THE JOURNAL OF

PHYSICAL CHEMISTRY

Volume 68, Number 12 December, 1964

Kendall Award Symposium on Behavior of Surfactants at Interfaces and in Solution, *Philadelphia, Pennsylvania, April 6–8, 1964*

NOTES

Important Notice to Authors

Professor Frederick T. Wall officially will assume the editorship of *The Journal of Physical Chemistry* effective January 1, 1965. New manuscripts submitted to *The Journal of Physical Chemistry* should be sent directly to Professor Wall addressed as follows:

Dr. Frederick T. Wall, Editor, *The Journal of Physical Chemistry*
Department of Chemistry, University of California
Santa Barbara, California

AUTHOR INDEX

THE JOURNAL OF
PHYSICAL CHEMISTRY

VOLUME 68, NUMBER 12 DECEMBER 15, 1964

Soap Films and Some Problems in Surface and Colloid Chemistry[1]

by Karol J. Mysels

Department of Chemistry, University of Southern California, Los Angeles, California 90007
(Received May 19, 1964)

Once their behavior is understood, soap films become a powerful tool for the study of surface and colloidal phenomena. This is because their geometry is well defined, their monolayer structure is relatively simple, and their behavior is easily observed. The formation and evolution of relatively thick films are controlled by ordinary hydrodynamics, without any indication of the existence of rigidified aqueous layers near the surface. Thinner films show the effect of both double-layer repulsion and van der Waals attractions. These forces balance at a thickness of the order of 100 Å. Some problems in the interpretation of recent measurements of these equilibrium thicknesses and some approaches leading to further information about these forces are discussed. Under certain conditions the films thin even further to about 45 Å. This is a thermodynamically stable state, which, though first observed by Newton, is still far from understood.

Soap films—the gossamer sheets which form a child's soap bubble, the pleasurable head on beer, or the distressing overflowing foam of the production vessel—have a respectable scientific history since the days when Robert Hooke[2] first called the attention of the Royal Society and of Newton to the optical phenomena which they exhibit. They have assisted in the development of the theory of optics,[3] of capillary forces,[4,5] and of minimal area problems[6]; they have served as delicate tools for detecting the magnetism of gases[7] and as analog computers in solving differential equations with complicated boundary conditions.[8] Today soap films serve science again in the elucidation of a number of problems in surface and colloid chemistry such as those of phase transitions in monolayers, of the structure of solvent in the neighborhood of a surface, of Gibbs film elasticity, of the magnitude of the double-layer repulsion, of the law of van der Waals attraction at

(1) Based on the Kendall Award Lecture presented at the 148th National Meeting of the American Chemical Society, Philadelphia, Pa., April, 1964. It reviews our work on films of ionic surfactants, which began under a 1-year grant from the American Chemical Society Petroleum Research Fund, was supported for several years by the Air Force Office of Scientific Research, and now continues with support from the National Science Foundation.

(2) R. Hooke, Communication to the Royal Society, March 28, 1672; T. Birch, "History of the Royal Society," Vol. III, A. Millard, London, 1757, p. 29.

(3) I. Newton, "Opticks," Book I, Part 2, expt. 4; Book II, Part 1, obs. 17–21, London, 1704.

medium range, and of factors governing specific ionic interactions.

Experimental Background. Just as the classical applications of soap films required the development of appropriate new techniques—since Newton first put a soap bubble under a bell jar to protect it from air currents and excessive evaporation[3]—so the recent developments have required new experimental approaches to produce the desired quantitative data. In addition, a new look was needed at the basic mechanisms by which a soap film is formed initially as a rather thick sheet of the order of 1 μ and then thins more or less gradually to an equilibrium structure whose thickness may be somewhat less than 50 Å.[9]

The basic condition for observing soap films over any length of time is that evaporation be absent so that closed vessels and good thermostats or minute circular films completely surrounded by a meniscus[10] are used. Plateau's[4,11] expedient of adding a hygroscopic agent, glycerine, to prevent bursting by evaporation has the basic disadvantage that the composition of the film changes all the time so that its behavior becomes much more complicated.

Soap films are almost always observed in reflected light so that the interference of the beams reflected by their front and rear surfaces produces colors or variations of intensity by which film thickness can be estimated and the motion of patches of different thicknesses observed. The direct and reflected beams may be either separate or combined by means of a semitransparent mirror.

Visual observations are easiest when the films are large and flat. For this reason most of our work involved films several centimeters on a side or in diameter. Vertical films such as shown in Fig. 1 are most easily produced by submerging a rectangular frame in a solution and then withdrawing it partially. Horizontal films such as shown in Fig. 2 and 3 can be supported by the top of a funnel with a narrowed mouth. Very slight curvatures may then be produced by slight changes of air pressure inside the funnel.

Phase Transitions and Film Elasticity. There is a striking difference between two types of films. One, the mobile film, thins in minutes, shows turbulent motions along the edges, and has a horizontal layering of interference colors. The other, the rigid film, thins in hours, shows little motion, and has a generally irregular arrangement of colors. Most ionic surfactant solutions give mobile films. Rigid films are formed by a few combinations of surfactants capable of giving rigid monolayers[12] by tight packing of adsorbed molecules,[13] the two-dimensional equivalent of solid bodies. The transition between the two—the "melting" of

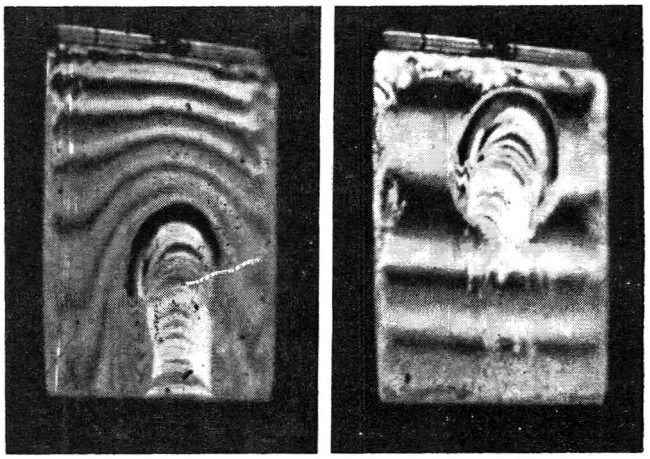

Figure 1. A rigid film (left) changes largely to a mobile one (right) as the total surface is rapidly expanded. Note that most fringes have become horizontal and that a remaining rigid area has risen to the top of the film. Film height is about 3 cm.

the rigid film—can be effected by a slight change of temperature[14] and also by an isothermal change in the surface area available per molecule as we found a few years ago with Dr. J. Skewis. The apparatus used was the same as devised for measuring Gibbs film elasticity.[15] A rectangular frame is rapidly raised from the solution or lowered into it. Both frames operate within a square bottle, 5 × 5 cm. As the total area of the solution is quite small, this motion of the second frame produces large percentage changes in the area available per adsorbed molecule before sur-

(4) J. Plateau, "Statique Experimentale et Theorique des Liquides Soumis aux Seulles Forces Mcleculaires," Gauthier-Villars, Paris, 1873.

(5) J. W. Gibbs, *Trans. Connecticut Acad.*, **3**, 108, 343 (1876–8); "Collected Works," Vol. I, Longmans Green, New York, N. Y., 1928, 1931: (a) p. 300; (b) pp. 301–303; (c) p. 309.

(6) R. Courant and H. Robbins, "What is Mathematics?" Oxford University Press, New York, N. Y., 1941.

(7) M. Faraday, *Phil. Trans. Roy. Soc. London*, **141**, 7 (1851).

(8) L. Prandtl, *Physik. Z.*, **4**, 758 (1903); B. Johnston, *Civil Eng.* (N. Y.), **5**, 698 (1935).

(9) K. J. Mysels, K. Shinoda, and S. Frankel, "Soap Films—Studies of Their Thinning," Pergamon Press, New York, N. Y., 1959: (a) Chapter III; (b) p. 34–38, 85–88, pl. II; (c) p. 20–24; (d) p. 38–40; (e) p. 36; (f) p. 58–60; (g) p. 74–76; (h) Chapter V; (i) p. 69–71.

(10) A. Scheludko and D. Exerowa, *Kolloid-Z.*, **155**, 39 (1957).

(11) C. V. Boys, "Soap Bubbles and the Forces Which Mould Them," Society for Promoting Christian Knowledge, London, 1890, 1912, and recent reprints, Appendix.

(12) J. Ross and M. B. Epstein, *J. Phys. Chem.*, **62**, 533 (1958).

(13) A. Wilson, M. B. Epstein, and J. Ross, *J. Colloid Sci.*, **12**, 345 (1957).

(14) M. B. Epstein, J. Ross, and C. W. Jakob, *ibid.*, **9**, 50 (1954); M. B. Epstein, A. Wilson, C. W. Jakob, L. E. Conroy, and J. Ross, *J. Phys. Chem.*, **58**, 860 (1954).

(15) K. J. Mysels, M. C. Cox, and J. D. Skewis, *ibid.*, **65**, 1107 (1961).

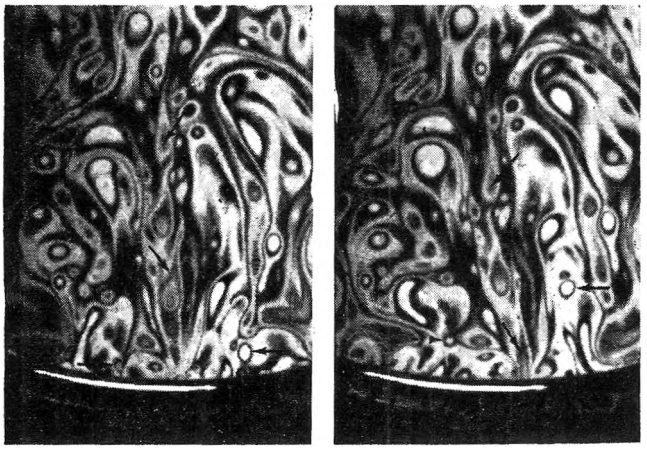

Figure 2. Marginal regeneration in an almost horizontal mobile film. Similarly oriented arrows indicate the same regions of the film in two successive stages which show the motion of thicker regions towards the border and that of the thinner ones away from it. The rim of the supporting funnel is at the bottom. The area shown is about 6 mm. across.

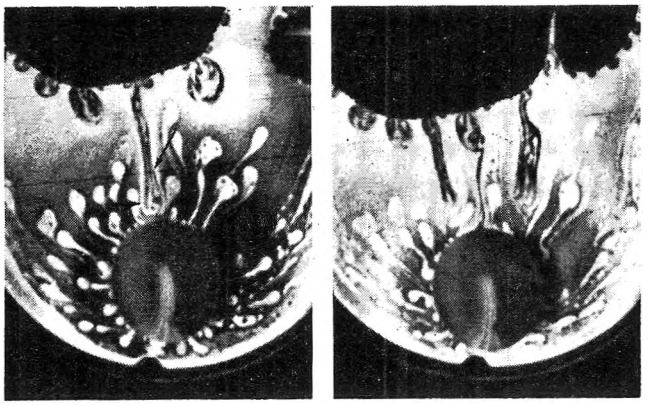

Figure 3. An almost horizontal mobile film. The round feature near the bottom edge is a droplet of solution some 4 mm. in diameter. The whole thick patch indicated by arrows on the left has been sucked in by the border of the drop as shown on the right. Note also the growth of the black film and the formation of thicker film areas by the displaced liquid.

face equilibrium is re-established. Hence the surface (or parts of it) loses its rigidity when the auxiliary frame is drawn out and becomes rigid again as it is lowered. Figure 1 shows selected frames from a color movie[16] recording the process.

The expansion and contraction of the area of the observed film as the auxiliary frame oscillates up and down can be evaluated from a photographic record. The corresponding variation of surface tension of the system can be recorded simultaneously. This gives[15] the two quantities needed to calculate the film elasticity E as defined by Gibbs.[5b]

$$E = 2\mathrm{d}\sigma/\mathrm{d}\ln s \qquad (1)$$

where σ is the surface tension, and s the area of the film.

Gibbs[5b] has also shown that in a two-component system this elasticity should be given by

$$E = 4\Gamma^2(\mathrm{d}\mu/\mathrm{d}G) \qquad (2)$$

where Γ is the surface density of the solute, μ its chemical potential, and G its total amount present per unit film surface. Verification of this relation requires experiments on rigorously purified systems since the presence of enough contaminant to form a fraction of a monolayer is enough to completely vitiate the results. We are now developing techniques[17] for working with pure surfaces, and as these are perfected it should become possible to test eq. 2 and perhaps use soap films to measure Γ and $\mathrm{d}\mu$.

Thinning Mechanisms. Rigid films thin primarily by the gravitational outflow of the solution from between the two immobile surface layers, and this seems to obey the simple laws of hydrodynamics.[9a] As the constraining surfaces are so near each other, the ordinary viscosity of water reduces the rate of outflow to the point where it takes hours for the film to thin.

In mobile films the situation is more complex. Their rapid thinning involves the relative motion of whole patches of film, the two surfaces and the intralamellar solution moving together over easily visible areas and shearing against adjacent patches of the film. This motion is due to two different causes. The first is gravity[5c,9b] which causes the thinner (and therefore lighter) areas to move upwards replacing the ones that are thicker (and therefore heavier), thus leading to the horizontal stratification of colors. The other is the effect of the capillary suction at the border where there must always be a curved meniscus (the so-called Plateau border) through which the excess liquid flows down to the level of the bulk solution.[9d] This suction exerts a greater force upon a thick film than upon a thin film, thus causing the thick film to be pulled into the border while thin film is simultaneously pulled out of the border to replace the lost area of the film. This "marginal regeneration" mechanism[9c] is best observed in almost horizontal films where the effects of gravity are minimized.[9e] Figures 2 and 3 show the reality of marginal regeneration by stills from two color movies of such films. Whereas the details of the pulling-in process are difficult to analyze theoretically[9f] and have not yet been isolated experimentally, the pulling-out has been studied further as we shall see shortly.

(16) First shown at the 1960 Colloid Symposium at Lehigh University.

(17) P. Elworthy and K. J. Mysels, to be published.

As the film becomes thinner it reaches a point where it appears black because of the disappearance (or more exactly great reduction) of the reflected light as the two surfaces come close together. This low intensity of the reflected beam can still be measured photoelectrically and gives a sensitive measure of film thickness. To the naked eye, however, the film is invisible. This illusion is heightened by the sharp and abrupt transition between the uniformity of this black film and the colorful and smooth variations of the neighboring thicker film. Perrin likened it to the clean cut produced with a punch.[18] However, recent careful observations by Miss McEntee[19] have shown that a transition region can sometimes be seen in horizontal films. This boundary is frequently the site of a third thinning mechanism as the area of black film grows spontaneously at the expense of the thicker film. The film disproportionates, and the excess liquid, originally present in the area whose thickness decreases, is forced into a thicker welt which gradually grows in thickness and in area and then flows to a lower level by gravity (Fig. 3).[9g]

van der Waals Forces. The forces causing the growth of the black film must be van der Waals attractions between molecules, as has been emphasized by Overbeek.[20] Here these forces are exerted over distances of the order of the film thickness, *i.e.*, some hundreds of angstroms. This is a range in which these forces cannot be studied directly by most other techniques, yet it is also the range of significance in the interaction of colloidal particles.

Furthermore this intermediate range is of more general interest because it includes the transition region in which the distance dependence of van der Waals forces—or, more specifically, London dispersion forces—changes from the inverse seventh to the inverse eighth power. Hence, quantitative measurements in this domain would provide a severe test of the theories which have predicted correctly the short range as well as the retarded, long range behavior but do also specify[21] the still untested details of the transition region.

In this transition region, the distances are too long and the dispersion forces are too weak to be studied by their effect on the individual molecules. At the same time, the distances are too short and the forces are too strong to allow the application of the elegant and sensitive methods using macroscopic plates and lenses.[22] Yet, the simplest apparatus permits the direct observation of their effects in soap films.

At first sight it may be surprising that the same forces which cause the attraction of two glass plates across a thin film of vacuum should also cause the thinning of a material film having air (which is practically vacuum) on both sides. Yet quantitative calculations show[20,23] that the pressures involved are exactly the same in both cases, and the following simple picture explains qualitatively why this is so.

Let us consider a transition region between thin and thick film in the range where van der Waals forces are significant as indicated in Fig. 4. A water molecule, such as A, situated in this region will be subject to attractions by all its neighbors, but within sphere I these effects all cancel each other since, for every molecule such as B, there is one B′ located diametrically opposite. Beyond this sphere, however, there are molecules such as C and D which do not have any opposites, precisely because the film is wedge-shaped. Their attractions therefore do not cancel and give a resultant force directed towards the thick film and tending to move our molecule away from the black film. Thus, the thin film becomes thinner, and the thick one thicker under the influence of van der Waals forces.

The rate of this growth of black film can be measured quite readily as has been done for several systems by Overbeek and McEntee[19]; it depends on such factors as the thickness of the thick film and the ionic strength, but the kinetics of the process still need clarification. When this is achieved we may have a very simple way of estimating van der Waals forces in this range.

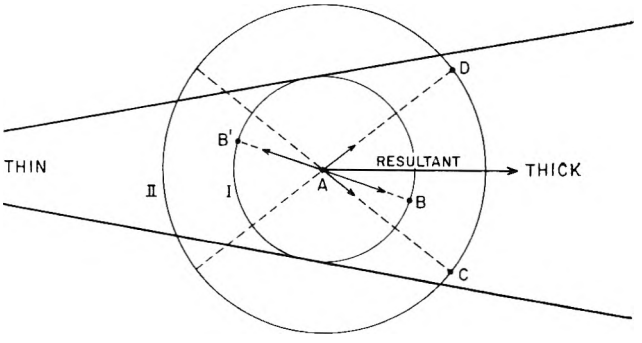

Figure 4. van der Waals forces in a transition region cause the intralamellar liquid to flow towards the thicker film.

(18) J. Perrin, *Ann. Phys.* (Paris), [9] **10**, 165 (1918).

(19) Unpublished results.

(20) J. Th. G. Overbeek, *J. Phys. Chem.*, **64**, 1178 (1960).

(21) H. B. G. Casimir and D. Polder, *Phys. Rev.*, **73**, 360 (1948); H. B. G. Casimir, *Proc. Koninkl. Ned. Akad. Wetenschap.*, **51**, 793 (1948); I. E. Dzyaloshinskii, E. M. Lifshits, and L. P. Pitaevskii, *Usp. Fiz. Nauk*, **73**, 381 (1961).

(22) *E.g.*, B. V. Derjaguin and I. I. Abrikosova, *Discussions Faraday Soc.*, 18, 24 (1954); J. A. Kitchener and A. P. Prosser, *Proc. Roy. Soc.* (London), **A242**, 403 (1957); W. Black, J. G. V. de Jongh, J. Th. G. Overbeek, and M. J. Sparnay, *Trans. Faraday Soc.*, **56**, 1597 (1960).

(23) A. Scheludko and D. Exerowa, *Kolloid-Z.*, **168**, 24 (1960).

The Nonrigidity of Water near the Surface. Acting alone, the van der Waals forces would cause a self-accelerating thinning and bursting of the film. In fact, however, once the black-film stage is reached, many films remain unchanged for an indefinite time. The fact that the limiting thickness depends on the ionic strength has naturally led to the invocation of the double-layer repulsion theory. This is especially convincing when the surfactant is ionogenic, although water surfaces and those of solutions of nonionic surfactants probably always have a surface potential.[24] However, there has been also a massive body of arguments that a rigidification of water near the surface, perhaps an ice-like formation, is important in preventing the approach of the two surfaces.[25] A very direct refutation of this latter idea can be obtained by a careful study of the pull-out of soap films.[26]

Frankel has analyzed the hydrodynamics in the narrow transition region between the Plateau border and the film proper and has shown[9b,27] that if one makes the assumptions that the surface of the solution is inextensible in this region and that the viscosity of the solution remains the same as in the bulk clear up to the surface, then it follows that the thickness δ is related to the velocity of pull-out, v, the viscosity, η, surface tension, γ, density, ρ, and gravity, g, by

$$\delta = 1.88 \frac{v^{2/3}\eta^{2/3}}{\gamma^{1/6}\rho^{1/2}g^{1/2}} \qquad (3)$$

Except for the numerical constant, this is the same formula which had been developed much earlier by Derjaguin[28] in connection with the very different problem of a liquid layer left on a solid inextensible substrate withdrawn from a liquid having a completely extensible surface and thus incapable of forming soap films.

The experimental test of Frankel's relation is somewhat difficult for thick (0.2–10 μ) films because of the need to extrapolate to zero film height where the experimentally accessible velocity of the frame approaches that of the film being withdrawn. Nevertheless, good agreement has been obtained for a variety of films having very different surface properties.[27] For thin films (<2000 Å.) the experimental problems are different, but, once these are overcome, it is possible to make very precise measurements.[26]

Equation 3 uses macroscopic, independently measured properties of the liquid to define a direct proportionality between the measured thickness and the two-thirds power of the velocity of pull-out as shown in Fig. 5. Any increased rigidity near the surface leads to an additional thickness, *i.e.*, to a positive intercept at the origin. Deviations from normal hydrodynamic behavior should alter the slope. Double-layer repulsions and van der Waals attraction should become noticeable for thin films and lead to larger and smaller thicknesses, respectively.[20,29] In fact, measurements on rigid films below some 800–1000 Å. showed marked deviations from the straight line, but higher thicknesses gave linear results which could be extrapolated to give an intercept of the order of two surface monolayers.[26] This is as would be expected for these rigid films and shows that there are no solidified layers of

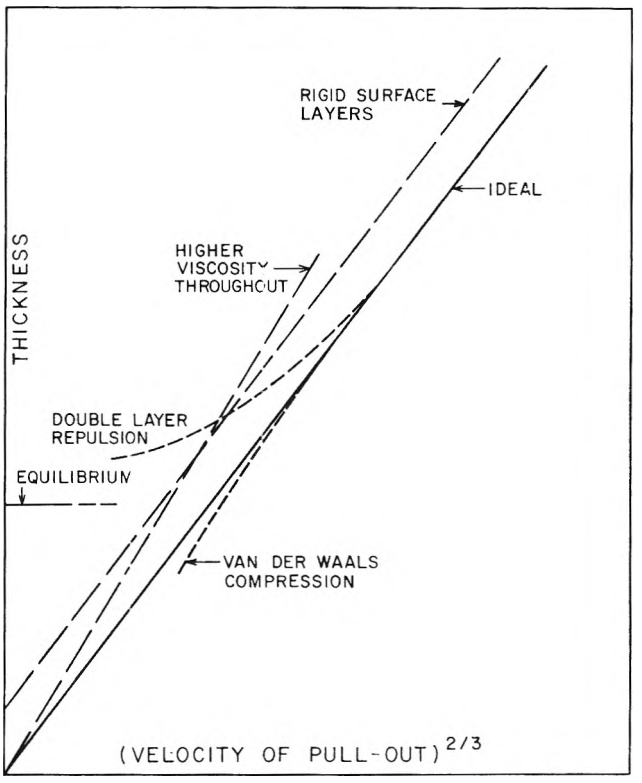

Figure 5. The relation between film thickness and rate of pull-out. Several types of deviations from the simple Frankel law are indicated schematically. At low speeds a thickness independent of rate indicates that a state of equilibrium has been reached.

(24) *E.g.*, D. Exerowa and A. Scheludko, paper submitted at the 4th International Congress on Surface Active Substances, Brussels, September, 1964.

(25) J. C. Henniker, *Rev. Mod. Phys.*, 21, 322 (1949); B. V. Derjaguin and A. S. Titijevskaya, *Discussions Faraday Soc.*, 18, 27 (1954); G. J. Dasher and A. J. Mabis, *J. Phys. Chem.*, 64, 77 (1960).

(26) J. Lyklema, P. C. Scholten, and K. J. Mysels, *ibid.*, in press.

(27) K. J. Mysels and M. C. Cox, *J. Colloid Sci.*, 17, 136 (1962).

(28) B. V. Derjaguin and S. M. Levi, "Fiziko-khimiya Naneseniya Tonkikh Sloev na Dvizhushchuyusya Podlozhki," USSR Acad. Sci., Moscow, 1959; B. V. Derjaguin, *Zh. Eksperim. i Teor. Fiz.*, 15, 9 (1945); see also B. V. Derjaguin and T. N. Voropayeva, *J. Colloid Sci.*, 19, 113 (1964).

(29) J. Lyklema, *Rec. trav. chim.*, 81, 890 (1962).

water within the experimental error of, say, 10 Å. for each surface, which is negligible in comparison with the equilibrium thicknesses.

Double-Layer Repulsion. These hydrodynamic experiments show, therefore, that in our systems the equilibrium thickness must depend only on repulsive forces (as opposed to structures). The obvious origin of such forces lies in the double-layer repulsion, *i.e.*, the total electric interaction of the two charged surfaces, as modified by the ion atmosphere of each. The theory of this interaction is well developed, based on the exact solution of the Boltzmann–Poisson equations with the assumption of point charges under the influence of the average potential.[30] Many proposed refinements[31] have only minor effects on the result. The repulsion increases very rapidly as the two charged planes approach each other beyond a certain point. The separation at which this repulsion becomes important increases rapidly as the ionic strength of the solution is lowered. The effect is shown schematically in Fig. 6 for two ionic strengths.

A necessary parameter in this calculation is the surface potential of the film. This is not easily accessible experimentally but fortunately is not of critical importance. A good estimate for this potential is 100 mv., based on electrokinetic measurements on micelles[32] which should have a surface similar to that of the soap films. A change of potential corresponds to a vertical shift of the repulsion lines of Fig. 6 by a factor of less than two, even if the potential is assumed to be infinite or only 60 mv., both highly unlikely possibilities. Such a vertical shift of these lines has only a slight percentage effect upon the thicknesses involved because of the almost vertical direction of the lines themselves.

Equilibrium Thickness. An evaluation of the van der Waals attractions can be also made on the basis of the estimated properties of water and gives values which are large for thin films but decrease so rapidly as the thickness increases that, for thick films, they become negligible compared to the hydrostatic suction due to the height of the film above bulk level. Figure 6 shows also the net resultant of these van der Waals and hydrostatic thinning forces. The intersections of this line with those representing the double-layer repulsion give, therefore, the theoretically anticipated thicknesses.

This theoretical development has essentially the same basis as has been used in the modern discussion of the diuturnity[33a] and flocculation of hydrophobic colloids.[33b] The main difference is that there it leads to the prediction of a kinetic process involving, in addition, the theory of the rate at which particles approach

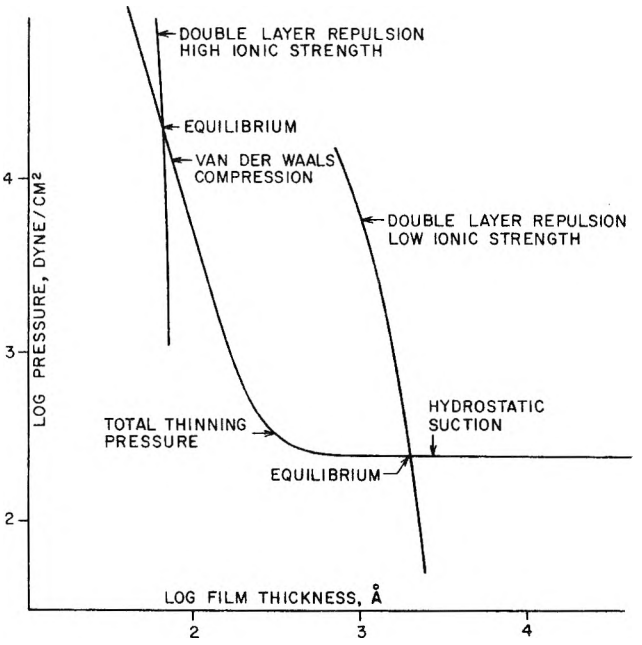

Figure 6. The intersection between double-layer repulsion and the resultant of van der Waals attraction and hydrostatic suction gives the equilibrium thickness.

each other, the more complicated equations for spheres, and the uncertain, and generally polydisperse, dimensions of the particles. In soap films, on the contrary, the geometry is that of simple planes, and both calculation and experiment can deal with an equilibrium state with all the attendant simplification.

The equilibrium thicknesses can be obtained as the limit of the thickness at very small velocities of pull-out as indicated in Fig. 5. This is a very reliable measurement because the thickness does not vary significantly over a broad range of experimentally accessible low rates.[34] The same result is obtained by allowing a thick film to drain spontaneously until it does not change further with time.

A very different technique has been developed by Scheludko[10] who forms a microscopic film completely surrounded by a meniscus by controlled withdrawal

(30) *E.g.*, J. Th. G. Overbeek in "Colloid Science," H. R. Kruyt, Ed., Elsevier Publishing Co., Amsterdam, 1952, Chapter VI.

(31) D. A. Haydon in "Recent Progress in Surface Science," J. F. Danielli, K. C. A. Pankhurst, and A. C. Riddiford, Ed., Academic Press, New York, N. Y., 1964, Chapter 3.

(32) D. Stigter and K. J. Mysels, *J. Phys. Chem.*, 59, 45 (1955).

(33) (a) Typical hydrophobic colloids are unstable but very long lived, *i.e.*, diuturnal; (b) B. V. Derjaguin and L. Landau, *Acta Physicochim. URSS*, 14, 633 (1941); *J. Exptl. Theoret. Phys.* (USSR), 11, 802 (1941); E. J. W. Vervey and J. Th. G. Overbeek, "Theory of the Stability of Lyophobic Colloids," Elsevier Publishing Co., Amsterdam, 1948; H. R. Kruyt, "Colloid Science," Vol. I, Elsevier Publishing Co., Amsterdam, 1952.

(34) J. Lyklema and K. J. Mysels, to be published.

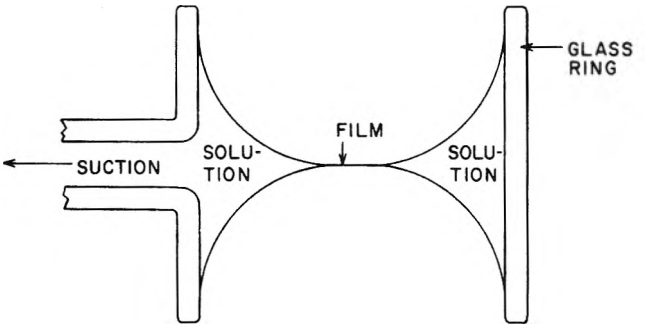

Figure 7. The principle of Scheludko's apparatus for producing films by gradual removal of liquid from a glass ring a few millimeters in diameter.

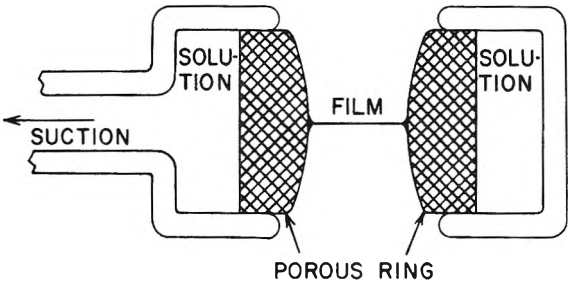

Figure 8. Apparatus for obtaining large hydrostatic suctions within a film produced by withdrawing liquid from a porous ring.

of liquid from a short piece of tubing, about 3 mm. in diameter, as indicated in Fig. 7. This technique gives excellent protection from evaporation and a rapid approach to equilibrium. The results obtained by these very different methods are quite concordant and agree qualitatively well with the theory. There are, however, quantitative discrepancies which are very disturbing. Thus, for example, the van der Waals attraction as calculated from these results seems to follow a third power dependence on distance for thicknesses[23,34] where it should be rather close to the fourth power.

Testing the Double-Layer Repulsion Theory. A test of the theory which involves both double-layer repulsion and van der Waals attraction simultaneously will always be complicated unless agreement is perfect since it is difficult to trace the source of any discrepancy. Hence, it would be better to test only one theory first, and that of the double-layer repulsion seems more easily isolated. Consideration of Fig. 6 shows that, at low ionic strengths, hydrostatic pressure is the dominant thinning force. A method for varying this pressure over a wide range should permit us to test the course of the double-layer repulsion curve independently of any van der Waals actions and at constant composition of the system.

Derjaguin and Titijevskaya[25] were able to cover a range of about 2 cm. of water (2×10^3 dynes/cm.) in an apparatus from which that of Fig. 7 was evolved and based on the same principle. The suction that can be applied in these instruments is limited by the capillary pressure of the orifice connecting the liquid to the outside; above this value air is drawn through the tube.

In order to overcome this limitation we are now developing a device for greatly extending this range of attainable pressures. It is shown schematically in Fig. 8. The film is formed in a tube of sintered glass or porous porcelain which permits easy passage of the liquid from the interior of the film but can support large air pressures up to several atmospheres (10^6 to 10^7 dynes/cm.). Once experimental difficulties are ironed out, this should permit an extremely straightforward test of the double-layer repulsion theory.

Light Scattering. Another new approach[35] to the problem of measuring the forces determining the equilibrium thickness of these films is now being developed in Overbeek's laboratory. It is based on the measurement of the intensity of light, not reflected—as is done in thickness measurements—but scattered at angles other than that of the reflection. This scattering is due to minute fluctuations in thickness caused by thermal agitation and resisted by the same forces which yield the equilibrium value. When further developed, light scattering should prove just as powerful a tool for the determination of thermodynamic parameters in these systems as it is accepted to be in bulk solutions.

The Second Black Film. In some systems there is a further stage of thinness, the abrupt transition from the "first" black film to a "second" black film. Whereas, the former, as discussed above, has a variable thickness depending on ionic strength, the latter has a constant thickness of about 45 Å. At this thickness the film still contains several layers of water molecules between the two outer surfactant layers. At first we thought[9i] that this second black film—like Perrin's stratified films[18]—was caused always by evaporation, and others have suggested that it was due to impurities, but now further work by Drs. Scholten and Jones has shown[36] that its appearance is not an artifact but an equilibrium phenomenon depending on temperature and on ionic strength.

(35) A. Vrij, "Interdisciplinary Conference on Electromagnetic Scattering," M. Kerker, Ed., Macmillan and Co., New York, N. Y., 1963, p. 387; *J. Colloid Sci.*, 19, 1 (1964).

(36) M. N. Jones, P. C. Scholten, and K. J. Mysels, to be published.

Our attention has been particularly attracted by the fact that this equilibrium between first and second black films is extremely sensitive to the nature of the counterions present. This is in marked contrast to the phenomena discussed heretofore, which are quite unspecific both with respect to the surfactant ion and with respect to the counterion. The second black film, on the other hand, exhibits the same kind of sensitivity to the specific nature of the counterion as so many colloidal and other phenomena, but this sensitivity seems to be greater by orders of magnitude. This makes it easy to discern the same kinds of influences that are apparent for example in the effect of counterions on the critical micelle concentration in bulk solutions of surfactants,[37] namely the role of the hydrated size of the ions and that of specific binding by hydrophobic bonds.

Thus here, as in many of the aspects which we have briefly reviewed, soap films offer an effective and unique tool to approach a problem in colloid and surface chemistry in addition to their intrinsic interest and aesthetic appeal.

(37) P. Mukerjee and K. J. Mysels, paper presented at the 131st National Meeting of the American Chemical Society, Miami, Fla., April, 1957, and unpublished results.

The Interaction of Water with Lecithin Micelles in Benzene

by P. H. Elworthy and D. S. McIntosh

Pharmacy Department, Royal College of Science and Technology, Glasgow, C.1., Scotland *(Received April 3, 1964)*

When water was introduced into the lecithin–benzene system, it was solubilized by the solute. Light scattering, viscosity, and diffusion measurements on the solubilized systems indicated that the number of monomers in the micelle was independent of solubilizate concentration between zero and 0.25 g. of water/g. of lecithin. The viscosity results indicated that as the water content was increased from zero to 0.055 g. of water/g. of lecithin, micellar asymmetry developed; the addition of more water caused an alteration in micellar structure, and spherical micelles were present at high water contents. A maximum solubilization of 0.33 g. of water/g. of lecithin was recorded.

The critical micelle concentration (c.m.c.) of lecithin in benzene at 25° has been reported[1] to be 33×10^{-5} %; above the c.m.c. small micelles containing four or five monomers are formed. A second association limit is present at 0.073%, where the small micelles aggregate into large ones.[2] The large micelles have the structure of bimolecular leaflets, with the polar head groups in the interior of the micelles and the hydrocarbon chains directed outward into the solvent[3]; at 25° the micellar weight was 55,000 to 57,000; at 40° it was 43,000. It was felt[4] that these large micelles might provide a biologically significant model of part of nerve myelin, as Finean[5] has shown that a similar bimolecular leaflet structure occurred in nerve myelin. Studies[6,7] of the effect of dielectric constant on micellization by lecithin have suggested a potential mechanism of cell wall permeability.

Although some solubilization studies[1,4] on the dry

(1) I. Blei and R. E. Lee, *J. Phys. Chem.*, **67**, 2085 (1963).

(2) P. H. Elworthy, *J. Chem. Soc.*, 813 (1959).

(3) P. H. Elworthy, *ibid.*, 1951 (1959).

(4) P. H. Elworthy, *ibid.*, 139 (1960).

(5) J. B. Finean, *Experientia*, **9**, 17 (1953).

(6) P. H. Elworthy and D. S. McIntosh, *J. Pharm. Pharmacol.*, **13**, 663 (1961).

(7) P. H. Elworthy and D. S. McIntosh, *Kolloid-Z.*, **195**, 27 (1964).

lecithin–benzene system have been made, it was felt that the large micelles would provide a more realistic biological model if water were present in the head group region of the bimolecular leaflets. The solubilization of water by lecithin has been studied by Demchenko,[8] who found the maximum quantity of water solubilized to be 0.33 g./g. of lecithin and to be independent of the solvents used (benzene, toluene, and xylene).

Experimental

Materials. Lecithin was prepared from chickens' egg yolks[9] by treatment with alumina to remove ninhydrin-reacting materials, followed by chromatography on silica to remove lysolecithin. It was deionized by dissolving in chloroform and stirring with mixed strong ion-exchange resins (biodeminrolit, B.D.H., previously well extracted with chloroform) for 2–3 hr. After several precipitations from dry ether into dry acetone, it was stored under dry acetone. The sample had N, 1.87%, P, 4.13%, I_2 no. 62. (Molecular weight calculated from N and P analysis figures = 750). Analar benzene was fractionally frozen and fractionally distilled, being stored over sodium, and had $n^{25}D$ 1.4979 (1.4981 Timmermans[10]). Tropaeolin 000 (Orange II) was recrystallized twice from water.

Light Scattering Measurements. The apparatus of Elworthy and McIntosh[6] was used. Solutions were made dust-free by filtering through sintered glass disks (mean pore size, 1 μ), concentrations being checked interferometrically after filtration. Solutions containing more than 0.15 g. of water/g. of lecithin could not be satisfactorily clarified either by filtering or by centrifuging. Specific refractive index increments (dn/dc) were measured on a Hilger–Rayleigh interference refractometer using Bauer's[11] technique for monochromatic light. All measurements were made at 20° using the 5461-Å. green line.

Diffusion Measurements. The modified interference refractometer was used as previously described[7]; Harned and Nuttall's treatment[12] of restricted diffusion was applied to measurements of concentrations at levels in the diffusion column $^1/_6$ and $^5/_6$ the column length. Differential diffusion coefficients were obtained, the concentration at the end of an experiment being determined from the interferometer reading after mixing the cell contents.

Viscosity Measurements. A suspended level dilution viscometer was used, the error in the relative viscosity being ±0.2%. A few representative solutions were checked for Newtonian flow in a Couette viscometer. Each intrinsic viscosity reported was obtained from eight to ten individual measurements as a function of concentration.

Solubilization of Tropaeolin 000. Powdered dye, the solution of lecithin in benzene, and a glass marble were placed in flasks whose stoppers were sealed in with parafilm. The flasks were rocked in a thermostat bath, samples being withdrawn occasionally. Optical densities were measured at 483 mμ in 1-cm. cells against benzene using a Hilger and Watts Uvispek. Uptake of dye was complete in 3 days. Negligible amounts of dye were taken up in dry benzene (optical density in 1-cm. cell = 0.006).

Solubilization of Water. Water was incorporated by either shaking the lecithin solution with a weighed quantity of water in a sealed flask or allowing dry lecithin to adsorb the required amount of water vapor and dissolve in dry benzene. No differences in behavior were observed between solutions made by the two methods. To give a value of the maximum water uptake, optical densities of 1% lecithin solutions containing various amounts of water were measured at 546 mμ (Fig. 2). Vapor phase equilibrium experiments between lecithin solutions and benzene with added water were carried out by connecting two flasks containing the solutions with a U-shaped adapter.

Results and Discussion

Figure 1 shows the results for the solubilization of Tropaeolin 000 by lecithin in benzene. The c.m.c. is 26×10^{-5}% at 20°. Taking this value with Blei and Lee's 33×10^{-5}% at 25° and mean value of 86×10^{-5} at 40° and using the standard relationships[13] derived for the two-phase model of micelle formation, $\Delta H_m = -10$ kcal. mole^{-1} and $\Delta S_m = -35$ cal. deg.$^{-1}$ mole^{-1} for the heat and entropy of micellization, respectively. These results must be treated tentatively because of the smallness of these micelles and the limitations of the pseudo-phase model of micellization.

The second association limit occurs at 0.075%, in reasonable agreement with the value found at 25° (0.073%). As we are interested in the large micelles, this higher transition concentration was used for cor-

(8) P. A. Demchenko, *Colloid J. USSR*, 22, 309 (1960).

(9) P. H. Elworthy and L. Saunders, *J. Chem. Soc.*, 330 (1957).

(10) J. Timmermans, "Physico-Chemical Constants of Pure Organic Compounds," Elsevier Publishing Co., New York, N. Y., 1950, p. 147.

(11) N. Bauer, K. Fajans, and S. Z. Lewin, "Physical Methods of Organic Chemistry," A. Weissberger, Ed., Vol. I, 3rd Ed., Interscience Publishers, Ltd., New York, N. Y., 1960, Part 2, p. 1139.

(12) H. S. Harned and R. L. Nuttall, *J. Am. Chem. Soc.*, 69, 736 (1947).

(13) K. Shinoda, "Colloidal Surfactants," Academic Press, London, 1963, p. 30.

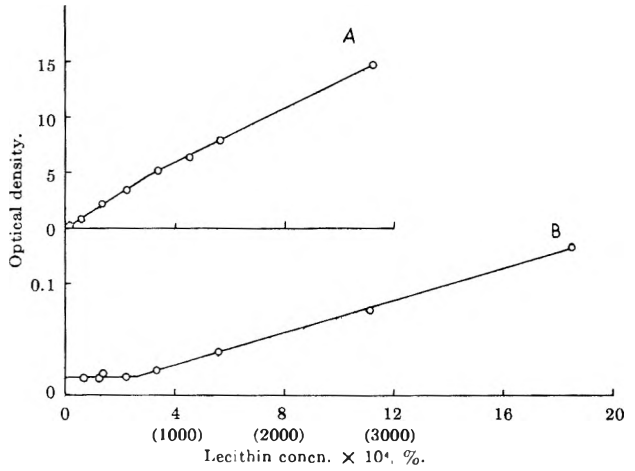

Figure 1. Solubilization of Tropaeolin 000 by lecithin in benzene in the absence of water. Determination of c.m.c. (B) and second association limit (A). Optical densities of solutions in 1-cm. cells. Values in parentheses are for the upper scale.

recting viscosity results for the presence of the small micelles, in the manner previously described[3]; the corrections are small. As irreproducible results for dye solubilization were obtained when water was present in the micelles, the value obtained in the dry condition was used in the correction procedure. The irreproducibility may be due to the effect of water on the nature of the micelles.

It is necessary to gain some idea of the location of the water in the lecithin–benzene system, as there is the possibility of a significant partition between the micelles and the surrounding benzene. Lecithin is intensely hygroscopic, making it seem likely that nearly all the water is associated with the solute; as the interpretation of the viscosity results depends to some extent on knowing the location of the water, an attempt was made to determine its position. Benzene saturated with water was equilibrated through the vapor phase with a 3% solution of lecithin in dry benzene. After 6–8 days, the presence of water in the benzene was no longer detectable, while it could be detected in the lecithin–benzene solution. Other tests indicated that there was no loss of water from the system, *i.e.*, transfer between water saturated and dry benzene gave the correct equilibrium distribution. Further tests on benzene saturated with water in vapor phase contact with a solution containing 0.15 g. of water/g. of lecithin also showed that an undetectable amount of water remained in the benzene at equilibrium.

If the partition of water favored the benzene rather than the micellar solute in the benzene, a significant amount of water would be expected to remain in the benzene in vapor contact with this system. There must be some equilibrium between the water in the micelles and in the surrounding benzene, and since the amount of water remaining in the benzene was too small to be detected, it seems reasonable to assume that almost all the water present is associated with the solute.

The maximum amount of water that could be solubilized by 1% solutions of lecithin in benzene was found to be 0.33 g. of water/g. of lecithin (Fig. 2), which agrees well with the value of Demchenko.[8]

The light scattering results are given in Fig. 3 as plots of $H(c - c_1)/(T - T_1)$ against $(c - c_1)$ where

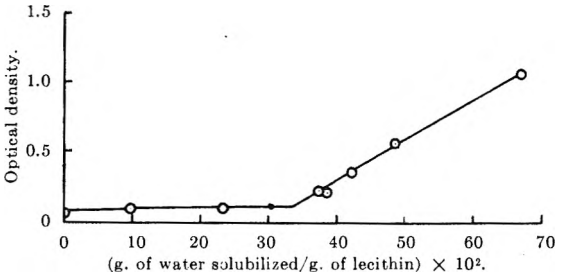

Figure 2. Optical densities (in 1-cm. cells) of 1% lecithin solutions in benzene as a function of the water content of the lecithin.

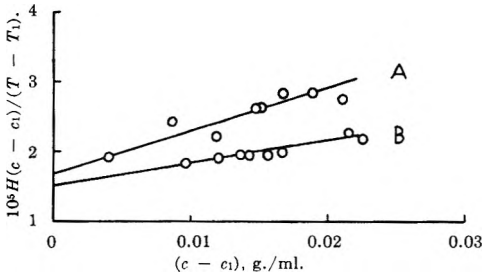

Figure 3. Light scattering results for lecithin in benzene: A, lecithin containing 0.053 g. of water/g. of lecithin; B, containing 0.105 g. of water/g. of lecithin.

$H = 32\pi^3 n_0^2 (dn/dc)^2 / 3\lambda^4 N$; c is the total concentration of lecithin plus solubilized water in g./ml., c_1 is the second association concentration, and T_1 is the turbidity at this concentration. Z_{45} values of close to unity were obtained (Table I) indicating that no dimensions of the micelles exceeded $\lambda/20$. The results have been corrected for depolarization. Micellar weights were calculated from the usual two-component theory

$$H(c - c_1)/(T - T_1) = 1/M + 2B(c - c_1) \quad (1)$$

Provided that the solubilizate is completely associated with the micelles, it seems reasonable to treat the

Table I

% (w/w) H_2O in lecithin	10^6D^a	M l.s.[b]	M_{ob}	M_{pro}	M_{solv}	M_{calcd}	dn/dc	Z_{45}[c]	ρ
5.3	...	59	..	..	..	63	−0.052	1.00	0.028
5.4	0.976	..	64	67	63	63	..	..	...
10.5	...	65	..	..	..	66	−0.058	1.01	0.050
25.5	0.962	..	71	73	71	75	..	..	...

[a] D = diffusion coefficient at c.m.c. in cm.^{2} sec.$^{-1}$. [b] All micellar weights × 10^{-3}, M_{calcd} = 60,000 + amount of water solubilized/micelle. [c] Z_{45} = dissymmetry at 45°.

system as essentially a two-component one. This treatment has been used elsewhere for the light scattering of solubilized systems.[14] Because of the smallness of the specific refractive index increments, the solutions possessed only small turbidities, and this, together with the ±7–10% error in the determination of molecular weights by light scattering,[15,16] make further checks on the micellar weight necessary. A combination of diffusion coefficients (after extrapolation to the second association concentration) (Fig. 4) and intrinsic viscosities (Fig. 5) give the micellar weights reported in Table I, which are calculated for three alternative interpretations of the deviation of the viscosity intercept from the Einsteinian value, *e.g.*, for oblate (M_{ob}), prolate (M_{pro}), ellipsoids of revolution, and for spherical particles solvated with solubilized water (M_{solv}).

The micellar weight grows as the amount of water solubilized increases. Under dry conditions,[7] M = 60,000, and the increase of micellar weight reported here, within experimental error, corresponds to 60,000 plus solubilized water. This indicates that the number of monomers per micelle remains reasonably constant, as the concentration of water solubilized increases.

The intercept from the viscosity runs (the same ratio of water to lecithin being maintained in each run) (Fig. 5) shows an increase from $[\eta]$ = 2.84 at zero water content to a peak value of $[\eta]$ = 3.94 at 0.055 g. of water/g. of lecithin, followed by a decrease when further water is incorporated. At 25°, under anhydrous conditions, $[\eta]$ = 2.82, close to the value found here at 20°. Using

$$[\eta] = \nu[\bar{V}_2 + W_1V_1^0] \qquad (2)$$

where ν = Simha's shape factor,[17] $\bar{V}_2$ = specific volume solute, W_1 = g. of solvating solvent per g. of solute, and V_1^0 = specific volume solvent; the viscosity intercepts for spherical particles using W = g. of water solubilized/g. of solute were calculated (Fig. 5B). This treatment does not account for the observed behavior of the viscosity intercepts at low water contents, indicating that changes in micellar shape occur in this region.

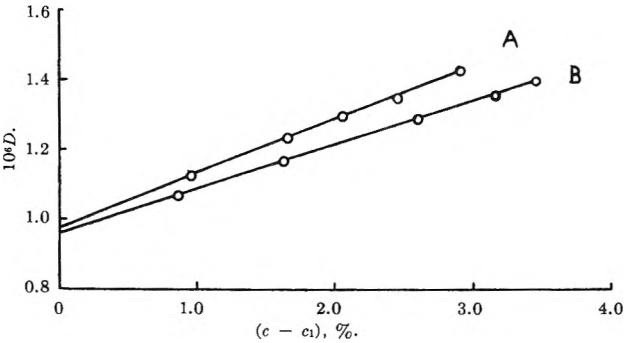

Figure 4. Diffusion coefficients (cm.^{2} sec.$^{-1}$) of lecithin in benzene: A, lecithin containing 0.054 g. of water/g. of lecithin; B, containing 0.255 g. of water/g. of lecithin.

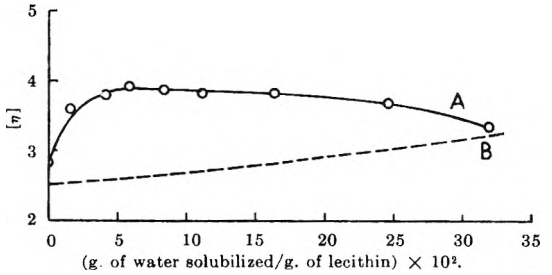

Figure 5. Intrinsic viscosities of lecithin–benzene systems as a function of the amount of water solubilized by lecithin: A, experimental; B, calculated for spherical micelles containing solubilized water.

A short extrapolation of Fig. 5 to 0.33 g. of water/g. of lecithin gives $[\eta]$ = 3.28, yielding W = 0.327 g. of water/g. of lecithin from eq. 2, assuming that the particles are spherical. The agreement between this value and the actual amount of water present indicates

(14) T. Nakagawa, K. Kuriyama, and H. Inouye, *J. Colloid Sci.*, 15, 268 (1960).

(15) N. Robinson and L. Saunders, *J. Pharm. Pharmacol.*, 11, 115T (1959).

(16) P. H. Elworthy and C. B. Macfarlane, *J. Chem. Soc.*, 537 (1962).

(17) R. Simha, *J. Phys. Chem.*, **44**, 25 (1940).

that the micelles do become spherical at this water content. A spherical cavity of radius 19.8 Å. in the micelle center would be filled by 0.327 g. of water/g. of lecithin.

Assuming, as in the calculations above, that no electrostriction of solubilized water takes place and that the micelles are unsolvated with respect to benzene (which seems reasonable from preceding work[3]), some idea of the changes of micellar shape occurring on addition of water may be gained using models of the lecithin micelles. Molecular models show that the polar head group can be represented as a block 7 × 8 Å., and, using the length of half the bimolecular leaflet (36 Å.), it is possible to calculate $[\eta]$ for a micelle of 80 monomers arranged to form prolate or oblate ellipsoids.

When water is absent, the short semiaxis for the prolate model is $b = (56 \times 40/\pi)^{1/3}$ enabling a/b to be found (a = 36 Å.), and this gives $[\eta] = 2.54$, rather lower than the experimental result. In the presence of water, we shall attempt to calculate $[\eta]$ at 0.055 g. of water/g. of lecithin, *i.e.*, at the peak of the intrinsic viscosity–water content curve. There are two principal ways of incorporating this amount of water. Firstly, it may lie in the gap between the two sheets of polar groups, and its incorporation would increase the a dimension; 0.055 g. of water/g. of lecithin corresponds to 2.3 water molecules per monomer, and even allowing a row of six water molecules between the two halves of the leaflet gives $[\eta] = 2.87$, which is much lower than the experimental value of 3.94 at this water content. Secondly, water may be inserted between the polar heads in each sheet, giving an increase in the cross-sectional micellar area, *i.e.*, an increase in b, the summation of the areas of polar heads plus the areas of water molecules giving $[\eta] = 2.62$. The third possibility is that both types of micellar expansion may occur, but these changes are likely to balance one another as far as asymmetry is concerned.

From water vapor sorption studies on lecithins[18,19] it was shown that 2.5 water molecules/molecule of lecithin represented the completion of first-layer sorption; this figure agrees reasonably well with the water content giving the peak value of $[\eta]$ in Fig. It was also shown, in interpreting the transport properties of lysolecithin, that this first layer might fit into cavities in the polar head group, with little increase in the effective monomer length.

A consideration of oblate ellipsoids is more difficult as decisions have to be made regarding the geometry of the sheet of polar head groups. Solubilization studies[4] indicated that the sheet of polar head groups was three times as long as it was wide. If the shorter dimension is taken as 32 Å. (= $2a$ = 4 × 8 Å.), then b^1 = 44.6 Å., using the mean of 44.6 and 36 Å. to give an average value of b; $[\eta] = 3.09$ in the absence of water. Incorporation of six rows of water molecules between the two polar sheets gives $[\eta] = 3.5$, while using the water to increase the area of the sheets gives $[\eta] = 3.6$. These calculations for the oblate model are tentative, being sensitive to the exact geometry of the lecithin head group, and having the drawback that the model does not exactly fit the oblate shape. Nevertheless, they do provide a guide to the development of micellar asymmetry.

Over-all, it appears that the micelles resemble oblate ellipsoids and that the addition of water initially increases their asymmetry. Above 0.055 g. of water/g. of lecithin, the micelles tend toward a more spherical shape as $[\eta]$ decreases with increases of solubilizate concentration. This change may represent a rearrangement of micellar structure. To prevent contact between the water-treated polar heads and benzene, as the volume of water in the micelle center grows, the micelle shape tends to become spherical and finally reaches this condition at 33% water.

This system, with water incorporated between two polar sheets of phosphatide materials, resembles part of the structures found in Finean's[5,20] X-ray studies of nerve myelin and has promise as a model of part of this structure.

Acknowledgment. We thank Miss M. Buchanan for the microanalyses.

(18) P. H. Elworthy, *J. Chem. Soc.*, 5385 (1961).

(19) P. H. Elworthy, *ibid.*, 4897 (1962).

(20) J. B. Finean and J. D. Robertson, *Brit. Med. Bull.*, **14**, 267 (1958).

The Solubility of Alkali Dinonylnapthalenesulfonates in Different Solvents and a Theory for the Solubility of Oil-Soluble Soaps

by R. C. Little and C. R. Singleterry

U. S. Naval Research Laboratory, Washington, D. C. 20390 *(Received March 26, 1964)*

The solubility of the alkali metal dinonylnaphthalenesulfonates parallels that of dinonylnaphthalene in low polarity solvents. In sulfonate–solvent systems showing limited solubility, the equilibrium is characteristic of a liquid–liquid pair having a critical solution temperature, the condensed soap phase behaving as an extremely viscous liquid. Micelle size in low polarity solvents decreases as the solubility parameter increases, probably because such a variation improves the match in solubility parameter between micelle and solvent by exposing more of the polar core. In moderately polar solvents, the sulfonate is freely soluble as an equilibrium mixture of monomer, dimer, and possibly higher units. Pure crystalline alkali metal carboxylates do not show high solubility in hydrocarbons unless they are heated to a temperature at which they pass over into a liquid-like phase; noncrystalline carboxylates, or mixtures of many different branched chain carboxylate species, have high or unlimited solubilities and appear to behave as liquid–liquid systems in much the same way as the alkali metal sulfonates.

Introduction

The behavior of the dinonylnaphthalenesulfonates has been well studied in benzene,[1,2] and this report is an extension of that work into other solvent systems with a view toward determining the influence of cation and solvent upon the apparent soap solubility (defined as the total solubility of associated and nonassociated sulfonate-derived species which are in thermodynamic equilibrium).

The published data on the solubility of soaps in various solvent environments are often difficult to interpret, each soap–solvent system appearing to have its own individual character.[3-10] Winsor[11] has attempted to clarify and classify some of this work. His theory, however, refers primarily to solutions containing water as an important component and is most readily exemplified in systems of high soap content.

The need for a more comprehensive theory of soap behavior in nonaqueous systems continues to exist.

Experimental

The lithium, sodium, and cesium salts of a special grade of dinonylnaphthalenesulfonic acid (HDNNS) (abbreviated LiDNNS, NaDNNS, and CsDNNS, respectively) were prepared by neutralization of an aqueous alcoholic solution of the acid by the appropriate base. The soaps were then lyophilized and stored in a desiccator over P_2O_5 until used. This acid and its salts have been described previously.[1]

All of the solvents used were ACS grade or better except for the 0.65, 1, 2, and 10 centistoke silicones, which were commercial samples. All solvents were passed through Linde molecular sieve materials and Florisil in order to remove water and polar contami-

(1) S. Kaufman and C. R. Singleterry, *J. Colloid Sci.*, **10**, 139 (1955).

(2) S. Kaufman and C. R. Singleterry, *ibid.*, **12**, 465 (1957).

(3) S. S. Marsden, Jr., and J. W. McBain, *J. Chem. Phys.*, **16**, 633 (1948).

(4) S. R. Palit and J. W. McBain, *Ind. Eng. Chem.*, **38**, 741 (1946).

(5) G. H. Smith and J. W. McBain, *J. Phys. Colloid Chem.*, **51**, 1189 (1947).

(6) P. N. Cheremisinoff, *J Am. Oil Chemists' Soc.*, **28**, 278 (1951).

(7) A. Bondi, *J. Colloid Sci.*, **5**, 458 (1950).

(8) S. M. Nelson and R. C. Pink, *J. Chem. Soc.*, 1744 (1952).

(9) H. Kambe, *Bull. Chem. Soc. Japan*, **35**, 265 (1962).

(10) I. Satake and R. Matuura, *Kolloid-Z.*, **176**, 31 (1961).

(11) P. A. Winsor, "Solvent Properties of Amphiphilic Compounds," Butterworth and Co., Ltd., London, 1954.

nants. A check on the efficiency of the percolations was made, in the case of dioxane, by means of a Karl Fischer titration. No water could be detected within the precision of the method. The cyclohexane used was of very high purity (99.92 mole %) and was obtained by fractional crystallization. The dimethylsiloxanes were specially prepared monodisperse species available from the Dow-Corning Corp. The nitroparaffins were fractionally distilled from the best available grade of Eastman Kodak solvents. Their boiling points and refractive indices corresponded closely to the literature values. The preparation and purification of the fluoro compounds have been described.[12] All solvents were stored over molecular sieve pellets in glass-stoppered bottles and were used as soon as possible after percolation.

Benzil (used for calibrating the osmometer) was twice crystallized from anhydrous ethanol, dried at 50°, and stored in a vacuum desiccator over P_2O_5 until used.

Methods

The apparatus used for the determination of the apparent soap solubility in various solvents consisted of a stationary NBS certified 0.1-deg. thermometer upon which was mounted a baffle to promote agitation. A rotator turned a solution cell within an air space surrounded by a bath of controlled temperature. A magnetic stirrer provided agitation of the bath while a copper heat exchange coil permitted easy change of temperature conditions by means of the thermostated reservoir. A solubility determination was made by preparing a sulfonate solution of known molality at a higher temperature and allowing it to cool at a rate of 0.1°/min. in the vicinity of the temperature at which precipitation would occur. Rates of cooling from 0.05 to 0.2°/min. gave the same results within the experimental error of ±0.2°. The point at which precipitation occurred was determined by visual observation of the turbidity in a concentrated light beam directed at a right angle to the observer.

It should be noted that the separating phase in the solvent-rich systems was soap saturated with solvent. The possibility of undercooling in these systems was explored by comparing the temperature for disappearance of turbidity upon warming with that for its appearance upon cooling. An undercooling no greater than 0.2° was observed and is considered to be within the precision of the solubility determinations.

Vapor pressure lowering data were obtained by means of a commercial thermoelectric device—the Mechrolab Model 301A osmometer. In all cases, a drying agent—Linde molecular sieves—was added to the solvent cup in order to maintain a water-free solvent atmosphere in the measuring chamber. Some difficulty was experienced with the osmometer in measuring solutions containing significant concentrations of ions. This was due to the fact that the thermistor leads of the nonaqueous type probe support are not insulated. Substitution of a matched pair of glass probe-type thermistors for the glass bead type furnished with the commercial unit eliminated this difficulty, which was apparently due to ionic conductance between the thermistor leads.

Liquid crystal systems were detected by means of crossed polaroid sheets. Conductivity measurements were made with a portable conductivity bridge, Industrial Instruments, Inc., Type RC16B1. Measurements were made at 35.02 ± 0.02° in a cell protected from atmospheric humidity by means of molecular sieve materials. The cell was surrounded by an oil bath.

Results

In order to facilitate discussion of the experimental results the sulfonate–solvent systems have been divided into four rather arbitrary classes based upon their experimental behavior (see Table I).

Type I. Sulfonate is Miscible with the Solvent in All Proportions; Micellar Size Is Constant in a Given Solvent. Figure 1 presents the data obtained from vapor pressure lowering measurements in terms of osmotic coefficient *vs.* concentration. Two generalizations may be made which are consistent with results previously obtained by Kaufman and Singleterry[2] on benzene solutions of lithium and sodium dinonyl-

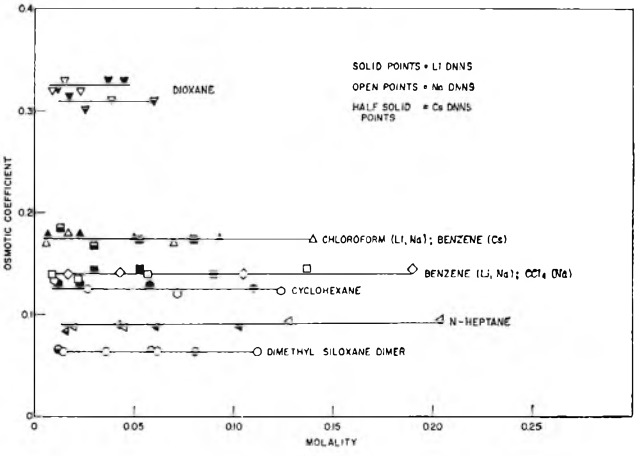

Figure 1. Osmotic coefficient *vs.* concentration for sulfonates in low polarity solvents (35°).

(12) P. D. Faurote, C. M. Henderson, C. M. Murphy, J. G. O'Rear, and H. Ravner, *Ind. Eng. Chem.*, **48**, 445 (1956).

Table I: Solubility of Sodium Dinonylnaphthalenesulfonate in Different Solvents

Solvent	Dielectric constant	NaDNNS, 1 *m* soln. at 25°	NaDNNS, 1 *m* soln. at −78°	DNN, 1 *m* soln. at 25°	DNN, 1 *m* soln. at −78°
		Type I solvents			
n-Heptane	1.924 (25°)	∞[a]	∞	∞	∞
Cyclohexane	2.01 (25°)	∞	f[b]	∞	f
Siloxane dimer	2.2 (25°)	∞	∞	∞	∞
Dioxane	2.21 (25°)	∞	f	∞	f
Carbon tetrachloride	2.24 (25°)	∞	f	∞	f
Benzene	2.27 (25°)	∞	f	∞	f
Chloroform	4.81 (25°)	∞	f	∞	f
		Type II solvents			
Ethyl acetate	6.02 (25°)	∞	∞	∞	∞
Methyl isobutyl ketone	13.11 (25°)	∞	∞	∞	∞
Acetone	20.7 (25°)	∞	0.12	∞	0.03
Ethanol	24.3 (25°)	∞	∞	0.09	i[c]
		Type III solvents			
Siloxane nonoamer	2.5–2.6 (25°)	0.20	i	∞	S[d]
Siloxane octamer	2.5–2.6 (25°)	0.30	i	∞	S
Siloxane heptamer	2.5–2.6 (25°)	S	i	∞	∞
Bis(ψ'-heptyl) β-methylglutarate	6.1 (20°)	0.0001	f	S.S.[e]	f
Ethyl perfluorobutyrate	...	0.0001	i	S.S.	i
Bis(ψ'-amyl) diphenate	8.0 (20°)	0.001	f	S.S	f
Bis(ψ'-propyl) diphenate	9.70 (20°)	0.01	f	S.S.	f
ψ'-Amyl alcohol	16.93 (20°)	0.04		i	
Nitroethane	28.6 (25°)	>1	i	∞	0.006
Nitromethane	36.6 (25°)	<0.001	f	S.S	f
Acetonitrile	36.7 (25°)	<0.001	f	S	f
Water	78.54 (25°)	d[f]	f	i	f
		Type IV solvents			
Silicones 10 centistokes and higher		i	i	∞	S
Silicones 100 centistokes and higher		i	i	Solubility decreases	
Monochloropentadecafluorodimethylcyclohexane		i	i	i	i

[a] ∞, miscible in all proportions. [b] f, solvent freezes. [c] i, insoluble. [d] S, soluble. [e] S.S., slightly soluble. [f] d, disperses.

naphthalenesulfonates. First, the aggregation number is independent of the concentration and, second, the aggregation numbers of the lithium and sodium salts are identical within the precision of the method. It should be noted here that aggregation numbers in benzene at 35° were lower (n = 7) than those from fluorescence depolarization studies (n = 10) at 25°.[2] The discrepancy is slightly greater than the absolute uncertainty estimated for the fluorescence depolarization method by Singleterry and Weinberger.[13] The consistency of results obtained by either method alone is much better, so that the relative aggregation numbers reported by the osmometer method are believed reliable to ±1 or better. The difference in micelle weight obtained by the two methods, however, merits further study.

Precise conductivity measurements on sulfonate solution in solvents of this type were not possible with the simple conductivity bridge used in this work. It is sufficient for purposes of this study to state that the specific conductivity of the solutions was less than 8 × 10^{-8} mho/cm., indicating that ionic concentrations of any soap species in solvents of this type must be extremely low. Table II lists the conductance results obtained.

Type II. Sulfonate Is Miscible in All Proportions with the Solvent, but the Extent of Association and/or Dissociation Is Concentration Dependent. Figure 2 illustrates the osmotic behavior which is characteristic of this solvent group. The sulfonates form conducting solutions in these solvents, as is shown by the data of Table II. Solutions in ethanol showed the highest conductance whereas solutions in ethyl acetate showed

(13) C. R. Singleterry and L. A. Weinberger, *J. Am. Chem. Soc.*, **73**, 4574 (1951).

Table II: Equivalent Conductance of Dinonylnaphthalenesulfonate Solutions at 35°

Solvent	Solvent type	Dielectric constant at 25°	Soap	Soap concentration, *M*	Equivalent conductance
Cyclohexane	I	2.01	LiDNNS	0.01	<0.005
Dioxane	I	2.21	LiDNNS	0.01	<0.005
Carbon tetrachloride	I	2.24	LiDNNS	0.01	<0.005
Benzene	I	2.27	LiDNNS	0.01	<0.005
Ethyl acetate	II	6.02	NaDNNS	0.018	0.036
1,1,5-Trihydroperfluoroamyl alcohol	III	16.93 (20°)	LiDNNS	0.002	0.18
1,1,5-Trihydroperfluoroamyl alcohol	III	16.93 (20°)	CsDNNS	0.002	0.97
Acetone	II	20.7	LiDNNS	0.002	12.2
Ethanol	II	24.3	LiDNNS	0.002	23.5
Ethanol	II	24.3	CsDNNS	0.002	27.7
Nitroethane	III	28.6	LiDNNS	0.002	0.13
Nitroethane	III	28.6	CsDNNS	0.002	36.4
Nitromethane	III	36.6	CsDNNS	0.002	63.2
Water	III	78.54	LiDNNS	0.002	72.2

the lowest. The decrease in the ability of the solvent to dissociate ion pairs reflects the decrease of dielectric constant. Two distinct processes appear to control osmotic behavior of sulfonate solutions from this solvent class—ionic dissociation and molecular association. The equilibria which apply in solvents of this type probably involve simple ions, ion pairs, triple ions, associated ion pairs, and larger clusters, perhaps both charged and neutral.

In ethanol, analysis of the data indicates that the equilibrium involves predominantly simple ions and ion pairs. An apparent equilibrium constant of 7.0–7.6 $\times$ 10^{-3} was found to fit the osmotic data for NaDNNS solutions over the experimental range of 0.002 to 0.04 *m* assuming the ion–ion pair model. Because the ethanol used contained some foreign ions which could not be removed by percolation, no serious attempt was made to determine the thermodynamic equilibrium constant, which would have required measurements in solutions so dilute as to permit serious interference by the foreign ions.

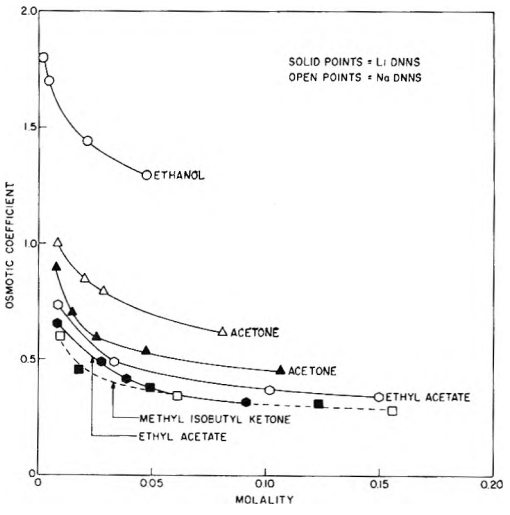

Figure 2. Concentration dependence of sulfonate osmotic coefficients in polar solvents (35°).

In acetone, methyl isobutyl ketone, and ethyl acetate, association products larger than simple ion pairs appear to be formed. In acetone solutions, the osmotic coefficient data indicate the formation of association products equivalent to sulfonate dimer and trimer (not necessarily neutral in charge); in ethyl acetate solutions, association products corresponding to clusters containing the equivalent of three and four sulfonate molecules (again not necessarily neutral in charge) appear to exist. Solvents of this type may or may not differentiate between the osmotic behavior of lithium and sodium soaps (see Fig. 2).

In water, the equilibrium appears to involve ions and much larger aggregates—probably aqueous micelles. This conclusion is supported by the following evidence: (1) high conductance at low soap concentrations (see Table II), (2) high light-scattering power of the dispersions, (3) ability to solubilize an oil-soluble dye—Sunbeam Yellow, and (4) easy passage of the dispersions through a 100-mμ Millipore filter.

Type III. Solubility Is Limited, and the Solubility Limit Varies with Temperature. The dinonylnaphthalenesulfonates exhibit a positive temperature coefficient for the solubility limit in solvents of this type. That is, the systems absorb heat when the sulfonates undergo solution in these solvents, and solubility increases with temperature. Figure 3 exemplifies, in a very general way, the type of behavior shown by the soaps in solvents of this type. Four solvent families belong to this group: (1) the higher members of the

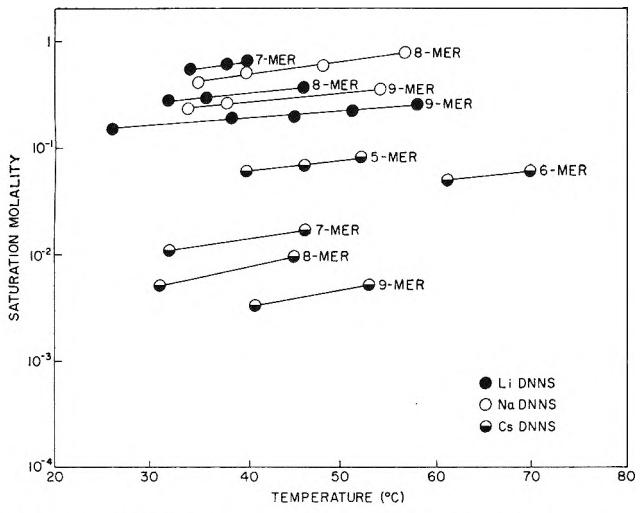

Figure 3. Solubility of the sulfonates in low molecular weight dimethylsiloxanes as a function of temperature: ●, LiDNNS; ○, NaDNNS; ◒, CsDNNS.

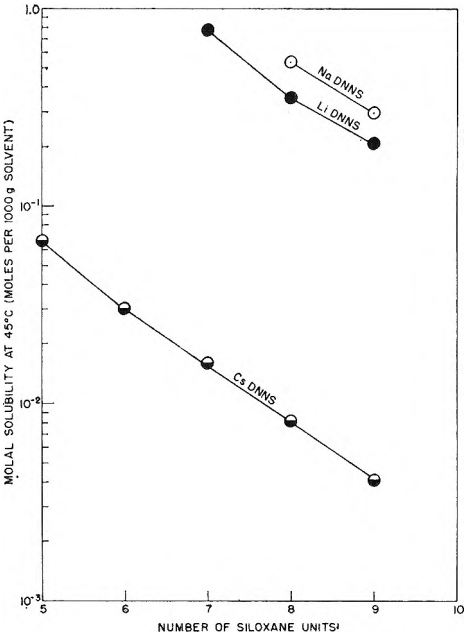

Figure 4. Solubility of the sulfonates in siloxane polymers at 45° as a function of polymer size.

polymethylsiloxanes, (2) fluorinated esters, (3) nitroparaffins, and (4) alkyl cyanides. It will be convenient to consider these families separately.

Polymethylsiloxanes. The dinonylnaphthalenesulfonates are dissolved by the lower homologs of the polydimethylsiloxanes in all proportions; this solubility extends up to the hexamer siloxane in the case of the lithium and sodium salts and to the trimer in the case of the cesium salt. The sulfonates exhibit limited solubility in the higher polysiloxane homologs, and Fig. 4 illustrates the effect of solvent homology upon the dinonylnaphthalenesulfonates. The most complete data are shown for the cesium salt. The plot of the log of the saturating molality *vs.* N, the number of siloxane units in the polymer chain, led to the descriptive equation for data taken at 45°

$$\log m = -0.289N + 0.225$$

Initial slopes for the NaDNNS and LiDNNS lines were found to be −0.247. The data for the cesium sulfonate over the experimental range 30 to 65° may be summarized to within 8% of the experimental by the empirical relation

$$\log m = A/T + BN + C$$

where $A = -1304$, $B = -0.289$, and $C = 4.33$. Differential heats of solution were not calculated from the solubility data because the activity of the sulfonates was not known.

Nitroparaffins. The solubility behavior of the sodium sulfonate in the first three nitro paraffins is shown in Table I. Solubility increases as the proportion of hydrocarbon in the solvent molecule is increased, going from barely detectable solubility in nitromethane to miscibility in all proportions with 1-nitropropane. The cesium sulfonate is much more soluble in nitroethane than either the lithium or sodium sulfonates. The cesium salt, moreover, has a moderate, though limited, solubility in nitromethane.

The conductance behavior of cesium sulfonate solutions as compared with lithium sulfonate solutions in Table II is of interest. In the solvent series—ethanol, nitroethane, nitromethane—the limiting conductance of the cesium salt increased along with the increase in dielectric constant in accordance with the Nernst–Thompson rule. On the other hand, the conductance of the lithium salt is two orders of magnitude less in nitroethane than in ethanol. While the cesium salt readily dissociates in nitroethane, the lithium salt does not. Osmotic measurements indicate that the lithium salt is moderately associated in both nitroethane ($\delta = 11.1$) and 1-nitropropane ($\delta = 10.2$) with an aggregation number of 5 in both solvents. The difference in conductance reflects the difference in cation radii; the small radius of the lithium ion favors coordination bonding to the sulfonate oxygen, which opposes ion dissociation. As would be expected, the solubility of the sulfonates in the nitroparaffin family increases very rapidly as the hydrocarbon radical is increased in size, paralleling the increased solubility of the HDNN hydrocarbon. Dinonylnaphthalene is completely miscible with nitroethane at 25°. The

sulfonates were found to be completely miscible with 1-nitropropane at 25°.

Fluoro Compounds. Table I lists the solubility characteristics of NaDNNS and DNN in a fluoro alcohol and several fluoro esters. Again, the low solubility of the dinonylnaphthalene parallels that of the sulfonates. Although the cesium and lithium salts formed conducting solutions in the ψ'-amyl alcohol, the limiting conductance was low as a result of the lower dielectric constant (16.93) and high viscosity of the alcohol.

Type IV. Soap May Show No Detectable Solubility. Solvents in this class include fluorocarbons and higher molecule weight silicones. The insolubility of the sulfonate approximately parallels the immiscibility of the dinonylnaphthalene.

Effect of Water on Solutions of the Dinonylnaphthalenesulfonates. The effect of water on solutions of dinonylnaphthalenesulfonates depends upon whether the solvent mixes with water freely and upon whether the salt shows limited or unlimited solubility in the solvent. It is convenient to discuss the effects of water-immiscible and water-miscible solvents separately.

Water-Immiscible Solvents. Simple water titrations indicate that water is solubilized in solutions of the dinonylnaphthalenesulfonates in excess of the amount soluble in the pure solvent. Solubilization of water by sulfonates in hydrocarbon solvents has been reported previously by Mathews and Hirschhorn[14] and by Kaufman and Singleterry.[2] Continued addition of water leads to a stable water-in-oil emulsion and finally, upon addition of a large excess of water, oil-in-water emulsions result which are partly stabilized by films of precipitated soap. When a small amount of water was added to sodium sulfonate swollen with about 5% benzene, the viscous mixture became flow birefringent. The addition of a further small amount of benzene destroyed the birefringence.

Water-Miscible Solvents. Water added to a concentrated solution of the DNNS soap in a solvent which was completely miscible with water led to the precipitation of liquid crystals. Six different solvents were found which gave this effect: ethanol, dioxane, acetone, glycerol, *n*-butylamine, and pyridine. Only two conditions seem necessary in order to produce the effect in the case of the dinonylnaphthalenesulfonates: (1) high solubility of the sulfonate in the solvent and (2) miscibility of the solvent and water in all proportions. Additional experiments with the DNNS salts and water alone indicate that even the water-miscible solvent itself is not needed to secure the effect since it was found that a thick paste of the sulfonate mixed with water in a mortar and pestle was birefringent. This liquid crystal, however, it is not necessarily equivalent to the liquid crystal which precipitates from the solvent upon addition of water. Aqueous solutions of the dispersed sulfonates are easily precipitated by the addition of a chloride solution of the corresponding cation. Although the coagulum was not initially birefringent, it could be made so by smearing it on a glass slide. These generalizations pertain only to the dinonylnaphthalenesulfonates, the aryl stearates forming liquid crystals under quite different conditions.[15]

Rheopectic properties were shown by the NaDNNS–dioxane–water system at mole percentages of 0.1, 1.0, and 98.9, respectively. The birefringent gel initially prepared slowly transformed over a 24-hr. period into an isotropic liquid (which showed flow birefringence). Gentle agitation of the liquid regenerated the gel which again slowly reverted to the isotropic liquid.

Nonsolubilization of Certain Nonionic Polar Molecules by Alkali Sulfonates. It was recognized that large polar organic molecules might possibly be present as impurities in either the soaps or the solvents employed. Experiments were designed to determine whether such molecules would be included in the sulfonate micelles or would exert independent osmotic effects in the solution. The systems examined included dinonylnaphthalene in a cyclohexane solution of NaDNNS and in a nitropropane solution of LiDNNS, a 9-siloxane polymer in a cyclohexane solution of NaDNNS, and 1-nitronaphthalene in a benzene solution of LiDNNS. In no case was there an indication of segregation of the additive in the micelles. The total osmotic activity was in all four cases the sum of that to have been expected from the sulfonate and the additive independently. This behavior contrasts with the distinct solubilization reported for acetic acid, methanol, *n*-propylamine, acetone, ethyl acetate, and ether.[16-18] It shows that any unsulfonated dinonylnaphthalene carried as a residual impurity in the soap would act independently in the solvent to lower the apparent micelle size found by vapor pressure osmometry.

Discussion

A Theory of Micellar Solubility in Nonaqueous Solvents. The solubility phenomena exhibited by oil-soluble soaps are too complex and depend upon too many factors to justify any hope of systematizing all

(14) M. B. Mathews and E. Hirschhorn, *J. Colloid Sci.*, 8, 86 (1953).

(15) J. Honig and C. R. Singleterry, *J. Phys. Chem.*, 60, 1114 (1956).

(16) W. D. Bascom and C. R. Singleterry, *J. Colloid Sci.*, 13, 569 (1958).

(17) S. Kaufman, *ibid.*, 17, 231 (1962).

(18) S. Kaufman, *J. Phys. Chem.*, 68, 2814 (1964).

the data by means of one simple theory. Nevertheless, the data available as a result of this and previous studies encourage an attempt to develop a theory applicable at least to the oil-soluble DNNS salts of the alkali cations. The attempt is especially promising for those solvents in which the sulfonate can be shown to exist in solution preponderantly as micelles whose size is independent of solute concentration. The solvents meeting this qualification include all of those listed as Type I solvents and those solvents of Type III having dielectric constants below 10 (siloxanes and fluoro esters).

The data of this report suggest the following generalizations about the solubility of the alkali metal sulfonates and their properties in micellar solutions in low polarity solvents.

(1) The equilibrium between solution and "solid" is effectively an equilibrium between sulfonate micelles of a characteristic size and a solvent-swollen sulfonate phase which is essentially a highly viscous liquid rather than a crystalline phase. The solubility phenomena observed are those characteristic of binary liquid systems.

(2) The solubility characteristics of the sulfonate are determined by the composition and properties of that exterior part of the micelle which is located so that it can interact with the molecules of the solvent. To a very rough first approximation this portion of the micelle consists of the DNNS radical; the cation and the charged sulfonate portion of the anion are considered to be located in the central region of the micelle. As a result of this structure, the solubility in hydrocarbon solvents parallels that of the hydrocarbon, dinonylnaphthalene, again to a rough first approximation.

(3) The solubility parameter of Hildebrand and co-workers,[19] rather than the dielectric constant or the dipole moment, is the property of a solvent which most accurately forecasts the micellar solubility of the alkali sulfonates in that solvent. As the solubility parameter of the solvent is increased, the micelles tend to assume a smaller size. This size reduction gives a looser packing of the DNNS tails and, thus, exposes the more interactive aromatic and polar parts in such a way as to reduce the difference between the solubility parameter of the solvent and the effective solubility parameter of the solvent-accessible portions of the micelle.

(4) As the solubility parameter of the solvent increases, this tendency to match solubility parameters leads to the breakdown of the micellar regime and produces systems which are most readily treated as concentration-dependent equilibrium mixtures of the monomer, dimer, trimer, and possibly tetramer. In solvents of high dielectric constant there may also be substantial dissociation into ions of various compositions. The interaction of the polar heads with the polar solvent molecules may also lead to solvation which modifies the effective solubility parameter of the solute.

The available data are generally consistent with these generalizations (see Table III). With all solvents having solubility parameters between 5 and 10; the alkali metal dinonylnaphthalenesulfonates are miscible in all proportions. Dinonylnaphthalene, with a solubility parameter of 7.5, is similarly miscible with these same solvents, although, as a result of the lower molecule volume, miscibility in the case of dinonylnaphthalene extends to slightly lower and higher values of the solubility parameter. Miscibility in all proportions is characteristic of liquid pairs whose solubility parameters do not differ by more than approximately 3.5 units.[19] The degree of mismatch tolerated is less if the effective molecular volumes differ by an order of magnitude, as in the case of the sulfonate micelles in a volatile solvent. Unlimited miscibility is not often encountered for pairs consisting of a crystalline solid and a liquid. The belief that the alkali metal sulfonates behave essentially as liquids in the presence of organic solvents is supported by the nature of the temperature–composition diagram observed for one case of limited sulfonate solubility, as shown in Fig. 5. Here the compositions of the two equilibrium phases are plotted as a function of the temperature for the case of LiDNNS in the dimethylsiloxane heptamer. The

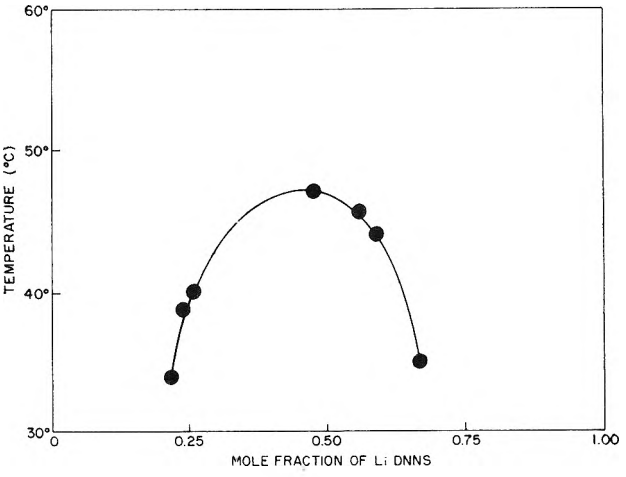

Figure 5. Mutual solubility of LiDNNS and dimethylsiloxane heptamer.

(19) J. H. Hildebrand and R. L. Scott, "The Solubility of Nonelectrolytes," 3rd Ed., Reinhold Publishing Corp., New York, N. Y., 1950.

Table III: Physical Properties of Selected Solvents

Solvent	Solubility parameter δ[a]	Dielectric constant ϵ[a]	Dipole moment	DNN solubility[b]	Surface tension[a]
D.c. 200, 10-cs. silicone		2.6	0[d]	m.a.p.	
Siloxane octamer	4.72[v,c]	2.5	0	m.a.p.	18.03
Siloxane hexamer	5.0[v]	2.5	0	m.a.p.	17.42
Siloxane pentamer	5.2[v]	2.5	0	m.a.p.	17.08
Monochloropentadecafluorodimethylcyclohexane	6.1[h]	Low	0	i	...
Siloxane dimer	6.5[v]	2.2	0	m.a.p.	14.82
Ethyl perfluorobutyrate	6.8[n]	...	...	s.s.	19–20?
Bis(ψ'-heptyl) β-methylglutarate	6.8[s]	6.1 (20°)	3.83	s.s.	25.6 (20°)
Squalane	7.1[s]	Low	0	m.a.p.	28.6
Bis(ψ'-amyl) diphenate	7.2[s]	8.0 (20°)	4.06	s.s.	28.4 (20°)
Diethyl ether	7.4[h]	4.34 (20°)	1.1	m.a.p.	17.0 (20°)
n-Heptane	7.45[h]	1.924	0	m.a.p.	19.27 (30°)
Dinonylnaphthalene	7.5[s]	Low	0	m.a.p.	31.2 (20°)
Bis(ψ'-propyl) diphenate	7.8[s]	9.7 (20°)	3.84	s.s.	31.1 (20°)
Hexadecane	8.0[h]	Low	0	m.a.p.	27.4 (20°)
Cyclohexane	8.2[h]	2.01	0	m.a.p.	25.3 (20°)
ψ'-Amyl alcohol	8.3[n]	16.93 (20°)	2.88	i	25 ?
n-Butylamine	8.5[n]	5.3	1.40	m.a.p.	19.7 (41°)
Carbon tetrachloride	8.6[h]	2.24	0	m.a.p.	27.0 (20°)
Isopropylbiphenyl	8.9[s]	Low	0	m.a.p.	34.8
Benzene	9.15[h]	2.27	0	m.a.p.	29.02 (20°)
Chloroform	9.3[h]	4.81	1.2	m.a.p.	27.1 (20°)
Methyl isobutyl ketone	9.5[n]	13.11 (20°)	...	m.a.p.	23.64 (20°)
Acetone	9.9[h]	20.7	2.7	m.a.p.	23.7 (20°)
Ethylacetate	9.9[n]	6.02	1.7	m.a.p.	24.3 (20°)
Dioxane	10.0[h]	2.21	0.45	m.a.p.	32.20 (30°)
Pyridine	10.7[h]	12.3	2.2	m.a.p.	38.0 (20°)
1-Nitropropane	10.2[n]	23.2 (30°)	3.6 (vapor)	m.a.p.	29.28
Nitroethane	11.1[h]	28.6	3.3	m.a.p.	32.3 (20°)
Acetonitrile	11.9[h]	36.7	3.5	s	29.3 (20°)
Nitromethane	12.6[h]	36.6	3.19	s.s.	36.8 (20°)
Ethanol	12.9[v]	24.3	1.7	0.09	22.75 (20°)
Glycerol	13.2[s]	42.5	2.56	i	63 (20°)
Methanol	14.4[h]	32.63	1.66	i	22.6 (20°)
Water	23.8[h]	78.54	1.84	i	72.75 (20°)

[a] At 25°, unless otherwise indicated. [b] Solubility notations: m.a.p., miscible in all proportions; i, insoluble; s, soluble; s.s., slightly soluble. [c] Calculation of δ values: [h], Hildebrand and Scott; [v] Heat of vaporization data; [n], Hildebrand rule; [s], surface tension data. [d] Calculation of the dipole moment of the silicones from their dielectric constants by the Onsager equation (J. B. Romans and C. R. Singleterry, *J. Chem. Eng. Data*, **6**, 56 (1961)) gave values of 0.0 ± 0.01.

curve is typical of a pair of liquids having a critical solution temperature (consolute temperature) above which they are miscible in all proportions. The sulfonate-rich equilibrium fractions at temperatures below the consolute point are seen to contain substantial amounts of silicone although their viscosities are so high that casual inspection might have classified them as soft solids. In the other cases of limited solubility examined, complete data were collected only for the composition of the solvent-rich phase, but these data are consistent with the picture developed for the Li-DNNS in siloxane heptamer. In several cases the critical solution temperature has been established.

The fact that practical oil-soluble soaps are usually either miscible with a solvent in all proportions or essentially insoluble is another observation which accords with the hypothesis that the oil-soluble soaps have the solubility characteristics of liquids. The range of solubility parameter mismatch permitting appreciable but limited miscibility is narrow. It corresponds to those pairs having critical solution temperatures only moderately higher than ambient. When the mismatch of parameters is greater, the consolute temperature is high and the mutual solubilities of solvent and soap become negligible. (The case of crystalline soaps is special and requires separate consideration.)

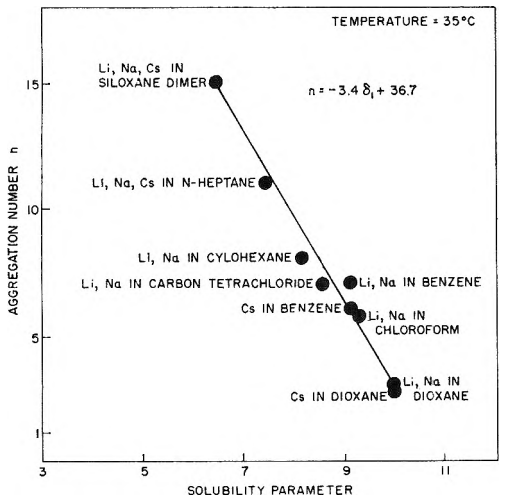

Figure 6. The dependence of the aggregation number of sulfonate micelles upon the solubility parameter of the solvent.

The Relation of Solubility Parameter to Micelle Size. Figure 6 shows that the micelle size of sodium dinonylnaphthalenesulfonate decreases approximately linearly with increasing solubility parameter of the solvent in the range of solvent solubility parameters between 6.5 and 10. The solvent effects noted by other workers[20-24] appear to show a similar relation although the data cover a much shorter range of solubility parameter, *e.g.*, for solutions of Aerosol OT, nonaethylene glycol laurate, monocaprin, calcium dinonylnaphthalenesulfonate, and sodium 2,6-di-*n*-alkylnaphthalene-1-sulfonates. The automatic matching of solubility parameters for micelle and solvent by reduction in micelle size and packing in solvents of high solubility parameter recalls the behavior of linear macromolecules in solvents of different solvent power. In the latter case, the polymer coil expands to permit greater interaction with the solvent as the solubility parameter for the solvent approximates that of the repeating unit in the polymer chain. In the case of the sulfonates, decrease in micelle size opens the structure and increases the opportunity for sulfonate–solvent interaction as uncoiling of a macromolecule does in polymer solutions.

The points for the oxygen-containing solvents at the lower end of the line in Fig. 6 are not mutually consistent with any simple extension of the best line through the points for hydrocarbon solvents. The nitroparaffins differ from dioxane in having strong permanent dipoles, which may introduce a new factor into the interaction between solvent and micelle. The data are insufficient for useful theorizing.

In solvents with solubility parameters lower than 6.5 the sulfonates exhibit limited solubility of the liquid–liquid type. Examination of molecular models suggests that an aggregate containing 15 to 20 DNNS units is as large as can be formed without radical deformation of the micelle toward a prolate or oblate spheroid of high eccentricity. This limit exists because the polar head of the sulfonate molecules has a smaller cross section than the branched hydrocarbon tail. If such a size limit is operative, the limited or negligible solubility in solvents of lower solubility parameter reflects the inability of the micelle to go further in adjusting its external shell to match the properties of the solvent. It may be expected that the micelle sizes of sulfonates showing limited solubility in solvents of lower solubility parameter will all lie near the limiting value noted above.

In an attempt to explain the observed relation of aggregation number to solubility parameter on a semiquantitative physical basis, a conceptual model was devised on the basis of five specific assumptions. These assumptions include those already made in the foregoing qualitative theory of soap solubility (monodisperse micelles having a central polar core and a liquid-like structure for the condensed sulfonate phase) plus two additional assumptions.

(1) When the sulfonate molecules associate to form aggregates or micelles, their polar heads are shielded so that the solubility parameter of the aggregate tends to approach the solubility parameter of the solvent.

(2) When a sulfonate molecule is added to an aggregate, the degree of shielding is increased, so that the solubility parameter of the aggregate is reduced by the amount K. The change in solubility parameter, $\Delta\bar{\delta}_2$, for n molecules forming an aggregate would be $(n - 1)K$. It is recognized that this assumption may be an oversimplification although it corresponds to the general trend of the shielding effect.

The basic equation to be operated upon is Hildebrand's expression for the free energy of mixing of two liquids[19]

$$\Delta F_m = RT(X_1 \ln X_1 + X_2 \ln X_2) + V_m(\delta_1 - \delta_2)^2\varphi_1\varphi_2 \quad (1)$$

where ΔF_m is the free energy of mixing, R is the gas constant, T is the absolute temperature, X is the mole fraction, V_m is the volume of mixing, δ is the solubility parameter, and φ is the volume fraction.

(20) A. Kitahara, T. Kobayashi, and T. Tachibana, *J. Phys. Chem.* **66**, 363 (1962).
(21) F. M. Fowkes, *ibid.*, **66**, 1843 (1962).
(22) E. Gonick, *J. Colloid Sci.*, **1**, 393 (1946).
(23) P. Debye and H. Coll, *ibid.*, **17**, 220 (1962).
(24) I. J. Heilweil, *ibid.*, **19**, 105 (1964).

If the solute molecules are predominantly in the associated state as monodisperse micelles, the mole fraction of micelles having an aggregation number n will be $X_2' \cong X_2/n$. The free energy of mixing of sulfonate micelles and solvent then becomes

$$\Delta F_m = RT\left[\left(1 - \frac{X_2}{n}\right)\ln\left(1 - \frac{X_2}{n}\right) + \frac{X_2}{n}\ln\frac{X_2}{n}\right] + V_m[\delta_1 - \bar{\delta}_2 + (n-1)K]^2\varphi_1\varphi_2 \quad (2)$$

where $\bar{\delta}_2$ refers to the solubility parameter of the nonassociated soap molecule. The free energy of mixing is then minimized with respect to the aggregation number, holding temperature, solvent mole fraction, and solvent solubility parameter constant

$$\left(\frac{\partial(\Delta F_m)}{\partial n}\right)_{X_1T\delta_1} = -\frac{X_2RT}{n^2}\ln\left(\frac{X_2}{n - X_2}\right) + 2V_mK\varphi_1\varphi_2[\delta_1 - \bar{\delta}_2 + (n-1)K] = 0 \quad (3)$$

Rearrangement yields

$$n = \frac{-\delta_1}{K} + \frac{1}{K}\left\{\bar{\delta}_2 + \left(\frac{RTX_2}{2\varphi_1\varphi_2V_mKn^3}\right)\left[\ln\left(\frac{X_2}{n - X_2}\right)\right]\right\} + 1 \quad (4)$$

This compares with the experimentally observed relation

$$n = -3.4\delta_1 + 36.7 \quad (5)$$

for sulfonates of the periodic group I cations.

Comparison of eq. 4 and 5 leads to values of $K = 0.295$ and $\bar{\delta}_2 = 10.5$ for aggregation numbers of 5 or greater. Evaluation of the complex term in eq. 4 showed that it amounted to 3% or less of the $\bar{\delta}_2$ value for aggregation numbers of 5 or greater. A simplified working form of eq. 4 for aggregates of 5 or more monomers would then be

$$n = \frac{-\delta_1}{K} + \frac{\bar{\delta}_2}{K} + 1 \quad (6)$$

Equation 4 is not applicable at high dilutions of solute, *i.e.*, in the region of the critical micelle concentration, since the assumption can no longer be made that $X_2' \leqq X_2/n$. The extrapolation of the linear eq. 6 to $n < 3$ is not strictly justifiable because the degree of hydrocarbon shielding is decreased by a much larger fraction in passing from $n = 3$ to $n = 2$ than in any step between adjacent higher values of n. The effect is even more pronounced if we pass to $n = 1$, and, in addition, the isolation of the ion-pair dipole from other dipoles with which it would interact will further increase the relative polarity of the monomer. It must therefore be expected that δ for the unsolvated monomer will be substantially greater than the 10.5 indicated by the extrapolation.

In order to determine whether a $\bar{\delta}_2$ of 10.5 or somewhat greater was a reasonable value, a crude calculation was devised, in which the heats of vaporization of typical group I ionic compounds were estimated at 298°K. from their boiling points using the Hildebrand rule. A solubility parameter of 45 was estimated for the ionic head, and the volume fractionwise combination of this value with the value of 7.5 for dinonylnaphthalene determined from surface tension measurements leads to an estimated value of 11.0 for the average solubility parameter of the soap molecule. Although the Hildebrand rule was not intended for estimating parameters of ionic compounds, the estimated parameter is in good agreement with the one derived from the semitheoretical treatment of the data and tends to validate the association model.

The controlling influence of solubility parameter match on micelle size is further substantiated by observations on the nonvariance of micelle size with temperature. Measurements of the vapor pressure lowering of benzene solutions of CsDNNS at 35 and 50° and of freezing point depression[2] led to a micellar aggregation of 5.8 over the 45° temperature range. This is to be expected under the theory proposed because, while δ values are somewhat temperature dependent, differences in δ values are relatively insensitive to change in temperature.

The association behavior of dinonylnaphthalenesulfonic acid in solvents of different solubility parameter does not parallel that of the alkali sulfonates. Kaufman[2] found the acid to be dimeric ($n = 1.7$) in benzene by freezing point depression. Vapor pressure osmometer measurements made at 35° in connection with the present study gave an association number of 2.0 in benzene and of 2.4 in siloxane dimer. It appears that here, as with the carboxylic acids, mutual hydrogen bonding to form an eight-numbered ring gives a configuration having lower free energy than does association into more complex units.

Nonmicellar Solubility of Dinonylnaphthalenesulfonates in Polar Solvents. When the solubility parameter of the solvent exceeds 10, it would be expected from the analogy with the solubility of dinonylnaphthalene hydrocarbon that sulfonate solubility would become limited. A few cases were in fact found in which the sulfonate solubility paralleled the decreasing solubility of the dinonylnaphthalene. Two of these solvents were nitromethane ($\delta = 12.6$) and nitroethane

(δ = 11.1). Acetone (δ = 9.9) permits mixing in all proportions at room temperature, but allows only limited solubility at −78°. In most solvents of high solubility parameter, however, the dinonylnaphthalenesulfonates were soluble in all proportions.

The solubility of the dinonylnaphthalenesulfonates in polar solvents having solubility parameters substantially higher than that estimated for the sulfonate monomer results from at least two causes. One is that the ionic end of the sulfonate molecule is solvated by coordination and/or hydrogen bonding with functional groups of the solvent in such a way as to improve the solubility parameter match between solvent and the solute units. The other cause is believed to be tail-to-tail association which increases the relative contribution of the polar heads to solute–solvent interaction in the more polar liquids. In the extreme case of water, this association leads to the formation of large aqueous micelles in which the polar heads lie on the exterior of the micelle.

It is recognized that the application of the solubility parameter concept to polar compounds goes beyond the original definition of δ in terms of London forces alone, but such an extension, which takes account of dipole forces as well as dispersion forces, has been made by Hildebrand and Scott.[19] Estimates of δ for polar molecules by the Hildebrand rule automatically include the electrostatic effects.

Solvents capable of coordination or hydrogen bonding include acetone, methyl isobutyl ketone, ethyl acetate, ethanol, and methanol. The work of Kaufman[17] has shown that alcohols are strongly solubilized from toluene solutions by sodium sulfonate and that hydrogen bonding of the solubilized alcohol can be detected by infrared examination. He found evidence of solubilization for acetone also,[18] but the effect was weaker. When the ketone is present in overwhelming proportions as the solvent species, even a modest tendency of the ketonic oxygen to coordinate with the cation will lead to substantial solvation. The osmotic coefficients of Fig. 2 suggest that the solvated dimer, and to a lesser extent the trimer, are the predominant solute species but that at low sulfonate concentrations appreciable proportions of the solvated monomer may exist. These conclusions apply particularly to solutions in methyl isobutyl ketone and ethyl acetate, whose dielectric constants are below 14.

Other work[25] has shown that the alkali sulfonates form strongly conducting solutions in alcohols and ketones and that some solutions in nitroparaffins are also conductors. In general, strong ionic conductance is coupled with a decreased tendency to sulfonate monomer association into dimers or larger aggregates: Both effects imply stronger solvation of one or both ions of the alkali sulfonate ion pair in these solvents.

It is of interest to examine the solubility and micellar phenomena observed for the group I dinonylnaphthalenesulfonates in relation to the general theory of micelle formation advanced by Winsor.[11] This author, considering systems containing an amphipathic compound in the presence of varying proportions of water and a hydrocarbon, postulates an equilibrium

$$\begin{bmatrix}\text{aqueous}\\ S_1\ \text{micelles}\end{bmatrix} \rightleftarrows \begin{bmatrix}\text{lamellar large (or liquid}\\ \text{crystals) ``G'' micelles}\end{bmatrix} \rightleftarrows \begin{bmatrix}\text{nonaqueous}\\ S_2\ \text{micelles}\end{bmatrix}$$

Such an equilibrium is most readily demonstrated in concentrated solutions in which the amphipath has a suitable balance of lipophilic and hydrophilic components. In the sulfonate systems of the present study, the transition from hydrocarbon to water environment was obtained by choosing a series of pure solvents of increasing polarity, rather than by varying the proportions of water and hydrocarbon present. Under these conditions the S_2 micelle decreases in size as the polarity of the liquid is increased, approaching monomeric dispersion in the lower alcohols; typical S_1 micelles are formed only in water. Progressive addition of water to dilute hydrocarbon solutions of the sulfonate does not lead to the separation of a liquid crystalline phase but, after a substantial solubilization of water, to the formation of water-in-oil or oil-in-water emulsions stabilized by precipitated sulfonate. However, addition of a small and critical amount of water to the solvent-free sulfonate, or to a sulfonate containing less than 10% of benzene, does produce a birefringent phase. Birefringence appears to depend upon some specific action of water; it was encountered in no system from which water was absent. The S_1 and S_2 micelles and the G liquid crystals of Winsor's model, thus, can be demonstrated in suitably chosen hydrocarbon–water–sulfonate systems, but the intermediate liquid crystalline phase can exist only in the presence of an overwhelming preponderance of the sulfonate. No indication of an intermediate G structure involving aggregates larger than the S type micelles was found in any water-free solvent of intermediate polarity.

Solubility Behavior of Crystalline Soaps. The relation of soap crystallinity to soap solubility has been discussed briefly by Kaufman and Singleterry.[26] They

(25) R. C. Little and C. R. Singleterry, *J. Phys. Chem.*, 68, 2709 (1964).

(26) S. Kaufman and C. R. Singleterry, *ibid.*, 62, 1257 (1958).

noted that the solubility of crystalline sodium 2-ethylhexylsebacate in benzene was undetectably small at room temperature but that it increased sharply in the neighborhood of 47° to give miscibility of soap and solvent in all proportions. This behavior recalls that of aqueous soap systems at the Krafft point. Similar sharp transitions in solubility have been reported for zinc laurate and stearate in various solvents.[27] Murray and Hartley[28] have explained the Krafft point in aqueous soap solutions as the temperature at which the solubility of the crystalline soap reaches the c.m.c. for micelle formation. At temperatures higher than the Krafft point the crystalline phase, therefore, cannot exist in equilibrium with micelles. The same explanation is applicable in principle to the sudden increases in solubility noted for amphipathic salts in low polarity solvents. However, as Winsor[11] has pointed out, the critical increase in solubility may sometimes occur as a sudden large increment accompanying a change of state from solid to liquid crystalline or liquid phases, either of which is likely to have a solubility greater than the c.m.c. for the micellar form. It should be noted that the temperature of a phase change such as melting or the formation of liquid crystals is lowered by the presence of a solvent which can swell or dissolve in one or both of the phases involved in the transition.

Kissa[29-31] has reported extensive data on the solubility of crystalline lithium salts of aliphatic and alicyclic acids (9–16 carbon atoms) at 27°. He found pure crystalline salts, whether straight-chain, branched, or alicyclic, to have low solubilities at this temperature, the normal chain acids being most insoluble. Although Kissa's data are for carboxylates, which do not always form the small isometric micelles characteristic of the sulfonates,[15,32,33] the theory proposed for the sulfonates appears capable of extension to the carboxylates. It may be noted that when Kissa mixed lithium salts of nine pure branched-chain acids, the solubility was increased 400-fold over the sum of their separate solubilities. The major change in the thermodynamic situation when the pure salts are mixed is that the condensed salt phase becomes a solid solution of geometrically unlike molecules which approaches the character of the viscous liquid phase just postulated for the sulfonates. The solubility then becomes that appropriate to a liquid–liquid mixture. Kissa reported difficulty in reaching equilibrium solubilities with some mixtures. It is thus not clear whether these mixed salt systems were above or below their critical solution temperatures. In the case of the nine-salt mixture, the fact that the solution passed to a gel as the concentration was increased suggests that this system was above the critical temperature and, so, was miscible in all proportions. The salts of isomeric mixed acids from commercial intermediates had solubilities as much as 1000 times that of some of the pure single salts of which they were composed. They appear to have been miscible with isooctane in all proportions but to have had limited liquid–liquid solubility in benzene, except for the lithium tridecanoate mixture which formed gels in concentrated solutions.

The differences in solubility behavior of the pure crystalline salts and of mixtures of the same pure salts are most readily understood if attention is focused on the different free energies of the solid phases involved, rather than on changes in micelle stability or structure as a result of mixing species. Straight-chain aliphatic radicals can pack closely in the crystal, allowing strong dispersion force interactions between the methylene groups of the chain.[34] The standard free energy decrease for a molecule passing from hydrocarbon solution into the crystal is relatively large and the solubility accordingly small. Mixing straight-chain salts causes only a minor decrease in the amount of interaction between chains, so mixtures of straight-chain salts show no enhanced solubility. In the small, nonaqueous micelle the hydrocarbon chains must be in rather intimate contact with the disordered solvent molecules rather than adlineated to each other as in the crystal, so the standard free energy change for micelle formation is less than that for crystal formation. Consequently, the micellar phase is unstable with respect to the crystal until the temperature of the system approaches the melting point of the soap, when there is usually a sharp transition to unlimited solubility. When, on the other hand, the carboxylate molecules are branched, the molecules cannot pack so closely in the crystal, and there is less dispersion force interaction between chains. In addition, the branched chains contain additional methyl groups, which interact less strongly than methylene groups. Mixing branched-chain species results in further decrease in geometrical economy of packing and in an increase in entropy which still further minimizes the free energy of solid formation and increases the equilibrium solu-

(27) E. P. Martin and R. C. Pink, *J. Chem. Soc.*, 1750 (1948).

(28) R. C. Murray and G. S. Hartley, *Trans. Faraday Soc.*, **31**, 183 (1935).

(29) E. Kissa, *J. Colloid Sci.*, **17**, 857 (1962).

(30) E. Kissa, *ibid.*, **18**, 147 (1963).

(31) E. Kissa, *ibid.*, accepted for publication.

(32) J. G. Honig and C. R. Singleterry, *J. Phys. Chem.*, **58**, 201 (1954).

(33) J. G. Honig and C. R. Singleterry, *ibid.*, **60**, 1108 (1956).

(34) W. C. Bigelow, E. Glass, and W. A. Zisman, *J. Colloid Sci.*, **2**, 563 (1947).

bility. As the complexity and heterogeneity of the molecules in the solid carboxylate phase are increased, a point is reached at which the mixture is in equilibrium with a higher concentration of dissolved species than is required for the formation of micelles. The solid phase then passes over completely to the micellar state unless the system is below the critical solution temperature, in which case a solvent-swollen "solid" phase equilibrates with the micellar solution, *i.e.*, there is limited micellar solubility.

Molecular Association in Pairs of Long-Chain Compounds.

II. Alkyl Alcohols and Sulfates

by H. C. Kung and E. D. Goddard

Research Center, Lever Brothers Company, Edgewater, New Jersey *(Received April 8, 1964)*

In our previous studies, which described the formation of 1:2 association complexes between alkyl alcohols and sulfates, sample preparation was by a dry melt method. The present work involves studies on samples prepared from aqueous or aqueous–ethanol solutions of lauryl alcohol and sulfate and of myristyl alcohol and sulfate. It is shown that, over a range of concentration, mixing ratio, and solvent composition, the specimens which settle out of solution have a composition corresponding to a 1:2 alcohol–sulfate ratio and that their differential thermal, infrared, and X-ray patterns correspond to those of the previously reported complexes. No evidence of free alcohol was obtained. Difficulty was encountered in preparing the "1:1" adducts reported by other workers; however, although some samples having approximately the 1:1 composition were obtained, the above techniques showed the adducts to be of an ill-defined nature and to contain uncombined alcohol under the test conditions used. It is also shown that reaction between alkyl alcohols and sulfates is rapid when the alcohol is melted.

It has been shown in a previous paper[1] that alkyl alcohols and sodium alkyl sulfates combine to form 1:2 association complexes with the release of a considerable amount of energy. In these studies samples were prepared by a melt method in order to avoid the effects of solvent inclusion. As there is interest in the interaction of the above species when present in aqueous solution or at aqueous interfaces, it seemed desirable to establish whether or not the same complexes form in an aqueous environment. Work of this type has been done previously. In their studies on phase relations in the system sodium lauryl or myristyl sulfate, lauryl alcohol, and water, Epstein,[2] *et al.*, isolated crystalline adducts in which the ratio of alcohol to sulfate was 1:2; later 1:1 adducts were isolated.[3] However, little information on these adducts, other than their composition, was published.

The purpose of this work was to prepare such adducts and to establish their identity or nonidentity to the melt-prepared complexes by use of the differential thermal analysis (DTA), infrared, and X-ray tech-

(1) H. C. Kung and E. D. Goddard, *J. Phys. Chem.*, **67**, 1965 (1963).

(2) M. B. Epstein, A. Wilson, C. W. Jakob, L. E. Conroy, and J. Ross, *ibid.*, **58**, 860 (1954).

(3) M. B. Epstein, A. Wilson, J. Gershman, and J. Ross, *ibid.*, **60**, 1051 (1956).

niques used previously.[1] In addition, further experiments have been carried out to establish the conditions under which interaction occurs in the absence of solvent.

Experimental

The specimens of lauryl alcohol (LOH), myristyl alcohol (MOH), sodium lauryl sulfate (NaLS), and myristyl sulfate (NaMS) have been described previously.[1] Adducts were prepared as follows: appropriate quantities (see Tables I and II) of long-chain alcohol, long-chain sulfate, and water or water–ethanol were stirred together at room temperature. The solvent was generally added last. In some experiments a small amount of sodium chloride was included.[3] Stirring was continued while heating to 75–80° and maintaining at this temperature for a few minutes. The systems were more or less turbid at this point and were then allowed to cool slowly to room temperature. Crystals of adduct grew as small, thin plates. After separation and drying over phosphorus pentoxide, their content of long-chain alcohol was determined by the method of Epstein, *et al.*[2] This involves transferring a weighed amount of the crystals into a fritted glass filter funnel and extracting with successive small portions of heated petroleum ether to constant weight. The water content of the crystals, where tested, was found to be <0.1%.

Table I: Composition of Solutions and Adducts. LOH–NaLS

	Initial solution, g./100 ml. of water			% by wt. of LOH in adduct
	NaLS	LOH	NaCl	
1	0.805	0.154	...	24.1
2	0.810	0.414	0.12	25.8
3	0.801	0.542	0.12	25.1
4	0.800	0.605	0.12	26.1
5	0.813	0.425	0.12	38.3
6	0.803	0.553	0.12	39.8

Table II: Composition of Solutions and Adducts. MOH–NaMS

	Initial solution, g./100 ml. of water			% by wt. of MOH in adduct
	NaMS	MOH	NaCl	
7	0.812	0.207	0.12	24.7
8	2.4	0.41	...	24.3
9	2.3[a]	0.68	...	24.9
10	0.801	0.409	0.12	36.2

[a] Water replaced by 50:50 water–ethanol.

In addition to 1:2 alcohol–sulfate complexes Epstein, *et al.*,[3] reported that 1:1 adducts will form if conditions are appropriate. To favor formation of the adduct with the higher level of alcohol the relative amount of alcohol to sulfate in the starting mixture was increased. Although this yielded the desired result for the myristyl system (see Table II), it was ineffective for the lauryl system. We therefore resorted to additional cooling of some of the mixtures of this series (members 5 and 6, Table I) at 5° to accomplish our purpose.

To obtain an idea of their mutual reactivity in the absence of water, long-chain alcohol and sulfate, in amounts equivalent to a 1:2 molar ratio, were mixed for a few minutes at room temperature and then placed in the DTA equipment for a thermal study.

The DTA, infrared, and X-ray procedures used have been previously described. For DTA the specimens were cooled where necessary to 0–10° before starting the experiment, and a heating rate of 1.6°/min. was used. For infrared studies the materials were dispersed as a mull in Nujol.

Results

Composition of Adducts. Composition data for the initial mixtures and the separated adducts are given in Tables I and II. In the lauryl system, two compositions of adduct are approached—that corresponding to a mole ratio of 1:2 LOH–NaLS (24.5% LOH) and that to a mole ratio of 1:1 (39.3% LOH). Evidence of a continuum of crystal composition was not obtained.[3] In the myristyl system, for which the theoretical MOH contents of the 1:2 and 1:1 MOH–NaMS compositions are 25.3 and 40.4%, respectively, results are similar. However, evidence for the formation of an adduct with the 1:1 composition is less convincing in this case.

DTA. The DTA patterns of adducts 1–4, Table I, were similar to one another and to that of the 1LOH–2-NaLS composition formed by the melt method. Curve a, Fig. 1, obtained for adduct 1, is given as an example. The pattern consists of a large endothermic peak near 60°. There is a complete absence of a peak caused by melting of LOH. We interpreted[1] a similar pattern for the melt-prepared 1:2 mixture as indicating the existence of a 1:2 complex having a melt decomposition point near 60°. The differential thermogram of adduct 5 (curve b, Fig. 1) consists of five peaks of various sizes. The peak near 24° is probably caused by melting of the alcohol (or alcohol-rich eutectic) and that at 60° by the melting and decomposition

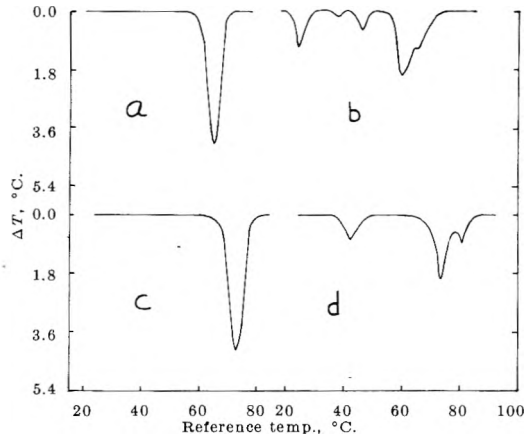

Figure 1. DTA curves of crystallized adducts: a, adduct 1; b, adduct 5; c, adduct 7; d, adduct 10.

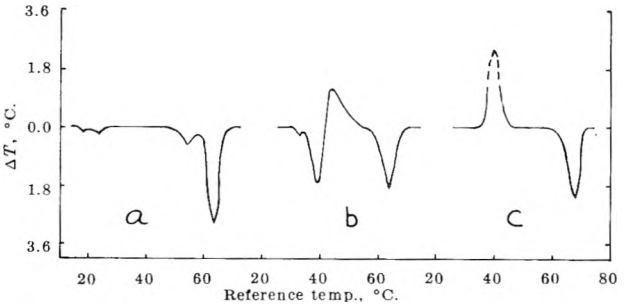

Figure 2. DTA curves of LOH–NaLS and MOH–NaMS mixtures: a, b, mixtures of 1LOH and 2NaLS, 1MOH and 2NaMS, respectively, made at room temperature; c, shock-cooled mixture of 1MOH and 2NaMS (see text).

of the complex. The nature of the other peaks is not clear. It appears that this adduct is not a single entity but a mixture of several species, despite its composition which approaches the 1LOH–1NaLS mole ratio. Adduct 6 gave a similar pattern to that of adduct 5.

Essentially the same DTA patterns were obtained with adducts 8 and 9 as was obtained with adduct 7; this is shown as curve c, Fig. 1. No peak due to melting of MOH is evident. The endothermic peak near 70° suggests incongruent melting of a 1MOH–2-NaMS molecular complex since this is the peak characteristic of decomposition of the complex formed by the dry melt method. The thermogram for adduct 10 has three peaks, that at 41° being associated with free MOH (or eutectic) and that at 74° very likely with the decomposition of the 1:2 complex. The origin of the peak near 80° is not establ shed.

Differential thermograms for 1:2 mixtures made at room temperature in the absence of water are given in Fig. 2. For the myristyl pair there is a peak at 38° corresponding to the melting of the alcohol. This is followed by a broad exothermic peak at 43°. We interpret this as indicating that reaction starts, very soon after the MOH is molten, to form the complex which subsequently decomposes as shown by the endothermic peak at 64°. We note also that the areas of the exothermic and second endothermic peaks are approximately the same. This is consistent with our interpretation which associates the second endothermic peak with the melt decomposition of the complex. However, under the conditions of this experiment, the temperature of the peak is slightly lower than before. For the LOH–NaLS system mixed at room temperature the thermogram consists of a major endothermic peak at 60° and minor peaks at 18, 23, and 54°. This suggests that during room temperature mixing, at which temperature the LOH is liquid, reaction to form the complex had gone virtually to completion. The melt decomposition of the complex formed in this way agrees satisfactorily with that observed previously.

The third curve in Fig. 2 represents the heating pattern of a 1MOH–2NaMS mixture which had been heated beyond the melt decomposition temperature in the DTA apparatus and cooled suddenly to room temperature with cold dry air.[1] While we note the complete absence of an endothermic peak in the temperature range of melting of MOH, there is a sharp exothermic peak in this area. Our interpretation is that the mutual disposition of MOH and NaMS molecules in this mixture, which was "frozen" in by the rapid cooling, is so favorable for subsequent reaction that, on heating to the melting point of the alcohol, interaction to form the complex is almost instantaneous.

Infrared. Sections of spectra in the hydroxyl band stretching region for a series of melt-prepared mixtures of MOH and NaMS are presented in Fig. 3. In this region the 1MOH–2NaMS composition is characterized by a sharp absorption peak at 2.86 μ, free alcohol by a broad band at 3 μ, and NaMS by the absence of absorption. Superpositioning of the 3-μ band and the 2.86-μ peak is evident in mixtures richer in alcohol than the 1:2 composition. The crystalline adducts 7, 8, and 9, whose compositions were all close to the 1:2 molar ratio, had very similar absorption spectra which matched that of the melt-prepared 1:2 complex; the curve for adduct 7 is shown in Fig. 3. Adduct 10 gave a spectrum with a relatively broad band consisting of a peak at 2.84 μ and two shoulders; this suggests the presence of free MOH in the adduct (see curve j, Fig. 3).

Infrared spectra of adducts 1, 3, 5, and 6 were also

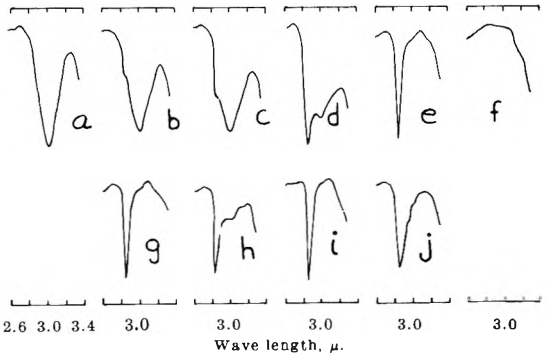

Figure 3. Sections of infrared spectra: a, MOH; b, 80.0% MOH and 20.0% NaMS; c, 60.0% MOH and 40.0% NaMS; d, 40.0% MOH and 60.0% NaMS; e, 25.3% MOH and 74.7% NaMS; f, NaMS; g, adduct 3; h, adduct 5; i, adduct 7; j, adduct 10.

obtained. Those of adducts 1 and 3, which show a sharp peak at 2.85 μ, were almost identical with that of the 1LOH–2NaLS complex prepared by the melt method. The spectra of adducts 5 and 6 differ from the former in that they consist of a sharp peak at 2.83 μ and a broad band around 3 μ which indicates the presence of free alcohol in addition to the hydrogen-bonded complex. The spectra for adducts 3 and 5 are shown in Fig. 3.

Spectra reported by Kaufman[4] for methanol and an organic sulfonate in toluene are relevant to the above. Whereas methanol alone has the characteristic, broad 3 μ band, its dilute toluene solution has a sharp peak at 2.76 μ which is characteristic of free hydroxyl groups. Addition of the organic sulfonate leads to superpositioning of a broad band at 2.95 μ on the sharp peak; this is probably the result of the clustering of several methanol molecules around each sulfonate.

X-Ray. X-Ray measurements on the separated adducts gave support to the findings by the DTA and infrared methods. Diffraction patterns of adducts 7, 8, and 9 matched each other and that of the melt-prepared 1MOH–2NaMS complex; all closely resembled the pattern of Lingafelter's ι-phase of sodium alkyl sulfates.[5] Adduct 10, however, which contains 36% MOH, gave rise to a pattern which is intermediate between that of the 1:2 complex and the melt-prepared 40% MOH–60% NaMS mixture.

In the same way, the diffraction patterns of adducts 1, 2, and 3, which are very close to the 1:2 composition, all resembled that of the melt-prepared 1LOH–2NaLS complex, and all have the ι-phase characteristics. However, slight changes in line intensities and positions of weak lines were evident among the patterns. The patterns of adducts 5 and 6, in which the excess LOH is presumably in the liquid state, also resembled the above.

The above results confirm the earlier work on adducts isolated by Mr. Ryer[6] of this laboratory. With 90% water–10% ethanol as solvent and a 2.4% level of NaMS, the MOH content was varied from 0.1 to 0.6%; with water as solvent and a 0.6–0.8% level of NaMS, the MOH level was varied from 0.025–0.06%. Heating and cooling these mixtures led to adducts which in all cases gave Lingafelter's ι-phase pattern and a content of MOH, when determined, of around 27%.

Discussion

Extraction analysis, DTA, infrared, and X-ray investigations have all provided evidence that the adducts with the 1:2 composition, which were separated from aqueous media, are identical with the 1:2 molecular complexes formed by the melt method. The ability to form the same species under such widely varied conditions lends considerable support to the existence of the postulated complexes. Aside from the fact that the composition of some of the adducts approaches the 1:1 molar ratio, no evidence has been obtained, either from investigation of the adducts or the melt-prepared materials, that mixtures having the 1:1 composition are molecular compounds; rather it seems likely that they are made up of the 1:2 complex with excess alcohol occluded or possibly partially in solid solution. It should be noted, however, that isolation of the adducts involved a drying step at room temperature, and there is a possibility that this may have resulted in the breakdown of a (hydrated) 1:1 adduct formed at lower temperatures.

The results on heating mixtures of long-chain alcohol and sulfate have demonstrated that interaction to form the complex starts soon after the alcohol is melted; such interaction can readily be seen by observation of the pairs on the hot stage of a microscope. Accordingly, since LOH is liquid at room temperature, the question may be raised as to whether the 1LOH–2NaLS complex exists in an aqueous environment or whether it is formed during the subsequent separation —for example, during the drying process. We believe the former to be the case, in view of the analogous behavior of the myristyl pair and the fact that MOH is solid at room temperature. One role of water in the

(4) S. Kaufman, *J. Colloid Sci.*, 17, 231 (1962).

(5) F. F. Rawlings and E. C. Lingafelter, *J. Am. Chem. Soc.*, 77, 870 (1955); F. F. Rawlings, Jr., Ph.D. Thesis, University of Washington, Seattle, Wash., 1951.

(6) F. V. Ryer, unpublished work.

aqueous system is to provide, for the component pairs, the mobility required for interaction.

The interaction tendency of alcohol–sulfate pairs makes understandable the difficulties always encountered in removing the last traces of long-chain alcohol from a long-chain sulfate specimen. Already a tedious procedure for the lauryl system, purification of the myristyl and longer homologs has proved formidable.[7] The present work indicates that procedures involving heating of the specimen to the melt decomposition temperature of the 1:2 complex would facilitate purification: thus, using the technique of vacuum extraction, we have found a marked increase in the rate of MOH removal from the 1MOH–2NaMS complex as the melt decomposition temperature is approached.

In the work carried out on the three-component system, long-chain alcohol, sulfate, and water, we have restricted investigation to extreme regions of the ternary phase diagram, *viz.*, to regions completely water-free or in which water is the major constituent (>97%). There have been several more complete studies of ternary detergent–amphiphile–water systems. In briefly describing some of these it is appropriate to start with the water-free systems studied by McBain, *et al.*,[8,9] who obtained evidence of 1:1 and 1:2 palmitic acid–sodium palmitate and of 1:1 oleic acid–potassium oleate associations. Furthermore, their phase diagrams bear a striking resemblance, in the areas of relevance, to the partial phase diagram we constructed for the MOH–NaMS system.[1] McBain and Stewart[10] also point out that in the oleic acid–potassium oleate–water system the boundary confining the water-rich isotropic region corresponds to the 1:2 acid–soap ratio. Similarly, Dervichian[11] has found an upper limit of solubility of octanol and potassium caproate (or laurate) in water to correspond to the 1:2 molar ratio and indicates that such stoichiometry is encountered only if the chain length of the amphiphile is sufficiently long. In the extensive work of Lawrence[12,13] and recent work of Ekwall[14] no significance is apparently attached to changes taking place at or near stoichiometric ratios. Most of Lawrence's work has been concerned with amphiphiles of chain length lower than twelve carbon atoms. He has, however, reported[13] the separation, from LOH–NaLS–water mixtures, of crystals of a "solid solution" of these three components whose composition varies with that of the starting system. Unfortunately, details of the compositions involved were not given.

It remains to consider how widespread the existence and formation of stoichiometric complexes between long-chain polar and long-chain ionic materials are. That such formation occurs under certain conditions is, as we have shown, now well established; and we will show in another publication that complex formation is by no means limited to the pairs of compounds discussed above. However, further work, both in bulk phase and at interfaces, is required to establish to what extent it is responsible for the diverse phenomena which have led various workers to suspect and postulate its existence. Such phenomena are spontaneous emulsification, mesomorphic phase formation, the position of phase boundaries, inhibition of precipitation of anionic detergents by heavy metal or long-chain cations, abnormal viscosity and surface tension effects, foam stability, slow draining films, monolayer penetration, and others. That attraction and interaction of the two species are involved in several of the above phenomena there seems little doubt.

In conclusion, evidence has been brought forward that the same 1:2 alkyl alcohol–sulfate complex is formed whether the association is allowed to take place *via* the melt or *via* aqueous solution. The *raison d'être* of the complexes, which can form under such a wide variety of conditions, we believe is associated with the limited stability of the alkyl sulfate structure. Stabilization is achieved in the complex by hydrogen bonding and charge separation. As soon as it is molten, an alkyl alcohol can react with a solid alkyl sulfate with the formation of the complex, and the release of a considerable amount of energy.

Acknowledgments. The authors wish to thank Messrs. H. Lemaire and E. Mecheski for preparation and purification of materials and the Lever Brothers Co. for permission to publish this paper.

(7) K. J. Mysels, personal communication.

(8) J. W. McBain and M. C. Field, *J. Chem. Soc.*, 920 (1933).

(9) J. W. McBain and A. Stewart, *ibid.*, 924 (1933).

(10) J. W. McBain and A. Stewart, *ibid.*, 928 (1933).

(11) D. G. Dervichian, *Proc. Intern. Congr. Surface Activity, 2nd, London*, **1**, 327 (1957); *Discussions Faraday Soc.*, **25**, 68 (1958).

(12) A. J. Hyde, D. M. Langbridge, and A. S. C. Lawrence, *ibid.*, **18**, 239 (1954).

(13) A. S. C. Lawrence, *ibid.*, **25**, 51, 70 (1958).

(14) P. Ekwall, I. Danielsson, and L. Mandell, *Proc. Intern. Congr. Surface Activity, 3rd, Cologne*, **1**, 189, 193 (1960).

The Penetration of Water and Aqueous Soap Solutions into Fatty Substances Containing One or Two Polar Groups

by A. S. C. Lawrence, A. Bingham, C. B. Capper, and K. Hume

Department of Chemistry, Sheffield University, Sheffield, England *(Received March 17, 1964)*

The minimum temperature of penetration of aqueous soap solutions into amphiphiles has been measured for the permutations of the even number alkyltrimethylammonium bromides from C_8 to C_{18} and fatty acids and alkanols from C_{12} to C_{20}. The penetration of water into amphiphiles has been studied by freezing point, vapor pressure, and X-ray diffraction methods and it has been shown that this considerable solubility of water in polar fatty substances, themselves insoluble in water, is general. Alkanols form a solid solution melting to liquid, fatty acids only liquid; fatty amines form a binary liquid crystalline phase and so do substances containing two OH groups, such as monoglycerides, hexadecane-1,2-diol, and α-hydroxypalmitic acid. Monolaurin forms a shallow eutectic with lauric acid while the T_{pen} minimum into this system forms a very deep one at the same composition which may be important in the intestinal absorption of fat. The monolaurin–water system above T_{pen} is a single liquid crystalline phase up to about 33% water; beyond this and to high dilution, the system is a suspension of lc spherulites in water. It is pointed out that the phosphatides and cerebrosides are almost certainly similar, each with its T_{pen} dependent upon the fatty acids present.

It has been shown that the effect of temperature upon phase equilibria in the ternary soap–water amphiphile systems may be represented by the simple general diagram shown in Fig. 1.[1] Here the system is shown as a binary one of some selected soap–water ratio as one component and the amphiphile as the other; the Krafft point of the soap is used as one melting point, and the melting point of the amphiphile is used as the other. This picture applies to the carboxylates, alkyl sulfates, and alkyltrimethylammonium bromide soaps with the usual amphiphiles having a hydrocarbon chain of five or more carbon atoms.

T_E is clearly the important minimum temperature at which the ternary liquid crystalline phase can exist; below it this association is broken by the component with the highest freezing point separating as solid; it may be the soap, the amphiphile, or water. The location of T_E by construction of Fig. 1 is extremely tedious and difficult, but it may be found very simply and accurately when it is realized that T_E is also the minimum temperature at which a soap solution penetrates into an amphiphile or at which water penetrates into soap plus amphiphile. This temperature T_{pen} is easily observed by placing a very small amount of amphiphile upon a glass microscope slide with a drop of soap solution, covering with a cover glass, and observing on a heating stage by a polarizing microscope. It is preferable to use a single crystal or fragment of one. Penetration shows first as formation of a membrane around the crystal flake, followed, when the temperature is held at this point, by penetration into the crystal and extrusion of myelin tubular forms. The concentrations and quantities used are irrelevant.[1] At equilibrium, the ternary composition has its proper place in one or another phase area, lying somewhere on the tie line connecting the original soap concentration in water with the amphiphile corner of the triangular diagram. However, we are not looking at the final stage; we are watching the equilibration process of soap and water penetration between the

(1) A. S. C. Lawrence, *Discussions Faraday Soc.*, 25, 53 (1958), "Surface Activity and Detergency," K. Durham, Ed., London, 1961, pp. 158–192; *Nature*, 183, 1491 (1959); *J. Soc. Chem. Ind.*, 1764 (1961); A. W. Ralston, "Fatty Acids."

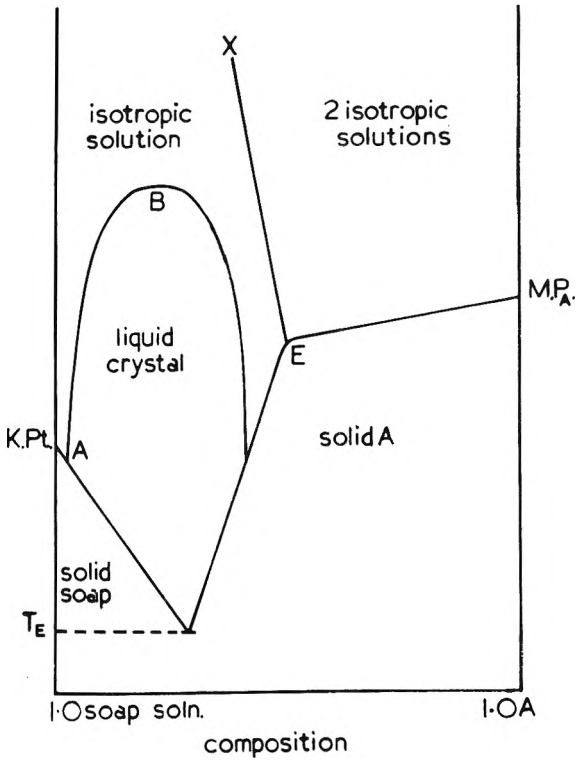

Figure 1. General temperature–composition diagram for soap–water–amphiphile systems.

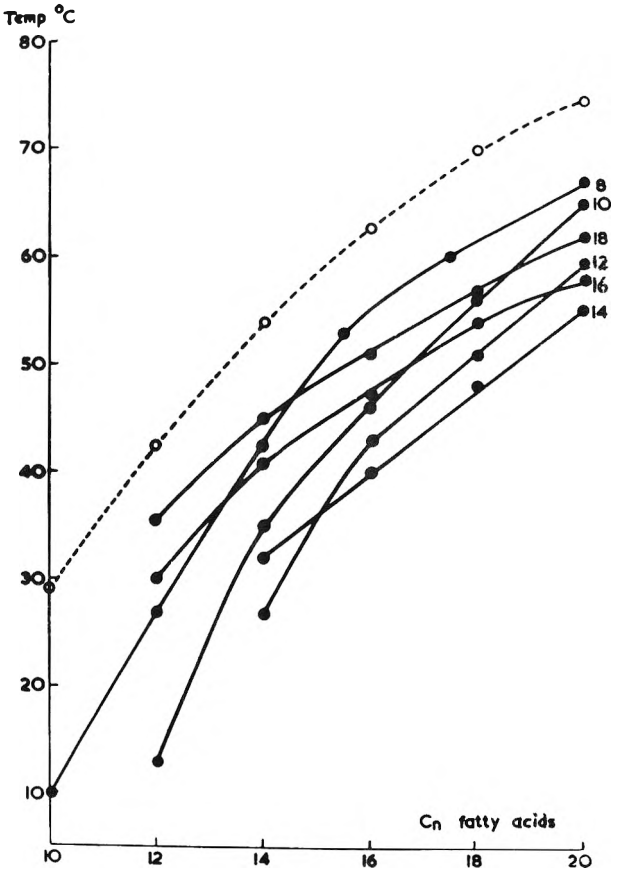

Figure 2. T_{pen} for even number alkyltrimethylammonium bromide soaps plotted against C_n in fatty acids.

layers of polar groups in the bimolecular leaflet of amphiphile. We see the formation and build-up of ternary liquid crystalline phase because it is formed more rapidly than it redissolves in the excess of soap solution. This is because of its extremely high viscosity.

Since reporting preliminary figures for T_{pen} for a number of soaps and amphiphiles,[1] we have made a systematic examination of the even number alkyltrimethylammonium bromide soaps from C_8 to C_{18} with the even number fatty acids and alkanols from C_{12} to C_{20}. In Fig. 2 each curve shows T_{pen} for one of the homologous series of soaps plotted against the number of C atoms in the fatty acids; Fig. 3 shows the results for alkanols. There is crossing over and lack of order, but, when the same results are plotted against C_n in the soaps, the family of curves for acids and alkanols reveal the order shown in Fig. 4a and 4b.

Effect of Water upon Fatty Alkanols and Acids

In Fig. 5 the bottom line shows an effect which misled us at first with the alkanols but which does not appear in the acids. A change is seen but penetration and liquid crystalline phase formation does not set in until a higher temperature, both transition temperatures being sharp. The effect of water alone was therefore tried upon the alkanols and fatty acids by measuring their melting points on the hot stage in the pure dry state and repeating with a drop of water upon the substance. Figure 5 shows that water lowers the melting point of the acids and increases that of the alkanols. If single crystals are used, the lower temperature transition is seen in the solid alkanols; in polarized light with crossed Nicols, the specimen is silvery white; at the transition temperature, this birefringence disappears as if a blind were drawn inwards from each edge of the platelet; craze lines appear also. The values for T_{pen} for the soaps into the alkanols shown in Fig. 3 and 4b are the transition of alkanol plus soap and water to form the ternary liquid crystalline phase and not the lower water penetration values.

The effect of water upon the freezing points of dodecanol and decanoic acid was examined; mixtures with increasing amounts of water were made up a few degrees above the melting points of the substances and agitated gently for several days. Freezing points were measured and repeated after further mixing; solution of the water is very slow as it takes place across the small interface. The eutectoid curves shown in Fig. 6

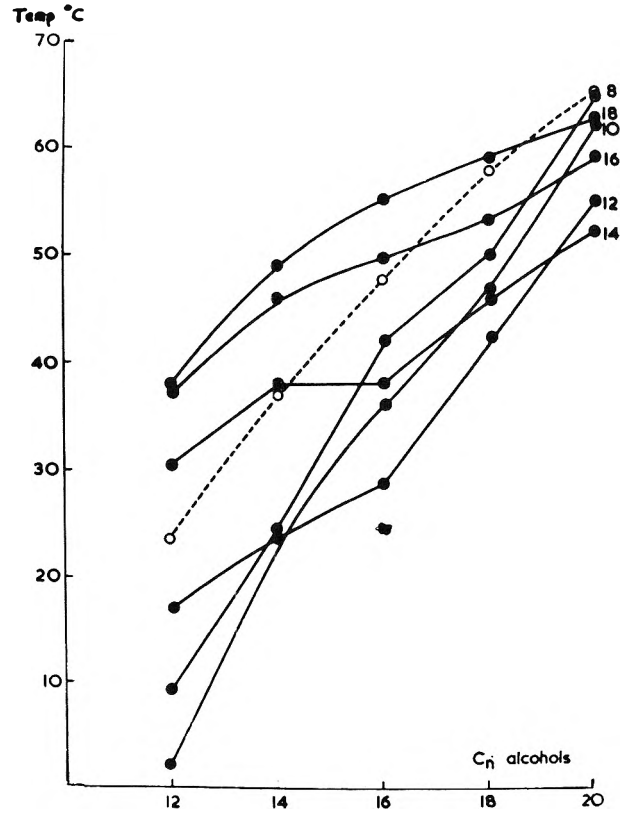

Figure 3. T_{pen} for even number alkyltrimethylammonium bromide soaps plotted against C_n in n-alkanols.

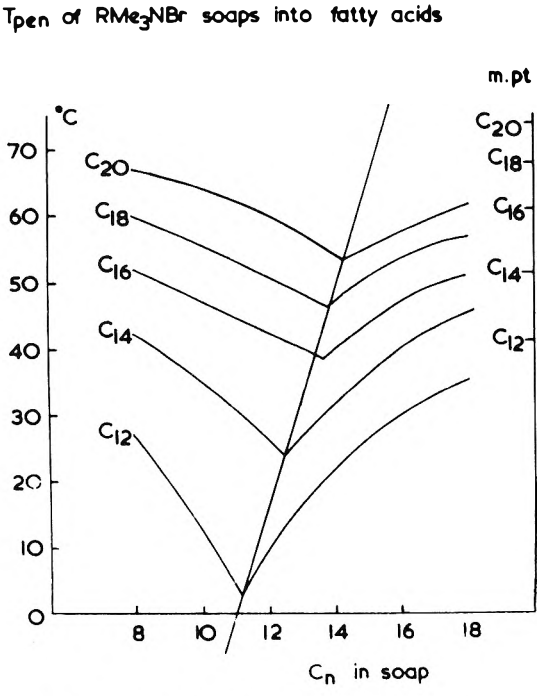

Figure 4a. T_{pen} *vs.* C_n in soaps with fatty acids.

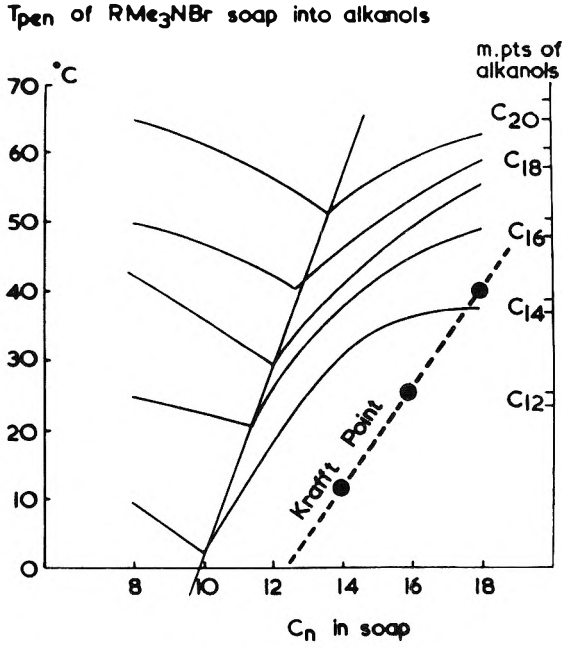

Figure 4b. T_{pen} *vs.* C_n in soaps with n-alkanols.

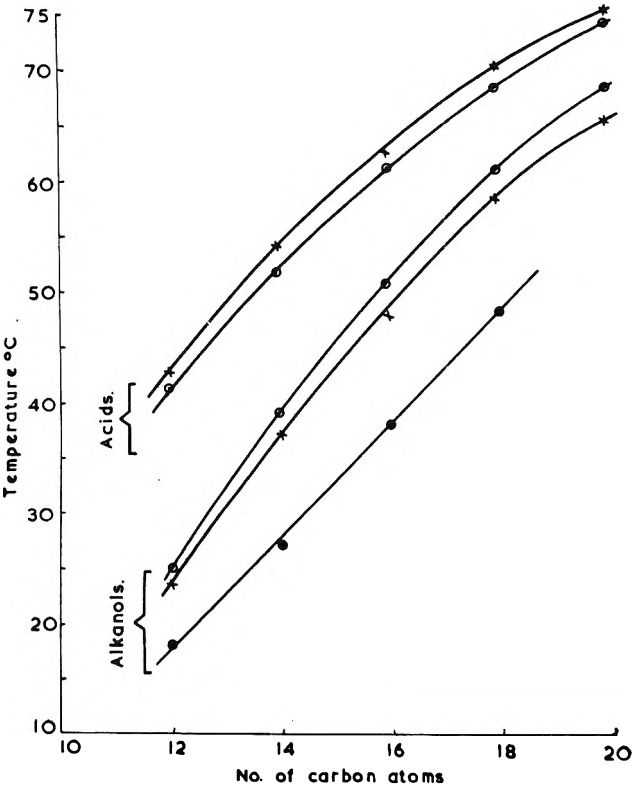

Figure 5. Melting points of fatty acids and alkanols; anhydrous and in presence of water. Lower curve for alkanols is the minimum temperature at which water penetrates to form solid hydrate. ×, melting point of pure compound; ○, melting point in water; ●, loss of birefringence (alcohols only).

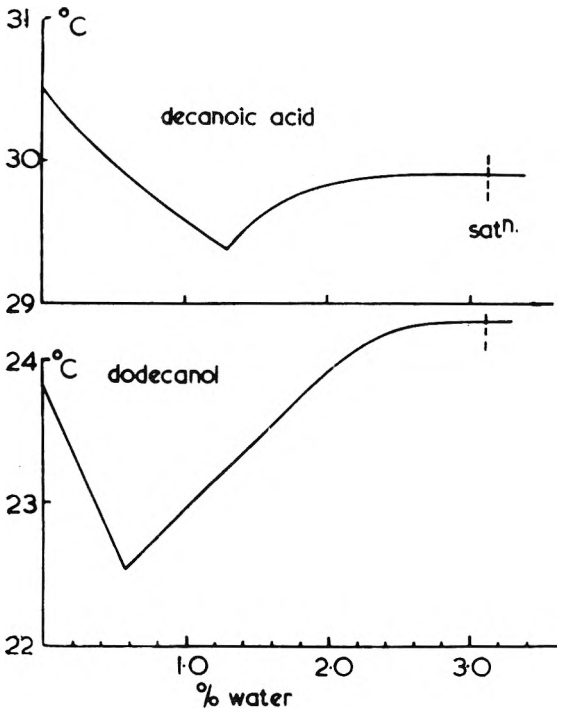

Figure 6. Freezing point *vs.* % water in dodecanol and in decanoic acid.

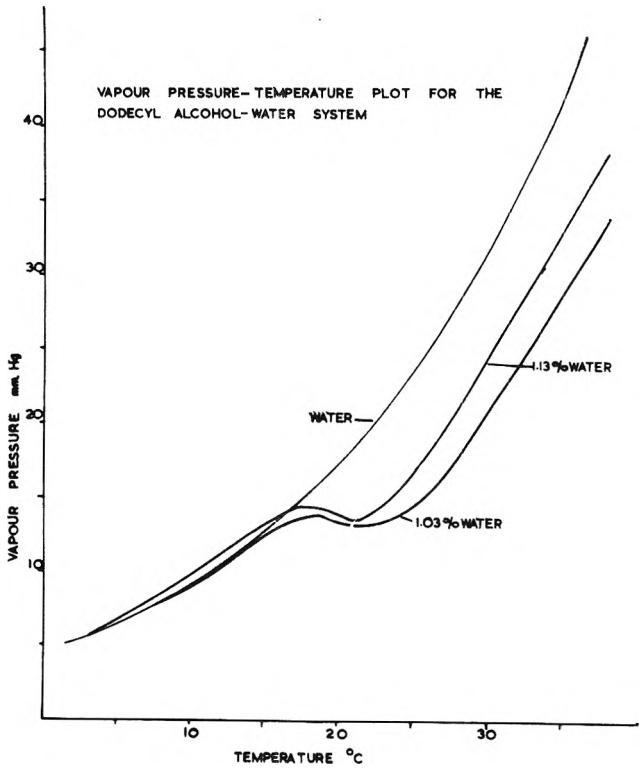

Figure 7. Log vapor pressure *vs.* $1/T$ for water and dodecanol containing two concentrations of water.

were obtained; saturation was in each case about one-third of a molecule of water per molecule of substance. The results resemble part of the familiar two-component system in which compound formation occurs with two eutectics; the rising melting point which is terminated by saturation could, if continued, reach 0° for 100% water only *via* a second eutectic.

The vapor pressure of dodecanol and water was measured as a function of temperature; the specimen was placed in a small flask fitted with a tap for evacuation and a U-tube mercury manometer. Outgassing was difficult and loss of water was dealt with by completing a series of measurements and then analyzing for water by the Karl Fischer reagent. The apparatus was placed in a thermostat and the temperature raised in small steps, at least 24 hr. at each temperature being allowed. As anticipated, the vapor pressure was that of pure water up to the lower transition temperature at 16°; as the water passes into the dodecanol, the rise is halted; the vapor pressure then rises again as the temperature is raised. Figure 7 shows the results for two concentrations of water and that, above the transition, the vapor pressure of the hydrate is less than that of water. Most curiously, however, the slopes of water and water in dodecanol are almost identical, and therefore so are their ΔH_{vap} values. No significant difference was found between the infrared spectra of the anhydrous dodecanol and its hydrate.

The existence of a hydrate of dodecanol was first shown by Bernal and very briefly reported[2]; Trapeznikov has also shown the existence of hydrates of both alkanols and fatty acids while studying monolayers, salt effects, and surface pressure changes with temperature.[3] From these he distinguishes solid hydrate, liquid crystalline, and liquid structures each existing inside definite temperature ranges. We have not, however, observed any sign of liquid crystals, and solid hydrate separates directly from the liquid. On all other points, our observations confirm those of Trapeznikov.

McBain and Marsden examined such a commercial monolaurin and reported that its aqueous systems are liquid crystalline and that the long X-ray spacings increased from 40 Å. for the anhydrous substance to 150 Å. for the 25% in water liquid crystalline phase.[4] Clearly, a very large amount of water can penetrate into the smectic layer lattice, but X-ray diffraction

(2) J. D. Bernal, *Nature*, 129, 870 (1932); *Z. Krist.*, 83, 153 (1932).

(3) A. A. Trapeznikov, *Acta Physiochim. URSS*, 19, 553 (1944); 20, 589 (1945); *Compt. Rend. Acad. Sci. URSS*, 47, 275, 417 (1945); *Dokl. Akad. Nauk SSSR*, 277, 435 (1945); *Zh. Khim.*, 19, 228 (1955); *Proc. Intern. Congr. Surface Activity, 2nd, London*, 1, 121 (1957).

(4) J. W. McBain and S. S. Marsden, Jr., *J. Chem. Phys.*, 15, 211, (1947).

results of these authors suggest that the binary mixture is still a single smectic phase with 75% water whereas our results show about 35% as the maximum in the pure monoglyceride. Although this addition of soap to monoglycerides is widely practiced commercially, no work upon the nature of its effects seems to have been published. The solubility of water in fatty acids has also been studied extensively by Ralston.[1,5]

No attention has been paid to the results of these workers although it is obvious that observations of melting points and the use of melting points as criteria of purity of fatty acids and alkanols is entirely unreliable unless the substances are rigorously dried.

Bernal found that the hydrate is hexagonal whereas the anhydrous dodecanol is of low symmetry, either monoclinic or triclinic. Dr. A. J. Smith of this department has kindly made the X-ray examination of our hydrate and found the same results. He also found that the hydrate cooled to 10°, *i.e.*, below T_{pen}, had reverted to the anhydrous form.

Amphiphiles Containing Two Functional Groups

When 1-monolaurin, m.p. 62.5°, is heated with a drop of water, it passes sharply to a liquid crystalline phase at 40°; this is the β-crystal modification; the α-form melts at 44° and has a T_{pen} by water well below room temperature. Hexadecane-1,2-diol, m.p. 74.5°, also passes to liquid crystalline phase some 15° below its melting point, T_{pen} = 60.5°, but α-hydroxypalmitic acid, m.p. 60.5°, requires heating to its melting point at which melting of the solid and penetration of water to give liquid crystalline phase occur simultaneously. Lecithin shows the same phase change in water at room temperature. Nonionic soaps such as Triton X45 and X100 also form a binary liquid crystalline phase with water although the two O atoms are separated by two methylene groups. 1,6-Hexamethylene glycol does not show this behavior. 1-Monolaurin at 40° continues to take up water to form a single liquid crystalline phase until about 35% is reached; this works out at 8.3 molecules of water per molecule of monoglyceride or about four per OH group. When further water is added, the system becomes a dispersion of liquid crystalline phase in water; this has been followed down to 0.4%. Below T_{pen} it becomes solid in liquid water. With bile acid salts, a ternary liquid crystalline phase is based upon the binary monolaurin one as in the case reported by us for octylamine with soap and water.[6] In the latter case, there is also the binary soap liquid crystalline range, and the ternary one forms a band across the triangular diagram. The bile acid salts do not form a binary liquid crystalline phase.[7]

Table I[a]: 1-Monoglycerides

	α-Form[b]		β-Form[b]	
	M.p., °C.	T_{pen}, °C.	M.p., °C.	T_{pen}, °C.
1-Monocaprin	27	<<Room temp.	52.5	27.5
1-Monolaurin	44	<Room temp.	62.5	40
1-Monomyristin	56	34	69	49.5
1-Monostearin	74	60.5	81.5	65

[a] We are indebted to Unilever Ltd. for these pure specimens whose melting points show good agreement with literature values; we are also grateful to Unilever Ltd. for the specimen of very pure dodecanol. [b] The β-form is obtained by crystallization from a solvent and the α-form from melts.

The Systems Monoglyceride–Fatty Acid–Water

The T_{pen} for water forming liquid crystalline phase with monolaurin of 40° is about 104°F., and the property would seem to be of no importance *in vivo*. However, under such conditions, there may also be present two molecules of fatty acid from whatever triglyceride the monoglyceride was formed. Examination of the binary system monolaurin and lauric acid showed eutectic formation (Fig. 8) and a lower T_{pen} eutectoid. The steep fall on the left-hand side is defined by K_f for the monoglyceride; from the known small change of ΔH_f of aliphatic series, we can predict that all monoglycerides will have similar slopes. The small fall on the right-hand side is bogus in that the solid separating is not pure fatty acid; all that one can predict is that the higher the freezing point (f.p.) of the acid, the nearer one will get to the genuine fall so that the higher fatty acids should show increasingly steep fall, and that oleic with its low freezing point will be flattest. The T_{pen} curve reminds us of our pair of stearic and palmitic acids which form a eutectic and a lower eutectic for T_{pen} by soap solution.[1] In that case, as in this, the two minima were for the same composition. In Fig. 8 the minimum is a little less than one molecule of lauric acid per molecule of monolaurin, which is 42.2%.

In vivo, we shall have not only the $-\Delta T$ due to the primary monoglyceride–fatty acid eutectic, but we shall have mixtures of monoglycerides with their $-\Delta T$; fatty acids are all different, and there will be another $-\Delta T$ on that side of the graph, and, finally, the presence of bile acid salts will lower T_{pen} by yet another

(5) A. W. Ralston, *J. Am. Chem. Soc.*, **64**, 1516 (1942).

(6) A. Hofman, *Biochem. Biophys. Acta*, **70**, 306 (1963); R. Collison and A. S. C. Lawrence, *Trans. Faraday Soc.*, **55**, 662 (1959).

(7) R. Vold and J. W. McBain, *J. Am. Chem. Soc.*, **63**, 1296 (1941).

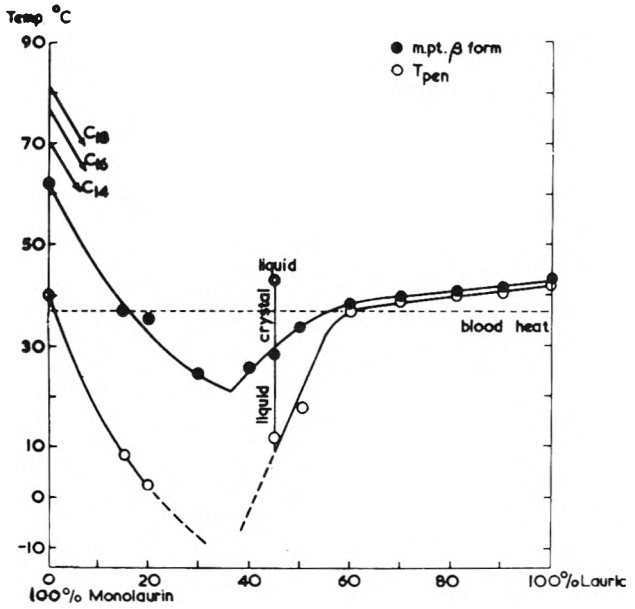

Figure 8. Melting point and T_{pen} for the binary system, monolaurin–lauric acid.

$-\Delta T$ increment. In the absorption of fats in man, his blood temperature is the only one that matters, and the sum of all the trends suggest that mixtures of up to two molecules of fatty acid per monoglyceride for any of them and their combinations will be in the labile liquid crystalline state at blood heat. We do not yet know the upper limit at which the liquid crystalline phase melts to isotropic liquid, except for the single value shown in Fig. 8, but it is probably nearly parallel to the T_{pen} curve.

It has been shown that the processes of absorption of fats involves polar solubilization of the amphiphilic monoglyceride, and its two fatty acid molecules enzymatically split off from the fat, any unhydrolyzed triglyceride remaining undissolved. In view of the well-known enhancement of nonpolar solubilization by amphiphiles, this fractionation needs explanation. The penetration of water into the monoglycerides plus fatty acids is a transition from very poor solubility of the monoglycerides in other fats to the labile liquid crystalline state coupled also with the eutectic lowering of freezing points which brings all the substances into this physical state at body temperature over a wide range of concentration. Whatever the importance of these physical changes and the mechanism by which the solubilization is terminated and the bile acid salts liberated, we still need physiological evidence of the loci of these changes. Since the bile acids are weak ones, more attention to pH changes seems needed.

Monoglycerides have been used widely, usually with a small amount of soap, and it has been suggested that monostearin crystallizes out as solid in the oil droplets. Indeed, it is reported that this separation is reduced if fatty acid is added to the monoglyceride, and it is suggested that it acts by enhancing formation of a protein interfacial layer.[8] Clearly, the temperature of the transition of the monostearin (plus fatty acid and soap which will pull it down) should be determined, but if water penetrates, why not protein with it? It has seemed most improbable to us, for some time, that triglycerides could possibly interact with proteins to form lipo protein, and the most likely form in which the fat could act would be as phosphatide. Now it seems likely that the monoglycerides could do this provided that they were above their natural T_{pen} or had had this reduced by fatty acids or even by lecithin.

The Bile Acid Salts

All the phenomena so far discussed are obviously connected with hydrogen bonding, and it is of interest to see that bile acid salts are not truly soaps because of the OH groups in the hydrocarbon part of the molecule. G. M. Rowles has made a study in our laboratory of sodium cholate, sodium taurodesoxycholate, sodium glycodeoxycholate, and sodium taurocholate with octanol and water. Each of these substances contains two or three OH groups, and the result is that, for solubilization, they are hydrotropes rather than soaps and that the large ring system is equivalent to only C_7 paraffin chain. On the other hand, they have the low critical micelle concentrations characteristic of soaps.

Discussion

It seems that we have a whole group of amphiphiles whose hydrophobic part is large enough to make them almost insoluble in water but in which considerable amounts of water can dissolve. The log of solubility in g./100 ml. of the alkanols from C_4 to C_8 gives a linear plot against C_n; that is over a range of solubility of *ca.* 8% down to 0.07%, but not for the inverse solubility. The partially miscible substances such as butanol and aniline are notably less soluble in water whan water is in them. On heating, the solubility of butanol decreases slightly in water, reaching a minimum at about 55°. The lower amines are miscible with water at sufficiently low temperatures but show a lower consolute temperature on heating, *e.g.*, NEt_3 and nicotine.[8] Some, such as dipropylamine, are not miscible with water at 0° because their lower consolute temperatures are below zero; this is shown by addition of soap which lifts them into sight. Upper consolute temperatures above T_{crit} of water can also be brought down, *e.g.*,

(8) M. J. Hayes, "Rheology of Emulsions," P. Sherman, Ed., London, 1963, p. 139.

0.74 *M* CTAB lifts the lower consolute temperature of 50–50 diisopropylamine and water from 27 to 169°, and the upper consolute temperature has been lowered to 212°.[9] Octylamine and its higher homologs form a binary liquid crystalline phase with water,[5,10] but this property seems to require two oxygens as either diol, α-hydroxy acid or monoglyceride. With one oxygen we get the rise or fall of melting points as described for the fatty acids and alcohols. In general, it seems that, where a liquid crystalline phase forms, its upper limit of transition to isotropic solution of water is above the melting point of the anhydrous substance.

The ethylene oxide chain nonionic soaps are interesting insofar as the two O groups are separated by two carbon atoms but nevertheless form a binary liquid crystalline phase with water. The lower consolute temperature *vs.* composition curve for the system Triton X45 is strikingly similar to the unusual one given by octylamine; both show elevation by soap, and C_{12}-TAB greatly increases the thermal stability of the liquid crystalline phase, *i.e.*, the longer hydrophobic chain effect. With the nonionic soap, urea acts as a peptizer for low nonionic soap concentrations, but as an H-bond competitor above about 60%. The most interesting feature of this work is the direct link between the monoglycerides and the phosphatides, and between the cerebrosides and sphingomyelin. None of these is soluble in water; water dissolves in all of them showing myelins and forming a binary liquid crystalline phase.[10] Presumably lecithin is, like monolaurin, an emulsion of liquid crystalline phase in water, down to the lowest concentrations; its T_{pen} would appear to be below room temperature, but synthetic lecithins containing the saturated fatty acids might be expected to show a T_{pen} above room temperature for the higher ones. The solid monohydrates of cholesterol and *p*-toluidine seem to be separate from the cases discussed here; they are stoichiometric and must depend upon considerations of packing in the crystalline state, even if attachment of the water involves hydrogen bonding. Walker has shown that the vapor pressure curve *vs.* temperature for *p*-toluidine shows no break down to 5°.[11]

(9) D. Langbridge, A. S. C. Lawrence, and R. Stenson, *J. Colloid Sci.*, 11, 585 (1956).

(10) Unpublished work from this laboratory.

(11) R. J. Friswell, *J. Soc. Chem. Ind.*, 27, 253 (1908); L. Lewy, *Ber.*, 19, 2728 (1886); J. Walker and H. H. Beveridge, *J. Chem. Soc.*, 91, 1797 (1907).

The Effect of Varying Centrifugal Field and Interfacial Area on the Ultracentrifugal Stability of Emulsions[1,2]

by Robert D. Vold and Robert C. Groot

Department of Chemistry, University of Southern California, Los Angeles, California 90007
(Received April 4, 1964)

The steady-state rate at which oil separates from 50 vol. % emulsions of Nujol in water stabilized with 0.2 or 0.4% sodium dodecyl sulfate and the quantity separating rapidly near the beginning of ultracentrifugation were determined as a function of ultracentrifugal speed and of specific interfacial area. The rate of separation of oil is directly proportional to the strength of the applied centrifugal field and varies inversely with the specific interfacial area of the emulsion. The data obtained are consistent with the hypothesis that the observed rate of separation of oil is a measure of the rate of coalescence between the polyhedral "drops" in the flocculated emulsion layer and the bulk oil phase. The initial rapid separation of a considerable quantity of oil near the beginning of ultracentrifugation is attributed to initial distortion of the drops with temporary excessive increase in area as they transform from spherical to polyhedral shape.

Introduction

Despite recent utilization[3-7] of the analytical ultracentrifuge to study creaming and coalescence phenomena in emulsions, there is still considerable uncertainty as to the locus of coalescence and the nature of the rate-determining step in the process. In the present experiments the effect was determined of changing the average drop size and the ultracentrifugal speed on the steady-state rate of separation of oil from an emulsion and the quantity separating rapidly on commencement of centrifugation. The data obtained support the view that the rate of appearance of oil under these experimental conditions is indeed a measure of the intrinsic rate of coalescence rather than a reflection of the rate of transport of either oil or aqueous phase through the flocculated emulsion. The results on the effect of change in interfacial area find further application in predicting the effect of changes in emulsification technique, since these usually result in changes in area with consequent changes in adsorption of surfactant and in ultracentrifugal stability.

A limited direct microscopic determination of size distribution in these emulsions was also undertaken to confirm the inferences drawn from the results of determinations of interfacial area.

Experimental Methods and Materials

The same sample of Nujol was used as in previous work.[5] Except where otherwise specified, a purified preparation of SDS (Princen II) was used as before.[7]

Ultracentrifugal and Adsorption Studies. The steady-state rate of separation of oil from emulsions in an ultracentrifugal field and the amount of oil separating rapidly near the beginning of centrifugation (extrapolated per cent oil separated at zero time) were determined as described previously.[5-7] In an attempt to improve the reproducibility in the present experiments, two batches of emulsion were always prepared as similarly as possible and then combined to make a

(1) This is a partial report of work done under contract with the U. S. Department of Agriculture and authorized by the Research and Marketing Act. The contract was supervised by the Northern Utilization Research and Development Division of the Agricultural Research Service.

(2) This work was reported in part at the Kendall Award Symposium of the Division of Colloid Chemistry at the 147th National Meeting of the American Chemical Society at Philadelphia, Pa., April, 1964.

(3) E. R. Garrett, *J. Pharm. Sci.*, **51**, 35 (1962).

(4) S. J. Rehfeld, *J. Phys. Chem.*, **66**, 1966 (1962).

(5) R. D. Vold and R. C. Groot, *ibid.*, **66**, 1969 (1962).

(6) R. D. Vold and R. C. Groot, *J. Soc. Cosmetic Chemists*, **15**, 233 (1963).

(7) R. D. Vold and R. C. Groot, *J. Colloid Sci.*, **19**, 384 (1964).

single sample, each being made from 150 ml. of Nujol and 120 ml. of 0.2% sodium dodecyl sulfate (SDS) solution, with subsequent incorporation under conditions of minimum agitation of additional SDS solution to give any desired total concentration and a 50–50 oil–water volume ratio. Specific interfacial areas were determined from the adsorption isotherms of a set of emulsions of the same drop size distribution but varying initial concentrations of SDS from 0.2 to 0.6%, assuming a limiting area per adsorbed molecule of 50 Å.^{2}.

Characterizing data on the emulsions used are given in Table I. Attention is called to the large differences in equilibrium concentration of SDS in the aqueous phase of emulsions of the same initial composition, resulting merely from changing the number of times the emulsion was passed through the homogenizer and sometimes occurring with different samples given the same preparative treatment. Since the stability of the emulsion is very sensitive to changes in the equilibrium concentration of emulsifier this may well account for the occasional poor reproducibility of behavior of emulsions assumed to be identical because of identical initial composition and similar preparative technique. It was noted that the effectiveness of the homogenizer decreased with age. Initially the molar concentration of SDS in the equilibrium aqueous phase was 3.7×10^{-3} after four passes through the homogenizer and 1.6×10^{-3} after twelve passes, while after a year many more passes were required to reach similar concentrations. With these emulsions, if the initial concentration of SDS was 0.2%, the concentration of SDS in the equilibrium phase was always below the critical micelle concentration (c.m.c.) while, if it was 0.4%, the equilibrium concentration was above the c.m.c.

Table I: Characterizing Data on the 50 Vol. % Nujol–Water–SDS Emulsions Used and Ultracentrifugal Stability at 39,460 R.p.m.

Emulsion	Specific interfacial area, cm.^{2} $\times 10^{-4}$/ml. of oil	Initial concn. of SDS, %	Equil. concn. of SDS in aq. phase, moles $\times 10^4$/l.	Fraction of saturation adsorption	Rate of oil sepn., %/min.	Extrapolated % oil sepn. at zero time
3-012122	1.14	0.2	3.92[a]	..	0.67	17
2-020607	1.64	0.2	3.45	0.64	0.63	24
1-092122	1.92	0.2	3.00	0.64	0.55	25
1-110708	1.85	0.2	2.84	0.66	0.50	21
2-010910	1.93	0.2	2.78	0.65	0.49	23
2-120506	2.66	0.2	2.00	0.56	0.27	21
2-121213	2.56	0.2	1.94	0.59	0.32	22
2-101819	1.97	0.2	3.30	0.56	..	..
2-081617	1.58	0.2	3.17	0.71	0.54	18
2-082728	1.70	0.2	3.21	0.66	..	..
2-112829	1.62	0.2	3.34	0.67	..	..
2-082021	1.64	0.4	3.13	0.90	..	..
2-082122	1.92	0.4	2.89	0.85	..	..
2-102425	1.71	0.2	3.04	..	0.42	20

[a] The concentration in this case was determined from a master plot of area *vs.* concentration in the aqueous phase of the 0.2% SDS system (ref. 5) since this particular experimental point was clearly in error. Ultracentrifuge runs were made at only this one concentration with this emulsion.

With emulsions containing an initial concentration of 0.2% SDS in the aqueous phase, the steady-state rate of separation of oil was usually reached after 10 to 20 min. of centrifugation, with no obvious dependence of the time on centrifugal speed between 12,500 and 56,100 r.p.m. As the initial concentration of SDS in the aqueous phase was increased, the time required to reach a constant rate of oil separation at 39,460 r.p.m. increased, leveling off at 35 to 45 min. at initial concentrations such that the equilibrium concentration was above the c.m.c.

Microscopic Technique. Brownian motion was avoided, and a suitable number of drops were obtained in the microscopic field by diluting the emulsion appropriately with a 10% gelatin solution containing the same concentration of SDS present in the equilibrium aqueous phase of the emulsion. Direct magnifications of 430 and 970 were obtained using a microscope with a calibrated scale, with photographic enlargement to 1000 and 2000, respectively. The number of drops in each size class, taken in 1-μ steps, was then determined by measurement of the diameters of the drops on the photographs, generally measuring a total of about 350 drops in three different fields. In almost all cases reasonably good straight lines were obtained when the data were plotted according to the usual log normal distribution curve

$$F(D) = \frac{1}{\ln \sigma_g \sqrt{2\pi}} \int_{-\infty}^{\ln D} \exp\left[-\frac{1}{2 \ln^2 \sigma_g} \times (\ln D - \ln D_{50})^2 \right] d \ln D$$

This permits comparison of the size distribution of different emulsions in terms of the two parameters of this curve, σ_g and D_{50}. D_{50} is the geometric mean diameter (the diameter of the drop of which the logarithm is the mean value of the logarithms of all the drops), and $\sigma_g = D_{84}/D_{50}$ and is a measure of the width of the distribution. Because of the relatively small number of drops counted, the precision obtained was not high, the uncertainty being about $\pm 10\%$ in the average value of D_{50} in the case of seven supposedly identical preparations.

Results

Microscopic Observations. It is of interest to compare the drop size obtained by direct microscopic observation with that calculable from the specific interfacial area. In the case of a Nujol–water–SDS (50–50–0.2%) emulsion, the mean diameter was 3.2 μ and the standard deviation of the logarithmic distribution, σ_g, was 1.75. A similar emulsion having a specific interfacial area of 1.9×10^4 cm.^{2}/ml. of oil would have a number average drop diameter (D_{50}) of 3.16 μ if it were monodisperse. That the two results are in apparent agreement shows that all the smaller drops were not detected and counted microscopically, since, for the present polydisperse emulsion, the area average diameter should have been about twice as large as the number average diameter. The microscopically determined average diameter is useful nevertheless for direct comparison of similar emulsions and for rough correlation of the specific interfacial area with an actual drop size distribution.

The microscopic observations serve to confirm directly that our procedure of blending a more concentrated SDS solution into a previously prepared emulsion stock is accomplished without changing the size distribution. Thus, the values of D_{50} and σ_g obtained on a Nujol–water–SDS (50–50–0.4%) emulsion prepared by adding more concentrated SDS solution to a 0.2% emulsion were 3.4 μ and 1.75, respectively, compared to 3.2 μ and 1.80 on the initial stock.

In earlier work[5] it was found that the rate of separation of oil from Nujol–water–SDS (50–50–0.2%) emulsions was faster the purer the SDS and that the interfacial area of these emulsions changed only slightly with time. Since we have now shown that the ultracentrifugal stability decreases with decreasing interfacial area, it is not surprising to find the average drop diameter in such an emulsion decreased from 3.2 to 2.3 μ when Fisher Scientific Co. technical SDS was used instead of a pure product. This effect is also in the same direction as that anticipated from the nature of the probable impurities in the technical product.[5] The drop size in Nujol emulsions was not determined as a function of age, but none of a series of 20% heat-bodied linseed oil (M37 oil)–80% water–1% technical SDS emulsions showed any systematic change in average drop size with time over periods up to 1 month.

With emulsions made by mechanical mixing followed by fourfold (or more) passage through a Cenco hand homogenizer, the drop size obtained decreased with decreasing viscosity of the oil. For example, in one set of observations D_{50} was found to be 8.6 μ for an M37 oil–water–technical SDS (20–80–0.5%) emulsion, 2.2 μ for a Nujol–water–technical SDS (50–50–0.2%) emulsion, and too small to size in a cetane–water–technical SDS (50–50–0.5%) emulsion even at a magnification of 970. The average drop size in the Nujol emulsion was reduced by successive passes through the homogenizer, but that in the M37 oil emulsions was not changed by this treatment.

Dependence of Stability on Interfacial Area. The dependence of the ultracentrifugal stability of Nujol–water–SDS emulsions on the interfacial area—and hence on the average drop size—is shown in Fig. 1, the data for emulsions B being taken from earlier work.[5] In agreement with previous results, the rate of separation of oil is seen to decrease rapidly with increasing equilibrium concentration of SDS in the aqueous phase, irrespective of the interfacial area of the emulsion, and to become constant or decrease only slowly after the equilibrium concentration exceeds the c.m.c. It is also apparent that the rate of separation of oil decreases as the interfacial area of the emulsion increases and therefore as the average drop size decreases.

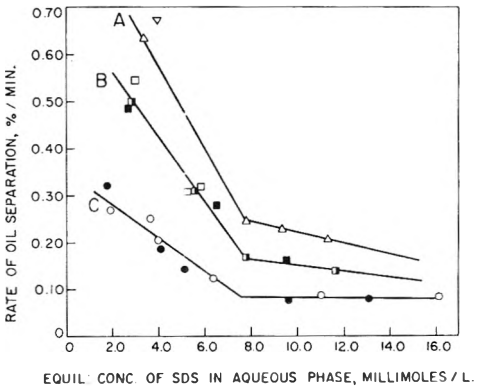

Figure 1. Dependence of the rate of oil separation at 39,460 r.p.m. on the equilibrium concentration of SDS in the aqueous phase of Nujol–water–SDS (50–50–0.2%) emulsions of different specific interfacial area. The emulsions and their respective specific interfacial areas (cm.^{2}/ml. of oil $\times 10^{-4}$): A, △, 1.64; B, □, 1.92; B, ◨, 1.85; B, ■, 1.93; C, ○, 2.66; C, ●, 2.56; —, ▽, 1.14.

This is brought out clearly in Fig. 2, which shows the rate of separation of oil at three different equilibrium concentrations of SDS below the c.m.c. as a function of the specific interfacial area of the emulsion. At 0.0039 *M* SDS the rate appears to decrease very nearly linearly with increasing area. At higher concentrations, the rate also decreases regularly with increasing area, but apparently less than proportionally at high areas.

It should be emphasized that, in making these comparisons, the rates for emulsions of different specific area can be compared only at equal equilibrium concen-

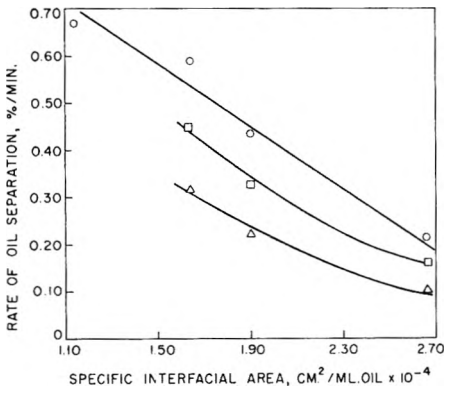

Figure 2. Dependence of the rate of oil separation at 39,460 r.p.m. at equal equilibrium concentrations of SDS in the aqueous phase on the specific interfacial area of Nujol–water–SDS (50–50–0.2%) emulsions. Comparisons made at 0.0039 *M*, ○; 0.0055 *M*, □; 0.0070 *M*, △.

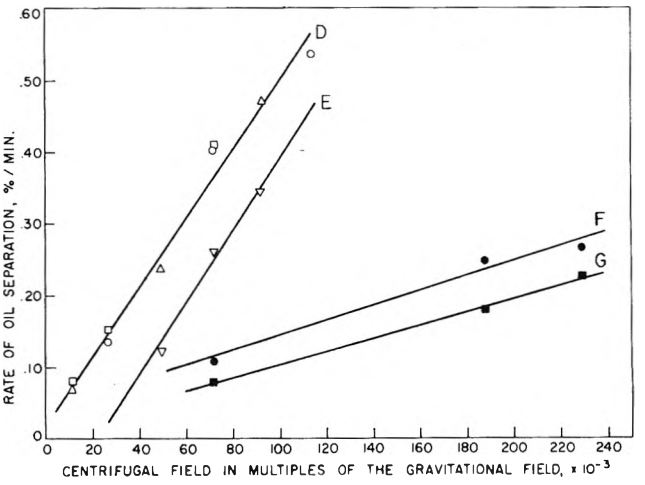

Figure 3. Dependence of the rate of oil separation from 50 vol. % Nujol–water–SDS emulsions on the applied centrifugal force. The aqueous phase of emulsions D and E contained initially 0.2% SDS; F and G, 0.4% SDS. The emulsions and their respective specific interfacial areas (cm.²/ml. of oil × 10^{-4}): D, ○, 1.58; D, △, 1.62; D, □, 1.70; E, ▽, 1.97; F, ●, 1.64; G, ■, 1.92.

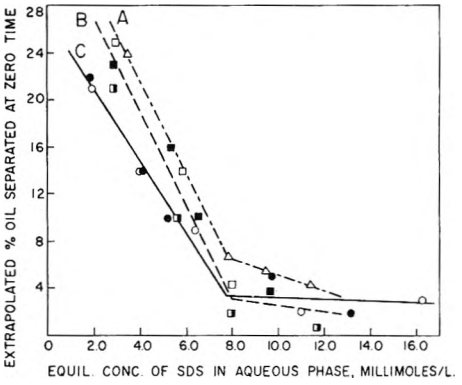

Figure 4. Dependence of the extrapolated per cent oil separated at zero time at 39,460 r.p.m. on the equilibrium concentration of SDS in the aqueous phase of Nujol–water–SDS (50–50–0.2%) emulsions of different specific interfacial area. The emulsions and their respective specific interfacial areas (cm.²/ml. of oil × 10^{-4}): A, △, 1.64; B, □, 1.92; B, ◪, 1.85; B, ■, 1.93; C, ○, 2.66; C, ●, 2.56.

trations of SDS. Only under these conditions will there be the same fractional saturation of the interface with adsorbed SDS, and it has been shown that the stability is directly proportional to the extent of coverage of the interface with adsorbed emulsifier.[7] Thus, a finer emulsion may appear to be less stable than a coarser one if direct comparison is made of the two prepared with the same initial concentration of stabilizer, because of the lower equilibrium concentration resulting, in the first case, from the larger quantity going to the interface. This explains the seemingly anomalous observation that a Nujol–water–technical SDS (50–50–0.2%) emulsion, prepared by the standard method using the homogenizer, separated oil at a steady-state rate of 0.074%/min. at an ultracentrifugal speed of 25,980 r.p.m., while an identical system, prepared using only mechanical stirring, had separated no oil after 30 min. of ultracentrifugation.

The data of Fig. 3 on effect of centrifugal field on ultracentrifugal stability provide further confirmation that the rate of oil separation from the emulsion decreases as the specific interfacial area increases. Here, however, since determinations were not carried out at a series of different initial concentrations of SDS, it is not possible to compare the rates quantitatively at the same equilibrium concentration in the different emulsions.

It is evident from Fig. 4, despite the substantially poorer precision of the data,[5] that changing the specific interfacial area has a similar effect on the amount of oil separated rapidly near the beginning of centrifugation. The amount decreases rapidly with increasing concentration of SDS until the c.m.c. is reached and decreases only slowly thereafter. At equal equilibrium concentration of SDS, the emulsions of greater specific interfacial area separate less oil although the scatter in the data prevents any quantitative correlation between area and amount separated.

In agreement with previous results,[7] the rate of oil separation found in these experiments varied linearly with the fraction of the interface covered with adsorbed SDS, extrapolating to zero rate of separation at complete saturation.

Effect of Centrifugal Field. The centrifugal force was calculated from the speed at which the ultracentrifuge

was run by the relation, $f = (0.1047)^2 n^2 rg/980$, where f is the ultracentrifugal force in multiples of g, the force of gravity, r is the distance in centimeters from the center of rotation to the center of the cell, 980 is the acceleration of gravity, n is the speed in r.p.m., and 0.1047 is the factor converting r.p.m. to radians per second. Since the radius to the midpoint of the cell is 6.500 cm., the length of the cell is 14.1 mm., and the movement of the oil–emulsion boundary only a few mm., no consequential error is introduced by using the average field strength rather than the exact value at the boundary.

Figure 3 shows that in all cases the rate of separation of oil from any individual emulsion increases directly proportional to the increase in ultracentrifugal force. The different lines obtained with different emulsions of identical initial concentration of SDS clearly result from differences in the specific interfacial areas of the emulsions, the emulsions with the smaller average drop size separating oil less rapidly at both 0.2% and 0.4% initial concentration of SDS. However, the rate of change with centrifugal force seems to be about the same independent of area, the slopes of lines D and E for 0.2% SDS emulsions being, respectively, 4.80 and 5.02 $\times$ 10^{-6}%/min./g. while those of lines F and G for 0.4% SDS emulsions are 1.03 and 0.97 $\times$ 10^{-6}%/min./g. Since these slopes are probably uncertain to about 5 to 6% because of the relative paucity of points, the values for each pair should probably be regarded as being the same within experimental error.

In addition to their theoretical value with respect to deducing the mechanism of the process, these results are also of considerable practical utility since they permit calculation of the rate of separation of oil to be expected at any centrifugal speed from the value obtained at a single speed.

Earlier, less systematic data obtained throughout the course of these studies in general had also indicated a linear relation between centrifugal field strength and steady-state rate of separation of oil. Thus, a different Nujol–water–SDS (50–50–0.2%) emulsion run at 39,460, 19,160, and 12,590 r.p.m. also gave three points on a line when the ultracentrifugal stability was plotted against the centrifugal force. Still earlier experiments with Nujol–water–technical SDS (50–50–1.0%) emulsions carried out with 38-g. samples of emulsion in 50 ml. of cellulose nitrate or nylon centrifuge tubes in a Servall SS-1 high speed angle centrifuge at speeds of 5000 to 13,500 r p.m. also gave a linear relation between the rate of separation of oil and the square of the speed of rotation. In these experiments the volume of oil separated was determined by separation of the layers in a separatory funnel after ultracentrifugation, followed by clarification and measurement of the volume of separated oil after low speed centrifugation in a basket-type centrifuge. This method was ultimately abandoned, however, because of failure to obtain reproducible results consistently. The only exception to the linear relation was a set of data on Nujol–water–technical SDS (50–50–0.2%) emulsions run at different speeds in the ultracentrifuge and reported in ref. 5, where the rate of increase of separation of oil seemed to be less at high speeds than would be required by a simple direct proportionality.

Figure 5 shows that the amount of oil separating rapidly during the first few minutes of ultracentrifugation is also directly proportional to the applied field strength. Here, however, the data are so much less precise that all the results with 0.2% SDS emulsions are best represented by a single line (DE) while those with 0.4% SDS fall on a different line (FG). The much greater protection against rapid separation of considerable oil conferred by the higher concentration of emulsifier in the aqueous phase is also clearly evident from this figure.

Discussion

There has been considerable question[3,5,7] concerning the mechanism of oil separation from an emulsion subjected to centrifugation, particularly as to the location where coalescence occurs leading to separation of observable bulk oil, the nature of the rate-determining step in this process, and the cause of the initial separation of a considerable quantity of oil at a rate much faster than the steady-state rate. The present data permit formulation of a more detailed analysis of these questions differing in some respects from that proposed previously.

Locus of Coalescence. The presently available evidence supports the view that coalescence in the centrifuging emulsion occurs at a rate significant compared to the duration of the experiment only at the interface between bulk oil and the flocculated emulsion, and that the observed rate of appearance of bulk oil is a measure of the rate of this coalescence. The constancy of the rate of separation of oil independent of the length of the column of flocculated emulsion during an experiment argues against the wall or the interior of the emulsion being the site of coalescence and also against the occurrence of stratification of drops according to size, since this would result in differing specific interfacial area at different depths in the emulsion with resultant change in the rate with duration of centrifugation. Moreover, the rate of separation of oil was found to be the same in Kell-F and in aluminum centerpieces.

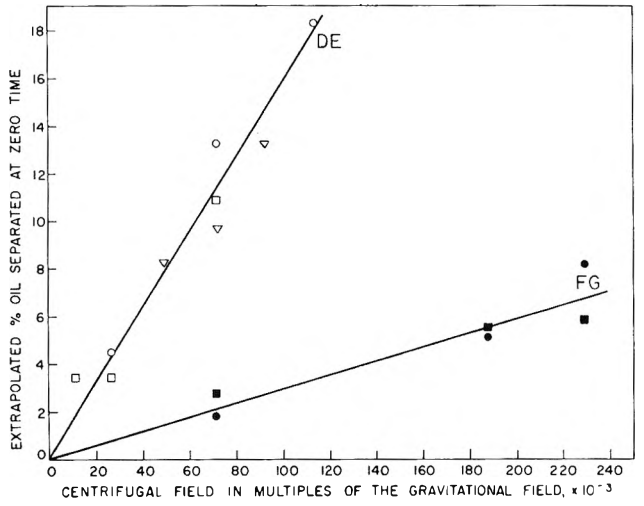

Figure 5. Dependence of the extrapolated per cent oil separated at zero time from 50 vol. % Nujol–water–SDS emulsions on the applied centrifugal force. The aqueous phase of emulsions D and E contained initially 0.2% SDS; F and G, 0.4% SDS. The emulsions and their respective specific interfacial areas (cm.²/ml. of oil $\times 10^{-4}$): D, O, 1.58; D, □, 1.70; E, ▽, 1.97; F, ●, 1.64; G, ■, 1.92.

The emulsion–water interface is an unlikely site for separation of oil, which would then have to be transported upward through the gel-like layer of flocculated emulsion counter to the downward flow of draining aqueous phase before joining the visible bulk phase on top. Moreover, the aqueous lamellae separating the oil drops would be thickest at the bottom of the column, and the probability of rupture decreases rapidly with increasing thickness.

Garrett's observation[3] that an emulsion resuspended after ultracentrifugation had the same "clearing time" on recentrifugation as the original emulsion is strongly indicative of the fact that appreciable coalescence is not occurring between "drops" in the layer of flocculated emulsion. However, this does not prove that the size distribution actually was unaffected but only that some of the same size of the smallest drops persisted unchanged. More significant is our finding that in a Nujol–water emulsion (2–102425) ultracentrifugation for 40 min. at 39,460 r.p.m. made no appreciable difference in the drop size distribution determined microscopically, D_{50} and σ_g being 2.9 μ and 1.66 before centrifugation and 2.7 and 1.65 after centrifugation. Further direct data on size distribution are needed, however, to fully establish this point.

That coalescence does not occur appreciably during centrifugation in the angle centrifuge used for separating the aqueous layer for analysis was already known.[7] Additional confirmation is furnished by the fact that a Nujol–water–SDS (50–50–0.2%) emulsion gave the same rate of oil separation in the ultracentrifuge at 39,460 r.p.m. with or without 15 min. prior centrifugation at 5000 r.p.m. in the angle centrifuge. If coalescence had occurred to a significant extent, the drop size distribution should have changed, with a consequent change in ultracentrifugal stability. Moreover, the reflectance of the emulsion layer in a Nujol–water–Triton X102 (50–50–0.25%) emulsion containing 0.017 g. of scarlet red/100 ml. of Nujol, which is proportional to the surface average diameter of the drops,[8] was the same after 1 and after 5 hr. of centrifugation in the angle centrifuge at 10,000 r.p.m.

There are grounds[7] for believing that, in the flocculated emulsion in the ultracentrifuge, the oil is present in space-filling polyhedra as in a foam, separated by thin lamellae of residual aqueous phase between the relatively flat surfaces, with a system of "holes" at the Plateau borders where the polyhedra meet. de Vries[9] has shown that in foams having a structure of this type the probability of collapse is greater, the smaller the thickness of the lamellae. Consequently, the bubble walls in the top layer of a foam are more liable to rupture than other lamellae because of their smaller thickness as a result of drainage under the influence of gravitation. By analogy, the same situation might be expected to occur with an emulsion in the ultracentrifuge since the aqueous lamellae separating the oil "drops" at the top surface would be expected to be thinner than those further down in the emulsion layer as residual water is spun out toward the bottom of the tube by the applied centrifugal field.

Rate-Determining Step in Separation of Oil. Based on the effect of salt on ultracentrifugal stability,[7] it was concluded that the rate of separation of oil from an emulsion in the ultracentrifuge was probably a measure of the rate of coalescence of "drops" with the bulk oil interface, determined by the extent of coverage of the interfaces with adsorbed SDS, the rheological characteristics of the adsorbed film, and the work required to rupture the adsorbed film of detergent and transport the oil through the residual water film. Neither the effect of drop size or ultracentrifugal field on the rate of separation of oil seem to provide much additional information concerning the details of this process.

The literature on the dependence of the probability of coalescence on drop size is rather confusing, some authors calculating or finding that it decreases with decreasing size[10] and others that it decreases with in-

(8) N. E. Lloyd, *J. Colloid Sci.*, **14**, 441 (1959).

(9) A. J. de Vries, *Rec. trav. chim.*, **77**, 383 (1958).

(10) E. G. Cockbain and T. S. McRoberts, *J. Colloid Sci.*, **8**, 440 (1953).

creasing size.[11,12] The situation is discussed most clearly by Charles and Mason[13] whose conclusion is that the stability of easily deformable drops should increase with increasing drop size but should decrease with drops which resist deformation. Since we are dealing here with relatively small drops with an adsorbed layer of SDS, it is perhaps not surprising to find that the stability decreases as the average drop size increases.

The approximately linear inverse dependence of the rate of oil separation on the specific interfacial area, and hence directly on the square of the average drop radius, r^2, suggests that coalescence may be occurring in a thin layer of bulk emulsion just below the bulk oil–emulsion interface as well as at the interface itself, even though the evidence already presented rules out extensive coalescence throughout the mass of the flocculated emulsion. This is not unreasonable since the water lamellae separating the dispersed oil would be expected to be thinnest at the top of the column.

If coalescence took place only at the interface, the observed rate of appearance of oil would be expected to depend on the number of drops in contact with the interface, which would be proportional to $1/r^2$ and remain constant. Next it might be assumed that the probability of coalescence depends only on the area of contact—a somewhat questionable assumption in the case of a polydisperse system since it does not allow for variation in rate of approach of the drop to the interface or of probability of rupture of the intervening water film with drop radius. On such a model the volume of oil released to the bulk phase due to coalescence of drops should, contrary to Fig. 2, vary with the cube of the drop radius since the volume of oil obtained on bursting a single drop is proportional to its volume and hence to r^3.

If, however, coalescence is occurring over a finite volume of the emulsion layer, consideration of the change of volume and surface with drop radius leads to the prediction that the rate of appearance of bulk oil should be inversely proportional to the specific interfacial area and hence directly to r^2. For the number of drops per volume element of emulsified oil is proportional to $1/r^3$ and the area per drop to r^2, resulting in a dependence of the specific interfacial area on $1/r$. Since the volume of oil released by a drop is proportional to r^3, the net effect is an over-all dependence on r^2. The data obtained tend to favor this view although they are not sufficiently extensive or unambiguous to permit a definitive decision. The real situation may be further complicated if stepwise coalescence occurs in the centrifugal field as is the case with coalescence under gravity.[13]

Intuitively it would be expected that as "drops" were pressed together harder by a stronger centrifugal field that oil would be squeezed out faster, and indeed Fig. 3 and 5 show that both the rate of separation of oil and the amount of oil lost rapidly near the beginning of ultracentrifugation increase directly proportional to the increase in centrifugal force. However, since the rate of sedimentation according to Stokes' law, the rate of Poiseuille flow, and the rate of viscous flow between infinite parallel planes all vary directly with the applied force, this in itself tells us little about the mechanism. If the distance of separation of the flattened polyhedral surfaces of the oil "drops" in the ultracentrifuge were determined by an equilibrium involving the centrifugal pressure and the electrostatic repulsion between the planes[14]—as actually seems unlikely in view of the unrealistically small calculated distance of the resultant spacing[7]—this distance would depend on a function in which the hyperbolic cosine varies directly with the applied pressure. Hence, the observed linear relation between applied centrifugal field and rate of oil separation constitutes further evidence that the rate of drainage of water from interlamellar films whose thickness is determined by the electrostatic repulsion due to the charge at the two interfaces is not the rate-determining step in the process.

Initial Rapid Separation of Oil. Frequently the absolute quantity of oil separated by supposedly identical emulsions after equal periods of ultracentrifugation differs widely,[5] because of considerable differences in the quantity of oil separated in the first 10 min. or so of centrifugation, even though the same steady-state rate of separation of oil is reached eventually. This effect was first attributed to the presence of a small amount of poorly dispersed oil or to lack of representative sampling. The direct proportionality now found between the amount of this rapidly separated oil and the applied centrifugal field (Fig. 5) shows that this is not a sufficient explanation, since different samples of the same emulsion should contain the same proportion of abnormally large oil drops and therefore separate the same amount of oil rapidly independent of the applied field.

It is now proposed[15] that the initial rapid separation of oil is due to irregular distortion of the originally spherical drops on application of the ultracentrifugal field, with resultant increase in area, as they are transformed to polyhedral shape. During this time there

(11) T. Gillespie and E. K. Rideal, *Trans. Faraday Soc.*, 52, 173 (1956).

(12) H. M. Princen, *J. Colloid Sci.*, 18, 178 (1963).

(13) G. E. Charles and S. G. Mason, *ibid.*, 15, 236 (1960).

(14) J. Th. G. Overbeek, *J. Phys. Chem.*, 64, 1178 (1960), discusses an analogous situation in soap films and gives many references.

(15) M. J. Vold, personal communication.

may be insufficient SDS present to protect them with an adsorbed film, with resultant rapid coalescence followed by somewhat slower transport of the free oil to the bulk phase. This hypothesis is apparently able to account for all the observations.

The proportionality between the applied centrifugal force and the amount of oil separated rapidly would be expected since the extent of deformation of the drops should depend on the magnitude of the distorting field. However, as found experimentally, this would not be expected to be as reproducible as the steady-state rate of oil separation since it depends on a variety of mechanical and geometrical factors which are difficult to control.

This hypothesis also accounts for the observation[7] that two emulsions with the same relative saturation of the interface with adsorbed SDS, brought about in one case by a high equilibrium concentration of SDS in the solution, and in the other by the presence of sodium chloride in a solution containing a low concentration of SDS, separate very different quantities of oil rapidly near the beginning of ultracentrifugation. In the example cited the emulsion with the higher concentration of SDS separates less than one-third as much oil initially as that with the lower concentration, despite the near equality of surface coverage. This is easily understandable if there is a large temporary increase in interfacial area immediately on exposure to the ultracentrifugal field, since, in the former case, the reserve SDS present in the solution can be adsorbed and can protect against coalescence, whereas, where the initial coverage was due to enhancement of adsorption of SDS by addition of NaCl, there is insufficient SDS left in solution to protect the new surface. The rapid decrease in the quantity of oil separated rapidly with increasing concentration of SDS in the system also supports this interpretation.

Further support for this interpretation of the phenomena occurring at the commencement of ultracentrifugation is found in the results of experiments to be reported in detail elsewhere, in which centrifugation was interrupted after oil had been separating at a constant rate for a period and then restarted. A considerable quantity of additional oil separated rapidly when centrifugation was again started, which is in accord with expectation if the phenomenon is due to initial deformation of the drops but cannot be accounted for simply in terms of a certain quantity of easily separable oil in the initial emulsion.

Acknowledgment. The authors wish to express their appreciation to Beatrice Levy and Robert L. Vold who made most of the microscopic observations reported in this paper.

The Correlation between Phase Inversion Temperature In Emulsion and Cloud Point in Solution of Nonionic Emulsifier

by Kōzō Shinoda and Haruhiko Arai

Department of Chemistry, Faculty of Engineering, Yokohama National University, Minamiku, Yokohama, Japan
(Received February 5, 1964)

A model has been advanced in which it is proposed to regard the cloud point in solution of nonionic agent as akin to the phase inversion temperature in emulsion. In the latter, the mixing is macroscopic, whereas in the former the mixing is microscopic or on the bimolecular leaflet scale, and the agent serves as an oil as well as an emulsifier. Phase inversion temperatures in hydrocarbon–water emulsions stabilized with polyoxyethylene alkyl phenyl ether have been determined for different hydrocarbons as a function of emulsifier concentration. It was found that the more soluble the hydrocarbon for a nonionic emulsifier, the lower is the phase inversion temperature, above which O/W type emulsions invert to W/O type. A similar rule, that the more soluble the nonionic emulsifier for a definite hydrocarbon, the lower the phase inversion temperature, also holds. The effects of polyoxyethylene chain length and hydrocarbon chain length of the emulsifier on the phase inversion temperature have been studied. It was found that the cloud points in solutions of nonionic emulsifiers saturated with various hydrocarbons and the phase inversion temperatures in emulsions were parallel, which supports the present model. The effect of temperature on the emulsion stability in connection with the phase inversion temperature is briefly discussed.

Introduction

Nonionic emulsifying agents dissolve in water in a molecular dispersion up to the solubility limit, and above this concentration the excess agent separates to form a phase solution above the cloud point temperature.[1] Below the cloud point the agent forms micelles which are composed of about 100 agent molecules. Since these micelles are much smaller than the wave length of light, the solution is transparent and the solubility increases enormously. Although the micellar solution is transparent, the formation of micelles is a phenomenon similar to a phase separation.[2]

By analogy with the change in emulsion type at the phase inversion temperature, we may regard the change in the state of solution above and below the cloud point as follows. Above the cloud point a surfactant-rich phase containing dissolved water separates; at this volume fraction a nonionic detergent (D) mixes with water (W). The mixing is almost on the bimolecular leaflet scale and may be regarded as the W/D type. Also, the detergent-rich phase dissolves into water as bimolecular leaflets or micelles below the cloud point. Something similar to a phase inversion on the bimolecular leaflet scale takes place in a surfactant solution near the cloud point, and the solution inverts to the D/W type. Thus, the concentrated solution readily disperses or diffuses into a dilute solution. This phenomenon may be designated as a pseudo-phase inversion.[3]

If we shake a 1:1 mixture of water and nonionic agent, the latter dissolves or disperses into water, and the whole system becomes an aqueous phase of the D/W type below the cloud point, whereas above the cloud point the water dissolves or disperses in the agent phase until the water phase disappears, *i.e.*, mixes in the W/D type.

(1) R. R. Balmbra, J. S. Clunie, J. M. Corkill, and J. F. Goodman, *Trans. Faraday Soc.*, **58**, 1661 (1962).

(2) K. Shinoda and E. Hutchinson, *J. Phys. Chem.*, **66**, 577 (1962).

(3) K. Shinoda, *Bull. Chem. Soc. Japan*, **35**, 1213 (1962).

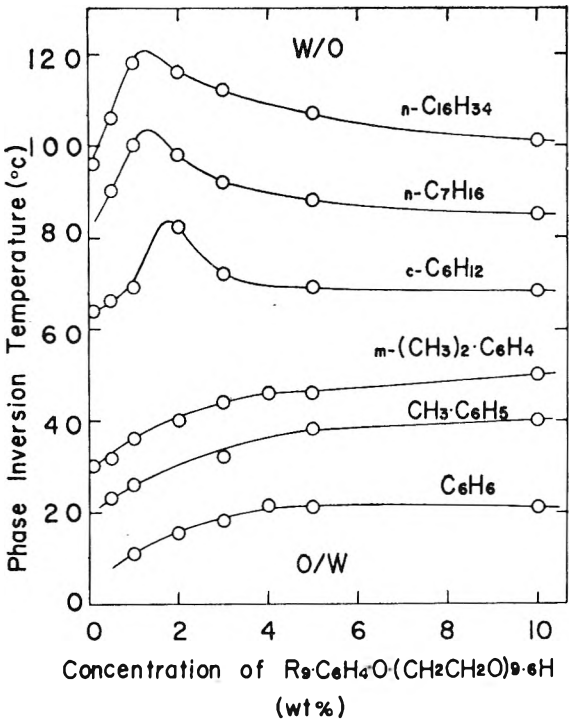

Figure 1. The effect of different hydrocarbons on the phase inversion temperature of emulsions (volume ratio = 1) *vs.* the concentration of polyoxyethylene(9.6) nonyl phenyl ether (wt. % in water).

A similar pseudo-phase inversion may occur near the cloud point in the presence of small amounts of added hydrocarbons, because the emulsifier molecules arrange side by side and end to end regardless of whether the mixing is of the D/W or W/D type. At the same time, the cloud point may be either raised or lowered by the presence of hydrocarbons. It was then expected that near the cloud point of the solution a phase inversion would occur from the O/W to the W/O type in an emulsion stabilized with a nonionic agent when the temperature was raised.

The present investigation was undertaken in order to obtain data on the phase inversion temperatures for various combinations of hydrocarbons and emulsifiers and to assure that the present model is correct. Although there are many works on emulsion type,[4,5] the data on the effects of temperature are meager.[6] It seemed very important to study the effect of temperature in order to eliminate confusions and get a better understanding of factors affecting the stability and type of emulsions formed. All other factors such as the phase volume ratio were held constant and only the temperature was changed to cause a phase inversion.

Experimental

Materials. Polyoxyethylene nonyl phenyl ether and polyoxyethylene (9.0) dodecyl phenyl ether were obtained from the Kao Soap Co. Samples were purified by extraction of polyethylene glycol into aqueous butanol solution.[7] These samples showed no pattern for polyethylene glycol on paper chromatographic analysis. The average chain lengths of the ethylene oxide adducts were determined from their respective hydroxyl values. Hexadecane and heptane were the standard fuels. Liquid paraffin (Drakeol 35) and dodecene (propylene tetramer) were commercial materials. Benzene, toluene, cyclohexane, and carbon tetrachloride were extra pure grade materials. Ethylbenzene, *m*-xylene, and α-methylnaphthalene were pure grade materials.

Procedure. Aqueous solutions of an emulsifier of varying concentration were placed in contact with equal volumes of hydrocarbons in test tubes and shaken vertically. Emulsion type was determined by conductivity, visual observation, dye solubility, and/or the phase dilution method. Since the emulsion was usually not stable near the phase inversion temperature, visual observation was easy and reliable

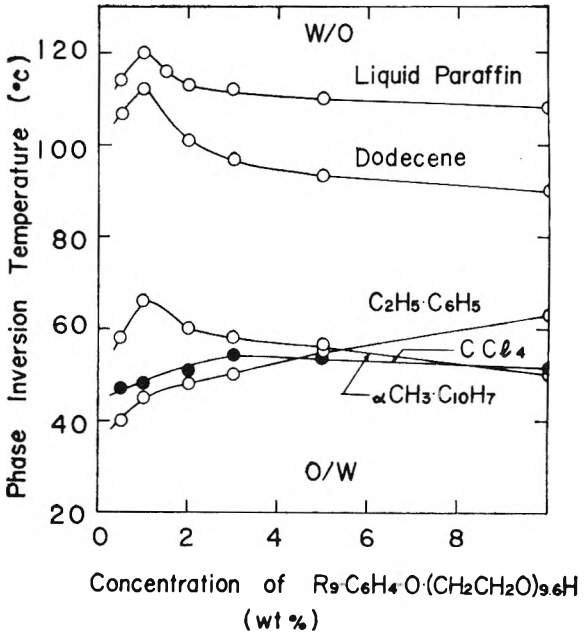

Figure 2. The effect of different hydrocarbons on the phase inversion temperature *vs.* the concentration of polyoxyethylene(9.6) nonyl phenyl ether.

(4) P. Becher, *J. Soc. Cosmetic Chemists*, 9, 141 (1958).
(5) J. T. Davies, *ibid.*, 12, 193 (1961).
(6) V. E. Wellman and H. V. Tartar, *J. Phys. Chem.*, 34, 379 (1930).
(7) K. Nagase and K. Sakaguchi, *J. Chem. Soc. Japan, Ind. Chem. Sect.*, 64, 635 (1961).

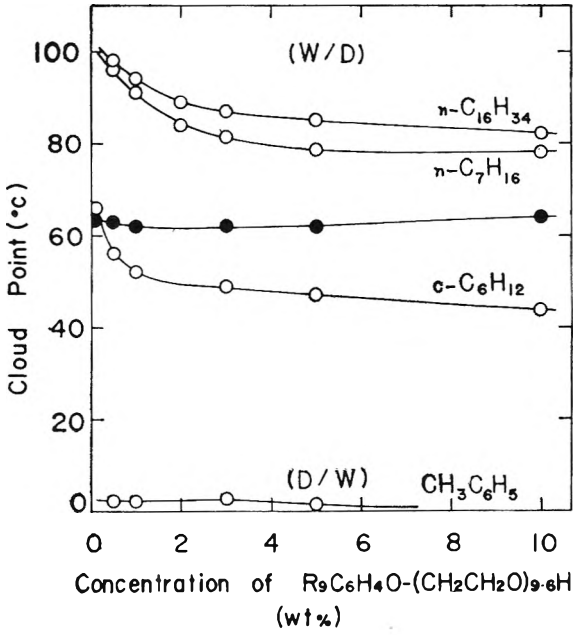

Figure 3. The cloud points of polyoxyethylene(9.6) nonyl phenyl ether solution saturated with different hydrocarbons. Filled circles express the cloud points in the absence of oil.

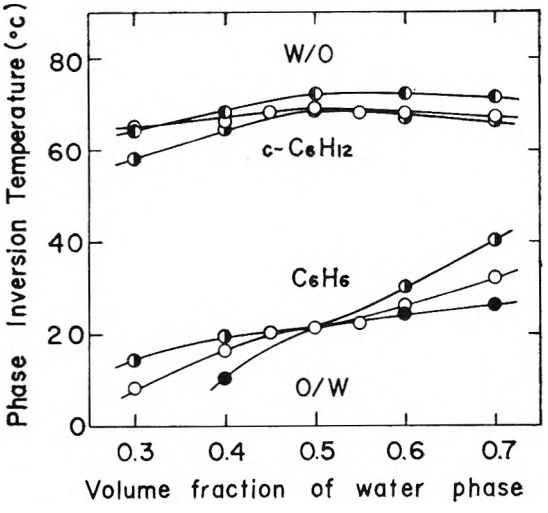

Figure 4. The effect of phase volume ratio on the phase inversion temperature for emulsions stabilized with i-$R_9C_6H_4O(CH_2CH_2O)_{9.6}H$; ◐, 3%; ●, 4%; ○, 5%; ◑, 10%.

in most cases studied. In cases when the phase inversion temperature was higher than the boiling point of oil or water, the emulsion type was determined by visual observation only in sealed test tubes. All the phase inversion temperature values reported are averages of several values. Experimental values were reproducible within ±2°. It was 1–2° lower in the case of horizontal shaking. Unlike the usual phase

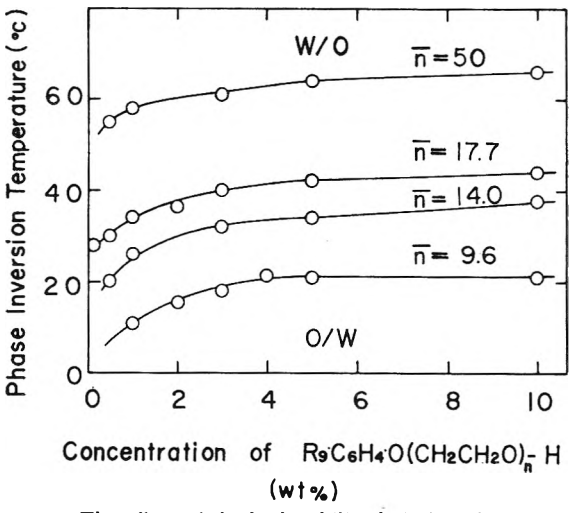

Figure 5. The effect of the hydrophilic chain length of the emulsifier on the phase inversion temperature in benzene–water emulsions (volume ratio = 1).

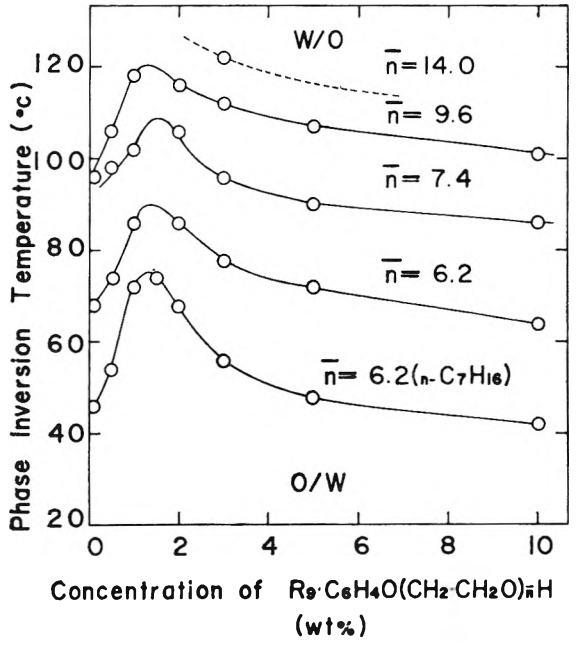

Figure 6. The effect of the hydrophilic chain length of the emulsifier on the phase inversion temperature in hexadecane–water emulsions (volume ratio = 1).

inversion study, only the temperature was changed to cause a phase inversion. The cloud points of emulsifier solutions saturated with various hydrocarbons were also observed. The values are not as accurate as the cloud points in the absence of hydrocarbons.

Results and Discussion

The Influence of Different Hydrocarbons on the Phase Inversion Temperature. The phase inversion temperature *vs.* the emulsifier concentration curves were de-

termined for different hydrocarbons and plotted in Fig. 1 and 2. The phase inversion temperature differs widely for different hydrocarbons. Benzene gave a phase inversion temperature of about 20° which was the lowest of any of the hydrocarbons examined. Polyoxyethylene(9.6) nonyl phenyl ether dissolved well in benzene at this temperature. On the other hand, hexadecane, which was the poorest solvent for the same emulsifier, gave the highest inversion temperature, about 110°. The more soluble the hydrocarbon for a definite nonionic emulsifier, the lower was the phase inversion temperature. This rule complements Bancroft's rule at a definite temperature. The cloud point curves in aqueous solutions saturated with different hydrocarbons were determined and plotted in Fig. 3. It was found that the cloud points and the phase inversion temperatures are parallel.

As the temperature had such a remarkable effect on the emulsion type in this system, it was expected that the change in phase volume ratio would not change the phase inversion temperature very much. Actually, it did not change much for a change of volume ratio from $^3/_2$ to $^2/_3$ as shown in Fig. 4.

The Effect of Hydrophilic Chain Length on the Phase Inversion Temperature. It was expected that the longer the hydrophilic chain, the higher the cloud point and/or the phase inversion temperature would be. This tendency was found in benzene–water and hexadecane–water systems using various polyoxyethylene nonyl phenyl ethers. The results are plotted in Fig. 5 and 6. The larger the hydrophilic group of the nonionic emulsifier, the higher was the phase inversion temperature.

The Effect of Hydrocarbon Chain Length of Emulsifier on the Phase Inversion Temperature. In order to determine the effect of the hydrocarbon chain length of the emulsifier on the phase inversion temperature, the phase inversion temperature curves were also determined for various hydrocarbons emulsified with polyoxyethylene(9.0) dodecyl phenyl ether. The results are plotted in Fig. 7.

The cloud point of 80° for polyoxyethylene(9.0) dodecyl phenyl ether saturated with hexadecane, is 7° lower than the cloud point of 87° for polyoxyethylene(9.6) nonyl phenyl ether. Thus the phase inversion temperatures are lower by about 7–8° for respective emulsions stabilized with the former emulsifier. Although the effect of the hydrocarbon chain length of the emulsifier on the phase inversion temperature was not large, the stability of the emulsion toward coalescence was appreciably better in the case of dodecyl phenyl ether than for nonyl phenyl ether.

Correlation between Phase Inversion Temperature and

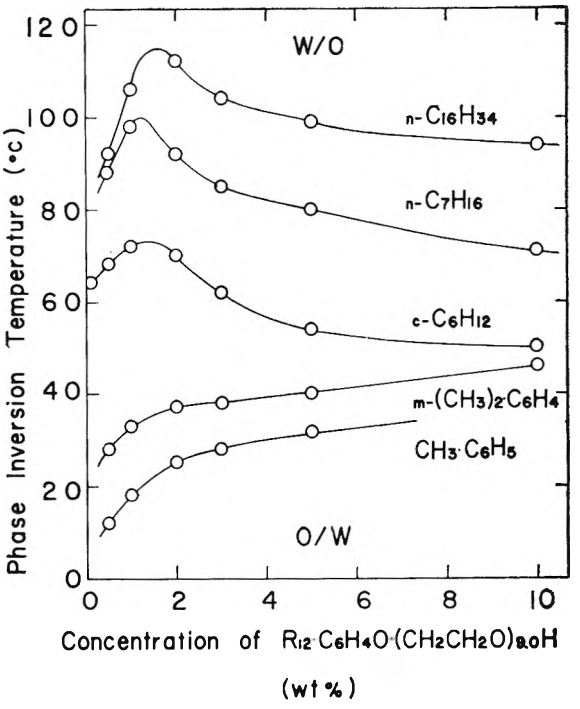

Figure 7. The effect of different hydrocarbons on the phase inversion temperature of the emulsions *vs.* the concentration of polyoxyethylene(9.0) dodecyl phenyl ether (wt. % in water).

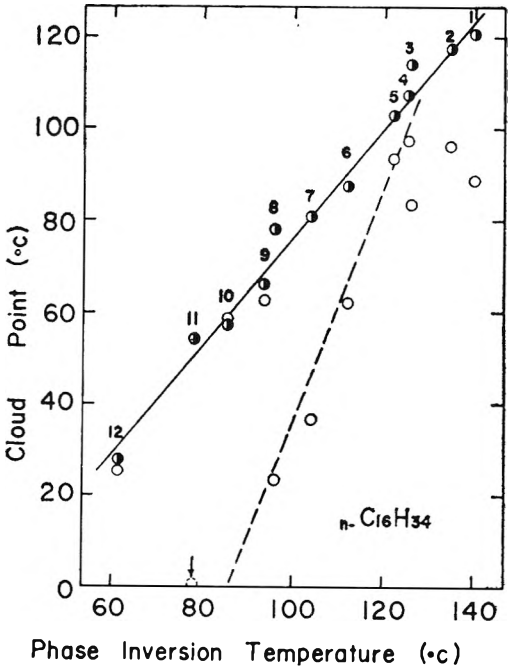

Figure 8. The correlation between the phase inversion temperatures in emulsion and the cloud points of emulsifiers in the absence of, O, or saturated with hexadecane, ◑; 1, Tween 40; 2, Tween 20; 3, Tween 60; 4, $R_{12}O(CH_2CH_2O)_{10}H$; 5, i-$R_9C_6H_4O(CH_2CH_2O)_{14}H$; 6, i-$R_9C_6H_4O(CH_2CH_2O)_{9.6}H$; 7, i-$R_{12}C_6H_4O(CH_2CH_2O)_{9.0}H$; 8, i-$R_9C_6H_4O(CH_2CH_2O)_{7.4}H$; 9, Pluronic L-44; 10, Pluronic L-64; 11, i-$R_9C_6H_4O(CH_2CH_2O)_{6.2}H$; 12, Pluronic L-62.

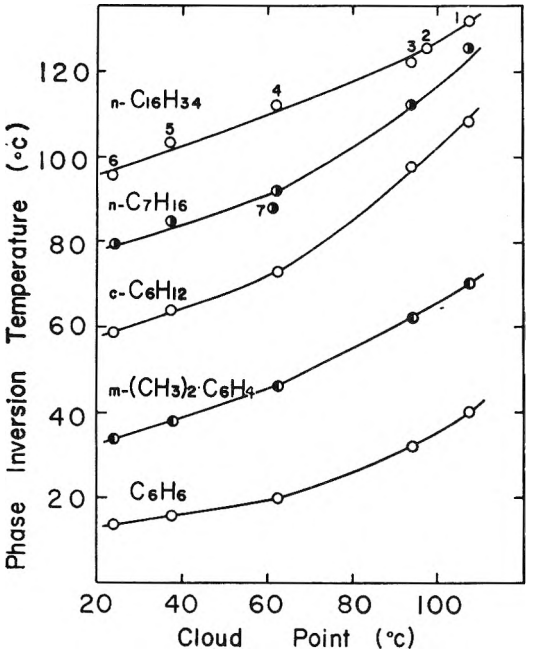

Figure 9. The correlation between the phase inversion temperatures in various hydrocarbon–water emulsions (volume ratio = 1) and the cloud points of emulsifiers in the absence of hydrocarbon; 1, i-$R_9C_6H_4O(CH_2CH_2O)_{17.7}H$; 2, $R_{12}O(CH_2CH_2O)_{10}H$; 3, i-$R_9C_6H_4O(CH_2CH_2O)_{14.0}H$; 4, i-$R_9C_6H_4O(CH_2CH_2O)_{9.6}H$; 5, i-$R_{12}C_6H_4O(CH_2CH_2O)_{9.0}H$; 6, i-$R_9C_6H_4O(CH_2CH_2O)_{7.4}H$; 7, $C_{18}H_{35}O(CH_2CH_2O)_{10}H$.

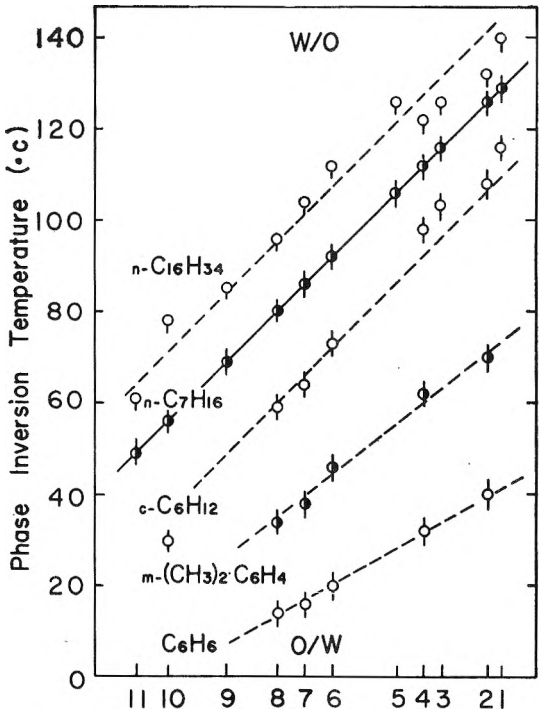

Figure 10. The correlation between the phase inversion temperatures in emulsions composed of different hydrocarbons; 1, Tween 40; 2, i-$R_9C_6H_4O(CH_2CH_2O)_{17.7}H$; 3, Tween 60; 4, i-$R_9C_6H_4O(CH_2CH_2O)_{14.0}H$; 5, $R_{12}O(CH_2CH_2O)_{10}H$; 6, i-$R_9C_6H_4O(CH_2CH_2O)_{9.6}H$; 7, i-$R_{12}C_6H_4O(CH_2CH_2O)_{9.0}H$; 8, i-$R_9C_6H_4O(CH_2CH_2O)_{7.4}H$; 9, Pluronic L-64; 10, i-$R_9C_6H_4O(CH_2CH_2O)_{6.2}H$; 11, Pluronic L-62.

Cloud Point. The correlation between the cloud points of aqueous solutions containing 3 wt. % of emulsifier without hexadecane and saturated with hexadecane and the phase inversion temperatures of hexadecane–water emulsions stabilized with various nonionic agents (3 wt. % for water) is shown in Fig. 8. Similar correlations were observed in solutions containing the other hydrocarbons.

It is clear from Fig. 8 that the phase inversion temperatures of emulsions and the cloud points when saturated with oil are quite parallel regardless of the type of nonionic agent.

This correlation does not hold well for cloud points in the absence of hydrocarbons as can be seen in Fig. 8. As for the polyoxyethylene type of nonionic agents, the cloud points and the phase inversion temperature change monotonically as shown is Fig. 9. This correlation is very useful to estimate the phase inversion temperatures from cloud points of nonionic agents in the absence of hydrocarbons.

Correlation among Phase Inversion Temperature, Oil, and Nonionic Emulsifier. The correlation between the phase inversion temperatures of emulsions composed of various hydrocarbons stabilized with various nonionic agents (3 wt. % for water) is shown in Fig. 10. The locations of the nonionic agents in the abscissa were determined so as to make the phase inversion temperatures in heptane–water emulsions *vs.* the nonionic agents fall on the straight line of slope 1. This correlation is also very useful to predict the phase inversion temperatures and/or to select the stable emulsifier in the emulsions.

Relation between the Emulsion Type and the Stability. It is generally supposed that the stability toward coalescence of emulsified droplets is nearly equal for homologous hydrocarbons stabilized with the same emulsifier. On the contrary, the stability is sometimes markedly different for such homologous oils. This is clearly shown by the data on phase inversion temperature. As can be seen in Fig. 1, the emulsion in the hexadecane–water system is of the O/W type, and that of the heptane–water system is of the W/O type at 100°. At this temperature the O/W type of emulsion of hexadecane–water is relatively stable, but that of heptane–water is unstable. At a lower temperature, for example at 80°, both systems were relatively stable, but the cyclohexane–water system was un-

stable. These relations on emulsion stability were qualitatively observed. The results are quite understandable with the aid of the phase inversion temperature data. The conclusion obtained by Benerito and Singleton,[8] "To provide emulsion stability at homogenization and sterilization temperatures the emulsifiers must be more hydrophilic than many O/W emulsifiers that are satisfactory in ordinary use and must have an increased affinity for water in the temperature range of 5 to 120°," is also readily understandable from the present data.

(8) R. R. Benerito and W. S. Singleton, *J. Am. Oil Chemists' Soc.*, 33, 364 (1956).

A Three-Component Light Scattering Theory for Surfactant Solutions Containing Added Electrolyte

by E. W. Anacker and A. E. Westwell

Department of Chemistry, Montana State College, Bozeman, Montana *(Received April 22, 1964)*

Although several light scattering procedures which lead in principle to "true" molecular weights of charged colloidal particles have recently appeared, the older Prins–Hermans–Mysels–Princen theory is still useful for estimating aggregation numbers of surfactant micelles. In the present paper, the theory is simplified and three working equations are developed. The new equations, the equations from the Prins–Hermans–Mysels–Princen theory, and the equations originating from two other approaches (Scatchard–Bregman and Stigter) are applied to scattering data obtained from solutions of dodecyltrimethylammonium bromide in 0.500 *m* NaBr. The calculated aggregation numbers are in reasonable agreement.

In recent years, several light scattering procedures[1–8] for calculating reliable molecular weights of charged colloidal particles in solutions containing added electrolyte have been developed. In their most exact formulations, these procedures require that turbidities and/or refractive index increments be measured with colloidal and supporting electrolyte solutions which have been dialyzed to equilibrium. Until membranes impermeable to monomeric as well as to aggregated surfactant ions are developed, the new procedures cannot be fully applied to the study of surfactant solutions. Monomeric surfactant ions which have diffused through a membrane into a solution originally consisting solely of solvent and supporting electrolyte will spontaneously aggregate to form micelles. When membrane equilibrium is established, the concentrations of all solute species will be the same on both sides of the membrane. This will be true even though a membrane impermeable to micelles as such may have been used. For this reason, the light scattering theory of Prins and Hermans[4] and of Mysels and Princen[5] (PHMP),

(1) A. Vrij, Thesis, University of Utrecht, 1959; A. Vrij and J. Th. G. Overbeek, *J. Colloid Sci.*, 17, 570 (1962).

(2) E. F. Casassa and H. Eisenberg, *J. Phys. Chem.*, 64, 753 (1960).

(3) D. Stigter, *ibid.*, 64, 842 (1960); "Proceedings of the Interdisciplinary Conference on Electromagnetic Scattering, Potsdam, N. Y., 1962," M. Kerker, Ed., The Macmillan Co., New York, N. Y., 1963, p. 303.

(4) W. Prins, Thesis, University of Leiden, 1955; W. Prins and J. J. Hermans, *Koninkl. Ned. Akad. Wetenschap. Proc.*, B59, 162 (1956).

which was developed specifically for surfactant solutions, is still of value.

In the PHMP procedure, one plots the quantity $H(\mathrm{d}n/\mathrm{d}c')_{m_{BX}}^2(c' - c_{cmc}')/\tau$ *vs.* $(c' - c_{cmc}')$ and uses the intercept α and limiting slope β to calculate an effective (thermodynamic) charge z and an aggregation number N from the relationships[6]

$$z = \frac{\beta(c_{cmc}' + fc_{BX}) + [(\beta/500)(c_{cmc}' + c_{BX})]^{1/2}}{\alpha(1 - 500\alpha E)} \quad (1)$$

$$N = {}^1/_2[zE + (1/1000\alpha)] + {}^1/_2[(zE - (1/1000\alpha))^2 - (z + z^2)E^2]^{1/2} \quad (2)$$

where $H = 32\pi^3n^2/3\mathbf{N}\lambda^4$, n is the solution refractive index, $\mathbf{N}$ is Avogadro's number, λ is the wave length under vacuum, c' is the surfactant molarity (primes refer to quantities in terms of monomer units), c_{cmc}' is the surfactant molarity at the critical micelle concentration, τ is the solution turbidity in excess of that at the critical micelle concentration, c_{BX} is the molarity of the supporting electrolyte BX, $f = (\mathrm{d}n/\mathrm{d}m_{BX})_{m'}/(\mathrm{d}n/\mathrm{d}m')$, m_{BX}, m_{BX} is the molality of the supporting electrolyte, m' is the molality of the surfactant, and $E = (c_{cmc}' + fc_{BX})/(c_{cmc}' + c_{BX})$. Temperature and pressure are assumed to be constant.

We note that turbidities are coupled with surfactant molarities, whereas refractive index increments are couched—wholly or in part—in terms of molalities. One of our objectives was to replace this curious mixture[7] of units with a consistent set.

In the PHMP theory, unaggregated monomer, supporting electrolyte, and micellar salt are regarded as solute components. The solvent, water, constitutes the fourth. The theory can be simplified, without introducing significant error, by treating the monomer, concentration assumed equal to that of the critical micelle concentration,[8] as part of the supporting electrolyte.[9] This device effectively reduces the number of components to three.

We consider a system of volume V and containing N_1 water molecules, N_2 micellar salt units, $R_NX_{N-z}X_z$ (each formula unit yields one micelle, $R_NX_{N-z}^{+z}$, and z counterions, X^-), and N_3 added salt units, BX. In solution there are N_2 micelles, N_3 co-ions, B^+, and $N_3 + zN_2$ counterions. Monomeric surfactant, present as the ions R^+ and X^-, is treated as part of the added salt, BX. Application of the general fluctuation theory of light scattering by multicomponent systems[10] in the manner employed by Prins and Hermans[4] leads to

$$\frac{HVn_2^2}{\tau^{\mp}} = \frac{[2N_3 + N_2(z + z^2)]\mathbf{N}}{N_3^2(f/N)^2 + [2N_3 + (z + z^2)N_3(f/N)^2 - 2fzN_3/N]N_2 + zN_2^2} \quad (3)$$

where $\tau^{\mp}$ is the turbidity in excess of water (assuming no depolarization and no dissymmetry), $f = n_3N/n_2$, $n_2 = (\mathrm{d}n/\mathrm{d}N_2)_{N_1,N_3}$, and $n_3 = (\mathrm{d}n/\mathrm{d}N_3)_{N_1,N_2}$. The ratio of refractive index increments of salt and surfactant, f, is the same here as in the PHMP theory. In the derivation of (3), we have assumed the constancy of all activity coefficients and have omitted certain small terms in the second derivatives of the free energy, F.[11]

Equation 3 is readily transformed into

$$N = \frac{2m_3(z'm_2')^{-1} + 1 - Hn_2'^2V^0m_3(\tau^{\mp})^{-1}f^2(m_3(z'm_2')^{-1} + 1)}{Hn_2'^2V^0(\tau^{\mp})^{-1}[m_3(2(z')^{-1} + z'f^2 - 2f) + m_2'] - z'} \quad (4)$$

where V^0 is the volume of solution containing 1 kg. of water, m_2' is the molality of the micellar salt (on a monomeric basis), m_3 is the molality of the added electrolyte, $z' = z/N$, and $n_2' = (\mathrm{d}n/\mathrm{d}m_2')_{m_3}$. From eq. 4, one computes values of N for various assumed values of z'. Presumably, the best z' is the one for which there is minimum variation in N for all solutions studied. This is the approach used by Johnson, *et al.*, in ultracentrifugation work.[12]

A graphical procedure for estimating N can be developed from eq. 3. Following Mysels' lead,[5] we solve for $\tau^{\mp}$, set $N_2 = 0$ to get $\tau_{cmc}^{\mp}$, and then form $\tau^{\mp} - \tau_{cmc}^{\mp} = \tau$. If the difference between n and n_{cmc} is ignored, we can rearrange the expression for τ to get

(5) K. J. Mysels, *J. Colloid Sci.*, **10**, 507 (1955); L. H. Princen and K. J. Mysels, *ibid.*, **12**, 594 (1957); K. J. Mysels and L. H. Princen, *J. Phys. Chem.*, **63**, 1696 (1959).

(6) E. W. Anacker, R. M. Rush, and J. S. Johnson, *ibid.*, **68**, 81 (1964).

(7) Brought to our attention by J. S. Johnson.

(8) P. Debye, *Ann. N. Y. Acad. Sci.*, **51**, 575 (1949).

(9) The refractive index increment and concentration of the supporting electrolyte are corrected for inclusion of the monomeric surfactant.

(10) F. Zernike, *Arch. Neerland. Sci.*, [3A] **4**, 74 (1918).

(11) Example: $(1/kT)(\mathrm{d}^2F/\mathrm{d}N_3^2)N_1,N_2 = N_3^{-1} + (N_3 + zN_2)^{-1} - 4[N_1 + (1 + z)N_2 + 2N_3]^{-1}$. Except for extremely high solute concentrations, the last term is negligible compared to the first two and may be omitted. T and k are the temperature and Boltzmann's constant, respectively.

(12) J. S. Johnson, K. A. Kraus, and G. Scatchard, *J. Phys. Chem.*, **58**, 1034 (1954).

$$\frac{Hn_2'^2V^0m_2'}{\tau} = \frac{2m_3 + (N)^{-1}(z + z^2)m_2'}{[2N + (2N)^{-1}(z + z^2)f^2 - 2fz]m_3 + zm_2'} \quad (5)$$

Expansion of (5) in powers of m_2' leads to

$$\frac{Hn_2'^2V^0m_2'}{\tau} = A + Bm_2' + \ldots \quad (6)$$

where

$$A = 4N[(2N - fz)^2 + zf^2]^{-1} \quad (7)$$

and

$$B = zA(2m_3)^{-1}[(1 + z)N^{-1} - A] \quad (8)$$

A and B are determined experimentally being, respectively, the intercept and limiting slope of the $Hn_2'^2V^0m_2'/\tau$ *vs.* m_2' plot. Equations 7 and 8 can be solved simultaneously to give relationships suitable for computing N. They are

$$z = [-2fm_3B \pm (8m_3B)^{1/2}]A^{-1}(fA - 2)^{-1} \quad (9)$$

$$N = z(z + 1)A(2m_3B + zA^2)^{-1} \quad (10)$$

An equation similar to (4) can be obtained by rearrangement of (5). It is

$$N = \frac{2m_3(z'm_2')^{-1} + 1 - Hn_2'^2V^0m_3(2\tau)^{-1}f^2}{Hn_2'^2V^0\tau^{-1}[m_3(2z'^{-1} + 2^{-1}z'f^2 - 2f) + m_2'] - z'} \quad (11)$$

Equation 11 is employed in the same manner as (4).

Before applying eq. 4, 6, and 11 to an actual situation, we would like to cite two other equations which have been used to compute micellar aggregation numbers from light scattering data. The first is that of Scatchard and Bregman.[13] It has given results comparable to those given by the PHMP procedure.[6] In the present symbolism and as adapted by Johnson,[6] the equation is

$$N^{-1} = \frac{H(dn/dm_2'^*)^2_{m_3^*}V^0m_2'^*}{\tau} \times \left[1 + \frac{(z'^2m_2'^*dn/dm_3^*)_{m_2'^*}}{4m_3^*(dn/dm_2'^*)_{m_3^*}}\right] - \frac{z'^2m_2'^*}{2m_3^*} \quad (12)$$

Equation 12 is used in the same way as eq. 4 and 11. The asterisks signify that Scatchard components[14] are involved. The micellar salt (component 2) is $R_NX_{N-z}X_z - {}^1/_2zBX$. Its molality, $m_2'^*$, equals m_2'. The supporting electrolyte (component 3) is still BX; its molality, m_3^*, is $m_3 + {}^1/_2z'm_2'$. In the case of the increments, $(dn/dm_3^*)_{m_2'^*} = (dn/dm_3)_{m_2'}$ and $(dn/dm_2'^*)_{m_3^*} = (dn/dm_2')_{m_3} - {}^1/_2z'(dn/dm_3)_{m_2'}$ A number of authors[2,12,14-16] have argued the case for the use of Scatchard components. Stigter[3] has pointed out a possible disadvantage in concentrated solutions.

The second equation we wish to cite is that of Stigter,[3] which he has applied to sodium lauryl sulfate and dodecylamine hydrochloride. It may be written in the form

$$H\mathbf{N}(dn/d\rho')_{\rho_4}^2(\rho' - \rho_3')/\tau = T_1[1 + T_2(\rho' - \rho_3') + \ldots] \quad (13)$$

where ρ', ρ_3', and ρ_4 are, respectively, the total surfactant concentration (in terms of monomer), the critical micelle concentration, and the added, 1–1 salt concentration—all in terms of formula units per unit volume. T_1, the intercept of the $H\mathbf{N}(dn/d\rho')_{\rho_4}^2(\rho' - \rho_3')/\tau$ *vs.* $(\rho' - \rho_3')$ plot, is given by

$$T_1 = (N + A_1\rho_3')[N + A_1\rho_3' + A_1\rho_4(dn/d\rho_4)_{\rho'}/(dn/d\rho')_{\rho_4}]^{-2} \quad (14)$$

A_1 represents the colloid–salt interaction and is evaluated by statistical thermodynamic methods.[3,17,18]

After A_1 has been evaluated, N may be determined from (14). The experimental information represented by the slope T_1T_2 of the scattering plot is replaced by the results of the statistical considerations and other experimental measurements. Evaluation of A_1 requires some notions about the micellar charge and radius, assuming spherical micelles. The charge can be obtained from electrophoretic mobility data[19] if the micelle radius is known. A first approximation to the radius can be calculated either from a rough value of the micellar weight and the micelle density or from the length of the extended surfactant ion (X-ray measurements). The aggregation number computed from (14) and following from the first radius approximation can be used with the micelle density to get a second approximation to the radius. This would lead to a new aggregation number from (14). A third cycle would probably not be justified unless the micelle density were known very accurately. Stigter[3] checks the statistical results by computing T_1T_2 and comparing the value obtained with the experimental slope of the scattering plot.

(13) G. Scatchard and J. Bregman, *J. Am. Chem. Soc.*, **81**, 6095 (1959).

(14) G. Scatchard, *ibid.*, **68**, 2315 (1946).

(15) J. T. Edsall, H. Edelhoch, R. Lontie, and P. R. Morrison, *ibid.*, **72**, 4641 (1950).

(16) R. S. Tobias and S. Y. Tyree, *ibid.*, **81**, 6385 (1959).

(17) D. Stigter and T. L. Hill, *J. Phys. Chem.*, **63**, 551 (1959).

(18) D. Stigter, *ibid.*, **64**, 838 (1960).

(19) D. Stigter and K. J. Mysels, *ibid.*, **59**, 45 (1955).

In accordance with the various procedures just described, we have computed aggregation numbers for dodecyltrimethylammonium bromide in 0.500 *m* NaBr.[20] The results are given in Table I. The N reported for an iterative procedure is a weighted mean value of the aggregation numbers calculated for the different solutions examined, the z' used in the calculations being that one providing the lowest weighted mean square deviation. The iterative procedure is illustrated by the deviation plots of Fig. 1, which summarize the computations involving eq. 11. In the graphical procedures, slopes and intercepts of the scattering plots were determined by a weighted least-squares procedure. The weighting factors used in all calculations were the surfactant concentrations in excess of the critical micelle concentration.

Table I: Dodecyltrimethylammonium Bromide Aggregation Numbers[a]

Procedure	Equations	N	z'
PHMP	1, 2	84 (79)[c]	0.17
Scatchard–Bregman	12	86	0.19
Stigter	13, 14	86 (70)[d]	0.30[b]
This work	4	89	0.20
This work	6, 9, 12	87 (81)[e]	0.19
This work	11	86	0.19

[a] Solvent 0.500 *m* NaBr; 31-32°. [b] Assumed value. [c] Equation 2: $N(z' = 0) = 1/1000\alpha$. [d] Equation 14: $N(A_1 = 0) = 1/T_1$. [e] $N(z' = 0) = 1/A$.

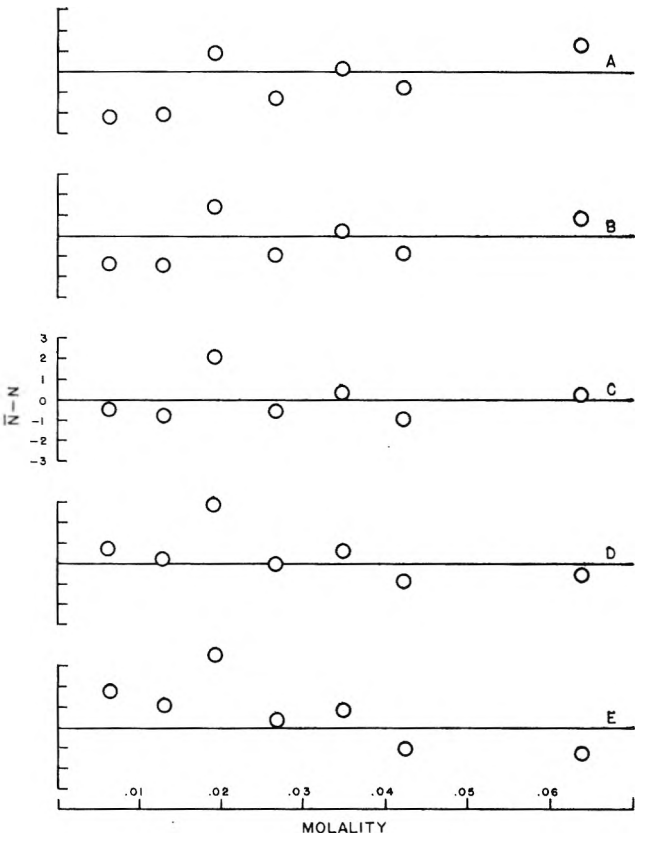

Figure 1. Aggregation numbers computed from eq. 11 as a function of z'. $\bar{N} = \Sigma w_i N_i / \Sigma w_i$. The weighting factor for solution i is w_i. $\bar{d}^2 = \Sigma w_i (\bar{N} - N_i)^2 / \Sigma w_i$. Plot A: $z' = 0.17$; $\bar{N} = 83.5$; $\bar{d}^2 = 1.38$. Plot B: $z' = 0.18$; $\bar{N} = 84.8$; $\bar{d}^2 = 0.88$. Plot C: $z' = 0.19$; $\bar{N} = 86.2$; $\bar{d}^2 = 0.84$. Plot D: $z' = 20$; $\bar{N} = 87.8$; $\bar{d}^2 = 1.10$. Plot E: $z' = 0.21$; $\bar{N} = 89.4$; $\bar{d}^2 = 2.19$.

In estimating A_1, which is required in Stigter's procedure, we assumed spherical micelles with specific volumes of 0.958 ml.,[6] a rough aggregation number of 90, and a charge of 27. The assumed degree of ionization of 0.30 seemed to be in line with the values calculated by Hoyer and Marmo[21] from electrophoretic mobility measurements for several long-chain quaternary ammonium chlorides in water. The experiments of Stigter and Mysels[19] indicate that the degree of ionization is relatively independent of salt concentration. Employment of the procedures described by Stigter[3] and by Stigter and Mysels[19] leads to an A_1 of -8.5×10^{-20} ml./molecule. The refractive index increments required in eq. 13 and 14 can be evaluated from data given by Anacker, Rush, and Johnson.[6]

In view of the uncertainties existing in the values employed for the various required refractive index increments, the aggregation numbers given in Table I are in reasonably good agreement. It is somewhat surprising that a higher aggregation number was not obtained from eq. 13 and 14. Stigter[3] recomputed the micellar weights of dodecylamine hydrochloride[22] and sodium lauryl sulfate[5] in aqueous sodium chloride solutions and found that the introduction of A_1 increases the values by some 10%. He indicated that at high added salt concentration one might have to introduce into the theoretical model long-range attraction between micelles. Princen and Mysels[5] have discussed difficulties which can be encountered in the PHMP theory in the presence of swamping electrolyte. For these reasons, additional comparisons of the several procedures at different added salt concentrations are desirable. There are insufficient data in the literature at present for this purpose.

(20) E. W. Anacker and H. M. Ghose, *J. Phys. Chem.*, **67**, 1713 (1963).

(21) H. W. Hoyer and A. Marmo, *ibid.*, **65**, 1807 (1961).

(22) L. M. Kushner, W. D. Hubbard, and R. A. Parker, *J. Res. Natl. Bur. Std.*, **59**, 113 (1957).

It is interesting to compare the aggregation numbers given by the graphical procedures for an assumed z' (or A_1) of 0. These values occur in Table I in parentheses. The large difference between the 70 given by Stigter's equations and the 79 given by the PHMP equations arises from the difference in the refractive index increments used. In one case the increment is measured at constant added salt molarity, whereas in the other it is measured at constant added salt molality.

Refractive index increments in terms of surfactant and added salt molalities arise simply and directly from Zernike's theory.[10] It is possible, of course, to convert to increments involving other concentration units. It is not evident, however, that there are enough advantages to warrant the introduction of the approximations that are usually required in such conversions.

Acknowledgment. This research was supported in part by a grant from the Petroleum Research Fund administered by the American Chemical Society. Grateful acknowledgment is hereby made to the donors of the fund.

Light Scattering Studies on Solutions of Decyltrimethylammonium Dodecyl Sulfate

by Horst W. Hoyer and Iris L. Doerr[1]

Hunter College of The City University of New York, New York 21, New York *(Received April 6, 1964)*

Solutions of decyltrimethylammonium dodecyl sulfate, whether prepared from equimolar concentrations of aqueous solutions of decyltrimethylammonium hydroxide and hydrogen dodecyl sulfate or from the solid salt, are highly turbid at concentrations of 1×10^{-4} M. Light scattering studies on solutions prepared according to the first procedure have shown that the scattering is due primarily to large particles. These solutions show considerable asymmetry in the angular distribution of the scattered light, the dissymmetry ratio for light scattered at 45 and 135° being 4.6. An extrapolation plot indicates that the particle weight of these scattering centers is about 1×10^9 g., corresponding to an equivalent spherical radius of approximately 7×10^{-6} cm. The experimental evidence indicates that such solutions consist of microemulsions with a high degree of stability. The solid salt, the preparation of which is described, forms colloidal solutions which separate into two phases within a short time.

Introduction

Solutions of salts in which both the anion and cation have amphipathic properties have been investigated by Scott, Tartar, and Lingafelter[2a] and by Anacker.[2b] The former group studied the conductance of the salts octyltrimethylammonium octanesulfonate (I) and decyltrimethylammonium decanesulfonate (II) and showed that these substances appeared to form micelles at concentrations much below that for corresponding salts in which only one ion is amphipathic. Anacker undertook light scattering studies on these compounds and

(1) A portion of this work is abstracted from the thesis of I. L. Doerr, submitted in partial fulfillment of the requirement for the degree of Master of Arts, Hunter College, February, 1964.

(2) (a) A. B. Scott, H. V. Tartar, and E. C. Lingafelter, *J. Am. Chem. Soc.*, **65**, 698 (1943); (b) E. W. Anacker, *J. Colloid Sci.*, **8**, 402 (1953).

found that compound II formed unstable emulsions while compound I and the salt octyltrimethylammonium decylsulfonate formed stable solutions with micelles of "molecular" weights equal to 21,600 and 89,700, respectively.

In this laboratory we have been concerned with the colloidal and electrophoretic properties of solutions of decyltrimethylammonium dodecyl sulfate and dodecyltrimethylammonium dodecyl sulfate[3] (hereafter designated as C_{10}–C_{12} and C_{12}–C_{12}, respectively). These substances showed surface activity at concentrations of 10^{-5} m with values of the critical micelle concentration of 1.9×10^{-4} M for the C_{10}–C_{12} and 3.0×10^{-5} M for C_{12}–C_{12}. The electrophoretic studies showed that the colloidal particles are not neutral but possess a positive charge which may be increased or decreased by providing an excess of either the amphipathic cation or anion.

Light scattering studies have proved to be a powerful tool for investigating the nature of colloidal particles in solution. It was hoped that this technique could help elucidate the nature of the fundamental particle present in solutions of the C_{10}–C_{12} compound.

Experimental

The preparation of the C_{10}–C_{12} compound has been described in a previous paper.[3] Briefly, the procedure involved conversion of the sodium dodecyl sulfate to the acid and of the decyltrimethylammonium iodide to the quaternary hydroxide by passage through the appropriate ion-exchange resin [Amberlite 120 (H^+ form) and IRA-402 (OH^- form)]. Equivalent quantities of the base and hydroxide were mixed to form a neutral stock solution which was diluted for the light scattering experiments.

It was later found that the salt can be readily prepared from the original sodium dodecyl sulfate and decyltrimethylammonium iodide. If a solution containing equivalent quantities of these compounds is kept for some time in an ice bath, a white crystalline solid separates. This melts to a viscous liquid from 163 to 165°. The chemical analysis of this salt is given in Table I. Except as indicated below, all experiments were made on dilutions of the stock solution prepared by the first procedure.

Table I: Elemental Analysis of Decyltrimethylammonium Dodecyl Sulfate

Element	Found, %	Calcd., %
C	64.44	64.22
H	11.91	12.00
N	3.01	3.24
S	6.89	7.17
I	None	None

The importance and difficulty of removing all extraneous matter from aqueous solutions which are to be used for light scattering studies are well known. We found that a standard 0.65-μ Millipore filter was an effective means of clarifying our solutions. Deionized water was passed repeatedly through such filters until its turbidity was 3.27×10^{-5}.

The light scattering experiments were made with a Brice-Phoenix Universal light scattering photometer which was calibrated against the standard opal glass supplied by the manufacturer. The refractive index gradient was obtained with a Brice-Phoenix differential refractometer, a value of dn/dc of 0.1406 being obtained with concentration units of grams per milliliter. In our work we used the green filter combination for isolating the 546-mμ wave length of mercury.

Results and Discussion

Scattering at 90°. Our initial studies were concerned with the determination of the intensity of the light scattered at 90° to the incident beam. As is well known, the molecular or particle weight for particles less than $^1/_{20}$ of the wave length of light is given by an extrapolation of the function HC/τ to zero concentration. H is a constant which takes into account the refractive index and, for our system, has the value 2.17×10^{-6}. τ is the excess turbidity, *i.e.*, the turbidity of the solution minus that of the solvent. For solutions of association colloids it is necessary to substitute $C - C_0$, where C_0 is the critical micelle concentration, for the concentration.

The results of these experiments are plotted in Fig. 1. Each point represents an average of three turbidity determinations. Application of Anacker's least-square method[4] to the conventional light scattering equation

$$\frac{H(C - C_0)}{\tau} = \frac{1}{M} + 2BC \qquad (1)$$

gave the plot of Fig. 2. The high value, 3.62×10^{-8} obtained for the intercept invalidates the use of eq. 1. Particles so large are greater than $^1/_{20}$ of the wave length of light and the scattered radiation must therefore show interference. Correction for this interference is described below.

The second point to emerge from these measurements is that the critical micelle concentration as determined for this system by the light scattering data is considerably lower than that obtained by dye solubilization. Using Anacker's least-square equation we obtain a value of 1.85×10^{-5} g./ml. for the c.m.c. The value

(3) H. W. Hoyer, A. Marmo, and M. Zoellner, *J. Phys. Chem.*, 65, 1804 (1961).

(4) E. W. Anacker, *J. Colloid Sci.*, 8, 402 (1953).

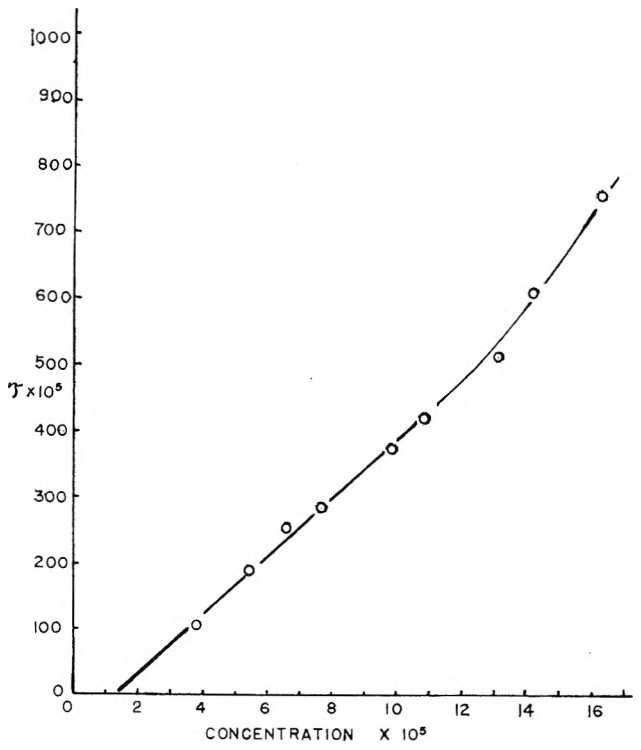

Figure 1. Excess turbidity *vs.* concentration for solutions of decyltrimethylammonium dodecyl sulfate. Concentrations are in grams per milliliter.

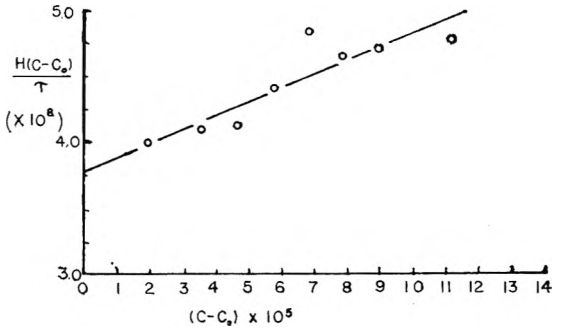

Figure 2. A least-square plot of light scattering data for solutions of decyltrimethylammonium dodecyl sulfate. Concentrations are in grams per milliliter.

obtained from dye solubilization measurements is 8.95×10^{-5} g./ml. It would seem that these two methods respond to different properties of our system. Further discussion of this point is reserved until after a consideration of additional light scattering data.

Dissymmetry Measurements. Two methods are available by which the intraparticle interference may be evaluated. By one method, the dissymmetry, *i.e.*, the ratio of the intensities of the scattered light at two angles, generally 45 and 135°, permits calculation of this correction factor. Doty and Steiner[5] give tables of these factors, $P(\theta)$, called the particle scattering factor, as a function of the dissymmetry, Z. Our values of Z, obtained in the concentration range of 8.71 to 4.35×10^{-5} g./ml. were not reproducible to better than 10%. No linear extrapolation of $1/(Z-1)$ to zero concentration was possible. The average value of Z was found to be 4.6 ± 0.4.

The most likely shape for a colloid-rich droplet suspended in water and subjected to interfacial tension would seem to be that of a sphere. Unfortunately, the dissymmetry method for determining particle size cannot be applied to spheres having a dissymmetry greater than about 1.5.[6] We then turned to the extrapolation method.

The Extrapolation Method. This method is the least dependent upon assumptions of particle shape and normally provides a more reliable determination of the particle weight and radius. Since all interference vanishes at a scattering angle of 0°, all particle scattering factors become unity at this angle. Zimm[7] suggested a simultaneous extrapolation to zero concentration and zero scattering angle which has become known as the Zimm plot. Essentially, this involves plotting HC/τ *vs.* $kC + \sin^2 \theta/2$, where k is an arbitrary constant, C the concentration, and θ the scattering angle. The Zimm plot for our data is given in Fig. 3. The intercept of both the zero concentration and the zero angle line on the ordinate is at 0.10×10^{-8}, corresponding to a particle weight of 1.0×10^{9}. Assuming a density of unity, this corresponds to particles with an equivalent spherical radius of 7.4×10^{-6} cm.

It would appear unlikely that the above results are more precise than 10 or 15%. However, they do lead to the conclusion that our C_{10}–C_{12} solution is actually a two-phase system, consisting of a relatively stable dispersion of a colloid-rich phase in an essentially aqueous phase.

The Question of Stability. Mysels[8] has introduced the terms diuturnal and caducous to designate unstable colloidal systems with different rates of flocculation. Caducous systems are short lived, flocculating perceptibly during the period of observation, while diuturnal system are unstable ones which flocculate at an imperceptible rate. We wished to establish whether our C_{10}–C_{12} system was a stable or a diuturnal one.

Prior work[3] had established that essentially the same system is obtained when one mixes equivalent quanti-

(5) P. Doty and R. F. Steiner, *J. Chem. Phys.*, **18**, 1211 (1950).

(6) P. Doty and J. T. Edsall, *Advan. Protein Chem.*, **6**, 87 (1951).

(7) B. H. Zimm, *J. Chem. Phys.*, **16**, 1093, 1098 (1948).

(8) K. J. Mysels, "Introduction to Colloid Chemistry," Interscience Publishers, Inc., New York, N. Y., 1959.

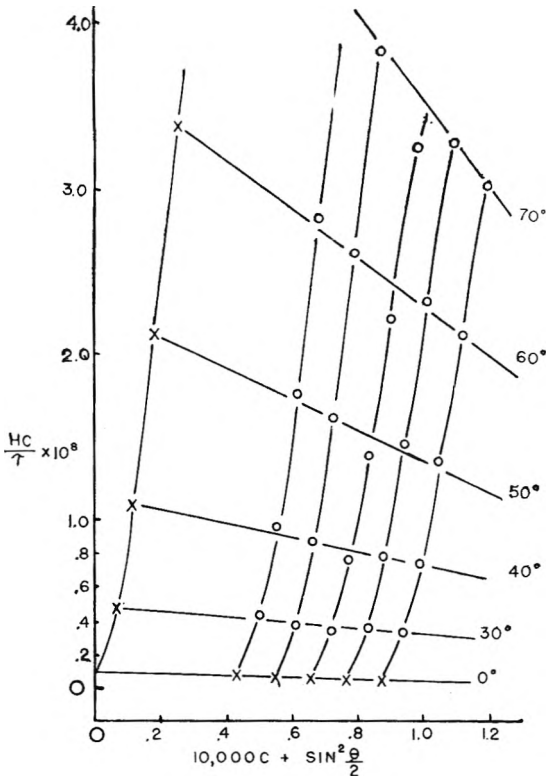

Figure 3. An extrapolation plot of the light scattering data for solutions of decyltrimethylammonium dodecyl sulfate.

ties of solutions of sodium dodecyl sulfate and decyltrimethylammonium iodide or the corresponding acidic and basic forms. We wished to prepare the same system from the solid salt and eventually discovered that the pure salt could be prepared by the simple procedure described in the Experimental part of this paper.

Solutions of this salt were readily prepared by heating. These had all the properties of the solutions prepared by the initial procedure except that of stability. Within 3 or 4 hr. after preparation, phase separation would occur. On the other hand, a sample prepared by the first procedure has stood on the laboratory shelf for more than 3 yr. with only a slight separation. It would seem that our system is an unstable one; that the first method of preparation, *i.e.*, from solutions, yields a diuturnal system while preparation from the solid salt yields a caducous one.

Centrifugation of the caducous system yields a clear solution with a turbidity from two to three times that of the water which we used. It may be that this slight excess turbidity is due to micelles existing in these extremely dilute solutions. This could account for the discrepancy between the critical micelle concentration obtained by light scattering and by dye solubilization. The latter method actually detects the colloid-rich phase and cannot respond to the low micelle concentrations which may, however, be detected by light scattering.

Conclusions

(1) Mixing aqueous solutions of sodium or hydrogen dodecyl sulfate with decyltrimethylammonium iodide or hydroxide results in the formation of a diuturnal two-phase system of colloid-rich material suspended in water.

(2) The colloid-rich phase consists of particles comparable in size with the wave length of light.

Micellar Weights of and Solubilization of Benzene by a Series of Tetradecylammonium Bromides. The Effect of the Size of the Charged Head[1a]

by Raymond L. Venable and Robert V. Nauman[1b]

Department of Chemistry, Louisiana State University, Baton Rouge, Louisiana *(Received May 4, 1964)*

Micellar weights of tetradecyltrimethylammonium, tetradecylpyridinium, and tetradecyltripropylammonium bromides were determined by light scattering experiments with aqueous and 0.05 *M* sodium bromide solutions. Critical concentrations were determined by surface tension measurements and confirmed by light scattering. The surface tension measurements were used in the Gibbs adsorption isotherm to calculate a head area parameter. Benzene was solubilized in varying concentrations of both aqueous and salt solutions of all the surfactants. In water the trimethyl salt had a 27,200 micellar weight and solubilized 2.10 to 2.36 benzene molecules per detergent monomer in micellar form. The comparable figures for the pyridinium salt were 26,000 and 2.14 to 2.45, and for the tripropyl salt they were 25,000 and 2.18 to 2.69. In 0.05 *M* sodium bromide solutions the micellar weights were 50,400, 97,600, and 40,700 for the trimethyl, pyridinium, and tripropyl salts. The comparable monomer to monomer solubilization figures were 4.41, 4.54, and 6.53 independent of concentration. A correlation of the head area parameter with the solubilization results suggests further experimentation.

Introduction

The role of the size of the hydrophilic portion of an aqueous surfactant on its solubilization ability has not been thoroughly established. By searching the literature one can find many papers on solubilization that contain information relative to the effect of specific types of hydrophilic groups on solubilization ability, but information from a single laboratory that is or could be used to discern the effect of the size of the hydrophilic portion on solubilization ability is rare.

Kolthoff and Stricks[2] studied the solubilization of large dye molecules in many surfactants and make possible the comparison of solubilization results in both aqueous and salt solutions of dodecylamine hydrochloride and sodium and potassium laurates. Many of the papers of McBain[3] contain information relative to the effect of the hydrophilic head.

Consideration of the available literature gave us the impression that the size of the hydrophilic portion of the surfactant is a relatively unimportant factor in correlating solubilization results. Our impression was strengthened by consulting the review literature in the field. Klevens[4] discusses the effect of the structure of the solubilizer on solubilization ability, but in his section on effect of substitution in the chain he says very little about the nature of the hydrophilic portion of the molecule. In his summary he says only, "The cationic detergents, such as dodecylamine hydrochloride, are more powerful solubilizers for hydrocarbons than the corresponding anionics of equal chain length." McBain and Hutchinson,[5] after discussing the effect of the ionic nature of the solubilizer, say, "It appears, in summary, that the differences between different types of materials containing the same long-chain hydrocarbon are relatively small, and that such differences as do exist may be explained in terms of the

(1) (a) This paper is based upon work submitted as a dissertation by R. L. Venable in partial fulfillment of the requirements for the Ph.D. degree at Louisiana State University, June, 1963; (b) to whom correspondence concerning this work should be addressed.

(2) I. M. Kolthoff and W. Stricks, *J. Phys. Colloid Chem.*, **52**, 915 (1948); **53**, 424 (1949).

(3) For example, see J. W. McBain and P. H. Richards, *Ind. Eng. Chem.*, **38**, 642 (1946).

(4) H. B. Klevens, *Chem. Rev.*, **47**, 1 (1950).

(5) M. E. L. McBain and E. Hutchinson, "Solubilization," Academic Press, New York, N. Y., 1955, Chapter 4, p. 85.

differences in the size of micelles formed by the various species." Harris[6] discusses surfactant structure and states, "For compounds with equal equivalent carbon chain lengths, the degree of solubilization is the same. An exception is the cationic type, which seems to provide an increased degree of solubilization over anionics."

Work done in this laboratory on sucrose monoesters[7] and a series of quaternary ammonium bromides[8] indicated that the amount of solubilization might be correlated with the void spaces caused by the size of the hydrophilic head. The experiments had not been designed to test this correlation, but they gave an indication that the influence of head size should be more carefully investigated in spite of the conclusions suggested in the literature.

A series of quaternary ammonium bromides was chosen as the result of our observing molecular models. The series allowed us to study the effect of similar (trimethylammonium and pyridinium) and dissimilar (trimethylammonium and tripropylammonium) head sizes in somewhat similar ionic environments. Surface tension measurements were used to locate the critical micelle concentration (c.m.c.) and were used in the Gibbs adsorption isotherm to calculate an area parameter to represent head size and correlate with solubilization. Light-scattering measurements were used to confirm c.m.c. values and to determine micellar weights. The amount of solubilization of benzene was determined by a spectrophotometric procedure. There is sufficient correlation between the head size parameter and solubilization to warrant a more detailed study.

Experimental Techniques

The surfactants, dodecylpyridinium bromide (LPB), tetradecylpyridinium bromide (TPB), tetradecyltrimethylammonium bromide (TTMAB), tetradecyltripropylammonium bromide (TTPAB), and hexadecyltripropylammonium bromide (HTPAB) were prepared by refluxing alkyl bromides and excesses of the appropriate amines in methanol or ethanol. After initial experiments gave peculiar results, only alkyl bromides that were shown to be pure by gas chromatography were used in the preparations. After the reaction was completed, the solvent was evaporated, and ether was added to precipitate the quaternary salt. Sometimes, the mixture had to be chilled to ice temperatures to ensure precipitation.

The surfactants were purified by repeated recrystallization from alcohol until there was no minimum in the surface tension results and reproducible light scattering results were obtained. Elemental analyses of all the surfactants were obtained; they confirmed the expected elemental composition.

Surface tensions were measured by the ring method using a Christian Becker balance designed for the purpose. The procedure was essentially that of Harkins and Jordan.[9] In treating the data, however, their correction factors were not explicitly applied. Measurements were made with a single ring on the triply distilled water that was used for light scattering measurements. The known surface tension of water was used to evaluate K in the equation, $\gamma = Kw$, in which γ is the surface tension and w is the weight required to pull the ring free. The determined K was used with measured w values to determine the other surface tensions. This procedure accounts for the correction factors that depend on the dimensions of the ring but does not correct for the different volumes that are raised by the ring. The solutions were thermostated prior to and during surface tension determinations by circulating water kept at 30.00 ± 0.01°.

A Brice–Phoenix light scattering photometer was used in these studies. The instrument was calibrated with the standard Cornell polymer solution for which a turbidity of 3.49×10^{-3} cm.$^{-1}$ was assumed for 436 mμ light. The common volume and refraction corrections were made. Some of the data have also been obtained with the Aminco photometer with no significant difference in results. The filter factors for the Brice–Phoenix instrument were re-evaluated with a Cary Model 14 spectrophotometer. Comparison of these factors with those given by the manufacturer and those determined with the photometer for 90° scattering showed deviation between extremes of 1.1, 2.0, 3.3, and 8.3% and deviations between Cary and 90° factors of 0.4, 1.5, 0.0, and 4.0% for transmittances of 0.453, 0.198, 0.125, and 0.0569. The Cary values were used in this work.

The water used in this work was laboratory distilled water which was redistilled once from alkaline permanganate followed by one redistillation. The two redistillations were carried out in a continuous closed system. This procedure gives water with a turbidity of $(8.0 \pm 0.4) \times 10^{-5}$ cm.$^{-1}$. This value is appreciably higher than that reported by Phillips and Mysels,[10] but it is a value that has been reproduced by several

(6) J. C. Harris, *J. Am. Oil Chemists' Soc.*, **35**, 428 (1958).

(7) R. V. Nauman and J. B. Sardieco, unpublished work appearing in J. Sardisco, M.S. Thesis, Louisiana State University, 1958.

(8) R. V. Nauman and E. E. Drott, unpublished work appearing in E. E. Drott, Ph.D. Dissertation, Louisiana State University, 1959.

(9) W. D. Harkins and H. F. Jordan, *J. Am. Chem. Soc.*, **52**, 1751 (1930).

(10) J. N. Phillips and K. J. Mysels, *J. Phys. Chem.*, **59**, 326 (1955).

investigators in our laboratories for about 3 years, and the water is at least reproducibly dirty.

Surfactant solutions were filtered once through ultrafine sintered glass filters. Concentrations were determined by differential refraction measurements after filtration. The refraction calibration curves were determined with solutions prepared by weight. The refraction measurements used for analysis and for molecular weight determinations were made with a Brice–Phoenix differential refractometer.

Solutions for turbidity measurements were prepared individually or were made by addition of measured volumes of a filtered concentrated stock solution to water or more dilute solutions. Investigation showed that dirt introduced by the dilution method was statistically constant; correction for the impurity turbidity gave results indistinguishable from those obtained from individually prepared and filtered samples. A comparison of the two methods is shown in Fig. 1.

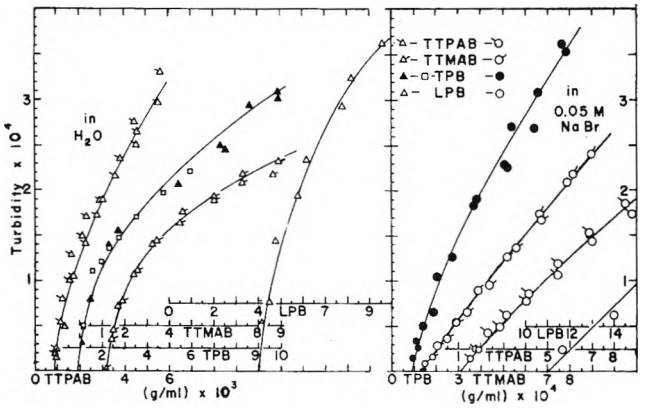

Figure 1. Turbidity *vs.* concentration.
△, tetradecyltripropylammonium bromide in water;
☆, tetradecyltrimethylammonium bromide in water;
▲, tetradecylpyridinium bromide in water (solutions made by dilution); □, tetradecylpyridinium bromide in water (solutions filtered individually); △, dodecylpyridinium bromide in water;
○, tetradecyltripropylammonium bromide in 0.05 *M* NaBr;
☆, tetradecyltrimethylammonium bromide in 0.05 *M* NaBr;
●, tetradecylpyridinium bromide in 0.05 *M* NaBr;
○, dodecylpyridinium bromide in 0.05 *M* NaBr.

Solubilization was determined spectrophotometrically. Excess benzene and detergent solutions were sealed in glass ampoules which were shaken at least 48 hr. at room temperature and then were thermostated at 30.00 ± 0.01°. The samples were kept in the thermostat until phase separation occurred, then the ampoule tip was broken, and weighed portions were immediately transferred into a measured amount of cyclohexane in a closed container. After extraction, the absorbancy of the cyclohexane phase at 255 mμ was determined.

Comparison with a calibration curve gave the benzene concentration. The efficiency of the extractions was determined independently and the immediate extraction from closed ampoules minimized loss of solubilizate that has plagued many solubilization experiments. Details of the method can be found elsewhere.[11] At least three series of seven or eight concentrations for each surfactant were run. Analyses were performed on each solution at least in duplicate.

Results and Discussions

1. Surface Tensions. Our surface tension data are shown in Fig. 2. Critical micelle concentrations and molecular areas determined from these data are given in Table I. The Gibbs adsorption equation[12] in the form (1/area) = $\Gamma = -(1/RT)(1/[2 \text{ or } 1])(\mathrm{d}\gamma/\mathrm{d} \ln c)$ was used to determine the areas per mole-

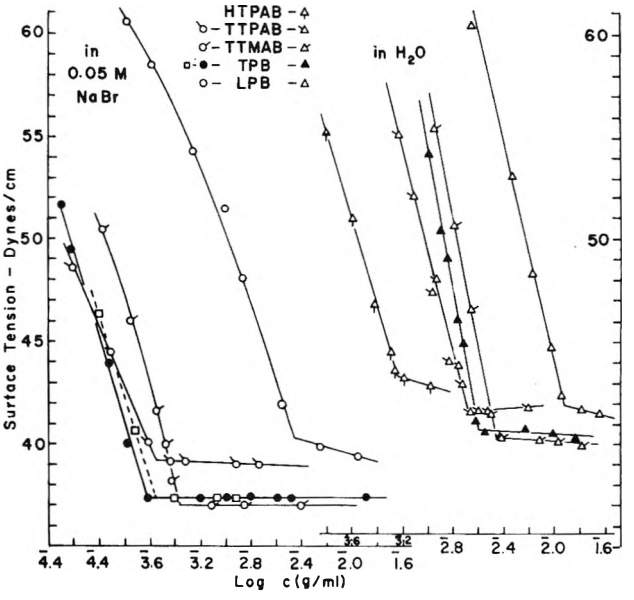

Figure 2. Surface tension *vs.* logarithm of concentration in g./ml. △, hexadecyltripropylammonium bromide in water;
☆, tetracecyltripropylammonium bromide in water;
☆, tetradecyltrimethylammonium bromide in water;
▲, tetradecylpyridinium bromide in water;
△, dodecylpyridinium bromide in water;
○, tetradecyltripropylammonium bromide in 0.05 *M* NaBr;
☆, tetradecyltrimethylammonium bromide in 0.05 *M* NaBr;
●, tetradecylpyridinium bromide in 0.05 *M* NaBr;
□, tetradecylpyridinium bromide in 0.05 *M* KBr;
○, dodecylpyridinium bromide in 0.05 *M* NaBr.

(11) E. L. Pye, J. B. Sardisco, and R. V. Nauman, to be published.
(12) J. W. Gibbs, "Collected Works," Vol. I, Longmans, Green and Co., New York, N. Y., 1928, pp. 218–237.

cule given in Table I. The factor 2 in the denominator was used in calculations dealing with solutions of surfactant ions in water, and the factor 1 was used when extraneous salt was present. The treatment of Guggenheim[13] is discussed in detail by Moilliet, Collie, and Black[14] as it applies to micellar solutions. At this time there will be no discussion of the physical significance of the area determination; it will be considered to be a parameter calculated from experiment that will be correlated with measured solubilizations.

Table I: Surface Tension Results

Surfactant	Critical micelle concentration (g./ml.) × 10⁴	Critical micelle concentration (moles/l.) × 10³	Area/molecule, Å.²
	In water		
LPB	39.7	12.1	59
TPB	9.15	2.57	60
TTMAB	11.8	3.51	61
TTPAB	8.6	2.05	89
HTPAB	2.58	0.57	91
	In 0.5 *M* sodium bromide		
LPB	12.0	3.66	48
TPB	0.86	0.24	48
TTMAB	1.43	0.42	39
TTPAB	1.16	0.276	64

Miles and Shedlovsky[15] showed that no minima occur in the surface tension–concentration curves when the surfactants are pure. This result was reconfirmed in this work. Shedlovsky and co-workers[16] observed changes with time in surface tensions of solutions of impure surfactants below the c.m.c. but found that no change with time occurs in these measurements after about 30 min. if the surfactants are pure. In this work small changes of surface tension with time were observed in all instances. These changes with one exception were not more than 0.5 dyne/cm. in 30 min. Later, LPB was purified by repeated recrystallization, and its surface tension at all concentrations was found to be constant for more than 10 min. after which no observations were made. These constant results agreed with the initial values found when there was a change with time. Initial values were used in the curves of Table I and in the area calculations.

Solutions of TTPAB were the only solutions to show large changes in surface tension with time; changes as large as 20 dynes/cm. were observed in 50 min. Purification which changed the turbidity results had no effect on the surface tension behavior. It seems unlikely that this behavior is real, but in this work it was reproduced.[17] Initial values were used for the area calculations.

Although this work is concerned primarily with solutions of the three detergents, TPB, TTMAB, and TTPAB, surface tensions were determined for aqueous solutions of LPB and HTPAB and for a 0.05 *M* NaBr solution of LPB as well for comparison purposes. Table I shows that there is a constancy in the area parameter for a particular kind of hydrophile. In aqueous solutions, the pyridinium group gives an area of 59 Å.² in the dodecyl salt and 60 Å.² in the tetradecyl salt. These results agree very well with results obtained by Greenland and Quirk,[18] by a very different method at a different interface. By X-ray diffraction analysis of hexadecylpyridinium bromide adsorbed on vermiculite from aqueous solution they found a 54-Å.² area for the adsorbed pyridine group lying flat on the clay surface.

The pyridinium area agrees well with the trimethylammonium area just as indicated by molecular models and the tripropylammonium area determined from solutions of the tetradecyl (89 Å.²) and the hexadecyl (91 Å.²) salts is larger as expected. The reproducibility of these determinations is 2 to 5 Å.².

In the salt solutions the two area results for the pyridinium group agree well; that of the trimethylammonium group is smaller than the pyridinium area, and that of the tripropylammonium is larger. All of the areas calculated from measurements on salt solutions are smaller than those obtained from measurements on aqueous solutions. The change in the pyridinium system with its more rigid hydrophilic head is appreciably less.

2. Molecular Weights. The light scattering data are shown in Fig. 1. The Princen–Mysels[19] treatment was used to calculate charge, p, aggregation number, m, micellar weight, mM_1, and micellar weight uncorrected for charge effects, $1/A$. These results are given in Table II along with differential refraction increments for the surfactants in aqueous solution and the monomeric molecular weights.

There are few results in the literature with which to compare our results. For TTMAB, Trap and

(13) E. A. Guggenheim, *Trans. Faraday Soc.*, **36**, 397 (1940).

(14) J. L. Moilliet, B. Collie, and W. Black, "Surface Activity," 2nd Ed., E. and F. N. Spon, Ltd., London, 1961, pp. 64–87.

(15) G. D. Miles and L. Shedlovsky, *J. Phys. Chem.*, **48**, 57 (1944).

(16) L. Shedlovsky, J. Ross, and C. W. Jakob, *J. Colloid Sci.*, **4**, 25 (1949).

(17) Recent preliminary work by Mr. Gary Brashier with a new group of preparations of TTPAB gives constant surface tensions from which areas are calculated which are nearly the same as those reported here.

(18) D. F. Greenland and J. P. Quirk, *J. Phys. Chem.*, **67**, 2886 (1963).

(19) L. H. Princen and K. J. Mysels, *J. Colloid Sci.*, **12**, 594 (1957).

Hermans[20] report 30,800 and 3.6×10^{-3} M and 53,400 and 1.3×10^{-3} M for the micellar weight and c.m.c. in water and in 0.05 N KBr. Debye[21] reports 25,300 and 3.4×10^{-3} M in water. Mysels[22] reports 3.41 $\times 10^{-3}$ M for the c.m.c. and 0.130 (12.2/93.5) for p/m. The Trap and Hermans results are probably high. When the other results are compared, they are as much in agreement as one can expect for light scattering results.

Table II: Turbidity Results

Surfactant	$(1/A) \times 10^{-3}$	$mM_1 \times 10^{-3}$	p/m	Mol. wt. $\times 10^{-3}$ (calcd.)	(dn/dc)
		In water			
LPB	14.9	17.7	0.166	17.9	0.174
TPB	22.3	26.0	0.136	25.9	0.175
TTMAB	23.2	27.2	0.143	23.7	0.154
TTPAB	22.7	25.6	0.114	20.1	0.160
		In 0.05 N NaBr			M_1
LPB	20.8	20.8	0.000	21.9	328
TPB	90.4	97.6	0.308	32.5	356
TTMAB	49.7	50.4	0.040	37.5	336
TTPAB	39.2	40.7	0.186	27.6	421

For TPB, Trap and Hermans report 28,100 and 4.1×10^{-3} M and 55,600 and 1.5×10^{-3} M for aqueous and 0.05 N KBr solutions. Our c.m.c. values are appreciably lower. In the 0.05 N salt the difference was so great that we repeated our experiments using a different preparation and KBr instead of the NaBr that we had used. The KBr solutions gave a 0.29×10^{-3} M c.m.c. compared with 0.24×10^{-3} M for the NaBr solutions. The comparison is shown in Fig. 2; the results are essentially the same as anticipated. Our micellar weight in 0.05 M NaBr is quite large but reproducible. Our other micellar weights are smaller than those of Trap and Hermans. Perhaps at this relatively high salt concentration the micelle is especially sensitive to temperature; Trap and Hermans worked at 30°; our light scattering instrument is not thermostated, and room temperature varied from 21 to 31°, probably being around 25° when our results were reproduced. Except perhaps for TPB in 0.05 M NaBr, all micellar weights are reasonable and consistent.

The areas of the hydrophiles were used with the linear extensions of the hydrocarbons chains that were suggested by Tartar[23a] to calculate a micellar weight.[23b] A spherical micelle with a radius equal to the chain extension was assumed. The calculated surface of the assumed sphere was divided by the area per head determined from the surface tension measurements to get an aggregation number. The micellar weights calculated from this crude model are given in Table II. They agree rather well with the experimental values in aqueous solution, but in 0.05 M salt where the micelle would not be expected to be spherical there is little correlation between calculated and measured values.

3. Solubilization. In this work the amount of material solubilized by the micellar part of the solution is desired. Consequently, the amounts of benzene dissolved in water, in 0.05 M NaBr, and in unmicellized surfactant were determined. The water determination also served as a check on the analytical procedure. The solubility of benzene in water was found to be 0.179 ± 0.002 g./100 ml. or 2.29×10^{-2} M. Arnold, *et al.*,[24] have reviewed the literature and have determined a value of 0.177 ± 0.002 g./100 ml. The solubility of benzene in 0.05 M NaBr was found by us to be 0.173 ± 0.002 g./100 ml. or 2.22×10^{-2} M. The solubility of benzene at the c.m.c. depends upon the surfactant but is in general about 0.09×10^{-2} M higher than the solubility in the solvent. The solubility of benzene at the c.m.c. will be called S_0.

The necessity for immediate extraction of the benzene removed from the sealed ampoules was shown by the following experiments with TTMAB. Usually two or three portions of the aqueous solution were transferred to the cyclohexane directly from the ampoule and weighed immediately for multiplicate determinations. In one group of experiments one portion from each ampoule was transferred directly and weighed immediately. Another portion was transferred to a beaker, and within a fraction of a

(20) H. J. L. Trap and J. J. Hermans, *Proc. Koninkl. Ned. Akad. Wetenschap*, **58B**, 97 (1955).

(21) P. Debye, *J. Phys. Colloid Chem.*, **53**, 1 (1949).

(22) K. J. Mysels, *J. Colloid Sci.*, **10**, 507 (1955).

(23) (a) H. V. Tartar, *ibid.*, **14**, 115 (1959). (b) One of the referees suggests that this calculation has no meaning because, "Once one assumes a spherical micelle having the radius of the fully extended chain, its molecular weight is fixed since the number of monomers which can be packed into such a sphere is determined. Hence, the surface area per head is also determined. Another way of looking at it is to say that the Tartar calculation implies that the area per head is proportional to the two-thirds power of the chain length." This argument suggests that all spherical micelles of surfactants having the same chain length would have the same aggregation number and the same head size. Whether the micelles are spherical is debatable, but all micelles with the same chain length do not have the same aggregation number and the same head size. We agree that the area per head is proportional to the two-thirds power of the chain length, but we are suggesting a different criterion for determining the proportionality constant than that of monomeric chain volume chosen by Tartar. It seems unnecessary to assume that the packing in the interior of the micelle is always the same and determines the micelle size.

(24) O. S. Arnold, C. A. Plank, E. E. Erickson, and F. P. Pike, *Chem. Eng. Data Ser.*, **3**, 253 (1958).

minute a part was pipetted into cyclohexane and weighed. The portions that had undergone intermediate transfer to the beakers gave results that were consistently lower than those from the directly transferred solutions by 5 to 10% of the total solubilizate.

Inadvertently, some solubilization experiments were performed before the surfactants were purified to an extent that resulted in reproducible turbidity and surface tension results. The very pure surfactants gave solutions in which phase separation occurred rapidly and cleanly; the other solutions gave emulsions that required weeks in some cases to break into separate phases. However, within experimental error, no difference in solubilization could be determined between solutions of the surfactants that were extremely pure and those that were only moderately pure.

Table III summarizes the solubilization results. It gives values taken at even surfactant concentrations from smooth curves for aqueous data and from least-square lines through all the experimental points for 0.05 M NaBr data. In aqueous solutions the solubilization increases slightly with surfactant concentration, but in 0.05 M NaBr the solubilization is concentration independent.

Table III: Solubilization Results

$(C - C_0)M \times 10^2$	$(S - S_0)M \times 10^2$				$(S - S_0)/(C - C_0)$			
	LPB[a]	TPB	TTMAB	TTPAB	LPB	TPB	TTMAB	TTPAB
				In water				
0.50	0.80	1.09	1.04	1.09	1.60	2.14	2.08	2.18
1.00	1.60	2.15	2.08	2.20	1.60	2.15	2.08	2.20
1.50	2.40	3.25	3.12	3.44	1.60	2.17	2.08	2.29
2.00	3.20	4.45	4.28	4.73	1.60	2.23	2.14	2.37
2.50	4.00	5.80	5.61	6.17	1.60	2.32	2.24	2.47
3.00	4.80	7.35	7.08	8.08	1.60	2.45	2.36	2.69
8.00	13.59				1.70			
				In 0.05 M NaBr				
0 → 3					2.27	4.54	4.41	6.53

[a] Solubilization results for LPB are available to $C - C_0 = 8 \times 10^{-2}$.

The solubilization of benzene in TPB and TTMAB is nearly the same in aqueous solutions; both the micellar weights and the hydrophile size are nearly the same also. TTPAB solubilizes a bit more benzene in water than do TPB and TTMAB on a mole solubilized to mole of monomer basis; the micellar weight of TTPAB is about the same as that of the other two but is probably a bit smaller, while the head size is significantly larger. In more concentrated solutions the increase in solubilization for a surfactant with the larger head but the same tail size is 0.28 to 0.46 as much as that shown by a two-carbon increase in tail length for the same head size. In dilute solution the solubilizations of all surfactants with the same chain length are nearly the same.

In 0.05 M NaBr there is no apparent correlation between micellar weights and solubilization. The solubilization ability of the tripropyl salt is now nearly as much greater than that of the other two tetradecyl salts as they are greater than that of the dodecyl salt.

Certainly the solubilization ability of these surfactants is not simply related to the head size parameter, but these results give sufficient encouragement to warrant more detailed investigation of the features of solution properties that commonly affect solubilization and surface tension.

It is tempting to try to rationalize the solubilizations with the observed micellar sizes, but the sizes reported here are representative of the micelles in the absence of solubilizate. Investigations are under way to determine micellar sizes in the presence of solubilizate, to study the micellar sizes and solubilization ability of trimethyl, triethyl, tripropyl, and tributyl surfactants in a series of salt solutions, and to extend the work to other solubilizates.

The Structure of the Micellar Solutions of Some Amphiphilic Compounds in Pure Water as Determined by Absolute Small-Angle X-Ray Scattering Techniques

by F. Reiss-Husson and Vittorio Luzzati[1]

Centre de recherches sur les Macromolécules, Strasbourg, France *(Received April 7, 1964)*

Micellar solutions of several amphiphiles in water, without added electrolytes, have been studied by small-angle X-ray scattering methods, based upon intensity measurements on an absolute scale. The concentration range goes from 5% to the appearance of a liquid crystalline phase (30 to 40% in most cases). Several amphiphiles have been studied at different temperatures: sodium lauryl sulfate (27 and 70°), sodium laurate (70°), myristate (80°), palmitate (80°), stearate (90°), and oleate (NaO, 27°), and cetyltrimethylammonium chloride (CTACl, 27°) and bromide (27, 50 and 70°). The interpretation of the experimental curves is discussed. It is shown that over various concentration ranges the micelles may be assumed to be monodisperse, their size and shape being independent of concentration. The analysis of the curves leads to the determination of the structure of the micelles. The structure is dependent on various parameters: nature of the amphiphile, temperature, and concentration. In most systems the micelles are spherical at low concentrations and become rod-like at high concentration. In two cases, the structure appears to be independent of the concentration: CTACl micelles are spherical from 5 to 38%; NaO micelles are rod-like from 4 to 20%. This polymorphism is discussed.

Introduction

For several years one of the main activities of our laboratory has been the study by X-ray diffraction of various structures of association colloids. Until now we have been mainly interested in liquid crystals, especially those of concentrated (generally over 30%) aqueous systems.[2] We are now reporting on the structure of micellar solutions which occur at lower concentrations.

We may note that, although the structure of micelles is quite well known, at least for a few systems, at very low concentrations close to the critical micelle concentration (c.m.c.), there is little definitive information about higher concentrations, where the effects of correlations between micelles become predominant and the interpretation of hydrodynamic and light-scattering experiments becomes uncertain. Structural analysis is best done in this region of concentrations by small angle X-ray scattering, a technique which has been used by several authors. McBain[3a] and Harkins[3b] were pioneers in this field, even though their work is now only of historical interest since the interpretation of experimental findings lacked a theoretical basis.[4-6] Others[7,8] have attempted a more rigorous interpretation of the experimental curves by trying to reconstruct their form on the basis of models of spherical micelles showing mutual correlations. It proved, however, to be difficult to distinguish the effect of the shape of micelles from that of their correlations. We have undertaken this problem by using an improved small-angle X-ray scattering technique, developed in our laboratory, which is based upon intensity measurements on an absolute scale.

(1) CNRS, Gif-sur-Yvette, France.

(2) V. Luzzati, H. Mustacchi, A. E. Skoulios, and F. Husson, *Acta Cryst.*, **14**, 219 (1961).

(3) (a) J. W. McBain and D. A. Hoffmann, *J. Phys. Colloid Chem.*, **53**, 39 (1949); (b) R. W. Mattoon, R. S. Stearns, and W. D. Harkins, *J. Chem. Phys.*, **15**, 209 (1947).

(4) A. Guinier and J. Fournet, "Small Angle X-Ray Scattering," John Wiley and Sons, Inc., New York, N. Y., 1955.

(5) M. L. Corrin, *J. Chem. Phys.*, **16**, 844 (1948).

(6) E. W. Hughes, *Nature*, **165**, 1017 (1950).

(7) G. W. Brady, *J. Chem. Phys.*, **19**, 1547 (1951).

(8) D. E. Andersen and G. B. Carpenter, *J. Am. Chem. Soc.*, **75**, 850 (1953).

Only a short account of the experimental results will be given here. A detailed description may be found in the Ph.D. dissertation of F. R.-H.[9] Furthermore, some special technical problems involved in the application of the small-angle X-ray scattering techniques to the study of micelles will be discussed elsewhere.

Experimental Technique

We have studied the following aqueous solutions: sodium lauryl sulfate (SLS) at 27 and 70°; sodium soaps: laurate (NaC_{12}) at 70°, myristate (NaC_{14}) at 80°, palmitate (NaC_{16}) at 80°, stearate (NaC_{18}) at 90°, and oleate (NaO) at 27°; cetyltrimethylammonium chloride and bromide (CTACl and CTAB) at 27 and at 27, 50, and 70°, respectively.

Solutions. The sodium soaps were prepared by neutralizing the fatty acids in methanolic solution with alcoholic sodium hydroxide, followed by precipitation and washing with anhydrous ether. The saturated fatty acids were obtained from Eastman Kodak, oleic acid from Prolabo and Fluka. We obtained commercially the SLS (Merck), the CTAB (Hochst), and the CTACl (Delta).

The concentration c (grams of amphiphile per gram of solution) of each solution was determined by drying the sample after the X-ray diffraction experiment. From c one calculates c_m, the weight concentration of micellized amphiphile, and c_e, the electronic concentration (the number of electrons of micellized amphiphile per electron of the solution), as

$$c_m = c - (\text{c.m.c.})$$

$$c_e = \left[1 + \frac{Z_0}{M_0}\frac{M_a}{Z_a}\frac{1 - c_m}{c_m}\right]^{-1}$$

where Z and M are the number of electrons and the mass of one molecule of amphiphile (subscript a) or of water (subscript 0). The c.m.c. (in g./g.) is negligible in comparison with the experimental values of c, except for SLS (c.m.c. = 2×10^{-3} at 25° and 3×10^{-3} at 70°),[10] NaC_{12} (7×10^{-3} at 25°),[11] and NaC_{14} (2.3×10^{-3} at 80°).[12]

The specific volumes are expressed in Å.^{3} e^{-1} (where e stands for electron). We have calculated the partial specific volumes of the hydrocarbon chain, ψ_{par}, for the several amphiphiles, on the basis of the partial volumes of the $-CH_2-$ and $-CH_3$ groups in molten paraffins (*cf.* ref. 9). We have measured pycnometrically the partial volumes of the amphiphiles, ψ. From this we have calculated the partial specific volumes, ψ_{pol}, of the polar groups $-COONa$, $-OSO_3Na$, $-N(CH_3)_3Br$, and $-N(CH_3)_3Cl$. Tables I and II summarize these values.

Table I: Partial Specific Volumes

Compd.	t, °C.	$\bar{V}_a$, cm.^{3} g.$^{-1}$	ψ, Å.^{3} e^{-1}	$\bar{V}_{par}$, cm.^{3} g.$^{-1}$	ψ_{par}, Å.^{3} e^{-1}	$\bar{V}_{pol}$, cm.^{3} g.$^{-1}$	ψ_{pol}, Å.^{3} e^{-1}
SLS	24	0.857	2.69	1.26	3.64	0.343	1.15
	70	0.922	2.83	1.30	3.77	0.386	1.29
NaC_{12}	70	0.966	2.97	1.31	3.80	0.227	0.77
NaC_{14}	70	1.010	3.03	1.29	3.75	0.228	0.77
NaC_{16}	80	1.035	3.11	1.29	3.74	0.228	0.77
NaC_{18}	90	1.059	3.17	1.29	3.74	0.229	0.77
NaO	27	0.997	3.00	1.215	3.55	0.226	0.77
CTAB	27	0.996	3.02	1.235	3.57	0.611	2.04
	50	1.014	3.08	1.26	3.64	0.617	2.06
	70	1.027	3.13	1.28	3.69	0.621	2.08
CTACl	27	1.11	3.26	1.235	3.57	0.817	2.50

Table II: Partial Specific Volumes of $-CH_2-$ and $-CH_3$ Groups of Molten Paraffins

t, °C.	$\bar{V}$ ($-CH_3$), cm.^{3} g.$^{-1}$	ψ ($-CH_3$), Å.^{3} e^{-1}	$\bar{V}$ ($-CH_2-$), cm.^{3} g.$^{-1}$	ψ ($-CH_2-$), Å.^{3} e^{-1}
27	2.18	6.04	1.16	3.39
50	2.29	6.36	1.18	3.44
70	2.39	6.62	1.19	3.48
80	2.44	6.76	1.20	3.50
90	2.48	6.90	1.21	3.52

X-Rays. The apparatus used for the absolute measure of the scattered intensity has been described elsewhere.[13] Its principle of operation is as follows. The copper $K\alpha_1$ line is isolated by a bent-quartz monochromator which focuses it as a short straight line on the entrance slit of a Geiger counter. The direct beam, defined by a system of slits, is very high and of negligible width; its energy is measured after attenuation by calibrated nickel filters. The solution, enclosed in a thin cell between mica windows, is placed at the center of a goniometer whose mobile arm carries the Geiger counter. The temperature of the sample is regulated automatically, and its thickness is measured on the basis of its absorption coefficient for X-rays.

The experiment consists in the recording of the intensity scattered by the solution, $I(s)$ (here $s = 2 \sin \theta/\lambda$, where 2θ is the angle between the scattered and direct beams and λ is the wave length), the energy of the direct beam, $\int i_0(s)ds$, and the thickness η of the sample, expressed in electrons/cm.^{2}. The experiment

(9) F. Reiss-Husson, Thesis, University of Strasbourg, 1963.
(10) B. D. Flockhart, *J. Colloid Sci.*, 16, 484 (1954).
(11) D. Eagland and F. Franks, *Nature*, **191**, 1003 (1961).
(12) P. Ekwall, *Z. physik. Chem.*, **A61**, 195 (1932).
(13) V. Luzzati, *Acta Cryst.*, 13, 939 (1960).

is then repeated with the solvent, *i.e.*, a solution having the concentration of the c.m.c. An experimental function

$$j_n(s) = \left[\frac{I(s)}{\eta\nu\int i_0(s)\mathrm{d}s}\right]_{\text{solution}} - \left[\frac{I(s)}{\eta\nu\int i_0(s)\mathrm{d}s}\right]_{\text{solvent}} \quad (1)$$

where ν is a constant equal to $7.29\lambda^2$, is thus obtained.

It can be shown that the function $j_n(s)$ depends only on the structure of the sample, *i.e.*, on the distribution of its electronic density,[13] and that it is independent of the experimental conditions.

Interpretation

For each amphiphile and at each temperature a series of low-angle diffraction experiments is performed at different concentrations. The experimental data are composed of the partial volumes ψ, ψ_{par}, and ψ_{pol} of the amphiphile and of the curves $j_n(s)$ (eq. 1), which are preferably divided by their corresponding concentrations c_e. (Besides the low angle scattering, one observes at $s \sim 4.5$ Å.$^{-1}$ a broad band, characteristic of the liquid configuration of the hydrocarbon chains.[1])

A few easily justified hypotheses are used along with the above data. Thus we assume that the interior of the micelle is occupied only by the $-CH_2-$ and CH_3- groups of the amphiphile and forms a paraffinic liquid of constant electronic density, ρ_{par}. We also assume that water and the unassociated molecules of the amphiphile form a region of constant electron density ρ_0 between the micelles. ρ_{par} and ρ_0 are known. One of the unknowns of the problem is the distribution of the electron density ρ_{pol} near the water–paraffin interface, in the region of the polar groups ($-COONa$, $-OSO_3Na$, etc.) and of the hydrated counterions. This distribution ρ_{pol} will be assumed here to be uniform; this assumption involves in fact only minor restrictions to the general validity of the mathematical treatment.[9]

There are several stages in the analysis of the experimental curves.

A. Analysis of the Total Intensity. It can be shown quite generally[13] that the following integral of the curve $j_n(s)/c_e$ can be related to the mean square fluctuation of the electronic density

$$2\pi\int_0^\infty \frac{sj_n(s)}{c_e}\mathrm{d}s = \frac{(\rho - \bar{\rho})^2}{c_e\bar{\rho}} \quad (2)$$

The experimental values of (2) furnish two types of information.

On the one hand, it is possible to show that when the shape and the dimensions of the scattering particles remain constant, as the concentration varies, the value of (2) remains constant. Thus, whenever the latter condition is satisfied, the micelles may be assumed to have constant shape and dimensions; we shall take such experimental observation as a suggestion that indeed the micelles remain identical.

On the other hand, and independently of the constancy of (2), one can separate the expression for the average square of the electron density into three parts stemming, respectively, from the aqueous region (ρ_0), the paraffinic kernel (ρ_{par}), and the polar layer (ρ_{pol}). Since the value of the first two terms is known, they can be subtracted from the total. The value of (2) yields therefore the contribution $C(\rho_{pol})$ of the polar layer. If one assumes in addition that all the micelles have the same shape and that ρ_{pol} is constant, one obtains the value of ρ_{pol}, which in this case is equal to $C(\rho_{pol})$.

B. The Two-Phase Region, Solution–Middle Phase. Separation into two phases, the micellar solution and the liquid crystalline middle phase, is observed at higher concentrations for all the amphiphiles studied. It is well known that the middle phase is formed by infinitely long cylindrical micelles located at the centers of a two-dimensional hexagonal lattice.[2] In the two-phase region the X-ray diffraction record shows simultaneously the broad band scattered by the micellar solution, with its one or two maxima (depending on the amphiphile), as well as the sharp diffraction lines of the middle phase (Fig. 1). In all cases except CTACl the maximum or maxima coincide in position with the first (and second) lines. This suggests that the structure of the two phases presents some similarities; more precisely, rod-shaped micelles exist in both phases. Those rods, which display crystalline order in the two dimensional lattice in the middle phase, show only loose correlations in the micellar solution. The

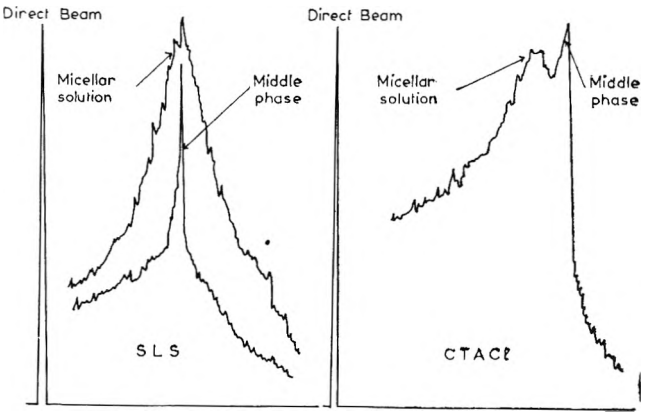

Figure 1. Microdensitometer tracing of photographic films, recorded in a small-angle X-ray scattering camera: SLS, $c_e = 0.30$ at 27°; CTACl, $c_e = 0.42$ at 27°. In both cases the micellar solution is found in equilibrium with the middle phase.

only exception which we have observed is CTACl at 25°. Here, the maximum of the band is located at a definitely lower angle than the first line of middle phase (Fig. 1). In this one case the micellar solution seems not to contain rods.

C. Measurement of the Mass and of the Radius of Gyration. In the study by X-ray diffraction of globular particles, it is possible in principle to determine the mass and the radius of gyration of the particles, once the effect of correlations has been eliminated by extrapolation to zero concentration.[4,13] This method cannot be used in most of the present systems because the curves $j_n(s)/c_e$, even when extrapolated to $c = 0$, show a maximum due to nonuniform electron density within each micelle. Only in the case of CTACl does this extrapolation yield a monotonic curve. Furthermore, the nonvariation of the integral (2) with concentration is, in this case, consistent with the micelles having a constant shape (Table III). We have drawn

Table III: Integral Intensity as a Function of Concentration for CTACl at 27°

c_e	$10^3 \times 2\pi \int_0^\infty \frac{s j_n(s)\, ds}{c_e}$
0.05	6.0
0.07	5.9
0.10	5.7
0.17	5.7
0.24	5.8
0.29	5.6
0.33	5.7
0.36	5.7
0.37	6.0
0.38	5.8

the curves $j_n(s)/c_e$ according to the method of Guinier[4] (Fig. 2). At finite concentrations a maximum is observed, the position of which approaches $s = 0$ as the concentration decreases. At $c = 0$ one obtains a straight line whose slope and intercept on the ordinate lead to the determination of the mass and of the radius of gyration of the micelles. These two parameters are in excellent agreement with the existence of spherical micelles having a paraffinic radius of 21.7 Å. (Table IV), a value which is compatible with the hydrocarbon chain length of CTACl.

D. Computation of the Function $j_n(s)/c_e$ for a Model. The definitive verification of a model is provided by the comparison of the experimental $j_n(s)/c_e$ curves with the calculated function corresponding to the model. This comparison is possible only at low concentrations, when the shape and the dimensions of the micelles

Table IV: Parameters of the Spherical Micelles of SLS, NaC_{12}, and CTACl[a]

Compound	t, °C.	R_{par}, Å.	R_{pol}, Å.	n	S_a, Å.²	$(S_a)_m$, Å.²
SLS	25	17.8	24.0	67	65	59
SLS	70	17.0	23.0	57	68	
NaC_{12}	70	12.5	24.4	25	76	51
CTACl	27	21.7	...	84	74	65

[a] n, number of monomers; S_a, specific surface, compared to $(S_a)_m$, specific surface in middle phase.[2]

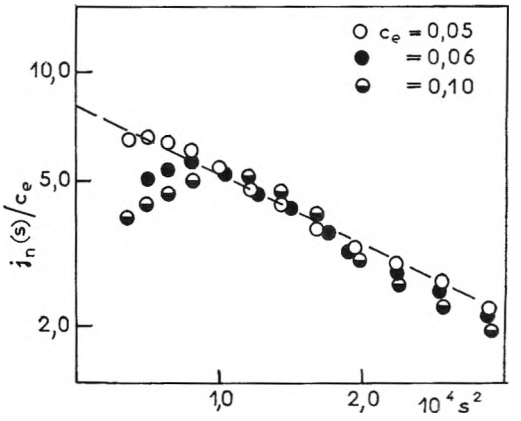

Figure 2. Guinier plots of the experimental curves $j_n(s)/c_e$ for CTACl, at 27°.

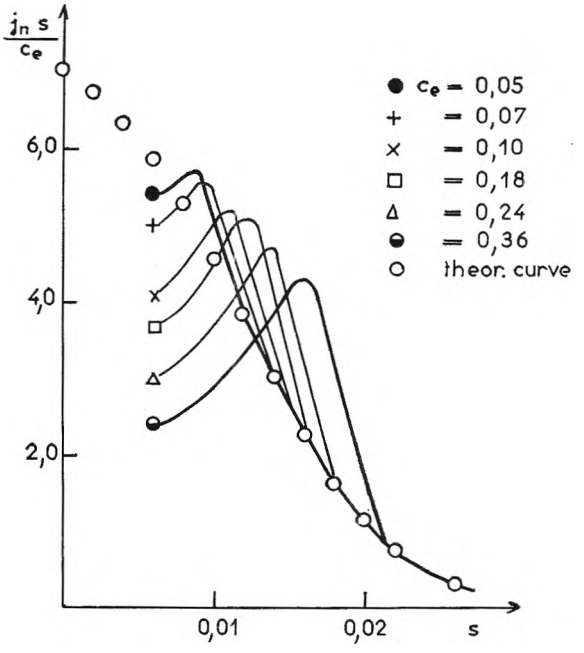

Figure 3. Comparison of experimental curves $j_n(s)/c_e$ for CTACl (at 27°) and the theoretical curve relevant to the spherical model (Table IV).

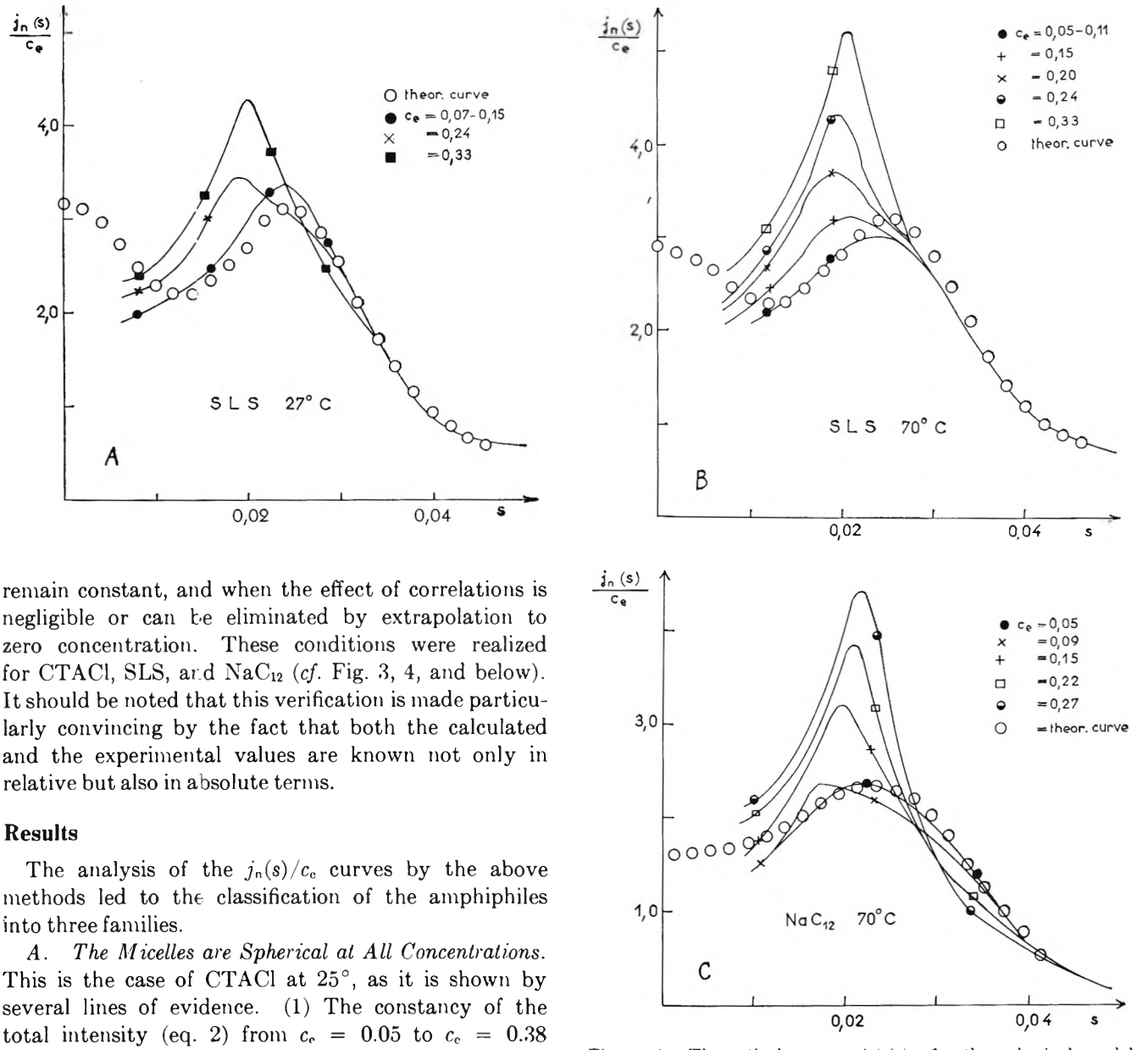

Figure 4. Theoretical curves $j_n(s)/c_e$ for the spherical model (Table IV) and experimental curves relevant to: A, SLS at 27°; B, SLS at 70°; C, NaC_{12} at 70°.

remain constant, and when the effect of correlations is negligible or can be eliminated by extrapolation to zero concentration. These conditions were realized for CTACl, SLS, and NaC_{12} (*cf.* Fig. 3, 4, and below). It should be noted that this verification is made particularly convincing by the fact that both the calculated and the experimental values are known not only in relative but also in absolute terms.

Results

The analysis of the $j_n(s)/c_e$ curves by the above methods led to the classification of the amphiphiles into three families.

A. The Micelles are Spherical at All Concentrations. This is the case of CTACl at 25°, as it is shown by several lines of evidence. (1) The constancy of the total intensity (eq. 2) from $c_e = 0.05$ to $c_e = 0.38$ (Table III) is consistent with the shape and the dimensions of the micelles remaining constant. (2) The analysis of the $j_n(s)$ curves based upon Guinier's law leads to the determination of the micellar weight and radius of gyration, the numerical values of which are in good agreement with the spherical model. (3) The calculated $j_n(s)$ curve for such spherical micelles agrees with the experimental curve in shape and absolute value when the correlation effects are eliminated by extrapolation to $c = 0$ (Fig. 3). It may be noted that, in this case, the maxima observed in $j_n(s)$ at high concentration are a consequence of the intermicellar correlations. (4) The existence of spherical micelles takes into account the observation that the bands of the micellar solution and the sharp reflections of the middle phase do not coincide in position in the concentration range in which both phases are present in equilibrium (Fig. 1).

B. The Micelles are Rods at All Concentrations. For NaO at 27° the integral (2) is again constant from $c = 0.05$ to $c = 0.20$, which corresponds to a constant value of ρ_{pol} (Fig. 5). The shape and the dimensions of the micelles seem then to remain constant, as in the case of CTACl. Here, however, the comparison between the concentrated solutions and the middle phase indicates that the micelles are very elongated rods (*cf.*

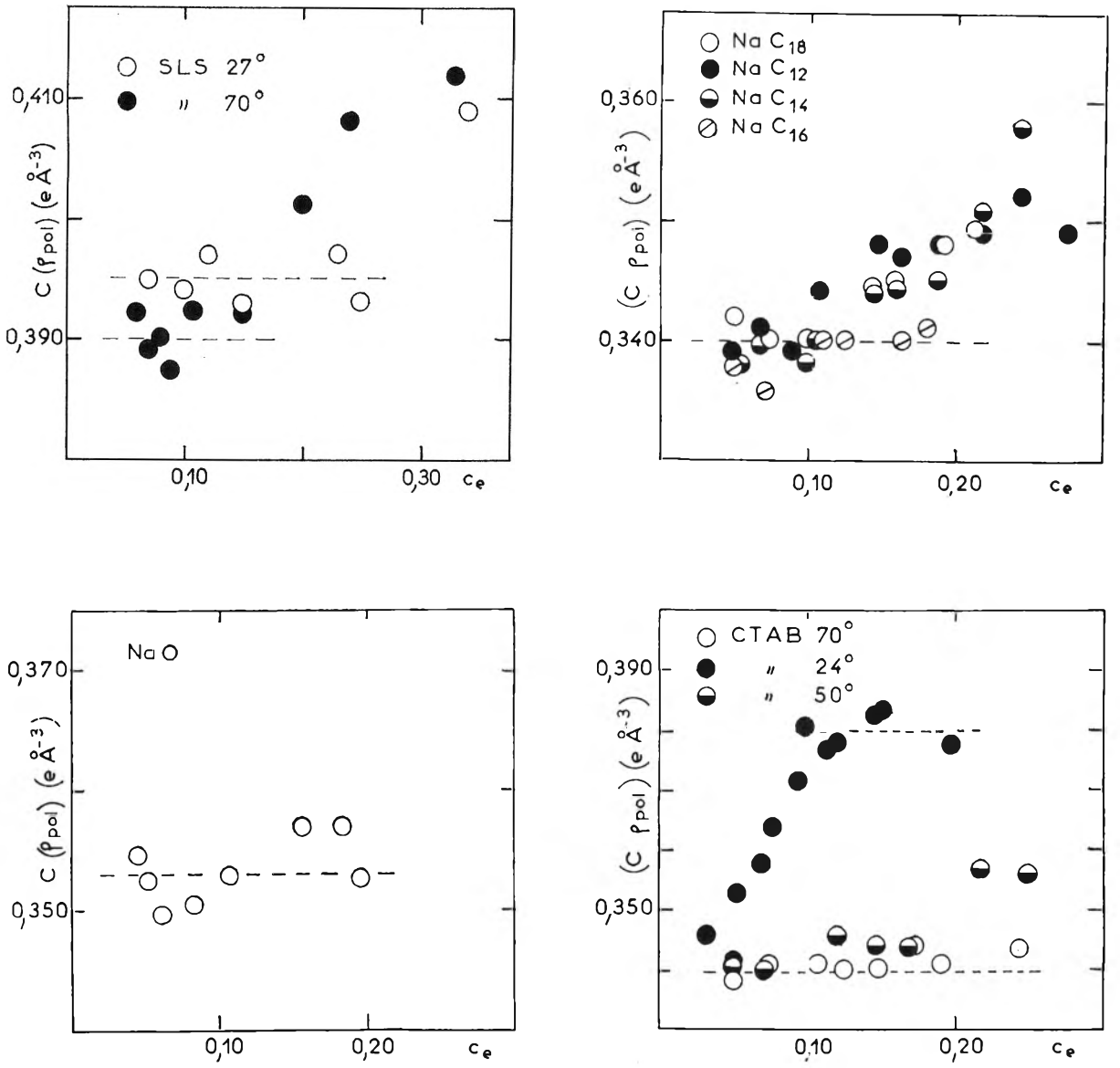

Figure 5. Plot of $C(\rho_{pol})$, as a function of concentration, for SLS, CTAB, and sodium soaps.

above). We have verified[9] that a model of very long rods, having the same diameter as those of the middle phase, but distributed without correlations, accounts for the shape of the $j_n(s)/c_e$ curves for large s, the region where the effect of correlations tends to disappear. This is all we could do in this case.

C. The Micelles Are Spheres at Low Concentrations and Become Rods at High Concentrations. This is the behavior of SLS at 27 and 70°, of the saturated sodium soaps, and of CTAB at 27, 50, and 70°. The change in the micellar form is indicated by the variation of the integral (2), which requires a corresponding variation of $C(\rho_{pol})$ (Fig. 5) within a range of concentrations whose limits can be approximately determined (Table V). This transition leads to the formation of rod-shaped micelles in the most concentrated solutions, as it is shown by the comparison of micellar solution and middle phase (*cf.* above).

In the case of SLS at 27 and 70°, of the saturated sodium soaps, and of CTAB at 50 and 70°, the micelles appear to remain the same over a small concentration range since ρ_{pol} remains constant. Furthermore, the micelles seem to be spherical over this concentration range, as it is suggested by SLS at 27 and 70° and by NaC_{12} at 70°. In these two cases, in which intermicellar correlations become negligible at low concentration,[9] the spherical models the parameters of which are listed in Table IV lead to an excellent agreement between

Table V: Approximate Concentration Ranges for the Different Types of Micelles

Amphiphile	t, °C.	Spherical micelles	Sphere–rod transition	Rod-like micelles	Middle phase
CTACl	27	0.05	0.40		0.40
NaO	27			0.04	0.20
SLS	27	0.07	0.25		0.40
SLS	70	0.05	0.15		0.40
NaC_{12}	70	0.05	0.10		0.36
NaC_{14}	70	0.06	0.10		0.28
NaC_{16}	80	0.05	0.18		0.23
NaC_{18}	90	0.05	0.16		0.22
CTAB	70	0.05	0.25		0.32
CTAB	50	0.05	0.17		0.26
CTAB	27		0.05	0.10	0.25

experimental and theoretical curves (Fig. 4). For the other amphiphiles the spherical model is compatible with the shape of the experimental curves for large s, but the direct determination of the micelle dimensions is hindered by the intermicellar correlations.

The behavior of CTAB at 27° is somewhat different. The value of $C(\rho_{pol})$ varies at low concentration (Fig. 5) and then remains constant in the range of c_e from 0.10 to 0.20. Here the transition from spheres to rods appears to occur at a low concentration, below 0.10.

Discussion

A few comments should be made on the limitations of the techniques used in this work. The small-angle X-ray scattering methods can provide a justification for the choice of one particular structure model; a rigorous proof of the uniqueness of the model is usually difficult to obtain. We made an effort in order to confirm our models by an extensive analysis of different systems, studied in a variety of experimental conditions, and by taking into account different lines of evidence. The techniques used are not very sensitive to polydispersity of the system, both in size and shape; statements about monodispersity and sphericity of the micelles should be taken to mean that the departure from these ideal conditions is not too large.

It is clear that the use of intensity measurements on an absolute scale is of essential importance for the interpretation of the experimental data. If only the shape of the scattering curves were known, the interpretation would remain ambiguous, since it would be difficult to disentangle the effects due to the internal structure of the micelles from those of the intermicellar correlations.

There is good agreement between the dimensions of micelles obtained by us and those determined by other methods; the size of the spherical micelles of SLS at 27° is close to that given by light scattering,[14] diffusion,[15] and sedimentation[16] for more dilute solutions. The rod shape of micelles of NaO and of CTAB at 27° is confirmed by some anisotropic properties of their solutions.[17] In general, our results agree with the view, expressed by several authors, that a transition takes place in micellar solutions, as a function of concentration.[18–21]

Our results show that the form of the micelles is a function of temperature, of concentration, and of the nature of the amphiphile. Such a polymorphism (further examples of which are encountered in the liquid crystalline phases formed by these amphiphiles[2]) requires that the hydrocarbon chains are liquid-like, since only a liquid can fill up uniformly the interior of volumes of different shapes: spheres, lamellae, rods, etc. In this respect, our results fully confirm the ideas of Hartley.[22] On the other hand, the existence of lamellar micelles can be shown to be incompatible with the experimental curves, at least in the systems described here.

From the few cases studied here it is difficult to draw any general conclusion about the influence of the chemical structure of the amphiphile, of the temperature, and of the concentration upon the shape of the micelles. One can, however, emphasize the role played by the average area available to each polar group at the water–paraffin interface; indeed, it should be noted that this area decreases as the concentration increases (Table IV), just as it does in the liquid crystals.[2]

Our method provides no information about the process by which micelles change from spheres to rods. The concentration at which the onset of this transformation takes place depends on the amphiphile and on the temperature but does not seem to be simply related to the thickness of the water layer separating neighboring micelles since it varies greatly from one amphiphile to another (*cf.* Table V).

(14) K. J. Mysels and L. H. Princen, *J. Phys. Chem.*, **63**, 1693 (1959).

(15) D. Stigter, R. J. Williams, and K. J. Mysels, *ibid.*, **59**, 330 (1955).

(16) P. J. Minhlieff, Thesis, University of Utrecht, 1958.

(17) K. G. Götz and K. Heckmann, *J. Colloid Sci.*, **13**, 266 (1958); *Z. physik. Chem.* (Frankfurt), **20**, 42 (1959).

(18) J. M. Corkill and K. W. Herrmann, *J. Phys. Chem.*, **67**, 934 (1963).

(19) P. A. Winsor, "Solvent Properties of Amphiphilic Compounds," Butterworth and Co., Ltd., London, 1954.

(20) J. Stauff, *Kolloid-Z.*, **96**, 245 (1941).

(21) W. D. Harkins, *J. Chem. Phys.*, **16**, 156 (1948).

(22) G. S. Hartley, "Progress in Chemistry of Fats and Other Lipids," Pergamon Press, London, 1955, p. 19.

For all the amphiphiles, except CTACl, the transition from micellar solutions to the liquid crystal corresponds to the establishment of a crystalline order among pre-existing but incompletely ordered micelles. In contrast, for CTACl, a much more drastic rearrangement occurs since even the shape of the micelles seems to change.

Acknowledgment. We wish to express our gratitude to Dr. K. J. Mysels who kindly helped us with the English translation of this paper.

Nonionic Surface-Active Compounds. VIII. Film Drainage Transition Temperatures by Surface Viscosity

by Paul Becher and Anthony J. Del Vecchio

Chemical Research Department, Atlas Chemical Industries, Inc., Wilmington, Delaware *(Received April 13, 1964)*

Film drainage transition temperatures (FDTT) have been studied for polyoxyethylene (12) lauryl alcohol in the presence of added lauryl alcohol, and of polyoxyethylene (23) lauryl alcohol in the presence of added lauryl and cetyl alcohol. The FDTT were determined principally by measurements of surface viscosity (although direct observations were also made) in the temperature range 10 to 60° and at total concentrations of 0.001 to 1.0 g./dl. The concentration of additive alcohol ranged up to 10%. In the absence of additive, fast-draining films are obtained in all cases; however, the addition of fatty alcohol gives rise to slow-draining films, with a transition to fast-draining, in complete analogy to the behavior of anionic materials. The FDTT for systems involving a particular alcohol appears to depend only on the mole ratio of nonionic agent and is independent of the nature of the agent. The analogy with melting point depression phenomena is indicated.

Introduction

It has been shown by Miles, Ross, and Shedlovsky[1] that films of aqueous solutions of ionic surface-active agents can be classified as either "fast-draining" or "slow-draining" films. Slow-draining films are usually found in systems containing hydrolyzable agents or in the presence of certain polar impurities, *e.g.*, fatty alcohols. Epstein, *et al.*,[2,3] have shown that such slow-draining films become fast-draining at higher temperatures, the transition between the two forms being quite sharp. This temperature is called the "film drainage transition temperature (FDTT)."

Systems exhibiting slow drainage are characterized by the existence of a high surface viscosity,[4] and Ross[5] has shown that the FDTT occurs at the same temperature as the transition from a region of high surface viscosity to one of low viscosity. As well as affording a mechanism for the transition in properties, the observation of surface viscosity permits a sharp determination of the transition temperature.

In the present study, the existence of film drainage transitions is demonstrated in systems of nonionic

(1) G. D. Miles, J. Ross, and L. Shedlovsky, *J. Am. Oil Chemists' Soc.*, **27**, 268 (1950).

(2) M. B. Epstein, J. Ross, and C. W. Jakob, *J. Colloid Sci.*, **9**, 50 (1954).

(3) M. B. Epstein, A. Wilson, C. W. Jakob, L. E. Conroy, and J. Ross, *J. Phys. Chem.*, **58**, 860 (1954).

(4) A. G. Brown, W. G. Thuman, and J. W. McBain, *J. Colloid Sci.*, **8**, 491 (1953).

(5) J. Ross, *J. Phys. Chem.*, **62**, 531 (1958).

surface-active agents, namely, polyoxyethylated fatty alcohols, in the presence of free fatty alcohol, in complete analogy to phenomena observed in ionic systems.

Experimental

Apparatus. Preliminary determination of FDTT's was made in film drainage tubes similar to those of Miles, *et al.*[1] The results reported herein, however, were obtained by measurement of the change in surface viscosity with temperature.

The instrument employed was of the oscillating-bob type. The bob used was of the "double-cone" type,[6] fabricated of stainless steel. In the present experiments it was suspended on a 26-gauge MacMichael wire, clamped at the top to a shaft supported by microbearings, and mechanically linked to a Statham Instruments Model Gl-1.5-300 strain gauge, the output of which is fed to a Brush Instruments Model BL-320 amplifier and recorded on a Brush Instruments Model BL-201 direct-writing magnetic oscillograph. A record of the damping of the bob's oscillations is thus obtained.

The logarithmic decrement, λ, is obtained by plotting the logarithm of the amplitude as a function of the number of swings (in effect, of the time). For a Newtonian surface this yields a straight line, the slope of which is the desired decrement. For non-Newtonian surfaces (such as are, in fact, obtained with slow-draining systems) the log decrement is a function of angle. For the purposes of the present investigation, the log decrement for some particular angular displacement of the bob may be used, and it was arbitrarily decided to use a value corresponding to 10°, λ_{10}.[7] Slopes were determined graphically.

Determinations were carried out in a jacketed cell, through which water from a constant temperature bath was circulated. Measurements were carried out in the range 10–60°. Temperatures were determined thermometrically.

A typical family of damping curves is shown in Fig. 1, for the system lauryl alcohol–polyoxyethylene (23) lauryl alcohol (7.5:92.5) at total concentration of 1.0 g./dl.

Materials. The surface-active agents investigated were commercial grade polyoxyethylated derivatives of lauryl alcohol containing, respectively, 12 and 23 moles of ethylene oxide. The former was studied in the presence of lauryl alcohol, the latter in the presence of lauryl and cetyl alcohols at alcohol:agent ratios by weight of 0:100, 2.5:97.5, 5.0:95.0, 7.5:92.5, and 10.0:90.0. These mixtures were prepared by blending the alcohols and surface-active agents directly. The mixtures were then studied at concentrations of 0.001, 0.010, 0.100, and 1.00 g./dl.

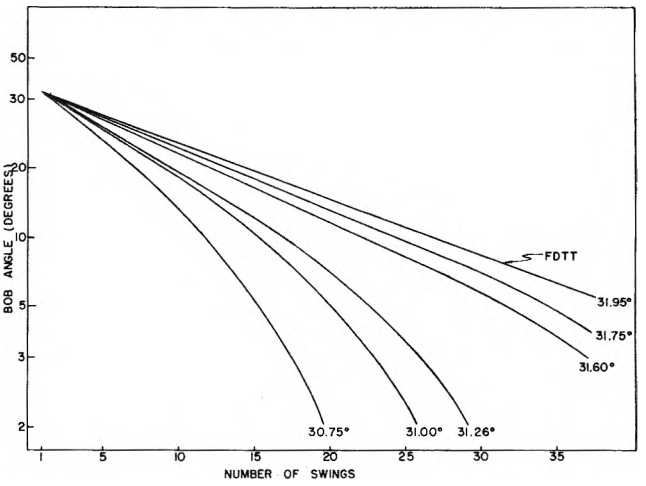

Figure 1. Typical family of damping curves as a function of temperature, for the system lauryl alcohol–polyoxyethylene (23) lauryl alcohol (7.5:92.5) at a total concentration of 1.0 g./dl.

Results and Discussion

The damping curves illustrated in Fig. 1 show that the onset of the FDTT is quite rapid. This is shown more strikingly in Fig. 2, where λ_{10} is plotted as a function of temperature. Although the scatter is quite marked, the maximum standard deviation is only of the order of $\pm 7\%$. It is possible that a major portion of the deviation is attributable to the errors inherent in graphical determination of the slopes.

The deviation becomes less pronounced the more closely the curves approach Newtonian behavior, since the slope can be determined with higher accuracy.

As can be seen from Fig. 2, the range of the transition is fairly sharp, being in this case of the order of 2°. We have arbitrarily chosen to designate as FDTT the temperature at which the log decrement reaches the value corresponding to pure substrate. With equal justice, the midpoint of the transition region might have been used, in which case the reported values would have been approximately 1° lower. The criterion employed gives better agreement with values obtained by direct observation in film drainage tubes, however.

The observed film drainage transition temperatures are reported in Tables I–III. Although the mole frac-

(6) P. Becher, "Emulsions: Theory and Practice," Reinhold Publishing Corp., New York, N. Y., 1957, p. 326.

(7) For the determination of absolute values of the surface viscosity, this quantity must be further corrected for the log decrement of the pure substrate, *i.e.*, water, and, in cases where the bulk viscosity of the substrate is affected by the solute, an additional correction for this factor must be made. Since the rheology of these surfaces is not considered, except qualitatively, in the present publication, the apparent log decrements are used.

Table I: Effect of Lauryl Alcohol on FDTT (°C.) of Polyoxyethylene (23) Lauryl Alcohol

% alcohol	Total concentration, g./dl. 1.0	0.10	0.01	0.001
0	[a]			
1.0	15.4	[a]		
2.5	20.4	[a]		
5.0	28.0	28.0	[a]	
7.5	32.0	30.4	[a]	
10.0	34.3	32.7	28.4	[a]

[a] Fast-draining down to 10°.

Table II: Effect of Lauryl Alcohol on FDTT (°C.) of Polyoxyethylene (12) Lauryl Alcohol

% alcohol	Total concentration, g./dl. 1.0	0.10	0.01	0.001
0	[a]			
1.0	13.5	[a]		
2.5	18.3	18.4	[a]	
5.0	22.7	22.7	[a]	
7.5	27.5	27.9	25.9	[a]
10.0	30.1	30.4	28.6	[a]

[a] Fast-draining down to 10°.

Table III: Effect of Cetyl Alcohol on FDTT (°C.) of Polyoxyethylene (23) Lauryl Alcohol

% alcohol	Total concentration, g./dl. 1.0	0.10	0.01	0.001
0	[a]			
1.0	29.0	22.1	[a]	
2.5	42.2	38.3	[a]	
5.0	49.5	50.0	[a]	
7.5	53.9	53.1	47.8	[a]
10.0	56.3	56.3	52.3	[a]

[a] Fast-draining down to 10°.

tion of fatty alcohol is, in general, slightly higher than those employed in studies with ionic materials,[3,5] the over-all behavior is quite consistent (even to the range of transition temperatures) with that reported previously.

The effect of total concentration on the FDTT appears to be similar to that reported for sodium lauryl sulfate–lauryl alcohol, *i.e.*, a steeply rising curve at low total concentration flattening out at higher concentrations.[8] Unfortunately, owing to the choice of concentrations in the present work, this is suggested only by the data at the higher alcohol concentrations.

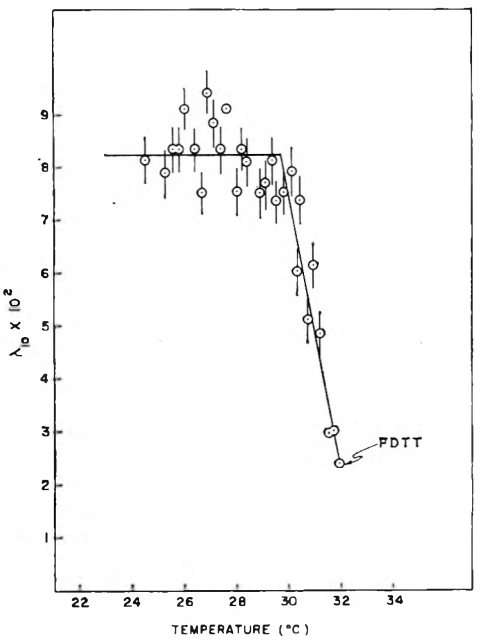

Figure 2. Log decrement at 10° (λ_{10}) for the system of Fig. 1.

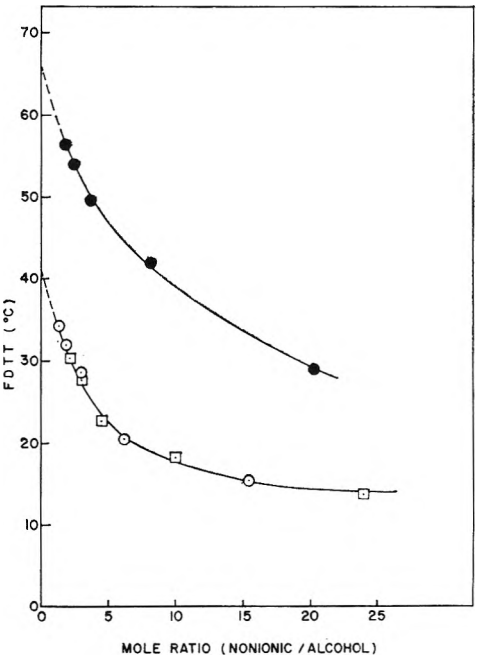

Figure 3. FDTT as a function of mole ratio of nonionic surface-active agent to fatty alcohol: ●, polyoxyethylene (23) lauryl alcohol–cetyl alcohol; ○, polyoxyethylene (23) lauryl alcohol–lauryl alcohol; □, polyoxyethylene (12) lauryl alcohol–lauryl alcohol.

The effect of the alcohol concentration is shown clearly in Fig. 3, where the FDTT is plotted as a func-

(8) *E.g.*, ref. 3, Fig. 1.

tion of the mole ratio of nonionic agent to alcohol at a total concentration of 1.0 g./dl.

Two significant observations can be made about these curves. The first is that the FDTT appears to be solely a function of the fatty alcohol employed and is independent of the nonionic used, since the data for both polyoxyethylene (12) and polyoxyethylene (23) lauryl alcohol in the presence of lauryl alcohol fall on the same curve. Furthermore, the curve for the lauryl alcohol-containing systems extrapolates to a temperature of 41.5°, while that for the cetyl alcohol-containing systems extrapolates to 68°, at zero mole ratio of nonionic.

These results are in excellent agreement with the results of a similar extrapolation in the system lauryl alcohol–sodium lauryl sulfate made by Ross[5] and with values for a transition in the surface viscosity of monolayers of the fatty alcohols reported previously. These are: lauryl alcohol, 41.5°,[5] and cetyl alcohol, 70[5] and 68°.[9]

It would therefore seem to be reasonable to regard these curves as in the nature of melting point depression curves, the departure from linearity (and, hence, from ideality) being possibly attributable to complex formation of the sort described by Epstein and co-workers[3] and, more recently, by Kung and Goddard.[10] In this connection, it is interesting to note that the difference in phase transition temperatures for the alcohols is of the same order of magnitude as the difference in their bulk melting points, although the two-dimensional "melting points" are some 20° higher.

Alternatively, one can think of these effects as being a two-dimensional vapor pressure lowering[11] with the complex formation resulting in deviation from Raoult's law.

Unfortunately, the present work was not extended to sufficiently low mole ratios to permit the precise calculation of a "transition temperature depression constant," although the extrapolations of Fig. 3 are such to suggest that a value of about 32° would be found for both fatty alcohols, when the concentration is expressed in terms of mole ratios. With this information, a more precise calculation of the extent of complex formation might be possible.

(9) A. Trapeznikov, *Acta Physicochim. URSS.* **20**, 597 (1945).

(10) H. C. Kung and E. D. Goddard, *J. Phys. Chem.*, **67**, 1965 (1963).

(11) N. K. Adam, "The Physics and Chemistry of Surfaces," 3rd Ed., Oxford University Press, London, 1941, pp. 70, 71.

Ideal Two-Dimensional Solutions. IV.

Penetration of Monolayers of Polymers

by Frederick M. Fowkes[1]

Shell Development Company, Emeryville, California *(Received May 7, 1964)*

Monomolecular films of polymers or proteins on the surface of water (or at liquid–liquid or liquid–solid interfaces) are often subject to swelling by penetration into the film of water, organic solvents, or surface-active molecules. This effect results in an expanded pressure–area isotherm which can be explained as a two-dimensional solution in which the polymer molecules of the film reduce the free energy of the penetrants. This concept leads to equations which accurately predict the degree of swelling. The equations are for athermal swelling (zero heat of mixing) and use a statistically derived entropy of dilution in which molecules of the penetrant and monomer units of the polymer occupy fixed sites. This expression allows for difference in size of the sites occupied by the penetrant and by the monomer units. The equations are useful for predicting penetration of polymer films by organic solvents or surface-active materials, or by water in the case of hydrophilic-expanded films of polymers. The results predicted by these equations check closely with experimental observation.

Introduction

Monolayers of surface-active polymers (including proteins) on the surface of water or at an oil–water interface are often subject to penetration by smaller molecules. The classical penetration experiments with polymers have been conducted with monolayers of protein on aqueous substrates from which surface-active molecules penetrate. Surface films of polymers having strongly hydrophilic polar groups are also subject to penetration by water molecules. A third kind of penetration occurs at an oil–water interface; here oil molecules penetrate between the oil-soluble groups of the polymer.

The thermodynamics of penetration have been discussed in four previous articles,[2-4] but these have been limited to the penetration of monolayers composed of fat derivatives such as stearic acid. These articles have shown that the penetrating molecules remain in a penetrated monolayer because their free energy has been decreased by dilution in the monolayer. This principle has been shown to explain penetration of solvent vapors, of solvent from aqueous or hydrocarbon substrates, or by surface-active molecules. The primary cause in such penetration is the formation of a surface or interfacial solution, and, since the activity coefficient of the penetrating molecules has proved experimentally to be unity, these monolayers have been termed "ideal two-dimensional solutions." It will be shown in this article that the same principles apply to polymeric monolayers although the form of the equation is somewhat different since the entropy change upon diluting a polymeric monolayer is different from the entropy change of diluting a monolayer of simple molecules.

The previous studies of ideal two-dimensional solutions have demonstrated two classes of monolayers on aqueous substrates. Monolayers of the most hydrophobic surface-active substances (such as stearic acid) tend to be anhydrous while monolayers of the less hydrophobic surface-active substances (such as sodium alkyl sulfates) tend to be fully solvated (penetrated by water) and form ideal two-dimensional aqueous solutions. Monolayers are generally in one state or the other; there appear to be very few in an intermediate state

(1) Sprague Electric Co., North Adams, Mass.

(2) F. M. Fowkes, *Proc. Intern. Congr. Surface Active Materials, 3rd, Cologne*, 2, 161 (1960).

(3) F. M. Fowkes, *J. Phys. Chem.*, **65**, 355 (1961).

(4) (a) F. M. Fowkes, *ibid.*, **66**, 385 (1962); (b) *ibid.*, **66**, 1863 (1962).

(partly solvated). Monolayers of surface-active materials are often in the solvated state at low pressures and discontinuously "invert" to the anhydrous state at some critical pressure; this occurs with stearic acid at pressures less than 0.1 dyne/cm., but with sodium dodecyl sulfate at 28–30 dynes/cm.[4a] In mixed monolayers of hydrophobic and hydrophilic surface-active substances this inversion is a function of mole ratio.[5] Surface films of polymers are also found in the anhydrous or fully solvated states. These have previously been described as condensed or expanded states.

Theory and Notation

When a monolayer is spread or adsorbed at an interface, it decreases the surface concentration of the molecules that were present in the first place. This decrease in free energy of the molecules initially presents results in their accumulation in the monolayer where they swell the monolayer and raise the film pressure, π.

The Boltzmann equation for the entropy of dilution of an ideal surface solution of simple molecules ($\Delta\bar{S}_1 = -R \ln x_1$) has proved adequate for all the applications so far described. However, in the case of polymer molecules this expression is not correct because the distribution of segments of a diluted polymer molecule is not random; adjacent monomer groups are always tied together and cannot be separated by dilution. Therefore, statistical distribution functions for the effect of dilution on the number of configurations which polymer molecules may have in solution or in monolayers must be used. Most of these expressions are based on a statistical mechanical treatment of solutions as a lattice of sites; the effect of dilution on the change in the total number of polymer configurations is calculated by a method developed by Miller.[6a] Singer[6b] has used such an expression for surface films of polymers. He assumed the surface to be a lattice of sites of equal area, some occupied and some unoccupied, and with this model had fair success in approximating the pressure–area curves for certain polymers.

An improvement over the Singer equations has recently been published by Motomura and Matuura[7]; their derivation also assumes a rigid lattice with sites vacant or occupied but considers, in addition, how intersegment attractions of various magnitudes can influence the configuration of the polymer. This adds an additional parameter which allows closer curve fitting; unfortunately, this parameter is not evaluated independently.

The treatment used in this paper is for polymers having such strongly adsorbed monomer groups that essentially all of the polar groups are bound to the substrate. A great many polar polymers (such as the wide variety of commercial nonash dispersant polymers, many of which are largely composed of long-chain alkyl methacrylates) behave in this fashion, especially when adsorbed or spread at an oil–water interface where the mobility of the interface favors rapid equilibration. This paper does not treat the case of weakly adsorbed polymers where a high proportion of the polymer chain can be looped out of the interface, especially at solid surfaces where equilibrium is seldom attained. Frisch and Simha[8] have developed a statistical treatment of monolayers of polymers which have only part of the monolayer bound to the surface. Silberberg[9] has given a general statistical treatment of the adsorption of polymers which allows for a wide range of energies of adsorption to be considered.

In this work a Flory–Huggins type of expression is used as developed by Guggenheim,[10] using the notation of Hildebrand and Scott.[11] The surface is considered to be a lattice of sites of equal area so arranged that each site has z nearest neighbor sites, and each monomer group in the polymer (component 2) is presumed to occupy one site. The number of sites occupied by a solvent molecule is m_1 and the number occupied by the polymer is m_2 (the degree of polymerization). The number of sites which are nearest neighbors to a polymer molecule is $zq_2 = (z - 2)m_2 + 2$. Similarly, for a solvent molecule, $zq_1 = (z - 2)m_1 + 2$. The coordination number z used by Singer[6b] and followers[12,13] is our $(z - 2)$. The fraction of sites occupied by solvent is θ_1 and by polymer is θ_2; $\theta_1 = 1 - \theta_2$.

The molar entropy change for the solvent molecules in a monolayer upon diluting a monolayer of pure solvent ($\theta_1^0 = 1$) to θ_1' is

$$\Delta\bar{S}_1' = -R\left[\ln \theta_1' - \frac{zq_1}{2} \ln\left(1 - \frac{2(m_2 - m_1)}{zq_1m_2}\theta_2'\right)\right] \quad (1)$$

and for the polymer molecules upon diluting a monolayer of pure polymer ($\theta_2^\circ = 1$) to θ_2' is as in eq. 2.

(5) F. M. Fowkes, *J. Phys. Chem.*, **67**, 1982 (1963).

(6) (a) A. R. Miller, "Theory of Solutions of High Polymers," Oxford University Press, London, 1948; (b) S. F. Singer, *J. Chem. Phys.*, **16**, 872 (1948).

(7) K. Motomura and R. Matuura, *J. Colloid Sci.*, **18**, 52 (1963).

(8) H. L. Frisch and R. Simha, *J. Chem. Phys.*, **27**, 702 (1957).

(9) A. Silberberg, *J. Phys. Chem.*, **66**, 1872 (1962).

(10) E. A. Guggenheim, *Proc. Roy. Soc.* (London), **A183**, 203 (1944).

(11) J. H. Hildebrand and R. L. Scott, "The Solubility of Nonelectrolytes," 3rd Ed., Reinhold Publishing Corp., New York, N. Y., 1950, pp. 406–415.

(12) (a) M. J. Schick, *J. Polymer Sci.*, **25**, 463 (1957); (b) J. T. Davies, *Biochim. Biophys. Acta*, **11**, 165 (1953).

(13) H. Hotta, *J. Colloid Sci.*, **9**, 504 (1954).

$$\Delta\bar{S}_2' = -R\left[\ln\theta_2' - \frac{zq_2}{2}\ln\left(1 - \frac{2(m_1 - m_2)}{zq_2m_1}\theta_1'\right)\right] \quad (2)$$

Equations 1 and 2 have been used for calculating the free energy change of dilution in the monolayer $(\partial G_i/\partial\theta_i)_{\gamma,P,T}$ by assuming that the heat of dilution (in the monolayer) is negligibly small (athermal mixing). This has often been justified for polymer solutions because only solvents giving small heats of dilution will dissolve polymers but is doubly justified for monolayers of polymers because heats of dilution in monolayers are far less than in bulk solution; this has been illustrated several times.[2-4] The free energy equation for relating changes of composition to surface tension γ is essentially the same as used previously[4b]

$$dG_i^\sigma = \left(\frac{\partial G_i^\sigma}{\partial\gamma}\right)_{T,P,\theta_i} d\gamma + \left(\frac{\partial G_i^\sigma}{\partial\theta_i}\right)_{T,P,\gamma} d\theta_i \quad (3)$$

where

$$\left(\frac{\partial G_i^\sigma}{\partial\theta_i}\right)_{T,P,\gamma} d\theta_i = -T\Delta\bar{S}_i'$$

and

$$\left(\frac{\partial G_i^\sigma}{d\gamma}\right)_{T,P,\theta i} = -N\bar{\sigma}_i$$

where $\bar{\sigma}_i$ is the partial molecular area of component i.

Equations 1, 2, and 3 can be used to calculate the effect of penetration of small molecules on the pressure–area isotherms for monomolecular films of polymers where the small penetrating molecules (component 1) dilute the polymer film and make it more expanded than an anhydrous surface film of the same polymer. Thus, if we have a pressure–area isotherm for a nonhydrated polymer spread at the water–air interface, the expansion of this monolayer because of penetration can be calculated. This calculation gives the pressure–area isotherm to be expected when solvent molecules penetrate the polymer monolayer by adsorption of vapor or by penetration from an aqueous or hydrocarbon substrate. In the use of eq. 1 and 2, certain simplifying assumptions can be made which result from the fact that $m_2 >> m_1$

$$\frac{m_1 - m_2}{(z-2)m_2 + 2} \approx \frac{-1}{z-2}$$

$$\frac{m_2 - m_1}{m_2} \approx 1$$

and $\ln\theta_2$ is a negligibly small term in eq. 2. By using these assumptions and $\theta_1 = 1 - \theta_2$, eq. 1 and 2 become

$$\Delta\bar{S}_1' = -R\left[\ln\theta_1 - \frac{zq_1}{2}\ln\left(1 - \frac{2(1-\theta_1)}{zq_1}\right)\right] \quad (4)$$

$$\Delta\bar{S}_2' = R\frac{zq_2}{2}\ln\left(1 + \frac{2(1-\theta_2)}{(z-2)m_1}\right) \quad (5)$$

Values of z may be determined experimentally by checking pressure–area curves *vs.* those calculated with various values of z. Values of four to six might be expected; actually, the results are not too sensitive to the values of z, however.

One method of using these equations is to consider the free energy of the solvent molecules in the monolayer under conditions that $dG_1^b = 0$, so that

$$\left(\frac{\partial G_1^\sigma}{\partial\gamma}\right)_\theta d\gamma = -\left(\frac{\partial G_1^\sigma}{\partial\theta_1}\right)_\gamma d\theta_1$$

This leads to

$$\frac{\bar{\sigma}_1}{kT}(\gamma_1^0 - \gamma') = -\ln\frac{\theta_1'}{\theta_1^0} - \left[\frac{(z-2)m_1 + 2}{2}\right]\ln\left[\frac{(z-2)m_1 + 2\theta_1'}{(z-2)m_1 + 2\theta_1^0}\right] \quad (6)$$

The preceding equation is similar to the equation of Singer[6b] which has been used primarily for polymer films at the air–water interface. In the use of this equation, it is assumed that the surface of water is a rigid lattice of sites of equal area and that the monomeric units of the polymer occupy one site at all film pressures; consequently, changes in area per molecule with change of film pressure are related to the change in the fraction of sites which are vacant. These conditions are at best a zero-order approximation of the structure of a polymer monolayer. However, they should fit monolayers at the water–hydrocarbon interface better than at aqueous surfaces because hydrocarbon molecules may occupy the sites unoccupied by monomeric units of the polymer. However, even at oil–water interfaces, the assumption that the area occupied by the monomer unit is independent of film pressure is undoubtedly incorrect. In this work the aim is to calculate changes in pressure–area isotherms which result from penetration, and, consequently, the pressure–area isotherm for the unpenetrated film is used as a standard. It is assumed that in this standard unpenetrated film all of the surface is occupied by monomer units, so that the pressure dependence of the area results entirely from changes in area occupied by the monomer units (sites). The change in area per site with pressure may be ascribed to compressibility or change of configuration of monomer groups. The larger area occupied by interfacial films as compared with anhydrous surface films (at the same film pressure) is ascribed to penetration of

solvent molecules which occupy sites; the area fraction θ_1 is calculated by eq. 6. When Singer's equation is used for penetrated films containing solvent molecules which occupy the same area as a polymer segment,[13] most of Singer's assumptions are justified, except for the nonexpandable lattice. Frisch and Simha[8] have considered only interfacial films with solvent molecules equal in size to the polymer segments; their equations are similar to (6), except they have made additional provisions for polymer molecules which are only partly in the surface. Although this study is limited to the discussion of polymers completely in the interface, there is provision for solvent molecules of various size (occupying more than one site), and there is also provision for calculating the entropy of dilution of the polymer (instead of only the solvent).

Obviously, penetrating molecules will not always have the same area (σ_1) as monomer segments (σ_2). The simplest way of handling this is to use σ_2 as the "site size"; then $m_1 = \sigma_1/\sigma_2$. It is found that a twofold increase in m_1 results in only a 10% increase in film pressures; thus, variations in σ_1/σ_2 result in minor but still significant variations in the pressure–area isotherms.

Application to Experimental Results

Penetration of Hydrocarbon Molecules into Polymer Films at the Oil–Water Interface. An experimental test of these formulas can be made with the pressure–area curves for polymethyl methacrylate monolayers which have been measured in this laboratory at both the air–water and cyclohexane–water interfaces by Schick.[12a] The film on the water surface has no solvent molecules in it, so $\theta_2 = 1$; calculated values of θ_1 allow construction of the expected pressure–area curve at the cyclohexane–water interface which may be compared with experiment (Fig. 1). These calculations are made with $m_1 = 1$, $z = 6$, $\bar{\sigma}_1 = 30$ Å.^{2}. A value of 6 for z agrees with Hotta's[13] studies of interfacial polymer films. When $m_1 = 1$ and $z = 6$, eq. 6 reduces to

$$\frac{\bar{\sigma}_1}{kT}(\gamma_1^0 - \gamma') = -\ln\frac{\theta_1'}{\theta_1^0} + 3\ln\left(\frac{2+\theta_1'}{2+\theta_1^0}\right) \quad (7)$$

and since in this example $\gamma^0 - \gamma' = \pi$ and $\theta_1^0 = 1$

$$\frac{\pi\bar{\sigma}_1}{kT} = +2.303\log\frac{(2+\theta_1')^3}{27\theta_1'}$$

The π–θ_1' relation obtained from this equation with $\bar{\sigma}_1 = 30$ Å.^{2} allows calculation of a pressure–area curve (Fig. 1) which is seen to fit the experimental pressure–area curve for polymethyl methacrylate (shown as circles) very well, except for points at the highest film pressures which are probably in error (because of the dissolving of some of the polymer film into cyclohexane).

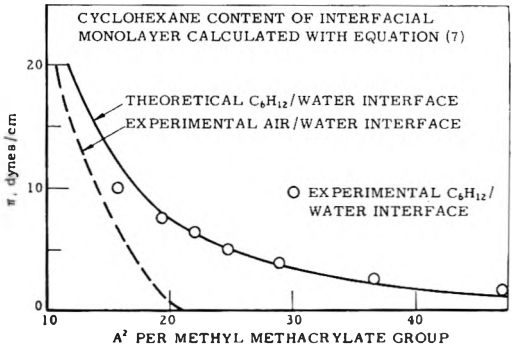

Figure 1. Pressure–area relations for surface and interfacial monolayers of polymethyl methacrylate at 25°.

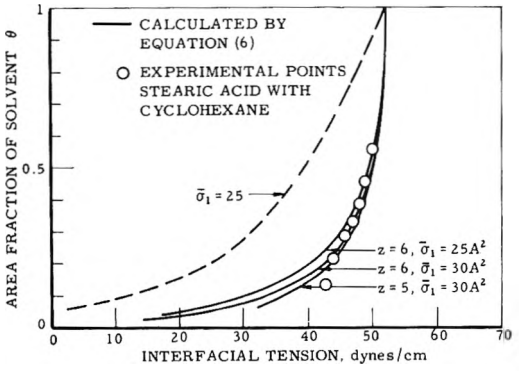

Figure 2. Cyclohexane content of monolayers at the cyclohexane–water interface.

The previous π–θ_1' relation can be used for a variety of similar polymers. It is best plotted as θ_1 *vs.* γ. Such plots, for $z = 5$ and 6, and for $\bar{\sigma}_1 = 25$ and 30 Å.^{2} are shown in Fig. 2 along with the experimental data for polymethyl methacrylate. It can be seen that the results are surprisingly insensitive to change in z and $\bar{\sigma}_1$.

For comparison the θ_1' *vs.* γ relation for interfacial monolayers of stearic acid is shown (as a dashed line) for the condition $\bar{\sigma}_1 = 25$ Å.^{2}. The contrast between the behavior of polymeric and monomeric films is seen to be very great. At a film pressure of 2 dynes/cm. ($\gamma = 50$ dynes/cm.) the polymer has squeezed out 50% of the solvent molecules from the monolayer, but stearic acid has squeezed out only 10%. One could say that in monolayers (as well as in solutions) polymers are poor solvents compared to simple compounds.

The tendency for polymeric monolayers to squeeze out solvent on increasing the film pressure (or free energy) is analogous to their tendency to precipitate from solution upon raising the heat of solution by adding a little nonsolvent. In both cases, in order to maintain equilibrium the increase in free energy is compensated

by demixing, precipitation from solution, or squeezing out of solvent from the monolayer.

Penetration of Solvent Vapors into Surface Films of Polymers. Solvent vapors penetrate and swell the monolayers which are spread on the surface of water; if the film is mechanically confined, the film pressure rises. This increase in film pressure has been accurately predicted (for monolayers of fatty derivatives) by equations for penetrated films acting as ideal two-dimensional solutions.[2-4] A similar treatment can be used for surface films of polymers.

If vapor and monolayers are in equilibrium, any change in the free energy of the vapor dG_1^v must equal the change in free energy of the vapor molecules in the monolayer

$$dG_1^v = \left(\frac{\partial G_1}{\partial \gamma}\right)_{\theta_1} d\gamma + \left(\frac{\partial G_1}{\partial \theta_1}\right)_{\gamma} d\theta_1$$

If the system has a negligible heat of mixing, eq. 4 can be used to evaluate the last term of the preceding and following equations

$$kT \, d \ln p_1^* = -\sigma_1 d\gamma - T dS_1$$

where p_1^* is the fugacity of the vapor. If the vapor performs as an ideal gas, the vapor pressure p_1 may be used instead of p_1^*. In integrated form the equation now becomes

$$kT \ln p_1/p_1^0 = \bar{\sigma}_1(\pi - \pi^0) + kT\left[\ln \theta_1 - \frac{zq_1}{2} \ln\left(1 - \frac{2(1-\theta_1)}{zq_1}\right)\right] \quad (8)$$

When saturated hexane vapor penetrates polymer molecules, we may use $m_1 = 1$, $z = 6$, $m_2 >> m_1$, and π^0 (the film pressure of saturated hexane vapor on a bare water surface) equals 4.0 dynes/cm. at 30°. Under these conditions

$$kT \ln p_2/p_2^0 = 0 = \bar{\sigma}_1(\pi - \pi^0) - kT \ln\left[\frac{(2+\theta_1)^3}{27\theta_1}\right]$$

This equation predicts swelling similar to that shown in Fig. 1.

Penetration of Surfactants into Polymer Molecules. If surfactants dissolved in the substrate penetrate a monolayer, at equilibrium the free energy will be the same in the bulk and in the surface film

$$dG_1^b = \left(\frac{\partial G_1}{\partial \gamma}\right)_{\theta_1} d\gamma + \left(\frac{\partial G_1}{\partial \theta_1}\right)_{\gamma} d\theta_1$$

If the penetration has negligible effect on dG_1^b, then eq. 6 can be used, and for $m_1 = 1$, $z = 6$, and $m_2 >> m_1$, one obtains

$$\pi = \pi_0 + \frac{kT}{\bar{\sigma}_1} \ln\left[\frac{(2+\theta_1)^3}{27\theta_1}\right] \quad (9)$$

Suitable examples are the penetration of water-soluble alcohols into protein films. Several such examples are in the literature but are not quantitative enough to test eq. 9.

Penetration of Water into Surface Films of Polymers. Crisp,[14] Llopis and Rebollo,[15] and Kawai[16] have all noted that some polymer films are condensed (such as polymethyl methacrylate) and others are expanded (polyvinyl acetate). It is proposed that the expanded polymer monolayers are fully hydrated and that at low pressures most of the area is occupied by water molecules. This is analogous to surface films of water-soluble substances in which the area and film pressure are determined by the penetration of water molecules into the surface film.[4a] In such films the water is diluted by the surface-active molecules, and equilibrium is only restored by rise of film pressure. It was found that in these films the partial molecular area of the surface-active molecules was determined by the polar groups and was pressure independent. Parallel behavior of hydrated polymer monolayers would mean that the size of the sites is pressure independent, and use of eq. 6 and 7 to determine the site fraction occupied by water (θ_1) gives directly the area per monomer group of film occupied by water ($\theta_1 \bar{\sigma}_1$), where $\bar{\sigma}_1$ (the average partial molecular area of water) is 9.7 Å.^{2}. For any given monomer one can then calculate the film pressure dependence of the surface area per unit weight of polymer film occupied by water (in m.^{2}/mg.). This is shown in

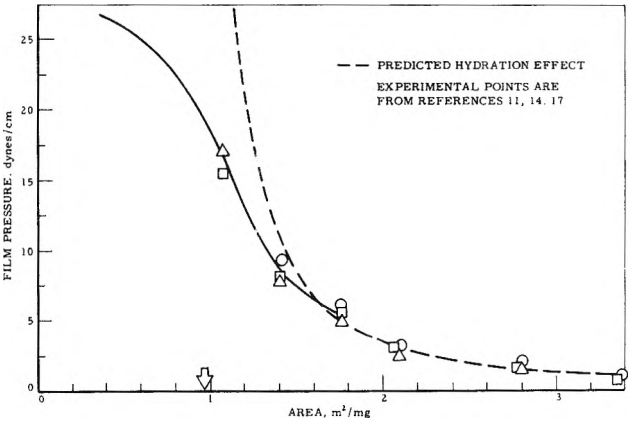

Figure 3. Pressure–area isotherms for polyvinyl acetate.

(14) D. J. Crisp, *J. Colloid Sci.*, 1, 49 (1946).
(15) J. Llopis and D. V. Rebollo, *ibid.*, 11, 543 (1956).
(16) T. Kawai, *J. Polymer Sci.*, 35, 401 (1959).

Fig. 3 for monolayers of polyvinyl acetate, and a fit of the experimental points to the curve

$$\pi = \frac{kT}{\bar{\sigma}_1} \ln\left[\frac{(2 + \theta_1)^3}{27\theta_1}\right]$$

gives the area of the acetate groups in 1 mg. of this polymer (arrow). Although a gradual (reversible) collapse of this film sets in at pressures over 8–10 dynes/cm., there is an excellent fit prior to collapse. The area occupied by the polymer before collapse is given by the arrow (0.96 m.^{2}/g. or 13.7 Å.^{2} per acetate group), and the additional area found experimentally is the water content of the monolayer.

Properties of Monolayers of ω-Monohalogenated Fatty Acids and Alcohols Adsorbed on Water[1]

by Marianne K. Bernett, N. L. Jarvis, and W. A. Zisman

U. S. Naval Research Laboratory, Washington, D. C. 20390 *(Received April 2, 1964)*

Force–area, surface potential–area, and surface moment–area relations of ω-monohalogenated compounds spread as monolayers on aqueous substrates were studied at various pH values in the absence or presence of multivalent ions. The compounds investigated were ω-monosubstituted bromo-, chloro-, and iodohexadecanoic acids, bromooctadecanoic acid, and fluorooctadecanol, along with their corresponding unsubstituted compounds. Mechanical properties of the substituted and unsubstituted alcohols were essentially the same and were not influenced by changes in pH or the presence of multivalent ions in the substrate. The halogenated hexadecanoic acids, however, gave unstable monolayers at all pH values on distilled and divalent ion-containing water at 20°; it was necessary to add tetravalent ions and lower the temperature to condense the monolayers to close-packed films. The change in surface potential of each substituted acid film was larger than that of any unsubstituted acid and showed the dipole orientation to be in the opposite direction. The vertical components of the apparent dipole moment were computed from the film potentials by use of the Helmholtz equation. Estimated values are given for the vertical components of the dipole contributed by the carbon–halogen bond. The results are discussed in terms of orientation and packing of the terminal polar groups and the resulting laterally induced polarization.

Introduction

The physical properties of monolayers of fatty acids or alcohols on water are known to be greatly altered by the replacement of one or more of the ω-, or terminal, hydrogen atoms by halogens. Various investigators[2–5] have reported that the presence of halogens on the ω-carbon atom of a fatty acid or alcohol not only causes it to form more unstable monolayers but also to lower the electrostatic surface potential change (ΔV) arising from

(1) Presented before the Colloid and Surface Chemistry Division at the 147th National Meeting of the American Chemical Society, Philadelphia, Pa., April 5–10, 1964

(2) (a) M. Gerovich and A. Frumkin, *J. Chem. Phys.*, **4**, 624 (1936); (b) M. Gerovich, A. Frumkin, and D. Vargin, *ibid.*, **6**, 906 (1938).

monolayer adsorption. Gerovich and co-workers[2a,b] determined that ΔV for a condensed insoluble monolayer of 16-bromohexadecanoic acid, adsorbed at the air–water interface, can be as low as −0.87 v., which is 1.26 v. less than that of the unbrominated acid under similar conditions. Davies[3] found that 16-bromohexadecanoic acid had a negative surface potential at both the oil–water and air–water interfaces. Fox[4] reported that a terminal $-CF_3$ group on octadecanoic acid and octadecylamine resulted in large and negative ΔV values for condensed monolayers at the air–water interface. More recently, Bernett and Zisman[5] found that condensed monolayers of a series of progressively fluorinated fatty acids would also give rise to large negative values of ΔV at the air–water interface.

This report describes the mechanical and electrical properties of the following compounds adsorbed as monolayers at the air–water interface: the ω-chloro-, ω-bromo-, and ω-iodohexadecanoic acids, ω-bromooctadecanoic acid, and ω-fluorooctadecanol. The objective of the investigation was to examine the effect of each of the terminal halogens on the packing, orientation, stability, and surface potential of the monolayers spread on aqueous substrates at various hydrogen ion concentrations. From the changes in surface potential, it was proposed to determine the dipole contributions of each terminal methylene halide group.

Experimental Materials and Procedures

Each organic acid and alcohol studied was a highly purified, white, crystalline solid. The *n*-hexadecanoic acid (m.p. 61.5°) and *n*-octadecanoic acid (m.p. 69.5°) were obtained from the Hormel Foundation, and the *n*-octadecanol (m.p. 59°) from Lachat Chemicals, Inc. Pure specimens of 18-fluorooctadecanol[6] (m.p. 60.5°) and 18-bromooctadecanoic acid (m.p. 72.0–73.0°) were generously donated for this investigation by Prof. F. L. M. Pattison of the University of Western Ontario and Dr. M. Stoll of Firmenich et Cie of Geneva, Switzerland, respectively. Pure 16-chlorohexadecanoic, 16-bromohexadecanoic, and 16-iodohexadecanoic acids (m.p. 61.0–61.5, 69.5–70.0, and 74.0–74.5°, respectively) were prepared specially for this study by Fox and Price[7] of this laboratory.

Spreading solutions of each polar compound in concentrations of 5×10^{-4} to 7×10^{-4} g./ml. were prepared in *n*-hexane (Fisher grade "purified" freshly percolated through adsorptive columns of activated silica gel and alumina). Each solution was delivered dropwise to the clean water surface of the modified Langmuir–Adam film balance with a calibrated self-adjusting micropipet, in a volume chosen to give a condensed film occupying an area from 200 to 240 cm.^{2}. The film balance used to measure the film pressure (F) *vs.* area per molecule (A) isotherms has been described in detail earlier.[5] It consisted of a shallow Pyrex glass trough with the rim lightly coated with paraffin, a paraffined mica float connected to the sides of the trough with end loops of thin polyethylene ribbon, and a Cenco duNuoy torsion head sensitive to a film pressure change of 0.05 dyne/cm. Surface potential measurements were made using essentially the same vibrating condenser apparatus described previously[5,8]; this device was sensitive to ±3.0 mv.

Aqueous substrates used in these experiments were prepared from water distilled once through a tin-lined still and then twice through an all-quartz still, and the water produced had a conductivity of 1×10^{-6} ohm^{-1} and a pH of 5.8 when in equilibrium at 20° with atmospheric carbon dioxide. Variations in pH were made by appropriate additions of either C.P. grade sulfuric acid or potassium hydroxide. The source of bivalent metallic ions for certain aqueous substrates was C.P. calcium chloride, and the source of tetravalent ions was C.P. thorium nitrate. The pH of the latter at the concentration of 5×10^{-4} M was 3.4 at 20° and 3.3 at 11°. All film balance experiments were made at either 20 ± 0.2° or 11 ± 1°.

Experimental Results

Force vs. Area Isotherms for Monolayers on Distilled Water. Both octadecanol and 18-fluorooctadecanol formed stable insoluble monolayers on distilled water at three different pH values at 20° (Fig. 1a and 1b). These monolayers behaved reversibly with film pressure up to 35 dynes/cm. and formed very condensed films having limiting areas per molecule (A_0) from 20.2 to 21.0 Å.^{2}, depending upon the pH. The steep linear portions of the F *vs.* A curves above 12 dynes/cm. indicated that both monolayers were solid condensed at such film pressures. At lower film pressures the fluoro alcohol was somewhat more expanded than the octadecanol monolayer which indicated that there was some repulsion between the terminal $-CH_2F$ groups. An examination of Stuart–Briegleb molecular ball models (Fig. 2) revealed that the substitution of a fluorine for a hydrogen atom on the terminal carbon atom did not cause a significant change in the molecular cross-sectional area. Therefore, the difference in size could not have

(3) J. T. Davies, *Trans. Faraday Soc.*, **49**, 949 (1953).

(4) H. W. Fox, *J. Phys. Chem.*, **61**, 1058 (1957).

(5) M. K. Bernett and W. A. Zisman, *ibid.*, **67**, 1534 (1963).

(6) F. L. M. Pattison, W. C. Howell, A. J. McNamara, J. C. Schneider, and J. F. Walker, *J. Org. Chem.*, **21**, 739 (1956).

(7) R. B. Fox and T. Price, *J. Chem. Eng. Data*, **8**, 612 (1963).

(8) W. A. Zisman, *Rev. Sci. Instr.*, **3**, 367 (1932).

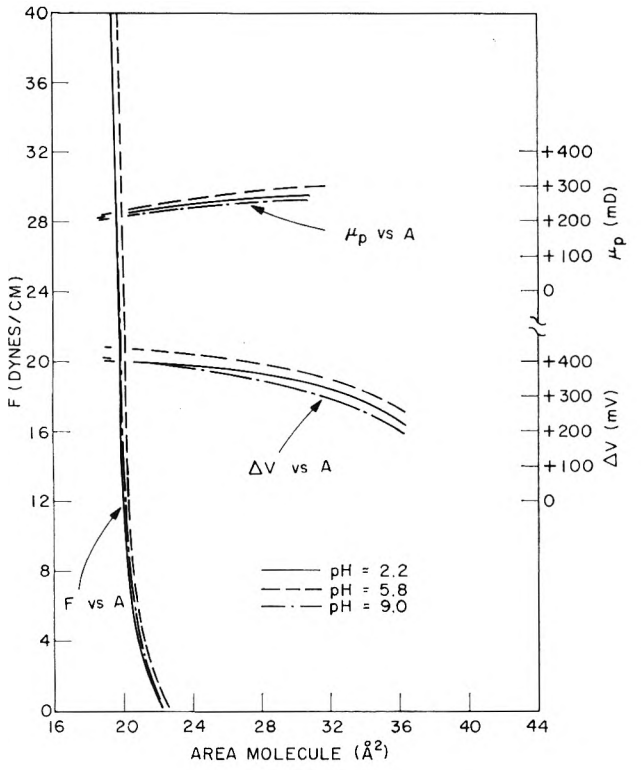

Figure 1a. Properties of octadecanol monolayers spread at 20° on substrate of distilled water.

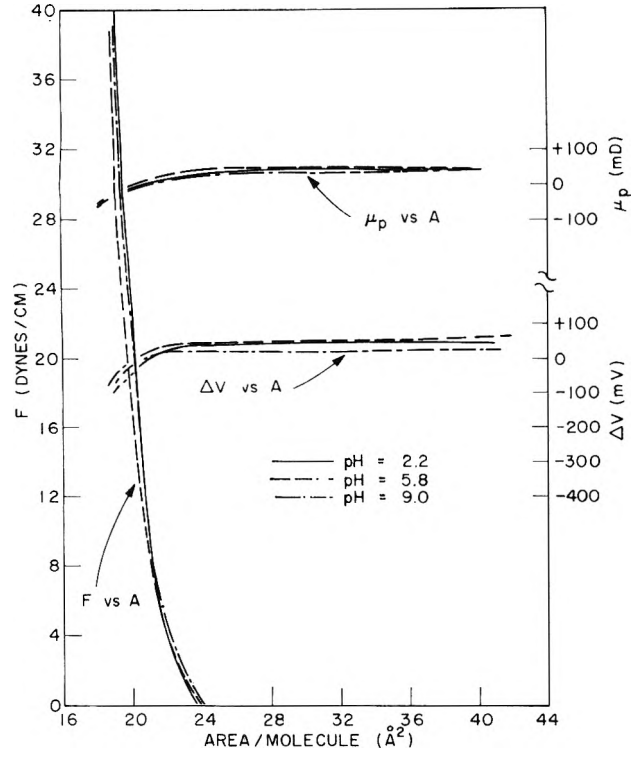

Figure 1b. Properties of 18-fluorooctadecanol monolayers spread at 20° on substrate of distilled water.

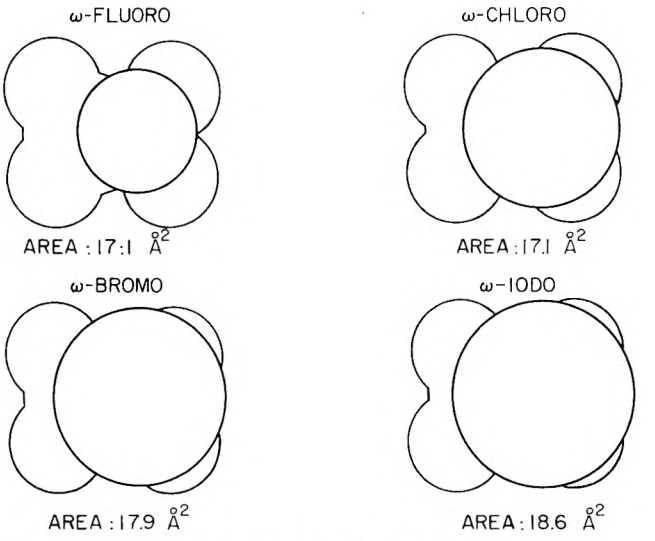

Figure 2. End views of terminally halogenated hydrocarbon chains.

caused the observed film expansion. The cause must be found elsewhere and will be discussed below. Varying the pH of the substrate over the range used had no significant influence on the *F vs. A* curve of the alcohol monolayers; this result is to be expected since the polar OH group was not ionizable under such conditions.

Monolayers of terminally chlorinated, brominated, or iodinated hexadecanoic acids collapsed at film pressures of only 2.0 to 5.5 dynes/cm. on distilled water at all pH values. This instability may have been caused by either steric hindrance to molecular close packing caused by the presence of these halogen atoms, which are considerably larger than hydrogen, or by repulsive forces acting between the similarly oriented terminal electrostatic dipoles. Figure 2, which gives the respective cross-sectional areas of ω-halogenated hydrocarbon chains (assuming the terminal carbon group does not rotate upon its axis), shows that the steric factor could be significant only with the ω-iodo and ω-bromo acids and even then could cause no more than a 10% increase in A_0. Hence, the observed instability in the acid monolayers must have been due to the repulsion between terminal dipoles; the same mechanism may have caused the expansion of the fluorooctadecanol monolayer mentioned before.

Gerovich, Frumkin, and Vargin[2b] also found that monomolecular films of 16-bromohexadecanoic acid were remarkably unstable and attributed the instability to the repulsive forces acting between similarly oriented C–Br dipoles. They reported obtaining stable films of 16-bromohexadecanoic acid by mixing it with various concentrations of hexadecanoic acid. They also suggested that more stable films could be obtained in the

presence of polyvalent cations, but they did not use this approach in their experiments, presumably because too little was known at that time about the structure of fatty acid films on neutral and alkaline solutions in the presence of polyvalent cations.

In our experiments with 16-iodohexadecanoic acid, it was found that the presence of iodide ions (I^-) in the aqueous substrate (as 0.01 *N* HI) did not alter the *F vs. A* or ΔV *vs. A* isotherms. If hydrolysis of the C–I bond had taken place, the presence of the common iodide ion should have had a suppressive effect and there would have resulted a somewhat different monolayer behavior. Evidence that the observed film instability did not arise from the hydrolysis of the carbon–halogen bond can also be found in the literature. Davies,[3] in his studies on monolayers of both 16-bromohexadecanoic acid and 16-hydroxyhexadecanoic acid on 1 *N* NaOH, assumed that the molecules of each compound could not be compressed above 7 dynes/cm. and tended to lie flat at the air–water interface up to those pressures. He obtained different surface potential values for each compound at equivalent areas per molecule, which indicated that the ω-C–Br bond had not been cleaved by hydrolysis.

Force vs. Area Isotherms for Monolayers on Solutions of Polyvalent Metallic Ions. It was our belief that the condensing effect of polyvalent ions on adsorbed monolayers of the higher fatty acids[9-12] could be used to stabilize and condense the monolayers of the terminally halogenated fatty acids. Each of the halogenated derivatives was therefore spread on 10^{-2} *M* $CaCl_2$ aqueous solutions at pH 2.2, 5.8, and 9.0. As expected, the *F vs. A* isotherms for octadecanol and 18-fluorooctadecanol monolayers on this substrate were identical with those obtained on distilled water. Although the stability of the halogenated acid monolayers was somewhat improved on the $CaCl_2$ solutions, they were still too unstable (even at pH 9.0) to give reliable *F. vs. A* isotherms.

An increase in the length of the hydrocarbon chain usually increases the stability of fatty acid monolayers. Accordingly, octadecanoic and 18-bromooctadecanoic acids were spread on 10^{-2} *M* $CaCl_2$ solutions at pH 3.9, 6.2, and 8.5 (Fig. 3a and 3b). The *F vs. A* isotherms obtained for octadecanoic acid agreed well with the re-

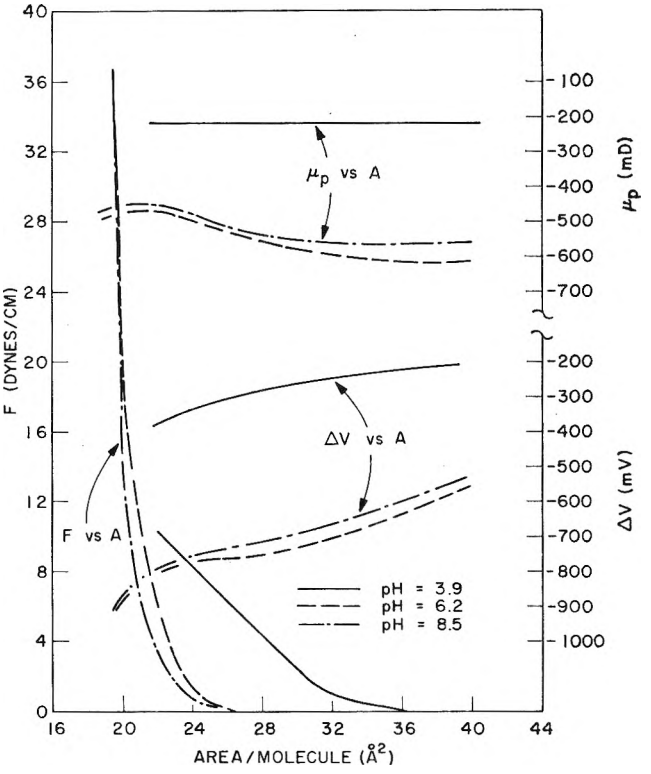

Figure 3b. Properties of 18-bromooctadecanoic acid monolayers spread at 20° on substrate containing 10^{-2} *M* $CaCl_2$.

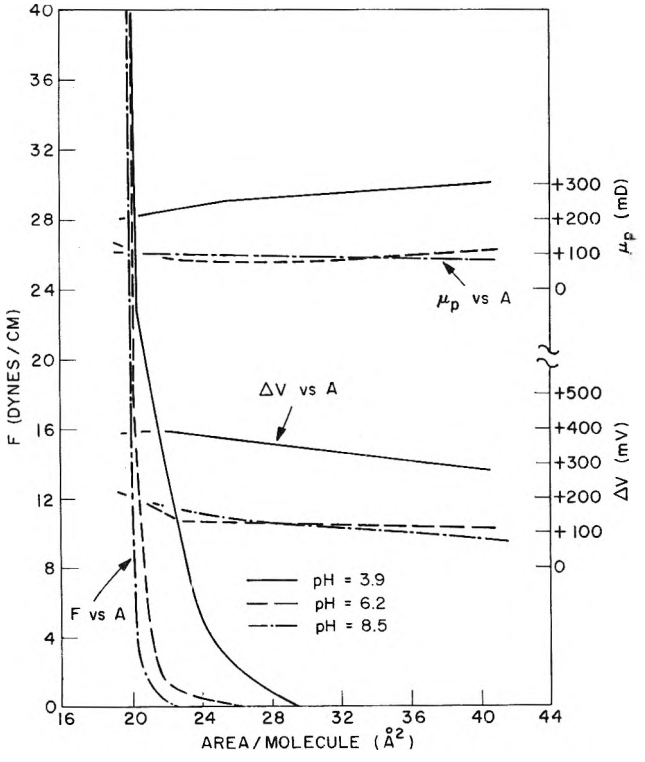

Figure 3a. Properties of octadecanoic acid monolayers spread at 20° on substrate containing 10^{-2} *M* $CaCl_2$.

(9) I. Langmuir and V. J. Schaefer, *J. Am. Chem. Soc.*, **58**, 284 (1936); **59**, 2400 (1937).

(10) W. A. Zisman, *J. Chem. Phys.*, **9**, 534 (1941).

(11) G. A. Wolstenholme and J. H. Schulman, *Trans. Faraday Soc.*, **46**, 475 (1950).

(12) J. A. Spink and J. V. Sanders, *ibid.*, **51**, 1154 (1955).

sults of Spink and Sanders.[12] The monolayer of 18-bromooctadecanoic acid was stable and reproducible at pH 6.2; at pH 8.5 it was close-packed with a value of A_0 of 20.4 Å.^{2}, the same as that of the unbrominated acid. Hence, increasing the length of the hydrocarbon chain from 16 to 18 carbon atoms increased the intermolecular cohesion sufficiently to stabilize the monolayer at the alkaline pH value in the presence of divalent calcium ions. In a recent study of monolayers of progressively fluorinated fatty acids, each of which contained a terminal $-CF_3$ group,[5] an 18-carbon aliphatic chain was the shortest permitting formation of stable monomolecular films on water at 20°.

Since the condensing effect of divalent ions in the aqueous substrate was not enough to overcome the large repulsive forces caused by terminal halogenation in the hexadecanoic acid monolayers, tetravalent thorium ions were added to distilled water to try to stabilize each monolayer. Many years ago Zisman[10] had shown that thorium salt solutions were able to solidify monolayers of straight-chain acids even at the oil–water interface and to condense branched-chain aliphatic acids having ten or more carbon atoms per molecule. Abramson and Ottewill[13] in a recent study of hydrolysis in thorium salt solutions found that a concentration of 5×10^{-5} M thorium nitrate was sufficient to completely condense monolayers of myristic acid. Therefore, a substrate containing 5×10^{-4} M thorium nitrate at the equilibrium pH value of 3.4 was used to determine the ability of tetravalent thorium ions to stabilize the monolayers of the ω-halogenated hexadecanoic acids. As would be expected, the F *vs.* A isotherms for octadecanol or 18-fluorooctadecanol on this substrate were not significantly different from those obtained on distilled water or on 10^{-2} M $CaCl_2$. The 18-fluorooctadecanol was again slightly more expanded than the octadecanol at lower film pressures and appeared to collapse at a somewhat lower area per molecule. Figure 4 shows the F *vs.* A isotherms of hexa-

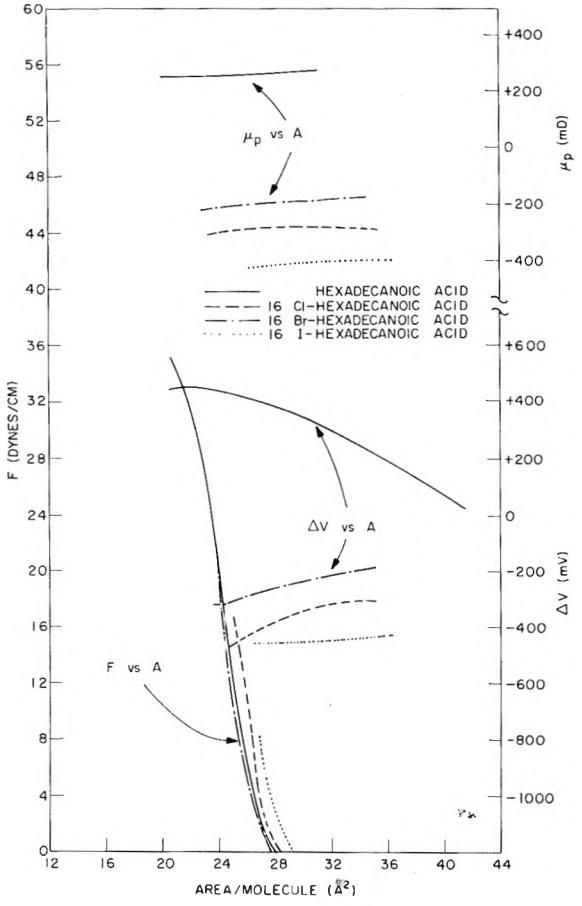

Figure 4. Properties of monolayers of 16-halogen hexadecanoic acids spread at 20° on substrate containing 5×10^{-4} M $Th(NO_3)_4$ and at pH 3.4.

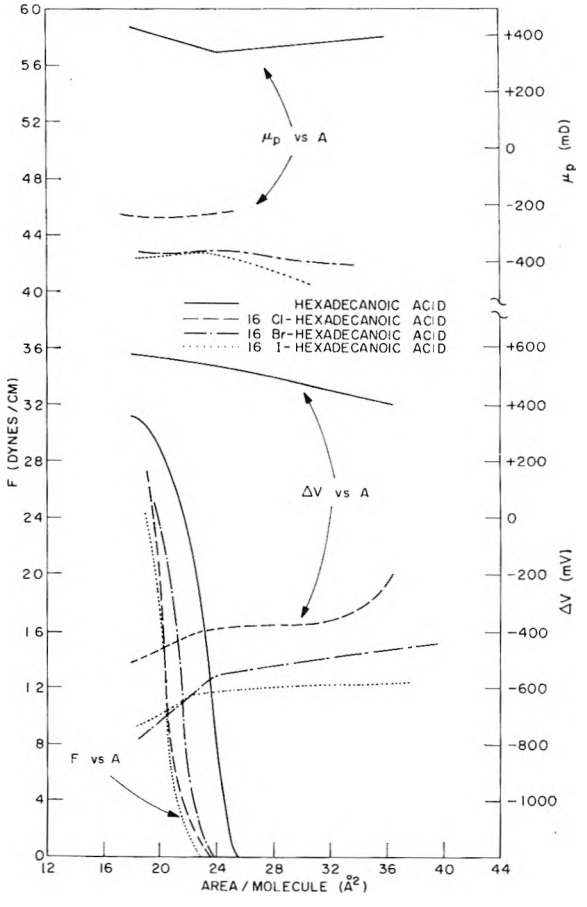

Figure 5. Properties of monolayers of 16-halogen hexadecanoic acids spread at 11° on substrate containing 5×10^{-4} M $Th(NO_3)_4$ and at pH 3.3.

(13) M. B. Abramson and R. H. Ottewill, *J. Colloid Sci.*, **17**, 883 (1962).

decanoic acid and its ω-halogenated derivatives on the thorium salt substrate. All of the *F vs. A* curves have the same shape and approximately the same value of A_0 (28 to 29 Å.^{2}). Whereas the monolayer of hexadecanoic acid supported film pressures up to 35 dynes/cm., the chloro-, bromo-, and iodohexadecanoic acid monolayers each collapsed at a lower film pressure (16, 12, and 8 dynes/cm., respectively). It should be noted that all A_0 values are still 60% greater than the cross-sectional areas per molecule determined from molecular models (Fig. 2). Thus these ω-halogenated hexadecanoic acid monolayers were condensed and stabilized by the presence of Th^{+4} ions in the aqueous substrate even though they had not been condensed to the closest possible packing.

Effect of Temperature on Monolayer Stability. It is well known that lowering the temperature will condense monolayers of paraffin derivatives.[14-16] Figure 5 gives the *F vs. A* isotherms of these acids on the thorium nitrate solutions at 11° and shows that the monolayers remained stable at higher film pressures with lower values of A_0 (19 to 20 Å.^{2}) than at 20°; *i.e.*, A_0 approached the value for closest packing given in Fig. 2. The *F vs. A* curves for octadecanol and 18-fluorooctadecanol in Fig. 6 shows that, whereas the monolayer of fluorinated alcohol behaved on this substrate very much like on other substrates, octadecanol was more expanded by about 1 Å.^{2}/molecule at lower film pressures.

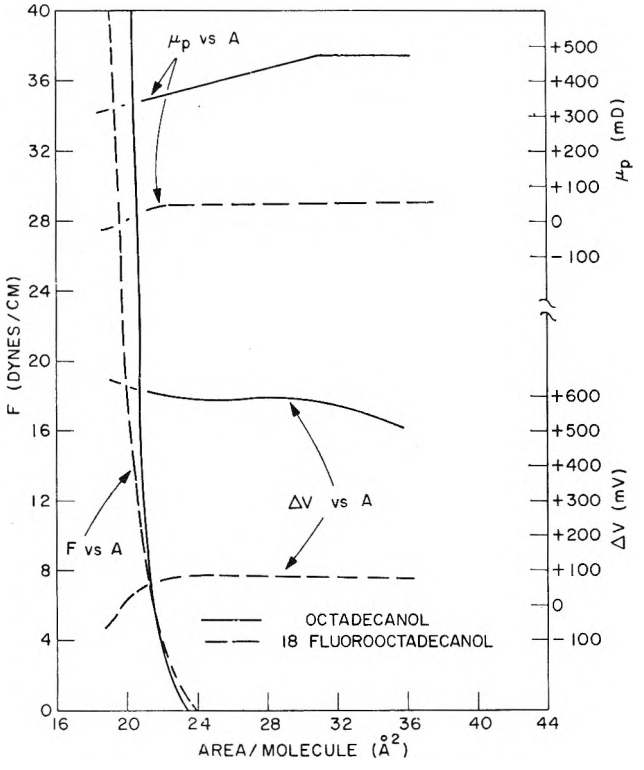

Figure 6. Properties of monolayers of octadecanols spread at 11° on substrate containing 5×10^{-4} *M* $Th(NO_3)_4$ and at pH 3.3.

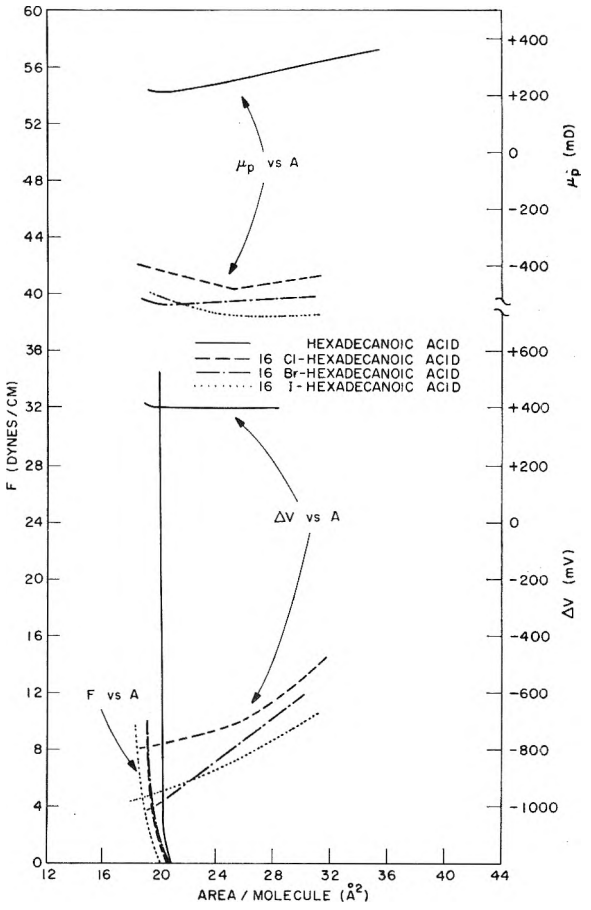

Figure 7. Properties of monolayers of 16-halogen hexadecanoic acids spread at 11° on substrate containing 10^{-2} *M* $CaCl_2$ and at pH 10.0.

Since decreasing the temperature from 20 to 11° effected the desired condensation and stabilization of the ω-halogenated hexadecanoic acid monolayers in the presence of thorium nitrate, *F vs. A* curves were also determined at 11° for each of these compounds on 10^{-2} *M* $CaCl_2$ at pH 1.8 as well as at pH 10.0. At pH 1.8 the *F vs. A* curves were nearly identical with those observed on acid substrates at 20°, while at pH 10.0 significant differences were found. *F vs. A* curves are given in Fig. 7 for those monolayers exhibiting changes in film properties with temperature at pH 10.0. At

(14) N. K. Adam, "The Physics and Chemistry of Surfaces," Oxford University Press, London, 1941, pp. 59–63, 72–74.

(15) W. D. Harkins, "The Physical Chemistry of Surface Films," Reinhold Publishing Corp., New York, N. Y., 1952, pp. 111, 112.

(16) J. T. Davies and E. K. Rideal, "Interfacial Phenomena," Academic Press, New York, N. Y., 1961, pp. 70, 71.

20° and pH 9.0 the 16-bromo and 16-iodo acids were too unstable to give reliable data; at 11° and at pH 10.0, however, they formed close-packed reproducible films which were stable up to pressures of 10 dynes/cm. The areas per molecule for the ω-halogenated hexadecanoic acids at collapse pressure were in each case approximately 19 Å.^{2}, which is comparable to the values obtained on the thorium nitrate substrate at 11°. Thus, the divalent calcium ions were ineffective in condensing monolayers of these halogenated acids at 20°, but became effective when the temperature was lowered to 11°.

Electrical Properties of Monolayers. The difference ΔV in the electrostatic potential between a clean water surface and the surface covered by a monolayer is known to be dependent upon the structure of the adsorbed molecules and, with adsorbed acidic or basic compounds, upon the pH and salt content of the aqueous substrate as well.[12,14,17,18] The ΔV *vs.* A isotherms for each of the compounds studied have been plotted, along with the corresponding F *vs.* A curves, in Fig. 1 and 3 through 7. Values of ΔV are given along the right-hand vertical scale in each figure. Values of ΔV for octadecanol and 18-fluorooctadecanol monolayers were independent of substrate pH or composition, except for octadecanol on 5×10^{-4} M $Th(NO_3)_4$ at 11° (Fig. 6), where ΔV was 200 mv. higher than on any of the other substrates. The ΔV *vs.* A curves for hexadecanoic and octadecanoic acids varied with the pH and the salt content of the substrate, the effect of varying pH alone being in good agreement with the results of Spink and Sanders.[12,17] ΔV was always positive for the unsubstituted acid or alcohol monolayers, and, as expected, ΔV was always negative for each ω-halogenated compound; at molecular close packing it was at least 1000 mv. less for the halogenated than for the unhalogenated acid.

The normal component of the molecular dipole moment (μ_p) was calculated from ΔV by using the classic equation of Helmholtz

$$\Delta V = 4\pi\eta\mu_p \qquad (1)$$

where η is the number of adsorbed polar molecules per cm.^{2}. Resulting values of μ_p have been plotted against A along the right-hand vertical scale of each figure.

It has long been realized that the value of μ_p so calculated is the resultant of several contributing dipoles in or associated with each molecule of the adsorbed film. These are (a) the permanent dipole in the adsorbed organic molecule, (b) the resultant arising from the reorientation of the surface water dipoles in the immediate vicinity of the polar hydrophilic group of the adsorbed organic molecule, and (c) the contribution of any ionic double layer present at the water–air interface. As is well known, contribution (a) can be considered the sum of vector contributions from each bonded pair of atoms in the organic molecule. In computing (a) it will be assumed (as is usual) that the net contribution from each unsubstituted polymethylene chain is zero; hence, the organic molecule contributes two moments, one due to the terminal polar $-CH_2X$ group (where X is a halogen atom) at one end of the paraffin chain and the other due to the hydrophilic polar group at the other end. It can also be assumed that contributions (b) and (c) do not alter the $-CH_2X$ dipole located at the outermost end of the paraffin chain because of its distance from the surface of the water substrate. Since at present it is impossible to separate the contributions of the hydrophilic polar group located in the water–air interface (from (a)), the water layer polarized by it (b), and the adjacent ionic double layer (c), it is usual to combine the three terms into the single term $\mu_{(0)p}$. Consequently, μ_p for the unhalogenated adsorbed molecule can be expressed as

$$\mu_p = \mu_{(0)p} + \mu_{(CH_3)p} \qquad (2)$$

where $\mu_{(CH_3)p}$ is the contribution of the terminal CH_3 group. When the adsorbed molecule has a halogen atom (X) on the ω-carbon atom, then

$$\mu_p = \mu_{(0)p} + \mu_{(CH_2X)p} \qquad (3)$$

From the assumptions made, it follows that $\mu_{(0)p}$, at a given value of η, should be the same for the halogenated and unhalogenated adsorbed compounds.

In Table I, values of ΔV are given for closely packed monolayers (at areas per molecule from 19.5 to 20 Å.^{2}) of each of the compounds studied. Values of ΔV for monolayers of both ω-substituted and nonsubstituted hexadecanoic acids and octadecanols were obtained on 5×10^{-4} $Th(NO_3)_4$ at 11° and pH 3.3, while those for octadecanoic acid and 18-bromooctadecanoic acid were measured on 10^{-2} M $CaCl_2$ at 20° and pH 8.5. From the measured value of ΔV (given in the third column) the corresponding value of μ_p was calculated from eq. 1 for each compound and is given in the fourth column. The value of $\mu_{(0)p}$ (given in the fifth column) for each unhalogenated compound was calculated from eq. 2 by using -0.3 D. as the vertical component of the dipole moment of the terminal methyl group, $\mu_{(CH_3)p}$, on the hydrocarbon chain, the terminal C–H bond being directed at an angle of 54° 44′ from the water surface. The best literature value for the

(17) J. A. Spink, *J. Colloid Sci.*, **18**, 512 (1963).

(18) E. D. Goddard and J. A. Ackilli, *ibid.*, **18**, 585 (1963).

Table I: Electrical Properties of Fatty Acids, Fatty Alcohols, and Their ω-Monohalogenated Derivatives

Compound	Area/molecule, Å.²	ΔV, mv.	μ_p, D.	$\mu_{(0)p}$[a] (calcd. from eq. 2), D.	$\mu_{(CH_3X)p}$ (calcd. from eq. 3), D.	$\mu_{(CH_2X)p}$ (calcd. by Davies' method), D.
On aqueous substrate: 5×10^{-4} *M* $Th(NO_3)_4$ at pH 3.3 and 11°						
Hexadecanoic acid	19.5	+565	+0.29	+0.59	...	...
16-Chlorohexadecanoic acid	19.5	−480	−0.25	+0.59	−0.84	−0.54
16-Bromohexadecanoic acid	19.5	−705	−0.37	+0.59	−0.96	−0.66
16-Iodohexadecanoic acid	19.5	−730	−0.38	+0.59	−0.97	−0.67
Octadecanol	20.0	+620	+0.35	+0.65	...	...
18-Fluorooctadecanol	19.5	−55	−0.03	+0.65	−0.68	−0.38
On aqueous substrate: 1×10^{-2} *M* $CaCl_2$ at pH 8.5 and 20°						
Octadecanoic acid	19.8	+200	+0.10	+0.40	...	...
18-Bromooctadecanoic acid	19.8	−910	−0.48	+0.40	−0.88	−0.58

[a] $\mu_{(CH_3)p} = -0.30$ D. from literature dipole moment C^+-H^-.

dipole moment of the terminal CH_3 group is approximately 0.4 D., with the polarity being C^+-H^-,[19] the same polarity as the carbon–halogen bond. Equation 3 was then used to compute the value given in the sixth column for each halogenated compound, assuming that $\mu_{(0)p}$ was the same for the halogenated and unhalogenated compounds.

The values of $\mu_{(CH_2X)p}$ ranged from −0.68 to −0.97 D. in going through the series of halogens from fluorine to iodine. In Fig. 8 the values of $\mu_{(CH_2X)p}$ are plotted against the covalent radii of the halogen atoms, and a rectilinear graph results. This should be expected, since the polarizability of an atom increases with the radius of its outer electron shell. It will be noted that the value of $\mu_{(CH_2X)p}$ for X = F was determined using a terminally halogenated alcohol, whereas for the other halogens the calculation was based on measurements on the terminally halogenated acids. Nevertheless, the deductions made should be valid because of the large number of carbon atoms separating the polar hydrophilic group and the polar CH_2X group. If one plots in Fig. 8 the value of $\mu_{(CH_2X)p}$ for the limiting case where X is replaced by a hydrogen atom (0.3 D.), the graphical point falls close to the extrapolated straight line plot defined by the halogen family.

Surface potential data for terminally halogenated derivatives have been treated in a somewhat different manner by both Gerovich[2b] and Davies.[16] They used the Helmholtz relationship to calculate μ_p for the halogenated and nonhalogenated compounds and then determined the values of each $\mu_{(CH_2X)p}$ from the amount that each of the halogens reduced μ_p. The last column in Table I shows the values for $\mu_{(CH_2X)p}$ obtained by their calculations. It can be seen that their results are lower by 0.3 D., the value of $\mu_{(CH_3)p}$, than those obtained by our calculations. In other words, they have assumed that the contribution of the terminal $-CH_3$ group can be neglected. Hence, except for the difference in the value assigned to $\mu_{(CH_3)p}$ the results of Gerovich and co-workers[2b] for 16-bromohexadecanoic acid agree well with ours.

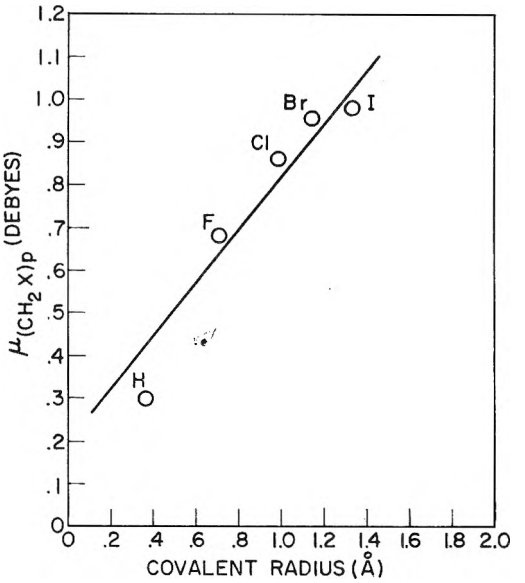

Figure 8. Relation of perpendicular moment of methylene–halogen group to the covalent radius of its respective halogen atom.

With an angle of 54° 44′ between the terminal C–X bond and the water surface, the apparent dipole moment of each $-CH_2X$ group, as determined from ΔV measurements, would be $\mu_{(CH_2X)p}/\sin 54° 44'$. In the third and fourth columns of Table II the dipole

(19) W. L. G. Gent, *Quart. Rev.* (London), 2, 383 (1948).

Table II: Comparison of Observed Values of Dipole Moments for CH_2X Group with Literature Values

Compound	ω-Terminal group	μ_{CH_2X}: $\mu\ (CH_2X)_p/\sin 54°\ 44'$, D.	μ_{CH_2X}: Lit.,[a] D.
18-Fluorooctadecanol	$-CH_2F$	0.80	1.9 to 2.1
16-Chlorohexadecanoic acid	$-CH_2Cl$	1.02	1.8 to 2.2
16-Bromohexadecanoic acid	$-CH_2Br$	1.15	1.9 to 2.2
18-Bromooctadecanoic acid	$-CH_2Br$	1.07	1.9 to 2.2
16-Iodohexadecanoic acid	$-CH_2I$	1.16	1.8 to 2.0

[a] See ref. 20 and 21.

moments obtained in this manner for each terminal halogen bond are compared with the values reported in the literature for the same dipoles.[20,21] It is apparent that our values are only about 50% of the literature values, which were obtained from measurements on appropriate halogenated compounds in the gaseous state or in dilute solution in a nonpolar solvent. The conclusion is unavoidable that the close packing of the similarly oriented polar molecules in the condensed monolayer caused mutual lateral induced polarization and thus lowered by 50% the contribution of the terminal CH_2X groups to the dipole moments.

Discussion

The results of this investigation demonstrate that the replacement of a hydrogen atom on the terminal carbon atom of a fatty acid or alcohol by a halogen atom will greatly reduce the stability of closely packed monolayers of the compounds. It was also found that the effect of the substituted chloro, bromo, and iodo atoms on monolayer stability is of approximately the same magnitude. Unlike the effect of ω-chloro, -bromo, and -iodo substitution on fatty acid monolayers, the substitution of fluorine on the ω-carbon of a fatty alcohol did not cause noticeable monolayer instability.

If the instability of the ω-halogenated hexadecanoic acid monolayers arose from steric hindrance to close packing because of the larger diameter of the terminal halogen atom as compared to hydrogen, one would expect the 16-iodohexadecanoic acid monolayer to be the most expanded and to collapse at lower film pressures than the bromo and chloro derivatives. However, if the disruptive influence was caused by an electrostatic repulsion between the large dipole moments of the terminal $-CH_2X$ groups in the neighboring adsorbed molecules, then each of the 16-halogen hexadecanoic acids should have roughly the same monolayer stability, for the literature values of the $-CH_2X$ bond dipole moments are approximately the same (Table II). All of the F *vs.* A data presented in this report strongly suggest that the monolayer instability arose primarily from mutual repulsion between the terminal dipole moments and not from steric hindrance related to the size of the halogen atoms. It was also shown in this investigation that the instability of the monolayers of terminally halogenated hexadecanoic acids could be overcome by decreasing the temperature of the system and by adding multivalent thorium or calcium ions to the aqueous substrate in order to take advantage of the condensing effect arising from their reaction with the adsorbed acid molecules.

Monohalogenation of the ω-carbon atoms also caused marked changes in the surface potential difference (ΔV) of condensed monolayers of fatty acids and alcohols adsorbed on water. Substitution of chloro-, bromo-, or iodo- for a terminal hydrogen atom in hexadecanoic acid was found to decrease ΔV by 1100 to 1300 mv. in a close-packed monolayer. However, the change in ΔV caused by replacement of the ω-hydrogen in octadecanol by fluorine was only 675 mv., appreciably less than the change caused by the substitution of the other halogens on hexadecanoic acid. From the literature values of the C–F dipole moment, which is equivalent to the dipole moment of the $-CH_2F$ group when obtained from a paraffin compound,[21] one would expect the decrease of ΔV to be as large as for the other halogens. The reason that the values of ΔV are not the same for each halogen may be that the dipole moment of each carbon–halogen bond in a closely packed monolayer is modified to a different extent by mutual lateral polarization. This possibility is reinforced by Fig. 8 which shows that the perpendicular component of the apparent dipole moment, $\mu_{(CH_2X)p}$, varies with the covalent radius (or polarizability) of the halogen atom.

The term $\mu_{(0)p}$ used in this report for the contribution of the polar adsorbing group to the molecular dipole moment is analogous to the term $\mu_{(COOH)aq}$ used previously by Bernett and Zisman.[5] The values reported here for $\mu_{(0)p}$ do not agree with those determined previously,[5] because here we have assumed a different polarity for the dipole moment of the terminal $-CH_3$ group. Bernett and Zisman used a value of 0.3 D. for the vertical component of the $-CH_3$ dipole moment, assuming a bond polarity of $C^-–H^+$. In the present study a value of 0.3 D. was also used, but we assumed the reverse polarity, $C^+–H^-$; this was done because values obtained by theoretical and

(20) J. W. Smith, "Electric Dipole Moments," Butterworths Scientific Publications, London, 1955, pp. 92, 119–125.

(21) C. P. Smyth, "Dielectric Behavior and Structure," McGraw-Hill Book Co., Inc., New York, N. Y., 1955, pp. 240–245.

spectroscopic methods[19] indicate that the true polarity of the C–H bond in a saturated aliphatic compound is C^{+}–H^{-}, giving the C–H bond the same polarity as the C–X bonds.

Influence of Water Structures on the Surface Pressure, Surface Potential, and Area of Soap Monolayers of Lithium, Sodium, Potassium, and Calcium

by D. F. Sears

Tulane University, School of Medicine, New Orleans, Louisiana

and Jack H. Schulman

Columbia University, School of Mines, Stanley Thompson Laboratories, New York, New York
(Received April 13, 1964)

Force–area and surface potential–area curves were obtained at 15, 25, and 37° for stearic acid on 0.1 *N* HCl and 0.5 *N* hydroxides of lithium, sodium, and potassium. Differences in areas per molecule at the same temperature and surface pressure on the different substrates indicated that the hydrated ion associated with the carboxyl group of the stearate determined the expansion of the monolayer. Areas per molecule increased in the sequence Li < Na < K. Trace amounts of calcium, when added to the hydroxide substrates, markedly decreased the expansion effected by the monovalent ions. On bicarbonate substrates of sodium and potassium, compression of the monolayer promoted removal of the respective cation. This removal allowed the area per molecule at high surface pressures to compress to the area of stearic acid on 0.1 *N* HCl. Calculation of the surface compressional modulus indicated that the monolayers on the hydroxide substrates were liquid expanded. The effect of temperature was examined by determining the change in surface pressure with change in temperature at constant area per molecule ($A\Delta\pi/\Delta T$). The values varied with temperature and with the compression of the monolayer. Stearic acid on the acid substrate gave $A\Delta\pi/\Delta T$ values which increased with increasing areas per molecule, whereas on hydroxide substrates the monolayers gave decreasing values with increasing area. Within the same temperature range and for the same area per soap molecule, values for $A\Delta\pi/\Delta T$ increased in the sequence Li < Na < K.

Introduction

Adam and Miller[1] reported expansion of fatty acid monolayers on alkali solutions of sodium and potassium. On 2 *N* hydroxides, limiting areas extrapolated to zero compression were 31 and 38 Å.²/molecule for sodium and potassium soaps, respectively. Experiments with adsorbed monolayers of sodium and potassium oleate at a benzene–water interface indicated that potassium

oleate monolayers were more expanded than sodium oleate.[2] This paper examines to what extent this expansion is due to the size of the hydrated sodium or potassium associated with the fatty acid monolayer.

Studies of ionic radii and hydration of ions have been reviewed by Stern and Amis.[3] The methods reviewed gave information concerning ion size in solution. It remains to be shown whether these measurements apply to ions at an interface. Information concerning the relative sizes of Na^+ and K^+ at an interface can be obtained from the monolayer technique after accounting for the effects of ionization and electrostatic repulsion between the molecules.

The hydrated sizes of Na^+ and K^+ are of biological significance. Cell membranes accumulate K^+ in the cell interior while excluding Na^+. Theories developed to account for the selectivity have been based in part on estimates of the size of hydrated ions derived from hydration numbers.

Some values taken from the extensive study of Stokes and Robinson[4] for n (the number of water molecules interacting with the cation with an energy large compared to kT) and for $\mathring{a}$ (the distance of closest approach to the hydrated cation by the anion, assumed to be unhydrated) are given in Table I. Values for

Table I

Salt	n	$\mathring{a}$
LiCl	7.1	4.32
NaCl	3.5	3.97
KCl	1.9	3.63

other salts of the same cations vary as a function of the anion size, but the same order, Li > Na > K, for n and $\mathring{a}$ was maintained.

Since it is at the cell membrane–water interface that ion transport occurs, knowledge of the properties of the cations in an interfacial region rather than in the bulk of a solution is pertinent for biological consideration. Structuring of water at interfaces is indicated.[5] The work of Derjaguin and Titijevskaya[6] on free films and froths showed that water layers adjacent to sodium oleate-adsorbed films were oriented to as much as ten molecules thick and were characterized by a low dielectric constant. At an interface, the hydration numbers given by Stokes and Robinson[4] for n may be expected to increase due to a reduction in thermal agitation.

This investigation was undertaken to measure the relative ion sizes with the monolayer technique. Force–area (π–A) and surface potential–area (ΔV–A) curves of stearic acid spread on 0.5 N hydroxides of lithium, sodium, and potassium were examined. Care was taken to remove traces of Ca^{+2} which might affect the results. At pH 13 saponification is essentially complete. The data reported here show that lithium, sodium, and potassium cause expansion of the monolayers of stearic acid and the limiting areas of these cations at the interface increase in the sequence Li < Na < K; this is the reverse of the sequence found for hydration sizes measured in the bulk solution.

Methods

π–A curves were obtained using a Wilhelmy balance which had a sensitivity of 0.2 dyne/cm. Both fused silica troughs and aluminum troughs coated with Teflon were used. No difference in the force–area curves could be detected because of differences in the troughs. Stearic acid was obtained from K and K Laboratories and was recrystallized six times, m.p. 68–69°. Normal hexane used for diluting the stearic acid was chromatographically pure. Substrate solutions were made with Pyrex distilled water. Sodium hexametaphosphate (Calgon) was added to the substrates (0.5 g./l.) to bind any calcium present. The acid and bicarbonate solutions were filtered over activated charcoal. Substrates were allowed to stand in the trough to accumulate any surface-active contaminants at the surface. The surface was then cleaned with a paraffined glass slide and suction. The temperature was regulated by surrounding the trough with water circulated from a water bath and was measured with a thermometer submerged in the substrate. Surface potentials were determined by the method described by Schulman and Rideal.[7] A Keithley electrometer with an input impedance of 10^{14} ohms was used.

Results

Figure 1 shows the π–A and ΔV–A curves for stearic acid on 0.1 N HCl and on 0.5 N solutions of lithium, sodium, and potassium hydroxides at 15°. Each

(1) N. K. Adam and J. G. F. Miller, *Proc. Roy. Soc.* (London), **A142**, 401 (1933).

(2) D. F. Sears and R. M. Eisenberg, *J. Gen. Physiol.*, **44**, 869 (1961).

(3) K. H. Stern and E. S. Amis, *Chem. Rev.*, **59**, 1 (1959).

(4) R. H. Stokes and R. A. Robinson, *J. Am. Chem. Soc.*, **70**, 1870 (1948).

(5) J. T. Davies and E. K. Rideal, "Interfacial Phenomena," Academic Press, New York, N. Y., 1962.

(6) B. F. Derjaguin and A. S. Titijevskaya, *Proc. Intern. Congr. Surface Activity, 2nd, London*, **1**, 211 (1957).

(7) J. H. Schulman and E. K. Rideal, *Proc. Roy. Soc.* (London), **A130**, 259 (1931); **A138**, 430 (1932).

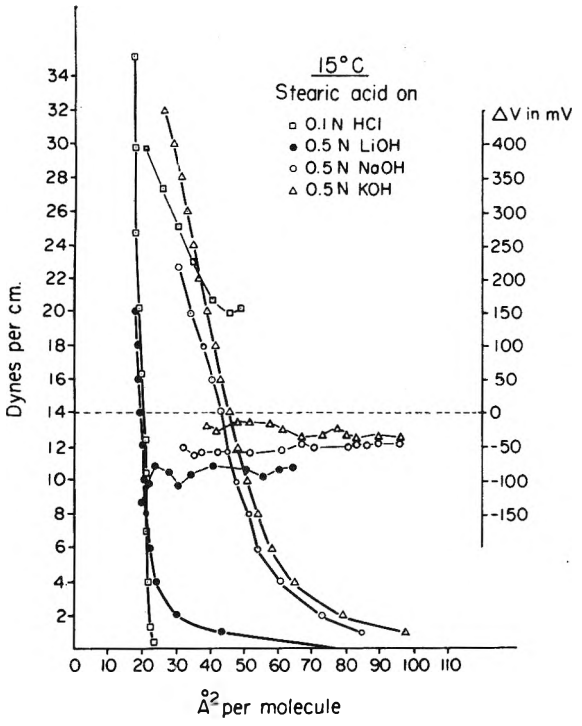

Figure 1. Force–area (bold lines) and surface potential–area (light lines) curves for stearic acid on various substrates at 15°. Each curve represents the average of three or more experiments on the respective substrates. The pH values for the alkali substrates at 15° were: LiOH, 12.6; NaOH, 13.2; and KOH, 13.4.

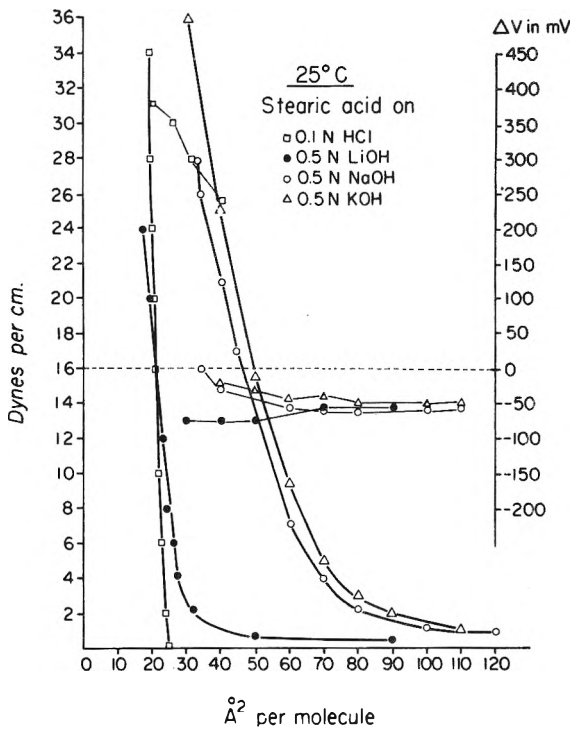

Figure 2. Force–area (bold lines) and surface potential–area (light lines) curves of stearic acid on substrates at 25°. Each curve represents the average of three or more experiments. The pH values for the alkali substrates were: LiOH, 12.6; NaOH, 13.2; KOH, 13.4.

curve represents the results from three or more experiments. Highest force values plotted for each curve are the breaking pressures with the exception of stearic acid on 0.1 *N* HCl which gave breaking pressures as high as 44 dynes/cm. ΔV–A values for stearic acid on 0.1 *N* HCl increased with compression to +390 mv., air with respect to water. For stearic acid spread on hydroxide solutions, ΔV was negative, air with respect to water. Erratic fluctuations of ΔV occurred at areas less than about 20 Å.²/molecule for the acid on LiOH, about 30 Å.²/molecule on NaOH, and 40 Å.²/molecule on KOH, which suggests that the monolayers had broken at these areas. For KOH, the π–A curves did not show an indication of breaking until about 25 Å.²/molecule. At pressures where coherent monolayers were obtained for all substrates, the area per molecule increased in the order H $\leq$ Li < Na < K, and the surface potentials were negative for the hydroxide solutions in the order Li > Na > K.

Figure 2 shows the results from experiments performed at 25° with the same group of solutions. π–A curves indicated that the monolayers were more expanded at this temperature than at 15°. The same order of expansion on the different substrates was observed. The highest pressures shown are the breaking pressures, except for stearic acid on HCl. Fluctuations of ΔV values suggested that breaks occurred at larger areas than indicated by π–A curves. ΔV values for the monolayers on hydroxides were still negative, air with respect to water, but, in the case of the sodium and potassium hydroxide substrates, they showed a tendency to become positive with compression.

Figure 3 shows the results from experiments performed at 37°. Further expansion was observed for each monolayer at this temperature as compared with 25°; however, the increase was slightly less than between 15 and 25°. The same order of expansion between the different substrates was observed, *i.e.*, Li < Na < K. At this temperature the ΔV–A curves were negative at large areas per molecule, but on sodium and potassium hydroxide the values became positive with compression. Since the π–A curves still showed the expansions associated with the respective cations, we ascribed the surface potential values to changes in the orientation of water about the acid–cation association.

Further evidence for the assumption that the orien-

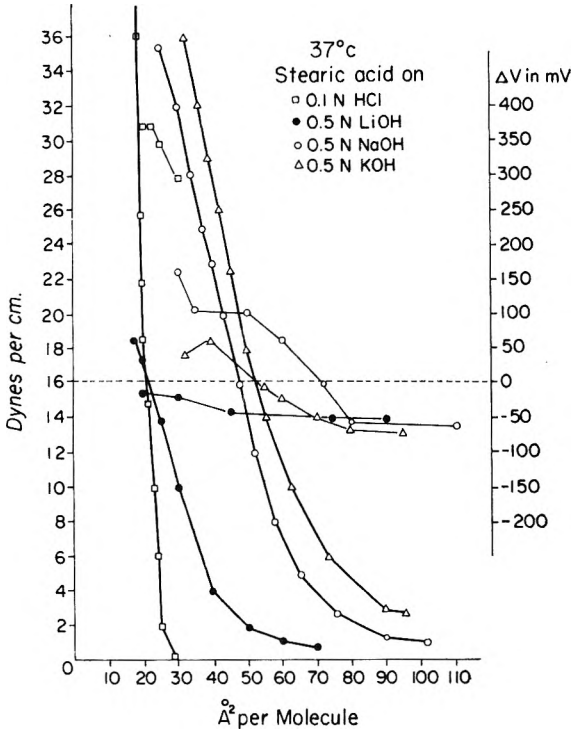

Figure 3. Force–area (bold lines) and surface potential–area (light lines) curves for stearic acid on substrates at 37°. Each curve represents the average of three or more experiments. The pH values for the alkali substrates at this temperature were: LiOH, 12.6; NaOH, 13.2; and KOH, 13.5.

tation of water caused the surface potential values was found when the millivolts per molecule was determined from the surface potential data. This was obtained from $\Delta V/N$, where N is the number of molecules/cm.^{2}. With compression at 15°, the electrical potential per molecule approached zero and the values were similar for all three hydroxide substrates. For the acid substrate the value decreased from a maximum value at 22 Å.^{2}/molecule of 86×10^{-14} mv. to 68×10^{-14} mv. at 17.5 Å.^{2}/molecule. This corresponds to a decrease in the dipole moment from 254 to 201 mD. due to compression. Since compression causes an alignment of molecules, it was expected that higher values of dipole moments would be obtained with compression rather than a decrease. The observed decrease of potential which occurred with both the acid and the hydroxide substrate could be explained on the basis of disorder in orientation of water molecules about the carboxyl end of the molecule.

The surface compressional modulus (C_s^{-1}) defined as

$$C_s^{-1} = (-1/A(\mathrm{d}A/\mathrm{d}\pi)_T)^{-1}$$

was calculated for each monolayer on hydroxide substrates. Values obtained varied within the range of 12.5 to 50, indicating that the monolayers were liquid expanded.

Figure 4 shows the effect of Ca^{+2} on monolayers with NaOH or KOH substrates at 25°. When approximately 0.006 g./l. of $Ca(OH)_2$ was added to 0.5 N NaOH or KOH, sufficient Ca^{+2} was present to condense the monolayers. Greater amounts of Ca^{+2} added to NaOH caused greater compression of the monolayer. At larger areas per molecule the effect of calcium was less marked than at smaller areas per molecule. Breaks in the force–area curves suggest different proportions of calcium to sodium or potassium associated with the stearate radical with progressive compression.

Experiments with 0.5 N Na and $KHCO_3$ as substrates were performed. The pH of these substrates was 8.5. Figure 5 shows curves on $NaHCO_3$ and $KHCO_3$ at 25°. At low surface pressures these π–A curves were expanded to resemble the curves on hydroxides. Surface potentials were negative. Compression resulted in limiting areas which were only slightly more expanded than stearic acid on 0.1 N HCl. Thus sodium or potassium was removed from the monolayer with increasing compression and the surface potential became positive in this case indicating the formation of

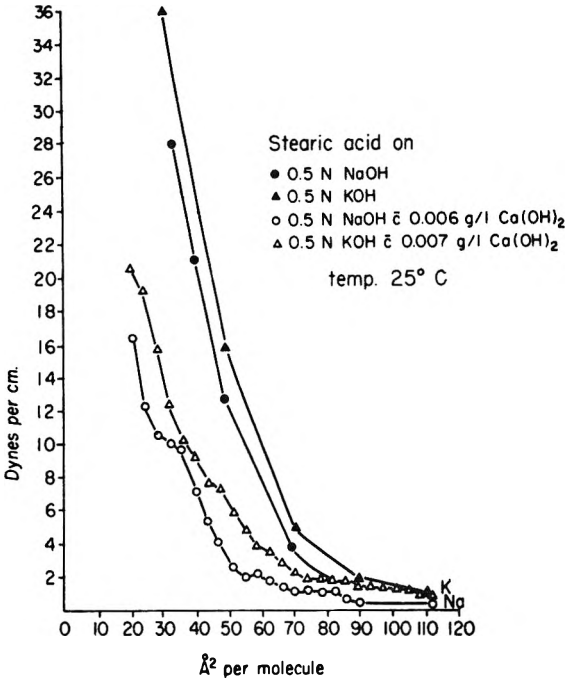

Figure 4. Effect of Ca^{+2} in the substrate without the addition of Calgon. Force–area curves for Na and K substrates from Fig. 2 were included for comparison. These two curves represent actual data from representative experiments and not averages as repeats of the experiments with calcium present agreed only qualitatively.

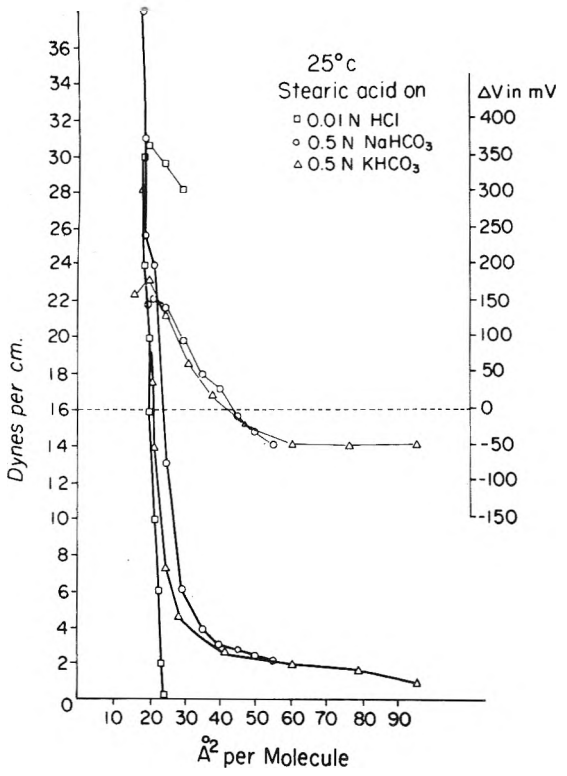

Figure 5. Force–area and surface potential–area curves of stearic acid on 0.5 N $NaHCO_3$ and $KHCO_3$. The pH of the bicarbonate substrates was 8.5 at 25°. The curves for stearic acid on 0.1 N HCl were included for comparison from Fig. 2. The sodium curve is more expanded than the potassium. Surface potentials on the bicarbonate substrates reverse sign during compression which did not occur with compression on 0.5 N hydroxides at this temperature.

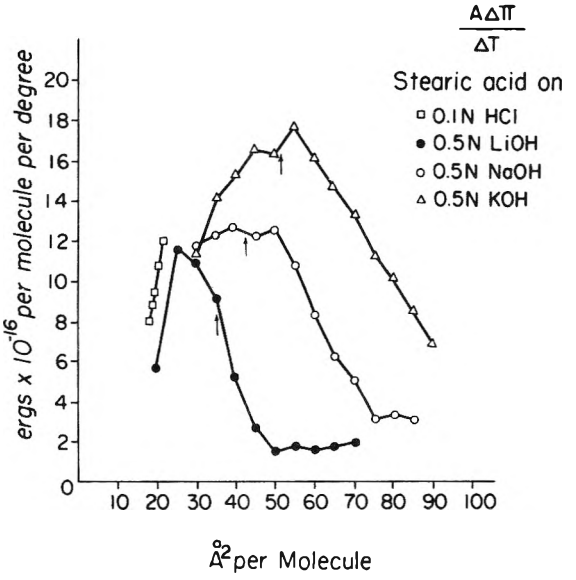

Figure 6. Plot of $A\Delta\pi/\Delta T$ values at different areas per molecule. The temperatures used were 15 and 37° to give ΔT as 22° and pressures at these two temperatures were measured at the areas indicated to give $\Delta\pi$. The small arrows indicate the estimated hydrated sizes of the cations based upon the assumptions discussed in the text. The magnitudes of the values are dependent upon the choice of temperatures as greater expansions, hence greater $\Delta\pi$ values, were obtained between 15 and 25° than between 25 and 35°. Thus measurements based upon ΔT of 10° between 15 and 25° would have given larger values for $A\Delta\pi/\Delta T$. However, the same relation between the curves is maintained.

the acid stearate. The sodium curves were more expanded than the potassium curves; similar results, *i.e.*, Na > K, were reported by Rogers and Schulman[8] for the alkyl sulfates.

The effect of temperature on the monolayers was examined on the basis of the relation $A\Delta\pi/\Delta T$, the change in surface pressure at constant area at two different temperatures. Since values for π corresponding to area from our experiments were available only at 15, 25, and 37°, the data are sufficient only to show the direction of the changes. The term $A\Delta\pi/\Delta T$ may be compared to Harkins'[9] expression for the entropy of expansion of a film on water

$$s_e = (\partial S/\partial\sigma_f)_{T,\sigma_w} = -(\partial\gamma_f/\partial T)_{\sigma_f}$$

where s_e is the entropy per unit area, S is the total entropy, σ_f is the molecular area of the film molecule, σ_w is the area of the water, and γ_f is the surface tension of the film. Values for $A\Delta\pi/\Delta T$ were determined from curves at 15 and 37°; for stearic acid on the acid substrate the values increased with increasing area per molecule, for the hydroxide substrates the values decreased with increasing area. Values obtained from data at 15 and 37° are shown in Fig. 6. On the acid substrate, stearic acid shows an increase in $A\Delta\pi/\Delta T$ which corresponds to increasing entropy, since

$$-(d\gamma/dT)_A = +(d\pi/dT)_A$$

Values are shown in ergs $\times 10^{-16}$/molecule deg.$^{-1}$. The decrease in values with increasing area per molecule on the hydroxide substrate indicates a decrease in the randomness of the orientation as expansion occurs.

Discussion

Stearic acid monolayers are expanded on hydroxide solutions in agreement with earlier reports in the literature. The degree of expansion varies with the specific cation. Adam[10] attributed the loss of adhesion

(8) J. Rogers and J. H. Schulman, *Proc. Intern. Congr. Surface Activity, 2nd, London*, **3**, 243 (1957).

(9) W. D. Harkins, "The Physical Chemistry of Surface Films," Reinhold Publishing Corp., New York, N. Y., 1952.

(10) N. K. Adam, "The Physics and Chemistry of Surfaces," Oxford University Press, London, 1941.

between the fatty acid molecules on the alkaline substrate and, consequently, the expansion of the monolayer to repulsion between the similar electrical charges on the adjacent end groups. Our experiments do not support this explanation. The reaction

$$H(FA) + B(OH) \longrightarrow B(FA) + HOH$$

is essentially complete at a pH which is three units higher than the pK of the acid. For the experiments at pH 13 on the hydroxides, the saponification of the fatty acid by the alkali would be complete. At a lower pH on the bicarbonates (8.5) the degree of association between the cation and the fatty acid could be less than complete, the actual degree of association depending upon two values, the pK of the anion and the pH at the interface. On the substrates at pH 8.5 compression was accompanied by the removal of cations as demonstrated by the force–area and surface potential–area curves. Both of these curves approached the values obtained for stearic acid spread on 0.1 N HCl with compression. The similarity of the curves at the two different regions of pH values (pH 1 and 8.5) indicate that the difference in degree of ionization of the fatty acid plays only a small role in determining the force–area relations of the monolayer as compared with the specific cation effect.

The question also arises with respect to the magnitude of the electrical field which would produce the repulsion of adjacent soap molecules. We found no information concerning the dipole moment of soap molecules other than the values obtained from the surface potential measurements. These measurements indicate that this moment is small. This also suggests that electrostatic repulsion between adjacent soap molecules was not an important factor in determining the expansion of the monolayer.

Replacement of Na^+ or K^+ by Ca^{+2} at pH 13 with compression of the monolayer as shown in Fig. 4 further demonstrates a specific effect which is attributable to characteristics of the cation. At large areas per molecule the Na^+ or K^+ could compete with the calcium for the stearate; however, with reduction of the area per molecule, calcium predominated by virtue of its two valences and finally replaced monovalent cations that due to hydration size could not compress to the area available.

Taking the diameter of a water molecule to be 2.7 Å. and assuming a sheath of water one molecule thick to be arranged about the cation with the crystalline radii given by Pauling,[11] the following areas per cation would be obtained: Li^+, 35.7 Å.^{2}; Na^+, 42.3 Å.^{2}; and K^+, 51.5 Å.^{2}.

In the bulk solution, thermal agitation does not allow a complete saturation of the sphere of water about the cation. Thus Stokes and Robinson[4] consider the water associated with the cation with an energy greater than kT. The size of the ions in the bulk would be related to the energy of hydration of the ion. However at the interface, in a layer of "soft ice,"[5] reduction in thermal energy may allow a more complete filling of the hydration region about the ion. Thus at the interface the size of the hydrated ion would be related to its actual crystalline size rather than to the energy of hydration. Figure 6 shows that the disorder in the soap monolayer decreased at areas per molecule *greater than that required for a completely filled hydration shell.*

Boyd[12] stated that hydration of the polar carboxyl groups in the monolayer gives a negative entropy contribution. The data presented in Fig. 6 suggest that increasing the area per molecule allows the orientation of water about the polar region which decreases the disorder in the soap monolayer. This did not occur in the case of the stearic acid spread on 0.1 N HCl where the interaction between the hydrocarbon groups played the major role in the structuring of the monolayer and increasing the area per molecule allowed greater disorder.

Comparison of the values for the different soaps at the same area per molecule shows that $A\Delta\pi/\Delta T$ is less for lithium than for sodium and less for sodium than for potassium. These results are consistent with a high degree of order between the head group and water which decreases in the sequence Li > Na > K. In water at 25°, the partial molal entropies according to the values listed in Gurney[13] are: Li, 4.7 e.u.; Na, 14.0 e.u.; and K, 24.2 e.u. Thus the order which exists in the soap monolayer is related to the order which exists between the water and the cations.

The results indicate that cation size is an important factor in characterizing soap monolayers, that the size is due to the hydration of the cation, and that the hydrated size in the surface region where structuring of water occurs leads to the size sequence Li < Na < K.

Acknowledgments. This work was supported by PHS Grants GM-07072-05 and NB-02067-05. We wish to thank Mr. Karl Dreher for his assistance.

(11) L. Pauling, "The Nature of the Chemical Bond," Cornell University Press, Ithaca, N. Y., 1960.

(12) G. E. Boyd, *J. Phys. Chem.*, **62**, 536 (1958).

(13) R. W. Gurney, "Ionic Processes in Solution," Dover Publications, Inc., New York, N. Y., 1962.

The Effect of Mechanically Produced Waves on the Properties of Monomolecular Layers

by Thomas W. Healy[1] and Victor K. La Mer

Department of Mineral Engineering, Columbia University, New York, New York *(Received January 27, 1964)*

Monolayers of *n*-paraffinic alcohols on water were subjected to the action of mechanically produced capillary waves, and the surface pressure–area per molecule isotherms were measured while the disturbance was present. For high amplitude capillary waves, the surface pressure behavior at pressures less than about 15 dynes cm.$^{-1}$ could be understood in terms of the increase in area due to the wave. At higher pressures, this increase in area was not sufficient to explain the isotherm for the wave-covered surface. Mechanisms relating to submergence and collapse of the monolayer are discussed, and the effect of capillary waves on the ability of monolayers to retard evaporation of water is considered.

Introduction

It is now well established that monolayers of long-chain alcohols and other surfactants can, under suitable conditions, retard the evaporation of water in the laboratory and in the field.[2] This principle has found application in field tests in the U. S. and Australia in particular, where significant savings of usable water have resulted.

The Columbia University Evaporimeter, developed by Archer and La Mer[3a] and improved by La Mer and Barnes[3b] is basically an instrument that uses the transport of water molecules as a probe to examine the properties of monolayers. This Evaporimeter is a surface balance with a desiccant assembly, suspended a few millimeters above the water surface, that records the mass of water per unit time that passes through a known area of the liquid–air interface that is either clean or covered with monolayer. The theory of this phenomenon and of the Evaporimeter have been well established in a series of experiments conducted at Columbia University by La Mer and co-workers over the past 12 years.[2]

In order to achieve reproducible results, free from the erratic disturbing effects of a current of air, and thus avoid the erroneous results which vitiate the work of earlier investigators, our investigations have been made exclusively under static conditions. It is of interest to extend these studied by introducing a mechanical vibration (*i.e.*, waves without wind)[4a,b] on the water surface and monitor the properties of the monolayer subjected to this disturbance.

A monolayer on a reservoir is subjected to continual disturbance by the action of wind. The monolayer moves laterally over a body of water as a "slick." In addition, the wind creates waves on the water surface that are either gravity waves, *i.e.*, of long wave length, or capillary waves, where the wave length is less than about 1.0 cm. The movement of slicks and the effect of gravity waves have been and are again receiving investigation.[4-6] The damping action of monomolecular layers on capillary waves (often referred to as ripples) has been investigated from the theoretical and practical point of view.[7-13] Since this investigation is oriented

(1) Department of Mineral Technology, University of California, Berkeley, Calif.

(2) V. K. La Mer, Ed., "Retardation of Evaporation," Academic Press, New York, N. Y., 1962.

(3) (a) R. J. Archer and V. K. La Mer, *J. Phys. Chem.*, **59**, 200 (1955); *Ann. N. Y. Acad. Sci.*, **58**, 807 (1954); (b) V. K. La Mer and G. T. Barnes, *Proc. Natl. Acad. Sci. U. S.*, **45**, 1274 (1959).

(4) (a) H. Lamb, "Hydrodynamics," 6th Ed., Dover, 1932; (b) on this topic, H. Lamb, *ibid.*, p. 60, has noted: "Owing to the irregular, eddying character of a wind blowing over a roughened surface, it is not easy to give more than a general explanation of the manner in which it generates and maintains waves."

(5) W. W. Mansfield, *Australian J. Appl. Sci.*, **10**, 73 (1959).

(6) I. K. H. McArthur, *Research*, **15**, 230 (1962).

(7) (a) J. T. Davies and E. K. Rideal, "Interfacial Phenomena," Academic Press, New York, N. Y., 1961, pp. 265-274; (b) J. T. Davies, *Chem. Ind.* (London), 906 (1962).

(8) W. D. Garrett and J. B. Bultman, *J. Colloid Sci.*, in press.

primarily toward the retardation of evaporation of monolayers, recourse to some of the wave-damping equations is made with minimal comment only.

The prime motivation for studying the effect of capillary wave action on evaporation suppression is that it is the capillary waves and not the gravity waves that are directly affected (*i.e.*, damped out) by the monolayer on the water surface. However, it is also important to keep in mind the interrelation between capillary and gravity waves. Capillary waves are thought to be generated by complex flow patterns either in the water or in the air, particularly in the region of the wave crests. Furthermore, the gravity waves, as they become steeper, can in fact generate a capillary wave pattern, even in the absence of wind, on the face of the gravity wave.[14] In this way, the capillary waves can play a significant role in the generation of waves by wind, in that they tend to delay the onset of breaking and therefore complete rupture of the monolayer. The fundamental importance of capillary waves on a water surface is that their formation tends to dissipate the energy of the gravity waves.

Theory of the Wave

We shall consider a section of water surface of length L cm. and breadth B cm. within which is contained a thin bar slightly less than B cm. long and oriented at right angles to the length of the water area. Let this bar oscillate in the surface at some frequency f c.p.s., and with an amplitude of a_0 cm. If the x-axis is along the length of the trough and the y-axis is at right angles to the water surface, then the oscillation is in the y–z plane. The wave profile is shown in Fig. 1.

The equation of the wave is

$$y = a_0 e^{-ux} \cos \frac{2\pi}{\lambda} x \qquad (1)$$

where u is the damping coefficient and λ is the wave length. We now require the area of the disturbed surface relative to the static surface. Let dS be the length of an element of the curve, then

$$dS = [1 + (dy/dx)^2]^{1/2} \qquad (2a)$$

$$= [{}^1/_2(dy/dx)^2 - {}^1/_8(dy/dx)^4 + {}^1/_{16}(dy/dx)^6]dx \qquad (2b)$$

$$= [1 + {}^1/_2(dy/dx)^2]dx \qquad (2c)$$

where eq. 2c is approximately true, provided $\lambda >> a$. The area of the disturbed or rippled surface, in terms of the length along the damped oscillation is S and is given by

$$S_{0\to n\lambda} = n\lambda - {}^1/_2 \int_0^{n\lambda} \left[\frac{d}{dx} \left(a_0 e^{-ux} \cos \frac{2\pi}{\lambda} x \right) \right]^2 dx \qquad (3)$$

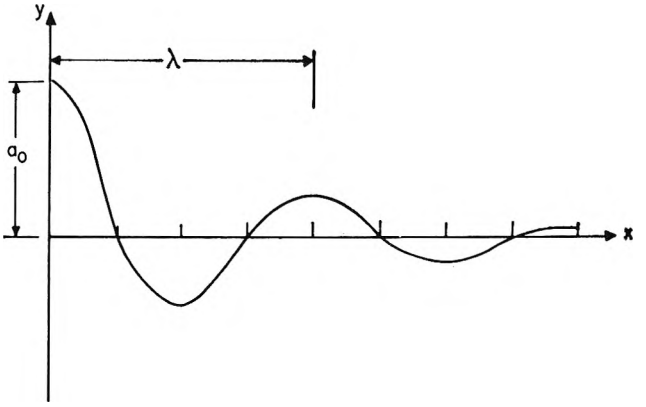

Figure 1. Schematic profile of damped oscillation of wave length, λ, in cm.

The surface pressure–area per molecule curve for the disturbed surface can be calculated from this equation and the corresponding curve for the static surface. Such a calculation involves the assumption that the decrease in surface pressure caused by the disturbance is due solely to the increased area of the rippled surface as compared to the static surface. For the present, a wave length (λ) of 0.5 cm. and an initial vibrator amplitude (a_0) of 0.0655 cm. were used for most experiments. The area of water surface onto which the disturbance was applied was 14.1 cm. × 30.0 cm. (*i.e.*, $n = 60$). For these conditions, the percentage increase in area of the disturbed surface can be expressed in terms of the damping coefficient (u). Since u is a function of the surface pressure, the increase in area at a given pressure can be calculated and the pressure–area diagram for a disturbed surface can be determined.

Experimental

Apparatus. Our Evaporimeter consists of a Langmuir trough of Pyrex glass, Wilhelmy plate assembly (the plate of roughened mica was suspended at right angles to the waves), desiccant box assembly to record the evaporation resistance of the monolayer,[2,3a] and a wave generator. The wave generator was a T-bar lying in the water surface, approximately 10 to 15 cm. from the Wilhelmy plate, which vibrated in and out with respect to this water surface. The T-bar was cemented to the voice coil of a 24-cm. speaker. The voice coil was approximately 1.9 cm. in diameter. The speaker

(9) F. C. Goodrich, *J. Phys. Chem.*, **66**, 1858 (1962).
(10) F. C. Goodrich, *Proc. Roy. Soc.* (London), **A260**, 481 (1961).
(11) R. G. Vines, *Australian J. Phys.*, **13**, 43 (1960).
(12) R. Dorrenstein, *Proc. Acad. Sci. Amsterdam*, **B54**, 260, 350 (1951).
(13) R. C. Brown, *Proc. Phys. Soc.* (London), **48**, 312, 323 (1936).
(14) M. S. Longuet-Higgins, *J. Fluid Mechanics*, **16**, 138 (1963).

was fed *via* an amplifier with a 60-c.p.s. signal from a Knight audio generator. The signal at the voice coil was monitored with a high-resistance voltmeter. The scale of the voltmeter was calibrated as described below, so as to read (in cm.) the initial amplitude of the vibrator. To calibrate the voltmeter, a small mark was made on the vertical bar of the T-bar, and the area around this mark was illuminated with stroboscopic light where the frequency of the stroboscope differed slightly from the frequency of the vibrator. The limits of motion of the mark were determined with a cathetometer. In this way, calibration curves of speaker volts *vs.* vibrator amplitude (cm.) were constructed at a number of frequencies. The apparatus and theory of the evaporation resistance technique have been described elsewhere.[2,3]

Materials. The straight-chain alcohols of 14–20 carbons were recently received, new high purity samples supplied by a manufacturer who also furnished gas chromatographs showing only one peak. The need for exceptional purity in these studies has been discussed in papers by La Mer and Aylmore,[15] and La Mer, Aylmore, and Healy.[16,17] All monolayers were spread from *n*-hexane solution in the standard manner.[3b]

Results

Figure 2 summarizes the results of surface pressure (Π)–area per molecule (A) experiments for *n*-paraffinic alcohols of 14–20 carbon atoms per chain when present as monolayers on static and disturbed surfaces. These results are for a wave of initial amplitude (a_0) of 0.0655 cm. and frequency of 60 c.p.s. A solid curve, A, is the conventional pressure–area diagram, *i.e.*, on a static surface, while the broken curve, B, represents the calculated curve for a disturbed surface assuming that the wave provides an additional area per molecule according to eq. 4. At surface pressures of 6.8, 13.8, 29.8, and 46.8 dynes cm.$^{-1}$, the corresponding damping coefficients are 0.175, 0.185, 0.23, and 0.32 from the results of Vines.[11]

In Fig. 3 is shown the effect of varying the initial amplitude of the wave. The area per molecule values of both figures refer to a static surface.

The effect of ripples on the specific resistance to evaporation is shown in Table I, where the quantities Π_s and Π_d refer to the surface pressure of monolayers on static and disturbed surfaces, while r_s and r_d refer to the specific evaporation resistance of monolayers on static and disturbed surfaces, respectively. The r_d values were calculated from the previously determined resistance–surface pressure curves of the alcohols[15,17] and from the results of Fig. 2.

Attempts to measure the evaporation resistance

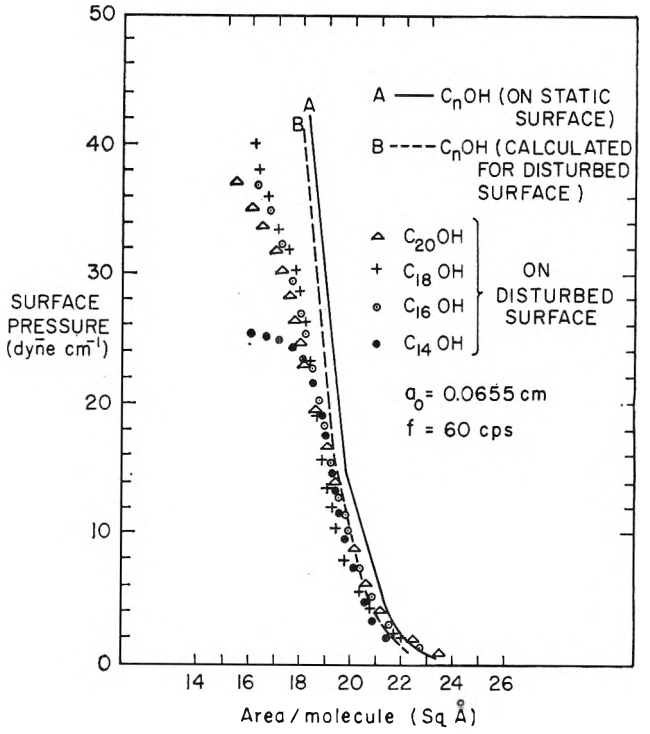

Figure 2. Surface pressure–area per molecule diagrams for pure *n*-paraffinic alcohols of from 14 to 20 carbons. Curve A is the conventional pressure–area diagram, *i.e.*, on a static surface. Curve B is the calculated pressure–area diagram assuming that the wave contributes only to increase in area. The four sets of points are the pressure–area experimental results for a disturbed surface.

while the surface was disturbed were only partially successful; a modification of the technique is required. However, preliminary results confirm the values of Table I. The important fact remains that such capillary waves as are here investigated, at pressures of the order of 30 dynes cm.$^{-1}$, reduce the evaporation resistance by the order of 25–30%.

Discussion

The present capillary ripple experiments were designed primarily to see the effect on monolayers of relatively high intensity disturbances. Previous workers had not detected any effect of the wave on the surface pressure (see, for example, the discussion following ref. 9), since the effective increase in area caused by the wave used by these investigators was negligible.

From Fig. 2 it can be seen that below about 15 dynes cm.$^{-1}$ the disturbed surface pressure–area results can be

(15) V. K. La Mer and L. A. G. Aylmore, *Proc. Natl. Acad. Sci. U. S.*, **48**, 316 (1962).

(16) V. K. La Mer, L. A. G. Aylmore, and T. W. Healy, *J. Phys. Chem.*, **67**, 2793 (1963).

(17) V. K. La Mer, L. A. G. Aylmore, and T. W. Healy, *Proc. Natl. Acad. Sci. U. S.*, in preparation.

Table I: Specific Resistance to Evaporation and Surface Pressure Value for Pure Straight-Chain Alcohol Monolayers on Static (s) and Disturbed (d) Surfaces[a]

Π_s	r_s	Π_d	r_d	Π_s	r_s	Π_d	r_d
	C_{14}				C_{16}		
12.3	0.22	7.3	0.15	7.7	0.58	5.1	0.43
19.0	0.33	11.5	0.21	14.3	0.94	10.2	0.74
28.4	0.42	17.5	0.30	26.0	1.30	15.4	0.98
38.5	0.55	21.5	0.34	34.6	1.50	20.3	1.10
Coll.[b]	..	24.4	0.37	43.0	2.0	25.4	1.22
Coll.[b]	..	25.3	0.38	Coll.[b]	..	32.3	1.40
	C_{18}				C_{20}		
8.1	1.15	4.2	0.5	5.8	2.0	4.0	1.0
15.6	1.90	8.0	1.15	15.0	4.5	11.4	3.8
31.0	2.70	15.5	1.90	28.6	6.5	16.6	4.8
40.0	3.40	23.2	2.30	36.0	7.8	19.5	5.2
Coll.[b]	..	30.3	2.70	Coll.[b]	..	24.6	5.9

[a] Units: Π, surface pressure in dynes cm.$^{-1}$; r, specific resistance to evaporation in sec. cm.$^{-1}$. [b] Collapse.

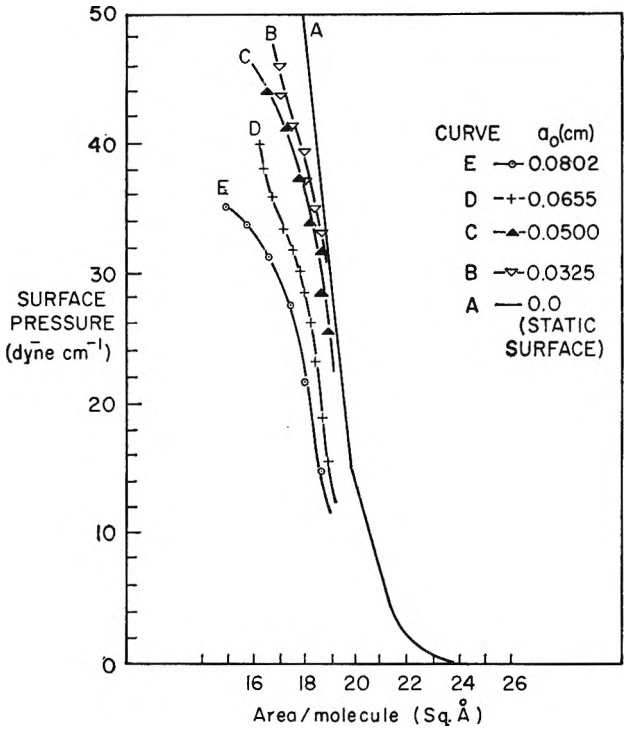

Figure 3. The effect of varying the initial amplitude of the wave on the pressure–area curves for pure octadecanol on a disturbed surface.

attributed to the increase in area associated with the rippled surface. However, above this pressure, the results for all alcohols indicate that there is a loss of alcohol from the monolayer. This may be attributed to either a *collapse-type process* in which the monolayer transforms into islands of duplex film, or to a process that we shall refer to as *submergence*, in which the film-forming molecules are transferred from the monolayer to the bulk water. This can be imagined to occur as follows: below a crest of the wave, the liquid can be thought to be a cylinder of revolution of fluid, revolving in the direction of propagation of the wave train.

This flow, together with the general stretching and compression of the monolayer, will result in surface pressure gradients being set up in the monolayer; the surfactant will not be uniformly distributed over the wave profile. Such a surface tension gradient will cause flow of molecules of the surfactant together with several layers of underlaying, partly bound water into the regions of lower pressure (Marongoni effect). It is probable that at the top and just forward of the crest there will be a region of higher surface pressure than along the portion of the wave between the crest and the trough. In this way, the flow of bulk water, interfacial water, and the flow of the monolayer molecules all tend to the point of inflection of the wave profile. It is reasonable to expect that with a sufficiently energetic wave that monolayer may be submerged at this point and carried under the surface. These effects are all maximized at this point of greatest amplitude of the capillary wave, which in the present experimental arrangement is at the wave generator. However, it must be pointed out that no breakage or turbulence was observed along the length of the T-bar lying in the water surface.

Since deviations of the surface pressure of the alcohols from curve B of Fig. 2 occur at pressures as low as 15 dynes cm.$^{-1}$, it is thought that a submergence mechanism is more appropriate than one analogous to collapse.

The pressure–area results for $C_{14}OH$ on a disturbed surface (see Fig. 2) show a distinct plateau around 26 dynes cm.$^{-1}$. Again in Fig. 3, at high initial amplitudes, the curve for $C_{18}OH$ shows a similar plateau. From the point of view of the use of such monolayers to retard evaporation of water, waves will limit the maximum attainable pressure. This loss of monolayer-forming molecules due to wave action with the accompanying reduction in surface pressure and, hence, the increase in evaporation, emphasizes the need of having excess material present in the monolayer. The grinder–duster technique described by Vines,[18] in which solid flakes of monolayer-forming material are present in the monolayer, is ideally suited to

(18) R. G. Vines in "Retardation of Evaporation," V. K. La Mer, Ed., Academic Press, New York, N. Y., 1962, p. 150.

provide immediate repair to sections of the monolayer damaged by wave action.

A final observation, which supports either the collapse or the submergence mechanism, is of interest. At all pressures below the region of the plateau, when the disturbance is removed, the static pressure is recovered. This rate of pressure recovery is an exponential curve, and successive application and removal of the disturbance show negligible hysteresis in the plot of recovery at pressure *vs.* time. In the plateau region, final approach to the static pressure after the initial rapid recovery of pressure is slow, so that successive application and removal of the disturbance is difficult to analyze.

Acknowledgment. We thank Dr. W. A. Zisman and Dr. W. D. Garrett of U. S. Naval Research Laboratories and Drs. Sylvester and Wiegel of the Civil Engineering Department of the University of California, Berkeley, Calif., for helpful discussions, and Mr. M. Jefferis for assistance in some of the experimental work.

The Effect of Solid Content on the Adsorption and Flocculation Behavior of Silica Suspensions

by Jacqueline C. Kane, Victor K. La Mer, and Henry B. Linford

Departments of Chemical and Mineral Engineering, Columbia University, New York, New York 10027
(Received February 19, 1964)

This research analyzes the authors' previously published results on flocculation in the silica–polymer system by considering both the theory of Smellie and La Mer and the modification of Healy and La Mer, which treats the adsorption phenomenon more fundamentally. The variation of P_m at decreasing solid content is explained in terms of secondary adsorption resulting from the increased time intervals between unit floc–unit floc collisions. A method for calculating b, the ratio of rate constants for the adsorption and desorption processes, and θ, the fraction of the solid surface covered, as a function of added polymer concentration, is outlined. An analysis of the deviations from the eighth power filtration law in terms of b is also presented. The basic assumption that the adsorption mechanism obeys a Langmuir-type equation has been justified. Preliminary calculations are included to indicate the geometrical dimensions that exist when flocculation occurs in the silica–polymer system.

Introduction

In 1958, Smellie and La Mer[1] published a quantitative theory of filtration of suspensions flocculated by high polymers. This theory was later modified by Healy and La Mer,[2] who interpreted the mechanism of the adsorption of high polymers by the substrate more fundamentally. They introduced the concept that a fraction of the total number of polymer segments interacted with a certain fraction of the active sites on the surface of the solid substrate and thus improved the picture of simple Langmuirian adsorption.

Since this approach does not affect the original theory in respect to either the kinetics of flocculation or the filtration mechanism, we compare the equations in the two theories for the purpose of interpreting the

(1) R. H. Smellie, Jr., and V. K. La Mer, *J. Colloid Sci.*, 13, 589 (1958).

(2) T. W. Healy and V. K. La Mer, *J. Phys. Chem.*, 66, 1835 (1962).

previously published data of Kane, La Mer, and Linford.[3]

Theoretical

In their treatment of the adsorption process, Smellie and La Mer[1] proposed that the equilibrium polymer concentration could be represented by

$$P = P_0 - k_{SL}W\theta \quad (1)$$

where P was the equilibrium polymer concentration, P_0 the initial polymer concentration, W the solid content, θ the fraction of surface covered, and k_{SL} the constant used by Smellie and La Mer dependent upon the fineness of grinding or specific surface area of the solid. In our previously published research on silica,[3] the pertinent quantities were expressed as

$$P \text{ and } P_0 = \frac{\text{g. of polymer}}{\text{g. of water}} \times 10^{-6}$$

$$W = \frac{\text{g. of solid}}{\text{g. of water}} \times 10^{-2}$$

$$k_{SL} = \frac{\text{g. of polymer adsorbed}}{\text{g. of solid}} \times 10^{-4}$$

(θ is dimensionless extending from 0 to 1)

Smellie and La Mer assumed that the adsorption process could be represented by an isotherm of the Langmuir type

$$\theta = \frac{bP}{1 + bP} \quad (2)$$

where b, as a first approximation and by analogy with the original derivation, is proportional to the ratio of the forward to reverse reaction rate constants for adsorption. Combining eq. 1 and 2 yields

$$\theta = \frac{b(P_0 - k_{SL}W\theta)}{1 + b(P_0 - k_{SL}W\theta)} \quad (3)$$

By employing the geometry involved in the limiting form of the Kozeny–Carman filtration equation, together with basic area and volume relationships, Smellie and La Mer derived the expression

$$Q - Q_0 = \frac{Q_0}{R_0^2} K^2W^4\theta^4(1 - \theta)^4 \quad (4)$$

Here Q and Q_0 are the refiltration rates with and without polymer, respectively, R_0 is the radius of a primary particle, K is a constant, and W and θ are defined above.

Rearranging and combining eq. 3 and 4 yields

$$\frac{P_0^{1/4}}{(Q - Q_0)^{1/4}} = A + BP_0 \quad (5)$$

or in a logarithmic form

$$\ln (P_0^4)/(Q - Q_0) = 8 \ln B + 8 \ln (P_m + P_0) \quad (5A)$$

Differentiating and setting the derivative equal to zero to correspond to an optimum gives

$$P_0 \text{ (optimum)} = P_m = \frac{(1 + bk_{SL}W)^2}{b} = \frac{1}{b} + 2k_{SL}W + bk_{SL}^2W^2 \quad (6)$$

For details of this derivation, the reader should consult ref. 1.

Healy and La Mer[2] proposed that when a polymer molecule concentrated at a solid–liquid interface, only β-segments per average polymer molecule adsorbed and covered surface sites, with the remainder of the molecule protruding into the surrounding medium as extended segments. It should be emphasized that these β-segments need not occupy β consecutive sites on the surface. In fact, it is most probable that loops of extended segments separate the adsorbed segments from each other, such that they can be treated as separate "small molecules," independent of other adsorbed segments along the polymer molecule.[4]

By introducing the parameter β in the original derivation of Smellie and La Mer, Healy and La Mer obtained

$$\beta(P_0 - P)N/sS_0 = \theta \quad (1A)$$

where

$$P = P_0 - k_H\theta/\beta \quad (1B)$$

and

$$k_H = sS_0/N \quad (1C)$$

In these equations, s is the number of sites per unit area of surface, S_0 is the total surface area of solid, N is Avogadro's number, P and P_0 are expressed in moles of polymer, and θ is again dimensionless. The subscript H refers to the constant of the Healy modification.

Reconciliation of the Theories. Since the two approaches are not mutually exclusive, an expression for k_{SL} in terms of k_H can be obtained by equating eq. 1 and 1B and dividing by θ.

(3) J. C. Kane, V. K. La Mer, and H. B. Linford, *J. Phys. Chem.*, 67, 1977 (1963).

(4) T. W. Healy, Ph.D. Dissertation, Columbia University, 1963.

$$\frac{k_{SL}W}{M} = \frac{(P_0 - P)}{\theta} = \frac{k_H}{\beta} \quad (7)$$

Since k_{SL} was expressed in weight units while k_H was in molar units, the molecular weight of polymer, M, has been included. Substituting for k_H from eq. 1C

$$k_{SL} = \frac{sS_0M}{N\beta W} \quad (8)$$

If the suspended particles are assumed to be spherical, and the density of the solid is ρ_s, then the surface area of the solid is

$$S_0 = 3W/R_0\rho_s \quad (9)$$

and eq. 8 becomes

$$k_{SL} = \frac{3sM/R_0\rho_sN}{\beta} \quad (10)$$

For dimensional consistency, it must be assumed that a surface site is equal in area to a polymer segment.[5]

Calculations of Values of θ and b. By definition, the optimum polymer concentration, P_m, is that concentration of polymer which maximizes the refiltration rate. From eq. 4, however, it is obvious that the refiltration rate can be a maximum only when the expression $\theta^4(1 - \theta)^4$ has its largest value. This occurs at $\theta = 0.5$. Figure 1 illustrates the functional dependence of $\theta(1 - \theta)$, the modifier of the Smoluchowski *coagulation* equation necessary to convert it into the Smellie and La Mer flocculation equation, upon the fraction of the surface covered. $\theta^2(1 - \theta)^2$, a quantity proportional to the floc size, and $\theta^4(1 - \theta)^4$, a quantity proportional to the rate of filtration, are also included. The importance of these quantities in interpreting flocculation and filtration has been emphasized recently by La Mer.[6]

Substituting $\theta = 0.5$ into eq. 4 produces

$$(Q - Q_0)_{max} = C/256 \quad (11)$$

where

$$C = \frac{Q_0}{R_0^2} K^2W^4 \quad (12)$$

Obviously, C becomes a known quantity once the maximum filtration improvement is determined. Subsequently, C can be used to evaluate the fraction of surface covered, θ, at refiltration rate improvement values, $(Q - Q_0)$ other than the maximum.

Equation 6 predicts a parabolic dependence of the optimum polymer concentration on the solid content; this has been verified experimentally for many flocculated clay–polymer systems. However, our recent experimental results[3] have shown that, for *silica dispersions* flocculated by various high polymers, the relationship is linear. These findings indicate that, for silica, the third term of eq. 6 is negligible in comparison to the terms $1/b$ and $2k_{SL}W$. Hence, for this system, the optimum polymer concentration can be expressed simply as

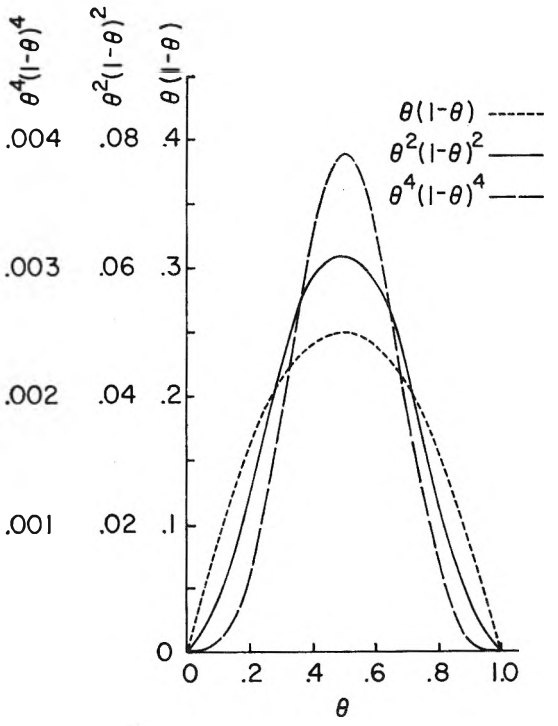

Figure 1. Variation of $\theta(1 - \theta)$, $\theta^2(1 - \theta)^2$, and $\theta^4(1 - \theta)^4$ with θ, the fraction of solid surface covered.

$$P_m = 1/b + 2k_{SL}W \quad (13)$$

where the slope of a plot of P_m *vs.* W is $2k_{SL}$. For more quantitative information about these plots, the reader should consult ref. 3.

Once both θ and k_{SL} are known, and since W and P are arbitrarily predetermined quantities, eq. 3 can be solved directly for b, *i.e.*

$$b = \frac{\theta}{(P_0 - k_{SL}W\theta)(1 - \theta)} \quad (14)$$

which combined with eq. 1 recovers the familiar form of the Langmuir equation

$$bP = \frac{\theta}{1 - \theta} \quad (15)$$

(5) R. Simha, H. Frisch, and F. Eirich, *J. Phys. Chem.*, **57**, 584 (1953).

(6) V. K. La Mer and T. W. Healy, *ibid.*, **67**, 2417 (1963).

Experimental

A detailed explanation of the experimental procedure, equipment, and materials employed in obtaining the data used in this paper has been published previously.[3] As in the earlier work the pH was held constant between values of 5.5 and 6.0.

Results and Discussion

The values of b calculated by eq. 14 appeared to be constant, within experimental limits, over a centrally located range of P_0 values. In all cases, this range corresponded to the linear portion of the s-shaped curves which typified the Smellie and La Mer plots of eq. 5 and 5A. Decreasing b values accompanied deviations which were *concave downward*, while increasing values of b produced *positive* deviations from linearity. See Fig. 4 of ref. 3. It was also noted that for flocculation of systems of different solid contents by a given polymer, the product bW, based on an average of the constant b values, was reasonably constant.

Furthermore, the magnitude of b increased with increasing molecular weight. Healy[4] demonstrated that for the calcium phosphate–polyacrylamide system, b has an optimum with respect to molecular weight. If these findings apply to other solid–polyacrylamide systems, then the optimum molecular weight of polyacrylamide for the silica system must be greater than 10 million.

On the average, the values of fractional surface coverage, θ, obtained by the calculations outlined above, ranged from 0.30 to 0.80. For example, see Fig. 2.

Figure 3 demonstrates graphically that the assumption of a Langmuirian-type adsorption is valid throughout a central range of surface coverage. The circled points are the result of plotting θ against the equilibrium polymer concentration calculated from the Smellie–La Mer theory, $P = P_0 - k_{SL}W\theta$. *This method of proof is valid since* P_0, k_{SL}, *and* W *were all determined experimentally*, and reference to the theoretical discussion will reassure the reader that the calculations of θ were accomplished without recourse to the assumption of Langmuirian adsorption.

The solid curve of Fig. 3 is a plot of the equilibrium polymer concentration obtained directly from a Langmuir-type equation, $P = \theta/b(1 - \theta)$, as a function of the fractional surface coverage, θ. The value of b used corresponded to an average of the b values of those points which comprised the linear portion of the eighth power Smellie–La Mer plots.

According to eq. 13, if P_m is linear with respect to W, then a plot of k_{SL} *vs.* W should be a horizontal straight line, independent of dilution. This has been verified experimentally for Jaguar + and ET-494, for Superfloc 16 above 2.5 g. of silica/100 g. of water, and for PAM 3 above 4 g. of silica/100 g. of water. See Fig. 4. As expected from the results of Healy[4] for the polyacrylamides, P_m decreased with increasing molecular weight at a given solid content.

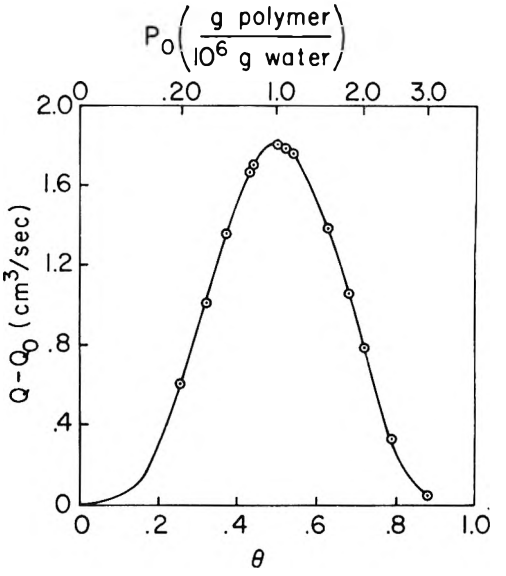

Figure 2. Typical plot of refiltration rate improvement as a function of the fraction of solid surface covered, θ, and the added polymer, P_0. Results are for ET-494 with 0.5 g. of silica/100 g. of water.

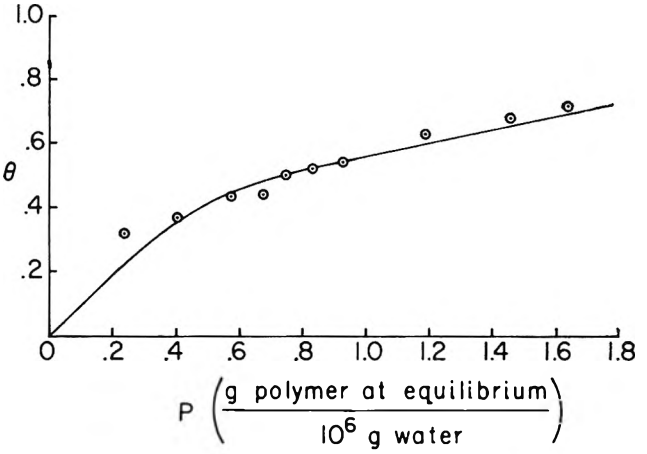

Figure 3. Langmuirian-type plot. Data of ET-494 with 0.5 g. of silica/100 g. of water.

Equation 10 can thus be written as

$$k_{SL} = J/\beta \tag{16}$$

where

$$J = 3sM/R_0\rho_s N \tag{17}$$

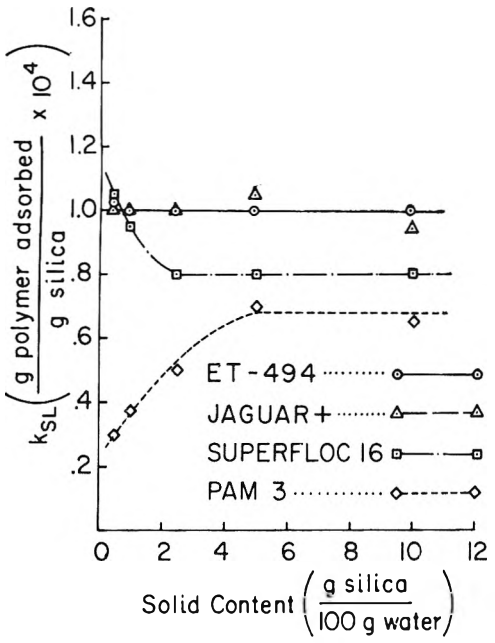

Figure 4. Variation of k_{SL} with solid content. Suspensions of different solid contents were prepared by mixing 5 g. of silica with various volumes of water.

As before, β is the number of segments of a polymer molecule adsorbed at the solid surface (the remainder, the greater part of each adsorbed molecule, extends into the surroundings) and represents an *average* value which can change by either molecular or segment adsorption. Obviously, J should be constant for any determination made using the same solid, suspension medium, polymer, and total weight of solids. Hence, for any system which obeys eq. 13, variations in k_{SL} must be attributed to a variation in β with decreasing solid content. The authors postulate the following types of behavior as the dilution is increased, keeping in mind that at high solid contents, and especially for high molecular weight polymers, the crowded environment may slow the adsorption of polymer molecules and consequent production of extended segments.

1. β Is Constant. This is the behavior of low molecular weight polymers which are completely adsorbed even at high dilution or which lack the chain flexibility necessary to change β by the adsorption of extended segments.

2. β Decreases. This is the behavior exhibited by polymers of intermediate molecular weight. Since, in this case, the extended segments of the polymer molecule are fairly short, adsorption will be continued by new molecules attaching at only a few segments to give a β decrease based on the number of adsorbed segments per *average* molecule.

3. β Increases. This is the behavior of high molecular weight polymers and in this case proceeds *via* a different mechanism. The long extended segments of the polymer molecule are favorably situated for a "wrap-around" type of adsorption which increases the number of adsorbed segments per average molecule.

This interpretation implies that at high dilution (<3 g. of solid/100 g. of water) the time interval between successive particle–particle collisions is greater than that necessary for secondary (continued) adsorption. In dilute suspensions then, adsorption will continue and flocculation will be slow with large flocs resulting. In concentrated suspensions, on the other hand, the rate of the flocculation reaction will be fast, continued adsorption will be slow, and the average floc size will be smaller. These two cases are illustrated schematically below where P and S are the polymer and solid, respectively.

$$P + S \rightleftharpoons PS_1 \overset{②}{\rightleftharpoons} PS_2$$

$$① \Downarrow \qquad \Downarrow ③$$

$$(PS)_{nR_1} \qquad (PS)_{nR_2}$$

Here PS_1 and PS_2 are, in the terminology of Healy,[7] unit flocs (single colloidal particles with molecules of polymer adsorbed), PS_2 resulting from the secondary adsorption of polymer on PS_1 *via* one of the mechanisms listed above. $(PS)_{nR_1}$ and $(PS)_{nR_2}$ are each macroflocs resulting from the bridging action of the polymer molecules between adjacent unit flocs of PS_1 or adjacent PS_2 flocs. Reaction 1 occurs if the solid content is high producing a floc of radius R_1, while reactions 2 and 3 proceed in dilute suspensions producing a floc of radius R_2, where R_1 is less than R_2. Qualitatively, we theorize that there will be a definite solid content at which the time necessary for reaction 2 to proceed will be less than that for reaction 1.

That the floc radius is indeed a function of the solid content can best be demonstrated by reference to eq. 4. Experimentally, it has been found that $(Q - Q_0)/Q_0$ varies by a factor of less than 2 when W^4 changes by 1.6×10^5 for a constant value of θ. Hence, K^2 must vary inversely with W^4 when R_0^2 and θ are constant. Since $K = Zk_1/k_2$ where Z is the proportionality constant between the number of particles and the solid content, k_1 is the rate constant of the floc formation, and k_2 is the deflocculation rate constant, and since $(Q - Q_0)/Q_0$ varies only slightly with W^4, then K, and hence the ratio k_1/k_2, must decrease with increasing W. Furthermore, k_1/k_2 is proportional to

(7) T. W. Healy and V. K. La Mer, *J. Colloid Sci.*, 19, 323 (1964).

Table I: Physical Characteristics of the Various Silica Suspensions

Solid content, g. of silica/ 100 g. of water	10^{-6} particles/ cm.^{3a}	Particulate length, l, μ	Mean free path, L, μ	Polymer molecules available/silica particle at P_m			
				Superfloc 16 mol. wt. = 4,000,000	PAM 3 mol. wt. = >10,000,000	ET-494 mol. wt. = 50,000	JAG+ mol. wt. = 200,000
10	9.1	48	88	2.66×10^5	8.60×10^4	2.69×10^7	6.31×10^6
5	4.6	60	175	2.66×10^5	9.27×10^4	2.60×10^7	6.98×10^6
2.5	2.3	76	350	2.66×10^5	6.60×10^4	2.60×10^7	6.65×10^6
1	0.91	103	878	3.15×10^5	4.97×10^4	2.60×10^7	6.65×10^6
0.5	0.46	130	1750	3.49×10^6	3.97×10^4	2.60×10^7	6.65×10^6
Extended length of polymer[b]				11.2 μ	28.2 μ	0.35 μ	0.25 μ

[a] The specific gravity of silica was taken as 2.65 g./cm.^{3}. [b] Extended length calculations were based on the nominal molecular weights listed in the headings of the table. Recent viscosity measurements by Healy on PAM 3, however, indicate that the actual molecular weight and hence the extended length of this polymer may be as much as four times as great as the nominal.

the radius of the floc, *i.e.*, $R = (k_1/k_2)n_0^2\theta^2(1-\theta)^2$; thus the decrease in the extent of flocculation, k_1/k_2, with increasing solid content is reflected in a smaller floc radius.

We are aware that we have not presented a quantitative explanation of the variation of β below solid contents of 3 g. of silica/100 g. of water. However, elementary calculations based on an average particle diameter of 20 μ do shed some light on the actual geometrical dimensions of the suspension. The following assumptions have been employed. (1) Due to coiling, the C–C, C–O, and C–N bond lengths can be taken as 1 Å. (2) A particle occupies a cubic particulate volume of particulate length l. (3) Mean free path length equations from kinetic theory can be applied. Table I summarizes the calculations.[8]

Acknowledgment. The authors wish to acknowledge the assistance of Dr. T. W. Healy, whose suggestions and ideas were most helpful in the preparation of this paper. The research has been supported by U. S. Public Health Service Grants RG-8389 and WP-00240-02.

(8) NOTE ADDED IN PROOF.—It is worthy of note that the values of k_{BL} in Fig. 4 are, at least, roughly proportional to the calculated values of the extended length of polymers in harmony with the basic concept of the bridging mechanism of flocculation by high polymers.

Adsorption at the Solid–Liquid Interface. II. Alcohols on Rutile from Solutions in *p*-Xylene

by G. D. Parfitt and I. J. Wiltshire

Department of Chemistry, University of Nottingham, Nottingham, England *(Received June 26, 1964)*

The adsorption by a pure rutile of alternate members of the homologous series of aliphatic straight-chain primary alcohols (ethanol to octadecanol) from solutions in *p*-xylene has been studied at 25°. The amount of each alcohol adsorbed at low relative concentrations reached a minimum value at hexanol and octanol, indicating the importance of solute–solvent interactions to the adsorption at the solid–liquid interface. Adsorbed water on the rutile surface caused a significant reduction in the extent of adsorption.

Introduction

From the significant amount of data that have been reported on adsorption at the solid–liquid interface, it is clear that the process is complicated by a large number of factors. Both adsorbate–adsorbent interactions and those between the components in solution, as well as the surface structure of the adsorbent, are important in determining the extent of adsorption. Furthermore, adsorption from nonpolar media onto polar surfaces is affected by the amount of water present in the system.[1]

The present paper is concerned with the adsorption by a pure rutile of alternate members of the homologous series of aliphatic straight-chain primary alcohols (ethanol to octadecanol) from solutions in *p*-xylene at 25°. Ethanol to dodecanol inclusive form binary liquid mixtures with *p*-xylene at 25° over the entire range of mole fraction, whereas for the remainder, the range of concentration available for adsorption studies is restricted by solubility.

Experimental

Materials. Two samples of pure rutile (>99.9%), supplied by British Titan Products Co. Ltd., of Billingham, County Durham, were prepared by hydrolysis of purified titanium tetrachloride and the product calcined at about 400°. Surface areas of 24.4 and 21.0 $m.^2 g.^{-1}$ were determined by the B.E.T. method using nitrogen at −195°. In the adsorption experiments, the sample of area 24.4 $m.^2 g.^{-1}$ was used with ethanol to octanol, respectively, and the other sample with the remaining alcohols. Before use, the rutile samples were outgassed to an ultimate pressure of 10^{-6} mm. and twice treated with spectroscopic oxygen at a pressure of about 10 cm. for 30 min., the residual oxygen being pumped off after each treatment. The temperature of the sample was maintained at 400° throughout and a liquid nitrogen trap isolated the sample from stopcock grease. The gray coloration in the samples outgassed at 400° was irreversibly removed by the oxygen treatment. This activation procedure is similar to that used by Hollabaugh and Chessick.[2]

p-Xylene (B.D.H. Ltd.) was distilled from phosphorus pentoxide and the fraction boiling at 139° was collected. From Karl Fischer measurements the *p*-xylene was found to contain 0.005% by weight of water.

Absolute commercial alcohol was refluxed with silver nitrate, distilled, and allowed to stand over calcium sulfate, finally distilled, and the fraction boiling at 78.5° collected. *n*-Butyl alcohol (B.D.H. Ltd.) was left to stand over molecular sieves Type 4A for 2 days, decanted, and distilled, the fraction boiling at 119° being collected. The remainder of the alcohols were Puriss grade from Fluka of Switzerland and were used as supplied. From analysis by g.l.c., infrared, and n.m.r. spectroscopy, all the alcohols were found to be of very high purity.

(1) W. Hirst and J. K. Lancaster, *Trans. Faraday Soc.*, **47**, 315 (1951).

(2) C. M. Hollabaugh and J. J. Chessick, *J. Phys. Chem.*, **65**, 109 (1961).

Procedure. In the majority of the adsorption experiments, samples of rutile after oxygen treatment (*ca.* 1 g.) and solution (*ca.* 5 g. made up by weight) were weighed into clean dry Pyrex adsorption tubes, which were then sealed by fusion and rotated in a water thermostat at 25.0 ± 0.2° for at least 12 hr., although adsorption equilibrium was found to be established in a shorter time. The tubes were then centrifuged at 2500 r.p.m. for 10 min. and returned to the thermostat before removing the clear supernatant liquid for analysis. The solutions were analyzed using a differential refractometer of the type designed by Brice and Halwer[3] with a cell obtained from the Phoenix Instrument Co. of Philadelphia, Pa. The original and equilibrium solutions were placed in the two compartments of the cell and the concentration of the unknown was found from a calibration using known solutions of concentration in the range under examination.

In the experiments carried out under very dry conditions using octanol and octadecanol as adsorbates, each sample of treated rutile in an evacuated thin-walled Pyrex bulb (similar to those used for heat of immersion experiments) was placed in an adsorption tube containing a known weight of the alcohol, which was then sealed to a vacuum apparatus. A tube containing a known weight of *p*-xylene over degassed rutile, used as a "getter" for water (previously filled and allowed to stand in a drybox), was attached to the apparatus, the contents of both tubes were frozen, and the apparatus then pumped down to 10^{-2} mm. The *p*-xylene was cold-distilled into the adsorption tube which was then sealed off under vacuum and the bulb was broken under the solution by ultrasonics.

The calorimeter used to measure heats of immersion consisted of a silvered dewar flask (capacity 350 ml.) fitted with a B55 Quickfit joint and included a heater, stirrer, sample holder and breaker, and a "Stantel" thermistor (resistance 1800 ohms and temperature coefficient 56 ohms/deg. at 20°) for temperature measurement. Resistance changes in the thermistor were measured using a Cambridge vernier potentiometer and a Tinsley Type V.S. 645 galvanometer, and the accuracy of temperature measurement was $\pm 1 \times 10^{-4}$°. The calorimeter was immersed in an oil thermostat at 25.0 ± 0.005°. Sample bulbs were blown from Pyrex glass and an average value of 0.150 cal. for the heat of bulb breaking was used to correct the measured heats of immersion.

Results and Discussion

The following heat of immersion values were obtained for samples of the activated rutile (three to five measurements in each case): (a) in water, 626 ± 13 ergs cm.$^{-2}$, (b) after exposure to the atmosphere, in water 282 ± 6 ergs cm.$^{-2}$, (c) in dry *p*-xylene over "getter," 131 ± 13 ergs cm.$^{-2}$, (d) in dry *p*-xylene after exposure of the xylene to the atmosphere, 166 ± 16 ergs cm.$^{-2}$, (e) in *p*-xylene saturated with water, 257 ± 12 ergs cm.$^{-2}$. The large difference between (a) and (b) is presumably the result of adsorption of water vapor from the atmosphere onto the activated rutile. Only a small increase in the heat of immersion in *p*-xylene resulted from exposure of the liquid to the atmosphere.

For adsorption from a two-component system the composite isotherm obeys the relation

$$n_0\Delta x/m = n_1^s(1 - x) - n_2^s x \qquad (1)$$

where Δx is the decrease in mole fraction of component 1 when n_0 moles of original solution are brought into contact with m grams of adsorbent, and n_1^s and n_2^s are the numbers of moles of components 1 and 2, respectively, which are adsorbed per gram of solid. To calculate the individual isotherms for the two components, it is usual[4] to assume that the adsorbed layer is one molecule thick as expressed in the relation

$$n_1^s/(n_1^s)_m + n_2^s/(n_2^s)_m = 1 \qquad (2)$$

where $(n_1^s)_m$ and $(n_2^s)_m$ are the corresponding numbers of moles required to cover 1 g. of adsorbent to the extent of a monolayer. Choice of values for $(n_1^s)_m$ and $(n_2^s)_m$ is often difficult, although where adsorption measurements from the vapor phase are possible, monolayer values derived from vapor isotherms have been used successfully[5] with the assumption that the molecules adopt the same orientation at both the solid–liquid and solid–vapor interfaces. With less volatile adsorbates, cross-sectional areas based on molecular models are usually used assuming a specific orientation at the surface and close-packing of the molecules. However, in the case of polar molecules adsorbed on a crystalline polar surface it is probable that localized adsorption occurs over specific sites which may not correspond to a close-packed monolayer.

In this work it has been assumed that *p*-xylene molecules are adsorbed with their major axis parallel to the surface of the adsorbent and an area of 45 Å.^{2} from a molecular model used in the calculation of $(n_2^s)_m$. The choice of an area for an adsorbed alcohol molecule has been based on the octadecanol composite isotherms as shown in Fig. 1. Since the octadecanol solutions are very dilute, eq. 1 reduces to $n_0\Delta x/m \sim n_1^s$ and the composite isotherm may therefore be taken as equiva-

(3) B. A. Brice and M. Halwer, *J. Opt. Soc. Am.*, **41**, 1033 (1951).
(4) G. D. Parfitt and E. Willis, *J. Phys. Chem.*, **68**, 1780 (1964).
(5) C. G. Gasser and J. J. Kipling, *ibid.*, **64**, 710 (1960).

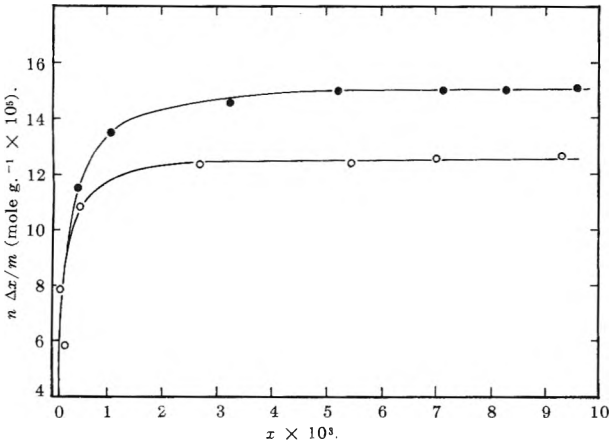

Figure 1. Composite isotherms for adsorption of octadecanol on rutile from p-xylene solutions: O, under normal conditions; ●, under dry conditions. Saturation mole fraction of octadecanol in p-xylene, 16×10^{-3}.

lent to the individual isotherm for the solute. The lower curve was obtained with samples of rutile which had been handled in the atmosphere after oxygen treatment, as was the case in the majority of the experiments reported here (called normal conditions), while the upper curve corresponds to the very dry conditions in which the bulbs containing the activated samples were broken under the solution.

At maximum coverage the areas occupied by an adsorbed octadecanol molecule, based on the B.E.T. area of 21.0 m.^{2} g.$^{-1}$, are 23.2 and 28.2 Å.^{2} in the dry and normal cases, respectively. We are inclined to the view that the 23.2 Å.^{2} per molecule represents the closest possible packing of the adsorbed molecules corresponding to localized adsorption over specific sites. Hollabaugh and Chessick[2] have suggested that the surface of rutile after outgassing at high temperature consists of Ti–O–Ti linkages and Ti–OH groups. From vapor adsorption isotherms for water and n-propyl alcohol, indicating both chemical and physical adsorption, they propose mechanisms which associate each adsorbed molecule with two titanium sites, either by reaction with a Ti–O–Ti group or localization over two Ti–OH in the case of physical adsorption. On this basis, an area of 11.4 Å.^{2} per Ti site was obtained using the B.E.T. area and the number of Ti–OH groups on a fully hydroxylated surface as determined from water vapor adsorption data. Such good agreement with our value of 23.2 Å.^{2} would make it seem reasonable to associate each octadecanol molecule with two Ti sites on the dry surface. Hollabaugh and Chessick, however, found a rather larger area of 26.6 Å.^{2} per n-propyl alcohol molecule in the monolayer from their

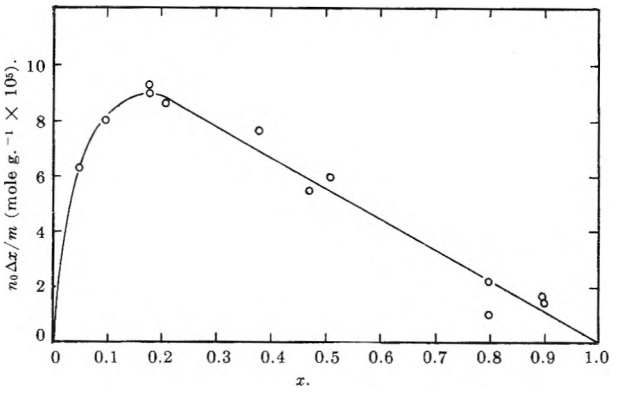

Figure 2a. Composite isotherm for adsorption of ethanol.

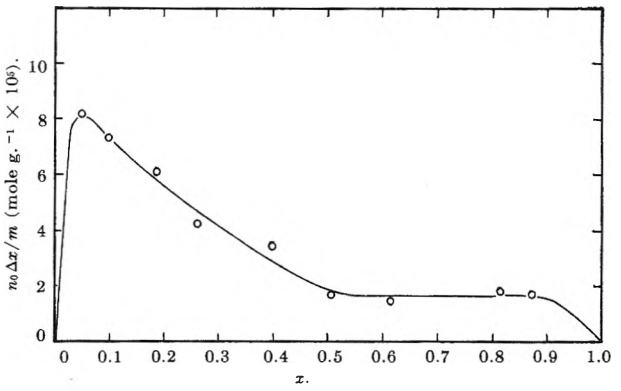

Figure 2b. Composite isotherm for adsorption of octanol.

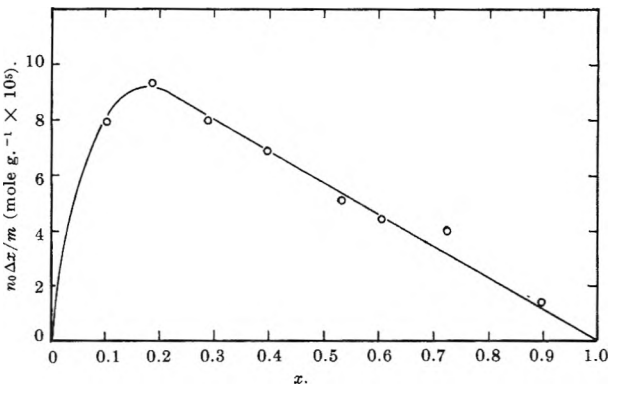

Figure 2c. Composite isotherm for adsorption of dodecanol.

vapor adsorption data. The reason for the discrepancy is not apparent.

On exposure of the activated rutile to the atmosphere, both chemisorption and physical adsorption of water molecules are likely to occur and the higher area per adsorbed octadecanol molecule is assumed to result from part of the fully hydroxylated surface being covered by physically adsorbed water. Comparison of our heat of immersion data with those of Hollabaugh

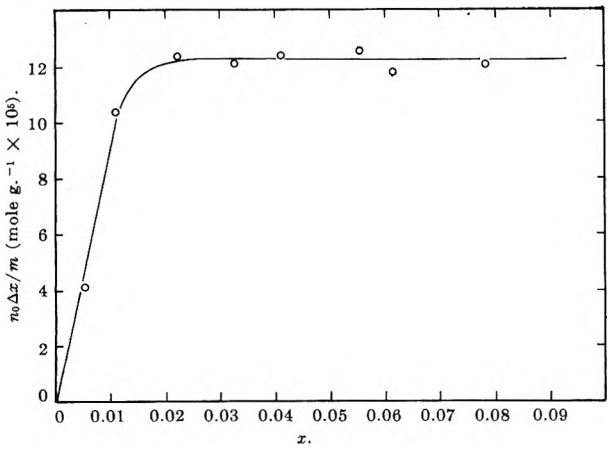

Figure 2d. Composite isotherm for adsorption of hexadecanol. Saturation mole fraction of hexadecanol in *p*-xylene, 0.11.

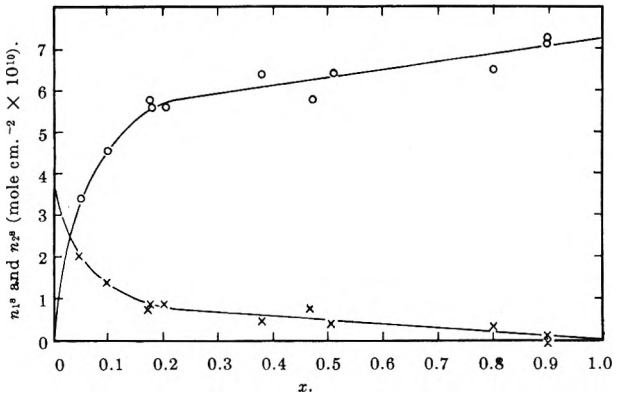

Figure 3a. Individual isotherms for adsorption of *p*-xylene (×) and ethanol (○).

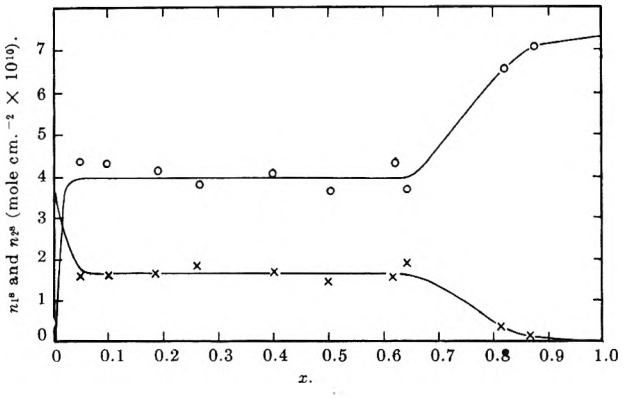

Figure 3b. Individual isotherms for adsorption of *p*-xylene (×) and octanol (○).

and Chessick would appear to confirm this view. The area of the surface which is available for adsorption of the two components in solution is therefore less for the normal than for the dry surface. Since eq. 2 assumes the adsorbed layer to be one molecule thick, it seems justifiable to use the lower surface area for the calculation of $(n_1^s)_m$ and $(n_2^s)_m$, assuming an area occupied by a physically adsorbed alcohol molecule of 23.2 Å.^{2}. On this basis, the area covered by octadecanol molecules at saturation in the normal case is 17.2 m.^{2} g.$^{-1}$ and the corresponding values of $(n_1^s)_m$ and $(n_2^s)_m$ have been used in the calculation of the individual isotherms, with the appropriate correction for the higher (B.E.T.) area sample used with ethanol to octanol, inclusive.

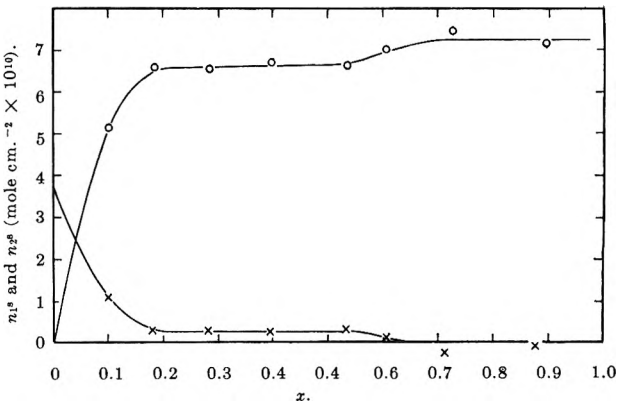

Figure 3c. Individual isotherms for adsorption of *p*-xylene (×) and dodecanol (○).

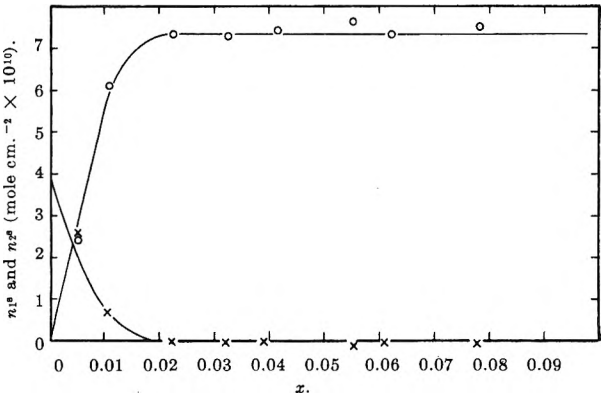

Figure 3d. Individual isotherms for adsorption of *p*-xylene (×) and hexadecanol (○).

The composite isotherms for the adsorption of ethanol, octanol, dodecanol, and hexadecanol onto rutile, which had been exposed to the atmosphere after oxygen treatment, are shown in Fig. 2, and the corresponding individual isotherms are shown in Fig. 3. Those for the remaining alcohols show intermediate behavior and have been omitted to save space.

The composite isotherms for the alcohols up to dodecanol show long linear portions which, under certain conditions,[6] would correspond to an adsorbed layer of

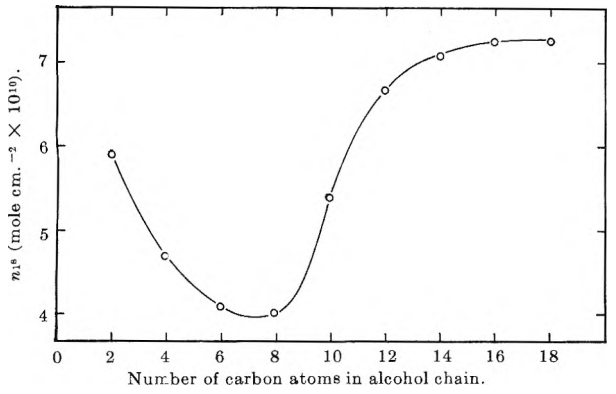

Figure 4. Adsorption of alcohol as a function of chain length at a 0.3 equilibrium mole fraction of alcohol in solution.

constant composition over a large concentration range. This occurs with butanol to dodecanol inclusive, the range of concentration over which the adsorbed layer shows constant composition decreasing with increasing chain length. It is perhaps surprising that this situation arises in the case of physical adsorption of alcohols on rutile when, purely on thermodynamic grounds, an increase in adsorption with concentration would be anticipated. Similar results were observed in the adsorption of a series of alkylbenzenes onto Graphon from solutions in *n*-heptane reported in part I of this series.[4] No adequate explanation has yet been proposed to account for this behavior.

The most striking results of this work is the variation of alcohol adsorption with chain length. At the lower end of the concentration range the amount of alcohol adsorbed at equilibrium mole fractions corresponding to the flat portions of the individual isotherms decreases from ethanol to hexanol and octanol and then increases up to the saturation value found with the long-chain alcohols. This effect is shown in Fig. 4 and clearly indicates the importance of solution interactions to the adsorption at the solid–liquid interface. At present the appropriate thermodynamic data are not available for these systems but it is of interest that the molar volumes of hexanol and *p*-xylene are similar, suggesting that a mixture of the two might represent the most ideal of all the alcohol–xylene mixtures used in this work. With the alkylbenzenes[4] no such minimum was observed, the adsorption of the alkyl benzene increasing with chain length.

Although adsorption experiments under dry conditions have been carried out with only one of the lower alcohols, namely octanol, it is particularly significant that in this case the amount adsorbed reaches saturation at a mole fraction in the region 0.2–0.3 suggesting much stronger solute–adsorbent interactions on the partially hydroxylated rutile, reducing the effect due to solution properties. Another possibility is that trace water in the solutions might contribute to the minimum. Further work on these aspects is in progress.

Acknowledgments. The authors are grateful to British Titan Products Co. Ltd. for preparing the samples of pure rutile and to Shell Research Ltd. for a grant to I. J. W.

(6) P. V. Cornford, J. J. Kipling, and E. H. M. Wright, *Trans. Faraday Soc.*, 58, 1 (1962).

Some Factors Influencing a High Energy Adsorption of Polar Molecules from Hydrocarbons onto a Solid Surface

by P. T. Dawson, G. T. Rich, and D. A. Haydon

Department of Colloid Science, University of Cambridge, Cambridge, England *(Received March 26, 1964)*

A study has been made of the adsorption of formic acid from benzene and of stearic acid and stearyl alcohol from benzene and aliphatic hydrocarbons onto three different specimens of rigorously dried pure rutile. The rutile was well characterized as to surface area, particle size, and pore distribution by electron microscopy and gas phase adsorption of nitrogen and formic acid. The nitrogen results indicated that the samples had porous structures arising from the void volume between aggregated particles. Vapor phase adsorption of formic acid showed a high energy (~80% irreversible) adsorption onto lattice points, giving monolayer coverages effectively the same in all specimens. From benzene, identical coverages were obtained, showing that the solvent did not effectively compete for sites. However, stearic acid and stearyl alcohol from benzene and aliphatic hydrocarbon, although giving an adsorption similar to each other, gave coverages smaller than those of formic acid, and which were smaller the smaller the particle size of the adsorbent. Results on adsorption at the hydrocarbon–water interface indicated that the increase in chain length alone is not responsible. It has been concluded that in all three samples the packing or association of the solid particles imposes a space restriction which limits the adsorption of C_{18} but not C_1 molecules.

Introduction

Adsorption from solution onto polar solid surfaces is known to be complicated by a number of factors. In particular, we should like to know more about how the adsorption is influenced by the size and shape of the solvent molecules, the chain flexibility of long-chain organic adsorbates, the pore and aggregate structure, particle sizes of the solid, and the extent of localization of the adsorbate molecules at the surface.

Previous investigations into adsorption onto metal oxides have revealed results of increasing complexity.[1] One clear point arising from studies of adsorption of long-chain acids from hydrocarbons is that an apparently close-packed acid film is not usually obtained.[2] Furthermore, adsorption from nonaqueous solvents[3] and from the vapor phase is very sensitive to the amount of water present. In this paper an attempt has been made to determine experimentally how some of the above factors influence adsorption onto titanium dioxide, by studying the adsorption of carboxylic acids from the vapor phase and from hydrocarbons under rigorously dry conditions. The results have been interpreted with the aid of data from a general investigation into the properties of the titanium dioxide used.[4]

Experimental

Adsorbent. Rutile (TiO_2) specimens were kindly provided by the British Titan Products Co. of Billingham, County Durham. They were prepared by the hydrolysis of pure $TiCl_4$ and the calcination of the resulting products. The calcination temperatures were approximately 600, 300–400, and 250° for the low, medium, and high area specimens, respectively. The

(1) (a) W. D. Harkins and D. M. Gans, *J. Am. Chem. Soc.*, **53**, 2804 (1931); (b) W. D. Harkins and D. M. Gans, *J. Phys. Chem.*, **36**, 86 (1932); (c) C. M. Hollabaugh and J. J. Chessick, *ibid.*, **65**, 109 (1961).

(2) H. E. Ries, M. F. L. Johnson, and J. S. Melik, *ibid.*, **53**, 638 (1949).

(3) W. Hirst and J. K. Lancaster, *Trans. Faraday Soc.*, **47**, 315 (1951).

(4) P. T. Dawson, Thesis, Cambridge University, 1963.

latter had to be recovered from its aqueous suspension after the hydrolysis by freeze-drying the suspension. The purity of the samples was 99.95%, the principal impurities being silica and chloride. The surface areas were determined by nitrogen adsorption using a conventional B.E.T. method. These were, respectively, 11.5, 44.8, and 158.0 m.²/g. The particle size distributions were found from electron microscope studies. The size (diameter) ranges of the primary particles in the specimens were, respectively, 0.01 to 0.3, 0.005 to 0.1, and 0.005 μ (almost monodisperse). A pore size distribution analysis based on a nonintersecting cylindrical pore model (described in more detail elsewhere) yielded the results shown in Fig. 1. The sharp peak at 25 Å. for the high area monodisperse sample indicates that the pores were between the particles in this specimen rather than in them. A more detailed examination of the low and intermediate area samples suggests that in these cases also the particles themselves, as opposed to aggregates of the particles, were not porous.

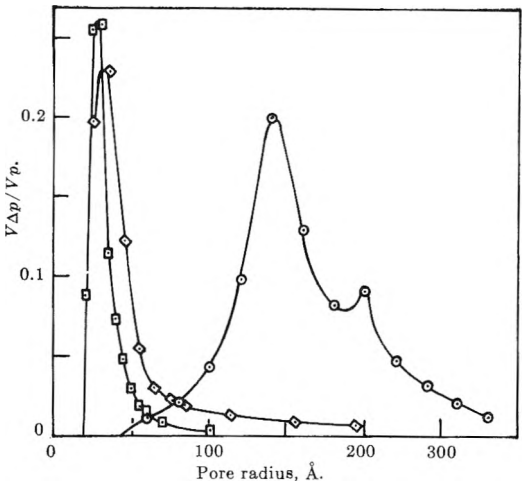

Figure 1. Pore size distribution curves for three rutiles (A, B, and C) prepared by hydrolysis of $TiCl_4$ and calcination at 600, 300–400, and 250°, respectively: ⊙, rutile A (11.5 m.²/g.); □, rutile B (158 m.²/g.); ◊, rutile C (44.8 m.²/g.).

For the adsorption studies described below, the oxides were heated to 250 ± 2° and degassed through liquid nitrogen traps for 50 hr. at $\sim 10^{-6}$ mm. Under these conditions the oxides did not noticeably change color, and they were not treated with O_2.[1c] The adsorption behavior of the oxides, prepared as described above, was accurately reproducible. For liquid phase adsorption measurements, the degassed samples were sealed off in thin-walled glass bulbs and transferred to a drybox for further manipulation.

Adsorbates. Formic acid of A.R. grade was used, from which dissolved gases were removed just prior to adsorption by evacuating the space above the sample. The acid had a saturated vapor pressure of 32.4 mm., which from the work of Coolidge[5] suggests the presence of approximately 1% water. The stearic acid and stearyl alcohol were of the highest grade available from Eastman Kodak and were recrystallized twice from acetone, twice from benzene, and then vacuum dried over phosphorus pentoxide. The benzene and petroleum ether (80–100° fraction) were A.R. grade solvents. They were first dried by standing over sodium wire, which was extruded directly into the solvent at intervals, until it remained clean and bright. The solvent was then passed through a 1-m. long column of Fluka active alumina (5016A) which, it is claimed, reduces the water content to less than 10 p.p.m. The outlet of this column was inside the drybox.

Vapor Phase Adsorption Apparatus. The adsorption of formic acid vapor was carried out by a conventional volumetric method. The formic acid dosage and equilibrium pressures were measured with a wide bore (25-mm. internal diameter) mercury manometer in which the heights of the menisci were determined to 0.01 mm. by means of a cathetometer. Adsorptions were carried out at 20°.

Liquid Phase Adsorption Apparatus and Procedure. Carefully dried solvents were used to prepare, in the drybox, suitable solutions for adsorption. The bulbs containing adsorbent were broken under the surfaces of these solutions in the drybox and the containing bottles immediately stoppered and sealed. The bottles were then shaken for several hours in a thermostat at 20°. Samples of the supernatant liquid were withdrawn in the drybox and analyzed either by titration with alcoholic potassium hydroxide under nitrogen, in the case of formic acid, or by spreading on a Langmuir trough, in the cases of stearic acid and stearyl alcohol.

Results

Adsorption of Formic Acid Vapor. It is known from the work of Coolidge that formic acid forms dimers in the vapor phase. Consequently, in the volumetric procedure adopted, a correction for nonideality was necessary. For the present investigation, however, Coolidge's results did not extend to sufficiently high relative pressures of formic acid and his experiments were repeated and extended.[4] This work will be described elsewhere, but the results agreed accurately with those of Coolidge in the overlap region, and at relative pressures >0.95 showed that trimers and possibly higher polymers begin to form.

(5) A. S. Coolidge, *J. Am. Chem. Soc.*, **50**, 2166 (1928).

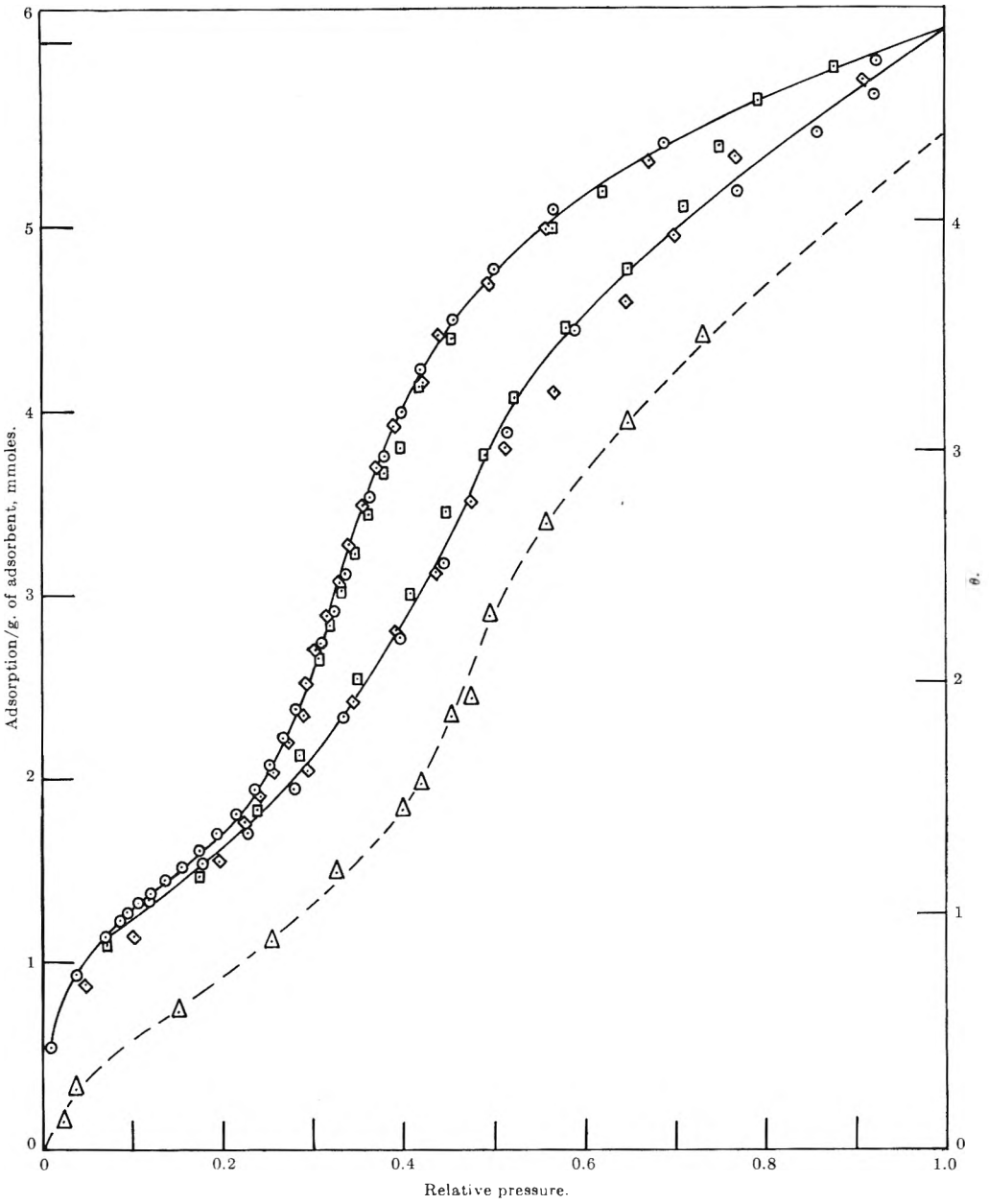

Figure 2. The adsorption and desorption at 20° of formic acid on rutile B (158 m.²/g.) which had been activated at 250 ± 2° at ~10^{-6} mm. for 50 hr.: ⊙, first cycle; ⊡, second cycle; ⊕, third cycle; ⧋, after treatment of the activated material with formic acid vapor and evacuation at 20°.

The adsorption and desorption of formic acid on rutile B is shown in Fig. 2. The reproducibility is illustrated by the agreement of three successive cycles. The total pore volume calculated from the hysteresis loop (0.227 cc./g.) agrees closely with the value obtained from nitrogen adsorption. If, after adsorbing formic acid at 20° onto a sample which had been degassed at 250°, the sample is then evacuated at 20° and a second isotherm determined, the lower curve is obtained. The difference between the two adsorption curves is approximately the same at all the equilibrium acid pressures.

Rutiles A and C showed similar behavior to B, although the differences between adsorption onto 250°-activated specimens and onto the same specimens after evacuation at 20° were not, in terms of surface coverage, exactly the same. The adsorption curves for rutile A are shown in Fig. 3. The broken curve

Table I: A Comparison of the Plateau (or Monolayer) Adsorption Values at 20° for the Three Rutiles. The Oxides were Degassed for 50 hr. at 250 ± 2° and ~10^{-6} mm.

		Adsorption, molecules/cm.² × 10^{-14}					
		Formic acid		Stearic acid		Octadecyl alcohol	
	Specific surface area, m.²/g.	Vapor phase	Benzene	Benzene	Petroleum ether	Benzene	Petroleum ether
Rutile A	11.5	3.85 (3.60 irr.)	4.04	3.12	3.32	3.35	3.30
Rutile C	44.8	3.75 (3.12 irr.)	3.75	1.93			
Rutile B	158	3.75 (2.40 irr.)	3.95	2.31			

in this figure shows the formic acid adsorption onto the rutile after it had been treated with water vapor and evacuated at 20°.

The θ plotted on the right-hand axis of Fig. 2 and 3 is the surface coverage and was calculated from the expression

$$\theta = \frac{\text{no. of acid molecules adsorbed/g. of oxide} \times \text{area of acid molecule}}{\text{specific surface area determined by nitrogen adsorption}}$$

The cross-sectional area of the formic acid molecule was assumed to be similar to that of other normal chain carboxylic acids in the vertical orientation, namely 20.8 Å.².[6]

Adsorption from Hydrocarbons. Adsorption and desorption results for formic and stearic acids from benzene to rutiles A, B, and C are shown in Fig. 4. For convenience the corresponding coverages are given on the right-hand axis. The extents of adsorption on the plateaus of the isotherms have been collected in Table I.

In calculating the coverages, the molecules have been assumed to be vertically oriented and therefore to have a cross-sectional area of 20.8 Å.² per molecule. The highly polar and nonpolar nature of the titanium dioxide and benzene, respectively, make this assumption reasonable and, moreover, experimental evidence of the vertical orientation has been found.[7] It can be seen from the desorption results that the acid molecules were extremely strongly adsorbed; in fact, no suggestion of desorption could be detected in any of the systems examined. As the bulk concentrations of acid were very low, the number of molecules adsorbed was given directly by the change in the bulk concentration. The rise in the adsorption of stearic acid onto rutile C at low concentrations is thought to be due to the systems having had insufficient time for equilibrium at the higher concentrations. The adsorptions of

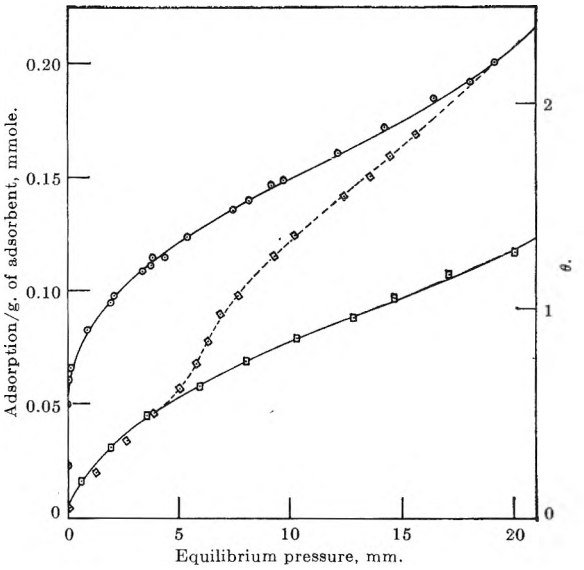

Figure 3. The adsorption at 20° of formic acid vapor on rutile A (11.5 m.²/g.) activated as in Fig. 2: ⊙, directly after activation; ⊡, after treatment with formic acid vapor and evacuation at 20°; ⊕, after treatment with water vapor and evacuation at 20°.

stearic acid from petroleum ether and of octadecyl alcohol from benzene and petroleum ether were measured only in the plateau region of the adsorption isotherm. The results are shown in Table I.

Discussion

Formic Acid Adsorption. In Fig. 2 and 3 the adsorption of formic acid has been plotted against the relative pressure of the acid. The isotherms do not show a well-defined linear region or a very distinct knee, and no clear estimate of the monolayer adsorption is possible by conventional means. However, by comparing the adsorption isotherm for the oxide degassed at

(6) S. J. Gregg, *Trans. Inst. Chem. Engrs.* (London), **25**, 40 (1947).
(7) J. J. Kipling and E. H. M. Wright, *Nature*, **200**, 1157 (1963).

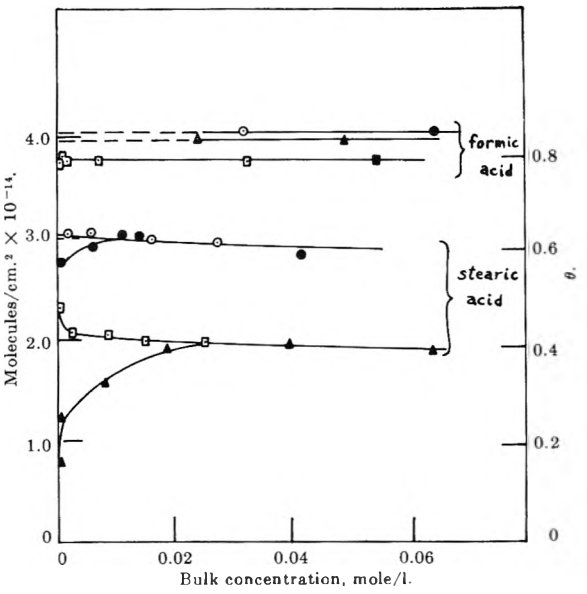

Figure 4. The adsorption at 20° of formic and stearic acids from dry benzene onto the three rutiles, activated as in Fig. 2: ⊙, rutile A (11.5 m.²/g.); □, ■, rutile C (44.8 m.²/g.); △, ▲, rutile B (158 m.²/g.). Open points indicate the desorption and filled points the adsorption isotherms.

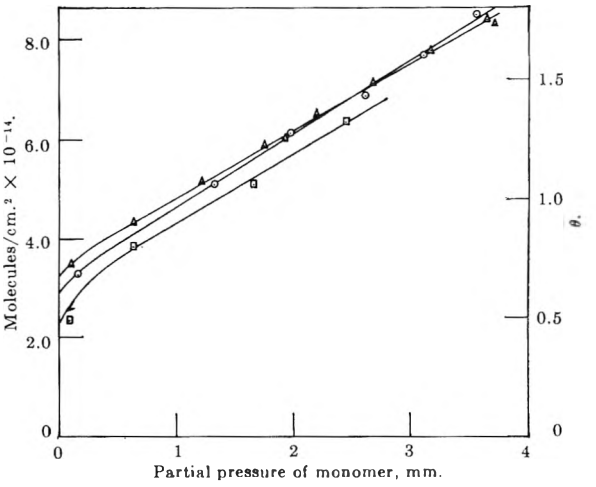

Figure 5. The adsorption of formic acid vapor at 20° onto the three rutile specimens (activated as in Fig. 2) plotted as a function of the partial pressure of the monomeric acid: △, rutile A (11.5 m.²/g.); □, rutile B (158 m.²/g.); ⊙, rutile C (44.8 m.²/g.).

250° with the isotherm for a formic acid-treated specimen degassed at 20°, we can infer that sufficient acid is irreversibly adsorbed at 20° to give approximately half-coverage. The precise values of the adsorption of irreversibly adsorbed acid are given in Table I. In order to attempt an estimate of the monolayer adsorption of the acid, we shall use the fact that the equilibrium vapor phase over the lower part of the isotherm contains monomeric and dimeric molecules.[4,5] From the chemical nature of titanium dioxide and formic acid we may conclude that by far the strongest bonds between the acid and the surface will be either the hydrogen bond or the ionic bond resulting from the formation of a formate. Only the monomeric acid would form such bonds. We therefore conclude from rough calculations that since the first layer is evidently complete at relative pressures of ~0.1 (*i.e.*, where the monomer concentration is still of the same order of magnitude as that of the dimer) the adsorption of dimer in the first layer is likely to be negligible. If we now plot the adsorption against the partial pressure of the monomer, we obtain the curves shown in Fig. 5. As can be seen, there is a well-defined linear portion and a knee, from which a fairly accurate monolayer adsorption can be read. These values are shown in Table I.

The question now arises as to why the monolayer adsorptions are all about the same per unit area, but correspond to coverages of less than unity. One obvious reason is that as the adsorption is clearly a very strong one, over half the molecules being irreversibly adsorbed, the film is no doubt highly localized on specific sites. If the spacing of the localized molecules is a little larger than the diameter of the formic acid molecule, and it is energetically unfavorable to displace the molecules laterally from their sites to make room for the completion of the monolayer, then the observed coverages of less than unity for the monolayer would be expected. While this may be the principal explanation, there may be another contributing factor. It is shown in Fig. 3 that in the first stages, the adsorption of formic acid onto oxide previously treated with formic acid and degassed at 20°, is almost the same as the adsorption onto oxide previously treated with water vapor and degassed at 20°. Thus, irreversibly adsorbed water competes with, and is not displaced by, formic acid. [The complete explanation for the course of this curve at higher pressures is not entirely obvious, although it is very probable that ultimately some of the residual adsorbed water is displaced by the formic acid. This is consistent with the eventual merging with the upper isotherm.] If, therefore, after degassing the original oxide at 250°, about one-fifth of the surface was covered by adsorbed water, we should not expect to obtain a complete monolayer of formic acid. In fact, detailed studies on the water adsorption[4] suggested that at the most only one-tenth of the surface was originally covered by water. It is therefore concluded that both the above mechanisms probably contribute to the results.

The similar first-layer adsorption values for the three rutiles suggests that either the site spacing or the amount of water remaining on the surface after degassing at 250°, or both, is very similar for each oxide. On the other hand, the variation in the amount of formic acid irreversibly adsorbed at 20° reveals that the proportion of the sites with a high energy decreases with the increase in specific surface area. In fact, the larger the surface area, the lower the temperature at which the oxide was calcined. It is, therefore, quite possible that the initial heat treatment of the rutile was responsible for the number of high energy sites.

The maximum adsorption of formic acid from dry benzene gives values which agree to within experimental error with the monolayer vapor phase values. It is not known to what extent this adsorption was effectively irreversible at 20°. All that can be said is that no desorption could be detected for bulk phase concentrations down to 5×10^{-5} mole/l. It seems reasonable to suppose that the irreversible adsorption was similar in extent to that found for the vapor phase systems.

By comparison of the benzene results with those for the vapor phase, we conclude that the benzene does not effectively compete for space in the monolayer. This is easy to understand in the present systems, since the benzene, having no polar group, would be expected to have a relatively small energy of interaction with the surface.[8] If, conversely, we assume that the benzene would have no influence on the adsorption, the results of adsorption from benzene (which do not involve any suppositions regarding the relative adsorption of monomers and dimers) confirm our interpretation of the vapor phase data.

The Adsorption of C_{18} Molecules. The adsorption isotherms of stearic acid from benzene showed the same qualitative features as the formic acid adsorption. The maximum adsorption obtained, however, was not only much lower than that for formic acid, but was considerably different for the three rutile specimens. This lower adsorption evidently was not related to the particular combination of carboxyl group and long chain, since the results for octadecyl alcohol from benzene are very similar. It is probable that, owing to the high energy of the adsorption, the size and shape of the hydrocarbon solvent is of very minor importance. This is borne out to some extent by the results of adsorption from petroleum ether (Table I).

Investigations into the adsorption of normal aliphatic alcohols from benzene and aliphatic hydrocarbons to a water surface[9] have shown that the effective cross-sectional area of the molecules is, to a first approximation, independent of chain length. There does not, therefore, appear to be any possibility that there is a space limitation in the plane of a flat surface for the C_{18} chains.

It seems that the explanation of the low adsorption of C_{18} relative to C_1 molecules is that the packing or aggregation of the oxides results in a space limitation for the former, but not for the latter. This conclusion is supported by the fact that the stearic acid adsorption per unit area is largest for the oxide with the largest pores and smallest for the oxides with the smallest pores. It can be shown that the London–van der Waals forces between the particles are very unlikely to be sufficiently large to prevent adsorption occurring between particles held together by these forces. As the pore volume analyses indicate that the pores are almost certainly between rather than in the particles, it is possible that the pores which are significant in limiting the adsorption are formed by adjacent particles which have partially coalesced or grown together at quite localized points.

The Adsorption Bonds. It is not possible to say anything definite from this investigation about the nature of the bonds between the acids and the oxides, but there are some implications in the experimental results. Smith[10] has concluded from infrared adsorption studies of adsorbed carboxylic acids on various specimens of titanium dioxide that both ionic and hydrogen-bonded acids may be found on the surface of one specimen. Those molecules bound ionically were shown to be irreversibly adsorbed, while the hydrogen-bonded molecules could be washed off in excess solvent. In the present rutile specimens it is concluded from the formic acid adsorption that both reversibly and irreversibly adsorbed acid is present. It is possible that these molecules may be hydrogen- and ionically bonded, respectively, but evidence of water adsorption[4] is in some ways difficult to reconcile with this. It was pointed out above that water molecules may become irreversibly adsorbed and so limit the adsorption on the first layer of formic acid. There is some evidence[4] that the water which does this is hydrogen-bonded and not in a dissociated, chemically bonded state. If this is so, hydrogen bonding cannot be entirely ruled out in the present systems for the irreversibly adsorbed acids.

Acknowledgments. P. T. Dawson and G. T. Rich are indebted to the Department of Scientific and Industrial Research and to Imperial Chemical Industries

(8) A. V. Kiselev and D. P. Poshkus, *Dokl. Akad. Nauk SSSR*, **120**, 4 (1958).

(9) G. T. Rich and D. A. Haydon, unpublished results.

(10) I. T. Smith, *Nature*, **201**, 67 (1964).

(Paints Division), respectively, for maintenance grants. The authors also wish to thank Dr. I. T. Smith of the Paint Research Station, Teddington, for discussions on several points.

The Influence of Detergents on the Dewetting of Calcium Palmitate

by F. van Voorst Vader and H. Dekker

Unilever Research Laboratory, Mercatorweg 2, Vlaardingen, The Netherlands *(Received April 13, 1964)*

The changes in surface composition of a solid because of replacement of one adjoining fluid by another can be derived from measurements of the contact angle between these two fluids and the solid interface and of the interfacial tension between the fluids. The changes in the solid surface are calculated from these data by means of formulas combining Young's equation with the Gibbs adsorption equations valid at the two solid–fluid interfaces considered. This method was applied to the system calcium palmitate–aqueous buffered detergent solution–air in the pH range 7.5–9.2. It was found that the calcium palmitate becomes nearly completely covered by a monolayer of acid soap on replacing the buffer solution by air in the absence of detergent. The presence of potassium N-lauroyl-N-methyltaurate, ethoxylated lauryl alcohol, or bis(methylsulfinyl)dodecane in the solution markedly reduces the increase in fatty acid adsorption during dewetting. It was found by direct titration that the presence of these detergents increased the fatty acid adsorption at the interface of calcium palmitate–solution.

Introduction

The hydrophylic character of calcium soaps can be greatly enhanced by adding detergents (so-called "scum dispersants") to their aqueous suspensions. In order to explain this behavior, the influence of a number of dispersants on the surface composition of calcium palmitate against dispersant solution and against air was investigated.

The values of the differences between the adsorption at the interfaces of calcium palmitate against these two phases were derived from contact angle and surface tension measurements. In addition, the values of these adsorptions at the calcium palmitate solution interface itself were determined by titration and electrokinetic measurements. In this way, a fairly complete picture of the surface phenomena connected with the phase change at the calcium palmitate surface during dewetting is obtained.

Thermodynamics

Consider a three-phase system consisting of an aqueous suspension of calcium palmitate (CaP_2) and air, where the aqueous phase contains Ca^{2+}, H^+, K^+, P^- (palmitate), Cl^-, and D^- (dispersant) ions and HP (palmitic acid) as solutes. Changes in the surface tension ($d\gamma$) at each of the three interfaces solid–air (SA), solid–liquid (SW), and air–liquid (AW) are related to the adsorption of these solutes at the interfaces by means of the relevant Gibbs adsorption isotherm

$$-d\gamma = \Gamma_P d\mu_P + \Gamma_{Ca} d\mu_{Ca} + \Gamma_{HP} d\mu_{HP} + \Gamma_K d\mu_K + \Gamma_D d\mu_D \quad (1)$$

where Γ is the adsorption relative to water, and μ is the thermodynamic potential.

In formula 1 the adsorptions of H^+, OH^-, and Cl^- ions at the calcium palmitate interface have been

neglected. The choice of Γ_{HP} rather than Γ_{H^+} as parameter implies that all hydrogen ions adsorbed at the interface are assumed to be attached to the COO^- groups present there and that the contribution of H^+ ions to the ionic double-layer charge at the interface is negligible. The validity of this assumption was proved in the case of carboxylate soap solutions.[1]

The following relations exist between the thermodynamic potentials given in formula 1

$$d\mu_H = d\mu_{HP} - d\mu_P \quad \text{(dissociation equilibrium of fatty acid)} \quad (2)$$

$$2d\mu_P + d\mu_{Ca} = 0 \quad \text{(solubility product of } CaP_2) \quad (3)$$

$$\Gamma_P + \Gamma_D = 2\Gamma_{Ca} + \Gamma_K \quad \text{(electroneutrality of adsorbed layer)} \quad (4)$$

Substituting (2), (3), and (4) in formula 1

$$d\gamma = -\Gamma_{HP}(d\mu_H - {}^1/_2 d\mu_{Ca}) - \Gamma_K(d\mu - {}^1/_2 d\mu_{Ca}) - \Gamma_D(d\mu_D + {}^1/_2 d\mu_{Ca}) \quad (5)$$

The changes in surface tension ($d\gamma$), at each of the three interfaces are related by the differential form of Young's equation

$$d\gamma_{SA} - d\gamma_{SW} = d(\gamma_{AW} \cos \vartheta) \quad (6)$$

where ϑ is the contact angle. It is assumed that the whole system is in thermodynamic equilibrium; in that case it is irrelevant whether the solutes are soluble in both fluids or in only one of them.[2] Substituting the expressions for $d\gamma$ at the SA and the SW interfaces in eq. 6

$$\frac{-d(\gamma_{AW} \cos \vartheta)}{RT} = \{(\Gamma_{HP})_{SA} - (\Gamma_{HP})_{SW}\} \times d \ln \frac{[H^+]}{\sqrt{[Ca^{2+}]}} + \{(\Gamma_K)_{SA} - (\Gamma_K)_{SW}\} d \ln \frac{[K^+]}{\sqrt{[Ca^{2+}]}} + \{(\Gamma_D)_{SA} - (\Gamma_D)_{SW}\} d \ln [D^+]\sqrt{[Ca^{2+}]} \quad (7)$$

where R is the gas constant; T = absolute temperature, and the $[H^+]$, etc., represent the activities of the relevant ionic species. In the case of a nonionic additive (N) eq. 7 is modified to

$$\frac{-d(\gamma_{AW} \cos \vartheta)}{RT} = \{(\Gamma_{HP})_{SA} - (\Gamma_{HP})_{SW}\} \times d \ln \frac{[H^+]}{\sqrt{[Ca^{2+}]}} + \{(\Gamma_K)_{SA} - (\Gamma_K)_{SW}\} d \ln \frac{[K^+]}{\sqrt{[Ca^{2+}]}} + \{(\Gamma_N)_{SA} - (\Gamma_N)_{SW}\} d \ln [N] \quad (8)$$

In the absence of dispersant, the last term on the right-hand side of formula 8 is omitted.

In these formulas, all adsorption differences are determined by quantities that can be varied independently and are readily measurable. They allow the changes in the adsorption of fatty acid, potassium ions, and dispersant ions on wetting the calcium palmitate to be deduced from suitable measurements of the contact angle and surface tension of the aqueous phase by varying, respectively, the pH, the potassium ion concentration, and the dispersant concentration at constant calcium ion concentration.

In our measurements, a dilute potassium borate–boric acid buffer was added to the solution to stabilize the pH value. It has been shown that the activity coefficients of such buffer solutions are nearly equal to those of potassium chloride solutions of equal ionic strength.[1] It is assumed that neither borate ions nor boric acid contribute to the adsorption.

Since it has been assumed that all adjoining phases are in equilibrium, the limits of the validity of the formulas derived above must be investigated separately. Three possible causes for instability of the calcium palmitate may arise: (1) formation of mixed crystals of calcium palmitate and, *e.g.*, fatty acid; (2) formation of solid fatty acid, by transformation of calcium palmitate; (3) formation of solid acid potassium soap.

In the pH range investigated (pH >7.5) no mixed crystals of calcium palmitate and fatty acids or of calcium palmitate and acid potassium soap are known.

No chemical transformation of the calcium palmitate will occur as long as the ionic product of the reaction products remains below their solubility product. Thus, transformation to palmitic acid is impossible as long as

$$[HP] = \frac{[H^+][P^-]}{I_{HP}} = \frac{[H^+]}{I_{HP}} \sqrt{\frac{S_{CaP_2}}{[Ca^{2+}]}} < [HP]_s$$

or

$$\frac{[H^+]}{\sqrt{[Ca^{2+}]}} < \frac{I_{HP}[HP]_s}{\sqrt{S_{CaP_2}}} = 10^{-3.7} \quad (9)$$

where $I_{HP} = [H^+][P^-][HP]^{-1} = 10^{-5}$ mole/l. is the ionization product of palmitic acid, and $[HP]_s = 10^{-7.5}$ mole/l. is the saturation concentration of this acid. $S_{CaP_2} = [Ca^{2+}][P^-]^2 = 10^{-17.5}$ mole^3/l.^{3} is the solubility of calcium palmitate.[3]

Since the highest value of $[H^+]$ used in our experiments is $<10^{-7}$, it follows that $[Ca]^{2+} > 0.5 \times 10^{-6}$ mole/l. is sufficient to prevent precipitation of palmitic acid. The formation of acid soap KHP_2 cannot occur if

(1) F. van V. Vader, *Trans. Faraday Soc.*, **57**, 2263 (1961).
(2) E. H. Lucassen-Reynders, *J. Phys. Chem.*, **67**, 969 (1963).
(3) J. Lucassen, unpublished results.

$$[H^+][K^+][P^-]^2 = [H^+][K^+]\frac{S_{CaP_2}}{[Ca^{2+}]} < S_{KHP_2}$$

where $S_{KHP_2} = 10^{-20}$ mole^4/l.^{4} is the solubility product of acid potassium palmitate.[3] Thus

$$\frac{[H^+][K^+]}{[Ca^{2+}]} < \frac{S_{KHP_2}}{S_{CaP_2}} = 10^{-2.5} \qquad (10)$$

Since the lowest value of $[H^+]$ in our experiments is about 10^{-9}, $[K^+]/[Ca^{2+}] < 4 \times 10^6$ is sufficient to prevent precipitation of acid potassium palmitate.

In our experiments, both conditions were fulfilled.

Experimental

The contact angles were measured using Bartell's method.[4] The required hydraulic radius of the calcium palmitate plugs was obtained from permeability measurements using the solution as mobile phase.[2] Surface tensions of solutions containing ionic surfactants, or nonionics at concentrations near the critical micellar concentration (c.m.c.), were measured using the drop-weight method. For solutions containing low concentrations of nonionics the Wilhelmy plate method was used.

A rough estimation of the potassium ion adsorption at the calcium palmitate–solution interface was obtained by measuring the ζ-potential between the solid and the solution by means of electroendosmotic measurements. An apparatus similar to that described by Sparnaay was used.[5] The plugs were made from the same batch of equilibrated Ca palmitate that was used for the contact angle measurements.

The adsorption of palmitic acid at the calcium palmitate–solution interface was determined both in the presence and in the absence of dispersants by comparing the amount of HCl needed for a certain change in pH of a calcium palmitate slurry to the amount needed for an identical change in a blank solution. The blank solution contained KCl, $CaCl_2$, and dispersant in concentrations about equal to those in the slurry. They were chosen in such a way that inequalities (9) and (10) were satisfied. The solutions were kept in stoppered polythene bottles under humid nitrogen that was free from CO_2. Their pH was fixed at 10–11 by adding KOH solution. The adsorption of palmitic acid at the Ca palmitate surface at higher pH values is neglected. Small amounts of 0.1 N HCl were then added under vigorous stirring. After 1–2 hr. a clear supernatant liquid layer was present over the calcium palmitate slurry. Both the glass electrode and the reference electrode of the pH meter were dipped into this layer and the pH was measured. The pH of the blank solution was also measured.

At the end of the experiment, the surface area of the calcium palmitate in the slurry was determined by permeametry. The change in fatty acid adsorption owing to the change in the pH of the slurry was then calculated by dividing the excess of HCl used on the slurry by the surface area of the sample.

In the same way, the amount of dispersant adsorbed at the calcium palmitate–solution interface was determined by dividing the difference between the concentration added and the equilibrium concentration by the surface area of the sample.

Materials. Calcium palmitate of suitable particle size was prepared by adding 1 N alcoholic KOH solution to 50 g. of molten palmitic acid (m.p. 55.2–59°) and 500 ml. of hot water in a beaker until spontaneous emulsification was observed. Then the contents were emulsified by stirring with a polytron. The emulsion, under a nitrogen blanket, was slowly introduced into a slowly stirred solution of 12.5 g. of calcium chloride (dry weight) in 8 l. of distilled water at 20° kept at pH ~10 by gradual addition of alcoholic KOH solution. The reactants were introduced through tubes extending to the bottom of the vessel in order to avoid air entrainment. After digesting for 3–4 hr. at 70°, the calcium palmitate was filtered and washed with distilled water until calcium ions could no longer be demonstrated by complexometric titration of 100 ml. of the effluent. The product was then dried at 100°.

Determination of the calcium and of the carboxylic acid content showed the product to be 98–99% pure. Its average particle size, as estimated both by microscopic observation and by permeametry was between 0.5 and 5 μ in the several samples used.

Potassium tetraborate, $K_2B_4O_7$, was prepared by heating K_2CO_3 (analytical grade) with twice the equivalent amount of boric acid (analytical grade) in a quartz vessel until the evolution of carbon dioxide ceased.

Potassium N-lauroyl-N-methyltaurate, $C_{11}H_{23}C(=O)N(CH_3)$, $(C_2H_4SO_3K)$, was prepared by treating potassium methyltaurate with lauroyl chloride in an acetone–water mixture. After completion of the reaction, lauric acid was removed by acidification and extraction with light petroleum. The product was recrystallized from 90% ethanol. The c.m.c. was 4.4 mmoles/l. The stock solution was foam fractionated before use.

Ethoxylated lauryl alcohol, average composition $C_{12}H_{25}(OC_2H_4)_{10}OH$, was freed from lauryl alcohol by

(4) (a) F. E. Bartell and H. J. Osterhof, *Ind. Eng. Chem.*, 19, 1277 (1927); (b) F. E. Bartell and F. C. Benner, *J. Phys. Chem.*, 46, 836 (1942).

(5) M. J. Sparnaay, *Rec. trav. chim.*, 79, 950 (1960).

Table I: Data on Contact Angle Measurements on Buffered Ca Palmitate Plugs

Additive	Additive added, mmole/l.	Plug data: ϵ[a]	Plug data: S_v,[b] cm.$^{-1}$ × 10^{-4}	Plug data: $-\Delta P$,[c] dyne/cm.^{2} × 10^{-3}	Equilibrium values: pH	[K^+], mmole/l.	[Ca^{2+}], mmole/l.	[Additive], mmole/l.	γ_{AW}, erg/cm.^{2}	$\gamma_{AW} \times \cos\theta$ erg/cm.^{2}	$(\Gamma_D)_{AW}$, mole/cm.^{2} × 10^{10}	ζ, mv.	θ, deg.
None	...	0.615	2.97	103	7.55	52.9	1.26	None	72.7	5.6	None	−33.2	86
	...	0.471	1.94	540	8.50	55.7	0.77	None	74.5	24.9	None	−51.6	70
	...	0.442	2.21	1067	9.20	43.9	0.51	None	72.2	38.1	None	−56.8	58
	...	0.778	2.43	215	9.0	56.8	0.65	None	73.1	31.0	None		65
	...	0.415	1.03	515	9.0	28.8	0.61	None	72.9	35.0	None		61
K N-lauroyl-N-methyltaurate	4.51	0.524	4.74	672	9.0	12.25	0.06[d]	4.31	48.4	15.6	1.24		71
	2.24	0.586	4.32	451	9.0	12.15	0.04[d]	2.11	53.25	14.8	0.72		74
	4.63	0.574	4.75	456	7.75	12.5	0.06[d]	4.39	46.9	13.3	1.07		73.5
	4.52	0.550	4.16	343	9.05	24.3	0.08	4.22	44.0	10.1	1.47		77
Ethoxylated lauryl alcohol	4.86×10^{-2}	0.628	4.07	351	8.8	12.11	0.03	2.1×10^{-3}	59.3	14.6	0.268		76
	4.88×10^{-2}	0.553	5.73	406	7.7	12.31	0.05	2.4×10^{-3}	53.3	8.78	0.161		81
	5.45×10^{-2}	0.608	5.83	338.5	7.7	13.9	0.04	1.8×10^{-3}	59.3	9.00	0.177		83
	0.930	0.486	8.31	348	8.95	14.14	1.3[d]	0.07	39.4	3.95	1.77		84
	0.927	0.512	9.20	262	8.05	14.10	2.0[d]	0.08	38.4	2.98	1.68		86
Bis(methylsulfinyl)dodecane	0.524	0.532	5.44	569	8.85	11.2	0.68	Unknown	43.0	11.9	Unknown		74
	0.566	0.556	5.52	536	7.8	12.0	0.85	Unknown	43.3	12.1	Unknown		74

[a] Volume fraction of liquid in the plug. [b] Specific surface area of the solid. [c] Capillary pressure across the stationary L–A interface. [d] Values not reliable because of incomplete removal of solid Ca palmitate.

extraction from a 1:1 alcoholic solution with light petroleum and freed from ionic components by percolation through a column of Dowex ion-exchange resin. Its critical micellar concentration (c.m.c.) was determined spectroscopically[6] and equals 9.9×10^{-5} mole/l.

1,2-Bis(methylsulfinyl)dodecane (m.p. 107–108.5°) was prepared as

$$C_{10}H_{21}C_H{=}CH_2 - CH_3SSCH_3 \xrightarrow{CH_3SO_3H} C_{10}H_{21}CH(SCH_3)CH_2SCH_3$$

$$\xrightarrow[HAc,(0°)]{H_2O_2} C_{10}H_{21}CH(SCH_3)-CH_2SCH_3 \quad (\overset{\|}{O} \qquad \overset{\|}{O})$$

The final product was purified by elution from an Al_2O_3 column using a 7 to 3 mixture of benzene and chloroform; c.m.c.: 5×10^{-5} mole/l.

Analytical. The concentration of lauroylmethyltaurate was determined by the cetylbenzyldimethylammonium chloride (CBC) method (methylene blue as indicator).[7] The equilibrium concentration of the ethoxylated lauryl alcohol was determined by a turbidimetric method due to Kho and Scholten.[8]

Measurements. In preliminary experiments on the system calcium palmitate–distilled water–air a contact angle of 89° 51′ ± 11′ was found. This value was not affected by slight variations in the method of preparing the calcium palmitate. The contact angle of the system palmitic acid–distilled water–air was obtuse (96° 54′).

In the case of buffered solutions, the calcium palmitate was equilibrated with the aqueous phases by mixing known amounts of its thoroughly washed aqueous slurry, concentrated solutions of the buffer, KCl, $CaCl_2$, dispersant, and doubly distilled water that was free from CO_2. The mixture was then stirred under a nitrogen blanket at room temperature during 45 hr. Plugs were prepared in glass plugholders by compression to 3 atm. during 1 hr.

After determining the mean hydraulic radius and the equilibrium displacement pressure against air, the plug was washed with distilled water, dried, and weighed in order to determine its porosity. In the equilibrium liquid pressed out of the plug, the calcium ion concentration was determined complexometrically.[9] There was no difference between advancing and receding contact angles in these systems. In order to find the

(6) S. Ross and J. F. Olivier, *J. Phys. Chem.*, **63**, 1671 (1959).

(7) F. Barr, J. Oliver, and W. V. Stubbings, *J. Soc. Chem. Ind.* (London), **67**, 45 (1948).

(8) G. S. Siggia, *Soap Chem. Specialities*, **3**, 51 (1958).

(9) G. Schwarzenbach, "Die Komplexometrische Titration," Ferdinand Enke Verlag, Stuttgart, 1956, p. 60.

Table II: Changes in Adsorption at the Surface of Calcium Palmitate during the Transition Solution–Air

Dispersant	pH range	(K^+) range, mequiv./l.	Average values of $(\Gamma_{SA} - \Gamma_{SW})$ moles/cm.^{2} × 10^{10} HP	K^+	Dispers.	$(\Gamma_D)_{SW}$,[a] moles/cm.^{2} × 10^{10}	$(\Gamma_{HP})_{SW}$,[b] moles/cm.^{2} × 10^{10}
None	7.55–8.50	50	4.1	...	...	...	
	8.50–9.20	50	3.8	...	...	...	1.9
	9.00	28.8–56.8	...	2.6	...	...	
Taurate							
4.5 mmole/l.	7.75–9.00	12.2	0.33	...	...		
4.5 mmole/l.	9.00	12.2–24.3	...	3.35	...	1.2	3.4
2.2–4.5 mmole/l.	9.00	12.3	...	...	−0.46		
Eth. ox. laur. alc.							
0.002 mmole/l.	7.7–8.8	12.2	0.96	...	...	0.17	...
0.07 mmole/l.	8.05–8.95	14.1	0.19	...	...	1.7	3.7
Sulfinyldodecane	7.8–8.85	11.6	<0.1	...	...	...	...

[a] From Table I (average values). [b] From titration measurements (Fig. 1).

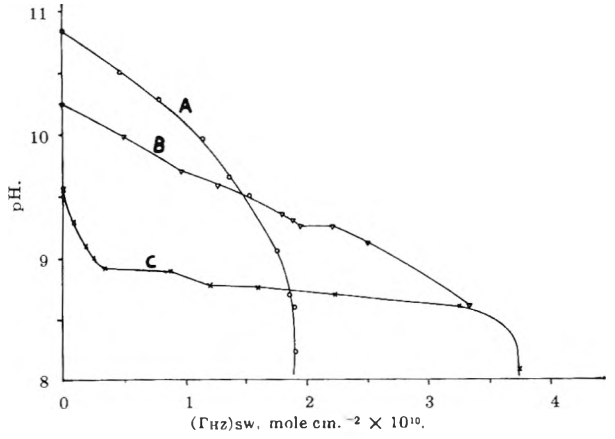

Figure 1. Adsorption of fatty acid at the calcium palmitate–solution interface against pH of solution. A: No surfactant present; $[K^+]$ = 10 mmoles/l., $[Ca^{2+}]$ = 0.29 mmole/l. B: In the presence of 4.48 mmoles/l. potassium lauroylmethyltaurate; $[K^+]$ = 18 mmoles/l., $[Ca^{2+}]$ = 0.51 mmole/l. C: In the presence of 0.31 mmole/l. ethoxylated lauryl alcohol; $[K^+]$ = 12 mmoles/l., $[Ca^{2+}]$ = 1.24 mmoles/l.

total amount of water and calcium palmitate present in the equilibrium slurry, all calcium palmitate was again collected, washed, dried, and weighed at the end of the experiment. The results obtained are collected in Table I.

In the presence of scum dispersants, accurate determination of the calcium ion concentration in the equilibrium liquid is often impossible, because of deflocculation of a small part of the Ca palmitate crystals to an extremely fine dispersion that cannot be separated off. In some cases, the calcium ion concentration found exceeds that of the original solution; this must be due to small amounts of calcium ion liberated by the plugs. The data show that the measurements can be combined in pairs in which the square root of the Ca^{2+} concentration was sufficiently constant, so that its contribution could be neglected in applying eq. 7 or 8.

The results of the measurements of the adsorption of fatty acid at the calcium palmitate–solution interface by means of titration are given in Fig. 1.

It must be noted that the adsorption values obtained by this method are only rough estimates. The large increase in fatty acid adsorption on adding dispersants at not too high pH values may be assumed to be a real effect and was found in all experiments. It explains the observations of Lottermoser and Flammer,[10] that the addition of taurate solutions to calcium soap dispersion increases the pH of the solution since an increase of the fatty acid adsorption will liberate a corresponding quantity of OH^- ions in the solution.

Discussion

On introducing the values given in Table I into formulas 7 or 8, the changes in the various adsorptions due to the transition aqueous solution–air are obtained. All activity coefficients of the ionic species were calculated using the simplified Güntelberg formula.[11] All ionized buffer ions were assigned a single negative charge; this was found to yield correct results in earlier investigations.[1] The results are collected in Table II. This table shows positive values for $(\Gamma_{SA} - \Gamma_{SL})$ both in the case of potassium ion adsorption and in the case of fatty acid adsorption.

(10) A. Lottermoser and H. F. Flammer, *Kolloid-Beih.*, 45, 359 (1937).
(11) G. A. Solomin, *Gidrokhim. Materialy*, 28, 1230 (1959).

This means that the adsorption of both these components increases when the solid falls dry.

Absolute values of the K^+ adsorption at the SW interface were roughly estimated by applying Stern's theory[12] to the electrophoretic data reported in Table I. Assuming that the measured ζ-potentials are equal to the potential in the Stern layer,[5] it follows that the values of $(\Gamma_K)_{SW}$ are about 0.5 to 1 $\times$ 10^{-10} mole/cm.^{2}.

If we still take into account the estimated values of the fatty acid adsorption (2×10^{-10} mole/cm.^{2}) at the solid–solution interface, it follows that at the air–solid interface these adsorptions become, respectively, $(\Gamma_K)_{SA} = 3.3 \times 10^{-10}$ mole/cm.^{2}, and $(\Gamma_{HP})_{SA} = 5.8 \times 10^{-10}$ mole/cm.^{2}. This implies that under the conditions of our experiments the surface of the calcium palmitate crystals against air is completely covered with a monolayer strongly resembling acid soap. Thus, the surface properties, *e.g.*, the properties determining the wetting of dry calcium palmitate should be comparable to those of acid potassium palmitate crystals. It has been noted that, compared with calcium soaps, acid potassium soaps are flotated very readily by air.

For the rewetting process a reaction at the three-phase boundary air–water–solid is required, in which most of the H^+ ions and K^+ ions at the surface are replaced by Ca^{2+} ions. If the Ca^{2+} concentration in the aqueous phase is low, this process will proceed only slowly since it will be governed by the diffusion velocity of the Ca^{2+} ions toward the three-phase boundary. It was observed qualitatively that wetting of dry Ca palmitate is improved on increasing the Ca^{2+} concentration of the solution.

Moreover, the H^+ ions liberated on wetting the Ca palmitate will tend to lower the pH locally at the three-phase boundary, thus increasing the contact angle and making wetting more difficult (*cf.* Table I). In analogy to the adsorption of potassium ions and fatty acid at the surface of aqueous carboxylate soap solutions, the fatty acid adsorption at the SA interface increases on lowering the pH.

At sufficiently low pH values, the Ca soap surface is probably completely covered by a fatty acid monolayer and the contact angle will become obtuse.

The most conspicious result of the presence of the dispersant is the far lower change of the fatty acid adsorption during transition of the Ca soap from water to air. However, the low value of $(\Gamma_{HP})_{SA} - (\Gamma_{HP})_{SW}$ does not imply a low level of fatty acid adsorption. As is seen from the value of $(\Gamma_{HP})_{SW}$ in Table II, the presence of the dispersant markedly increases the fatty acid adsorption at the SW interface. Therefore, the dispersant appears to reduce the differences in composition of the SA and SW interfaces. The greater similarity of these interfaces will reduce any hysteresis effects during wetting and dewetting.

However, the presence of dispersant does not markedly decrease the contact angles. In the presence of potassium lauroylmethyltaurate the contact angles are in the range of 73°, and in the presence of ethoxylated lauryl alcohol, between 80° and 73°, which are only slightly lower than the values obtained in the absence of dispersants.

In the presence of 1,2-bis(methylsulfinyl)dodecane no change in fatty acid adsorption at the Ca palmitate interface can be discovered on replacing the aqueous phase by air.

Conclusion

It follows from the discussion given above, that the influence of detergents on the wetting of calcium palmitate can be correlated with their influence on the equilibrium surface composition of this solid. It must, however, be realized that, in practice, wetting and dewetting frequently occur under conditions of non-equilibrium. Then, dynamic effects must be taken into account, which must be studied separately and may considerably influence the effectiveness of a given scum dispersant.

Acknowledgment. Thanks are due to Dr. J. R. Nooi for the synthesis of bis(methylsulfinyl)dodecane.

(12) F. van V. Vader, *Proc. Intern. Congr. Surface Activity, 3rd Cologne*, 2, 276 (1960).

Surfactant Adsorption at the Solid–Liquid Interface—Dependence of Mechanism on Chain Length

by P. Somasundaran, Thomas W. Healy, and D. W. Fuerstenau

Department of Mineral Technology, University of California, Berkeley, California *(Received April 20, 1964)*

At low concentrations, alkylammonium ions affect the ζ-potential of quartz in nearly the same way as do sodium ions; at a certain concentration of alkylammonium ions there is a sudden change in the electrokinetic potential. This has been attributed to the formation of "hemimicelles" or two-dimension aggregates of the long chain ions. As in micelle formation, the cohesive or van der Waals interaction between hydrocarbon chains reduces the work of bringing the polar groups together into aggregates at the solid–liquid interface. We have measured the ζ-potential–concentration curves for quartz in the presence of alkylammonium acetates of chain length from 10 to 18 carbons. From the variation with chain length of the concentration of surfactant at zero ζ-potential, it is possible to determine the value of the van der Waals cohesive energy. Our value of $0.97kT$ or 580 cal./mole, in good agreement with literature values, substantiates the hemimicelle hypothesis and strengthens the validity of electrokinetic techniques.

Introduction

In a previous publication,[1] evidence was presented for the occurrence of lateral interaction between hydrocarbon chains of alkylammonium ions adsorbed at the quartz–aqueous solution interface. It was concluded that in dilute solutions alkylammonium ions are adsorbed as individual ions; once the adsorbed ions reach a certain critical concentration at the solid–liquid interface, they begin to associate into two-dimensional patches of ions in much the same way as they associate into three-dimensional aggregates to form micelles in bulk solution. The forces responsible for this association at the surface will be the same as those operating in the bulk, except that coulombic attraction for the surface adsorption sites will aid the association.

Because of the proposed appearance of these adsorbed surfactant ions, the patches of associated ions have been termed "hemimicelles."[2] The critical concentration at which the association is observed is referred to as the hemimicelle concentration, C_{HM}, in moles/liter. Electrokinetic, adsorption density, contact angle, and flotation-rate data all show an abrupt change in behavior at the hemimicelle concentration. Such correlation of interfacial parameters has been demonstrated for the system quartz–dodecylammonium acetate, both in terms of the pH effect[3] and in terms of the effect of the concentration of dodecylammonium acetate at fixed pH.[4] Contact angle studies by Zisman for the adsorption of amines and carboxylic acids on platinum[5] also suggest that lateral interaction between adsorbed surfactant species takes place at a certain critical concentration.

The adsorption isotherm of alkyl surfactants at the solid–water interface for such solids as silica and alumina, while not extensively investigated, does show a general pattern[6–8]; the isotherm consists of two regions which join at a distinct point which we have termed

(1) D. W. Fuerstenau, *J. Phys. Chem.*, **60**, 981 (1956).

(2) A. M. Gaudin and D. W. Fuerstenau, *Trans. AIME*, **202**, 958 (1955).

(3) D. W. Fuerstenau, *ibid.*, **208**, 1365 (1957).

(4) D. W. Fuerstenau, T. W. Healy, and P. Somasundaran, *ibid.*, in press.

(5) E. G. Shafrin and W. A. Zisman, in "Monomolecular Layers," H. Sobotka, Ed., American Academy of Arts and Sciences, Washington, D. C., 1954, p. 129.

(6) P. L. deBruyn, *Trans. AIME*, **202**, 291 (1955).

(7) K. Shinoda, *et al.*, "Colloidal Surfactants," Academic Press, New York, N. Y., 1963, Chapter 3.

(8) M. J. Jaycock and R. H. Ottewill, *Bull. Inst. Mining Met.*, **73**, 497 (1963).

the "hemimicelle concentration." Adsorption is more extensive for concentrations greater than the hemimicelle concentration. No quantitative description of the adsorption process has been presented that accounts for the break in the isotherm and the concomitant change in slope.

In the investigation reported in this paper, quantitative evidence of the occurrence of lateral interaction between adsorbed alkyl surfactant ions, *i.e.*, hemimicelle formation at the solid–liquid interface, has been obtained from determinations of the effect of chain length on the electrokinetic potential of silica in aqueous solutions of alkylammonium acetates. Based on the Stern–Grahame model of the electrical double layer, it has also been possible to examine the range of application of ζ-potential data and to use these data to interpret certain properties of adsorption isotherms for the system silica–dodecylammonium acetate at neutral pH.

Theory

For the examination of the effects of surfactant species at solid–liquid interfaces, the following model of the electrical double layer will be applied. Hydrogen and hydroxyl ions are potential-determining ions for silica,[9-11] and the surface charge of silica might be considered to result from adsorption–dissociation of water molecules at broken silicon–oxygen bonds, depicted schematically as

$$\text{–Si–OH}_2^+ \overset{H^+}{\rightleftharpoons} \text{–Si–OH} \overset{OH^-}{\rightleftharpoons} \text{–Si–O}^- + H_2O$$

Let the closest approach of positive counterions to this negative surface be at the plane distance δ out from the surface. In accordance with the Stern–Grahame model, the diffuse layer charge can be expressed by the exact form of the Guoy–Chapman equation for the potential at plane δ, *i.e.*, ψ_δ. The diffuse layer charge, expressed as charge within a column out from the plane δ and of unit area of cross section, is given by

$$\sigma_d = -\sqrt{\frac{2\epsilon kT}{\pi}}\sqrt{n_0}\sinh\left(\frac{Ze\psi_\delta}{2kT}\right) \qquad (1)$$

where ϵ is the dielectric constant, k is Boltzmann's constant, T is the absolute temperature, Z is the valence including sign, e is the electronic charge, and n_0 is the number of ions/cc. in the bulk. For 1–1 valent electrolytes, the adsorption density of positive counterions, expressed as moles/cm.^{2} of surface at 25°, eq. 1 becomes

$$\Gamma_d^+ = 6.1 + 10^{-11}\sqrt{C}[(\exp -19.46\psi_\delta) - 1] \qquad (2)$$

where ψ_δ is in volts and C is the bulk concentration in moles/cm.^{3}.

Grahame's treatment of the compact double layer,[12] based on Stern's original concept,[13] leads to an expression for the adsorption of positive counterions at the plane δ, which is of the form

$$\Gamma_\delta^+ = 2rC\exp(-W_\delta/kT) \qquad (3)$$

where r is the radius of the adsorbed ion at the plane δ and W_δ is the work to bring the ion from the bulk of the solution up to the plane δ. For the purposes of this paper it is unnecessary to subdivide the plane δ into inner and outer Helmholtz planes as does Grahame in his detailed treatment of the double layer.[12]

The work W_δ can be divided into electrostatic and chemical work terms, so that for cation adsorption

$$W_\delta = Z_+e\psi_\delta - \phi \qquad (4)$$

where for the case of adsorption of alkyl surfactants, such as dodecylammonium ion, ϕ is the van der Waals energy in units of kT associated with removal of the alkyl chain from its aqueous environment. For an alkyl chain of n carbon atoms, assuming that

$$\phi/kT = n\phi'/kT$$

then ϕ' is the van der Waals energy of interaction per CH_2 group between adjacent chains of adsorbed surfactant molecules. This interaction takes place at the bulk concentration referred to as the hemimicelle concentration, $C = C_{HM}$, by analogy to the critical micelle concentration of surfactant solutions. At surface coverages where this association between the chains takes place, the adsorption isotherm, for $C > C_{HM}$, is described by

$$\Gamma_\delta^+ = 2rC\exp(Z_+e\psi_\delta - n\phi')/kT \qquad (5)$$

Equations 5 in logarithmic form can be differentiated to give

$$\frac{d\ln\Gamma}{d\ln C} = \frac{d\ln\Gamma_\delta^+}{d\ln C} = 1 - \frac{dy}{d\ln C} + \frac{\phi'}{kT}\left(\frac{dn}{d\ln C}\right) \qquad (6)$$

where Γ is the experimental value of the adsorption density and

(9) E. J. Verwey, *Rec. trav. chim.*, **60**, 625 (1941).

(10) D. J. O'Connor and A. S. Buchanan, *Trans. Faraday Soc.*, **52**, 397 (1956).

(11) A. M. Gaudin and D. W. Fuerstenau, *Trans. AIME*, **202**, 66 (1955).

(12) D. C. Grahame, *Chem. Rev.*, **40**, 441 (1947).

(13) O. Stern, *Z. Elektrochem.*, **30**, 508 (1924).

$$y = \frac{Z_+ e\psi_\delta}{kT}$$

The differential ($dn/d \ln C$) expresses the fact that the effective number of carbons that can be removed totally from an aqueous environment by hydrocarbon chain association increases as the surface coverage increases. At the C_{HM}, the effective value of n is zero; at a monolayer, $n = 12$ for dodecylammonium acetate. That the effective value of n increases linearly with $\ln C$ over this range has been verified by Fuerstenau and Modi for alkyl sulfates at the alumina–water interface.[14]

If after association of the alkyl chains the potential is reduced to zero, it follows from eq. 5 that

$$\ln C_0 = -n(\phi'/kT) - \ln (\Gamma_\delta{}^+)_0 - \ln 2r \quad (7)$$

where $C = C_0$ at $\psi_\delta = 0$. If the ratio of the adsorption density at $\psi_\delta = 0$ to the factor $2r$ is relatively independent of chain length, then the natural logarithm of the concentration of alkyl surfactant ions at $\psi_\delta = 0$ should be a linear function of the alkyl chain length with a slope equal to $-\phi'/kT$.

In obtaining the above equations, no simplifying assumptions have been made other than to assume the Stern-Grahame model of the double layer. The potential ψ_δ is the potential of the Stern layer, and for successful use of eq. 6 and 7, an estimate of ψ_δ is required. A convenient measure of the potential at plane δ is the electrokinetic or ζ-potential, defined as the potential at a plane (or layer[15]) at which shearing occurs within the double layer. We feel that ζ-potential studies can be used to interpret these phenomena because (1) the potential difference between plane δ and the shear plane is small compared to the total potential difference across the double layer, provided the ionic strength is less than about 10^{-1} M and (2) ζ-potentials, when expressed as a change in ζ with respect to a change in some other parameter as illustrated by eq. 6, do in fact give agreement between theory and experiment. These agreements will be presented later in the paper. The following formal substitutions are suggested

$$\frac{d\psi_\delta}{d \ln C} \equiv \frac{d\zeta}{d \ln C} \quad (8)$$

in eq. 6, and in eq. 7

$$\left(\frac{d\psi_\delta}{dn}\right)_{\zeta=0} = 0 \quad (9)$$

Equation 9 can similarly be expressed as: at $\zeta = 0$ (*i.e.*, experimentally observed), there is no change in ψ_δ with change in chain length of the adsorbed surfactant. If $\psi_\delta = 0$, then ζ must be zero, and there is probably negligible error involved in assuming that at low ionic strengths ψ_δ is zero when ζ is zero.

Experimental

Brazilian quartz, 48 × 65 and 28 × 35 mesh, was used in this investigation. It was prepared by leaching with concentrated hydrochloric acid, washing free of chloride ions, and then stored in distilled water. The alkyl amines were obtained from Armour Industrial Chemical Co., Chicago, Ill. All amines were dissolved in ether anhydrous, then added to the equimolar quantity of glacial acetic acid, and the acetate obtained was recrystallized from ether anhydrous, dried at room temperature in a desiccator, and stored in a cool place. The conductivity water used for making reagent solutions was prepared in a quartz still from laboratory distilled water. Conductivity was less than 8×10^{-7} ohm^{-1} cm.$^{-1}$. The water was stored and dispensed in a carbon dioxide-free atmosphere. All measurements were conducted at pH values ranging from 6.5 to 6.9.

The apparatus used for streaming potential studies[16] is based on the same principles and assembly described earlier with few modifications. The cell assembly mainly consists of a porous plug filled with 48 × 65 mesh quartz particles. A layer of 28 × 35 mesh particles placed at the two ends prevents any of the 48 × 65 mesh particles from passing through the holes in the electrode. The potential developed is fed into an E-H Laboratory Model 215 electrometer, with an input impedance in excess of 10^{14} ohms, and the output is fed to a Beckman recorder (Type 93500) through a Cahn recorder control. For measurements of resistance less than 10^5 ohms, a General Radio Co. (Type 1650-A) impedance bridge was used. For measurements of higher resistances, a precision resistor of resistance approximately equal to that of the test solution was placed in parallel with the electrodes. The resistance of the plug with the test solution is then given by the relation

$$R_1 = R_2 \frac{E_1 - E_2}{E_2} \quad (10)$$

where R_1 is resistance of plug with the test solution, R_2 is the known resistance, E_1 is the streaming potential without using R_2, and E_2 is that with R_2 in parallel. A correction for variation of dielectric constant of the

(14) H. J. Modi and D. W. Fuerstenau, *J. Electrochem. Soc.*, 106, 336 (1959).

(15) J. Lyklema and J. Th. G. Overbeek, *J. Colloid Sci.*, 16, 501 (1961).

(16) D. W. Fuerstenau, *Mining Eng.*, 8, 834 (1956).

medium with temperature, even though small, was made. The formula used in calculating ζ-potentials after applying the correction is

$$\zeta = [9.69 + 0.05(t - 25)] \times 10^4 \frac{E\lambda}{P} \text{ (mv.)} \quad (11)$$

where ζ is ζ-potential in mv., t is temperature of the solution in °C., E is the streaming potential in volts, P is the driving pressure in cm., and λ is the specific conductivity of the solution in ohm^{-1} cm.$^{-1}$.

Results

The ζ-potential–concentration curves for quartz in the presence of long chain amines at pH 6.5–6.9 and at 22–25° are given in Fig. 1 for alkyl chain lengths from 10 to 18 carbon atoms. Included in this figure is the ζ-potential–concentration curve for quartz in the presence of ammonium acetate under the same conditions.

All alkylammonium ions change the sign of the ζ-potential, but ammonium ion itself does not. The effect of increase in alkyl chain length is to lower successively the hemimicelle concentration, *i.e.*, the bulk concentration at which van der Waals interaction takes place between adsorbed ions at the solid–liquid interface.

For comparison, the critical micelle concentrations for the alkylammonium acetates are C_0, 4×10^{-2} M; C_{12}, 1.3×10^{-2} M; C_{14}, 4×10^{-3} M; C_{16}, 8×10^{-4} M; and C_{18} 3×10^{-4} M. All major changes in the electrokinetic curves occur at concentrations far below the respective c.m.c. values.

Discussion

The concentration C_0, at which the ζ-potential is reduced to zero is plotted in Fig. 2 as a function of the alkyl chain length (n) of the ammonium acetate. The linear relation between log C_0 and n as predicted by eq. 7 is verified; the slope of this line in terms of the van der Waals cohesive energy per CH_2 group is $0.97kT$ or 580 cal./mole. This value is in excellent agreement with values of ϕ' determined from solubility data[17] or from studies of micelle formation as a function of alkyl chain length of monofunctional surfactants.[18,19] Values of ϕ' determined from properties of surfactant solutions vary from 1.0 to $1.1kT$. That an acceptable value of ϕ' has been obtained from this analysis is substantial evidence in favor of the hemimicelle hypothesis. It is the operation of this van der Waals interaction energy that is the fundamental postulate of the hemimicelle theory. It is significant that the value of ϕ' obtained for hydrocarbon chain association at a solid–liquid interface is slightly less than the usual

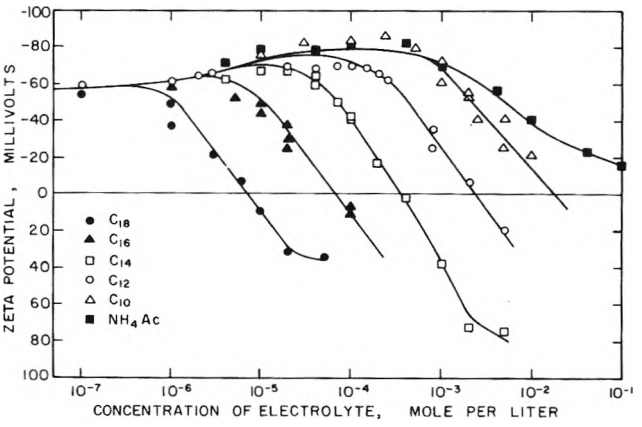

Figure 1. Effect of hydrocarbon chain length on the ζ-potential of quartz in solutions of alkylammonium acetates and in solutions of ammonium acetate.

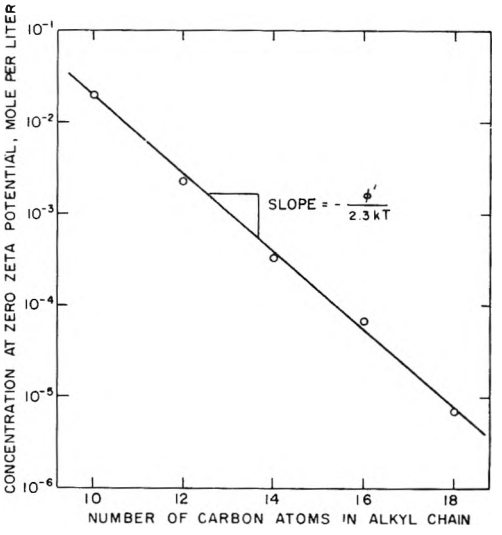

Figure 2. Variation of the concentration of alkylammonium acetate at zero ζ-potential as a function of alkyl chain length.

value of 600–625 cal./mole deduced from micelle phenomena. This is probably due to the fact that complete association into a hydrocarbon liquid state is precluded on steric grounds for hemimicelles, since van der Waals interaction is restricted to two dimensions.

The observed linear relationship between the logarithm of the concentration of surfactant at $\zeta = 0$ and the chain length (eq. 7 and Fig. 2) means that $(\Gamma_\delta^+)_0/2r$ is independent of chain length, where $(\Gamma_\delta^+)_0$ is the adsorption density of cations at plane δ at $\zeta = 0$ and $2r$

(17) A. W. Ralston, "Fatty Acids and Their Derivatives," John Wiley and Sons, Inc., New York, N. Y., 1948.

(18) D. Stigter and J. Th. G. Overbeek, *Proc. 2nd Intern. Congr. Surface Activity London*, 1, 311 (1958).

(19) K. Shinoda, *Bull. Chem. Soc. Japan*, 26, 191 (1955); *J. Chem. Phys.*, 58, 1136 (1954).

is the volume of charge at unit cross-sectional area through plane δ. This finding implies that the electrostatic contribution to the energy of adsorption is located entirely within the charged polar head of the surfactant ion and is not affected by hydrocarbon chain association. Use of eq. 5, other than in differential form, would therefore require the value of the radius of the charged polar head group and not the "radius" of the whole surfactant molecule. A possible cancelling of the effect of $(\Gamma_\delta{}^+)_0$ and $2r$ should not be overlooked and will have to be evaluated in subsequent research.

Use of eq. 6 requires estimates of both the hemimicelle concentration and the concentration corresponding to monolayer coverage. Location of the hemimicelle concentration is partly obscured by the interference of surface conductance effects which, for example, are responsible for the maximum in the ζ–log C data of Fig. 1. Surface conductance effects that are observed in streaming potential experiments on porous plugs are not observed if the experiments are carried out in capillary systems. The validity of the extrapolation of the alkylammonium curves up to the ammonium acetate curve to locate the hemimicelle concentration has been discussed by Davies and Rideal.[20]

The present electrokinetic data for the system quartz–dodecylammonium acetate leads to a value for the slope of the logarithmic adsorption isotherm for $C > C_{HM}$ of approximately 2.5–3.0 to be compared with the experimentally determined value of 1.6–2.3.[6] The C_{HM} values obtained from the previous adsorption data and the present electrokinetic experiments are 1.5×10^{-4} M and approximately 10^{-4} M DDA, respectively. Notice that at low surface coverages before association of the alkyl chains, Guoy–Chapman theory, eq. 1, predicts a maximum limiting slope for the logarithmic adsorption isotherm of 0.5, but as the potential changes with concentration and approaches $C = C_{HM}$, the slope will become less than 0.5.

These agreements between the experimentally determined adsorption parameters and those deduced from ζ-potentials with the aid of Stern–Grahame double layer theory are of considerable interest. Primarily, they strengthen the assumption of the equivalence between changes in ζ and changes in ψ_δ and, therefore, of the utility of electrokinetic results when analyzed in terms of differential quantities.

The above model of the adsorption process of alkyl surfactants can be considered appropriate for systems where the adsorption is purely physical adsorption. Alkylammonium ions on quartz fulfill this condition. Cases where the adsorption is clearly a chemisorption phenomena, where besides the van der Waals contribution to the work of adsorption there is a specific chemical interaction term, will require a more detailed treatment. Such systems as oleate on hematite appear to be of this category.

Acknowledgments. The authors wish to thank the National Science Foundation, Washington, D. C., for support of this work, and Armour Industrial Chemical Company for the high-purity amines used in this investigation.

(20) J. T. Davies and E. K. Rideal, "Interfacial Phenomena," 1st Ed., Academic Press, New York, N. Y., 1961, p. 121.

A Study of the Surface pH of Micelles Using Solubilized Indicator Dyes

by Pasupati Mukerjee[1] and Kalyan Banerjee

Department of Physical Chemistry, Indian Association for the Cultivation of Science, Calcutta 32, India *(Received April 16, 1964)*

Attempts have been made to determine H^+ concentrations at the surface of micelles using indicator dyes, bromophenol blue and bromocresol green. In the presence of cationic micelles, the dyes are incorporated almost exclusively in the micelles, presumably with the hydrophilic groups exposed at the surface and the hydrophobic parts buried. The apparent indicator constants (K_a) for the surface, in terms of the average $[H^+]$ of the system, have been determined for cationic micelles of three chain lengths at several ionic strengths, two counterions (Cl^- and Br^-), and two temperatures. The distribution of bromophenol blue between the anionic micelles of sodium lauryl sulfate and the bulk has also been investigated and the surface pK_a estimated. The differences between the bulk and surface pK values have been interpreted in terms of the electrical potential difference and changes in the intrinsic pK (pK_i) of the dye. Potential values intermediate between the Gouy–Chapman surface potentials and the electrokinetic potentials seem to be needed, as expected for the surface from recent theories. The surface pK_i seems to be higher than the bulk value, the difference increasing with increasing charge density of the micelles. This effect is ascribed to the lowering of the effective dielectric constant at the surface. The change in pK_a with micellar concentration can be explained satisfactorily by the negative adsorption from the surface, in fair quantitative agreement with theoretical predictions. The pK_a varies linearly and substantially with the mole fraction of counterions. The effect is ascribed to different charge densities on the micelles and the larger effect of Br^- on the decrease of the effective dielectric constant at the surface.

Introduction

Micelles of association colloidal electrolytes (ACE), because of the comparatively high purity attainable for these systems and their thermodynamic stability, provide excellent model systems for studying colloid chemical phenomena in general. The possibilities of using micelles as models for ionized monolayers are less appreciated. Although there are problems associated with the difficulties of varying the charge density at will and the curvature of the monolayer, these are more than offset in some cases by the reproducibility and attainable purity of the interface, and the use of some of the more reliable experimental techniques easily applicable to bulk solutions containing micelles but difficult for ordinary interfaces.

The present study deals with the use of solubilized indicator dyes to determine the surface pH of micelles, as originally suggested by Hartley and Roe.[2a,b] Spectrophotometric methods are applicable such that apparent indicator constants (K) can often be determined to within 1–2%, corresponding to a variation in the apparent pH or pK (pK_a) by 0.005–0.01. If the pK_a values can be related to changes in the potential at the surface, 0.01 in pK_a corresponds to a 0.6 mv. change in the potential.

The interpretation of the surface pH data involves, on the one hand, the evaluation of the theories of double layers leading to predictions of the potentials, and, on the other hand, the change, if any, in the intrinsic pK (pK_i) from the bulk value ($pK_{i(b)}$) to its value at the surface of micelles ($pK_{i(s)}$). The problems are thus closely related to the analysis of titration curves of proteins and polyelectrolytes. Unlike most

(1) Department of Chemistry, University of Southern California, Los Angeles, Calif. 90007.

(2) (a) G. S. Hartley and J. W. Roe, *Trans. Faraday Soc.*, **36**, 101 (1940); (b) J. T. Davies and E. K. Rideal, "Interfacial Phenomena," Academic Press, New York, N. Y., 1961.

of the latter types of study, the work reported here is in terms of concentrations of H^+ rather than the electrometric pH. The corrections due to activity coefficients are quite uncertain for surfaces, particularly for high potentials. They can be introduced, however, when desirable.

Experimental

Materials. The cationic association colloids studied were lauryl trimethylammonium chloride (LTAC), the corresponding bromide (LTAB) and the myristyl (MTAB) and cetyl (CTAB) homologs of the latter. The bromide salts were pure preparations donated by Deosan Ltd., London. LTAC was a pure sample obtained from Armour and Co., Chicago, Ill.

The sodium lauryl sulfate (NaLS) used was a highly purified preparation donated by Prof. K. J. Mysels of the University of Southern California.

The indicator dyes were the sulfonphthalein dyes bromophenol blue (BPB) and bromocresol green (BCG) obtained from the British Drug Houses Ltd.

Apparatus. Absorbance measurements were done in a Hilger spectrophotometer with a thermostated cell chamber. The temperature was controlled to within 0.2–0.5°.

Experimental Procedure. Absorbances were measured at the band maxima determined for each system. The dye concentration was usually in the range 2–3 $\times 10^{-5}$ M. The absorbances of the yellow (Y^-) and the blue (B^{-2}) forms of the dye were used to calculate R, the ratio of $[Y^-]$ and $[B^{-2}]$ by using the relative molar extinction coefficients. KCl or KBr were used for varying ionic strengths and HCl and HBr for varying $[H^+]$ for the cationic ACE's containing Cl^- or Br^-, except when the counterion composition was varied intentionally.

Results

K_a Values for Cationic ACE's at the C.m.c. The apparent indicator constant K_a is defined as $[H^+]/R$, where $[H^+]$ is the average value for the solution. At a constant ionic strength and constant concentration of the cationic ACE, the R values varied linearly with H^+ concentration. K_a was usually determined at three to seven different $[H^+]$ values. The average variation in K_a was in the range 0.6–3%.

The concentration of the ACE in the micellar form, *i.e.*, in excess of the estimated critical micelle concentration (c.m.c.), in the measurements where the concentration variation of the ACE was not explicitly studied, was 0.2–0.4%. Thus, several micelles were present per dye ion. The finite concentration of micelles had a measurable effect on pK_a. The pK_a values were corrected to the c.m.c. (infinite dilution of micelles) on the basis of the interpretation of the concentration variation studies on CTAB in terms of negative adsorption (see later), and assuming that the other systems behave like CTAB in this regard. Since the maximum correction to pK_a was about 0.04 for systems other than CTAB, it is expected that the uncertainty of the ACE concentration correction is negligible.

Table I summarizes the pK_a values (corrected to the c.m.c.) for the various systems. The ionic strengths (μ) were calculated by adding the estimated c.m.c. to the concentration of the potassium salts added. There are occasional large discrepancies between the c.m.c. values reported in the literature. Most of the measurements were made at a sufficiently high concentration of added salt such that uncertainties in the estimated c.m.c. are small, as are the effects of any premicellar association. The probable errors in pK_a are indicated in some cases. For the others, it is estimated as ±0.01.

Table I: pK_a Values at the C.m.c.

ACE	Dye	Temp., °C.	μ	pK_a
CTAB	BPB	25	0.0077	2.12
			0.0102	2.22 ± 0.02
			0.0300	2.63
			0.100	3.05
			0.176	3.26 ± 0.02
			0.520	3.67 ± 0.02
			1.05	3.95 ± 0.03
MTAB	BPB	25	0.0121	2.28 ± 0.02
			0.0315	2.64
			0.100	3.00
LTAB	BPB	25	0.0332	2.62
			0.0520	2.77
			0.104	2.98
LTAC	BPB	25	0.0390	2.35
			0.107	2.64
CTAB	BPB	45	0.0077	2.00
			0.0300	2.50
			0.100	2.89
CTAB	BCG	25	0.0102	3.52
			0.0300	3.90
			0.100	4.38
CTAB (0.2%) in 0.1 M KCl	BPB	32	0.100	2.59

At 25°, the measurements for CTAB above μ = 0.1 pertain to possibly super-saturated solutions.[3]

(3) P. Debye and E. W. Anacker, *J. Phys. Colloid Chem.*, 55, 644 (1951).

No precipitation was observed, however, during measurements.

Effect of Micellar Concentration for Cationic Systems. The R values of BPB for fixed over-all $[H^-]$ concentration and added KBr are plotted against the micellar concentration of CTAB in Fig. 1 as R/R_{cmc}. At three ionic strengths and two temperatures, the variation was found to be linear within a scatter of less than 1%

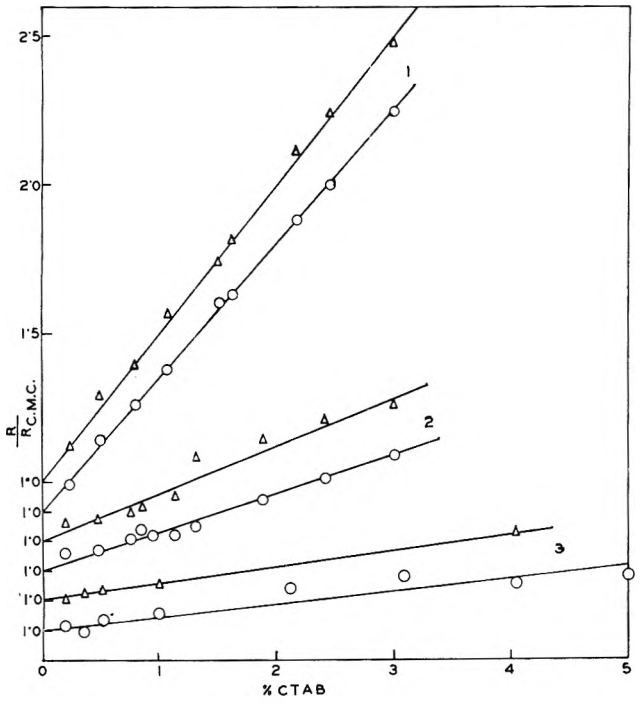

Figure 1. Variation in R with micellar concentration of CTAB: ⊙, 25°; △, 45°; μ_{cmc}: 1, 0.0077; 2, 0.0300; 3, 0.100.

at $\mu = 0.0077$, 2% at $\mu = 0.03$, and 3% at $\mu = 0.1$. Turbidity corrections were applied. The correction on R did not exceed 3%. R_{cmc} values were obtained from linear extrapolations of the R values to the c.m.c.

R Values for NaLS. These are shown in Fig. 2 as a function of the NaLS concentration in the micellar form (*i.e.*, after subtracting the c.m.c.) in sodium acetate–acetic acid buffers at two pH values, adjusted to $\mu = 0.100$ with NaCl. These curves are quite nonlinear.

Effect of Counterion Composition Variation. This was studied by measuring R values for various concentrations of CTAB at constant values of $[H^+]$ and KCl ($\mu = 0.1$). The R values in this case for mixed counterions show a much more pronounced relative change with CTAB concentration (Fig. 3) than for CTAB in KBr (Fig. 1).

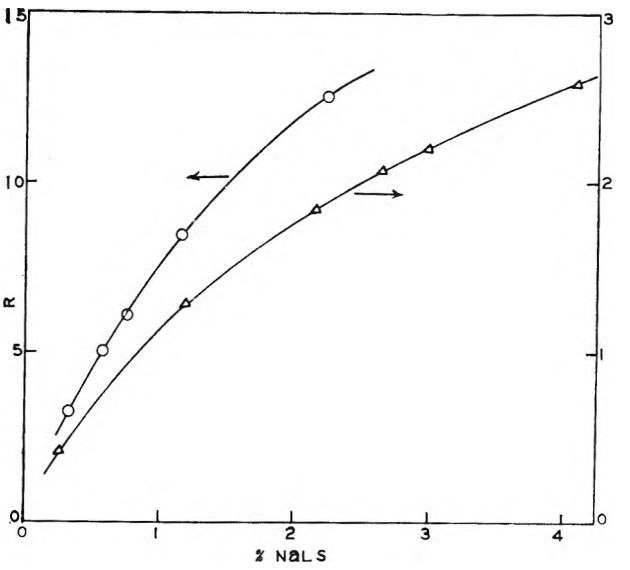

Figure 2. Variation in R with micellar concentration of NaLS in sodium acetate–acetic acid buffer adjusted to 0.100μ with NaCl: O, pH 4.10; △, pH 5.02, temperature 25°.

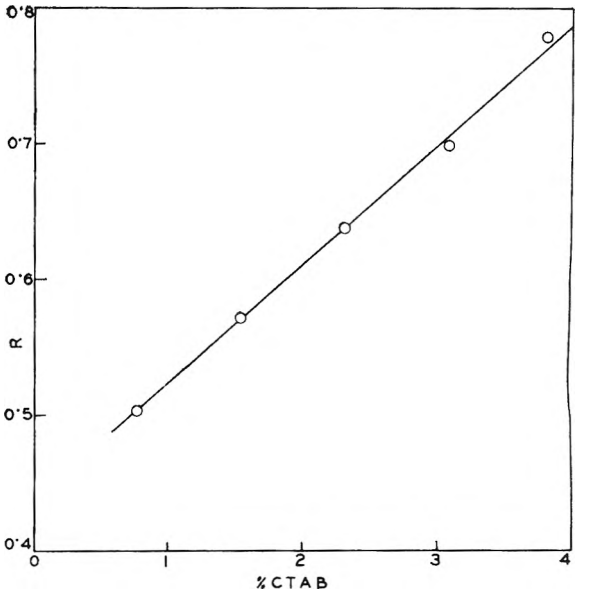

Figure 3. Variation in R with micellar concentration of CTAB in KCl (0.100μ) at 28.5°.

Discussion

The pK_a values are calculated in terms of the over-all $[H^+]$. The H^+ concentration at the surface is different because of the electrical potential difference of the surface with respect to the bulk. The interpretation of the pK_a values involves the equation (for 25°)[2a,b]

$$pK_a = pK_{i(s)} - \psi/59.16 \quad (1)$$

where $pK_{i(s)}$ is the intrinsic pK of the dye at the surface, in the solubilized state, and ψ the appropriate potential, in mv., operative for the plane in which the dissociable –OH groups of the dye are located, assuming that the $[H^+]$ follows the Boltzmann distribution. $pK_{i(s)}$ and ψ are not independently determinable. The interpretation, therefore, involves the evaluation of various estimates with regard to $pK_{i(s)}$ and ψ.

The basic assumption of this work is that the presence of the dye ion in the micelle does not alter its surface properties and the dye can be used as an indicator of these properties. The assumption is expected to be quite sound because of the low concentration of the dye used (one dye for several micelles as a rule) and is supported by the observed similarity of the relative pK_a values at different ionic strengths when two different dyes are used for the same ACE (see later).

It has been shown previously that such low proportions of oppositely charged dye do not affect the conductivity of micelles.[4]

In the case of cationic ACE's, the further assumption is made that, in the presence of micelles, all of the dye is solubilized. This assumption is justified by the following arguments. (1) The solubilities of salts of dyes and detergents of opposite charge in water have been estimated to be very low[4] and the distribution coefficients between micelles and the bulk estimated in some cases are very high.[5] (2) The blue form of BPB is bleached by OH^- ion. In CTAB micelles, the dye is inaccessible to this attack. Duynstee and Grunwald[6] found that under conditions where the pseudo-first-order rate constant in the bulk is 9×10^{-5} sec.$^{-1}$, in the presence of 0.01 M CTAB there is no change in color in 37 hr. The distribution coefficient K_D (vol./vol.) between micelles and the bulk is, therefore, greater than 3×10^5. (3) The K_D value estimated for the yellow form of BPB between NaLS micelles and the bulk is about 1.3×10^3 (see later). For cationic micelles, the electrostatic factor is expected to increase it to above 10^6. At the minimum micellar volume fraction of 0.002 used, less than 0.1% of the yellow form of the dye is expected to be in the bulk and much less of the double-charged blue form. (4) At $\mu = 0.1$, where intermicellar interactions are weak, the R values increase by only about 20% as the CTAB concentration is increased from a value somewhat above the c.m.c. (6×10^{-3} N) to 0.137 N. (See Fig. 1.) For LTAB, the change is about 35% in R as the micellar of LTAB is increased from about 0.008 to 0.159 N. Both of these small changes are, moreover, well explained by negative adsorption from the micelle surface (see later). It seems, therefore, that any variation in the distribution ratio must be small, and the distribution is effectively complete in favor of the micelles.

Ionic Strength Variation and the Effects on ψ and $pK_{i(s)}$. With increasing μ, it is expected that ψ decreases and, therefore, pK_a increases. In the present study, pK_a seems to vary linearly with log μ as shown in Fig. 4 where pK_a – log μ is plotted against log μ, to magnify the deviations. The average deviation from the straight lines is 0.01 unit in pK_a, no deviation exceeding 0.02 unit. For CTAB, the linearity persists to high ionic strengths where very large and rod-like micelles form.[3] The $dpK_a/d \log \mu$ slopes, given in Table II, show a consistent increase with chain length.

Table II: Variations in pK_a with μ

ACE	Dye	Temp., °C.	$dpK_a/d \log \mu$
CTAB	BPB	25	0.85 ± 0.01
MTAB	BPB	25	0.78 ± 0.02
LTAB	BPB	25	0.72 ± 0.03
LTAC	BPB	25	0.66 ± 0.04
CTAB	BCG	25	0.87 ± 0.02
CTAB	BPB	45	0.80 ± 0.02

With CTAB, BCG, and BPB, in spite of the large difference in pK_a, lead to the same value of the slope within experimental error, suggesting that the measured slope is characteristic of the ACE system.

To correlate the variations in pK_a with variations in ψ, the Gouy–Chapman potentials (ψ_G) were estimated from the molecular weight data of Trap and Hermans[7] for the bromides and Kushner, *et al.*,[8] for LTAC, using the numerical tables of Loeb, Wiersema, and Overbeek[9] for the spherical double layers. In these calculations, the molecular weights, uncorrected for charge effects, were used because of the uncertainty of the corrections and because the relevant ionic strengths involved here require substantial contributions from inorganic salts in which case the corrections are small and largely cancel relatively. In the calculations of the micellar radii, the partial molal volumes of the chloride micelles estimated previously[10] were used.

(4) P. Mukerjee and K. J. Mysels, *J. Am. Chem. Soc.*, **77**, 2937 (1955).

(5) E. F. J. Duynstee and E. Grunwald, *ibid.*, **81**, 4542 (1959).

(6) E. F. J. Duynstee and E. Grunwald, *ibid.*, **81**, 4540 (1959).

(7) H. J. L. Trap and J. J. Hermans, *Koninkl. Ned. Akad. Wetenschap. Proc.*, **B58**, 97 (1955).

(8) L. M. Kushner, W. D. Hubbard, and R. A. Parker, *J. Res. Natl. Bur. Std.*, **59**, 113 (1957).

(9) A. L. Loeb, J. Th. G. Overbeek, and P. H. Wiersema, "The Electrical Double Layer around a Spherical Colloid Particle," the M.I.T. Press, Cambridge, Mass., 1961.

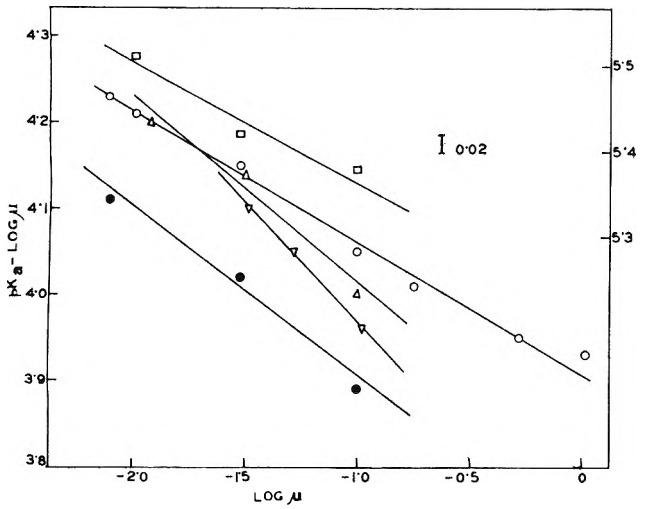

Figure 4. Plots of $pK_a - \log \mu$ *vs.* $\log \mu$: O, CTAB; △, MTAB; ▽, LTAB (all at 25° with BPB); ●, CTAB at 45° with BPB; □, CTAB at 25° with BCG (right-hand ordinate).

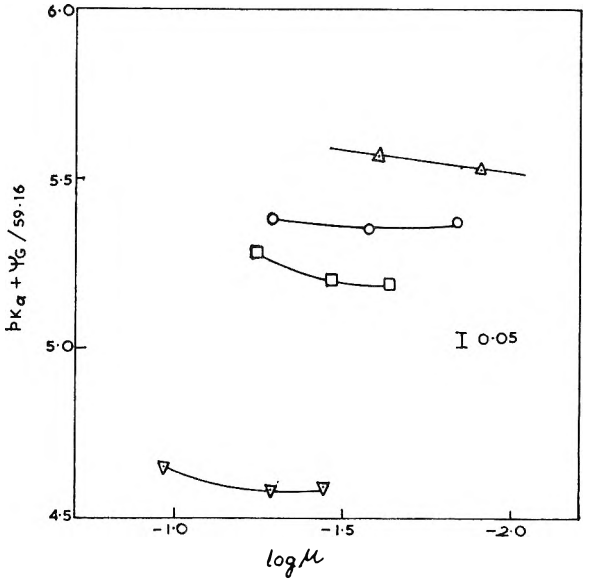

Figure 5. Plots of $pK_a + \psi_G/59.16$ *vs.* $\log \mu$: △, CTAB; ○, MTAB; ⊡, LTAB; ▽, LTAC.

By subtracting the partial molal volumes of Cl^-,[11] neglecting electrostriction effects, the partial molal volumes of the micelles without any counterions were estimated and used to calculate radii and charge densities of micelles without the counterions. The values for CTAB were obtained by extrapolation from the LTAB and MTAB values.

If $pK_{i(s)}$ remains constant when only μ is varied, it is expected from eq. 1 that $-d(\psi/59.16)/d \log \mu$ will equal $dpK_a/d \log \mu$. When $-\psi_G/59.16$ values are plotted against log μ, the curves are somewhat nonlinear and the average slopes are all less than unity, mainly because of the increase in the molecular weight and charge density with μ, and in qualitative agreement with $dpK_a/d \log \mu$ values. The values of the slopes of the ψ_G plots are, however, somewhat smaller in general. This is illustrated in Fig. 5, where $pK_a + \psi_G/59.16$ is plotted against log μ. The variations with μ seem to be barely significant, since errors in molecular weight of 10 and 20% correspond to about 0.033 and 0.066 in $\psi_G/59.16$.

Much more significant are the high values of $pK_a + \psi_G/59.16$, their chain-length dependence, and the dependence on counterions. Clearly, if ψ_G is to replace ψ, $pK_{i(s)}$, which equals $pK_a + \psi_G/59.16$, must vary with chain length, ionic strength, and different counterions. The bulk value, $pK_{i(b)}$, for BPB, was determined to be 4.01 and 3.84 for $\mu = 0.01$ and 0.1 in HBr + KBr systems. Clearly, also, when ψ_G is used for ψ, $pK_{i(s)} > pK_{i(b)}$.

For explanations of surface pH, it has sometimes been suggested that the ζ-potential is the operative one.[2a,b] This seems unlikely in general; the adsorbed dye is likely to remain on the surface in the tightly bound layer rather than on the shear layer. Since the Booth ζ-potentials, not available for the present systems, are usually about 0.55 times ψ_G,[12] the use of ζ-potentials would require much less change in $pK_{i(s)}$ from $pK_{i(b)}$ than ψ_G. But, now, $pK_{i(s)}$ would be less than $pK_{i(b)}$ in many cases, but not in all. This seems physically implausible.

That $pK_{i(s)} \neq pK_{i(b)}$ seems to be established by the constant difference of 1.30 ± 0.02 in the apparent pK_a of BPB and BCG for CTAB at three ionic strengths, as compared to the difference in $pK_{i(b)}$ of 0.77 ± 0.03 over the ionic strengths of 0 to 0.5.[13] The alternative explanation in terms of different placement of the dye with respect to the micellar surface seems unlikely.

That $pK_{i(s)}$ should be greater than $pK_{i(b)}$ seems reasonable if it is accepted that the effective dielectric constant at the micelle surface is lower than the bulk value because of dielectric saturation,[14] the high concentration of ions,[15] and the proximity of the hydrocarbon core of the micelle. An interpretation of the charge-transfer spectra of dodecylpyridinium iodide

(10) P. Mukerjee, *J. Phys. Chem.*, **66**, 1733 (1962).

(11) P. Mukerjee, *ibid.*, **65**, 740 (1961).

(12) J. Th. G. Overbeek and D. Stigter, *Rec. trav. chim.*, **75**, 1264 (1956).

(13) H. T. S. Britton, "Hydrogen Ions," 4th Ed., Chapman and Hall, London, 1955.

(14) F. Booth, *J. Chem. Phys.*, **19**, 391, 1327, 1615 (1951).

(15) M. J. Sparnaay, *Rec. trav. chim.*, **77**, 872 (1958).

micelles, in comparison to ion-pair spectra in various solvents, has recently led to an estimate of 36 for the dielectric constant at the surface.[16] With lowering of the dielectric constant, an increase in pK_i is expected and observed for weak acids.[17] Also, the increase in pK_i is usually greater when pK_i is greater, which may explain the difference between the pK_a values of BPB and BCG as compared to $pK_{i(b)}$ values.

As a corollary of the above explanation, it may be expected that $pK_{i(s)}$ should be greater as the charge density increases at constant μ for the same counterion. This seems to explain most of the chain-length dependence as shown in Fig. 6, where $pK_a + \psi_G/59.16$ is plotted against the charge density. The variation with charge density is quite significant. Although the range covered is small, the expected extrapolation to a value of about 4.0 ($pK_{i(b)}$) at zero charge density is not unreasonable. The ionic strength effect at constant charge density seems to be significant also, but not adequately interpretable at the moment.

In Fig. 6, on any reasonable extrapolation of the line for bromides, a significant difference between LTAB and LTAC remains. It seems that $pK_{i(s)}$ is lower for the chloride than the bromide at the same μ and charge density. Presumably, the larger and the more polarizable Br^- produces a greater lowering of the effective polarity at the micelle surface than Cl^-. Molar decrements in the dielectric constant of water

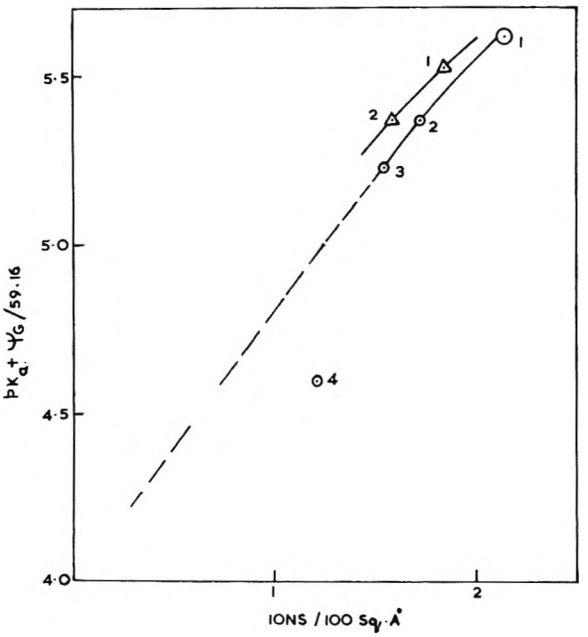

Figure 6. Plots of $pK_a + \psi_G/59.16$ *vs.* charge density. 1, CTAB; 2, MTAB; 3, LTAB; 4, LTAC; ⊙, log μ = −1.40; △, log μ = −1.90; circle for CTAB estimated by extrapolation.

for NaCl and NaI[18] (data do not seem to be available for Br^-) are 11 and 15, respectively, suggesting the influence of the size and polarizability of the cation.

pK_a for NaLS. The discussion above suggests that a $pK_{i(s)}$ value higher than $pK_{i(b)}$ and a ψ-value higher than the ζ-potentials are consistent with the data for cationic ACE's. No conclusion is possible, however, as to how well ψ is represented by ψ_G. A pK_a value for NaLS was estimated to provide some sidelight.

To analyze the variation in R with the micellar concentration of the anionic NaLS, it was assumed that in a well-buffered system of constant bulk pH and μ, and a high value of the latter (μ = 0.1) where intermicellar interactions can be neglected to a good first approximation, ψ remains constant. If the value of R is R_b in the bulk and R_s at the surface, $[H^+]_b/R_s = K_a$. R_b can be experimentally determined in the absence of micelles. To determine R_s, K_D must be estimated. Defining K_D, for the yellow form, as $[Y^-]_m/[Y^-]_b$ where $[Y^-]_m$ is the concentration in the micelles, it can be shown that the experimentally measured R is given by

$$R = \frac{[Y^-]}{[B^{-z}]} = \frac{1 + K_D\varphi_m}{1/R_b + K_D\varphi_m/R_s} \qquad (2)$$

where φ_m is the volume fraction of micelles. Rearranging, we have

$$\frac{R/R_b - 1}{\varphi_m} = K_D - RK_D/R_s \qquad (3)$$

In Fig. 7, the left-hand side is plotted against R at various values of φ_m. A micellar density of 1.1 g./ml. was assumed for calculating φ_m.

The two curves in Fig. 7 for two different values of pH_b are fairly satisfactory straight lines. From the intercepts, the K_D values of 1.13 and 1.52 × 10^3 are obtained. The R_s values from the slopes and the intercepts lead to pK_a values of 5.65 ± 0.07 at pH_b of 4.10 and 5.68 ± 0.02 at pH_b of 5.02. The estimated mean value is 5.67 ± 0.03.

The small difference in the estimated K_D values may be due to various causes, in particular the presence of acetic acid in the buffered systems, which may alter the properties of the micelles. The calculated concentrations of acetic acid, 0.008 and 0.015 *M*, are fairly

(16) P. Mukerjee and A. Ray, to be published.

(17) H. S. Harned and B. B. Owen, "The Physical Chemistry of Electrolytic Solutions," 3rd Ed., Reinhold Publishing Corp., New York, N. Y., 1958.

(18) J. B. Hasted, D. M. Ritson, and C. H. Collie, *J. Chem. Phys.*, 16, 1 (1948).

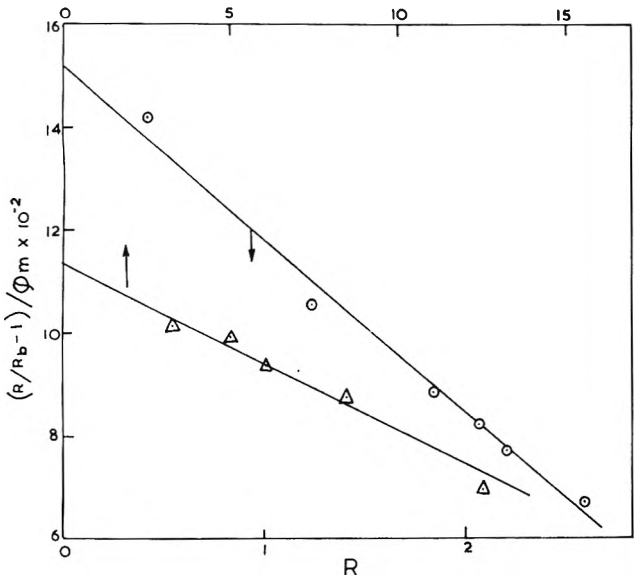

Figure 7. See text: △, pH 4.10; ⊙, pH 5.02.

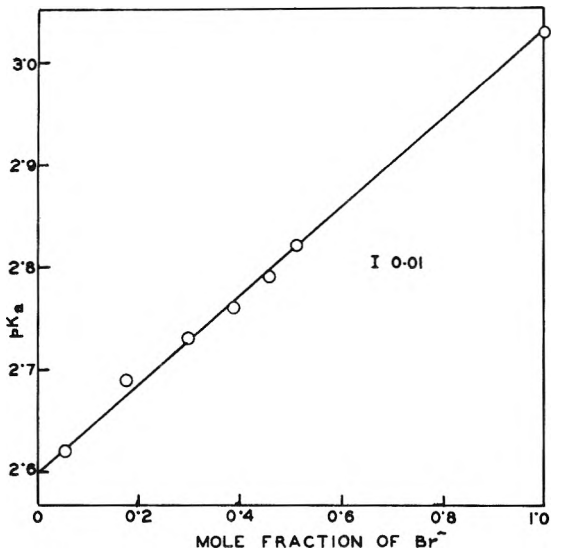

Figure 8. Variation in pK_a in the cetyl (Cl^- + Br^-) system, temperature 28.5°.

small, however, and in view of the small variation in pK_a it is felt that the pK_a values are reliable.

If the $pK_{i(b)}$ value of 3.84 is used for $pK_{i(s)}$ to calculate ψ, the value of NaLS at $\mu = 0.1$ is -108 mv. as compared to the estimated ψ_G of -132 and ζ or -68 mv.[12] A lower value of $pK_{i(s)}$ brings ψ closer to ψ_G and a higher value brings it closer to ζ. The same $pK_{i(s)}$ for LTAC (at $\mu = 0.1$) gives $\psi = 72$ mv. as compared to estimated $\psi_G = 120$ mv. and $\zeta = 64$ mv. A higher $pK_{i(s)}$ here brings ψ closer to ψ_G.

A consistent explanation seems to require that ψ is roughly midway between ψ_G and ζ and $pK_{i(s)}$ is higher than $pK_{i(b)}$. This explanation is in accord with the Stern model and other recent models of the double layer. It is interesting that some recent hydrolysis rate studies of long chain alkyl sulfates at the micellar surface also require potentials intermediate between ψ_G and ζ,[19] for an explanation of the electrostatic effects. The ideas developed in this paper should be of some use in understanding ionic reactions on micelle surfaces.[5,6,20]

It is to be noted that an apparently higher value of $pK_{i(s)}$ may be caused by the partial inaccessibility of the dissociable –OH group of the yellow singly charged form of the dye, if some of the –OH groups are buried inside the micelle. However, this is energetically unlikely, in view of the well-known hydrophilic character of the –OH group. The extrapolation of $pK_{i(s)}$ values to a value close to $pK_{i(b)}$ as the charge density on the micelles tends to zero also argues against the importance of this factor.

Counterion Composition Variation. The effect of the counterion composition variation on pK_a seemed to be of some interest. For this, the micellar concentration variation data with CTAB in 0.1 *M* KCl (Fig. 3) were used, after applying corrections due to negative adsorption (less than 0.07 unit). Independent estimates of pK_a for CTAB in KCl and CTAB in KBr (Table I) were corrected for small temperature differences. The data are plotted in Fig. 8 as a function of the mole fraction of the counterions. The variation is accurately linear over the whole range. The variation in pK_a is caused by the different effects of these ions on the local polarity at the micelle surface and the formation of micelles of different charge densities, as the comparison of LTAB and LTAC micelles have shown. It seems, however, that there is no preference for either of the cations in the intermediate range, indicating little preferential adsorption of the Br^- with respect to the Cl^-.

Negative Adsorption. The linear increase of the *R* values with micellar concentration (Fig. 1) is a strikingly simple result which can be explained qualitatively by the increase in the H^+ concentration of the bulk and its effective ionic strength by negative adsorption from the micelle surface,[9] both factors increasing *R*. To evaluate the extent of negative adsorption, we note that the variation of the $dpK_a/d \log \mu$ (at the c.m.c.) from unity is primarily due to the increase in the molecular weight with higher μ. At a constant overall concentration of the added salt, if the molecular

(19) J. L. Kurz, *J. Phys. Chem.*, **66**, 2239 (1962).

(20) E. W. Anacker, R. M. Rush, and J. S. Johnson, *ibid.*, **68**, 81 (1964).

weight is assumed to remain constant for varying micellar concentration, a value of unity for $dpK_a/d \log \mu$ is a good approximation such that R should vary in the same ratio as μ when $[H^+]$ is constant. At constant μ, similarly, R varies in the same ratio as $[H^+]$. Therefore as C_m, the concentration of micelles in equivalents/liter, increases, μ and $[H^+]$ values of the bulk should both increase by a factor of $1 + \alpha C_m/\mu_{cmc}$ compared to their values at the c.m.c., α being the negative adsorption factor, and R/R_{cmc} should increase by the square of this factor. To evaluate α, therefore, $\sqrt{R/R_{cmc}}$ should be plotted against C_m/μ_{cmc}.

The experimental data at $\mu_{cmc} = 0.0077$ (Fig. 1) are very well represented by straight lines, and R_{cmc} values were chosen by extrapolation on this basis. On plotting the square root of the R/R_{cmc} values, curved lines are obtained and the value of α changes continuously from 0.0635 ± 0.0015 at the c.m.c. to 0.050 ± 0.001 for 3% CTAB. Thus, the negative adsorption factor seems to be somewhat dependent upon the concentration of micelles, but not excessively so. The variation is presumably due to the interaction of the double layers. At the higher values of μ, although the R values are displayed in Fig. 1 as varying linearly with C_m, the scatter of the points does not allow a clear evaluation of the variation of α with C_m except to state that it is smaller than in the case of $\mu = 0.0077$, as expected.

The α-values estimated near the c.m.c. are shown in Table III. The variation with ionic strength is slight, but temperature seems to have an appreciable effect.

Table III: Negative Adsorption Factors at the C.m.c.

ACE	Temp., °C.	μ_{cmc}	α
CTAB	25	0.0077	0.0635 ± 0.0015
	25	0.0300	0.067 ± 0.004
	25	0.100	0.082 ± 0.015
	45	0.0077	0.0705 ± 0.0015
	45	0.0300	0.083 ± 0.005
	45	0.100	0.100 ± 0.015
LTAB	25	0.100	0.095 ± 0.015

To compare the experimental α-values with theoretical predictions, we have calculated α from the tables of Loeb, Wiersema, and Overbeek[9] by using ψ_G and ζ, assumed to be equal to $0.55\ \psi_G$. We have assumed that the shear layers are located 2 Å. away from the surface for ψ_G. The calculated values (25°) for CTAB at $\mu = 0.0125$ and 0.025 are 0.068 and 0.065 using ψ_G and 0.058 and 0.056 using ζ. The agreement is satisfactory considering that the percentage of errors in α is nearly proportional to that in the charge density. The recently published molecular weight of LTAB micelles in 0.1 M NaBr[20] leads to α-values of 0.140 and 0.119 using ψ_G and ζ. The experimental value (Table III) here is somewhat low.

Calorimetric Studies of the Micellization of Dimethyl-*n*-alkylamine Oxides[1]

by L. Benjamin

Miami Valley Laboratories, The Procter and Gamble Company, Cincinnati, Ohio *(Received February 10, 1964)*

Heat of solution measurements have been made with a series of dimethyl-*n*-alkylamine oxides (DC_nAO) in water. The derived partial molal enthalpy values, $\bar{H}_2$, allow estimates to be made of the standard free energies of micellization ($\Delta F_m°$) to furnish the corresponding entropy changes, $\Delta S_m°$. The well-known regular decrease in $\Delta F_m°$ with increasing chain length is seen to be due to a parallel decrease in $\Delta H_m°$ since the entropy of micellization is essentially independent of chain length. The chain lengths studied are C_8, C_9, C_{10}, and C_{12}. Below the critical micelle concentration (c.m.c.) considerable heats of dilution are found with the shorter chain length compounds while $\bar{H}_2$ values are more nearly constant for the C_{10} and C_{12} compounds. In all cases $\bar{H}_2$ is found to be essentially constant above the c.m.c., even up to the point of separation of a mesomorphic phase (30–50% w./w.). The positive values of $\Delta H_m°$ are interpreted in terms of hydrophobic bonding present during micellization. Data obtained for $DC_{12}AO$ in dilute HCl solutions, where the surfactant is cationic, show a negative value for $\Delta H_m°$ and indicate a lower entropy change for the ionic species than for the nonionic species. Comparison with published data for ionic surfactants shows that this is generally true and is interpreted as resulting from the disrupting influence of ionic head groups on the ordering of water around the monomer.

Introduction

Considerable attention has been given in the last decade to a study of the thermodynamics of surfactant solutions, the objective being to understand the factors which govern the formation of micelles. Standard free energies ($\Delta F_m°$) and enthalpies ($\Delta H_m°$) of micellization have been derived from critical micelle concentrations (c.m.c.) and their temperature dependence, respectively. In addition, calorimetric ΔH_m and heat capacity values have been obtained for certain ionic surfactants.[2-5]

It has been concluded from these studies that the entropy increase during micellization contributes largely to the free energy change and overrides the unfavorable enthalpy term. Structural changes in the solvent, associated with loss of hydration of the hydrocarbon chain when the surfactant enters the micelle, are thought to be responsible for the positive $\Delta S_m°$ values, and, thus, micelle formation is partially a result of what has been termed hydrophobic bonding. A statistical mechanical treatment of the latter has recently been presented.[6]

The present work concerns calorimetric measurement of $\Delta H_m°$ values for a homologous series of nonionic surfactants, the dimethyl-*n*-alkylamine oxides (DC_nAO), and the application of such data to the thermodynamics of micellization in these systems. Other calorimetric data are available only for ionic surfactants where interpretation is somewhat complicated by varying electrical interactions.[2-5] Following a consideration of nonionic micellization according to the law of mass action, the experimental data are interpreted particularly in terms of the thermodynamic

(1) Paper presented at the Kendall Award Symposium, Division of Colloid Science of the American Chemical Society, Philadelphia, Pa., April, 1964.

(2) (a) E. D. Goddard and G. C. Benson, *Trans. Faraday Soc.*, **52**, 409 (1956); (b) E. D. Goddard, C. A. J. Hoeve, and G. C. Benson, *J. Phys. Chem.*, **61**, 593 (1957).

(3) P. White and G. C. Benson, *J. Colloid Sci.*, **13**, 584 (1958).

(4) P. White and G. C. Benson, *J. Phys. Chem.*, **64**, 599 (1960).

(5) P. White and G. C. Benson, *Trans. Faraday Soc.*, **55**, 1025 (1959).

(6) (a) G. Nemethy and H. A. Scheraga, *J. Chem. Phys.*, **36**, 3382, 3401 (1962); (b) G. Nemethy and H. A. Scheraga, *J. Phys. Chem.*, **66**, 1773 (1962).

changes which occur as a function of surfactant chain length. Heat of solution and solubility measurements of certain aliphatic alcohols have also been measured as an aid to the interpretation.

Monomer–Micelle Equilibrium. Since micelles are formed only above a fairly critical concentration, a phase separation model can often be used to represent micellization (*e.g.*, ref. 7). An alternative approach involves applying the law of mass action,[8] and for high aggregation numbers (n) the two methods become equivalent.[7] For nonionic surfactants we may write

$$n \text{ monomer} \overset{K_m}{\rightleftharpoons} (\text{micelle})_n$$

Assuming monodispersity, *i.e.*, a single n value and writing activities equal to concentrations (m)

$$K_m = \frac{1 - \alpha}{n\alpha^n m^{n-1}} \qquad (1)$$

where α is the fraction of monomer present. In a manner similar to that proposed by Phillips,[8] the c.m.c. may be defined as the concentration at which the monomer fraction shows maximum curvature as a function of total concentration, m. Thus, at the c.m.c. (m_0)

$$\left(\frac{d^3\alpha}{dm^3}\right) = 0 \qquad (2)$$

With no mathematical approximations it can be shown from eq. 1 and 2 that

$$\left[\frac{1 - \alpha_0}{\alpha_0}\right]^4 n^2(2n - 1)(3n - 1) + \left[\frac{1 - \alpha_0}{\alpha_0}\right]^3 2n(2n - 1)(3n + 1) - \left[\frac{1 - \alpha_0}{\alpha_0}\right]^2 3n(3n - 1)(n - 3) - \left[\frac{1 - \alpha_0}{\alpha_0}\right] \times 2n(n + 3)(n - 2) + (n - 3)(n - 2) = 0 \qquad (3)$$

Equation 3 has been solved for α_0, the monomer fraction at the defined c.m.c., using a computer. A number of n values between 5 and 100 were chosen, and in all cases α_0 was found to be essentially the same as one also calculates using only the last two terms of eq. 3. In this case

$$\alpha_0 = \frac{2n(n + 3)}{2n^2 + 7n - 3} \simeq \frac{2n}{1 + 2n}$$

for large n. Values of α_0 obtained for this limiting case agree with those derived by Phillips for ionic surfactants in the presence of swamping electrolyte.[8]

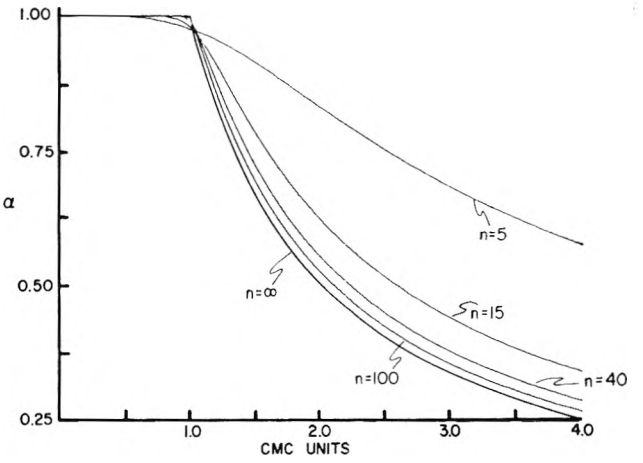

Figure 1. Monomer fraction for various aggregation numbers (n).

Variations of α as a function of m/m_0 have been computed for various n values using eq. 1, and representative curves are shown in Fig. 1. Each curve contains 100 points and was drawn directly under control of the computer. The curves for large n values approach that shown for phase separation ($n = \infty$). With lower n values, the c.m.c. (as detected experimentally) is less "critical" and should be thought of more as a range of concentration in which the presence of micelles first becomes noticeable. From eq. 1 the standard free energy of micellization per surfactant monomer is given by

$$\Delta F_m^\circ = \frac{-RT}{n} \ln K = 2.303RT\left[\frac{(n - 1)}{n} \log m_0 + C\right] \qquad (4)$$

where C is a function of n and varies from 0.455 for $n = 5$ to 0.041 for $n = 100$. For large n values, eq. 4 is seen to reduce to the form

$$\Delta F_m^\circ = 2.303RT \log m_0 \qquad (5)$$

which is the equation derived from the phase separation model.

Experimental Studies

Integral heats of solution, ΔH_s, were determined at 25° using two calorimeters. Most results were obtained with a simple vacuum-flask calorimeter employing thermistors for temperature measurement; its use has been described elsewhere.[9] Data obtained in this

(7) K. Shinoda and E. Hutchinson, *J. Phys. Chem.*, 66, 577 (1962).
(8) J. N. Phillips, *Trans. Faraday Soc.*, 51, 561 (1955).
(9) L. Benjamin, *J. Chem. Eng. Data*, 7, 239 (1962).

way were found with a precision of ±0.4% for heat changes of greater than about two calories. An adiabatic calorimeter[10] was used to study dilute solutions and for runs where dilute HCL was the solvent. Data obtained with this instrument were more precise (±0.1% for heat changes greater than 1 cal.). In dilute solutions very small heat changes (less than 0.2 cal.) had to be measured with dimethyldodecylamine oxide ($DC_{12}AO$) and alcohols, and consequently these were obtained with low precision. Both instruments were checked by measuring the heat of solution of NaCl in water, and appropriate corrections were made for the heat associated with opening blank sample cells. For concentrated solutions, it was sometimes necessary to measure ΔH_s values by successive solution of solute in the solution from a previous run. Heat of dilution measurements were also made in a few instances in order to obtain data for concentrated solutions.

The preparation of the amine oxides used in this study has been described.[11] Because of their hygroscopicity, the compounds were vacuum-dried over P_2O_5 before use and transferred to calorimeter sample cells in a drybox. The 1-hexanol and 1-octanol used for solubility and heat of solution studies were obtained by fractional distillation of commercial samples. Vapor phase chromatography showed the 1-hexanol and 1-octanol to be 98.2 and 99.3% pure, respectively. Water used in these studies was distilled and subsequently passed through an ion-exchange column.

Results

ΔH_s data are shown in Fig. 2 for dimethyldecylamine oxide ($DC_{10}AO$). Apart from the values at low concentration, the inverted curve is very similar to those in Fig. 1, as expected. Changes in the interaction of surfactant with its surroundings are more apparent from variations in partial molal enthalpy of the solute, $\bar{H}_2$, derived according to[2a]

$$\bar{H}_2 - \bar{H}_2^\circ = \Delta H_s + m\frac{d\Delta H_s}{dm} \qquad (6)$$

where $\bar{H}_2^\circ$ refers to the (partial) molal enthalpy of the solid surfactant.[12] Partial molal enthalpies obtained by application of this equation are also shown in Fig. 2 and exhibit a step variation as has been reported for ionic surfactants[2b,3,5] and which is required for true phase equilibrium. Corresponding enthalpy variations are shown in Fig. 3–5 for DC_8AO, DC_9AO, and $DC_{12}AO$ (octyl, nonyl, and dodecyl chain lengths, respectively). It is interesting to note that ΔH_s variations at the c.m.c. are less sharp for DC_8AO. This is expected for a surfactant with an aggregation number of 15 (determined for this compound by light scattering techniques[13]) as seen from Fig. 1.

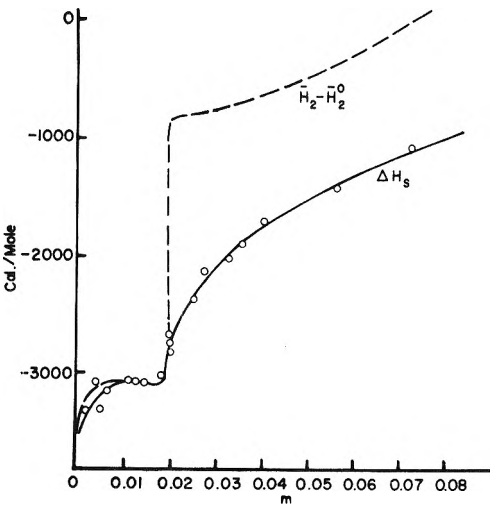

Figure 2. Heat of solution and partial molal enthalpy variation with molality of aqueous $DC_{10}AO$ at 25°.

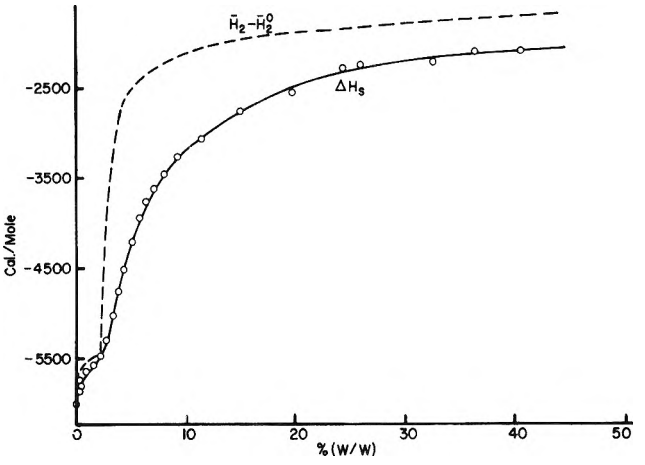

Figure 3. Heat of solution and partial molal enthalpy variation with concentration of DC_8AO solutions at 25°.

An important feature of these systems is the near constancy of $\bar{H}_2$ between the c.m.c. values and the concentrations at which a mesomorphic phase, known as middle,[14] is formed (30–50% w./w.). Such behavior is in contrast to that found with ionic surfactants[2b,3,5] and in-

(10) L. Benjamin, *Can. J. Chem.*, 41, 2210 (1963).

(11) K. W. Herrmann, *J. Phys. Chem.*, 66, 295 (1962).

(12) If concentrations are expressed in weight per cent. c, the appropriate form of this equation is

$$\bar{H}_2 - \bar{H}_2^\circ \quad \Delta H_s + \frac{c(100 - c)}{100}\frac{d\Delta H_s}{dc}$$

(13) K. W. Herrmann, private communication.

(14) V. Luzzati, E. Mustacchi, and A. Skoulios, *Nature*, 180, 600 (1957).

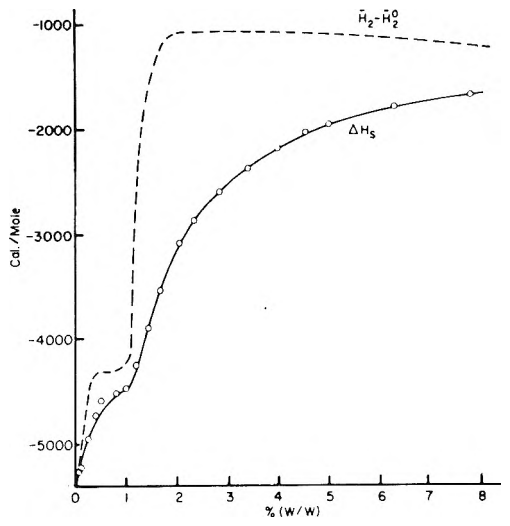

Figure 4. Heat of solution and partial molal enthalpy variation with concentration of DC_9AO solutions at 25°.

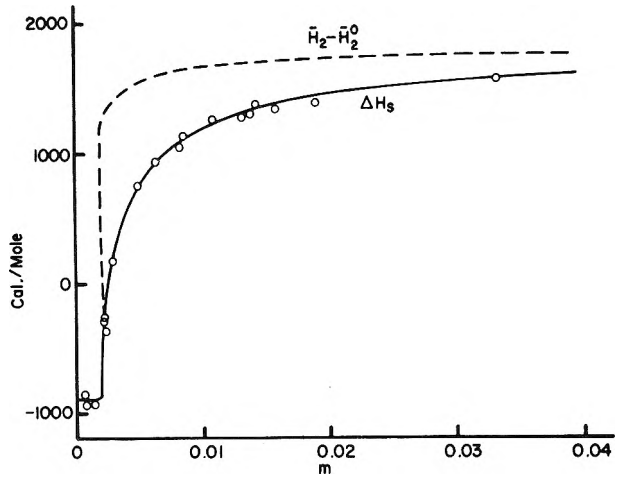

Figure 5. Heat of solution and partial molal enthalpy variation with molality of aqueous $DC_{12}AO$ at 25°.

dicates that little change takes place in the energy of interaction of the surfactant molecule with its surroundings, even though interaction between aggregate species has to be expected at these high concentrations.

In the monomer region below the c.m.c., $\bar{H}_2$ is not constant, as was also the case with ionic surfactants. However, it appears that as the chain length increases, $\bar{H}_2$ has a tendency to become more constant (*cf.* data for $DC_{10}AO$, Fig. 2). Little can be said about the variations of $\bar{H}_2$ below the c.m.c. of $DC_{12}AO$ because of low experimental precision, but, in view of the trend shown by the shorter chain length surfactants the approximate constancy of $\bar{H}_2$ has been assumed in assigning a value at infinite dilution. Enthalpy changes below the c.m.c. may be associated with dimerization or other preaggregation processes, and the ΔH_s curves for DC_8AO and DC_9AO are consistent with such an explanation. Departures from ideality due to interactions not involving association are equally likely, however.

The most important data to be derived from these results are enthalpies of micellization, and these have been defined for the ideal case as the change in $\bar{H}_2$ which occurs at the c.m.c.[2a] Where monomer solutions are nonideal the heat of dilution of the monomer from the c.m.c. to infinite dilution has to be included to obtain the standard enthalpy of micellization

$$\Delta H_m^\circ = \bar{H}_2 \text{ (just above the c.m.c.)} - \bar{H}_2^* \text{ (infinite dilution)}$$

In all cases ΔH_m° is positive as has always previously been observed calorimetrically at 25°.[2b,3,5,7]

This is not true at higher temperatures, however,[15] and a small negative value of ΔH_m° is also found for $DC_{12}AO$ in acid solution at 25°. This may be seen in Fig. 6. Amine oxides are readily protonated,[11] and the acid form has a pK_a value close to 5. In 0.1 *N* HCl, therefore, the surfactant is present almost entirely as the cationic form in the concentration range studied, while in 0.01 *N* HCl the cationic form is present at low concentration with the fraction of nonionic form present (β) increasing sharply above about 0.01 *m*. As the nonionic form has a c.m.c. of 0.002 *m*, it will form micelles in the concentration region in which it is present in HCl solutions. The curve for 0.01 *N* HCl (solid line, Fig. 6) has thus been calculated using the pK_a value to obtain β and a value of 2250 cal./mole

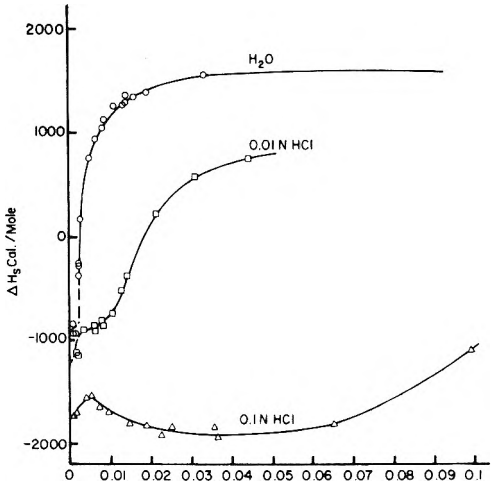

Figure 6. Heat of solution variation with molality of $DC_{12}AO$ in aqueous and dilute HCl solutions at 25°.

(15) L. Benjamin, unpublished work.

for the difference in $\bar{H}_2$ for the nonionic micellar species and the cationic species (essentially all monomer). This is a reasonable value for the process considered. The agreement with experimental points is good, especially since ideality of the solute species was assumed in obtaining β, and the pK_a value used was for monomer–monomer equilibrium. Even in 0.1 N HCl some nonionic surfactant is present at high concentrations, and ΔH_s is seen to begin to increase (Fig. 6).

Thermodynamics of Micellization. Standard free energies of micellization obtained according to eq. 5 depended on the concentration units used and on the choice of standard states. It is convenient to adopt the hypothetical standard state of mole fraction unity referred to the infinitely dilute solution.[8,11] The process considered is then

hydrated monomer (hypothetical) $X_2 = 1$ $\xrightarrow{\Delta F_m^\circ,\ \Delta H_m^\circ}$ micelle (hydrated) $X_m = 1$ $\bar{H}_2 = \bar{H}_2$ just above c.m.c.

$\Delta F = 0$

hydrated monomer X_2 = c.m.c. $\bar{H}_2 = \bar{H}_2$ just below c.m.c:

Table I shows the observed thermodynamic data for the nonionic surfactants studied. In calculating free energy changes, use has been made of c.m.c. values obtained from these calorimetric studies, although similar values have also been observed by other techniques.

Table I: Thermodynamic Data for Micellization of Amine Oxides at 25°

Surfactant	$\Delta F_m^{\circ a}$	$\Delta H_m^{\circ a}$	$T\Delta S_m^{\circ a}$
DC_8AO	−3.5	4.0	7.5
DC_9AO	−4.1	4.4	8.5
$DC_{10}AO$	−4.8	2.7	7.5
$DC_{12}AO$	−6.1	2.6	8.7

[a] All kcal./mole.

As has been generally noted for micellization, the negative standard free energy term is the result of an unfavorable positive enthalpy change and a favorable increase in entropy (ΔS_m°), the latter term dominating. This behavior, typical of hydrophobic bonding,[6a] is thought to result from the release of ordered water associated with the monomer during the micellization process. Additional support for such a conclusion is obtained from heat capacity studies[2b,4,15] and theoretical calculations[6] (an alternative explanation for the entropy effect, involving the hydrocarbon chain, has also been proposed[16]). Energy has to be supplied to "melt" these "icebergs" or "flickering clusters,"[17] and increased entropy results.

An important feature of the data is the essentially constant entropy of micellization for the chain length range C_8–C_{12} (Table I). Thus, the well-known decrease in ΔF_m° with increasing chain length according to the "rule of three" (*cf.* ref. 16) is accompanied by a corresponding decrease in ΔH_m°, the entropy change being constant at about 25 e.u. Similar behavior is also observed with ionic surfactants. Thermodynamic data for all ionic compounds for which calorimetric ΔH_m° values are available are shown in Table II, including provisional data for sodium dodecyl sulfate.[15] Free energy changes have again been calculated from eq. 5 assuming ideality and using calorimetric c.m.c. values.[18] The roughly constant entropy value is somewhat lower (~18 e.u.) than with the nonionic surfactants studied. According to the interpretation above, one would therefore conclude that less ordered water is released during micellization of ionic surfactants than with nonionic species. It is reasonable to suppose that the presence of large anions has a structure-breaking influence on the solvent,[17] and the ionic monomer would therefore have less ordered water associated with it.[20]

Table II: Thermodynamic Data for Micellization of Ionic Surfactants at 25°

Surfactant	$\Delta F_m^{\circ a}$	$\Delta H_m^{\circ a}$	$T\Delta S_m^{\circ a}$
Potassium octanoate	−2.9	3.3[b]	6.2
Sodium octyl sulfate	−3.6	1.5[b]	5.1
Sodium decyl sulfate	−4.5	1.0[b]	5.5
Sodium dodecyl sulfate[c]	−5.2	−0.3	4.9
$[DC_{12}AOH]^+Cl^-$	−5.5	−0.3	5.2

[a] All kcal./mole. [b] Estimated from data in ref. 2b. [c] See ref. 15.

Chain Length Effects. It is of interest to consider why it is that for a given type of surfactant, for chain

(16) R. H. Aranow and L. Witten, *J. Phys. Chem.*, **64**, 1643 (1960).

(17) H. S. Frank and M. W. Evans, *J. Chem. Phys.*, **13**, 507 (1945).

(18) Depending on the way the micelle and monomer species are defined for ionic sufactants, an equation may be derived, analogous to eq. 5, but differing by a factor two which becomes unity in the presence of excess added electrolyte.[7,8,19] Also, when the surfactant in the micelle is completely dissociated, eq. 5 is applicable, and this extreme condition has been assumed for the present treatment; it is applicable, in any case, for $DC_{12}AO$ in 0.1 N HCl because of the electrolyte effect.

(19) E. Matijevic and B. A. Pethica, *Trans. Faraday Soc.*, **54**, 587 (1958).

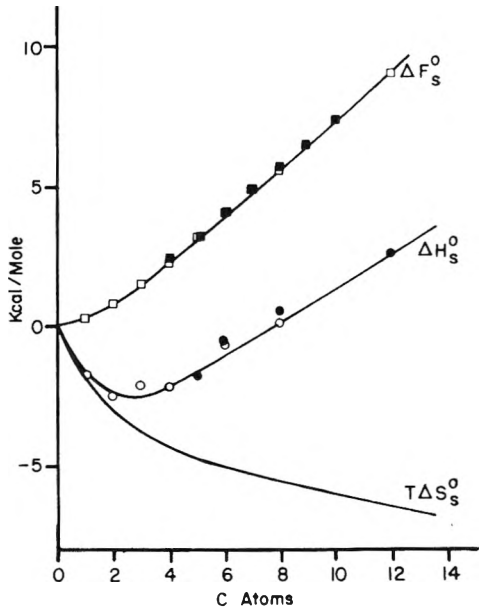

Figure 7. Standard free energies ($\Delta F_s°$), enthalpies ($\Delta H_s°$), and entropies ($\Delta S_s°$) of solution of normal aliphatic alcohols in water at 25°. Calorimetric data, O; solubility–temperature data, ●; free energy data, □ and ■.

lengths C_7 to C_{12} at least, $\Delta S_m°$ is constant, and differences in $\Delta H_m°$ values essentially parallel $\Delta F_m°$ changes. With the head-group effect removed we are left with the process

$$(-CH_2-)_{aq} \longrightarrow (-CH_2-) \text{ micelle} \cong (-CH_2-) \text{ in hydrocarbon environment}$$

This is the extreme case of hydrophobic bonding,[21] and the corresponding thermodynamic parameters for the transfer from aqueous to nonpolar environments have been calculated for amino acid side chains (ref. 6b, Table XI). That the free energy change for the process is −830 cal./mole of CH_2 is well known and is associated with the "rule of three" (*cf.* ref. 16). Thus, free energy changes of micellization, solution, and adsorption for long chain length compounds all show about this same increment per CH_2 group (*e.g.*, ref. 11, 22, 23). The enthalpy and entropy contributions to the process have been estimated as −140 cal./mole of CH_2 and +2.9 e.u., respectively, using solubility and vaporization data for short chain length hydrocarbons (C_1 to C_4) and extrapolating to longer chain lengths where the hydrocarbon is liquid at room temperature.[2b]

A better estimate of the thermodynamic changes associated with hydrophobic bonding, particularly for chain lengths greater than C_4, may be obtained from the solution data of aliphatic alcohols. These are shown in Fig. 7.[24] Where available, published or measured calorimetric $\Delta H_s°$ (heat of solution at infinite dilution) data are used; otherwise, these values are estimated from the temperature variation of solubility. Relative solubilities were determined for 1-hexanol using gas chromatographic analysis of the saturated solutions, and a radioactive technique was used with 1-dodecanol. Except for the shorter chain lengths, ideality of solutions at saturation has been assumed, and the slight solubility of water in the alcohol at equilibrium has been ignored. It is apparent from Fig. 7 that for chain lengths greater than C_4, where the influence of the alcohol head group is presumably negligible, more than two-thirds of the free energy of solution is enthalpic (~590 cal./mole of CH_2 for $\Delta H_s°$) in contrast to the predominant role of the entropy term which would be deduced from the data for short chain length alcohols. Data for an analogous process, the desorption from the air–water surface into water, provide supporting evidence for the importance of the enthalpy term with longer chain length alcohols and carboxylic acids.[22]

Returning to the micellization data (Tables I and II), for the chain lengths studied, C_7 to C_{12}, the situation is very similar to that found previously, and the roughly constant entropy term is about 18–20 e.u. for the alcohols and ionic surfactants and 25 e.u. for the amine oxides. The calorimetric data are insufficiently precise to show whether $\Delta S_m°$ values actually increase slightly with increasing chain length as is suggested by the data in Fig. 7. It appears, therefore, that although entropy changes provide the driving force for micellization (and similar processes) with short chain length compounds, with longer chain lengths the enthalpy term predominates for additional CH_2 increments. A physical picture of the surfactant monomer consistent with such

(20) This is supported by measurements of the partial molal heat capacity ($\bar{C}_{p_2}$) of DC_9AO[15]; the higher $\bar{C}_{p_2}$ value obtained for monomers of this compound than for potassium octanoate,[4] even after allowing for the extra CH_2 group, shows that the amine oxide head group is a better structure-maker than the carboxylate head group plus cation.

(21) In protein systems only partial interaction of adjacent hydrocarbon chains may occur leading to less extensive hydrophobic bonding.[6b]

(22) J. T. Davies and E. K. Rideal, "Interfacial Phenomena," Academic Press, New York, N. Y., and London, 1961.

(23) D. A. Haydon and F. H. Taylor, *Phil. Trans. Roy. Soc. London, Ser. A*, **252**, 225 (1960).

(24) Data for MeOH from L. Benjamin and G. C. Benson, *J. Phys. Chem.*, **67**, 858 (1963); EtOH from "Selected Values of Chemical Thermodynamic Properties," Circular 500 of the National Bureau of Standards, U. S. Govt. Printing Office, Washington, D. C., 1952; *n*-PrOH data from W. Dimmling and E. Lange, *Z. Elektrochem.*, **55**, 322 (1951); *n*-BuOH data from G. J. Young, J. J. Chessick, and F. H. Healey, *J. Phys. Chem.*, **60**, 394 (1956); 1-pentanol data from F. Fontein, *Z. physik. Chem.*, **73**, 212 (1910); 1-hexanol data from H. Fuhner, *Ber.*, **57**, 510 (1924). Free energy data (except for dodecanol) from J. A. V. Butler, D. W. Thomson, and W. H. Maclennan; *J. Chem. Soc.*, 674 (1933), and K. Kinoshita, H. Ishikawa, and K. Shinoda, *Bull. Chem. Soc. Japan*, **31**, 1081 (1958).

data is one in which the hydrocarbon chain curls up when possible in order to reduce the degree of contact with the water. Such changes in hydration might be expected to begin to take place above C_4 chain lengths as is found with alcohols (Fig. 7). The entropy of solution per CH_2 group is approximately twice as large below C_5 chain lengths as above for the alcohols, in semiquantitative agreement with a curled-chain model.

Acknowledgment. The author wishes to thank Mr N. E. Gilman for assistance in making the measurements and Mr. F. P. Krause for the radiotracer studies with dodecanol.

The Association and Hydration of Sodium Dodecyl Sulfate in the Submicellar Concentration Range

by Felix Franks[1a] and Harold T. Smith[1b]

Department of Chemistry, University of Pittsburgh, Pittsburgh, Pennsylvania, and the Department of Chemical Technology, Institute of Technology, Bradford 7, Yorkshire, England
(Received February 26, 1964)

The magnetic float technique has been employed to carry out density measurements on sodium dodecyl sulfate solutions in the submicellar concentration range and on the sodium salt of 2′-hydroxy-5′-sulfophenylazo-2-naphthol. The slope of the partial molar volume curve of the solute, $\partial \bar{V}_2/\partial m^{1/2}$, deviates from the Debye–Hückel limiting slope even at very low concentrations, and the negative deviations of $\bar{V}_2$ increase with rising concentration. The results are interpreted in terms of ionic dimerization as a result of hydrophobic bonding and a resultant shift in the hydration equilibrium.

Introduction

In recent years, several investigations of dilute solutions of surfactants have been carried out to produce evidence of preassociation or dimerization below the critical micelle concentration, c.m.c. Although McBain and his co-workers reported deviations from normal 1–1 electrolyte behavior in dilute solutions of ionic surfactants[2] and his findings have received support from careful conductance and transference studies on sodium dodecyl sulfate (SDS),[3] the experimental results have been challenged by van Voorst Vader,[4] who carried out e.m.f. measurements with a DS′/HgDS(s), Hg(l) electrode, and more recently by Parfitt on the basis of a conductance study of SDS, and the application of the Fuoss–Onsager equation to the experimental results.[5]

Thus, although it is accepted that in carboxylic soap solutions acid soaps such as HX·X′ do exist, there appears to be no clear-cut evidence that such preassociation does take place in aqueous solutions of alkyl sulfates and sulfonates. In the present study, the density was chosen as a physical property likely to provide high precision results capable of unam-

(1) (a) Visiting NASA Research Associate, 1963–1964; University of Pittsburgh; (b) Department of Chemical Technology, Institute of Technology, Bradford 7, Yorks., England.

(2) (a) M. E. L. McBain and W. B. Dye, *J. Am. Chem. Soc.*, **61**, 321 (1939); (b) M. E. L. McBain, *J. Colloid Sci.*, **10**, 223 (1955).

(3) P. Mukerjee, K. J. Mysels, and C. I. Dulin, *J. Phys. Chem.*, **62**, 1390 (1958).

(4) F. van Voorst Vader, *Trans. Faraday Soc.*, **57**, 110 (1961).

(5) G. D. Parfitt and A. L. Smith, *J. Phys. Chem.*, **66**, 942 (1962).

biguous interpretation in terms of partial molar volume changes.

Density measurements on SDS solutions at 23° have been reported, but they cover mainly the micellar concentration range.[6] Of more immediate interest are some measurements on sodium dodecyl sulfonate[7] which show a pronounced curvature in the density *vs.* concentration plots, although no explanation is advanced for this unexpected decrease in the partial molar volume, $\bar{V}_2$, of the dodecyl sulfonate ions below the c.m.c.

It has been established that dimerization takes place in solutions of some azo dyestuffs, and a spectrophotometric study of the dimerization equilibrium in aqueous solutions of the sodium salt of Solochrome Violet R (SVR), 2′-hydroxy-5′-sulfophenylazo-2-naphthol, has recently been reported.[8] Thus in order to obtain more evidence for the existence of preassociation equilibria, density measurements were also carried out on solutions of SVR in the concentration range 0.5–4 × 10^{-4} *m*.

Experimental

The experiments here described were performed as a preliminary investigation to ascertain whether density measurements would constitute a suitable method for the study of dimerization in dilute solutions. The precision aimed at was one part in 10^5. In the light of the results obtained, a more refined apparatus, capable of a precision of five parts in 10^7, has now been constructed and will be described in due course.

Materials. Dried Analar grade sodium chloride was used for the calibration experiments. The sample of SDS employed had been prepared by the usual method[9] but had been stored for several months. As there is some evidence that SDS decomposes during storage,[10] the sample was extracted several times with ether and dried *in vacuo*. A standard solution of purified SVR was kindly supplied by Mr. E. Coates.[8] Deionized water equilibrated with CO_2 was used throughout.

Apparatus and Method of Operation. A modification of the magnetic float technique was employed.[11] The Pyrex cell was firmly mounted on a water-tight brass base which contained the solenoid. The dimensions of the float were chosen such that it would just float when immersed in water at 20.00°. The whole assembly was mounted in a thermostat capable of a temperature control of ±0.01°. The current supply consisted of a 12-v. battery connected in series with a 10,000-ohm resistance box for approximate adjustment, and a 12-ohm continuously variable resistance for fine adjustment of the solenoid current which was measured by the potential drop across a standard 2-ohm resistance. The circuit was completed by a switch and a tapping key which allowed the float to be pulled to the bottom of the cell by applying a booster current to the solenoid.

After the cell and its contents had reached thermal equilibrium, the current was adjusted to 70 ma. The float was then pulled down to the base of the cell and kept there for about 1 min. The current was then gradually reduced until buoyancy caused the float to rise. The potential drop across the standard resistance was then measured to 0.1 mv. The float was calibrated with standard solutions of sodium chloride of known densities.[12] To minimize errors due to adsorption, the cell and float were left in contact with a concentrated solution of SDS (or SVR) overnight. The cell was then thoroughly rinsed and allowed to dry at room temperature.

Results

Figures 1 and 2 show the specific volumes of solutions of SDS and SVR at 20° as functions of the solute weight fraction w_2. The partial molar volumes were obtained from large scale graphs by the method of intercepts, and they are shown as functions of $m^{1/2}$ in Fig. 3 and 4 for SDS and SVR, respectively. The density measurements on SVR did not extend down to sufficiently low concentrations for reliable $\bar{V}_2$ values to be obtained over the whole association range.

The partial molar volumes at infinite dilution, $\bar{V}_2^0$, had to be obtained by extrapolating the specific volume curves to zero concentration and taking the limiting slope; they are thus subject to a degree of uncertainty. Their correct order of magnitude can be roughly checked by comparing $\bar{V}_2^0$ with the molar volume of the pure substance, V_2^0. Table I shows such a comparison for a variety of compounds. It is well known that for compounds containing aliphatic or aromatic residues $\bar{V}_2^0 < V_2^0$, and the relative volume difference $100(V_2^0 - \bar{V}_2^0)/V_2^0$ is usually of the order of 10%.

The initial slope of the $\bar{V}_2$ *vs.* $m^{1/2}$ plot is obtained from the Debye–Hückel limiting law for 1–1 electrolytes and is given by

(6) L. M. Kushner, B. C. Duncan, and J. I. Hoffman, *J. Res. Natl. Bur. Std.*, **49**, 85 (1952).

(7) K. A. Wright and H. V. Tartar, *J. Am. Chem. Soc.*, **61**, 544 (1939).

(8) E. Coates and B. Rigg, *Trans. Faraday Soc.*, **57**, 1637 (1961).

(9) E. E. Dreger, G. I. Klein, G. D. Miles, L. Shedlovsky, and J. Ross, *Ind. Eng. Chem.*, **36**, 610 (1944).

(10) B. Pethica, private communication.

(11) D. A. MacInnes and M. O. Dayhoff, *Rev. Sci. Instr.*, **22**, 642 (1951).

(12) "International Critical Tables," Vol. III, 1928, p. 79.

$$\bar{V}_2 = \bar{V}_2^0 + k\Gamma^{1/2}$$

where

$$\Gamma = \Sigma c_i z_i^2$$

$$k = 2.303\nu RTk' \times {}^1/_2 \left[\frac{3\partial \ln D}{\partial P} - \frac{\partial \ln c_i}{\partial P}\right]$$

$$k' = 1.290\nu^{-1}\Sigma\nu_i z_i^2 (DT)^{-3/2} \times 10^6$$

The uncertainty in k arises out of a lack of reliable data concerning the pressure dependence of D, the dielectric constant, and the compressibility of the solution; the problem of assigning a reasonable value to k has recently been discussed by Redlich and Meyer,[13]

Table I: Molar Volumes of Pure Compounds and Partial Molar Volumes at Infinite Dilution in Aqueous Solution

	V_2^0, ml. mole^{-1}	$\bar{V}_2^0$, ml. mole^{-1}	$100(V_2^0 - \bar{V}_2^0)/V_2^0$
Ethane	55	50	9
Benzene	89	83	7
Phenol	88	82	6
Ethanol	58.4	55	6
SDS	271	246	9
SVR	300	270	10

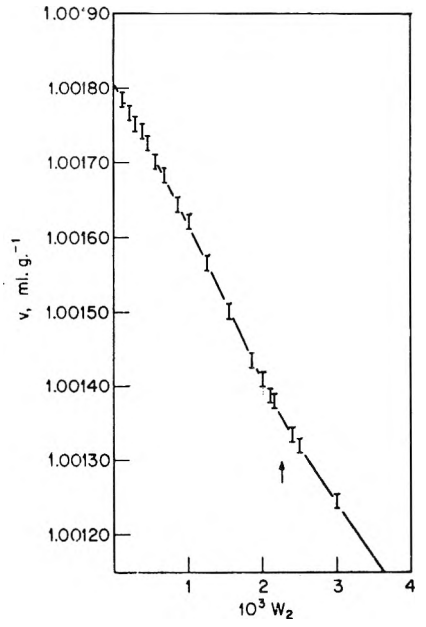

Figure 1. Specific volumes of aqueous solutions of SDS at 20° as a function of weight fraction. The arrow indicates the c.m.c.

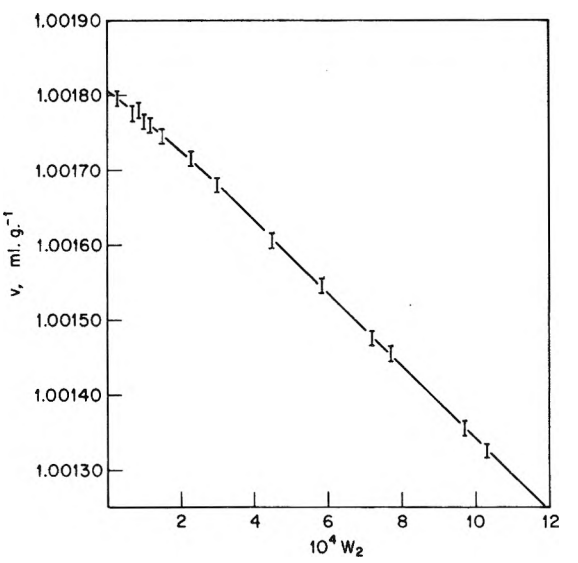

Figure 2. Specific volumes of aqueous solutions of SVR at 20° as a function of weight fraction.

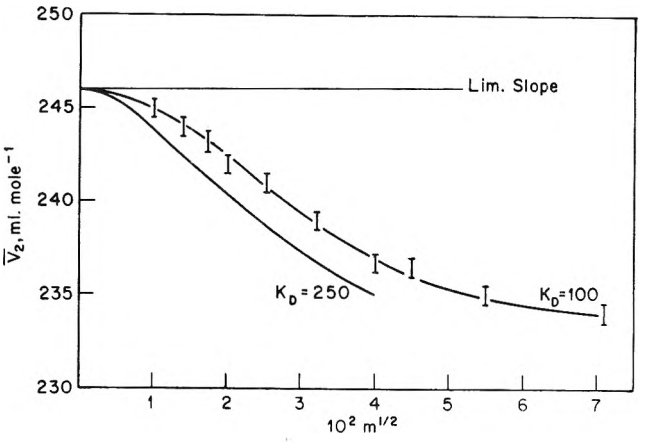

Figure 3. Experimental and calculated partial molar volumes of SDS. The calculated volumes obtained by putting $K_D = 250$ are included.[3]

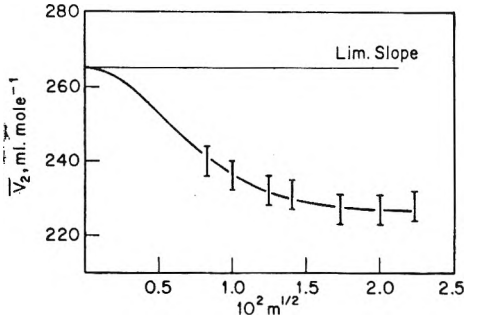

Figure 4. Experimental and calculated partial molar volumes of SVR.

(13) O. Redlich and D. M. Meyer, *Chem. Rev.*, **64**, 221 (1964).

and Fig. 3 and 4 include the small positive limiting slope based on their calculations.

Discussion

The volumetric behavior of SDS and SVR, *i.e.*, negative ($\bar{V}_2^0 - V_2^0$) values which become more negative with rising concentration, resembles that of other soluble compounds with hydrocarbon groups, *e.g.*, alcohols[14] and tetraalkylammonium halides.[15] The magnitude of the deviations from the limiting law is much greater than can be accounted for by a decrease in the electrostriction effects with increasing ionic concentration, and the shape of the $\bar{V}_2$ curves is in qualitative agreement with the postulate of an equilibrium of the type

$$2DS' \rightleftharpoons DS_2''$$

such as has in fact been demonstrated in the case of SVR.[8] Assuming as a first approximation that the monomer partial molar volume is constant and independent of concentration, then

$$\bar{V}_2 = \left(\frac{\partial V}{\partial n_2}\right)_{T,P,n_1} = \frac{\partial V}{\partial m_D} \times \frac{\partial m_D}{\partial m} \qquad (1)$$

where m_D is the molal concentration of dimers, from which an estimate of the dimerization constant K_D can be obtained. Neglecting the term in m_D^2, and setting all activity coefficients equal to unity, we can write

$$m_D = \frac{K_D m^2}{1 - 4K_D m}; \quad \frac{\partial m_D}{\partial m} = \frac{2K_D m(1 + 2K_D m)}{(1 + 4K_D m)^2}$$

which, at high concentrations, has a limiting value of 0.25. Now $\partial V/\partial m_D$ in eq. 1 is the volume change ΔV_D, due to dimerization, and it is obtained by multiplying the high concentration asymptotic ($\bar{V}_2^0 - \bar{V}_2$) values in Fig. 3 and 4 by the limiting value of $\partial m_D/\partial m$. ΔV_D is thus given as ~160 and 48 ml. mole^{-1} for SVR and SDS, respectively. The results can now be fitted to eq. 1 in the intermediate concentration range and the best values for K_D obtained. For SVR, K_D = 2000, as derived by Coates and Rigg,[8] provides a good fit to our data, whereas for SDS the best fit is given by K_D = 100 which is in reasonable agreement with K_D = 250 obtained from conductance measurements on very dilute solutions.[3]

The nature of ΔV_D is most readily accounted for on the basis of a partial dehydration of the hydrocarbon chains upon dimerization

$$2DS' \cdot qH_2O^* \rightleftharpoons DS_2'' \cdot rH_2O^* + (q - r)H_2O$$

where H_2O^* refers to "structured" water, as defined by the formalisms of Frank and Evans[16] or Némethy and Scheraga.[17] This species of water of hydration, to which have been ascribed some of the structural properties of ice[17] or of inert gas hydrates,[18] differs from bulk water by virtue of its lower density, and hence ΔV_D is negative. Since $(q - r)$ will increase with increasing chain length, ΔV_D should do likewise. The very large ΔV_D of SVR reflects the greater degree of hydration, and hence the higher solubility, of aromatic compounds over that of aliphatic compounds with the same number of carbon atoms.

If the driving force for the formation of the dimer is taken as the hydrophobic bond, as discussed by Némethy and Scheraga,[19] then for a homologous series

$$\Delta G_D = -RT \ln K_D = n\Delta G\phi + \Delta G_{mix}$$

where $\Delta G\phi$ is the free energy of formation of a hydrophobic bond, n is the number of such bonds formed per dimer, and ΔG_{mix} is the free energy of demixing associated with the formation of the dimer. The latter term would be expected to increase only slowly with increasing chain length, so that K_D would be affected mainly by the first term which has been estimated as −0.6 kcal. mole^{-1}.[19] That K_D is indeed affected by the length of the hydrocarbon chain has been established by pNa measurements on a series of alkyl sulfates.[20] These have demonstrated that the behavior of $C_{10}H_{21}SO_4Na$ closely follows that of NaCl, but that progressively larger deviations are observed for SDS and $C_{14}H_{29}SO_4Na$ which cannot be accounted for by the usual ion size corrections to the Debye–Hückel limiting law.

High precision density measurements on a range of alkyl sulfates and on some homologous aromatic compounds at several temperatures are now in progress, and the results will be reported in due course.

(14) A. G. Mitchell and W. F. K. Wynne-Jones, *Discussions Faraday Soc.*, **15**, 161 (1953).

(15) W. Y. Wen and S. Saito, *J. Phys. Chem.*, **68**, 2639 (1964).

(16) H. S. Frank and M. W. Evans, *J. Chem. Phys.*, **13**, 507 (1945).

(17) G. Némethy and H. A. Scheraga, *ibid.*, **36**, 3401 (1962).

(18) H. S. Frank and A. S. Quist, *ibid.*, **34**, 604 (1961).

(19) G. Némethy and H. A. Scheraga, *J. Phys. Chem.*, **66**, 1173 (1962).

(20) L. Shedlovsky, C. W. Jakob, and M. B. Epstein, *ibid.*, **67**, 2075 (1963).

Effect of Electrolyte and Urea on Micelle Formation[1]

by M. J. Schick

Lever Brothers Company, Research Center, Edgewater, New Jersey *(Received April 6, 1964)*

The effect of counterion hydration on the critical micelle concentration (c.m.c.) of some *n*-dodecyl sulfates has been studied in aqueous salt solutions as a function of counterion concentration maintaining a constant similion. In order to supplement this study of hydration effects in the electrical double layer on the micellar periphery, the effect of urea on micelle formation and on hydrophobic bonding in the micellar core of some *n*-alkyl sulfates has been investigated as a function of urea concentration and temperature. The increments in c.m.c. values on urea addition increase in the following order: lithium *n*-dodecyl sulfate, sodium *n*-decyl sulfate, sodium *n*-dodecyl sulfate, tetramethylammonium (TMA) *n*-dodecyl sulfate. These results are interpreted in terms of the structural concepts of water. For comparison with the data on ionic detergents, the effect of urea on the c.m.c. of *n*-dodecyl ether alcohol sulfates in aqueous solutions and of polyoxyethylene alkanols in aqueous and in electrolyte solutions has also been studied as a function of urea concentration and temperature. Increments in c.m.c. values of the polyoxyethylene alkanols on urea addition are attributed to increased hydration of the ethylene oxide chain caused by a reduction of the cooperative structure of water.

Introduction

Recent investigations[2-7] have supported the contention that changes in water structure are an important factor in micelle formation. Therefore, an investigation has been carried out to increase our experimental knowledge of the effect of these changes in water structure upon micelle formation of ionic, nonionic, and the intermediate *n*-alkyl ether alcohol sulfate detergents. In addition, the effect of changing counterions has been examined.

Corrin and Harkins[8] have shown in a study of the aggregation of long-chain electrolytes (1) that the c.m.c. is related to only the concentration of the counterion and the nature of the similion is without effect, and (2) that the c.m.c. of a long-chain electrolyte is a linear function of the logarithm of the total concentration of the counterion. This holds only for univalent counterions and has been treated theoretically by Hobbs.[9]

The effect of changing counterions has been the subject of several investigations.[10-15] For example, the effect of univalent cations on the c.m.c. of sodium *n*-dodecyl sulfate has been reported by Goddard, *et al.*,[10] of univalent anions on the c.m.c. of dodecylpyridinium chloride by Lange,[11] and of univalent anions on the c.m.c. of dodecyltrimethylammonium bromide by Anacker and Ghose.[12] However, these

(1) Paper presented in the Kendall Award Symposium on Behavior of Surfactants at Interfaces and in Solution at the 147th National Meeting of the American Chemical Society, Philadelphia, Pa., April 5–10, 1964.

(2) E. D. Goddard, C. A. J. Hoeve, and G. C. Benson, *J. Phys. Chem.*, **61**, 593 (1957).

(3) E. D. Goddard and G. C. Benson, *Can. J. Chem.*, **35**, 986 (1957).

(4) P. Mukerjee and A. Ray, *J. Phys. Chem.*, **67**, 190 (1963).

(5) W. Bruning and A. Holtzer, *J. Am. Chem. Soc.*, **83**, 4865 (1961).

(6) K. W. Herrmann, *J. Phys. Chem.*, **66**, 295 (1962).

(7) M. J. Schick, *ibid.*, **67**, 1796 (1963).

(8) M. L. Corrin and W. D. Harkins, *J. Am. Chem. Soc.*, **69**, 683 (1947).

(9) M. E. Hobbs, *J. Phys. Colloid Chem.*, **55**, 675 (1951).

(10) E. D. Goddard, O. Harva, and T. G. Jones, *Trans. Faraday Soc.*, **49**, 980 (1953).

(11) H. Lange, *Kolloid-Z.*, **121**, 66 (1951).

(12) E. W. Anacker and H. M. Ghose, *J. Phys. Chem.*, **67**, 1713 (1963).

(13) J. M. Corkill and J. F. Goodman, *Trans. Faraday Soc.*, **58**, 206 (1962).

(14) K. J. Mysels and L. H. Princen, *J. Phys. Chem.*, **63**, 1698 (1959).

(15) E. W. Anacker, R. M. Rush, and J. S. Johnson, *ibid.*, **68**, 81 (1964).

three investigations dealt with solutions containing mixtures of counterions,[10-12] in which the possibility of formation of micelles with mixed counterion layers exists as shown by Corkill and Goodman.[13] In contrast, Mysels and Princen have compared the c.m.c. values of some *n*-dodecyl sulfates in solutions containing a single counterion.[14] In the present investigation, these data have been amplified with a study of the c.m.c. values of lithium, sodium, and tetramethylammonium *n*-dodecyl sulfates in salt solutions containing a single counterion and a constant similion over the concentration range 0–0.4 *M*.

Mukerjee and Ray[4] and Bruning and Holtzer[5] have used dissolved urea as a probe for investigating the water structure contribution to micelle formation and hydrophobic bonding. The choice of urea is based on its two outstanding properties in aqueous solutions, namely, its great ability to undergo hydrogen bonding with water because of the presence of three potential centers on each molecule and its small effect on the polarity of water.[4] Urea actually increases the dielectric constant of water appreciably and the surface tension slightly. At high concentrations urea modifies the "iceberg" structure around solute molecules as has been inferred from micellization and protein denaturation studies without unduly affecting interfacial effects.[4,5,16,17] In order to supplement our initial study of the hydration effects in the counterion layer of ionic micelles an attempt was made to elucidate the detailed nature of hydrophobic bonding in the micellar core of ionic micelles. In analogy with the two investigations cited above,[4,5] this was achieved by studying the effect of urea on the c.m.c. of *n*-alkyl sulfates. For comparison with the data on *n*-alkyl sulfates the effect of urea on the c.m.c. of *n*-alkyl ether alcohol sulfates and of polyoxyethylene alkanols has also been studied.

Experimental

Lithium *n*-dodecyl sulfate was prepared by treating Givaudan 1-dodecanol (99.6%) with SO_3 (Baker Sulfan). Dry nitrogen was passed over the liquid SO_3 and the vapors introduced into the stirred 1-dodecanol at 40–50°. The *n*-dodecyl sulfuric acid was neutralized by addition to an aqueous solution of LiOH until the paste was at pH 8. The paste was dried and recrystallized three times from 2-propanol. The molecular weight of lithium *n*-dodecyl sulfate was determined by conversion to the free acid through ion exchange and subsequent titration. The observed molecular weight was 273.1 as compared to the theoretical one of 272.4.

Tetramethylammonium *n*-dodecyl sulfate was prepared by a similar procedure as lithium *n*-dodecyl sulfate. The *n*-dodecyl sulfuric acid was neutralized by addition to an aqueous solution of tetramethylammonium hydroxide until the paste was at pH 8. The paste was dried and recrystallized four times from 2-propanol and five times from ethanol. The observed molecular weight was 339.9 as compared to the theoretical one, 339.6.

Sodium *n*-dodecyl sulfate was prepared by the method of Dreger, *et al.*,[18] recrystallized several times from ethanol, and extracted with petroleum ether. The synthesis of the sodium *n*-dodecyl ether alcohol sulfates has been referred to before.[7] The purity of these materials was readily checked from the shape of the surface tension *vs.* logarithm of concentration plots near the c.m.c. The origin of the polyoxyethylene alkanols has been described previously.[7] The water was redistilled from alkaline permanganate. Analytical reagent grade electrolytes and urea were used.

For the procedure of the surface tension measurements see our previous communication.[7]

Results

Changes in the c.m.c., *i.e.*, the maximum concentration of molecular dispersion, are a measure of the balance of forces causing the formation of micelles.[19] Moreover, since interpretation of the experimentally measured behavior of micelles in terms of their structure requires extrapolation to conditions under which interaction between the micelles is negligible or, in other words, zero concentration, we were concerned with establishing this concentration, *i.e.*, the c.m.c. Throughout this investigation, the c.m.c. values were taken from the sharp breaks in the surface tension *vs.* logarithm of detergent concentration plots.[7,19]

Ionic Detergents. The effect of the hydration of univalent counterions on the c.m.c. values of some *n*-dodecyl sulfates has been studied as a function of counterion concentration maintaining a constant similion at 25.0° and is illustrated in Fig. 1. In aqueous solutions, the c.m.c. values decreased in the order of diminished hydration of counterions, *viz.*, Table I, from n-$C_{12}H_{25}SO_4Li$ (7.9×10^{-3} *M*), n-$C_{12}H_{25}SO_4Na$ (7.2×10^{-3} *M*) to n-$C_{12}H_{25}SO_4TMA$ (4.8×10^{-3}

(16) D. B. Wetlaufer, S. K. Malik, L. Stoller, and R. L. Coffin, *J. Am. Chem. Soc.*, **86**, 508 (1964).

(17) W. Kauzman, *Advan. Protein Chem.*, **14**, 1 (1959).

(18) E. E. Dreger, G. I. Keim, G. D. Miles, L. Shedlovsky, and J. Ross, *Ind. Eng. Chem.*, **36**, 610 (1944).

(19) M. J. Schick, S. M. Atlas, and F. R. Eirich, *J. Phys. Chem.*, **66**, 1326 (1962).

Table I: Effect of Urea on the C.m.c. of Some *n*-Alkyl Sulfate Solutions

n-Alkyl sulfate	Urea, *M*	C.m.c., *M*			C.m.c./c.m.c.(0)		
		10°	25°	45°	10°	25°	45°
n-$C_{10}H_{21}$–SO_4Na	0		3.1×10^{-2}			1.00	
n-$C_{10}H_{21}$–SO_4Na	1		3.2×10^{-2}			1.03	
n-$C_{10}H_{21}$–SO_4Na	2		3.5×10^{-2}			1.13	
n-$C_{10}H_{21}$–SO_4Na	3		3.7×10^{-2}			1.19	
n-$C_{10}H_{21}$–SO_4Na	4.5		4.3×10^{-2}			1.39	
n-$C_{10}H_{21}$–SO_4Na	6		5.0×10^{-2}			1.61	
n-$C_{12}H_{25}$–SO_4Na	0	7.4×10^{-3}	7.2×10^{-3}	7.6×10^{-3}	1.00	1.00	1.00
n-$C_{12}H_{25}$–SO_4Na	1		7.4×10^{-3}			1.03	
n-$C_{12}H_{25}$–SO_4Na	2		8.0×10^{-3}			1.11	
n-$C_{12}H_{25}$–SO_4Na	3	1.06×10^{-2}	9.0×10^{-3}	9.1×10^{-3}	1.43	1.25	1.20
n-$C_{12}H_{25}$–SO_4Na	4.5		1.02×10^{-2}			1.42	
n-$C_{12}H_{25}$–SO_4Na	6	1.41×10^{-2}	1.20×10^{-2}	1.15×10^{-2}	1.91	1.67	1.52
n-$C_{12}H_{25}$–SO_4Li	0	7.0×10^{-3}	7.9×10^{-3}	8.0×10^{-3}	1.00	1.00	1.00
n-$C_{12}H_{25}$–SO_4Li	1		8.0×10^{-3}			1.01	
n-$C_{12}H_{25}$–SO_4Li	2		8.2×10^{-3}			1.04	
n-$C_{12}H_{25}$–SO_4Li	3	8.0×10^{-3}	8.8×10^{-3}	8.9×10^{-3}	1.14	1.11	1.11
n-$C_{12}H_{25}$–SO_4Li	4.5		9.4×10^{-3}			1.19	
n-$C_{12}H_{25}$–SO_4Li	6	1.0×10^{-2}	1.0×10^{-2}	1.05×10^{-2}	1.43	1.27	1.31
n-$C_{12}H_{25}$–SO_4TMA[a]	0	4.8×10^{-3}	4.8×10^{-3}	6.3×10^{-3}	1.00	1.00	1.00
n-$C_{12}H_{25}$–SO_4TMA[a]	1		5.0×10^{-3}			1.04	
n-$C_{12}H_{25}$–SO_4TMA[a]	2		5.8×10^{-3}			1.20	
n-$C_{12}H_{25}$–SO_4TMA[a]	3	6.6×10^{-3}	6.9×10^{-3}	7.9×10^{-3}	1.37	1.43	1.25
n-$C_{12}H_{25}$–SO_4TMA[a]	4.5		7.9×10^{-3}			1.65	
n-$C_{12}H_{25}$–SO_4TMA[a]	6	1.0×10^{-2}	1.0×10^{-2}	1.08×10^{-2}	2.08	2.08	1.72
n-$C_{16}H_{33}$–SO_4Na	0			6.0×10^{-4}			1.00
n-$C_{16}H_{33}$–SO_4Na	3			6.4×10^{-4}			1.07
n-$C_{16}H_{33}$–SO_4Na	6			7.9×10^{-4}			1.31

[a] Tetramethylammonium.

M).[10,14,20] These results are in line with those reported by Mysels and Princen,[14] who concluded that hydrated ions are less closely attached to the aggregates than unhydrated ones and, therefore, contribute less to their formation. It is worth noting that these c.m.c. values determined by the surface tension method are somewhat lower compared to those of the light-scattering method, but follow the same order. The results of Fig. 1 follow the general relation that the logarithm of the c.m.c. of a colloidal electrolyte is a linear function of the logarithm of the total concentration of the counterion.[8] These results may also be expressed by the equations

$$\log (\text{c.m.c.}) = -3.55 - 0.68 \log (Li^+) \quad (1)$$

$$\log (\text{c.m.c.}) = -3.60 - 0.66 \log (Na^+) \quad (2)$$

$$\log (\text{c.m.c.}) = -3.65 - 0.57 \log (TMA^+) \quad (3)$$

The intercepts vary with the degree of hydration of the counterions,[20] and the slopes decrease slightly in the order n-$C_{12}H_{25}SO_4Li$, n-$C_{12}H_{25}SO_4Na$, to n-$C_{12}H_{25}SO_4$ TMA. The latter may be attributed to a reduction in the effect of shielding of charges when the counterions are more closely attached to the aggregates. These results conform with earlier predictions of Goddard, *et al.*,[10] and Lange.[11]

In addition to this study of hydration effects in the counterion layer of *n*-dodecyl sulfates, the object of this investigation was also to understand hydrophobic bonding in the micellar core of ionic detergents. Therefore, the effect of urea on the c.m.c. of *n*-dodecyl sulfate solutions has been determined as a function of urea concentration and the pertinent data are given in Table I and Fig. 2. Only at high urea concentrations was a marked increase in c.m.c. observed, which followed an almost linear relation between c.m.c./c.m.c. (0) *vs.* urea concentration in the region of 2 to 6 moles/l. of urea. The ratio of the c.m.c. in the presence of urea to the c.m.c. in the absence of urea, c.m.c./c.m.c. (0), has been adopted as a convenient way of representing the data.[4] The c.m.c. determinations of the *n*-dodecyl sulfates given in Table I have been carried out at 10.0, 25.0, and 45.0°, whereas those of sodium *n*-decyl sulfate and sodium *n*-hexadecyl sulfate have

(20) E. R. Nightingale, *J. Phys. Chem.*, 66, 894 (1962).

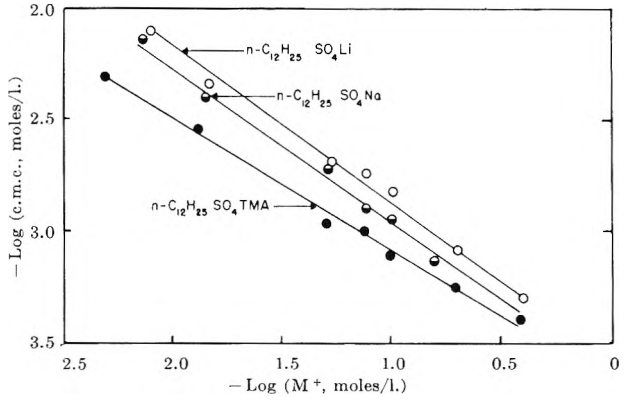

Figure 1. Log–log plot of the effects of salts on the c.m.c. of some *n*-dodecyl sulfate solutions at 25.0°.

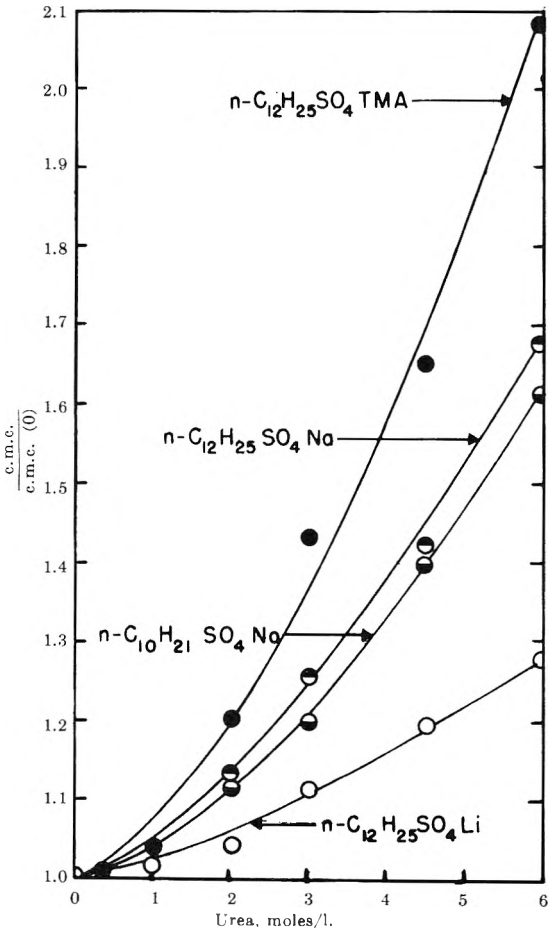

Figure 2. Effect of urea on the c.m.c. of some *n*-alkylsulfate solutions at 25.0°.

been limited to one temperature, *i.e.*, 25.0 and 45.0°, respectively. Sodium *n*-hexadecyl sulfate is insoluble below 45.0°. No significant difference in susceptibility to changes in c.m.c. on urea addition was observed at 25.0° between sodium *n*-decyl sulfate and sodium *n*-dodecyl sulfate within experimental accuracy. In contrast, a much lower increase in c.m.c. on urea addition was observed with sodium *n*-hexadecyl sulfate than with the shorter chain homolog at 45.0° The increments in c.m.c. values of *n*-dodecyl sulfates on urea addition decrease on raising the temperature from 10.0 to 45.0°. These results are at variance with those of Mukerjee and Ray,[4] who observed no temperature dependence in the c.m.c. of dodecylpyridinium iodide solutions on urea addition. The effect of urea on the c.m.c. of *n*-dodecyl sulfates as a function of the hydration of the counterions is shown in Fig. 2. The increments in c.m.c. values on urea addition, in the concentration region from 0 to 6 *M*, increase in the order of diminished hydration of the counterion[14,20]: lithium *n*-dodecyl sulfate, sodium *n*-dodecyl sulfate to TMA *n*-dodecyl sulfate.

Nonionic Detergents. For comparison with the data on ionic detergents, the effect of urea on the c.m.c. of sodium *n*-dodecyl ether alcohol sulfates and polyoxyethylene alkanols in aqueous solutions has also been studied as a function of urea concentration and the pertinent data are given in Tables II and III. With the sodium ether alcohol sulfates, the increments in c.m.c. values on urea addition increase with increasing length of the polyether chain. Thus, the transition from the moderate effects of ionic detergents to the larger effects of nonionic detergents with comparable hydrophobic groups, *viz.*, Tables I and III, is reflected in these results. With the polyoxyethylene alkanols, the increments in c.m.c. values on urea addition increase in the order of their c.m.c. values in the absence of urea: 1-hexadecanol + 30 EO, 1-dodecanol + 7 EO, and 1-dodecanol + 30 EO. The effect of 6 *M* urea on the c.m.c. values of polyoxyethylene alkanol solutions as a function of temperature is shown in Fig. 3. For comparison, data of sodium *n*-dodecyl sulfate and of sodium *n*-dodecyl ether alcohol sulfates have been included and are represented by the dotted lines. The values of c.m.c./c.m.c. (0) in the c.m.c./c.m.c. (0) *vs.* temperature plots of the polyoxyethylene alkanols decrease with increasing temperature and follow the order: 1-dodecanol + 30 EO, 1-dodecanol + 7 EO, and 1-hexadecanol + 30 EO. In analogy the c.m.c./c.m.c. (0) values in the c.m.c./c.m.c. (0) *vs.* temperature plots of sodium *n*-dodecyl sulfate and the intermediate sodium *n*-dodecyl ether alcohol sulfates decrease in the temperature range from 10.0 to 45.0°. An interpretation of these data of polyoxyethylene compounds is given in the discussion in terms of changes in the hydration of the ethylene oxide chains.

Finally, the effect of urea on the c.m.c. of 1-dodeca-

Table II: Effect of Urea on the C.m.c. of Sodium *n*-Dodecyl Ether Alcohol Sulfate Solutions

	Urea, *M*	C.m.c., *M*			C.m.c./c.m.c.(0)		
		10°	25°	45°	10°	25°	45°
n-$C_{12}H_{25}$-$(OC_2H_4)_3$-SO_4Na	0	1.1×10^{-4}	1.0×10^{-4}	1.2×10^{-4}	1.00	1.00	1.00
	3	1.55×10^{-4}	1.5×10^{-4}	1.93×10^{-4}	1.41	1.50	1.61
	6	2.85×10^{-4}	2.5×10^{-4}	2.70×10^{-4}	2.60	2.50	2.25
n-$C_{12}H_{25}$-$(OC_2H)_{17.5}$-SO_4Na	0	6.5×10^{-5}	6.0×10^{-5}	4.5×10^{-5}	1.00	1.00	1.00
	3	1.3×10^{-4}	1.2×10^{-4}	7.02×10^{-5}	2.00	2.00	1.56
	6	2.48×10^{-4}	2.2×10^{-4}	1.41×10^{-4}	3.80	3.70	3.13

Table III: Effect of Urea on the C.m.c. of Polyoxyethylene Alkanols in Aqueous Solutions

Hydrophobe	*n*EO	Urea, *M*	C.m.c., *M*			C.m.c./c.m.c.(0)		
			10°	25°	45°	10°	25°	45°
n-Dodecanol	7	0	8.0×10^{-5}	5.0×10^{-5}	2.8×10^{-5}	1.00	1.00	1.00
n-Dodecanol		3	1.2×10^{-4}	6.25×10^{-5}	3.4×10^{-5}	1.50	1.25	1.22
n-Dodecanol		6	2.08×10^{-4}	1.25×10^{-4}	5.6×10^{-5}	2.60	2.50	2.00
n-Dodecanol	30	0	9.0×10^{-5}	8.0×10^{-5}	4.8×10^{-5}	1.00	1.00	1.00
n-Dodecanol		3	3.6×10^{-4}	1.6×10^{-4}	6.7×10^{-6}	4.00	2.00	1.40
n-Dodecanol		6	7.2×10^{-4}	2.5×10^{-4}	9.45×10^{-5}	8.00	3.13	1.97
n-Hexadecanol	30	0	2.0×10^{-5}	1.1×10^{-5}	5.0×10^{-6}	1.00	1.00	1.00
n-Hexadecanol		3	3.2×10^{-5}	1.6×10^{-5}	6.35×10^{-6}	1.60	1.45	1.27
n-Hexadecanol		6	4.0×10^{-5}	2.0×10^{-5}	7.9×10^{-6}	2.00	1.82	1.58

nol + 30 EO in electrolyte solutions has been determined at 25.0°, and the results are listed in Table IV. In previous communications we have shown that at a specific temperature the lowering of the c.m.c. of a nonionic detergent on electrolyte addition is proportional to the electrolyte concentration, but inversely proportional

Table IV: Effect of Urea on the C.m.c. of *n*-Dodecanol + 30 EO in Electrolyte Solutions at 25.0°

Solvent	Urea, *M*	C.m.c., *M*	$\frac{\text{C.m.c.}}{\text{C.m.c. (0)}}$
H_2O	0	8.0×10^{-5}	
0.43 *M* NaCl	0	3.0×10^{-5}	1.00
0.43 *M* NaCl	3	4.5×10^{-5}	1.50
0.43 *M* NaCl	6	1.0×10^{-4}	3.34
0.86 *M* NaCl	0	2.0×10^{-5}	1.00
0.86 *M* NaCl	3	5.0×10^{-5}	2.50
0.86 *M* NaCl	6	1.2×10^{-4}	6.00
0.86 *M* NaCNS	0	5.5×10^{-5}	1.00
0.86 *M* NaCNS	3	8.7×10^{-5}	1.58
0.86 *M* NaCNS	6	1.1×10^{-4}	2.00
0.86 *M* $^1/_2Na_2SO_4$	0	1.2×10^{-5}	1.00
0.86 *M* $^1/_2Na_2SO_4$	3	2.9×10^{-5}	2.40
0.86 *M* $^1/_2Na_2SO_4$	6	3.6×10^{-5}	3.00
0.86 *M* LiCl	0	4.0×10^{-5}	1.00
0.86 *M* LiCl	3	5.0×10^{-5}	1.25
0.86 *M* LiCl	6	8.0×10^{-5}	2.00
0.86 *M* TMACl[a]	0	3.0×10^{-5}	1.00
0.86 *M* TMACl[a]	3	5.7×10^{-5}	1.90
0.86 *M* TMACl[a]	6	1.0×10^{-4}	3.33

[a] Tetramethylammonium chloride.

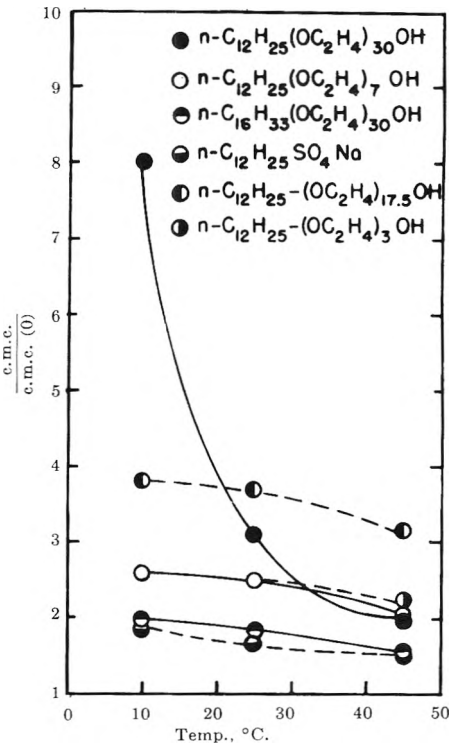

Figure 3. Effect of 6 *M* urea on the c.m.c. of polyoxyethylene alkanol solutions as a function of temperature.

to the lyotropic number of the anions.[7,19,21] The effect of variations in the lyotropic number of the anions is more pronounced than that of the cations. This also follows from the results of Table IV, which demonstrate both the effects of electrolyte concentration and lyotropic number. In contrast, the c.m.c. of 1-dodecanol + 30 EO is raised on urea addition (see Table III). From this it follows that two opposing effects must take place in this simultaneous addition of electrolyte and urea to 1-dodecanol + 30 EO solutions. Let us now compare the results in Table IV at the highest urea concentration level, *i.e.*, 6 *M*. In general, the magnitude of the c.m.c./c.m.c. (0) values in these solutions correlates with the lowering of the c.m.c. in electrolyte solutions containing no urea. Thus, the increase in c.m.c./c.m.c. (0) values is proportional to the electrolyte concentration, 3.34 for 0.43 *M* NaCl and 6.00 for 0.86 *M* NaCl but is inversely proportional to the lyotropic number of the anions, 2.00 for 0.86 *M* NaCNS and 3.00 for 0.86 *M* $^1/_2Na_2SO_4$, or cations 2.00 for 0.86 *M* LiCl and 3.33 for 0.86 *M* TMACl. No marked difference of the effect of variations in the lyotropic number of the anions compared to that of the cations in c.m.c./c.m.c. (0) in the presence of 6 *M* urea was observed in contrast to the large difference in the absence of urea.

Discussion

Water has always provided an interesting scientific challenge. In order to explain the properties of water and to elucidate its structure, many qualitative and quantitative theories have been proposed. Several of the more recent theories of water structure and the influence of various ions on it are given in the papers referred to below.[22-32] In particular, interest has been focused on the relation between hydrophobic bonding in proteins and water structure.[16,17,30-32] From the results of our previous communications[7,19] and related investigations,[2-6,33] it was inferred that changes in the water medium are an important factor in stabilizing an equilibrium size distribution in micelle formation. Therefore, it seems appropriate to interpret the results of this investigation in terms of the structural concepts of water.

Let us first define the "iceberg" picture and the role of ions and urea in aqueous solutions more accurately. The currently accepted hypothesis for micelle formation of ionic detergents invokes the "iceberg" structure of water.[2,22] Goddard, Hoeve, and Benson have given an explanation for the observed positive values for $\Delta\bar{H}_m$ at lower temperatures in terms of a water (so-called "iceberg") structure around the hydrocarbon chain of the single ions.[2,22] The hydrocarbon chain surrounded by the water structure represents a comparatively low energy state but the concomitant restriction of motion provides a driving force to aggregation, which is an entropy effect at lower temperatures.[3] Furthermore, Frank and Wen[25] and Nightingale[20] have shown a gradation of ions in their effect of altering the structure of water. Thus, alkali metal ions are structure breakers whereas the tetramethylammonium ion is a structure promoter in aqueous solutions. According to Frank and Wen,[25] structure breaking ions orient the neighboring solvent molecules, restricting their participation in hydrogen-bonded water clusters and leading to a region of disorder around the solvated solute molecules. The role of urea may be defined similarly. In order to explain the observed anomalously low viscosities of urea solutions, Rupley[34] suggests that urea disrupts the water structure. The proposed mechanism of the disruption of water structure by urea follows the same line as that given before for the structure breaking by ions.[34] Thus, we are led to hypothesize that ions and urea may modify the "iceberg" structure around the hydrocarbon chain of the single ions and consequently affect micelle formation of ionic detergents.

The effects in the electrical double layer of ionic micelles are considered first. The decrease in c.m.c. values of the *n*-dodecyl sulfates, see Table I, can be simply related to diminished hydration of the univalent cations,[29] *i.e.*, from Li^+, Na^+ to TMA^+, for which Mysels and Princen[14] have given a plausible explanation in terms of differences in the closeness of attachment of the counterions to the aggregates. However, in order to explain the drastic decrease in c.m.c. by the symmetrical tetramethylammonium ion despite

(21) M. J. Schick, *J. Colloid Sci.*, **17**, 810 (1962).

(22) H. S. Frank and M. W. Evans, *J. Chem. Phys.*, **13**, 507 (1945).

(23) F. S. Feates and D. J. G. Ives, *J. Chem. Soc.*, 2798 (1956).

(24) H. S. Frank, *Proc. Roy. Soc.* (London), **A247**, 481 (1958).

(25) H. S. Frank and W. Y. Wen, *Discussions Faraday Soc.*, **24**, 133 (1957).

(26) H. S. Frank, "Desalineation Research Conference," Publication 942 of National Academy of Science, National Research Conference, Washington, D.C., 1962, p. 141.

(27) H. S. Frank, "The Effects of Solutes on the Structure of Water," Paper presented at the 144th National Meeting of the American Chemical Society, New York, N. Y., September 9-13, 1963.

(28) R. P. Marchi and H. Eyring, *J. Phys. Chem.*, **68**, 221 (1964).

(29) E. R. Nightingale, *ibid.*, **63**, 1381 (1959).

(30) G. Némethy and H. A. Scheraga, *J. Chem. Phys.*, **36**, 3382 (1962).

(31) G. Némethy and H. A. Scheraga, *ibid.*, **36**, 3401 (1962).

(32) G. Némethy and H. A. Scheraga, *J. Phys. Chem.*, **66**, 1773 (1962).

(33) J. M. Corkill, J. F. Goodman, and S. P. Harrold, *Trans. Faraday Soc.*, **60**, 202 (1964).

(34) J. A. Rupley, *J. Phys. Chem.*, **68**, 2002 (1964).

a reduction in electrostatic interaction, Mysels[35] suggests that other nonelectrostatic interactions between hydrophobic surfaces of aggregates and ions must also be at work. Contact between these hydrophobic surfaces of aggregates and ions can reduce the hydrocarbon–water interface in the solution and, consequently, stabilize an equilibrium size distribution at a lower concentration level. From this it follows that other functions besides the electrostatic interaction may be assigned to counterions in micelle formation.

In line with the "iceberg" picture, it is anticipated that a structure-promoting ion should enhance micelle formation, whereas a structure-breaking ion should reduce it. This is confirmed to a large extent by our results of the *n*-dodecyl sulfates. The structure-promoting tetramethylammonium ion exhibits a drastic decrease in c.m.c. from the high values in the presence of the structure breaking alkali metal ions, as shown in Table I. In contrast, the discrepancy between the c.m.c. values of the lithium and sodium *n*-dodecyl sulfates is small and follows the order of hydration rather than the efficacy of structure breaking. The wide discrepancy between the effect of structure-promoting and structure-breaking ions on micelle formation is shown also in the results of urea addition to *n*-dodecyl sulfates, as illustrated in Fig. 2. The highly ordered "icebergs" around the solute molecules in the presence of structure promoting tetramethylammonium ion are more susceptible to modification by urea than the disordered "icebergs" around the solute molecules in the presence of structure-breaking alkali metal ions. The c.m.c./c.m.c. (0) values follow the same order as the c.m.c. values. These results suggest a multiplicity of functions for the counterions in micelle formation; however, further work is required to explain the relative contributions from electrostatic interaction, ion hydration, water structure changes by ions, and other factors. Likewise, the argument of the "iceberg" picture is useful to explain the results of the temperature dependence of the c.m.c. of *n*-dodecyl sulfate solutions in the presence of urea, as given in Table I. On raising the temperature, a gradual decrease of ordered regions in water occurs above 25.0°.[28] Consequently, it is anticipated that the modification of the "iceberg" structure around solute molecules on urea addition gradually decreases at temperatures above 25.0°. This is borne out by our results of Table I, which show a decrease in the increments in c.m.c. values of the *n*-dodecyl sulfates on urea addition, on raising the temperature from 10.0 to 45.0°.

Secondly, the effects exhibited by nonionic micelles are considered. It is generally recognized that the over-all solubility of nonionic detergents depends on the extent of hydration of the hydrophilic group through formation of hydrogen bonds between ether oxygens and water molecules.[21] The c.m.c. values of nonionic detergents depend on the balance of forces between the van der Waals interactions in the hydrophobic groups and the opposing hydration of the ethylene oxide chains. Therefore, it is expected, if we accept the validity of Rupley's[34] postulate of the disruption of water structure by urea, that addition of urea to polyoxyethylene surfactants increases the hydration of the ethylene oxide chains and consequently raises the c.m.c. values of these solutions. Thus, the marked increments in c.m.c. values of polyoxyethylene alkanol solutions on urea addition, as shown in Table III, may be attributed to increased hydration caused by a decrease of ordered regions in water.

As may be deduced from the inverse solubility relation, the hydration of the ethylene oxide chains decreases with increasing temperature.[21] This is attributed to the fact that at higher temperatures the tendency of water to hydrogen bond to the ether oxygens is reduced. Consequently, the c.m.c. values of nonionic detergents decrease with increasing temperature.[7] It has been stressed already that on raising the temperature, a gradual decrease of ordered regions in water occurs above 25.0°.[28] Therefore, it is anticipated that the effect of urea on the hydration of the ethylene oxide chain gradually decreases at temperatures above 25.0°. This follows also from our results given in Fig. 3, which show a decrease in the increments in c.m.c. values of the polyoxyethylene alkanols in the presence of 6 *M* urea on raising the temperature from 10.0 to 45.0°. After having given an explanation for the temperature dependence of c.m.c. values in urea solutions of *n*-dodecyl sulfates and polyoxyethylene 1-dodecanols, it is clear that both these explanations apply to the intermediate *n*-dodecyl ether alcohol sulfates.

Finally, the results of Table IV on the addition of electrolyte and urea to 1-dodecanol + 30 EO solutions are briefly discussed. The effects of electrolytes on nonionic detergents have been attributed to a salting-out mechanism.[13,21] The magnitude of this salting out effect depends on the electrolyte concentration and lyotropic number of the "counterion," see Table IV. It is concluded from examination of the two opposing effects that nonionic detergents under con-

(35) K. J. Mysels, Final Report Project NR 356-254, Office of Naval Research Contract NONR-274 (004).

ditions of maximum dehydration of the ethylene oxide chain on electrolyte addition are prone to maximum hydration of the ethylene oxide chain on urea addition.

Acknowledgment. The author wishes to express his gratitude to Lever Brothers Co. for permission to publish this paper, to Mr. D. Manning and Mr. E. Beyer for carrying out the experimental work, and to Mr. W. Pease for synthesizing the ionic detergents.

Thermodynamic Properties of Solutions of Homogeneous *p,t*-Octylphenoxyethoxyethanols (OPE_{1-10})

by E. H. Crook, G. F. Trebbi, and D. B. Fordyce

Research Laboratories, Rohm and Haas Co., Philadelphia, Pennsylvania *(Received April 8, 1964)*

Surface tension as a function of concentration and temperature has been determined for aqueous solutions of single species *p,t*-octylphenoxyethoxyethanols (OPE_{1-10}). From these data surface tension at the critical micelle concentration ($\gamma_{c.m.c.}$), area per molecule, and c.m.c. have been obtained and are presented as a function of temperature and ethylene oxide chain length. $\gamma_{c.m.c.}$ decreases with temperature, the dependence being greatest for compounds with ethylene oxide chain lengths greater than five EO units. This behavior may be attributed to the dehydration of the surfactant molecules which form a lower surface energy film at the air–water interface. Area per molecule at the air–water interface increases as a function of temperature due to the greater surface area swept out by the molecules with increased thermal-kinetic motion. Applying the pseudo-phase model of micellization, changes in enthalpy (ΔH_m^T) and entropy (ΔS_m^T) of micellization are calculated for OPE_{1-10}. ΔH_m^T and ΔS_m^T increase with increasing EO chain length and decrease with temperature. With increasing EO chain length, this corresponds to a greater positive energetic contribution to the micellization process due to the breaking of an increasing number of hydrogen bonds, and with increasing temperature at constant EO chain length, there is a reduced contribution to the energetics of the micellization process because of a lesser degree of initial hydrogen bonding.

Introduction

In a previous investigation,[1] the surface tension of single species OPE_{1-10} as a function of concentration was determined at 25°. At this temperature, several conclusions were drawn as to the effect of ethylene oxide chain length on the surface physicochemical properties of these compounds. Only a few recent investigations[2-10] have dealt with the effect of temperature on the surface tension properties of nonionic surfactants. It is commonly known that temperature has a drastic effect upon the bulk properties of certain nonionic compounds. This is demonstrated by the so-called "cloud point" phenomenon.[11,12] In this investigation a systematic study of the effect of temperature

(1) E. H. Crook, D. B. Fordyce, and G. F. Trebbi, *J. Phys. Chem.*, **67**, 1987 (1963).

(2) M. J. Schick, *ibid.*, **67**, 1796 (1963).

(3) M. J. Schick, *J. Colloid Sci.*, **17**, 801 (1962).

(4) J. M. Corkill, J. F. Goodman, and R. H. Ottewill, *Trans. Faraday Soc.*, **57**, 1627 (1961).

upon the surface tension properties of solutions of homogeneous OPE_{1-10} is presented.

Experimental

Materials. Details of the preparation and characterization of single species OPE_{1-10} have been presented elsewhere.[1,13] All of the water used in the preparation of solutions was distilled from alkaline permanganate solution and had a specific conductance of $<1 \times 10^{-6}$ ohm^{-1} cm.$^{-1}$, which indicates the substantial absence of inorganic contaminants.

Apparatus. Two Du Noüy tensiometers were used to measure the surface tension of the aqueous surfactant solutions. Calibration of the tensiometers was carried out with water by determining its surface tension as a function of temperature. Temperatures both above and below room temperature were obtained by circulating a thermostated mineral oil through specially designed chambers (Fig. 1) which enclosed the Du Noüy ring and surfactant solution. Temperature constancy was obtained within *ca.* 25 min. as was initially determined with a thermistor probe situated at the center of the surfactant solution. Uniformity of temperature was better than $\pm 0.5°$ over the entire depth of the inner chamber of the cell. There was a $<1°$ temperature gradient between the constant temperature bath and the inner chamber of the cell.

Procedure. Stock solutions or dispersions of the appropriate surfactants were prepared by dissolution of the corresponding pure material in water and subsequent equilibration for 24 hr. at room temperature. Subsequent dilutions were prepared from these stock solutions and were equilibrated for 24 hr. before surface tension measurements were carried out. To initiate a run, an acid-cleaned Tannin dish was placed in the inner compartment of the constant temperature cell. Thirty milliliters of surfactant solution was carefully added *via* a pipet. The stem of the Du Noüy ring, with its adapter, was then inserted through the bottom of the cover of the constant temperature chamber and held firmly in place until the top had been fitted onto the main body of the constant temperature chamber. The adapter, which was attached to the stem of the Du Noüy ring, was then inserted into the appropriate receptacle in the arm of the Du Noüy tensiometer. Some lateral movement of the main body of the constant temperature cell was often necessary to ensure free movement of the Du Noüy ring through the orifice (*ca.* 3.5-mm. diameter) in the top of the cell. This adjustment was provided by the swinging arm of the tensiometer to which the main body of the cell was attached. Orientation of the ring with respect to the air–water interface was accomplished by illuminating the ring from a top porthole and viewing through a porthole located on the side. Necessary adjustments were then made by rotating the stem of the ring until the ring was parallel to the surface of the surfactant solution. Once the correct orientation was obtained, surface tension values were determined in the conventional manner. Measurements were carried out between 15 and 85° in 10° increments. Four to six readings were obtained at a given temperature and an average value was recorded.

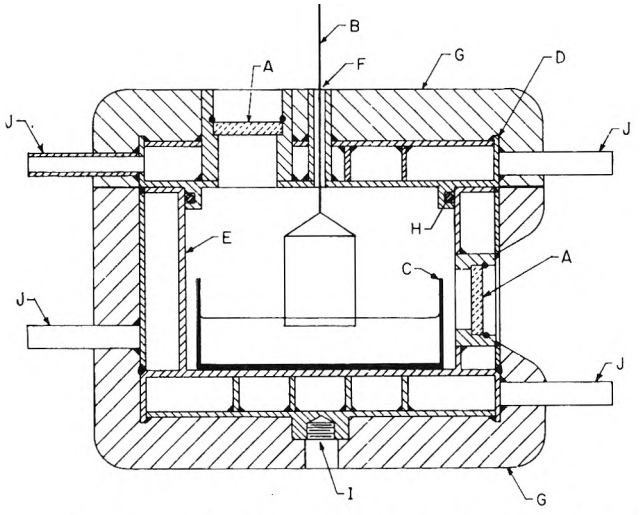

Figure 1. Constant temperature cell for surface tension determination: A, circular glass portholes; B, Du Noüy ring and adapter; C, Tannin dish; D, cell cover; E, cell body; F, 3.5-mm. orifice; G, insulation; H, "O" ring; I, tapped base for attachment to tensiometer platform; J, inlets and outlets for thermostatted liquid.

Results and Discussion

From surface tension *vs.* concentration plots at various temperatures, the parameters: surface tension at the critical micelle concentration, $\gamma_{c.m.c.}$ (Fig. 2 and 3), area per molecule at the air–water interface (Fig. 4 and

(5) P. H. Elworthy and A. T. Florence, *J. Pharm. Pharmacol.*, **16**, 851 (1963).

(6) M. E. Ginn, F. B. Kinney, and J. C. Harris, *J. Am. Oil Chemists' Soc.*, **37**, 183 (1960).

(7) T. Nakagawa, H. Inoue, K. Tori, and K. Kuriyama, *J. Chem. Soc. Japan*, **79**, 1194 (1958).

(8) C. A. J. Hoeve and G. C. Benson, *J. Phys. Chem.*, **61**, 1149 (1957).

(9) K. W. Herrmann, *ibid.*, **66**, 295 (1962).

(10) I. Reich, *ibid.*, **50**, 257 (1956).

(11) W. N. Maclay, *J. Colloid Sci.*, **11**, 272 (1956).

(12) T. Nakagawa and K. Tori, *Kolloid-Z.*, **168**, 132 (1960).

(13) R. C. Mansfield and J. E. Locke, *J. Am. Oil Chemists' Soc.*, **41**, 267 (1964).

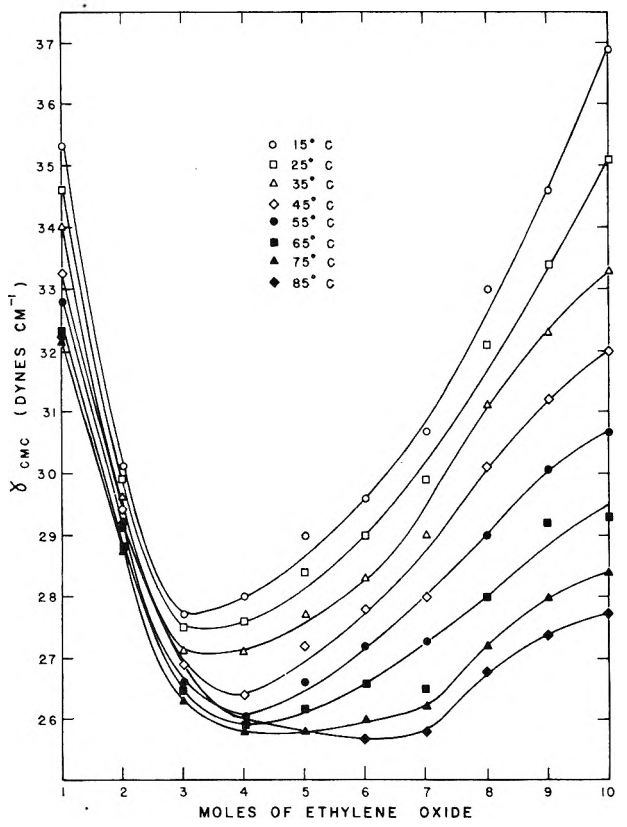

Figure 2. Plot of $\gamma_{c.m.c.}$ *vs.* ethylene oxide chain length (t = 15–85°).

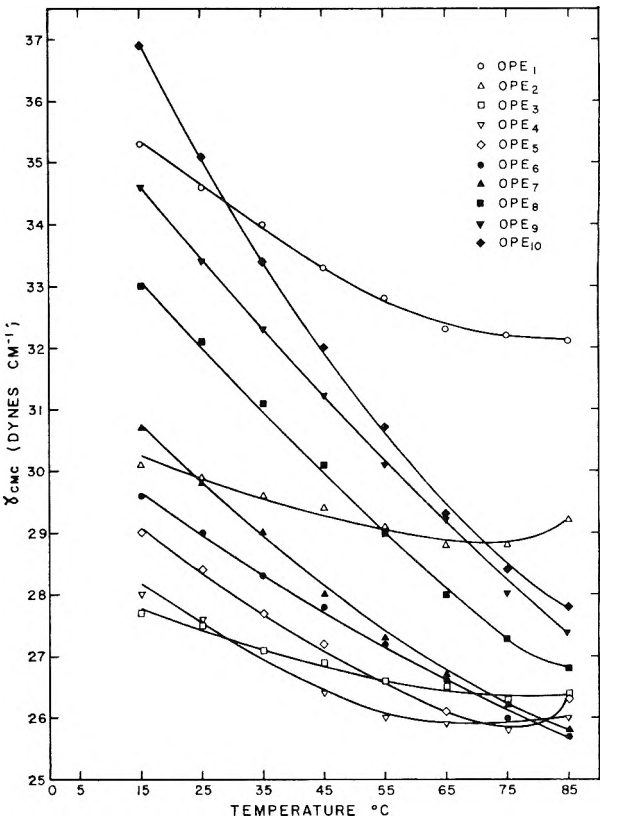

Figure 3. Plot of $\gamma_{c.m.c.}$ *vs.* temperature (OPE_{1-10}).

5), and critical micelle concentration, c.m.c. (Fig. 6 and 7), were determined. Calculated values of the enthalpy (ΔH_m^T) and entropy (ΔS_m^T) of micellization which were determined from plots of log c.m.c. *vs.* $1/T$ data are presented in Fig. 8 and 9. $\Delta(\Delta H_m)$ *vs.* t°C. is presented in Fig. 10.

$\gamma_{c.m.c.}$ *vs. Temperature.* From Fig. 2 it is clear that OPE_{3-7} are the most surface-active members of the OPE series at all temperatures that were studied. It is noteworthy that the relative order of surface activity within the series varies with temperature. This is to be expected since the HLB (hydrophile–lipophile balance) of the individual molecules will change with temperature. For example, at 15° OPE_3 is the most surface active molecule of the series, while between 35 and 65° OPE_4 becomes the most surface-active entity, and finally OPE_5 and OPE_6 are the most surface-active molecules at higher (75–85°) temperatures. This effect occurs as the molecules become more hydrophobic as a consequence of increasing dehydration of the EO chains as the temperature increases. Also of interest is an apparent limiting surface tension (25.8 dynes cm.$^{-1}$) which occurs in the OPE series in the range of 75 to 85°. This is necessarily related to a unique value of HLB which gives rise to an optimum molecular packing at the air–water interface of OPE–water systems.

With shorter EO chain length members, values of $\gamma_{c.m.c.}$ approach the surface tensions of alkylated phenols (γ = 39–41 dynes cm.$^{-1}$) as the EO chain length decreases. It is likely that with octyl phenol and perhaps OPE_1 an insoluble monolayer forms at the air–water interface. This could account for the observed high surface tension values.

Maintaining the EO chain length constant (Fig. 3), the surface tension at the c.m.c. decreases with increasing temperature, which behavior is analogous to the surface tension dependence of pure liquids, *e.g.*, benzene, hexane, or molten NaCl. The decrease of surface tension at the c.m.c. with temperature, however, is nonlinear while conventional liquids usually show a linear decrease of surface tension with temperature. Such deviations from linearity for all of the systems studied can be related to the effect of temperature on the interactions between the surfactant molecules and the water molecules. Such interactions are present and sensitive to temperature because of the large degree of hydrogen bonding which exists in the system and, in fact, is responsible for the solubility of the OPE molecules. With longer chain length OPE's (*e.g.*,

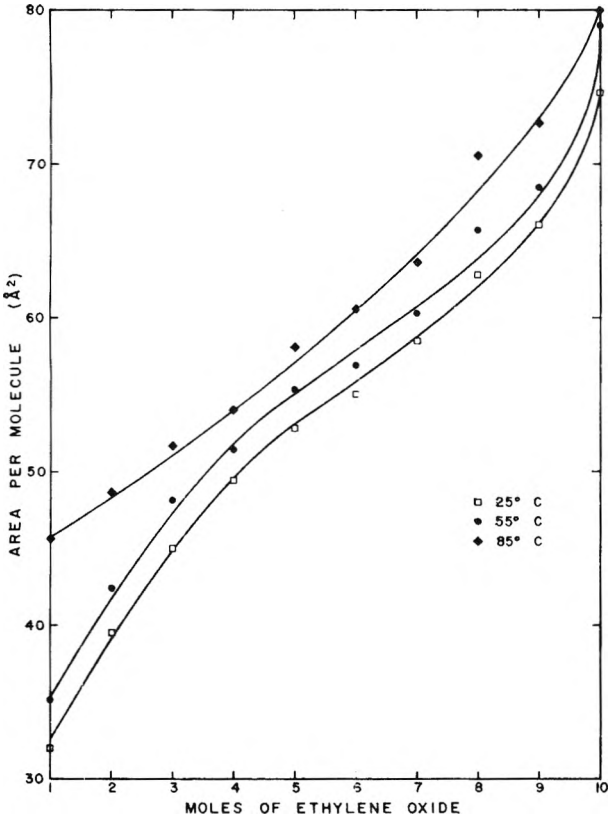

Figure 4. Area per molecule *vs.* ethylene oxide chain length (t = 25, 55, and 85°).

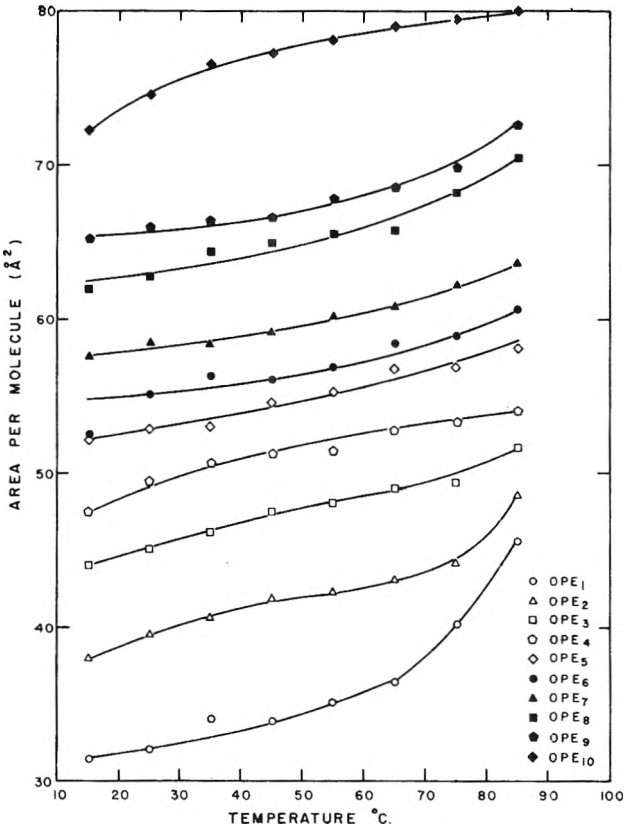

Figure 5. Area per molecule *vs.* temperature (OPE_{1-10}).

OPE_{10}) the EO chain is greatly hydrated. As thermal energy is imparted to the system, many of the existing hydrogen bonds are ruptured and a corresponding decrease in the surface tension occurs as the hydrophobicity of the molecules increases. For shorter chain length OPE's (*e.g.*, OPE_4) the dehydration effect will be somewhat less pronounced since the surfactant molecule binds considerably less water, *i.e.*, is more hydrophobic, to begin with. In fact, at higher temperatures, the surface tension at the c.m.c. of OPE_{1-5} either approaches a limiting value or in some cases, actually increases. This behavior is caused by the continuously changing HLB of the surfactant as the temperature increases and with the shorter EO chain lengths can lead to a less surface-active structure.

In interpretation of the properties of EO containing molecules dissolved in aqueous systems, two opposing thermally controlled effects must be considered: (i) the dehydration of the EO chains which results in an increase of hydrophobic character of the molecule with increasing temperature, and (ii) increase of solubility with increasing temperature due to kinetic–thermal effects. With longer EO chain length OPE's, the first effect overbalances the thermal solubility effect, but with shorter EO chain length molecules, which have only a few oxygen atoms available for hydrogen bonding, the second effect plays an important role and in some instances (*e.g.*, OPE_{1-5}) predominates. This trend will be further demonstrated in the discussion of c.m.c. as a function of temperature.

Area per Molecule vs. Temperature. From Fig. 4 and 5 it is clear that the area per molecule at the air–water interface is an increasing function of EO chain length and temperature. The result obtained as a function of EO chain length has been reported previously[1,14] as being due to poorer packing at the air–water interface since the hydrated, coiled EO chains sweep out a greater surface area as their length increases. As the EO chain length approaches zero, the area per molecule approaches that of the hydrophobe itself,[1,15] the *p,t*-octylphenyl group.

The increase of area per molecule at the air–water interface with temperature is presumed to be primarily a kinetic–thermal effect. An increase of molecular mo-

(14) M. J. Schick, S. M. Atlas, and F. R. Eirich, *J. Phys. Chem.*, 66, 1326 (1962).

(15) M. J. Schick and E. A. Beyer, *J. Am. Oil Chemists' Soc.*, 40, 66 (1963).

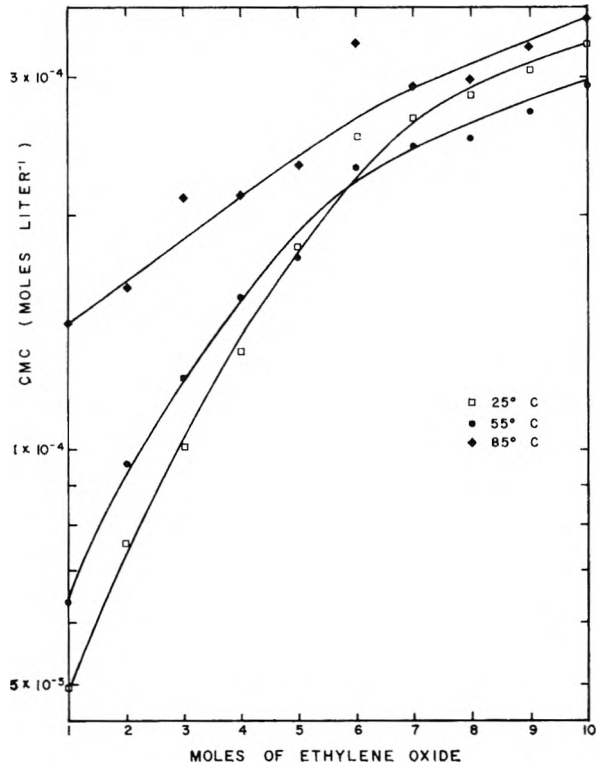

Figure 6. C.m.c. *vs.* ethylene oxide chain length (t = 25, 55, and 85°).

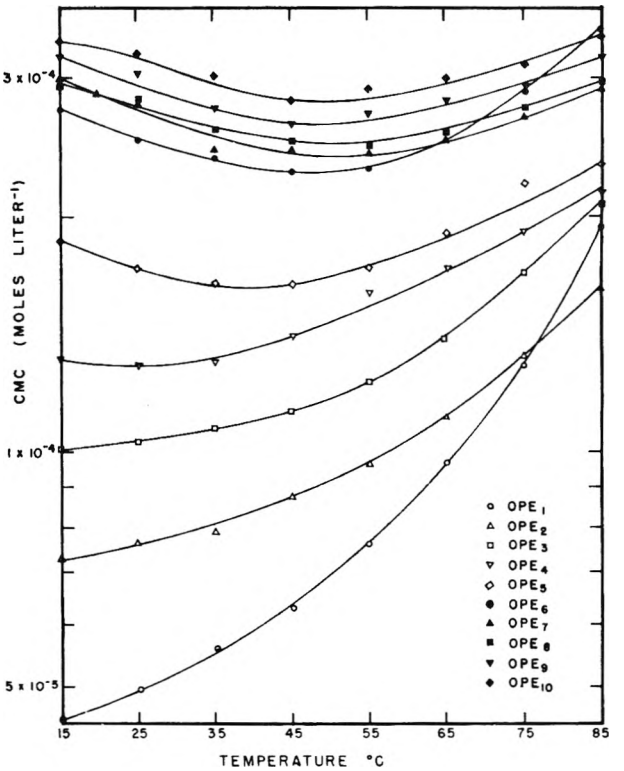

Figure 7. C.m.c. *vs.* temperature (OPE_{1-10}).

tion with increasing temperature results in poorer packing of the adsorbed molecules and a consequent increase of area occupied per molecular unit. This thermal effect is opposed by the influence of the decreased hydration of the EO chains (which consequently sweep out less area under static conditions) which undergo further dehydration with increasing temperature. With all of the OPE's studied, the former area-increasing effect predominates over the latter area-decreasing effect.

C.m.c. vs. Temperature. The data plotted in Fig. 6 show that the c.m.c. at constant temperature is an increasing function of EO chain length within the OPE series. This result is in agreement with previous studies[1,15-18] with nonionic surfactants. Such behavior is directly related to the increase of hydrophilicity of the OPE molecules with increased EO chain length; *i.e.*, longer EO chain length surfactant molecules being more water soluble because of increased oxygen atom content, form micelles at higher concentrations than do the shorter EO chain length molecules.

In Fig. 7 for the surfactants, OPE_{5-10}, the c.m.c. initially decreases, then increases, as the temperature of the system is increased. The initial decrease of the c.m.c. with temperature is undoubtedly a result of the decreased solubility of the surfactant because of the rupture of hydrogen bonds, *i.e.*, the onset of micellization occurs at a lower concentration. As the temperature increases further, the thermal solubility effects begin to exert their influence and finally predominate as the c.m.c. attains a minimum value and finally increases with temperature. Structurally, this corresponds to an initial increasing aggregation of micelles followed at higher temperatures by a partial disintegration of these highly dehydrated aggregates into smaller aggregates. Such behavior has been observed[19] with some of these materials (OPE_{5-8}). One notes first that with increasing temperature the turbidity of the aqueous system increases, reaches a maximum, and then decreases, thus reflecting a corresponding change in aggregation number.

The c.m.c. values of OPE_{1-4} increase monotonically with temperature. The insolubilizing effect of dehydration is much less pronounced and indeed the kinetic-thermal solubility effects predominate. The average

(16) L. Hsiao, H. N. Dunning, and P. B. Lorenz, *J. Phys. Chem.*, 60, 657 (1956).

(17) F. V. Nevolin, T. G. Tipisova, N. A. Polyakova, and A. M. Semenova, *J. prakt. Chem.*, 15, 206 (1962).

(18) H. Lange, *Proc. Intern. Congr. Surface Activity, 3rd Cologne*, 1, 279 (1961).

(19) E. H. Crook, D. B. Fordyce, and G. F. Trebbi, *J. Am. Oil Chemists' Soc.*, 41, 231 (1964).

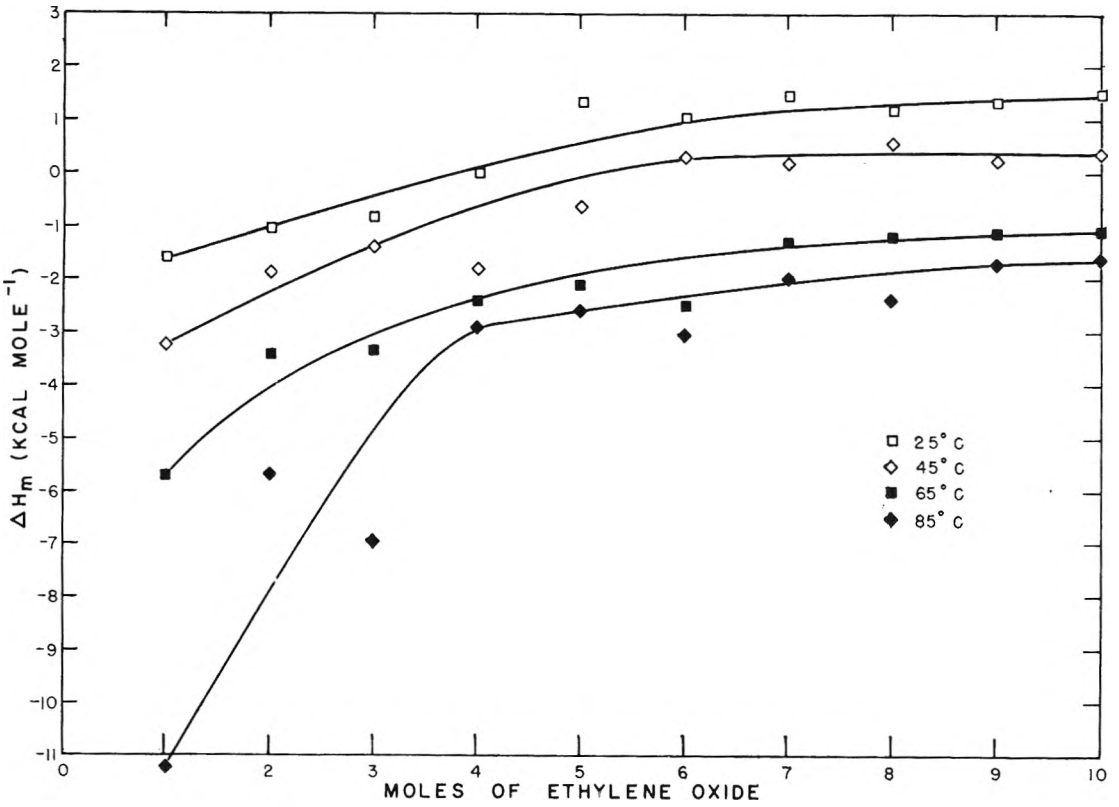

Figure 8. ΔH_m *vs.* ethylene oxide chain length (t = 25, 45, 65, and 85°).

slope of the curve is more positive the shorter the EO chain length, which fact is consistent with the decreased dehydration of the EO chain of the smallest OPE molecules.

One of the referees has pointed out that some of the systems studied may have precipitated as the temperature was raised, so that kinks in the surface tension *vs.* concentration curves may correspond to solubility effects rather than to c.m.c. effects. For solutions of all the compounds studied (OPE_{1-10}) insolubility is already present or attained in the 15–85° temperature range (*e.g.*, 1% solutions of OPE_{1-6} all have "cloud points" below 0° while 1% solutions of OPE_{7-10} have "cloud points" of 28, 54, 68 and 78°, respectively) at concentrations in excess of the c.m.c. This "cloud point" corresponds to an aggregation of micelles such that a distinct phase separation occurs in the system, as is evidenced by turbidity. As is shown in Fig. 7, no simple correlation exists between this cloud point phenomenon and the dependence of the c.m.c. on temperature, since solutions of OPE_{4-6} which exhibit turbidity over the entire temperature range show both positive and negative slopes within the c.m.c. *vs.* temperature plot over the temperature interval studied. Also, the compounds, OPE_{7-10}, all show a reverse of sign of slope of c.m.c. *vs.* temperature at 45°, thus being independent of EO chain length. Consequently, it is believed that the obtained c.m.c. values are indeed indicative of a primary micellization process which is coincidental in some cases with aggregation rather than due to any simple insolubility effects which are independent of a micellar structure.

Thermodynamics of Micellization. Two general theories have been proposed to account for the thermodynamics of micellization, *i.e.*, the phase separation model[20-22] and the mass action model.[23] In principle, it is identical to treat micelle formation either as a mass action equilibrium or as a pseudo-phase.[24] If, however, the aggregation number of the micelle is small, the mass action model is used, while if the aggregation number is large, the phase separation model is applied.[25] Since the aggregation numbers of the micelles of ethoxylates

(20) A. E. Alexander, *Trans. Faraday Soc.*, **38**, 54 (1942).

(21) K. Shinoda, *Bull. Chem. Soc. Japan*, **26**, 101 (1953).

(22) E. Hutchinson, A. Inaba, and L. G. Bailey, *Z. physik. Chem.* (Frankfurt), **5**, 344 (1955).

(23) J. N. Phillips, *Trans. Faraday Soc.*, **51**, 561 (1955).

(24) K. Shinoda and E. Hutchinson, *J. Phys. Chem.*, **66**, 577 (1962).

(25) K. Shinoda, *et al.*, "Colloidal Surfactants," Academic Press, London, 1963, p. 37.

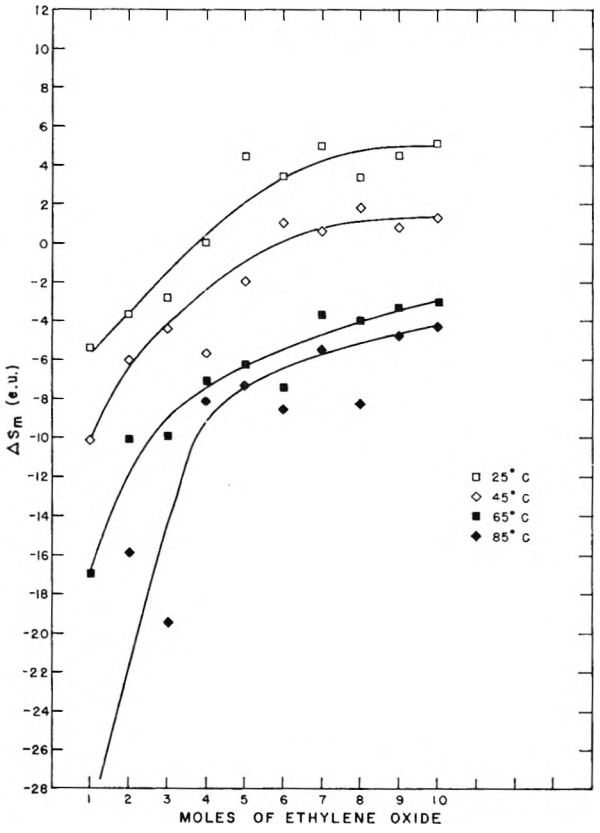

Figure 9. ΔS_m *vs.* ethylene oxide chain length (t = 25, 45, 65, and 85°).

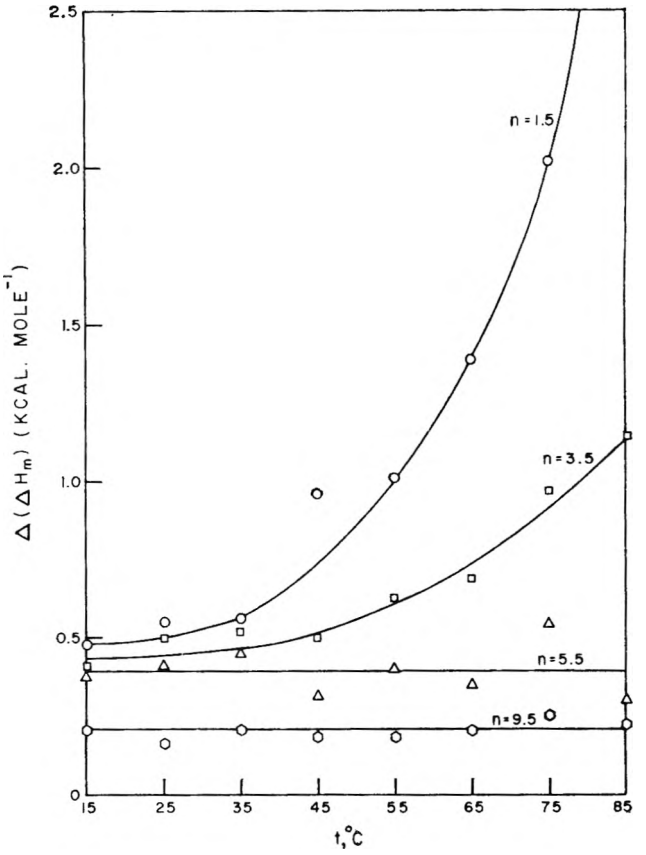

Figure 10. Increment of ΔH_m per EO unit *vs.* temperature (average EO chain length = 1.5, 3.5, 5.5, 9.5).

of alkyl phenols are greater than 100 for EO chain lengths of ten or less,[14,26,27] the pseudo-phase model has been applied to the present results.

With this model, the c.m.c. corresponds to the saturation solubility of the molecular species. If this concentration is exceeded, a new phase is formed. Stainsby and Alexander[28] have proposed the calculation of the change in enthalpy (ΔH_m^T) and entropy (ΔS_m^T) of micellization from the temperature dependence of the c.m.c. according to a Clausius–Clapeyron type of relationship

$$\Delta H_m^T = -RT^2(\partial \ln \text{c.m.c.}/\partial T)_p \qquad (1)$$

Since the micellization process is considered a phase transition, $\Delta F_m^T = 0$, and thus

$$\Delta S_m^T = \Delta H_m^T/T \qquad (2)$$

Recent criticism[29] of this method has centered about the need for values of ΔH_m^T and ΔS_m^T which are corrected for: (i) the change of activity with concentration of the surface-active molecules, and (ii) the change of aggregation number with temperature. With compounds having small c.m.c. values it has been shown[30] that the change of activity with concentration is equal to unity and thus does not contribute to any errors in thermodynamic functions derived from c.m.c. as a function of temperature data. This certainly applies to single species OPE_{1-10} in which the mole fraction c.m.c. varies from 7.8×10^{-7} to 6.1×10^{-6} (for OPE_1 and OPE_{10}, respectively). In this investigation the aggregation number of the compounds as a function of temperature was not determined. If the aggregation number is large (as it is[14,26,27] with ethoxylated adducts of alkyl phenols) the fraction of solute in the aggregated form will be negligible and the correction to be applied to the change in enthalpy and entropy will be very small and can be neglected.[31] On these grounds it is believed that the thermodynamic parameters derived from the temperature dependence of the c.m.c. of

(26) C. W. Dwiggins, Jr., R. J. Bolen, and H. N. Dunning, *J. Phys. Chem.*, **64**, 1175 (1960).

(27) P. Becher, *J. Colloid Sci.*, **16**, 49 (1961).

(28) G. Stainsby and A. E. Alexander, *Trans. Faraday Soc.*, **46**, 587 (1950).

(29) K. Shinoda, *et al.*, ref. 25, p. 129.

(30) K. Shinoda, *et al.*, ref. 25, p. 36.

(31) K. Shinoda, *et al.*, ref. 25, p. 35.

OPE_{1-10} are good approximations to the more accurate values which could possibly be obtained *via* calorimetric determinations of the heat of dilution.[32-34]

Values of ΔH_m^T and ΔS_m^T as a function of EO chain length at various temperatures are presented in Fig. 8 and 9. ΔH_m^T and ΔS_m^T at a given temperature become less negative and in some cases positive as a function of increasing EO chain length. ΔH_m^T and ΔS_m^T for a given EO chain length molecule decrease with increasing temperature: in some cases (OPE_{4-10}) passing from positive to negative values while in others becoming increasingly more negative (OPE_{1-3}).

There are two main structural processes[35] which oppose one another during micellization; (i) the destruction of a considerable portion of the "iceberg" water structure about the monomeric units of surfactant during their incorporation into the micelle with a consequent desolvation of water molecules, and (ii) the rearrangement of a substantial number (>100) of randomly oriented monomeric molecules into a well-ordered micellar structure. From an entropy viewpoint the former process should lead to a positive change in entropy in the transition from a monomeric to a micellar state, while the latter process would lead to a negative value of the change in entropy.

With OPE_{1-10} at 25° the change in entropy upon micellization becomes more positive as the EO chain length increases. This result is consistent with the desolvation of H_2O molecules outweighing the ordering process of the surfactant molecules, and increasingly so as the EO chain length and consequently the number of hydrogen-bound water molecules increase. At EO chain lengths less than four, the change in entropy still increases with EO chain length but the ordering effect of micellization predominates over the desolvation effect simply because of the reduced number of hydrogen-bound water molecules.

With increased temperature, *e.g.*, 65 or 85°, the ΔS_m^T values are all negative, which indicates that the micellar ordering process is more important than the desolvation effect over the entire range of OPE_{1-10}. This result is entirely consistent with the less solvated initial structure of the monomeric surfactant molecules at these temperatures (which can no longer overbalance the ordering process that occurs during micellization).

The present results are entirely in accord with those of Schick[3] who calculated ΔH_m^T and ΔS_m^T for molecularly distilled fractions of EO adducts (ranging from 10 to 50 EO units) of *t*-octylphenol and nonylphenol. In the temperature interval studied (25 to 55°) with compounds of EO chain length longer than those investigated in the present work, the obtained ΔH_m^T and ΔS_m^T values are positive. This agrees with the trend of the present results obtained for the longest EO chain length compound which was studied, *i.e.*, OPE_{10}.

In Fig. 10 is plotted the increment in ΔH_m ($\Delta(\Delta H_m)$) per unit increase in EO chain length as a function of temperature for several average EO chain length molecules. In general, the increment in ΔH_m decreases as a function of increasing EO chain length and approaches a limiting value of *ca.* 200 cal. $mole^{-1}$ in the range of ethylene oxide chain length of 6 to 10 units (and by implication at longer EO chain lengths). At shorter EO chain lengths (OPE_{1-5}) the increment in ΔH_m per unit of EO is strongly temperature dependent above 35°. This is due to the strong dehydration effect of temperature on the small number of water molecules which are bound to such short EO chains; *i.e.*, at higher temperatures (*e.g.*, 65°) the difference in the energy of micellization between OPE_1 and OPE_2 is larger than the same parameter evaluated at 35°. For the longer EO chain length molecules (OPE_{6-10}), the values of $\Delta(\Delta H_m)$ are practically temperature-independent because the number of bound water molecules is not as drastically increased on a fractional basis in a transition from OPE_{8-9}, whether evaluated at 35 or 65°, as would be the case with the shorter EO chain length compounds. The same explanation applies to the increment of ΔS_m as a function of temperature evaluated at several average EO chain lengths.

Acknowledgments. The authors express their gratitude to Messrs. R. C. Mansfield and J. E. Locke for the preparation and characterization of OPE_{1-10} and to Drs. K. A. Booman and F. A. Blankenship for their useful comments pertaining to the manuscript.

(32) P. White and G. C. Benson, *J. Colloid Sci.*, **13**, 584 (1958); *Trans. Faraday Soc.* **55**, 1025 (1959); *J. Phys. Chem.*, **64**, 599 (1960).

(33) E. D. Goddard, C. A. J. Hoeve, and G. C. Benson, *ibid.*, **61**, 593 (1957).

(34) E. Hutchinson, K. E. Manchester, and L. Winslow, *ibid.*, **58**, 1124 (1954).

(35) H. S. Frank and M. W. Evans, *J. Chem. Phys.* **13**, 507 (1945).

On the Viscoelectric Effect in Colloidal Solutions[1]

by D. Stigter

Western Regional Research Laboratory,[2] Albany, California *(Received August 6, 1964)*

The viscoelectric effect for charged colloidal particles is represented as an apparent shift, Δ, of the shear surface. The value of Δ is not very sensitive to the type of kinetic experiment. Comparison of theoretical values with an experimental value $\Delta < 1$ Å. for ionic detergent micelles suggests that the Lyklema–Overbeek estimate of the viscoelectric constant of water is considerably too high.

Introduction

In a discussion of electrokinetic theory, Lyklema and Overbeek[3] have introduced the viscoelectric effect. This is the change of the viscosity η of a liquid under the influence of an electric field E. The treatment is based on the relation[4]

$$\eta = \eta_0(1 + fE^2) \qquad (1)$$

where η_0 is the bulk viscosity of the liquid, E is derived from electric double layer theory, and the viscoelectric constant f for water is estimated

$$f = 10.2 \times 10^{-12} \text{ v.}^{-2} \text{ cm.}^2 \qquad (2)$$

The results suggest that inclusion of the viscoelectric effect in electrokinetic theory raises the calculated ζ-potential substantially in most practical cases. This paper presents evidence to the contrary. The viscoelectric effect is introduced into the theory of intrinsic viscosity and of the rate of self-diffusion of charged colloidal particles with a relatively thin double layer. The treatment is applied to ionic micelles in aqueous detergent solutions and compared with the viscoelectric effect in micellar electrophoresis. The results are compared also with experimental viscosity data on micelles.

Apparent Shift of Shear Surface

We wish to develop a convenient representation of the viscoelectric effect. To this end we consider shearing motion in a 1–1-valent salt solution contained between two infinitely large, flat surfaces of shear located at $x = 0$ and $x = x_0$ in a rectangular coordinate system; see Fig. 1. The liquid is at rest at $x = 0$ and has a velocity in the z direction $v_z = v_0$ at $x = x_0$. In the solution, when no pressure gradient is imposed, the equations of viscous flow reduce to

$$\frac{\partial}{\partial x}\left(\eta \frac{\partial v_z}{\partial x}\right) = 0; \; v_x = v_y = 0 \qquad (3)$$

where η may be a function of x. Integration with respect to x yields

$$\eta \partial v_z/\partial x = \text{constant} \qquad (4)$$

Remembering the definition of η, it is evident that the constant in eq. 4 equals the shearing force F per unit area in the liquid parallel to the flat surfaces. For example, on the stationary surface we have in the case of uniform viscosity $\eta = \eta_0$

$$F = \eta_0(\partial v_z/\partial x)_{x=0} = \eta_0 v_0/x_0 \qquad (5)$$

We now assume that the surface at $x = 0$ is charged such that the electrostatic potential at $x = 0$ is ζ while the potential in the bulk of the solution vanishes. When the surface charge gives rise to a variable viscosity in the solution near $x = 0$, we define an effective shear surface at $x = \Delta$, where Δ is evaluated from

$$F = \eta \partial v_z/\partial x = \eta_0 v_0/(x_0 - \Delta) \qquad (6)$$

(1) Presented in part at the Kendall Award Symposium of the Division of Colloid and Surface Chemistry at the 147th National Meeting of the American Chemical Society, Philadelphia, Pa., April, 1964.

(2) A laboratory of the Western Utilization Research and Development Division, Agricultural Research Service, U. S. Department of Agriculture.

(3) J. Lyklema and J. Th. G. Overbeek, *J. Colloid Sci.*, 16, 501 (1961).

(4) E. N. da C. Andrade and C. Dodd, *Proc. Roy. Soc.* (London), A204, 449 (1951).

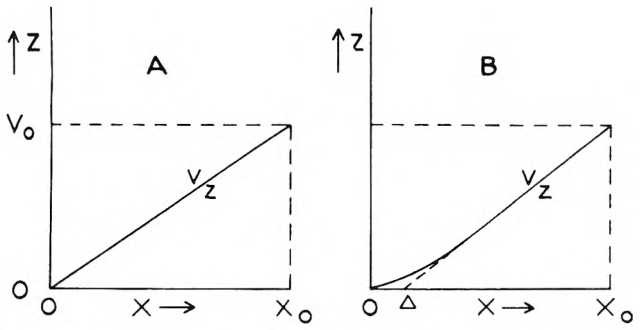

Figure 1. Liquid velocity v_z between two flat plates, at $x = 0$ and $x = x_0$, in shear motion: A, with constant liquid viscosity; B, with increased viscosity in liquid near $x = 0$.

Introducing eq. 1 for η, and assuming $x_0/\Delta \to \infty$, we find from eq. 6

$$\Delta = x_0 - \int_0^{x_0} \frac{dx}{1 + fE^2} = \int_0^{\infty} \frac{fE^2}{1 + fE^2}\, dx \quad (7)$$

Specializing now for E to the Gouy–Chapman theory of the flat double layer, as in ref. 3, the result is, for $A < 1$

$$\Delta = A^{1/2}(1 - A)^{-1/2}\kappa^{-1}\,[\arctan\{A^{1/2}(1 - A)^{-1/2} \times \cosh(e\zeta/2kT)\} - \arctan A^{1/2}(1 - A)^{-1/2}] \quad (8a)$$

and for $A > 1$

$$\Delta = A^{1/2}(A - 1)^{-1/2}(2\kappa)^{-1}\,[\ln\{A^{1/2}\cosh(e\zeta/2kT) - (A - 1)^{1/2}\}\{A^{1/2} + (A - 1)^{1/2}\} - \ln\{A^{1/2}\cosh(e\zeta/2kT) + (A - 1)^{1/2}\}\{A^{1/2} - (A - 1)^{1/2}\}] \quad (8b)$$

where $A = 32\pi cRTf/1000\epsilon$, c is the concentration of salt in moles/liter, and κ is the reciprocal thickness of the double layer.

If an effective shear surface is introduced, eq. 1 for the variable viscosity is replaced by a step function wherein the change from $\eta = \eta_0$ to $\eta = \infty$ occurs at distance Δ from the true surface of shear. The advantage of an effective shear surface is, of course, that it permits one to apply the usual hydrodynamic relations derived with $\eta = \eta_0$, such as the Stokes friction law and the Einstein viscosity theory for spheres. Indeed, it can be shown that in translation as well as in rotation of spheres in viscous liquid the liquid velocity at the surface of the sphere is purely tangential. Hence, for diffusion and intrinsic viscosity of charged spheres with radius a, eq. 8 applies in the limiting case that $a/\Delta \to \infty$. Incidentally, in a complete analysis of viscosity and self-diffusion one should also take into account the interaction between the charged colloid particle and the mobile ions in its double layer. At present we assume that such interactions may be separated from the viscoelectric effect and can be described satisfactorily, *e.g.*, by the expressions derived by Booth.[5]

Lyklema and Overbeek[3] report their results as a correction factor to the Helmholtz–Smoluchowski electrophoresis equation. With the help of the potential distance relation in a flat Gouy–Chapman double layer, this correction factor can be translated into an apparent shift Δ of the shear surface. This representation greatly facilitates the comparison between the viscoelectric effect in, say, viscosity and electrophoresis. It is obvious that, for a given structure of the double layer, the exact value of Δ depends upon the volume forces on the solution in the double layer region. Hence, we anticipate that Δ for electrophoresis differs from Δ for viscosity. This is borne out by the example given in the next section.

Application to Detergent Micelles

We have applied eq. 8 to micelles of sodium dodecyl sulfate in aqueous sodium chloride solutions, using eq. 2 for f and assuming that one-half of the number of counterions is inside the true shear surface of the micelles.[6] As the theory has been developed for a flat double layer, the present calculations neglect the curvature of the micelle surface or, rather, we assume $\kappa a = \infty$, a being the radius of the spherical micelle.

The results for Δ, recorded in Table I, range from 7 to 14 Å. Introduction of the curvature of the micelle surface should decrease the calculated values of Δ, particularly those at low ionic strength. This correction for curvature is difficult to evaluate. However, the theory for the flat surface, $\kappa a = \infty$, should be ap-

Table I: Viscoelectric Shift (Δ) of Shear Surface of Micelles of Sodium Dodecyl Sulfate in Aqueous Sodium Chloride Solutions Calculated for $\kappa a = \infty$

Ionic strength, mole/l.	κa	Δ, Å	
		Intrinsic viscosity	Electrophoresis
0.0085	0.66	14.8	9.0
0.0153	0.91	13.5	9.2
0.0333	1.4	11.8	8.6
0.0523	1.8	10.7	7.8
0.101	2.5	9.3	7.0

(5) F. Booth, *Proc. Roy. Soc.* (London), **A203**, 533 (1950); *J. Chem. Phys.*, **22**, 1956 (1954).

(6) D. Stigter, submitted for presentation at the IVth International Congress on Surface-Active Substances, Brussels, September, 1964.

proached reasonably well for $\kappa a = 2.5$ in Table I. In this case one does not expect a very large correction for curvature. Thus it seems safe to conclude that the theory based on eq. 1 and 2 predicts Δ values of several Å.

The second observation on Table I is that Δ is of the same order of magnitude for viscosity as for electrophoresis.

At this point we introduce some conclusions derived in a concerted analysis[6] of various experiments on micelles of sodium dodecyl sulfate in which the viscoelectric effect was disregarded. The viscosity of micellar solutions, and also the rate of self-diffusion of micelles, showed that the shear surface of micelles coincides within 1 Å. with the surface enveloping the hydrated heads of the micellized ions. This means that, up to a distance of less than 1 Å. from this envelope, the viscosity of water may be treated as a constant. Consequently, the experimental value of Δ is less than 1 Å. and, for all practical purposes, the viscoelectric effect may be neglected in the interpretation of intrinsic viscosity data.

Returning now to Table I we conclude that (a) the viscoelectric effect may also be neglected in the interpretation of micellar electrophoresis; (b) the viscoelectric constant of water, as estimated by Lyklema and Overbeek,[3] eq. 2, is probably too high, perhaps even by one order of magnitude.

This author agrees with the final suggestion by Lyklema and Overbeek[3] that "a determination of the viscoelectric constant for water and aqueous solutions [is] highly desirable."

On the Adsorption of Counterions at the Surface of Detergent Micelles[1]

by D. Stigter

Western Regional Research Laboratory,[2] Albany, California *(Received August 24, 1964)*

This paper presents a model of an ionic micelle in which the electric double layer is divided into a Gouy–Chapman layer outside and a Stern layer inside the shear surface. In the Stern layer the discrete nature and the size of the counterions and of the ionic headgroups are introduced as well as a specific adsorption potential $\Delta\mu^\circ$ of the counterions. The potential $\Delta\mu^\circ$ is calculated as a residue from the equation for the adsorption equilibrium of counterions between the Stern layer and the bulk solution. The theory is applied to micelles of sodium dodecyl sulfate and of dodecyl ammonium chloride, both in aqueous sodium chloride solutions. Using the charge and size of kinetic micelles as determined from various experiments, we find $\Delta\mu^\circ \approx 0.5kT$. There is no significant trend of $\Delta\mu^\circ$ with ionic strength. The uncertainty in $\Delta\mu^\circ$ is due mainly to uncertainties in the precise location of the shear surface, in the dimensions of ions, and to approximations in the ion distribution inside the Stern layer. The results, although developed for prolate ellipsoidal micelles, are not very sensitive to micelle shape. From the repulsion between the micelle core with low dielectric constant and an ion in water, one expects for the sodium counterion $\Delta\mu^\circ \approx 0.25kT$ and for the chloride counterion $\Delta\mu^\circ \approx 0.45kT$. The present results suggest that dehydration of counterions at the micelle surface is insignificant and that the distribution of small ions is governed almost wholly by electrostatic and dimensional factors.

Introduction

Micelles in ionic detergent solutions are interesting objects of research. On one hand, their structure is simple enough to be explored extensively with present experimental techniques. On the other hand, micelles have in common with more complex systems certain interesting features which may be studied fruitfully in the simpler system of micellar solutions. An example is the interaction between small ions and charged colloidal particles, the subject of this paper.

The most advanced theoretical model of a micelle discussed so far is a sphere with a uniform surface charge surrounded by a Gouy–Chapman diffuse double layer. The shortcomings of this model are at least twofold. First, it was found some time ago that the model is inconsistent with the low electrophoretic mobility of micelles and suggested that micelles have a rough rather than a smooth surface.[3] Second, the Gouy–Chapman theory itself has some serious defects.[4] For example, it neglects the dimensions of small ions and recognizes only Coulomb interaction forces.

On the basis of present experimental information, we may introduce a more detailed model of ionic micelles. The new feature is a Stern layer[4] at the micelle surface where correction of the Gouy–Chapman theory is most necessary. In the Stern layer we take into account the geometry of the micelle surface and the size of the counterions. Furthermore, we allow for a specific adsorption potential of the counterions in the Stern layer.

The starting point of the theory is the equilibrium between the counterions in the bulk solution and in the Stern layer or, stated otherwise, the equality of the electrochemical potential of the counterions, η, in the two regions. Indicating properties of counterions in the bulk solution and in the Stern layer with subscripts

(1) Presented in part at the Kendall Award Symposium of the Division of Colloid and Surface Chemistry, 147th National Meeting of the American Chemical Society, Philadelphia, Pa., April, 1964.

(2) A laboratory of the Western Utilization Research and Development Division, Agricultural Research Service, U. S. Department of Agriculture.

(3) D. Stigter and K. J. Mysels, *J. Phys. Chem.*, 59, 45 (1955).

(4) J. Th. G. Overbeek in "Colloid Science," Vol. I, H. R. Kruyt, Ed., Elsevier Publishing Co., New York, N. Y., 1952.

b and s, respectively, we write conventionally for counterions in the bulk, outside the double layers

$$\eta_b = \mu_b^\circ + kT \ln \rho_b + kT \ln f_b + ze\psi_b \quad (1)$$

μ_b° is the standard chemical potential, ρ_b is the concentration (number density), f_b is the relevant single ion activity coefficient, and $ze\psi_b$ is the electrostatic potential energy of a counterion with charge ze in the bulk solution. As ψ_b is constant outside the double layers, we follow common practice and set $\psi_b = 0$.

We may express η_s formally in a similar way

$$\eta_s = \mu_s^\circ + kT \ln \rho_s + ze\psi_s \quad (2)$$

where ρ_s is the effective concentration of the counterions in the Stern layer and $ze\psi_s$ is their electrostatic potential energy in the field of the neighboring ions. There is no rigorous treatment for ρ_s and for ψ_s. The problems are similar to those in the theory of concentrated solutions. In fact, the entropy term $kT \ln \rho_s$ and the energy term $ze\psi_s$ cannot be separated explicitly, as in eq. 2, except in certain approximate treatments. The approach in this paper is based on a cell model of the Stern layer that does allow separate evaluation of ρ_s and ψ_s.

As in most theories, our model is a compromise between tractability and reality. Although the present choice is not fully satisfactory, it allows us to decide which features of the model require refinement. The test quantity in the theory is the difference $\Delta\mu^\circ = \mu_s^\circ - \mu_b^\circ$ which is found as the final term in the equilibrium equation $\eta_b = \eta_s$. With eq. 1 and 2 we have

$$\Delta\mu^\circ = \mu_s^\circ - \mu_b^\circ = kT \ln (f_b \rho_b / \rho_s) - ze\psi_s \quad (3)$$

The term $\Delta\mu^\circ$ is generally called the specific adsorption energy of a counterion in the Stern layer. We note that this quantity is a free energy.

We can identify one positive (repulsive) contribution to $\Delta\mu^\circ$. In general, when an electrostatic charge approaches a region of lower dielectric constant, its self-energy increases. For this reason, μ° increases when a counterion approaches the hydrocarbon core of a micelle. This contribution to $\Delta\mu^\circ$ can be calculated from a model. Comparison with the result of eq. 3 for $\Delta\mu^\circ$ in various practical cases yields a rough test of the theory. A satisfactory model might then be used to treat other topics in micelle theory, *e.g.*, the micelle–monomer equilibrium and the micelle size distribution.

The applications of eq. 3 in this paper are restricted to two detergent systems for which sufficient experimental information is available: sodium dodecyl sulfate and dodecyl ammonium chloride, both in aqueous sodium chloride solutions at 25°. We start with a discussion of the model and the derivation of some parameters from experiments. This part has been nearly completed in previous reports[5,6] and a brief summary suffices.

Model of Micelle

Figure 1 shows a partial cross section of the model of a sodium dodecyl sulfate micelle. The interior of the micelle is formed by n associating hydrocarbon chains. The density of this core, as extrapolated from the density of liquid hydrocarbons at 25°, is 0.802 g./ml. Small micelles have a spherical core with a radius not exceeding the length of the straight dodecyl chain of 16.6 Å. Larger micelles, with $n \geq n_0 = 54.7$, have a prolate ellipsoidal core with a short semi-axis of 16.6 Å. and a long semi-axis of $16.6\, n/n_0$ Å.

Between the smooth surface of the core and the smooth shear surface is the aqueous Stern layer which contains the n ionic heads of the micellized detergent ions and $(1 - \alpha)n$ counterions. The core and the Stern layer together form the "kinetic micelle."

The charge of the kinetic micelle is neutralized by an excess of αn counterions in the surrounding Gouy–Chapman diffuse double layer. The reciprocal thickness, κ, of the diffuse double layer is determined by the (effective) ionic strength of the solution, that is, by the concentration outside the double layer of nonmicellized (monomeric) detergent and of foreign salt.

The model, as described so far, is essentially defined by three parameters: the association number n, the thickness s of the Stern layer, and the fraction α of the total number of counterions located outside the shear

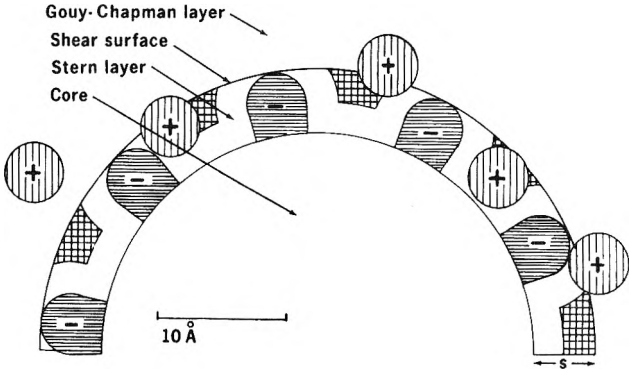

Figure 1. Partial cross section of sodium dodecyl sulfate micelle. Crosshatched area in Stern layer is available to the centers of sodium ions.

(5) D. Stigter in "Electromagnetic Scattering," M. Kerker, Ed., Pergamon Press, New York, N. Y., 1963, p. 303.

(6) D. Stigter, presented at the IVth International Congress on Surface-Active Substances, Brussels, September, 1964.

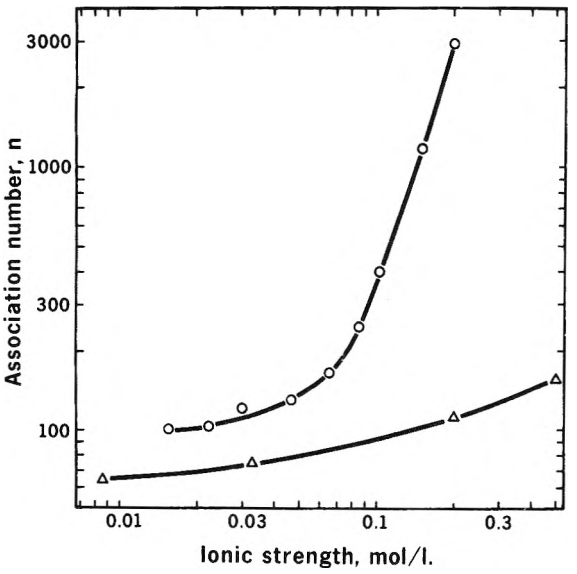

Figure 2. Association number, n, of micelles in aqueous sodium chloride solutions. Circles: dodecyl ammonium chloride, experiments by Kusher, Hubbard, and Parker[7]; triangles: sodium dodecyl sulfate, experiments by Mysels and Princen.[8]

surface. In order to determine these parameters we have carried out a concerted analysis of various experiments.[5,6]

The association number n is determined[5] from light scattering data.[7,8] As shown in Fig. 2, n increases with increasing ionic strength and, furthermore, n depends on the particular type of detergent.

The thickness of the Stern layer follows from the viscosity of micellar solutions and from the rate of self-diffusion of micelles. We find[6] that, within 1 Å., s equals the length of the hydrated ionic head of the micellized ions.

Information on micelle shape is also obtained. Viscosity data indicate[6] that large micelles behave like flexible rods as is consistent with the assumed fluid structure of micelles. Small angle X-ray scattering[9] has confirmed the liquid nature of micelles.

The values of α derived[6] from electrophoresis and from electric conductance of micelles range from 0.4 to 0.6.

The present treatment requires a rather detailed model of the Stern layer. We assume that the ions in the Stern layer remain hydrated and behave like hard spheres. A diameter of 4.6 Å. is taken for both sodium and sulfate ions and 3.8 Å. for chloride and ammonium ions. In addition, we take s = 4.6 Å. for the dodecyl sulfate micelle and s = 2.7 Å. for the dodecyl ammonium micelle. Actually, there is considerable uncertainty about the size of hydrated ions.[10] Because of this uncertainty, we shall investigate the effect on our results of a variation of 0.5 Å. in s and in the ionic radii.

Effective Concentration of Counterions in the Stern Layer

In Fig. 1 the crosshatched sections indicate the free volume of the Stern layer, that is, the volume that is available to the centers of the counterions. Figure 3 shows a schematic top view of the Stern layer, again for sodium dodecyl sulfate, with α = 0.5. The n fixed SO_4^- groups are arranged hexagonally, leaving $n/2$ face-centered sites or cells for the sodium ions. With this regular arrangement, elementary geometry suffices to make an estimate of the free volume v per sodium site, as a function of the micelle size. The results are presented in Fig. 4. It is apparent that the uncertainties in the values of s and of the ionic radii may cause an error of a factor 2 in v.

The concentration ρ_s of the counterions in the Stern layer is, of course, connected with the free volume in the Stern layer. At α = $^1/_2$ a crude estimate is $\rho_s = 1/v$. This estimate of ρ_s is too high for two rea-

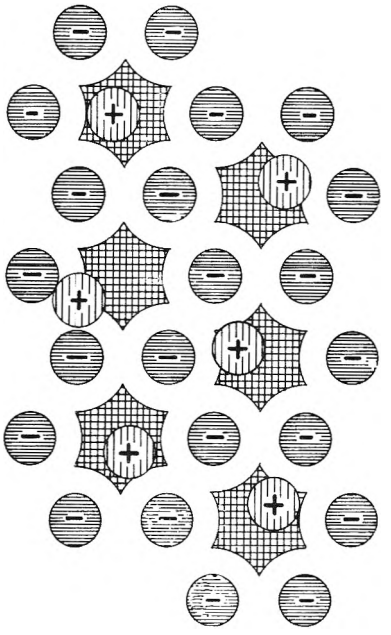

Figure 3. Top view of Stern layer of sodium dodecyl sulfate micelle at the level of the centers of fixed sulfate groups. Crosshatched sections are available to center of sodium ions.

(7) L. M. Kushner, W. D. Hubbard, and R. A. Parker, *J. Res. Natl. Bur. Std.*, 59, 113 (1957).

(8) K. J. Mysels and L. H. Princen, *J. Phys. Chem.*, 63, 1696 (1959).

(9) Fr. Reiss-Husson and V. Luzzati, *ibid.*, 68, 3504 (1964).

(10) R. A. Robinson and R. H. Stokes, "Electrolyte Solutions," Butterworths, London, 1959.

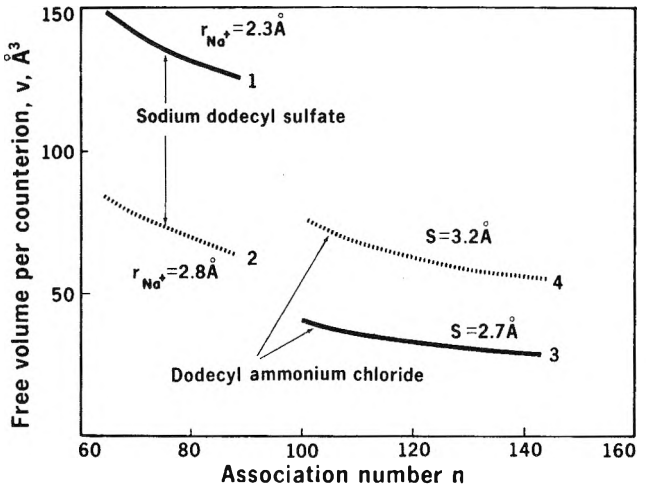

Figure 4. Volume, v, per adsorption cell in Stern layer *vs.* association number, n, of detergent micelles, calculated with smoothed values from broken lines in Fig. 5 of ref. 6: curve 1, sodium dodecyl sulfate, with s = 4.6 Å. and diameters of sodium ion and of sulfate group = 4.6 Å.; curve 2, model as for curve 1, except that diameter of sodium ion = 5.6 Å.; curve 3, dodecyl ammonium chloride, with s = 2.7 Å. and diameter of chloride ion and of ammonium group = 3.8 Å.; curve 4, model as for curve 3 except that s = 3.2 Å.

sons which are both connected with the liquid structure of the micelle.

In the first place, the arrangement of the fixed charges is not at all regular. Therefore, the average overlap of excluded volumes around fixed charges is larger than evaluated above and, consequently, the average value of v is also larger.

In the second place, the cell theory assumes that each cell is occupied by one counterion which is restricted to movement inside the cell. Actually, this restriction is too severe. In general, the relevant correction for communal entropy is difficult.[11] In a simple case a rigorous treatment shows that ρ_s is a factor e' less than predicted by the cell theory,[11] e' = 2.718... being the base of the natural logarithms.

In the present applications we distribute the $(1 - \alpha)n$ counterions in the total free volume of the Stern layer $nv/2$ and we add a factor e' for communal entropy

$$\rho_s = 2(1 - \alpha)/ve' \qquad (4)$$

Expression 4 for ρ_s is perhaps not very satisfactory. One might abandon the cell theory altogether and consider the ions in the Stern layer as an imperfect two-dimensional gas. However, it was found that the ion concentration is much too high for an application of the approximate van der Waals approach. The virial expansion method might be more practical, provided that it can be carried through to sufficiently high terms. This problem was not studied in any detail.

Electrostatics of the Stern Layer

We wish to derive the average electrostatic potential due to the interaction with the neighboring ions ψ_s of a counterion in the Stern layer. To this end the ion distribution is divided into several parts and the contribution of each part to ψ_s is evaluated separately. We have: (a) the potential ψ_d due to the ions in the Gouy–Chapman diffuse double layer; (b) the potential ψ_f due to the fixed ionic charges in the Stern layer; and (c) the potential ψ_c, caused by the counterions in the Stern layer, excepting the one counterion in the cell under consideration.

The effect of micelle shape is introduced in an approximate way as follows. We first evaluate ψ_s for spherical micelles with a core radius $a = 16.6(n/n_0)^{1/3}$ Å. Subsequently, we apply to ψ_s a correction for the deviation from spherical shape of the micelle which will be estimated later.

We assume that the dielectric constant is a step function with ϵ_c 2 inside a sphere with radius b and ϵ_w 78.5 outside this sphere. We set b equal to the core radius a and, in addition, we shall investigate the effect on ψ_s of a variation of b.

We evaluate ψ_s in the center of an adsorption cell and we shall consider, to some extent, the variations of ψ_s within a cell.

We now return to the shape factor in ψ_s. Let us consider a particle with volume V and electric charge e in a medium with dielectric constant ϵ. The surface potential ψ of the particle may be written as

$$\psi = \frac{e}{\epsilon}\left(\frac{3V}{4\pi}\right)^{1/3} S_0 = \frac{e}{\epsilon r_0} S_0 \qquad (5)$$

where r_0 is the radius of a sphere with volume V. S_0 is a shape factor which equals unity for spherical particles.

Standard texts on electricity show that the equipotential surface around a uniform line charge is the family of prolate ellipsoids with foci at the ends of the line charge. Thus we find for the shape factor of prolate ellipsoidal particles with axis ratio p

$$S_0 = \frac{(1 - E^2)^{1/3}}{2E} \ln \frac{1 + E}{1 - E} = 1 - \frac{1}{45}E^4 - \frac{64}{2835}E^6 + \qquad (6)$$

(11) See, *e.g.*, T. L. Hill, "Introduction to Statistical Thermodynamics," Addison Wesley, Reading, Mass., 1961, p. 290.

where the eccentricity of the ellipsoid is $E = \sqrt{1 - 1/p^2}$.

Expression 5 has to be corrected for the effect of the electric double layer that is present around charged micelles in aqueous salt solutions. The presence of a double layer, with thickness $1/\kappa$, around a particle changes both the cofactor, $e/\epsilon r_0$, and the shape factor. We are concerned with the change of the shape factor from S_0 to S. In limiting cases this change is obvious; for

$$\kappa r_0 \longrightarrow 0,\ S \longrightarrow S_0$$

and for

$$\kappa r_0 \longrightarrow \infty,\ S \longrightarrow 1$$

Furthermore, a reasonable guess is, for

$$\kappa r_0 = 1,\ S = (S_0 + 1)/2$$

A simple interpolation function satisfying the above three cases is

$$S = (S_0 + \kappa r_0)/(1 + \kappa r_0) \qquad (7)$$

With equations 6 and 7 we shall estimate S for micelles in aqueous sodium chloride solutions.

Contribution of Diffuse Double Layer to Stern Potential. In order to evaluate ψ_d we start with the total electrostatic potential, ζ, in the spherical shear surface with radius $a + s$. In the Gouy–Chapman model we have[3]

$$\zeta = \frac{1}{\beta}\,\frac{\alpha n e}{\epsilon_w(a + s)[1 + \kappa(a + s)]} \qquad (8)$$

The factor β, also denoted[12] $I/I(\mathrm{DH})$, corrects the Debye–Hückel relation between the surface potential ζ and the particle charge αne. Numerical values of β as a function of the parameters $e\zeta/kT$ and $\kappa(a + s)$ are available.[3,12]

The desired potential ψ_d is found by subtracting from ζ the potential at the uniformly charged surface of the kinetic micelle without diffuse double layer

$$\psi_d = \zeta - \frac{\alpha n e}{\epsilon_w(a + s)} \qquad (9)$$

Contribution of Fixed Charges to Stern Potential. In the present model the Stern layer contains discrete ionic charges. It is of interest to establish the difference from the simpler, more conventional model which possesses a uniform surface charge instead of a Stern layer. The difference is demonstrated with the help of a planar, hexagonal array of point charges e as shown in Fig. 5. This array is the same as that of the fixed charges in Fig. 3, provided that the curvature of the micelle surface is disregarded. In order to evaluate

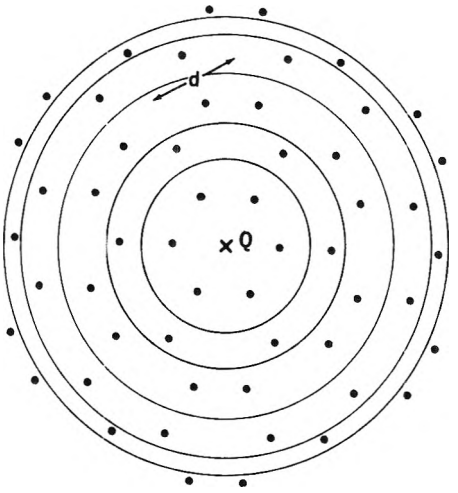

Figure 5. Plane hexagonal array of fixed charges, with repeat distance d. Potential in Q for discrete point charges is given by series 10, for uniformly smeared-out charges by series 11.

the potential ψ_Q at the center of a cell, we divide the array into groups of equivalent neighbors of the central charge, separated by concentric circles in Fig. 5. The potential in Q is written as the sum of successive group contributions, starting with that of the six nearest neighbors

$$\psi_Q = \frac{e}{\epsilon d}(10.39 + 5.20 + 7.86 + 5.77 + \ldots) \qquad (10)$$

ϵ is the dielectric constant of the medium and d is the repeat distance of the array along a trigonal axis.

We now smear out the charges over the appropriate rings so that the plane of the array has a uniform charge density $4e/d^2\sqrt{3}$. Similar to eq. 10 the potential in Q can be written as the sum of contributions from successive charged rings and we find

$$\psi_Q = \frac{e}{\epsilon d}(13.20 + 5.47 + 7.73 + 5.93 + \ldots) \qquad (11)$$

The comparison between corresponding terms in eq. 10 and 11 reveals that only with the nearest neighbors the discreteness of the charges is important. The more distant charges may be smeared out without changing ψ_Q significantly. Consequently, in the evaluation of ψ_f we treat the six nearest ionic heads as discrete charges and we smear out the remainder of the fixed charges over the appropriate surface. This procedure is also, at least to some degree, in accord with a fluid nature of the Stern layer.

(12) A. L. Loeb, J. Th. G. Overbeek, and P. H. Wiersema, "The Electrical Double Layer Around a Spherical Colloid Particle," Massachusetts Institute of Technology Press, Cambridge, Mass., 1960.

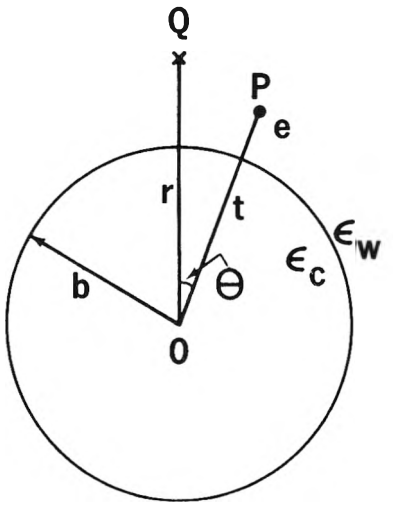

Figure 6. Cross section through dielectric sphere with charge e in P. Potential in Q is given by eq. 13.

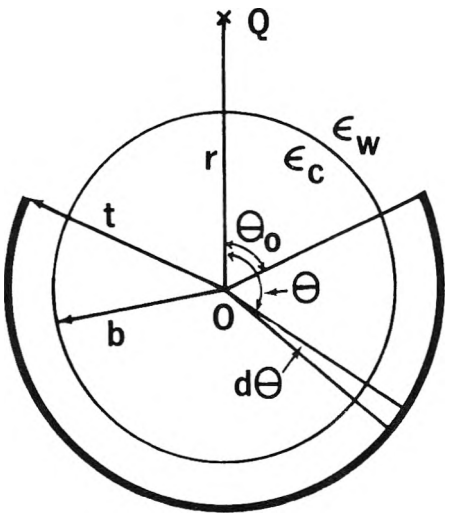

Figure 7. Cross section through dielectric sphere with uniform surface charge of density $ne/4\pi t^2$ in concentric spherical surface with radius t between $\theta = \theta_0$ and $\theta = \pi$. Potential in Q is given by eq. 15.

The introduction of discrete charges in the Stern layer destroys the spherical symmetry of the charge distribution. To obtain the proper solution of Laplace's equation, $\Delta\psi = 0$, we first look at the potential field of a single charge in the Stern layer.

Let the charge e in Fig. 6 be in P at distance t from the center O of the micelle. The position vector r makes an angle θ with OP. Modification of the field around an electric charge near a dielectric sphere under vacuum[13] gives for the present situation, in the region $r > b$

$$\psi = \frac{e}{\epsilon_w t}\sum_{l=0}^{\infty}\left[\left(\frac{r}{t}\right)^l + \frac{(\epsilon_w - \epsilon_c)l}{\epsilon_w(l+1) + \epsilon_c l}\left(\frac{b}{t}\right)^l\left(\frac{b}{r}\right)^{l+1}\right]P_l(\cos\theta) \quad (12)$$

where $P_l(\cos\theta)$ are Legendre functions.

The summation in eq. 12 is carried out similarly to one by Kirkwood and Westheimer,[14] who derived the potential for a point charge inside a dielectric sphere, $t < b$ in Fig. 6. With the abbreviations $b^2/tr = x$ and $\epsilon_c/\epsilon_w = \omega$, eq. 12 is converted into

$$\psi = \frac{e}{\epsilon_w(t^2 - 2tr\cos\theta + r^2)^{1/2}} + \frac{e(1+\omega)}{\epsilon_w b(1+\omega)} \times \left\{\frac{x}{(1 - 2x\cos\theta + x^2)^{1/2}} - x^{\omega/(1+\omega)} \times \int_0^{x^{1/(1+\omega)}} \frac{dy}{(1 - 2y^{1+\omega}\cos\theta + y^{2+2\omega})^{1/2}}\right\} \quad (13)$$

With eq. 13 we evaluate the contribution to ψ_f of the six nearest neighbor fixed ionic charges. The parameters t, r, and x are derived from the micelle model as specified above and θ is obtained from an approximate expression

$$\theta = 4\sqrt{\pi/3n}/\sqrt[4]{3} \quad (14)$$

which is exact for $\theta \to 0$.

It remains to find the potential of the $(n - 6)$ smeared-out, fixed charges. This requires the potential in a point Q near a partially charged dielectric sphere (Fig. 7). In the surface t = constant, between $\theta = \theta_0$ and $\theta = \pi$, the charge density is $ne/4\pi t^2$. This surface is divided into rings between θ and $\theta + d\theta$. The contribution of a charged ring to the potential in Q is obtained with eq. 13. The total potential is found by integrating with respect to θ between the limits θ_0 and π. The potential in Q is

$$\psi = \frac{ne}{2\epsilon_w t}\left\{1 + \frac{t}{r} - \left(1 - 2\frac{t}{r}\cos\theta_0 + \frac{t^2}{r^2}\right)^{1/2}\right\} + \frac{ne(1-\omega)}{2\epsilon_w b(1+\omega)} \times \left\{1 - x - (1 - 2x\cos\theta_0 + x^2)^{1/2} + x^{\omega/(1+\omega)} \times \int_0^{x^{1/(1+\omega)}} \frac{(1 - 2y^{1+\omega}\cos\theta_0 + y^{2+2\omega})^{1/2} - 1 + y^{1+\omega}}{y^{1+\omega}}dy\right\} \quad (15)$$

(13) See, *e.g.*, C. J. F. Böttcher, "Theory of Electric Polarization," Elsevier Publishing Co., New York, N. Y., 1952, p. 102.

(14) J. G. Kirkwood and F. H. Westheimer, *J. Chem. Phys.*, **6**, 506 (1938).

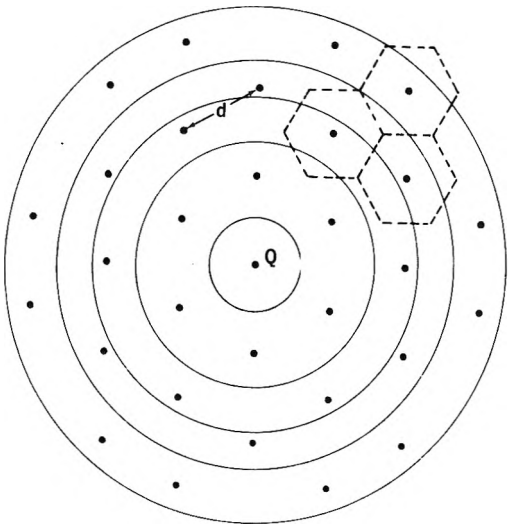

Figure 8. Plane trigonal array of counterions with repeat distance d. Hexagonal cells indicate arrangement of fixed ions. Potential in Q for discrete counterions is given by series 16, for uniformly smeared-out counterions by series 17.

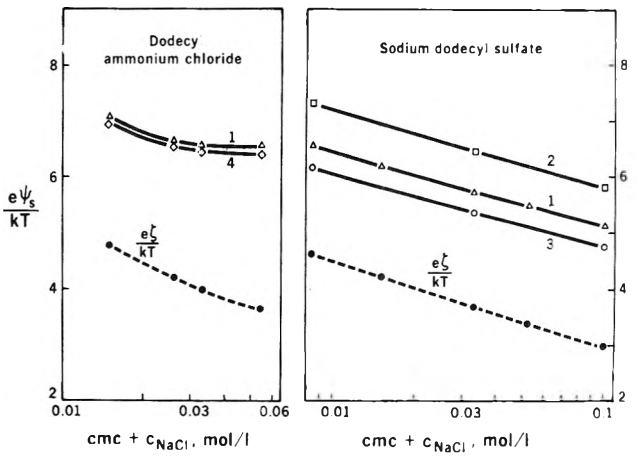

Figure 9. Absolute values of surface potentials *vs.* ionic strength for detergent micelles in aqueous sodium chloride solutions at 25°. Comparison of the Stern potential ψ_s calculated for various models (solid lines) with the ζ-potential (broken lines). In all cases the smoothed α-values have been used from the broken lines in Fig. 5 of ref. 6: curve 1, regular, face-centered hexagonal array of charges in Stern layer; change from $\epsilon_w = 78.5$ to $\epsilon_c = 2$ at surface of micelle core; shape factor $S = 1$; curve 2, model as for curve 1, except that one nearest-neighbor sulfate group is as close as possible to the central sodium ion; curve 3, model as for curve 1, except that the change of ϵ occurs at 2.3 Å. from the core, at the level of the centers of the fixed ions; curve 4, model as for curve 1, but including shape factor S for prolate ellipsoids according to eq. 7.

The contribution of the $(n - 6)$ smeared out fixed charges to ψ_f is derived with eq. 15, where $\cos\theta_0 = 1 - 12/n$ as follows from solid geometry.

Contribution of Counterions in Stern Layer to Stern Potential. The discussion of ψ_c follows closely that of ψ_f. We start with the case of $\alpha = {}^1/_2$. In the regular plane array, as shown in Fig. 8, the counterions form a trigonal lattice with repeat distance d. Some of the $n/2$ hexagonal cells formed by the fixed charges are also indicated in Fig. 8. The charges are divided into equivalent groups, separated by the circles in Fig. 8, and the potential in the central site Q is evaluated as the sum of group contributions. Counting all counterions discretely we find

$$\psi_Q = \frac{e}{\epsilon d}(\infty + 6 + 3.46 + 3 + 4.54 + \ldots) \quad (16)$$

For the uniformly smeared-out charges the equivalent series is

$$\psi_Q = \frac{e}{\epsilon d}(3.81 + 6.27 + 3.83 + 2.70 + 4.60 + \ldots) \quad (17)$$

The main difference between the series 16 and 17 is in the leading term, that is, the contribution of the central ion. But this term refers to the self-potential of the central counterion which should be omitted altogether in the evaluation of the Stern potential. Indeed, the Stern potential, as defined in this treatment, deals with the interionic interaction only. Possible changes of the self-potential of an adsorbed counterion are properly counted with the *specific* adsorption potential as discussed later.

In the actual case of micelles, when $\alpha \neq {}^1/_2$, $\alpha n - 1$ counterions are smeared out over $(n/2 - 1)$ cells, that is, over $(1 - 2/n)$th part of the total surface of the sphere. The desired potential ψ_c is now obtained from eq. 15 in which n is replaced by $[(1 - \alpha)n - 1]/[1 - 2/n]$ and with $\cos\theta_0 = 1 - 4/n$.

The Stern Potential. We are now in a position to evaluate the Stern potential $\psi_s = \psi_d + \psi_f + \psi_c$. In Fig. 9 we compare the ζ-potential with the results of ψ_s for various models in two micellar systems. It appears that ζ is 50 to 75 mv., that is, about 2 to 3 units in $e\zeta/kT$, lower than ψ_s. This difference has but one major cause.

The ζ-potential is derived for a uniformly charged sphere. This means that ζ is an average surface potential to which all ions contribute.

On the other hand, in evaluating ψ_s we specifically exclude the central counterion because we wish to incorporate in ψ_s only the interactions with neighboring ions. Now, the potential of the central, smeared-out counterion is quite significant. It is represented, in the case of a plane surface, by the leading term of

series 17. For spherical micelles we find from eq. 15 that the omission of the central smeared ion lowers $e\psi_s/kT$ by 2.2 to 3.0 units in all cases. Further details of the model may change ψ_s only by small amounts.

The present model of the ion distribution in the Stern layer is very schematic. In all cases ψ_s was calculated for the center of a hexagonal cell. There are, of course, potential variations within a cell. The potential at the center is minimal. A crude estimate is that variations up to 0.4 unit in $e\psi_s/kT$ occur within a cell. Another estimate is obtained when we allow variation in the position of a neighboring fixed ionic group. Curves 1 in Fig. 9 are for regular arrays of ions. However, ψ_s is raised to curve 2 when one neighboring sulfate group is moved toward the central sodium ion. It is likely that curves 1 represent a low estimate of the Stern potential.

Another difficulty is the change of the dielectric constant near the micelle surface. An increase of the radius of the dielectric sphere by 2.3 Å. lowers $e\psi_s/kT$ from curve 1 to curve 3.

We have also tested the effect of micelle shape on ψ_s. The introduction of the shape factor S from eq. 7 lowers ψ_s from curve 1 to curve 4 for dodecyl ammonium chloride. It is evident that this shape effect is hardly significant. For micelles of sodium dodecyl sulfate the correction for shape is even smaller.

In further studies one might introduce an intermediate dielectric constant for the Stern layer. In addition, one might improve the ion distribution in the Stern layer by using, say, a two-dimensional Debye–Hückel approach.

The Specific Adsorption Potential $\Delta\mu^\circ$ of Counterions in the Stern Layer

With the information collected so far we can now evaluate $\Delta\mu^\circ$ by means of eq. 3. The activity coefficient f_b is identified with the average activity coefficient in an aqueous sodium chloride solution[15] at concentration c_{NaCl} + c.m.c. The charge of the kinetic micelle may be evaluated from micellar electrophoresis and also from the conductance of micelles. We have used both sets of data[6] for α in the present calculations. In Fig. 10 the results for $\Delta\mu^\circ$ are plotted *vs.* ionic strength. In each of the micelle systems the considerable spread of $\Delta\mu^\circ$ is due mostly to the uncertainty in α which gives rise to errors in ρ_s and ψ_s. The micelle charges derived from micellar conductance[6] are by no means definite. A thorough study of this method, both theoretical and experimental, would be very helpful.

There are additional errors in ρ_s and in ψ_s which are reflected in $\Delta\mu^\circ$. Some refinements in the theory are possible as pointed out before. However, a large error in v, and hence in $\Delta\mu^\circ$, may be due to our inaccurate knowledge of the thickness of the Stern layer and of ionic radii. Direct experimental determination of these parameters with sufficient accuracy does not seem feasible. The comparison of micelle systems differing only in, say, the type of counterion presents itself as an indirect way of testing the geometric assumptions of the Stern layer model.

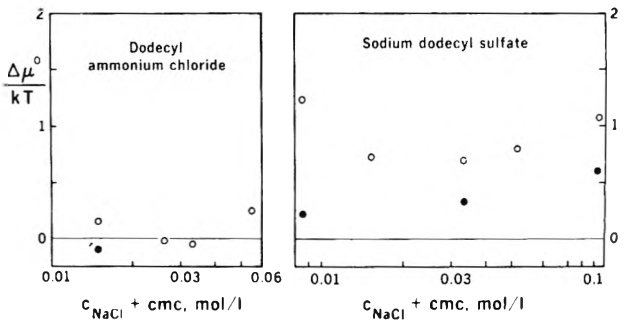

Figure 10. Specific adsorption potential $\Delta\mu^\circ$ of counterions in the Stern layer of micelles in aqueous sodium chloride solutions *vs.* ionic strength at 25°: open circles, micelle charge derived from micelle electrophoresis[6]; solid circles, micelle charge derived from micelle conductance.[6]

Before further discussion of the data in Fig. 10, we evaluate an electrostatic contribution to $\Delta\mu^\circ$. The electrostatic energy (self-energy), ϕ, of a counterion increases when the ion moves from the bulk of the aqueous solution to the micelle surface. This change, $\Delta\phi$, increases the adsorption potential $\Delta\mu^\circ$ of the counterion.

Let the counterion be a sphere with radius δ and charge e, located in point Q of Fig. 6. The surface potential of the ion, ψ_δ, is derived with eq. 13. The desired change of self energy is

$$\Delta\phi = (1/2)e[\psi_\delta(r) - \psi_\delta(r = \infty)] \qquad (18)$$

When we treat the ion as a point charge, that is, assuming $\delta/(r - b) \to 0$, eq. 18 and 13 yield

$$\Delta\phi = \frac{e^2(1 - \omega)b}{2\epsilon_w(1 + \omega)(r^2 - b^2)} - \frac{e^2(1 - \omega)}{2\epsilon_w b(1 + \omega)}\left(\frac{b}{r}\right)^{2\omega/(1+\omega)} \int_{(b/r)^{2/(1+\omega)}}^{} \frac{dy}{1 - y^{1+\omega}} \qquad (19)$$

In the case of the flat interface, $b/(r - b) \to \infty$, eq. 19 is converted into

$$\Delta\phi = \frac{e^2(1 - \omega)}{4\epsilon_w(1 + \omega)(r - b)} \qquad (20)$$

(15) H. S. Harned and B. B. Owen, "The Physical Chemistry of Electrolytic Solutions," 2nd Ed., Reinhold Publishing Corp., New York, N. Y., 1950, pp. 360, 362.

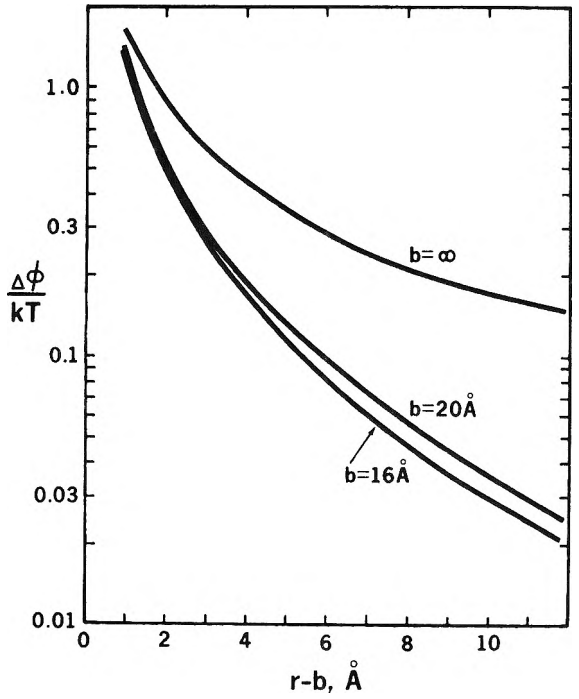

Figure 11. Change of self-energy $\Delta\phi$ of monovalent ion in water *vs.* distance $r - b$ from surface of sphere with dielectric constant $\epsilon_c = 2$ and radius $b = 16$ Å., $b = 20$ Å., and $b = \infty$.

It is observed that according to eq. 20 the influence of the dielectricum on ϕ may be represented by the action of a virtual point charge $(1 - \omega)e/(1 + \omega)$ situated in the mirror point, that is, at distance $2(r - b)$ across the interface from the real charge e. For this reason $\Delta\phi$, in eq. 20, is often called an image term. The corresponding term in eq. 19 is the first one on the right-hand side. The other term in eq. 19 is the correction for curvature of the interface.

In Fig. 11 we have plotted $\Delta\phi$ *vs.* the distance between the charge and the interface for dielectric spheres and also for a flat interface. The data show that curvature of the interface may reduce $\Delta\phi$ considerably. A radius of 16 to 20 Å. is representative for micelles. For the counterions in the Stern layer, $\Delta\phi$ may vary because of the finite thickness of the Stern layer.

In the present model we estimate $\Delta\phi = 0.15$ to 0.3 kT for sodium dodecyl sulfate and $\Delta\phi = 0.3$ to $0.55kT$ for dodecyl ammonium chloride. These values compare favorably with the results of $\Delta\mu^\circ$ in Fig. 10, but the agreement might be fortuitous. The uncertainty in $\Delta\mu^\circ$ is perhaps of the order of $1kT$. Moreover, there might be other contributions than $\Delta\phi$ to $\Delta\mu^\circ$. One possibility would be a significant decrease of the free energy of hydration of the counterions due to disarrangement of water molecules around the ions in the Stern layer. This effect would add a positive (repulsive) term in $\Delta\mu^\circ$.

We have no theoretical reason to anticipate a pronounced trend of $\Delta\mu^\circ$ with ionic strength. Therefore, the absence of a special trend of $\Delta\mu^\circ$ in Fig. 10 supports the present model, in particular the assumption that the distance s between core surface and shear surface does not depend on the ionic strength (compare Fig. 4). This reinforces the conclusion of a previous paper that for micelles a dependence of s on ionic strength due to the viscoelectric effect is insignificant.[16]

Strictly speaking, a factor $\exp(-\Delta\phi/kT)$ should be introduced into the Poisson–Boltzmann equation that gives the ion distribution in the diffuse double layer. Such a factor would tend to lower the ion concentration near the interface and, consequently, imply a more extended diffuse double layer around the micelles. However, Fig. 11 indicates that at a distance larger than 3 or 4 Å. from the core surface, $\Delta\phi$ drops to a small fraction of kT. Thus it is a good approximation to neglect the image term in the region outside the shear surface of micelles.

In conclusion, it should be mentioned that there is a considerable body of literature on the Stern layer in various double layer systems including detergent monolayers at a dielectric interface.[17-19] Now a micelle might be viewed as a detergent monolayer adsorbed onto itself. Therefore, one expects a similarity between the theory of micelles and of monolayers. However, there are considerable differences. One reason is that the experimental information of the two systems is quite different. Another reason is that in monolayer theory the statistical treatments of the Stern layer are essentially based on dilute solution theories whereas for the Stern layer of micelles we have used approximations devised to deal with concentrated solutions.

(16) D. Stigter, *J. Phys. Chem.*, **68**, 3600 (1964).

(17) D. A. Haydon and F. H. Taylor, *Phil. Trans. Roy. Soc.* (London), **A252**, 225 (1960); **A253**, 255 (1960).

(18) S. Levine, J. Mingins, and G. M. Bell, *J. Phys. Chem.*, **67**, 2095 (1963).

(19) S. Levine, G. M. Bell, and B. A. Pethica, *J. Chem. Phys.*, **40**, 2304 (1964).

Ultrafiltration of Nonionic Detergent Solutions[1]

by Hans Schott

Research Center, Lever Brothers Company, Edgewater, New Jersey *(Received April 6, 1964)*

The ultrafiltration of nonionic detergent solutions through cellophane was used as a method of purification. Since the hydrated micelles are about twice the average pore size, the ultrafiltrate consisted chiefly of water-soluble impurities and nonassociated detergent molecules. This permitted removal of carbonylated oxidation products, polyethylene glycol, and sodium chloride. Because of the low c.m.c., the loss of detergent was small. Some fractionation occurred; molecules of longer EO chains filtered through preferentially. Below the c.m.c., purified detergent passed the membrane unhindered. Above it, the detergent concentration in the ultrafiltrate increased linearly with the filtrand concentration. This line intersected the 45° line through the origin at the c.m.c., which can be determined in this manner. The increase in ultrafiltrate concentration was chiefly due to increasing monomer concentration of the filtrand although a few micelles also permeated the membrane, as was shown by the dye tagging technique. An approximately linear increase of monomer concentration with over-all detergent concentration was thus shown by ultrafiltration.

Introduction

Although McBain[2] studied the ultrafiltration of sodium oleate and potassium laurate as long ago as 1922, additional application of this technique to association colloids has been scant and limited to other anionic detergents.[3-5]

Nonionic detergents differ from anionic ones in three pertinent aspects. The membranes used in previous work, *viz.*, cellophane[3] and nitrocellulose,[2,4,5] are negatively charged, and their charge was probably increased by adsorption of anionic detergent. Electrostatic repulsion may have prevented the passage of anionic micelles through the membranes and possibly reduced that of trimers, dimers, and even monomers. Micelles of anionic detergents tagged with a water-insoluble dye did not permeate cellophane in dialysis[6,7] and ultrafiltration experiments.[4] Lacking a pronounced electric charge, nonionic micelles can be prevented from filtering through the membrane only by sieving action.

On the other hand, nonionic micelles are considerably larger than anionic ones, having similar aggregation numbers but much larger monomer molecular weights. Their large size will improve the retention of nonionic micelles by sieving. The slow rate of dissociation of nonionic micelles on dilution[8] is also likely to benefit the retention of micelles during ultrafiltration by minimizing the effect of concentration fluctuations at the membrane in changing the proportion of micelles to monomers.

Experimental

Materials. The detergent used most extensively, molecularly distilled polyoxyethylated 1-dodecanol averaging 30 ethylene oxide (EO) units (C12EO30), was received from Dr. M. J. Schick. The micellar molecular weight of this particular sample, determined by light scattering,[9] was 82,000, which corresponds to

(1) Presented at the 147th National Meeting of the American Chemical Society in Philadelphia, Pa., April 6–10, 1964.

(2) J. W. McBain and W. J. Jenkins, *J. Chem. Soc.*, 121, 2325 (1922).

(3) J. W. McBain, Y. Kawakami, and H. P. Lucas, *J. Am. Chem. Soc.*, **55**, 2762 (1933).

(4) E. Hutchinson, *Z. physik. Chem.*, 21, 38 (1959).

(5) E. Hutchinson and P. M. Shaffer, *ibid.*, **31**, 397 (1962).

(6) R. B. Dean and J. R. Vinograd, *J. Phys. Chem.*, **46**, 1091 (1942).

(7) K. J. Mysels, P. Mukerjee, and M. Abu-Hamdiyyah, *ibid.*, **67**, 1943 (1963).

(8) P. Becher and N. K. Clifton, *J. Colloid Sci.*, **14**, 519 (1959).

(9) M. J. Schick, S. M. Atlas, and F. R. Eirich, *J. Phys. Chem.*, **66**, 1326 (1962).

a diameter of 64 Å. if spherical shape is assumed. Since diameters measured by sedimentation velocity are about one-third larger,[9] the hydrated micelle has a diameter of about 85 Å. Extrapolation of data referring to commercial polyoxyethylated dodecanols[10] results in approximately 52 and 73 Å. for the diameter of a spherical micelle of C12EO30 as measured by light scattering and as calculated by including water of hydration, respectively.

Igepal CO-880, a branched nonylphenol with an average of 30 EO units (NPh30EO) made by General Aniline and Film Corp., was also used. For another commercial NPh30EO, the micellar molecular weight determined by light scattering was 29,700.[10] This corresponds to a diameter of 45 Å. for a spherical micelle and to 62 Å. if the water of hydration is included.[10] For molecularly distilled NPh30EO, a micellar molecular weight of 67,000 has been found by light scattering,[9] which corresponds to a spherical micelle of 59-Å. diameter.

Orange OT (F. D. and C. Orange No. 2; 1-*o*-tolylazo-2-naphthol, mol. wt. 262.3), a water-insoluble dye used for solubilization experiments, was purified by twice precipitating it from acetone solutions with water, followed by three recrystallizations from ethanol.[11] The melting point of 130–131° was the same as that of a sample synthesized in the laboratory. Carbowax 1540 and Carbowax 600 are polyethylene glycols of Union Carbide Chemicals Co. with nominal molecular weights 1300–1600 and 600, respectively.

Ultrafilter. The LKB ultrafilter[12] consists of a cylindrical nylon framework 9.5 cm. long with a 2.7-cm. o.d. over which a tubular cellophane membrane is stretched. The upper end is sealed off by tying the membrane into a double knot. The lower end is closed by a perforated rubber stopper having a glass tube flush with the upper surface, through which vacuum is applied and the ultrafiltrate removed. The supported membrane is mounted in the center of a cylindrical glass container which is filled with the solution being filtered (filtrand). This container has a jacket for circulating water of constant temperature. Its lower end is closed by a perforated rubber stopper directly beneath the first one, and the glass tube which drains the ultrafiltrate runs through it as well. This simple and inexpensive setup affords filtration rates of 20–30 cm.^{3}/hr. The ultrafiltrate runs down the inside surface of the membrane and the frame, thereby practically eliminating dialysis.

Membrane. Seamless regenerated cellulose tubing, Type Visking 36 DC, was used; its diameter was 2.74 cm. After the glycerine with which the cellophane is plasticized was washed out, the specific water content of the membrane, defined[13] by Ferry's eq. 7, was 0.80 g./cm.^{3}. The cellophane had a thickness of 40 μ when wet and 18.3 μ when dry. The average pore diameter, determined from pressure–flow rate data obtained with detergent solutions, was 34 Å. according to Ferry's eq. 4, which assumes that all capillaries run perpendicular to the membrane.[13]

The carboxyl content of the cellophane was found to be 7 ± 1 μequiv./g. by direct titration[14] and 11 ± 2 μequiv./g. by the calcium acetate method.[15] Cellophane from three different rolls was used. The rolls are designated 1, 2, and 3; the different membranes from each roll are designated by letters.

Procedure. Ultrafiltrations were carried out at 25.0 ± 0.5°. The volume of filtrand was initially 710 cm.^{3}. It was usually kept constant by gradual addition of water in order to avoid an increase in filtrand concentration during filtration and to keep the membrane covered with solution, except for experiments with very dilute solutions or with solutions containing solubilized dye. In most experiments below the c.m.c., the filtrand was replenished with more of the initial filtrand. Filtrand concentrations listed are the arithmetic mean values of initial and final concentrations. The solid contents of filtrands and ultrafiltrates were determined by drying aliquots at 75° *in vacuo*. In a typical experiment, the filtrand consisted initially of 710 g. of a 0.700% C12EO30 solution. After 8 hr., 176 g. of solution containing 0.079 g. of detergent had filtered through. The filtrand concentration was thereby reduced to 0.689%.

Stirring of the filtrand was necessary to avoid building up a layer of very concentrated solution near the membrane.[13] The effect of the rate of stirring was not investigated except to make certain that the ultrafiltrate concentration did not increase when the r.p.m. of the stirrer was reduced to one-fifth. The filtrations were carried out under vacuum; evaporation of water never exceeded 2% if the pressure did not come within 4 mm. of the pressure at which the ultrafiltrate boiled. The effect of net pressure on rate of filtration and on ultrafiltrate concentration is shown in Table I. Rates

(10) P. Becher, *J. Colloid Sci.*, 16, 49 (1961).

(11) R. J. Williams, J. N. Phillips, and K. J. Mysels, *Trans. Faraday Soc.*, 51, 728 (1955).

(12) LKB Instruments, Inc., Washington 14, D. C.

(13) J. D. Ferry, *Chem. Rev.*, 18, 373 (1936).

(14) S. M. Neale and W. A. Stringfellow, *Trans. Faraday Soc.*, 33, 881 (1937).

(15) P. A. McGee, W. F. Fowler, and W. O. Kenyon, *J. Am. Chem. Soc.*, 69, 347 (1947).

of flow were directly proportional to applied pressure. Except for filtration under gravity, where dialysis may have contributed, the ultrafiltrate concentration was independent of the rate of filtration. Values of filtrand and ultrafiltrate concentrations obtained with different membranes from the same roll of cellophane were in good agreement, but there were distinct variations from roll to roll.

Table I: Effect of Pressure on Rate of Flow and Ultrafiltrate Concentration of C12EO28

Membrane	Pressure difference, mm.	Rate of flow, g./hr.	Filtrand concentration, %	Ultrafiltrate concentration, %
1-H	6[a]	0.54	0.502	0.0389
1-K	5[a]	0.52	0.488	0.0380
1-H	165	4.47	0.488	0.0304
1-K	368	10.12	0.498	0.0307
1-C	722	21.00	0.493	0.0305
2-C	168	4.46	0.490	0.0401
2-A	368	10.51	0.437	0.0377
2-C	720	21.92	0.440	0.0379
2-B	725	21.90	0.492	0.0399
2-B	728	22.80	0.303	0.0306

[a] By gravity; all other filtrations were at constant volume.

In dye solubilization experiments, an excess of dye was suspended in C12EO30 solutions of different concentration. The solutions were kept in dark bottles under nitrogen. Six to eight days of agitation on a jar-rolling mill were followed by 10–14 days of storage at 25.0 ± 0.1°. Most of the excess dye settled on standing. The finely dispersed dye suspended in the decanted supernatant was removed by filtration through a tightly packed plug of absorbent cotton.[16] This removed all nonsolubilized dye because doubling the detergent concentration of a filtered sample by the addition of solid detergent did not increase its absorbancy.

Conductance measurements were made with a dipping cell immersed in the filtrand and an alternating current conductance bridge. Surface tensions were measured at 25.0 ± 0.1° with a sand-blasted platinum Wilhelmy plate. In the range between the critical micelle concentration (c.m.c.) and one-half of the c.m.c., the surface tension was not very sensitive to changes in concentration.

Spectroscopic Methods. 1. Infrared. A Beckman IR-5A infrared spectrophotometer and 0.1-mm. sodium chloride cells were used to detect the presence of carbonyl groups in C12EO30 by their absorption band at 5.8 μ and to determine variations in the EO chain length. For the second objective, five molecularly distilled polyoxyethylated dodecanol samples of known EO content[9] were used to establish a calibration curve. The ratio of the absorbancy of the stretching vibrations of the C–H bond at 3.4 μ to that of the C–O bond at 9.0 μ, determined with 1.5% solutions in carbon tetrachloride, became nearly independent of the chain length above 23 EO units. Therefore, the ratio of the absorbancy of the two weaker and less readily assigned bands at 7.75 and 6.9 μ was used. The base line for the 6.9-μ band was drawn from 6.7 to 7.1 μ; that of the 7.75-μ band, from 7.1 to 8.3 μ. All measurements, including the calibration data of Table II, were made with 8.0% solutions in tetrachloroethylene. In the 20–30-EO range, careful work affords a reproducibility of ±1 EO unit. Nondistilled EO adducts of 1-dodecanol did not fall on the same calibration curve. In the presence of carbonyl, the estimated number of EO units was low.

Table II: Infrared Absorbancy of EO Adducts of 1-Dodecanol

n[a]	Absorbancy (A) at 7.75 μ	Absorbancy (A) at 6.8 μ	Ratio $\frac{A_{7.75\,\mu}}{A_{6.8\,\mu}}$
3.5	0.121	0.368	0.330
7	0.186	0.328	0.568
14	0.246	0.311	0.792
23	0.282	0.304	0.928
30	0.293	0.300	0.977
PEG[b]	0.269	0.254	1.056

[a] Number of EO units per detergent molecule. [b] Carbowax 1540.

2. Visible. Orange OT used in solubilization experiments has an absorption maximum at 492–493 mμ when dissolved in aqueous C12EO30 solutions. Spectra were taken with a Perkin-Elmer 202 ultraviolet-visible spectrophotometer and with a Beckman DK-2 recording spectrophotometer, using quartz cells 0.5, 1, 5, and 10 cm. long. The plateau at 700 mμ nearly coincided with the base line of the blank and was used as reference (I_0). At the 492-mμ absorption maximum Beer's law was obeyed up to the highest absorbancy tested, namely, 0.9. The absorbancy, log I_0/I, is the product of the molar extinction coefficient ϵ, molar concentration c, and path length l in cm. Acidification of solutions[11] did not change absorbancies. The

(16) M. W. Rigg and F. W. J. Liu, *J. Am. Oil Chemists' Soc.*, **30**, 14 (1953).

molar extinction coefficient of Orange OT at 492 mμ was determined by adding very small volumes of acetone solutions with a micrometer syringe to aqueous 2.00% solutions of C12EO30 The acetone content of the aqueous solutions did not exceed 0.2%. Since the highest dye concentration was less than one-fifth of the solubility limit, little or no dye precipitated when the acetone solution was added to the C12EO30 solution. The best value of ϵ, 1.73×10^4 l./mole cm. (see Table III) is in good agreement with Kolthoff's

Table III: Molar Extinction Coefficient of Orange OT at 493 mμ

Mg. of Orange OT/ 1000 g. of C12EO28 solution	log $(I_0/I)/l = \epsilon c$, cm.$^{-1}$	ϵ, (l./mole cm.) $\times 10^{-4}$
1.740	0.114	1.726
3.529	0.234	1.740
3.793	0.251	1.737
6.714	0.450	1.759
13.482	0.905	1.762

1.98×10^4 value[17] determined in an alcohol–water mixture, but is an order of magnitude lower than the value determined by Williams, Phillips, and Mysels in sodium dodecyl sulfate solutions.[11]

3. Ultraviolet. Variations in the EO chain length of NPh30EO were estimated by the absorbancy of the 276–277-mμ band, which is due to the alkylbenzene portion of the molecule. The EO portion merely dilutes the chromophore.[18] The methanol solutions obeyed Beer's law at the 277-mμ maximum. The molar extinction coefficient was found to be 1510 ± 21 l./mole cm. for three commercial polyoxyethylated nonylphenol samples containing nominally 15, 20, and 30 EO units, respectively. The method affords a reproducibility of ±0.5 EO unit in the range of composition of NPh30EO.

Results and Discussion

Ultrafiltration as a Method of Purification. 1. C12EO30. Infrared spectra of the C12EO30 sample showed a weak carbonyl band at 5.8 μ.[19] When a given portion of this detergent was subjected to a continuous series of ultrafiltrations, the initial ultrafiltrate portions had abnormally high solid contents, and their solid residues had high carbonyl contents. The relation between concentration of filtrand and of ultrafiltrate free of carbonyl is represented by the line CBA of Fig. 1, whereas the triangular points of line EB represent the successive solid contents during

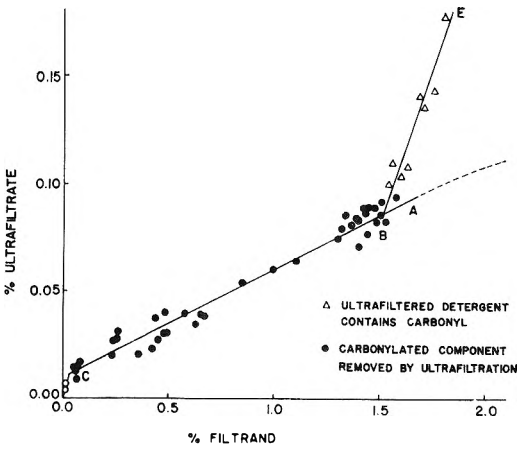

Figure 1. Relationship between the concentrations of filtrand and ultrafiltrate for C12EO30/C12EO28, expressed as wt. %.

the early stages of the ultrafiltration of a given detergent sample when the initial filtrand concentration was 1.8%. The further the ultrafiltration proceeded, the less carbonyl was found in ultrafiltrate and filtrand, while the concentration gradually changed from E to B. After the first 10–15% of the detergent had been removed by ultrafiltration, both filtrand and further ultrafiltrate were free of carbonyl, and their concentration relationship fell on the line CA at point B. The C12EO30 sample contained 6–7% of this carbonylated impurity. The ease with which it was removed by ultrafiltration indicates that it was soluble in water and probably not associated in micelles.

Even though it had been molecularly distilled, the C12EO30 sample was not quite homogeneous, and successive ultrafiltrations produced some fractionation; molecules of longer EO chains filtered through preferentially. The detergent in the initial ultrafiltrate contained approximately 45 EO units. After the first 16% of the detergent had been removed, the EO chain length of the detergent filtering through had decreased to 28. It remained constant at 28 until about 55% of the sample was removed, then drifted down, reaching 20 after removal of 80% of the detergent. All quantitative work was done while this 39% portion containing 28 EO units, designated C12EO28, was being filtered.

Commercial polyoxyethylated detergents usually contain small amounts of alkali salts resulting from neutralization of the ethoxylation catalyst. The removal of electrolytes by ultrafiltration was studied

(17) I. M. Kolthoff and W. Stricks, *J. Phys. Colloid Chem.*, **52**, 915 (1948).

(18) J. Kelly and E. L. Greenwald, *J. Phys. Chem.*, **62**, 1096 (1958).

(19) J. M. Corkill, J. F. Goodman, and R. H. Ottewill, *Trans. Faraday Soc.*, **57**, 1627 (1961).

by adding small amounts of sodium sulfate and of sodium chloride, respectively, to C12EO28 filtrands. The rate of salt removal was followed by the decrease in conductance of the filtrand and checked by chemical analysis of successive ultrafiltrate portions. The conductance data followed first-order kinetics. The specific rate constants are listed in Table IV.

Table IV: First-Order Velocity Constants for Removal of Electrolytes by Ultrafiltration[a]

Electrolyte	Initial concentration, molarity × 10^4	—Rate constants, hr.$^{-1}$, determined by— Electric resistance	Chemical analysis[b]	Rate of flow
NaCl	2.67	0.0132	0.0135	0.0200
NaCl	4.66	0.0192	0.0205	0.0230
Na_2SO_4	2.61	0.0049	0.0048	0.0220

[a] Filtrand contained initially 0.400% C12EO28; ultrafiltration at constant volume. [b] Chloride was determined by Volhard's method; sulfate gravimetrically as $BaSO_4$.

Comparison of the values obtained by conductance or by chemical analysis with the values derived from the flow rate of the ultrafiltrate indicates that sodium chloride passed almost freely through the membrane. Sodium sulfate was strongly retained, passing through the membrane at only one-fifth of the rate of the ultrafiltrate. The detergent was even more strongly retained; the first-order velocity constant for its removal was about 0.0016 hr.$^{-1}$. With filtrands containing initially 0.40% C12EO28, removal of 95% of the salt present coincided with removal of 23–26% of the detergent in the case of sodium chloride but 58% in the case of sodium sulfate. Removal of electrolyte from nonionic detergent solutions by ultrafiltration seems worthwhile only for chloride and perhaps for other univalent anions. The presence of electrolytes at the 10^{-4} M level did not significantly affect the relationship between the C12EO28 concentrations in filtrand and ultrafiltrate.

2. NPh30EO. After discarding the initial ultrafiltrate containing the first 7–8% of this detergent, the EO chain length of the detergent filtering through had decreased from about 50 to 30. It remained constant at 30 until at least 28% of the detergent had been removed, and all quantitative work was done while this 20% portion was being filtered.

Polyethylene glycols may be an impurity in commercial polyoxyethylated detergents. The feasibility of removing them by ultrafiltration was investigated by adding 0.0185% of Carbowax 600 to a filtrand containing 0.53% NPh30EO. The specific first-order rate constant for removal of the polyethylene glycol, as determined by the ultraviolet spectra of successive ultrafiltrates and by their solid contents, was 0.0238 hr.$^{-1}$. The constants for the rate of flow of the ultrafiltrates and for the removal of detergent were 0.0298 and 0.0028 hr.$^{-1}$, respectively. This indicates that the retention of polyethylene glycol by the membrane is slight, and that, in order to remove 95% of it, one loses 28% of the detergent.

Relationship between the Concentrations of Filtrand and Ultrafiltrate. This relationship, shown in Fig. 1–3, is seen to change abruptly at the c.m.c. Working below the c.m.c. with detergent solutions which had been purified previously by filtering off the initial 16% of the detergent for C12EO30 and the initial 8% for NPh30EO resulted in ultrafiltrates with lower solid contents than the respective filtrands. This was probably because of the presence of small amounts of water-insoluble impurities in the filtrands, which remained solubilized even below the c.m.c., holding back some of the detergent. Surface tensions of the filtrands were about equal to those of their respective ultrafiltrates. When the ultrafiltrates of previous filtrations were used as filtrands, the concentrations of the ultrafiltrates were equal to or only very slightly below those of their filtrands. These points fell just barely below or directly on the 45° line through the origin in Fig. 2 and 3, indicating that little or no detergent is retained when solutions of highly purified nonionic detergents below the c.m.c. are filtered through cellophane.

Above the c.m.c., points fell on the straight line CBA up to filtrand concentrations of approximately 1.8%. For C12EO28, the equation of this line, calculated by the method of least squares from 39 points determined with six membranes from roll 1, is

$$U = 0.0104 + 0.0495F \qquad (1)$$

where U and F are the solid contents of ultrafiltrate and filtrand, respectively, expressed in wt. %. The variance about the line is 2.15×10^{-5}. This line intersects the 45° line observed below the c.m.c., for which $U = F$, at 0.0109%. The c.m.c. for C12EO-28, determined as the concentration at which the break in the surface tension *vs.* log. concentration plot occurred, was 0.0106%. Interpolation from the c.m.c. values of a series of molecularly distilled polyoxyethylated dodecanols, which included the present starting material,[9] gave 0.0105% as the c.m.c. for C12EO28. The 45° line through the origin and the line ABC intersect almost precisely at the aforementioned c.m.c. value since the coordinates of point C were $U = F =$

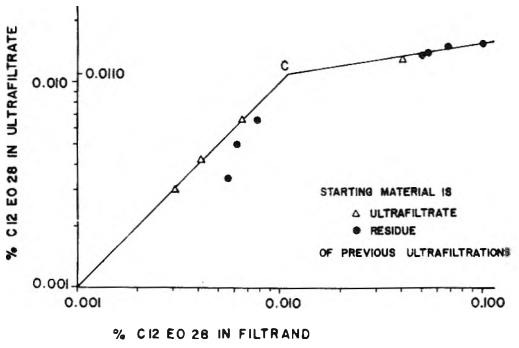

Figure 2. Relationship between the concentrations of filtrand and ultrafiltrate for C12EO28; low concentration region on expanded log–log scale.

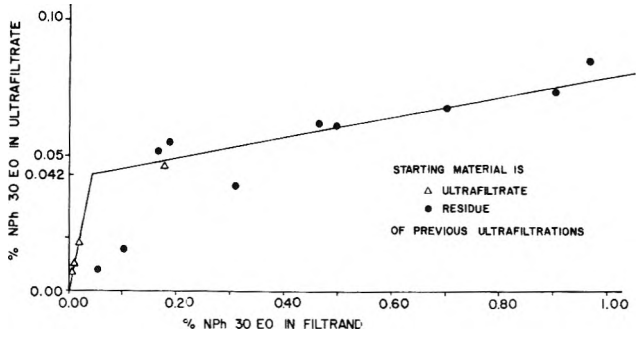

Figure 3. Relationship between the concentrations of filtrand and ultrafiltrate for NPh30EO, expressed as wt. %.

0.0109%. Plotting the few measurements made with roll 2 gave a line slightly above ABC and having a slightly greater slope, but which intersected the 45° line at the same point, namely, 0.0109%.

For NPh30EO, the least-squares equation of line ABC obtained from eight points determined with three membranes from roll 1, is

$$U = 0.0406 + 0.0382F \qquad (2)$$

The variance about this line is 2.37×10^{-5}. It intersects the 45° line through the origin at 0.0422%. The c.m.c. of Igepal CO-880 at 25° was reported[20] as 0.0385–0.0462%, so that point C represents the c.m.c. of NPh30EO as well.

Ultrafiltration therefore offers a method for determining the c.m.c. of nonionic detergents. For this purpose, filtrand concentrations in the range of 0.2 to 1.0% are recommended. Higher concentrations may give points in the nonlinear region beyond point A. The weighing error or the large volume of water to be evaporated on determining the solid contents of very dilute ultrafiltrates dictates the lower limit.

Above filtrand concentrations of approximately 1.8%, line CBA curves toward the filtrand concentration axis. For instance, a 3.45% filtrand of C12EO28 gave an ultrafiltrate containing 0.116% solids, considerably below the 0.181% value calculated by eq. 1. The ultrafiltrate of a filtrand containing 2.56% NPh-30EO had 0.0736% solids instead of 0.1387% as calculated by eq. 2. The rates of flow of these ultrafiltrates were unexceptional.

Dye Solubilization Experiments. The nonzero slope of CBA could be due to limited permeability of the membrane to micelles and/or to an increase in the monomer concentration with increasing concentration of filtrand. The permeability of cellophane to micelles was investigated with Orange OT. The pure dye, synthesized in the laboratory, was insoluble in water at 25°; aqueous suspensions centrifuged at 8000 or 17,000 *g* and 25.0 ± 0.5° did not show the characteristic absorption maximum at 493 mμ. The reported solubility value of 0.2 mg./l. in pure water at 30°[16] may be due to incomplete removal of suspending agents which are probably admixed with commercial dye samples. Moreover, virtually no dissolved Orange OT could be detected after exposure to C12EO28 solutions below the c.m.c. Therefore, dye appearing in the ultrafiltrate is most likely solubilized in detergent micelles. Table V shows that, for a given roll of cellophane, the 493-mμ absorbancy of the ultrafiltrate increased with increasing filtrand concentration. This indicates that the membrane had a few pores large enough to pass micelles, and the dye solubilized within them. It is also seen that solubilization of Orange OT did not affect the relation between filtrand and ultrafiltrate concentration; eq. 1, which was determined for roll

Table V: Ultrafiltration of C12EO28 Solutions Saturated with Orange OT

Membrane	Average filtrand concentration, %	Ultrafiltrate concentration, Observed, %	Ultrafiltrate concentration, Calculated by eq. 1, %	Absorbancy of ultrafiltrate for 1.00-cm. cell ×10⁴	Monomer concentration in filtrand, calculated by eq. 3, %
1-H	0.088	0.0180	0.0148	12.4	0.0174
1-I	0.301	0.0248	0.0253	23.1	0.0237
1-H	0.680	0.0385	0.0440	42.3	0.0365
3-K	0.238	0.0199	0.0222	9.5	0.0194
3-L	0.456	0.0269	0.0330	11.4	0.0264
3-K	0.582	0.0391	0.0392	30.7	0.0376

(20) L. Hsiao, H. N. Dunning and P. B. Lorenz, *J. Phys. Chem.*, 60, 657 (1956).

1 in the absence of dye, predicted equally well the concentration of ultrafiltrates obtained in the presence of dye.

The dye content of detergent solutions saturated with Orange OT, expressed as ϵc, increased linearly with detergent concentration up to 0.40% (*cf.* Table VI).

Table VI: Solubilization of Orange OT by C12EO28

Detergent concentration, % C12EO28	Absorbancy for 1.00-cm. cell	Micelles per solubilized dye molecule: At constant monomer concentration of 0.011%	Micelles per solubilized dye molecule: Corrected for increasing monomer-concentration
	Solutions saturated with dye		
0.662	1.443	0.95	0.91
0.576	1.325	0.90	0.86
0.567	1.107	1.06	1.02
0.500	1.100	0.94	0.90
0.350	0.688	1.04	0.99
0.275	0.515	1.08	1.03
0.200	0.383	1.04	0.99
0.139	0.241	1.12	1.06
0.088	0.164	0.99	0.93
0.050	0.075	1.10	1.00
	Ultrafiltrates of saturated solutions		
0.039	0.00307	19.3	1.00 by
0.038	0.00423	13.4	analogy to
0.027	0.00114	29.6	above data
0.025	0.00231	12.8	
0.020	0.00124	15.3	
0.018	0.00095	15.5	

This straight line intersects the % detergent axis at 0.011%, which is the c.m.c. of C12EO28, indicating that no dye solubilization occurs below the c.m.c.[16,17] Together with the fact that solubilized dye did not affect the relation between filtrand and ultrafiltrate concentration, this shows that the method of dye solubilization for determining the c.m.c.[11,17] is applicable to nonionic detergents.

The solubilization limit of Orange OT in C12EO28 solutions at 25° is calculated in the upper half of Table VI based on the assumption that the micellar molecular weight, namely 82,000,[9] is independent of detergent concentration. Since the Debye plots used in determining micellar molecular weights by light scattering were linear at least up to 0.5% detergent,[9] this assumption is valid at least up to that concentration. In the third column, a constant monomer concentration of 0.011% is assumed throughout and subtracted from the detergent concentration, in order to obtain the fraction of detergent aggregating into micelles and from it the molar ratio of micelles to solubilized dye molecules. In the last column, this ratio is corrected for the increase in monomer concentration with increasing detergent concentration (see below). The result for all saturated solutions was a molar ratio of detergent micelles to dye molecules of 1.0 ± 0.1, *i.e.*, each micelle enfolded one dye molecule. The weight of solubilized dye amounts to only 0.32% of the weight of the micelle which it saturates or 2.82% of the hydrocarbon portion thereof.

Mysels, *et al.*,[7] showed by dialysis that for sodium dodecyl sulfate, the activity of monomer as well as that of micelles increases appreciably with increasing concentration above the c.m.c. Their experimental demonstration was simplified by the virtual impermeability of cellophane to the anionic micelles. Some of the C12EO28 did go through the membrane in the form of micelles. However, their contribution to the total amount of detergent in the ultrafiltrate could be determined because each micelle became tagged with one dye molecule when the filtrand was saturated with Orange OT. It is seen in the lower half of Table VI that in the ultrafiltrates, out of an amount of detergent sufficient to form 13–30 micelles, only one micelle was shown by the dye tag actually to have permeated the membrane as such. The remainder, comprising the bulk of the ultrafiltered detergent, must have existed in the filtrand as monomer. The term monomer is used here to include dimers, trimers, etc., *i.e.*, species small enough to permeate the membrane with relative ease and too small to solubilize Orange OT.

The monomer concentration of the filtrand shown in the last column of Table V was calculated on the assumption that the micellar molecular weight was constant at 82,000. Since the proportion of original micelles is very small, an increase in the micellar molecular weight with concentration would introduce only minor changes. As can be seen from the data of Table V, there is an approximately linear relationship between the calculated monomer concentration in the filtrand (M) and the total detergent concentration (F) expressed as wt. %, at least in the range of 0.09 to 0.70% C12EO28. The least-squares equation relating these two quantities is

$$M = 0.01247 + 0.03676F \qquad (3)$$

The increase in monomer concentration is appreciable. As the detergent concentration goes up from 0.10 to 0.54%, the monomer content doubles. Below the c.m.c., $M = F$, and this 45° line intersects the line represented by eq. 3 at 0.013%, namely, the c.m.c., as it should be.

Acknowledgment. The author is indebted to the Lever Brothers Co. for permission to publish this paper and to Dr. S. Goldwasser for discussions on infrared spectroscopy.

Experimental Investigation on the "Dimpling" of Thin Liquid Films

by D. Platikanov

Institute of Physical Chemistry, Bulgarian Academy of Sciences, Sofia, Bulgaria *(Received April 13, 1964)*

In order to provide an experimental check of the Frankel–Mysels theory for the shape of the "dimpling" during the approach of two interfaces, measurements were carried out on microscopic, circular, thinning liquid films on a solid substrate and on similar foam (soap) films. The shape of the "dimple" was given by the interference picture obtained by photographing the films in reflected monochromatic light. The decreasing of the thickness in the center of the film was measured interferometrically with a photomultiplier. Films of water, aqueous KCl, aniline, ethanol, and oleic acid were used. A shape corresponding to the Frankel–Mysels theory but with a slightly smaller "dimple" was obtained for films on a substrate. For foam films the shape evolved in a different way. In all cases practically plane-parallel films were obtained when the diameters of the films and their thicknesses were sufficiently small. This is in accordance with the assumptions used in the dynamic method for measuring the disjoining pressure in thin liquid films.

The properties of thin microscopic circular films, formed when a gas bubble or a liquid drop approaches an interface, are of utmost importance for the behavior of the respective disperse systems (foams, emulsions, flotation systems, etc.). When the films are sufficiently thin, an additional pressure arises—the so-called disjoining pressure—caused by the deformation of the double electric layers and by van der Waals forces. Recently,[1–3] a dynamic method has been developed for the measurement of the disjoining pressure in thin liquid films as a function of their thickness. This method is based on the assumption that thin liquid films are plane-parallel and that the liquid flows out of them as if between two parallel rigid disks. Thus the equation of Reynolds can be used for the rate of thinning of the film

$$\frac{d(1/h^2)}{dt} = \frac{4}{3\eta r_0^2} P$$

where h is the thickness of the film, r_0 is its radius, and η is the viscosity. As shown earlier,[3] when one of the surfaces of the film dilutes freely, the numerical factor is $^{16}/_{3}$. For both cases the general equation will be

$$\frac{d(1/h^2)}{dt} = \frac{16}{3n^2\eta r_0^2} P \qquad (1)$$

where n is the number of surfaces at which the flow rate is zero. The pressure $P = P_\sigma + \Pi$ is a sum of the capillary pressure $P_\sigma = 2\sigma/R$ (σ is the surface tension, R is the radius of the bubble or the drop) and of the disjoining pressure Π. To apply eq. 1 to the dynamic method for the measurement of Π, the experimental conditions in previous works[1–3] were chosen so that in the thickness range under investigation the films were plane-parallel, which was controlled visually.

(1) A. Scheludko, *Kolloid-Z.*, **155**, 39 (1957).

(2) A. Scheludko and D. Exerowa, *ibid.*, **165**, 148 (1959); **168**, 24 (1960).

(3) A. Scheludko and D. Platikanov, *ibid.*, **175**, 150 (1961).

It is established, however,[4-7] that when a bubble or a drop approaches an interface, the film obtained between the latter and the flattened part of the bubble is not plane, but has a central part thicker than its periphery. Thus a "dimple" is formed, entrapped by a thinner "barrier ring." A hydrodynamic theory for the profile and evolution of this dimple was developed by Frankel and Mysels.[8] This theory takes into consideration only the capillary pressure, but neglects the disjoining pressure which arises at low film thicknesses and depends on this thickness. According to this theory the thickness h in the center of the film (the maximum thickness) is given by the equation

$$h = \left[\frac{0.0096n^2\eta r_0^6}{\sigma R}\right]^{1/4} \frac{1}{(t - t_0)^{1/4}} \qquad (2)$$

and the thickness z_0 at the barrier ring (the minimum thickness) by

$$z_0 = \left[\frac{0.090n^2\eta r_0^2 R}{\sigma}\right]^{1/2} \frac{1}{(t - t_0)^{1/2}} \qquad (3)$$

where t_0 is the time of formation of the hypothetic dimple with infinite thickness. The last equation coincides almost completely with eq. 1, which on integration becomes

$$h = \left[\frac{0.094n^2\eta r_0^2 R}{\sigma}\right]^{1/2} \frac{1}{(t - t_0)^{1/2}} \qquad (4)$$

(for a flat film $h = z_0$). From eq. 2 and 3 one obtains the expression

$$\frac{z_0}{h} = 3.066 \frac{R}{r_0^2} h \qquad (5)$$

which indicates, that the dimple should become relatively more pronounced as the film thins.

The disagreement between these results and the experimental data which serve as a base of the dynamic method[1-3] for the measurement of the disjoining pressure requires elucidation. In the present work thin liquid circular films on a solid substrate, as well as free foam films were studied and the results compared with the Frankel and Mysels theory.[8]

Experimental

A number of liquids with different viscosity were examined: water, aqueous KCl solutions, ethanol, aniline, and oleic acid.

The microscopic circular films on solid substrate were obtained in cell a (Fig. 1). A small glass plate, e, with well-polished surfaces was laid down on the bottom of the cell and the liquid under study was poured in (f). A vertical tube with a radius $R = 2.4 \times 10^{-2}$ cm. was placed above the plate so that the gap between its lower end and the plate was smaller than the radius R. With the aid of a mercury-sealed micrometric screw, air is pressed slowly through the capillary, d, until the concave liquid meniscus is lowered sufficiently to approach the glass plate. Thereupon a circular film is formed at point g. The micrometric screw makes it possible to obtain films with different radii, r_0, although the radius R of the "semibubble" remains constant. In this case the capillary pressure depends[9] on r_0

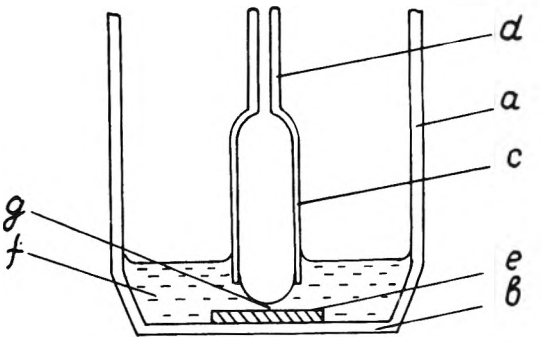

Figure 1. Cell for the investigations of circular liquid films on a solid substrate.

$$P_\sigma = 2\sigma \frac{R}{R^2 - r_0^2} \qquad (6)$$

When $r_0 << R$, r_0 may be neglected in eq. 6.

The films thus obtained are illuminated with a monochromatic beam, observed and photographically recorded through the plane-parallel bottom, b, of the cell. At definite intervals the interference pattern displayed by the film is photographed. From these photographs the thickness h and z_0 as well as the profiles of the dimple and of the barrier ring were calculated. Since the thicknesses could be determined from these photographs only with an accuracy of about $\pm$ 0.03 μ, the values of h were also measured directly by means of a photomultiplier, which registered the intensity of the beam reflected by the center of the film. The plots of photocurrent–time were used to calculate the h–t plots. The latter overlapped the respective curves calculated from the photographs.

(4) B. Derjaguin and M. Kusakov, *Acta Physicochim. URSS*, **10**, 25 (1939).

(5) G. A. Elton, *Proc. Roy. Soc.* (London), **A194**, 275 (1948).

(6) P. S. Prokhorov, *Discussions Faraday Soc.*, **18**, 41 (1954).

(7) R. S. Allan, G. E. Charles, and S. G. Mason, *J. Colloid Sci.*, **16**, 150 (1961).

(8) S. P. Frankel and K. J. Mysels, *J. Phys. Chem.*, **66**, 190 (1962).

(9) D. Exerowa, I. Ivanov, and A. Scheludko, *Godishnik Sofiiskiya Univ. Khim. Fak.*, **56**, 157 (1961/62).

Pictures of films of 0.1 N aqueous solutions of KCl[10] show that a dimple with a regular circular form is formed in the center of the film and thins slowly with time. Simultaneously, the film is rapidly thinning at its periphery—the barrier ring. They also show that the bigger the radius r_0 of the film, the more pronounced the dimple. When $r_0 < 5 \times 10^{-3}$ cm., practically no dimple is formed. The profiles of a film having $r_0 = 1.4 \times 10^{-2}$ cm. taken at intervals from 1 to 300 sec. after its formation are shown in Fig. 2. The film thickness scale is 200 times that of its radius, so that in reality the curvature of the dimple is many times smaller than shown. After a prolonged evolution, the dimpling of films in 0.1 N KCl solution disappears completely and $h = z_0 \approx 300$ Å. These profiles are not to be seen in Fig. 2, because it is rather difficult to maintain the radius r_0 at a constant value for very long periods of time. The time dependences of h and z_0 are given in Fig. 3. The curves are calculated by eq. 2 and 3, respectively ($\eta = 0.01$, $\sigma = 72.7$, $n = 2$), whereas the points are experimental. The same results are represented in Fig. 4 plotting z_0/h against h. The dotted line is calculated by eq. 5.

The photographs of aniline films—a liquid with considerably higher viscosity—show the same picture but the process of thinning is much slower. Here one can observe the initial stages of the formation of the dimple, which in the case of water proceeds very quickly. The profiles of a film with $r_0 = 1.6 \times 10^{-2}$ cm. obtained at intervals from 1 to 900 sec. after its formation are shown in Fig. 5. The data for h and z_0 are given in Fig. 6 and 7, in a manner similar to that for the 0.1 N KCl solution. (The theoretical curves were calculated for $\eta = 4.48 \times 10^{-2}$, $\sigma = 37$, $n = 2$.)

The results with ethanol films are somewhat different. Inasmuch as the surface of ethanol against air dilates freely ($n = 1$),[11] the rate of thinning is considerably higher. Furthermore, ethanol forms quite thick (*ca.* 1400 Å.) equilibrium films upon glass and z_0 cannot reach lower values. Consequently, the barrier ring offers only small resistance to the flow of the liquid, so that h decreases rapidly to reach an equilibrium value, at which the whole film is already plane-parallel. The profiles of a film with a radius $r_0 = 1.25 \times 10^{-2}$ cm. obtained at intervals from 4 to 30 sec. from its formation are shown in Fig. 8, and the results for h and z_0 are given in Fig. 9. The curves in the latter are calculated by eq. 2 and 3 with $\eta = 1.20 \times 10^{-2}$, $\sigma = 22.3$, $n = 1$. Similar results are obtained with films of pure doubly distilled water.

The experiments on free foam films were carried out as described previously.[2] Films of 5×10^{-3}% OP20 (a nonionic surfactant) in 0.1 N KCl aqueous solution were studied. Dimples were observed with films having a radius of *ca.* 10^{-2} cm. Their form as a rule was irregular, located asymmetrically with respect to the center of the film and unstable. As the film thins, the dimple shifts toward the edge and suddenly and rapidly flows out to the bulk of liquid. Very often dimples are not formed at all but a number of thicker "channels" directed to the periphery can be seen through which the liquid flows rapidly toward the edges. Such a flow through "channels" was usually observed at large diameters of the films.[12] At radii lower than *ca.* 10^{-2} cm., no thickenings—either dimples

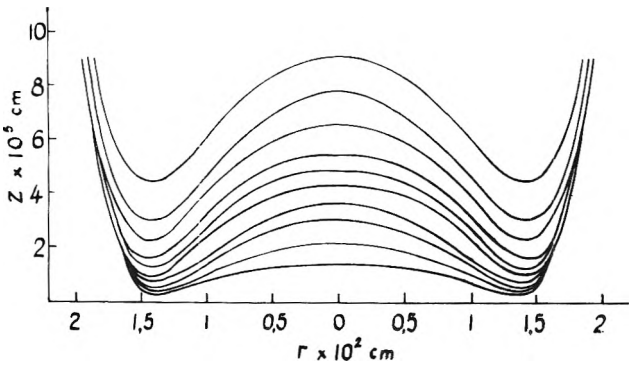

Figure 2. Profiles of a film of 0.1 N KCl solution on glass; film radius, 1.4×10^{-2} cm. The curves, beginning from the top correspond, respectively, to 1, 3, 6, 12, 20, 60, 100, 200, and 300 sec. from the formation of the film.

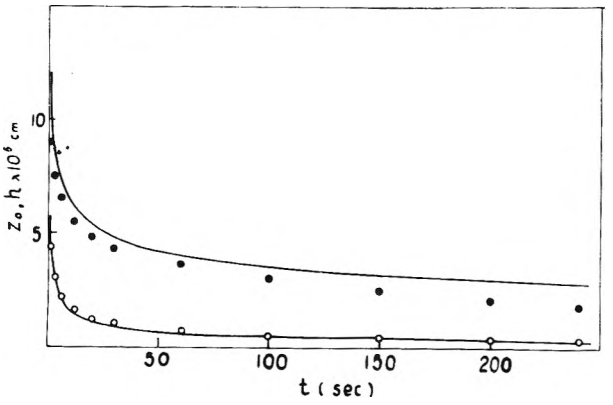

Figure 3. Plot of h (filled circles) and z_0 (open circles) *vs.* time of thinning for the film of Fig. 2.

(10) KCl was added in order to eliminate the positive electrostatic disjoining pressure.

(11) As was previously established,[1-3] infinitesimal quantities of surface active agents in water solutions are sufficient to reduce the surface flow rate of the film to zero. In the case of aniline this was obtained by the addition of 0.5% $C_{10}H_{21}OH$. The surface flow of pure ethanol, however, is free, which is proven by the fact that free foam films cannot be obtained from pure ethanol.

(12) A. Scheludko and D. Exerowa, *Izv. Khim. Inst. Bulgar. Akad. Nauk.*, 7, 123 (1959).

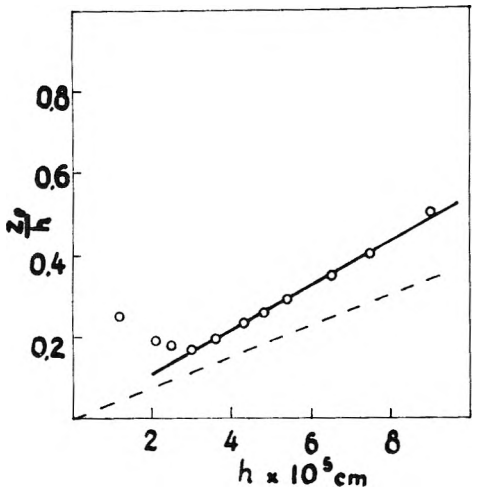

Figure 4. Plot of z_0/h *vs.* h for the film of Fig. 2.

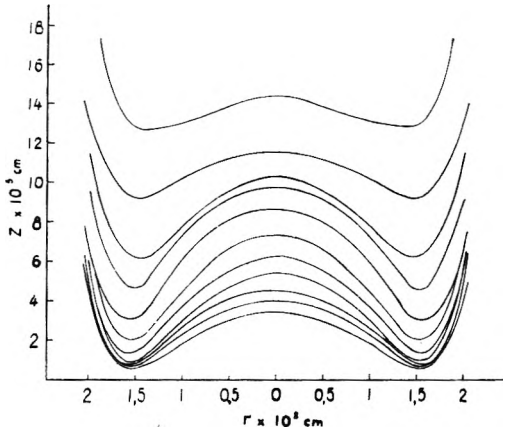

Figure 5. Profiles of a film of aniline on glass; film radius, 1.6×10^{-2} cm. The curves, beginning from the top correspond, respectively, to 1, 3, 6, 12, 30, 60, 180, 300, 450, 600, and 900 sec. from the formation of the film.

or channels--are formed and the films are plane-parallel. When the film thins to *ca.* 1000 Å. it is in all cases plane-parallel. Inasmuch as water is a liquid of low viscosity, the phenomena described above proceed very rapidly. Therefore films of oleic acid which thin considerably more slowly were also studied. The series of pictures in Fig. 10 demonstrates the characteristic evolution of a dimple in the case of small free foam films. The dimple obtained in thin liquid films between two drops of another liquid undergoes a similar evolution.[13]

Discussion

The results show that the theory of Frankel and Mysels,[8] which considers the simplified model of a flow strictly symmetrical with respect to the center, in a steady-state form, and at a constant surface

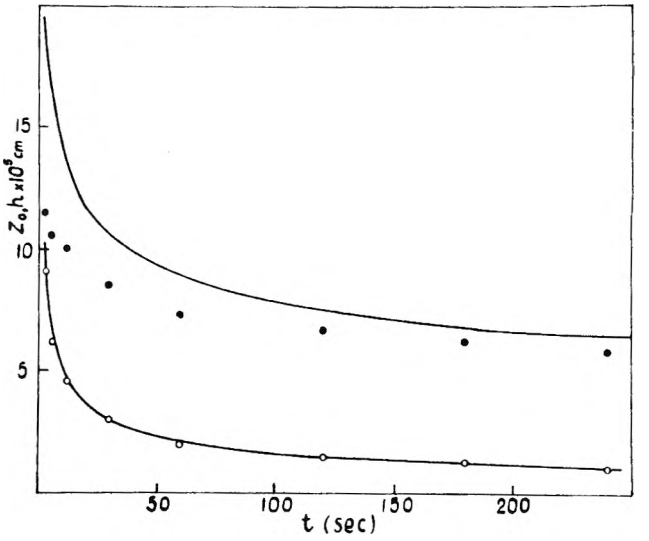

Figure 6. Plot of h (filled circles) and z_0 (open circles) *vs.* time of thinning for the film of Fig. 5.

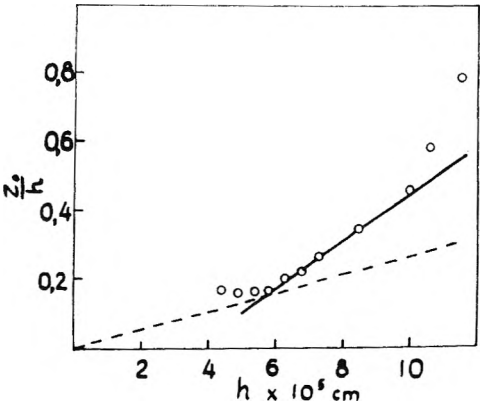

Figure 7. Plot of z_0/h *vs.* h for the film of Fig. 5.

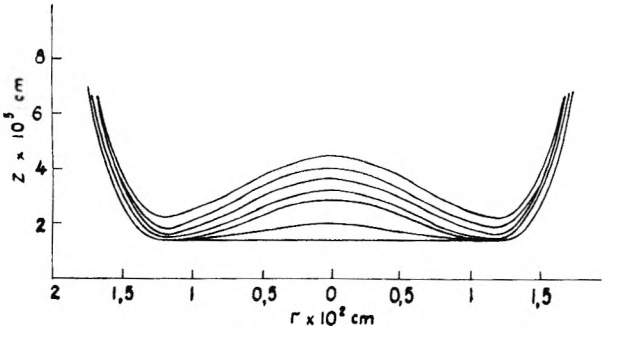

Figure 8. Profiles of a film of ethanol on glass; film radius, 1.25×10^{-2} cm. The curves, beginning from the top correspond, respectively, to 4, 6, 8, 12, 16, 20, and 30 sec. from the formation of the film.

(13) D. Platikanov and E. Manev, *Izv. Inst. Fizikokhim. Bulgar. Akad. Nauk.*, **4**, 185 (1964).

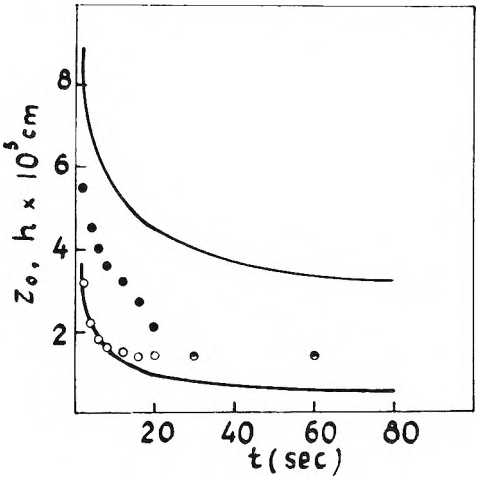

Figure 9. Plot of h (filled circles) and z_0 (open circles) *vs.* time of thinning for the film of Fig. 8.

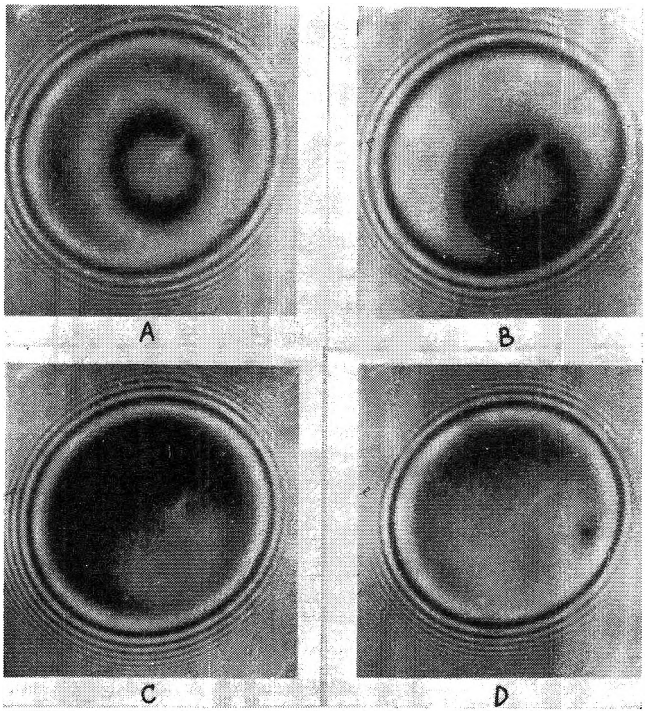

Figure 10. Evolution of the dimple in a free foam film of oleic acid: A, 15 sec., B, 20 sec., C, 45 sec., D, 70 sec. after the formation of the film.

tension along the film, is approximately followed in the case of thin liquid films on solid substrates. Obviously, comparison with the theory is possible only for thicknesses at which any disjoining pressure (a component of the pressure dependent on the thickness) is absent. In this thickness range, the presence of a dimple is indeed observed and its evolution can be followed and is consistent with the theory. In all cases, however, the dimple is somewhat less pronounced than expected by theory. In the case of high viscosity liquid films (aniline) it was established that in the initial stages of its evolution the dimple is considerably less pronounced. The respective ratios z_0/h are not only higher than the theoretical values but their h dependence strongly deviates from the linear as shown by the points with abcissas 10.6×10^{-5} and 11.5×10^{-5} in Fig. 7.

The results with films on a solid substrate indicate that in the presence of a positive disjoining pressure the dimple quickly flattens out, which is quite natural (Fig. 8, and the points corresponding to small h in Fig. 4 and 7). The problem becomes much more complicated when a negative disjoining pressure is present. Unfortunately, no such cases could be realized in the course of the present experiments. The studies of free foam films[1,2,9] have shown that negative disjoining pressure alone is not capable of distorting a plane film to a concave one. It seems that a similar behavior is shown by liquid films on mercury,[3] where ruptures (holes), occurring uniformly along the film surface were observed. The rupture of the film is possible only at a negative value of the disjoining pressure. The formation of holes all over the surface and not only at the periphery is definite evidence that the film is plane-parallel.

The observations of free foam films leave little doubt that, on account of lability of form, the flow is much more complicated, and the symmetry in the flowing of the film is spontaneously disturbed. In this way the expulsion of the thicker parts and the formation of flat films becomes possible and in the latter, provided that they are sufficiently thin, no dimpling occurs.

A further development of the theory concerning the initial stages of dimple formation could perhaps elucidate the lack of dimpling in sufficiently thin flat films (even in the presence of negative disjoining pressure) as well as in all kinds of films with small radii.

As a conclusion, it should be noted that in the case of circular liquid films on a solid substrate, the theory of Frankel and Mysels accounts fairly well for the observed shapes. This indicates that some of the basic factors determining the hydrodynamics of thin liquid films are now understood. A development of the theory for the initial stage of the dimpling no doubt would be of interest. In order to include the phenomena occurring with larger free liquid films, however, the theory needs substantial and very complicated modifications. Free liquid films which are sufficiently small and thin are practically plane-parallel, so that the use of Reynolds' equation with the dynamic method for the determination of the disjoining pressure is justi-

fied. This is true also for thin liquid films upon a solid substrate, but only at considerably smaller radii of the films.

Acknowledgment. The author thanks Prof. Dr. A. Scheludko for his constant encouragement and helpful discussions.

On the Interaction between Macromolecules and Colloidal Electrolytes

by C. Botré, F. De Martiis, and M. Solinas

Istituto di Chimica Farmaceutica and Centro di Studio per la Chimica del Farmaco e dei Prodotti biologicamente attivi del CNR, Università, Rome, Italy *(Received April 27, 1964)*

The interaction in aqueous solution between sodium lauryl sulfate either with water-insoluble (such as polyvinyl acetate) or water-soluble (such as bovine serum albumin) macromolecules was studied. Potentiometric determinations with permselective membrane electrodes or cationic glass electrodes and specific conductivity were employed in this investigation. Several evidences clearly confirm the formation of a "complex" between macromolecule and colloidal electrolyte. Data are also reported about the shift observed in the c.m.c. values, as well as the binding of sodium and calcium ions in solution of these complexes. In spite of the poor solubility of the calcium salt of a detergent in aqueous solution, it is shown that the solution of the "complex" before precipitation may sequester significant amounts of calcium. The behavior of the complex was studied both as a function of the molar detergent–polymer ratio and as a function of the concentration of the complex in solution. On the basis of these experiments, a theoretical approach is proposed to treat the complex as a polyelectrolyte.

Introduction

It was shown that water-insoluble polymers can be dissolved in a solution of ionic detergents.[1] The mechanism of solubilization was explained by assuming the formation of a "complex" between the macromolecule and the detergent. Similar "complexes" are also built up in the presence of surfactants and a water-soluble polymer such as polyvinylpyrrolidone.[2] With molecules other than detergents, as for instance an azo dye,[3] similar interactions occur. The common feature in all these complexes is, however, their polyelectrolyte character. In the field of biologically important macromolecules, the interaction with colloidal electrolytes was also studied by many authors.[4-9]

The study reported below refers to the complexes resulting by an interaction between sodium lauryl sulfate (NaLS) and polyvinyl acetate (PVAc) or bovine serum albumin (BSA).

Experimental

Material. Crystallized BSA obtained from Armour Laboratories was dialyzed against water by allowing the solution to stand for 5 days at 3°, and then the resulting solution was lyophilized. Polyvinyl acetate was a sample supplied by Polymer Consultants Ltd., England. The molecular weight, determined by light-scattering

(1) I. Isemura and A. Imanishi, *J. Polymer Sci.*, **33**, 337 (1958).

(2) S. Saito, *J. Colloid. Sci.*, **15**, 283 (1960).

(3) H. P. Frank, S. Barkin, and F. R. Eirich, *J. Phys. Chem.*, **61**, 1375 (1957).

(4) G. Strauss and U. P. Strauss, *ibid.*, **62**, 1321 (1958).

(5) M. Brauer and U. P. Strauss, *ibid.*, **64**, 228 (1960).

(6) B. P. Brand and P. Johnson, *Trans. Faraday Soc.*, **52**, 438 (1956).

(7) D. F. Waugh, *J. Phys. Chem.*, **65**, 1793 (1961).

(8) B. S. Harrap and J. H. Schulman, *Discussions Faraday Soc.*, **13**, 197 (1953).

(9) I. Blei, *J. Colloid. Sci.*, **15**, 370 (1960).

measurements, gave a value corresponding to about 975 monomers/molecule. Sodium lauryl sulfate was prepared according to Dreger.[10]

Procedure. Potentiometric determinations of the activity of Na^+ ions were performed with both membrane electrodes and a couple of a sodium-responsive electrode (Beckman 39278)–liquid bridge calomel, in a wide range of polymer–detergent concentration.

In this latter case, the activity of sodium ions was calculated by means of a calibration curve, which allowed the conversion of e.m.f. values into activities. This was obtained by diluting a sodium chloride solution stepwise, recording the e.m.f. of the cell and plotting it *vs.* the logarithm of Na^+ ion activity at each step. A linear plot[11] of the e.m.f. against log a_{Na} was obtained. The a_{Na^+} values of the solution were calculated from the measured e.m.f. by interpolating the calibration curve. This was done by assuming that $\gamma_{Na^+} = \gamma_{\pm(NaCl)}$ in the calibrating solution.

The sequestering power determinations were performed following the procedure already described.[12,13] Conductometric titrations were performed in a thermostatic bath at 25 and 30°. In some cases, the potentiometric and the conductometric determinations were carried out simultaneously.

Results and Discussion

In previous papers,[14,15] the behavior of aqueous solutions of colloidal electrolytes was studied by means of e.m.f. measurements and discussed in terms of an interaction between counterions and micelles, the latter being treated as a spherical polyelectrolyte. It is assumed that the liquid junction potential remains effectively unchanged, regardless of the nature of the solution, since the concentration of NaCl in the liquid bridge is higher than the concentration of the experimental solution.

In Fig. 1 the activity coefficient of sodium ions is reported as a function of concentration of sodium lauryl sulfate in solution (open points, plot a). The c.m.c. value, C_0, is marked by the discontinuity in the plot. The concentration of NaLS at this point is 8.0×10^{-3} M, and the γ_{Na} value is 0.56.

In the same Fig. 1 (full points, plot b), the behavior of γ_{Na} refers to a solution of NaLS with PVAc dissolved. The molar NaLS–PVAc ratio was 2.61. As extensively discussed in a previous work,[14] it is assumed that above c.m.c. any addition of detergent increases the number of micelles since both the concentration of monomers and the number of monomers per micelle are considered to be constant in solution. Furthermore, since the value of the dielectric constant of the solution containing the NaLS–PVAc complex is nearly coincident with

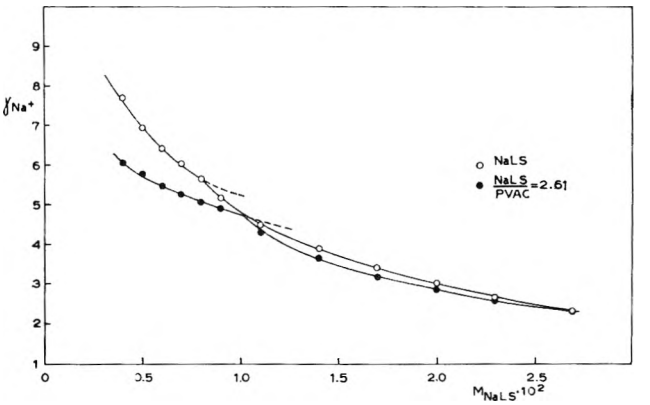

Figure 1. γ_{Na^+} *vs.* concentration expressed as molarity of NaLS. Open points refer to NaLS solution; full points, to a solution of NaLS–PVAc complex.

the one of simple NaLS solution, no influence on γ_{Na} was considered. As may be seen, an apparent shift toward higher concentrations in c.m.c. is observed. This shift from C_0 to C can be ascribed to an amount of free monomers removed from the equilibrium monomer micelle by an oriented absorption of the monomers on the polymeric chain of the PVAc, as elsewhere discussed.[1]

The relationship which gives the γ_{ex} value (γ_{ex} being the experimental value of the activity coefficient) at the concentration corresponding to the c.m.c. of NaLS in solution of the "complex" NaLS–PVAc may be written as

$$\gamma_{ex} = \frac{\gamma_{Na^+} C_0 + \gamma_{Na^+} \alpha (C - C_0)}{C} \qquad (1)$$

When the complex with a NaLS–PVAc ratio of 2.61 is present in solution, the concentration of NaLS itself required to form micelles is $C = 1.0 \times 10^{-2}$. At this point, the value γ_{ex} is 0.48.

So, replacing the experimental data in (1)

$$0.48 = \frac{0.56 \times 8 \times 10^{-3} + 0.56\alpha(10 \times 10^{-3} - 8 \times 10^{-3})}{10 \times 10^{-3}} \qquad (1')$$

(10) E. E. Dreger, G. I. Keim, G. A. Miles, L. Shedlovsky, and J. Ross, *Ind. Eng. Chem.*, **36**, 610 (1944).

(11) F. Ascoli, C. Botré, and A. M. Liquori, *J. Mol. Biol.*, **3**, 202 (1961).

(12) F. Ascoli and C. Botré, *Farmaco* (Pavia), **17**, 213 (1962).

(13) C. Botré, V. Crescenzi, and A. Mele, *J. Nucl. Chem.*, **8**, 369 (1958).

(14) C. Botré, V. Crescenzi, and A. Mele, *J. Phys. Chem.* **63**, 650 (1959).

(15) L. Shedlovsky, C. W. Jakob, and M. B. Epstein, *ibid.*, **67**, 2075 (1963).

the degree of dissociation, α, of Na^+ ions in the complex NaLS–PVAc may be obtained. This value of α is about 0.28.

If a cylindrical model is assumed for the polyelectrolyte complex, then, on the basis of a relation proposed by Oosawa, the degree of dissociation, α, of counterions in solution may be evaluated

$$\ln \frac{1-\alpha}{\alpha} = \ln \frac{\phi}{1-\phi} + q\alpha \ln \frac{1}{\phi} \qquad (2)$$

$$q = \frac{e_0^2}{DTkb} \qquad (3)$$

where α = degree of dissociation, e_0 = charge, b = distance between neighboring charged groups, ϕ = volume fraction of the polyelectrolyte, D = dielectric constant of water, and T and k have the usual meaning.

In the case within the range of complex concentrations considered, the value of ϕ being small compared with unity, the relation (2) may be written as

$$\ln \phi = \ln \frac{1-\alpha}{\alpha} - \alpha q \ln \frac{1}{\phi} \qquad (4)$$

therefore, $q = 1$. By assuming for our complex a = 15 Å. and b = 2.5 Å., the value of α is 0.32. At c.m.c. this value of α is in good agreement with the value of 0.28 determined experimentally.

It is to be pointed out that the hypothesis to treat the polyelectrolyte complex with a cylindrical model may be successful if this treatment is applied to a relatively dilute solution where mainly detergent molecules, and not aggregates, are present inside the polyelectrolyte complex. In fact, in a more concentrated solution, the contribution of the γ_{Na} value is mainly determined by micelles, while the role played by the complex becomes negligible. This is in agreement with the experiments, and no significant differences in γ_{Na} values may be observed in the presence or absence of the complex when the concentration of NaLS is higher than 2.5×10^{-2} M.

From such an interaction results the polyelectrolyte character of the complex which is expressed by the typical behavior of γ_{Na} upon dilution. Obviously, the charge density on the macroion is closely dependent upon the degree of binding of the detergent molecules on the polymeric chain. When partially hydrolyzed samples of PVAc are employed, the number of active sites for the adsorption of detergent molecules on the polymeric chain is lowered. Therefore, the charge density on the macromolecular complex is also lowered, and an increase of γ_{Na} is found.

Above c.m.c., as discussed elsewhere,[14] the situation is more or less the same, as in simple NaLS solutions. In both cases, in fact, the steep decrease of γ_{Na} may be explained, considering the micelles as highly charged spherical polyelectrolytes. On the surface of the micelle, the high electrostatic field, determined by the ionic heads of the detergent toward water, affects the distribution of Na^+ ions in solution significantly. The consequent interaction between micelles and counterions leads to the lowering of free charges on the former because of an extensive binding of sodium counterions.

Furthermore, a striking difference may be observed in the binding of divalent cations, *i.e.*, Ca^{+2} ions. In fact, when Ca^{+2} ions are added to a solution of detergent, a precipitation of the calcium salt takes place. On the contrary, in detergent solutions containing dissolved PVAc, after addition of Ca^{+2} ions, significant amounts of calcium are held in solution before the formation of a precipitate.

To test the sequestering ability of this complex, the binding of Ca^{+2} was evaluated according to a method described elsewhere.[12] To evaluate the binding of Ca^{+2} ions in solution of the complex, a potentiometric system was set up which employs both glass cationic electrodes and membrane electrodes. The sensitivity of cationic glass electrodes is very high toward monovalent cations while the sensitivity toward divalent cations is very low (near zero). It was observed that Ca^{+2} ions in the range of concentration used in sequestering power determinations do not alter the potential difference due to Na^+ ions alone and recorded by the couple of electrodes—cationic glass electrode–calomel electrode.

In Fig. 2 (system A), a combination of the negatively charged membrane electrode, prepared according to Neihof,[16] and the sodium electrode is reported. Neglecting the junctions, the e.m.f. $\Delta E_{1,2}$ is given by the expression

$$-\Delta E_{1,2} = \frac{RT}{F}\left[t_{Na^+} \ln \frac{a_{Na_2^+}}{a_{Na_1^+}} + {}^1/_2 t_{Ca^{+2}} \ln \frac{a_{Ca_2^{+2}}}{a_{Ca_1^{+2}}}\right] \qquad (5)$$

and the e.m.f. ΔE_{Na} is given by

$$-\Delta E_{Na} = K \log a_{Na_2^+} \qquad (6)$$

where R, T, and F have the usual meaning, $a_{Na_1^+}$ and $a_{Ca_1^{+2}}$ are Na^+ and Ca^{+2} ion activities in reference solution, and $a_{Na_2^+}$ is the ion activity measured with the Na electrode. Furthermore, across the membrane one has

$$t_{Na^+} + t_{Ca^{+2}} = 1.0 \qquad (7)$$

t_{Na^+} and $t_{Ca^{+2}}$ being the transference numbers of sodium and calcium, respectively. They are functions

(16) R. Neihof, *J. Phys. Chem.*, **58**, 916 (1954).

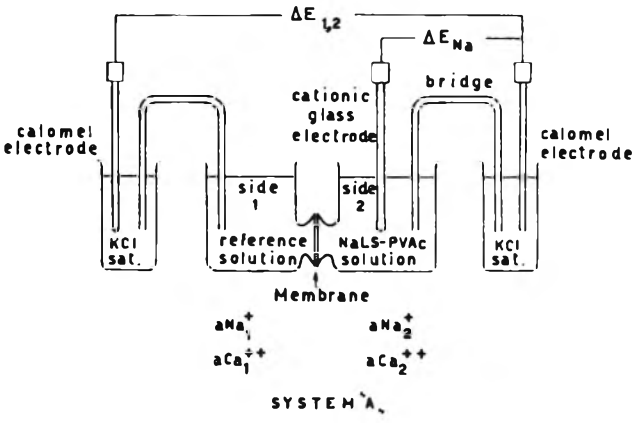

Figure 2. Apparatus for membrane electrode titration.

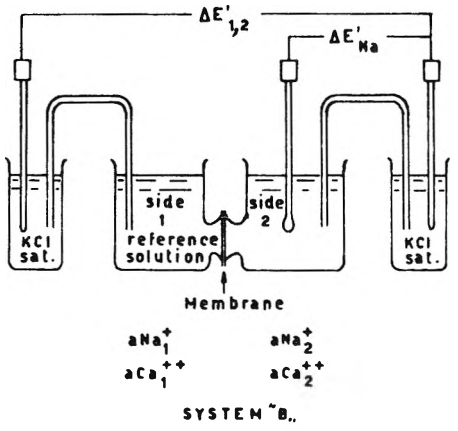

Figure 3. Reference electrode system for membrane titration.

of a_{Na^+} and $a_{Ca^{+2}}$ so that it is impossible to determine $a_{Ca^{+2}}$ by direct use of (5)–(7). This difficulty has been overcome by using a reference system (Fig. 3) analogous to the first one and schematized hereafter as system B and characterized by the e.m.f. values, $\Delta E'_{1,2}$ and $\Delta E_{Na}'$.

The titration is performed as follows. The solution of the complex is placed in one half-cell (side 2 of system A) and NaCl solution is placed in the other one (side 1 of system A). This latter solution is diluted or concentrated in order to have an e.m.f. equal to zero so that the activities of Na^+ ion are equal in the two half-cells. The composition of the solution in side 1, 1′, and 2′ of the two systems A and B are kept identical with each other throughout the titrations. After each addition of equal amounts of $CaCl_2$ in both half-cells of the system and in half-cell 1′ of system B, the potential differences ΔE_{Na} and $\Delta E_{Na}'$ are read. A solution of NaCl is now added to the half-cell 2′ of the system B until $\Delta E_{Na}'$ matches ΔE_{Na} (obviously taking into account the necessary corrections due to small differences in the calibration curves of the two sodium electrodes). $CaCl_2$ solution is now added to the half-cell 2′ of system B until $\Delta E_{1,2}'$ matches $\Delta E_{1,2}$. The amount of Ca^{+2} ions added to the half-cell 2′, therefore, corresponds to the Ca^{+2} ions not bound by the sequestering agent in the half-cell 2 of system A. The difference between the Ca^{+2} ions added to side 1′ and side 2′ of system B indicates the amount of sequestered Ca^{+2} ions.

The above described steps are repeated after each addition of $CaCl_2$ to both half-cells of system A. Thus, the calcium sequestered as a function of Ca^{+2} ions present in a solution containing a fixed concentration of sequestering agent is obtained. In agreement with the polyelectrolyte character of the complex, the amount of calcium sequestered is a function of the concentration of complex in solution (Fig. 4), and of the NaLS–PVAc ratio (Fig. 5), which is in close correlation to the charge density on the polymeric chain.

The strong electrostatic interaction between Ca^{+2} ions and the macroanion leads to a release of Na^+ ions and is evident from the plots of Fig. 4. In fact, the two plots differ from each other only in the total amount of complex in solution, the NaLS–PVAc ratio being the same in both cases. The curves of Fig. 4 and 5 are calculated by using eq. 5 with $t_{Ca^{+2}} = 1$ and $t_{Na^+} = 0$. On the other hand, by taking into account the sodium release by means of the preceding procedure, the plots become more or less coincident giving a straight line with a slope of 45° (broken lines both in Fig. 4 and 5).

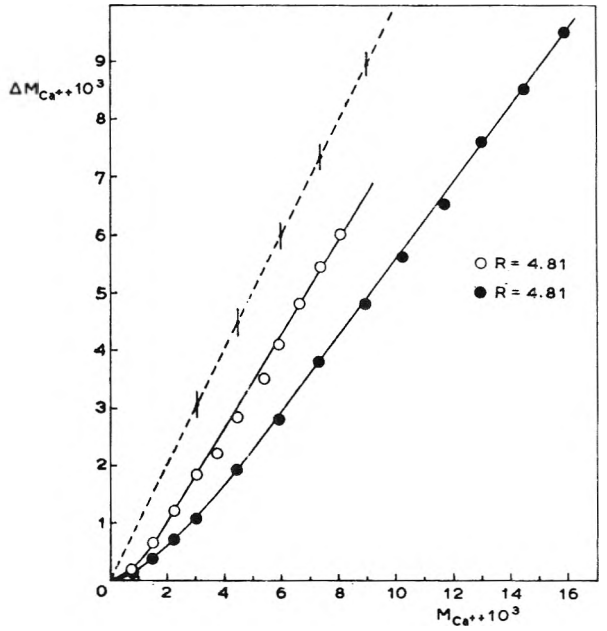

Figure 4. Sequestering power of NaLS–PVAc. The three plots refer to the same amount of PVAc present in solution but at different NaLS–PVAc ratios. By increasing the detergent concentration, the total amount of Ca^{+2} sequestered is increased.

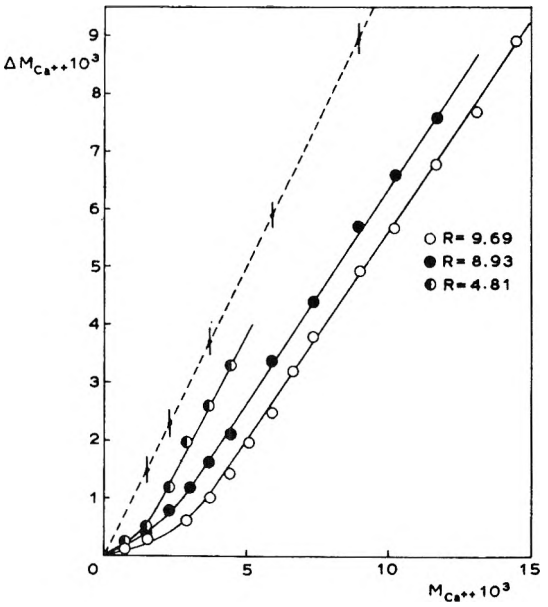

Figure 5. Sequestering power of the complex toward calcium ions. The ordinate represents the amount of Ca^{+2} sequestered; the abscissa, the total amount of Ca^{+2} present in solution. The two plots refer to the same NaLS–PVAc ratio but at different concentrations of the complex.

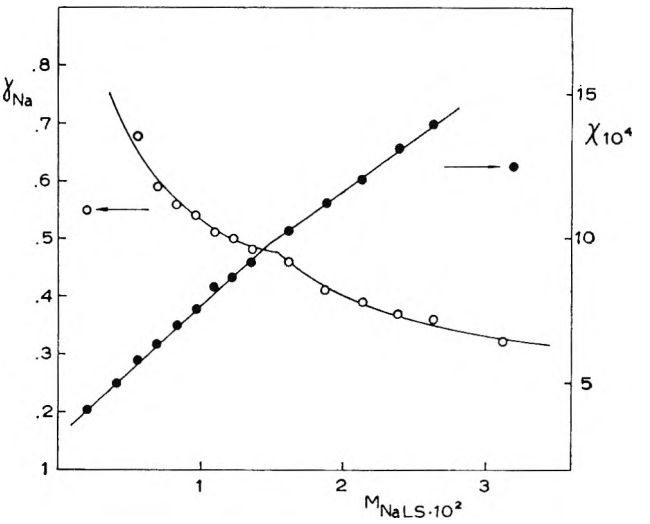

Figure 6. γ_{Na^+} (open circlets, left ordinate) and specific conductivity χ (full circlets, right ordinate) *vs.* the molarity of NaLS in a solution of the BSA–NaLS complex.

As it may be seen, the correction due to the sodium release is significant particularly when the concentration of ions in solution is large. However, the accuracy of released sodium ions in solution of surface active agents is significantly affected, probably by the adsorption of detergent on the surface of the glass. In fact, the poor suitability of glass electrodes for measuring pH in solution of detergents and similar substances was pointed out by Nebe,[17] who found some errors in pH measurements. Nevertheless, our aim was to study such a behavior in a semiquantitative way.

The formation of a complex, with charge density strongly dependent on the charge density on the macroion, as well as on the ionic strength of the medium, was also found in solution of NaLS and BSA. In Fig. 6 (left ordinate, open points), the activity coefficient of sodium ions γ_{Na} is reported as a function of the concentration of the lauryl sulfate in solution of the NaLS–BSA complex. As may be seen, a discontinuity may be observed, such a discontinuity also being evident with specific conductivity measurements of the same solution (right ordinate, full points). On the other hand, when the same experiment is performed in presence of $CaCl_2$, 5×10^{-4} *M*, the discontinuity in the activity coefficient of sodium ions and in the specific conductivity is no longer detectable.

In agreement with other authors,[9,18] it could be assumed that "micellar clusters" might be formed when the detergent acts on the macromolecule. Divalent cations might reduce the net charge of the complex as shown by previous plots. Such a reduction of the net charge of the complex was also claimed by some of the previously mentioned authors who ascribed to Ca^{+2} ions also an increase in solubilizing power of several protein detergent complexes.

Acknowledgments. The authors wish to express their best thanks to Colgate-Palmolive Co., New York, N.Y., for having sponsored and financially supported this work, and to Dr. L. Shedlovsky for the useful discussion of the manuscript. The authors also wish to thank Prof. A. M. Liquori for his extremely useful suggestions and stimulating discussions.

(17) E. Nebe, *J. Electroanal. Chem.*, A21 (63) II/1959 52.

(18) E. G. Jackson and U. P. Strauss, *J. Polymer Sci.*, 7, 473 (1951).

Interaction of Electromagnetic Radiation with Matter. I. Theory of Optical Rotatory Power: Topic B. Digonal Dihedral Compounds and Compounds of Lower Symmetry[1a]

by Andrew D. Liehr[1b]

Mellon Institute, Pittsburgh, Pennsylvania 15213, Bell Telephone Laboratories, Inc., Murray Hill, New Jersey 07971 *(Received May 28, 1964)*

A belief is not true because it is useful.—Amiel

A complete theory of the electronic properties of digonal dihedral compounds and compounds of lower symmetry, both organic and inorganic, is chalked, with special emphasis upon their optical rotatory power. Molecular orbitals are constructed, many electron configurations fabricated, and sundry spectral parameters reckoned. A number of points of general interest have been discovered and underscored: (1) overlap can be used as a bond criterion for orbitals of the selfsame symmetry solely; for orbitals of different eurythmy a nonunit (nonconstant) weight function of identical symmetry as the molecular Hamiltonian must be used; (2) short of a full quantum mechanical computation, there exists no sure means by which the absolute sign of the molecular orbital variational parameters and hence, the optical rotatory powers can be determined; (3) the finished optical rotatory power depends both linearly and quadratically upon the amplitude of the covalent strength, with quadratic dominance at high strengths; (4) the rotational and spectral powers are functionally relatively insensitive to the explicit appearance of the angles of ligand orbital (lone pair, bond pair, acceptor, or donor) cant (as the quadratic ligand–ligand terms tend to dominate), but covertly extremely sensitive to their implicit appearance (since the parametric magnitude of odd ligand additaments hangs immediately upon them); (5) there is a direct correspondence between the rotational and spectral powers of spin-free transition metal electronic configurations and their spin-free half-shell supplements and numerous direct and indirect relationships between these and other systems; (6) the principal determinant of rotatory direction is the relative ligand orbital (lone pair, bond pair, donor, or acceptor) constellation; (7) there is no prime difference in origin of optical rotary and spectral intensive power in organic and inorganic compounds; (8) optical rotatory transitions to or from bonded and antibonded electronic states, both organic and inorganic, turn electromagnetic radiation either parallely or oppositely dependent upon conditions; (9) configurational interaction, whether electronically or nuclearly induced, is of essential import in optical rotivity and intensity calculations; (10) there exist no simple addition invariance connections for eurythmically abased compounds. Representatives have been manifested, a road for future progress laid, and a map for closer theoretical–experimental reciprocation drawn.

(1) (a) Presented at the Eighth International Conference on Coordination Chemistry, Vienna, Austria, Sept. 7–11, 1964; an amplified account of this lecture, as well as of that (the non-Faraday portion) presented at the Sixth International Conference on Coordination Chemistry, Wayne State University, Detroit, Mich., Aug. 27–Sept. 1, 1961 (this latter lecture is not that published in the conference proceedings, "Advances in the Chemistry of Coordination Compounds," S. Kirschner, Ed., The Macmillan Co., New York, N. Y., 1961), may be found in *Progr. Transition Metal Chem.*, 1 and 3 (1965 and 1966). (b) Mellon Institute, Pittsburgh, Pa.

TABLE OF CONTENTS

In continuation of our quest of the primeval source of optical rotatory power in chemical compounds, we have embarked upon a critical surveyal of the electronic characteristics of inorganic and organic aggregates of low symmetry. The initial fruits of this surveyal are here reported. They are divided into these main categories: Division A, the transition metal digonal dihedral compounds; Division B, the transition metal compounds of lower symmetry; Division C, the nontransition metal compounds (carbon and others); Division D, the conclusion; and Division E, the acknowledgments. We start with Division A, the transition metal digonal dihedral compounds.

Division A

Transition Metal Digonal Dihedral Compounds

I. Introduction

The potency of natural optical rotatory power as a structural tool has nowhere been better demonstrated than in its use to fix the nonplanarity and nontetrahedrality of four-coordinated platinum or palladium amine complexes[2,3] or the relative conformation of carbon compounds.[4] However, despite this stereochemical success, the electronic source of the optical rotatory power has remained as mysterious as ever, notwithstanding the many efforts and some advances which have been made to uncover its origin.[4,5] What we wish

(2) F. M. Jaeger and J. ter Berg, *Proc. Roy. Acad. Sci.* (Amsterdam), **40**, 490 (1937).

(3) W. Theilacker, *Z. anorg. allgem. Chem.*, **234**, 161 (1937).

(4) For a surveyal of the carbon (and other) problem read (a) "Optical Rotatory Power: A General Discussion," *Trans. Faraday Soc.*, **26**, 265 (1930); (b) G. Kortüm, *Z. angew. Chem.*, **43**, 341 (1930); *Physik. Z.*, **31**, 641 (1930); "Neuere Forschungen über die optische Aktivität chemischer Moleküle," Sammlung chemischer und chemisch-technischer Vorträge [N.F.], Heft 10, Enke, Stuttgart, 1932; W. Kuhn and K. Freudenberg, "Hand- und Jahrbuch der chemischen Physik," Band 8, Abschnitt III, A. Eucken and K. L. Wolf, Ed., Akademische Verlagsgesellschaft, Leipzig, 1932; "Stereochemie," K. Freudenberg, Ed., F. Deuticke, Leipzig and Vienna, 1932-1933, Books 1-3 [note especially the paired articles by W. Kuhn, Book 1, pp. 317-434 and by K. Freudenberg, Book 2, pp. 662-720]; (c) S. Mitchell, "The Cotton Effect and Related Phenomena," G. Bell and Sons, Ltd., London, 1933; (d) T. M. Lowry, "Optical Rotatory Power," Longmans, Green, and Co., London and New York, N. Y., 1935; (e) G. Bruhat, "Traite de Polarimétrie," Editions de la Revue d'Optique théorique et instrumentale, Paris, 1930; M. Delepine, "Traite de Chimie Organique," V. Grignard, Ed., Vol. I, Masson, Paris, 1935, pp. 833-1008; E. Darmois, *ibid.*, Vol. II, 1948, pp. 1-58; P. A. Levene and A. Rothen, "Organic Chemistry," Vol. 2, 1st Ed., H. Gilman, Ed., John Wiley and Sons, Inc., New York, N. Y., 1938, pp. 1779-1849; R. L. Shriner, R. Adams, and C. S. Marvel, *ibid.*, Vol. 1, 2nd Ed., 1943, pp. 214-488; J. R. Partington, "An Advanced Treatise on Physical Chemistry," Vol. 4, Longmans, Green and Co., London and New York, N. Y., 1953, pp. 290-391; W. Klyne, "Determination of Organic Structures by Physical Methods," Vol. 1, E. A. Braude and F. C. Nachod, Ed., Academic Press, Inc., New York, N. Y., 1955, pp. 73-130; G. G. Lyle and R. E. Lyle, *ibid.*, Vol. 2, F. C. Nachod and W. D. Phillips, Ed., 1962, pp. 1-92; W. Heller and D. D. Fitts, "Technique of Organic Chemistry," Vol. I, Part III, A. Weissberger, Ed., 3rd Ed., Interscience Publishers Inc., New York, N. Y., and London, 1960, pp. 2147-2333; W. Klyne and A. C. Parker, *ibid.*, pp. 2335-2385; W. Klyne, "Advances in Organic Chemistry: Methods and Results," R. A. Raphael, E. C. Taylor, and H. Wynberg, Ed., Vol. 1, Interscience Publishers Inc., New York, N. Y., and London, 1960, pp. 239-348; E. L. Eliel, "Stereochemistry of Carbon Compounds," McGraw-Hill Book Co., Inc., New York, N. Y., and London 1962; T. M. Lowry *Chem. Ind.* (London), 477 (1935); H. M. Powell, *Endeavour*, **15**, 20 (1956); V. Sykora, *Chemie* (Prague), **9**, 400 (1957); O. Cervinka, *ibid.*, 637 (1957); J. A. Schellman, *Compt. rend. trav. lab. Carlsberg, Sèr. Chim.*, **30**, 363 (1958); K. Nakanishi, *Kagaku No Ryoiko*, **13**, 2 (1959); K. Imahori, *ibid.*, **13**, 92 (1959); M.-L. Huang, *Ko Hsueh T'ung Pao*, 255 (1959); K. Imabori, *Tampakushitsu Kakusan Koso*, **5**, 549, 606 (1960); S. S. Yufit and V. F. Kucherov, *Usp. Khim.*, **31**, 474 (1962); R. D. Gillard, *Analyst*, **88**, 825 (1963); O. N. Perti, *Agra Univ. J. Res.*, 11, 175, 15 (1962); (f) "Progress in Stereochemistry," Vol. 1-3, W. Klyne and P. B. D. de la Mare, Ed., Butterworths, London and Washington, D. C., 1954-1962; (g) C. Djerassi, *Record Chem. Progr.*, **20**, 101 (1959); "Optical Rotatory Dispersion," McGraw-Hill Book Co., Inc., New York, N. Y., and London, 1960; *Science*, **134**, 649 (1961); *Chem. Eng. News*, **39**, 88 (Aug. 21, 1961); (h) "Rotatory Dispersion: Related Theory and Application," Conference Proceedings, B. H. Levedahl and T. W. James, Ed., *Tetrahedron*, **13**, 1-240 (1961); as well as the classic papers by W. Kuhn and collaborators: (i) W. Kuhn, *Ber.*, **63B**, 190 (1930); (j) W. Kuhn, K. Freudenberg, and I. Bumann, *ibid.*, 2380 (1930), W. Kuhn, K. Freudenberg, and I. Wolf, *ibid.*, 2367 (1930); (k) W. Kuhn and E. Braun, *Z. physik. Chem.*, **8B**, 281 (1930); (l) W. Kuhn, *Naturwiss.*, **19**, 854 (1931); (m) K. Freudenberg and W. Kuhn, *Ber.*, **64B**, 703 (1931); (n) W. Kuhn, H. Eyer, and K. Freudenberg, *Z. physiol. Chem.*, **202**, 97 (1931); (o) W. Kuhn and H. K. Gore, *Z. physik. Chem.*, **12B**, 389 (1931); (p) W. Kuhn and H. L. Lehmann, *Chem. Weekblad.*, **28**, 517 (1931) [collate K. Scheringa, *ibid.*, **28**, 363, 655 (1931); **29**, 218 (1932)]; *Z. Elektrochem.*, **37**, 549 (1931); *Z. physik. Chem.*, **18B**, 32 (1932); (q) W. Kuhn, *Ber.*, **66B**, 166 (1933) [see also the companion piece by K. Freudenberg, *ibid.*, 177 (1933)]; *IX Congr. Intern. quim. pura applicada*, **4**, 181 (1934); (r) W. Kuhn and H. Biller, *Z. physik. Chem.*, **29B**, 1, 256 (1935); (s) H. B. Elkins and W. Kuhn, *J. Am. Chem. Soc.*, **57**, 296 (1935); (t) W. Kuhn, *Z. physik. Chem.*, **31B**, 23 (1936); (u) W. Kuhn, *Naturwiss.*, **26**, 289, 305 (1938); (v) W. Kuhn and R. Rometsch, *Helv. Chim. Acta*, **27**, 1080, 1946 (1944); (w) R. Rometsch and W. Kuhn, *ibid.*, **29**, 1483 (1946); (x) W. Kuhn, *Z. Elektrochem.*, **56**, 506 (1952); (y) W. Kuhn, *Angew. Chem.*, **68**, 93 (1956); (z) W. Kuhn, *Z. Elektrochem.*, **62**, 28 (1958); *Ann. Rev. Phys. Chem.*, **9**, 417 (1958); ref. 4h, p. 1; "Rotatory Dispersion and the Vibrating Momentum of Optically Active Absorption Bands," Advances in Molecular Spectroscopy, Conference Proceedings, A. Mangini, Ed., Pergamon-Macmillan, New York, N. Y., 1962, pp. 34-38.

(5) The extent and diversity of such efforts is best appreciated by a view of the works of (a) P. Drude, "Theory of Optics" (translation, 1st Ed., 1900, by C. R. Mann and R. A. Millikan), Dover, New York, N. Y., 1960; (b) J. Stark, *Jahrb. Radioakt. Elektronik*, **11**, 194 (1914); "Prinzipien der Atomdynamik," Vol. 3, Leipzig, 1915, p. 262 ff.; (c) C. W. Oseen, *Ann. Physik*, **48**, 1 (1915); (d) M. Born, *Physik. Z.*, **16**, 251, 437 (1915); *Ann. Physik*, **55**, 177 (1918) [see also the related work of A. Lande, *ibid.*, **56**, 225 (1918); R. Gans, *Z. Physik*, **17**, 353 (1923); **27**, 164 (1924); G. L. Palumbo, *Ann. Physik*, **79**, 533 (1926) (Appendix by R. Gans); V. Bursian and A. Timorew, *Z. Physik*, **38**, 475 (1926)]; (e) F. Gray, *Phys. Rev.*, **7**, 472 (1916); (f) J. J. Thomson, *Phil. Mag.*, [vi] **40**, 713 (1920); (g) R. de Malleman, *Ann. Phys.*, (10) **2**, 137 (1924); **4**, 456 (1925); *Compt. rend. Acad. Sci. Paris*, **181**, 298 (1925); **184**, 1374 (1927); *Rev. gen. Sci. pures appl.*, **38**, 453 (1927); *Compt. rend. Acad. Sci. Paris*, **188**, 705 (1929); (h) W. Kuhn, *Z. physik. Chem.*, **4B**, 14 (1929); see ref. 4a, p. 293; *Z. physik. Chem.*, **20B**, 325 (1933); W. Kuhn and K. Bein, *ibid.*, **22B**, 406 (1933); **24B**, 335 (1934); (i) M. Born, "Optik," Julius Springer, Berlin, 1933; *Proc. Roy. Soc.* (London), **A150**, 84 (1935); B. Y. Oke, *ibid.*, **A153**, 539 (1936); (j) S. F. Boys, *ibid.*, **A144**, 655 (1934); (k) J. M. Kooy, Jr., "Theory of Optical Activity," Thesis, University of Leiden, 1936; (l) J. G. Kirkwood, *J. Chem. Phys.*, **5**, 479 (1937), **7**, 139 (1939); D. D. Fitts and J. G. Kirkwood, *J. Am. Chem. Soc.*, **77**, 4940 (1955); D. D. Fitts, M. Siegel, and K. Mislow, *ibid.*, **80**, 480 (1958); (m) E. U. Condon, W. Altar, and H. Eyring, *J. Chem. Phys.*, **5**, 753 (1937); E. U. Condon, *Rev. Mod. Phys.*, **9**, 432 (1937); E. Gorin, J. Walter, and H. Eyring, *J. Chem. Phys.*, **6**, 824 (1938); E. Gorin, W. Kauzmann, and J. Walter, *ibid.*, **7**, 327 (1939); L. L. Jones and H. Eyring, ref. 4h, p. 235; T. Watanabe and H. Eyring, *J. Chem. Phys.*, **40**, 3411 (1964); (n) W. Kauzmann, "Theory of

to do in this article is to present a model, an extension of our previous one for octahedral six-coordinate molecules,[6] which will explain the occurrence of the phenomenon of natural optical rotatory power in four- (and other) coordinate systems. We shall show that optical rotatory power can be qualitatively and quantitatively accounted for by a simple model of dihedrally twisted local electronic charge densities. In subsequent papers we shall demonstrate the capabilities of similar models to explain forced optical rotatory power in a variety of other situations.

II. Theory

§1. Molecular Orbitals for Digonal Dihedral Compounds: Zero Spin-Orbit Forces

1.1 *The σ-Molecular Orbitals.* In Fig. 1 through 9 we diagrammatically display the geometries of a series of typical σ-bonded [neglecting so-called "ammonia" framework hyperconjugative effects] digonal dihedral complex cations. Figures 1 through 4 depict the idealized disposition of the ligand σ-bond orbitals which we assume in our subsequent numerical toil, and Fig. 10, 11, and 12 a typical, but not all inclusive, level scheme. Mark particularly the clear provisos in Fig. 1, 2, 3, 4, 7, 8, 9 for angles of cant α and ι (defined in Fig. 9) between the ligand orbitals and the metal orbitals. [The metal orbitals are in this paper taken to be aligned octahedrally along the x', y', and z' axes of the figures.]

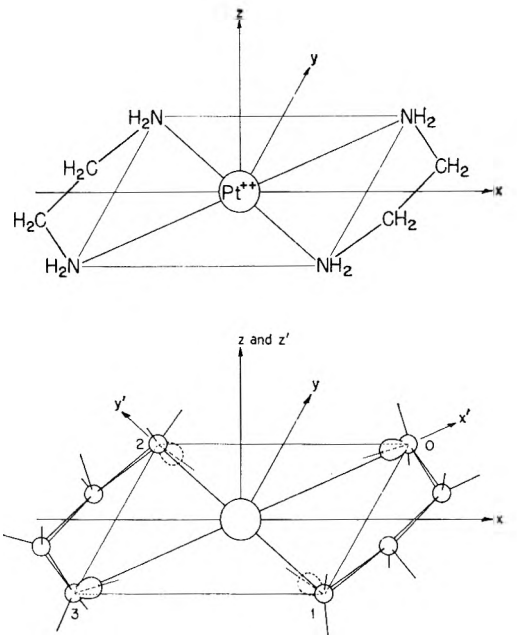

Figure 1. The idealized complanately bonded right-angled geometry of the bis(ethylenediamine)platinum(II) cation and its associate localized ligand orbital spatial disposition for the Δ(λ,λ) conformation [for conformational conventions see Fig. 5 and 7]. The upward-directed localized ligand (nitrogen) orbital (*i.e.* directed toward positive z-values) is leagued with the upward-placed adjacent ligand (carbon) kernel.

If, as in Part I, Topic A,[6] we designate the localized

Optical Rotary Power," Thesis, Princeton University, 1940; W. Kauzmann, J. E. Walter, and H. Eyring, *Chem. Rev.*, **26**, 339 (1940) [*erratum*, J. F. Lane, *Science*, **113**, 577 (1951)]; W. Kauzmann and H. Eyring, *J. Chem. Phys.*, **9**, 41 (1941); S. Bernstein, W. Kauzmann, and E. S. Wallis, *J. Org. Chem.*, **6**, 319 (1941); W. Kauzmann, *J. Am. Chem. Soc.*, **64**, 1626 (1942); W. Kauzmann, F. B. Clough, and I. Tobias, ref. 4h, p. 57; (o) M. V. Vol'kenshtein, *Dokl. Akad. Nauk SSSR*, **71**, 447, 643 (1950); *Zh. Eksptl. Teoret. Fiz.*, **20**, 342 (1950); *Izv. Akad. Nauk SSSR, Ser. Fiz.*, **17**, 574 (1953); M. V. Vol'kenshtein and M. P. Kruchek, *Opt. Spectry.*, **9**, 243 (1960); *Zh. Strukt. Khim.*, **2**, 59 (1961); M. V. Vol'kenshtein and I. O. Levitan, *ibid.*, **3**, 80, 87 (1962); S. Yamana, *Bull. Chem. Soc. Japan*, **31**, 558 (1958); **33**, 1741 (1960); (p) H. Looyenga, "Optical Rotation and Molecular Structure," Thesis, University of Leiden, 1955; (q) W. E. Moffitt, *J. Chem. Phys.*, **25**, 1189 (1956); (r) A. J. Moscowitz, "On Optical Activity—Hexahelicene," Thesis, Harvard University, 1957, and to be published; ref. 4h, p. 48; *Advan. Chem. Phys.*, **4**, 67 (1962); K. Mislow, M. A. W. Glass, A. J. Moscowitz, and C. Djerassi, *J. Am. Chem. Soc.*, **83**, 2771 (1961); A. J. Moscowitz, E. Charney, U. Weiss, and H. Ziffer, *ibid.*, **83**, 4661 (1961); W. E. Moffitt, R. B. Woodward, A. J. Moscowitz, W. Klyne, and C. Djerassi, *ibid.*, **83**, 4013 (1961); C. Djerassi, R. Records, E. Bunnenberg, K. Mislow, and A. J. Moscowitz, *ibid.*, **84**, 870 (1962); A. J. Moscowitz, K. Mislow, M. A. W. Glass, and C. Djerassi, *ibid.*, **84**, 1945 (1962); E. Bunnenberg, C. Djerassi, K. Mislow, and A. J. Moscowitz, *ibid.*, **84**, 2823 (1962); L. S. Forster, A. J. Moscowitz, J. G. Berger, and K. Mislow, *ibid.*, **84**, 4353 (1962); A. J. Moscowitz and K. Mislow, *ibid.*, **84**, 4605 (1962); J. de Heer and A. J. Moscowitz, to be published; L. C. Snyder and A. J. Moscowitz, to be published; (s) E. Wasserman, "Nonconjugated Interactions in Pi Electron Systems," Thesis, Harvard University, 1958; *Rev. Mod. Phys.*, **32**, 443 (1960), and to be published; (t) S. Sugano *J. Chem. Phys.*, **33**, 1883 (1960); M. Shinada and S. Sugano, to be published; (u) A. Julg. *Tetrahedron*, **12**, 146 (1961); M. Maestro and S. Merlino, *Gazz. chim. ital.*, **93**, 477 (1963) (v) R. Deen, "Optical Rotatory Dispersion of Some Organic Molecules," Thesis, University of Leiden, 1961; R. Deen and H. J. C. Jacobs, *Proc. Roy. Acad. Sci.* (Amsterdam), **64B**, 313 (1961); (w) T. S. Piper, *J. Am. Chem. Soc.*, **83**, 3908 (1961); T. S. Piper and A. G. Karipides, *Mol. Phys.*, **5**, 475 (1962); A. G. Karipides and T. S. Piper, *J. Chem. Phys.*, **40**, 674 (1964); (x) N. K. Hamer, *Mol. Phys.*, **5**, 339 (1962); (y) H. Poulet, *J. chim. phys.*, **59**, 584 (1962); (z) Kwang-Hsien Hsu, "Theory of Optical Rotatory Power," Thesis, Columbia University, 1951; D. J. Caldwell, "Selected Topics in the Theory of Optical Rotation," Thesis, Princeton University, 1962; J. P. Ranck, "Optical Rotatory Dispersion of Complexes of Transition Metals with Asymmetric Ligands," Thesis. Princeton University, 1962; D. J. Caldwell and H. Eyring, *Rev. Mod. Phys.*, **35**, 577 (1963); (aa) Th. Bürer, *Mol. Phys.*, **6**, 541 (1963). Highly critical reviews which underscore the successes as well as the failures of these efforts may be found in (bb) T. M. Lowry, ref. 4d; E. U. Condon, ref. 5m; W. Kauzmann, J. E. Walter, and H. Eyring, ref. 5n; P. Szarvas, *Magyar Kem. Folyoirat*, **46**, 1 (1940); M. V. Vol'kenshtein, *Usp. Khim.*, **9**, 1089, 1252 (1940); E. Hückel, *Z. Elektrochem.*, **50**, 13 (1944); J. P. Mathieu, "Les Théories Moléculaires du Pouvoir Rotatoire Naturel," Centre National de la Recherche Scientifique, Gauthier-Villars, Paris, 1946; "Activité Optique Naturelle," Handbuch der Physik, Band XXVIII, Spektroskopie II, S. Flügge, Ed., Springer-Verlag, Berlin, 1957, pp. 333–432; G. W. van Vloten, *Chem. Weekblad.*, **48**, 977 (1952); S. F. Mason, *Quart. Rev.* (London), **17**, 20 (1963); D. J. Caldwell and H. Eyring, *Ann. Rev. Phys. Chem.*, **15**, 281 (1964). The rigorous quantum mechanical basis (independent of model) of optical rotation is given in (cc) L. Rosenfeld, *Z. Physik*, **52**, 161 (1928); G. Temple, ref. 4a; M. Born and P. Jordan, "Elementare Quantenmechanik," Julius Springer, Berlin, 1930; H. Eyring, J. Walter, and G. E. Kimball, "Quantum Chemistry," John Wiley and Sons, Inc., New York, N. Y., and London; M. V. Vol'kenshtein, "Molekulyarnaya optika," Gosudarst. Izd. Tekh.-Teoret. Lit., Moscow, Leningrad, 1951; W. Kauzmann, "Quantum Chemistry: An Introduction," Academic Press, Inc., New York, N. Y., 1957, and in ref. 5bb.

(6) A. D. Liehr, *J. Phys. Chem.*, **68**, 665 (1964).

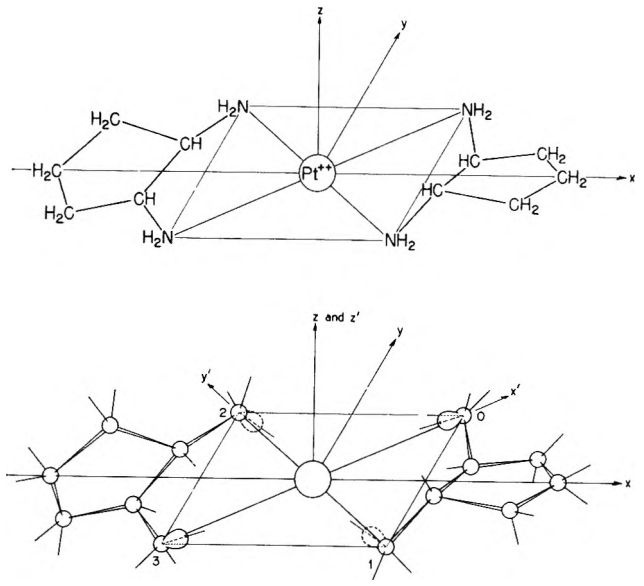

Figure 2. The idealized complanately bonded right-angled geometry of the bis(cyclopentanediamine)platinum(II) cation and its associate localized ligand orbital spatial disposition for the $\Lambda(\delta,\delta)$ conformation [for conformational conventions, see Fig. 6 and 8]. The upward-directed localized ligand (nitrogen) orbital (*i.e.*, directed toward positive z-values) is leagued with the downward-placed adjacent ligand (carbon) kernel. [Thus, bisethylenediamine (Fig. 1) and biscyclopentanediamine (Fig. 2) pseudo-complanate compounds of the same over-all conformation rotate oppositely. Hence, relative conformation of coordination compounds with nonhomomorphic ligands *cannot* be secured from relative rotational signs alone: comparative localized ligand orbital patterns need also to be known.]

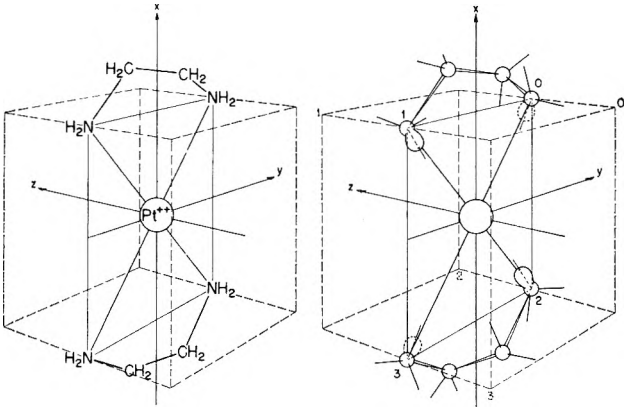

Figure 3. The idealized complanately bonded right-angled geometry of the bis(ethylenediamine)platinum(II) cation in the $\Delta(\lambda,\lambda)$ conformation [for conformational conventions, see Fig. 5 and 7] and its associate localized ligand orbital spatial disposition viewed as a tetrahedral affiliate.

ligand σ-bond orbitals by the symbol λ_j ($j = 0, 1, 2, 3$), we may approximate the digonal dihedral one-electron σ-like molecular orbitals, Λ_s, as a linear combination of these localized orbitals [but see the qualifications of this statement in footnote 4, ref. 6].

$$\Lambda_s = \sum_{j=0}^{3} a_{js}\lambda_j \qquad (1)$$

As our molecular framework has the symmetry D_2, the three twofold axes being the x, y, and z axes pictured in Fig. 1, 2, 3, 4, 7, and 8, we can demand consistently that our molecular orbitals, Λ_s, be digonally symmetric; that is, that [recall that in ordinary space $\mathcal{C}_2(y)$ equals $\mathcal{C}_2(x)\mathcal{C}_2(z)$]

$$\mathcal{C}_2(z)\Lambda_{s_z}^{(s_x)} = s_z\Lambda_{s_z}^{(s_x)};\ \mathcal{C}_2(x)\Lambda_{s_z}^{(s_x)} = s_x\Lambda_{s_z}^{(s_x)};$$
$$\mathcal{C}_2(y)\Lambda_{s_z}^{(s_x)} = s_xs_z\Lambda_{s_z}^{(s_x)}\ (s_z,\ s_x = \pm) \qquad (2)$$

In the localized representation, eq. 1, for the one-electron molecular orbitals, $\Lambda_{s_z}^{(s_x)}$, we find that the $a_{js_z}^{s_x}$ equal 1, s_x, s_xs_z, s_z times $a_{0s_z}^{s_x}$, respectively, for ($j = 0$, 1, 2, 3), (s_x, $s_z = \pm$), or that [letting s_xs_z equal s_y]

$$\Lambda_{s_z}^{(s_x)} = a_{0s_z}^{s_x}\{\lambda_0 + s_x\lambda_1 + s_y\lambda_2 + s_z\lambda_3\} \qquad (3)$$

where the constants $a_{0s_z}^{s_x}$ are determined solely by normalization. Printed in full and classified as to their proper D_2 symmetry species [see Table II], these one-electron orbitals subsume the form[7]

$$\Lambda_+^{(+)}(a_1) = a_{0+}^{+}\{\lambda_0 + \lambda_1 + \lambda_2 + \lambda_3\}$$
$$\Lambda_+^{(-)}(b_1) = a_{0+}^{-}\{\lambda_0 - \lambda_1 - \lambda_2 + \lambda_3\}$$
$$\Lambda_-^{(-)}(b_2) = a_{0-}^{-}\{\lambda_0 - \lambda_1 + \lambda_2 - \lambda_3\}$$
$$\Lambda_-^{(+)}(b_3) = a_{0-}^{+}\{\lambda_0 + \lambda_1 - \lambda_2 - \lambda_3\} \qquad (4)$$

With the neglect of localized ligand–ligand overlap, the constants $a_{0s_z}^{s_x}$ uniformly equal one-half.

Table I: Definition of the $\mathcal{C}_2(z)$, $\mathcal{C}_2(y)$, and $\mathcal{C}_2(x)$ Symmetry Operations

k	$\mathcal{C}_2(z)k$	$\mathcal{C}_2(x)k$	$\mathcal{C}_2(y)k$	(kl)	$\mathcal{C}_2(z)(kl)$	$\mathcal{C}_2(x)(kl)$	$\mathcal{C}_2(y)(kl)$
0	3	1	2	(01)	(32)	(10)	(23)
1	2	0	3	(23)	(10)	(32)	(01)
2	1	3	0	x'	$-x'$	$-y'$	y'
3	0	2	1	y'	$-y'$	$-x'$	x'

(7) These selfsame equations could also have been derived by use of the localized orbital formalism of eq. 13 through 15 of ref. 6. In this formalism, eq. 1 of this paper would be recast as $\Lambda_s = b_{0s}(01) + b_{1s}(23)$, and the application of $\mathcal{C}_2(y)$ and $\mathcal{C}_2(x)$ as in eq. 2 would then imply b_{1s} equals s_yb_{0s}, and (10) equals $s_x(01)$ and (32) equals $s_x(23)$. [*Cf.* Table I. For comparison, mark that in ref. 6, the operation $\mathcal{C}_3(z')$, $\mathcal{C}_2(y')$, and complex conjugation, *, together implied that (51) equaled (15)*, (40) equaled (04)*, and (32) equaled (23)*]. Whence if (01) is approximated as $\lambda_0 + c_{01}\lambda_1$ and (23) as $\lambda_2 + c_{23}\lambda_3$ we find c_{01} and c_{23} equal s_z and eq. 3 and 4 are recreated [similar comments hold with regard to eq. 10 and 16 of ref. 6.]

Table II: The D_2 Point Group and Transformation Standards

D_2	E	$C_2(z)$	$C_2(y)$	$C_2(x)$	Transformation standards
A	1	1	1	1	$x^2, y^2, z^2, x'y', x'^2 + y'^2, z'^2, \Lambda_+^{(+)}$
B_1	1	1	−1	−1	$z, \ell_z, z', \ell_{z'}, xy, x'^2 - y'^2, \Lambda_+^{(-)}$
B_2	1	−1	1	−1	$y, \ell_y, x' + y', \ell_x' + \ell_y', xz, x'z' - y'z', \Lambda_-^{(-)}$
B_3	1	−1	−1	1	$x, \ell_x, x' - y', \ell_x' - \ell_y', yz, x'z' + y'z', \Lambda_-^{(+)}$

Table III: Definition of the Local σ- and π-Orbitals Utilized

j	σ_j^c	π_j^c	$\tilde{\pi}_j^s$
0	$k_s(2s)_{A_0} - k_p \cos \iota \cos \alpha\ (2p_{z'})_{A_0}$	$k_p \cos \iota \sin \alpha\ (2p_{y'})_{A_0}$	$k_p \sin \iota\ (2p_{z'})_{A_0}$
1	$k_s(2s)_{A_1} + k_p \cos \iota \cos \alpha\ (2p_{y'})_{A_1}$	$-k_p \cos \iota \sin \alpha\ (2p_{z'})_{A_1}$	$-k_p \sin \iota\ (2p_{z'})_{A_1}$
2	$k_s(2s)_{A_2} - k_p \cos \iota \cos \alpha\ (2p_{y'})_{A_2}$	$k_p \cos \iota \sin \alpha\ (2p_{z'})_{A_2}$	$-k_p \sin \iota\ (2p_{z'})_{A_2}$
3	$k_s(2s)_{A_3} + k_p \cos \iota \cos \alpha\ (2p_{z'})_{A_3}$	$-k_p \cos \iota \sin \alpha\ (2p_{y'})_{A_3}$	$k_p \sin \iota\ (2p_{z'})_{A_3}$

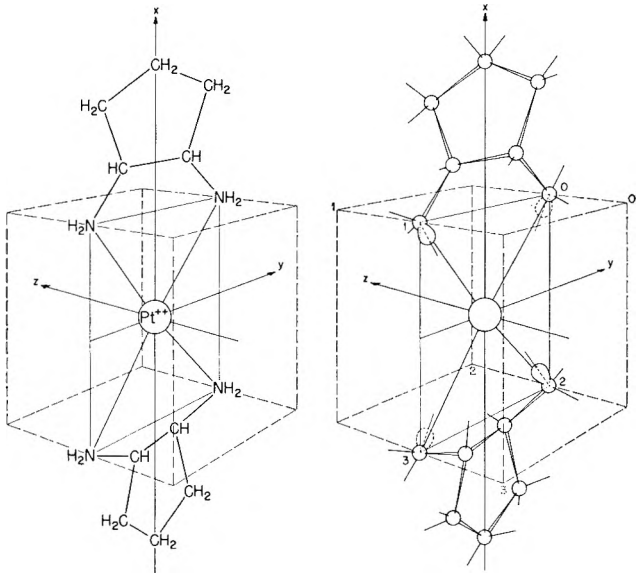

Figure 4. The idealized complanately bonded right-angled geometry of the bis(cyclopentanediamine)platinum(II) cation in the $\Lambda(\delta,\delta)$ conformation [for conformational conventions, see Fig. 6 and 8] and its associate localized ligand orbital spatial disposition viewed as a tetrahedral affiliate.

For ease of later computations, it is expedient to parcel the localized ligand orbitals λ_j into a "σ-part" and a "π-part" which are separately directed along the axes x', y', and z' of Fig. 1, 2, 3, 4, 7, 8, 9, and 13.[8] We may then scribe

$$\lambda_0 = \sigma_{x'0} + \pi_{y'0} + \tilde{\pi}_{z'0};\ \lambda_1 = \sigma_{y'1} + \pi_{x'1} + \tilde{\pi}_{z'1}$$
$$\lambda_2 = \sigma_{y'2} + \pi_{x'2} + \tilde{\pi}_{z'2};\ \lambda_3 = \sigma_{x'3} + \pi_{y'3} + \tilde{\pi}_{z'3} \qquad (5)$$

where $[w = x', y', z';\ j = 0, 1, 2, 3]$[8]

$$\sigma_{wj}^c = k_s ns \mp k_p \cos \iota \cos \alpha\ np\sigma_{wj}$$
$$\pi_{wj}^c = \pm k_p \cos \iota \sin \alpha\ np\pi_{wj}$$
$$\tilde{\pi}_{wj}^s = \pm k_p \sin \iota\ np\tilde{\pi}_{wj} \qquad (6)$$

and where the superscripts c and s have been introduced in eq. 6 to witness the attendance of the factors $k_p \cos \iota \cos \alpha$ (or $\sin \alpha$) and $k_p \sin \iota$ in the σ- and π-like functions. [If these factors are absent the superscripts c and s are to be discarded. See Fig. 13a.] The factor $\mp$ in the σ_{wj}^c expression of eq. 6 gives the phase required for maximum σ-bonding strength; the factors $\pm$ in the π_{wj}^c and $\tilde{\pi}_{wj}^s$ expressions give the phases needed for proper symmetrization and orientation [compare Fig. 1, 2, 3, 4, 7, 8, 9, and 13b and Table III]. In this idiom, eq. 3 and 4 become

$$\Lambda_{s_z}^{(s_x)} = \Sigma_{s_z}^{(s_x)c} + \Pi_{s_z}^{(s_x)c} + \tilde{\Pi}_{s_z}^{(s_x)s} \qquad (7)$$

$$\Lambda_+^{(+)}(a_1) = \Sigma_+^{(+)c}(a_{1g}) + \Pi_+^{(+)c}(b_{1g}) + \tilde{\Pi}_+^{(+)s}(b_{1u})$$
$$\Lambda_+^{(-)}(b_1) = \Sigma_+^{(-)c}(b_{2g}) + \Pi_+^{(-)c}(a_{2g}) + \tilde{\Pi}_+^{(-)s}(a_{2u})$$
$$\Lambda_-^{(-)}(b_2) = \Sigma_-^{(-)c}(e_{ub}) + \Pi_-^{(-)c}(e_{ub}) - \tilde{\Pi}_-^{(-)s}(e_{gb})$$
$$\Lambda_-^{(+)}(b_3) = \Sigma_-^{(+)c}(e_{ua}) + \Pi_-^{(+)c}(e_{ua}) + \tilde{\Pi}_-^{(+)s}(e_{ga}) \qquad (8)$$

where

$$\Sigma_{s_z}^{(s_x)c} = a_{s_z}^{\sigma s_x}\{\sigma_0^c + s_x\sigma_1^c + s_y\sigma_2^c + s_z\sigma_3^c\}$$
$$\Pi_{s_z}^{(s_x)c} = a_{s_z}^{\pi s_x}\{\pi_0^c + s_x\pi_1^c + s_y\pi_2^c + s_z\pi_3^c\}$$
$$\tilde{\Pi}_{s_z}^{(s_x)s} = a_{s_z}^{\tilde{\pi} s_x}\{\tilde{\pi}_0^s + s_x\tilde{\pi}_1^s + s_y\tilde{\pi}_2^s + s_z\tilde{\pi}_3^c\} \qquad (9)$$

(8) This parcelment is accomplished by the techniques of footnote 7 and Fig. 4b of ref. 6, with the angular identification of the angles α and φ_α of ref. 6 with $90° - \iota$ and $\pm\alpha$ here [*cf.* Fig. 1, 2, 3, 4, 7, 8, 9, and 13].

$$
\begin{aligned}
\Sigma_+^{(+)c}(a_{1g}) &= a_+^{\sigma+}\{\sigma_0^c + \sigma_1^c + \sigma_2^c + \sigma_3^c\} \\
\Sigma_+^{(-)c}(b_{2g}) &= a_+^{\sigma-}\{\sigma_0^c - \sigma_1^c - \sigma_2^c + \sigma_3^c\} \\
\Sigma_-^{(-)c}(e_{ub}) &= a_-^{\sigma-}\{\sigma_0^c - \sigma_1^c + \sigma_2^c - \sigma_3^c\} \\
\Sigma_-^{(+)c}(e_{ub}) &= a_-^{\sigma+}\{\sigma_0^c + \sigma_1^c - \sigma_2^c - \sigma_3^c\} \\
\Pi_+^{(+)c}(b_{1g}) &= a_+^{\pi+}\{\pi_0^c + \pi_1^c + \pi_2^c + \pi_3^c\} \\
\Pi_+^{(-)c}(a_{2g}) &= a_+^{\pi-}\{\pi_0^c - \pi_1^c - \pi_2^c + \pi_3^c\} \\
\Pi_-^{(-)c}(e_{ub}) &= a_-^{\pi-}\{\pi_0^c - \pi_1^c + \pi_2^c - \pi_3^c\} \\
\Pi_-^{(+)c}(e_{ua}) &= a_-^{\pi+}\{\pi_0^c + \pi_1^c - \pi_2^c - \pi_3^c\} \\
\tilde{\Pi}_+^{(+)s}(b_{1u}) &= a_+^{\tilde{\pi}+}\{\tilde{\pi}_0^s + \tilde{\pi}_1^s + \tilde{\pi}_2^s + \tilde{\pi}_3^s\} \\
\tilde{\Pi}_+^{(-)s}(a_{2u}) &= a_+^{\tilde{\pi}-}\{\tilde{\pi}_0^s - \tilde{\pi}_1^s - \tilde{\pi}_2^s + \tilde{\pi}_3^s\} \\
\tilde{\Pi}_-^{(-)s}(e_{gb}) &= a_-^{\tilde{\pi}-}\{\tilde{\pi}_0^s - \tilde{\pi}_1^s + \tilde{\pi}_2^s - \tilde{\pi}_3^s\} \\
\Pi_-^{(+)s}(e_{gb}) &= a_-^{\tilde{\pi}+}\{\tilde{\pi}_0^s + \tilde{\pi}_1^s - \tilde{\pi}_2^s - \tilde{\pi}_3^s\} \qquad (10)
\end{aligned}
$$

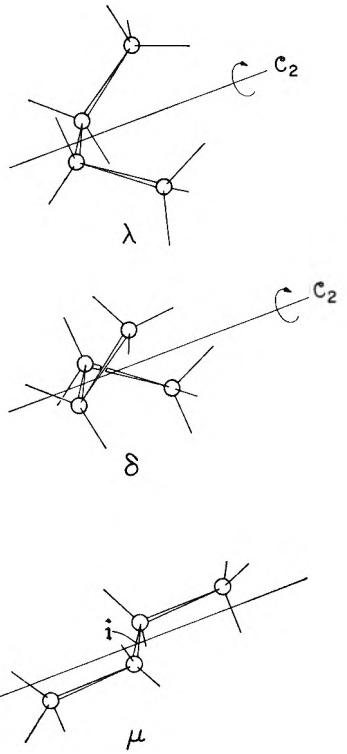

Figure 5. Conformational conventions for the ligand ethylenediamine. The lambda (λ) conformer is defined as that obtained by a clockwise left-hand screw rotation (*i.e.*, a clockwise rotation with the left hand which advances the left thumb outward toward the eyes of the observer) of *less than* 180° which will take the bottommost (*i.e.*, on the palm side of the hand) branch of the ligand into contingence with the topmost (*i.e.*, at the thumb side of the hand); the delta (δ) conformer as that obtained by the contrary (mirror image) right-hand counterclockwise rotation; and the *meso* (μ) conformer as that obtained by an internal inversion (i) [Fig. 5] or reflection (σ_v) [Fig. 6] which will take all ligand parts into themselves.

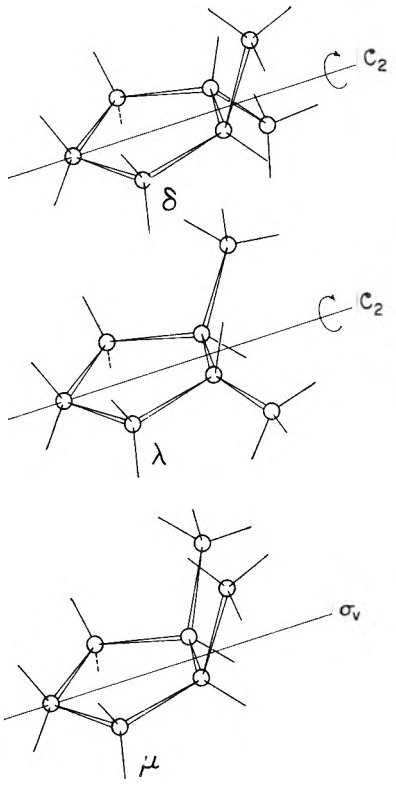

Figure 6. Conformational conventions for the ligand cyclopentanediamine (read caption to Fig. 5 for detail).

and where the subscript w equals x', y', z', which is made superfluous by Fig. 13 and Table III, has been dropped. The quadrate (D_{4h}) species classification [Table IV] has been added to the symbols $\Sigma_{s_z}^{(s_z)c}$, $\Pi_{s_x}^{(s_z)c}$, $\tilde{\Pi}_{s_z}^{(s_z)s}$ (s_x, $s_z = \pm$), in eq. 8 and 10 for tutorial clarity.

The construction of the one-electron molecular orbitals of a digonal dihedral compound is now straightforward: it is only required to sum the compatibly oriented and symmetrized localized ligand molecular orbitals, with suitable multiplicative variational constants, to the proper central atom orbitals [collate Tables II, IV, and V]. If we let these multiplicative constants be η or $\eta^\star$ (the star * denotes quantities allied to different orbitals of the same species, here to the second orbital of species a), ρ_1, ρ_2, and ρ_3 for the ligand functions $\Lambda_+^{(+)}(a_1)$, $\Lambda_+^{(-)}(b_1)$, $\Lambda_-^{(-)}(b_2)$, and $\Lambda_-^{(+)}(b_3)$, separately, we find that

$$
\begin{aligned}
a(x^2 - y^2) &= N_a\{d_{x^2-y^2} + \eta\Lambda_+^{(+)}\} \\
a^\star(3z^2 - r^2) &= N_{a^\star}\{d_{3z^2-r^2} + \eta^\star\Lambda_+^{(+)}\} \\
b_1(xy) &= N_{b_1}\{d_{xy} + \rho_1\Lambda_+^{(-)}\} \\
b_2(xz) &= N_{b_2}\{d_{xz} + \rho_2\Lambda_-^{(-)}\} \\
b_3(yz) &= N_{b_3}\{d_{yz} + \rho_3\Lambda_-^{(+)}\} \qquad (11)
\end{aligned}
$$

Table IV: Ligand Group Orbital Transformation Properties

Ligand group orbital designation[a]					Ligand group representation	Transformation properties[b]						
D_2	$D_{4h}(T_d)$	$D_{4h}(O_h)$	T_d	O_h		$\mathcal{C}_4(z \text{ or } z')$	i	$\mathcal{C}_2(z \text{ or } z')$	$\mathcal{C}_2(x)$	$\mathcal{C}_2(y)$	$\mathcal{C}_2(x')$	$\mathcal{C}_2(y')$
a	...	...	...	...	$A_+^{(+)}$	...	...	$A_+^{(+)}$	$A_+^{(+)}$	$A_+^{(+)}$	...	...
b_1	...	...	...	...	$A_+^{(-)}$	...	...	$A_+^{(-)}$	$-A_+^{(-)}$	$-A_+^{(-)}$	...	...
b_2	...	...	...	...	$A_-^{(-)}$	...	...	$-A_-^{(-)}$	$A_-^{(-)}$	$-A_-^{(-)}$	...	...
b_3	...	...	...	...	$A_-^{(+)}$	...	...	$-A_-^{(+)}$	$-A_-^{(+)}$	$A_-^{(+)}$	...	...
a	$a_{1g}(a_1)$	$a_{1g}(\sqrt{2/3}a_{1g} - \sqrt{1/3}e_{ga})$	a_1	$\sqrt{2/3}a_{1g} - \sqrt{1/3}e_{ga}$	$\Sigma_+^{(+)c}$	$\Sigma_+^{(+)c}$	$\Sigma_+^{(+)c}$	$\Sigma_+^{(+)c}$	$\Sigma_+^{(+)c}$	$\Sigma_+^{(+)c}$	$\Sigma_+^{(+)c}$	$\Sigma_+^{(+)c}$
b_1	$b_{2g}(-t_{2b})$	$b_{1g}(e_{gb})$	$-t_{2b}$	e_{gb}	$\Sigma_+^{(-)c}$	$-\Sigma_+^{(-)c}$	$\Sigma_+^{(-)c}$	$\Sigma_+^{(-)c}$	$-\Sigma_+^{(-)c}$	$-\Sigma_+^{(-)c}$	$\Sigma_+^{(-)c}$	$\Sigma_-^{(-)c}$
b_2	$e_{ub}(-t_{2a})$	$\sqrt{1/2}(e_{uc}(t_{1uc}) + e_{ub}(t_{1ub}))$	$-t_{2a}$	$\sqrt{1/2}(t_{1uc} + t_{1ub})$	$\Sigma_-^{(-)c}$	$\Sigma_-^{(+)c}$	$-\Sigma_-^{(-)c}$	$-\Sigma_-^{(-)c}$	$\Sigma_-^{(-)c}$	$-\Sigma_-^{(-)c}$	$\Sigma_-^{(+)c}$	$-\Sigma_-^{(+)c}$
b_3	$e_{ua}(t_{2c})$	$\sqrt{1/2}(e_{ua}(t_{1uc}) - e_{ub}(t_{1ub}))$	t_{2c}	$\sqrt{1/2}(t_{1uc} - t_{1ub})$	$\Sigma_-^{(+)c}$	$-\Sigma_-^{(-)c}$	$-\Sigma_-^{(+)c}$	$-\Sigma_-^{(+)c}$	$-\Sigma_-^{(+)c}$	$\Sigma_-^{(+)c}$	$\Sigma_-^{(-)c}$	$-\Sigma_-^{(-)c}$
a	$b_{1g}\left(\frac{1}{2}e_a - \frac{\sqrt{3}}{2}e_b\right)$	$b_{2g}(t_{2ga})$	$\frac{1}{2}e_a - \frac{\sqrt{3}}{2}e_b$	t_{2ga}	$\Pi_+^{(+)c}$	$-\Pi_+^{(+)c}$	$\Pi_+^{(+)c}$	$\Pi_+^{(+)c}$	$\Pi_+^{(+)c}$	$\Pi_+^{(+)c}$	$-\Pi_+^{(+)c}$	$-\Pi_+^{(+)c}$
b_1	$a_{2g}\left(-\frac{1}{2}t_{2b} - \frac{\sqrt{3}}{2}t_{1b}\right)$	$a_{2g}(t_{1ga})$	$-\frac{1}{2}t_{2b} - \frac{\sqrt{3}}{2}t_{1b}$	t_{1ga}	$\Pi_+^{(-)c}$	$\Pi_+^{(-)c}$	$\Pi_+^{(-)c}$	$\Pi_+^{(-)c}$	$-\Pi_+^{(-)c}$	$-\Pi_+^{(-)c}$	$-\Pi_+^{(-)c}$	$-\Pi_+^{(-)c}$
b_2	$e_{ub}\left(\frac{1}{2}t_{2a} - \frac{\sqrt{3}}{2}t_{1a}\right)$	$\frac{1}{2}(e_{ua}(t_{1uc}) + e_{ua}(t_{2uc}) + e_{ub}(t_{1ub}) + e_{ub}(t_{2ub}))$	$\frac{1}{2}t_{2a} - \frac{\sqrt{3}}{2}t_{1a}$	$\frac{1}{2}(t_{1ub} + t_{2ub} + t_{1uc} + t_{2uc})$	$\Pi_-^{(-)c}$	$-\Pi_-^{(+)c}$	$-\Pi_-^{(-)c}$	$-\Pi_-^{(-)c}$	$\Pi_-^{(-)c}$	$-\Pi_-^{(-)c}$	$-\Pi_-^{(+)c}$	$\Pi_-^{(+)c}$
b_3	$e_{ua}(-t_{2c})$	$\frac{1}{2}(e_{ub}(t_{1ub}) + e_{ub}(t_{2ub}) - e_{ua}(t_{1uc}) - e_{ua}(t_{2uc}))$	$-t_{2c}$	$\frac{1}{2}(t_{1ub} + t_{2ub} - t_{1uc} - t_{2uc})$	$\Pi_-^{(+)c}$	$\Pi_-^{(-)c}$	$-\Pi_-^{(+)c}$	$-\Pi_-^{(+)c}$	$-\Pi_-^{(+)c}$	$\Pi_-^{(+)c}$	$-\Pi_-^{(-)c}$	$\Pi_-^{(-)c}$
a	$b_{1u}\left(\frac{\sqrt{3}}{2}e_a + \frac{1}{2}e_b\right)$	$b_{2u}(t_{2ua})$	$\frac{\sqrt{3}}{2}e_a + \frac{1}{2}e_b$	t_{2ua}	$\tilde{\Pi}_+^{(+)g}$	$-\tilde{\Pi}_+^{(+)g}$	$-\tilde{\Pi}_+^{(+)g}$	$\tilde{\Pi}_+^{(+)g}$	$\tilde{\Pi}_+^{(+)g}$	$\tilde{\Pi}_+^{(+)g}$	$-\tilde{\Pi}_+^{(+)g}$	$-\tilde{\Pi}_+^{(+)g}$
b_1	$a_{2u}\left(-\frac{\sqrt{3}}{2}t_{2b} + \frac{1}{2}t_{1b}\right)$	$a_{2u}(t_{1ua})$	$-\frac{\sqrt{3}}{2}t_{2b} + \frac{1}{2}t_{1b}$	t_{1ua}	$\tilde{\Pi}_+^{(-)g}$	$\tilde{\Pi}_+^{(-)g}$	$-\tilde{\Pi}_+^{(-)g}$	$\tilde{\Pi}_+^{(-)g}$	$-\tilde{\Pi}_+^{(-)g}$	$-\tilde{\Pi}_+^{(-)g}$	$-\tilde{\Pi}_+^{(-)g}$	$-\tilde{\Pi}_+^{(-)g}$
b_2	$e_{gb}\left(-\frac{\sqrt{3}}{2}t_{2a} - \frac{1}{2}t_{1a}\right)$	$\frac{1}{2}(e_{gb}(t_{1gb}) + e_{gb}(t_{2gb}) - e_{ga}(t_{1gc}) - e_{ga}(t_{2gc}))$	$-\frac{\sqrt{3}}{2}t_{2a} - \frac{1}{2}t_{1a}$	$\frac{1}{2}(t_{1gb} + t_{2gb} - t_{1gc} - t_{2gc})$	$\tilde{\Pi}_-^{(-)g}$	$-\tilde{\Pi}_-^{(+)g}$	$\tilde{\Pi}_-^{(-)g}$	$-\tilde{\Pi}_-^{(-)g}$	$\tilde{\Pi}_-^{(-)g}$	$-\tilde{\Pi}_-^{(+)g}$	$-\tilde{\Pi}_-^{(+)g}$	$\tilde{\Pi}_-^{(+)g}$
b_3	$e_{ga}(-t_{2c})$	$\frac{1}{2}(e_{ga}(t_{1gc}) + e_{ga}(t_{2gc}) + e_{gb}(t_{1gb}) + e_{gb}(t_{2gb}))$	$-t_{2c}$	$\frac{1}{2}(t_{1gb} + t_{2gb} + t_{1gc} + t_{2gc})$	$\tilde{\Pi}_-^{(+)g}$	$\tilde{\Pi}_-^{(-)g}$	$\tilde{\Pi}_-^{(+)g}$	$-\tilde{\Pi}_-^{(+)g}$	$-\tilde{\Pi}_-^{(+)g}$	$\tilde{\Pi}_-^{(+)g}$	$-\tilde{\Pi}_-^{(-)g}$	$\tilde{\Pi}_-^{(-)g}$

[a] The tetrahedral (T_d) orbital orientation is that of C. J. Ballhausen and A. D. Liehr, *J. Mol. Spectry.*, **2**, 342 (1958) [*errata, ibid.*, **4**, 190 [(1960)]]. The octahedral (O_h) orbital orientation is that derivable from the octahedral nuclear coordinate displacements of A. D. Liehr and C. J. Ballhausen, *Ann. Phys.* [N. Y.], **3**, 304 (1958), with the outward bond stretches replaced by positively signed inward σ-bond orbitals and inward bond stretches replaced by negatively signed inward σ-bond orbitals and with the sign of the $S_{2g}(e_g)$ displacement reversed. The subscripts a and b for the tetrahedral (T_d) and octahedral (O_h) e-orbitals designate functions oriented along the z (T_d) and z' (O_h) axis and in the x–y (T_d) and x'–y' (O_h) plane [Fig. 10], serially; the subscripts a, b, and c for the tetrahedral (T_d) and octahedral (O_h) t_2 or t_1 orbitals designate functions oriented in the x–y, x–z, and y–z (T_d) and x'–y', x'–z', and y'–z' (O_h) planes or along the z, y, and x (T_d) and z', y', and x' (O_h) axes [Fig. 10], separately; and the subscripts a and b for the tetragonal ($D_{4h}(T_d$ or $O_h)$) e-orbitals designate functions oriented in the y–z and x–z (T_d) and y'–z' and x'–z' (O_h) planes or along the x and y (T_d) and x' and y' (O_h) axes [Fig. 10], sequentially. [b] The transformations $\mathcal{C}_2(z \text{ or } z')$, $\mathcal{C}_2(y)$, and $\mathcal{C}_2(x)$ are as defined in Table I with the addition that these transformations applied to the coordinates $\{z, z'\}$ yield $\{z, z'\}$, $\{-z, -z'\}$, and $\{-z, -z'\}$, individually [Fig. 10]. The transformations $\mathcal{C}_4(z \text{ or } z')$, i, $\mathcal{C}_2(x')$, and $\mathcal{C}_2(y')$ are defined as these transformations which replace atoms numbered $\{0, 1, 2, 3\}$ and coordinate axes labeled $\{x, y, z\}$ and $\{x', y', z'\}$ by atoms numbered $\{1, 3, 0, 2\}$, $\{3, 2, 1, 0\}$, $\{0, 2, 1, 3\}$, and $\{3, 1, 2, 0\}$ and by coordinate axes labeled $\{-y, x, z\}$, $\{-x, -y, -z\}$, $\{y, x, -z\}$, and $(-y, -x, -z\}$ and $\{-y', x', z'\}$, $\{-x', -y', -z'\}$, $\{x', -y', -z'\}$, and $\{-x', y', z'\}$, respectively, with all (positive sense) rotations taken as counterclockwise [Fig. 10 and 13].

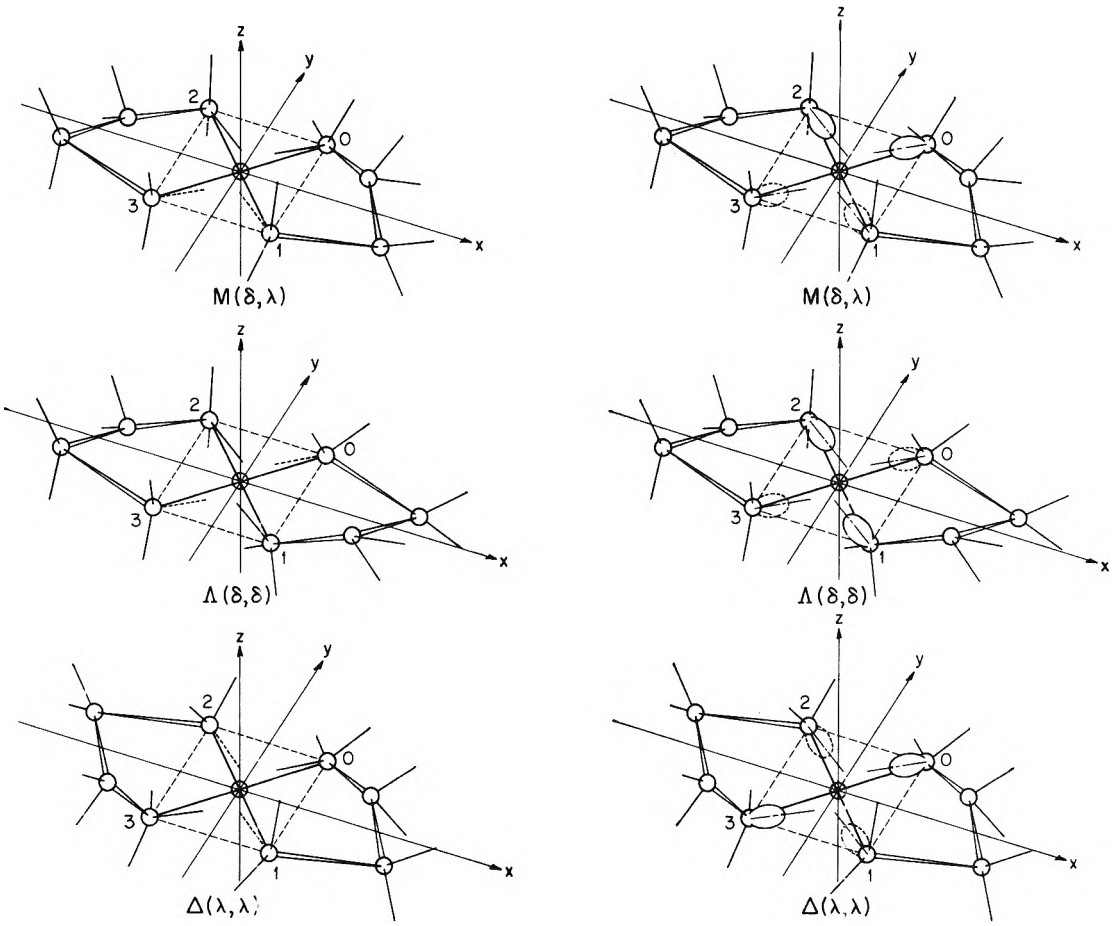

Figure 7. Conformational conventions and localized ligand orbital spatial dispositions for (pseudo) complanate bisethylenediamine complexes. The over-all delta (Δ) conformer is defined as that which fashions a two-bladed screw propeller whose smoothed lateralmost surface edges are right-handed or Δ-helices (*i.e.*, a two-bladed screw propeller which moves forward toward the observer when rotated counterclockwise—view Fig. 47). As this over-all conformer is formed only by ligands of lambda (λ) constitution, it is most completely designated as Δ(λ,λ). The over-all lambda (Λ) conformer is defined contrarily. Since it likewise is set wholly by ligands of delta (δ) fixture, it is also most fully designated as Λ(δ,δ). The over-all *meso* (M) conformer is defined as that which fashions a two-bladed counter-screw propeller whose smoothed lateralmost surface edges are one right-handed or Δ- and one left-handed or Λ-helices (*i.e.*, a two-bladed screw propeller which remains translationally immobile under clockwise or counterclockwise rotation but gyroscopically pivots about axes perpendicular to its principal (translational) axis of rotation). It is composed solely of paired ligands of δ- and λ-structure, and is therefore totally designated as M(δ,λ). As in Fig. 1 and 2, the upward-directed localized ligand (nitrogen) donor (lone pair) orbitals (symbolized by a full line) are allied with the upward-lodged adjacent ligand (carbon) kernels, and the downward-directed localized ligand (nitrogen) donor (lone pair) orbitals (symbolized by a dashed line) with the downward-lodged adjacent ligand (carbon) kernels in Fig. 7, and *vice versa* in Fig. 8; wherefore, identical conformers of pseudo-complanate bisethylenediamine and biscyclopentanediamine aggregates, for the same (metallochromophoric) electronic jump, rotate electromagnetic radiation contrarily.

where N_a, $N_a{}^\star$, N_{b_1}, N_{b_2}, and N_{b_3} are the molecular normalization constants which we choose to be real.

$$N_a = \{1 + 2\eta S[d_{3z^2-r^2};\ \Lambda_+{}^{(+)}] - \eta^2\}^{-1/2}$$
$$N_{a^\star} = \{1 + 2\eta^\star S[d_{x^2-y^2};\ \Lambda_+{}^{(+)}] + \eta^{\star 2}\}^{-1/2}$$
$$N_{b_1} = \{1 + 2\rho_1 S[d_{xy};\ \Lambda_+{}^{(-)}] + \rho_1{}^2\}^{-1/2}$$
$$N_{b_2} = \{1 + 2\rho_2 S[d_{xz};\ \Lambda_-{}^{(-)}] + \rho_2{}^2\}^{-1/2}$$
$$N_{b_3} = \{1 + 2\rho_3 S[d_{yz};\ \Lambda_-{}^{(+)}] + \rho_3{}^2\}^{-1/2} \qquad (12)$$

The connection between these functions and those correspondent to their tetrahedral and octahedral progenitors is as portrayed in Fig. 10, 11, and 12 and tabulated in Tables IV and V.[9]

1.2 *The π-Molecular Orbitals.* If localized ligand functions exist which present true ligand–central atom

(9) Note, in sharp contrast to ref. 6 [*cf.* footnotes 14 and 17 of ref. 6], that all the functions of eq. 11 and 12 are truly dihedrally dissymmetric since pseudo-octahedrality or tetrahedrality was nowhere invoked in their construction [study Tables III and IV].

Table V: Central Atom Orbital Transformation Properties

Central atom orbital designation[a]					d and p representations		Transformation properties		
D_2	$D_{4h}(T_d)$	$D_{4h}(O_h)$	T_d	O_h	T_d	O_h	$C_3(z)$	$C_3(y)$	$C_3(x)$
a	$a_{1g}(e)$	$a_{1g}(e_g)$	e_a	e_{ga}	$d_{3z^2-r^2}$	$d_{3z'^2-r^2}$	a	a	a
a	$b_{1g}(e)$	$b_{2g}(t_{2g})$	e_b	$-t_{2ga}$	$d_{x^2-y^2}$	$-d_{x'y'}$	a	a	a
b_1	$b_{2g}(t_2)$	$b_{1g}(t_{2g})$	t_{2a}	e_{gb}	d_{xy}	$d_{x'^2-y'^2}$	b_1	$-b_1$	$-b_1$
b_2	$e_{gb}(t_2)$	$\sqrt{1/2}(e_{gb}(t_{2g}) - e_{ga}(t_{2g}))$	t_{2b}	$\sqrt{1/2}(t_{2gb} - t_{2gc})$	d_{xz}	$\sqrt{1/2}(d_{x'z'} - d_{y'z'})$	$-b_2$	b_2	$-b_2$
b_3	$e_{ga}(t_2)$	$\sqrt{1/2}(e_{gb}(t_{2g}) + e_{ga}(t_{2g}))$	t_{2c}	$\sqrt{1/2}(t_{2gb} + t_{2gc})$	d_{yz}	$\sqrt{1/2}(d_{x'z'} + d_{y'z'})$	$-b_3$	$-b_3$	b_3
b_1	$a_{2u}(t_2)$	$a_{2u}(t_{1u})$	t_{2a}	t_{1ua}	p_z	$p_{z'}$	b_1	$-b_1$	$-b_1$
b_2	$e_{ub}(t_2)$	$\sqrt{1/2}(e_{ua}(t_{1u}) + e_{ub}(t_{1u}))$	t_{2b}	$\sqrt{1/2}(t_{1uc} + t_{1ub})$	p_y	$\sqrt{1/2}(p_{x'} + p_{y'})$	$-b_2$	b_2	$-b_2$
b_3	$e_{ua}(t_2)$	$\sqrt{1/2}(e_{ua}(t_{1u}) - e_{ub}(t_{1u}))$	t_{2c}	$\sqrt{1/2}(t_{1uc} - t_{1ub})$	p_x	$\sqrt{1/2}(p_{x'} - p_{y'})$	$-b_3$	$-b_3$	b_3

[a] The octahedral, tetrahedral, and tetragonal specie subscripts a, b, and c of columns two, three, four, and five are appended as indicated by their orbital representatives, columns six and seven. To elucidate, $e_{gb}(t_{2g})[D_{4h}(O_h)] \sim x'z$ or y', $e_{gb}(t_2)[D_{4h}(T_d)] \sim xz$ or y, $t_{2b}[T_d] \sim xz$ or y, $t_{2gb}[O_h] \sim x'z'$ or y', and so forth [the coordinate bases are as shown in Fig. 10]. In this notation and functional orientation we have $C_3(x = y = z)[T_d]$ or $C_3(x' = y' = z')[O_h]\{a,b,c\}$ equals $\{b,c,a\}$ and $C_4(z \text{ or } z')[D_{4h}]\{a,b\}$ equals $\{b,-a\}$.

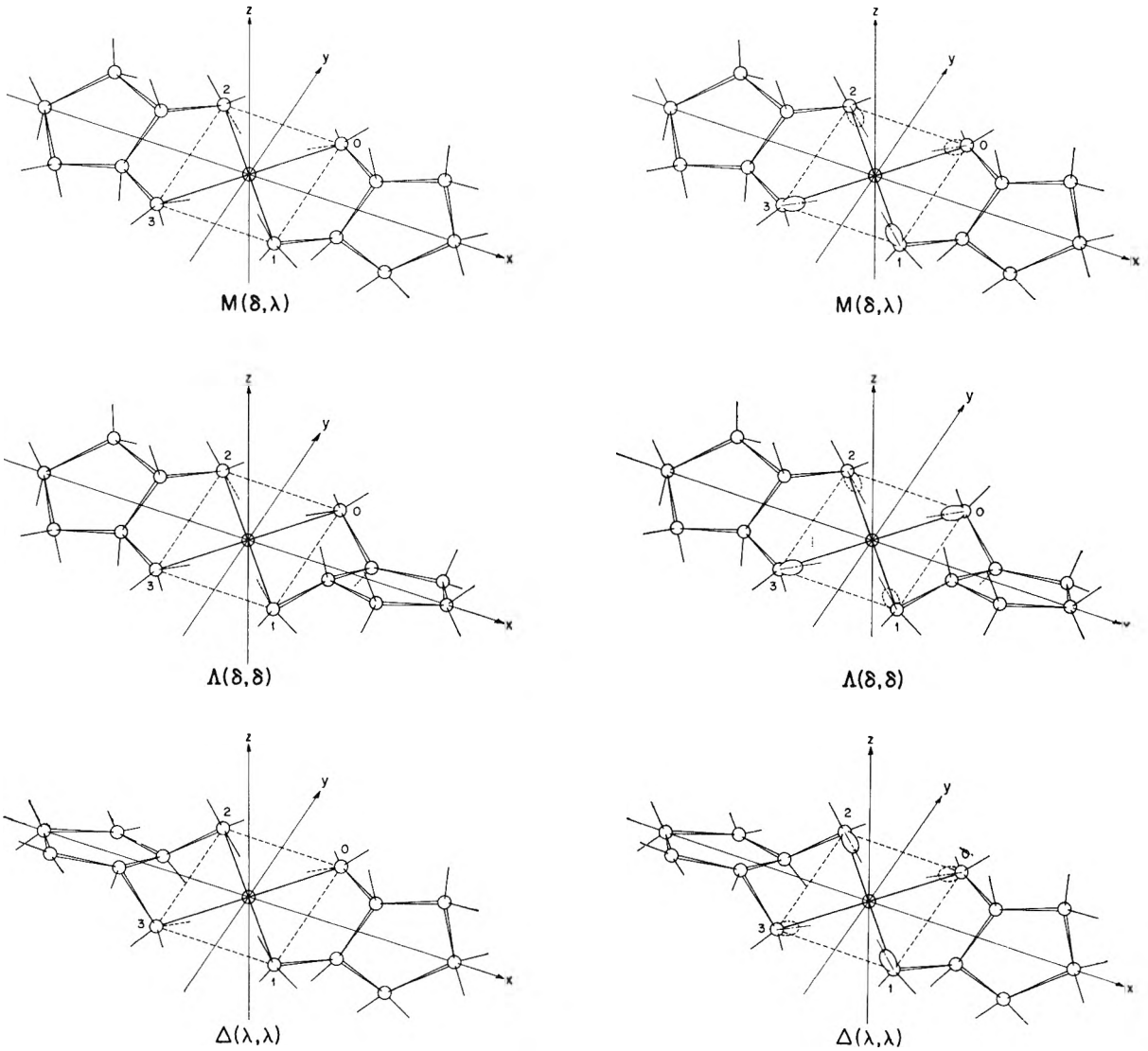

Figure 8. Conformational conventions and localized ligand orbital spatial dispositions for (pseudo) complanate biscyclopentanediamine complexes (read caption to Fig. 7 for detail).

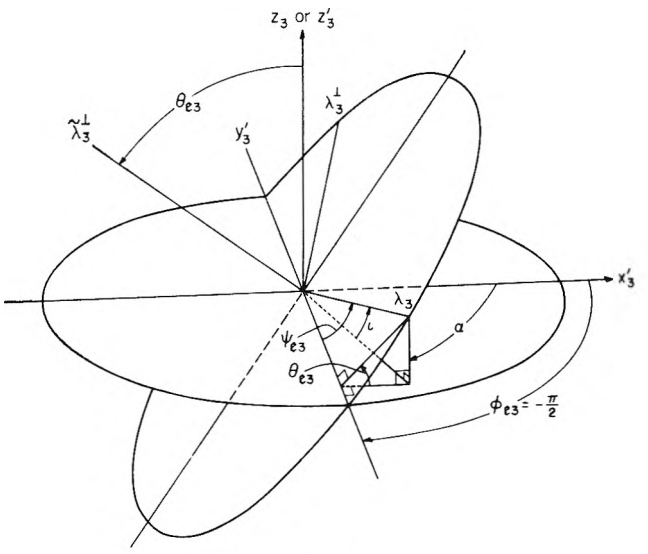

$$\cos(90-\alpha)\cos\iota = \cos\psi_{e3}$$
$$\sin(90-\alpha)\cos\iota = \sin\psi_{e3}\cos\theta_{e3}$$
$$\sin\iota = \sin\psi_{e3}\sin\theta_{e3}$$

Figure 9. Definition of the angles of cant α and ι and of the Euler angles ϕ_e, θ_e, ψ_e and a sample (at coordinate position three. At this position the σ-like orbital λ_3 is directed in the x_3', $-y_3'$, z_3' octant, and the π-like orbitals $\lambda_3^{\perp}$ and $\tilde{\lambda}_3^{\perp}$ in the x_3', y_3', z_3' and $-x_3'$, 0, z_3' octants, each) specification of their interconnection.

π-bond potentialities, the above molecular orbital analysis must be amended accordingly. Figures 14 through 17 portray the geometry and idealized local ligand orbital disposition, each, for a series of typical π-bonded digonal dihedral complex anions, and Fig. 18 and 19 show a possible, but not essential, level pattern. Once more the σ- and π-ligand frameworks are canted to the central atom–ligand axes, which have been here picked to be the x', y', z' axes for presentational simplicity.

To obtain the needed truly π-bonding linear combination, we proceed as in §1.1, eq. 1 through 12. We once more partition the available localized ligand orbitals when possible. If we signify by $\lambda_j^{\perp}$ and $\tilde{\lambda}_j^{\perp}$ the localized π-like ligand orbitals perpendicular to those of eq. 1 through 4 [*cf.* Fig. 9, 16b, and 17b],[10] we may write symbolically

$$\kappa_0^{\perp} = \sigma_{x'0} + \pi_{y'0} + \tilde{\pi}_{z'0}; \quad \kappa_1^{\perp} = \sigma_{y'1} + \pi_{x'1} + \tilde{\pi}_{z'1}$$
$$\kappa_2^{\perp} = \sigma_{y'2} + \pi_{x'2} + \tilde{\pi}_{z'2}; \quad \kappa_3^{\perp} = \sigma_{x'3} + \pi_{y'3} + \tilde{\pi}_{z'3} \qquad (13)$$

where $\kappa^{\perp}$ equals $\lambda^{\perp}$ or $\tilde{\lambda}^{\perp}$. The explicit specialization of eq. 13 to a form analogous to §1.1, eq. 6 is slightly involved. What is required is the Eulerian specification, $\mathbf{A}_j$, of the canted orbital (axis) system $\{\lambda_j, \lambda_j^{\perp}, \tilde{\lambda}_j^{\perp}\}$ relative to the uncanted system $\{p_{x'j}, p_{y'j}, p_{z'j}\}$ [view Fig. 9, 13, 16b, and 17b][11]

$$\begin{bmatrix} \lambda_j \\ \lambda_j^{\perp} \\ \tilde{\lambda}_j^{\perp} \end{bmatrix} = \mathbf{A}_j \begin{bmatrix} p_{x'j} \\ p_{y'j} \\ p_{z'j} \end{bmatrix} \qquad (14)$$

Equation 14 reduces to eq. 6, §1.1, whenever interest is confined solely to the orbital λ_j. In this case the three Eulerian angles, $(\phi_{cj}, \theta_{cj}, \psi_{cj})$, which particularize $\mathbf{A}_j$, convert to the two substitute angles, α_j and ι_j, of §1.1 [as an instance, witness Fig. 9]. The correct one-electron digonal dihedral localized ligand molecular orbitals are then given by a form identical with eq. 7 and 8 of §1.1 with the exception that the localized σ-, π-, and $\tilde{\pi}$-like functions now have a somewhat more complex appearance than that of eq. 6, §1.1 [recall the similar circumstance in ref. 6] due to the occurrence in their definitions of more complex multiplicative angular factors for the atomic-like functions $np_{\sigma_{wj}}$, $np_{\pi_{wj}}$, and $np_{\tilde{\pi}_{wj}}$ of eq. 6.

The molecular orbitals for a σ- and π-bonded digonal dihedral complex are now secured as before. The appropriate generalizations of eq. 7 through 10 of §1.1 are combined with the apt central atom orbitals to form proper molecular orbitals for the compound, whose form is identical with eq. 11, §1.1. This mathematical confluence of the σ-bonded and σ,π-bonded one-electron molecular orbitals, as in the trigonal dihedral case, ref. 6, is of wide consequence for the optical intensity and rotativity computations which follow.[12]

§2. Molecular Orbitals for Digonal Dihedral Compounds: Nonzero Spin-Orbit Forces

The meet tetragonal one-electron spin-orbital functions for states of octahedral of tetrahedral lineage $e_{(\delta)}^{(g)}$ and $t_{2(\delta)}^{(g)}$ have been constituted earlier by the author.[13] To adapt these functions to the current inquiry, it is but necessary to express the tetragonal basis (axes x', y',

(10) Alternatively, as explained in footnote 15 of ref. 6, the equivalent localized ligand orbital representation $\{\lambda_j, \lambda_j<, \tilde{\lambda}_j<\}$ of Fig. 16a and 17a could be used.

(11) For a marvellously clear exposition of Eulerian coordinate geometry, read H. Goldstein, "Classical Mechanics," Addison-Wesley, Cambridge, Mass., 1951. Our Eulerian matrix **A** and its angular depiction is identical with Goldstein's.

(12) It is important to note here that, in contrast to our treatment of the trigonal dihedral problem, ref. 6, no orbitals, gerade or ungerade, have been omitted in our formulation of σ-bonded or σ,π-bonded digonal dihedral molecular orbitals. Thus we can expect digonal dihedral optical intensities and rotativities which are considerably enhanced with respect to the trigonal dihedral ones of ref. 6

(13) A. D. Liehr, *J. Phys. Chem.*, **64**, 43 (1960).

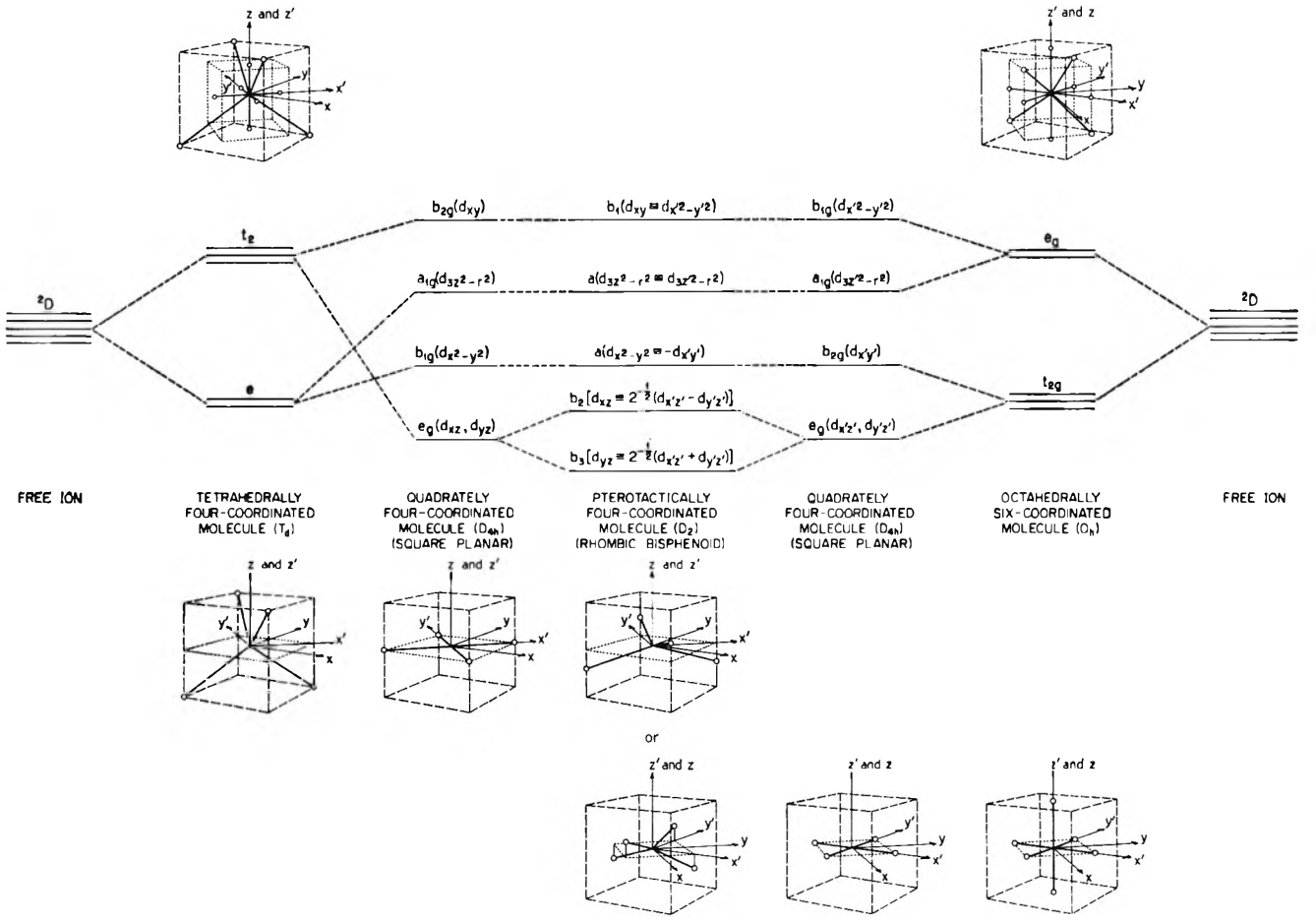

Figure 10. A correlational ligand field energy level diagram for the central atom of a pterotactically four-coordinated (digonal dihedral) compound. The order of the levels has been surmised from qualitative electronic overlap considerations. Note especially the placement of the $a(d_{3z^2-r^2})$ level. It is dictated by the large overlap of the $d_{3z^2-r^2}$ central atom orbital with the ligand σ-bond orbitals. This latter overlap is $-\sqrt{1/3}a_+^{\sigma+}/a_+^{\sigma-}$ or approximately minus the square root of one-third times that of the strongly σ-bonded central atom d_{xy} orbital with the ligand σ-bond orbitals. In turn, the overlap of central atom $d_{x^2-y^2}$ strongly π-bonded orbital is $\sqrt{2}\cot\iota\sin\alpha\, a_+^{\pi+}/a_-^{\tilde{\pi}-\text{or}+}$ (note that this quantity vanishes when α, ι go to zero, the pure σ-bond limit) times that of the moderately π-bonded d_{xz} and d_{yz} orbitals (for compounds with true π-bonded ligand possibilities, and with α, ι zero, the multiplicative factor is $\sqrt{2}\, a_+^{\pi+}/a_-^{\tilde{\pi}-\text{or}+}$, where the canted σ-bond ligand orbital parameters α, ι, and k_p have been suitably suppressed in the ligand–ligand normalization equations, eq. A-21 of the Appendix, section XII, § 5.7. With compounds of such possibilities, the ratio of the strong σ-bond overlap (d_{xy}) to the strong π-bond overlap ($d_{x^2-y^2}$) is $\sim -2.7a_+^{\sigma-}/a_+^{\pi+}$ [bis(ethylenediamine)copper(II) cation]. The location of the $b_2(d_{xz})$ level above the $b_3(d_{yz})$ level is made on steric grounds [*cf.* Fig. 1, 2, 3, 4, 7, 8].

z') in terms of the digonal dihedral basis (axes x, y, z) [mark Fig. 10 and 13]

$$d_{x'y'} = -d_{x^2-y^2},\ d_{x'z'} = \sqrt{1/2}(d_{xz} + d_{yz}),\ d_{y'z'} = \sqrt{1/2}(d_{yz} - d_{xz}),\ d_{3z'^2-r^2} = d_{3z^2-r^2},\ d_{x'^2-y'^2} = d_{xy}$$
$$\zeta'(\pm 1/2) = e^{\mp \pi i/8}\zeta(\pm 1/2) \qquad (15)$$

and substitute in eq. 15 of ref. 13.[14]

When the digonal dihedral basis orbitals $d_{x^2-y^2}$, $d_{3z^2-r^2}$, d_{xy}, d_{xz}, and d_{yz} are abbreviated by their digonal dihedral species denominations, a, a*, b_1, b_2, and b_3, sequentially, and eq. 15 is entered into eq. 15 of ref. 13, we find the wanted digonal (octahedrally oriented) spin orbital wave functions to be[15]

$$\gamma_{5(\substack{a\\b})}^{(7)}(t_{2g}) = \gamma_{5(\substack{a\\b})}^{D(1)}(t_{2g}) = \gamma_{7(\substack{a\\b})}(t_{2g}) = \frac{ie^{\pm \pi i/8}}{\sqrt{3}}\left\{a\zeta(\mp 1/2) \mp \sqrt{2}d\pi_{\pm}(\pm 1/2)\right\}$$

$$\gamma_{5(\substack{a\\b})}^{(8)}(t_{2g}) = \gamma_{5(\substack{a\\b})}^{D(2)}(t_{2g}) = \gamma_{8(\substack{a\\b})}(t_{2g}) = \frac{ie^{\pm \pi i/8}}{\sqrt{3}}\left\{\sqrt{2}a\zeta(\mp 1/2) \pm d\pi_{\pm}\zeta(\pm 1/2)\right\}$$

(14) The conversion of the spatial functions from the tetragonal $\{x', y', z'\}$ to the digonal $\{x, y, z\}$ representation is self-evident and needs no further comment. The same is not true for the conversion of the spin functions from the tetragonal $\zeta'(\pm 1/2)$ to the digonal $\zeta(\pm 1/2)$

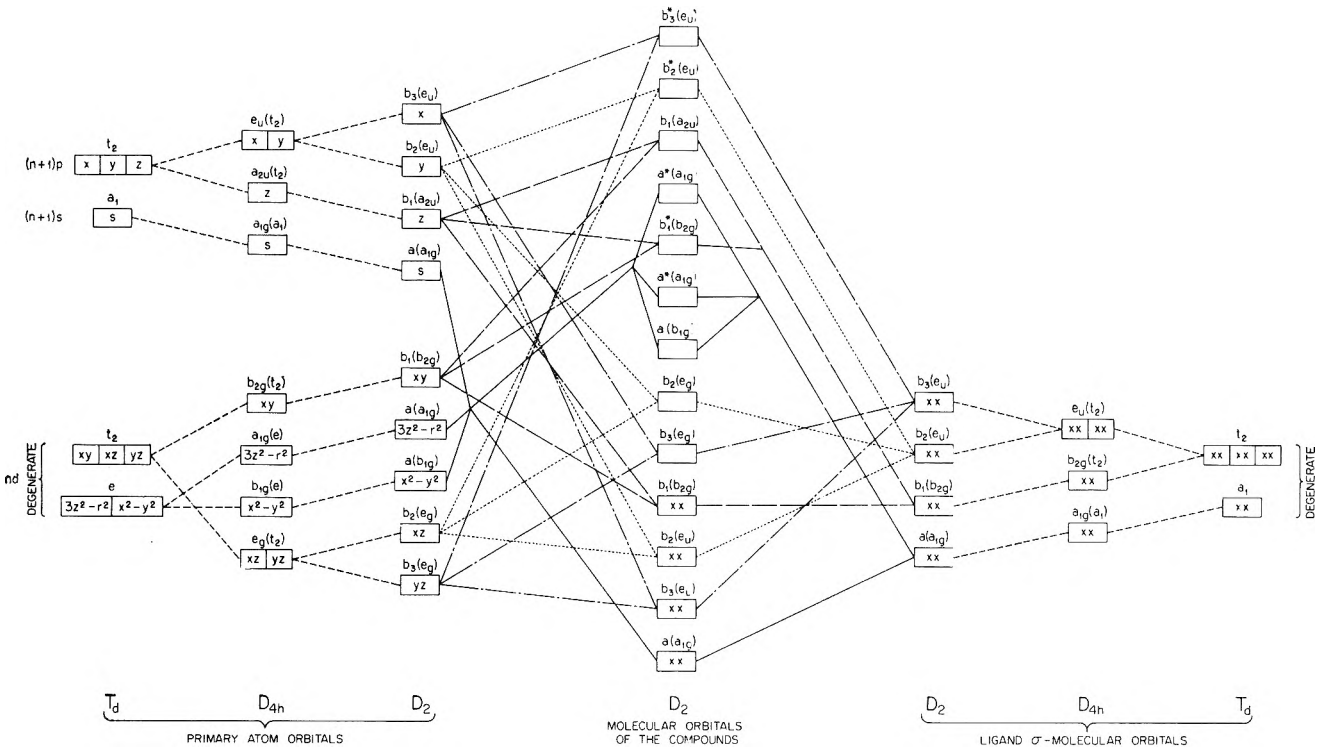

Figure 11. Correlational molecular orbital energy level diagram for a pterotactically four-coordinated (digonal dihedral) σ-bonded compound. The figure illustrates the confluence of the tetrahedrate, quadrate, and pterotactate diagrams. Level orders have been surmised as in Fig. 10.

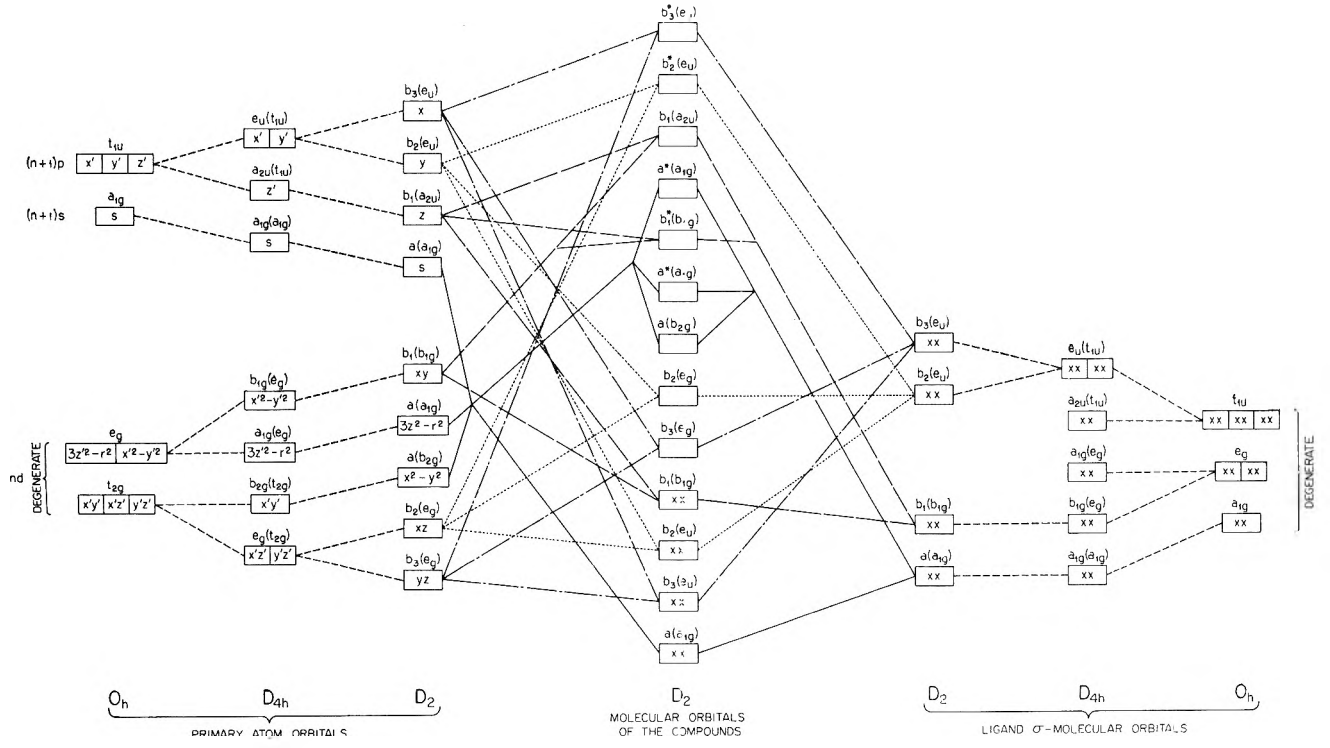

Figure 12. Correlational molecular orbital energy level diagram for a pterotactically four-coordinated (digonal dihedral) σ-bonded compound. The figure illustrates the confluence of the octahedrate, quadrate, and pterotactate diagrams. Level orders have been surmised as in Fig. 10.

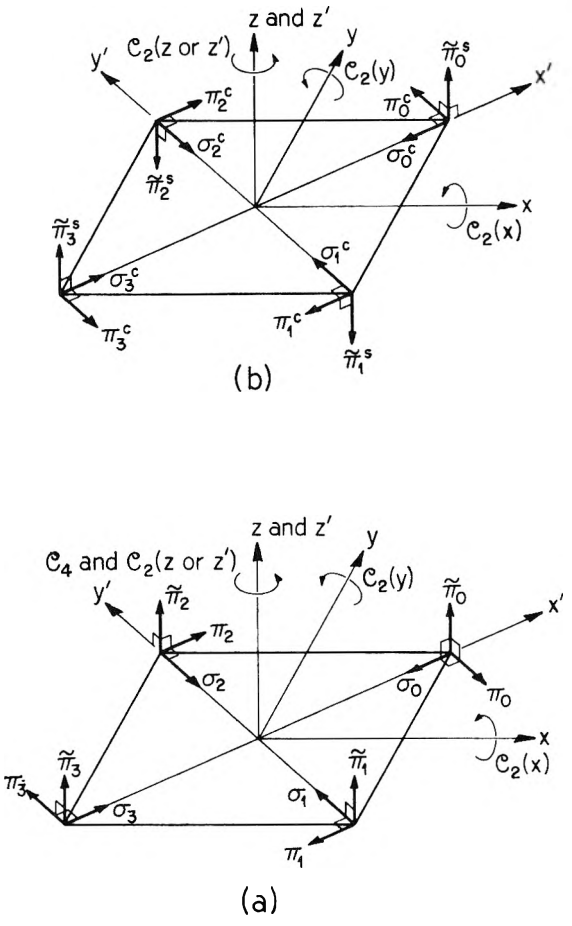

Figure 13. Picturization of the local atomic orbital rectilinear basis. Figure 13a specifies the right-handed quadrately symmetric basis, $\{\sigma_j, \pi_j, \bar{\pi}_j\}$ (j = 0, 1, 2, 3), and σ_j are as blocked in Table III and eq. 6 with α, ι equal zero and π_j and $\bar{\pi}_j$ are $-(2p_{y'})_{A_0}$, $-(2p_{x'})_{A_1}$, $(2p_{x'})_{A_2}$, $(2p_{y'})_{A_3}$, and $(2p_{z'})_{A_j}$, respectively, for j equal 0, 1, 2, 3 serially. Figure 13b specifies the related left-handed pterotactately symmetric basis, $\{\sigma_j^c, \pi_j^c, \bar{\pi}_j^s\}$ (j = 0, 1, 2, 3), with σ_j^c, π_j^c, and $\bar{\pi}_j^s$ as stamped in Table III and eq. 6.

representation, and some direction is required. Two methods of procedure may be followed. As each is differently instructive we outline both here. The first method invokes the invariance of physical points under arbitrary coordinate transformations, $\mathcal{P}$; that is, that $\mathcal{P}\vec{r}$ equals $\vec{r}$ and $\mathcal{P}\Upsilon$ equals Υ for any coordinate vector $\vec{r}$ in physical space or any spin (state) vector Υ in spin space. In physical space this invariance demand requires that the coordinates $\{x', y', z'\}$ or $\{x, y, z\}$ transform inversely ("contragradiently") to their basis vectors $\{\hat{i}', \hat{j}', \hat{k}'\}$ or $\{\hat{i}, \hat{j}, \hat{k}\}$, where $\vec{r} = x'\hat{i}' + y'\hat{j}' + z'\hat{k}' = x\hat{i} + y\hat{j} + z\hat{k}$; in spin space it exacts that the coordinates $\{c'(+1/2), c'(-1/2)\}$ or $\{c(+1/2), c(-1/2)\}$ transform inversely ("contragradiently") to their "basis vectors" $\{\zeta'(+1/2), \zeta'(-1/2)\}$ or $\{\zeta(+1/2), \zeta(-1/2)\}$, where $\Upsilon = c'(+1/2)\zeta'(+1/2) + c'(-1/2)\zeta'(-1/2) = c(+1/2)\zeta(+1/2) + c(-1/2)\zeta(-1/2)$. Hence, if the usual physical coordinate and spin coordinate ("spinor") transformations have matrix representations $\mathbf{A}^{-1}$ and $\mathbf{Q}^{-1}$, individually, then the physical coordinate basis vectors and the spin coordinate basis vectors have matrix representations $\mathbf{A}$ and $\mathbf{Q}$. Specifically, for the counterclockwise coordinate replacement transformation (rotation), $\mathcal{C}_8(z$ or $z')$, for which $\mathcal{C}_8(z$ or $z')\{x', y', z'\}$ equals $\{x, y, z\}$, we have $\mathcal{C}_8(z$ or $z')\zeta'(\pm 1/2)$ equals $\zeta(\pm 1/2)$, equals $e^{\pm \pi i/8}\zeta'(\pm 1/2)$ where $\zeta(\pm 1/2)$ are the spin basis vectors correspondent to the new physica coordinates $\{x, y, z\}$. [To derive the last equality, $\mathcal{C}_8(z$ or $z')\zeta'(\pm 1/2)$ equals $e^{\pm \pi i/8}\zeta'(\pm 1/2)$, from standard spin coordinate ("spinor") transformation tabulations, such as those of Goldstein,[11] extreme care must be taken to ensure that the tabulated general transformation and the utilized special transformation are of the same sense. As an instance, we here use counterclockwise coordinate *replacement* transformations, whereas Goldstein[11] employs counterclockwise coordinate *transplacement* ("goes into") transformations, and so our transformations are *inverse* to his. Thus, to use Goldstein's[11] tabulations with our conventions (which we have done), one must always take an inverse. This stipulation implies that for physical and spin coordinate transformations we use his $\mathbf{A}^{-1}$ and $\mathbf{Q}^{-1}$ matrix representations, and for physical and spin basis vector transformations we use his $\mathbf{A}$ and $\mathbf{Q}$ matrix representations. In particular, for the transformation $\mathcal{C}_8(z$ or $z')$ discussed above, we use Goldstein's[11] matrices $\mathbf{A}^{-1}$ and $\mathbf{Q}$ with Eulerian angles $(\phi_\ell, \theta_\ell, \psi_\ell)$ equal $(\pi/4, 0, 0)$ and obtain the physical coordinate and spin basis vector identities quoted earlier.] The second method invokes an analogy. One simply notes that as the counterclockwise replacement transformation (rotation), $\mathcal{C}_8(z$ or $z')$, supplants the orbital basis functions $\{d_{x'z'}, d_{y'z'}\}$ with $\{d_{xz}, d_{yz}\}$ that it must also supplant the spin basis functions $\{\zeta'(+1/2), \zeta'(-1/2)\}$ with $\{\zeta(+1/2), \zeta(-1/2)\}$, and as the usual[11] spinor transformation, $\mathbf{Q}$, correspondent to $\mathcal{C}_8(z$ or $z')$ supplants $\{\zeta'(+1/2), \zeta'(-1/2)\}$ with $\{e^{+\pi i/8}\zeta'(+1/2), e^{-\pi i/8}\zeta'(-1/2)\}$, we conclude that $\zeta(\pm 1/2)$ equals $e^{\pm \pi i/8}\zeta'(\pm 1/2)$ in agreement with method one. A third method based on the fixity of quantum mechanical expectation values (in this case on the numerical stability of the Pauli spin expectation value $\langle \sigma_x' \rangle$ upon basis change) also exists, but as it is detailed at length in the excellent book of D. Bohm ["Quantum Theory," Prentice-Hall, Inc., New York, N. Y., 1951], albeit in an entirely different context, we shall not describe it here.

(15) The spin orbital functions of eq. 16 have been digonally oriented such that

$$\mathcal{C}_2(z)\gamma_7\binom{a}{b} = \mp i\gamma_7\binom{a}{b};\quad \mathcal{C}_2(x)\gamma_7\binom{a}{b} = \mp e^{\mp \pi i/4}\gamma_7\binom{b}{a};\quad \gamma_5^D\binom{a}{b} = \gamma_7\binom{a}{b}$$

$$\mathcal{C}_2(z)\gamma_8\binom{a}{b} = \mp i\gamma_8\binom{a}{b};\quad \mathcal{C}_2(x)\gamma_8\binom{a}{b} = \mp e^{\mp \pi i/4}\gamma_8\binom{b}{a};\quad \gamma_5^D\binom{a}{b} = \gamma_8\binom{a}{b}$$

$$\mathcal{C}_2(z)\gamma_8\binom{c}{d} = \mp i\gamma_8\binom{c}{d};\quad \mathcal{C}_2(x)\gamma_8\binom{c}{d} = e^{\pm \pi i/4}\gamma_8\binom{d}{c};\quad \gamma_5^D\binom{a}{b} = \gamma_8\binom{a}{b}$$

in which the 180° rotations $\mathcal{C}_2(z)$, $\mathcal{C}_2(y)$, and $\mathcal{C}_2(x)$ of spin space are defined in accord with Goldstein[11] as $\mathcal{C}_2(z) = i\sigma_z$, $\mathcal{C}_2(y) = i\sigma_y$, $\mathcal{C}_2(x) = i\sigma_x$, where σ_z, σ_y, and σ_x are the Pauli spin matrices. This definition implies that $\mathcal{C}_2(z) = \mathcal{C}_2(y)\mathcal{C}_2(x)$, $\mathcal{C}_2(y) = \mathcal{C}_2(x)\mathcal{C}_2(z)$, $\mathcal{C}_2(x) = \mathcal{C}_2(z)\mathcal{C}_2(y)$, as usual, but that $\mathcal{C}_2(w)^{-1}$ equals $-\mathcal{C}_2(w)$ (w = z, y, z), in spin space [as $i\sigma_z = -\sigma_y\sigma_x = \sigma_x\sigma_y$, $i\sigma_y = -\sigma_x\sigma_z = \sigma_z\sigma_x$, $i\sigma_x = -\sigma_z\sigma_y = \sigma_y\sigma_z$, and $(i\sigma_w)^{-1}$ equals $-i\sigma_w$ (w = z, y, x)[11]].

The uncommon reverse relationship of $\mathcal{C}_2(w)$ in spin space may be reconciled with the familiar physical space relationship, $\mathcal{C}_2(w)^{-1}$ equals $\mathcal{C}_2(w)$ (w = z, y, x) by use of the 360° rotation, $\mathcal{C}_1(w)$, which in the absence of spin is normally held to be equivalent to the identity ("do nothing") rotation (operation), $\mathcal{I}$. In the presence of spin we equate the rotation $\mathcal{C}_1(w)$ with the Janus ("two faced") operation, $\mathcal{J}$, which multiplies a function by plus or minus one, dependent upon whether it is a physical or integral spin function or a half-integral spin function, respectively. Then, $\mathcal{C}_2(w)^{-1}$ equals $\mathcal{J}\mathcal{C}_2(w)$ equals $\mathcal{C}_2(w)\mathcal{J}$, and $\mathcal{J}^2$, which may be thought equivalent to the 720° rotation $\mathcal{C}_{1/2}(w)$ [recall that a counterclockwise rotation by the angle $2\pi/n$ is designated by $\mathcal{C}_n$], equals (in a mathematical sense) $\mathcal{I}$. The Janus operation, $\mathcal{J}$, being purely multiplicative (*i.e.*, diagonal in matrix terminology), is universally commutative, $\mathcal{J}\mathcal{O}$ equals $\mathcal{O}\mathcal{J}$ for any operation $\mathcal{O}$. Hark that because of the physical space ambiguity of $\mathcal{C}_2(w)$ and $\mathcal{C}_2(w)^{-1}$ one *cannot* construct a unique spin space matrix representation of $\mathcal{C}_2(w)$ from Eulerian angular specifications [*e.g.*, physically the Eulerian sets $(0, \pi, 0)$ and $(0, -\pi, 0)$ produce the same coordinate transformation $\{x, y, z\}$ replaced by $\{x, -y, -z\}$, but abstractly they produce inverse transformations $\mathcal{C}_2(x)$ and $\mathcal{C}_2(x)^{-1}$, separately]. Twofold rotations $\mathcal{C}_2(q)$, in spin space about arbitrary axes, q, are generated by the relation $\mathcal{C}_2(q) = i\sigma_q = i\vec{\sigma}\cdot\hat{q} = i\sigma_{x'}(\hat{i}\cdot\hat{q}) + i\sigma_{y'}(\hat{j}'\cdot\hat{q}) + i\sigma_{z'}(\hat{k}'\cdot\hat{q}) = i\sigma_x(\hat{i}\cdot\hat{q}) + i\sigma_y(\hat{j}\cdot\hat{q}) + i\sigma_z(\hat{k}\cdot\hat{q})$. As samples, $\mathcal{C}_2(x')\zeta'(\pm 1/2)$ equals $i\sigma_{x'}\zeta'(\pm 1/2)$ equals $i\zeta'(\mp 1/2)$, $\mathcal{C}_2(x)\zeta'(\pm 1/2)$ equals $((1/\sqrt{2})i\sigma_{x'} - (1/\sqrt{2})i\sigma_{y'})\zeta'(\pm 1/2)$ equals $\pm e^{\pm \pi i/4}\zeta'(\mp 1/2)$, $\mathcal{C}_2(x)\zeta(\pm 1/2)$ equals $i\sigma_x\zeta(\pm 1/2)$ equals $i\zeta(\mp 1/2)$, $\mathcal{C}_2(y')\zeta'(\pm 1/2)$ equals $i\sigma_{y'}\zeta'(\pm 1/2)$ equals $\mp\zeta'(\mp 1/2)$, $\mathcal{C}_2(y)\zeta'(\pm 1/2)$ equals $((1/\sqrt{2})i\sigma_{x'} + (1/\sqrt{2})i\sigma_{y'})\zeta'(\pm 1/2)$ equals $\mp e^{\mp \pi i/4}\zeta'(\mp 1/2)$, $\mathcal{C}_2(y)\zeta(\pm 1/2)$ equals $i\sigma_y\zeta(\pm 1/2)$ equals $\mp\zeta(\mp 1/2)$, $\mathcal{C}_2(z'$ or $z)\zeta'(\pm 1/2)$ equals $i\sigma_{z'}\zeta'(\pm 1/2)$ equals $\pm i\zeta'(\pm 1/2)$, $\mathcal{C}_2(z)\zeta(\pm 1/2)$ equals $i\sigma_z\zeta(\pm 1/2)$ equals $\pm i\zeta(\pm 1/2)$, and so on.

$$\gamma_{5(\substack{a\\b})}^{(8)\prime}(t_{2g}) = \gamma_{5(\substack{a\\b})}^{D(3)}(t_{2g}) = \gamma_{8(\substack{c\\d})}(t_{2g}) = e^{\pm \pi i/8} d\pi_{\mp}\zeta(\pm 1/2)$$

$$\gamma_{5(\substack{a\\b})}^{(8)}(e_g) = \gamma_{5(\substack{c\\d})}^{D(1)}(e_g) = \gamma_{8(\substack{a\\b})}(e_g) = \pm e^{\pm \pi i/8} b_1\zeta(\mp 1/2)$$

$$\gamma_{5(\substack{a\\b})}^{(8)\prime}(e_g) = \gamma_{5(\substack{a\\b})}^{D(2)}(e_g) = \gamma_{8(\substack{c\\d})}(e_g) = \pm e^{\pm \pi i/8} a^{\star}\zeta(\mp 1/2) \quad (16)$$

where $d\pi_{\pm}$ equals $\sqrt{1/2}(d_{xz} \pm id_{yz})$ equals $\sqrt{1/2}(b_2 \pm ib_3)$. The insertion of eq. 11 and its accompaniments, eq. 7 through 10, into eq. 16 gives the sought-for σ-bonded or σ,π-bonded digonal dihedral one-electron spin-orbital molecular orbitals. Figures 20a,b,c,d picture the conjunction of the two views, that with and without spin-orbit forces, in both octahedral and non-octahedral orientation, for the one- and nine-electron couple.

§3. The Optical Rotatory Power

3.1 *Matrix Elements.* The tally of the needful matrix elements is routine. The employment of eq. 7 through 11 and of Tables I through V produces the basic spinless one-electron molecular orbital matrix elements.

$$\left\langle b_2 \left| \frac{\vec{p}}{\vec{m}} \right| b_2 \right\rangle \equiv 0$$

$$\left\langle b_2 \left| \frac{\vec{p}}{\vec{m}} \right| b_3 \right\rangle = \hat{k} N_{b_2} N_{b_3} \begin{bmatrix} \rho_2 L[\Lambda_-^{(-)};\ d_{yz}] + \rho_3 L[d_{xz};\ \Lambda_-^{(+)}] + \rho_2\rho_3 L[\Lambda_-^{(-)};\ \Lambda_-^{(+)}] \\ -i\mu_B + \rho_2 M[\Lambda_-^{(-)};\ d_{yz}] + \rho_3 M[d_{xz};\ \Lambda_-^{(+)}] + \rho_2\rho_3 M[\Lambda_-^{(-)};\ \Lambda_-^{(+)}] \end{bmatrix}$$

$$\left\langle b_2 \left| \frac{\vec{p}}{\vec{m}} \right| a \right\rangle = \hat{j} N_{b_2} N_a \begin{bmatrix} \eta L[d_{xz};\ \Lambda_+^{(+)}] + \rho_2 L[\Lambda_-^{(-)};\ d_{x^2-y^2}] + \rho_2\eta L[\Lambda_-^{(-)};\ \Lambda_+^{(+)}] \\ -i\mu_B + \eta M[d_{xz};\ \Lambda_+^{(+)}] + \rho_2 M[\Lambda_-^{(-)};\ d_{x^2-y^2}] + \rho_2\eta M[\Lambda_-^{(-)};\ \Lambda_+^{(+)}] \end{bmatrix}$$

$$\left\langle b_2 \left| \frac{\vec{p}}{\vec{m}} \right| a^{\star} \right\rangle = \hat{j} N_{b_2} N_{a^{\star}} \begin{bmatrix} \eta^{\star} L[d_{xz};\ \Lambda_+^{(+)}] + \rho_2 L[\Lambda_-^{(-)};\ d_{3z^2-r^2}] + \rho_2\eta^{\star} L[\Lambda_-^{(-)};\ \Lambda_+^{(+)}] \\ i\sqrt{3}\mu_B + \eta^{\star} M[d_{xz};\ \Lambda_+^{(+)}] + \rho_2 M(\Lambda_-^{(-)};\ d_{3z^2-r^2}] + \rho_2\eta^{\star} M[\Lambda_-^{(-)};\ \Lambda_+^{(+)}] \end{bmatrix}$$

$$\left\langle b_2 \left| \frac{\vec{p}}{\vec{m}} \right| b_1 \right\rangle = \hat{i} N_{b_2} N_{b_1} \begin{bmatrix} \rho_1 L[d_{xz};\ \Lambda_+^{(-)}] + \rho_2 L[\Lambda_-^{(-)};\ d_{xy}] + \rho_2\rho_1 L[\Lambda_-^{(-)};\ \Lambda_+^{(-)}] \\ i\mu_B + \rho_1 M[d_{xz};\ \Lambda_+^{(-)}] + \rho_2 M[\Lambda_-^{(-)};\ d_{xy}] + \rho_2\rho_1 M[\Lambda_-^{(-)};\ \Lambda_+^{(-)}] \end{bmatrix}$$

$$\left\langle b_3 \left| \frac{\vec{p}}{\vec{m}} \right| b_3 \right\rangle \equiv 0$$

$$\left\langle b_3 \left| \frac{\vec{p}}{\vec{m}} \right| a \right\rangle = \hat{i} N_{b_3} N_a \begin{bmatrix} \eta L[d_{yz};\ \Lambda_+^{(+)}] + \rho_3 L[\Lambda_-^{(+)};\ d_{x^2-y^2}] + \rho_3\eta L[\Lambda_-^{(+)};\ \Lambda_+^{(+)}] \\ -i\mu_B + \eta M[d_{yz};\ \Lambda_+^{(+)}] + \rho_3 M[\Lambda_-^{(+)};\ d_{x^2-y^2}] + \rho_3\eta M[\Lambda_-^{(+)};\ \Lambda_+^{(+)}] \end{bmatrix}$$

$$\left\langle b_3 \left| \frac{\vec{p}}{\vec{m}} \right| a^{\star} \right\rangle = \hat{i} N_{b_3} N_{a^{\star}} \begin{bmatrix} \eta^{\star} L[d_{yz};\ \Lambda_+^{(+)}] + \rho_3 L[\Lambda_-^{(+)};\ d_{3z^2-r^2}] + \rho_3\eta^{\star} L[\Lambda_-^{(+)};\ \Lambda_+^{(+)}] \\ -i\sqrt{3}\mu_B + \eta^{\star} M[d_{yz};\ \Lambda_+^{(+)}] + \rho_3 M[\Lambda_-^{(+)};\ d_{3z^2-r^2}] + \rho_3\eta^{\star} M[\Lambda_-^{(+)};\ \Lambda_+^{(+)}] \end{bmatrix}$$

$$\left\langle b_3 \left| \frac{\vec{p}}{\vec{m}} \right| b_1 \right\rangle = \hat{j} N_{b_3} N_{b_1} \begin{bmatrix} \rho_1 L[d_{yz};\ \Lambda_+^{(-)}] + \rho_3 L[\Lambda_-^{(+)};\ d_{xy}] + \rho_3\rho_1 L[\Lambda_-^{(+)};\ \Lambda_+^{(-)}] \\ -i\mu_B + \rho_1 M[d_{yz};\ \Lambda_+^{(-)}] + \rho_3 M[\Lambda_-^{(+)};\ d_{xy}] + \rho_3\rho_1 M[\Lambda_-^{(+)};\ \Lambda_+^{(-)}] \end{bmatrix}$$

$$\left\langle a \left| \frac{\vec{p}}{\vec{m}} \right| a \right\rangle \equiv 0$$

$$\left\langle a \left| \frac{\vec{p}}{\vec{m}} \right| a^{\star} \right\rangle \equiv 0$$

$$\left\langle a \left| \frac{\vec{p}}{\vec{m}} \right| b_1 \right\rangle = \hat{k} N_a N_{b_1} \begin{bmatrix} \eta L[\Lambda_+^{(+)};\ d_{xy}] + \rho_1 L[d_{x^2-y^2};\ \Lambda_+^{(-)}] + \eta\rho_1 L[\Lambda_+^{(+)};\ \Lambda_+^{(-)}] \\ -i2\mu_B + \eta M[\Lambda_+^{(+)};\ d_{xy}] + \rho_1 M[d_{x^2-y^2};\ \Lambda_+^{(-)}] + \eta\rho_1 M[\Lambda_+^{(+)};\ \Lambda_+^{(-)}] \end{bmatrix}$$

$$\left\langle a^{\star} \left| \frac{\vec{p}}{\vec{m}} \right| a^{\star} \right\rangle \equiv 0$$

$$\left\langle a^{\star} \left| \frac{\vec{p}}{\vec{m}} \right| b_1 \right\rangle = \hat{k} N_{a^{\star}} N_{b_1} \begin{bmatrix} \eta^{\star} L[\Lambda_+^{(+)};\ d_{xy}] + \rho_1 L[d_{3z^2-r^2};\ \Lambda_+^{(-)}] + \eta^{\star}\rho_1 L[\Lambda_+^{(+)};\ \Lambda_+^{(-)}] \\ \eta^{\star} M[\Lambda_+^{(+)};\ d_{xy}] + \rho_1 M[d_{3z^2-r^2};\ \Lambda_+^{(-)}] + \eta^{\star}\rho_1 M[\Lambda_+^{(+)};\ \Lambda_+^{(-)}] \end{bmatrix}$$

$$\left\langle b_1 \left| \frac{\vec{p}}{\vec{m}} \right| b_1 \right\rangle \equiv 0 \quad (17)$$

where the integrals $L[\chi_1;\ \chi_2]$ and $M[\chi_1;\ \chi_2]$ are as defined in the Appendix, section XII, §5.6, eq. A-14 through 17.

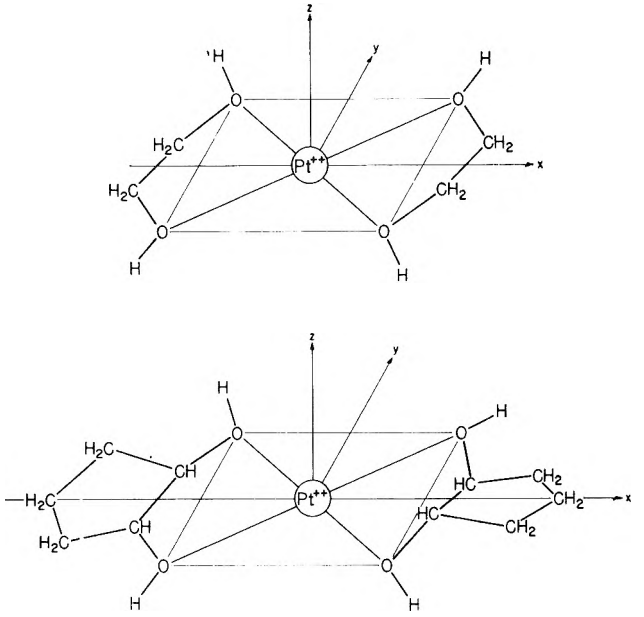

Figure 14. The idealized complanately bonded right-angled $\Delta(\lambda,\lambda)$ and $\Lambda(\delta,\delta)$ geometry of the bis(ethylene glycol)-platinum(II) and the bis(cyclopentane glycol)platinum(II) cations, individually. Their tetrahedral affiliation is as in Fig. 3 and 4, with appropriate label change. Their adjacent (ligand) carbon stations are as in Fig. 1 and 2.

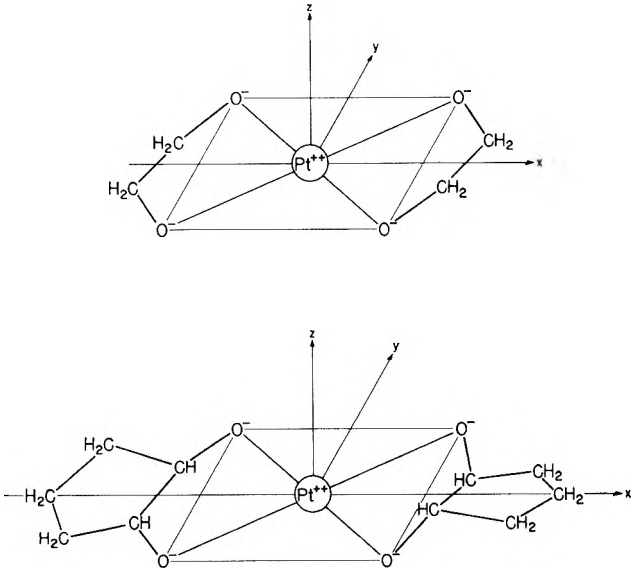

Figure 15. The idealized complanately bonded right-angled $\Delta(\lambda,\lambda)$ and $\Lambda(\delta,\delta)$ geometry of the bis(ethylene glycolate)-platinum(II) and the bis(cyclopentane glycolate)platinum(II) anions, individually. Their tetrahedral affiliation is as in Fig. 3 and 4, with appropriate label change. Their adjacent (ligand) carbon stations are as in Fig. 1 and 2.

The supplementation of eq. 17 with the magnitudes

$$\langle\zeta(\pm 1/2)|2\vec{S}|\zeta(\pm 1/2)\rangle = \pm\mu_B\hat{k}$$

$$\langle\zeta(\pm 1/2)|2\vec{S}|\zeta(\mp 1/2)\rangle = \mu_B(\hat{i} \mp i\hat{j}) \quad (18)$$

permits the compilation of the basic one-electron molecular spin-orbital matrix terms. The empanelment of these terms is greatly eased by the abridgement

$$\begin{aligned}
\langle b_2|\vec{p}|b_3\rangle &= \bar{l}_{0a}\hat{k},\ \langle b_2|\vec{m}|b_3\rangle = -im_{0a}\hat{k}\\
\langle b_2|\vec{p}|a\rangle &= \bar{l}_{0b}\hat{j},\ \langle b_2|\vec{m}|a\rangle = -im_{0b}\hat{j}\\
\langle b_3|\vec{p}|a\rangle &= \bar{l}_{0c}\hat{i},\ \langle b_3|\vec{m}|a\rangle = -im_{0c}\hat{i}\\
\langle b_2|\vec{p}|a^\star\rangle &= l_{1a}\hat{j},\ \langle b_2|\vec{m}|a^\star\rangle = -im_{1a}\hat{j}\\
\langle b_2|\vec{p}|b_1\rangle &= l_{1b}\hat{i},\ \langle b_2|\vec{m}|b_1\rangle = -im_{1b}\hat{i}\\
\langle b_3|\vec{p}|a^\star\rangle &= l_{2a}\hat{i},\ \langle b_3|\vec{m}|a^\star\rangle = -im_{2a}\hat{i}\\
\langle b_3|\vec{p}|b_1\rangle &= l_{2b}\hat{j},\ \langle b_3|\vec{m}|b_1\rangle = -im_{2b}\hat{j}\\
\langle a|\vec{p}|a^\star\rangle &= l_{0a}\hat{o},\ \langle a|\vec{m}|a^\star\rangle = -im_{0a}\hat{o}\\
\langle a|\vec{p}|b_1\rangle &= l_{0b}\hat{k},\ \langle a|\vec{m}|b_1\rangle = -im_{0b}\hat{k}\\
\langle a^\star|\vec{p}|b_1\rangle &= \bar{l}_0\hat{k},\ \langle a^\star|\vec{m}|b_1\rangle = -i_0\bar{m}\hat{k} \quad (19)
\end{aligned}$$

where l betokens r or $-ip$ dependent upon the representation $e\vec{r}$ or $(\hbar/i)\vec{\nabla}$, respectively, used for the electric dipole operator, $\vec{p}$, and where $\hat{o}$ is the "unit" null vector. In this garb the spin-orbital matrix constituents become[16] as in eq. 20.

(16) The connectiveness of the $\gamma_{5\binom{a}{b}}$ matrix members is a direct issuance of their momentum reversal, $\mathcal{K}$, and their counterclockwise rotational, $\mathcal{C}_2(x)$, symmetry [for the definition of the momentum reversal operator, $\mathcal{K}$, read footnote 25 of ref. 6, and for that of $\mathcal{C}_2(x)$ confer footnote 15 of this paper]. As $\mathcal{K}\gamma_{5\binom{a}{b}}$ equals $\pm\gamma_{5\binom{b}{a}}$ for all $\gamma_{5\binom{a}{b}}$ recorded in eq. 16, and as $\mathcal{K}\vec{p}$ equals $\pm\vec{p}$ dependent upon the representation used for $\vec{p}$, and $\mathcal{K}\vec{m}$ equals $-\vec{m}$, we deduce

$$\left\langle \gamma_{5a}\left|\begin{matrix}\vec{p}\\ \vec{m}\end{matrix}\right|\gamma_{5a}\right\rangle = \begin{bmatrix}\pm\\ -\end{bmatrix}\left\langle \gamma_{5b}\left|\begin{matrix}\vec{p}\\ \vec{m}\end{matrix}\right|\gamma_{5b}\right\rangle^*$$

$$\left\langle \gamma_{5a}\left|\begin{matrix}\vec{p}\\ \vec{m}\end{matrix}\right|\gamma_{5b}\right\rangle = \begin{bmatrix}\mp\\ +\end{bmatrix}\left\langle \gamma_{5b}\left|\begin{matrix}\vec{p}\\ \vec{m}\end{matrix}\right|\gamma_{5a}\right\rangle^*$$

where the asterisk * again [recall footnote 7] indicates complex conjugation. Similarly, from the $\mathcal{C}_2(x)\gamma_{5\binom{a}{b}}$ relations of footnote 15, we secure for any true vector or pseudo vector $\vec{v}$ ($\vec{v} = \vec{p}$ or m)

$$\langle\gamma_{5a}^{(7,8)\text{ or }(8)'}|v_x, v_y, v_z|\gamma_{5a}^{(7,8)\text{ or }(8)'}\rangle = \langle\gamma_{5b}^{(7,8)\text{ or }(8)'}|v_x, -v_y, -v_z|\gamma_{5b}^{(7,8)\text{ or }(8)'}\rangle$$

$$\langle\gamma_{5a}^{(7,8)\text{ or }(8)'}|v_x, v_y, v_z|\gamma_{5a}^{(8)'\text{ or }(7,8)}\rangle = -\langle\gamma_{5b}^{(7,8)\text{ or }(8)'}|v_x, -v_y, -v_z|\gamma_{5b}^{(8)'\text{ or }(7,8)}\rangle$$

$$\langle\gamma_{5a}^{(7,8)\text{ or }(8)'}|v_x, v_y, v_z|\gamma_{5b}^{(7,8)\text{ or }(8)'}\rangle = -i\langle\gamma_{5b}^{(7,8)\text{ or }(8)'}|v_x, -v_y, -v_z|\gamma_{5a}^{(7,8)\text{ or }(8)'}\rangle$$

$$\langle\gamma_{5a}^{(7,8)\text{ or }(8)'}|v_x, v_y, v_z|\gamma_{5b}^{(8)'\text{ or }(7,8)}\rangle = i\langle\gamma_{5b}^{(7,8)\text{ or }(8)'}|v_x, -v_y, -v_z|\gamma_{5a}^{(8)'\text{ or }(7,8)}\rangle$$

regardless of the origin, t_{2g} or e_g, of the spin-orbitals.

These kinships plus those derivable from matrix Hermiticity and $\mathcal{C}_2(z)$ symmetry then govern the form of eq. 20 [for example, the joint usage of the momentum reversal, $\mathcal{K}$, and the twofold rotational,

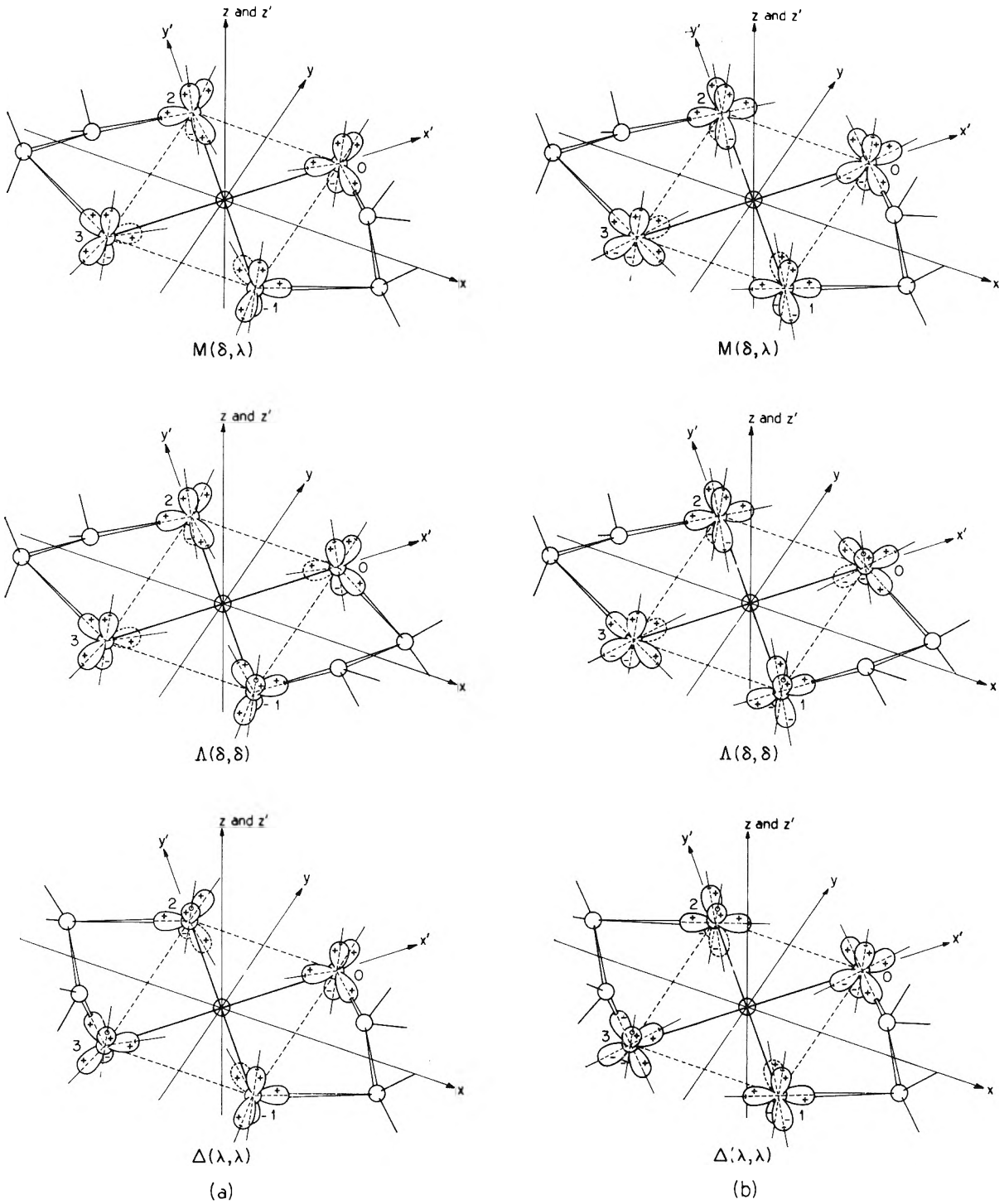

Figures 16a and 16b. The localized ligand orbital spatial disposition for the idealized complanately bonded right-angled conformations of the bis(ethylene glycol or glycolate) platinum(II) cation or anion. Figure 16a displays the spatial disposition under the premise of isosceles hybridization and Fig. 16b under the premise of digonal hybridization. Figure 7 suitably modified shows it under tetrahedral hybridization [read division C, section VIII for the precise sense of the word hybridization used here]. The actual disposition is presumably intermediate between these extreme types.

$C_2(x)$, connections aloft and a segregation of the individual component matrix terms into real and imaginary parts quickly shows that $\langle v_x \rangle_{aa' \text{ or } bb'}$ and $\langle v_{y,z} \rangle_{aa \text{ or } bb}$ are real, $\langle v_z \rangle_{aa \text{ or } bb}$ and $\langle v_{y,z} \rangle_{aa' \text{ or } bb'}$ are pure imaginary, and $e^{\pi i/4}\langle v_x \rangle_{ab \text{ or } a'b'}$, $e^{\pi i/4}\langle v_{y,z} \rangle_{ab' \text{ or } a'b}$ and $e^{-\pi i/4}\langle v_x \rangle_{ab' \text{ or } a'b}$, $e^{-\pi i/4}\langle v_{y,z} \rangle_{ab \text{ or } a'b'}$ are real for $\vec{v}$ pure imaginary, and *vice versa* for $\vec{v}$ real; and the $C_2(z)$ functional invariance of footnote 15 implies that $\langle v_{x,y} \rangle_{aa,aa',bb,bb'}$ and $\langle v_z \rangle_{ab,ab',a'b',a'b}$ are zero, and hence that $\langle \vec{v} \rangle_{aa,aa',bb,bb'}$ is parallel to the $\hat{k}$ axis and $\langle \vec{v} \rangle_{ab,ab',a'b',a'b}$ is perpendicular to it for any $\gamma_{S\binom{a}{b}}^{(7,8)}$ or $\gamma_{S\binom{a}{b}}^{(8)}$, spin molecular orbital, regardless of source, t_{2g} or e_g.]

$$\left\langle \gamma_{5\binom{a}{b}}^{(8)\prime}(t_{2g}) \left| \begin{matrix}\vec{p}\\ \vec{m}\end{matrix} \right| \gamma_{5\binom{a}{b}}^{(7)}(t_{2g}) \right\rangle = \hat{k}\sqrt{2/3}\begin{bmatrix} \Re e\bar{l}_{0a} \\ 0 \end{bmatrix}$$

$$\left\langle \gamma_{5\binom{a}{b}}^{(8)\prime}(t_{2g}) \left| \begin{matrix}\vec{p}\\ \vec{m}\end{matrix} \right| \gamma_{5\binom{b}{a}}^{(7)}(t_{2g}) \right\rangle = \frac{e^{\pm \pi i/4}}{\sqrt{6}}\begin{bmatrix} i(\bar{l}_{0c}\hat{i} \pm i\bar{l}_{0b}\hat{j}) \\ (\bar{m}_{0c} + 2\mu_B)\hat{i} \mp i(\bar{m}_{0b} + 2\mu_B)\hat{j} \end{bmatrix}$$

$$\left\langle \gamma_{5\binom{a}{b}}^{(8)\prime}(t_{2g}) \left| \begin{matrix}\vec{p}\\ \vec{m}\end{matrix} \right| \gamma_{5\binom{a}{b}}^{(8)}(t_{2g}) \right\rangle = -\hat{k}\sqrt{1/3}\begin{bmatrix} \Re e\bar{l}_{0a} \\ 0 \end{bmatrix}$$

$$\left\langle \gamma_{5\binom{a}{b}}^{(8)\prime}(t_{2g}) \left| \begin{matrix}\vec{p}\\ \vec{m}\end{matrix} \right| \gamma_{5\binom{b}{a}}^{(8)}(t_{2g}) \right\rangle = \frac{e^{\pm \pi i/4}}{\sqrt{3}}\begin{bmatrix} i(\bar{l}_{0c}\hat{i} \mp i\bar{l}_{0b}\hat{j}) \\ (\bar{m}_{0c} - \mu_B)\hat{i} \mp i(\bar{m}_{0b} - \mu_B)\hat{j} \end{bmatrix}$$

$$\left\langle \gamma_{5\binom{a}{b}}^{(7)}(t_{2g}) \left| \begin{matrix}\vec{p}\\ \vec{m}\end{matrix} \right| \gamma_{5\binom{a}{b}}^{(8)}(t_{2g}) \right\rangle = \pm\hat{k}\frac{\sqrt{2}}{3}\begin{bmatrix} \Im m\bar{l}_{0a} \\ -(\bar{m}_{0a} + 2\mu_B) \end{bmatrix}$$

$$\left\langle \gamma_{5\binom{a}{b}}^{(7)}(t_{2g}) \left| \begin{matrix}\vec{p}\\ \vec{m}\end{matrix} \right| \gamma_{5\binom{b}{a}}^{(8)}(t_{2g}) \right\rangle = \frac{e^{\mp \pi i/4}}{3\sqrt{2}}\begin{bmatrix} i((\bar{l}_{0c} + 2\Re e\bar{l}_{0c})\hat{i} \pm i(\bar{l}_{0b} + 2\Re e\bar{l}_{0b})\hat{j}) \\ (\bar{m}_{0c} + 2\mu_B)\hat{i} \pm i(\bar{m}_{0b} + 2\mu_B)\hat{j} \end{bmatrix}$$

$$\left\langle \gamma_{5\binom{a}{b}}^{(8)\prime}(t_{2g}) \left| \begin{matrix}\vec{p}\\ \vec{m}\end{matrix} \right| \gamma_{5\binom{a}{b}}^{(8)\prime}(e_g) \right\rangle = 0$$

$$\left\langle \gamma_{5\binom{a}{b}}^{(8)\prime}(t_{2g}) \left| \begin{matrix}\vec{p}\\ \vec{m}\end{matrix} \right| \gamma_{5\binom{b}{a}}^{(8)\prime}(e_g) \right\rangle = \mp\frac{e^{\pm \pi i/4}}{\sqrt{2}}\begin{bmatrix} l_{2a}\hat{i} \mp il_{1a}\hat{j} \\ -i(m_{2a}\hat{i} \mp im_{1a}\hat{j}) \end{bmatrix}$$

$$\left\langle \gamma_{5\binom{a}{b}}^{(8)\prime}(t_{2g}) \left| \begin{matrix}\vec{p}\\ \vec{m}\end{matrix} \right| \gamma_{5\binom{a}{b}}^{(8)}(e_g) \right\rangle = 0$$

$$\left\langle \gamma_{5\binom{a}{b}}^{(8)\prime}(t_{2g}) \left| \begin{matrix}\vec{p}\\ \vec{m}\end{matrix} \right| \gamma_{5\binom{b}{a}}^{(8)}(e_g) \right\rangle = \mp\frac{e^{\mp \pi i/4}}{\sqrt{2}}\begin{bmatrix} l_{1b}\hat{i} \pm il_{2b}\hat{j} \\ -i(m_{1b}\hat{i} \pm im_{2b}\hat{j}) \end{bmatrix}$$

$$\left\langle \gamma_{5\binom{a}{b}}^{(7)}(t_{2g}) \left| \begin{matrix}\vec{p}\\ \vec{m}\end{matrix} \right| \gamma_{5\binom{a}{b}}^{(8)\prime}(e_g) \right\rangle = 0$$

$$\left\langle \gamma_{5\binom{a}{b}}^{(7)}(t_{2g}) \left| \begin{matrix}\vec{p}\\ \vec{m}\end{matrix} \right| \gamma_{5\binom{b}{a}}^{(8)\prime}(e_g) \right\rangle = \mp\frac{e^{\mp \pi i/4}}{\sqrt{3}}\begin{bmatrix} l_{2a}\hat{i} \pm il_{1a}\hat{j} \\ -i(m_{2a}\hat{i} \pm im_{1a}\hat{j}) \end{bmatrix}$$

$$\left\langle \gamma_{5\binom{a}{b}}^{(7)}(t_{2g}) \left| \begin{matrix}\vec{p}\\ \vec{m}\end{matrix} \right| \gamma_{5\binom{a}{b}}^{(8)}(e_g) \right\rangle = \mp\hat{k}\sqrt{1/3}\begin{bmatrix} il_{0b} \\ m_{0b} \end{bmatrix}$$

$$\left\langle \gamma_{5\binom{a}{b}}^{(7)}(t_{2g}) \left| \begin{matrix}\vec{p}\\ \vec{m}\end{matrix} \right| \gamma_{5\binom{b}{a}}^{(8)}(e_g) \right\rangle = \mp\frac{e^{\pm \pi i/4}}{\sqrt{3}}\begin{bmatrix} l_{1b}\hat{i} \mp il_{2b}\hat{j} \\ -i(m_{1b}\hat{i} \mp im_{2b}\hat{j}) \end{bmatrix}$$

$$\left\langle \gamma_{5\binom{a}{b}}^{(8)}(t_{2g}) \left| \begin{matrix}\vec{p}\\ \vec{m}\end{matrix} \right| \gamma_{5\binom{a}{b}}^{(8)\prime}(e_g) \right\rangle = 0$$

$$\left\langle \gamma_{5\binom{a}{b}}^{(8)}(t_{2g}) \left| \begin{matrix}\vec{p}\\ \vec{m}\end{matrix} \right| \gamma_{5\binom{b}{a}}^{(8)\prime}(e_g) \right\rangle = \pm\frac{e^{\mp \pi i/4}}{\sqrt{6}}\begin{bmatrix} l_{2a}\hat{i} \pm il_{1a}\hat{j} \\ -i(m_{2a}\hat{i} \pm im_{1a}\hat{j}) \end{bmatrix}$$

$$\left\langle \gamma_{5\binom{a}{b}}^{(8)}(t_{2g}) \left| \begin{matrix}\vec{p}\\ \vec{m}\end{matrix} \right| \gamma_{5\binom{a}{b}}^{(8)}(e_g) \right\rangle = \mp\hat{k}\sqrt{2/3}\begin{bmatrix} il_{0b} \\ m_{0b} \end{bmatrix}$$

$$\left\langle \gamma_{5\binom{a}{b}}^{(8)}(t_{2g}) \left| \begin{matrix}\vec{p}\\ \vec{m}\end{matrix} \right| \gamma_{5\binom{b}{a}}^{(8)}(e_g) \right\rangle = \pm\frac{e^{\pm \pi i/4}}{\sqrt{6}}\begin{bmatrix} l_{1b}\hat{i} \mp il_{2b}\hat{j} \\ -i(m_{1b}\hat{i} \mp im_{2b}\hat{j}) \end{bmatrix}$$

$$\left\langle \gamma_{5(\substack{a\\b})}^{(8)\prime}(e_g) \left| \begin{matrix} \vec{p} \\ \vec{m} \end{matrix} \right| \gamma_{5(\substack{a\\b})}^{(8)\prime}(e_g) \right\rangle = \mp \hat{k} \begin{bmatrix} 0 \\ \mu_B \end{bmatrix}$$

$$\left\langle \gamma_{5(\substack{a\\b})}^{(8)\prime}(e_g) \left| \begin{matrix} \vec{p} \\ \vec{m} \end{matrix} \right| \gamma_{5(\substack{b\\a})}^{(8)\prime}(e_g) \right\rangle = -e^{\mp \pi i/4} \begin{bmatrix} 0 \\ \mu_B(\hat{i} \pm i\hat{j}) \end{bmatrix}$$

$$\left\langle \gamma_{5(\substack{a\\b})}^{(8)\prime}(e_g) \left| \begin{matrix} \vec{p} \\ \vec{m} \end{matrix} \right| \gamma_{5(\substack{a\\b})}^{(8)}(e_g) \right\rangle = \hat{k} \begin{bmatrix} \bar{\bar{l}}_0 \\ -i\bar{\bar{m}}_0 \end{bmatrix}$$

$$\left\langle \gamma_{5(\substack{a\\b})}^{(8)\prime}(e_g) \left| \begin{matrix} \vec{p} \\ \vec{m} \end{matrix} \right| \gamma_{5(\substack{b\\a})}^{(8)}(e_g) \right\rangle = 0$$

$$\left\langle \gamma_{5(\substack{a\\b})}^{(8)}(e_g) \left| \begin{matrix} \vec{p} \\ \vec{m} \end{matrix} \right| \gamma_{5(\substack{a\\b})}^{(8)}(e_g) \right\rangle = \mp \hat{k} \begin{bmatrix} 0 \\ \mu_B \end{bmatrix}$$

$$\left\langle \gamma_{5(\substack{a\\b})}^{(8)}(e_g) \left| \begin{matrix} \vec{p} \\ \vec{m} \end{matrix} \right| \gamma_{5(\substack{b\\a})}^{(8)}(e_g) \right\rangle = -e^{\mp \pi i/4} \begin{bmatrix} 0 \\ \mu_B(\hat{i} \pm i\hat{j}) \end{bmatrix}$$

$$\left\langle \gamma_{5(\substack{a\\b})}^{(8)\prime}(t_{2g}) \left| \begin{matrix} \vec{p} \\ \vec{m} \end{matrix} \right| \gamma_{5(\substack{a\\b})}^{(8)\prime}(t_{2g}) \right\rangle = \pm \hat{k} \begin{bmatrix} \Im m\bar{l}_{0a} \\ -(\bar{m}_{0a} - \mu_B) \end{bmatrix}$$

$$\left\langle \gamma_{5(\substack{a\\b})}^{(8)\prime}(t_{2g}) \left| \begin{matrix} \vec{p} \\ \vec{m} \end{matrix} \right| \gamma_{5(\substack{b\\a})}^{(8)\prime}(t_{2g}) \right\rangle = 0$$

$$\left\langle \gamma_{5(\substack{a\\b})}^{(7)}(t_{2g}) \left| \begin{matrix} \vec{p} \\ \vec{m} \end{matrix} \right| \gamma_{5(\substack{a\\b})}^{(7)}(t_{2g}) \right\rangle = \mp 1/3 \hat{k} \begin{bmatrix} 2\Im m\bar{l}_{0a} \\ -(2\bar{m}_{0a} + \mu_B) \end{bmatrix}$$

$$\left\langle \gamma_{5(\substack{a\\b})}^{(7)}(t_{2g}) \left| \begin{matrix} \vec{p} \\ \vec{m} \end{matrix} \right| \gamma_{5(\substack{b\\a})}^{(7)}(t_{2g}) \right\rangle = \frac{e^{\mp \pi i/4}}{3} \begin{bmatrix} -2(\Im m\bar{l}_{0c}\hat{i} \pm i\Im m\bar{l}_{0b}\hat{j}) \\ (2\bar{m}_{0c} + \mu_B)\hat{i} \pm i(2\bar{m}_{0b} + \mu_B)\hat{j} \end{bmatrix}$$

$$\left\langle \gamma_{5(\substack{a\\b})}^{(8)}(t_{2g}) \left| \begin{matrix} \vec{p} \\ \vec{m} \end{matrix} \right| \gamma_{5(\substack{a\\b})}^{(8)}(t_{2g}) \right\rangle = \mp 1/3 \hat{k} \begin{bmatrix} \Im m\bar{l}_{0a} \\ -(\bar{m}_{0a} - \mu_B) \end{bmatrix}$$

$$\left\langle \gamma_{5(\substack{a\\b})}^{(8)}(t_{2g}) \left| \begin{matrix} \vec{p} \\ \vec{m} \end{matrix} \right| \gamma_{5(\substack{b\\a})}^{(8)}(t_{2g}) \right\rangle = \frac{2e^{\mp \pi i/4}}{3} \begin{bmatrix} \Im m\bar{l}_{0c}\hat{i} \pm i\Im m\bar{l}_{0b}\hat{j} \\ -((\bar{m}_{0c} - \mu_B)\hat{i} \pm i(\bar{m}_{0b} - \mu_B)\hat{j}) \end{bmatrix} \tag{20}$$

It is to be particularly heeded that the magnetic dipole transition moments which are posted as simple multiples of μ_B in eq. 20 are born of spin alone.[17]

3.2 *Rotational and Spectral Strengths.* The usual electronic dipole length rotational and spectral strengths

$$\begin{aligned} \mathcal{R}_{ab} &= \Im m\left\{\left\langle a\left|\sum_j e\vec{r}_j\right|b\right\rangle \cdot \left\langle b\left|\sum_j \vec{m}_j\right|a\right\rangle\right\} \\ \mathcal{S}_{ab} &= \left\langle a\left|\sum_j e\vec{r}_j\right|b\right\rangle \cdot \left\langle b\left|\sum_j e\vec{r}_j\right|a\right\rangle = \left|\left\langle a\left|\sum_j e\vec{r}_j\right|b\right\rangle\right|^2 \\ \mathfrak{M}_{ab} &= \left\langle a\left|\sum_j \vec{m}_j\right|b\right\rangle \cdot \left\langle b\left|\sum_j \vec{m}_j\right|a\right\rangle = \left|\left\langle a\left|\sum_j \vec{m}_j\right|b\right\rangle\right|^2 \end{aligned} \tag{21}$$

and the less usual electronic dipole velocity rotational and spectral strengths

$$\mathcal{P}_{ab} = \Re e\left\{\left\langle a\left|\sum_j \frac{\hbar}{i}\vec{\nabla}_j\right|b\right\rangle \cdot \left\langle b\left|\sum_j \vec{m}_j\right|a\right\rangle\right\}$$

$$\mathcal{O}_{ab} = \left\langle a\left|\sum_j \frac{\hbar}{i}\vec{\nabla}_j\right|b\right\rangle \cdot \left\langle b\left|\sum_j \frac{\hbar}{i}\vec{\nabla}_j\right|a\right\rangle = \left|\left\langle a\left|\sum_j \frac{\hbar}{i}\vec{\nabla}_j\right|b\right\rangle\right|^2 \tag{22}$$

where for exact wave functions [$\mathcal{P}$ may be thought of as short for pirouettal or pirouettory and $\mathcal{O}$ for optical; E_a and E_b are the energies of the states a and b and m is the mass of the electron]

(17) It is no contradiction of Kramers' theorem for the matrix elements $\langle \gamma_{5(\substack{a\\b})}|\vec{p}\ \gamma_{5(\substack{a\\b})}\rangle$ and $\langle \gamma_{5(\substack{a\\b})}|\vec{p}|\gamma_{5(\substack{b\\a})}\rangle$ not to vanish when $\vec{p}$ has the representation $(\hbar/i)\vec{\nabla}$, as $(\hbar/i)\vec{\nabla}$ is not an operator for an electric perturbation. [*Cf.* the remarks of footnote 26 of ref. 6. The momentum reversal and group theoretical arguments of that footnote must be modified when $\vec{p}$ equals $(\hbar/i)\vec{\nabla}$, as in this event the momentum reversal, group theoretical, and complex conjugational properties of $\vec{p}$ and $\vec{m}$ become indistinguishable.]

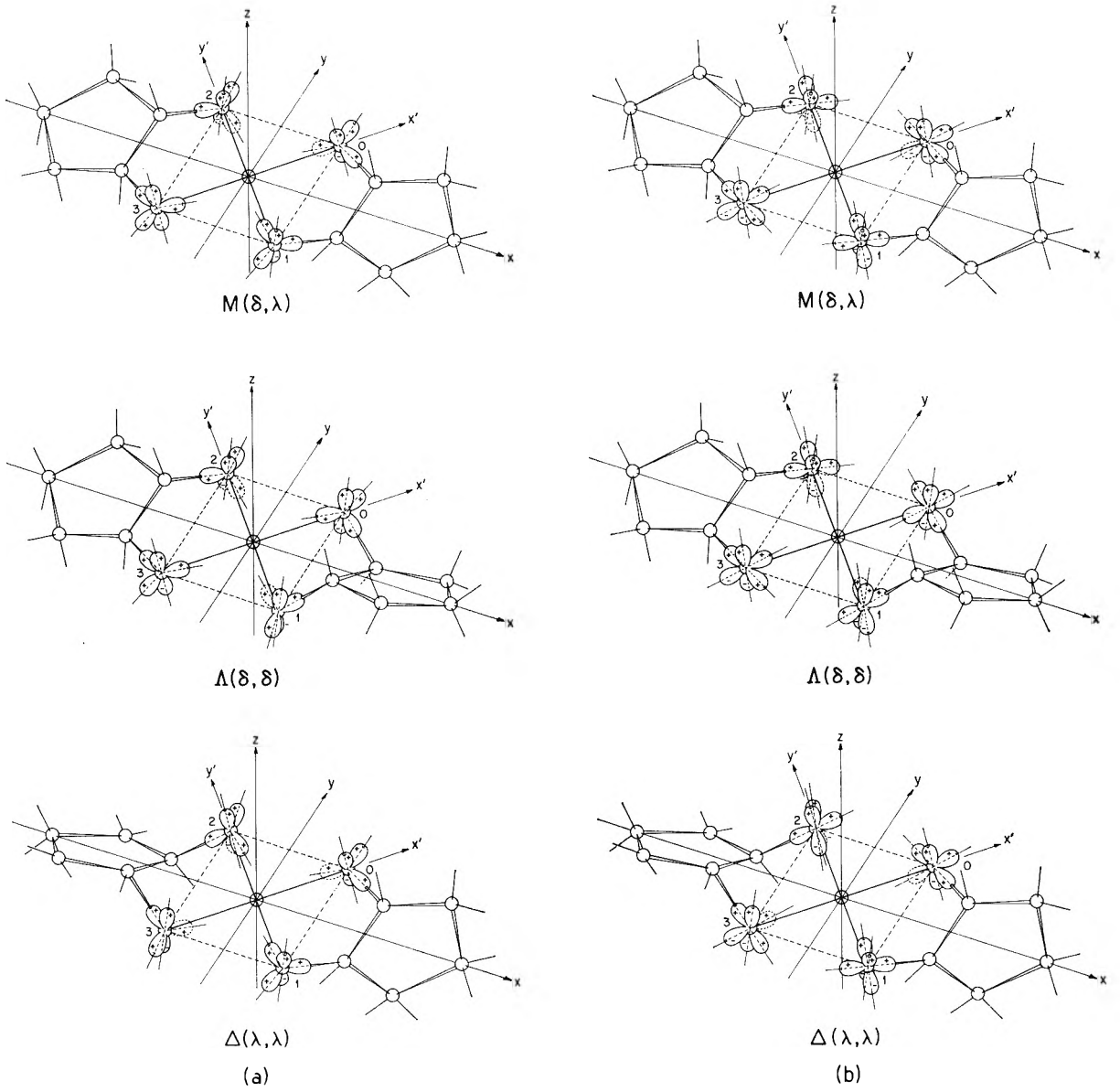

Figures 17a and 17b. The localized ligand orbital spatial disposition for the idealized complanately bonded right-angled conformations of the bis(cyclopentane glycol or glycolate) platinum(II) cation or anion. Figure 17a displays the spatial disposition under the premise of isosceles hybridization and Fig. 17b under the premise of digonal hybridization. Figure 8 properly altered pictures it under tetrahedral hybridization [read division C, section VIII for the exact meaning of the word hybridization used here]. The actual disposition is presumably intermediate between these extreme types. Mind the electronic antipodality of biscyclopentane and bis(ethylene glycol) derivatives of the same over-all nuclear conformation [compare Fig. 7 and 8].

$$\mathcal{P}_{ab} = \frac{m(E_b - E_a)}{\hbar e}\,\mathcal{R}_{ab};\quad \mathcal{O}_{ab} = \frac{m^2(E_b - E_a)^2}{\hbar^2 e^2}\,\mathcal{S}_{ab} \tag{23}$$

are now readily cataloged.

(a) No Configuration Interaction: Zero Spin-Orbit Forces. The installation of eq. 17 and 19 into eq. 21 and 22 gives the pertinent basic spinless one-electron rotational and spectral strengths. To save type, we set $\mathcal{W}_{ab}$ equal to $\mathcal{R}_{ab}$ or $\mathcal{P}_{ab}$, $\mathfrak{X}_{ab}$ equal to $\mathcal{S}_{ab}$ or $\mathcal{O}_{ab}$, and g equal to r or p [$\mathcal{W}$ may be considered as brief for whirlatory and $\mathfrak{X}$ for chromatory].

$$\mathcal{W}[b_2 \rightarrow b_2] \equiv 0,\ \mathfrak{X}[b_2 \rightarrow b_2] = 0,\ \mathfrak{M}[b_2 \rightarrow b_2] \equiv 0$$

$$\mathcal{W}[b_2 \rightarrow b_3] = \bar{g}_{0a}\bar{m}_{0a},\ \mathfrak{X}[b_2 \rightarrow b_3] = \bar{g}_{0a}{}^2,\ \mathfrak{M}[b_2 \rightarrow b_3] = \bar{m}_{0a}{}^2$$

$$\mathcal{W}[b_3 \rightarrow b_3] \equiv 0,\ \mathfrak{X}[b_3 \rightarrow b_3] \equiv 0,\ \mathfrak{M}[b_3 \rightarrow b_3] \equiv 0$$

$$\mathfrak{W}[b_2 \rightarrow a] = \bar{g}_{0b}\bar{m}_{0b},\ \mathfrak{X}[b_2 \rightarrow a] = \bar{g}_{0b}{}^2,\ \mathfrak{M}[b_2 \rightarrow a] = \bar{m}_{0b}{}^2$$

$$\mathfrak{W}[b_3 \rightarrow a] = \bar{g}_{0c}\bar{m}_{0c},\ \mathfrak{X}[b_3 \rightarrow a] = \bar{g}_{0c}{}^2,\ \mathfrak{M}[b_3 \rightarrow a] = \bar{m}_{0c}{}^2$$

$$\mathfrak{W}[b_2 \rightarrow a^*] = g_{1a}m_{1a},\ \mathfrak{X}[b_2 \rightarrow a^*] = g_{1a}{}^2,\ \mathfrak{M}[b_2 \rightarrow a^*] = m_{1a}{}^2$$

$$\mathfrak{W}[b_2 \rightarrow b_1] = g_{1b}m_{1b},\ \mathfrak{X}[b_2 \rightarrow b_1] = g_{1b}{}^2,\ \mathfrak{M}[b_2 \rightarrow b_1] = m_{1b}{}^2$$

$$\mathfrak{W}[b_3 \rightarrow a^*] = g_{2a}m_{2a},\ \mathfrak{X}[b_3 \rightarrow a^*] = g_{2a}{}^2,\ \mathfrak{M}[b_3 \rightarrow a^*] = m_{2a}{}^2$$

$$\mathfrak{W}[b_3 \rightarrow b_1] = g_{2b}m_{2b},\ \mathfrak{X}[b_3 \rightarrow b_1] = g_{2b}{}^2,\ \mathfrak{M}[b_3 \rightarrow b_1] = m_{2b}{}^2$$

$$\mathfrak{W}[a \rightarrow a] \equiv 0,\ \mathfrak{X}[a \rightarrow a] \equiv 0,\ \mathfrak{M}[a \rightarrow a] \equiv 0$$

$$\mathfrak{W}[a \rightarrow a^*] \equiv 0,\ \mathfrak{X}[a \rightarrow a^*] \equiv 0,\ \mathfrak{M}[a \rightarrow a^*] \equiv 0$$

$$\mathfrak{W}[a \rightarrow b_1] = g_{0b}m_{0b},\ \mathfrak{X}[a \rightarrow b_1] = g_{0b}{}^2,\ \mathfrak{M}[a \rightarrow b_1] = m_{0b}{}^2$$

$$\mathfrak{W}[a^* \rightarrow a^*] \equiv 0,\ \mathfrak{X}[a^* \rightarrow a^*] \equiv 0,\ \mathfrak{M}[a^* \rightarrow a^*] \equiv 0$$

$$\mathfrak{W}[a^* \rightarrow b_1] = \bar{\bar{g}}_0\bar{\bar{m}}_0,\ \mathfrak{X}[a^* \rightarrow b_1] = \bar{\bar{g}}_0{}^2,\ \mathfrak{M}[a^* \rightarrow b_1] = \bar{\bar{m}}_0{}^2$$

$$\mathfrak{W}[b_1 \rightarrow b_1] \equiv 0,\ \mathfrak{X}[b_1 \rightarrow b_1] \equiv 0,\ \mathfrak{M}[b_1 \rightarrow b_1] \equiv 0 \quad (24)$$

(*b*) *No Configuration Interaction: Nonzero Spin-Orbit Forces.* The inlay of eq. 20 into eq. 21 and 22 composes the appropriate basic one-electron spin-orbital rotational and spectral strengths epitomized beneath. Again $\mathfrak{W}_{ab}$ equals $\mathfrak{R}_{ab}$ or $\mathfrak{P}_{ab}$, $\mathfrak{X}_{ab}$ equals $\mathfrak{S}_{ab}$ or $\mathfrak{O}_{ab}$, and g equals r or p.

$$\mathfrak{W}[\gamma_{5(\substack{a\\b})}{}^{(8)'}(t_{2g}) \longrightarrow \gamma_{5(\substack{a\\b})}{}^{(7)}(t_{2g})] = 0$$

$$\mathfrak{X}[\gamma_{5(\substack{a\\b})}{}^{(8)'}(t_{2g}) \longrightarrow \gamma_{5(\substack{a\\b})}{}^{(7)}(t_{2g})] = {}^2/_3\bar{r}_{0a}{}^2 \text{ or } 0$$

$$\mathfrak{M}[\gamma_{5(\substack{a\\b})}{}^{(8)'}(t_{2g}) \longrightarrow \gamma_{5(\substack{a\\b})}{}^{(7)}(t_{2g})] = 0$$

$$\mathfrak{W}[\gamma_{5(\substack{a\\b})}{}^{(8)'}(t_{2g}) \longrightarrow \gamma_{5(\substack{b\\a})}{}^{(7)}(t_{2g})] = {}^1/_6\{\bar{g}_{0b}(\bar{m}_{0b} + 2\mu_B) + \bar{g}_{0c}(\bar{m}_{0c} + 2\mu_B)\}$$

$$\mathfrak{X}[\gamma_{5(\substack{a\\b})}{}^{(8)'}(t_{2g}) \longrightarrow \gamma_{5(\substack{b\\a})}{}^{(7)}(t_{2g})] = {}^1/_6\{\bar{g}_{0b}{}^2 + \bar{g}_{0c}{}^2\}$$

$$\mathfrak{M}[\gamma_{5(\substack{a\\b})}{}^{(8)'}(t_{2g}) \longrightarrow \gamma_{5(\substack{b\\a})}{}^{(7)}(t_{2g})] = {}^1/_6\{(\bar{m}_{0b} + 2\mu_B)^2 + (\bar{m}_{0c} + 2\mu_B)^2\}$$

$$\mathfrak{W}[\gamma_{5(\substack{a\\b})}{}^{(8)'}(t_{2g}) \longrightarrow \gamma_{5(\substack{a\\b})}{}^{(8)}(t_{2g})] = 0$$

$$\mathfrak{X}[\gamma_{5(\substack{a\\b})}{}^{(8)'}(t_{2g}) \longrightarrow \gamma_{5(\substack{a\\b})}{}^{(8)}(t_{2g})] = {}^1/_3\bar{r}_{0a}{}^2 \text{ or } 0$$

$$\mathfrak{M}[\gamma_{5(\substack{a\\b})}{}^{(8)'}(t_{2g}) \longrightarrow \gamma_{5(\substack{a\\b})}{}^{(8)}(t_{2g})] = 0$$

$$\mathfrak{W}[\gamma_{5(\substack{a\\b})}{}^{(8)'}(t_{2g}) \longrightarrow \gamma_{5(\substack{b\\a})}{}^{(8)}(t_{2g})] = {}^1/_3\{\bar{g}_{0b}(\bar{m}_{0b} - \mu_B) + \bar{g}_{0c}(\bar{m}_{0c} - \mu_B)\}$$

$$\mathfrak{X}[\gamma_{5(\substack{a\\b})}{}^{(8)'}(t_{2g}) \longrightarrow \gamma_{5(\substack{b\\a})}{}^{(8)}(t_{2g})] = {}^1/_3\{\bar{g}_{0b}{}^2 + \bar{g}_{0c}{}^2\}$$

$$\mathfrak{M}[\gamma_{5(\substack{a\\b})}{}^{(8)'}(t_{2g}) \longrightarrow \gamma_{5(\substack{b\\a})}{}^{(8)}(t_{2g})] = {}^1/_3\{(\bar{m}_{0b} - \mu_B)^2 + (\bar{m}_{0c} - \mu_B)^2\}$$

$$\mathfrak{W}[\gamma_{5(\substack{a\\b})}{}^{(7)}(t_{2g}) \longrightarrow \gamma_{5(\substack{a\\b})}{}^{(8)}(t_{2g})] = 0 \text{ or } {}^2/_9\bar{p}_{0a}(\bar{m}_{0a} + 2\mu_B)$$

$$\mathfrak{X}[\gamma_{5(\substack{a\\b})}{}^{(7)}(t_{2g}) \longrightarrow \gamma_{5(\substack{a\\b})}{}^{(8)}(t_{2g})] = 0 \text{ or } {}^2/_9\bar{p}_{0a}{}^2$$

$$\mathfrak{M}[\gamma_{5(\substack{a\\b})}{}^{(7)}(t_{2g})] \longrightarrow \gamma_{5(\substack{a\\b})}{}^{(8)}(t_{2g})] = {}^2/_9(\bar{m}_{0a} + 2\mu_B)^2$$

$$\mathfrak{W}[\gamma_{5(\substack{a\\b})}{}^{(7)}(t_{2g}) \longrightarrow \gamma_{5(\substack{b\\a})}{}^{(8)}(t_{2g})] = {}^1/_6\{\bar{r}_{0c}(\bar{m}_{0c} + 2\mu_B) + \bar{r}_{0b}(\bar{m}_{0b} + 2\mu_B)\}$$

or

$${}^1/_{18}\{\bar{p}_{0c}(\bar{m}_{0c} + 2\mu_B) + \bar{p}_{0b}(\bar{m}_{0b} + 2\mu_B)\}$$

$$\mathfrak{X}[\gamma_{5(\substack{a\\b})}{}^{(7)}(t_{2g}) \longrightarrow \gamma_{5(\substack{b\\a})}{}^{(8)}(t_{2g})] = {}^1/_2\{\bar{r}_{0c}{}^2 + \bar{r}_{0b}{}^2\} \text{ or } {}^1/_{18}\{\bar{p}_{0c}{}^2 + \bar{p}_{0b}{}^2\}$$

$$\mathfrak{M}[\gamma_{5(\substack{a\\b})}{}^{(7)}(t_{2g}) \longrightarrow \gamma_{5(\substack{b\\a})}{}^{(8)}(t_{2g})] = {}^1/_{18}\{(\bar{m}_{0c} + 2\mu_B)^2 + (\bar{m}_{0b} + 2\mu_B)^2\}$$

$$\mathfrak{W}[\gamma_{5(\substack{a\\b})}{}^{(8)'}(t_{2g}) \longrightarrow \gamma_{5(\substack{a\\b})}{}^{(8)'}(e_g)] = \mathfrak{X}[\gamma_{5(\substack{a\\b})}{}^{(8)'}(t_{2g}) \longrightarrow \gamma_{5(\substack{a\\b})}{}^{(8)'}(e_g)] = \mathfrak{M}[\gamma_{5(\substack{a\\b})}{}^{(8)'}(t_{2g}) \longrightarrow \gamma_{5(\substack{a\\b})}{}^{(8)'}(e_g)] = 0$$

$$\mathfrak{W}[\gamma_{5(\substack{a\\b})}{}^{(8)'}(t_{2g}) \longrightarrow \gamma_{5(\substack{b\\a})}{}^{(8)'}(e_g)] = {}^1/_2\{g_{2a}m_{2a} - g_{1a}m_{1a}\}$$

$$\mathfrak{X}[\gamma_{5(\substack{a\\b})}{}^{(8)'}(t_{2g}) \longrightarrow \gamma_{5(\substack{b\\a})}{}^{(8)'}(e_g)] = {}^1/_2\{g_{2a}{}^2 + g_{1a}{}^2\}$$

$$\mathfrak{M}[\gamma_{5(\substack{a\\b})}{}^{(8)'}(t_{2g}) \longrightarrow \gamma_{5(\substack{b\\a})}{}^{(8)'}(e_g)] = {}^1/_2\{m_{2a}{}^2 + m_{1a}{}^2\}$$

$$\mathfrak{W}[\gamma_{5(\substack{a\\b})}{}^{(8)'}(t_{2g}) \longrightarrow \gamma_{5(\substack{a\\b})}{}^{(8)}(e_g)] = \mathfrak{X}[\gamma_{5(\substack{a\\b})}{}^{(8)'}(t_{2g}) \longrightarrow \gamma_{5(\substack{a\\b})}{}^{(8)}(e_g)] = \mathfrak{M}[\gamma_{5(\substack{a\\b})}{}^{(8)'}(t_{2g}) \longrightarrow \gamma_{5(\substack{a\\b})}{}^{(8)}(e_g)] = 0$$

$$\mathfrak{W}[\gamma_{5(\substack{a\\b})}{}^{(8)'}(t_{2g}) \longrightarrow \gamma_{5(\substack{b\\a})}{}^{(8)}(e_g)] = {}^1/_2\{g_{1b}m_{1b} + g_{2b}m_{2b}\}$$

$$\mathfrak{X}[\gamma_{5(\substack{a\\b})}{}^{(8)'}(t_{2g}) \longrightarrow \gamma_{5(\substack{b\\a})}{}^{(8)}(e_g)] = {}^1/_2\{g_{1b}{}^2 + g_{2b}{}^2\}$$

$$\mathfrak{M}[\gamma_{5(\substack{a\\b})}{}^{(8)'}(t_{2g}) \longrightarrow \gamma_{5(\substack{b\\a})}{}^{(8)}(e_g)] = {}^1/_2\{m_{1b}{}^2 + m_{2b}{}^2\}$$

$$\mathfrak{W}[\gamma_{5(\substack{a\\b})}{}^{(7)}(t_{2g}) \longrightarrow \gamma_{5(\substack{a\\b})}{}^{(8)'}(e_g)] = \mathfrak{X}[\gamma_{5(\substack{a\\b})}{}^{(7)}(t_{2g}) \longrightarrow \gamma_{5(\substack{a\\b})}{}^{(8)'}(e_g)] = \mathfrak{M}[\gamma_{5(\substack{a\\b})}{}^{(7)}(t_{2g}) \longrightarrow \gamma_{5(\substack{a\\b})}{}^{(8)'}(e_g)] = 0$$

$$\mathfrak{W}[\gamma_{5(\substack{a\\b})}{}^{(7)}(t_{2g}) \longrightarrow \gamma_{5(\substack{a\\b})}{}^{(8)'}(e_g)] = {}^1/_3\{g_{1a}m_{1a} + g_{2a}m_{2a}\}$$

$$\mathfrak{X}[\gamma_{5(\substack{a\\b})}{}^{(7)}(t_{2g}) \longrightarrow \gamma_{5(\substack{b\\a})}{}^{(8)'}(e_g)] = {}^1/_3\{g_{1a}{}^2 + g_{2a}{}^2\}$$

$$\mathfrak{M}[\gamma_{5(\substack{a\\b})}{}^{(7)}(t_{2g}) \longrightarrow \gamma_{5(\substack{b\\a})}{}^{(8)'}(e_g)] = {}^1/_3\{m_{1a}{}^2 + m_{1b}{}^2\}$$

$$\mathfrak{W}[\gamma_{5(\substack{a\\b})}{}^{(7)}(t_{2g}) \longrightarrow \gamma_{5(\substack{a\\b})}{}^{(8)}(e_g)] = {}^1/_3g_{0b}m_{0b}$$

$$\mathfrak{X}[\gamma_{5(\substack{a\\b})}{}^{(7)}(t_{2g}) \longrightarrow \gamma_{5(\substack{a\\b})}{}^{(8)}(e_g)] = {}^1/_3g_{0b}{}^2$$

$$\mathfrak{M}[\gamma_{5(\substack{a\\b})}{}^{(7)}(t_{2g}) \longrightarrow \gamma_{5(\substack{a\\b})}{}^{(8)}(e_g)] = {}^1/_3m_{0b}{}^2$$

$$\mathfrak{W}[\gamma_{5(\substack{a\\b})}{}^{(7)}(t_{2g}) \longrightarrow \gamma_{5(\substack{b\\a})}{}^{(8)}(e_g)] = {}^1/_3\{g_{1b}m_{1b} + g_{2b}m_{2b}\}$$

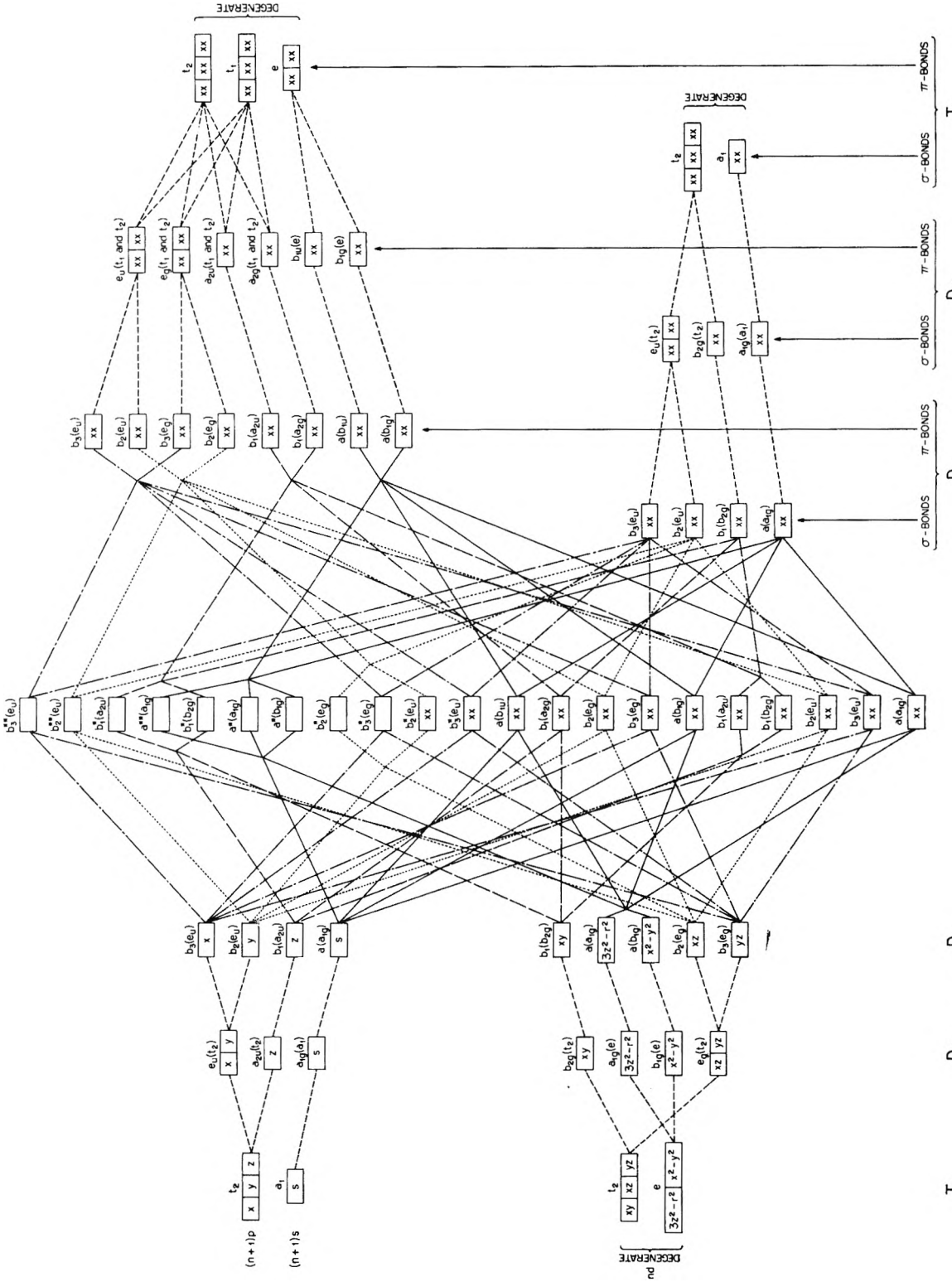

Figure 18. Correlational molecular orbital energy level diagram for a pterotactically four-coordinated (digonal dihedral) σ,π-bonded compound. The figure images the junction of the tetrahedrate, quadrate, and peterotactate diagrams. Level orders have been opined as in Fig. 10.

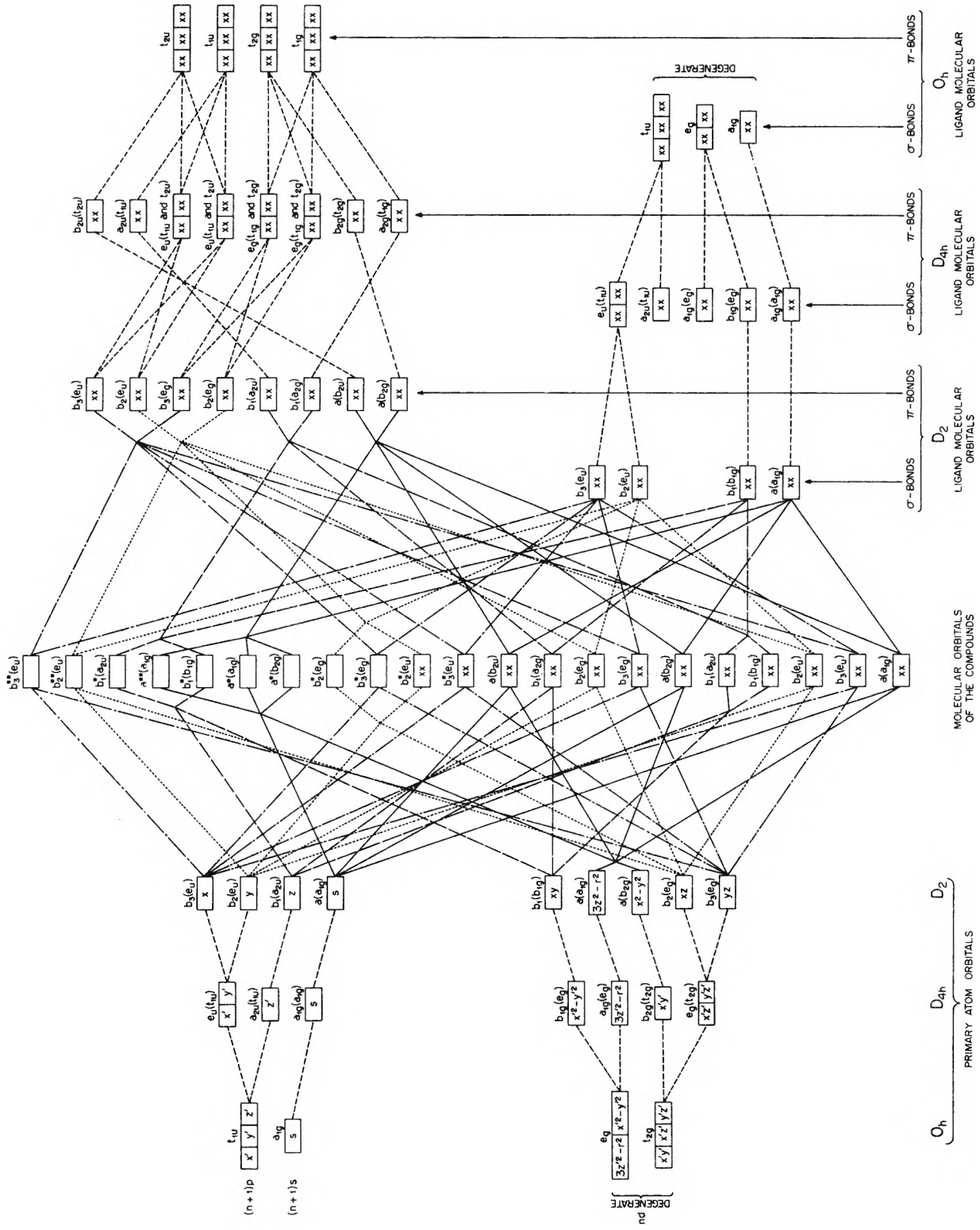

Figure 19. Correlational molecular orbital energy level diagram for a pterotactically four-coordinated (digonal dihedral) σ,π-bonded compound. The figure images the junction of the octahedrate, quadrate, and peterotactate diagrams. Level orders have been opined as in Fig. 10.

$$\mathfrak{X}[\gamma_{5(\substack{a\\b})}{}^{(7)}(t_{2g}) \longrightarrow \gamma_{5(\substack{b\\a})}{}^{(8)}(e_g)] = {}^1/_3\{g_{1b}{}^2 + g_{2b}{}^2\}$$

$$\mathfrak{M}[\gamma_{5(\substack{a\\b})}{}^{(7)}(t_{2g}) \longrightarrow \gamma_{5(\substack{b\\a})}{}^{(8)}(e_g)] = {}^1/_3\{m_{1b}{}^2 + m_{2b}{}^2\}$$

$$\mathfrak{W}[\gamma_{5(\substack{a\\b})}{}^{(8)}(t_{2g}) \longrightarrow \gamma_{5(\substack{a\\b})}{}^{(8)'}(e_g)] =$$

$$\mathfrak{X}[\gamma_{5(\substack{a\\b})}{}^{(8)}(t_{2g}) \longrightarrow \gamma_{5(\substack{a\\b})}{}^{(8)'}(e_g)] =$$

$$\mathfrak{M}[\gamma_{5(\substack{a\\b})}{}^{(8)}(t_{2g}) \longrightarrow \gamma_{5(\substack{a\\b})}{}^{(8)'}(e_g)] = 0$$

$$\mathfrak{W}[\gamma_{5(\substack{a\\b})}{}^{(8)}(t_{2g}) \longrightarrow \gamma_{5(\substack{b\\a})}{}^{(8)'}(e_g)] = {}^1/_6\{g_{2a}m_{2a} + g_{1a}m_{1a}\}$$

$$\mathfrak{X}[\gamma_{5(\substack{a\\b})}{}^{(8)}(t_{2g}) \longrightarrow \gamma_{5(\substack{b\\a})}{}^{(8)'}(e_g)] = {}^1/_6\{g_{2a}{}^2 + g_{1a}{}^2\}$$

$$\mathfrak{M}[\gamma_{5(\substack{a\\b})}{}^{(8)}(t_{2g}) \longrightarrow \gamma_{5(\substack{b\\a})}{}^{(8)'}(e_g)] = {}^1/_6\{m_{2a}{}^2 + m_{1a}{}^2\}$$

$$\mathfrak{W}[\gamma_{5(\substack{a\\b})}{}^{(8)}(t_{2g}) \longrightarrow \gamma_{5(\substack{a\\b})}{}^{(8)}(e_g)] = {}^2/_3 g_{0b}m_{0b}$$

$$\mathfrak{X}[\gamma_{5(\substack{a\\b})}{}^{(8)}(t_{2g}) \longrightarrow \gamma_{5(\substack{a\\b})}{}^{(8)}(e_g)] = {}^2/_3 g_{0b}{}^2$$

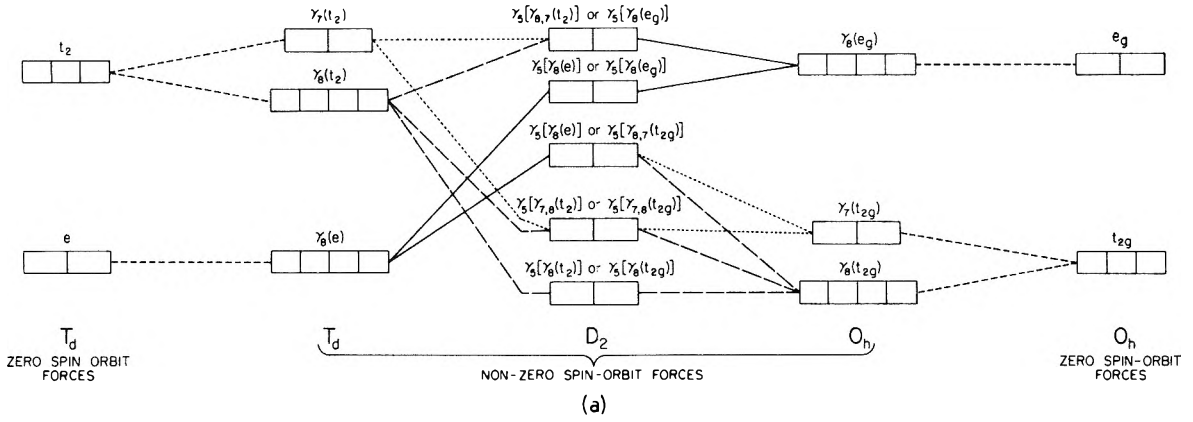

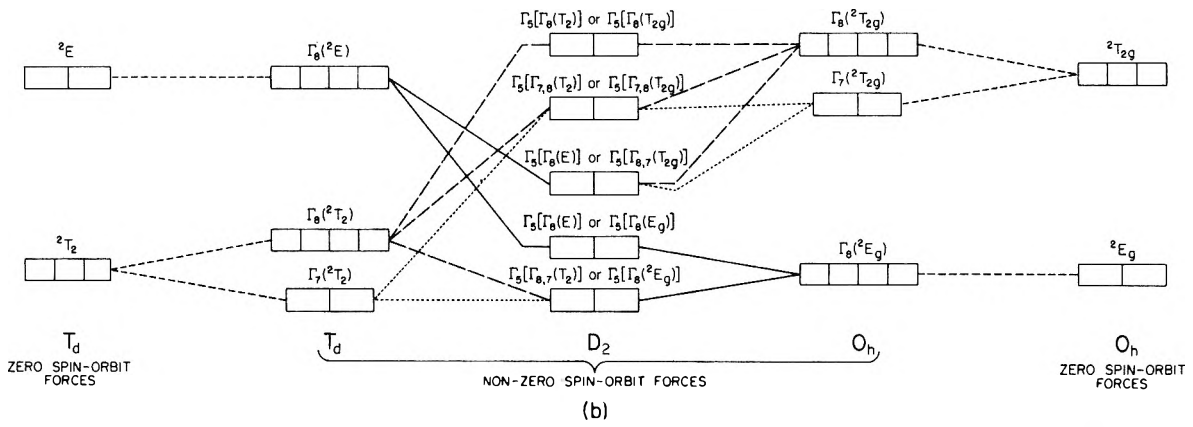

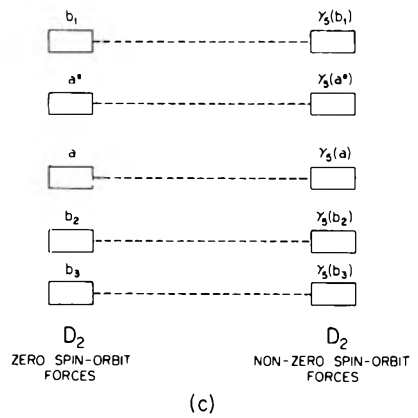

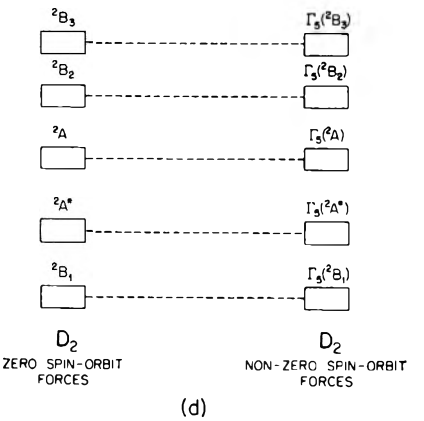

Figure 20. Concurrence of the tetrahedrate, octahedrate, and peterotactate zero and nonzero molecular spin-orbital energy level diagrams for a one- [(a) and (c)] and nine- [(b) and (d)] electron digonal dihedral transition metal compound.

$$\mathfrak{M}[\gamma_{5(\substack{a\\b})}{}^{(8)}(t_{2g}) \longrightarrow \gamma_{5(\substack{a\\b})}{}^{(8)}(e_g)] = {}^{2}/_{3}m_{0b}{}^{2}$$

$$\mathfrak{W}[\gamma_{5(\substack{a\\b})}{}^{(8)}(t_{2g}) \longrightarrow \gamma_{5(\substack{b\\a})}{}^{(8)}(e_g)] = {}^{1}/_{6}\{g_{1b}m_{1b} + g_{2b}m_{2b}\}$$

$$\mathfrak{X}[\gamma_{5(\substack{a\\b})}{}^{(8)}(t_{2g}) \longrightarrow \gamma_{5(\substack{b\\a})}{}^{(8)}(e_g)] = {}^{1}/_{6}\{g_{1b}{}^{2} + g_{2b}{}^{2}\}$$

$$\mathfrak{M}[\gamma_{5(\substack{a\\b})}{}^{(8)}(t_{2g}) \longrightarrow \gamma_{5(\substack{b\\a})}{}^{(8)}(e_g)] = {}^{1}/_{6}\{m_{1b}{}^{2} + m_{2b}{}^{2}\}$$

$$\mathfrak{W}[\gamma_{5(\substack{a\\b})}{}^{(9)'}(e_g) \longrightarrow \gamma_{5(\substack{a\\b})}{}^{(8)'}(e_g)] =$$
$$\mathfrak{X}[\gamma_{5(\substack{a\\b})}{}^{(8)'}(e_g) \longrightarrow \gamma_{5(\substack{a\\b})}{}^{(8)'}(e_g)] = 0$$

$$\mathfrak{M}[\gamma_{5(\substack{a\\b})}{}^{(8)'}(e_g) \longrightarrow \gamma_{5(\substack{a\\b})}{}^{(8)'}(e_g)] = \mu_B{}^{2}$$

$$\mathfrak{W}[\gamma_{5(\substack{a\\b})}{}^{(8)'}(e_g) \longrightarrow \gamma_{5(\substack{b\\a})}{}^{(8)'}(e_g)] =$$
$$\mathfrak{X}[\gamma_{5(\substack{a\\b})}{}^{(8)'}(e_g) \longrightarrow \gamma_{5(\substack{b\\a})}{}^{(8)'}(e_g)] = 0$$

$$\mathfrak{M}[\gamma_{5(\substack{a\\b})}{}^{(8)'}(e_g) \longrightarrow \gamma_{5(\substack{b\\a})}{}^{(8)'}(e_g)] = 2\mu_B{}^{2}$$

$$\mathfrak{W}[\gamma_{5(\substack{a\\b})}{}^{(8)'}(e_g) \longrightarrow \gamma_{5(\substack{a\\b})}{}^{(8)}(e_g)] = \bar{\bar{g}}_0\bar{\bar{m}}_0$$

$$\mathfrak{X}[\gamma_{5(\substack{a\\b})}{}^{(8)'}(e_g) \longrightarrow \gamma_{5(\substack{a\\b})}{}^{(8)}(e_g)] = \bar{\bar{g}}_0{}^{2}$$

$$\mathfrak{M}[\gamma_{5(\substack{a\\b})}{}^{(9)'}(e_g) \longrightarrow \gamma_{5(\substack{a\\b})}{}^{(8)}(e_g)] = \bar{\bar{m}}_0{}^{2}$$

$$\mathfrak{W}[\gamma_{5(\substack{a\\b})}{}^{(3)'}(e_g) \longrightarrow \gamma_{5(\substack{b\\a})}{}^{(8)}(e_g)] =$$
$$\mathfrak{X}[\gamma_{5(\substack{a\\b})}{}^{(8)'}(e_g) \longrightarrow \gamma_{5(\substack{b\\a})}{}^{(8)}(e_g)] =$$
$$\mathfrak{M}[\gamma_{5(\substack{a\\b})}{}^{(8)'}(e_g) \longrightarrow \gamma_{5(\substack{b\\a})}{}^{(8)}(e_g)] = 0$$

$$\mathfrak{W}[\gamma_{5(\substack{a\\b})}{}^{(8)}(e_g) \longrightarrow \gamma_{5(\substack{a\\b})}{}^{(8)}(e_g)] =$$
$$\mathfrak{X}[\gamma_{5(\substack{a\\b})}{}^{(8)}(e_g) \longrightarrow \gamma_{5(\substack{a\\b})}{}^{(8)}(e_g)] = 0$$

$$\mathfrak{M}[\gamma_{5(\substack{a\\b})}{}^{(8)}(e_g) \longrightarrow \gamma_{5(\substack{a\\b})}{}^{(8)}(e_g)] = \mu_B{}^{2}$$

$$\mathfrak{W}[\gamma_{5(\substack{a\\b})}{}^{(8)}(e_g) \longrightarrow \gamma_{5(\substack{b\\a})}{}^{(8)}(e_g)] =$$
$$\mathfrak{X}[\gamma_{5(\substack{a\\b})}{}^{(8)}(e_g) \longrightarrow \gamma_{5(\substack{b\\a})}{}^{(8)}(e_g)] = 0$$

$$\mathfrak{M}[\gamma_{5(\substack{a\\b})}{}^{(8)}(e_g) \longrightarrow \gamma_{5(\substack{b\\a})}{}^{(8)}(e_g)] = 2\mu_B{}^{2}$$

$$\mathfrak{W}[\gamma_{5(\substack{a\\b})}{}^{(8)'}(t_{2g}) \longrightarrow \gamma_{5(\substack{a\\b})}{}^{(8)'}(t_{2g})] = 0 \text{ or } \bar{p}_{0a}(\bar{m}_{0a} - \mu_B)$$

$$\mathfrak{X}[\gamma_{5(\substack{a\\b})}{}^{(8)'}(t_{2g}) \longrightarrow \gamma_{5(\substack{a\\b})}{}^{(8)'}(t_{2g})] = 0 \text{ or } \bar{p}_{0a}{}^{2}$$

$$\mathfrak{M}[\gamma_{5(\substack{a\\b})}{}^{(8)'}(t_{2g}) \longrightarrow \gamma_{5(\substack{a\\b})}{}^{(8)'}(t_{2g})] = (\bar{m}_{0a} - \mu_B)^{2}$$

$$\mathfrak{W}[\gamma_{5(\substack{a\\b})}{}^{(8)'}(t_{2g}) \longrightarrow \gamma_{5(\substack{b\\a})}{}^{(8)'}(t_{2g})] =$$
$$\mathfrak{X}[\gamma_{5(\substack{a\\b})}{}^{(8)'}(t_{2g}) \longrightarrow \gamma_{5(\substack{b\\a})}{}^{(8)'}(t_{2g})] =$$
$$\mathfrak{M}[\gamma_{5(\substack{a\\b})}{}^{(8)'}(t_{2g}) \longrightarrow \gamma_{5(\substack{b\\a})}{}^{(8)'}(t_{2g})] = 0$$

$$\mathfrak{W}[\gamma_{5(\substack{a\\b})}{}^{(7)}(t_{2g}) \longrightarrow \gamma_{5(\substack{a\\b})}{}^{(7)}(t_{2g})] = 0 \text{ or } {}^{2}/_{9}\bar{p}_{0a}(2\bar{m}_{0a} + \mu_B)$$

$$\mathfrak{X}[\gamma_{5(\substack{a\\b})}{}^{(7)}(t_{2g}) \longrightarrow \gamma_{5(\substack{a\\b})}{}^{(7)}(t_{2g})] = 0 \text{ or } {}^{4}/_{9}\bar{p}_{0a}{}^{2}$$

$$\mathfrak{M}[\gamma_{5(\substack{a\\b})}{}^{(7)}(t_{2g}) \longrightarrow \gamma_{5(\substack{a\\b})}{}^{(7)}(t_{2g})] = {}^{1}/_{9}(2\bar{m}_{0a} + \mu_B)^{2}$$

$$\mathfrak{W}[\gamma_{5(\substack{a\\b})}{}^{(7)}(t_{2g}) \longrightarrow \gamma_{5(\substack{b\\a})}{}^{(7)}(t_{2g})] = 0$$
$$\text{or } {}^{2}/_{9}\{\bar{p}_{0c}(2\bar{m}_{0c} + \mu_B) + \bar{p}_{0b}(2\bar{m}_{0b} + \mu_B)\}$$

$$\mathfrak{X}[\gamma_{5(\substack{a\\b})}{}^{(7)}(t_{2g}) \longrightarrow \gamma_{5(\substack{b\\a})}{}^{(7)}(t_{2g})] = 0 \text{ or } {}^{4}/_{9}\{\bar{p}_{0c}{}^{2} + \bar{p}_{0b}{}^{2}\}$$

$$\mathfrak{M}[\gamma_{5(\substack{a\\b})}{}^{(7)}(t_{2g}) \longrightarrow \gamma_{5(\substack{b\\a})}{}^{(7)}(t_{2g})] =$$
$${}^{1}/_{9}\{(2\bar{m}_{0c} + \mu_B)^{2} + (2\bar{m}_{0b} + \mu_B)^{2}\}$$

$$\mathfrak{W}[\gamma_{5(\substack{a\\b})}{}^{(8)}(t_{2g}) \longrightarrow \gamma_{5(\substack{a\\b})}{}^{(3)}(t_{2g})] = 0 \text{ or } {}^{1}/_{9}\bar{p}_{0a}(\bar{m}_{0a} - \mu_B)$$

$$\mathfrak{X}[\gamma_{5(\substack{a\\b})}{}^{(8)}(t_{2g}) \longrightarrow \gamma_{5(\substack{a\\b})}{}^{(8)}(t_{2g})] = 0 \text{ or } {}^{1}/_{9}\bar{p}_{0a}{}^{2}$$

$$\mathfrak{M}[\gamma_{5(\substack{a\\b})}{}^{(8)}(t_{2g}) \longrightarrow \gamma_{5(\substack{a\\b})}{}^{(8)}(t_{2g})] = {}^{1}/_{9}(\bar{m}_{0a} - \mu_B)^{2}$$

$$\mathfrak{W}[\gamma_{5(\substack{a\\b})}{}^{(8)}(t_{2g}) \longrightarrow \gamma_{5(\substack{b\\a})}{}^{(8)}(t_{2g})] = 0$$
$$\text{or } {}^{4}/_{9}\{\bar{p}_{0c}(\bar{m}_{0c} - \mu_B) + \bar{p}_{0b}(\bar{m}_{0b} - \mu_B)\}$$

$$\mathfrak{X}[\gamma_{5(\substack{a\\b})}{}^{(8)}(t_{2g}) \longrightarrow \gamma_{5(\substack{b\\a})}{}^{(8)}(t_{2g})] = 0 \text{ or } {}^{4}/_{9}\{\bar{p}_{0c}{}^{2} + \bar{p}_{0b}{}^{2}\}$$

$$\mathfrak{M}[\gamma_{5(\substack{a\\b})}{}^{(8)}(t_{2g}) \longrightarrow \gamma_{5(\substack{b\\a})}{}^{(3)}(t_{2g})] =$$
$${}^{4}/_{9}\{(\bar{m}_{0c} - \mu_B)^{2} + (\bar{m}_{0b} - \mu_B)^{2}\} \quad (25)$$

These single rotational and spectral strengths sum to the full rotational and spectral strengths filed below

$$\mathfrak{W}[\gamma_5{}^{(8)'}(t_{2g}) \longrightarrow \gamma_5{}^{(7)}(t_{2g})] =$$
$${}^{1}/_{6}\{\bar{g}_{0b}(\bar{m}_{0b} + 2\mu_B) + \bar{g}_{0c}(\bar{m}_{0c} + 2\mu_B)\}$$

$$\mathfrak{X}[\gamma_5{}^{(8)'}(t_{2g}) \longrightarrow \gamma_5{}^{(7)}(t_{2g})] = {}^{2}/_{3}\bar{r}_{0a}{}^{2} + {}^{1}/_{6}\bar{r}_{0b}{}^{2} + {}^{1}/_{6}\bar{r}_{0c}{}^{2}$$
$$\text{or } {}^{1}/_{6}\bar{p}_{0b}{}^{2} + {}^{1}/_{6}\bar{p}_{0c}{}^{2}$$

$$\mathfrak{M}[\gamma_5{}^{(8)'}(t_{2g}) \longrightarrow \gamma_5{}^{(7)}(t_{2g})] = {}^{1}/_{6}\{(\bar{m}_{0b} + 2\mu_B)^{2} + (\bar{m}_{0c} + 2\mu_B)^{2}\}$$

$$\mathfrak{W}[\gamma_5{}^{(8)'}(t_{2g}) \longrightarrow \gamma_5{}^{(8)}(t_{2g})] =$$
$${}^{1}/_{3}\{\bar{g}_{0b}(\bar{m}_{0b} - \mu_B) + \bar{g}_{0c}(\bar{m}_{0c} - \mu_B)\}$$

$$\mathfrak{X}[\gamma_5{}^{(8)'}(t_{2g}) \longrightarrow \gamma_5{}^{(8)}(t_{2g})] = {}^{1}/_{3}\{\bar{r}_{0a}{}^{2} + \bar{r}_{0b}{}^{2} + \bar{r}_{0c}{}^{2}\}$$
$$\text{or } {}^{1}/_{3}\{\bar{p}_{0b}{}^{2} + \bar{p}_{0c}{}^{2}\}$$

$$\mathfrak{M}[\gamma_5{}^{(8)'}(t_{2g}) \longrightarrow \gamma_5{}^{(8)}(t_{2g})] = {}^{1}/_{3}\{(\bar{m}_{0b} - \mu_B)^{2} + (\bar{m}_{0c} - \mu_B)^{2}\}$$

$$\mathfrak{W}[\gamma_5{}^{(7)}(t_{2g}) \longrightarrow \gamma_5{}^{(8)}(t_{2g})] =$$
$${}^{1}/_{6}\{\bar{r}_{0c}(\bar{m}_{0c} + 2\mu_B) + \bar{r}_{0b}(\bar{m}_{0b} + 2\mu_B)\}$$
$$\text{or } {}^{2}/_{9}\bar{p}_{0a}(\bar{m}_{0a} + 2\mu_B) + {}^{1}/_{18}\bar{p}_{0c}(\bar{m}_{0c} + 2\mu_B) + {}^{1}/_{18}\bar{p}_{0b}(\bar{m}_{0b} + 2\mu_b)$$

$$\mathfrak{X}[\gamma_5{}^{(7)}(t_{2g}) \longrightarrow \gamma_5{}^{(8)}(t_{2g})] = {}^{1}/_{2}\{\bar{r}_{0c}{}^{2} + \bar{r}_{0b}{}^{2}\}$$
$$\text{or } {}^{2}/_{9}\bar{p}_{0a}{}^{2} + {}^{1}/_{18}\bar{p}_{0c}{}^{2} + {}^{1}/_{18}\bar{p}_{0b}{}^{2}$$

$$\mathfrak{M}[\gamma_5{}^{(7)}(t_{2g}) \longrightarrow \gamma_5{}^{(8)}(t_{2g})] =$$
$${}^{2}/_{9}(\bar{m}_{0a} + 2\mu_B)^{2} + {}^{1}/_{18}(\bar{m}_{0c} + 2\mu_B)^{2} + {}^{1}/_{18}(\bar{m}_{0b} + 2\mu_B)^{2}$$

$$\mathfrak{W}[\gamma_5{}^{(8)'}(t_{2g}) \longrightarrow \gamma_5{}^{(8)'}(e_g)] = {}^{1}/_{2}\{g_{2a}m_{2a} + g_{1a}m_{1a}\}$$

$$\mathfrak{X}[\gamma_5{}^{(8)'}(t_{2g}) \longrightarrow \gamma_5{}^{(8)'}(e_g)] = {}^{1}/_{2}\{g_{1a}{}^{2} + g_{2a}{}^{2}\}$$

$$\mathfrak{M}[\gamma_5{}^{(8)'}(t_{2g}) \longrightarrow \gamma_5{}^{(8)'}(e_g)] = {}^{1}/_{2}\{m_{1a}{}^{2} + m_{2a}{}^{2}\}$$

$$\mathfrak{W}[\gamma_5{}^{(8)'}(t_{2g}) \longrightarrow \gamma_5{}^{(8)}(e_g)] = {}^{1}/_{2}\{g_{1b}m_{1b} + g_{2b}m_{2b}\}$$

$$\mathfrak{X}[\gamma_5{}^{(8)'}(t_{2g}) \longrightarrow \gamma_5{}^{(8)}(e_g)] = {}^{1}/_{2}\{g_{1b}{}^{2} + g_{2b}{}^{2}\}$$

$$\mathfrak{M}[\gamma_5{}^{(8)'}(t_{2g}) \longrightarrow \gamma_5{}^{(8)}(e_g)] = {}^{1}/_{2}\{m_{1b}{}^{2} + m_{2b}{}^{2}\}$$

$$\mathfrak{W}[\gamma_5{}^{(7)}(t_{2g}) \longrightarrow \gamma_5{}^{(8)'}(e_g)] = {}^{1}/_{3}\{g_{1a}m_{1a} + g_{2a}m_{2a}\}$$

$$\mathfrak{X}[\gamma_5^{(7)}(t_{2g}) \longrightarrow \gamma_5^{(8)'}(e_g)] = {}^1/_3\{g_{1a}^2 + g_{2a}^2\}$$
$$\mathfrak{M}[\gamma_5^{(7)}(t_{2g}) \longrightarrow \gamma_5^{(8)'}(e_g)] = {}^1/_3\{m_{1a}^2 + m_{2a}^2\}$$
$$\mathfrak{W}[\gamma_5^{(7)}(t_{2g}) \longrightarrow \gamma_5^{(8)}(e_g)] = {}^1/_3\{g_{0b}m_{0b} + g_{1b}m_{1b} + g_{2b}m_{2b}\}$$

$$\mathfrak{X}[\gamma_5^{((7)}(t_{2g}) \longrightarrow \gamma_5^{(8)}(e_g)] = {}^1/_3\{g_{0b}^2 + g_{1b}^2 + g_{2b}^2\}$$
$$\mathfrak{M}[\gamma_5^{(7)}(t_{2g}) \longrightarrow \gamma_5^{(8)}(e_g)] = {}^1/_3\{m_{0b}^2 + m_{1b}^2 + m_{2b}^2\}$$
$$\mathfrak{W}[\gamma_5^{(8)}(t_{2g}) \longrightarrow \gamma_5^{(8)'}(e_g)] = {}^1/_6\{g_{1a}m_{1a} + g_{2a}m_{2a}\}$$
$$\mathfrak{X}[\gamma_5^{(8)}(t_{2g}) \longrightarrow \gamma_5^{(8)'}(e_g)] = {}^1/_6\{g_{1a}^2 + g_{2a}^2\}$$
$$\mathfrak{M}[\gamma_5^{(8)}(t_{2g}) \longrightarrow \gamma_5^{(8)'}(e_g)] = {}^1/_6\{m_{1a}^2 + m_{2a}^2\}$$
$$\mathfrak{W}[\gamma_5^{(8)}(t_{2g}) \longrightarrow \gamma_5^{(8)}(e_g)] = {}^2/_3g_{0b}m_{0b} + {}^1/_6g_{1b}m_{1b} + {}^1/_6g_{2b}m_{2b}$$

$$\mathfrak{X}[\gamma_5^{(8)}(t_{2g}) \longrightarrow \gamma_5^{(8)}(e_g)] = {}^2/_3g_{0b}^2 + {}^1/_6g_{1b}^2 + {}^1/_6g_{2b}^2$$
$$\mathfrak{M}[\gamma_5^{(8)}(t_{2g}) \longrightarrow \gamma_5^{(8)}(e_g)] = {}^2/_3m_{0b}^2 + {}^1/_6m_{1b}^2 + {}^1/_6m_{2b}^2$$
$$\mathfrak{W}[\gamma_5^{(8)'}(e_g) \longrightarrow \gamma_5^{(8)'}(e_g)] = \mathfrak{X}[\gamma_5^{(8)'}(e_g) \longrightarrow \gamma_5^{(8)'}(e_g)] = 0$$

$$\mathfrak{M}[\gamma_5^{(8)'}(e_g) \longrightarrow \gamma_5^{(8)'}(e_g)] = 3\mu_B^2$$
$$\mathfrak{W}[\gamma_5^{(8)'}(e_g) \longrightarrow \gamma_5^{(8)}(e_g)] = \bar{\bar{g}}_0\bar{\bar{m}}_0$$
$$\mathfrak{X}[\gamma_5^{(8)'}(e_g) \longrightarrow \gamma_5^{(8)}(e_g)] = \bar{\bar{g}}_0^2$$
$$\mathfrak{M}[\gamma_5^{(8)'}(e_g) \longrightarrow \gamma_5^{(8)}(e_g)] = \bar{\bar{m}}_0^2$$
$$\mathfrak{W}[\gamma_5^{(8)}(e_g) \longrightarrow \gamma_5^{(8)}(e_g)] = \mathfrak{X}[\gamma_5^{(8)}(e_g) \longrightarrow \gamma_5^{(8)}(e_g)] = 0$$

$$\mathfrak{M}[\gamma_5^{(8)}(e_g) \longrightarrow \gamma_5^{(8)}(e_g)] = 3\mu_B^2$$
$$\mathfrak{W}[\gamma_5^{(8)'}(t_{2g}) \longrightarrow \gamma_5^{(8)'}(t_{2g})] = 0 \text{ or } \bar{p}_{0a}(\bar{m}_{0a} - \mu_B)$$
$$\mathfrak{X}[\gamma_5^{(8)'}(t_{2g}) \longrightarrow \gamma_5^{(8)'}(t_{2g})] = 0 \text{ or } \bar{p}_{0a}^2$$
$$\mathfrak{M}[\gamma_5^{(8)'}(t_{2g}) \longrightarrow \gamma_5^{(8)'}(t_{2g})] = (\bar{m}_{0a} - \mu_B)^2$$
$$\mathfrak{W}[\gamma_5^{(7)}(t_{2g}) \longrightarrow \gamma_5^{(7)}(t_{2g})] = 0 \text{ or } {}^2/_9\{\bar{p}_{0a}(2\bar{m}_{0a} + \mu_B) + \bar{p}_{0b}(2\bar{m}_{0b} + \mu_B) + \bar{p}_{0c}(2\bar{m}_{0c} + \mu_B)\}$$

$$\mathfrak{X}[\gamma_5^{(7)}(t_{2g}) \longrightarrow \gamma_5^{(7)}(t_{2g})] = 0 \text{ or } {}^4/_9\{\bar{p}_{0a}^2 + \bar{p}_{0b}^2 + \bar{p}_{0c}^2\}$$
$$\mathfrak{M}[\gamma_5^{(7)}(t_{2g}) \longrightarrow \gamma_5^{(7)}(t_{2g})] = {}^1/_9\{(2\bar{m}_{0a} + \mu_B)^2 + (2\bar{m}_{0b} + \mu_B)^2 + (2\bar{m}_{0c} + \mu_B)^2\}$$

$$\mathfrak{W}[\gamma_5^{(8)}(t_{2g}) \longrightarrow \gamma_5^{(8)}(t_{2g})] = 0 \text{ or } {}^1/_9\bar{p}_{0a}(\bar{m}_{0a} - \mu_B) + {}^4/_9\bar{p}_{0b}(\bar{m}_{0b} - \mu_B) + {}^4/_9\bar{p}_{0c}(\bar{m}_{0c} - \mu_B)$$

$$\mathfrak{X}[\gamma_5^{(8)}(t_{2g}) \longrightarrow \gamma_5^{(8)}(t_{2g})] = 0 \text{ or } {}^1/_9\bar{p}_{0a}^2 + {}^4/_9\bar{p}_{0b}^2 + {}^4/_9\bar{p}_{0c}^2$$
$$\mathfrak{M}[\gamma_5^{(8)}(t_{2g}) \longrightarrow \gamma_5^{(8)}(t_{2g})] = {}^1/_9(\bar{m}_{0a} - \mu_B)^2 + {}^4/_9(\bar{m}_{0b} - \mu_B)^2 + {}^4/_9(\bar{m}_{0c} - \mu_B)^2 \quad (26)$$

(*c*) *Configuration Interaction: Zero and Nonzero Spin-Orbit Forces.* The admission of configuration interaction to eq. 24, 25, and 26 proceeds identically as in ref. 6. Note though that no essential alteration of eq. 24 is engendered by so doing, in sharp contrast to eq. 25 and 26.

3.3 *Dissymmetry Factors.* The apropos dissymmetry factors with and without configuration interaction for both zero and nonzero spin-orbit forces are easily fabricated from their definition

$$G_{ab} = 4\frac{\nu}{\nu_{ab}}\frac{\mathfrak{R}_{ab}}{\mathfrak{S}_{ab}} = 8\pi\frac{m\nu}{e}\frac{\mathfrak{P}_{ab}}{\mathfrak{O}_{ab}} \quad (27)$$

and from eq. 24, 25, and 26, and hence need not be listed here.[18]

III. Applications

§4. The Many-Electron Systems: Wave Functions and Matrix Elements

4.1 *The One- and Nine-Electron Case.* The apt rotatory and refractory parameters for one-electron systems have already been put down in eq. 17 through 26. Hence, the nine-electron case is all that need be attended at this instance. The fit orbital wave functions are

(*a*) *No Configuration Interaction: Zero Spin-Orbit Forces.* (*i*) *Wave Functions: One Electron*

$$^2A[^2T_{2g}(t_{2g}^1)]:a$$
$$^2B_{(\frac{2}{3})}[^2T_{2g}(t_{2g}^1)]:(\pm)b_{(\frac{2}{3})}$$
$$^2A[^2E_g(e_g^1)]:a^*$$
$$^2B_1[^2E_g(e_g^1)]:b_1 \quad (28)$$

(*ii*) *Wave Functions: Nine Electrons*

$$^2A[^2E_g(t_{2g}^6e_g^3)]:|b_2\bar{b}_2b_3\bar{b}_3a\bar{a}a^*\bar{b}_1b_1|$$
$$^2B_1[^2E_g(t_{2g}^6e_g^3)]:|b_2\bar{b}_2b_3\bar{b}_3a\bar{a}a^*\bar{a}^*b_1|$$
$$^2A[^2T_{2g}(t_{2g}^5e_g^4)]:|b_2\bar{b}_2b_3\bar{b}_3aa^*\bar{a}^*b_1\bar{b}_1|$$
$$^2B_{(\frac{2}{3})}[^2T_{2g}(t_{2g}^5e_g^4)]:|b_2b_3\bar{b}_{(\frac{2}{3})}a\bar{a}a^*\bar{a}^*b_1\bar{b}_1| \quad (29)$$

(18) Note in passing that the specific integral expressions of ref. 6 for $\mathfrak{R}_{ab}$, $\mathfrak{S}_{ab}$, and G_{ab}, ref. 6, eq. 47, 49, 52, 53, 54, 55, 58, 60, 61, and 62, may be facilely metamorphosed into a catholic form parallel to eq. 24, 25, and 26 of this article by the simple use of the ecumenical matrix definitions and their special structures of ref. 6, footnote 49. Read Appendix, section XII, §6, of the present work.

where in eq. 28 and 29 the spin function $\zeta(+1/2)$ is appended to a molecular orbital on its initial appearance in a determinant and the spin function $\zeta(-1/2)$ (indicated by an overhead bar) on its last. An itemization of the wanted matrix components with these functions demonstrates that the nine- and one-electron situations are connected as follows.

(iii) Matrix Elements: One Electron

$$\left\langle {}^2B_{(\frac{2}{3})}[{}^2T_{2g}(t_{2g}{}^1)] \left|\frac{\vec{p}}{\vec{m}}\right| {}^2A[{}^2T_{2g}(t_{2g}{}^1)] \right\rangle = (\pm)\left\langle b_{(\frac{2}{3})} \left|\frac{\vec{p}}{\vec{m}}\right| a \right\rangle$$

$$\left\langle {}^2B_{(\frac{2}{3})}[{}^2T_{2g}(t_{2g}{}^1)] \left|\frac{\vec{p}}{\vec{m}}\right| {}^2A[{}^2E_g(e_g{}^1)] \right\rangle = (\pm)\left\langle b_{(\frac{2}{3})} \left|\frac{\vec{p}}{\vec{m}}\right| a^\star \right\rangle$$

$$\left\langle {}^2B_{(\frac{2}{3})}[{}^2T_{2g}(t_{2g}{}^1)] \left|\frac{\vec{p}}{\vec{m}}\right| {}^2B_1[{}^2E_g(e_g{}^1)] \right\rangle = (\pm)\left\langle b_{(\frac{2}{3})} \left|\frac{\vec{p}}{\vec{m}}\right| b_1 \right\rangle$$

$$\left\langle {}^2A[{}^2T_{2g}(t_{2g}{}^1)] \left|\frac{\vec{p}}{\vec{m}}\right| {}^2A[{}^2E_g(e_g{}^1)] \right\rangle \equiv 0$$

$$\left\langle {}^2A[{}^2T_{2g}(t_{2g}{}^1)] \left|\frac{\vec{p}}{\vec{m}}\right| {}^2B_1[{}^2E_g(e_g{}^1)] \right\rangle = \left\langle a \left|\frac{\vec{p}}{\vec{m}}\right| b_1 \right\rangle$$

$$\left\langle {}^2A[{}^2E_g(e_g{}^1)] \left|\frac{\vec{p}}{\vec{m}}\right| {}^2B_1[{}^2E_g(e_g{}^1)] \right\rangle = \left\langle a^\star \left|\frac{\vec{p}}{\vec{m}}\right| b_1 \right\rangle \qquad (30)$$

(iv) Matrix Elements: Nine Electrons

$$\left\langle {}^2B_1[{}^2E_g(t_{2g}{}^6e_g{}^3)] \left|\frac{\vec{p}}{\vec{m}}\right| {}^2A[{}^2E_g(t_{2g}{}^6e_g{}^3)] \right\rangle = -\left\langle a^\star \left|\frac{\vec{p}}{\vec{m}}\right| b_1 \right\rangle$$

$$\left\langle {}^2B_1[{}^2E_g(t_{2g}{}^6e_g{}^3)] \left|\frac{\vec{p}}{\vec{m}}\right| {}^2A[{}^2T_{2g}(t_{2g}{}^5e_g{}^4)] \right\rangle = -\left\langle a \left|\frac{\vec{p}}{\vec{m}}\right| b_1 \right\rangle$$

$$\left\langle {}^2B_1[{}^2E_g(t_{2g}{}^6e_g{}^3)] \left|\frac{\vec{p}}{\vec{m}}\right| {}^2B_{(\frac{2}{3})}[{}^2T_{2g}(t_{2g}{}^5e_g{}^4)] \right\rangle = (\mp)\left\langle b_{(\frac{2}{3})} \left|\frac{\vec{p}}{\vec{m}}\right| b_1 \right\rangle$$

$$\left\langle {}^2A[{}^2E_g(t_{2g}{}^6e_g{}^3)] \left|\frac{\vec{p}}{\vec{m}}\right| {}^2A[{}^2T_{2g}(t_{2g}{}^5e_g{}^4)] \right\rangle \equiv 0$$

$$\left\langle {}^2A[{}^2E_g(t_{2g}{}^6e_g{}^3)] \left|\frac{\vec{p}}{\vec{m}}\right| {}^2B_{(\frac{2}{3})}[{}^2T_{2g}(t_{2g}{}^5e_g{}^4)] \right\rangle = (\mp)\left\langle b_{(\frac{2}{3})} \left|\frac{\vec{p}}{\vec{m}}\right| a^\star \right\rangle$$

$$\left\langle {}^2A[{}^2T_{2g}(t_{2g}{}^5e_g{}^4)] \left|\frac{\vec{p}}{\vec{m}}\right| {}^2B_{(\frac{2}{3})}[{}^2T_{2g}(t_{2g}{}^5e_g{}^4)] \right\rangle = (\mp)\left\langle b_{(\frac{2}{3})} \left|\frac{\vec{p}}{\vec{m}}\right| a \right\rangle \qquad (31)$$

Due to the broad correspondence of the forecasts which can be promulgated on the basis of eq. 31 to those which can be promulgated on the basis of the nonzero spin-orbit force equation, eq. 34 of the next paragraph ,§4.1b, we shall postpone consideration of the issuance of this equation till after eq. 34 of that paragraph, and there present a concurrent inquisition of the one- and nine-electron orbital and spin-orbital prophecies.

(b) No Configuration Interaction: Nonzero Spin-Orbit Forces. The proper spin-orbit wave functions are as succeeds.

(i) Wave Functions: One Electron

$$\Gamma_{5(\frac{a}{b})}[\Gamma_{8(\frac{a}{b})}({}^2T_{2g})] : \gamma_{5(\frac{a}{b})}{}^{(8)}(t_{2g})$$

$$\Gamma_{5(\frac{a}{b})}[\Gamma_{8(\frac{c}{d})}({}^2T_{2g})] : \gamma_{5(\frac{c}{b})}{}^{(8)'}(t_{2g})$$

$$\Gamma_{5(\frac{a}{b})}[\Gamma_{7(\frac{a}{b})}({}^2T_g)] : \gamma_{5(\frac{a}{b})}{}^{(7)}(t_{2g})$$

$$\Gamma_{5(\frac{a}{b})}[\Gamma_{8(\frac{a}{b})}({}^2E_g)] : \gamma_{5(\frac{a}{b})}{}^{(8)}(e_g)$$

$$\Gamma_{5(\frac{a}{b})}(\Gamma_{8(\frac{c}{d})}({}^2E_g)] : \gamma_{5(\frac{a}{b})}{}^{(8)'}(e_g) \qquad (32)$$

In eq. 32 and 33 the molecular spin orbital $\gamma_{5a}(t_{2g}$ or $e_g)$ has been put ahead of $\gamma_{5b}(t_{2g}$ or $e_g)$. A chronicle of the required matrix parts with these functions manifests that the nine- and one-electron electron situations are tied as shown.

(ii) Wave Functions: Nine Electrons

$$\Gamma_{5(\frac{a}{b})}[\Gamma_{8(\frac{c}{d})}({}^2E_g)] : |\gamma_5{}^{(8)}(t_{2g})^2\gamma_5{}^{(8)'}(t_{2g})^2\gamma_5{}^{(7)}(t_{2g})^2\gamma_5{}^{(8)}(e_g)^2\gamma_{5(\frac{a}{b})}{}^{(8)'}(e_g)^1|$$

$$\Gamma_{5(\frac{a}{b})}[\Gamma_{8(\frac{a}{b})}({}^2E_g)] : |\gamma_5{}^{(8)}(t_{2g})^2\gamma_5{}^{(8)'}(t_{2g})^2\gamma_5{}^{(7)}(t_{2g})^2\gamma_{5(\frac{a}{b})}{}^{(8)}(e_g)^1\gamma_5{}^{(8)'}(e_g)^2|$$

$$\Gamma_{5(\frac{a}{b})}[\Gamma_{7(\frac{a}{b})}({}^2T_{2g})] : \gamma_5{}^{(8)}(t_{2g})^2\gamma_5{}^{(8)'}(t_{2g})^2\gamma_{5(\frac{a}{b})}{}^{(7)}(t_{2g})^1\gamma_5{}^{(8)}(e_g)^2\gamma_5{}^{(8)'}(e_g)^2|$$

$$\Gamma_{5(\frac{a}{b})}[\Gamma_{8(\frac{c}{d})}({}^2T_{2g})] : \gamma_5{}^{(8)}(t_{2g})^2\gamma_{5(\frac{a}{b})}{}^{(8)'}(t_{2g})^1\gamma_5{}^{(7)}(t_{2g})^2\gamma_5{}^{(8)}(e_g)^2\gamma_5{}^{(8)'}(e_g)^2|$$

$$\Gamma_{5(\frac{a}{b})}[\Gamma_{8(\frac{a}{b})}({}^2T_{2g})] : |\gamma_{5(\frac{a}{b})}{}^{(8)}(t_{2g})^1\gamma_5{}^{(8)'}(t_{2g})^2\gamma_5{}^{(7)}(t_{2g})^2\gamma_5{}^{(8)}(e_g)^2\gamma_5{}^{(8)'}(e_g)^2| \qquad (33)$$

(*iii*) *Matrix Elements: One Electron.* These are the same as eq. 20.

(*iv*) *Matrix Elements: Nine Electrons*

$$\left\langle \Gamma_{5(^{a}_{b})}[\Gamma_{8(^{c}_{d})}(^{2}E_{g})] \left| \frac{\vec{p}}{\vec{m}} \right| \Gamma_{5(^{a}_{b})}[\Gamma_{8(^{c}_{d})}(^{2}E_{g})] \right\rangle = \left\langle \gamma_{5(^{a}_{b})}{}^{(8)'}(e_g) \left| \frac{\vec{p}}{\vec{m}} \right| \gamma_{5(^{a}_{b})}{}^{(8)'}(e_g) \right\rangle$$

$$\left\langle \Gamma_{5(^{a}_{b})}[\Gamma_{8(^{c}_{d})}(^{2}E_{g})] \left| \frac{\vec{p}}{\vec{m}} \right| \Gamma_{5(^{b}_{a})}[\Gamma_{8(^{d}_{c})}(^{2}E_{g})] \right\rangle = \left\langle \gamma_{5(^{a}_{b})}{}^{(8)'}(e_g) \left| \frac{\vec{p}}{\vec{m}} \right| \gamma_{5(^{b}_{a})}{}^{(8)'}(e_g) \right\rangle$$

$$\left\langle \Gamma_{5(^{a}_{b})}[\Gamma_{8(^{c}_{d})}(^{2}E_{g})] \left| \frac{\vec{p}}{\vec{m}} \right| \Gamma_{5(^{a}_{b})}[\Gamma_{8(^{a}_{b})}(^{2}E_{g})] \right\rangle = -\left\langle \gamma_{5(^{b}_{a})}{}^{(8)}(e_g) \left| \frac{\vec{p}}{\vec{m}} \right| \gamma_{5(^{b}_{a})}{}^{(8)'}(e_g) \right\rangle$$

$$\left\langle \Gamma_{5(^{a}_{b})}[\Gamma_{8(^{c}_{d})}(^{2}E_{g})] \left| \frac{\vec{p}}{\vec{m}} \right| \Gamma_{5(^{b}_{a})}[\Gamma_{8(^{b}_{a})}(^{2}E_{g})] \right\rangle = \left\langle \gamma_{5(^{a}_{b})}{}^{(8)}(e_g) \left| \frac{\vec{p}}{\vec{m}} \right| \gamma_{5(^{b}_{a})}{}^{(8)'}(e_g) \right\rangle$$

$$\left\langle \Gamma_{5(^{a}_{b})}[\Gamma_{8(^{c}_{d})}(^{2}E_{g})] \left| \frac{\vec{p}}{\vec{m}} \right| \Gamma_{5(^{a}_{b})}[\Gamma_{7(^{a}_{b})}(^{2}T_{2g})] \right\rangle = -\left\langle \gamma_{5(^{b}_{a})}{}^{(7)}(t_{2g}) \left| \frac{\vec{p}}{\vec{m}} \right| \gamma_{5(^{b}_{a})}{}^{(8)'}(e_g) \right\rangle$$

$$\left\langle \Gamma_{5(^{a}_{b})}[\Gamma_{8(^{c}_{d})}(^{2}E_{g})] \left| \frac{\vec{p}}{\vec{m}} \right| \Gamma_{5(^{b}_{a})}[\Gamma_{7(^{b}_{a})}(^{2}T_{2g})] \right\rangle = \left\langle \gamma_{5(^{a}_{b})}{}^{(7)}(t_{2g}) \left| \frac{\vec{p}}{\vec{m}} \right| \gamma_{5(^{b}_{a})}{}^{(8)'}(e_g) \right\rangle$$

$$\left\langle \Gamma_{5(^{a}_{b})}[\Gamma_{8(^{c}_{d})}(^{2}E_{g})] \left| \frac{\vec{p}}{\vec{m}} \right| \Gamma_{5(^{a}_{b})}[\Gamma_{8(^{a}_{b})}(^{2}T_{2g})] \right\rangle = -\left\langle \gamma_{5(^{b}_{a})}{}^{(8)'}(t_{2g}) \left| \frac{\vec{p}}{\vec{m}} \right| \gamma_{5(^{b}_{a})}{}^{(8)'}(e_g) \right\rangle$$

$$\left\langle \Gamma_{5(^{a}_{b})}[\Gamma_{8(^{c}_{d})}(^{2}E_{g})] \left| \frac{\vec{p}}{\vec{m}} \right| \Gamma_{5(^{b}_{a})}[\Gamma_{8(^{d}_{c})}(^{2}T_{2g})] \right\rangle = \left\langle \gamma_{5(^{a}_{b})}{}^{(8)'}(t_{2g}) \left| \frac{\vec{p}}{\vec{m}} \right| \gamma_{5(^{a}_{b})}{}^{(8)'}(e_g) \right\rangle$$

$$\left\langle \Gamma_{5(^{a}_{b})}[\Gamma_{8(^{c}_{d})}(^{2}E_{g})] \left| \frac{\vec{p}}{\vec{m}} \right| \Gamma_{5(^{a}_{b})}[\Gamma_{8(^{a}_{b})}(^{2}T_{2g})] \right\rangle = -\left\langle \gamma_{5(^{b}_{a})}{}^{(8)}(t_{2g}) \left| \frac{\vec{p}}{\vec{m}} \right| \gamma_{5(^{b}_{a})}{}^{(8)'}(e_g) \right\rangle$$

$$\left\langle \Gamma_{5(^{a}_{b})}[\Gamma_{8(^{c}_{d})}(^{2}E_{g})] \left| \frac{\vec{p}}{\vec{m}} \right| \Gamma_{5(^{b}_{a})}[\Gamma_{8(^{b}_{a})}(^{2}T_{2g})] \right\rangle = \left\langle \gamma_{5(^{a}_{b})}{}^{(8)}(t_{2g}) \left| \frac{\vec{p}}{\vec{m}} \right| \gamma_{5(^{b}_{a})}{}^{(8)'}(e_g) \right\rangle$$

$$\left\langle \Gamma_{5(^{a}_{b})}[\Gamma_{8(^{a}_{b})}(^{2}E_{g})] \left| \frac{\vec{p}}{\vec{m}} \right| \Gamma_{5(^{a}_{b})}[\Gamma_{8(^{a}_{b})}(^{2}E_{g})] \right\rangle = \left\langle \gamma_{5(^{a}_{b})}{}^{(8)}(e_g) \left| \frac{\vec{p}}{\vec{m}} \right| \gamma_{5(^{a}_{b})}{}^{(8)}(e_g) \right\rangle$$

$$\left\langle \Gamma_{5(^{a}_{b})}[\Gamma_{8(^{a}_{b})}(^{2}E_{g})] \left| \frac{\vec{p}}{\vec{m}} \right| \Gamma_{5(^{b}_{a})}[\Gamma_{8(^{b}_{a})}(^{2}E_{g})] \right\rangle = \left\langle \gamma_{5(^{a}_{b})}{}^{(8)}(e_g) \left| \frac{\vec{p}}{\vec{m}} \right| \gamma_{5(^{b}_{a})}{}^{(8)}(e_g) \right\rangle$$

$$\left\langle \Gamma_{5(^{a}_{b})}[\Gamma_{8(^{a}_{b})}(^{2}E_{g})] \left| \frac{\vec{p}}{\vec{m}} \right| \Gamma_{5(^{a}_{b})}[\Gamma_{7(^{a}_{b})}(^{2}T_{2g})] \right\rangle = -\left\langle \gamma_{5(^{b}_{a})}{}^{(7)}(t_{2g}) \left| \frac{\vec{p}}{\vec{m}} \right| \gamma_{5(^{b}_{a})}{}^{(8)}(e_g) \right\rangle$$

$$\left\langle \Gamma_{5(^{a}_{b})}[\Gamma_{8(^{a}_{b})}(^{2}E_{g})] \left| \frac{\vec{p}}{\vec{m}} \right| \Gamma_{5(^{b}_{a})}[\Gamma_{7(^{b}_{a})}(^{2}T_{2g})] \right\rangle = \left\langle \gamma_{5(^{a}_{b})}{}^{(7)}(t_{2g}) \left| \frac{\vec{p}}{\vec{m}} \right| \gamma_{5(^{b}_{a})}{}^{(8)}(e_g) \right\rangle$$

$$\left\langle \Gamma_{5(^{a}_{b})}[\Gamma_{8(^{a}_{b})}(^{2}E_{g})] \left| \frac{\vec{p}}{\vec{m}} \right| \Gamma_{5(^{a}_{b})}[\Gamma_{8(^{c}_{d})}(^{2}T_{2g})] \right\rangle = -\left\langle \gamma_{5(^{b}_{a})}{}^{(8)'}(t_{2g}) \left| \frac{\vec{p}}{\vec{m}} \right| \gamma_{5(^{b}_{a})}{}^{(8)}(e_g) \right\rangle$$

$$\left\langle \Gamma_{5(^{a}_{b})}[\Gamma_{8(^{b}_{a})}(^{2}E_{g})] \left| \frac{\vec{p}}{\vec{m}} \right| \Gamma_{5(^{b}_{a})}[\Gamma_{8(^{d}_{c})}(^{2}T_{2g})] \right\rangle = \left\langle \gamma_{5(^{a}_{b})}{}^{(8)'}(t_{2g}) \left| \frac{\vec{p}}{\vec{m}} \right| \gamma_{5(^{b}_{a})}{}^{(8)}(e_g) \right\rangle$$

$$\left\langle \Gamma_{5(^{a}_{b})}[\Gamma_{8(^{a}_{b})}(^{2}E_{g})] \left| \frac{\vec{p}}{\vec{m}} \right| \Gamma_{5(^{a}_{b})}[\Gamma_{8(^{a}_{b})}(^{2}T_{2g})] \right\rangle = -\left\langle \gamma_{5(^{b}_{a})}{}^{(8)}(t_{2g}) \left| \frac{\vec{p}}{\vec{m}} \right| \gamma_{5(^{b}_{a})}{}^{(8)}(e_g) \right\rangle$$

$$\left\langle \Gamma_{5(^{a}_{b})}[\Gamma_{8(^{b}_{a})}(^{2}E_{g})] \left| \frac{\vec{p}}{\vec{m}} \right| \Gamma_{5(^{b}_{a})}[\Gamma_{8(^{b}_{a})}(^{2}T_{2g})] \right\rangle = \left\langle \gamma_{5(^{a}_{b})}{}^{(8)}(t_{2g}) \left| \frac{\vec{p}}{\vec{m}} \right| \gamma_{5(^{b}_{a})}{}^{(8)}(e_g) \right\rangle$$

$$\left\langle \Gamma_{5(^{a}_{b})}[\Gamma_{7(b)}(^{2}T_{2g})] \left| \frac{\vec{p}}{\vec{m}} \right| \Gamma_{5(^{a}_{b})}[\Gamma_{7(^{a}_{b})}(^{2}T_{2g})] \right\rangle = \left\langle \gamma_{5(^{a}_{b})}{}^{(7)}(t_{2g}) \left| \frac{\vec{p}}{\vec{m}} \right| \gamma_{5(^{a}_{b})}{}^{(7)}(t_{2g}) \right\rangle$$

$$\left\langle \Gamma_{5(^{a}_{b})}[\Gamma_{7(^{b}_{a})}(^{2}T_{2g})] \left| \frac{\vec{p}}{\vec{m}} \right| \Gamma_{5(^{b}_{a})}[\Gamma_{7(^{b}_{a})}(^{2}T_{2g})] \right\rangle = \left\langle \gamma_{5(^{a}_{b})}{}^{(7)}(t_{2g}) \left| \frac{\vec{p}}{\vec{m}} \right| \gamma_{5(^{b}_{a})}{}^{(7)}(t_{2g}) \right\rangle$$

$$\left\langle \Gamma_{5(^{a}_{b})}[\Gamma_{7(^{b}_{a})}(^{2}T_{2g})] \left| \frac{\vec{p}}{\vec{m}} \right| \Gamma_{5(^{b}_{a})}[\Gamma_{8(^{c}_{d})}(^{2}T_{2g})] \right\rangle = -\left\langle \gamma_{5(^{b}_{a})}{}^{(8)'}(t_{2g}) \left| \frac{\vec{p}}{\vec{m}} \right| \gamma_{5(^{a}_{b})}{}^{(7)}(t_{2g}) \right\rangle$$

$$\left\langle \Gamma_{5(b)}^{(a)}[\Gamma_{7(b)}^{(a)}(^2T_{2g})] \left|\frac{\vec{p}}{\vec{m}}\right| \Gamma_{5(a)}^{(b)}[\Gamma_{8(c)}^{(d)}(^2T_{2g})] \right\rangle = \left\langle \gamma_{5(b)}^{(a)(8)'}(t_{2g}) \left|\frac{\vec{p}}{\vec{m}}\right| \gamma_{5(a)}^{(b)(7)}(t_{2g}) \right\rangle$$

$$\left\langle \Gamma_{5(b)}^{(a)}[\Gamma_{7(b)}^{(a)}(^2T_{2g})] \left|\frac{\vec{p}}{\vec{m}}\right| \Gamma_{5(b)}^{(a)}[\Gamma_{8(b)}^{(a)}(^2T_{2g})] \right\rangle = -\left\langle \gamma_{5(a)}^{(b)(\xi)}(t_{2g}) \left|\frac{\vec{p}}{\vec{m}}\right| \gamma_{5(a)}^{(b)(7)}(t_{2g}) \right\rangle$$

$$\left\langle \Gamma_{5(b)}^{(a)}[\Gamma_{7(b)}^{(a)}(^2T_{2g})] \left|\frac{\vec{p}}{\vec{m}}\right| \Gamma_{5(a)}^{(b)}[\Gamma_{8(a)}^{(b)}(^2T_{2g})] \right\rangle = \left\langle \gamma_{5(b)}^{(a)(3)}(t_{2g}) \left|\frac{\vec{p}}{\vec{m}}\right| \gamma_{5(a)}^{(b)(7)}(t_{2g}) \right\rangle$$

$$\left\langle \Gamma_{5(b)}^{(a)}[\Gamma_{8(d)}^{(c)}(^2T_{2g})] \left|\frac{\vec{p}}{\vec{m}}\right| \Gamma_{5(h)}^{(a)}[\Gamma_{8(d)}^{(c)}(^2T_{2g})] \right\rangle = \left\langle \gamma_{5(b)}^{(a)(8)'}(t_{2g}) \left|\frac{\vec{p}}{\vec{m}}\right| \gamma_{5(b)}^{(a)(8)'}(t_{2g}) \right\rangle$$

$$\left\langle \Gamma_{5(b)}^{(a)}[\Gamma_{8(d)}^{(c)}(^2T_{2g})] \left|\frac{\vec{p}}{\vec{m}}\right| \Gamma_{5(a)}^{(b)}[\Gamma_{8(c)}^{(d)}(^2T_{2g})] \right\rangle = \left\langle \gamma_{5(b)}^{(a)(8)'}(t_{2g}) \left|\frac{\vec{p}}{\vec{m}}\right| \gamma_{5(a)}^{(b)(8)'}(t_{2g}) \right\rangle$$

$$\left\langle \Gamma_{5(b)}^{(a)}[\Gamma_{8(d)}^{(c)}(^2T_{2g})] \left|\frac{\vec{p}}{\vec{m}}\right| \Gamma_{5(b)}^{(a)}[\Gamma_{8(b)}^{(a)}(^2T_{2g})] \right\rangle = -\left\langle \gamma_{5(a)}^{(b)(3)}(t_{2g}) \left|\frac{\vec{p}}{\vec{m}}\right| \gamma_{5(a)}^{(b)(8)'}(t_{2g}) \right\rangle$$

$$\left\langle \Gamma_{5(b)}^{(a)}[\Gamma_{8(d)}^{(c)}(^2T_{2g})] \left|\frac{\vec{p}}{\vec{m}}\right| \Gamma_{5(a)}^{(b)}[\Gamma_{8(b)}^{(a)}(^2T_{2g})] \right\rangle = \left\langle \gamma_{5(b)}^{(a)(8)}(t_{2g}) \left|\frac{\vec{p}}{\vec{m}}\right| \gamma_{5(a)}^{(b)(8)'}(t_{2g}) \right\rangle$$

$$\left\langle \Gamma_{5(b)}^{(a)}[\Gamma_{8(b)}^{(a)}(^2T_{2g})] \left|\frac{\vec{p}}{\vec{m}}\right| \Gamma_{5(b)}^{(a)}[\Gamma_{8(b)}^{(a)}(^2T_{2g})] \right\rangle = \left\langle \gamma_{5(b)}^{(a)(8)}(t_{2g}) \left|\frac{\vec{p}}{\vec{m}}\right| \gamma_{5(b)}^{(a)(8)}(t_{2g}) \right\rangle$$

$$\left\langle \Gamma_{5(b)}^{(a)}[\Gamma_{8(b)}^{(a)}(^2T_{2g})] \left|\frac{\vec{p}}{\vec{m}}\right| \Gamma_{5(a)}^{(b)}[\Gamma_{8(a)}^{(b)}(^2T_{2g})] \right\rangle = \left\langle \gamma_{5(a)}^{(b)(8)}(t_{2g}) \left|\frac{\vec{p}}{\vec{m}}\right| \gamma_{5(b)}^{(a)(8)}(t_{2g}) \right\rangle \quad (34)$$

The injection of eq. 31 and 34 into eq. 22, 23, and 27 exhibits that the one- and nine-electron digonal rotational and spectral strengths are directly coupled in the *selfsame* manner as were correspondent trigonal strengths [compare ref. 6, Fig. 14 and the present Fig. 21]. The association is not happenstance, but is a firm consequence of the one-electron character of the matrix operators $\vec{p}$ and $\vec{m}$. This occurrence and its implications will be discussed at length in section IV. The nine-electron rotational and spectral strengths, with apropos notational modifications of the bracketed transition states, are given by eq. 24, 25, 26, and 27.

4.2 *The Two- and Eight-Electron Case.* As in ref. 6, we confine attention to singly excited electronic configurations solely, with no penalty of lost generality. The wave functions of concerns are then as stamped underneath.[19]

(*a*) *No Configuration Interaction: Zero Spin-Orbit Forces.* (*i*) *Wave Functions: Two Electrons*

$$^3B_1[^3T_{1g}(t_{2g}^2)]: |b_2b_3|$$

$$^3B_{(\frac{2}{3})}[^3T_{1g}(t_{2g}^2)]: |b_{(\frac{2}{3})}a|$$

$$^3B_1[^3T_{1g}(t_{2g}e_g)]: |ab_1|$$

$$^3B_{(\frac{2}{3})}[^3T_{1g}(t_{2g}e_g)]: (\mp)^1/_2\{\sqrt{3}|b_{(\frac{2}{3})}a^*| - |b_{(\frac{3}{2})}b_1|\}$$

$$^3A[^3T_{2g}(t_{2g}e_g)]: |aa^*|$$

$$^3B_{(\frac{2}{3})}[^3T_{2g}(t_{2g}e_g)]: (\mp)^1/_2\{|b_{(\frac{2}{3})}a^*| + \sqrt{3}|b_{(\frac{3}{2})}b_1|\}$$

$$^3B_1[^3A_{2g}(e_g^2)]: |a^*b_1|$$

$$^1A[^1T_{2g}(t_{2g}^2)]: \frac{1}{\sqrt{2}}\{|b_2\bar{b}_2| - |b_3\bar{b}_3|\}$$

$$^1B_{(\frac{2}{3})}[^1T_{2g}(t_{2g}^2)]: \frac{1}{\sqrt{2}}\{|b_{(\frac{2}{3})}\bar{a}| - |\bar{b}_{(\frac{2}{3})}a|\}$$

$$^1A[^1E_g(t_{2g}^2)]: \frac{1}{\sqrt{6}}\{2|a\bar{a}| - |b_2\bar{b}_2| - |b_3\bar{b}_3|\}$$

$$^1B_1[^1E_g(t_{2g}^2)]: -\frac{1}{\sqrt{2}}\{|b_2\bar{b}_3| - |\bar{b}_2b_3|\}$$

$$^1A[^1A_{1g}(t_{2g}^2)]: \frac{1}{\sqrt{3}}\{|b_3\bar{b}_2| + |b_2\bar{b}_3| + |a\bar{a}|\} \quad (35)$$

(19) The digonal wave functions both here and elsewhere (inclusive of the one- and nine-electron functions) have all been manufactured as outlined in ref. 6, footnotes 38 and 43. The functions are octahedrally oriented with respect to $\mathcal{C}_4(z'$ or $z)$ such that $\mathcal{C}_3(x' = y' = z')$ internally permutes the triply degenerate species T_1 and T_2 and transforms the doubly degenerate species E in a fashion identical with that for the atomic-like orbitals s, $p_{x',y',z'}$, and $d_{x'^2-y'^2}$, $d_{3z'^2-r^2}$, $d_{x'y'}$, $d_{x'z'}$, and $d_{y'z'}$. The functions are subsequently digonally oriented with respect to $\mathcal{C}_2(x)$. As an instance, we elect $\mathcal{C}_4(z'$ or $z)$ $T_{(\frac{1}{2})a}$ to equal $(\pm)T_{(\frac{1}{2})a}$ and $\mathcal{C}_3(x' = y' = z')$ $T_{(\frac{1}{2})a,b,c}$ to equal $T_{(\frac{1}{2})b,c,a}$, so that T_{1a}, $\sqrt{1/2}\{T_{1c} \pm T_{1b}\}$ and T_{2a}, $\sqrt{1/2}\{T_{2c} \pm T_{2b}\}$ under $\mathcal{C}_2(x)$ behave as B_1, $B_{(\frac{2}{3})}$ and A, $B_{(\frac{2}{3})}$, individually; and we elect $\mathcal{C}_4(z'$ or $z)$ $E_{(\frac{a}{b})}$ to equal $\pm E_{(\frac{a}{b})}$ and $\mathcal{C}_3(x' = y' = z')$ $E_{(\frac{a}{b})}$ to equal $-1/2E_{(\frac{a}{b})} \mp (\sqrt{3}/2)E_{(\frac{b}{a})}$, so that E_a, E_b behave as A, B_1, individually. [Note that this orientation for $A(T_2)$, $B_{(\frac{2}{3})}(T_2)$ is somewhat different from that which would be obtained from the two "natural" choices, $\{d_{x'y'}, \sqrt{1/2}(d_{x'z'} \mp d_{y'z'})\}$ and $\{-d_{x'y'}, \sqrt{1/2}(d_{x'z'} \mp d_{y'z'})\}$, where T_{2a} equals $\pm d_{x'y'}$, T_{2b} equals $\pm d_{x'z'}$, and T_{2c} equals $\pm d_{y'z'}$, each, which choices are suggested by the definitions of $T_{2(\frac{b}{c})}$ in terms of $\mathcal{C}_3^{\pm 1}(x' = y' = z')T_{2a}$ and of $A(T_2)$, $B_{(\frac{2}{3})}(T_2)$ in terms of $d_{z^2-y^2}$, d_{xz}, and d_{yz} [look at Fig. 10]. Our contrary election was stimulated by our desire to define parallel shapes for both T_1 and T_2 digonal forms.]

(ii) Wave Functions: Eight Electrons. Octahedral Orientation

$$^3B_1[^3A_{2g}(t_{2g}^6e_g^2)]: |b_2\bar{b}_2b_3\bar{b}_3a\bar{a}a^*b_1|$$

$$^3A[^3T_{2g}(t_{2g}^5e_g^3)]: |b_2\bar{b}_2b_3\bar{b}_3aa^*b_1\bar{b}_1|$$

$$^3B_{(\frac{2}{3})}[^3T_{2g}(t_{2g}^5e_g^3)]: -1/2\{|b_2b_3\bar{b}_{(\frac{3}{2})}a\bar{a}a^*b_1\bar{b}_1| + \sqrt{3}\,|b_2\bar{b}_{(\frac{2}{3})}b_3a\bar{a}a^*\bar{a}^*b_1|\}$$

$$^3B_1[^3T_{1g}(t_{2g}^5e_g^3)]: |b_2\bar{b}_2b_3\bar{b}_3aa^*\bar{a}^*b_1|$$

$$^3B_{(\frac{2}{3})}[^3T_{1g}(t_{2g}^5e_g^3)]: -1/2\{\sqrt{3}\,|b_2b_3\bar{b}_{(\frac{3}{2})}a\bar{a}a^*b_1\bar{b}_1| - |b_2\bar{b}_{(\frac{2}{3})}b_3a\bar{a}a^*\bar{a}^*b_1|\}$$

$$^3B_1[^3T_{1g}(t_{2g}^4e_g^4)]: |b_2b_3a\bar{a}a^*\bar{a}^*b_1\bar{b}_1|$$

$$^3B_{(\frac{2}{3})}[^3T_{1g}(t_{2g}^4e_g^4)]: (\pm)|b_2b_3\bar{b}_{(\frac{2}{3})}aa^*\bar{a}^*b_1\bar{b}_1|$$

$$^1A[^1E_g(t_{2g}^6e_g^2)]: \frac{1}{\sqrt{2}}\{|b_2\bar{b}_2b_3\bar{b}_3a\bar{a}b_1\bar{b}_1| - |b_2\bar{b}_2b_3\bar{b}_3a\bar{a}a^*\bar{a}^*|\}$$

$$^1B_1[^1E_g(t_{2g}^6e_g^2)]: \frac{1}{\sqrt{2}}\{|b_2\bar{b}_2b_3\bar{b}_3a\bar{a}a^*\bar{b}_1| - |b_2\bar{b}_2b_3\bar{b}_3a\bar{a}\bar{a}^*b_1|\}$$

$$^1A[^1A_{1g}(t_{2g}^6e_g^2)]: \frac{1}{\sqrt{2}}\{|b_2\bar{b}_2b_3\bar{b}_3a\bar{a}a^*\bar{a}^*| + |b_2\bar{b}_2b_3\bar{b}_3a\bar{a}b_1\bar{b}_1|\}$$

$$^1B_1[^1T_{1g}(t_{2g}^5e_g^3)]: -\frac{1}{\sqrt{2}}\{|b_2\bar{b}_2b_3\bar{b}_3aa^*\bar{a}^*\bar{b}_1| - |b_2\bar{b}_2b_3\bar{b}_3\bar{a}a^*\bar{a}^*b_1|\}$$

$$^1B_{(\frac{2}{3})}[^1T_{1g}(t_{2g}^5e_g^3)]: \frac{1}{2\sqrt{2}}\{\sqrt{3}|b_2b_3\bar{b}_{(\frac{3}{2})}a\bar{a}\bar{a}^*b_1\bar{b}_1| - \sqrt{3}|\bar{b}_2b_{(\frac{3}{2})}\bar{b}_3a\bar{a}a^*b_1\bar{b}_1| + |b_{(\frac{2}{3})}\bar{b}_2\bar{b}_3a\bar{a}a^*\bar{a}^*b_1| - |b_2\bar{b}_{(\frac{2}{3})}b_3a\bar{a}a^*\bar{a}^*\bar{b}_1|\}$$

$$^1A[^1T_{2g}(t_{2g}^5e_g^3)]: -\frac{1}{\sqrt{2}}\{|b_2\bar{b}_2b_3\bar{b}_3a\bar{a}a^*b_1\bar{b}_1| - |b_2\bar{b}_2b_3\bar{b}_3\bar{a}aa^*b_1\bar{b}_1|\}$$

$$^1B_{(\frac{2}{3})}[^1T_{2g}(t_{2g}^5e_g^3)]: \frac{1}{2\sqrt{2}}\{|b_2b_3\bar{b}_{(\frac{3}{2})}a\bar{a}\bar{a}^*b_1\bar{b}_1| - |\bar{b}_2b_{(\frac{3}{2})}\bar{b}_3a\bar{a}a^*b_1\bar{b}_1| - \sqrt{3}|b_{(\frac{2}{3})}\bar{b}_2\bar{b}_3a\bar{a}a^*\bar{a}^*b_1| + \sqrt{3}|b_2\bar{b}_{(\frac{2}{3})}b_3a\bar{a}a^*\bar{a}^*\bar{b}_1|\}$$

$$^1A[^1T_{2g}(t_{2g}^4e_g^4)]: -\frac{1}{\sqrt{2}}\{|b_3\bar{b}_3a\bar{a}a^*\bar{a}^*b_1\bar{b}_1| - |b_2\bar{b}_2a\bar{a}a^*\bar{a}^*b_1\bar{b}_1|\}$$

$$^1B_{(\frac{2}{3})}[^1T_{2g}(t_{2g}^4e_g^4)]: (\pm)\frac{1}{\sqrt{2}}\{|b_2b_3\bar{b}_{(\frac{3}{2})}a\bar{a}a^*\bar{a}^*b_1\bar{b}_1| - |\bar{b}_2b_{(\frac{3}{2})}\bar{b}_3aa^*\bar{a}^*b_1\bar{b}_1|\}$$

$$^1A[^1E_g(t_{2g}^4e_g^4)]: -\frac{1}{\sqrt{6}}\{2|b_2\bar{b}_2b_3\bar{b}_3a^*\bar{a}^*b_1\bar{b}_1| - |b_3\bar{b}_3a\bar{a}a^*\bar{a}^*b_1\bar{b}_1| - |b_2\bar{b}_2a\bar{a}a^*\bar{a}^*b_1\bar{b}_1|\}$$

$$^1B_1[^1E_g(t_{2g}^4e_g^4)]: -\frac{1}{\sqrt{2}}\{|b_2\bar{b}_3a\bar{a}a^*\bar{a}^*b_1\bar{b}_1| - |\bar{b}_2b_3a\bar{a}a^*\bar{a}^*b_1\bar{b}_1|\}$$

$$^1A[^1A_{1g}(t_{2g}^4e_g^4)]: -\frac{1}{\sqrt{3}}\{|b_2\bar{b}_2b_3\bar{b}_3a^*\bar{a}^*b_1\bar{b}_1| + |b_3\bar{b}_3a\bar{a}a^*\bar{a}^*b_1\bar{b}_1| + |b_2\bar{b}_2a\bar{a}a^*\bar{a}^*b_1\bar{b}_1|\} \qquad (36)$$

The rotatory and spectral matrix elements are then rapidly obtained from eq. 35 and 36.

(iii) Matrix Elements: Two Electrons

$$\left\langle {}^3B_1[{}^3T_{1g}(t_{2g}^2)]\left|\frac{\vec{p}}{\vec{m}}\right|{}^3B_{(\frac{2}{3})}[{}^3T_{1g}(t_{2g}^2)]\right\rangle = (\pm)\left\langle b_{(\frac{3}{2})}\left|\frac{\vec{p}}{\vec{m}}\right|a\right\rangle$$

$$\left\langle {}^3B_1[{}^3T_{1g}(t_{2g}^2)]\left|\frac{\vec{p}}{\vec{m}}\right|{}^3B_1[{}^3T_{1g}(t_{2g}e_g)]\right\rangle \equiv 0$$

$$\left\langle {}^3B_1[{}^3T_{1g}(t_{2g}^2)]\left|\frac{\vec{p}}{\vec{m}}\right|{}^3B_{(\frac{2}{3})}[{}^3T_{1g}(t_{2g}e_g)]\right\rangle = -1/2\left\{\sqrt{3}\left\langle b_{(\frac{3}{2})}\left|\frac{\vec{p}}{\vec{m}}\right|a^*\right\rangle + \left\langle b_{(\frac{2}{3})}\left|\frac{\vec{p}}{\vec{m}}\right|b_1\right\rangle\right\}$$

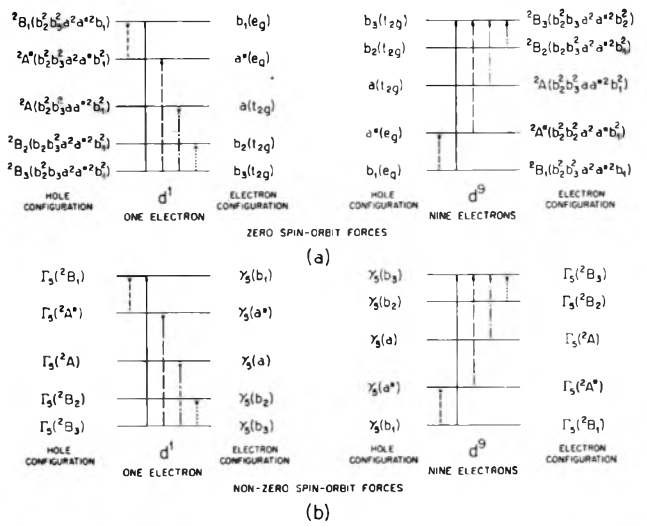

Figure 21. Graphic portrayal of the conjugate one- and nine-electron digonal dihedral electronic transitions in both the orbital (a) and spin-orbital (b) bases. Correspondent transition dyads are limned by correspondent lines.

$$\left\langle {}^3B_1[{}^3T_{1g}(t_{2g}{}^2)] \left| \frac{\vec{p}}{\vec{m}} \right| {}^3A[{}^3T_{2g}(t_{2g}e_g)] \right\rangle = 0$$

$$\left\langle {}^3B_1[{}^3T_{1g}(t_{2g}{}^2)] \left| \frac{\vec{p}}{\vec{m}} \right| {}^3B_{(\frac{2}{3})}[{}^3T_{2g}(t_{2g}e_g)] \right\rangle =$$

$$-1/2 \left\{ \left\langle b_{(\frac{2}{3})} \left| \frac{\vec{p}}{\vec{m}} \right| a^\star \right\rangle - \sqrt{3} \left\langle b_{(\frac{2}{3})} \left| \frac{\vec{p}}{\vec{m}} \right| b_1 \right\rangle \right\}$$

$$\left\langle {}^3B_1[{}^3T_{1g}(t_{2g}{}^2)] \left| \frac{\vec{p}}{\vec{m}} \right| {}^3B_1[{}^3A_{2g}(e_g{}^2)] \right\rangle \equiv 0$$

$$\left\langle {}^3B_2[{}^3T_{1g}(t_{2g}{}^2)] \left| \frac{\vec{p}}{\vec{m}} \right| {}^3B_3[{}^3T_{1g}(t_{2g}{}^2)] \right\rangle = \left\langle b_2 \left| \frac{\vec{p}}{\vec{m}} \right| b_3 \right\rangle$$

$$\left\langle {}^3B_{(\frac{2}{3})}[{}^3T_{1g}(t_{2g}{}^2)] \left| \frac{\vec{p}}{\vec{m}} \right| {}^3B_1[{}^3T_{1g}(t_{2g}e_g)] \right\rangle =$$

$$- \left\langle b_{(\frac{2}{3})} \left| \frac{\vec{p}}{\vec{m}} \right| b_1 \right\rangle$$

$$\left\langle {}^3B_{(\frac{2}{3})}[{}^3T_{1g}(t_{2g}{}^2)] \left| \frac{\vec{p}}{\vec{m}} \right| {}^3B_{(\frac{2}{3})}[{}^3T_{1g}(t_{2g}e_g)] \right\rangle \equiv 0$$

$$\left\langle {}^3B_{(\frac{2}{3})}[{}^3T_{1g}(t_{2g}{}^2)] \left| \frac{\vec{p}}{\vec{m}} \right| {}^3B_{(\frac{3}{2})}[{}^3T_{1g}(t_{2g}e_g)] \right\rangle =$$

$$(\mp)^1/_2 \left\langle a \left| \frac{\vec{p}}{\vec{m}} \right| b_1 \right\rangle$$

$$\left\langle {}^3B_{(\frac{2}{3})}[{}^3T_{1g}(t_{2g}{}^2)] \left| \frac{\vec{p}}{\vec{m}} \right| {}^3A[{}^3T_{2g}(t_{2g}e_g)] \right\rangle =$$

$$- \left\langle b_{(\frac{2}{3})} \left| \frac{\vec{p}}{\vec{m}} \right| a^\star \right\rangle$$

$$\left\langle {}^3B_{(\frac{2}{3})}[{}^3T_{1g}(t_{2g}{}^2)] \left| \frac{\vec{p}}{\vec{m}} \right| {}^3B_{(\frac{2}{3})}[{}^3T_{2g}(t_{2g}e_g)] \right\rangle \equiv 0$$

$$\left\langle {}^3B_{(\frac{2}{3})}[{}^3T_{1g}(t_{2g}{}^2)] \left| \frac{\vec{p}}{\vec{m}} \right| {}^3B_{(\frac{3}{2})}[{}^3T_{2g}(t_{2g}e_g)] \right\rangle =$$

$$(\pm) \frac{\sqrt{3}}{2} \left\langle a \left| \frac{\vec{p}}{\vec{m}} \right| b_1 \right\rangle$$

$$\left\langle {}^3B_{(\frac{2}{3})}[{}^3T_{1g}(t_{2g}{}^2)] \left| \frac{\vec{p}}{\vec{m}} \right| {}^3B_1[{}^3A_{2g}(e_g{}^2)] \right\rangle = 0 \qquad (37)$$

(iv) Matrix Elements: Eight Electrons. Octahedral Orientation

$$\left\langle {}^3B_1[{}^3A_{2g}(t_{2g}{}^6e_g{}^2)] \left| \frac{\vec{p}}{\vec{m}} \right| {}^3A[{}^3T_{2g}(t_{2g}{}^5e_g{}^3)] \right\rangle = \left\langle a \left| \frac{\vec{p}}{\vec{m}} \right| b_1 \right\rangle$$

$$\left\langle {}^3B_1[{}^3A_{2g}(t_{2g}{}^6e_g{}^2)] \left| \frac{\vec{p}}{\vec{m}} \right| {}^3B_{(\frac{2}{3})}[{}^3T_{2g}(t_{2g}{}^5e_g{}^3)] \right\rangle =$$

$$(\mp)^1/_2 \left\{ \left\langle b_{(\frac{2}{3})} \left| \frac{\vec{p}}{\vec{m}} \right| b_1 \right\rangle - \sqrt{3} \left\langle b_{(\frac{3}{2})} \left| \frac{\vec{p}}{\vec{m}} \right| a^\star \right\rangle \right\}$$

$$\left\langle {}^3B_1[{}^3A_{2g}(t_{2g}{}^6e_g{}^2)] \left| \frac{\vec{p}}{\vec{m}} \right| {}^3B_1[{}^3T_{1g}(t_{2g}{}^5e_g{}^3)] \right\rangle \equiv 0$$

$$\left\langle {}^3B_1[{}^3A_{2g}(t_{2g}{}^6e_g{}^2)] \left| \frac{\vec{p}}{\vec{m}} \right| {}^3B_{(\frac{2}{3})}[{}^3T_{1g}(t_{2g}{}^5e_g{}^3)] \right\rangle =$$

$$(\mp)^1/_2 \left\{ \sqrt{3} \left\langle b_{(\frac{2}{3})} \left| \frac{\vec{p}}{\vec{m}} \right| b_1 \right\rangle + \left\langle b_{(\frac{3}{2})} \left| \frac{\vec{p}}{\vec{m}} \right| a^\star \right\rangle \right\}$$

$$\left\langle {}^3B_1[{}^3A_{2g}(t_{2g}{}^6e_g{}^2)] \left| \frac{\vec{p}}{\vec{m}} \right| {}^3B_1[{}^3T_{1g}(t_{2g}{}^4e_g{}^4)] \right\rangle \equiv 0$$

$$\left\langle {}^3B_1[{}^3A_{2g}(t_{2g}{}^6e_g{}^2)] \left| \frac{\vec{p}}{\vec{m}} \right| {}^3B_{(\frac{2}{3})}[{}^3T_{1g}(t_{2g}{}^4e_g{}^4)] \right\rangle = 0$$

$$\left\langle {}^1B_1[{}^1E_g(t_{2g}{}^6e_g{}^2)] \left| \frac{\vec{p}}{\vec{m}} \right| {}^1A[{}^1E_g(t_{2g}{}^6e_g{}^2)] \right\rangle =$$

$$\left\{ \left\langle a^\star \left| \frac{\vec{p}}{\vec{m}} \right| b_1 \right\rangle - \left\langle b_1 \left| \frac{\vec{p}}{\vec{m}} \right| a^\star \right\rangle \right\}$$

$$\left\langle {}^1B_1[{}^1E_g(t_{2g}{}^6e_g{}^2)] \left| \frac{\vec{p}}{\vec{m}} \right| {}^1A[{}^1A_{1g}(t_{2g}{}^6e_g{}^2)] \right\rangle =$$

$$\left\{ \left\langle b_1 \left| \frac{\vec{p}}{\vec{m}} \right| a^\star \right\rangle + \left\langle a^\star \left| \frac{\vec{p}}{\vec{m}} \right| b_1 \right\rangle \right\}$$

$$\left\langle {}^1B_1[{}^1E_g(t_{2g}{}^6e_g{}^2)] \left| \frac{\vec{p}}{\vec{m}} \right| {}^1A[{}^1T_{2g}(t_{2g}{}^5e_g{}^3)] \right\rangle = \left\langle a \left| \frac{\vec{p}}{\vec{m}} \right| b_1 \right\rangle$$

$$\left\langle {}^1B_1[{}^1E_g(t_{2g}{}^6e_g{}^2)] \left| \frac{\vec{p}}{\vec{m}} \right| {}^1B_{(\frac{2}{3})}[{}^1T_{2g}(t_{2g}{}^5e_g{}^3)] \right\rangle =$$

$$(\mp)^1/_2 \left\{ \left\langle b_{(\frac{2}{3})} \left| \frac{\vec{p}}{\vec{m}} \right| b_1 \right\rangle + \sqrt{3} \left\langle b_{(\frac{3}{2})} \left| \frac{\vec{p}}{\vec{m}} \right| a^\star \right\rangle \right\}$$

$$\left\langle {}^1B_1[{}^1E_g(t_{2g}{}^6e_g{}^2)] \left| \frac{\vec{p}}{\vec{m}} \right| {}^1B_1[{}^1T_{1g}(t_{2g}{}^5e_g{}^3)] \right\rangle \equiv 0$$

$$\left\langle {}^1B_1[{}^1E_g(t_{2g}{}^6e_g{}^2)] \left| \frac{\vec{p}}{\vec{m}} \right| {}^1B_{(\frac{2}{3})}[{}^1T_{1g}(t_{2g}{}^5e_g{}^3)] \right\rangle =$$

$$(\pm)^1/_2 \left\{ \left\langle b_{(\frac{3}{2})} \left| \frac{\vec{p}}{\vec{m}} \right| a^\star \right\rangle - \sqrt{3} \left\langle b_{(\frac{2}{3})} \left| \frac{\vec{p}}{\vec{m}} \right| b_1 \right\rangle \right\}$$

$$\left\langle {}^1B_1[{}^1E_g(t_{2g}^6e_g^2)]\left|\frac{\vec{p}}{\vec{m}}\right|{}^1A[{}^1T_{2g}(t_{2g}^4e_g^4)]\right\rangle = 0$$

$$\left\langle {}^1B_1[{}^1E_g(t_{2g}^6e_g^2)]\left|\frac{\vec{p}}{\vec{m}}\right|{}^1B_{(\frac{2}{3})}[{}^1T_{2g}(t_{2g}^4e_g^4)]\right\rangle = 0$$

$$\left\langle {}^1B_1[{}^1E_g(t_{2g}^6e_g^2)]\left|\frac{\vec{p}}{\vec{m}}\right|{}^1A[{}^1E_g(t_{2g}^4e_g^4)]\right\rangle = 0$$

$$\left\langle {}^1B_1[{}^1E_g(t_{2g}^6e_g^2)]\left|\frac{\vec{p}}{\vec{m}}\right|{}^1B_1[{}^1E_g(t_{2g}^4e_g^4)]\right\rangle \equiv 0$$

$$\left\langle {}^1B_1[{}^1E_g(t_{2g}^6e_g^2)]\left|\frac{\vec{p}}{\vec{m}}\right|{}^1A[{}^1A_{1g}(t_{2g}^4e_g^4)]\right\rangle = 0$$

$$\left\langle {}^1A[{}^1E_g(t_{2g}^6e_g^2)]\left|\frac{\vec{p}}{\vec{m}}\right|{}^1A[{}^1A_{1g}(t_{2g}^6e_g^2)]\right\rangle \equiv 0$$

$$\left\langle {}^1A[{}^1E_g(t_{2g}^6e_g^2)]\left|\frac{\vec{p}}{\vec{m}}\right|{}^1A[{}^1T_{2g}(t_{2g}^5e_g^3)]\right\rangle \equiv 0$$

$$\left\langle {}^1A[{}^1E_g(t_{2g}^6e_g^2)]\left|\frac{\vec{p}}{\vec{m}}\right|{}^1B_{(\frac{2}{3})}[{}^1T_{2g}(t_{2g}^5e_g^3)]\right\rangle =$$
$$(\pm)^1/_2\left\{\left\langle b_{(\frac{2}{3})}\left|\frac{\vec{p}}{\vec{m}}\right|a^\star\right\rangle - \sqrt{3}\left\langle b_{(\frac{3}{2})}\left|\frac{\vec{p}}{\vec{m}}\right|b_1\right\rangle\right\}$$

$$\left\langle {}^1A[{}^1E_g(t_{2g}^6e_g^2)]\left|\frac{\vec{p}}{\vec{m}}\right|{}^1B_1[{}^1T_{1g}(t_{2g}^5e_g^3)]\right\rangle = \left\langle a\left|\frac{\vec{p}}{\vec{m}}\right|b_1\right\rangle$$

$$\left\langle {}^1A[{}^1E_g(t_{2g}^6e_g^2)]\left|\frac{\vec{p}}{\vec{m}}\right|{}^1B_{(\frac{3}{2})}[{}^1T_{1g}(t_{2g}^5e_g^3)]\right\rangle =$$
$$(\pm)^1/_2\left\{\left\langle b_{(\frac{2}{3})}\left|\frac{\vec{p}}{\vec{m}}\right|b_1\right\rangle + \sqrt{3}\left\langle b_{(\frac{3}{2})}\left|\frac{\vec{p}}{\vec{m}}\right|a^\star\right\rangle\right\}$$

$$\left\langle {}^1A[{}^1E_g(t_{2g}^6e_g^2)]\left|\frac{\vec{p}}{\vec{m}}\right|{}^1A[{}^1T_{2g}(t_{2g}^4e_g^4)]\right\rangle \equiv 0$$

$$\left\langle {}^1A[{}^1E_g(t_{2g}^6e_g^2)]\left|\frac{\vec{p}}{\vec{m}}\right|{}^1B_{(\frac{2}{3})}[{}^1T_{2g}(t_{2g}^4e_g^4)]\right\rangle = 0$$

$$\left\langle {}^1A[{}^1E_g(t_{2g}^6e_g^2)]\left|\frac{\vec{p}}{\vec{m}}\right|{}^1A[{}^1E_g(t_{2g}^4e_g^4)]\right\rangle \equiv 0$$

$$\left\langle {}^1A[{}^1E_g(t_{2g}^6e_g^2)]\left|\frac{\vec{p}}{\vec{m}}\right|{}^1B_1[{}^1E_g(t_{2g}^4e_g^4)]\right\rangle = 0$$

$$\left\langle {}^1A[{}^1E_g(t_{2g}^6e_g^2)]\left|\frac{\vec{p}}{\vec{m}}\right|{}^1A[{}^1A_{1g}(t_{2g}^4e_g^4)]\right\rangle \equiv 0$$

$$\left\langle {}^1A[{}^1A_{1g}(t_{2g}^6e_g^2)]\left|\frac{\vec{p}}{\vec{m}}\right|{}^1A[{}^1T_{2g}(t_{2g}^5e_g^3)]\right\rangle \equiv 0$$

$$\left\langle {}^1A[{}^1A_{1g}(t_{2g}^6e_g^2)]\left|\frac{\vec{p}}{\vec{m}}\right|{}^1B_{(\frac{2}{3})}[{}^1T_{2g}(t_{2g}^5e_g^3)]\right\rangle =$$
$$(\pm)^1/_2\left\{\left\langle b_{(\frac{2}{3})}\left|\frac{\vec{p}}{\vec{m}}\right|a^\star\right\rangle + \sqrt{3}\left\langle b_{(\frac{3}{2})}\left|\frac{\vec{p}}{\vec{m}}\right|b_1\right\rangle\right\}$$

$$\left\langle {}^1A[{}^1A_{1g}(t_{2g}^6e_g^2)]\left|\frac{\vec{p}}{\vec{m}}\right|{}^1B_1[{}^1T_{1g}(t_{2g}^5e_g^3)]\right\rangle =$$
$$-1/_2\left\langle a\left|\frac{\vec{p}}{\vec{m}}\right|b_1\right\rangle$$

$$\left\langle {}^1A[{}^1A_{1g}(t_{2g}^6e_g^2)]\left|\frac{\vec{p}}{\vec{m}}\right|{}^1B_{(\frac{2}{3})}[{}^1T_{1g}(t_{2g}^5e_g^3)]\right\rangle =$$
$$(\mp)^1/_2\left\{\left\langle b_{(\frac{2}{3})}\left|\frac{\vec{p}}{\vec{m}}\right|b_1\right\rangle - \sqrt{3}\left\langle b_{(\frac{3}{2})}\left|\frac{\vec{p}}{\vec{m}}\right|a^\star\right\rangle\right\}$$

$$\left\langle {}^1A[{}^1A_{1g}(t_{2g}^6e_g^2)]\left|\frac{\vec{p}}{\vec{m}}\right|{}^1A[{}^1T_{2g}(t_{2g}^4e_g^4)]\right\rangle \equiv 0$$

$$\left\langle {}^1A[{}^1A_{1g}(t_{2g}^6e_g^2)]\left|\frac{\vec{p}}{\vec{m}}\right|{}^1B_{(\frac{2}{3})}[{}^1T_{2g}(t_{2g}^4e_g^4)]\right\rangle = 0$$

$$\left\langle {}^1A[{}^1A_{1g}(t_{2g}^6e_g^2)]\left|\frac{\vec{p}}{\vec{m}}\right|{}^1A[{}^1E_g(t_{2g}^4e_g^4)]\right\rangle \equiv 0$$

$$\left\langle {}^1A[{}^1A_{1g}(t_{2g}^6e_g^2)]\left|\frac{\vec{p}}{\vec{m}}\right|{}^1B_1[{}^1E_g(t_{2g}^4e_g^4)]\right\rangle = 0$$

$$\left\langle {}^1A[{}^1A_{1g}(t_{2g}^6e_g^2)]\left|\frac{\vec{p}}{\vec{m}}\right|{}^1A[{}^1A_{1g}(t_{2g}^4e_g^4)]\right\rangle \equiv 0 \qquad (38)$$

For later work it is also of interest to addend at this place the wave functions and matrix elements of the nonoctahedrally oriented single assignational eight-electron digonal configurations.

(v) Wave Functions: Eight Electrons. Nonoctahedral Orientation

$${}^1A^{(1)}: |b_2\bar{b}_2b_3\bar{b}_3a\bar{a}a^\star\bar{a}^\star|$$

$${}^1A^{(2)}: |b_2\bar{b}_2b_3\bar{b}_3a\bar{a}b_1\bar{b}_1|$$

$${}^1A^{(3)}: -\frac{1}{\sqrt{2}}\{|b_2\bar{b}_2b_3\bar{b}_3a\bar{a}^\star b_1\bar{b}_1| - |b_2\bar{b}_2b_3\bar{b}_3\bar{a}a^\star b_1\bar{b}_1|\}$$

$${}^1A^{(4)}: |b_2\bar{b}_2b_3\bar{b}_3a^\star\bar{a}^\star b_1\bar{b}_1|$$

$${}^1A^{(5)}: |b_3\bar{b}_3a\bar{a}a^\star\bar{a}^\star b_1\bar{b}_1|$$

$${}^1A^{(6)}: |b_2\bar{b}_2a\bar{a}a^\star\bar{a}^\star b_1\bar{b}_1|$$

$${}^1B_1{}^{(1)}: \frac{1}{\sqrt{2}}\{|b_2\bar{b}_2b_3\bar{b}_3a\bar{a}a^\star\bar{b}_1| - |b_2\bar{b}_2b_3\bar{b}_3a\bar{a}\bar{a}^\star b_1|\}$$

$${}^1B_1{}^{(2)}: -\frac{1}{\sqrt{2}}\{|b_2\bar{b}_2b_3\bar{b}_3aa^\star\bar{a}^\star\bar{b}_1| - |b_2\bar{b}_2b_3\bar{b}_3\bar{a}a^\star\bar{a}^\star b_1|\}$$

$${}^1B_1{}^{(3)}: -\frac{1}{\sqrt{2}}\{|b_2\bar{b}_3a\bar{a}a^\star\bar{a}^\star b_1\bar{b}_1| - |\bar{b}_2b_3a\bar{a}a^\star\bar{a}^\star b_1\bar{b}_1|\}$$

$${}^1B_2{}^{(1)}: \frac{1}{\sqrt{2}}\{|b_2\bar{b}_2b_3a\bar{a}a^\star\bar{a}^\star\bar{b}_1| - |b_2\bar{b}_2\bar{b}_3a\bar{a}a^\star\bar{a}^\star b_1|\}$$

$${}^1B_2{}^{(2)}: \frac{1}{\sqrt{2}}\{|b_2b_3\bar{b}_3a\bar{a}\bar{a}^\star b_1\bar{b}_1| - |\bar{b}_2b_3\bar{b}_3a\bar{a}a^\star b_1\bar{b}_1|\}$$

$${}^1B_2{}^{(3)}: \frac{1}{\sqrt{2}}\{|b_2b_3\bar{b}_3\bar{a}a^\star\bar{a}^\star b_1\bar{b}_1| - |\bar{b}_2b_3\bar{b}_3aa^\star\bar{a}^\star b_1\bar{b}_1|\}$$

$${}^1B_3{}^{(1)}: \frac{1}{\sqrt{2}}\{|b_2b_3\bar{b}_3a\bar{a}a^\star\bar{a}^\star\bar{b}_1| - |\bar{b}_2b_3\bar{b}_3a\bar{a}a^\star\bar{a}^\star b_1|\}$$

$$^1B_3^{(3)}: \frac{1}{\sqrt{2}}\{|b_2\bar{b}_2b_3a\bar{a}\bar{a}^*b_1\bar{b}_1| - |b_2\bar{b}_2\bar{b}_3aaa^*b_1\bar{b}_1|\}$$

$$^1B_3^{(2)}: \frac{1}{\sqrt{2}}\{|b_2\bar{b}_2b_3\bar{a}a^*\bar{a}^*b_1\bar{b}_1| - |b_2\bar{b}_2\bar{b}_3aa^*\bar{a}^*b_1\bar{b}_1|\}$$

$$^3A: |b_2\bar{b}_2b_3\bar{b}_3aa^*b_1\bar{b}_1|$$

$$^3B_1^{(1)}: |b_2\bar{b}_2b_3\bar{b}_3a\bar{a}a^*b_1|$$

$$^3B_1^{(2)}: |b_2\bar{b}_2b_3\bar{b}_3aa^*\bar{a}^*b_1|$$

$$^3B_1^{(3)}: |b_2b_3a\bar{a}a^*\bar{a}^*b_1\bar{b}_1|$$

$$^3B_2^{(1)}: |b_2\bar{b}_2b_3a\bar{a}a^*\bar{a}^*b_1|$$

$$^3B_2^{(2)}: |b_2b_3\bar{b}_3a\bar{a}a^*b_1\bar{b}_1|$$

$$^3B_2^{(3)}: |b_2b_3\bar{b}_3aa^*\bar{a}^*b_1\bar{b}_1|$$

$$^3B_3^{(1)}: |b_2b_3\bar{b}_3a\bar{a}a^*\bar{a}^*b_1|$$

$$^3B_3^{(2)}: |b_2\bar{b}_2b_3a\bar{a}a^*b_1\bar{b}_1|$$

$$^3B_3^{(3)}: |b_2\bar{b}_2b_3aa^*\bar{a}^*b_1\bar{b}_1| \qquad (39)$$

(*vi*) *Matrix Elements: Eight Electrons. Nonoctahedral Orientation*

$$\left\langle {}^1A^{(j)} \left| \frac{\vec{p}}{\vec{m}} \right| {}^1A^{(k)} \right\rangle \equiv\equiv 0 \quad (j, k = 0, 1, 2, 3, 4, 5, 6)$$

$$\left\langle {}^1A^{(1)} \left| \frac{\vec{p}}{\vec{m}} \right| {}^1B_1^{(1)} \right\rangle = \sqrt{2}\left\langle a^* \left| \frac{\vec{p}}{\vec{m}} \right| b_1 \right\rangle$$

$$\left\langle {}^1A^{(1)} \left| \frac{\vec{p}}{\vec{m}} \right| {}^1B_1^{(2)} \right\rangle = -\sqrt{2}\left\langle a \left| \frac{\vec{p}}{\vec{m}} \right| b_1 \right\rangle$$

$$\left\langle {}^1A^{(1)} \left| \frac{\vec{p}}{\vec{m}} \right| {}^1B_1^{(3)} \right\rangle = 0$$

$$\left\langle {}^1A^{(1)} \left| \frac{\vec{p}}{\vec{m}} \right| {}^1B_{(\frac{2}{3})}^{(1)} \right\rangle = \sqrt{2}\left\langle b_{(\frac{3}{2})} \left| \frac{\vec{p}}{\vec{m}} \right| b_1 \right\rangle$$

$$\left\langle {}^1A^{(1)} \left| \frac{\vec{p}}{\vec{m}} \right| {}^1B_{(\frac{2}{3})}^{(2)} \right\rangle = 0$$

$$\left\langle {}^1A^{(1)} \left| \frac{\vec{p}}{\vec{m}} \right| {}^1B_{(\frac{2}{3})}^{(3)} \right\rangle = 0$$

$$\left\langle {}^3B_1^{(1)} \left| \frac{\vec{p}}{\vec{m}} \right| {}^3B_1^{(2,3)} \right\rangle \equiv 0$$

$$\left\langle {}^3B_1^{(1)} \left| \frac{\vec{p}}{\vec{m}} \right| {}^3A \right\rangle = \left\langle a \left| \frac{\vec{p}}{\vec{m}} \right| b_1 \right\rangle$$

$$\left\langle {}^3B_1^{(1)} \left| \frac{\vec{p}}{\vec{m}} \right| {}^3B_{(\frac{2}{3})}^{(1)} \right\rangle = -\left\langle b_{(\frac{3}{2})} \left| \frac{\vec{p}}{\vec{m}} \right| a^* \right\rangle$$

$$\left\langle {}^3B_1^{(1)} \left| \frac{\vec{p}}{\vec{m}} \right| {}^3B_{(\frac{2}{3})}^{(2)} \right\rangle = \left\langle b_{(\frac{3}{2})} \left| \frac{\vec{p}}{\vec{m}} \right| b_1 \right\rangle$$

$$\left\langle {}^3B_1^{(1)} \left| \frac{\vec{p}}{\vec{m}} \right| {}^3B_{(\frac{2}{3})}^{(3)} \right\rangle = 0 \qquad (40)$$

These functions and matrices are conjoined to those of eq. 36 and 38 by the matrix connectives

$$\begin{bmatrix} {}^1A[{}^1E_g(t_{2g}^6e_g^2)] \\ {}^1A[{}^1A_{1g}(t_{2g}^6e_g^2)] \\ {}^1A[{}^1T_{2g}(t_{2g}^5e_g^3)] \\ {}^1A[{}^1T_{2g}(t_{2g}^4e_g^4)] \\ {}^1A[{}^1E_g(t_{2g}^4e_g^4)] \\ {}^1A[{}^1A_{1g}(t_{2g}^4e_g^4)] \end{bmatrix} = \begin{bmatrix} -\frac{1}{\sqrt{2}} & \frac{1}{\sqrt{2}} & 0 & 0 & 0 & 0 \\ \frac{1}{\sqrt{2}} & \frac{1}{\sqrt{2}} & 0 & 0 & 0 & 0 \\ 0 & 0 & 1 & 0 & 0 & 0 \\ 0 & 0 & 0 & 0 & -\frac{1}{\sqrt{2}} & \frac{1}{\sqrt{2}} \\ 0 & 0 & 0 & -\frac{2}{\sqrt{6}} & \frac{1}{\sqrt{6}} & \frac{1}{\sqrt{6}} \\ 0 & 0 & 0 & -\frac{1}{\sqrt{3}} & -\frac{1}{\sqrt{3}} & -\frac{1}{\sqrt{3}} \end{bmatrix} \begin{bmatrix} {}^1A^{(1)} \\ {}^1A^{(2)} \\ {}^1A^{(3)} \\ {}^1A^{(4)} \\ {}^1A^{(5)} \\ {}^1A^{(6)} \end{bmatrix}$$

$$\begin{bmatrix} {}^1B_1[{}^1E_g(t_{2g}^6e_g^2)] \\ {}^1B_1[{}^1T_{1g}(t_{2g}^5e_g^3)] \\ {}^1B_1[{}^1E_g(t_{2g}^4e_g^4)] \end{bmatrix} = \begin{bmatrix} 1 & 0 & 0 \\ 0 & 1 & 0 \\ 0 & 0 & 1 \end{bmatrix} \begin{bmatrix} {}^1B_1^{(1)} \\ {}^1B_1^{(2)} \\ {}^1B_1^{(3)} \end{bmatrix}$$

$$\begin{bmatrix} {}^1B_2[{}^1T_{1g}(t_{2g}^5e_g^3)] \\ {}^1B_2[{}^1T_{2g}(t_{2g}^5e_g^3)] \\ {}^1B_2[{}^1T_{2g}(t_{2g}^4e_g^4)] \end{bmatrix} = \begin{bmatrix} -1/2 & \frac{\sqrt{3}}{2} & 0 \\ \frac{\sqrt{3}}{2} & 1/2 & 0 \\ 0 & 0 & 1 \end{bmatrix} \begin{bmatrix} {}^1B_2^{(1)} \\ {}^1B_2^{(2)} \\ {}^1B_2^{(3)} \end{bmatrix}$$

$$\begin{bmatrix} {}^1B_3[{}^1T_{1g}(t_{2g}^5e_g^3)] \\ {}^1B_3[{}^1T_{2g}(t_{2g}^5e_g^3)] \\ {}^1B_3[{}^1T_{2g}(t_{2g}^4e_g^4)] \end{bmatrix} = \begin{bmatrix} 1/2 & -\frac{\sqrt{3}}{2} & 0 \\ -\frac{\sqrt{3}}{2} & -1/2 & 0 \\ 0 & 0 & 1 \end{bmatrix} \begin{bmatrix} {}^1B_3^{(1)} \\ {}^1B_3^{(2)} \\ {}^1B_3^{(3)} \end{bmatrix}$$

$$[{}^3A[{}^3T_{2g}(t_{2g}^5e_g^3)]] = [1][{}^3A]$$

$$\begin{bmatrix} {}^3B_1[{}^3A_{2g}(t_{2g}^6e_g^2)] \\ {}^3B_1[{}^3T_{1g}(t_{2g}^5e_g^2)] \\ {}^3B_1[{}^3T_{1g}(t_{2g}^4e_g^4)] \end{bmatrix} = \begin{bmatrix} 1 & 0 & 0 \\ 0 & 1 & 0 \\ 0 & 0 & 1 \end{bmatrix} \begin{bmatrix} {}^3B_1^{(1)} \\ {}^3B_1^{(2)} \\ {}^3B_1^{(3)} \end{bmatrix}$$

$$\begin{bmatrix} {}^3B_2[{}^3T_{2g}(t_{2g}^5e_g^3)] \\ {}^3B_2[{}^3T_{1g}(t_{2g}^5e_g^3)] \\ {}^3B_2[{}^3T_{1g}(t_{2g}^4e_g^4)] \end{bmatrix} = \begin{bmatrix} -\frac{\sqrt{3}}{2} & -1/2 & 0 \\ 1/2 & -\frac{\sqrt{3}}{2} & 0 \\ 0 & 0 & 1 \end{bmatrix} \begin{bmatrix} {}^3B_2^{(1)} \\ {}^3B_2^{(2)} \\ {}^3B_2^{(3)} \end{bmatrix}$$

$$\begin{bmatrix} {}^3B_3[{}^3T_{2g}(t_{2g}^5e_g^3)] \\ {}^3B_3[{}^3T_{1g}(t_{2g}^5e_g^3)] \\ {}^3B_3[{}^3T_{1g}(t_{2g}^4e_g^4)] \end{bmatrix} = \begin{bmatrix} \frac{\sqrt{3}}{2} & 1/2 & 0 \\ -1/2 & \frac{\sqrt{3}}{2} & 0 \\ 0 & 0 & 1 \end{bmatrix} \begin{bmatrix} {}^3B_3^{(1)} \\ {}^3B_3^{(2)} \\ {}^3B_3^{(3)} \end{bmatrix} \tag{41}$$

From eq. 37, 38, and 40 we see that the rotational and spectral strengths and dissymmetry factors are simply related in a formal algebraic manner to the one-electron mathematical rotational, spectral, and dissymmetry expressions of eq. 24 and 27. Attend that, unlike the one- and nine-electron case, there is no formal equivalence of the two- and eight-electron rotational and spectral strengths for any functional orientation. This circumstance arises as the electronic hops of usual practical import are not electron-hole complements [inspect Fig. 22].

(*b*) *No Configuration Interaction: Nonzero Spin-Orbit Forces. Two and Eight Electrons.* As in ref. 6, we shall defer a study of this representation to future works.

(*c*) *Configuration Interaction: Zero and Nonzero Spin-Orbit Forces.* Configuration interaction, if extreme enough, can alter the results of §4.2b and c appreciably. To visualize this fact one need only compare the two extremes, eq. 38 and 40. The discussion of the intermediates progresses as in ref. 6, §4.2c. Note however, that the breakdown of pseudo cubicity here allows much stronger rotations for the eight-electron ${}^3A_{2g}$ to ${}^3T_{1g}$ electronic shifts than for the trigonal dihedral situation of ref. 6, and that the upsurge of spin-orbit reciprocity permits the appearance of nonzero rotations and intensions for spin-forbidden bands.

4.3 *The Three- and Seven-Electron Case.* The apposite single electron excitations of harmonious posture wanted for this research are put below. Other excitations are the substance of subsequent effort.[20]

(*a*) *No Configuration Interaction: Zero Spin-Orbit Forces.* (*i*) *Wave Functions: Three Electrons*

${}^4B_1[{}^4A_{2g}(t_{2g}^3)]: |b_2b_3a|$

${}^4A[{}^4T_{2g}(t_{2g}^2e_g)]: |b_2b_3b_1|$

(20) The $d^{3,4,5}$ state functions are fabricated from the $d^{1,2,3}$ basic state functions constructed as in footnote 19 by means of parentage concepts. For example, ${}^4T_{1g}(t_{2g}{}^2e_g) + {}^4T_{2g}(t_{2g}{}^2e_g)$ equals ${}^3T_{1g}(t_{2g}{}^2) \times {}^2E_g(e_g)$, and ${}^3E_g(t_{2g}{}^3e_g)$ equals ${}^4A_{2g}(t_{2g}{}^3) \times {}^2E_g(e_g)$. The d^{10-n} and $d^{5\pm n}$, or more generally, the $t_{2g}{}^{6-l}$, $e_g{}^{4-m}$, and $t_{2g}{}^{6-l}e_g{}^{4-m}$, state functions are structured from the correspondent d^n and $d^{6\mp n}$ or $t_{2g}{}^l$, $e_g{}^m$, and $t_{2g}{}^le_g{}^m$ basic state functions built earlier. To illustrate ${}^3T_{2g}(t_{2g}{}^5e_g{}^3) \sim {}^3T_{2g}(t_{2g}e_g) \sim {}^3T_{2g}(t_{2g}{}^5e_g) \sim {}^3T_{2g}(t_{2g}e_g{}^3)$, ${}^3T_{1g}(t_{2g}{}^4) \sim {}^3T_{1g}(t_{2g}{}^2) \sim {}^3T_{1g}(t_{2g}{}^2e_g{}^4) \sim {}^3T_{1g}(t_{2g}{}^4e_g{}^4)$, and so on. Care must be punctiliously exercised in these generalized electron-hole electrons to ensure a consistent choice of determinantal phase. We have picked the standard determinantal order to be $b_2\bar{b}_2b_3\bar{b}_3a\bar{a}a^\star\bar{a}^\star b_1\bar{b}_1$, where the bar denotes spin minus one-half, and have always taken the hole configuration (ℌ) to have the inverse spin order from that of its electron progenitor (ℭℌ) [for instance, $\sqrt{1/2}\{|a^\star\bar{b}_1| - |\bar{a}^\star b_1|\}$ (electron progenitor (2ℌ)) $\Longleftrightarrow \sqrt{1/2}\{|\bar{a}^\star b_1| - |\bar{a}^\star\bar{b}_1|\}$ (hole (ℌ)) $\Longleftrightarrow \sqrt{1/2}\{|b_2\bar{b}_2b_3\bar{b}_3a\bar{a}a^\star b_1| - |b_2\bar{b}_2b_3\bar{b}_3aa\bar{a}^\star b_1|\}$ (electron (ℭ)) and $\sqrt{1/2}\{|b_2\bar{b}_2| - |b_3\bar{b}_3|\}$ (electron progenitor (ℭℌ)) $\Longleftrightarrow \sqrt{1/2}\{|\bar{b}_2b_2| - |\bar{b}_3b_3|\} \equiv -\sqrt{1/2}\{|b_2\bar{b}_2| - |b_3\bar{b}_3|\}$ (hole (ℌ)) $\Longleftrightarrow -\sqrt{1/2}\{|b_3\bar{b}_3a\bar{a}a^\star\bar{a}^\star b_1\bar{b}_1| - |b_2\bar{b}_2a\bar{a}a^\star\bar{a}^\star b_1\bar{b}_1|\}$ (electron (ℭ))]. With a meticulous observance of phase, many electron transformational characteristics are neatly established in their conjugate hole representation.

$$^4B_{(\frac{3}{3})}[^4T_{2g}(t_{2g}{}^2e_g)]: -{}^1/_2\{\sqrt{3}|b_{(\frac{3}{3})}aa^*| + |b_{(\frac{3}{2})}ab_1|\}$$

$$^4B_1[^4T_{1g}(t_{2g}{}^2e_g)]: |b_2b_3a^*|$$

$$^4B_{(\frac{3}{3})}[^4T_{1g}(t_{2g}{}^2e_g)]: -{}^1/_2\{|b_{(\frac{3}{3})}aa^*| - \sqrt{3}|b_{(\frac{3}{2})}ab_1|\}$$

$$^4B_1[^4T_{1g}(t_{2g}e_g{}^2)]: |aa^*b_1|$$

$$^4B_{(\frac{3}{3})}[^4T_{1g}(t_{2g}e_g{}^2)]: (\mp)|b_{(\frac{3}{2})}a^*b_1|$$

$$^2A[^2E_g(t_{2g}{}^3)]: \frac{1}{\sqrt{2}}\{|b_2\bar{b}_2a| - |b_3\bar{b}_3a|\}$$

$$^2B_1[^2E_g(t_{2g}{}^3)]: \frac{1}{\sqrt{6}}\{2|b_2b_3\bar{a}| - |b_2\bar{b}_3a| - |\bar{b}_2b_3a|\}$$

$$^2A[^2T_{2g}(t_{2g}{}^3)]: \frac{1}{\sqrt{2}}\{|b_2\bar{b}_2a| + |b_3\bar{b}_3a|\}$$

$$^2B_{(\frac{3}{3})}[^2T_{2g}(t_{2g}{}^3)]: (\pm)\frac{1}{\sqrt{2}}\{(\pm)|b_2b_3\bar{b}_{(\frac{3}{2})}| + |b_{(\frac{3}{3})}a\bar{a}|\}$$

$$^2B_1[^2T_{1g}(t_{2g}{}^3)]: \frac{1}{\sqrt{2}}\{|b_2\bar{b}_3a| - |\bar{b}_2b_3a|\}$$

$$^2B_{(\frac{3}{3})}[^2T_{1g}(t_{2g}{}^3)]: (\pm)\frac{1}{\sqrt{2}}\{(\mp)|b_2b_3\bar{b}_{(\frac{3}{2})}| + |b_{(\frac{3}{3})}a\bar{a}|\} \quad (42)$$

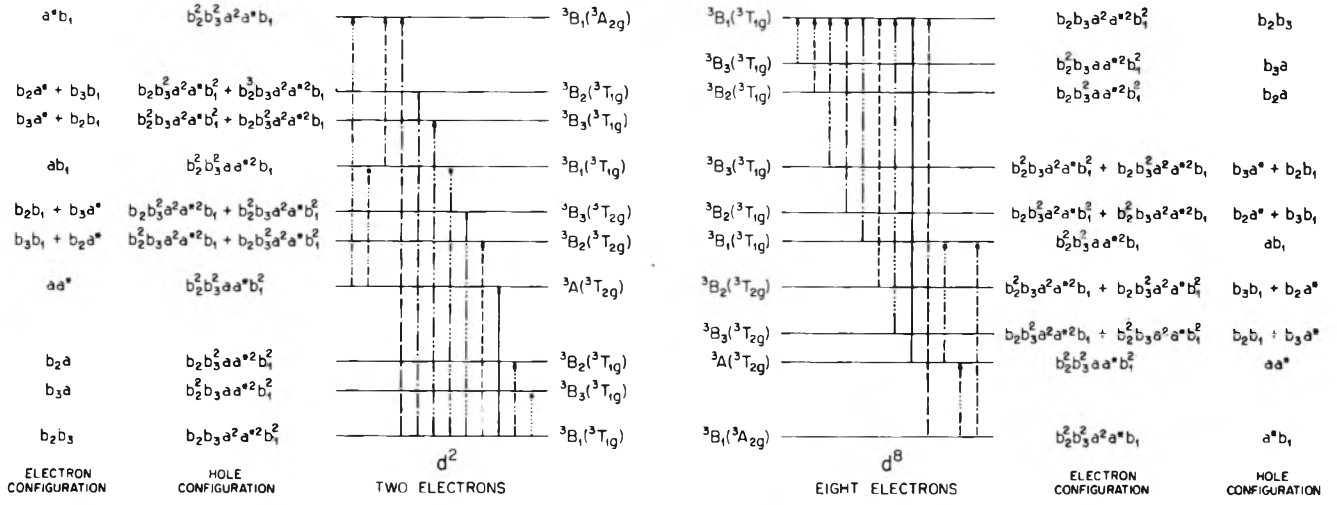

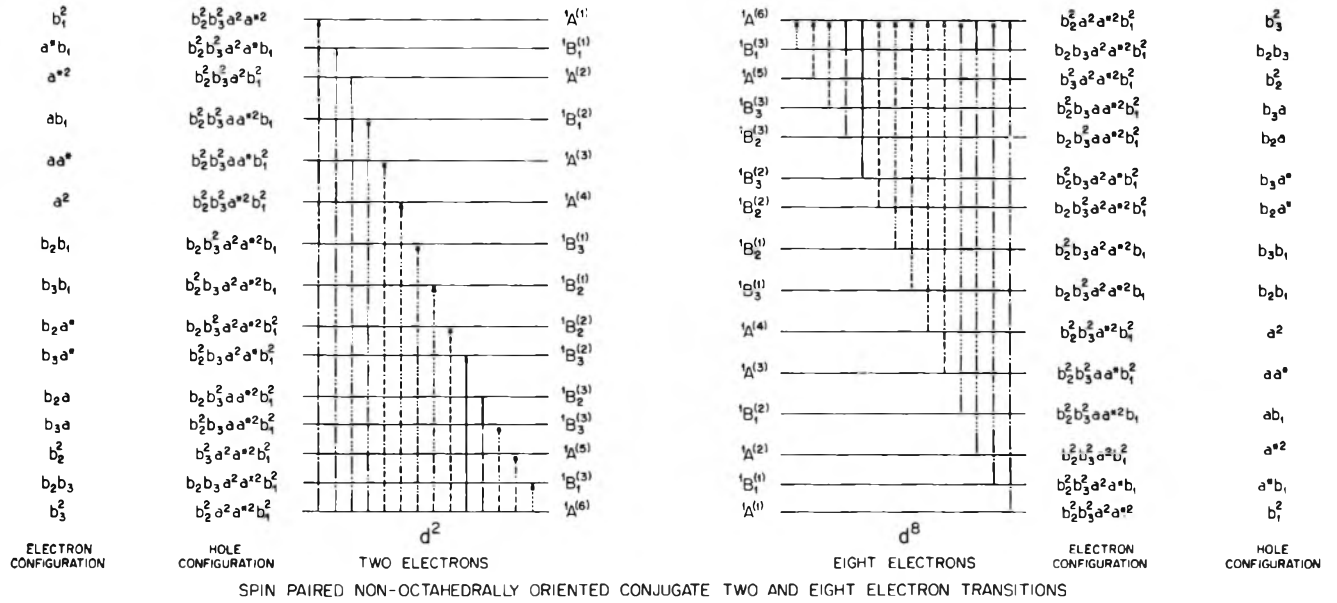

Figure 22. Graphic portrayal of the conjugate two- and eight-electron digonal dihedral electronic transitions in the orbital basis for both (spin-free) octahedral and (spin-paired) nonoctahedral orientations. Correspondent transition dyads are limned by correspondent lines.

(ii) Wave Functions: Seven Electrons

$^4B_1[^4T_{1g}(t_{2g}^5e_g^2)]: |b_2\bar{b}_2b_3\bar{b}_3aa^*b_1|$

$^4B_{(\frac{2}{3})}[^4T_{1g}(t_{2g}^5e_g^2)]: -|b_2\bar{b}_{(\frac{2}{3})}b_3a\bar{a}a^*b_1|$

$^4A[^4T_{2g}(t_{2g}^4e_g^3)]: |b_2b_3a\bar{a}a^*\bar{a}^*b_1|$

$^4B_{(\frac{2}{3})}[^4T_{2g}(t_{2g}^4e_g^3)]:$

$$(\mp)^1/_2\{\sqrt{3}|b_2b_3\bar{b}_{(\frac{2}{3})}aa^*b_1\bar{b}_1| + |b_2\bar{b}_{(\frac{2}{3})}b_3aa^*\bar{a}^*b_1|\}$$

$^4B_1[^4T_{1g}(t_{2g}^4e_g^3)]: |b_2b_3a\bar{a}a^*b_1\bar{b}_1|$

$^4B_{(\frac{2}{3})}[^4T_{1g}(t_{2g}^4e_g^3)]:$

$$(\mp)^1/_2\{|b_2b_3\bar{b}_{(\frac{3}{2})}aa^*b_1\bar{b}_1| - \sqrt{3}|b_2\bar{b}_{(\frac{2}{3})}b_3aa^*\bar{a}^*b_1|\}$$

$^4B_1[^4A_{2g}(t_{2g}^3e_g^4)]: |b_2b_3aa^*\bar{a}^*b_1\bar{b}_1|$

$^2A[^2E_g(t_{2g}^6e_g)]: |b_2\bar{b}_2b_3\bar{b}_3a\bar{a}a^*|$

$^2B_1[^2E_g(t_{2g}^6e_g)]: |b_2\bar{b}_2b_3\bar{b}_3a\bar{a}b_1|$

$$^2B_1[^2T_{1g}(t_{2g}^5e_g^2)]: \frac{1}{\sqrt{6}}\{2|b_2\bar{b}_2b_3\bar{b}_3\bar{a}a^*b_1| - |b_2\bar{b}_2b_3\bar{b}_3a\bar{a}^*b_1| - |b_2\bar{b}_2b_3\bar{b}_3aa^*\bar{b}_1|\}$$

$$^2B_{(\frac{2}{3})}[^2T_{1g}(t_{2g}^5e_g^2)]: -\frac{1}{\sqrt{6}}\{2|b_{(\frac{2}{3})}\bar{b}_2\bar{b}_3a\bar{a}a^*b_1| - |b_2\bar{b}_{(\frac{2}{3})}b_3a\bar{a}\bar{a}^*b_1| - |b_2\bar{b}_{(\frac{2}{3})}b_3a\bar{a}a^*\bar{b}_1|\}$$

$^2A[^2T_{2g}(t_{2g}^5e_g^2)]:$

$$\frac{1}{\sqrt{2}}\{|b_2\bar{b}_2b_3\bar{b}_3ab_1\bar{b}_1| - |b_2\bar{b}_2b_3\bar{b}_3aa^*\bar{a}^*|\}$$

$$^2B_{(\frac{2}{3})}[^2T_{2g}(t_{2g}^5e_g^2)]: -\frac{1}{2\sqrt{2}}\{\sqrt{3}|b_2\bar{b}_{(\frac{2}{3})}b_3aa^*\bar{b}_1| - \sqrt{3}|b_2\bar{b}_{(\frac{2}{3})}b_3a\bar{a}\bar{a}^*b_1| - |b_2b_3\bar{b}_{(\frac{3}{2})}aa\bar{a}^*\bar{a}^*| + |b_2b_3\bar{b}_{(\frac{3}{2})}a\bar{a}b_1\bar{b}_1|\}$$

$^2B_1[^2T_{1g}(t_{2g}^5e_g^2)]:$

$$\frac{1}{\sqrt{2}}\{|b_2\bar{b}_2b_3\bar{b}_3aa^*\bar{b}_1| - |b_2\bar{b}_2b_3\bar{b}_3a\bar{a}^*b_1|\}$$

$$^2B_{(\frac{2}{3})}[^2T_{1g}(t_{2g}^5e_g^2)]: \frac{1}{2\sqrt{2}}\{|b_2\bar{b}_{(\frac{2}{3})}b_3a\bar{a}a^*\bar{b}_1| - |b_2\bar{b}_{(\frac{2}{3})}b_3a\bar{a}\bar{a}^*b_1| + \sqrt{3}|b_2b_3\bar{b}_{(\frac{3}{2})}aa\bar{a}^*\bar{a}^*| - \sqrt{3}|b_2b_3\bar{b}_{(\frac{3}{2})}a\bar{a}b_1\bar{b}_1|\}$$

$^2A[^2T_{2g}(t_{2g}^5e_g^2)]:$

$$\frac{1}{\sqrt{2}}\{|b_2\bar{b}_2b_3\bar{b}_3aa^*\bar{a}^*| + |b_2\bar{b}_2b_3\bar{b}_3ab_1\bar{b}_1|\}$$

$^2B_{(\frac{2}{3})}[^2T_{2g}(t_{2g}^5e_g^2)]:$

$$\frac{1}{\sqrt{2}}\{|b_2b_3\bar{b}_{(\frac{3}{2})}a\bar{a}a^*\bar{a}^*| + |b_2b_3\bar{b}_{(\frac{3}{2})}a\bar{a}b_1\bar{b}_1|\} \quad (43)$$

From these functions the gyratory and optical matrix displays are facilely gotten.

(iii) Matrix Elements: Three Electrons

$$\left\langle {}^4B_1[{}^4A_{2g}(t_{2g}^3)] \left|\frac{\vec{p}}{\vec{m}}\right| {}^4A[{}^4T_{2g}(t_{2g}^2e_g)] \right\rangle = \left\langle a \left|\frac{\vec{p}}{\vec{m}}\right| b_1 \right\rangle$$

$$\left\langle {}^4B_1[{}^4A_{2g}(t_{2g}^3)] \left|\frac{\vec{p}}{\vec{m}}\right| {}^4B_{(\frac{2}{3})}[{}^4T_{2g}(t_{2g}^2e_g)] \right\rangle =$$

$$(\mp)^1/_2\left\{\left\langle b_{(\frac{2}{3})} \left|\frac{\vec{p}}{\vec{m}}\right| b_1 \right\rangle - \sqrt{3}\left\langle b_{(\frac{3}{2})} \left|\frac{\vec{p}}{\vec{m}}\right| a^* \right\rangle\right\}$$

$$\left\langle {}^4B_1[{}^4A_{2g}(t_{2g}^3)] \left|\frac{\vec{p}}{\vec{m}}\right| {}^4B_1[{}^4T_{1g}(t_{2g}^2e_g)] \right\rangle \equiv 0$$

$$\left\langle {}^4B_1[{}^4A_{2g}(t_{2g}^3)] \left|\frac{\vec{p}}{\vec{m}}\right| {}^4B_{(\frac{2}{3})}[{}^4T_{1g}(t_{2g}^2e_g)] \right\rangle =$$

$$(\pm)^1/_2\left\{\sqrt{3}\left\langle b_{(\frac{2}{3})} \left|\frac{\vec{p}}{\vec{m}}\right| b_1 \right\rangle + \left\langle b_{(\frac{3}{2})} \left|\frac{\vec{p}}{\vec{m}}\right| a^* \right\rangle\right\}$$

$$\left\langle {}^4B_1[{}^4A_{2g}(t_{2g}^3)] \left|\frac{\vec{p}}{\vec{m}}\right| {}^4B_1[{}^4T_{1g}(t_{2g}e_g^2)] \right\rangle \equiv 0$$

$$\left\langle {}^4B_1[{}^4A_{2g}(t_{2g}^3)] \left|\frac{\vec{p}}{\vec{m}}\right| {}^4B_{(\frac{2}{3})}[{}^4T_{1g}(t_{2g}e_g^2)] \right\rangle = 0 \quad (44)$$

(iv) Matrix Elements: Seven Electrons

$$\left\langle {}^4B_1[{}^4T_{1g}(t_{2g}^5e_g^2)] \left|\frac{\vec{p}}{\vec{m}}\right| {}^4B_{(\frac{2}{3})}[{}^4T_{1g}(t_{2g}^5e_g^2)] \right\rangle =$$

$$(\pm)\left\langle b_{(\frac{3}{2})} \left|\frac{\vec{p}}{\vec{m}}\right| a \right\rangle$$

$$\left\langle {}^4B_1[{}^4T_{1g}(t_{2g}^5e_g^2)] \left|\frac{\vec{p}}{\vec{m}}\right| {}^4A[{}^4T_{2g}(t_{2g}^4e_g^3)] \right\rangle = 0$$

$$\left\langle {}^4B_1[{}^4T_{1g}(t_{2g}^5e_g^2)] \left|\frac{\vec{p}}{\vec{m}}\right| {}^4B_{(\frac{2}{3})}[{}^4T_{2g}(t_{2g}^4e_g^3)] \right\rangle =$$

$$-1/_2\left\{\left\langle b_{(\frac{3}{2})} \left|\frac{\vec{p}}{\vec{m}}\right| a^* \right\rangle - \sqrt{3}\left\langle b_{(\frac{3}{2})} \left|\frac{\vec{p}}{\vec{m}}\right| b_1 \right\rangle\right\}$$

$$\left\langle {}^4B_1[{}^4T_{1g}(t_{2g}^5e_g^2)] \left|\frac{\vec{p}}{\vec{m}}\right| {}^4B_1[{}^4T_{1g}(t_{2g}^4e_g^3)] \right\rangle \equiv 0$$

$$\left\langle {}^4B_1[{}^4T_{1g}(t_{2g}^5e_g^2)] \left|\frac{\vec{p}}{\vec{m}}\right| {}^4B_{(\frac{2}{3})}[{}^4T_{1g}(t_{2g}^4e_g^3)] \right\rangle =$$

$$1/_2\left\{\sqrt{3}\left\langle b_{(\frac{3}{2})} \left|\frac{\vec{p}}{\vec{m}}\right| a^* \right\rangle + \left\langle b_{(\frac{3}{2})} \left|\frac{\vec{p}}{\vec{m}}\right| b_1 \right\rangle\right\}$$

$$\left\langle {}^4B_1[{}^4T_{1g}(t_{2g}^5e_g^2)] \left|\frac{\vec{p}}{\vec{m}}\right| {}^4B_1[{}^4A_{2g}(t_{2g}^3e_g^4)] \right\rangle \equiv 0$$

$$\left\langle {}^4B_2[{}^4T_{1g}(t_{2g}^5e_g^2)] \left|\frac{\vec{p}}{\vec{m}}\right| {}^4B_3[{}^4T_{1g}(t_{2g}^5e_g^2)] \right\rangle =$$

$$\left\langle b_2 \left|\frac{\vec{p}}{\vec{m}}\right| b_3 \right\rangle$$

$$\left\langle {}^4B_{(\frac{2}{3})}[{}^4T_{1g}(t_{2g}^5e_g^2)]\left|\frac{\vec{p}}{\vec{m}}\right|{}^4A[{}^4T_{2g}(t_{2g}^4e_g^3)]\right\rangle = -\left\langle b_{(\frac{2}{3})}\left|\frac{\vec{p}}{\vec{m}}\right|a^*\right\rangle$$

$$\left\langle {}^4B_{(\frac{2}{3})}[{}^4T_{1g}(t_{2g}^5e_g^2)]\left|\frac{\vec{p}}{\vec{m}}\right|{}^4B_{(\frac{2}{3})}[{}^4T_{2g}(t_{2g}^4e_g^3)]\right\rangle \equiv 0$$

$$\left\langle {}^4B_{(\frac{2}{3})}[{}^4T_{1g}(t_{2g}^5e_g^2)]\left|\frac{\vec{p}}{\vec{m}}\right|{}^4B_{(\frac{3}{2})}[{}^4T_{2g}(t_{2g}^4e_g^3)]\right\rangle = (\pm)\frac{\sqrt{3}}{2}\left\langle a\left|\frac{\vec{p}}{\vec{m}}\right|b_1\right\rangle$$

$$\left\langle {}^4B_{(\frac{2}{3})}[{}^4T_{1g}(t_{2g}^5e_g^2)]\left|\frac{\vec{p}}{\vec{m}}\right|{}^4B_1[{}^4T_{1g}(t_{2g}^4e_g^3)]\right\rangle = \left\langle b_{(\frac{2}{3})}\left|\frac{\vec{p}}{\vec{m}}\right|b_1\right\rangle$$

$$\left\langle {}^4B_{(\frac{2}{3})}[{}^4T_{1g}(t_{2g}^5e_g^2)]\left|\frac{\vec{p}}{\vec{m}}\right|{}^4B_{(\frac{2}{3})}[{}^4T_{1g}(t_{2g}^4e_g^3)]\right\rangle \equiv 0$$

$$\left\langle {}^4B_{(\frac{2}{3})}[{}^4T_{1g}(t_{2g}^5e_g^2)]\left|\frac{\vec{p}}{\vec{m}}\right|{}^4B_{(\frac{3}{2})}[{}^4T_{1g}(t_{2g}^4e_g^3)]\right\rangle = (\pm)^{1/2}\left\langle a\left|\frac{\vec{p}}{\vec{m}}\right|b_1\right\rangle$$

$$\left\langle {}^4B_{(\frac{2}{3})}[{}^4T_{1g}(t_{2g}^5e_g^2)]\left|\frac{\vec{p}}{\vec{m}}\right|{}^4B_1[{}^4A_{2g}(t_{2g}^3e_g^4)]\right\rangle = 0$$

$$\left\langle {}^2A[{}^2E_g(t_{2g}^6e_g)]\left|\frac{\vec{p}}{\vec{m}}\right|{}^2B_1[{}^2E_g(t_{2g}^6e_g)]\right\rangle = \left\langle a^*\left|\frac{\vec{p}}{\vec{m}}\right|b_1\right\rangle$$

$$\left\langle {}^2A[{}^2E_g(t_{2g}^6e_g)]\left|\frac{\vec{p}}{\vec{m}}\right|{}^2B_1[{}^2T_{1g}(t_{2g}^5e_g^2)]\right\rangle = \sqrt{3/2}\left\langle a\left|\frac{\vec{p}}{\vec{m}}\right|b_1\right\rangle$$

$$\left\langle {}^2A[{}^2E_g(t_{2g}^6e_g)]\left|\frac{\vec{p}}{\vec{m}}\right|{}^2B_{(\frac{3}{2})}[{}^2T_{1g}(t_{2g}^5e_g^2)]\right\rangle = (\mp)\sqrt{3/2}\left\langle b_{(\frac{3}{2})}\left|\frac{\vec{p}}{\vec{m}}\right|b_1\right\rangle$$

$$\left\langle {}^2A[{}^2E_g(t_{2g}^6e_g)]\left|\frac{\vec{p}}{\vec{m}}\right|{}^2A[{}^2T_{2g}(t_{2g}^5e_g^2)]\right\rangle \equiv 0$$

$$\left\langle {}^2A[{}^2E_g(t_{2g}^6e_g)]\left|\frac{\vec{p}}{\vec{m}}\right|{}^2B_{(\frac{2}{3})}[{}^2T_{2g}(t_{2g}^5e_g^2)]\right\rangle = (\mp)\frac{1}{2\sqrt{2}}\left\{\left\langle b_{(\frac{2}{3})}\left|\frac{\vec{p}}{\vec{m}}\right|a^*\right\rangle - \sqrt{3}\left\langle b_{(\frac{3}{2})}\left|\frac{\vec{p}}{\vec{m}}\right|b_1\right\rangle\right\}$$

$$\left\langle {}^2A[{}^2E_g(t_{2g}^6e_g)]\left|\frac{\vec{p}}{\vec{m}}\right|{}^2B_1[{}^2T_{1g}(t_{2g}^5e_g^2)]\right\rangle = -\frac{1}{\sqrt{2}}\left\langle a\left|\frac{\vec{p}}{\vec{m}}\right|b_1\right\rangle$$

$$\left\langle {}^2A[{}^2E_g(t_{2g}^6e_g)]\left|\frac{\vec{p}}{\vec{m}}\right|{}^2B_{(\frac{2}{3})}[{}^2T_{1g}(t_{2g}^5e_g^2)]\right\rangle = (\mp)\frac{1}{2\sqrt{2}}\left\{\sqrt{3}\left\langle b_{(\frac{2}{3})}\left|\frac{\vec{p}}{\vec{m}}\right|a^*\right\rangle + \left\langle b_{(\frac{3}{2})}\left|\frac{\vec{p}}{\vec{m}}\right|b_1\right\rangle\right\}$$

$$\left\langle {}^2A[{}^2E_g(t_{2g}^6e_g)]\left|\frac{\vec{p}}{\vec{m}}\right|{}^2A[{}^2T_{2g}(t_{2g}^5e_g^2)]\right\rangle \equiv 0$$

$$\left\langle {}^2A[{}^2E_g(t_{2g}^6e_g)]\left|\frac{\vec{p}}{\vec{m}}\right|{}^2B_{(\frac{2}{3})}[{}^2T_{2g}(t_{2g}^5e_g^2)]\right\rangle = (\mp)\frac{1}{\sqrt{2}}\left\langle b_{(\frac{2}{3})}\left|\frac{\vec{p}}{\vec{m}}\right|a^*\right\rangle$$

$$\left\langle {}^2B_1[{}^2E_g(t_{2g}^6e_g)]\left|\frac{\vec{p}}{\vec{m}}\right|{}^2B_1[{}^2T_{1g}(t_{2g}^5e_g^2)]\right\rangle \equiv 0$$

$$\left\langle {}^2B_1[{}^2E_g(t_{2g}^6e_g)]\left|\frac{\vec{p}}{\vec{m}}\right|{}^2B_{(\frac{2}{3})}[{}^2T_{1g}(t_{2g}^5e_g^2)]\right\rangle = (\pm)\sqrt{3/2}\left\langle b_{(\frac{3}{2})}\left|\frac{\vec{p}}{\vec{m}}\right|a^*\right\rangle$$

$$\left\langle {}^2B_1[{}^2E_g(t_{2g}^6e_g)]\left|\frac{\vec{p}}{\vec{m}}\right|{}^2A[{}^2T_{2g}(t_{2g}^5e_g^2)]\right\rangle = -\frac{1}{\sqrt{2}}\left\langle a\left|\frac{\vec{p}}{\vec{m}}\right|b_1\right\rangle$$

$$\left\langle {}^2B_1[{}^2E_g(t_{2g}^6e_g)]\left|\frac{\vec{p}}{\vec{m}}\right|{}^2B_{(\frac{2}{3})}[{}^2T_{2g}(t_{2g}^5e_g^2)]\right\rangle = (\pm)\frac{1}{2\sqrt{2}}\left\{\left\langle b_{(\frac{2}{3})}\left|\frac{\vec{p}}{\vec{m}}\right|b_1\right\rangle + \sqrt{3}\left\langle b_{(\frac{3}{2})}\left|\frac{\vec{p}}{\vec{m}}\right|a^*\right\rangle\right\}$$

$$\left\langle {}^2B_1[{}^2E_g(t_{2g}^6e_g)]\left|\frac{\vec{p}}{\vec{m}}\right|{}^2B_1[{}^2T_{1g}(t_{2g}^5e_g^2)]\right\rangle \equiv 0$$

$$\left\langle {}^2B_1[{}^2E_g(t_{2g}^6e_g)]\left|\frac{\vec{p}}{\vec{m}}\right|{}^2B_{(\frac{2}{3})}[{}^2T_{1g}(t_{2g}^5e_g^2)]\right\rangle = (\mp)\frac{1}{2\sqrt{2}}\left\{-\sqrt{3}\left\langle b_{(\frac{2}{3})}\left|\frac{\vec{p}}{\vec{m}}\right|b_1\right\rangle + \left\langle b_{(\frac{3}{2})}\left|\frac{\vec{p}}{\vec{m}}\right|a^*\right\rangle\right\}$$

$$\left\langle {}^2B_1[{}^2E_g(t_{2g}^6e_g)]\left|\frac{\vec{p}}{\vec{m}}\right|{}^2A[{}^2T_{2g}(t_{2g}^5e_g^2)]\right\rangle = -\frac{1}{\sqrt{2}}\left\langle a\left|\frac{\vec{p}}{\vec{m}}\right|b_1\right\rangle$$

$$\left\langle {}^2B_1[{}^2E_g(t_{2g}^6e_g)]\left|\frac{\vec{p}}{\vec{m}}\right|{}^2B_{(\frac{2}{3})}[{}^2T_{2g}(t_{2g}^5e_g^2)]\right\rangle = (\mp)\frac{1}{\sqrt{2}}\left\langle b_{(\frac{2}{3})}\left|\frac{\vec{p}}{\vec{m}}\right|b_1\right\rangle \quad (45)$$

We uncover from eq. 44 and 45 that the rotational and spectral strengths of the three- and seven-electron conundrum are simply linked to those of the two- and eight-electron problems priorly discussed. In truth, we behold an exact one-to-one correspondence of the two- and seven-electron spin-free rotational and spec-

tral strengths and of the three- and eight-electron strengths, severally. The seven-electron spin-paired rotational and spectral strengths are joined multiplicatively to the one, four, six, and nine [refer §3.1, 3.2, 4.1, and 4.4] spin-free strengths and to certain of the five- and eight-electron spin paired strengths [confer §4.2 and 4.5] as we shall see in §4.4 and 4.5. The broad repercussions of this correspondence will be sounded in section IV.

(*b*) *No Configuration Interaction: Nonzero Spin-Orbit Forces. Three and Seven Electrons.* The comments appropriate to this paragraph are identical with those of §4.2b.

(*c*) *Configuration Interaction: Zero and Nonzero Spin-Orbit Forces. Three and Seven Electrons.* The effects of configuration interaction are exactly as outlined in §4.2c.

4.4 *The Four- and Six-Electron Case.* In agreement with the confinement of §4.2, we fasten our scan of the four- and six-electron puzzle on the single electron excitations alone, the left-overs to remain for later study. With this bound, the applicable digonally situated determinantal functions for the four- and six-electron bunches are as penned alow.[21]

(*a*) *No Configuration Interaction: Zero Spin-Orbit Forces.* (*i*) *Wave Functions: Four Electrons*

$$^5A[^5E_g(t_{2g}{}^3e_g)]:|b_2b_3ab_1|$$

$$^5B_1[^5E_g(t_{2g}{}^3e_g)]:-|b_2b_3aa^*|$$

$$^5A[^5T_{2g}(t_{2g}{}^2e_g{}^2)]:|b_2b_3a^*b_1|$$

$$^5B_{(\frac{2}{3})}[^5T_{2g}(t_{2g}{}^2e_g{}^2)]:|b_{(\frac{3}{2})}aa^*b_1|$$

$$^3B_1[^3T_{1g}(t_{2g}{}^4)]:|b_2b_3a\bar{a}|$$

$$^3B_{(\frac{2}{3})}[^2T_{1g}(t_{2g}{}^4)]:(\pm)|b_2b_3\bar{b}_{(\frac{3}{2})}a|$$

$$^1A[^1E_g(t_{2g}{}^4)]:-\frac{1}{\sqrt{6}}\{2|b_2\bar{b}_2b_3\bar{b}_3|-|b_3\bar{b}_3a\bar{a}|-|b_2\bar{b}_2a\bar{a}|\}$$

$$^1B_1[^1E_g(t_{2g}{}^4)]:-\frac{1}{\sqrt{2}}\{|b_2\bar{b}_3a\bar{a}|-|\bar{b}_2b_3a\bar{a}|\}$$

$$^1A[^1T_{2g}(t_{2g}{}^4)]:-\frac{1}{\sqrt{2}}\{|b_3\bar{b}_3a\bar{a}|-|b_2\bar{b}_2a\bar{a}|\}$$

$$^1B_{(\frac{2}{3})}[^1T_{2g}(t_{2g}{}^4)]:(\pm)\frac{1}{\sqrt{2}}\{|b_2b_3\bar{b}_{(\frac{3}{2})}\bar{a}|-|\bar{b}_2b_{(\frac{3}{2})}\bar{b}_3a|\}$$

$$^1A[^1A_{1g}(t_{2g}{}^4)]:-\frac{1}{\sqrt{3}}\{|b_2\bar{b}_2b_3\bar{b}_3|+|b_3\bar{b}_3a\bar{a}|+|b_2\bar{b}_2a\bar{a}|\}$$

$$^3A[^3E_g(t_{2g}{}^3e_g)]:\frac{1}{2\sqrt{3}}\{3|b_2b_3a\bar{b}_1|-|b_2b_3\bar{a}b_1|-|b_2\bar{b}_3ab_1|-|\bar{b}_2b_3ab_1|\}$$

$$^3B_1[^3E_g(t_{2g}{}^3e_g)]:-\frac{1}{2\sqrt{3}}\{3|b_2b_3a\bar{a}^*|-|b_2b_3\bar{a}a^*|-|b_2\bar{b}_3aa^*|-|\bar{b}_2b_3aa^*|\}$$

$$^3B_1[^3T_{1g}(t_{2g}{}^3e_g)]:\frac{1}{\sqrt{2}}\{|b_2\bar{b}_3aa^*|-|\bar{b}_2b_3aa^*|\}$$

(21) The computation of the requisite functions is greatly eased if it is noted that the cumulative products $o_1\bar{o}_1+o_2\bar{o}_2$, $o_1\bar{o}_2-o_2\bar{o}_1$, $\{(o_1\bar{o}_1-o_2\bar{o}_2),-(o_1\bar{o}_2+o_2\bar{o}_1)\}$; $u_1\bar{u}_1+u_2\bar{u}_2+u_3\bar{u}_3$, $\{2u_1\bar{u}_1-u_2\bar{u}_2-u_3\bar{u}_3,\sqrt{3}(u_2\bar{u}_3-u_3\bar{u}_2)\}$, $\{u_2\bar{u}_3-u_3\bar{u}_2,u_3\bar{u}_1-u_1\bar{u}_3,u_1\bar{u}_2-u_2\bar{u}_1\}$, $\{u_2\bar{u}_3+u_3\bar{u}_2,u_3\bar{u}_1+u_1\bar{u}_3,u_1\bar{u}_2+u_2\bar{u}_1\}$; $\{o_1u_1,(-\frac{1}{2}o_1-(\sqrt{3}/2)o_2)u_2,(-\frac{1}{2}o_1+(\sqrt{3}/2)o_2)u_3\}$, $\{o_2u_1,((\sqrt{3}/2)o_1-\frac{1}{2}o_2)u_2,(-(\sqrt{3}/2)o_1-\frac{1}{2}o_2)u_3\}$; $a\bar{a}$; $\{ao_1,ao_2\}$; au_1, au_2, $au_3\}$, of basis functions $\{o_1,o_2\}$, $\{\bar{o}_1,\bar{o}_2\}$; $\{u_1,u_2,u_3\}$. $\{\bar{u}_1,\bar{u}_2,\bar{u}_3\}$; $a,\bar{a}$, of species $\{E_a,E_b\}$; $\{T_{(\frac{1}{2})a},T_{(\frac{1}{2})b},T_{(\frac{1}{2})c}\}$; $A_{(\frac{1}{2})}$, separately, which are oriented as in footnote 19, are composite functions, properly oriented, of species A_1, A_2, $\{E_a,E_b\}$; A_1, $\{E_a,E_b\}$, $\{T_{1a},T_{1b},T_{1c}\}$, $\{T_{2a},T_{2b},T_{2c}\}$ [u, ū of same species T_1 and T_2] or A_2, $\{E_b,E_a\}$, $\{T_{2a},T_{2b},T_{2c}\}$, $\{T_{1a},T_{1b},T_{1c}\}$ [u, ū of different species T_1 and T_2]; $\{T_{1a},T_{1b},T_{1c}\}$, $\{T_{2a},T_{2b},T_{2c}\}$ [o, u of species E, T_1] or $\{T_{2a},T_{2b},T_{2c}\}$, $\{T_{1a},T_{1b},T_{1c}\}$ [o, u of species E, T_2]; A_1 [a, ā of same species A_1 or A_2] or A_2 [a, ā of different species A_1 and A_2]; $\{E_a,E_b\}$ [a, o of species A_1, E] or $\{E_b,E_a\}$ [a, o of species A_2, E]; $\{T_{(\frac{1}{2})a},T_{(\frac{1}{2})b},T_{(\frac{1}{2})c}\}$ [a, u of species A_1, $T_{(\frac{1}{2})}$] or $\{T_{(\frac{2}{1})a},T_{(\frac{2}{1})b},T_{(\frac{2}{1})c}\}$ [a, u of species A_2, $T_{(\frac{1}{2})}$]. This declaration is quickly proved either by direct application of the $\mathcal{C}_4(z'$ or $z)$ and $\mathcal{C}_3(x'=y'=z')$ operators [footnote 19] to the registered cumulative products, or by oblique reference to tensorial algebraic considerations [*cf.* (a) Y. Tanabe and S. Sugano, *J. Phys. Soc. Japan*, 9, 753 (1954), *et seq.*; (b) M. E. Rose, "Multipole Fields," John Wiley and Sons, Inc., New York, N. Y., 1955; "Elementary Theory of Angular Momentum," John Wiley and Sons, Inc., New York, N. Y., 1957; (c) U. Fano and G. Racah, "Irreducible Tensorial Sets," Academic Press, New York, N. Y., 1959; (d) J. S. Griffith, "The Irreducible Tensor Method for Molecular Symmetry Groups," Prentice-Hall, Englewood Cliffs, N. J., 1962; (e) S. R. Polo, "Studies on Crystal Field Theory," R.C.A. Laboratories Report, 1963, and to be published. Note that the direct application is a simple way of deriving the tensorial coupling coefficients tabulated in ref. 21a,b,c,d,e]. Since all nuclear permutation (symmetry) operators, $\mathcal{P}$, such as $\mathcal{C}_4(z'$ or $z)$, $\mathcal{C}_3(x'=y'=z')$, and $\mathcal{C}_2(x)$, commute with the determinantal electronic antisymmetrization operator, $\mathcal{A}$, the product classifications and expressions recorded above are equally valid for the determinantal and nondeterminantal cumulative products, and both kinds of products transform isomorphously. As both the nuclear permutation operators $\mathcal{P}$ and the antisymmetrization operator $\mathcal{A}$ equals $(1/\sqrt{N!})\sum_P(-1)^P$, where the summation, Σ, is over all two-electron permutations, P, are orthonormalization preservative, the end functions $\mathcal{A}\mathcal{P}\prod_j\mathfrak{v}_j(n_j)$ equal $\mathcal{P}\mathcal{A}\prod_j\mathfrak{v}_j(n_j)$, where n_j is the numbered electron associated with orbital $\mathfrak{v}_j$ generated by $\mathcal{P}$, are orthonormal, if the initial orbitals $\mathfrak{v}_j$ were so. The process $\mathcal{A}\mathcal{P}$ or $\mathcal{P}\mathcal{A}$ applied to a function is entirely analogous to that of the addition of a set of orthonormal functions to obtain a final orthonormal (new) function. Observe that since $\mathcal{P}\mathcal{A}\mathfrak{e}\cdot\mathfrak{h}$ transforms as $\mathcal{A}\mathcal{P}\mathfrak{e}\cdot\mathfrak{h}$, and since $\mathcal{A}\mathcal{P}\mathfrak{e}\cdot\mathfrak{h}$ equals $\mathcal{A}(\mathcal{P}\mathfrak{e}\cdot\mathcal{P}\mathfrak{h})$ equals $\mathcal{A}\mathfrak{e}\cdot\mathfrak{h}$ for a closed shell, our argument also proves that electron ($\mathfrak{e}$) and hole ($\mathfrak{h}$) configurations transform contragradiently ("inversely") and that therefore the electron and the electron equivalent of the hole ($\mathfrak{e}\mathfrak{h}$) transform cogradiently ("parallelly"). For example, in footnote 20, the eight-electron ($\mathfrak{e}$) and the two-electron hole equivalent ($\mathfrak{e}\mathfrak{h}$) transform parallelly and the eight-electron (or two-electron hole equivalent) and the hole ($\mathfrak{h}$) transform oppositely [the hole ($\mathfrak{h}$) and the electron equivalent of the hole ($\mathfrak{e}\mathfrak{h}$) transform oppositely by construction].

$$^3B_{(\frac{2}{3})}[^3T_{1g}(t_{2g}{}^3e_g)]: \frac{1}{2\sqrt{2}}\{|b_2b_3\bar{b}_{(\frac{3}{2})}a^\star| +$$

$$(\mp)|b_{(\frac{2}{3})}aāa^\star| + \sqrt{3}\,|b_2\bar{b}_{(\frac{2}{3})}b_3b_1| + (\mp)\sqrt{3}|b_{(\frac{3}{2})}\,aāb_1|\}$$

$$^3A[^3T_{2g}(t_{2g}{}^3e_g)]: \frac{1}{\sqrt{2}}\{|b_2\bar{b}_3ab_1| - |\bar{b}_2b_3ab_1|\}$$

$$^3B_{(\frac{2}{3})}[^3T_{2g}(t_{2g}{}^3e_g)]: \frac{1}{2\sqrt{2}}\{\sqrt{3}\,|b_2b_3\bar{b}_{(\frac{3}{2})}a^\star| +$$

$$(\mp)\sqrt{3}\,|b_{(\frac{2}{3})}aāa^\star| - |b_2\bar{b}_{(\frac{2}{3})}b_3b_1| + (\pm)|b_{(\frac{3}{2})}aāb_1|\}$$

$$^3A[^3A_{1g}(t_{2g}{}^3e_g)]: \frac{1}{2\sqrt{3}}\{2|b_2b_3āb_1| - |b_2\bar{b}_3ab_1| -$$

$$|\bar{b}_2b_3ab_1| + \sqrt{3}\,|b_2\bar{b}_2aa^\star| - \sqrt{3}\,|b_3\bar{b}_3aa^\star|\}$$

$$^3A[^3E_g(t_{2g}{}^3e_g)]: \frac{1}{2\sqrt{3}}\{\sqrt{3}\,|b_2\bar{b}_2aa^\star| - \sqrt{3}\,|b_3\bar{b}_3aa^\star| -$$

$$2|b_2b_3āb_1| + |b_2\bar{b}_3ab_1| + |\bar{b}_2b_3ab_1|\}$$

$$^3B_1[^3E_g(t_{2g}{}^3e_g)]: -\frac{1}{2\sqrt{3}}\{\sqrt{3}\,|b_2\bar{b}_2ab_1| -$$

$$\sqrt{3}\,|b_3\bar{b}_3ab_1| + 2|b_2b_3āa^\star| - |b_2\bar{b}_3aa^\star| - |\bar{b}_2b_3aa^\star|\}$$

$$^3B_1[^3A_{2g}(t_{2g}{}^3e_g)]: \frac{1}{2\sqrt{3}}\{\sqrt{3}\,|b_2\bar{b}_2ab_1| -$$

$$\sqrt{3}\,|b_3\bar{b}_3ab_1| - 2|b_2b_3āa^\star| + |b_2\bar{b}_3aa^\star| + |\bar{b}_2b_3aa^\star|\}$$

$$^3A[^3T_{2g}(t_{2g}{}^3e_g)]: \frac{1}{\sqrt{2}}\{|b_2\bar{b}_2aa^\star| + |b_3\bar{b}_3aa^\star|\}$$

$$^3B_{(\frac{2}{3})}[^3T_{2g}(t_{2g}{}^3e_g)]: -\frac{1}{2\sqrt{2}}\{|b_2b_3\bar{b}_{(\frac{3}{2})}a^\star| +$$

$$(\pm)|b_{(\frac{2}{3})}aāa^\star| + \sqrt{3}\,|b_2\bar{b}_{(\frac{2}{3})}b_3b_1| +$$

$$(\pm)\sqrt{3}\,|b_{(\frac{3}{2})}aāb_1|\}$$

$$^3B_1[^3T_{1g}(t_{2g}{}^3e_g)]: \frac{1}{\sqrt{2}}\{|b_2\bar{b}_2ab_1| + |b_3\bar{b}_3ab_1|\}$$

$$^3B_{(\frac{2}{3})}[^3T_{1g}(t_{2g}{}^3e_g)]: -\frac{1}{2\sqrt{2}}\{\sqrt{3}\,|b_2b_3\bar{b}_{(\frac{3}{2})}a^\star| +$$

$$(\pm)\sqrt{3}\,|b_{(\frac{2}{3})}aāa^\star| - |b_2\bar{b}_{(\frac{2}{3})}b_3b_1| +$$

$$(\mp)|b_{(\frac{3}{2})}aāb_1|\} \quad (46)$$

(ii) Wave Functions: Six Electrons

$$^5A[^5T_{2g}(t_{2g}{}^4e_g{}^2)]: |b_2b_3aāa^\star b_1|$$

$$^5B_{(\frac{2}{3})}[^5T_{2g}(t_{2g}{}^4e_g{}^2)]: (\pm)|b_2\bar{b}_{(\frac{2}{3})}b_3aa^\star b_1|$$

$$^5A[^5E_g(t_{2g}{}^3e_g{}^3)]: |b_2b_3aa^\star ā^\star b_1|$$

$$^5B_1[^5E_g(t_{2g}{}^3e_g{}^3)]: -|b_2b_3aa^\star b_1\bar{b}_1$$

$$^1A[^1A_{1g}(t_{2g}{}^6)]: |b_2\bar{b}_2b_3\bar{b}_3aā|$$

$$^1B_1[^1T_{1g}(t_{2g}{}^5e_g)]: \frac{1}{\sqrt{2}}\{|b_2\bar{b}_2b_3\bar{b}_3a\bar{b}_1| - |b_2\bar{b}_2b_3\bar{b}_3āb_1|\}$$

$$^1B_{(\frac{2}{3})}[^1T_{1g}(t_{2g}{}^5e_g)]: -\frac{1}{2\sqrt{2}}\{\sqrt{3}\,|b_2b_3\bar{b}_{(\frac{3}{2})}aāā^\star| -$$

$$\sqrt{3}\,|\bar{b}_2b_{(\frac{3}{2})}\bar{b}_3aāa^\star| - |b_2\bar{b}_{(\frac{2}{3})}b_3aa\bar{b}_1| + |b_{(\frac{2}{3})}\bar{b}_2\bar{b}_3aāb_1|\}$$

$$^1A[^1T_{2g}(t_{2g}{}^5e_g)]: \frac{1}{\sqrt{2}}\{|b_2\bar{b}_2b_3\bar{b}_3aā^\star| - |b_2\bar{b}_2b_3\bar{b}_3āa^\star|\}$$

$$^1B_{(\frac{2}{3})}[^1T_{2g}(t_{2g}{}^5e_g)]: -\frac{1}{2\sqrt{2}}|b_2b_3\bar{b}_{(\frac{3}{2})}aāā^\star| -$$

$$|\bar{b}_2b_{(\frac{3}{2})}\bar{b}_3aāa^\star| + \sqrt{3}\,|b_2\bar{b}_{(\frac{2}{3})}b_3aa\bar{b}_1| -$$

$$\sqrt{3}\,|b_{(\frac{2}{3})}\bar{b}_2\bar{b}_3aāb_1| \quad (47)$$

Triplet wave functions $^3B_1[^3T_{1g}(t_{2g}{}^5e_g)]$, $^3A[^3T_{2g}(t_{2g}{}^5e_g)]$, $^3B_{(\frac{2}{3})}[^3T_{1,2g}(t_{2g}{}^5e_g)]$ correspondent to those of $^1B_1[^1T_{1g}(t_{2g}{}^5e_g)]$, $^1A[^1T_{2g}(t_{2g}{}^5e_g)]$, $^1B_{(\frac{2}{3})}[^1T_{1,2g}(t_{2g}{}^5e_g)]$ impressed on high are swiftly fabricated by circumspect exploit of their two-electron (partial) hole equivalents $^3B_1[^3T_{1g}(t_{2g}e_g)]$, $^3A[^3T_{2g}(t_{2g}e_g)]$, $^3B_{(\frac{2}{3})}[^3T_{1,2g}(t_{2g}e_g)]$ of eq. 35, compliant with the restrictive prescriptions of footnotes 19 and 20.

These functions allow the spiratory and spectral matrix contents to be indexed.

(iii) Matrix Elements: Four Electrons

$$\left\langle {}^5B_1[{}^5E_g(t_{2g}{}^3e_g)]\left|\frac{\vec{p}}{\vec{m}}\right|{}^5A[{}^5E_g(t_{2g}{}^3e_g)]\right\rangle =$$

$$-\left\langle a^\star\left|\frac{\vec{p}}{\vec{m}}\right|b_1\right\rangle$$

$$\left\langle {}^5B_1[{}^5E_g(t_{2g}{}^3e_g)]\left|\frac{\vec{p}}{\vec{m}}\right|{}^5A[{}^5T_{2g}(t_{2g}{}^2e_g{}^2)]\right\rangle = \left\langle a\left|\frac{\vec{p}}{\vec{m}}\right|b_1\right\rangle$$

$$\left\langle {}^5B_1[{}^5E_g(t_{2g}{}^3e_g)]\left|\frac{\vec{p}}{\vec{m}}\right|{}^5B_{(\frac{2}{3})}[{}^5T_{2g}(t_{2g}{}^2e_g{}^2)]\right\rangle =$$

$$(\pm)\left\langle b_{(\frac{2}{3})}\left|\frac{\vec{p}}{\vec{m}}\right|b_1\right\rangle$$

$$\left\langle {}^5A[{}^5E_g(t_{2g}{}^3e_g)]\left|\frac{\vec{p}}{\vec{m}}\right|{}^5A[{}^5T_{2g}(t_{2g}{}^2e_g{}^2)]\right\rangle \equiv 0$$

$$\left\langle {}^5A[{}^5E_g(t_{2g}{}^3e_g)]\left|\frac{\vec{p}}{\vec{m}}\right|{}^5B_{(\frac{2}{3})}[{}^5T_{2g}(t_{2g}{}^2e_g{}^2)]\right\rangle =$$

$$(\pm)\left\langle b_{(\frac{2}{3})}\left|\frac{\vec{p}}{\vec{m}}\right|a^\star\right\rangle$$

$$\left\langle {}^3B_{(\frac{2}{3})}[{}^3T_{1g}(t_{2g}{}^4)]\left|\frac{\vec{p}}{\vec{m}}\right|{}^3B_1[{}^3T_{1g}(t_{2g}{}^4)]\right\rangle =$$

$$(\mp)\left\langle b_{(\frac{3}{2})}\left|\frac{\vec{p}}{\vec{m}}\right|a\right\rangle$$

$$\left\langle {}^3B_{(\frac{2}{3})}[{}^3T_{1g}(t_{2g}{}^4)]\left|\frac{\vec{p}}{\vec{m}}\right|{}^3B_1[{}^3E_g(t_{2g}{}^3e_g)]\right\rangle =$$

$$(\pm)\frac{2}{\sqrt{3}}\left\langle b_{(\frac{3}{2})}\left|\frac{\vec{p}}{\vec{m}}\right|a^\star\right\rangle$$

$$\left\langle {}^3B_{(\frac{2}{3})}[{}^3T_{1g}(t_{2g}{}^4)]\left|\frac{\vec{p}}{\vec{m}}\right|{}^3A[{}^3E_g(t_{2g}{}^3e_g)]\right\rangle =$$
$$(\mp)\frac{2}{\sqrt{3}}\left\langle b_{(\frac{3}{2})}\left|\frac{\vec{p}}{\vec{m}}\right|b_1\right\rangle$$

$$\left\langle {}^3B_{(\frac{2}{3})}[{}^3T_{1g}(t_{2g}{}^4)]\left|\frac{\vec{p}}{\vec{m}}\right|{}^3B_1[{}^3T_{1g}(t_{2g}{}^3e_g)]\right\rangle =$$
$$\frac{1}{\sqrt{2}}\left\langle b_{(\frac{3}{2})}\left|\frac{\vec{p}}{\vec{m}}\right|a^\star\right\rangle$$

$$\left\langle {}^3B_{(\frac{2}{3})}[{}^3T_{1g}(t_{2g}{}^4)]\left|\frac{\vec{p}}{\vec{m}}\right|{}^3B_{(\frac{2}{3})}[{}^3T_{1g}(t_{2g}{}^3e_g)]\right\rangle \equiv 0$$

$$\left\langle {}^3B_{(\frac{2}{3})}[{}^3T_{1g}(t_{2g}{}^4)]\left|\frac{\vec{p}}{\vec{m}}\right|{}^3B_{(\frac{3}{2})}[{}^3T_{1g}(t_{2g}{}^3e_g)]\right\rangle =$$
$$(\mp)^1/_2\sqrt{{}^3/_2}\left\langle a\left|\frac{\vec{p}}{\vec{m}}\right|b_1\right\rangle$$

$$\left\langle {}^3B_{(\frac{2}{3})}[{}^3T_{1g}(t_{2g}{}^4)]\left|\frac{\vec{p}}{\vec{m}}\right|{}^3A[{}^3T_{2g}(t_{2g}{}^3e_g)]\right\rangle =$$
$$\frac{1}{\sqrt{2}}\left\langle b_{(\frac{3}{2})}\left|\frac{\vec{p}}{\vec{m}}\right|b_1\right\rangle$$

$$\left\langle {}^3B_{(\frac{2}{3})}[{}^3T_{1g}(t_{2g}{}^4)]\left|\frac{\vec{p}}{\vec{m}}\right|{}^3B_{(\frac{2}{3})}[{}^3T_{2g}(t_{2g}{}^3e_g)]\right\rangle \equiv 0$$

$$\left\langle {}^3B_{(\frac{2}{3})}[{}^3T_{1g}(t_{2g}{}^4)]\left|\frac{\vec{p}}{\vec{m}}\right|{}^3B_{(\frac{3}{2})}[{}^3T_{2g}(t_{2g}{}^3e_g)]\right\rangle =$$
$$(\pm)\frac{1}{2\sqrt{2}}\left\langle a\left|\frac{\vec{p}}{\vec{m}}\right|b_1\right\rangle$$

$$\left\langle {}^3B_{(\frac{2}{3})}[{}^3T_{1g}(t_{2g}{}^4)]\left|\frac{\vec{p}}{\vec{m}}\right|{}^3A[{}^3A_{1g}(t_{2g}{}^3e_g)]\right\rangle =$$
$$(\pm)\frac{1}{2\sqrt{3}}\left\{-\left\langle b_{(\frac{3}{2})}\left|\frac{\vec{p}}{\vec{m}}\right|b_1\right\rangle+\sqrt{3}\left\langle b_{(\frac{2}{3})}\left|\frac{\vec{p}}{\vec{m}}\right|a^\star\right\rangle\right\}$$

$$\left\langle {}^3B_{(\frac{2}{3})}[{}^3T_{1g}(t_{2g}{}^4)]\left|\frac{\vec{p}}{\vec{m}}\right|{}^3B_1[{}^3E_g(t_{2g}{}^3e_g)]\right\rangle =$$
$$(\mp)\frac{1}{2\sqrt{3}}\left\{\sqrt{3}\left\langle b_{(\frac{2}{3})}\left|\frac{\vec{p}}{\vec{m}}\right|b_1\right\rangle-\left\langle b_{(\frac{3}{2})}\left|\frac{\vec{p}}{\vec{m}}\right|a^\star\right\rangle\right\}$$

$$\left\langle {}^3B_{(\frac{2}{3})}[{}^3T_{1g}(t_{2g}{}^4)]\left|\frac{\vec{p}}{\vec{m}}\right|{}^3A[{}^3E_g(t_{2g}{}^3e_g)]\right\rangle =$$
$$(\pm)\frac{1}{2\sqrt{3}}\left\{\sqrt{3}\left\langle b_{(\frac{2}{3})}\left|\frac{\vec{p}}{\vec{m}}\right|a^\star\right\rangle+\left\langle b_{(\frac{3}{2})}\left|\frac{\vec{p}}{\vec{m}}\right|b_1\right\rangle\right\}$$

$$\left\langle {}^3B_{(\frac{2}{3})}[{}^3T_{1g}(t_{2g}{}^4)]\left|\frac{\vec{p}}{\vec{m}}\right|{}^3B_1[{}^3A_{2g}(t_{2g}{}^3e_g)]\right\rangle =$$
$$(\pm)\frac{1}{2\sqrt{3}}\left\{\sqrt{3}\left\langle b_{(\frac{2}{3})}\left|\frac{\vec{p}}{\vec{m}}\right|b_1\right\rangle+\left\langle b_{(\frac{3}{2})}\left|\frac{\vec{p}}{\vec{m}}\right|a^\star\right\rangle\right\}$$

$$\left\langle {}^3B_{(\frac{2}{3})}[{}^3T_{1g}(t_{2g}{}^4)]\left|\frac{\vec{p}}{\vec{m}}\right|{}^3A[{}^3T_{2g}(t_{2g}{}^3e_g)]\right\rangle =$$
$$-\frac{1}{\sqrt{2}}\left\langle b_{(\frac{2}{3})}\left|\frac{\vec{p}}{\vec{m}}\right|a^\star\right\rangle$$

$$\left\langle {}^3B_{(\frac{2}{3})}[{}^3T_{1g}(t_{2g}{}^4)]\left|\frac{\vec{p}}{\vec{m}}\right|{}^3B_{(\frac{2}{3})}[{}^3T_{2g}(t_{2g}{}^3e_g)]\right\rangle \equiv 0$$

$$\left\langle {}^3B_{(\frac{2}{3})}[{}^3T_{1g}(t_{2g}{}^4)]\left|\frac{\vec{p}}{\vec{m}}\right|{}^3B_{(\frac{3}{2})}[{}^3T_{2g}(t_{2g}{}^3e_g)]\right\rangle =$$
$$(\pm)^1/_2\sqrt{{}^3/_2}\left\langle a\left|\frac{\vec{p}}{\vec{m}}\right|b_1\right\rangle$$

$$\left\langle {}^3B_{(\frac{2}{3})}[{}^3T_{1g}(t_{2g}{}^4)]\left|\frac{\vec{p}}{\vec{m}}\right|{}^3B_1[{}^3T_{1g}(t_{2g}{}^3e_g)]\right\rangle =$$
$$-\frac{1}{\sqrt{2}}\left\langle b_{(\frac{3}{2})}\left|\frac{\vec{p}}{\vec{m}}\right|b_1\right\rangle$$

$$\left\langle {}^3B_{(\frac{2}{3})}[{}^3T_{1g}(t_{2g}{}^4)]\left|\frac{\vec{p}}{\vec{m}}\right|{}^3B_{(\frac{2}{3})}[{}^3T_{1g}(t_{2g}{}^3e_g)]\right\rangle \equiv 0$$

$$\left\langle {}^3B_{(\frac{2}{3})}[{}^3T_{1g}(t_{2g}{}^4)]\left|\frac{\vec{p}}{\vec{m}}\right|{}^3B_{(\frac{3}{2})}[{}^3T_{1g}(t_{2g}{}^3e_g)]\right\rangle =$$
$$(\mp)\frac{1}{2\sqrt{2}}\left\langle a\left|\frac{\vec{p}}{\vec{m}}\right|b_1\right\rangle$$

$$\left\langle {}^3B_1[{}^3T_{1g}(t_{2g}{}^4)]\left|\frac{\vec{p}}{\vec{m}}\right|{}^3B_1[{}^3E_g(t_{2g}{}^3e_g)]\right\rangle \equiv 0$$

$$\left\langle {}^3B_1[{}^3T_{1g}(t_{2g}{}^4)]\left|\frac{\vec{p}}{\vec{m}}\right|{}^3A[{}^3E_g(t_{2g}{}^3e_g)]\right\rangle =$$
$$\frac{2}{\sqrt{3}}\left\langle a\left|\frac{\vec{p}}{\vec{m}}\right|b_1\right\rangle$$

$$\left\langle {}^3B_1[{}^3T_{1g}(t_{2g}{}^4)]\left|\frac{\vec{p}}{\vec{m}}\right|{}^3B_1[{}^3T_{1g}(t_{2g}{}^3e_g)]\right\rangle \equiv 0$$

$$\left\langle {}^3B_1[{}^3T_{1g}(t_{2g}{}^4)]\left|\frac{\vec{p}}{\vec{m}}\right|{}^3B_{(\frac{2}{3})}[{}^3T_{1g}(t_{2g}{}^3e_g)]\right\rangle =$$
$$\frac{1}{2\sqrt{2}}\left\{-\left\langle b_{(\frac{3}{2})}\left|\frac{\vec{p}}{\vec{m}}\right|a^\star\right\rangle+\sqrt{3}\left\langle b_{(\frac{2}{3})}\left|\frac{\vec{p}}{\vec{m}}\right|b_1\right\rangle\right\}$$

$$\left\langle {}^3B_1[{}^3T_{1g}(t_{2g}{}^4)]\left|\frac{\vec{p}}{\vec{m}}\right|{}^3A[{}^3T_{2g}(t_{2g}{}^3e_g)]\right\rangle = 0$$

$$\left\langle {}^3B_1[{}^3T_{1g}(t_{2g}{}^4)]\left|\frac{\vec{p}}{\vec{m}}\right|{}^3B_{(\frac{2}{3})}[{}^3T_{2g}(t_{2g}{}^3e_g)]\right\rangle =$$
$$-\frac{1}{2\sqrt{2}}\left\{\sqrt{3}\left\langle b_{(\frac{3}{2})}\left|\frac{\vec{p}}{\vec{m}}\right|a^\star\right\rangle+\left\langle b_{(\frac{2}{3})}\left|\frac{\vec{p}}{\vec{m}}\right|b_1\right\rangle\right\}$$

$$\left\langle {}^3B_1[{}^3T_{1g}(t_{2g}{}^4)]\left|\frac{\vec{p}}{\vec{m}}\right|{}^3A[{}^3A_{1g}(t_{2g}{}^3e_g)]\right\rangle =$$
$$-\frac{1}{\sqrt{3}}\left\langle a\left|\frac{\vec{p}}{\vec{m}}\right|b_1\right\rangle$$

$$\left\langle {}^3B_1[{}^3T_{1g}(t_{2g}{}^4)]\left|\frac{\vec{p}}{\vec{m}}\right|{}^3B_1[{}^3E_g(t_{2g}{}^3e_g)]\right\rangle \equiv 0$$

$$\left\langle {}^3B_1[{}^3T_{1g}(t_{2g}{}^4)]\left|\frac{\vec{p}}{\vec{m}}\right|{}^3A[{}^3E_g(t_{2g}{}^3e_g)]\right\rangle =$$
$$\frac{1}{\sqrt{3}}\left\langle a\left|\frac{\vec{p}}{\vec{m}}\right|b_1\right\rangle$$

$$\left\langle {}^3B_1[{}^3T_{1g}(t_{2g}^4)] \left| \frac{\vec{p}}{\vec{m}} \right| {}^3B_1[{}^3A_{2g}(t_{2g}^3 e_g)] \right\rangle \equiv 0$$

$$\left\langle {}^3B_1[{}^3T_{1g}(t_{2g}^4)] \left| \frac{\vec{p}}{\vec{m}} \right| {}^3A[{}^3T_{2g}(t_{2g}^4 e_g)] \right\rangle = 0$$

$$\left\langle {}^3B_1[{}^3T_{1g}(t_{2g}^4)] \left| \frac{\vec{p}}{\vec{m}} \right| {}^3B_{(\frac{2}{3})}[{}^3T_{2g}(t_{2g}^3 e_g)] \right\rangle =$$

$$\frac{1}{2\sqrt{2}} \left\{ \sqrt{3} \left\langle b_{(\frac{2}{3})} \left| \frac{\vec{p}}{\vec{m}} \right| b_1 \right\rangle - \left\langle b_{(\frac{3}{2})} \left| \frac{\vec{p}}{\vec{m}} \right| a^\star \right\rangle \right\}$$

$$\left\langle {}^3B_1[{}^3T_{1g}(t_{2g}^4)] \left| \frac{\vec{p}}{\vec{m}} \right| {}^3B_1[{}^3T_{1g}(t_{2g}^3 e_g)] \right\rangle \equiv 0$$

$$\left\langle {}^3B_1[{}^3T_{1g}(t_{2g}^4)] \left| \frac{\vec{p}}{\vec{m}} \right| {}^3B_{(\frac{2}{3})}[{}^3T_{1g}(t_{2g}^3 e_g)] \right\rangle =$$

$$-\frac{1}{2\sqrt{2}} \left\{ \sqrt{3} \left\langle b_{(\frac{3}{2})} \left| \frac{\vec{p}}{\vec{m}} \right| a^\star \right\rangle + \left\langle b_{(\frac{2}{3})} \left| \frac{\vec{p}}{\vec{m}} \right| b_1 \right\rangle \right\} \tag{48}$$

(iv) Matrix Elements: Six Electrons

$$\left\langle {}^5A[{}^5T_{2g}(t_{2g}^4 e_g^2)] \left| \frac{\vec{p}}{\vec{m}} \right| {}^5B_{(\frac{2}{3})}[{}^5T_{2g}(t_{2g}^4 e_g^2)] \right\rangle =$$

$$(\pm) \left\langle a \left| \frac{\vec{p}}{\vec{m}} \right| b_{(\frac{2}{3})} \right\rangle$$

$$\left\langle {}^5A[{}^5T_{2g}(t_{2g}^4 e_g^2)] \left| \frac{\vec{p}}{\vec{m}} \right| {}^5A[{}^5E_g(t_{2g}^3 e_g^3)] \right\rangle \equiv 0$$

$$\left\langle {}^5A[{}^5T_{2g}(t_{2g}^4 e_g^2)] \left| \frac{\vec{p}}{\vec{m}} \right| {}^5B_1[{}^5E_g(t_{2g}^3 e_g^3)] \right\rangle =$$

$$-\left\langle a \left| \frac{\vec{p}}{\vec{m}} \right| b_1 \right\rangle$$

$$\left\langle {}^5B_{(\frac{2}{3})}[{}^5T_{2g}(t_{2g}^4 e_g^2)] \left| \frac{\vec{p}}{\vec{m}} \right| {}^5A[{}^5E_g(t_{2g}^3 e_g^3)] \right\rangle =$$

$$(\mp) \left\langle b_{(\frac{2}{3})} \left| \frac{\vec{p}}{\vec{m}} \right| a^\star \right\rangle$$

$$\left\langle {}^5B_{(\frac{2}{3})}[{}^5T_{2g}(t_{2g}^4 e_g^2)] \left| \frac{\vec{p}}{\vec{m}} \right| {}^5B_1[{}^5E_g(t_{2g}^3 e_g^3)] \right\rangle =$$

$$(\mp) \left\langle b_{(\frac{2}{3})} \left| \frac{\vec{p}}{\vec{m}} \right| b_1 \right\rangle$$

$$\left\langle {}^1A[{}^1A_{1g}(t_{2g}^6)] \left| \frac{\vec{p}}{\vec{m}} \right| {}^1B_1[{}^1T_{1g}(t_{2g}^5 e_g)] \right\rangle =$$

$$\sqrt{2} \left\langle a \left| \frac{\vec{p}}{\vec{m}} \right| b_1 \right\rangle$$

$$\left\langle {}^1A[{}^1A_{1g}(t_{2g}^6)] \left| \frac{\vec{p}}{\vec{m}} \right| {}^1B_{(\frac{2}{3})}[{}^1T_{1g}(t_{2g}^5 e_g)] \right\rangle =$$

$$(\mp) \frac{1}{\sqrt{2}} \left\{ \sqrt{3} \left\langle b_{(\frac{2}{3})} \left| \frac{\vec{p}}{\vec{m}} \right| a^\star \right\rangle - \left\langle b_{(\frac{3}{2})} \left| \frac{\vec{p}}{\vec{m}} \right| b_1 \right\rangle \right\}$$

$$\left\langle {}^1A[{}^1A_{1g}(t_{2g}^6)] \left| \frac{\vec{p}}{\vec{m}} \right| {}^1A[{}^1T_{2g}(t_{2g}^5 e_g)] \right\rangle \equiv 0$$

$$\left\langle {}^1A[{}^1A_{1g}(t_{2g}^6)] \left| \frac{\vec{p}}{\vec{m}} \right| {}^1B_{(\frac{2}{3})}[{}^1T_{2g}(t_{2g}^5 e_g)] \right\rangle =$$

$$(\mp) \frac{1}{\sqrt{2}} \left\{ \sqrt{3} \left\langle b_{(\frac{3}{2})} \left| \frac{\vec{p}}{\vec{m}} \right| b_1 \right\rangle + \left\langle b_{(\frac{2}{3})} \left| \frac{\vec{p}}{\vec{m}} \right| a^\star \right\rangle \right\} \tag{49}$$

On account of the spin equivocality and fructificity of the four- and six-electron assortment, we discern that no simple kinship exists either within itself or between the one-, two-, three-, seven-, eight-, or nine-electron allotments. Nonetheless, within a circumscribed patch such kinships can be uprooted. To illustrate: (1) the quintet four and six electronic state pirouettory and optical strengths are identical with one another and with the one- and nine-electron strengths, and are multiplicatively connected to the spin-paired seven-electron strengths; (2) some of the triplet state four-electron verticilatory and chromatic strengths are formally one-half those of the correspondent two- and seven- spin-free electron strengths; and (3) the singlet six-electron helical and spectral strengths are formally twice those of the kindred three- and eight-electron strengths. These kinships will be again asserted in section IV.

(b) N_Q Configuration Interaction: Nonzero Spin-Orbit Forces. Four and Six Electrons. The remarks apropos of this paragraph are the same as those of §4.2b.

(c) Configuration Interaction: Zero and Nonzero Spin-Orbit Forces. Four and Six Electrons. The aftermaths of configuration interaction are coequal to those of §4.2c.

4.5 *The Five-Electron Case.* Along with our antecedent declarations of §4.2, we conduct our inquest of the five-electron tangle with attention to the single-electron excitations solely, the residuum to be shelved for impendent investment. In this frame, the germane digonally disposed cubical many-electron functions for the five-electron troop are as engraved underneath.

(a) No Configuration Interaction: Zero Spin-Orbit Forces. (i) Wave Functions: Five Electrons

$${}^6A[{}^6A_{1g}(t_{2g}^3 e_g^2)]: |b_2 b_3 a a^\star b_1|$$

$${}^4B_1[{}^4T_{1g}(t_{2g}^4 e_g)]: |b_2 b_3 a \bar{a} a^\star|$$

$${}^4B_{(\frac{2}{3})}[{}^4T_{1g}(t_{2g}^4 e_g)]:$$

$$(\pm)^1/_2 \{ \sqrt{3} |b_2 \bar{b}_{(\frac{2}{3})} b_3 a b_1| - |b_2 b_3 \bar{b}_{(\frac{3}{2})} a a^\star| \}$$

$${}^4A[{}^4T_{2g}(t_{2g}^4 e_g)]: |b_2 b_3 a \bar{a} b_1|$$

$${}^4B_{(\frac{2}{3})}[{}^4T_{2g}(t_{2g}^4 e_g)]:$$

$$(\mp)^1/_2 \{ |b_2 \bar{b}_{(\frac{2}{3})} b_3 a b_1| + \sqrt{3} |b_2 b_3 \bar{b}_{(\frac{3}{2})} a a^\star| \}$$

$$^2A[^2T_{2g}(t_{2g}^5)]: |b_2\bar{b}_2b_3\bar{b}_3a|$$

$$^2B_{(\frac{2}{3})}[^2T_{2g}(t_{2g}^5)]: |b_2b_3\bar{b}_{(\frac{3}{2})}a\bar{a}|$$

$$^2B_1[^2A_{2g}(t_{2g}^4e_g)]: -\frac{1}{2\sqrt{3}}\{2|b_2\bar{b}_2b_3\bar{b}_3b_1| - |b_3\bar{b}_3a\bar{a}b_1| - |b_2\bar{b}_2a\bar{a}b_1| - \sqrt{3}\,|b_2\bar{b}_3a\bar{a}a^*| + \sqrt{3}\,|\bar{b}_2b_3a\bar{a}a^*|\}$$

$$^2B_1[^2T_{1g}(t_{2g}^4e_g)]: \frac{1}{\sqrt{6}}\{2|b_2b_3a\bar{a}\bar{a}^*| - |b_2\bar{b}_3a\bar{a}a^*| - |\bar{b}_2b_3a\bar{a}a^*|\}$$

$$^2B_{(\frac{2}{3})}[^2T_{1g}(t_{2g}^4e_g)]: (\pm)\frac{1}{2\sqrt{6}}\{2\sqrt{3}\,|b_2\bar{b}_{(\frac{2}{3})}b_3a\bar{b}_1| - \sqrt{3}\,|b_2\bar{b}_{(\frac{2}{3})}b_3\bar{a}b_1| - \sqrt{3}\,|b_{(\frac{2}{3})}\bar{b}_2\bar{b}_3ab_1| - 2|b_2b_3\bar{b}_{(\frac{3}{2})}a\bar{a}^*| + |b_2b_3\bar{b}_{(\frac{3}{2})}\bar{a}a^*| + |\bar{b}_2b_{(\frac{3}{2})}\bar{b}_3aa^*|\}$$

$$^2A[^2T_{2g}(t_{2g}^4e_g)]: -\frac{1}{\sqrt{2}}\{|b_3\bar{b}_3a\bar{a}a^*| - |b_2\bar{b}_2a\bar{a}a^*|\}$$

$$^2B_{(\frac{2}{3})}[^2T_{2g}(t_{2g}^4e_g)]: (\pm)\frac{1}{2\sqrt{2}}\{\sqrt{3}\,|b_2\bar{b}_{(\frac{2}{3})}b_3\bar{a}b_1| - \sqrt{3}\,|b_{(\frac{2}{3})}\bar{b}_2\bar{b}_3ab_1| + |\bar{b}_2b_{(\frac{3}{2})}\bar{b}_3aa^*| - |b_2b_3\bar{b}_{(\frac{3}{2})}\bar{a}a^*|\}$$

$$^2A[^2E_g(t_{2g}^4e_g)]: -\frac{1}{2\sqrt{3}}\{2|b_2\bar{b}_2b_3\bar{b}_3a^*| - |b_3\bar{b}_3a\bar{a}a^*| - |b_2\bar{b}_2a\bar{a}a^*| - \sqrt{3}\,|b_2\bar{b}_3a\bar{a}b_1| + \sqrt{3}\,|\bar{b}_2b_3a\bar{a}b_1|\}$$

$$^2B_1[^2E_g(t_{2g}^4e_g)]: \frac{1}{2\sqrt{3}}\{2|b_2\bar{b}_2b_3\bar{b}_3b_1| - |b_3\bar{b}_3a\bar{a}b_1| - |b_2\bar{b}_2a\bar{a}b_1| + \sqrt{3}\,|b_2\bar{b}_3a\bar{a}a^*| - \sqrt{3}\,|\bar{b}_2b_3a\bar{a}a^*|\}$$

$$^2A[^2T_{2g}(t_{2g}^4e_g)]: \frac{1}{\sqrt{6}}\{2|b_2b_3a\bar{a}\bar{b}_1| - |b_2\bar{b}_3a\bar{a}b_1| - |\bar{b}_2b_3a\bar{a}b_1|\}$$

$$^2B_{(\frac{2}{3})}[^2T_{2g}(t_{2g}^4e_g)]: (\mp)\frac{1}{2\sqrt{6}}\{2|b_2\bar{b}_{(\frac{2}{3})}b_3a\bar{b}_1| - |b_2\bar{b}_{(\frac{2}{3})}b_3\bar{a}b_1| - |b_{(\frac{2}{3})}\bar{b}_2\bar{b}_3ab_1| + 2\sqrt{3}\,|b_2b_3\bar{b}_{(\frac{3}{2})}a\bar{a}^*| - \sqrt{3}\,|b_2b_3\bar{b}_{(\frac{3}{2})}\bar{a}a^*| - \sqrt{3}\,|\bar{b}_2b_{(\frac{3}{2})}\bar{b}_3aa^*|\}$$

$$^2B_1[^2T_{1g}(t_{2g}^4e_g)]: -\frac{1}{\sqrt{2}}\{|b_3\bar{b}_3a\bar{a}b_1| - |b_2\bar{b}_2a\bar{a}b_1|\}$$

$$^2B_{(\frac{2}{3})}[^2T_{1g}(t_{2g}^4e_g)]: (\mp)\frac{1}{2\sqrt{2}}\{|b_2\bar{b}_{(\frac{2}{3})}b_3\bar{a}b_1| - |b_{(\frac{2}{3})}\bar{b}_2\bar{b}_3ab_1| - \sqrt{3}\,|\bar{b}_2b_{(\frac{3}{2})}\bar{b}_3aa^*| + \sqrt{3}\,|b_2b_3\bar{b}_{(\frac{3}{2})}\bar{a}a^*|\}$$

$$^2A[^2A_{1g}(t_{2g}^4e_g)]: -\frac{1}{2\sqrt{3}}\{2|b_2\bar{b}_2b_3\bar{b}_3a^*| - |b_3\bar{b}_3a\bar{a}a^*| - |b_2\bar{b}_2a\bar{a}a^*| + \sqrt{3}\,|b_2\bar{b}_3a\bar{a}b_1| - \sqrt{3}\,|\bar{b}_2b_3a\bar{a}b_1|\}$$

$$^2A[^2E_g(t_{2g}^4e_g)]: -\frac{1}{\sqrt{3}}\{|b_2\bar{b}_2b_3\bar{b}_3a^*| + |b_3\bar{b}_3a\bar{a}a^*| + |b_2\bar{b}_2a\bar{a}a^*|\}$$

$$^2B_1[^2E_g(t_{2g}^4e_g)]: -\frac{1}{\sqrt{3}}\{|b_2\bar{b}_2b_3\bar{b}_3b_1| + |b_3\bar{b}_3a\bar{a}b_1| + |b_2\bar{b}_2a\bar{a}b_1|\} \quad (50)$$

These configurational functions enable the vortical and photical matrix segments to be gathered.

(ii) Matrix Elements: Five Electrons

$$\left\langle ^2A[^2T_{2g}(t_{2g}^5)]\left|\frac{\vec{p}}{\vec{m}}\right|{}^2B_{(\frac{2}{3})}[^2T_{2g}(t_{2g}^5)]\right\rangle = (\mp)\left\langle b_{(\frac{2}{3})}\left|\frac{\vec{p}}{\vec{m}}\right|a\right\rangle$$

$$\left\langle ^2A[^2T_{2g}(t_{2g}^5)]\left|\frac{\vec{p}}{\vec{m}}\right|{}^2B_1[^2A_{2g}(t_{2g}^4e_g)]\right\rangle = -\frac{1}{\sqrt{3}}\left\langle a\left|\frac{\vec{p}}{\vec{m}}\right|b_1\right\rangle$$

$$\left\langle ^2A[^2T_{2g}(t_{2g}^5)]\left|\frac{\vec{p}}{\vec{m}}\right|{}^2B_1[^2T_{1g}(t_{2g}^4e_g)]\right\rangle = 0$$

$$\left\langle ^2A[^2T_{2g}(t_{2g}^5)]\left|\frac{\vec{p}}{\vec{m}}\right|{}^2B_{(\frac{2}{3})}[^2T_{1g}(t_{2g}^4e_g)]\right\rangle = {}^1/_2\sqrt{{}^3/_2}\left\{\left\langle b_{(\frac{2}{3})}\left|\frac{\vec{p}}{\vec{m}}\right|a^*\right\rangle - \sqrt{3}\left\langle b_{(\frac{3}{2})}\left|\frac{\vec{p}}{\vec{m}}\right|b_1\right\rangle\right\}$$

$$\left\langle ^2A[^2T_{2g}(t_{2g}^5)]\left|\frac{\vec{p}}{\vec{m}}\right|{}^2A[^2T_{2g}(t_{2g}^4e_g)]\right\rangle \equiv 0$$

$$\left\langle ^2A[^2T_{2g}(t_{2g}^5)]\left|\frac{\vec{p}}{\vec{m}}\right|{}^2B_{(\frac{2}{3})}[^2T_{2g}(t_{2g}^4e_g)]\right\rangle = {}^1/_2\left\{\left\langle b_{(\frac{2}{3})}\left|\frac{\vec{p}}{\vec{m}}\right|a^*\right\rangle - \sqrt{3}\left\langle b_{(\frac{3}{2})}\left|\frac{\vec{p}}{\vec{m}}\right|b_1\right\rangle\right\}$$

$$\left\langle ^2A[^2T_{2g}(t_{2g}^5)]\left|\frac{\vec{p}}{\vec{m}}\right|{}^2A[^2E_g(t_{2g}^4e_g)]\right\rangle \equiv 0$$

$$\left\langle ^2A[^2T_{2g}(t_{2g}^5)]\left|\frac{\vec{p}}{\vec{m}}\right|{}^2B_1[^2E_g(t_{2g}^4e_g)]\right\rangle = \frac{1}{\sqrt{3}}\left\langle a\left|\frac{\vec{p}}{\vec{m}}\right|b_1\right\rangle$$

$$\left\langle ^2A[^2T_{2g}(t_{2g}^5)]\left|\frac{\vec{p}}{\vec{m}}\right|{}^2A[^2T_{2g}(t_{2g}^4e_g)]\right\rangle \equiv 0$$

$$\left\langle ^2A[^2T_{2g}(t_{2g}^5)]\left|\frac{\vec{p}}{\vec{m}}\right|{}^2B_{(\frac{2}{3})}[^2T_{2g}(t_{2g}^4e_g)]\right\rangle = {}^1/_2\sqrt{{}^3/_2}\left\{\sqrt{3}\left\langle b_{(\frac{2}{3})}\left|\frac{\vec{p}}{\vec{m}}\right|a^*\right\rangle + \left\langle b_{(\frac{3}{2})}\left|\frac{\vec{p}}{\vec{m}}\right|b_1\right\rangle\right\}$$

$$\left\langle ^2A[^2T_{2g}(t_{2g}^5)]\left|\frac{\vec{p}}{\vec{m}}\right|{}^2B_1[^2T_{1g}(t_{2g}^4e_g)]\right\rangle = 0$$

$$\left\langle {}^2A[{}^2T_{2g}(t_{2g}^5)] \left|\frac{\vec{p}}{\vec{m}}\right| {}^2B_{(\frac{2}{3})}[{}^2T_{1g}(t_{2g}^4e_g)] \right\rangle =$$
$$\frac{1}{2\sqrt{2}} \left\{ \sqrt{3} \left\langle b_{(\frac{2}{3})} \left|\frac{\vec{p}}{\vec{m}}\right| a^* \right\rangle + \left\langle b_{(\frac{3}{2})} \left|\frac{\vec{p}}{\vec{m}}\right| b_1 \right\rangle \right\}$$

$$\left\langle {}^2A[{}^2T_{2g}(t_{2g}^5)] \left|\frac{\vec{p}}{\vec{m}}\right| {}^2A[{}^2A_{1g}(t_{2g}^4e_g)] \right\rangle \equiv 0$$

$$\left\langle {}^2A[{}^2T_{2g}(t_{2g}^5)] \left|\frac{\vec{p}}{\vec{m}}\right| {}^2A[{}^2E_g(t_{2g}^4e_g)] \right\rangle \equiv 0$$

$$\left\langle {}^2A[{}^2T_{2g}(t_{2g}^5)] \left|\frac{\vec{p}}{\vec{m}}\right| {}^2B_1[{}^2E_g(t_{2g}^4e_g)] \right\rangle =$$
$$-\frac{1}{\sqrt{3}} \left\langle a \left|\frac{\vec{p}}{\vec{m}}\right| b_1 \right\rangle$$

$$\left\langle {}^2B_{(\frac{2}{3})}[{}^2T_{2g}(t_{2g}^5)] \left|\frac{\vec{p}}{\vec{m}}\right| {}^2B_1[{}^2A_{2g}(t_{2g}^4e_g)] \right\rangle =$$
$$(\pm)\frac{1}{2\sqrt{3}} \left\{ \left\langle b_{(\frac{2}{3})} \left|\frac{\vec{p}}{\vec{m}}\right| b_1 \right\rangle - \sqrt{3} \left\langle b_{(\frac{3}{2})} \left|\frac{p}{\vec{m}}\right| a^* \right\rangle \right\}$$

$$\left\langle {}^2B_{(\frac{2}{3})}[{}^2T_{2g}(t_{2g}^5)] \left|\frac{\vec{p}}{\vec{m}}\right| {}^2B_1[{}^2T_{1g}(t_{2g}^4e_g)] \right\rangle =$$
$$\sqrt{3/2} \left\langle b_{(\frac{3}{2})} \left|\frac{\vec{p}}{\vec{m}}\right| a^* \right\rangle$$

$$\left\langle {}^2B_{(\frac{2}{3})}[{}^2T_{2g}(t_{2g}^5)] \left|\frac{\vec{p}}{\vec{m}}\right| {}^2B_{(\frac{2}{3})}[{}^2T_{1g}(t_{2g}^4e_g)] \right\rangle \equiv 0$$

$$\left\langle {}^2B_{(\frac{2}{3})}[{}^2T_{2g}(t_{2g}^5)] \left|\frac{\vec{p}}{\vec{m}}\right| {}^2B_{(\frac{3}{2})}[{}^2T_{1g}(t_{2g}^4e_g)] \right\rangle =$$
$$(\pm)\frac{3}{2\sqrt{2}} \left\langle a \left|\frac{\vec{p}}{\vec{m}}\right| b_1 \right\rangle$$

$$\left\langle {}^2B_{(\frac{2}{3})}[{}^2T_{2g}(t_{2g}^5)] \left|\frac{\vec{p}}{\vec{m}}\right| {}^2A[{}^2T_{2g}(t_{2g}^4e_g)] \right\rangle =$$
$$-\frac{1}{\sqrt{2}} \left\langle b_{(\frac{2}{3})} \left|\frac{\vec{p}}{\vec{m}}\right| a^* \right\rangle$$

$$\left\langle {}^2B_{(\frac{2}{3})}[{}^2T_{2g}(t_{2g}^5)] \left|\frac{\vec{p}}{\vec{m}}\right| {}^2B_{(\frac{2}{3})}[{}^2T_{2g}(t_{2g}^4e_g)] \right\rangle \equiv 0$$

$$\left\langle {}^2B_{(\frac{2}{3})}[{}^2T_{2g}(t_{2g}^5)] \left|\frac{\vec{p}}{\vec{m}}\right| {}^2B_{(\frac{3}{2})}[{}^2T_{2g}(t_{2g}^4e_g)] \right\rangle =$$
$$(\mp)\frac{\sqrt{3}}{2} \left\langle a \left|\frac{\vec{p}}{\vec{m}}\right| b_1 \right\rangle$$

$$\left\langle {}^2B_{(\frac{2}{3})}[{}^2T_{2g}(t_{2g}^5)] \left|\frac{\vec{p}}{\vec{m}}\right| {}^2A[{}^2E_g(t_{2g}^4e_g)] \right\rangle =$$
$$(\pm)\frac{1}{2\sqrt{3}} \left\{ \left\langle b_{(\frac{2}{3})} \left|\frac{\vec{p}}{\vec{m}}\right| a^* \right\rangle - \sqrt{3} \left\langle b_{(\frac{3}{2})} \left|\frac{\vec{p}}{\vec{m}}\right| b_1 \right\rangle \right\}$$

$$\left\langle {}^2B_{(\frac{2}{3})}[{}^2T_{2g}(t_{2g}^5)] \left|\frac{\vec{p}}{\vec{m}}\right| {}^2B_1[{}^2E_g(t_{2g}^4e_g)] \right\rangle =$$
$$(\mp)\frac{1}{2\sqrt{3}} \left\{ \left\langle b_{(\frac{2}{3})} \left|\frac{\vec{p}}{\vec{m}}\right| b_1 \right\rangle + \sqrt{3} \left\langle b_{(\frac{3}{2})} \left|\frac{\vec{p}}{\vec{m}}\right| a^* \right\rangle \right\}$$

$$\left\langle {}^2B_{(\frac{2}{3})}[{}^2T_{2g}(t_{2g}^5)] \left|\frac{\vec{p}}{\vec{m}}\right| {}^2A[{}^2T_{2g}(t_{2g}^4e_g)] \right\rangle =$$
$$\sqrt{3/2} \left\langle b_{(\frac{3}{2})} \left|\frac{\vec{p}}{\vec{m}}\right| b_1 \right\rangle$$

$$\left\langle {}^2B_{(\frac{2}{3})}[{}^2T_{2g}(t_{2g}^5)] \left|\frac{\vec{p}}{\vec{m}}\right| {}^2B_{(\frac{2}{3})}[{}^2T_{2g}(t_{2g}^4e_g)] \right\rangle \equiv 0$$

$$\left\langle {}^2B_{(\frac{2}{3})}[{}^2T_{2g}(t_{2g}^5)] \left|\frac{\vec{p}}{\vec{m}}\right| {}^2B_{(\frac{3}{2})}[{}^2T_{2g}(t_{2g}^4e_g)] \right\rangle =$$
$$(\mp)^{1/2}\sqrt{3/2} \left\langle a \left|\frac{\vec{p}}{\vec{m}}\right| b_1 \right\rangle$$

$$\left\langle {}^2B_{(\frac{2}{3})}[{}^2T_{2g}(t_{2g}^5)] \left|\frac{\vec{p}}{\vec{m}}\right| {}^2B_1[{}^2T_{1g}(t_{2g}^4e_g)] \right\rangle =$$
$$-\frac{1}{\sqrt{2}} \left\langle b_{(\frac{2}{3})} \left|\frac{\vec{p}}{\vec{m}}\right| b_1 \right\rangle$$

$$\left\langle {}^2B_{(\frac{2}{3})}[{}^2T_{2g}(t_{2g}^5)] \left|\frac{\vec{p}}{\vec{m}}\right| {}^2B_{(\frac{2}{3})}[{}^2T_{1g}(t_{2g}^4e_g)] \right\rangle \equiv 0$$

$$\left\langle {}^2B_{(\frac{2}{3})}[{}^2T_{2g}(t_{2g}^5)] \left|\frac{\vec{p}}{\vec{m}}\right| {}^2B_{(\frac{3}{2})}[{}^2T_{1g}(t_{2g}^4e_g)] \right\rangle =$$
$$(\pm)\frac{1}{2\sqrt{2}} \left\langle a \left|\frac{\vec{p}}{\vec{m}}\right| b_1 \right\rangle$$

$$\left\langle {}^2B_{(\frac{2}{3})}[{}^2T_{2g}(t_{2g}^5)] \left|\frac{\vec{p}}{\vec{m}}\right| {}^2A[{}^2A_{1g}(t_{2g}^4e_g)] \right\rangle =$$
$$(\pm)\frac{1}{2\sqrt{3}} \left\{ \left\langle b_{(\frac{2}{3})} \left|\frac{\vec{p}}{\vec{m}}\right| a^* \right\rangle + \sqrt{3} \left\langle b_{(\frac{3}{2})} \left|\frac{\vec{p}}{\vec{m}}\right| b_1 \right\rangle \right\}$$

$$\left\langle {}^2B_{(\frac{2}{3})}[{}^2T_{2g}(t_{2g}^5)] \left|\frac{\vec{p}}{\vec{m}}\right| {}^2A[{}^2E_g(t_{2g}^4e_g)] \right\rangle =$$
$$(\mp)\frac{1}{\sqrt{3}} \left\langle b_{(\frac{2}{3})} \left|\frac{\vec{p}}{\vec{m}}\right| a^* \right\rangle$$

$$\left\langle {}^2B_{(\frac{2}{3})}[{}^2T_{2g}(t_{2g}^5)] \left|\frac{\vec{p}}{\vec{m}}\right| {}^2B_1[{}^2E_g(t_{2g}^4e_g)] \right\rangle =$$
$$(\mp)\frac{1}{\sqrt{3}} \left\langle b_{(\frac{2}{3})} \left|\frac{\vec{p}}{\vec{m}}\right| b_1 \right\rangle \quad (51)$$

Like the four- and six-electron circumstance, the multifaricity of the spin-electronic states checks any even regular concert of the five electron vortical and photical strengths with those of the one-, two-, three-four-, six-, seven-, eight-, or nine-electron collects. Still special relationships exist in limited areas. Exemplificatively, the four- and five- spin-paired digonally directed cubical electron congregations of the legally allowed single electron leaps can be put in a one to one association with each other so that their vertigal and photical strengths become (for the most part) equal when the digonal and cubical specie labels A and B_1, B_2 and B_3, A_1 and A_2, and T_1 and T_2 are interchanged, that is, so that the $A(T_{1g})$, $B_{(\frac{2}{3})}(T_{1g})$ to $A(T_{1g})$, $B_{(\frac{2}{3})}(T_{1g})$

transition of the four-electron case corresponds to the $B_1(T_{2g})$, $B_{(\frac{2}{3})}(T_{2g})$ to $B_1(T_{2g})$, $B_{(\frac{2}{3})}(T_{2g})$ transition of the five-electron case, and so on [three exceptions to this rule exist; one of the four-electron $A(T_{1g})$, $B_{(\frac{2}{3})}(T_{1g})$ to $A(E_g)$, $B_1(E_g)$ transitions is four times as strong as the associate five-electron transition, and one each of the four-electron $A(T_{1g})$, $B_{(\frac{2}{3})}(T_{1g})$ to $A(T_{1g})$, $B_1(T_{2g})$, $B_{(\frac{2}{3})}(T_{1,2g})$ transitions is one-third as strong as its correspondent five-electron transition]. It therefore follows that the five-electron vertigal and photical strengths are also linked to those of the two- and seven-electron spin-free (and hence other) situations, just as were the four-electron strengths of §4.4. In addition, there is a direct multiplicative relationship between the two sets of $^2A[^2T_{2g}(t_{2g}^5)]$, $^2B_{(\frac{2}{3})}[^2T_{2g}(t_{2g}^5)]$ to $^2A[^2E_g(t_{2g}^4e_g)]$, $^2B_1[^2E_g(t_{2g}^4e_g)]$ five-electron spin-paired rotational and spectral strengths and the associate sets of $^2A[^2E_g(t_{2g}^6e_g)]$, $^2B_1[^2E_g(t_{2g}^6e_g)]$ to $^2A[^2T_{2g}(t_{2g}^5e_g^2)]$, $^2B_{(\frac{2}{3})}[^2T_{2g}(t_{2g}^5e_g^2)]$ seven-electron spin-paired strengths [collate eq. 45 with eq. 51], as well as several other less direct relationships.

(*b*) *No Configuration Interaction: Nonzero Spin-Orbit Forces. Five Electrons.* The statements relevant to this paragraph are coincident with those of §4.2b.

(*c*) *Configuration Interaction: Zero and Nonzero Spin-Orbit Forces. Five Electrons.* The harvests of configuration interaction are consonant with those of §4.2c.

4.6 *A Numerical Example: The Bisethylenediamine and Bisglycolato Copper(II) Cation and Anion.* To evince that the electrical asymmetries invoked in the precedent paragraphs are of a proper order to rationalize the measured optical rotations of digonal dihedral transition metal compounds, we shall here document with a numerical exemplar. Entertain the σ- and σ,π-bonded complex ions bis(ethylenediamine)copper(II) and bis(glycolato)copper(II), separately, and suppose for simplicity that these are depictable by a linear combination of Slater type metallic and ligand atomic orbitals with Slater (effective charge) exponents 7.85 (Cu: 3d), 3.80 and 3.90 (N: 2s, 2p), 4.4456 (O: 2s, 2p, or 2p), with the metal and ligand nuclear centers separated by a space of 2.00 Å., as in ref. 6. Also suppose as in ref. 6 that the ligand σ-bond 2s- and 2p-like content k_s and k_p are $^1/_2$ and $\sqrt{3}/2$ each, that the ligand–metal σ,π mixture parameters $N_a\eta a_+^{\sigma,\pi,\bar{\pi}+}$, $N_a{}^\star\eta^\star a_+^{\sigma,\pi,\bar{\pi}+}$, $N_{b_1}\rho_1 a_+^{\sigma,\pi,\bar{\pi}-}$, $N_{b_2}\rho_2 a_-^{\sigma,\pi,\bar{\pi}-}$, $N_{b_3}\rho_3 a_-^{\sigma,\pi,\bar{\pi}+}$ are $^1/_{20}$, $^1/_{20}$, $-1/2\sqrt{2}$, $^1/_{26}$, $^1/_{20}$, apiece,[22] that metal multiplicative factors N_a, $N_a{}^\star$, N_{b_1}, N_{b_2}, N_{b_3} are unity, and that the angles of ligand–metal orbital cant, α and ι, are 5°. With these modest estimates the rotational, $\mathfrak{R}$, and spectral, $\mathfrak{S}$, strengths for bis(ethylenediamine)copper(II) in the conformations of Fig. 1 and 3 become, in the limit of zero spin-orbit forces

$$\mathfrak{R}[^2B_1(E_g) \rightarrow {}^2A(E_g)] \approx 7.6 \times 10^{-3}B$$

$$\mathfrak{S}[^2B_1(E_g) \rightarrow {}^2A(E_g)] \approx 6.7 \times 10^{-3}D^2,$$

$$\mathfrak{M}[^2B_1(E_g) \rightarrow {}^2A(E_g)] \approx 8.6 \times 10^{-7}V^2$$

$$\mathfrak{R}[^2B_1(E_g) \rightarrow {}^2A(T_{2g})] \approx -1.5B$$

$$\mathfrak{S}[^2B_1(E_g) \rightarrow {}^2A(T_{2g})] \approx 6.7 \times 10^{-5}D^2,$$

$$\mathfrak{M}[^2B_1(E_g) \rightarrow {}^2A(T_{2g})] \approx 3.4V^2$$

$$\mathfrak{R}[^2B_1(E_g) \rightarrow {}^2B_{(\frac{2}{3})}(T_{2g})] \approx (\pm)37B$$

$$\mathfrak{S}[^2B_1(E_g) \rightarrow {}^2B_{(\frac{2}{3})}(T_{2g})] \approx 0.16D^2,$$

$$\mathfrak{M}[^2B_1(E_g) \rightarrow {}^2B_{(\frac{2}{3})}(T_{2g})] \approx 0.86V^2$$

$$\mathfrak{R}[^2A(E_g) \rightarrow {}^2A(T_{2g})] \equiv 0$$

$$\mathfrak{S}[^2A(E_g) \rightarrow {}^2A(T_{2g})] \equiv 0, \quad \mathfrak{M}[^2A(E_g) \rightarrow {}^2A(T_{2g})] \equiv 0$$

$$\mathfrak{R}[^2A(E_g) \rightarrow {}^2B_{(\frac{2}{3})}(T_{2g})] \approx (\pm)2B$$

$$\mathfrak{S}[^2A(E_g) \rightarrow {}^2B_{(\frac{2}{3})}(T_{2g})] \approx 1 \times 10^{-4}D^2,$$

$$\mathfrak{M}[^2A(E_g) \rightarrow {}^2B_{(\frac{2}{3})}(T_{2g})] \approx 2.6V^2$$

$$\mathfrak{R}[^2A(T_{2g}) \rightarrow {}^2B_{(\frac{2}{3})}(T_{2g})] \approx 3.1B$$

$$\mathfrak{S}[^2A(T_{2g}) \rightarrow {}^2B_{(\frac{2}{3})}(T_{2g})] \approx 1.1 \times 10^{-3}D^2,$$

$$\mathfrak{M}[^2A(T_{2g}) \rightarrow {}^2B_{(\frac{2}{3})}(T_{2g})] \approx 0.86V^2$$

$$\mathfrak{R}[^2B_2(T_{2g}) \rightarrow {}^2B_3(T_{2g})] \approx -6.7B$$

$$\mathfrak{S}[^2B_2(T_{2g}) \rightarrow {}^2B_3(T_{2g})] \approx 5.2 \times 10^{-3}D^2,$$

$$\mathfrak{M}[^2B_2 \rightarrow {}^2B_3(T_{2g})] \approx 0.86V^2 \quad (52)$$

where the symbols B, D, and V denote the fundamental units of rotational and spectral strength, the Biot [10^{-40} c.g.s.], the Debye [10^{-18} c.g.s.], and the Van Vleck [10^{-20} c.g.s.].[23] If besides the transition frequencies involved $\nu[^2B_1(E_g) \rightarrow {}^2A(E_g)]$, $\nu[^2B_1(E_g) \rightarrow {}^2A(T_{2g})]$, $\nu[^2B_1(E_g) \rightarrow {}^2B_{(\frac{2}{3})}(T_{2g})]$, $\nu[^2A(E_g) \rightarrow {}^2A(T_{2g})]$,

(22) Mark that if the normalization of the ligand function $\Sigma_{s_z}(s_z)_c$, $\Pi_{s_z}(s_z)_c$, $\tilde{\Pi}_{s_z}(s_z)_s$ is taken to be $^1/_2$ the variational constants $\eta a_+^{\sigma,\pi,\bar{\pi}+}$, $\eta^\star a_+^{\sigma,\pi,\bar{\pi}+}$, $\rho_1 a_+^{\sigma,\pi,\bar{\pi}-}$, $\rho_2 a_-^{\sigma,\pi,\bar{\pi}-}$, $\rho_3 a_-^{\sigma,\pi,\bar{\pi}+}$ become $^1/_2\eta\epsilon_+^{\sigma,\pi,\bar{\pi}+}$, $^1/_2\eta^\star\epsilon_+^{\sigma,\pi,\bar{\pi}+}$, $^1/_2\rho_1\epsilon_+^{\sigma,\pi,\bar{\pi}-}$, $^1/_2\rho_2\epsilon_-^{\sigma,\pi,\bar{\pi}-}$, $^1/_2\rho_3\epsilon_-^{\sigma,\pi,\bar{\pi}+}$ where the $\epsilon_\pm^{\sigma,\pi,\bar{\pi}\pm}$ are the true variational factors and the η, $\eta^\star$, ρ_1, ρ_2, ρ_3 are convenient sequesteral coefficients which may be set equal to unity if desired. The signs of the variational constants are somewhat ambiguous, as some cannot be fixed by overlap considerations as in ref. 6, footnote 48 [note, however, that this same ambiguity actually occurred in the trigonal problem also, but that it was there craftily disguised and glossed over]. This occurrence is especially critical for the dominant odd ligand–ligand contributions. We have here assumed that sign for these odd ligand orbital constants matches that for the companionate even ligand orbital constants. Understandably, this circumstance casts some doubt upon the signed forecasts of the rotational strengths in eq. 52 and 53.

(23) The Van Vleck as a unit of magnetic dipole strength is introduced here to remove the vexation of the usage of a nonunit conversion factor in the comparison of experimental and theoretical results. It is the analog of the Biot and the Debye, whose (theoretical) "natural" units would be $e\mu_B$ and ea_0, where e, μ_B, and a_0 are the electronic charge, the Bohr magneton, and the Bohr radius (infinite nuclear mass) [just as the (theoretical) "natural" unit of the magnetic dipole moment is μ_B].

$\nu[^2A(E_g) \rightarrow {}^2B_{(\frac{2}{3})}(T_{2g})]$, $\nu[^2A(T_{2g}) \rightarrow {}^2B_{(\frac{2}{3})}(T_{2g})]$, $\nu[^2B_2(T_{2g}) \rightarrow {}^2B_3(T_{2g})]$ are elected to be 5×10^3 cm.$^{-1}$, 1.2×10^4 cm.$^{-1}$, 1.5×10^4 cm.$^{-1}$, 7×10^3 cm.$^{-1}$, 1×10^4 cm.$^{-1}$, 3×10^3 cm.$^{-1}$, 3×10^2 cm.$^{-1}$, distributively, the electric oscillator strengths f and the electric dissymmetry factors G scale to [24,25]

$$G[^2B_1(E_g) \rightarrow {}^2A(E_g)] \approx 0.91 \times 10^{-7}\nu, \qquad f[^2B_1(E_g) \rightarrow {}^2A(E_g)] \approx 1.6 \times 10^{-5}$$

$$G[^2B_1(E_g) \rightarrow {}^2A(T_{2g})] \approx -0.75 \times 10^{-3}\nu, \qquad f[^2B_1(E_g) \rightarrow {}^2A(T_{2g})] \approx 3.8 \times 10^{-7}$$

$$G[^2B_1(E_g) \rightarrow {}^2B_{(\frac{2}{3})}(T_{2g})] \approx (\pm)\,6.2 \times 10^{-6}\nu, \qquad f[^2B_1(E_g) \rightarrow {}^2B_{(\frac{2}{3})}(T_{2g})] \approx 1.1 \times 10^{-3}$$

$$G[^2A(E_g) \rightarrow {}^2A(T_{2g})] = \text{indeterminate}, \qquad f[^2A(E_g) \rightarrow {}^2A(T_{2g})] \equiv 0$$

$$G[^2A(E_g) \rightarrow {}^2B_{(\frac{2}{3})}(T_{2g})] \approx (\pm)8 \times 10^{-4}\nu, \qquad f[^2A(E_g) \rightarrow {}^2B_{(\frac{2}{3})}(T_{2g})] \approx 4.7 \times 10^{-7}$$

$$G[^2A(T_{2g}) \rightarrow {}^2B_{(\frac{2}{3})}(T_{2g})] \approx 3.8 \times 10^{-4}\nu, \qquad f[^2A(T_{2g}) \rightarrow {}^2B_{(\frac{2}{3})}(T_{2g})] \approx 1.6 \times 10^{-6}$$

$$G[^2B_2(T_{2g}) \rightarrow {}^2B_3(T_{2g})] \approx -1.7 \times 10^{-3}\nu, \qquad f[^2B_2(T_{2g}) \rightarrow {}^2B_3(T_{2g})] \approx 7.3 \times 10^{-7} \quad (53)$$

where ν is the frequency of the observant light in cm^{-1}. The numbers in eq. 52 and 53 are to within ± 5 in the second significant figure due to evaluational approximations. The rotational and spectral strengths and the dissymmetry factors of eq. 52 and 53 for the $^2B_{(\frac{2}{3})}(T_{2g})$ electronic states are not identically equal in magnitude for the parameterization chosen, but the approximational errors and the subtractive cancellation of significant figures precludes a reliable estimate of their difference [this difference is within the error limit quoted previously].[26]

If the more liberal (probably excessively so) assessment of the ligand–metal σ,π-copulative constants and cantation angles, $1/2\sqrt{3}$, $1/2\sqrt{3}$, $-1/2\sqrt{2}$, $1/2\sqrt{3}$, $1/2\sqrt{3}$, and 15° is made the rotational and electric spectral strengths increase enormously.

$$\Re[^2B_1(E_g) \rightarrow {}^2A(E_g)] \approx 0.23B, \qquad \$[^2B_1(E_g) \rightarrow {}^2A(E_g)] \approx 1.9 \times 10^{-2}D^2$$

$$\mathfrak{M}[^2B_1(E_g) \rightarrow {}^2A(E_g)] \approx 2.8 \times 10^{-4}V^2$$

$$\Re[^2B_1(E_g) \rightarrow {}^2A(T_{2g})] \approx -27B, \qquad \$[^2B_1(E_g) \rightarrow {}^2A(T_{2g})] \approx 2.1 \times 10^{-2}D^2$$

$$\Re[^2B_1(E_g) \rightarrow {}^2B_{(\frac{2}{3})}(T_{2g})] \approx (\pm)210, \qquad \$[^2B_1(E_g) \rightarrow {}^2B_{(\frac{2}{3})}(T_{2g})] \approx 5.1D^2$$

$$\Re[^2A(E_g) \rightarrow {}^2A(T_{2g})] \equiv 0, \quad \$[^2A(E_g) \rightarrow {}^2A(T_{2g})] \equiv 0$$

$$\Re[^2A(E_g) \rightarrow {}^2B_{(\frac{2}{3})}(T_{2g})] \approx (\pm)320B, \qquad \$[^2A(E_g) \rightarrow {}^2B_{(\frac{2}{3})}(T_{2g})] \approx 3.9D^2$$

$$\Re[^2A(T_{2g}) \rightarrow {}^2B_{(\frac{2}{3})}(T_{2g})] \approx 190B, \qquad \$[^2A(T_{2g}) \rightarrow {}^2B_{(\frac{2}{3})}(T_{2g})] \approx 4.3D^2$$

$$\Re[^2B_2(T_{2g}) \rightarrow {}^2B_3(T_{2g})] \approx -53B, \qquad \$[^2B_2(T_{2g}) \rightarrow {}^2B_3(T_{2g})] \approx 0.33D^2 \quad (54)$$

The magnetic spectral strengths not listed are not much changed from their magnitudes (which arose from the intrinsic metallic orbital magnetic moments) of eq. 52. The correspondent dissymmetry factors and oscillator strengths are readily obtained from (54). In general they are seen to decrease and increase, respectively, by factors of 10 to 10^4. The upsurge in rotational and electric spectral strengths upon growth of metal–ligand amalgamation is a consequence of ascendant ligand–ligand electric dipole moment contributions [look at eq. 8, 11, and 17].

Because of the expanded orbital basis which allows greater metal–ligand intimacy, and the emanant rise of

(24) With the units for electric and magnetic dipole vigor employed above, the Debye and the Van Vleck, the expressions for the oscillator strengths become

$$f[N \rightarrow X]_{\text{electric}} = 4.705 \times 10^{-7}\nu[N \rightarrow X, \text{cm.}^{-1}]\ \$[N \rightarrow X, D^2]$$

$$f[N \rightarrow X]_{\text{magnetic}} = 4.705 \times 10^{-11}\nu[N \rightarrow X, \text{cm.}^{-1}]\ \mathfrak{M}[N \rightarrow X, V^2]$$

Note that the fundamental units of B, D^2, and V^2 are all the same—a unit electrical charge in e.s.u. squared times a unit length in cm. squared [thus the fundamental units of the Bohr magneton are the same as those of the Debye and the square root of the Biot!].

(25) Whenever $\mathfrak{M}/\$$ nears or exceeds unity [recall V^2/D^2 equals 10^{-4}] for an electronic transition, eq. 27 for the dissymmetry factor must be modified either by a designation such as "electric dissymmetry factor" or by the alteration of its denominators with a replacement of $\$_{ab}$ by $\$_{ab} + \mathfrak{M}_{ab}$ or of $\mathcal{O}_{ab}$ by $\mathcal{O}_{ab} + \mathfrak{M}_{ab}$.

(26) The subtractive difficulties occur only for values of the metal-ligand mixture parameters in the neighborhood of $1/_{20}$. Indeed, for values lower than this the rotational and spectral strengths of the $^2A(E_g, T_{2g}) \rightarrow {}^2B_{(\frac{2}{3})}(T_{2g})$, $^2B_1(E_g) \rightarrow {}^2A(E_g)$ transitions pass through zero and the rotational strengths change sign. For the especially sensitive $^2A(E_g) \rightarrow {}^2B_{(\frac{2}{3})}(T_{2g})$ transition this crossover point takes place at the mixture parameter value of $\sim 1/_{24}$, hence the uncertainties referred to above. For the $^2A(T_{2g}) \rightarrow {}^2B_{(\frac{2}{3})}(T_{2g})$ and $^2B_1(E_g) \rightarrow {}^2A(E_g)$ hops the critical specification falls in a region of less physical interest, parameter values of $\sim 1/_{40}$ and $\sim 1/_{165}$. The other transitions do not exhibit such cancellative difficulties. The possibility of internal compensation arises because of the occurrence of opposed linear (metal–ligand contributions) and quadratic (ligand–ligand contributions) to the electric dipole length matrix elements [view eq. 17]. At values of the parameters not too much greater than $1/_{20}$, the quadratic ligand–ligand terms so dominate as to render the linear metal–ligand terms but small correctives [an exception to this rule is the $\langle b_2|\vec{er}|b_3\rangle$ matrix term in which the linear term dominates in practical situations]. The unusually large magnitude of the $^2B_1(E_g) \rightarrow {}^2B_{(\frac{2}{3})}(T_{2g})$ rotational and spectral strengths stems from the large (even) ligand σ-molecular orbital content in the b_1 orbitals (the b_1 orbital is σ-bonding in the quadrate limit), which creates a large ligand–ligand electric dipole moment when a digonal field infuses odd σ-bond character into the $b_{(\frac{2}{3})}$ orbitals.

ligand–ligand contributions, the rotational and spectral strengths for the bis(glycolato)copper(II) anion should be bigger than those for the bis(ethylenediamine)copper(II) cation in eq. 51, 52, and 54, despite the decreased magnitude of the metal–ligand integrals due to the increased magnitude of the ligand Slater (effective nuclear charge) exponents [read ref. 6, §4.6]. However, the sign of its rotational strength will be invariant and equal to that of the bis(ethylenediamine)copper(II) cation of the same over-all ionic conformation.

Unfortunately, experimental data are scarce and no detailed experimental–theoretical comparison can be made.[27] However, the size of our rotational and spectral strengths is of the correct order.

IV. Discussion

The discussion of the digonal dihedral findings, for the most part, runs along the lines identical with those detailed in ref. 6, and, hence, need not be recounted here, except in where differences or variances occur. Of the differences, the most striking is the major importance of the ligand orbital out-of-plane cant, without which central atom optical activity, either rotational or (nonvibronic) spectral [to first order] would disappear by virtue of local electric symmetry. It is this local electronic nonplanarity which dictates the common union of even and odd one-electron ligand molecular orbitals with the even central atom orbitals, in sharp contrast to the trigonal case where local trigonality alone served to induce optical activity. Of course, nonplanarity is also a contributent in the trigonal dihedral problem, but it is not the prime motivator as here [compare Fig. 1 through 8 with 23 and 24 and Fig. 11 through 17 with 25].[28] Nonplanarity, except in unusual instances, cannot alter the sign of the trigonal central atom activity; it can only moderate its amplitude slightly. Thus the trigonal axial and skew axial ligand constellation [Fig. 23] for the same over-all molecular conformation rotate similarly in metallochromophoric absorption segments.[29] This happenstance is certainly not the case for the digonal compounds where oppositely skewed ligands may induce either parallel or opposite central atom rotativity dependent upon the local ligand orbital conformation [study Fig. 1 through 8 and 14 through 17], and where local ligand electronic nonplanarity is a prerequisite for central atom activity.[30]

Inextricably wedded to the difference in digonal and trigonal sensitivity to ligand architectural idiosyncrasy is the digonal–trigonal variance in ligand–ligand import. For the trigonal dihedral problem as treated previously, the concept of pseudo-octahedrality eliminated automatically all contributions of the ligand–ligand type in σ-bonded complexes except in the internal one-electron t_{2g}- to t_{2g}-like transition [there was also a minor contribution to the magnetic moment of t_{2g}- to e_g-like transition. Read footnote 73 of ref. 6]. However, even were this concept dropped and large ligand–ligand terms admitted, the authoritative rotational and spectral terms would still be of predominant external trigonal molecular conformational origin rather than of internal aplanar ligand constellational cause. Ligand–ligand terms from this latter source, though significant, are of a lower order of magnitude for the trigonal situation. For the digonal circumstance there is neither a possibility for pseudo octahedrality or tetrahedrality nor a possibility for external digonal molecular contribution; there is solely the possiblity of internal

(27) Measurements have been made on platinum(II) complexes of undetermined conformations.[2] Our results are not inconsistent with these experiments. As further measurements are sure to be made it is not out of place to report in this spot the order of magnitude of the signed electric and magnetic dipole strengths to be expected. [The estimates are recorded in units of eÅ. and μ_B, where e is the electronic charge, Å. is the Ångstrom unit, and μ_B is the Bohr magneton. The top half corresponds to the parameterization of eq. 52 and the bottom half to that of eq. 54.]

$\bar{r}_{0a}$	$\bar{r}_{0(\frac{b}{c})}$	r_{0a}	r_{0b}
1.5×10^{-2}	7×10^{-3}	0	-1.7×10^{-3}
1.2×10^{-1}	4.3×10^{-1}	0	-3.0×10^{-2}
$r(\frac{1}{2})_a$	$r(\frac{1}{2})_b$		r_0
2.5×10^{-3}	-8.3×10^{-2}		-1.7×10^{-2}
4.1×10^{-1}	-4.7×10^{-1}		-2.9×10^{-2}

$\bar{m}_{0a}$	$\bar{m}_{0(\frac{b}{c})}$	m_{0a}	m_{0b}
1	1	0	2
1	1	0	2
$m(\frac{1}{2})_a$	$m(\frac{1}{2})_b$		$\bar{m}_0$
$(\mp)\sqrt{3}$	$(\mp)\,1$		-1.0×10^{-3}
$(\mp)\sqrt{3}$	$(\mp)\,1$		-1.8×10^{-2}

NOTE ADDED IN PROOF.—Since this article has gone to press, two experimental reports have appeared on the nature of the rotations in cobalt *l*-propylenediamine compounds, one of which supports our naive numerical work (R. A. D. Wentworth and T. S. Piper, *Inorg. Chem.*, in press), and one of which does not (J. H. Dunlop and R. D. Gillard, *Mol. Phys.*, **7**, 493 (1963–4)). It will be interesting to see which view prevails.

(28) With regard to the problem of ligand conformational preference in trigonal, digonal, and other transition metal compounds be sure to study the fundamental papers of (a) E. J. Corey and J. C. Bailar, Jr., *J. Am. Chem. Soc.*, **81**, 2620 (1959); (b) K. Nakatsu, N. Shiro, Y. Saito, and H. Kuroya, *Bull. Chem. Soc. Japan*, **30**, 158 (1957); (c) Y. Saito and H. Iwasaki, *ibid.*, **35**, 1131 (1962); (d) F. P. Dwyer, T. E. MacDermott, and A. M. Sargeson, *J. Am. Chem. Soc.*, **85**, 2913 (1963); F. P. Dwyer and T. E. MacDermott, *ibid.*, **85**, 2916 (1963); F. P. Dwyer, A. M. Sargeson, and L. B. Jones, *ibid.*, **86**, 590 (1964); and (e) Y. Saito, H. Iwasaki, and H. Ota, *Bull. Chem. Soc. Japan*, **36**, 1543 (1963).

(29) There is some indicative experimental evidence in support of this positive theoretical declaration. Read T. E. MacDermott and A. M. Sargeson, *Australian J. Chem.*, **16**, 334 (1963).

(30) Local metal–ligand bond nonplanarity and nonorthogonality, however, as in the case of the trigonal dihedral problem, have little effect upon the (qualitative) digonal dihedral rotatory and refractory power.

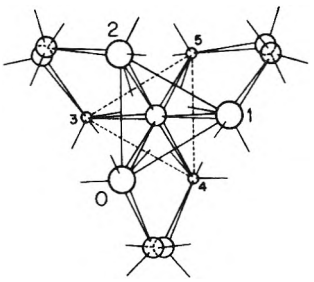

Λ(δ, δ, δ)

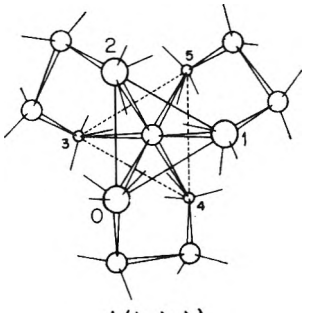

Λ(λ, λ, λ)

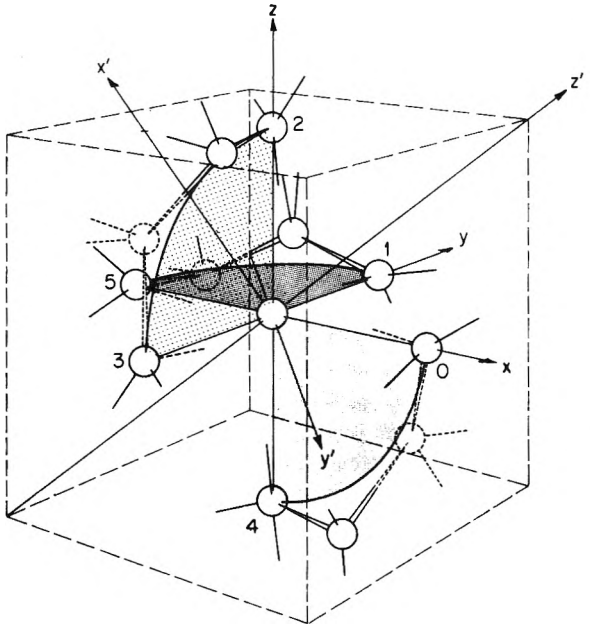

Λ(δ, δ, δ)

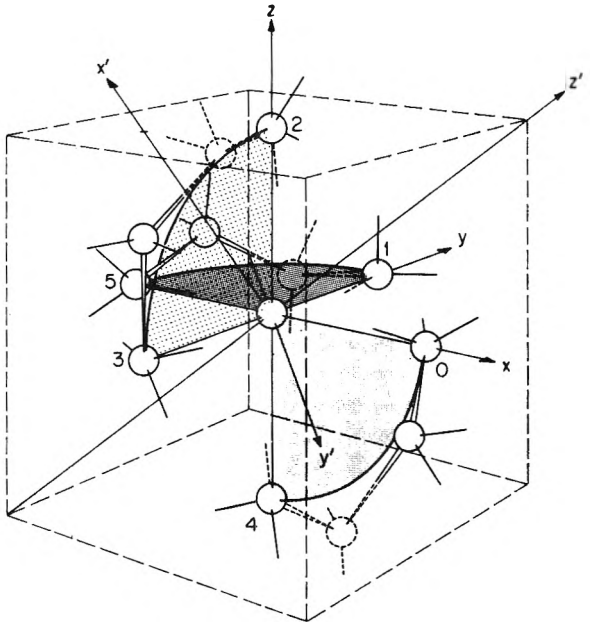

Λ(λ, λ, λ)

Figure 23. The lambda (Λ) conformation of the tris(ethylenediamine)cobalt(III) cation in its two principal (extreme) isomeric forms, Λ(δ,δ,δ) [the observed form[28b]] and Λ(λ,λ,λ) [its internally reversed form]. [We here make the convention that the parenthesized lower case deltas (δ) and lambdas (λ) designate the attached ligand conformations (recall Fig. 5 and 6), written in order of their affixment, with the conformation of the ligand attached to position 0 first, position 1 second, and position 2 third, and with the proviso that the coordination positions be numbered as in Fig. 23 and that positions 0, 1, and 2 not be welded one to the other. We hope this convention will find favor. We believe it is more convenient and extensible than that recently proposed by Corey and Bailar[28a] (our Λ(δ,δ,δ) equals Corey and Bailar's *lel* pattern and our Λ(λ,λ,λ) their ob pattern). For example, mixed Λ(δ,δ,λ), Λ(λ,δ,λ), etc., constellations are readily (and exactly) specified.]

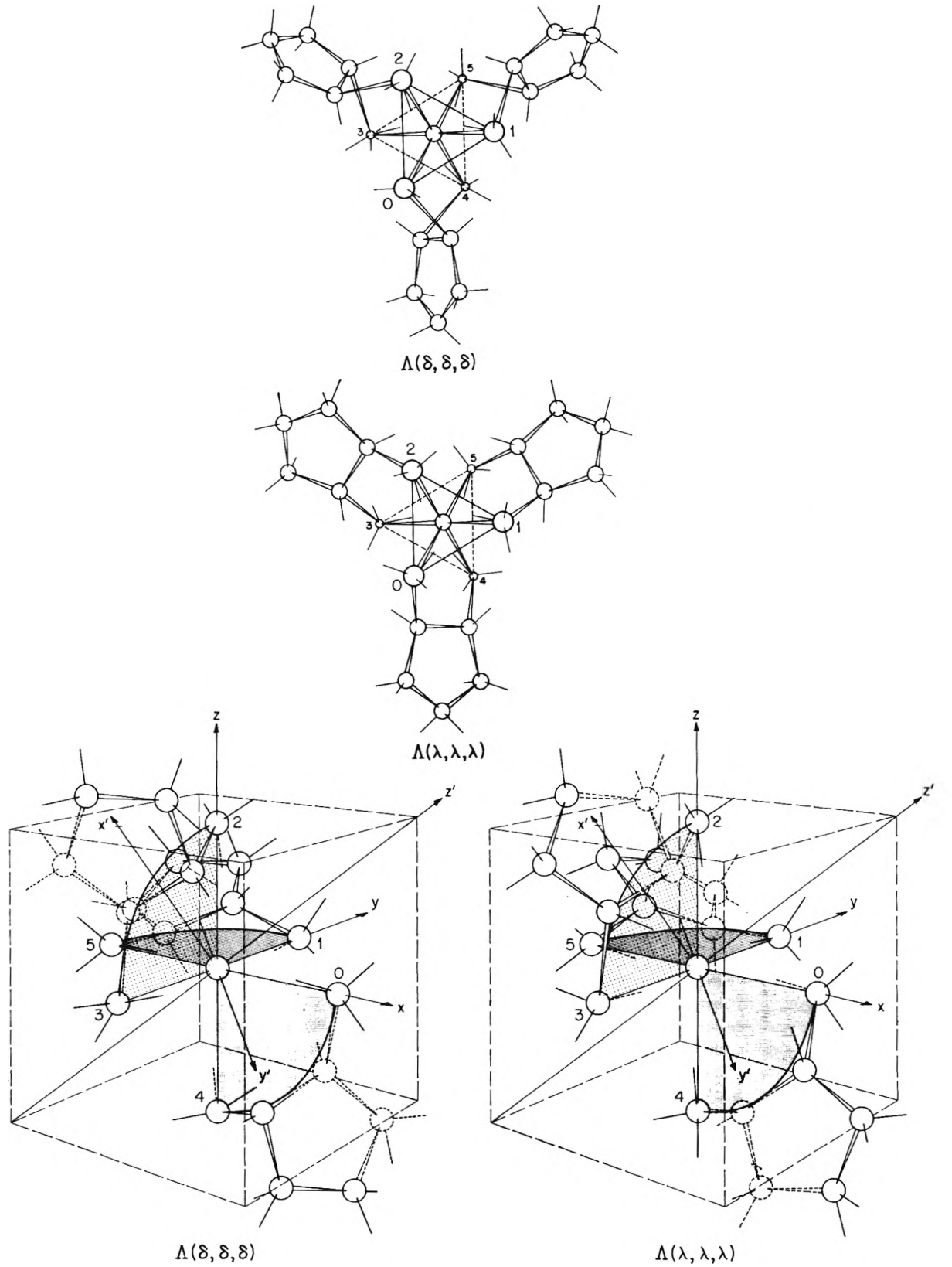

Figure 24. The lambda(Λ) conformation of the tris(cyclopentanediamine)cobalt(III) cation in its two principal (extreme) isomeric forms, Λ(δ,δ,δ) and Λ(λ,λ,λ).

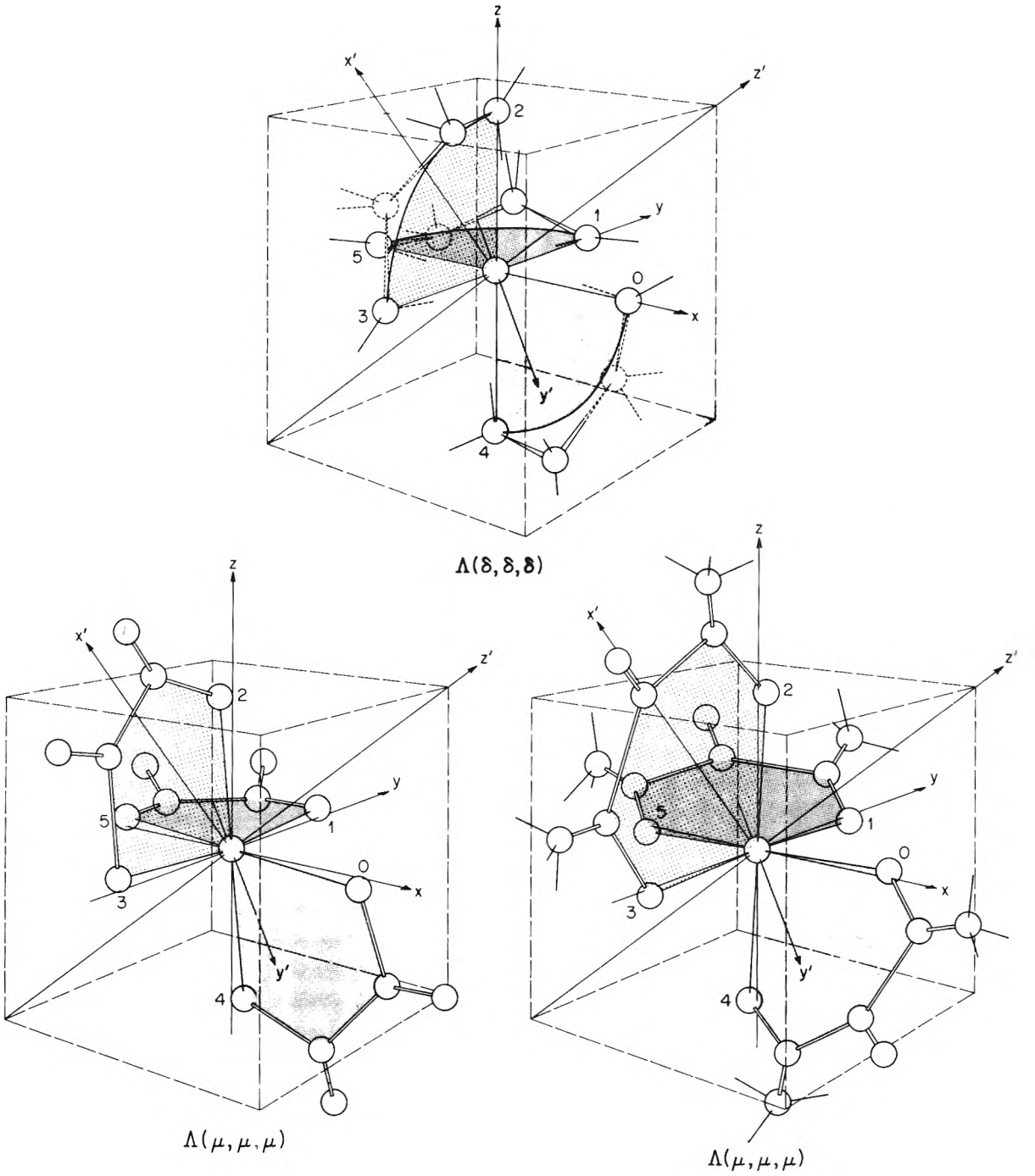

Figure 25. The lambda (Λ) conformations of the cobalt(III) tris(ethylene glycol) (top), trisoxalato (left), and trisacetylacetonato (right) cations and anions in their Λ(δ,δ,δ), Λ(μ,μ,μ), and Λ(μ,μ,μ) forms, respectively. [The lower case mu's (μ) indicate a *meso*-architecture for the bound ligand. The conventions are as stipulated in Fig. 23.]

aplanar ligand contribution[31]; hence, the digonal–trigonal contrast.[32, 33]

The loss of pseudo cubicity, besides the induction of large ligand–ligand contributions, has another funda-

(31) Although the internal aplanar ligand contributions are of "lower order" (*i.e.*, not the main causative) for trigonal structures, this does not mean they are negligible or small. It only implies that they are not sign determinative. [They add no new parts to the externally induced ligand–ligand supplements.]

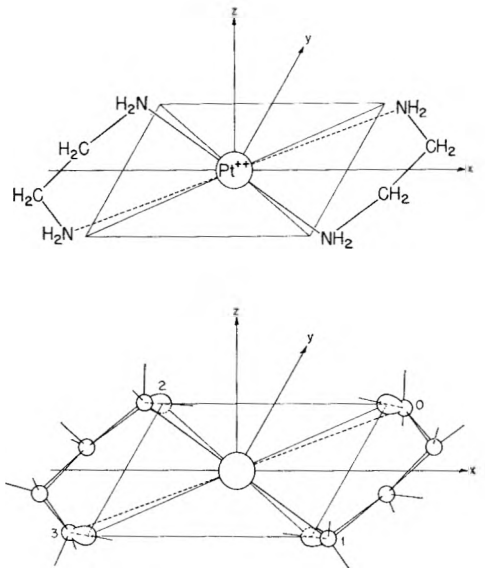

Figure 26. The factualized noncomplanately bonded acute-angled geometry of the bis(ethylenediamine)platinum(II) cation and its associate localized ligand orbital spatial disposition for the $\Delta(\lambda,\lambda)$ conformation. Adjacent (ligand) carbon postures are as in Fig. 1.

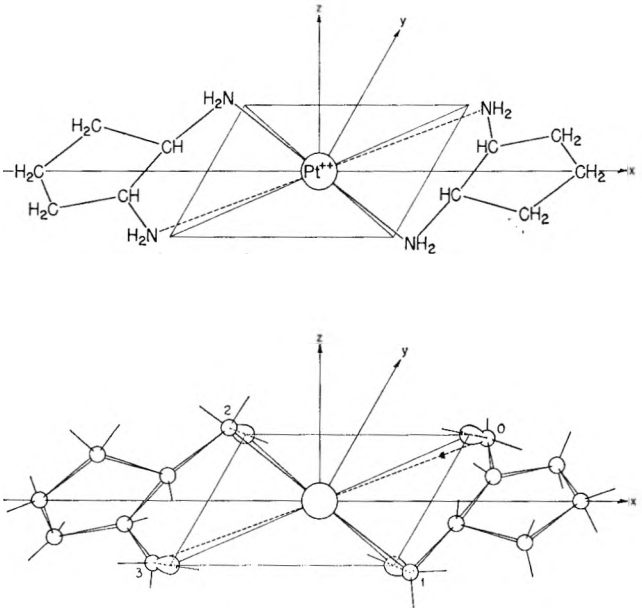

Figure 27. The factualized noncomplanately bonded acute-angled geometry of the bis(cyclopentanediamine)platinum(II) cation and its associate localized ligand orbital spatial disposition for the $\Lambda(\delta,\delta)$ conformation. Adjacent (ligand) carbon postures are as in Fig. 2.

mental sequent. There are no simple sum rules for digonal dihedral compounds. The sums, $\sum_{j(t_{2g}\rightarrow e_g)} r_j m_j$, which equal $\bar{r}_{0b}\bar{m}_{0b} + \bar{r}_{0c}\bar{m}_{0c} + r_{1a}m_{1a} + r_{2a}m_{2a} - r_{0b}m_{0b} - \bar{\bar{r}}_0\bar{\bar{m}}_0$ and $r_{0a}m_{0a} + r_{0b}m_{0b} + r_{1a}m_{1a} + r_{1b}m_{1b} + r_{2a}m_{2a} + r_{2b}m_{2b}$ in the tetrahedral (η equals $\eta^\star$, ρ equals ρ_1, ρ_2, ρ_3) and octahedral ($\eta^\star$ equals ρ_1, ρ equals η, ρ_2, ρ_3) limits, separately, reduce to $\sim 8.5B$, $410B$ and $\sim -0.7B$, $-27B$ in the two numerations of eq. 52, 54, which algebraically approximate to $2\bar{r}_{0(^b_c)}\bar{m}_{0(^b_c)} - r_{0b}m_{0b}$ and $r_{0b}m_{0b}$, separately.[34] Again a digonal–trigonal contrast.[35]

Lastly, the want of good digonal dihedral wave functions creates an essential ambiguity. This ambiguity was mentioned before in ref. 6, section II, footnote 22 and ref. 6, section IV—it is the formal, but not actual, duality of the coordinate, $\vec{er}$, and the momental, $(\hbar/i)\vec{\nabla}$, representations for the electric dipole operator, $\vec{p}$. In both the trigonal and digonal (or any other) case, the poorness of the existent wave functions makes this duality an enigma, as one does not know *a priori* which representation actually represents the truth in any specific instance, although there is some practical evidence that the momentum representation (which is actually that of the untransformed theory) is best [read footnote 22, ref. 6]. To illustrate this enigma in somewhat dramatic fashion consider two examples: (i) a matrix component between $^1A[^1E_g(e_g^2)]$ and $^1B_1[^1E_g(e_g^2)]$ electronic states, Ψ_A and Ψ_B, respectively, and (ii) a matrix component between the $^1B_1[^3T_{1g}(t_{2g}^2)]$ and $^1B_{(\frac{2}{3})}[^3T_{1g}(t_{2g}e_g)]$ electronic states, Φ_{B_1} and $\tilde{\Phi}_{B(\frac{2}{3})}$, respectively, where Ψ_A equals $\sqrt{1/2}\{|a^\star\bar{a}^\star| - |b_1\bar{b}_1|\}$, Ψ_B equals $-\sqrt{1/2}\{|a^\star\bar{b}_1| - |\bar{a}^\star b_1|\}$, Φ_{B_1} equals $|b_2\bar{b}_3|$, and $\tilde{\Phi}_{B(\frac{2}{3})}$ equals $(\mp)1/2\{\sqrt{3}|b_{(\frac{2}{3})}a^\star| - |b_{(\frac{2}{2})}b_1|\}$. If we

(32) This contrast is one more of semantics and practics than of dialectics and mathematics. The heightened rotativity and intensity in both instances springs from the impact of even-odd σ–σ, and to a lesser extent, for σ-bonded complexes, π–π and σ–π (σ,π-bonded complexes give equal weight to σ–σ and π–π contributions and higher weight to σ–π contributions), ligand–ligand contributions to the electric dipole matrix components due to a loss of pseudo cubicity, and to consequent breakdowns of even–odd orbital distinctions [in the trigonal case this breakdown manifests itself in the separate admixture of $\Sigma_0^{(+)}$ and $\Sigma_\pm^{(1)}$, $\Sigma_\pm^{(2)}$ terms into the $a_1(t_{2g})$ and $e_\pm(t_{2g}, e_g)$ one-electron pseudo-octahedral trigonal molecular orbitals].

(33) The digonal and trigonal situations are in agreement on more ordinary ligand substituent isomer effects, however. These will have but slight influence on the central atom rotational and spectral strengths so long as they do not alter the localized ligand–metal electronic charge disposition significantly. They certainly cannot alter its sign without a gross concomitant stereochemical molecular charge [*i.e.*, sign alterations can only occur if substituent steric hindrance causes a structural rearrangement which transfigures the gross molecular form (for example induces a transition from an over-all Λ to an over-all Δ form, in Piper's[5w] notation)].

(34) A few terms in the sums do actually algebraically cancel independent of the numeration. As a sample, the linear η and $\eta^\star$ terms in the tetrahedral (η equals $\eta^\star$, ρ equals ρ_1, ρ_2, ρ_3) and octahedral ($\eta^\star$ equals ρ_1, ρ equals η, ρ_2, ρ_3) sums cancel, and certain metal–ligand and ligand–ligand terms both linear in ρ and quadratic in $\eta\rho$, $\eta^\star\rho$, ρ^2, η^2, or $\eta^{\star 2}$ also cancel. This incomplete cancellation is not unexpected due to the great structural difference between the digonal, tetrahedral, and octahedral systems [eye Fig. 3, 4, 10, 28, and 29].

(35) Of course, in the quadrate limit we do get a digonal–trigonal analogy as the rotational strengths all identically vanish, as all transitions are then even–even.

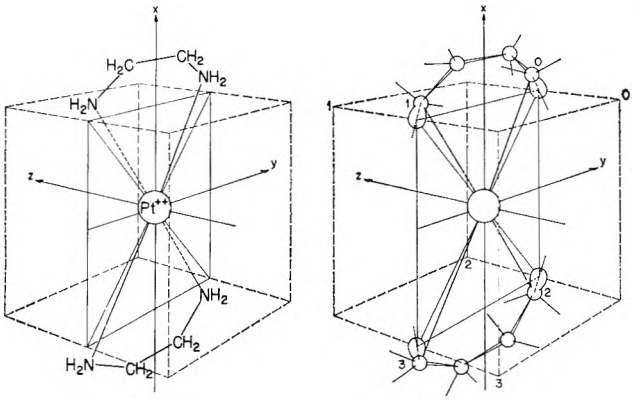

Figure 28. The factualized noncomplanately bonded acute-angled geometry of the bis(ethylenediamine)platinum(II) cation in the $\Delta(\lambda,\lambda)$ conformation and its associate localized ligand orbital spatial disposition viewed as a tetrahedral affiliate.

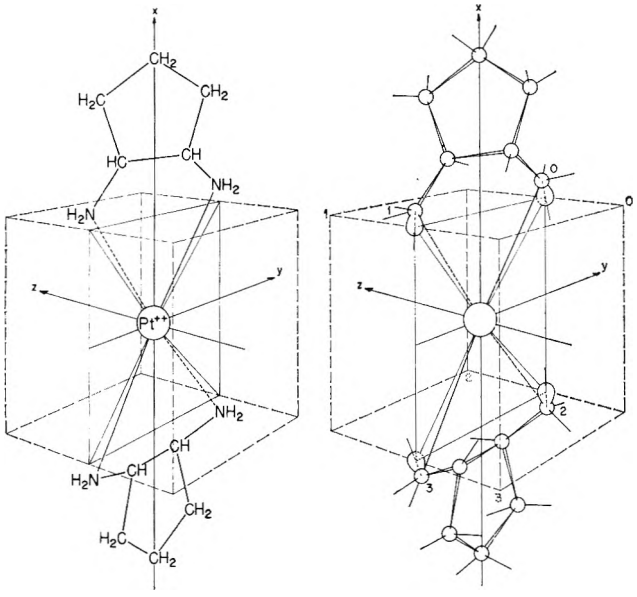

Figure 29. The factualized noncomplanately bonded acute-angled geometry of the bis(cyclopentanediamine)platinum(II) cation in the $\Lambda(\delta,\delta)$ conformation and its associate localized ligand orbital spatial disposition viewed as a tetrahedral affiliate.

let $\vec{p}$ equal $e\vec{r}$ or $(\hbar/i)\vec{\nabla}$, we find with the use of the matrix identity (for *exact* wave functions), $\left\langle a \left| \frac{\hbar}{i}\vec{\nabla} \right| b \right\rangle$ equals $\frac{im}{\hbar e}(E_a - E_b)\langle a|e\vec{r}|b\rangle$,[36] that $\langle\Psi_{B_1}|\vec{p}|\Psi_A\rangle$ equals $\langle a^\star|\vec{p}|b_1\rangle - \langle b_1|\vec{p}|a^\star\rangle$, and $\langle\Phi_{B_1}|\vec{p}|\tilde{\Phi}_{B(\frac{2}{3})}\rangle$ equals $-{}^1/_2\{\sqrt{3}\langle b_{(\frac{3}{2})}|\vec{p}|a^\star\rangle + \langle b_{(\frac{2}{3})}|\vec{p}|b_1\rangle\}$ can be expressed in a quintuple of connections

$$\left\langle \Psi_{B_1}\left|\frac{\hbar}{i}\vec{\nabla}\right|\Psi_A\right\rangle = \frac{im}{\hbar}(E_B - E_A)\langle\Psi_{B_1}|\vec{r}|\Psi_A\rangle =$$

$$\frac{im}{\hbar}(E_B - E_A)\{\langle a^\star|\vec{r}|b_1\rangle - \langle b_1|\vec{r}|a^\star\rangle\}$$

$$\left\langle \Psi_{B_1}\left|\frac{\hbar}{i}\vec{\nabla}\right|\Psi_A\right\rangle = \left\langle a^\star\left|\frac{\hbar}{i}\vec{\nabla}\right|b_1\right\rangle - \left\langle b_1\left|\frac{\hbar}{i}\vec{\nabla}\right|a\right\rangle =$$

$$\frac{im}{\hbar}\{(E_{a\star} - E_{b_1})\langle a^\star|\vec{r}|b_1\rangle - (E_{b_1} - E_{a\star})\langle b_1|\vec{r}|a^\star\rangle\}$$

and

$$\left\langle \Phi_{B_1}\left|\frac{\hbar}{i}\vec{\nabla}\right|\tilde{\Phi}_{B(\frac{2}{3})}\right\rangle = \frac{im}{\hbar}(E_{B_1} - E_{B(\frac{2}{3})})\langle\Phi_{B_1}|\vec{r}|\tilde{\Phi}_{B(\frac{2}{3})}\rangle =$$

$$-\frac{im}{2\hbar}(E_{B_1} - E_{B(\frac{2}{3})})\{\sqrt{3}\langle b_{(\frac{3}{2})}|\vec{r}|a^\star\rangle + \langle b_{(\frac{2}{3})}|\vec{r}|b_1\rangle\}$$

$$\left\langle \Phi_{B_1}\left|\frac{\hbar}{i}\vec{\nabla}\right|\tilde{\Phi}_{b_{(\frac{2}{3})}}\right\rangle = -{}^1/_2\left\{\sqrt{3}\left\langle b_{(\frac{3}{2})}\left|\frac{\hbar}{i}\vec{\nabla}\right|a^\star\right\rangle + \left\langle b_{(\frac{2}{3})}\left|\frac{\hbar}{i}\vec{\nabla}\right|b_1\right\rangle\right\} =$$

$$-\frac{im}{2\hbar}\{\sqrt{3}(E_{b_{(\frac{2}{3})}} - E_{a^\star})\langle b_{(\frac{2}{3})}|\vec{r}|a^\star\rangle + (E_{b_{(\frac{2}{3})}} - E_{b_1})\langle b_{(\frac{2}{3})}|\vec{r}|b_1\rangle\}$$

in which numerous logical self-contradictions appear. These contradictions become obvious when there are substituted into the quintuples the *incorrect* identifications (incorrect as the momental-coordinate identity requires *both* $\mathcal{H}\Upsilon$ equals $E\Upsilon$ and $\int\Upsilon^*\mathcal{H}\Upsilon$ equals E, not just the latter alone) E_A equals E_B equals $E_{a^\star} + E_{b_1}$ and E_{B_1} equals $E_{b_2} + E_{b_3}$, $E_{B_{(\frac{2}{3})}}$ equals ${}^1/_4(3(E_{b_{(\frac{2}{3})}} + E_{a^\star}) + (E_{b_{(\frac{3}{2})}} + E_{b_1}))$, upon which substitution (with the use of matrix Hermiticity) we see that the first quintuple requires that either $E_{a^\star} - E_{b1}$ or $\langle a^\star|\vec{r}|b_1\rangle$ vanish, neither of which requirements is true. The explanation of these contradictions is, of course, that sums of determinants of even *exact* one-electron orbital functions can *never* be eigenfunctions of any Hamiltonian, except by fortunate chance.[37] As it is not yet sure which of the

(36) This identity is readily proved with the commutator equality, $(\hbar/i)\vec{\nabla}_j$ equals $(im/\hbar)[\mathcal{H}, \vec{r}_j]$, which holds for any Hamiltonian, $\mathcal{H}$, which contains $(\hbar/i)\vec{\nabla}_j$ only in the kinetic form $\sum_k -(\hbar^2/2m)\nabla_k^2$ [this commutator equality is independent of all functional additaments of the potential form $V(\vec{r}_i, \vec{r}_j, \vec{r}_k, \ldots \vec{r}_n, \vec{r}_{ij}, \vec{r}_{jk}, \ldots \vec{r}_{in} \ldots)$].

(37) For example, for the determinantal sums Ψ_A, Ψ_B, Φ_{B1}, $\tilde{\Phi}_{B(\frac{2}{3})}$ printed above, we have at best $\mathcal{H}\Psi_A$ equals $\sqrt{1/2}\{2E_{a^\star}|a^\star\bar{a}^\star| - 2E_{b_1}|b_1\bar{b}_1|\}$, $\mathcal{H}\Psi_B$ equals $(E_{a^\star} + E_{b_1})\Psi_B$, $\mathcal{H}\Phi_{B_1}$ equals $(E_{b_2} + E_{b_3})\Phi_1$, and $\mathcal{H}\tilde{\Phi}_{B(\frac{2}{3})}$ equals $(\mp)^1/_2\{(E_{b_{(\frac{2}{3})}} + E_{a^\star})\sqrt{3}|b_{(\frac{3}{2})}a^\star| - (E_{b_{(\frac{3}{2})}} + E_{b_1})|b_{(\frac{3}{2})}b_{b_1}|\}$, when the Hamiltonian, $\mathcal{H}$, is a one-electron sum, $\mathcal{H}$ equals $\sum_j\{-(\hbar^2/2m)\nabla_j^2 + v(r_j) + \xi(r_j)\vec{\ell}_j\cdot\vec{s}_j + \ldots$.

Table VI: The Spin-Free d^n (n = 1, 2, 3, 4, 5, 6, 7, 8, 9), Digonal Dihedral (Octahedrally Oriented) Rotational and Spectral Strengths for Zero Spin-Orbital Forces[a]

n	Transitions	Rotational strengths	Spectral strengths: Electric	Spectral strengths: Magnetic
1 (s = 2)	$^2B_2(T_{2g}) \rightarrow {}^2B_1(T_{2g})$	$\bar{g}_{0a}\bar{m}_{0a}$	$\bar{g}_{0a}^2$	$\bar{m}_{0a}^2$
and	$^2B_{(\frac{2}{3})}(T_{2g}) \rightarrow {}^2A(T_{2g})$	$\bar{g}_{0(\frac{b}{c})}\bar{m}_{0(\frac{b}{c})}$	$\bar{g}_{0(\frac{b}{c})}^2$	$\bar{m}_{0(\frac{b}{c})}^2$
6 (s = 5)	$\rightarrow {}^2A(E_g)$	$g_{(\frac{1}{2})a}m_{(\frac{1}{2})a}$	$g_{(\frac{1}{2})a}^2$	$m_{(\frac{1}{2})a}^2$
	$\rightarrow {}^2B_1(E_g)$	$g_{(\frac{1}{2})b}m_{(\frac{1}{2})b}$	$g_{(\frac{1}{2})b}^2$	$m_{(\frac{1}{2})b}^2$
	$^4A(T_{2g}) \rightarrow {}^4A(E_g)$	0	0	0
	$\rightarrow {}^4B_1(E_g)$	$g_{0b}m_{0b}$	g_{0b}^2	m_{0b}^2
	$^6A(E_g) \rightarrow {}^6B_1(E_g)$	$\bar{\bar{g}}_0\bar{\bar{m}}_0$	$\bar{\bar{g}}_0^2$	$\bar{\bar{m}}_0^2$
2 (s = 3)	$^6B_1(T_{1g}) \rightarrow {}^6B_{(\frac{2}{3})}(T_{1g})$	$\bar{g}_{0(\frac{c}{b})}\bar{m}_{0(\frac{c}{b})}$	$\bar{g}_{0(\frac{c}{b})}^2$	$\bar{m}_{0(\frac{c}{b})}^2$
and	$\rightarrow {}^6A(T_{2g})$	0	0	0
7 (s = 4)	$\rightarrow {}^6B_{(\frac{2}{3})}(T_{2g})$	$^1/_4(g_{(\frac{2}{1})a} - \sqrt{3}g_{(\frac{1}{2})b})(m_{(\frac{2}{1})a} - \sqrt{3}m_{(\frac{1}{2})b})$	$^1/_4(g_{(\frac{2}{1})a} - \sqrt{3}g_{(\frac{1}{2})b})^2$	$^1/_4(m_{(\frac{2}{1})a} - \sqrt{3}m_{(\frac{1}{2})b})^2$
	$\rightarrow {}^6B_1(T_{1g})$	0	0	0
	$\rightarrow {}^6B_{(\frac{2}{3})}(T_{1g})$	$^1/_4(\sqrt{3}g_{(\frac{2}{1})a} + g_{(\frac{1}{2})b})(\sqrt{3}m_{(\frac{2}{1})a} + m_{(\frac{1}{2})b})$	$^1/_4(\sqrt{3}g_{(\frac{2}{1})a} + g_{(\frac{1}{2})b})^2$	$^1/_4(\sqrt{3}m_{(\frac{2}{1})a} + m_{(\frac{1}{2})b})^2$
	$\rightarrow {}^6B_1(A_{2g})$	0	0	0
	$^6B_2(T_{1g}) \rightarrow {}^6B_3(T_{1g})$	$\bar{g}_{0a}\bar{m}_{0a}$	$\bar{g}_{0a}^2$	$\bar{m}_{0a}^2$
	$^6B_{(\frac{2}{3})}(T_{1g}) \rightarrow {}^6A(T_{2g})$	$g_{(\frac{1}{2})a}m_{(\frac{1}{2})a}$	$g_{(\frac{1}{2})a}^2$	$m_{(\frac{1}{2})a}^2$
	$\rightarrow {}^6B_{(\frac{2}{3})}(T_{2g})$	0	0	0
	$\rightarrow {}^6B_{(\frac{3}{2})}(T_{2g})$	$^3/_4g_{0b}m_{0b}$	$^3/_4g_{0b}^2$	$^3/_4m_{0b}^2$
	$\rightarrow {}^6B_1(T_{1g})$	$g_{(\frac{1}{2})b}m_{(\frac{1}{2})b}$	$g_{(\frac{1}{2})b}^2$	$m_{(\frac{1}{2})b}^2$
	$\rightarrow {}^6B_{(\frac{2}{3})}(T_{1g})$	0	0	0
	$\rightarrow {}^6B_{(\frac{3}{2})}(T_{1g})$	$^1/_4g_{0b}m_{0b}$	$^1/_4g_{0b}^2$	$^1/_4m_{0b}^2$
	$\rightarrow {}^6B_1(A_{2g})$	0	0	0
3 (s = 4)	$^6B_1(A_{2g}) \rightarrow {}^6A(T_{2g})$	$g_{0b}m_{0b}$	g_{0b}^2	m_{0b}^2
and	$\rightarrow {}^6B_{(\frac{2}{3})}(T_{2g})$	$^1/_4(g_{(\frac{1}{2})b} - \sqrt{3}g_{(\frac{2}{1})a})(m_{(\frac{1}{2})b} - \sqrt{3}m_{(\frac{2}{1})a})$	$^1/_4(g_{(\frac{1}{2})b} - \sqrt{3}g_{(\frac{2}{1})a})^2$	$^1/_4(m_{(\frac{1}{2})b} - \sqrt{3}m_{(\frac{2}{1})a})^2$
8 (s = 3)	$\rightarrow {}^6B_1(T_{1g})$	0	0	0
	$\rightarrow {}^6B_{(\frac{2}{3})}(T_{1g})$	$^1/_4(\sqrt{3}g_{(\frac{1}{2})b} + g_{(\frac{2}{1})a})(\sqrt{3}m_{(\frac{1}{2})b} + m_{(\frac{2}{1})a})$	$^1/_4(\sqrt{3}g_{(\frac{1}{2})b} + g_{(\frac{2}{1})a})^2$	$^1/_4(\sqrt{3}m_{(\frac{1}{2})b} + m_{(\frac{2}{1})a})^2$
	$\rightarrow {}^6B_1(T_{1g})$	0	0	0
	$\rightarrow {}^6B_{(\frac{2}{3})}(T_{1g})$	0	0	0
4 (s = 5)	$^6B_1(E_g) \rightarrow {}^6A(E_g)$	$\bar{\bar{g}}_0\bar{\bar{m}}_0$	$\bar{\bar{g}}_0^2$	$\bar{\bar{m}}_0^2$
and	$\rightarrow {}^6A(T_{2g})$	$g_{0b}m_{0b}$	g_{0b}^2	m_{0b}^2
9 (s = 2)	$\rightarrow {}^6B_{(\frac{2}{3})}(T_{2g})$	$g_{(\frac{1}{2})b}m_{(\frac{1}{2})b}$	$g_{(\frac{1}{2})b}^2$	$m_{(\frac{1}{2})b}^2$
	$^4A(E_g) \rightarrow {}^4A(T_{2g})$	0	0	0
	$\rightarrow {}^4B_{(\frac{2}{3})}(T_{2g})$	$g_{(\frac{1}{2})a}m_{(\frac{1}{2})a}$	$g_{(\frac{1}{2})a}^2$	$m_{(\frac{1}{2})a}^2$
	$^4A(T_{2g}) \rightarrow {}^4B_{(\frac{2}{3})}(T_{2g})$	$\bar{g}_{0(\frac{b}{c})}\bar{m}_{0(\frac{b}{c})}$	$\bar{g}_{0(\frac{b}{c})}^2$	$\bar{m}_{0(\frac{b}{c})}^2$
	$^2B_2(T_{2g}) \rightarrow {}^2B_3(T_{2g})$	$-\bar{g}_{0a}\bar{m}_{0a}$	$\bar{g}_{0a}^2$	$\bar{m}_{0a}^2$
5	$^6A(A_{1g}) \rightarrow {}^{2,4}B_1(T_{1g})$	0	0	0
	$\rightarrow {}^{2,4}B_{(\frac{2}{3})}(T_{1g})$			
	$\rightarrow {}^{2,4}A(T_{2g})$			
	$\rightarrow {}^{2,4}B_{(\frac{2}{3})}(T_{2g})$			
	$\rightarrow {}^{2,4}B_1(A_{2g})$			
	$\rightarrow {}^{2,4}A(E_g)$			
	$\rightarrow {}^{2,4}B_1(E_g)$			
	$\rightarrow {}^{2,4}A(A_{1g})$			

[a] The quantities $\bar{g}_{0a,b,c}$, g_0, $g_{0a,b}$, $g_{1a,b}$, $g_{2a,b}$, $\bar{m}_{0a,b,c}$, m_0, $m_{0a,b}$, $m_{1a,b}$, $m_{2a,b}$ (g = r, p), are as defined specially and generally in § 3.1, eq. 17 and 19.

Table VII: The Spin-Paired d^n (n = 1, 2, 3, 4, 5, 6, 7, 8, 9), Digonal Dihedral (Octahedrally Oriented) Rotational and Spectral Strengths for Zero Spin-Orbit Forces[a]

n	Transitions	Rotational strengths	Spectral strengths: Electric	Spectral strengths: Magnetic
4	$^3B_2(T_{1g}) \rightarrow {}^3B_3(T_{1g})$	$-\bar{g}_{0a}\bar{m}_{0a}$	$\bar{g}_{0a}^2$	$\bar{m}_{0a}^2$
	$^3B_{(\frac{2}{3})}(T_{1g}) \rightarrow {}^3B_1(T_{1g})$	$\bar{g}_{0(\frac{c}{b})}\bar{m}_{0(\frac{c}{b})}$	$\bar{g}_{0(\frac{c}{b})}^2$	$\bar{m}_{0(\frac{c}{b})}^2$
	$\rightarrow {}^3B_1(E_g)$	$^4/_3 g_{(\frac{2}{1})a} m_{(\frac{2}{1})a}$	$^4/_3 g_{(\frac{2}{1})a}^2$	$^4/_3 m_{(\frac{2}{1})a}^2$
	$\rightarrow {}^3A(E_g)$	$^4/_3 g_{(\frac{2}{1})b} m_{(\frac{2}{1})b}$	$^4/_3 g_{(\frac{2}{1})b}^2$	$^4/_3 m_{(\frac{2}{1})b}^2$
	$\rightarrow {}^3B_1(T_{1g})$	$^1/_2 g_{(\frac{2}{1})a} m_{(\frac{2}{1})a}$	$^1/_2 g_{(\frac{2}{1})a}^2$	$^1/_2 m_{(\frac{2}{1})a}^2$
	$\rightarrow {}^3B_{(\frac{2}{3})}(T_{1g})$	0	0	0
	$\rightarrow {}^3B_{(\frac{3}{2})}(T_{1g})$	$^3/_8 g_{0b} m_{0b}$	$^3/_8 g_{0b}^2$	$^3/_8 m_{0b}^2$
	$\rightarrow {}^3A(T_{2g})$	$^1/_2 g_{(\frac{2}{1})b} m_{(\frac{2}{1})b}$	$^1/_2 g_{(\frac{2}{1})b}^2$	$^1/_2 m_{(\frac{2}{1})b}^2$
	$\rightarrow {}^3B_{(\frac{2}{3})}(T_{2g})$	0	0	0
	$\rightarrow {}^3B_{(\frac{3}{2})}(T_{2g})$	$^1/_8 g_{0b} m_{0b}$	$^1/_8 g_{0b}^2$	$^1/_8 m_{0b}^2$
	$\rightarrow {}^3A(A_{1g})$	$^1/_{12}(\sqrt{3}g_{(\frac{1}{2})a} - g_{(\frac{2}{1})b})(\sqrt{3}m_{(\frac{1}{2})a} - m_{(\frac{2}{1})b})$	$^1/_{12}(\sqrt{3}g_{(\frac{1}{2})a} - g_{(\frac{2}{1})b})^2$	$^1/_{12}(\sqrt{3}m_{(\frac{1}{2})a} - m_{(\frac{2}{1})b})^2$
	$\rightarrow {}^3B_1(E_g)$	$^1/_{12}(\sqrt{3}g_{(\frac{1}{2})b} - g_{(\frac{2}{1})a})(\sqrt{3}m_{(\frac{1}{2})b} - m_{(\frac{2}{1})a})$	$^1/_{12}(\sqrt{3}g_{(\frac{1}{2})b} - g_{(\frac{2}{1})a})^2$	$^1/_{12}(\sqrt{3}m_{(\frac{1}{2})b} - m_{(\frac{2}{1})a})^2$
	$\rightarrow {}^3A(E_g)$	$^1/_{12}(\sqrt{3}g_{(\frac{1}{2})a} + g_{(\frac{2}{1})b})(\sqrt{3}m_{(\frac{1}{2})a} + m_{(\frac{2}{1})b})$	$^1/_{12}(\sqrt{3}g_{(\frac{1}{2})a} + g_{(\frac{2}{1})b})^2$	$^1/_{12}(\sqrt{3}m_{(\frac{1}{2})a} + m_{(\frac{2}{1})b})^2$
	$\rightarrow {}^3B_1(A_{2g})$	$^1/_{12}(\sqrt{3}g_{(\frac{1}{2})b} + g_{(\frac{2}{1})a})(\sqrt{3}m_{(\frac{1}{2})b} + m_{(\frac{2}{1})a})$	$^1/_{12}(\sqrt{3}g_{(\frac{1}{2})b} + g_{(\frac{2}{1})a})^2$	$^1/_{12}(\sqrt{3}m_{(\frac{1}{2})b} + m_{(\frac{2}{1})a})^2$
	$\rightarrow {}^3A(T_{2g})$	$^1/_2 g_{(\frac{1}{2})a} m_{(\frac{1}{2})a}$	$^1/_2 g_{(\frac{1}{2})a}^2$	$^1/_2 m_{(\frac{1}{2})a}^2$
	$\rightarrow {}^3B_{(\frac{2}{3})}(T_{2g})$	0	0	0
	$\rightarrow {}^3B_{(\frac{3}{2})}(T_{2g})$	$^3/_8 g_{0b} m_{0b}$	$^3/_8 g_{0b}^2$	$^3/_8 m_{0b}^2$
	$\rightarrow {}^3B_1(T_{1g})$	$^1/_2 g_{(\frac{1}{2})b} m_{(\frac{1}{2})b}$	$^1/_2 g_{(\frac{1}{2})b}^2$	$^1/_2 m_{(\frac{1}{2})b}^2$
	$\rightarrow {}^3B_{(\frac{2}{3})}(T_{1g})$	0	0	0
	$\rightarrow {}^3B_{(\frac{3}{2})}(T_{1g})$	$^1/_8 g_{0b} m_{0b}$	$^1/_8 g_{0b}^2$	$^1/_8 m_{0b}^2$
	$^3B_1(T_{1g}) \rightarrow {}^3B_1(E_g)$	0	0	0
	$\rightarrow {}^3A(E_g)$	$^4/_3 g_{0b} m_{0b}$	$^4/_3 g_{0b}^2$	$^4/_3 m_{0b}^2$
	$\rightarrow {}^3B_1(T_{1g})$	0	0	0
	$\rightarrow {}^3B_{(\frac{2}{3})}(T_{1g})$	$^1/_8(\sqrt{3}g_{(\frac{1}{2})b} - g_{(\frac{2}{1})a})(\sqrt{3}m_{(\frac{1}{2})b} - m_{(\frac{2}{1})a})$	$^1/_8(\sqrt{3}g_{(\frac{1}{2})b} - g_{(\frac{2}{1})a})^2$	$^1/_8(\sqrt{3}m_{(\frac{1}{2})b} - m_{(\frac{2}{1})a})^2$
	$\rightarrow {}^3A(T_{2g})$	0	0	0
	$\rightarrow {}^3B_{(\frac{2}{3})}(T_{2g})$	$^1/_8(\sqrt{3}g_{(\frac{2}{1})a} + g_{(\frac{1}{2})b})(\sqrt{3}m_{(\frac{2}{1})a} + m_{(\frac{1}{2})b})$	$^1/_8(\sqrt{3}g_{(\frac{2}{1})a} + g_{(\frac{1}{2})b})^2$	$^1/_8(\sqrt{3}m_{(\frac{2}{1})a} + m_{(\frac{1}{2})b})^2$
	$\rightarrow {}^3A(A_{1g})$	$^1/_3 g_{0b} m_{0b}$	$^1/_3 g_{0b}^2$	$^1/_3 m_{0b}^2$
	$\rightarrow {}^3B_1(E_g)$	0	0	0
	$\rightarrow {}^3A(E_g)$	$^1/_3 g_{0b} m_{0b}$	$^1/_3 g_{0b}^2$	$^1/_3 m_{0b}^2$
	$\rightarrow {}^3B_1(A_{2g})$	0	0	0
	$\rightarrow {}^3A(T_{2g})$	0	0	0
	$\rightarrow {}^3B_{(\frac{2}{3})}(T_{2g})$	$^1/_8(\sqrt{3}g_{(\frac{1}{2})b} - g_{(\frac{2}{1})a})(\sqrt{3}m_{(\frac{1}{2})b} - m_{(\frac{2}{1})a})$	$^1/_8(\sqrt{3}g_{(\frac{1}{2})b} - g_{(\frac{2}{1})a})^2$	$^1/_8(\sqrt{3}m_{(\frac{1}{2})b} - m_{(\frac{2}{1})a})^2$
	$\rightarrow {}^3B_1(T_{1g})$	0	0	0
	$\rightarrow {}^3B_{(\frac{2}{3})}(T_{1g})$	$^1/_8(\sqrt{3}g_{(\frac{2}{1})a} + g_{(\frac{1}{2})b})(\sqrt{3}m_{(\frac{2}{1})a} + m_{(\frac{1}{2})b})$	$^1/_8(\sqrt{3}g_{(\frac{2}{1})a} + g_{(\frac{1}{2})b})^2$	$^1/_8(\sqrt{3}m_{(\frac{2}{1})a} + m_{(\frac{1}{2})b})^2$
5	$^2A(T_{2g}) \rightarrow {}^2B_{(\frac{2}{3})}(T_{2g})$	$\bar{g}_{0(\frac{b}{c})}\bar{m}_{0(\frac{b}{c})}$	$\bar{g}_{0(\frac{b}{c})}^2$	$\bar{m}_{0(\frac{b}{c})}^2$
	$\rightarrow {}^2B_1(A_{2g})$	$^1/_3 g_{0b} m_{0b}$	$^1/_3 g_{0b}^2$	$^1/_3 m_{0b}^2$
	$\rightarrow {}^2B_1(T_{1g})$	0	0	0
	$\rightarrow {}^2B_{(\frac{2}{3})}(T_{1g})$	$^3/_8(g_{(\frac{1}{2})a} - \sqrt{3}g_{(\frac{2}{1})b})(m_{(\frac{1}{2})a} - \sqrt{3}m_{(\frac{2}{1})b})$	$^3/_8(g_{(\frac{1}{2})a} - \sqrt{3}g_{(\frac{2}{1})b})^2$	$^3/_8(m_{(\frac{1}{2})a} - \sqrt{3}m_{(\frac{2}{1})b})^2$
	$\rightarrow {}^2A(T_{2g})$	0	0	0
	$\rightarrow {}^2B_{(\frac{2}{3})}(T_{2g})$	$^1/_8(g_{(\frac{1}{2})a} - \sqrt{3}g_{(\frac{2}{1})b})(m_{(\frac{1}{2})a} - \sqrt{3}m_{(\frac{2}{1})b})$	$^1/_8(g_{(\frac{1}{2})a} - \sqrt{3}g_{(\frac{2}{1})b})^2$	$^1/_8(m_{(\frac{1}{2})a} - \sqrt{3}m_{(\frac{2}{1})b})^2$
	$\rightarrow {}^2A(E_g)$	0	0	0
	$\rightarrow {}^2B_1(E_g)$	$^1/_3 g_{0b} m_{0b}$	$^1/_3 g_{0b}^2$	$^1/_3 m_{0b}^2$
	$\rightarrow {}^2A(T_{2g})$	0	0	0

Table VII (*Continued*)

n	Transitions	Rotational strengths	Spectral strengths: Electric	Spectral strengths: Magnetic
5	$\rightarrow {}^2B_{(\frac{2}{3})}(T_{2g})$	$^3/_8(\sqrt{3}g_{(\frac{1}{2})a} + g_{(\frac{2}{1})b})(\sqrt{3}m_{(\frac{1}{2})a} + m_{(\frac{2}{1})b})$	$^3/_8(\sqrt{3}g_{(\frac{1}{2})a} + g_{(\frac{2}{1})b})^2$	$^3/_8(\sqrt{3}m_{(\frac{1}{2})a} + m_{(\frac{2}{1})b})^2$
	$\rightarrow {}^2B_1(T_{1g})$	0	0	0
	$\rightarrow {}^2B_{(\frac{2}{3})}(T_{1g})$	$^1/_8(\sqrt{3}g_{(\frac{1}{2})a} + g_{(\frac{2}{1})b})(\sqrt{3}m_{(\frac{1}{2})a} + m_{(\frac{2}{1})b})$	$^1/_8(\sqrt{3}g_{(\frac{1}{2})a} + g_{(\frac{2}{1})b})^2$	$^1/_8(\sqrt{3}m_{(\frac{1}{2})a} + m_{(\frac{2}{1})b})^2$
	$\rightarrow {}^2A(A_{1g})$	0	0	0
	$\rightarrow {}^2A(E_g)$	0	0	0
	$\rightarrow {}^2B_1(E_g)$	$^1/_3g_{0b}m_{0b}$	$^1/_3g_{0b}{}^2$	$^1/_3m_{0b}{}^2$
$^2B_2(T_{2g})$	$\rightarrow {}^2B_2(T_{2g})$	$-\bar{g}_{0a}\bar{m}_{0a}$	$\bar{g}_{0a}{}^2$	$\bar{m}_{0a}{}^2$
$^2B_{(\frac{2}{3})}(T_{2g})$	$\rightarrow {}^2E_1(A_{2g})$	$^1/_{12}(\sqrt{3}g_{(\frac{2}{1})a} - g_{(\frac{1}{2})b})(\sqrt{3}m_{(\frac{2}{1})a} - m_{(\frac{1}{2})b})$	$^1/_{12}(\sqrt{3}g_{(\frac{2}{1})a} - g_{(\frac{1}{2})b})^2$	$^1/_{12}(\sqrt{3}m_{(\frac{2}{1})a} - m_{(\frac{1}{2})b})^2$
	$\rightarrow {}^2B_1(T_{1g})$	$^3/_2g_{(\frac{2}{1})a}m_{(\frac{2}{1})a}$	$^3/_2g_{(\frac{2}{1})a}{}^2$	$^3/_2m_{(\frac{2}{1})a}{}^2$
	$\rightarrow {}^2B_{(\frac{2}{3})}(T_{1g})$	0	0	0
	$\rightarrow {}^2B_{(\frac{3}{2})}(T_{1g})$	$^9/_8g_{0b}m_{0b}$	$^9/_8g_{0b}{}^2$	$^9/_8m_{0b}{}^2$
	$\rightarrow {}^2A(T_{2g})$	$^1/_2g_{(\frac{1}{2})a}m_{(\frac{1}{2})a}$	$^1/_2g_{(\frac{1}{2})a}{}^2$	$^1/_2m_{(\frac{1}{2})a}{}^2$
	$\rightarrow {}^2B_{(\frac{2}{3})}(T_{2g})$	0	0	0
	$\rightarrow {}^2B_{(\frac{3}{2})}(T_{2g})$	$^3/_8g_{0b}m_{0b}$	$^3/_8g_{0b}{}^2$	$^3/_8m_{0b}{}^2$
	$\rightarrow {}^2A(E_g)$	$^1/_{12}(\sqrt{3}g_{(\frac{2}{1})b} - g_{(\frac{1}{2})a})(\sqrt{3}m_{(\frac{2}{1})b} - m_{(\frac{1}{2})a})$	$^1/_{12}(\sqrt{3}g_{(\frac{2}{1})b} - g_{(\frac{1}{2})a})^2$	$^1/_{12}(\sqrt{3}m_{(\frac{2}{1})b} - m_{(\frac{1}{2})a})^2$
	$\rightarrow {}^2B_1(E_g)$	$^1/_{12}(g_{(\frac{1}{2})b} + \sqrt{3}g_{(\frac{2}{1})a})(m_{(\frac{1}{2})b} + \sqrt{3}m_{(\frac{2}{1})a})$	$^1/_{12}(g_{(\frac{1}{2})b} + \sqrt{3}g_{(\frac{2}{1})a})^2$	$^1/_{12}(m_{(\frac{1}{2})b} + \sqrt{3}m_{(\frac{2}{1})a})^2$
	$\rightarrow {}^2A(T_{2g})$	$^3/_2g_{(\frac{2}{1})b}m_{(\frac{2}{1})b}$	$^3/_2g_{(\frac{2}{1})b}{}^2$	$^3/_2m_{(\frac{2}{1})b}{}^2$
	$\rightarrow {}^2E_{(\frac{2}{3})}(T_{2g})$	0	0	0
	$\rightarrow {}^2E_{(\frac{3}{2})}(T_{2g})$	$^3/_8g_{0b}m_{0b}$	$^3/_8g_{0b}{}^2$	$^3/_8m_{0b}{}^2$
	$\rightarrow {}^2E_1(T_{1g})$	$^1/_2g_{(\frac{1}{2})b}m_{(\frac{1}{2})b}$	$^1/_2g_{(\frac{1}{2})b}{}^2$	$^1/_2m_{(\frac{1}{2})b}{}^2$
	$\rightarrow {}^2E_{(\frac{2}{3})}(T_{1g})$	0	0	0
	$\rightarrow {}^2E_{(\frac{3}{2})}(T_{1g})$	$^1/_8g_{0b}m_{0b}$	$^1/_8g_{0b}{}^2$	$^1/_8m_{0b}{}^2$
	$\rightarrow {}^2A(A_{1g})$	$^1/_{12}(g_{(\frac{1}{2})a} + \sqrt{3}g_{(\frac{2}{1})b})(m_{(\frac{1}{2})a} + \sqrt{3}m_{(\frac{2}{1})b})$	$^1/_{12}(g_{(\frac{1}{2})a} + \sqrt{3}g_{(\frac{2}{1})b})^2$	$^1/_{12}(m_{(\frac{1}{2})a} + \sqrt{3}m_{(\frac{2}{1})b})^2$
	$\rightarrow {}^2A(E_g)$	$^1/_3g_{(\frac{1}{2})a}m_{(\frac{1}{2})a}$	$^1/_3g_{(\frac{1}{2})a}{}^2$	$^1/_3m_{(\frac{1}{2})a}{}^2$
	$\rightarrow {}^2E_1(E_g)$	$^1/_3g_{(\frac{1}{2})b}m_{(\frac{1}{2})b}$	$^1/_3g_{(\frac{1}{2})b}{}^2$	$^1/_3m_{(\frac{1}{2})b}{}^2$
6	$^1A_1(A_{1g}) \rightarrow {}^1B_1(T_{1g})$	$2g_{0b}m_{0b}$	$2g_{0b}{}^2$	$2m_{0b}{}^2$
	$\rightarrow {}^1B_{(\frac{2}{3})}(T_{1g})$	$^1/_2(\sqrt{3}g_{(\frac{1}{2})a} - g_{(\frac{2}{1})b})(\sqrt{3}m_{(\frac{1}{2})a} - m_{(\frac{2}{1})b})$	$^1/_2(\sqrt{3}g_{(\frac{1}{2})a} - g_{(\frac{2}{1})b})^2$	$^1/_2(\sqrt{3}m_{(\frac{1}{2})a} - m_{(\frac{2}{1})b})^2$
	$\rightarrow {}^1A(T_{2g})$	0	0	0
	$\rightarrow {}^1B_{(\frac{2}{3})}(T_{2g})$	$^1/_2(\sqrt{3}g_{(\frac{2}{1})b} + g_{(\frac{1}{2})a})(\sqrt{3}m_{(\frac{2}{1})b} + m_{(\frac{1}{2})a})$	$^1/_2(\sqrt{3}g_{(\frac{2}{1})b} + g_{(\frac{1}{2})a})^2$	$^1/_2(\sqrt{3}m_{(\frac{2}{1})b} + m_{(\frac{1}{2})a})^2$
7	$^2A(E_g) \rightarrow {}^2B_1(E_g)$	g_0m_0	$g_0{}^2$	$m_0{}^2$
	$\rightarrow {}^2B_1(T_{1g})$	$^3/_2g_{0b}m_{0b}$	$^3/_2g_{0b}{}^2$	$^3/_2m_{0b}{}^2$
	$\rightarrow {}^2B_{(\frac{2}{3})}(T_{1g})$	$^3/_2g_{(\frac{2}{1})b}m_{(\frac{2}{1})b}$	$^3/_2g_{(\frac{2}{1})b}{}^2$	$^3/_2m_{(\frac{2}{1})b}{}^2$
	$\rightarrow {}^2A(T_{2g})$	0	0	0
	$\rightarrow {}^2B_{(\frac{2}{3})}(T_{2g})$	$^1/_8(g_{(\frac{1}{2})a} - \sqrt{3}g_{(\frac{2}{1})b})(m_{(\frac{1}{2})a} - \sqrt{3}m_{(\frac{2}{1})b})$	$^1/_8(g_{(\frac{1}{2})a} - \sqrt{3}g_{(\frac{2}{1})b})^2$	$^1/_8(m_{(\frac{1}{2})a} - \sqrt{3}m_{(\frac{2}{1})b})^2$
	$\rightarrow {}^2B_1(T_{1g})$	$^1/_2g_{0b}m_{0b}$	$^1/_2g_{0b}{}^2$	$^1/_2m_{0b}{}^2$
	$\rightarrow {}^2B_{(\frac{2}{3})}(T_{1g})$	$^1/_8(\sqrt{3}g_{(\frac{1}{2})a} + g_{(\frac{2}{1})b})(\sqrt{3}m_{(\frac{1}{2})a} + m_{(\frac{2}{1})b})$	$^1/_8(\sqrt{3}g_{(\frac{1}{2})a} + g_{(\frac{2}{1})b})^2$	$^1/_8(\sqrt{3}m_{(\frac{1}{2})a} + m_{(\frac{2}{1})b})^2$
	$\rightarrow {}^2A(T_{2g})$	0	0	0
	$\rightarrow {}^2B_{(\frac{2}{3})}(T_{2g})$	$^1/_2g_{(\frac{1}{2})a}m_{(\frac{1}{2})a}$	$^1/_2g_{(\frac{1}{2})a}{}^2$	$^1/_2m_{(\frac{1}{2})a}{}^2$
	$^2B_1(E_g) \rightarrow {}^2B_1(T_{1g})$	0	0	0
	$\rightarrow {}^2B_{(\frac{2}{3})}(T_{1g})$	$^3/_2g_{(\frac{2}{1})a}m_{(\frac{2}{1})a}$	$^3/_2g_{(\frac{2}{1})a}{}^2$	$^3/_2m_{(\frac{2}{1})a}{}^2$
	$\rightarrow {}^2A(T_{2g})$	$^1/_2g_{0b}m_{0b}$	$^1/_2g_{0b}{}^2$	$^1/_2m_{0b}{}^2$
	$\rightarrow {}^2B_{(\frac{2}{3})}(T_{2g})$	$^1/_8(g_{(\frac{1}{2})b} + \sqrt{3}g_{(\frac{2}{1})a})(m_{(\frac{1}{2})b} + \sqrt{3}m_{(\frac{2}{1})a})$	$^1/_8(g_{(\frac{1}{2})b} + \sqrt{3}g_{(\frac{2}{1})a})^2$	$^1/_8(m_{(\frac{1}{2})b} + \sqrt{3}m_{(\frac{2}{1})a})^2$

Table VII (*Continued*)

n	Transitions	Rotational strengths	Spectral strengths: Electric	Spectral strengths: Magnetic
7	$\rightarrow {}^2B_1(T_{1g})$	0	0	0
	$\rightarrow {}^2B_{(\frac{2}{3})}(T_{1g})$	$^1/_8(g_{(\frac{2}{1})a} - \sqrt{3}g_{(\frac{1}{2})b})(m_{(\frac{2}{1})a} - \sqrt{3}m_{(\frac{1}{2})b})$	$^1/_8(g_{(\frac{2}{1})a} - \sqrt{3}g_{(\frac{1}{2})b})^2$	$^1/_8(m_{(\frac{2}{1})a} - \sqrt{3}m_{(\frac{1}{2})b})^2$
	$\rightarrow {}^2A(T_{2g})$	$^1/_2g_{0b}m_{0b}$	$^1/_2g_{0b}{}^2$	$^1/_2m_{0b}{}^2$
	$\rightarrow {}^2B_{(\frac{2}{3})}(T_{2g})$	$^1/_2g_{(\frac{1}{2})b}m_{(\frac{1}{2})b}$	$^1/_2g_{(\frac{1}{2})b}{}^2$	$^1/_2m_{(\frac{1}{2})b}{}^2$
8	${}^1B_1(E_g) \rightarrow {}^1A(E_g)$	$4\bar{\bar{p}}_0\bar{\bar{m}}_0$ [b]	$4\bar{\bar{p}}_0{}^2$ [b]	$4\bar{\bar{m}}_0{}^2$
	$\rightarrow {}^1A(A_{1g})$	0 [c]	$4\bar{\bar{r}}_0{}^2$ [c]	0 [c]
	$\rightarrow {}^1A(T_{2g})$	$g_{0b}m_{0b}$	$g_{0b}{}^2$	$m_{0b}{}^2$
	$\rightarrow {}^1B_{(\frac{2}{3})}(T_{2g})$	$^1/_4(g_{(\frac{1}{2})b} + \sqrt{3}g_{(\frac{2}{1})a})(m_{(\frac{1}{2})b} + \sqrt{3}m_{(\frac{2}{1})a})$	$^1/_4(g_{(\frac{1}{2})b} + \sqrt{3}g_{(\frac{2}{1})a})^2$	$^1/_4(m_{(\frac{1}{2})b} + \sqrt{3}m_{(\frac{2}{1})a})^2$
	$\rightarrow {}^1B_1(T_{1g})$	0	0	0
	$\rightarrow {}^1B_{(\frac{2}{3})}(T_{1g})$	$^1/_4(g_{(\frac{2}{1})a} - \sqrt{3}g_{(\frac{1}{2})b})(m_{(\frac{2}{1})a} - \sqrt{3}m_{(\frac{1}{2})b})$	$^1/_4(g_{(\frac{2}{1})a} - \sqrt{3}g_{(\frac{1}{2})b})^2$	$^1/_4(m_{(\frac{2}{1})a} - \sqrt{3}m_{(\frac{1}{2})b})^2$
	$\rightarrow {}^1A(T_{2g})$	0	0	0
	$\rightarrow {}^1B_{(\frac{2}{3})}(T_{2g})$	0	0	0
	$\rightarrow {}^1A(E_g)$	0	0	0
	$\rightarrow {}^1B_1(E_g)$	0	0	0
	$\rightarrow {}^1A(A_{1g})$	0	0	0
	${}^1A(E_g) \rightarrow {}^1A(A_{1g})$	0	0	0
	$\rightarrow {}^1A(T_{2g})$	0	0	0
	$\rightarrow {}^1B_{(\frac{2}{3})}(T_{2g})$	$^1/_4(g_{(\frac{1}{2})a} - \sqrt{3}g_{(\frac{2}{1})b})(m_{(\frac{1}{2})a} - \sqrt{3}m_{(\frac{2}{1})b})$	$^1/_4(g_{(\frac{1}{2})a} - \sqrt{3}g_{(\frac{2}{1})b})^2$	$^1/_4(m_{(\frac{1}{2})a} - \sqrt{3}m_{(\frac{2}{1})b})^2$
	$\rightarrow {}^1B_1(T_{1g})$	$g_{0b}m_{0b}$	$g_{0b}{}^2$	$m_{0b}{}^2$
	$\rightarrow {}^1B_{(\frac{2}{3})}(T_{1g})$	$^1/_4(g_{(\frac{2}{1})b} + \sqrt{3}g_{(\frac{1}{2})a})(m_{(\frac{2}{1})b} + \sqrt{3}m_{(\frac{1}{2})a})$	$^1/_4(g_{(\frac{2}{1})b} + \sqrt{3}g_{(\frac{1}{2})a})^2$	$^1/_4(m_{(\frac{2}{1})b} + \sqrt{3}m_{(\frac{1}{2})a})^2$
	$\rightarrow {}^1A(T_{2g})$	0	0	0
	$\rightarrow {}^1B_{(\frac{2}{3})}(T_{2g})$	0	0	0
	$\rightarrow {}^1A(E_g)$	0	0	0
	$\rightarrow {}^1B_1(E_g)$	0	0	0
	$\rightarrow {}^1A(A_{1g})$	0	0	0
	$\rightarrow {}^1A(T_{2g})$	0	0	0
	$\rightarrow {}^1B_{(\frac{2}{3})}(T_{2g})$	$^1/_4(g_{(\frac{1}{2})a} + \sqrt{3}g_{(\frac{2}{1})b})(m_{(\frac{1}{2})a} + \sqrt{3}m_{(\frac{2}{1})b})$	$^1/_4(g_{(\frac{1}{2})a} + \sqrt{3}g_{(\frac{2}{1})b})^2$	$^1/_4(m_{(\frac{1}{2})a} + \sqrt{3}m_{(\frac{2}{1})b})^2$
	$\rightarrow {}^1B_1(T_{1g})$	$^1/_4g_{0b}m_{0b}$	$^1/_4g_{0b}{}^2$	$^1/_4m_{0b}{}^2$
	$\rightarrow {}^1B_{(\frac{2}{3})}(T_{1g})$	$^1/_4(g_{(\frac{2}{1})b} - \sqrt{3}g_{(\frac{1}{2})a})(m_{(\frac{2}{1})b} - \sqrt{3}m_{(\frac{1}{2})a})$	$^1/_4(g_{(\frac{2}{1})b} - \sqrt{3}g_{(\frac{1}{2})a})^2$	$^1/_4(m_{(\frac{2}{1})b} - \sqrt{3}m_{(\frac{1}{2})a})^2$
	$\rightarrow {}^1A(T_{2g})$	0	0	0
	$\rightarrow {}^1B_{(\frac{2}{3})}(T_{2g})$	0	0	0
	$\rightarrow {}^1A(E_g)$	0	0	0
	$\rightarrow {}^1B(E_g)$	0	0	0
	$\rightarrow {}^1A(A_{1g})$	0	0	0

[a] The quantities $\bar{g}_{0a,b,c}$, $\bar{\bar{g}}_0$, $g_{0a,b}$, $g_{1a,b}$, $g_{2a,b}$, $\bar{\bar{m}}_{0a,b,c}$, $\bar{\bar{m}}_0$, $m_{0a,b}$, $m_{1a,b}$, $m_{2c,b}$ ($g = r,p$) are as defined specially and generally in §3.1, eq. 17 and 19. [b] The dipole length forms vanish due to internal self-cancellation [confer eq. 38 and recall $\langle a^\star|\vec{v}|b_1\rangle$ equals $\langle b_1|\vec{v}|a^\star\rangle$ for $\vec{v}$ real ($\vec{v} = e\vec{r}$), but equals $-\langle b_1|\vec{v}|a^\star\rangle$ for $\vec{v}$ pure imaginary ($\vec{v} = (\hbar/i)\vec{\nabla}$, $\vec{m}$). [c] The dipole velocity forms vanish due to internal self-cancellation [confer eq. 38 and recall $\langle a^\star|\vec{v}|b_1\rangle$ equals $-\langle b_1|\vec{v}|a^\star\rangle$ for $\vec{v}$ pure imaginary ($\vec{v} = (\hbar/i)\vec{\nabla}$, $\vec{m}$), but equals $\langle b_1|\vec{v}|a^\star\rangle$ for $\vec{v}$ real ($\vec{v} = e\vec{r}$).

quintuplet forms is the more faithful for transition metal compounds, we have carried both in our algebra [eq. 19, 20, 24, 25, and 26 and Tables VI, VII, and VIII] and used the simplest (the coordinate representation) in our numerology [eq. 52, 53, and 54 and footnote 27].

V. Summary

The salient points of this division are the following.

(1) Digonal dihedral molecular orbitals may be unequivocally fixed in a directed localized ligand–metal orbital basis.

Table VIII: The Spin-Paired d^8 Digonal Dihedral (Nonoctahedrally Oriented) Rotational and Spectral Strengths for Zero Spin-Orbit Forces[a]

Transitions	Rotational strengths	Spectral strengths: Electric	Spectral strengths: Magnetic
$^1A^{(j)} = {}^1A^{(k)}$ $(j, k = 0, 1, 2, 3, 4, 5, 6)$	0	0	0
$^1A^{(1)} \rightarrow {}^1B_1^{(1)}$	$2\bar{g}_0\bar{m}_0$	$2\bar{g}_0^2$	$2\bar{m}_0^2$
$\rightarrow {}^1B_1^{(2)}$	$2g_{0b}m_{0b}$	$2g_{0b}^2$	$2m_{0b}^2$
$\rightarrow {}^1B_1^{(3)}$	0	0	0
$\rightarrow {}^1B_{(\frac{2}{3})}^{(1)}$	$2g_{(\frac{2}{1})b}m_{(\frac{2}{1})b}$	$2g_{(\frac{2}{1})b}^2$	$2m_{(\frac{2}{1})b}^2$
$\rightarrow {}^1B_{(\frac{2}{3})}^{(2)}$	0	0	0
$\rightarrow {}^1B_{(\frac{2}{3})}^{(3)}$	0	0	0
$^3B_1^{(1)} \rightarrow {}^3B_1^{(2,3)}$	0	0	0
$^3B_1^{(1)} \rightarrow {}^3A$	$g_{0b}m_{0b}$	g_{0b}^2	m_{0b}^2
$^3B_1^{(1)} \rightarrow {}^3B_{(\frac{2}{3})}^{(1)}$	$g_{(\frac{2}{1})a}m_{(\frac{2}{1})a}$	$g_{(\frac{2}{1})a}^2$	$m_{(\frac{2}{1})a}^2$
$^3B_1^{(1)} \rightarrow {}^3B_{(\frac{2}{3})}^{(2)}$	$g_{(\frac{1}{2})b}m_{(\frac{1}{2})b}$	$g_{(\frac{1}{2})b}^2$	$m_{(\frac{1}{2})b}^2$
$^3B_1^{(1)} \rightarrow {}^3B_{(\frac{2}{3})}^{(3)}$	0	0	0

[a] The quantities $\bar{g}_{0a,b,c}$, $\bar{\bar{g}}_0$, $g_{0a,b}$, $g_{1a,b}$, $g_{2a,b}$, $\bar{\bar{m}}_{0a,b,c}$, $\bar{\bar{m}}_0$, $m_{0a,b}$, $m_{1a,b}$, $m_{2a,b}$ $(g = r, p)$ are as defined specially and generally in §3.1, eq. 17 and 19.

(2) The optical rotatory and spectral powers are directly (but not linearly) proportional to the covalent strength of the compound.

(3) The electron-hole formalism is not straightly applicable to matrix manipulation of single-electron operator sums. In particular, it is not straightly applicable to optical rotatory and intensiveness matrix calculations.

(4) There is a direct correspondence between the rotational and spectral powers of d^n and d^{5+n} $(n = 0, 1, 2, 3, 4, 5)$ spin-free systems, between $d^{1,4,6,9}$ spin-free systems, and various indirect relationships between these and other d^n $(n = 0, 1, 2, 3, 4, 5, 6, 8, 9)$ configurations.

(5) The sign and magnitude of the optical rotation, the ellipticity, and the dissymmetry, for a given conformation, is directly dependent (but not linearly) upon the sign and magnitude of the covalency and hybridization parameters, the localized metal–metal, metal–ligand, and ligand–ligand transition moments, and the angles of bidental cant.

(6) Cubic magnetic and electric selection rules are nontrivially relaxed in zero order in digonal dihedral compounds.

(7) Strong natural electronic optical rotatory dispersion and dichroism are possible in the infrared and microwave regions of the spectrum for spin-orbitally coupled and uncoupled d^n electronic systems.

(8) Spin magnetic dipole transition moments alone, in conjunction with an allowed electric dipole transition moment, can induce large rotational strengths.

(9) To good approximation σ- and σ,π-bonded compounds are formally identical in their mathematical optical rotatativeness and intensiveness behavior.

(10) The optical rotatory and spectral powers of many electron digonal dihedral systems are expressed as multiples and simple sums of those of the primogenital one-electron system, but no simple addition invariance relationship exists for these expressions.

Division B

Transition Metal Compounds of Lower Symmetry

VI. Compounds of Unidigonal Dihedral Symmetry

Transition metal compounds of unidigonal dihedral (D_1) symmetry[38] of the usual sort fall naturally into three kinds: the monobidentate [Fig. 36a, b, 37, and 41], the dibidentate [Fig. 38a, b, 39, 40, and 41], and the polydentate [Fig. 42, 43, and 44].[39] The mathematical treatment of the first two kinds follows directly from that of the digonal dihedral and trigonal dihedral cases developed earlier in Division A of this paper and in ref. 6. This circumstance occurs due to our careful choice of functional orientation in these former two cases. Because of this careful choice with respect to the digonal twofold axis $C_2(x)$ and the trigonal twofold axis $C_2(y')$, the wave functions, and hence the matrix elements and rotational and spectral strengths, of unidi-

(38) The debased point group D_1 is identical with the primitative point group C_2.

(39) Monodentate compounds of D_1 symmetry are not possible as their essential simplicity imposes higher symmetry.

gonal dihedral chemicals can be written as simple sums of those of their correspondent digonal and trigonal forebears. To demonstrate, for the zero spin-orbit force problem the principle of descent in symmetry[40] immediately shows that the digonal dihedral functions, matrix elements, and rotational and spectral strengths of Division A are identically also the unidigonal dihedral monobidentate functions, matrix elements, and rotational and spectral strengths with the digonal–unidigonal dihedral species correspondence a, b_3, A, $B_3(D_2) \rightarrow$ a, $A(D_1)$, b_1, b_2, B_1, $B_2(D_2) \rightarrow$ b, $B(D_1)$, and that the trigonal dihedral functions $a_1(t_{2g}$ or $a_{1g})$, $a_2(t_{1u})$, $e_\pm(t_{2g}$ or $e_g)$, $e_\pm(t_{1u})$, $A_1(T_{2g}$ or $A_{1g})$, $A_2(T_{1g}$ or $A_{2g})$, $E_\pm(T_{2g}$ or $E_g)$, $E_\pm(T_{1g})$, of ref. 6 are straightly related to the unidigonal dihedral dibidentate functions by the functional correspondence

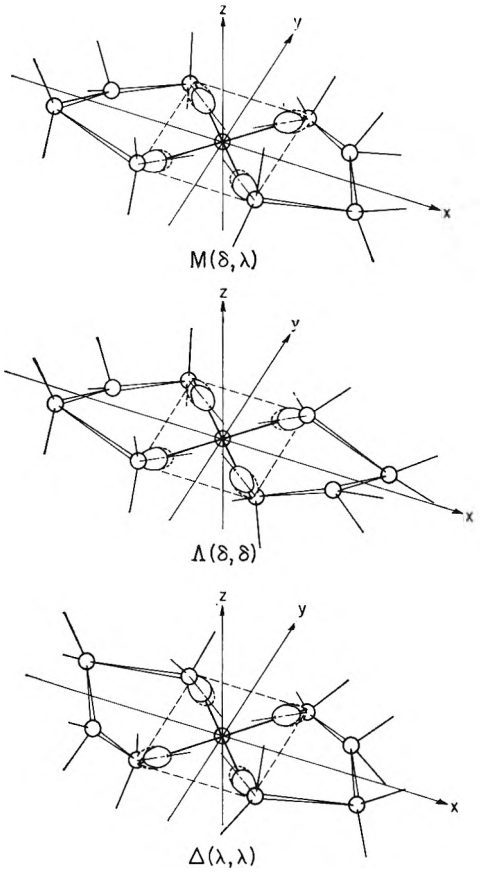

Figure 30. The localized ligand orbital spatial dispositions for the factualized noncomplanately bonded acute-angled conformations of the bisethylenediamine cation. The adjacent (ligand) carbon quarters are as in Fig. 7.

$$a_1(t_{2g} \text{ or } a_{1g})[D_3] = a(t_{2g} \text{ or } a_{1g})[D_1],$$
$$a_2(t_{1u})[D_3] = b(t_{1u})[D_1]$$

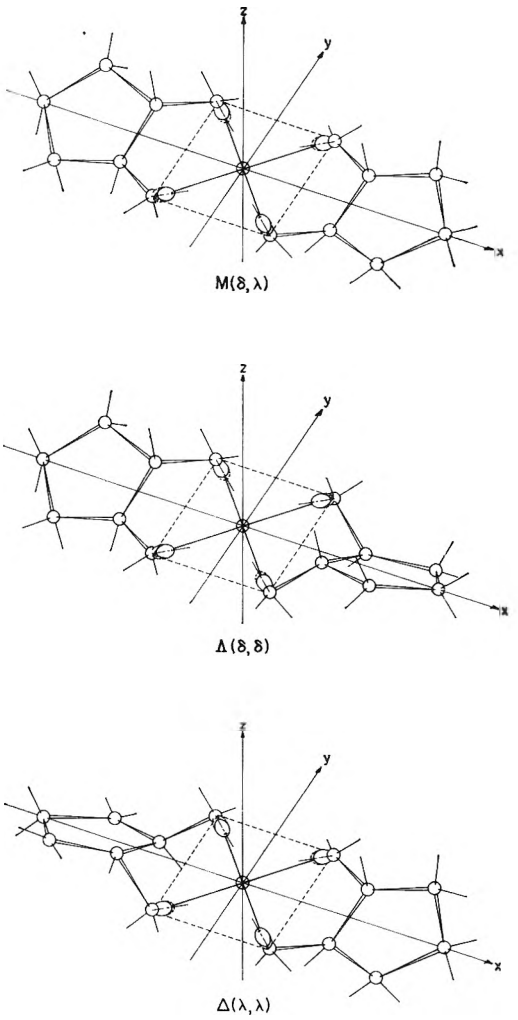

Figure 31. The localized ligand orbital spatial dispositions for the factualized noncomplanately bonded acute-angled conformation of the biscyclopentanediamine cation. The adjacent (ligand) carbon quarters are as in Fig. 8.

$$e_\pm(t_{2g} \text{ or } e_g)[D_3] = \sqrt{1/2}(e_A(t_{2g} \text{ or } e_g) \pm ie_B(t_{2g} \text{ or } e_g)[D_1],$$
$$e_\pm(t_{1u})[D_3] = \sqrt{1/2}(e_B(t_{1u}) \pm ie_A(t_{1u}))[D_1]$$

$$A_1(T_{2g} \text{ or } A_{1g})[D_3] = A(T_{2g} \text{ or } A_{1g})[D_1],$$
$$A_2(T_{1g} \text{ or } A_{2g})[D_2] = B(T_{1g} \text{ or } A_{2g})[D_1]$$

$$E_\pm(T_{2g} \text{ or } E_g)[D_3] = \sqrt{1/2}(E_A(T_{2g} \text{ or } E_g) \pm iE_B(T_{2g} \text{ or } E_g))[D_1],$$
$$E_\pm(T_{1g})[D_3] = \sqrt{1/2}(E_B(T_{1g}) \pm iE_A(T_{1g}))[D_1] \quad (55)$$

or

$$a(t_{2g} \text{ or } a_{1g})[D_1] = a_1(t_{2g} \text{ or } a_{1g})[D_3],$$
$$b(t_{1u})[D_1] = a_2(t_{1u})[D_3]$$

(40) Read, for example, A. D. Liehr, *J. Phys. Chem.*, **67**, 389, 471 (1963).

$$e_A(t_{2g} \text{ or } e_g)[D_1] = \sqrt{1/2}(e_+(t_{2g} \text{ or } e_g) + e_-(t_{2g} \text{ or } e_g))[D_3],$$

$$e_B(t_{2g} \text{ or } e_g)[D_1] = -i\sqrt{1/2}(e_+(t_{2g} \text{ or } e_g) - e_-(t_{2g} \text{ or } e_g))[D_3]$$

$$e_A(t_{1u})[D_1] = -i\sqrt{1/2}(e_+(t_{1u}) - e_-(t_{1u}))[D_3],$$

$$e_B(t_{1u})[D_1] = \sqrt{1/2}(e_+(t_{1u}) + e_-(t_{1u}))[D_3]$$

$$A(T_{2g} \text{ or } A_{1g})[D_1] = A_1(T_{2g} \text{ or } A_{1g})[D_3],$$

$$B(T_{1g} \text{ or } A_{2g})[D_1] = A_2(T_{1g} \text{ or } A_{2g})[D_3]$$

$$E_A(T_{2g} \text{ or } E_g)[D_1] = \sqrt{1/2}(E_+(T_{2g} \text{ or } E_g) + E_-(T_{2g} \text{ or } E_g))[D_3],$$

$$E_B(T_{2g} \text{ or } E_g)[D_1] = -i\sqrt{1/2}(E_+(T_{2g} \text{ or } E_g) - E_-(T_{2g} \text{ or } E_g))[D_3]$$

$$E_A(T_{1g})[D_1] = -i\sqrt{1/2}(E_+(T_{1g}) - E_-(T_{1g}))[D_3],$$

$$E_B(T_{1g})[D_1] = \sqrt{1/2}(E_+(T_{1g}) + E_-(T_{1g}))[D_3] \quad (56)$$

where e_A, e_B and E_A, E_B are the unidigonal dibidentate (D_1) a, b and A, B specie progeny of the trigonal (D_3) E specie primogenitor, so that the unidigonal dihedral dibidentate matrix elements and rotational and spectral strengths are but additive sets of the trigonal dihedral ones, to a first approximation, as illustrated in eq. 57 through 66 and in Tables IX and X.

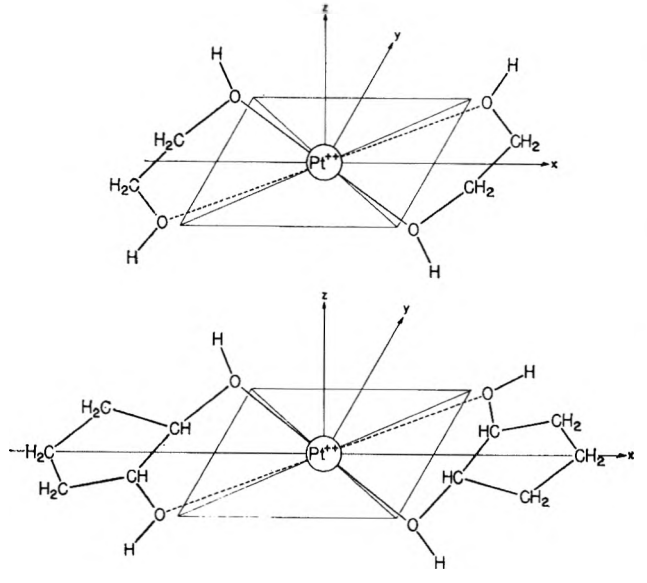

Figure 32. The factualized noncomplanately bonded acute-angled $\Delta(\lambda,\lambda)$ and $\Lambda(\delta,\delta)$ geometry of the bis(ethylene glycol)-platinum(II) and the bis(cyclopentane glycol)platinum(II) cations, distributively. Their tetrahedral affiliation is as in Fig. 28 and 29, with appropriate label change. Their adjacent (ligand) carbon sites are as in Fig. 1 and 2.

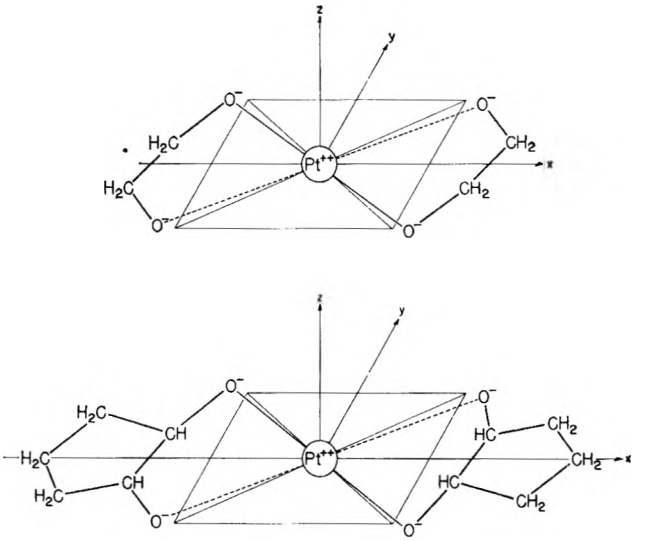

Figure 33. The factualized noncomplanately bonded acute-angled $\Delta(\lambda,\lambda)$ and $\Lambda(\delta,\delta)$ geometry of the bis(ethylene glycolate)-platinum(II) and the bis(cyclopentane glycolate)platinum(II) anions, distributively. Their tetrahedral affiliation is as in Fig. 28 and 29, with appropriate label change. Their adjacent (ligand) carbon sites are as in Fig. 1 and 2.

(i) *Matrix Elements: One Electron*

$$\left\langle {}^2A[{}^2T_{2g}(t_{2g})] \left| \frac{\vec{p}}{\vec{m}} \right| {}^2E_{(B)}^{(A)}[{}^2T_{2g}(t_{2g})] \right\rangle = \left\langle a(t_{2g}) \left| \frac{\vec{p}}{\vec{m}} \right| e_{(B)}^{(A)}(t_{2g}) \right\rangle$$

$$\left\langle {}^2A[{}^2T_{2g}(t_{2g})] \left| \frac{\vec{p}}{\vec{m}} \right| {}^2E_{(B)}^{(A)}[{}^2E_g(e_g)] \right\rangle = \left\langle a(t_{2g}) \left| \frac{\vec{p}}{\vec{m}} \right| e_{(B)}^{(A)}(e_g) \right\rangle$$

$$\left\langle {}^2E_{(B)}^{(A)}[{}^2T_{2g}(t_{2g})] \left| \frac{\vec{p}}{\vec{m}} \right| {}^2E_{(B)}^{(A)}[{}^2T_{2g}(t_{2g})] \right\rangle = \left\langle e_{(B)}^{(A)}(t_{2g}) \left| \frac{\vec{p}}{\vec{m}} \right| e_{(B)}^{(A)}(t_{2g}) \right\rangle$$

$$\left\langle {}^2E_{(B)}^{(A)}[{}^2T_{2g}(t_{2g})] \left| \frac{\vec{p}}{\vec{m}} \right| {}^2E_{(A)}^{(B)}[{}^2T_{2g}(t_{2g})] \right\rangle = \left\langle e_{(B)}^{(A)}(t_{1g}) \left| \frac{\vec{p}}{\vec{m}} \right| e_{(A)}^{(B)}(t_{2g}) \right\rangle$$

$$\left\langle {}^2E_{(B)}^{(A)}[{}^2T_{2g}(t_{2g})] \left| \frac{\vec{p}}{\vec{m}} \right| {}^2E_{(B)}^{(A)}[{}^2E_g(e_g)] \right\rangle = \left\langle e_{(B)}^{(A)}(t_{2g}) \left| \frac{\vec{p}}{\vec{m}} \right| e_{(B)}^{(A)}(e_g) \right\rangle$$

$$\left\langle {}^2E_{(B)}^{(A)}[{}^2T_{2g}(t_{2g})] \left| \frac{\vec{p}}{\vec{m}} \right| {}^2E_{(A)}^{(B)}[{}^2T_{2g}(t_{2g})] \right\rangle = \left\langle e_{(A)}^{(B)}(t_{2g}) \left| \frac{\vec{p}}{\vec{m}} \right| e_{(A)}^{(B)}(e_g) \right\rangle$$

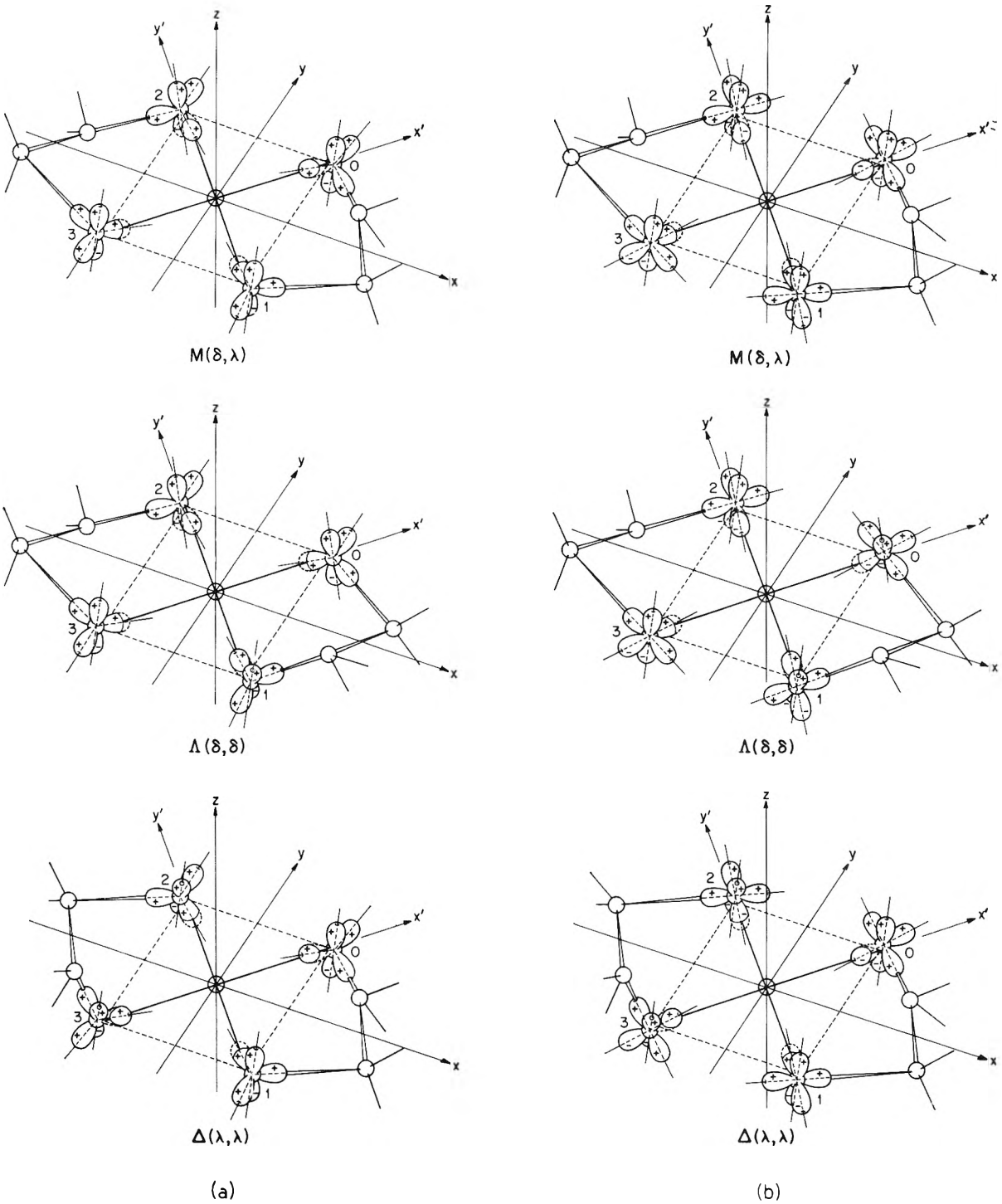

Figures 34a and 34b. The localized ligand orbital spatial disposition for the factualized noncomplanately bonded acute-angled conformations of the bis(ethylene glycol or glycolate) platinum(II) cation or anion. Figure 34a manifests the spatial disposition under the premise of isosceles hybridization and Fig. 34b under the premise of digonal hybridization. Figure 30 suitably modified illustrates it under tetrahedral hybridization [read Division C, section VIII for the precise sense of the word hybridization used here]. The actual disposition is presumably intermediate between these extreme types. The adjacent (ligand) carbon aspects are as in Fig. 7.

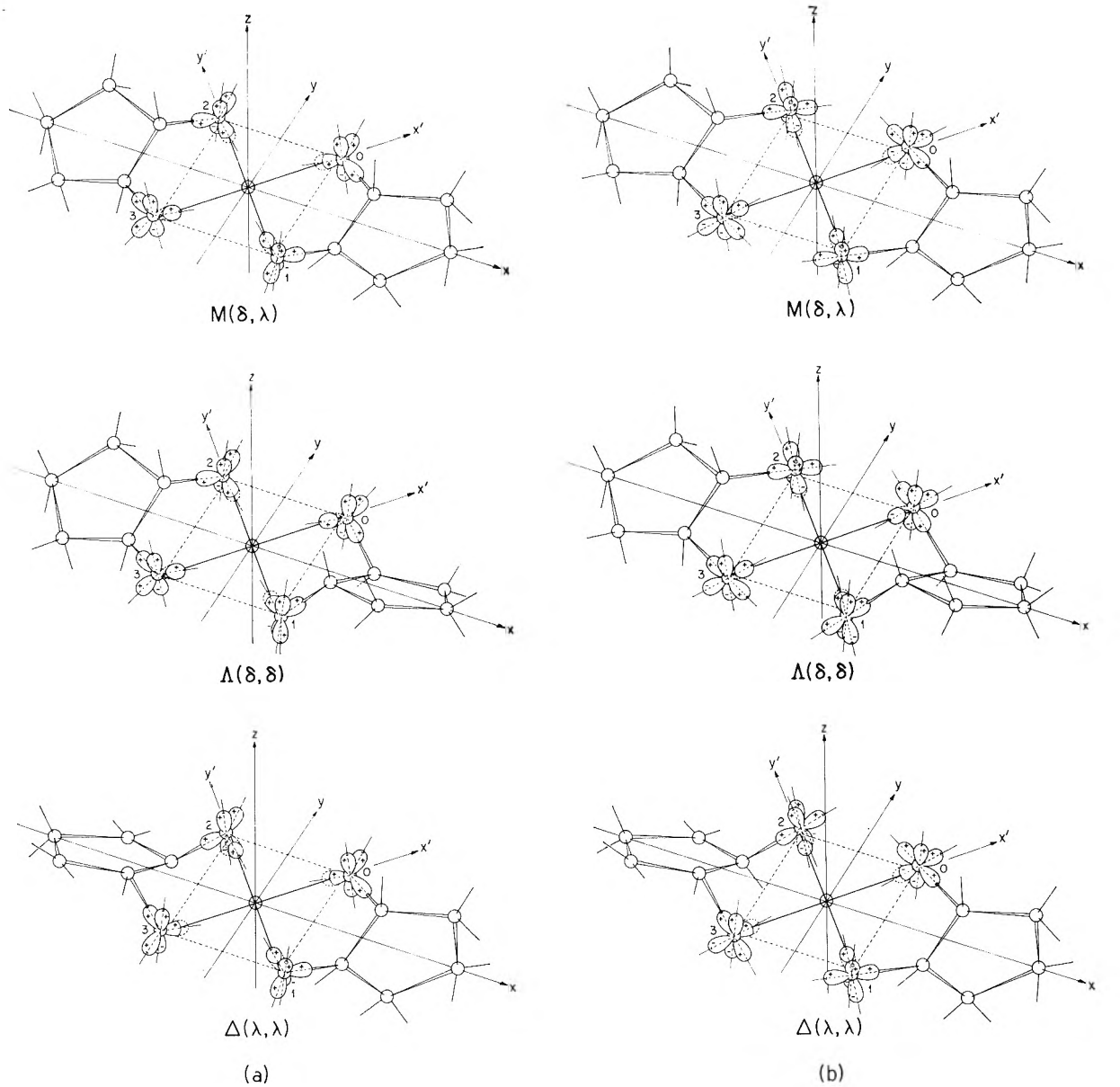

Figures 35a and 35b. The localized ligand orbital spatial disposition for the factualized noncomplanately bonded acute-angled conformations of the bis(cyclopentane glycol or glycolate) platinum(II) cation or anion. Figure 35a manifests the spatial disposition under the premise of isosceles hybridization and Fig. 35b under the premise of digonal hybridization. Figure 31 properly altered exhibits it under tetrahedral hybridization [read Division C, section VIII for the exact meaning of the word hybridization used here]. The actual disposition is presumably intermediate between these extreme types. The adjacent (ligand) carbon aspects are as in Fig. 8.

$$\left\langle {}^2\mathrm{E}_{(\substack{A\\B})}[{}^2\mathrm{E}_g(\mathrm{e}_g)]\left|\frac{\vec{\mathrm{p}}}{\vec{\mathrm{m}}}\right|{}^2\mathrm{E}_{(\substack{A\\B})}[{}^2\mathrm{E}_g(\mathrm{e}_g)]\right\rangle = \left\langle \mathrm{e}_{(\substack{A\\B})}(\mathrm{e}_g)\left|\frac{\vec{\mathrm{p}}}{\vec{\mathrm{m}}}\right|\mathrm{e}_{(\substack{A\\B})}(\mathrm{e}_g)\right\rangle$$

$$\left\langle {}^2\mathrm{E}_{(\substack{A\\B})}[{}^2\mathrm{E}_g(\mathrm{e}_g)]\left|\frac{\vec{\mathrm{p}}}{\vec{\mathrm{m}}}\right|{}^2\mathrm{E}_{(\substack{B\\A})}[{}^2\mathrm{E}_g(\mathrm{e}_g)]\right\rangle = \left\langle \mathrm{e}_{(\substack{A\\B})}(\mathrm{e}_g)\left|\frac{\vec{\mathrm{p}}}{\vec{\mathrm{m}}}\right|\mathrm{e}_{(\substack{B\\A})}(\mathrm{e}_g)\right\rangle \quad (57)$$

(ii) Matrix Elements: Two Electrons

$$\left\langle {}^3\mathrm{B}[{}^3\mathrm{T}_{1g}(\mathrm{t}_{2g}{}^2)]\left|\frac{\vec{\mathrm{p}}}{\vec{\mathrm{m}}}\right|{}^3\mathrm{E}_{(\substack{B\\A})}[{}^3\mathrm{T}_{1g}(\mathrm{t}_{2g}{}^2)]\right\rangle = (\pm)\left\langle \mathrm{e}_{(\substack{A\\B})}(\mathrm{t}_{2g})\left|\frac{\vec{\mathrm{p}}}{\vec{\mathrm{m}}}\right|\mathrm{a}(\mathrm{t}_{2g})\right\rangle$$

$$\left\langle {}^3\mathrm{B}[{}^3\mathrm{T}_{1g}(\mathrm{t}_{2g}{}^2)]\left|\frac{\vec{\mathrm{p}}}{\vec{\mathrm{m}}}\right|{}^3\mathrm{A}[{}^3\mathrm{T}_{2g}(\mathrm{t}_{2g}\mathrm{e}_g)]\right\rangle = \sqrt{2}\left\langle \mathrm{e}_-(\mathrm{t}_{2g})\left|\frac{\vec{\mathrm{p}}}{\vec{\mathrm{m}}}\right|\mathrm{e}_-(\mathrm{e}_g)\right\rangle$$

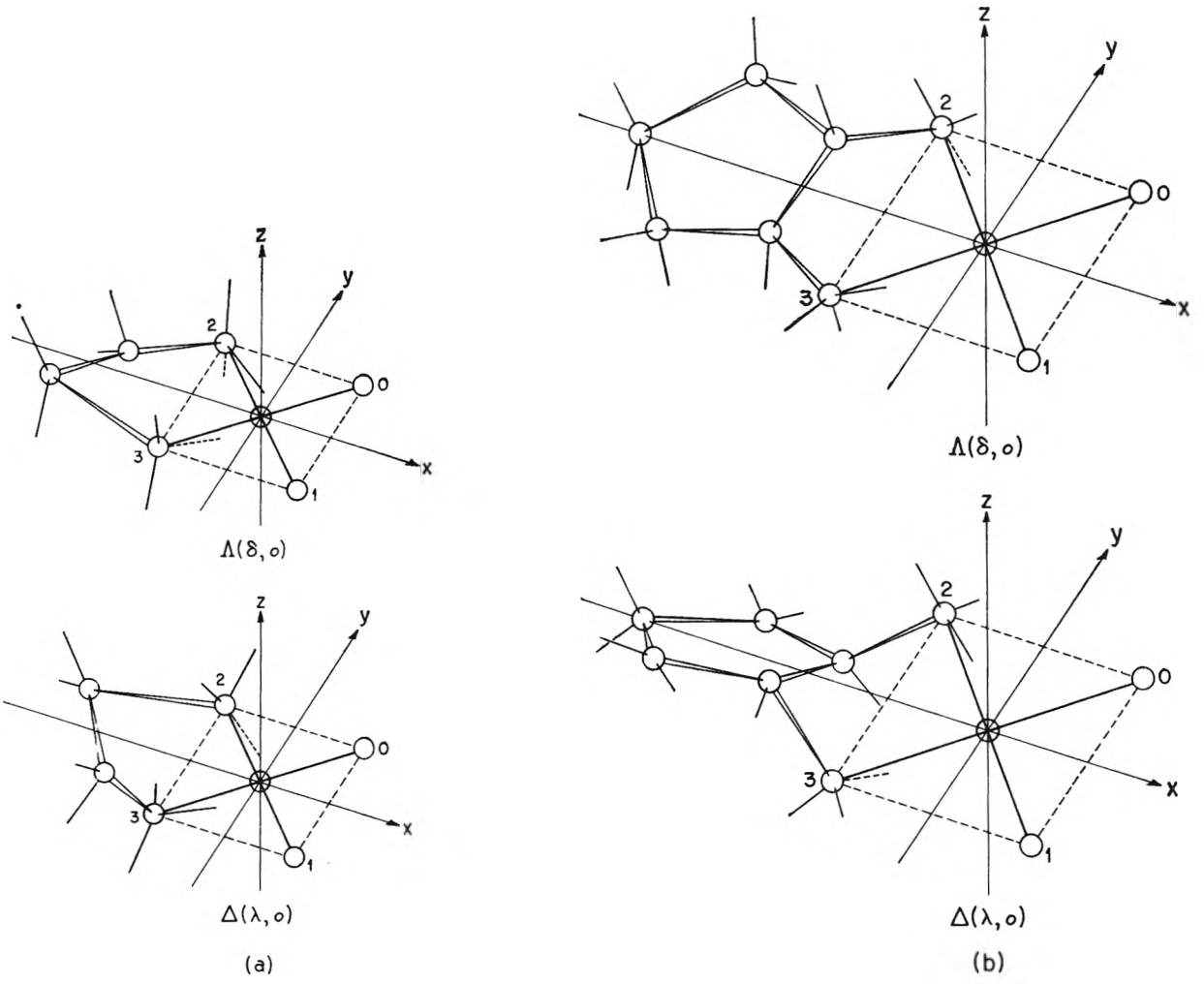

Figures 36a and 36b. The idealized complanately bonded right-angled geometries of the mono(ethylenediamine)platinum(II) [Fig. 36a] and mono(cyclopentanediamine)platinum(II) [Fig. 36b] cations in their $\Lambda(\delta,o)$ and $\Delta(\lambda,o)$ conformations. The associate localized ligand orbital spatial dispositions are indicated by the full (above the x–y plane) and dashed (below the x–y plane) lines. The carbon adjacent to the ligated nitrogen is up (above the x–y plane) when the localized nitrogen orbital is up (full line) and down (below the x–y plane) when the localized nitrogen orbital is down (dashed line) for mono(ethylenediamine)platinum(II) [Fig. 36a] and *vice versa* for mono(cyclopentanediamine)platinum(II) [Fig. 36b]. Hence, as rotatory sign depends primarily upon the localized ligand disposition and not the ligand backbone, identical conformers of mono(ethylenediamine)platinum(II) and mono(cyclopentanediamine) platinum(II) (or any metal), for metallochromphoric bands, rotate oppositely.

$$\left\langle {}^3B[{}^3T_{1g}(t_{2g}^2)] \left|\frac{\vec{p}}{\vec{m}}\right| {}^3E_{(A)}[{}^3T_{2g}(t_{2g}e_g)] \right\rangle = \begin{pmatrix}1\\-i\end{pmatrix}^{1/2} \left\{ \left\langle e_+(t_{2g}) \left|\frac{\vec{p}}{\vec{m}}\right| e_-(e_g) \right\rangle - (\pm) \left\langle e_-(t_{2g}) \left|\frac{\vec{p}}{\vec{m}}\right| e_+(e_g) \right\rangle \right\}$$

$$\left\langle {}^3B[{}^3T_{1g}(t_{2g}^2)] \left|\frac{\vec{p}}{\vec{m}}\right| {}^3B[{}^3T_{1g}(t_{2g}e_g)] \right\rangle = 0$$

$$\left\langle {}^3B[{}^3T_{1g}(t_{2g}^2)] \left|\frac{\vec{p}}{\vec{m}}\right| {}^3E_{(B)}[{}^3T_{1g}(t_{2g}e_g)] \right\rangle = \begin{pmatrix}-1\\i\end{pmatrix}^{1/2} \left\{ \left\langle e_+(t_{2g}) \left|\frac{\vec{p}}{\vec{m}}\right| e_-(e_g) \right\rangle + (\pm) \left\langle e_-(t_{2g}) \left|\frac{\vec{p}}{\vec{m}}\right| e_+(e_g) \right\rangle \right\}$$

$$\left\langle {}^3B[{}^3T_{1g}(t_{2g}^2)] \left|\frac{\vec{p}}{\vec{m}}\right| {}^3B[{}^3A_{2g}(e_g^2)] \right\rangle = 0$$

$$\left\langle {}^3E_{(B)}[{}^3T_{1g}(t_{2g}^2)] \left|\frac{\vec{p}}{\vec{m}}\right| {}^3E_{(A)}[{}^3T_{1g}(t_{2g}^2)] \right\rangle = \left\langle e_{(A)}(t_{2g}) \left|\frac{\vec{p}}{\vec{m}}\right| e_{(B)}(t_{1g}) \right\rangle_{\star}$$

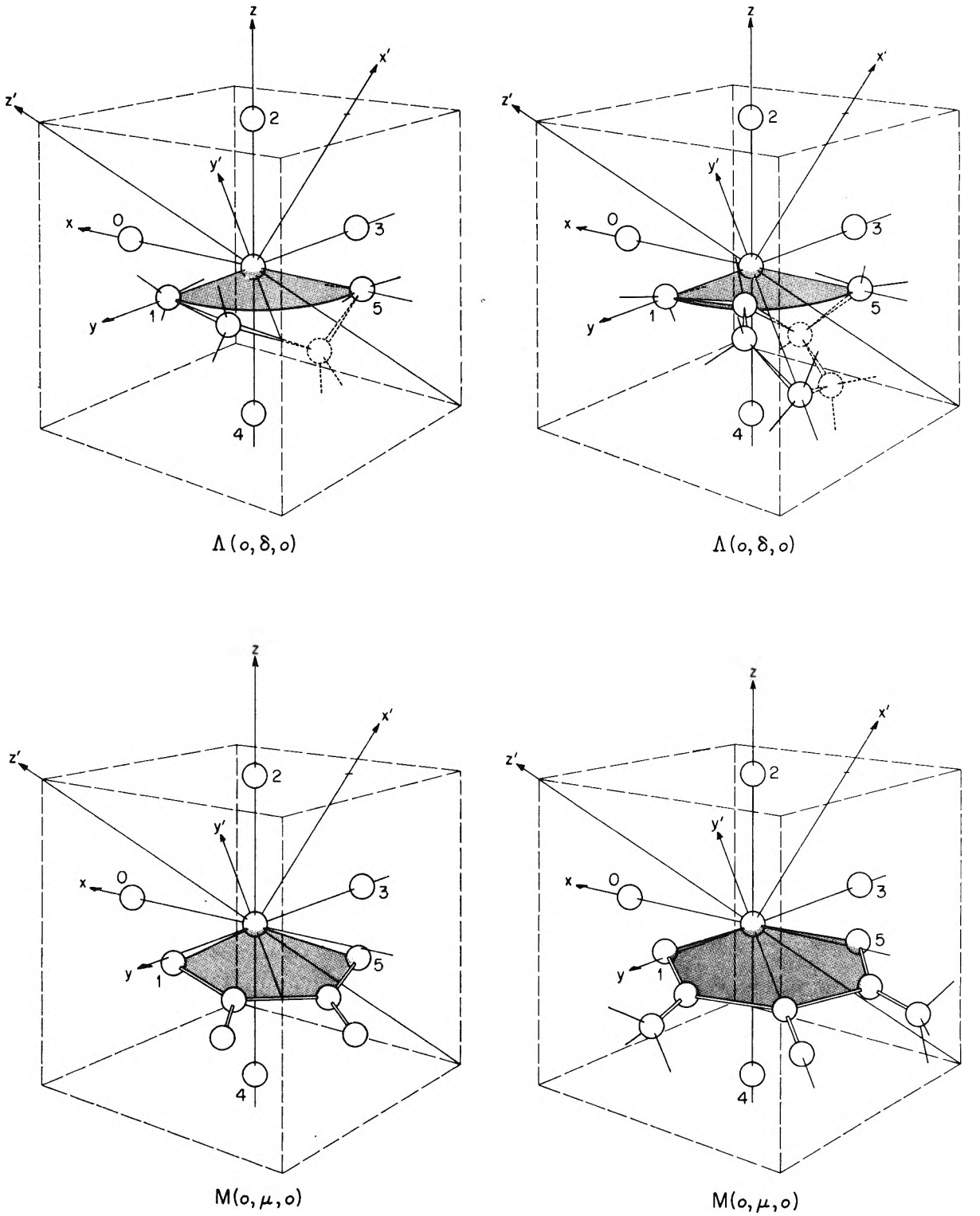

Figure 37. Exemplificative illustrations of the hexacoordinate optically active [Λ(o,δ,o) conformation] monoethylenediamine and monocyclopentanediamine (adjacent carbon locales as in Fig. 36a,b) and the optically inactive [M(o,μ,o) conformation] monooxalato and monoacetylacetonato metallate geometries.

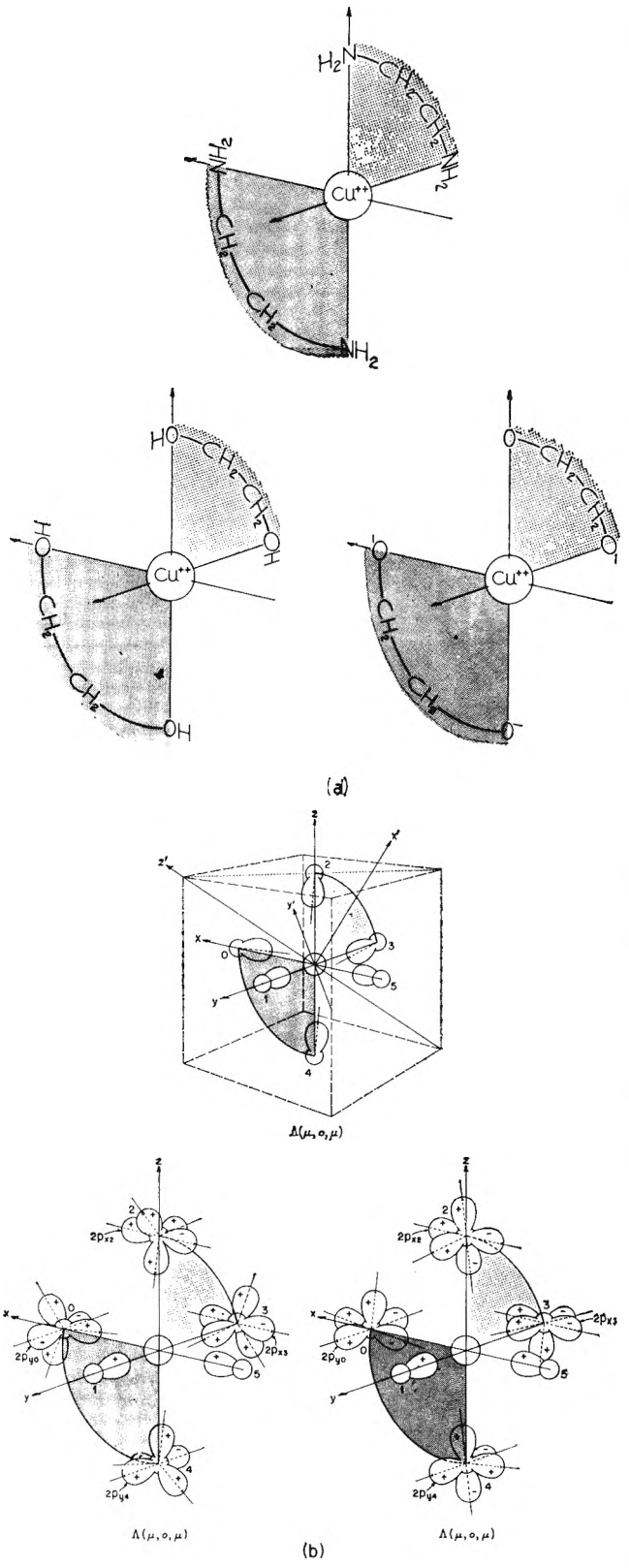

Figures 38a and 38b. Sample picturizations of some dibidentate optically active hexacoordinate metallate complexes in the idealized planar $\Lambda(\mu,o,\mu)$ conformation [regard Fig. 23 for conformational conventions].

$$\left\langle {}^3E_{(A)}^{(B)}[{}^3T_{1g}(t_{2g}^2)]\left|\frac{\vec{p}}{\vec{m}}\right|{}^3A[{}^3T_{2g}(t_{2g}e_g)]\right\rangle =$$
$$(\mp)\frac{i}{\sqrt{2}}\left\langle a(t_{2g})\left|\frac{\vec{p}}{\vec{m}}\right|e_{(A)}^{(B)}(e_g)\right\rangle$$

$$\left\langle {}^3E_{(A)}^{(B)}[{}^3T_{1g}(t_{2g}^2)]\left|\frac{\vec{p}}{\vec{m}}\right|{}^3E_{(B)}^{(A)}[{}^3T_{2g}(t_{2g}e_g)]\right\rangle =$$
$$(\mp)\frac{i}{2}\left\{\sqrt{2}\left\langle e_{(B)}^{(A)}(t_{2g})\left|\frac{\vec{p}}{\vec{m}}\right|e_{(A)}^{(B)}(e_g)\right\rangle_{\star} + \left\langle a(t_{2g})\left|\frac{\vec{p}}{\vec{m}}\right|e_B(e_g)\right\rangle\right\}$$

$$\left\langle {}^3E_{(A)}^{(U)}[{}^3T_{1g}(t_{2g}^2)]\left|\frac{\vec{p}}{\vec{m}}\right|{}^3E_{(A)}^{(B)}[{}^3T_{2g}(t_{2g}e_g)]\right\rangle =$$
$$(\mp)\frac{i}{2}\left\{\sqrt{2}\left\langle e_{(B)}^{(A)}(t_{2g})\left|\frac{\vec{p}}{\vec{m}}\right|e_{(B)}^{(A)}(e_g)\right\rangle + (\pm)\left\langle a(t_{2g})\left|\frac{\vec{p}}{\vec{m}}\right|e_A(e_g)\right\rangle\right\}$$

$$\left\langle {}^3E_{(A)}^{(B)}[{}^3T_{1g}(t_{2g}^2)]\left|\frac{\vec{p}}{\vec{m}}\right|{}^3B[{}^3T_{1g}(t_{2g}e_g)]\right\rangle =$$
$$\frac{1}{\sqrt{2}}\left\langle a(t_{2g})\left|\frac{\vec{p}}{\vec{m}}\right|e_{(B)}^{(A)}(e_g)\right\rangle$$

$$\left\langle {}^3E_{(A)}^{(B)}[{}^3T_{1g}(t_{2g}^2)]\left|\frac{\vec{p}}{\vec{m}}\right|{}^3E_{(A)}^{(B)}[{}^3T_{1g}(t_{2g}e_g)]\right\rangle =$$
$$-{}^1/_2\left\{\sqrt{2}\left\langle e_{(B)}^{(A)}(t_{2g})\left|\frac{\vec{p}}{\vec{m}}\right|e_{(B)}^{(A)}(e_g)\right\rangle + (\mp)\left\langle a(t_{2g})\left|\frac{\vec{p}}{\vec{m}}\right|e_A(e_g)\right\rangle\right\}$$

$$\left\langle {}^3E_{(B)}^{(A)}[{}^3T_{1g}(t_{2g}^2)]\left|\frac{\vec{p}}{\vec{m}}\right|{}^3E_{(B)}^{(A)}[{}^3T_{1g}(t_{2g}e_g)]\right\rangle =$$
$$-{}^1/_2\left\{\sqrt{2}\left\langle e_{(B)}^{(A)}(t_{2g})\left|\frac{\vec{p}}{\vec{m}}\right|e_{(A)}^{(B)}(e_g)\right\rangle + \left\langle a(t_{2g})\left|\frac{\vec{p}}{\vec{m}}\right|e_B(e_g)\right\rangle\right\}$$

$$\left\langle {}^3E_{(A)}^{(B)}[{}^3T_{1g}(t_{2g}^2)]\left|\frac{\vec{p}}{\vec{m}}\right|{}^3B[{}^3A_{2g}(e_g^2)]\right\rangle = 0 \qquad (58)$$

(iii) Matrix Elements: Three Electrons

$$\left\langle {}^4B[{}^4A_{2g}(t_{2g}^3)]\left|\frac{\vec{p}}{\vec{m}}\right|{}^4A[{}^4T_{2g}(t_{2g}^2e_g)]\right\rangle =$$
$$\sqrt{2}\left\langle e_-(t_{2g})\left|\frac{\vec{p}}{\vec{m}}\right|e_-(e_g)\right\rangle$$

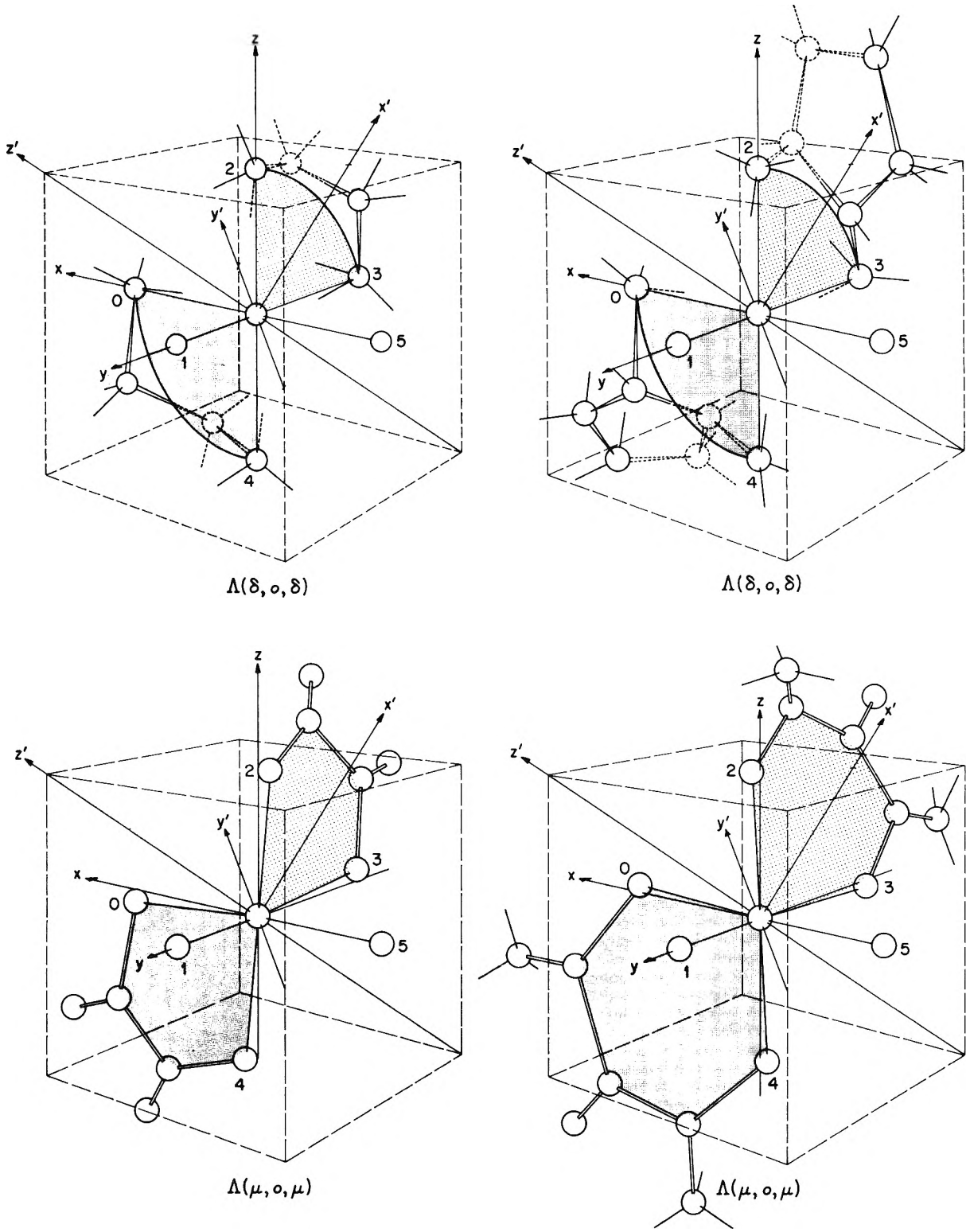

Figure 39. Modelistic portrait of the hexacoordinate optically active bisethylenediamine and biscyclopentanediamine [Λ(δ,o,δ) conformations] and the bisooxalato and bisacetylacetonato [Λ(μ,o,μ) conformations] metallate geometries and localized ligand orbital spatial dispositions [attend Fig. 36a,b for draftsman conventions (note that the planes are now the x–z and y–z planes, separately)].

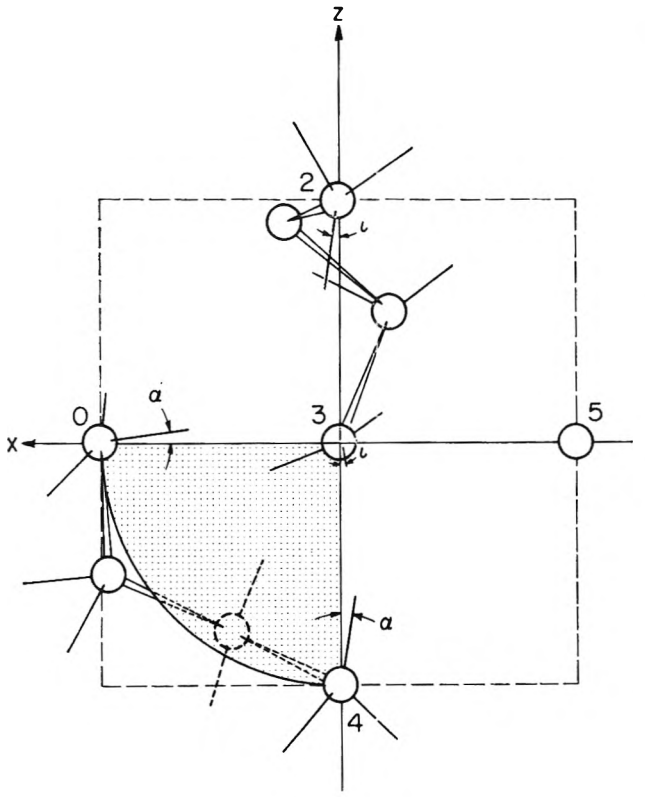

Figure 40. An axial (y-axis) cross-cut of the optically active hexacoordinate bisethylenediamine [$\Lambda(\delta,o,\delta)$ conformation] metallate geometry and localized ligand orbital spatial disposition of Fig. 39. Witness the dual orbital misdirectedness as measured by the two angles of canting α [in-plane (x–z or y–z as the case may be) misdirectedness] and ι [out-of-plane (x–z or y–z as the case may be) misdirectedness].

$$\left\langle {}^4B[{}^4A_{2g}(t_{2g}{}^3)] \left|\frac{\vec{p}}{m}\right| {}^4E_{(A)}[{}^4T_{2g}(t_{2g}{}^2e_g)] \right\rangle =$$
$$(\mp)\frac{i}{\sqrt{2}}\left\langle a(t_{2g}) \left|\frac{\vec{p}}{m}\right| e_{(A)}(e_g)\right\rangle -$$
$$\begin{pmatrix}1\\-i\end{pmatrix}^{1/2}\left\{\left\langle e_+(t_{2g}) \left|\frac{\vec{p}}{m}\right| e_-(e_g)\right\rangle -\right.$$
$$\left.(\pm)\left\langle e_-(t_{2g}) \left|\frac{\vec{p}}{m}\right| e_+(e_g)\right\rangle\right\}$$

$$\left\langle {}^4B[{}^4A_{2g}(t_{2g}{}^3)] \left|\frac{\vec{p}}{m}\right| {}^4B[{}^4T_{1g}(t_{2g}{}^2e_g)] \right\rangle = 0$$

$$\left\langle {}^4B[{}^4A_{2g}(t_{2g}{}^3)] \left|\frac{\vec{p}}{m}\right| {}^4E_{(A)}[{}^4T_{1g}(t_{2g}{}^2e_g)] \right\rangle =$$
$$-\frac{1}{\sqrt{2}}\left\langle a(t_{2g}) \left|\frac{\vec{p}}{m}\right| e_{(A)}(e_g)\right\rangle +$$
$$\begin{pmatrix}1\\-i\end{pmatrix}^{1/2}\left\{\left\langle e_+(t_{2g}) \left|\frac{\vec{p}}{m}\right| e_-(e_g)\right\rangle +\right.$$
$$\left.(\pm)\left\langle e_-(t_{2g}) \left|\frac{\vec{p}}{m}\right| e_+(e_g)\right\rangle\right\}$$

$$\left\langle {}^4B[{}^4A_{2g}(t_{2g}{}^3)] \left|\frac{\vec{p}}{m}\right| {}^4B[{}^4T_{1g}(t_{2g}e_g{}^2)] \right\rangle = 0$$

$$\left\langle {}^4B[{}^4A_{2g}(t_{2g}{}^3)] \left|\frac{\vec{p}}{m}\right| {}^4E_{(B)}[{}^4T_{1g}(t_{2g}e_g{}^2)] \right\rangle = 0 \qquad (59)$$

(iv) Matrix Elements: Four Electrons

$$\left\langle {}^5E_{(A)}[{}^5E_g(t_{2g}{}^3e_g)] \left|\frac{\vec{p}}{m}\right| {}^5E_{(B)}[{}^5E_g(t_{2g}{}^3e_g)] \right\rangle =$$
$$\left\langle e_{(A)}(e_g) \left|\frac{\vec{p}}{m}\right| e_{(B)}(e_g)\right\rangle$$

$$\left\langle {}^5E_{(A)}[{}^5E_g(t_{2g}{}^3e_g)] \left|\frac{\vec{p}}{m}\right| {}^5E_{(B)}[{}^5E_g(t_{2g}{}^3e_g)] \right\rangle =$$
$$\left\langle e_{(A)}(e_g) \left|\frac{\vec{p}}{m}\right| e_{(B)}(e_g)\right\rangle$$

$$\left\langle {}^5E_{(A)}[{}^5E_g(t_{2g}{}^3e_g)] \left|\frac{\vec{p}}{m}\right| {}^5A[{}^5T_{2g}(t_{2g}{}^2e_g{}^2)] \right\rangle =$$
$$-\left\langle a(t_{2g}) \left|\frac{\vec{p}}{m}\right| e_{(B)}(e_g)\right\rangle$$

$$\left\langle {}^5E_{(A)}[{}^5E_g(t_{2g}{}^3e_g)] \left|\frac{\vec{p}}{m}\right| {}^5E_{(B)}[{}^5T_{2g}(t_{2g}{}^2e_g{}^2)] \right\rangle =$$
$$\left\langle e_{(B)}(t_{2g}) \left|\frac{\vec{p}}{m}\right| e_{(B)}(e_g)\right\rangle$$

$$\left\langle {}^5E_{(A)}[{}^5E_g(t_{2g}{}^3e_g)] \left|\frac{\vec{p}}{m}\right| {}^5E_{(A)}[{}^5T_{2g}(t_{2g}{}^2e_g{}^2)] \right\rangle =$$
$$-\left\langle e_{(B)}(t_{2g}) \left|\frac{\vec{p}}{m}\right| e_{(A)}(e_g)\right\rangle_{\star}$$

$$\left\langle {}^5A[{}^5T_{2g}(t_{2g}{}^2e_g{}^2)] \left|\frac{\vec{p}}{m}\right| {}^5E_{(B)}[{}^5T_{2g}(t_{2g}{}^2e_g{}^2)] \right\rangle =$$
$$\left\langle e_{(B)}(t_{2g}) \left|\frac{\vec{p}}{m}\right| a(t_{2g})\right\rangle$$

$$\left\langle {}^5E_{(B)}[{}^5T_{2g}(t_{2g}{}^2e_g{}^2)] \left|\frac{\vec{p}}{m}\right| {}^5E_{(B)}[{}^5T_{2g}(t_{2g}{}^2e_g{}^2)] \right\rangle =$$
$$-\left\langle e_{(A)}(t_{2g}) \left|\frac{\vec{p}}{m}\right| e_{(B)}(t_{2g})\right\rangle$$

$$\left\langle {}^5E_{(B)}[{}^5T_{2g}(t_{2g}{}^2e_g{}^2)] \left|\frac{\vec{p}}{m}\right| {}^5E_{(A)}[{}^5T_{2g}(t_{2g}{}^2c_g{}^2)] \right\rangle =$$
$$\left\langle e_{(B)}(t_{2g}) \left|\frac{\vec{p}}{m}\right| e_{(A)}(t_{2g})\right\rangle_{\star}$$

$$\left\langle {}^3B[{}^3T_{1g}(t_{2g}{}^4)] \left|\frac{\vec{p}}{m}\right| {}^3E_{(A)}[{}^3T_{1g}(t_{2g}{}^4)] \right\rangle =$$
$$\left\langle a(t_{2g}) \left|\frac{\vec{p}}{m}\right| e_{(B)}(t_{2g})\right\rangle$$

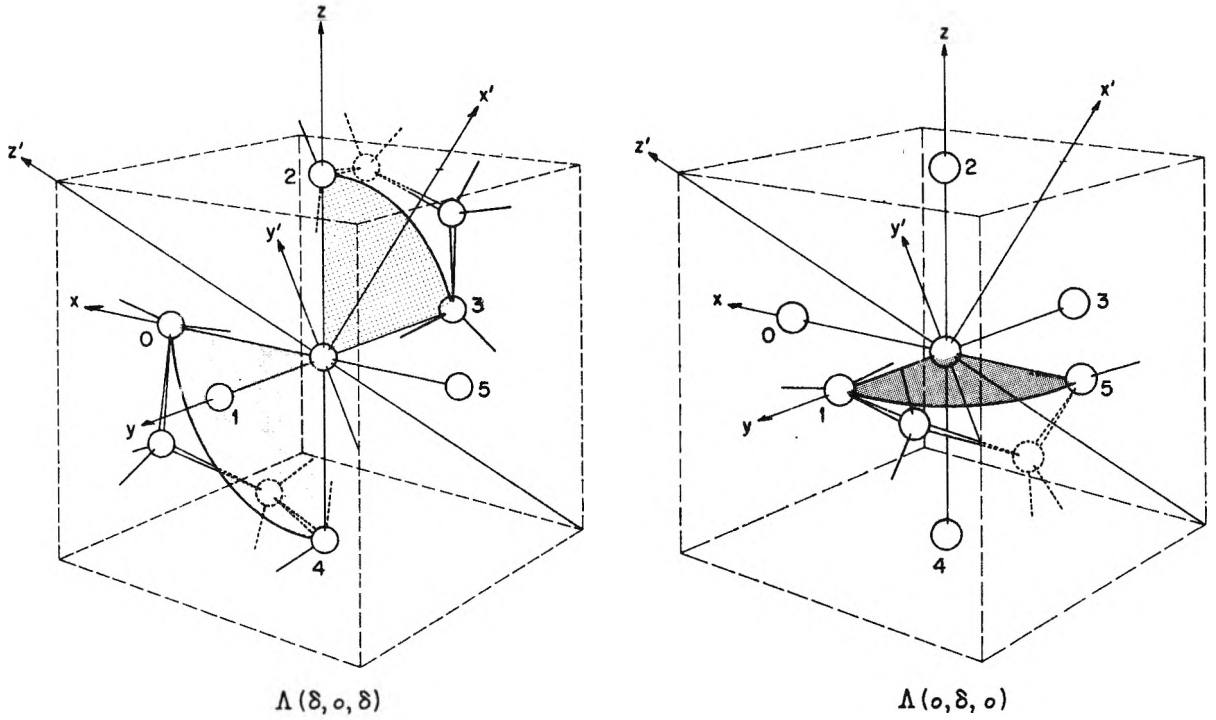

Figure 41. Schematic outline of the hexacoordinate optically active bis(ethylene glycol) [Λ(δ,o,δ) conformation] and mono(ethylene glycol) [Λ(o,δ,o) conformation] metallate geometries and localized ligand orbital spatial dispositions [attend Fig. 36a,b for draftsman conventions (mark that the planes are now the x–y, x–z, and y–z planes, singly)].

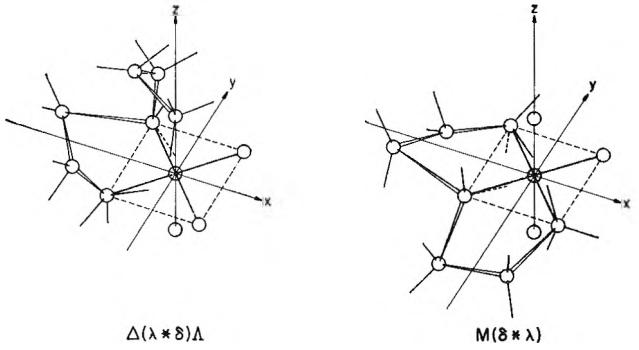

Figure 42. Artistic sketch of the optically distinct monodiethylenediamine metallate stereoisomers in their Δ(λ*δ)Λ and M(δ*λ) conformations [we make the convention that the over-all conformation of a fused ligand be indexed as a composite of its fragmented parts, with the act of composition indicated by an interspersed asterisk *. The over-all complexed conformation is signified, as in Fig. 7, 8, and 23, in terms of its screw propeller properties about its principal (partial in the present case) twofold, threefold, fourfold, etc., axis (here it is a partial threefold axis, $\mathcal{C}_3(x = \sqrt{2}z)$, for the Δ(λ*δ)Λ structure and a partial fourfold axis, $\mathcal{C}_4(z)$, and its contained mirror plane, $\sigma_v[x = y]$, for the M(δ*λ) structure)]. The draftsman conventions are as given in Fig. 36a,b. The capital delta (Δ) and lambda (Λ) indicate that the over-all molecular conformation of the two tridentate halves with respect to the partial threefold axis, $\mathcal{C}_3(x = \sqrt{2}z)$ [or the two partial twofold axis, $\mathcal{C}_2(x)$ and $\mathcal{C}_2(-x = y = z)$], are opposed.

$$\left\langle {}^3B[{}^3T_{1g}(t_{2g}^4)] \left|\frac{\vec{p}}{\vec{m}}\right| {}^3E_{(A)}[{}^3E_g(t_{2g}{}^3e_g)] \right\rangle =$$

$$(\pm)i\,\frac{2}{\sqrt{3}} \left\langle a(t_{2g}) \left|\frac{\vec{p}}{\vec{m}}\right| e_{(A)}(e_g) \right\rangle$$

$$\left\langle {}^3B[{}^3T_{1g}(t_{2g}^4)] \left|\frac{\vec{p}}{\vec{m}}\right| {}^3B[{}^3T_{1g}(t_{2g}{}^3e_g)] \right\rangle = 0$$

$$\left\langle {}^3B[{}^3T_{1g}(t_{2g}^4)] \left|\frac{\vec{p}}{\vec{m}}\right| {}^3E_{(B)}[{}^3T_{1g}(t_{2g}{}^3e_g)] \right\rangle =$$

$$-\frac{1}{\sqrt{3}} \left\langle a(t_{2g}) \left|\frac{\vec{p}}{\vec{m}}\right| e_{(B)}(e_g) \right\rangle -$$

$$\begin{pmatrix} 1 \\ -i \end{pmatrix} \frac{1}{2\sqrt{6}} \left\{ \left\langle e_+(t_{2g}) \left|\frac{\vec{p}}{\vec{m}}\right| e_-(e_g) \right\rangle + \right.$$

$$\left. (\pm) \left\langle e_-(t_{2g}) \left|\frac{\vec{p}}{\vec{m}}\right| e_+(e_g) \right\rangle \right\}$$

$$\left\langle {}^3B[{}^3T_{1g}(t_{2g}^4)] \left|\frac{\vec{p}}{\vec{m}}\right| {}^3A[{}^3T_{2g}(t_{2g}{}^3e_g)] \right\rangle =$$

$$-\frac{1}{\sqrt{3}} \left\langle e_-(t_{2g}) \left|\frac{\vec{p}}{\vec{m}}\right| e_-(e_g) \right\rangle$$

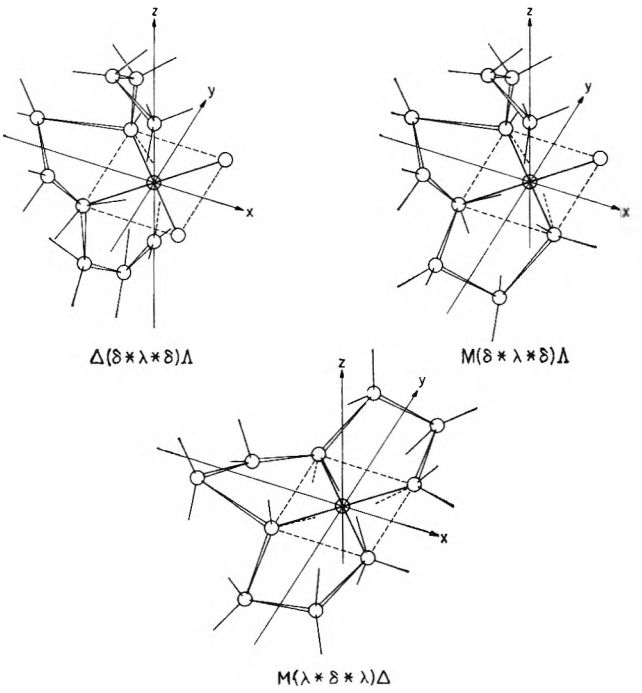

Figure 43. An idealized skeletal framework for the optically distinct monotriethylenediamine metallate stereoisomers in their Δ(δ*λ*δ)Λ, M(δ*λ*δ)Λ, and M(λ*δ*λ)Δ conformations. The stereochemical conventions are as in Fig. 42. [Witness the twofold symmetry of the Δ(δ*λ*δ)Λ and M(λ*δ*λ)Δ isomers. Over-all classification with respect to this axis or the partial threefold of pseudo-fourfold axis yields identical results, as must be if no further detailed specification is offered by means of subscripts. Perhaps for tangled structures of this sort a system of superscripts for chelate position coordination and subscripts for over-all axis classification should be used for ligand fragment and over-all designations, respectively. In this event a standard denumerative procedure must be kept.]

$$\left\langle {}^3B[{}^3T_{1g}(t_{2g}{}^4)] \left| \frac{\vec{p}}{\vec{m}} \right| {}^3E_{(A/B)}[{}^3T_{2g}(t_{2g}{}^3e_g)] \right\rangle =$$
$$(\mp)\frac{i}{\sqrt{3}} \left\langle a(t_{2g}) \left| \frac{\vec{p}}{\vec{m}} \right| e_{(B/A)}(e_g) \right\rangle +$$
$$\begin{pmatrix} 1 \\ -i \end{pmatrix} \frac{1}{2\sqrt{6}} \left\{ \left\langle e_+(t_{2g}) \left| \frac{\vec{p}}{\vec{m}} \right| e_-(e_g) \right\rangle - \right.$$
$$\left. (\pm) \left\langle e_-(t_{2g}) \left| \frac{\vec{p}}{\vec{m}} \right| e_+(e_g) \right\rangle \right\}$$

$$\left\langle {}^3B[{}^3T_{1g}(t_{2g}{}^4)] \left| \frac{\vec{p}}{\vec{m}} \right| {}^3A[{}^3A_{1g}(t_{2g}{}^3e_g)] \right\rangle =$$
$$\sqrt{2/3} \left\langle e_-(t_{2g}) \left| \frac{\vec{p}}{\vec{m}} \right| e_-(e_g) \right\rangle$$

$$\left\langle {}^3B[{}^3T_{1g}(t_{2g}{}^4)] \left| \frac{\vec{p}}{\vec{m}} \right| {}^3E_{(A/B)}[{}^3E_g(t_{2g}{}^3e_g)] \right\rangle =$$
$$\begin{pmatrix} -1 \\ i \end{pmatrix} \frac{1}{\sqrt{6}} \left\{ \left\langle e_+(t_{2g}) \left| \frac{\vec{p}}{\vec{m}} \right| e_-(e_g) \right\rangle + \right.$$
$$\left. (\mp) \left\langle e_-(t_{2g}) \left| \frac{\vec{p}}{\vec{m}} \right| e_+(e_g) \right\rangle \right\}$$

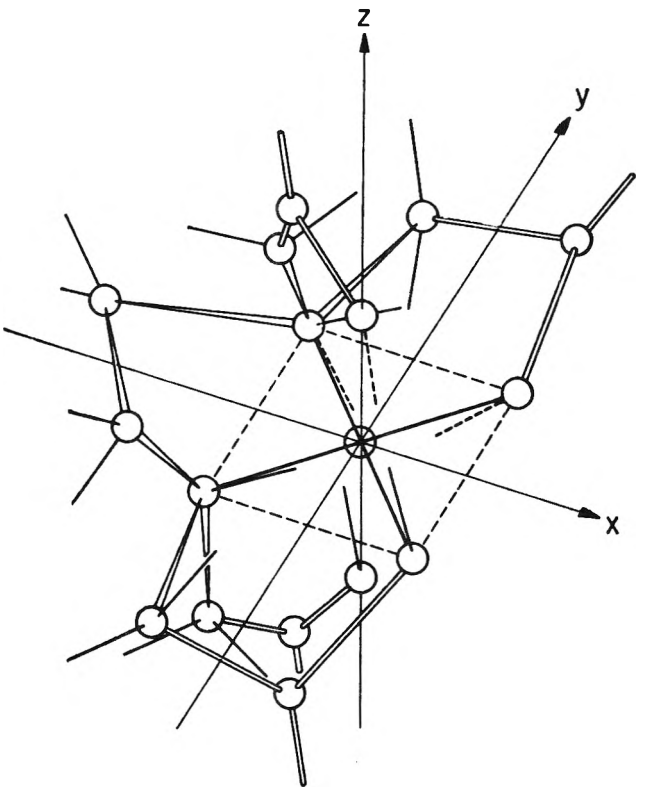

$$\Delta(\tilde{\delta} * \tilde{\delta} * \lambda * \tilde{\delta} * \tilde{\delta})$$

Figure 44. A fanciful network for the undigonal dihedral monoethylenediaminetetraacetate metallate structure in the $\Delta(\tilde{\delta}*\tilde{\delta}*\lambda*\tilde{\delta}*\tilde{\delta})$ conformation, where the δ (or λ) tilde betokens an acetate fragmental absolute conformation [if the nitrogen–acetate fragment be planar the conformation be $\Delta(\tilde{\mu}*\tilde{\mu}*\lambda*\tilde{\mu}*\tilde{\mu})$]. Over-all classification is made with respect to the twofold axis.

$$\left\langle {}^3B[{}^3T_{1g}(t_{2g}{}^4)] \left| \frac{\vec{p}}{\vec{m}} \right| {}^3B[{}^3A_{2g}(t_{2g}{}^3e_g)] \right\rangle = 0$$

$$\left\langle {}^3B[{}^3T_{1g}(t_{2g}{}^4)] \left| \frac{\vec{p}}{\vec{m}} \right| {}^3A[{}^3T_{2g}(t_{2g}{}^3e_g)] \right\rangle =$$
$$\left\langle e_-(t_{2g}) \left| \frac{\vec{p}}{\vec{m}} \right| e_-(e_g) \right\rangle$$

$$\left\langle {}^3B[{}^3T_{1g}(t_{2g}{}^4)] \left| \frac{\vec{p}}{\vec{m}} \right| {}^3E_{(A/B)}[{}^3T_{2g}(t_{2g}{}^3e_g)] \right\rangle =$$
$$\begin{pmatrix} 1 \\ -i \end{pmatrix} \frac{1}{2\sqrt{2}} \left\{ \left\langle e_+(t_{2g}) \left| \frac{\vec{p}}{\vec{m}} \right| e_-(e_g) \right\rangle + \right.$$
$$\left. (\mp) \left\langle e_-(t_{2g}) \left| \frac{\vec{p}}{\vec{m}} \right| e_+(e_g) \right\rangle \right\}$$

$$\left\langle {}^3B[{}^3T_{1g}(t_{2g}{}^4)] \left| \frac{\vec{p}}{\vec{m}} \right| {}^3B[{}^3T_{1g}(t_{2g}{}^3e_g)] \right\rangle = 0$$

$$\left\langle {}^3B[{}^3T_{1g}(t_{2g}{}^4)] \left|\frac{\vec{p}}{\vec{m}}\right| {}^3E_{(A)}^{(B)}[{}^3T_{1g}(t_{2g}{}^3e_g)] \right\rangle =$$
$$\binom{-1}{i} \frac{1}{2\sqrt{2}} \left\{ \left\langle e_+(t_{2g}) \left|\frac{\vec{p}}{\vec{m}}\right| e_-(e_g) \right\rangle + (\pm) \left\langle e_-(t_{2g}) \left|\frac{\vec{p}}{\vec{m}}\right| e_+(e_g) \right\rangle \right\}$$

$$\left\langle {}^3E_{(A)}^{(B)}[{}^3T_{1g}(t_{2g}{}^4)] \left|\frac{\vec{p}}{\vec{m}}\right| {}^3E_{(B)}^{(A)}[{}^3T_{1g}(t_{2g}{}^4)] \right\rangle =$$
$$-\left\langle e_{(B)}^{(A)}(t_{2g}) \left|\frac{\vec{p}}{\vec{m}}\right| e_{(A)}^{(B)}(t_{2g}) \right\rangle_{\star}$$

$$\left\langle {}^3E_{(A)}^{(B)}[{}^3T_{1g}(t_{2g}{}^4)] \left|\frac{\vec{p}}{\vec{m}}\right| {}^3E_{(B)}^{(A)}[{}^3E_g(t_{2g}{}^3e_g)] \right\rangle =$$
$$(\pm)\, i \frac{2}{\sqrt{3}} \left\langle e_{(B)}^{(A)}(t_{2g}) \left|\frac{\vec{p}}{\vec{m}}\right| e_{(A)}^{(B)}(e_g) \right\rangle$$

$$\left\langle {}^3E_{(A)}^{(B)}[{}^3T_{1g}(t_{2g}{}^4)] \left|\frac{\vec{p}}{\vec{m}}\right| {}^3E_{(A)}^{(B)}[{}^3E_g(t_{2g}{}^3e_g)] \right\rangle =$$
$$(\mp)\, i \frac{2}{\sqrt{3}} \left\langle e_{(B)}^{(A)}(t_{2g}) \left|\frac{\vec{p}}{\vec{m}}\right| e_{(B)}^{(A)}(e_g) \right\rangle$$

$$\left\langle {}^3E_{(A)}^{(B)}[{}^3T_{1g}(t_{2g}{}^4)] \left|\frac{\vec{p}}{\vec{m}}\right| {}^3B[{}^3T_{1g}(t_{2g}{}^3e_g)] \right\rangle =$$
$$-\frac{1}{2\sqrt{3}} \left\langle a(t_{2g}) \left|\frac{\vec{p}}{\vec{m}}\right| e_{(B)}^{(A)}(e_g) \right\rangle + \binom{-1}{i} \frac{1}{\sqrt{6}} \left\{ \left\langle e_+(t_{2g}) \left|\frac{\vec{p}}{\vec{m}}\right| e_-(e_g) \right\rangle + (\pm) \left\langle e_-(t_{2g}) \left|\frac{\vec{p}}{\vec{m}}\right| e_+(e_g) \right\rangle \right\}$$

$$\left\langle {}^3E_{(A)}^{(B)}[{}^3T_{1g}(t_{2g}{}^4)] \left|\frac{\vec{p}}{\vec{m}}\right| {}^3E_{(A)}^{(B)}[{}^3T_{1g}(t_{2g}{}^3e_g)] \right\rangle =$$
$$(\mp) \frac{1}{2\sqrt{6}} \left\{ \left\langle a(t_{2g}) \left|\frac{\vec{p}}{\vec{m}}\right| e_A(e_g) \right\rangle + (\mp)\sqrt{2} \left\langle e_{(B)}^{(A)}(t_{2g}) \left|\frac{\vec{p}}{\vec{m}}\right| e_{(B)}^{(A)}(e_g) \right\rangle \right\}$$

$$\left\langle {}^3E_{(A)}^{(B)}[{}^3T_{1g}(t_{2g}{}^4)] \left|\frac{\vec{p}}{\vec{m}}\right| {}^3E_{(B)}^{(A)}[{}^3T_{1g}(t_{2g}{}^3e_g)] \right\rangle =$$
$$\frac{1}{2\sqrt{6}} \left\{ \sqrt{2} \left\langle e_{(B)}^{(A)}(t_{2g}) \left|\frac{\vec{p}}{\vec{m}}\right| e_{(A)}^{(B)}(e_g) \right\rangle + \left\langle a(t_{2g}) \left|\frac{\vec{p}}{\vec{m}}\right| e_B(e_g) \right\rangle \right\} + (\mp) \frac{i}{2\sqrt{3}} \left\{ \left\langle e_+(t_{2g}) \left|\frac{\vec{p}}{\vec{m}}\right| e_+(e_g) \right\rangle - \left\langle e_-(t_{2g}) \left|\frac{\vec{p}}{\vec{m}}\right| e_-(e_g) \right\rangle \right\}$$

$$\left\langle {}^3E_{(A)}^{(B)}[{}^3T_{1g}(t_{2g}{}^4)] \left|\frac{\vec{p}}{\vec{m}}\right| {}^3A[{}^3T_{2g}(t_{2g}{}^3e_g)] \right\rangle =$$
$$(\pm) \frac{i}{2\sqrt{3}} \left\langle a(t_{2g}) \left|\frac{\vec{p}}{\vec{m}}\right| e_{(A)}^{(B)}(e_g) \right\rangle + \binom{-1}{i} \frac{1}{\sqrt{6}} \left\{ \left\langle e_+(t_{2g}) \left|\frac{\vec{p}}{\vec{m}}\right| e_-(e_g) \right\rangle + (\mp) \left\langle e_-(t_{2g}) \left|\frac{\vec{p}}{\vec{m}}\right| e_+(e_g) \right\rangle \right\}$$

$$\left\langle {}^3E_{(A)}^{(B)}[{}^3T_{1g}(t_{2g}{}^4)] \left|\frac{\vec{p}}{\vec{m}}\right| {}^3E_{(B)}^{(A)}[{}^3T_{2g}(t_{2g}{}^3e_g)] \right\rangle =$$
$$(\mp) \frac{i}{2\sqrt{6}} \left\{ \sqrt{2} \left\langle e_{(B)}^{(A)}(t_{2g}) \left|\frac{\vec{p}}{\vec{m}}\right| e_{(A)}^{(B)}(e_g) \right\rangle_{\star} + \left\langle a(t_{2g}) \left|\frac{\vec{p}}{\vec{m}}\right| e_B(e_g) \right\rangle \right\}$$

$$\left\langle {}^3E_{(A)}^{(B)}[{}^3T_{1g}(t_{2g}{}^4)] \left|\frac{\vec{p}}{\vec{m}}\right| {}^3E_{(A)}^{(B)}[{}^3T_{2g}(t_{2g}{}^3e_g)] \right\rangle =$$
$$(\mp) \frac{i}{2\sqrt{6}} \left\{ \sqrt{2} \left\langle e_{(B)}^{(A)}(t_{2g}) \left|\frac{\vec{p}}{\vec{m}}\right| e_{(B)}^{(A)}(e_g) \right\rangle + (\pm) \left\langle a(t_{2g}) \left|\frac{\vec{p}}{\vec{m}}\right| e_A(e_g) \right\rangle \right\}$$

$$\left\langle {}^3E_{(A)}^{(B)}[{}^3T_{1g}(t_{2g}{}^4)] \left|\frac{\vec{p}}{\vec{m}}\right| {}^3E_{(B)}^{(A)}[{}^3E_g(t_{2g}{}^3e_g)] \right\rangle =$$
$$(\pm) \frac{i}{\sqrt{6}} \left\langle a(t_{2g}) \left|\frac{\vec{p}}{\vec{m}}\right| e_B(e_g) \right\rangle - \frac{1}{2\sqrt{3}} \left\{ \left\langle e_+(t_{2g}) \left|\frac{\vec{p}}{\vec{m}}\right| e_+(e_g) \right\rangle - \left\langle e_-(t_{2g}) \left|\frac{\vec{p}}{\vec{m}}\right| e_-(e_g) \right\rangle \right\}$$

$$\left\langle {}^3E_{(A)}^{(B)}[{}^3T_{1g}(t_{2g}{}^4)] \left|\frac{\vec{p}}{\vec{m}}\right| {}^3E_{(A)}^{(B)}[{}^3E_g(t_{2g}{}^3e_g)] \right\rangle =$$
$$\frac{i}{\sqrt{6}} \left\langle a(t_{2g}) \left|\frac{\vec{p}}{\vec{m}}\right| e_A(e_g) \right\rangle$$

$$\left\langle {}^3E_{(A)}^{(B)}[{}^3T_{1g}(t_{2g}{}^4)] \left|\frac{\vec{p}}{\vec{m}}\right| {}^3A[{}^3A_{1g}(t_{2g}{}^3e_g)] \right\rangle =$$
$$(\mp) \frac{i}{\sqrt{6}} \left\langle a(t_{2g}) \left|\frac{\vec{p}}{\vec{m}}\right| e_{(A)}^{(B)}(e_g) \right\rangle + \binom{-1}{i} \frac{1}{2\sqrt{3}} \left\{ \left\langle e_+(t_{2g}) \left|\frac{\vec{p}}{\vec{m}}\right| e_-(e_g) \right\rangle + (\mp) \left\langle e_-(t_{2g}) \left|\frac{\vec{p}}{\vec{m}}\right| e_+(e_g) \right\rangle \right\}$$

$$\left\langle {}^3E_{(A)}^{(B)}[{}^3T_{1g}(t_{2g}{}^4)] \left|\frac{\vec{p}}{\vec{m}}\right| {}^3B[{}^3A_{2g}(t_{2g}{}^3e_g)] \right\rangle =$$
$$\frac{1}{\sqrt{6}} \left\langle a(t_{2g}) \left|\frac{\vec{p}}{\vec{m}}\right| e_{(B)}^{(A)}(e_g) \right\rangle + \binom{-1}{i} \frac{1}{2\sqrt{3}} \left\{ \left\langle e_+(t_{2g}) \left|\frac{\vec{p}}{\vec{m}}\right| e_-(e_g) \right\rangle + (\pm) \left\langle e_-(t_{2g}) \left|\frac{\vec{p}}{\vec{m}}\right| e_+(e_g) \right\rangle \right\}$$

$$\left\langle {}^3E_{(A)}^{(B)}[{}^3T_{1g}(t_{2g}^4)]\left|\frac{\vec{p}}{m}\right|{}^3A[{}^3T_{2g}(t_{2g}^3e_g)]\right\rangle =$$
$$(\pm)\frac{i}{2}\left\langle a(t_{2g})\left|\frac{\vec{p}}{m}\right|e_{(A)}^{(B)}(e_g)\right\rangle$$

$$\left\langle {}^3E_{(A)}^{(B)}[{}^3T_{1g}(t_{2g}^4)]\left|\frac{\vec{p}}{m}\right|{}^3E_{(B)}^{(A)}[{}^3T_{2g}(t_{2g}^3e_g)]\right\rangle =$$
$$(\pm)\frac{i}{2\sqrt{2}}\left\{\sqrt{2}\left\langle e_{(B)}^{(A)}(t_{2g})\left|\frac{\vec{p}}{m}\right|e_{(A)}^{(B)}(e_g)\right\rangle_{\star}+\left\langle a(t_{2g})\left|\frac{\vec{p}}{m}\right|e_B(e_g)\right\rangle\right\}$$

$$\left\langle {}^3E_{(A)}^{(B)}[{}^3T_{1g}(t_{2g}^4)]\left|\frac{\vec{p}}{m}\right|{}^3E_{(B)}^{(A)}[{}^3T_{2g}(t_{2g}^3e_g)]\right\rangle =$$
$$(\pm)\frac{i}{2\sqrt{2}}\left\{\sqrt{2}\left\langle e_{(B)}^{(A)}(t_{2g})\left|\frac{\vec{p}}{m}\right|e_{(A)}^{(B)}(e_g)\right\rangle+(\pm)\left\langle a(t_{2g})\left|\frac{\vec{p}}{m}\right|e_A(e_g)\right\rangle\right\}$$

$$\left\langle {}^3E_{(A)}^{(B)}[{}^3T_{1g}(t_{2g}^4)]\left|\frac{\vec{p}}{m}\right|{}^3B[{}^3T_{1g}(t_{2g}^3e_g)]\right\rangle =$$
$$-{}^1/_2\left\langle a(t_{2g})\left|\frac{\vec{p}}{m}\right|e_{(A)}^{(B)}(e_g)\right\rangle$$

$$\left\langle {}^3E_{(A)}^{(B)}[{}^3T_{1g}(t_{2g}^4)]\left|\frac{\vec{p}}{m}\right|{}^3E_{(B)}^{(A)}[{}^3T_{1g}(t_{2g}^3e_g)]\right\rangle =$$
$$-\frac{1}{2\sqrt{2}}\left\{\sqrt{2}\left\langle e_{(B)}^{(A)}(t_{2g})\left|\frac{\vec{p}}{m}\right|e_{(B)}^{(A)}(e_g)\right\rangle+(\mp)\left\langle a(t_{2g})\left|\frac{\vec{p}}{m}\right|e_A(e_g)\right\rangle\right\}$$

$$\left\langle {}^3E_{(A)}^{(B)}[{}^3T_{1g}(t_{2g}^4)]\left|\frac{\vec{p}}{m}\right|{}^3E_{(B)}^{(A)}[{}^3T_{1g}(t_{2g}^3e_g)]\right\rangle =$$
$$\frac{1}{2\sqrt{2}}\left\{\sqrt{2}\left\langle e_{(B)}^{(A)}(t_{2g})\left|\frac{\vec{p}}{m}\right|e_{(A)}^{(B)}(e_g)\right\rangle_{\star}-\left\langle a(t_{2t})\left|\frac{\vec{p}}{m}\right|e_B(e_g)\right\rangle\right\} \quad (60)$$

(v) Matrix Elements: Five Electrons

$$\left\langle {}^2A[{}^2T_{2g}(t_{2g}^5)]\left|\frac{\vec{p}}{m}\right|{}^2E_{(B)}^{(A)}[{}^2T_{2g}(t_{2g}^5)]\right\rangle =$$
$$-\left\langle e_{(B)}^{(A)}(t_{2g})\left|\frac{\vec{p}}{m}\right|a(t_{2g})\right\rangle$$

$$\left\langle {}^2A[{}^2T_{2g}(t_{2g}^5)]\left|\frac{\vec{p}}{m}\right|{}^2B[{}^2A_{2g}(t_{2g}^4e_g)]\right\rangle =$$
$$\sqrt{{}^2/_3}\left\langle e_-(t_{2g})\left|\frac{\vec{p}}{m}\right|e_-(e_g)\right\rangle$$

$$\left\langle {}^2A[{}^2T_{2g}(t_{2g}^5)]\left|\frac{\vec{p}}{m}\right|{}^2B[{}^2T_{1g}(t_{2g}^4e_g)]\right\rangle =$$
$$-\sqrt{3}\left\langle e_-(t_{2g})\left|\frac{\vec{p}}{m}\right|e_-(e_g)\right\rangle$$

$$\left\langle {}^2A[{}^2T_{2g}(t_{2g}^5)]\left|\frac{\vec{p}}{m}\right|{}^2E_{(B)}^{(A)}[{}^2T_{1g}(t_{2g}^4e_g)]\right\rangle =$$
$$\begin{pmatrix}1\\-i\end{pmatrix}{}^1/_2\sqrt{{}^3/_2}\left\{\left\langle e_+(t_{2g})\left|\frac{\vec{p}}{m}\right|e_-(e_g)\right\rangle+(\mp)\left\langle e_-(t_{2g})\left|\frac{\vec{p}}{m}\right|e_+(e_g)\right\rangle\right\}$$

$$\left\langle {}^2A[{}^2T_{2g}(t_{2g}^5)]\left|\frac{\vec{p}}{m}\right|{}^2A[{}^2T_{2g}(t_{2g}^4e_g)]\right\rangle = 0$$

$$\left\langle {}^2A[{}^2T_{2g}(t_{2g}^5)]\left|\frac{\vec{p}}{m}\right|{}^2E_{(B)}^{(A)}[{}^2T_{2g}(t_{2g}^4e_g)]\right\rangle =$$
$$\frac{1}{\sqrt{3}}\left\langle a(t_{2g})\left|\frac{\vec{p}}{m}\right|e_{(B)}^{(A)}(e_g)\right\rangle+\begin{pmatrix}1\\-i\end{pmatrix}\frac{1}{2\sqrt{6}}\left\{\left\langle e_+(t_{2g})\left|\frac{\vec{p}}{m}\right|e_-(t_{2g})\right\rangle+(\pm)\left\langle e_-(t_{2g})\left|\frac{\vec{p}}{m}\right|e_+(e_g)\right\rangle\right\}$$

$$\left\langle {}^2A[{}^2T_{2g}(t_{2g}^5)]\left|\frac{\vec{p}}{m}\right|{}^2E_{(B)}^{(A)}[{}^2E_g(t_{2g}^4e_g)]\right\rangle =$$
$$\begin{pmatrix}1\\-i\end{pmatrix}\frac{1}{\sqrt{6}}\left\{\left\langle e_+(t_{2g})\left|\frac{\vec{p}}{m}\right|e_-(e_g)\right\rangle+(\pm)\left\langle e_-(t_{2g})\left|\frac{\vec{p}}{m}\right|e_+(e_g)\right\rangle\right\}$$

$$\left\langle {}^2A[{}^2T_{2g}(t_{2g}^5)]\left|\frac{\vec{p}}{m}\right|{}^2A[{}^2T_{2g}(t_{2g}^4e_g)]\right\rangle = 0$$

$$\left\langle {}^2A[{}^2T_{2g}(t_{2g}^5)]\left|\frac{\vec{p}}{m}\right|{}^2E_{(B)}^{(A)}[{}^2T_{2g}(t_{2g}^4e_g)]\right\rangle =$$
$$\begin{pmatrix}-1\\i\end{pmatrix}{}^1/_2\sqrt{{}^3/_2}\left\{\left\langle e_+(t_{2g})\left|\frac{\vec{p}}{m}\right|e_-(e_g)\right\rangle+(\pm)\left\langle e_-(t_{2g})\left|\frac{\vec{p}}{m}\right|e_+(e_g)\right\rangle\right\}$$

$$\left\langle {}^2A[{}^2T_{2g}(t_{2g}^5)]\left|\frac{\vec{p}}{m}\right|{}^2B[{}^2T_{1g}(t_{2g}^4e_g)]\right\rangle =$$
$$\frac{1}{\sqrt{3}}\left\langle e_-(t_{2g})\left|\frac{\vec{p}}{m}\right|e_-(e_g)\right\rangle$$

$$\left\langle {}^2A[{}^2T_{2g}(t_{2g}^5)]\left|\frac{\vec{p}}{m}\right|{}^2E_{(A)}^{(B)}[{}^2T_{1g}(t_{2g}^4e_g)]\right\rangle =$$
$$(\mp)\frac{i}{\sqrt{3}}\left\langle a(t_{2g})\left|\frac{\vec{p}}{m}\right|e_{(A)}^{(B)}(e_g)\right\rangle+\begin{pmatrix}1\\-i\end{pmatrix}\frac{1}{2\sqrt{6}}\left\{\left\langle e_+(t_{2g})\left|\frac{\vec{p}}{m}\right|e_-(e_g)\right\rangle+(\mp)\left\langle e_-(t_{2g})\left|\frac{\vec{p}}{m}\right|e_+(e_g)\right\rangle\right\}$$

$$\left\langle {}^2A[{}^2T_{2g}(t_{2g}^5)] \left|\frac{\vec{p}}{\vec{m}}\right| {}^2A[{}^2A_{1g}(t_{2g}^4 e_g)] \right\rangle = 0$$

$$\left\langle {}^2A[{}^2T_{2g}(t_{2g}^5)] \left|\frac{\vec{p}}{\vec{m}}\right| {}^2E_{(B)}^{(A)}[{}^2E_g(t_{2g}^4 e_g)] \right\rangle = \frac{1}{\sqrt{3}} \left\langle a(t_{2g}) \left|\frac{\vec{p}}{\vec{m}}\right| e_{(B)}^{(A)}(e_g) \right\rangle$$

$$\left\langle {}^2E_{(B)}^{(A)}[{}^2T_{2g}(t_{2g}^5)] \left|\frac{\vec{p}}{\vec{m}}\right| {}^2E_{(A)}^{(B)}[{}^2T_{2g}(t_{2g}^5)] \right\rangle = \left\langle e_{(B)}^{(A)}(t_{2g}) \left|\frac{\vec{p}}{\vec{m}}\right| e_{(A)}^{(B)}(t_{2g}) \right\rangle_{\star}$$

$$\left\langle {}^2E_{(B)}^{(A)}[{}^2T_{2g}(t_{2g}^5)] \left|\frac{\vec{p}}{\vec{m}}\right| {}^2B[{}^2A_{2g}(t_{2g}^4 e_g)] \right\rangle = (\mp)\frac{i}{\sqrt{6}} \left\langle a(t_{2g}) \left|\frac{\vec{p}}{\vec{m}}\right| e_{(A)}^{(B)}(e_g) \right\rangle + \binom{-1}{i} \frac{1}{2\sqrt{3}} \left\{ \left\langle e_+(t_{2g}) \left|\frac{\vec{p}}{\vec{m}}\right| e_-(e_g) \right\rangle + (\mp) \left\langle e_-(t_{2g}) \left|\frac{\vec{p}}{\vec{m}}\right| e_+(e_g) \right\rangle \right\}$$

$$\left\langle {}^2E_{(B)}^{(A)}[{}^2T_{2g}(t_{2g}^5)] \left|\frac{\vec{p}}{\vec{m}}\right| {}^2B[{}^2T_{1g}(t_{2g}^4 e_g)] \right\rangle = (\mp)\, i\frac{\sqrt{3}}{2} \left\langle a(t_{2g}) \left|\frac{\vec{p}}{\vec{m}}\right| e_{(A)}^{(B)}(e_g) \right\rangle$$

$$\left\langle {}^2E_{(B)}^{(A)}[{}^2T_{2g}(t_{2g}^5)] \left|\frac{\vec{p}}{\vec{m}}\right| {}^2E_{(A)}^{(B)}[{}^2T_{1g}(t_{2g}^4 e_g)] \right\rangle = (\pm)\frac{i}{2}\sqrt{3/2} \left\{ \sqrt{2} \left\langle e_{(B)}^{(A)}(t_{2g}) \left|\frac{\vec{p}}{\vec{m}}\right| e_{(A)}^{(B)}(e_g) \right\rangle - \left\langle a(t_{2g}) \left|\frac{\vec{p}}{\vec{m}}\right| e_B(e_g) \right\rangle \right\}$$

$$\left\langle {}^2E_{(B)}^{(A)}[{}^2T_{2g}(t_{2g}^5)] \left|\frac{\vec{p}}{\vec{m}}\right| {}^2E_{(B)}^{(A)}[{}^2T_{1g}(t_{2g}^4 e_g)] \right\rangle = (\mp)\frac{i}{2}\sqrt{3/2} \left\{ \sqrt{2} \left\langle e_{(B)}^{(A)}(t_{2g}) \left|\frac{\vec{p}}{\vec{m}}\right| e_{(B)}^{(A)}(e_g) \right\rangle + (\pm) \left\langle a(t_{2g}) \left|\frac{\vec{p}}{\vec{m}}\right| e_A(e_g) \right\rangle \right\}$$

$$\left\langle {}^2E_{(B)}^{(A)}[{}^2T_{2g}(t_{2g}^5)] \left|\frac{\vec{p}}{\vec{m}}\right| {}^2A[{}^2T_{2g}(t_{2g}^4 e_g)] \right\rangle = -\frac{1}{2\sqrt{3}} \left\langle a(t_{2g}) \left|\frac{\vec{p}}{\vec{m}}\right| e_{(B)}^{(A)}(e_g) \right\rangle + \binom{-1}{i} \frac{1}{\sqrt{6}} \left\{ \left\langle e_+(t_{2g}) \left|\frac{\vec{p}}{\vec{m}}\right| e_-(e_g) \right\rangle + (\pm) \left\langle e_-(t_{2g}) \left|\frac{\vec{p}}{\vec{m}}\right| e_+(e_g) \right\rangle \right\}$$

$$\left\langle {}^2E_{(B)}^{(A)}[{}^2T_{2g}(t_{2g}^5)] \left|\frac{\vec{p}}{\vec{m}}\right| {}^2E_{(B)}^{(A)}[{}^2T_{2g}(t_{2g}^4 e_g)] \right\rangle = -\frac{1}{2\sqrt{6}} \left\{ \sqrt{2} \left\langle e_{(B)}^{(A)}(t_{2g}) \left|\frac{\vec{p}}{\vec{m}}\right| e_{(B)}^{(A)}(e_g) \right\rangle + (\mp) \left\langle a(t_{2g}) \left|\frac{\vec{p}}{\vec{m}}\right| e_A(e_g) \right\rangle \right\}$$

$$\left\langle {}^2E_{(B)}^{(A)}[{}^2T_{2g}(t_{2g}^5)] \left|\frac{\vec{p}}{\vec{m}}\right| {}^2E_{(A)}^{(B)}[{}^2T_{2g}(t_{2g}^4 e_g)] \right\rangle = -\frac{1}{2\sqrt{6}} \left\{ \sqrt{2} \left\langle e_{(B)}^{(A)}(t_{2g}) \left|\frac{\vec{p}}{\vec{m}}\right| e_{(A)}^{(B)}(e_g) \right\rangle + \left\langle a(t_{2g}) \left|\frac{\vec{p}}{\vec{m}}\right| e_B(e_g) \right\rangle \right\} + (\pm)\frac{i}{2\sqrt{3}} \left\{ \left\langle e_+(t_{2g}) \left|\frac{\vec{p}}{\vec{m}}\right| e_+(e_g) \right\rangle - \left\langle e_-(t_{2g}) \left|\frac{\vec{p}}{\vec{m}}\right| e_-(e_g) \right\rangle \right\}$$

$$\left\langle {}^2E_{(B)}^{(A)}[{}^2T_{2g}(t_{2g}^5)] \left|\frac{\vec{p}}{\vec{m}}\right| {}^2E_{(B)}^{(A)}[{}^2E_g(t_{2g}^4 e_g)] \right\rangle = (\pm)\frac{1}{\sqrt{6}} \left\langle a(t_{2g}) \left|\frac{\vec{p}}{\vec{m}}\right| e_A(e_g) \right\rangle$$

$$\left\langle {}^2E_{(B)}^{(A)}[{}^2T_{2g}(t_{2g}^5)] \left|\frac{\vec{p}}{\vec{m}}\right| {}^2E_{(A)}^{(B)}[{}^2E_g(t_{2g}^4 e_g)] \right\rangle = -\frac{1}{\sqrt{6}} \left\langle a(t_{2g}) \left|\frac{\vec{p}}{\vec{m}}\right| e_B(e_g) \right\rangle + (\mp)\frac{i}{2\sqrt{3}} \left\{ \left\langle e_+(t_{2g}) \left|\frac{\vec{p}}{\vec{m}}\right| e_+(e_g) \right\rangle - \left\langle e_-(t_{2g}) \left|\frac{\vec{p}}{\vec{m}}\right| e_-(e_g) \right\rangle \right\}$$

$$\left\langle {}^2E_{(B)}^{(A)}[{}^2T_{2g}(t_{2g}^5)] \left|\frac{\vec{p}}{\vec{m}}\right| {}^2A[{}^2T_{2g}(t_{2g}^4 e_g)] \right\rangle = \frac{\sqrt{3}}{2} \left\langle a(t_{2g}) \left|\frac{\vec{p}}{\vec{m}}\right| e_{(B)}^{(A)}(e_g) \right\rangle$$

$$\left\langle {}^2E_{(B)}^{(A)}[{}^2T_{2g}(t_{2g}^5)] \left|\frac{\vec{p}}{\vec{m}}\right| {}^2E_{(B)}^{(A)}[{}^2T_{2g}(t_{2g}^4 e_g)] \right\rangle = -1/2\sqrt{3/2} \left\{ \sqrt{2} \left\langle e_{(B)}^{(A)}(t_{2g}) \left|\frac{\vec{p}}{\vec{m}}\right| e_{(B)}^{(A)}(e_g) \right\rangle + (\mp) \left\langle a(t_{2g}) \left|\frac{\vec{p}}{\vec{m}}\right| e_A(e_g) \right\rangle \right\}$$

$$\left\langle {}^2E_{(B)}^{(A)}[{}^2T_{2g}(t_{2g}^5)] \left|\frac{\vec{p}}{\vec{m}}\right| {}^2E_{(A)}^{(B)}[{}^2T_{2g}(t_{2g}^4 e_g)] \right\rangle = 1/2\sqrt{3/2} \left\{ \sqrt{2} \left\langle e_{(B)}^{(A)}(t_{2g}) \left|\frac{\vec{p}}{\vec{m}}\right| e_{(A)}^{(B)}(e_g) \right\rangle_{\star} - \left\langle a(t_{2g}) \left|\frac{\vec{p}}{\vec{m}}\right| e_B(e_g) \right\rangle \right\}$$

$$\left\langle {}^2E_{(B)}^{(A)}[{}^2T_{2g}(t_{2g}^5)]\left|\frac{\vec{p}}{m}\right|{}^2B[{}^2T_{1g}(t_{2g}^4e_g)]\right\rangle =$$
$$(\mp)\frac{i}{2\sqrt{3}}\left\langle a(t_{2g})\left|\frac{\vec{p}}{m}\right|e_{(A)}^{(B)}(e_g)\right\rangle +$$
$$\begin{pmatrix}1\\-i\end{pmatrix}\frac{1}{\sqrt{6}}\left\{\left\langle e_+(t_{2g})\left|\frac{\vec{p}}{m}\right|e_-(e_g)\right\rangle -\right.$$
$$\left.(\pm)\left\langle e_-(t_{2g})\left|\frac{\vec{p}}{m}\right|e_+(e_g)\right\rangle\right\}$$

$$\left\langle {}^2E_{(B)}^{(A)}[{}^2T_{2g}(t_{2g}^5)]\left|\frac{\vec{p}}{m}\right|{}^2E_{(A)}^{(B)}[{}^2T_{1g}(t_{2g}^4e_g)]\right\rangle =$$
$$(\mp)\frac{i}{2\sqrt{6}}\left\{\sqrt{2}\left\langle e_{(B)}^{(A)}(t_{2g})\left|\frac{\vec{p}}{m}\right|e_{(A)}^{(B)}(e_g)\right\rangle -\right.$$
$$\left.\left\langle a(t_{2g})\left|\frac{\vec{p}}{m}\right|e_B(e_g)\right\rangle\right\}$$

$$\left\langle {}^2E_{(B)}^{(A)}[{}^2T_{2g}(t_{2g}^5)]\left|\frac{\vec{p}}{m}\right|{}^2E_{(B)}^{(A)}[{}^2T_{1g}(t_{2g}^4e_g)]\right\rangle =$$
$$(\pm)\frac{i}{2\sqrt{6}}\left\{\sqrt{2}\left\langle e_{(B)}^{(A)}(t_{2g})\left|\frac{\vec{p}}{m}\right|e_{(B)}^{(A)}(e_g)\right\rangle +\right.$$
$$\left.(\pm)\left\langle a(t_{2g})\left|\frac{\vec{p}}{m}\right|e_A(e_g)\right\rangle\right\}$$

$$\left\langle {}^2E_{(B)}^{(A)}[{}^2T_{2g}(t_{2g}^5)]\left|\frac{\vec{p}}{m}\right|{}^2A[{}^2A_{1g}(t_{2g}^4e_g)]\right\rangle =$$
$$\frac{1}{\sqrt{6}}\left\langle a(t_{2g})\left|\frac{\vec{p}}{m}\right|e_{(B)}^{(A)}(e_g)\right\rangle +$$
$$\begin{pmatrix}-1\\i\end{pmatrix}\frac{1}{2\sqrt{3}}\left\{\left\langle e_+(t_{2g})\left|\frac{\vec{p}}{m}\right|e_-(e_g)\right\rangle +\right.$$
$$\left.(\pm)\left\langle e_-(t_{2g})\left|\frac{\vec{p}}{m}\right|e_+(e_g)\right\rangle\right\}$$

$$\left\langle {}^2E_{(B)}^{(A)}[{}^2T_{2g}(t_{2g}^5)]\left|\frac{\vec{p}}{m}\right|{}^2E_{(B)}^{(A)}[{}^2E_g(t_{2g}^4e_g)]\right\rangle =$$
$$\frac{1}{\sqrt{3}}\left\langle e_{(B)}^{(A)}(t_{2g})\left|\frac{\vec{p}}{m}\right|e_{(B)}^{(A)}(e_g)\right\rangle$$

$$\left\langle {}^2E_{(B)}^{(A)}[{}^2T_{2g}(t_{2g}^5)]\left|\frac{\vec{p}}{m}\right|{}^2E_{(A)}^{(B)}[{}^2E_g(t_{2g}^4e_g)]\right\rangle =$$
$$\frac{1}{\sqrt{3}}\left\langle e_{(B)}^{(A)}(t_{2g})\left|\frac{\vec{p}}{m}\right|e_{(A)}^{(B)}(e_g)\right\rangle \quad (61)$$

(vi) Matrix Elements: Six Electrons

$$\left\langle {}^5A[{}^5T_{2g}(t_{2g}^4e_g^2)]\left|\frac{\vec{p}}{m}\right|{}^5E_{(B)}^{(A)}[{}^5T_{2g}(t_{2g}^4e_g^2)]\right\rangle =$$
$$\left\langle a(t_{2g})\left|\frac{\vec{p}}{m}\right|e_{(B)}^{(A)}(t_{2g})\right\rangle$$

$$\left\langle {}^5A[{}^5T_{2g}(t_{2g}^4e_g^2)]\left|\frac{\vec{p}}{m}\right|{}^5E_{(B)}^{(A)}[{}^5E_g(t_{2g}^3e_g^3)]\right\rangle =$$
$$-\left\langle a(t_{2g})\left|\frac{\vec{p}}{m}\right|e_{(B)}^{(A)}(e_g)\right\rangle$$

$$\left\langle {}^5E_{(B)}^{(A)}[{}^5T_{2g}(t_{2g}^4e_g^2)]\left|\frac{\vec{p}}{m}\right|{}^5E_{(B)}^{(A)}[{}^5T_{2g}(t_{2g}^4e_g^2)]\right\rangle =$$
$$-\left\langle e_{(B)}^{(A)}(t_{2g})\left|\frac{\vec{p}}{m}\right|e_{(D)}^{(A)}(t_{2g})\right\rangle$$

$$\left\langle {}^5E_{(B)}^{(A)}[{}^5T_{2g}(t_{2g}^4e_g^2)]\left|\frac{\vec{p}}{m}\right|{}^5E_{(A)}^{(B)}[{}^5T_{2g}(t_{2g}^4e_g^2)]\right\rangle =$$
$$\left\langle e_{(A)}^{(B)}(t_{2g})\left|\frac{\vec{p}}{m}\right|e_{(A)}^{(B)}(t_{2g})\right\rangle_{\star}$$

$$\left\langle {}^5E_{(B)}^{(A)}[{}^5T_{2g}(t_{2g}^4e_g^2)]\left|\frac{\vec{p}}{m}\right|{}^5E_{(B)}^{(A)}[{}^5E_g(t_{2g}^3e_g^3)]\right\rangle =$$
$$-\left\langle e_{(B)}^{(A)}(t_{2g})\left|\frac{\vec{p}}{m}\right|e_{(B)}^{(A)}(e_g)\right\rangle$$

$$\left\langle {}^5E_{(B)}^{(A)}[{}^5T_{2g}(t_{2g}^4e_g^2)]\left|\frac{\vec{p}}{m}\right|{}^5E_{(A)}^{(B)}[{}^5E_g(t_{2g}^3e_g^3)]\right\rangle =$$
$$-\left\langle e_{(B)}^{(A)}(t_{2g})\left|\frac{\vec{p}}{m}\right|e_{(A)}^{(B)}(e_g)\right\rangle$$

$$\left\langle {}^5E_{(B)}^{(A)}[{}^5E_g(t_{2g}^3e_g^3)]\left|\frac{\vec{p}}{m}\right|{}^5E_{(B)}^{(A)}[{}^5E_g(t_{2g}^3e_g^3)]\right\rangle =$$
$$\left\langle e_{(B)}^{(A)}(e_g)\left|\frac{\vec{p}}{m}\right|e_{(B)}^{(A)}(e_g)\right\rangle$$

$$\left\langle {}^5E_{(B)}^{(A)}[{}^5E_g(t_{2g}^3e_g^3)]\left|\frac{\vec{p}}{m}\right|{}^5E_{(A)}^{(B)}[{}^5E_g(t_{2g}^3e_g^3)]\right\rangle =$$
$$\left\langle e_{(B)}^{(A)}(e_g)\left|\frac{\vec{p}}{m}\right|e_{(A)}^{(B)}(e_g)\right\rangle$$

$$\left\langle {}^1A[{}^1A_{1g}(t_{2g}^6)]\left|\frac{\vec{p}}{m}\right|{}^1B[{}^1T_{1g}(t_{2g}^5e_g)]\right\rangle =$$
$$2\left\langle e_-(t_{2g})\left|\frac{\vec{p}}{m}\right|e_-(e_g)\right\rangle$$

$$\left\langle {}^1A[{}^1A_{1g}(t_{2g}^6)]\left|\frac{\vec{p}}{m}\right|{}^1E_{(A)}^{(B)}[{}^1T_{1g}(t_{2g}^5e_g)]\right\rangle =$$
$$(\mp)\,i\left\langle a(t_{2g})\left|\frac{\vec{p}}{m}\right|e_{(A)}^{(B)}(e_g)\right\rangle +$$
$$\begin{pmatrix}-1\\i\end{pmatrix}\frac{1}{\sqrt{2}}\left\{\left\langle e_+(t_{2g})\left|\frac{\vec{p}}{m}\right|e_-(e_g)\right\rangle +\right.$$
$$\left.(\mp)\left\langle e_-(t_{2g})\left|\frac{\vec{p}}{m}\right|e_+(e_g)\right\rangle\right\}$$

$$\left\langle {}^1A[{}^1A_{1g}(t_{2g}^6)]\left|\frac{\vec{p}}{m}\right|{}^1A[{}^1T_{2g}(t_{2g}^5e_g)]\right\rangle = 0$$

$$\left\langle {}^1A[{}^1A_{1g}(t_{2g}^6)]\left|\frac{\vec{p}}{m}\right|{}^1E_{(B)}^{(A)}[{}^1T_{2g}(t_{2g}^5e_g)]\right\rangle =$$
$$-\left\langle a(t_{2g})\left|\frac{\vec{p}}{m}\right|e_{(B)}^{(A)}(e_g)\right\rangle +$$
$$\begin{pmatrix}1\\-i\end{pmatrix}\frac{1}{\sqrt{2}}\left\{\left\langle e_+(t_{2g})\left|\frac{\vec{p}}{m}\right|e_-(e_g)\right\rangle +\right.$$
$$\left.(\pm)\left\langle e_-(t_{2g})\left|\frac{\vec{p}}{m}\right|e_+(e_g)\right\rangle\right\} \quad (62)$$

(vii) Matrix Elements: Seven Electrons

$$\left\langle {}^4B[{}^4T_{1g}(t_{2g}{}^5e_g{}^2)]\left|\frac{\vec{p}}{\vec{m}}\right|{}^4E_{(A)}^{(B)}[{}^4T_{1g}(t_{2g}{}^5e_g{}^2)]\right\rangle = -\left\langle e_{(B)}^{(A)}(t_{2g})\left|\frac{\vec{p}}{\vec{m}}\right|a(t_{2g})\right\rangle$$

$$\left\langle {}^4B[{}^4T_{1g}(t_{2g}{}^5e_g{}^2)]\left|\frac{\vec{p}}{\vec{m}}\right|{}^4A[{}^4T_{2g}(t_{2g}{}^4e_g{}^3)]\right\rangle = \sqrt{2}\left\langle e_-(t_{2g})\left|\frac{\vec{p}}{\vec{m}}\right|e_-(e_g)\right\rangle$$

$$\left\langle {}^4B[{}^4T_{1g}(t_{2g}{}^5e_g{}^2)]\left|\frac{\vec{p}}{\vec{m}}\right|{}^4E_{(B)}^{(A)}[{}^4T_{2g}(t_{2g}{}^4e_g{}^3)]\right\rangle = \begin{pmatrix}1\\-i\end{pmatrix}{}^1/_2\left\{\left\langle e_+(t_{2g})\left|\frac{\vec{p}}{\vec{m}}\right|e_-(e_g)\right\rangle - (\pm)\left\langle e_-(t_{2g})\left|\frac{\vec{p}}{\vec{m}}\right|e_+(e_g)\right\rangle\right\}$$

$$\left\langle {}^4B[{}^4T_{1g}(t_{2g}{}^5e_g{}^2)]\left|\frac{\vec{p}}{\vec{m}}\right|{}^4B[{}^4T_{1g}(t_{2g}{}^4e_g{}^3)]\right\rangle = 0$$

$$\left\langle {}^4B[{}^4T_{1g}(t_{2g}{}^5e_g{}^2)]\left|\frac{\vec{p}}{\vec{m}}\right|{}^4E_{(A)}^{(B)}[{}^4T_{1g}(t_{2g}{}^4e_g{}^3)]\right\rangle = \begin{pmatrix}-1\\i\end{pmatrix}{}^1/_2\left\{\left\langle e_+(t_{2g})\left|\frac{\vec{p}}{\vec{m}}\right|e_-(e_g)\right\rangle + (\pm)\left\langle e_-(t_{2g})\left|\frac{\vec{p}}{\vec{m}}\right|e_+(e_g)\right\rangle\right\}$$

$$\left\langle {}^4B[{}^4T_{1g}(t_{2g}{}^5e_g{}^2)]\left|\frac{\vec{p}}{\vec{m}}\right|{}^4B[{}^4A_{2g}(t_{2g}{}^3e_g{}^4)]\right\rangle = 0$$

$$\left\langle {}^4E_{(A)}^{(B)}[{}^4T_{1g}(t_{2g}{}^5e_g{}^2)]\left|\frac{\vec{p}}{\vec{m}}\right|{}^4E_{(B)}^{(A)}[{}^4T_{1g}(t_{2g}{}^5e_g{}^2)]\right\rangle = \left\langle e_{(B)}^{(A)}(t_{2g})\left|\frac{\vec{p}}{\vec{m}}\right|e_{(A)}^{(B)}(t_{2g})\right\rangle_{\star}$$

$$\left\langle {}^4E_{(A)}^{(B)}[{}^4T_{1g}(t_{2g}{}^5e_g{}^2)]\left|\frac{\vec{p}}{\vec{m}}\right|{}^4A[{}^4T_{2g}(t_{2g}{}^4e_g{}^3)]\right\rangle = (\mp)\frac{i}{\sqrt{2}}\left\langle a(t_{2g})\left|\frac{\vec{p}}{\vec{m}}\right|e_{(A)}^{(B)}(e_g)\right\rangle$$

$$\left\langle {}^4E_{(A)}^{(B)}[{}^4T_{1g}(t_{2g}{}^5e_g{}^2)]\left|\frac{\vec{p}}{\vec{m}}\right|{}^4E_{(A)}^{(A)}[{}^4T_{2g}(t_{2g}{}^4e_g{}^3)]\right\rangle = (\mp)\frac{i}{2}\left\{\sqrt{2}\left\langle e_{(B)}^{(A)}(t_{2g})\left|\frac{\vec{p}}{\vec{m}}\right|e_{(A)}^{(B)}(e_g)\right\rangle_{\star} + \left\langle a(t_{2g})\left|\frac{\vec{p}}{\vec{m}}\right|e_B(e_g)\right\rangle\right\}$$

$$\left\langle {}^4E_{(A)}^{(B)}[{}^4T_{1g}(t_{2g}{}^5e_g{}^2)]\left|\frac{\vec{p}}{\vec{m}}\right|{}^4E_{(A)}^{(B)}[{}^4T_{2g}(t_{2g}{}^4e_g{}^3)]\right\rangle = (\mp)\frac{i}{2}\left\{\sqrt{2}\left\langle e_{(B)}^{(A)}(t_{2g})\left|\frac{\vec{p}}{\vec{m}}\right|e_{(B)}^{(A)}(e_g)\right\rangle + (\pm)\left\langle a(t_{2g})\left|\frac{\vec{p}}{\vec{m}}\right|e_A(e_g)\right\rangle\right\}$$

$$\left\langle {}^4E_{(A)}^{(B)}[{}^4T_{1g}(t_{2g}{}^5e_g{}^2)]\left|\frac{\vec{p}}{\vec{m}}\right|{}^4B[{}^4T_{1g}(t_{2g}{}^4e_g{}^3)]\right\rangle = -\frac{1}{\sqrt{2}}\left\langle a(t_{2g})\left|\frac{\vec{p}}{\vec{m}}\right|e_{(B)}^{(A)}(e_g)\right\rangle$$

$$\left\langle {}^4E_{(A)}^{(B)}[{}^4T_{1g}(t_{2g}{}^5e_g{}^2)]\left|\frac{\vec{p}}{\vec{m}}\right|{}^4E_{(A)}^{(B)}[{}^4T_{1g}(t_{2g}{}^4e_g{}^3)]\right\rangle = -{}^1/_2\left\{\sqrt{2}\left\langle e_{(B)}^{(A)}(t_{2g})\left|\frac{\vec{p}}{\vec{m}}\right|e_{(B)}^{(A)}(e_g)\right\rangle + (\mp)\left\langle a(t_{2g})\left|\frac{\vec{p}}{\vec{m}}\right|e_A(e_g)\right\rangle\right\}$$

$$\left\langle {}^4E_{(A)}^{(B)}[{}^4T_{1g}(t_{2g}{}^5e_g{}^2)]\left|\frac{\vec{p}}{\vec{m}}\right|{}^4E_{(B)}^{(A)}[{}^4T_{1g}(t_{2g}{}^4e_g{}^3)]\right\rangle = -{}^1/_2\left\{\sqrt{2}\left\langle e_{(B)}^{(A)}(t_{2g})\left|\frac{\vec{p}}{\vec{m}}\right|e_{(A)}^{(B)}(e_g)\right\rangle + \left\langle a(t_{2g})\left|\frac{\vec{p}}{\vec{m}}\right|e_B(e_g)\right\rangle\right\}$$

$$\left\langle {}^4E_{(A)}^{(B)}[{}^4T_{1g}(t_{2g}{}^5e_g{}^2)]\left|\frac{\vec{p}}{\vec{m}}\right|{}^4B[{}^4A_{2g}(t_{2g}{}^3e_g{}^4)]\right\rangle = 0$$

$$\left\langle {}^2E_{(B)}^{(A)}[{}^2E_g(t_{2g}{}^6e_g)]\left|\frac{\vec{p}}{\vec{m}}\right|{}^2E_{(A)}^{(B)}[{}^2E_g(t_{2g}{}^6e_g)]\right\rangle = \left\langle e_{(B)}^{(A)}(e_g)\left|\frac{\vec{p}}{\vec{m}}\right|e_{(A)}^{(B)}(e_g)\right\rangle$$

$$\left\langle {}^3E_{(B)}^{(A)}[{}^2E_g(t_{2g}{}^6e_g)]\left|\frac{\vec{p}}{\vec{m}}\right|{}^2B[{}^2T_{1g}(t_{2g}{}^5e_g{}^2)]\right\rangle = (\pm)\,i\sqrt{3/2}\left\langle a(t_{2g})\left|\frac{\vec{p}}{\vec{m}}\right|e_{(A)}^{(B)}(e_g)\right\rangle$$

$$\left\langle {}^2E_{(B)}^{(A)}[{}^2E_g(t_{2g}{}^6e_g)]\left|\frac{\vec{p}}{\vec{m}}\right|{}^2E_{(A)}^{(B)}[{}^2T_{1g}(t_{2g}{}^5e_c{}^2)]\right\rangle = (\pm)\,i\sqrt{3/2}\left\langle e_{(B)}^{(A)}(t_{2g})\left|\frac{\vec{p}}{\vec{m}}\right|e_{(A)}^{(B)}(e_g)\right\rangle_{\star}$$

$$\left\langle {}^2E_{(B)}^{(A)}[{}^2E_g(t_{2g}{}^6e_g)]\left|\frac{\vec{p}}{\vec{m}}\right|{}^2E_{(B)}^{(A)}[{}^2T_{1g}(t_{2g}{}^5e_g{}^2)]\right\rangle = (\pm)\,i\sqrt{3/2}\left\langle e_{(B)}^{(A)}(t_{2g})\left|\frac{\vec{p}}{\vec{m}}\right|e_{(D)}^{(A)}(e_g)\right\rangle$$

$$\left\langle {}^2E_{(B)}^{(A)}[{}^2E_g(t_{2g}{}^6e_g)]\left|\frac{\vec{p}}{\vec{m}}\right|{}^2A[{}^2T_{2g}(t_{2g}{}^5e_g{}^2)]\right\rangle = \begin{pmatrix}-1\\i\end{pmatrix}{}^1/_2\left\{\left\langle e_+(t_{2g})\left|\frac{\vec{p}}{\vec{m}}\right|e_-(e_g)\right\rangle + (\pm)\left\langle e_-(t_{2g})\left|\frac{\vec{p}}{\vec{m}}\right|e_+(e_g)\right\rangle\right\}$$

$$\left\langle {}^2E_{(B)}^{(A)}[{}^2E_g(t_{2g}{}^6e_g)]\left|\frac{\vec{p}}{\vec{m}}\right|{}^2E_{(B)}^{(A)}[{}^2T_{2g}(t_{2g}{}^5e_g{}^2)]\right\rangle = (\mp)\,{}^1/_2\left\langle a(t_{2g})\left|\frac{\vec{p}}{\vec{m}}\right|e_A(e_g)\right\rangle$$

$$\left\langle {}^2E_{(B)}^{(A)}[{}^2E_g(t_{2g}^6e_g)]\left|\frac{\vec{p}}{\vec{m}}\right|{}^2E_{(A)}^{(B)}[{}^2T_{2g}(t_{2g}^5e_g^2)]\right\rangle =$$
$$1/2\left\langle a(t_{2g})\left|\frac{\vec{p}}{\vec{m}}\right|e_B(e_g)\right\rangle +$$
$$(\mp)\frac{i}{2\sqrt{2}}\left\{\left\langle e_+(t_{2g})\left|\frac{\vec{p}}{\vec{m}}\right|e_+(e_g)\right\rangle -\left\langle e_-(t_{2g})\left|\frac{\vec{p}}{\vec{m}}\right|e_-(e_g)\right\rangle\right\}$$

$$\left\langle {}^2E_{(B)}^{(A)}[{}^2E_g(t_{2g}^6e_g)]\left|\frac{\vec{p}}{\vec{m}}\right|{}^2B[{}^2T_{1g}(t_{2g}^5e_g^2)]\right\rangle =$$
$$\begin{pmatrix}-1\\ i\end{pmatrix}1/2\left\{\left\langle e_+(t_{2g})\left|\frac{\vec{p}}{\vec{m}}\right|e_-(e_g)\right\rangle -(\pm)\left\langle e_-(t_{2g})\left|\frac{\vec{p}}{\vec{m}}\right|e_+(e_g)\right\rangle\right\}$$

$$\left\langle {}^2E_{(B)}^{(A)}[{}^2E_g(t_{2g}^6e_g)]\left|\frac{\vec{p}}{\vec{m}}\right|{}^2E_{(A)}^{(B)}[{}^2T_{1g}(t_{2g}^5e_g^2)]\right\rangle =$$
$$(\pm)\frac{i}{2}\left\langle a(t_{2g})\left|\frac{\vec{p}}{\vec{m}}\right|e_B(e_g)\right\rangle -$$
$$\frac{1}{2\sqrt{2}}\left\{\left\langle e_+(t_{2g})\left|\frac{\vec{p}}{\vec{m}}\right|e_+(e_g)\right\rangle -\left\langle e_-(t_{2g})\left|\frac{\vec{p}}{\vec{m}}\right|e_-(e_g)\right\rangle\right\}$$

$$\left\langle {}^2E_{(B)}^{(A)}[{}^2E_g(t_{2g}^6e_g)]\left|\frac{\vec{p}}{\vec{m}}\right|{}^2E_{(B)}^{(A)}[{}^2T_{1g}(t_{2g}^5e_g^2)]\right\rangle =$$
$$\frac{i}{2}\left\langle a(t_{2g})\left|\frac{\vec{p}}{\vec{m}}\right|e_A(e_g)\right\rangle$$

$$\left\langle {}^2E_{(B)}^{(A)}[{}^2E_g(t_{2g}^6e_g)]\left|\frac{\vec{p}}{\vec{m}}\right|{}^2A[{}^2T_{2g}(t_{2g}^5e_g^2)]\right\rangle =$$
$$-\frac{1}{\sqrt{2}}\left\langle a(t_{2g})\left|\frac{\vec{p}}{\vec{m}}\right|e_{(B)}^{(A)}(e_g)\right\rangle$$

$$\left\langle {}^2E_{(B)}^{(A)}[{}^2E_g(t_{2g}^6e_g)]\left|\frac{\vec{p}}{\vec{m}}\right|{}^2E_{(B)}^{(A)}[{}^2T_{2g}(t_{2g}^5e_g^2)]\right\rangle =$$
$$\frac{1}{\sqrt{2}}\left\langle e_{(B)}^{(A)}(t_{2g})\left|\frac{\vec{p}}{\vec{m}}\right|e_{(B)}^{(A)}(e_g)\right\rangle$$

$$\left\langle {}^2E_{(B)}^{(A)}[{}^2E_g(t_{2g}^6e_g)]\left|\frac{\vec{p}}{\vec{m}}\right|{}^2E_{(A)}^{(B)}[{}^2T_{2g}(t_{2g}^5e_g^2)]\right\rangle =$$
$$-\frac{1}{\sqrt{2}}\left\langle e_{(B)}^{(A)}(t_{2g})\left|\frac{\vec{p}}{\vec{m}}\right|e_{(A)}^{(B)}(e_g)\right\rangle_{\star} \quad (63)$$

(viii) Matrix Elements: Eight Electrons

$$\left\langle {}^3B[{}^3A_{2g}(t_{2g}^6e_g^2)]\left|\frac{\vec{p}}{\vec{m}}\right|{}^3A[{}^3T_{2g}(t_{2g}^5e_g^3)]\right\rangle =$$
$$\sqrt{2}\left\langle e_-(t_{2g})\left|\frac{\vec{p}}{\vec{m}}\right|e_-(e_g)\right\rangle$$

$$\left\langle {}^3B[{}^3A_{2g}(t_{2g}^6e_g^2)]\left|\frac{\vec{p}}{\vec{m}}\right|{}^3E_{(B)}^{(A)}[{}^3T_{2g}(t_{2g}^5e_g^3)]\right\rangle =$$
$$(\mp)\frac{i}{\sqrt{2}}\left\langle a(t_{2g})\left|\frac{\vec{p}}{\vec{m}}\right|e_{(A)}^{(B)}(e_g)\right\rangle -$$
$$\begin{pmatrix}1\\ -i\end{pmatrix}1/2\left\{\left\langle e_+(t_{2g})\left|\frac{\vec{p}}{\vec{m}}\right|e_-(e_g)\right\rangle -(\pm)\left\langle e_-(t_{2g})\left|\frac{\vec{p}}{\vec{m}}\right|e_+(e_g)\right\rangle\right\}$$

$$\left\langle {}^3B[{}^3A_{2g}(t_{2g}^6e_g^2)]\left|\frac{\vec{p}}{\vec{m}}\right|{}^3B[{}^3T_{1g}(t_{2g}^5e_g^3)]\right\rangle = 0$$

$$\left\langle {}^3B[{}^3A_{2g}(t_{2g}^6e_g^2)]\left|\frac{\vec{p}}{\vec{m}}\right|{}^3E_{(A)}^{(B)}[{}^3T_{1g}(t_{2g}^5e_g^3)]\right\rangle =$$
$$-\frac{1}{\sqrt{2}}\left\langle a(t_{2g})\left|\frac{\vec{p}}{\vec{m}}\right|e_{(B)}^{(A)}(e_g)\right\rangle +$$
$$\begin{pmatrix}1\\ -i\end{pmatrix}1/2\left\{\left\langle e_+(t_{2g})\left|\frac{\vec{p}}{\vec{m}}\right|e_-(e_g)\right\rangle +(\pm)\left\langle e_-(t_{2g})\left|\frac{\vec{p}}{\vec{m}}\right|e_+(e_g)\right\rangle\right\}$$

$$\left\langle {}^3B[{}^3A_{2g}(t_{2g}^6e_g^2)]\left|\frac{\vec{p}}{\vec{m}}\right|{}^3B[{}^3T_{1g}(t_{2g}^4e_g^4)]\right\rangle = 0$$

$$\left\langle {}^3B[{}^3A_{2g}(t_{2g}^6e_g^2)]\left|\frac{\vec{p}}{\vec{m}}\right|{}^3E_{(A)}^{(B)}[{}^3T_{1g}(t_{2g}^4e_g^4)]\right\rangle = 0 \quad (64)$$

(ix) Matrix Elements: Nine Electrons

$$\left\langle {}^2E_{(B)}^{(A)}(E_g)\left|\frac{\vec{p}}{\vec{m}}\right|{}^2E_{(A)}^{(B)}(E_g)\right\rangle =$$
$$-\left\langle e_{(B)}^{(A)}(e_g)\left|\frac{\vec{p}}{\vec{m}}\right|e_{(B)}^{(A)}(e_g)\right\rangle$$

$$\left\langle {}^2E_{(B)}^{(A)}(E_g)\left|\frac{\vec{p}}{\vec{m}}\right|{}^2E_{(A)}^{(B)}(E_g)\right\rangle =$$
$$\left\langle e_{(B)}^{(A)}(e_g)\left|\frac{\vec{p}}{\vec{m}}\right|e_{(A)}^{(B)}(e_g)\right\rangle_{\star}$$

$$\left\langle {}^2E_{(B)}^{(A)}(E_g)\left|\frac{\vec{p}}{\vec{m}}\right|{}^2A(T_{2g})\right\rangle = -\left\langle a(t_{2g})\left|\frac{\vec{p}}{\vec{m}}\right|e_{(B)}^{(A)}(e_g)\right\rangle$$

$$\left\langle {}^2E_{(B)}^{(A)}(E_g)\left|\frac{\vec{p}}{\vec{m}}\right|{}^2E_{(B)}^{(A)}(T_{2g})\right\rangle =$$
$$-\left\langle e_{(B)}^{(A)}(t_{2g})\left|\frac{\vec{p}}{\vec{m}}\right|e_{(B)}^{(A)}(e_g)\right\rangle$$

$$\left\langle {}^2E_{(B)}^{(A)}(E_g)\left|\frac{\vec{p}}{\vec{m}}\right|{}^2E_{(A)}^{(B)}(T_{2g})\right\rangle =$$
$$\left\langle e_{(B)}^{(A)}(t_{2g})\left|\frac{\vec{p}}{\vec{m}}\right|e_{(A)}^{(B)}(e_g)\right\rangle_{\star}$$

$$\left\langle {}^2A(T_{2g}) \left| \frac{\vec{p}}{\vec{m}} \right| {}^2E_{(B)}^{(A)}(T_{2g}) \right\rangle =$$
$$(\pm) \left\langle e_{(B)}^{(A)}(t_{2g}) \left| \frac{\vec{p}}{\vec{m}} \right| a(t_{2g}) \right\rangle$$
$$\left\langle {}^2E_{(B)}^{(A)}(T_{2g}) \left| \frac{\vec{p}}{\vec{m}} \right| {}^2E_{(B)}^{(A)}(T_{2g}) \right\rangle =$$
$$- \left\langle e_{(B)}^{(A)}(t_{2g}) \left| \frac{\vec{p}}{\vec{m}} \right| e_{(B)}^{(A)}(t_{2g}) \right\rangle$$
$$\left\langle {}^2E_{(B)}^{(A)}(T_{2g}) \left| \frac{\vec{p}}{\vec{m}} \right| {}^2E_{(A)}^{(B)}(T_{2g}) \right\rangle =$$
$$\left\langle e_{(B)}^{(A)}(t_{2g}) \left| \frac{\vec{p}}{\vec{m}} \right| e_{(A)}^{(B)}(t_{2g}) \right\rangle_{\star} \quad (65)$$

(*x*) *Matrix Elements: The Unidigonal–Trigonal Connections*

$$\left\langle a(t_{2g}) \left| \frac{\vec{p}}{\vec{m}} \right| e_{(B)}^{(A)}(t_{2g}) \right\rangle = \begin{pmatrix} \begin{bmatrix} -\bar{r}_0 \\ -i\bar{m}_0 \end{bmatrix} \hat{j}' \\ \begin{bmatrix} \bar{r}_0 \\ i\bar{m}_0 \end{bmatrix} \hat{i}' \end{pmatrix}$$
$$\left\langle a(t_{2g}) \left| \frac{\vec{p}}{\vec{m}} \right| e_{(B)}^{(A)}(e_g) \right\rangle = \begin{pmatrix} \begin{bmatrix} r_0 \\ -im_0 \end{bmatrix} \hat{j}' \\ \begin{bmatrix} -r_0 \\ im_0 \end{bmatrix} \hat{i}' \end{pmatrix}$$
$$\left\langle e_{(B)}^{(A)}(t_{2g}) \left| \frac{\vec{p}}{\vec{m}} \right| e_{(B)}^{(A)}(e_g) \right\rangle = (\pm) \sqrt{1/2} \begin{bmatrix} r_2 \\ -im_2 \end{bmatrix} \hat{j}'$$
$$\left\langle e_{(B)}^{(A)}(t_{2g}) \left| \frac{\vec{p}}{\vec{m}} \right| e_{(A)}^{(B)}(e_g) \right\rangle =$$
$$\sqrt{1/2} \begin{bmatrix} r_2 \\ -im_2 \end{bmatrix} \hat{i}' + (\pm) \begin{bmatrix} r_1 \\ -im_1 \end{bmatrix} \hat{k}'$$
$$\left\langle e_{(B)}^{(A)}(t_{2g}) \left| \frac{\vec{p}}{\vec{m}} \right| e_{(B)}^{(A)}(t_{2g}) \right\rangle = (\pm) \sqrt{1/2} \begin{bmatrix} \bar{r}_0^{\ddagger} \text{ or } 0 \\ 0 \end{bmatrix} \hat{j}'$$
$$\left\langle e_{(B)}^{(A)}(t_{2g}) \left| \frac{\vec{p}}{\vec{m}} \right| e_{(A)}^{(B)}(t_{2g}) \right\rangle =$$
$$\sqrt{1/2} \begin{bmatrix} \bar{r}_0^{\ddagger} \text{ or } 0 \\ 0 \end{bmatrix} \hat{i}' + (\pm) i \begin{bmatrix} 0 \text{ or } \bar{p}_0^{\mp} \\ \bar{m}_0^{\mp} \end{bmatrix} \hat{k}'$$
$$\left\langle e_{(B)}^{(A)}(e_g) \left| \frac{\vec{p}}{\vec{m}} \right| e_{(B)}^{(A)}(e_g) \right\rangle = (\pm) \sqrt{1/2} \begin{bmatrix} \bar{r}_0 \\ 0 \end{bmatrix} \hat{j}'$$
$$\left\langle e_{(B)}^{(A)}(e_g) \left| \frac{\vec{p}}{\vec{m}} \right| e_{(A)}^{(B)}(e_g) \right\rangle =$$
$$\sqrt{1/2} \begin{bmatrix} \bar{r}_0 \text{ or } 0 \\ 0 \end{bmatrix} \hat{i}' + (\mp) i \begin{bmatrix} 0 \text{ or } \bar{p}_0^{\ddagger} \\ \bar{m}_0^{\ddagger} \end{bmatrix} \hat{k}'$$

with the auxiliary sums

$$1/2 \left\{ \left\langle e_+(t_{2g}) \left| \frac{\vec{p}}{\vec{m}} \right| e_-(e_g) \right\rangle + \left\langle e_-(t_{2g}) \left| \frac{\vec{p}}{\vec{m}} \right| e_+(e_g) \right\rangle \right\} = \sqrt{1/2} \begin{bmatrix} r_2 \\ -im_2 \end{bmatrix} \hat{j}'$$
$$1/2 \left\{ \left\langle e_+(t_{2g}) \left| \frac{\vec{p}}{\vec{m}} \right| e_-(e_g) \right\rangle - \left\langle e_-(t_{2g}) \left| \frac{\vec{p}}{\vec{m}} \right| e_+(e_g) \right\rangle \right\} = \sqrt{1/2} \begin{bmatrix} -ir_2 \\ -m_2 \end{bmatrix} \hat{i}'$$
$$1/2 \left\{ \left\langle e_+(t_{2g}) \left| \frac{\vec{p}}{\vec{m}} \right| e_+(e_g) \right\rangle - \left\langle e_-(t_{2g}) \left| \frac{\vec{p}}{\vec{m}} \right| e_-(e_g) \right\rangle \right\} = \begin{bmatrix} ir_1 \\ m_1 \end{bmatrix} \hat{k}' \quad (66)$$

where the subscript $\star$ on the angular brackets indicates a reversal of the sign of its $\hat{i}'$ vectorial component and where the symbols $\bar{g}_0^{\dagger}$, $\bar{g}_0^{\ddagger}$, and $\bar{g}_0$ ($g = r,p,m$) are as defined in section XII, Appendix §6.1.

Similarly, for the nonzero spin-orbit force problem, the unidigonal monodentate and dibidentate wave functions, matrix elements, and rotational and spectral strengths are again simple linear combinations of the digonal dihedral and the trigonal dihedral nonzero spin-orbit results. To exhibit, the principle of descent in symmetry[40] swiftly evinces that the digonal and trigonal wave functions of division A of this article and of ref. 6 are linked to the unidigonal monodentate and bidentate wave functions by the functional conjunction

$$\gamma_{5a}^{(7 \text{ or } 8)D}(t_{2g} \text{ or } e_g)[D_2] = \frac{e^{\pi i/8}}{\sqrt{2}} (\gamma_3^{(7 \text{ or } 8)D}(t_{2g} \text{ or } e_g) + \gamma_4^{(7 \text{ or } 8)D}(t_{2g} \text{ or } e_g))[D_1],$$
$$\gamma_{5b}^{(7 \text{ or } 8)D}(t_{2g} \text{ or } e_g)[D_2] = \frac{e^{-\pi i/8}}{\sqrt{2}} (\gamma_3^{(7 \text{ or } 8)D}(t_{2g} \text{ or } e_g) - \gamma_4^{(7 \text{ or } 8)D}(t_{2g} \text{ or } e_g))[D_1]$$
$$\gamma_{5a}^{(8)'D}(t_{2g} \text{ or } e_g)[D_2] = \frac{e^{\pi i/8}}{\sqrt{2}} (\gamma_4^{(8)'D}(t_{2g} \text{ or } e_g) + \gamma_3^{(8)'D}(t_{2g} \text{ or } e_g))[D_1],$$
$$\gamma_{5b}^{(8)'D}(t_{2g} \text{ or } e_g)[D_2] = \frac{e^{-\pi i/8}}{\sqrt{2}} (\gamma_4^{(8)'D}(t_{2g} \text{ or } e_g) - \gamma_3^{(8)'D}(t_{2g} \text{ or } e_g))[D_1]$$
$$\gamma_{6a}^{(7 \text{ or } 8)T}(t_{2g} \text{ or } e_g)[D_3] = \frac{1}{\sqrt{2}} (\bar{\gamma}_3^{(7 \text{ or } 8)T}(t_{2g} \text{ or } e_g) + \bar{\gamma}_4^{(7 \text{ or } 8)T}(t_{2g} \text{ or } e_g))[D_1],$$
$$\gamma_{6b}^{(7 \text{ or } 8)T}(t_{2g} \text{ or } e_g)[D_3] = \frac{i}{\sqrt{2}} (\bar{\gamma}_3^{(7 \text{ or } 8)T}(t_{2g} \text{ or } e_g) - \bar{\gamma}_4^{(7 \text{ or } 8)T}(t_{2g} \text{ or } e_g))[D_1]$$
$$\gamma_4^{(8)T}(t_{2g} \text{ or } e_g)[D_3] = \bar{\gamma}_3^{(8)'T}(t_{2g} \text{ or } e_g)[D_1],$$
$$\gamma_5^{(8)T}(t_{2g} \text{ or } e_g)[D_3] = \bar{\gamma}_4^{(8)'T}(t_{2g} \text{ or } e_g)[D_1] \quad (67)$$

or

$$\gamma_3^{(7\text{ or }8)D}(t_{2g}\text{ or }e_g)[D_1] = \sqrt{1/2}(e^{-\pi i/8}\gamma_{5a}^{(7\text{ or }8)D}(t_{2g}\text{ or }e_g) + e^{\pi i/8}\gamma_{5b}^{(7\text{ or }8)D}(t_{2g}\text{ or }e_g))[D_2],$$

$$\gamma_4^{(7\text{ or }8)D}(t_{2g}\text{ or }e_g)[D_1] = \sqrt{1/2}(e^{-\pi i/8}\gamma_{5a}^{(7\text{ or }8)D}(t_{2g}\text{ or }e_g) - e^{\pi i/8}\gamma_{5b}^{(7\text{ or }8)D}(t_{2g}\text{ or }e_g))[D_2]$$

$$\gamma_3^{(8)'D}(t_{2g}\text{ or }e_g)[D_1] = \sqrt{1/2}(e^{-\pi i/8}\gamma_{5a}^{(8)'D}(t_{2g}\text{ or }e_g) - e^{\pi i/8}\gamma_{5b}^{(8)'D}(t_{2g}\text{ or }e_g))[D_2],$$

$$\gamma_4^{(8)'D}(t_{2g}\text{ or }e_g)[D_1] = \sqrt{1/2}(e^{-\pi i/8}\gamma_{5a}^{(8)'D}(t_{2g}\text{ or }e_g) + e^{\pi i/8}\gamma_5^{(8)'D}(t_{2g}\text{ or }e_g))[D_2]$$

$$\bar{\gamma}_3^{(7\text{ or }8)T}(t_{2g}\text{ or }e_g)[D_1] = \sqrt{1/2}(\gamma_{6a}^{(7\text{ or }8)T}(t_{2g}\text{ or }e_g) - i\gamma_{6b}^{(7\text{ or }8)T}(t_{2g}\text{ or }e_g))[D_3],$$

$$\bar{\gamma}_4^{(7\text{ or }8)T}(t_{2g}\text{ or }e_g)[D_1] = \sqrt{1/2}(\gamma_{6a}^{(7\text{ or }8)T}(t_{2g}\text{ or }e_g) + i\gamma_{6b}^{(7\text{ or }8)T}(t_{2g}\text{ or }e_g))[D_3]$$

$$\bar{\gamma}_3^{(8)'T}(t_{2g}\text{ or }e_g)[D_1] = \gamma_4^{(8)T}(t_{2g}\text{ or }e_g)[D_3],$$
$$\bar{\gamma}_4^{(8)'T}(t_{2g}\text{ or }e_g)[D_1] = \gamma_5^{(8)T}(t_{2g}\text{ or }e_g)[D_3] \qquad (68)$$

where γ_3^D, γ_4^D and $\bar{\gamma}_3^T$, $\bar{\gamma}_4^T$ are the unidigonal mono- and dibidentate (D_1) γ_3, γ_4 specie offspring of the digonal (D_2) and trigonal (D_3) $\gamma_{5(\frac{a}{b})}^D$ and $\gamma_{6(\frac{a}{b})}^T$, γ_4^T, γ_5^T specie parents, separately,[41] so that the unidigonal dihedral mono- and dibidentate individual matrix elements and rotational and spectral strengths are once more a serial sum of the digonal dihedral and trigonal dihedral ones, singly.

$$\left\langle \gamma_{(\frac{3}{4})}^{(7\text{ or }8)D} \left| \frac{\vec{p}}{\vec{m}} \right| \gamma_{(\frac{3}{4})}^{(7\text{ or }8)D} \right\rangle = {}^1/_2 \left\{ \left\langle \gamma_{5a}^{(7\text{ or }8)D} \left| \frac{\vec{p}}{\vec{m}} \right| \gamma_{5a}^{(7\text{ or }8)D} \right\rangle + (\pm)e^{\pi i/4} \left\langle \gamma_{5a}^{(7\text{ or }8)D} \left| \frac{\vec{p}}{\vec{m}} \right| \gamma_{5b}^{(7\text{ or }8)D} \right\rangle + (\pm)e^{-\pi i/4} \left\langle \gamma_{5b}^{(7\text{ or }8)D} \left| \frac{\vec{p}}{\vec{m}} \right| \gamma_{5a}^{(7\text{ or }8)D} \right\rangle + \left\langle \gamma_{5b}^{(7\text{ or }8)D} \left| \frac{\vec{p}}{\vec{m}} \right| \gamma_{5b}^{(7\text{ or }8)D} \right\rangle \right\}$$

$$\left\langle \gamma_{(\frac{3}{4})}^{(8)'D} \left| \frac{\vec{p}}{\vec{m}} \right| \gamma_{(\frac{5}{4})}^{(8)'D} \right\rangle = {}^1/_2 \left\{ \left\langle \gamma_{5a}^{(8)'D} \left| \frac{\vec{p}}{\vec{m}} \right| \gamma_{5a}^{(8)'D} \right\rangle + (\mp)e^{\pi i/4} \left\langle \gamma_{5a}^{(8)'D} \left| \frac{\vec{p}}{\vec{m}} \right| \gamma_{5b}^{(8)'D} \right\rangle + (\mp)e^{-\pi i/4} \left\langle \gamma_{5b}^{(8)'D} \left| \frac{\vec{p}}{\vec{m}} \right| \gamma_{5a}^{(8)'D} \right\rangle + \left\langle \gamma_{5b}^{(8)'D} \left| \frac{\vec{p}}{\vec{m}} \right| \gamma_{5b}^{(8)'D} \right\rangle \right\}$$

$$\left\langle \gamma_{(\frac{3}{4})}^{(8)'D} \left| \frac{\vec{p}}{\vec{m}} \right| \gamma_{(\frac{5}{3})}^{(8)'D} \right\rangle = {}^1/_2 \left\{ \left\langle \gamma_{5a}^{(8)'D} \left| \frac{\vec{p}}{\vec{m}} \right| \gamma_{5a}^{(8)'D} \right\rangle + (\pm)e^{\pi i/4} \left\langle \gamma_{5a}^{(8)'D} \left| \frac{\vec{p}}{\vec{m}} \right| \gamma_{5b}^{(8)'D} \right\rangle + (\mp)e^{-\pi i/4} \left\langle \gamma_{5b}^{(8)'D} \left| \frac{\vec{p}}{\vec{m}} \right| \gamma_{5a}^{(8)'D} \right\rangle + \left\langle \gamma_{5b}^{(8)'D} \left| \frac{\vec{p}}{\vec{m}} \right| \gamma_{5b}^{(8)'D} \right\rangle \right\}$$

$$\left\langle \gamma_{(\frac{3}{4})}^{(8)'D} \left| \frac{\vec{p}}{\vec{m}} \right| \gamma_{(\frac{3}{4})}^{(7\text{ or }8)D} \right\rangle = {}^1/_2 \left\{ \left\langle \gamma_{5a}^{(8)'D} \left| \frac{\vec{p}}{\vec{m}} \right| \gamma_{5a}^{(7\text{ or }8)D} \right\rangle + (\pm)e^{\pi i/4} \left\langle \gamma_{5a}^{(8)'D} \left| \frac{\vec{p}}{\vec{m}} \right| \gamma_{5b}^{(7\text{ or }8)D} \right\rangle + (\mp)e^{-\pi i/4} \left\langle \gamma_{5b}^{(8)'D} \left| \frac{\vec{p}}{\vec{m}} \right| \gamma_{5a}^{(7\text{ or }8)D} \right\rangle + \left\langle \gamma_{5b}^{(8)'D} \left| \frac{\vec{p}}{\vec{m}} \right| \gamma_{5b}^{(7\text{ or }8)D} \right\rangle \right\}$$

(41) The unidigonal (D_1) species γ_3, γ_4 are as defined by E. Fick [*Z. Physik*, **147**, 307 (1957)], $\mathcal{C}_2(x)\gamma_{(\frac{3}{4})}^D = (\pm)i\gamma_{(\frac{3}{4})}^D$, $\mathcal{C}_2(y')\bar{\gamma}_{(\frac{3}{4})}^T = (\pm)i\bar{\gamma}_{(\frac{3}{4})}^T$ and are Kramers' pairs (that is, they are coupled by momentum reversal,[6,13,41] $\mathcal{K}\gamma_{(\frac{3}{4})}^D = \mp\gamma_{(\frac{4}{3})}^D$, $\mathcal{K}\gamma_{(\frac{3}{4})}^{'D} = \pm\gamma_{(\frac{4}{3})}^{'D}$, and $\mathcal{K}\bar{\gamma}_{(\frac{3}{4})}^T = \mp i\gamma_{(\frac{4}{3})}^T$, as[6,13,41] $\mathcal{K}\gamma_{5(\frac{a}{b})}^D = \pm\gamma_{5(\frac{b}{a})}^D$ and $\mathcal{K}\gamma_{6(\frac{a}{b})}^T = \pm\gamma_{6(\frac{b}{a})}^T$, $\mathcal{K}\gamma_{(\frac{4}{3})}^T = \mp i\gamma_{(\frac{5}{4})}^T$). This digonal $\mathcal{C}_2(x)$ symmetry and

$$\left\langle \gamma_{(\frac{3}{4})}^{(8)'D} \left|\frac{\vec{p}}{\vec{m}}\right| \gamma_{(\frac{4}{3})}^{(7\text{ or }8)D} \right\rangle =$$
$$\tfrac{1}{2}\left\{\left\langle \gamma_{6a}^{(8)'D} \left|\frac{\vec{p}}{\vec{m}}\right| \gamma_{6a}^{(7\text{ or }8)D} \right\rangle + (\mp)e^{\pi i/4}\left\langle \gamma_{6a}^{(8)'D} \left|\frac{\vec{p}}{\vec{m}}\right| \gamma_{6b}^{(7\text{ or }8)D} \right\rangle + (\mp)e^{-\pi i/4}\left\langle \gamma_{6b}^{(8)'D} \left|\frac{\vec{p}}{\vec{m}}\right| \gamma_{6a}^{(7\text{ or }8)D} \right\rangle + \left\langle \gamma_{6b}^{(8)'D} \left|\frac{\vec{p}}{\vec{m}}\right| \gamma_{6b}^{(7\text{ or }8)D} \right\rangle\right\}$$

$$\left\langle \bar{\gamma}_{(\frac{3}{4})}^{(7\text{ or }8)T} \left|\frac{\vec{p}}{\vec{m}}\right| \bar{\gamma}_{(\frac{3}{4})}^{(7\text{ or }8)T} \right\rangle =$$
$$\tfrac{1}{2}\left\{\left\langle \gamma_{6a}^{(7\text{ or }8)T} \left|\frac{\vec{p}}{\vec{m}}\right| \gamma_{6a}^{(7\text{ or }8)T} \right\rangle + (\mp)i\left\langle \gamma_{6a}^{(7\text{ or }8)T} \left|\frac{\vec{p}}{\vec{m}}\right| \gamma_{6b}^{(7\text{ or }8)T} \right\rangle + (\pm)i\left\langle \gamma_{6b}^{(7\text{ or }8)T} \left|\frac{\vec{p}}{\vec{m}}\right| \gamma_{6a}^{(7\text{ or }8)T} \right\rangle + \left\langle \gamma_{6b}^{(7\text{ or }8)T} \left|\frac{\vec{p}}{\vec{m}}\right| \gamma_{6b}^{(7\text{ or }8)T} \right\rangle\right\}$$

$$\left\langle \bar{\gamma}_{(\frac{3}{4})}^{(7\text{ or }8)T} \left|\frac{\vec{p}}{\vec{m}}\right| \bar{\gamma}_{(\frac{4}{3})}^{(7\text{ or }8)T} \right\rangle =$$
$$\tfrac{1}{2}\left\{\left\langle \gamma_{6a}^{(7\text{ or }8)T} \left|\frac{\vec{p}}{\vec{m}}\right| \gamma_{6a}^{(7\text{ or }8)T} \right\rangle + (\pm)i\left\langle \gamma_{6a}^{(7\text{ or }8)T} \left|\frac{\vec{p}}{\vec{m}}\right| \gamma_{6b}^{(7\text{ or }8)T} \right\rangle + (\pm)i\left\langle \gamma_{6b}^{(7\text{ or }8)T} \left|\frac{\vec{p}}{\vec{m}}\right| \gamma_{6a}^{(7\text{ or }8)T} \right\rangle - \left\langle \gamma_{6b}^{(7\text{ or }8)T} \left|\frac{\vec{p}}{\vec{m}}\right| \gamma_{6b}^{(7\text{ or }8)T} \right\rangle\right\}$$

$$\left\langle \bar{\gamma}_{(\frac{3}{4})}^{(8)'T} \left|\frac{\vec{p}}{\vec{m}}\right| \gamma_{(\frac{3}{4})}^{(8)'T} \right\rangle = \left\langle \gamma_{(\frac{4}{3})}^{(8)T} \left|\frac{\vec{p}}{\vec{m}}\right| \gamma_{(\frac{4}{3})}^{(8)T} \right\rangle$$

$$\left\langle \bar{\gamma}_{(\frac{3}{4})}^{(8)'T} \left|\frac{\vec{p}}{\vec{m}}\right| \bar{\gamma}_{(\frac{4}{3})}^{(8)'T} \right\rangle = \left\langle \gamma_{(\frac{4}{3})}^{(8)T} \left|\frac{\vec{p}}{\vec{m}}\right| \gamma_{(\frac{4}{3})}^{(8)T} \right\rangle$$

$$\left\langle \bar{\gamma}_{(\frac{3}{4})}^{(8)'T} \left|\frac{\vec{p}}{\vec{m}}\right| \bar{\gamma}_{(\frac{3}{4})}^{(7\text{ or }8)T} \right\rangle =$$
$$\sqrt{\tfrac{1}{2}}\left\{\left\langle \gamma_{(\frac{4}{3})}^{(8)T} \left|\frac{\vec{p}}{\vec{m}}\right| \gamma_{6a}^{(7\text{ or }8)T} \right\rangle + (\mp)i\left\langle \gamma_{(\frac{4}{3})}^{(8)T} \left|\frac{\vec{p}}{\vec{m}}\right| \gamma_{6b}^{(7\text{ or }8)T} \right\rangle\right\}$$

$$\left\langle \bar{\gamma}_{(\frac{3}{4})}^{(8)'T} \left|\frac{\vec{p}}{\vec{m}}\right| \gamma_{(\frac{4}{3})}^{(7\text{ or }8)T} \right\rangle =$$
$$\sqrt{\tfrac{1}{2}}\left\{\left\langle \gamma_{(\frac{4}{3})}^{(8)T} \left|\frac{\vec{p}}{\vec{m}}\right| \gamma_{6a}^{(7\text{ or }8)T} \right\rangle + (\pm)i\left\langle \gamma_{(\frac{4}{3})}^{(8)T} \left|\frac{\vec{p}}{\vec{m}}\right| \gamma_{6b}^{(7\text{ or }8)T} \right\rangle\right\} \quad (69)$$

$$\left\langle \gamma_{(\frac{3}{4})}^{(8)'D}(t_{2g}) \left|\frac{\vec{p}}{\vec{m}}\right| \gamma_{(\frac{3}{4})}^{(7)D}(t_{2g}) \right\rangle =$$
$$(\pm)\frac{i}{\sqrt{6}}\begin{bmatrix} i\bar{l}_{0c} \\ (\bar{m}_{0c}+2\mu_B)\end{bmatrix}\hat{i}$$

$$\left\langle \gamma_{(\frac{3}{4})}^{(8)'D}(t_{2g}) \left|\frac{\vec{p}}{\vec{m}}\right| \gamma_{(\frac{4}{3})}^{(7)D}(t_{2g}) \right\rangle =$$
$$\sqrt{\tfrac{2}{3}}\begin{bmatrix} \Re\mathrm{e}\bar{l}_{0a} \\ 0\end{bmatrix}\hat{k} + (\mp)\frac{i}{\sqrt{6}}\begin{bmatrix} \bar{l}_{0b} \\ -i(\bar{m}_{0b}+2\mu_B)\end{bmatrix}\hat{j}$$

$$\left\langle \gamma_{(\frac{3}{4})}^{(8)'D}(t_{2g}) \left|\frac{\vec{p}}{\vec{m}}\right| \gamma_{(\frac{3}{4})}^{(8)D}(t_{2g}) \right\rangle =$$
$$(\pm)\frac{i}{\sqrt{3}}\begin{bmatrix} i\bar{l}_{0c} \\ (\bar{m}_{0c}-\mu_B)\end{bmatrix}\hat{i}$$

$$\left\langle \gamma_{(\frac{3}{4})}^{(8)'D}(t_{2g}) \left|\frac{\vec{p}}{\vec{m}}\right| \gamma_{(\frac{4}{3})}^{(8)D}(t_{2g}) \right\rangle =$$
$$-\sqrt{\tfrac{1}{3}}\begin{bmatrix} \Re\mathrm{e}\bar{l}_{0a} \\ 0\end{bmatrix}\hat{k} + (\mp)\frac{i}{\sqrt{3}}\begin{bmatrix} \bar{l}_{0b} \\ -i(\bar{m}_{0b}-\mu_B)\end{bmatrix}\hat{j}$$

$$\left\langle \gamma_{(\frac{3}{4})}^{(7)D}(t_{2g}) \left|\frac{\vec{p}}{\vec{m}}\right| \gamma_{(\frac{3}{4})}^{(8)D}(t_{2g}) \right\rangle =$$
$$(\pm)\frac{1}{3\sqrt{2}}\begin{bmatrix} i(\bar{l}_{0c}+2\Re\mathrm{e}\bar{l}_{0c}) \\ (\bar{m}_{0c}+2\mu_B)\end{bmatrix}\hat{i}$$

$$\left\langle \gamma_{(\frac{3}{4})}^{(7)D}(t_{2g}) \left|\frac{\vec{p}}{\vec{m}}\right| \gamma_{(\frac{4}{3})}^{(8)D}(t_{2g}) \right\rangle =$$
$$\frac{\sqrt{2}}{3}\begin{bmatrix} \Im\mathrm{m}\bar{l}_{0a} \\ -(\bar{m}_{0a}+2\mu_B)\end{bmatrix}\hat{k} + (\pm)\frac{1}{3\sqrt{2}}\begin{bmatrix} (\bar{l}_{0b}+2\Re\mathrm{e}\bar{l}_{0b}) \\ -i(\bar{m}_{0b}+2\mu_B)\end{bmatrix}\hat{j}$$

$$\left\langle \gamma_{(\frac{3}{4})}^{(8)'D}(t_{2g}) \left|\frac{\vec{p}}{\vec{m}}\right| \gamma_{(\frac{3}{4})}^{(8)'D}(e_g) \right\rangle = (\pm)\frac{i}{\sqrt{2}}\begin{bmatrix} l_{2a} \\ -im_{2a}\end{bmatrix}\hat{i}$$

$$\left\langle \gamma_{(\frac{3}{4})}^{(8)'D}(t_{2g}) \left|\frac{\vec{p}}{\vec{m}}\right| \gamma_{(\frac{4}{3})}^{(8)'D}(e_g) \right\rangle = (\pm)\frac{i}{\sqrt{2}}\begin{bmatrix} il_{1a} \\ m_{1a}\end{bmatrix}\hat{j}$$

$$\left\langle \gamma_{(\frac{3}{4})}^{(8)'D}(t_{2g}) \left|\frac{\vec{p}}{\vec{m}}\right| \gamma_{(\frac{3}{4})}^{(8)D}(e_g) \right\rangle = (\mp)\frac{1}{\sqrt{2}}\begin{bmatrix} l_{1b} \\ -im_{1b}\end{bmatrix}\hat{i}$$

$$\left\langle \gamma_{(\frac{3}{4})}^{(8)'D}(t_{2g}) \left|\frac{\vec{p}}{\vec{m}}\right| \gamma_{(\frac{4}{3})}^{(8)D}(e_g) \right\rangle = (\pm)\frac{1}{\sqrt{2}}\begin{bmatrix} il_{2b} \\ m_{2b}\end{bmatrix}\hat{j}$$

$$\left\langle \gamma_{(\frac{3}{4})}^{(7)D}(t_{2g}) \left|\frac{\vec{p}}{\vec{m}}\right| \gamma_{(\frac{3}{4})}^{(8)'D}(e_g) \right\rangle = (\pm)\frac{1}{\sqrt{3}}\begin{bmatrix} l_{2a} \\ -im_{2a}\end{bmatrix}\hat{i}$$

$$\left\langle \gamma_{(\frac{3}{4})}^{(7)D}(t_{2g}) \left|\frac{\vec{p}}{\vec{m}}\right| \gamma_{(\frac{4}{3})}^{(8)'D}(e_g) \right\rangle = (\pm)\frac{1}{\sqrt{3}}\begin{bmatrix} il_{1a} \\ m_{1a}\end{bmatrix}\hat{j}$$

trigonal $\mathcal{C}_2(y')$ symmetry establishes that all matrix members of the type $\langle\vec{v}\rangle_{33\text{ or }44}$ and $\langle\vec{v}\rangle_{34\text{ or }43}$ between unidigonal γ_3 and γ_4 type molecular spin orbitals are parallel and perpendicular, respectively, to the digonal $\hat{i}$ and the trigonal $\hat{j}'$ axes, as the case may be, regardless of their cubic origin, γ_7, γ_8, t_{2g}, or e_g [*cf.* eq. 70 and 72].

$$\left\langle \gamma_{(\frac{3}{4})}^{(7)D}(t_{2g}) \left| \frac{\vec{p}}{\vec{m}} \right| \gamma_{(\frac{3}{4})}^{(8)D}(e_g) \right\rangle = (\mp)\frac{i}{\sqrt{3}}\begin{bmatrix} l_{1b} \\ -im_{1b} \end{bmatrix}\hat{i}$$

$$\left\langle \gamma_{(\frac{3}{4})}^{(7)D}(t_{2g}) \left| \frac{\vec{p}}{\vec{m}} \right| \gamma_{(\frac{4}{3})}^{(8)D}(e_g) \right\rangle = -\sqrt{1/3}\begin{bmatrix} il_{0b} \\ m_{0b} \end{bmatrix}\hat{k} + (\mp)\frac{i}{\sqrt{3}}\begin{bmatrix} il_{2b} \\ m_{2b} \end{bmatrix}\hat{j}$$

$$\left\langle \gamma_{(\frac{3}{4})}^{(8)D}(t_{2g}) \left| \frac{\vec{p}}{\vec{m}} \right| \gamma_{(\frac{3}{4})}^{(8)'D}(e_g) \right\rangle = (\mp)\frac{1}{\sqrt{6}}\begin{bmatrix} l_{2a} \\ -im_{2a} \end{bmatrix}\hat{i}$$

$$\left\langle \gamma_{(\frac{3}{4})}^{(8)D}(t_{2g}) \left| \frac{\vec{p}}{\vec{m}} \right| \gamma_{(\frac{4}{3})}^{(8)'D}(e_g) \right\rangle = (\mp)\frac{1}{\sqrt{6}}\begin{bmatrix} il_{1a} \\ m_{1a} \end{bmatrix}\hat{j}$$

$$\left\langle \gamma_{(\frac{3}{4})}^{(8)D}(t_{2g}) \left| \frac{\vec{p}}{\vec{m}} \right| \gamma_{(\frac{3}{4})}^{(8)D}(e_g) \right\rangle = (\pm)\frac{i}{\sqrt{6}}\begin{bmatrix} l_{1b} \\ -im_{1b} \end{bmatrix}\hat{i}$$

$$\left\langle \gamma_{(\frac{3}{4})}^{(8)D}(t_{2g}) \left| \frac{\vec{p}}{\vec{m}} \right| \gamma_{(\frac{4}{3})}^{(8)D}(e_g) \right\rangle = -\sqrt{2/3}\begin{bmatrix} il_{0b} \\ m_{0b} \end{bmatrix}\hat{k} + (\pm)\frac{i}{\sqrt{6}}\begin{bmatrix} il_{2b} \\ m_{2b} \end{bmatrix}\hat{j}$$

$$\left\langle \gamma_{(\frac{3}{4})}^{(8)'D}(e_g) \left| \frac{\vec{p}}{\vec{m}} \right| \gamma_{(\frac{3}{4})}^{(8)'D}(e_g) \right\rangle = (\pm)\begin{bmatrix} 0 \\ \mu_B \end{bmatrix}\hat{i}$$

$$\left\langle \gamma_{(\frac{3}{4})}^{(8)'D}(e_g) \left| \frac{\vec{p}}{\vec{m}} \right| \gamma_{(\frac{4}{3})}^{(8)'D}(e_g) \right\rangle = -\begin{bmatrix} 0 \\ \mu_B \end{bmatrix}\hat{k} + (\mp)\begin{bmatrix} 0 \\ i\mu_B \end{bmatrix}\hat{j}$$

$$\left\langle \gamma_{(\frac{3}{4})}^{(8)'D}(e_g) \left| \frac{\vec{p}}{\vec{m}} \right| \gamma_{(\frac{3}{4})}^{(8)D}(e_g) \right\rangle = 0$$

$$\left\langle \gamma_{(\frac{3}{4})}^{(8)'D}(e_g) \left| \frac{\vec{p}}{\vec{m}} \right| \gamma_{(\frac{4}{3})}^{(8)D}(e_g) \right\rangle = \begin{bmatrix} \bar{l}_0 \\ -i\bar{m}_0 \end{bmatrix}\hat{k}$$

$$\left\langle \gamma_{(\frac{3}{4})}^{(8)D}(e_g) \left| \frac{\vec{p}}{\vec{m}} \right| \gamma_{(\frac{4}{3})}^{(8)D}(e_g) \right\rangle = (\mp)\begin{bmatrix} 0 \\ \mu_B \end{bmatrix}\hat{i}$$

$$\left\langle \gamma_{(\frac{3}{4})}^{(8)D}(e_g) \left| \frac{\vec{p}}{\vec{m}} \right| \gamma_{(\frac{4}{3})}^{(8)D}(e_g) \right\rangle = -\begin{bmatrix} 0 \\ \mu_B \end{bmatrix}\hat{k} + (\pm)\begin{bmatrix} 0 \\ \mu_B \end{bmatrix}\hat{j}$$

$$\left\langle \gamma_{(\frac{3}{4})}^{(8)'D}(t_{2g}) \left| \frac{\vec{p}}{\vec{m}} \right| \gamma_{(\frac{3}{4})}^{(8)'D}(t_{2g}) \right\rangle = 0$$

$$\left\langle \gamma_{(\frac{3}{4})}^{(8)'D}(t_{2g}) \left| \frac{\vec{p}}{\vec{m}} \right| \gamma_{(\frac{4}{3})}^{(8)'D}(t_{2g}) \right\rangle = \begin{bmatrix} \Im m\bar{l}_{0a} \\ -(\bar{m}_{0a} - \mu_B) \end{bmatrix}\hat{k}$$

$$\left\langle \gamma_{(\frac{3}{4})}^{(7)D}(t_{2g}) \left| \frac{\vec{p}}{\vec{m}} \right| \gamma_{(\frac{3}{4})}^{(7)D}(t_{2g}) \right\rangle = (\pm)^1/_3\begin{bmatrix} -2\Im m\bar{l}_{0c} \\ (2\bar{m}_{0c} + \mu_B) \end{bmatrix}\hat{i}$$

$$\left\langle \gamma_{(\frac{3}{4})}^{(7)D}(t_{2g}) \left| \frac{\vec{p}}{\vec{m}} \right| \gamma_{(\frac{4}{3})}^{(7)D}(t_{2g}) \right\rangle = -1/_3\begin{bmatrix} 2\Im m\bar{l}_{0a} \\ -(2\bar{m}_{0a} + \mu_B) \end{bmatrix}\hat{k} + (\pm)\frac{i}{3}\begin{bmatrix} 2\Im m\bar{l}_{0b} \\ -(2\bar{m}_{0b} + \mu_B) \end{bmatrix}\hat{j}$$

$$\left\langle \gamma_{(\frac{3}{4})}^{(8)D}(t_{2g}) \left| \frac{\vec{p}}{\vec{m}} \right| \gamma_{(\frac{3}{4})}^{(8)D}(t_{2g}) \right\rangle = (\pm)^2/_3\begin{bmatrix} \Im m\bar{l}_{0c} \\ -(\bar{m}_{0c} - \mu_B) \end{bmatrix}\hat{i}$$

$$\left\langle \gamma_{(\frac{3}{4})}^{(8)D}(t_{2g}) \left| \frac{\vec{p}}{\vec{m}} \right| \gamma_{(\frac{4}{3})}^{(8)D}(t_{2g}) \right\rangle = -1/_3\begin{bmatrix} \Im m\bar{l}_{0a} \\ -(\bar{m}_{0a} - \mu_B) \end{bmatrix}\hat{k} + (\mp)\frac{2i}{3}\begin{bmatrix} \Im m\bar{l}_{0b} \\ -(\bar{m}_{0b} - \mu_B) \end{bmatrix}\hat{j} \tag{70}$$

$$\mathcal{W}[\gamma_{(\frac{3}{4})}^{(8)'D}(t_{2g}) \longrightarrow \gamma_{(\frac{3}{4})}^{(7)D}(t_{2g})] = {}^1/_6\bar{g}_{0c}(\bar{m}_{0c} + 2\mu_B)$$

$$\mathfrak{X}[\gamma_{(\frac{3}{4})}^{(8)'D}(t_{2g}) \longrightarrow \gamma_{(\frac{3}{4})}^{(7)D}(t_{2g})] = {}^1/_6\bar{g}_{0c}{}^2$$

$$\mathfrak{M}[\gamma_{(\frac{3}{4})}^{(8)'D}(t_{2g}) \longrightarrow \gamma_{(\frac{3}{4})}^{(7)D}(t_{2g})] = {}^1/_6(\bar{m}_{0c} + 2\mu_B)^2$$

$$\mathcal{W}[\gamma_{(\frac{3}{4})}^{(8)'D}(t_{2g}) \longrightarrow \gamma_{(\frac{4}{3})}^{(7)D}(t_{2g})] = {}^1/_6\bar{g}_b(\bar{m}_{0b} + 2\mu_B)$$

$$\mathfrak{X}[\gamma_{(\frac{3}{4})}^{(8)'D}(t_{2g}) \longrightarrow \gamma_{(\frac{4}{3})}^{(7)D}(t_{2g})] = ({}^2/_3\bar{r}_{0a}{}^2 \text{ or } 0) + {}^1/_6\bar{g}_{0b}{}^2$$

$$\mathfrak{M}[\gamma_{(\frac{3}{4})}^{(8)'D}(t_{2g}) \longrightarrow \gamma_{(\frac{4}{3})}^{(7)D}(t_{2g})] = {}^1/_6(\bar{m}_{0b} + 2\mu_B)^2$$

$$\mathcal{W}[\gamma_{(\frac{3}{4})}^{(8)'D}(t_{2g}) \longrightarrow \gamma_{(\frac{4}{3})}^{(8)D}(t_{2g})] = {}^1/_3\bar{g}_{0c}(\bar{m}_{0c} - \mu_B)$$

$$\mathfrak{X}[\gamma_{(\frac{3}{4})}^{(8)'D}(t_{2g}) \longrightarrow \gamma_{(\frac{3}{4})}^{(8)D}(t_{2g})] = {}^1/_3\bar{g}_{0c}{}^2$$

$$\mathfrak{M}[\gamma_{(\frac{3}{4})}^{(8)'D}(t_{2g}) \longrightarrow \gamma_{(\frac{3}{4})}^{(8)D}(t_{2g})] = {}^1/_3(\bar{m}_{0c} - \mu_B)^2$$

$$\mathcal{W}[\gamma_{(\frac{3}{4})}^{(8)'D}(t_{2g}) \longrightarrow \gamma_{(\frac{4}{3})}^{(8)D}(t_{2g})] = {}^1/_3\bar{g}_{0b}(\bar{m}_{0b} - \mu_B)$$

$$\mathfrak{X}[\gamma_{(\frac{3}{4})}^{(8)'D}(t_{2g}) \longrightarrow \gamma_{(\frac{4}{3})}^{(8)D}(t_{2g})] = ({}^1/_3\bar{r}_{0a}{}^2 \text{ or } 0) + {}^1/_3\bar{g}_{0b}{}^2$$

$$\mathfrak{M}[\gamma_{(\frac{3}{4})}^{(8)'D}(t_{2g}) \longrightarrow \gamma_{(\frac{4}{3})}^{(8)D}(t_{2g})] = {}^1/_3(\bar{m}_{0b} - \mu_B)^2$$

$$\mathcal{W}[\gamma_{(\frac{3}{4})}^{(7)D}(t_{2g}) \longrightarrow \gamma_{(\frac{3}{4})}^{(8)D}(t_{2g})] = {}^1/_6\bar{r}_{0c}(\bar{m}_{0c} + 2\mu_B) \text{ or } {}^1/_{18}\bar{p}_{0c}(\bar{m}_{0c} + 2\mu_B)$$

$$\mathfrak{X}[\gamma_{(\frac{3}{4})}^{(7)D}(t_{2g}) \longrightarrow \gamma_{(\frac{3}{4})}^{(8)D}(t_{2g})] = {}^1/_2\bar{r}_{0c}{}^2 \text{ or } {}^1/_{18}\bar{p}_{0c}{}^2$$

$$\mathfrak{M}[\gamma_{(\frac{3}{4})}^{(7)D}(t_{2g}) \longrightarrow \gamma_{(\frac{3}{4})}^{(8)D}(t_{2g})] = {}^1/_{18}(\bar{m}_{0c}{}^2 + 2\mu_B)^2$$

$$\mathcal{W}[\gamma_{(\frac{3}{4})}^{(7)D}(t_{2g}) \longrightarrow \gamma_{(\frac{4}{3})}^{(8)D}(t_{2g})] = {}^1/_6\bar{r}_{0b}(\bar{m}_{0b} + 2\mu_B) \text{ or } {}^2/_9\bar{p}_{0a}(\bar{m}_{0a} + 2\mu_B) + {}^1/_{18}\bar{p}_{0b}(\bar{m}_{0b} + 2\mu_B)$$

$$\mathfrak{X}[\gamma_{(\frac{3}{4})}^{(7)D}(t_{2g}) \longrightarrow \gamma_{(\frac{4}{3})}^{(8)D}(t_{2g})] = {}^1/_2\bar{r}_{0b}{}^2 \text{ or } {}^2/_9\bar{p}_{0a}{}^2 + {}^1/_{18}\bar{p}_{0b}{}^2$$

$$\mathfrak{M}[\gamma_{(\frac{3}{4})}^{(7)D}(t_{2g}) \longrightarrow \gamma_{(\frac{4}{3})}^{(8)D}(t_{2g})] = {}^2/_9(\bar{m}_{0a} + 2\mu_B)^2 + {}^1/_{18}(\bar{m}_{0b} + 2\mu_B)^2$$

$$\mathcal{W}[\gamma_{(\frac{3}{4})}^{(8)'D}(t_{2g}) \longrightarrow \gamma_{(\frac{3}{4})}^{(8)'D}(e_g)] = {}^1/_2g_{2a}m_{2a}$$

$$\mathfrak{X}[\gamma_{(\frac{3}{4})}^{(8)'D}(t_{2g}) \longrightarrow \gamma_{(\frac{3}{4})}^{(8)'D}(e_g)] = {}^1/_2 g_{2a}^2$$

$$\mathfrak{M}[\gamma_{(\frac{3}{4})}^{(8)'D}(t_{2g}) \longrightarrow \gamma_{(\frac{3}{4})}^{(8)'D}(e_g)] = {}^1/_2 m_{2a}^2$$

$$\mathfrak{W}[\gamma_{(\frac{3}{4})}^{(8)'D}(t_{2g}) \longrightarrow \gamma_{(\frac{4}{3})}^{(8)'D}(e_g)] = {}^1/_2 g_{1a} m_{1a}$$

$$\mathfrak{X}[\gamma_{(\frac{3}{4})}^{(8)'D}(t_{2g}) \longrightarrow \gamma_{(\frac{4}{3})}^{(8)'D}(e_g)] = {}^1/_2 g_{1a}^2$$

$$\mathfrak{M}[\gamma_{(\frac{3}{4})}^{(8)'D}(t_{2g}) \longrightarrow \gamma_{(\frac{4}{3})}^{(8)'D}(e_g)] = {}^1/_2 m_{1a}^2$$

$$\mathfrak{W}[\gamma_{(\frac{3}{4})}^{(8)'D}(t_{2g}) \longrightarrow \gamma_{(\frac{3}{4})}^{(8)D}(e_g)] = {}^1/_2 g_{1b} m_{1b}$$

$$\mathfrak{X}[\gamma_{(\frac{3}{4})}^{(8)'D}(t_{2g}) \longrightarrow \gamma_{(\frac{3}{4})}^{(8)D}(e_g)] = {}^1/_2 g_{1b}^2$$

$$\mathfrak{M}[\gamma_{(\frac{3}{4})}^{(8)'D}(t_{2g}) \longrightarrow \gamma_{(\frac{3}{4})}^{(8)D}(e_g)] = {}^1/_2 m_{1b}^2$$

$$\mathfrak{W}[\gamma_{(\frac{3}{4})}^{(8)'D}(t_{2g}) \longrightarrow \gamma_{(\frac{4}{3})}^{(8)D}(e_g)] = {}^1/_2 g_{2b} m_{2b}$$

$$\mathfrak{X}[\gamma_{(\frac{3}{4})}^{(8)'D}(t_{2g}) \longrightarrow \gamma_{(\frac{4}{3})}^{(8)D}(e_g)] = {}^1/_2 g_{2b}^2$$

$$\mathfrak{M}[\gamma_{(\frac{3}{4})}^{(8)'D}(t_{2g}) \longrightarrow \gamma_{(\frac{4}{3})}^{(8)D}(e_g)] = {}^1/_2 m_{2b}^2$$

$$\mathfrak{W}[\gamma_{(\frac{3}{4})}^{(7)D}(t_{2g}) \longrightarrow \gamma_{(\frac{3}{4})}^{(8)'D}(e_g)] = {}^1/_3 g_{2a} m_{2a}$$

$$\mathfrak{X}[\gamma_{(\frac{3}{4})}^{(7)D}(t_{2g}) \longrightarrow \gamma_{(\frac{3}{4})}^{(8)'D}(e_g)] = {}^1/_3 g_{2a}^2$$

$$\mathfrak{M}[\gamma_{(\frac{3}{4})}^{(7)D}(t_{2g}) \longrightarrow \gamma_{(\frac{3}{4})}^{(8)'D}(e_g)] = {}^1/_3 m_{2a}^2$$

$$\mathfrak{W}[\gamma_{(\frac{3}{4})}^{(7)D}(t_{2g}) \longrightarrow \gamma_{(\frac{4}{3})}^{(8)'D}(e_g)] = {}^1/_3 g_{1a} m_{1a}$$

$$\mathfrak{X}[\gamma_{(\frac{3}{4})}^{(7)D}(t_{2g}) \longrightarrow \gamma_{(\frac{4}{3})}^{(8)'D}(e_g)] = {}^1/_3 g_{1a}^2$$

$$\mathfrak{M}[\gamma_{(\frac{3}{4})}^{(7)D}(t_{2g}) \longrightarrow \gamma_{(\frac{4}{3})}^{(8)'D}(e_g)] = {}^1/_3 m_{1a}^2$$

$$\mathfrak{W}[\gamma_{(\frac{3}{4})}^{(7)D}(t_{2g}) \longrightarrow \gamma_{(\frac{3}{4})}^{(8)D}(e_g)] = {}^1/_3 g_{1b} m_{1b}$$

$$\mathfrak{X}[\gamma_{(\frac{3}{4})}^{(7)D}(t_{2g}) \longrightarrow \gamma_{(\frac{3}{4})}^{(8)D}(e_g)] = {}^1/_3 g_{1b}^2$$

$$\mathfrak{M}[\gamma_{(\frac{3}{4})}^{(7)D}(t_{2g}) \longrightarrow \gamma_{(\frac{3}{4})}^{(8)D}(e_g)] = {}^1/_3 m_{1b}^2$$

$$\mathfrak{W}[\gamma_{(\frac{3}{4})}^{(7)D}(t_{2g}) \longrightarrow \gamma_{(\frac{4}{3})}^{(8)D}(e_g)] = {}^1/_3\{g_{0b} m_{0b} + g_{2b} m_{2b}\}$$

$$\mathfrak{X}[\gamma_{(\frac{3}{4})}^{(7)D}(t_{2g}) \longrightarrow \gamma_{(\frac{4}{3})}^{(8)D}(e_g)] = {}^1/_3\{g_{0b}^2 + g_{2b}^2\}$$

$$\mathfrak{M}[\gamma_{(\frac{3}{4})}^{(7)D}(t_{2g}) \longrightarrow \gamma_{(\frac{4}{3})}^{(8)D}(e_g)] = {}^1/_3\{m_{0b}^2 + m_{2b}^2\}$$

$$\mathfrak{W}[\gamma_{(\frac{3}{4})}^{(8)D}(t_{2g}) \longrightarrow \gamma_{(\frac{3}{4})}^{(8)'D}(e_g)] = {}^1/_6 g_{2a} m_{2a}$$

$$\mathfrak{X}[\gamma_{(\frac{3}{4})}^{(8)D}(t_{2g}) \longrightarrow \gamma_{(\frac{3}{4})}^{(8)'D}(e_g)] = {}^1/_6 g_{2a}^2$$

$$\mathfrak{M}[\gamma_{(\frac{3}{4})}^{(8)D}(t_{2g}) \longrightarrow \gamma_{(\frac{3}{4})}^{(8)'D}(e_g)] = {}^1/_6 m_{2a}^2$$

$$\mathfrak{W}[\gamma_{(\frac{3}{4})}^{(8)D}(t_{2g}) \longrightarrow \gamma_{(\frac{4}{3})}^{(8)'D}(e_g)] = {}^1/_6 g_{1a} m_{1a}$$

$$\mathfrak{X}[\gamma_{(\frac{3}{4})}^{(8)D}(t_{2g}) \longrightarrow \gamma_{(\frac{4}{3})}^{(8)'D}(e_g)] = {}^1/_6 g_{1a}^2$$

$$\mathfrak{M}[\gamma_{(\frac{3}{4})}^{(8)D}(t_{2g}) \longrightarrow \gamma_{(\frac{4}{3})}^{(8)'D}(e_g)] = {}^1/_6 m_{1a}^2$$

$$\mathfrak{W}[\gamma_{(\frac{3}{4})}^{(8)D}(t_{2g}) \longrightarrow \gamma_{(\frac{3}{4})}^{(8)D}(e_g)] = {}^1/_6 g_{1b} m_{1b}$$

$$\mathfrak{X}[\gamma_{(\frac{3}{4})}^{(8)D}(t_{2g}) \longrightarrow \gamma_{(\frac{3}{4})}^{(8)D}(e_g)] = {}^1/_6 g_{1b}^2$$

$$\mathfrak{M}[\gamma_{(\frac{3}{4})}^{(8)D}(t_{2g}) \longrightarrow \gamma_{(\frac{3}{4})}^{(8)D}(e_g)] = {}^1/_6 m_{1b}^2$$

$$\mathfrak{W}[\gamma_{(\frac{3}{4})}^{(8)D}(t_{2g}) \longrightarrow \gamma_{(\frac{4}{3})}^{(8)D}(e_g)] = {}^2/_3 g_{0b} m_{0b} + {}^1/_6 g_{2b} m_{2b}$$

$$\mathfrak{X}[\gamma_{(\frac{3}{4})}^{(8)D}(t_{2g}) \longrightarrow \gamma_{(\frac{4}{3})}^{(8)D}(e_g)] = {}^2/_3 g_{0b}^2 + {}^1/_6 g_{2b}^2$$

$$\mathfrak{M}[\gamma_{(\frac{3}{4})}^{(8)D}(t_{2g}) \longrightarrow \gamma_{(\frac{4}{3})}^{(8)D}(e_g)] = {}^2/_3 m_{0b}^2 + {}^1/_6 m_{2b}^2$$

$$\mathfrak{W}[\gamma_{(\frac{3}{4})}^{(8)'D}(e_g) \longrightarrow \gamma_{(\frac{3}{4})}^{(8)'D}(e_g)] = \mathfrak{X}[\gamma_{(\frac{3}{4})}^{(8)'D}(e_g) \longrightarrow \gamma_{(\frac{3}{4})}^{(8)'D}(e_g)] = 0$$

$$\mathfrak{M}[\gamma_{(\frac{3}{4})}^{(8)'D}(e_g) \longrightarrow \gamma_{(\frac{3}{4})}^{(8)'D}(e_g)] = \mu_B^2$$

$$\mathfrak{W}[\gamma_{(\frac{3}{4})}^{(8)'D}(e_g) \longrightarrow \gamma_{(\frac{4}{3})}^{(8)'D}(e_g)] = \mathfrak{X}[\gamma_{(\frac{3}{4})}^{(8)'D}(e_g) \longrightarrow \gamma_{(\frac{4}{3})}^{(8)'D}(e_g)] = 0$$

$$\mathfrak{M}[\gamma_{(\frac{3}{4})}^{(8)'D}(e_g) \longrightarrow \gamma_{(\frac{4}{3})}^{(8)'D}(e_g)] = 2\mu_B^2$$

$$\mathfrak{W}[\gamma_{(\frac{3}{4})}^{(8)'D}(e_g) \longrightarrow \gamma_{(\frac{3}{4})}^{(8)D}(e_g)] = \mathfrak{X}[\gamma_{(\frac{3}{4})}^{(8)'D}(e_g)] \longrightarrow \gamma_{(\frac{3}{4})}^{(8)D}(e_g)] = \mathfrak{M}[\gamma_{(\frac{3}{4})}^{(8)'D}(e_g) \longrightarrow \gamma_{(\frac{3}{4})}^{(8)D}(e_g)] = 0$$

$$\mathfrak{W}[\gamma_{(\frac{3}{4})}^{(8)'D}(e_g) \longrightarrow \gamma_{(\frac{4}{3})}^{(8)D}(e_g)] = \bar{g}_0 \bar{\bar{m}}_0$$

$$\mathfrak{X}[\gamma_{(\frac{3}{4})}^{(8)'D}(e_g) \longrightarrow \gamma_{(\frac{4}{3})}^{(8)D}(e_g)] = \bar{g}_0^2$$

$$\mathfrak{M}[\gamma_{(\frac{3}{4})}^{(8)'D}(e_g) \longrightarrow \gamma_{(\frac{4}{3})}^{(8)D}(e_g)] = \bar{\bar{m}}_0^2$$

$$\mathfrak{W}[\gamma_{(\frac{3}{4})}^{(8)D}(e_g) \longrightarrow \gamma_{(\frac{3}{4})}^{(8)D}(e_g)] = \mathfrak{X}[\gamma_{(\frac{3}{4})}^{(8)D}(e_g) \longrightarrow \gamma_{(\frac{3}{4})}^{8(D)}(e_g)] = 0$$

$$\mathfrak{M}[\gamma_{(\frac{3}{4})}^{(8)D}(e_g) \longrightarrow \gamma_{(\frac{3}{4})}^{(8)D}(e_g)] = \mu_B^2$$

$$\mathfrak{W}[\gamma_{(\frac{3}{4})}^{(8)D}(e_g) \longrightarrow \gamma_{(\frac{4}{3})}^{(8)D}(e_g)] = \mathfrak{X}[\gamma_{(\frac{3}{4})}^{(8)D}(e_g) \longrightarrow \gamma_{(\frac{4}{3})}^{(8)D}(e_g)] = 0$$

$$\mathfrak{M}[\gamma_{(\frac{3}{4})}^{(8)D}(e_g) \longrightarrow \gamma_{(\frac{4}{3})}^{(8)D}(e_g)] = 2\mu_B^2$$

$$\mathfrak{W}[\gamma_{(\frac{3}{4})}^{(8)'D}(t_{2g}) \longrightarrow \gamma_{(\frac{3}{4})}^{(8)'D}(t_{2g})] = \mathfrak{X}[\gamma_{(\frac{3}{4})}^{(8)'D}(t_{2g}) \longrightarrow \gamma_{(\frac{3}{4})}^{(8)'D}(t_{2g})] = \mathfrak{M}[\gamma_{(\frac{3}{4})}^{(8)'D}(t_{2g}) \longrightarrow \gamma_{(\frac{3}{4})}^{(8)'D}(t_{2g})] = 0$$

$$\mathfrak{W}[\gamma_{(\frac{3}{4})}^{(8)'D}(t_{2g}) \longrightarrow \gamma_{(\frac{4}{3})}^{(8)'D}(t_{2g})] = 0 \text{ or } \bar{p}_{0a}(\bar{m}_{0a} - \mu_B)$$

$$\mathfrak{X}[\gamma_{(\frac{3}{4})}^{(8)'D}(t_{2g}) \longrightarrow \gamma_{(\frac{4}{3})}^{(8)'D}(t_{2g})] = 0 \text{ or } \bar{p}_{0a}^2$$

$$\mathfrak{M}[\gamma_{(\frac{3}{4})}^{(8)'D}(t_{2g}) \longrightarrow \gamma_{(\frac{4}{3})}^{(8)'D}(t_{2g})] = (\bar{m}_{0a} - \mu_B)^2$$

$$\mathfrak{W}[\gamma_{(\frac{3}{4})}^{(7)D}(t_{2g}) \longrightarrow \gamma_{(\frac{3}{4})}^{(7)D}(t_{2g})] = 0 \text{ or } {}^2/_9 \bar{p}_{0c}(2\bar{m}_{0c} + \mu_B)$$

$$\mathfrak{X}[\gamma_{(\frac{3}{4})}^{(7)D}(t_{2g}) \longrightarrow \gamma_{(\frac{3}{4})}^{(7)D}(t_{2g}) = 0 \text{ or } {}^4/_9 \bar{p}_{0c}^2$$

$$\mathfrak{M}[\gamma_{(\frac{3}{4})}^{(7)D}(t_{2g}) \longrightarrow \gamma_{(\frac{3}{4})}^{(7)D}(t_{2g})] = {}^1/_9(2\bar{m}_{0c} + \mu_B)^2$$

$$\mathfrak{W}[\gamma_{(\frac{3}{4})}^{(7)D}(t_{2g}) \longrightarrow \gamma_{(\frac{4}{3})}^{(7)D}(t_{2g})] = 0 \text{ or } {}^2/_9\{\bar{p}_{0a}(2\bar{m}_{0a} + \mu_B) + \bar{p}_{0b}(2\bar{m}_{0b} + \mu_B)\}$$

$$\mathfrak{X}[\gamma_{(\frac{3}{4})}^{(7)D}(t_{2g}) \longrightarrow \gamma_{(\frac{4}{3})}^{(7)D}(t_{2g})] = 0 \text{ or } {}^4/_9\{\bar{p}_{0a}^2 + \bar{p}_{0b}^2\}$$

$$\mathfrak{M}[\gamma_{(\frac{3}{4})}^{(7)D}(t_{2g}) \longrightarrow \gamma_{(\frac{4}{3})}^{(7)D}(t_{2g})] = {}^1/_9\{(2\bar{m}_{0a} + \mu_B)^2 + (2\bar{m}_{0b} + \mu_B)^2\}$$

$$\mathfrak{W}[\gamma_{(\frac{3}{4})}^{(8)D}(t_{2g}) \longrightarrow \gamma_{(\frac{3}{4})}^{(8)D}(t_{2g})] = 0 \text{ or } {}^4/_9 \bar{p}_{0c}(\bar{m}_{0c} - \mu_B)$$

$$\mathfrak{X}[\gamma_{(\frac{3}{4})}^{(8)D}(t_{2g}) \longrightarrow \gamma_{(\frac{3}{4})}^{(8)D}(t_{2g})] = 0 \text{ or } {}^4/_9 \bar{p}_{0c}^2$$

$$\mathfrak{M}[\gamma_{(\frac{3}{4})}^{(8)D}(t_{2g}) \longrightarrow \gamma_{(\frac{3}{4})}^{(8)D}(t_{2g})] = {}^{4}/_{9}(\bar{m}_{0c} - \mu_B)^2$$

$$\mathfrak{W}[\gamma_{(\frac{3}{4})}^{(8)D}(t_{2g}) \longrightarrow \gamma_{(\frac{4}{3})}^{(8)D}(t_{2g})] =$$
$$0 \text{ or } {}^{1}/_{9}\bar{p}_{0a}(\bar{m}_{0a} - \mu_B) + {}^{4}/_{9}\bar{p}_{0b}(\bar{m}_{0b} - \mu_B)$$

$$\mathfrak{X}[\gamma_{(\frac{3}{4})}^{(8)D}(t_{2g}) \longrightarrow \gamma_{(\frac{4}{3})}^{(8)D}(t_{2g})] =$$
$$0 \text{ or } {}^{1}/_{9}\bar{p}_{0a}{}^2 + {}^{4}/_{9}\bar{p}_{0b}{}^2$$

$$\mathfrak{M}[\gamma_{(\frac{3}{4})}^{(8)D}(t_{2g}) \longrightarrow \gamma_{(\frac{4}{3})}^{(8)D}(t_{2g})] =$$
$${}^{1}/_{9}(\bar{m}_{0c} - \mu_B)^2 + {}^{4}/_{9}(\bar{m}_{0b} - \mu_B)^2 \quad (71)$$

$$\left\langle \bar{\gamma}_{(\frac{3}{4})}^{(8)T}(t_{2g}) \left|\frac{\vec{p}}{\vec{m}}\right| \bar{\gamma}_{(\frac{3}{4})}^{(7)T}(t_{2g}) \right\rangle =$$
$$(\pm)\frac{1}{\sqrt{2}}\begin{bmatrix} -i\bar{l}_0 \\ {}^{1}/_{3}(\bar{m}_0 + 2\mu_B)\end{bmatrix}\hat{\jmath}'$$

$$\left\langle \bar{\gamma}_{(\frac{3}{4})}^{(8)T}(t_{2g}) \left|\frac{\vec{p}}{\vec{m}}\right| \bar{\gamma}_{(\frac{4}{3})}^{(7)T}(t_{2g}) \right\rangle =$$
$$\frac{\sqrt{2}}{3}\begin{bmatrix} i\bar{l}_0{}^{\ddagger} \\ (\bar{m}_0{}^{\ddagger} + 2\mu_B)\end{bmatrix}\hat{k}' + (\pm)\frac{i}{\sqrt{2}}\begin{bmatrix} -i\bar{l}_0 \\ {}^{1}/_{3}(\bar{m}_0 + 2\mu_B)\end{bmatrix}\hat{\imath}'$$

$$\left\langle \bar{\gamma}_{(\frac{3}{4})}^{(8)T}(t_{2g}) \left|\frac{\vec{p}}{\vec{m}}\right| \bar{\gamma}_{(\frac{3}{4})}^{(8)'T}(t_{2g}) \right\rangle =$$
$$(\pm)\frac{e^{\pm i\beta/4}}{\sqrt{6}}\begin{bmatrix} i(\sqrt{2}\bar{l}_0 + (\pm)i^{\ddagger} \\ -\sqrt{2}(\bar{m}_0 - \mu_B)\end{bmatrix}\hat{\jmath}'$$

$$\left\langle \bar{\gamma}_{(\frac{3}{4})}^{(8)T}(t_{2g}) \left|\frac{\vec{p}}{\vec{m}}\right| \bar{\gamma}_{(\frac{4}{3})}^{(8)'T}(t_{2g}) \right\rangle =$$
$$(\pm)\frac{e^{\mp i\beta/4}}{\sqrt{6}}\begin{bmatrix} (\sqrt{2}\bar{l}_0 + (\mp)i\bar{l}_0{}^{\ddagger}) \\ i\sqrt{2}(\bar{m}_0 - \mu_B)\end{bmatrix}\hat{\imath}'$$

$$\left\langle \bar{\gamma}_{(\frac{3}{4})}^{(7)T}(t_{2g}) \left|\frac{\vec{p}}{\vec{m}}\right| \bar{\gamma}_{(\frac{3}{4})}^{(8)'T}(t_{2g}) \right\rangle =$$
$$(\mp)\frac{e^{\pm i\beta/4}}{\sqrt{6}}\begin{bmatrix} i(\bar{l}_0 + (\mp)i\sqrt{2}\bar{l}_0{}^{\ddagger}) \\ -(\bar{m}_0 + 2\mu_B)\end{bmatrix}\hat{\jmath}'$$

$$\left\langle \bar{\gamma}_{(\frac{3}{4})}^{(7)T}(t_{2g}) \left|\frac{\vec{p}}{\vec{m}}\right| \bar{\gamma}_{(\frac{4}{3})}^{(8)'T}(t_{2g}) \right\rangle =$$
$$(\mp)\frac{e^{\mp i\beta/4}}{\sqrt{6}}\begin{bmatrix} (\bar{l}_0 + (\pm)i\sqrt{2}\bar{l}_0{}^{\ddagger}) \\ i(\bar{m}_0 + 2\mu_B)\end{bmatrix}\hat{\imath}'$$

$$\left\langle \bar{\gamma}_{(\frac{3}{4})}^{(8)'T}(t_{2g}) \left|\frac{\vec{p}}{\vec{m}}\right| \bar{\gamma}_{(\frac{3}{4})}^{(8)'T}(e_g) \right\rangle = 0$$

$$\left\langle \bar{\gamma}_{(\frac{3}{4})}^{(8)'T}(t_{2g}) \left|\frac{\vec{p}}{\vec{m}}\right| \bar{\gamma}_{(\frac{4}{3})}^{(8)'T}(e_g) \right\rangle = \begin{bmatrix} il_1 \\ m_1\end{bmatrix}\hat{k}'$$

$$\left\langle \bar{\gamma}_{(\frac{3}{4})}^{(7)T}(t_{2g}) \left|\frac{\vec{p}}{\vec{m}}\right| \bar{\gamma}_{(\frac{3}{4})}^{(8)'T}(e_g) \right\rangle =$$
$$(\pm)\frac{e^{\mp i\beta/4}}{\sqrt{6}}\begin{bmatrix} i(\sqrt{2}l_0 + (\pm)il_2) \\ (m_0 + (\pm)i\sqrt{2}m_2)\end{bmatrix}\hat{\jmath}'$$

$$\left\langle \bar{\gamma}_{(\frac{3}{4})}^{(7)T}(t_{2g}) \left|\frac{\vec{p}}{\vec{m}}\right| \bar{\gamma}_{(\frac{4}{3})}^{(8)'T}(e_g) \right\rangle =$$
$$(\pm)\frac{e^{\pm i\beta/4}}{\sqrt{6}}\begin{bmatrix} (l_0 + (\mp)i\sqrt{2}l_2) \\ -i(m_0 + (\mp)i\sqrt{2}m_2\end{bmatrix}\hat{\imath}'$$

$$\left\langle \bar{\gamma}_{(\frac{3}{4})}^{(8)T}(t_{2g}) \left|\frac{\vec{p}}{\vec{m}}\right| \bar{\gamma}_{(\frac{3}{4})}^{(8)'T}(e_g) \right\rangle =$$
$$(\mp)\frac{e^{\mp i\beta/4}}{\sqrt{6}}\begin{bmatrix} i(\sqrt{2}l_0 + (\mp)il_2) \\ (\sqrt{2}m_0 + (\mp)im_2)\end{bmatrix}\hat{\jmath}'$$

$$\left\langle \bar{\gamma}_{(\frac{3}{4})}^{(8)T}(t_{2g}) \left|\frac{\vec{p}}{\vec{m}}\right| \bar{\gamma}_{(\frac{4}{3})}^{(8)'T}(e_g) \right\rangle =$$
$$(\mp)\frac{e^{\pm i\beta/4}}{\sqrt{6}}\begin{bmatrix} (\sqrt{2}l_0 + (\pm)il_2) \\ -i(\sqrt{2}m_0 + (\pm)im_2)\end{bmatrix}\hat{\imath}'$$

$$\left\langle \bar{\gamma}_{(\frac{3}{4})}^{(8)'T}(t_{2g}) \left|\frac{\vec{p}}{\vec{m}}\right| \bar{\gamma}_{(\frac{3}{4})}^{(8)T}(e_g) \right\rangle = \frac{e^{\mp i\beta/4}}{\sqrt{2}}\begin{bmatrix} l_2 \\ -im_2\end{bmatrix}\hat{\jmath}'$$

$$\left\langle \bar{\gamma}_{(\frac{3}{4})}^{(8)'T}(t_{2g}) \left|\frac{\vec{p}}{\vec{m}}\right| \bar{\gamma}_{(\frac{4}{3})}^{(8)T}(e_g) \right\rangle = -\frac{e^{\mp i\beta/4}}{\sqrt{2}}\begin{bmatrix} ir_2 \\ m_2\end{bmatrix}\hat{\imath}'$$

$$\left\langle \bar{\gamma}_{(\frac{3}{4})}^{(7)T}(t_{2g}) \left|\frac{\vec{p}}{\vec{m}}\right| \bar{\gamma}_{(\frac{3}{4})}^{(8)T}(e_g) \right\rangle = (\pm)\frac{1}{\sqrt{6}}\begin{bmatrix} il_0 \\ m_0\end{bmatrix}\hat{\jmath}'$$

$$\left\langle \bar{\gamma}_{(\frac{3}{4})}^{(7)T}(t_{2g}) \left|\frac{\vec{p}}{\vec{m}}\right| \bar{\gamma}_{(\frac{4}{3})}^{(8)T}(e_g) \right\rangle =$$
$$\sqrt{{}^{2}/_{3}}\begin{bmatrix} il_1 \\ m_1\end{bmatrix}\hat{k}' + (\mp)\sqrt{{}^{1}/_{6}}\begin{bmatrix} l_0 \\ -im_0\end{bmatrix}\hat{\imath}'$$

$$\left\langle \bar{\gamma}_{(\frac{3}{4})}^{(8)T}(t_{2g}) \left|\frac{\vec{p}}{\vec{m}}\right| \bar{\gamma}_{(\frac{3}{4})}^{(8)T}(e_g) \right\rangle = (\mp)\sqrt{{}^{1}/_{3}}\begin{bmatrix} il_0 \\ m_0\end{bmatrix}\hat{\jmath}'$$

$$\left\langle \bar{\gamma}_{(\frac{3}{4})}^{(8)T}(t_{2g}) \left|\frac{\vec{p}}{\vec{m}}\right| \bar{\gamma}_{(\frac{4}{3})}^{(8)T}(e_g) \right\rangle =$$
$$\sqrt{{}^{1}/_{3}}\begin{bmatrix} il_1 \\ m_1\end{bmatrix}\hat{k}' + (\pm)\sqrt{{}^{1}/_{3}}\begin{bmatrix} l_0 \\ -im_0\end{bmatrix}\hat{\imath}'$$

$$\left\langle \bar{\gamma}_{(\frac{3}{4})}^{(8)'T}(e_g) \left|\frac{\vec{p}}{\vec{m}}\right| \bar{\gamma}_{(\frac{3}{4})}^{(8)'T}(e_g) \right\rangle = 0$$

$$\left\langle \bar{\gamma}_{(\frac{3}{4})}^{(8)'T}(e_g) \left|\frac{\vec{p}}{\vec{m}}\right| \bar{\gamma}_{(\frac{4}{3})}^{(8)'T}(e_g) \right\rangle =$$
$$e^{\pm i\beta/2}\begin{bmatrix} i\bar{\bar{l}}_0{}^{\ddagger} \\ (\bar{\bar{m}}_0{}^{\ddagger} + \mu_B)\end{bmatrix}\hat{k}'$$

$$\left\langle \bar{\gamma}_{(\frac{3}{4})}^{(8)T}(e_g) \left|\frac{\vec{p}}{\vec{m}}\right| \bar{\gamma}_{(\frac{3}{4})}^{(8)'T}(e_g) \right\rangle =$$
$$\frac{e^{\mp i\beta/4}}{\sqrt{2}}\begin{bmatrix} \bar{\bar{l}}_0 \\ -\sqrt{2}\mu_B\end{bmatrix}\hat{\jmath}'$$

$$\left\langle \bar{\gamma}_{(\frac{3}{4})}^{(8)T}(e_g) \left|\frac{\vec{p}}{\vec{m}}\right| \bar{\gamma}_{(\frac{4}{3})}^{(8)'T}(e_g) \right\rangle = \frac{e^{\pm i\beta/4}}{\sqrt{2}}\begin{bmatrix} -i\bar{\bar{l}}_0 \\ i\sqrt{2}\mu_B\end{bmatrix}\hat{\imath}'$$

$$\left\langle \bar{\gamma}_{(\frac{3}{4})}^{(8)T}(e_g) \left|\frac{\vec{p}}{\vec{m}}\right| \bar{\gamma}_{(\frac{3}{4})}^{(8)T}(e_g) \right\rangle = 0$$

$$\left\langle \bar{\gamma}_{(\frac{3}{4})}^{(8)T}(e_g) \left|\frac{\vec{p}}{\vec{m}}\right| \bar{\gamma}_{(\frac{4}{3})}^{(8)T}(e_g) \right\rangle = -\begin{bmatrix} i\bar{\bar{l}}_0{}^{\ddagger} \\ (\bar{\bar{m}}_0{}^{\ddagger} - \mu_B)\end{bmatrix}\hat{k}'$$

$$\left\langle \bar{\gamma}_{(\frac{3}{4})}^{(7)\mathrm{T}}(t_{2g}) \left| \frac{\vec{p}}{\vec{m}} \right| \bar{\gamma}_{(\frac{3}{4})}^{(7)\mathrm{T}}(t_{2g}) \right\rangle =$$

$$(\pm)^{1}/_{3}\begin{bmatrix} 0 \text{ or } 2\bar{p}_0 \\ -(2\bar{m}_0 + \mu_B) \end{bmatrix} \hat{\jmath}'$$

$$\left\langle \bar{\gamma}_{(\frac{3}{4})}^{(7)\mathrm{T}}(t_{2g}) \left| \frac{\vec{p}}{\vec{m}} \right| \bar{\gamma}_{(\frac{4}{3})}^{(7)\mathrm{T}}(t_{2g}) \right\rangle =$$

$$^{1}/_{3}\begin{bmatrix} i2\bar{l}_0^{\mp} \\ (2\bar{m}_0^{\mp} + \mu_B) \end{bmatrix} \hat{k}' + (\pm)\frac{i}{3}\begin{bmatrix} 0 \text{ or } 2\bar{p}_0 \\ -2(\bar{m}_0 + \mu_B) \end{bmatrix} \hat{\imath}'$$

$$\left\langle \bar{\gamma}_{(\frac{3}{4})}^{(8)\mathrm{T}}(t_{2g}) \left| \frac{\vec{p}}{\vec{m}} \right| \bar{\gamma}_{(\frac{3}{4})}^{(8)\mathrm{T}}(t_{2g}) \right\rangle =$$

$$(\pm)^{2}/_{3}\begin{bmatrix} 0 \text{ or } -\bar{p}_0 \\ (\bar{m}_0 - \mu_B) \end{bmatrix} \hat{\jmath}'$$

$$\left\langle \bar{\gamma}_{(\frac{3}{4})}^{(8)\mathrm{T}}(t_{2g}) \left| \frac{\vec{p}}{\vec{m}} \right| \bar{\gamma}_{(\frac{4}{3})}^{(8)\mathrm{T}}(t_{2g}) \right\rangle =$$

$$^{1}/_{3}\begin{bmatrix} i\bar{l}_0^{\mp} \\ (\bar{m}_0^{\mp} - \mu_B) \end{bmatrix} \hat{k}' + (\pm)\frac{2i}{3}\begin{bmatrix} 0 \text{ or } -\bar{p}_0 \\ (\bar{m}_0 - \mu_B) \end{bmatrix} \hat{\imath}'$$

$$\left\langle \bar{\gamma}_{(\frac{3}{4})}^{(8)'\mathrm{T}}(t_{2g}) \left| \frac{\vec{p}}{\vec{m}} \right| \bar{\gamma}_{(\frac{3}{4})}^{(8)'\mathrm{T}}(t_{2g}) \right\rangle = 0$$

$$\left\langle \bar{\gamma}_{(\frac{3}{4})}^{(8)'\mathrm{T}}(t_{2g}) \left| \frac{\vec{p}}{\vec{m}} \right| \bar{\gamma}_{(\frac{4}{3})}^{(8)'\mathrm{T}}(t_{2g}) \right\rangle =$$

$$-e^{\mp i\beta/2}\begin{bmatrix} i\bar{l}_0^{\mp} \\ (\bar{m}_0^{\mp} - \mu_B) \end{bmatrix} \hat{k}' \quad (72)$$

$$\mathfrak{W}[\bar{\gamma}_{(\frac{3}{4})}^{(8)\mathrm{T}}(t_{2g}) \longrightarrow \bar{\gamma}_{(\frac{3}{4})}^{(7)\mathrm{T}}(t_{2g})] = -^{1}/_{6}\bar{g}_0(\bar{m}_0 + 2\mu_B)$$

$$\mathfrak{X}[\bar{\gamma}_{(\frac{3}{4})}^{(8)\mathrm{T}}(t_{2g}) \longrightarrow \bar{\gamma}_{(\frac{3}{4})}^{(7)\mathrm{T}}(t_{2g})] = ^{1}/_{2}\bar{g}_0^{2}$$

$$\mathfrak{M}[\bar{\gamma}_{(\frac{3}{4})}^{(8)\mathrm{T}}(t_{2g}) \longrightarrow \bar{\gamma}_{(\frac{3}{4})}^{(7)\mathrm{T}}(t_{2g})] = ^{1}/_{18}(\bar{m}_0 + 2\mu_B)^{2}$$

$$\mathfrak{W}[\bar{\gamma}_{(\frac{3}{4})}^{(8)\mathrm{T}}(t_{2g}) \longrightarrow \bar{\gamma}_{(\frac{4}{3})}^{(7)\mathrm{T}}(t_{2g})] =$$
$$^{2}/_{9}\bar{g}_0^{\mp}(\bar{m}_0^{\mp} + 2\mu_B) - ^{1}/_{6}\bar{g}_0(\bar{m}_0 + 2\mu_B)$$

$$\mathfrak{X}[\bar{\gamma}_{(\frac{3}{4})}^{(8)\mathrm{T}}(t_{2g}) \longrightarrow \bar{\gamma}_{(\frac{4}{3})}^{(7)\mathrm{T}}(t_{2g})] = ^{2}/_{9}\bar{g}_0^{\mp 2} + ^{1}/_{2}\bar{g}_0^{2}$$

$$\mathfrak{M}[\bar{\gamma}_{(\frac{3}{4})}^{(8)\mathrm{T}}(t_{2g}) \longrightarrow \bar{\gamma}_{(\frac{4}{3})}^{(7)\mathrm{T}}(t_{2g})] =$$
$$^{2}/_{9}(\bar{m}_0^{\mp} + 2\mu_B)^{2} + ^{1}/_{18}(\bar{m}_0 + 2\mu_B)^{2}$$

$$\mathfrak{W}[\bar{\gamma}_{(\frac{3}{4})}^{(8)\mathrm{T}}(t_{2g}) \longrightarrow \bar{\gamma}_{(\frac{3}{4})}^{(8)'\mathrm{T}}(t_{2g})] = -^{1}/_{3}\bar{g}_0(\bar{m}_0 - \mu_B)$$

$$\mathfrak{X}[\bar{\gamma}_{(\frac{3}{4})}^{(8)\mathrm{T}}(t_{2g}) \longrightarrow \bar{\gamma}_{(\frac{3}{4})}^{(8)'\mathrm{T}}(t_{2g})] = ^{1}/_{6}\{2\bar{g}_0^{2} + \bar{g}_0^{\mp 2}\}$$

$$\mathfrak{M}[\bar{\gamma}_{(\frac{3}{4})}^{(8)\mathrm{T}}(t_{2g}) \longrightarrow \bar{\gamma}_{(\frac{3}{4})}^{(8)'\mathrm{T}}(t_{2g})] = ^{1}/_{3}(\bar{m}_0 - \mu_B)^{2}$$

$$\mathfrak{W}[\bar{\gamma}_{(\frac{3}{4})}^{(8)\mathrm{T}}(t_{2g}) \longrightarrow \bar{\gamma}_{(\frac{4}{3})}^{(8)'\mathrm{T}}(t_{2g})] = -^{1}/_{3}\bar{g}_0(\bar{m}_0 - \mu_B)$$

$$\mathfrak{X}[\bar{\gamma}_{(\frac{3}{4})}^{(8)\mathrm{T}}(t_{2g}) \longrightarrow \bar{\gamma}_{(\frac{4}{3})}^{(8)'\mathrm{T}}(t_{2g})] = ^{1}/_{6}\{2\bar{g}_0^{2} + \bar{g}_0^{\mp 2}\}$$

$$\mathfrak{M}[\bar{\gamma}_{(\frac{3}{4})}^{(8)\mathrm{T}}(t_{2g}) \longrightarrow \bar{\gamma}_{(\frac{4}{3})}^{(8)'\mathrm{T}}(t_{2g})] = ^{1}/_{3}(\bar{m}_0 - \mu_B)^{2}$$

$$\mathfrak{W}[\bar{\gamma}_{(\frac{3}{4})}^{(7)\mathrm{T}}(t_{2g}) \longrightarrow \bar{\gamma}_{(\frac{3}{4})}^{(8)'\mathrm{T}}(t_{2g})] = -^{1}/_{6}\bar{g}_0(\bar{m}_0 + 2\mu_B)$$

$$\mathfrak{X}[\bar{\gamma}_{(\frac{3}{4})}^{(7)\mathrm{T}}(t_{2g}) \longrightarrow \bar{\gamma}_{(\frac{3}{4})}^{(8)'\mathrm{T}}(t_{2g})] = ^{1}/_{6}\{\bar{g}_0^{2} + 2\bar{g}_0^{\mp 2}\}$$

$$\mathfrak{M}[\bar{\gamma}_{(\frac{3}{4})}^{(7)\mathrm{T}}(t_{2g}) \longrightarrow \bar{\gamma}_{(\frac{3}{4})}^{(8)'\mathrm{T}}(t_{2g})] = ^{1}/_{6}(\bar{m}_0 + 2\mu_B)^{2}$$

$$\mathfrak{W}[\bar{\gamma}_{(\frac{3}{4})}^{(8)'\mathrm{T}}(t_{2g}) \longrightarrow \bar{\gamma}_{(\frac{4}{3})}^{(8)'\mathrm{T}}(t_{2g})] = -^{1}/_{6}\bar{g}_0(\bar{m}_0 + 2\mu_B)$$

$$\mathfrak{X}[\bar{\gamma}_{(\frac{3}{4})}^{(7)\mathrm{T}}(t_{2g}) \longrightarrow \bar{\gamma}_{(\frac{4}{3})}^{(8)'\mathrm{T}}(t_{2g})] = ^{1}/_{6}\{\bar{g}_0^{2} + 2\bar{g}_0^{\mp 2}\}$$

$$\mathfrak{M}[\bar{\gamma}_{(\frac{3}{4})}^{(7)\mathrm{T}}(t_{2g}) \longrightarrow \bar{\gamma}_{(\frac{4}{3})}^{(8)'\mathrm{T}}(t_{2g})] = ^{1}/_{6}(\bar{m}_0 + 2\mu_B)^{2}$$

$$\mathfrak{W}[\bar{\gamma}_{(\frac{3}{4})}^{(8)'\mathrm{T}}(t_{2g}) \longrightarrow \bar{\gamma}_{(\frac{3}{4})}^{(8)'\mathrm{T}}(e_g)] =$$
$$\mathfrak{X}[\bar{\gamma}_{(\frac{3}{4})}^{(8)'\mathrm{T}}(t_{2g}) \longrightarrow \bar{\gamma}_{(\frac{3}{4})}^{(8)'\mathrm{T}}(e_g)] =$$
$$\mathfrak{M}[\bar{\gamma}_{(\frac{3}{4})}^{(8)'\mathrm{T}}(t_{2g}) \longrightarrow \bar{\gamma}_{(\frac{3}{4})}^{(8)'\mathrm{T}}(e_g)] = 0$$

$$\mathfrak{W}[\bar{\gamma}_{(\frac{3}{4})}^{(8)'\mathrm{T}}(t_{2g}) \longrightarrow \bar{\gamma}_{(\frac{4}{3})}^{(8)'\mathrm{T}}(e_g)] = g_1 m_1$$

$$\mathfrak{X}[\bar{\gamma}_{(\frac{3}{4})}^{(8)'\mathrm{T}}(t_{2g}) \longrightarrow \bar{\gamma}_{(\frac{4}{3})}^{(8)'\mathrm{T}}(e_g)] = g_1^{2}$$

$$\mathfrak{M}[\bar{\gamma}_{(\frac{3}{4})}^{(8)'\mathrm{T}}(t_{2g}) \longrightarrow \bar{\gamma}_{(\frac{4}{3})}^{(8)'\mathrm{T}}(e_g)] = m_1^{2}$$

$$\mathfrak{W}[\bar{\gamma}_{(\frac{3}{4})}^{(7)\mathrm{T}}(t_{2g}) \longrightarrow \bar{\gamma}_{(\frac{3}{4})}^{(8)'\mathrm{T}}(e_g)] = ^{1}/_{6}\{g_0 m_0 + 2g_2 m_2\}$$

$$\mathfrak{X}[\bar{\gamma}_{(\frac{3}{4})}^{(7)\mathrm{T}}(t_{2g}) \longrightarrow \bar{\gamma}_{(\frac{3}{4})}^{(8)'\mathrm{T}}(e_g)] = ^{1}/_{6}\{g_0^{2} + 2g_2^{2}\}$$

$$\mathfrak{M}[\bar{\gamma}_{(\frac{3}{4})}^{(7)\mathrm{T}}(t_{2g}) \longrightarrow \bar{\gamma}_{(\frac{3}{4})}^{(7)\mathrm{T}}(e_g)] = ^{1}/_{6}\{m_0^{2} + 2m_2^{2}\}$$

$$\mathfrak{W}[\bar{\gamma}_{(\frac{3}{4})}^{(7)\mathrm{T}}(t_{2g}) \longrightarrow \bar{\gamma}_{(\frac{4}{3})}^{(8)'\mathrm{T}}(e_g)] = ^{1}/_{6}\{g_0 m_0 + 2g_2 m_2\}$$

$$\mathfrak{X}[\bar{\gamma}_{(\frac{3}{4})}^{(7)\mathrm{T}}(t_{2g}) \longrightarrow \bar{\gamma}_{(\frac{4}{3})}^{(8)'\mathrm{T}}(e_g)] = ^{1}/_{6}\{g_0^{2} + 2g_2^{2}\}$$

$$\mathfrak{M}[\bar{\gamma}_{(\frac{3}{4})}^{(7)\mathrm{T}}(t_{2g}) \longrightarrow \bar{\gamma}_{(\frac{4}{3})}^{(8)'\mathrm{T}}(e_g)] = ^{1}/_{6}\{m_0^{2} + 2m_2^{2}\}$$

$$\mathfrak{W}[\bar{\gamma}_{(\frac{3}{4})}^{(8)\mathrm{T}}(t_{2g}) \longrightarrow \bar{\gamma}_{(\frac{3}{4})}^{(8)'\mathrm{T}}(e_g)] = ^{1}/_{6}\{2g_0 m_0 + g_2 m_2\}$$

$$\mathfrak{X}[\bar{\gamma}_{(\frac{3}{4})}^{(8)\mathrm{T}}(t_{2g}) \longrightarrow \bar{\gamma}_{(\frac{3}{4})}^{(8)'\mathrm{T}}(e_g)] = ^{1}/_{6}\{2g_0^{2} + g_2^{2}\}$$

$$\mathfrak{M}[\bar{\gamma}_{(\frac{3}{4})}^{(8)\mathrm{T}}(t_{2g}) \longrightarrow \bar{\gamma}_{(\frac{3}{4})}^{(8)'\mathrm{T}}(e_g)] = ^{1}/_{6}\{2m_0^{2} + m_2^{2}\}$$

$$\mathfrak{W}[\bar{\gamma}_{(\frac{3}{4})}^{(8)\mathrm{T}}(t_{2g}) \longrightarrow \bar{\gamma}_{(\frac{4}{3})}^{(8)'\mathrm{T}}(e_g)] = ^{1}/_{6}\{2g_0 m_0 + g_2 m_2\}$$

$$\mathfrak{X}[\bar{\gamma}_{(\frac{3}{4})}^{(8)\mathrm{T}}(t_{2g}) \longrightarrow \bar{\gamma}_{(\frac{4}{3})}^{(8)'\mathrm{T}}(e_g)] = ^{1}/_{6}\{2g_0^{2} + g_2^{2}\}$$

$$\mathfrak{M}[\bar{\gamma}_{(\frac{3}{4})}^{(8)\mathrm{T}}(t_{2g}) \longrightarrow \bar{\gamma}_{(\frac{4}{3})}^{(8)'\mathrm{T}}(e_g)] = ^{1}/_{6}\{2m_0^{2} + m_2^{2}\}$$

$$\mathfrak{W}[\bar{\gamma}_{(\frac{3}{4})}^{(8)'\mathrm{T}}(t_{2g}) \longrightarrow \bar{\gamma}_{(\frac{3}{4})}^{(8)\mathrm{T}}(e_g)] = ^{1}/_{2}g_2 m_2$$

$$\mathfrak{X}[\bar{\gamma}_{(\frac{3}{4})}^{(8)'\mathrm{T}}(t_{2g}) \longrightarrow \bar{\gamma}_{(\frac{3}{4})}^{(8)\mathrm{T}}(e_g)] = ^{1}/_{2}g_2^{2}$$

$$\mathfrak{M}[\bar{\gamma}_{(\frac{3}{4})}^{(8)'\mathrm{T}}(t_{2g}) \longrightarrow \bar{\gamma}_{(\frac{3}{4})}^{(8)\mathrm{T}}(e_g)] = ^{1}/_{2}m_2^{2}$$

$$\mathfrak{W}[\bar{\gamma}_{(\frac{3}{4})}^{(8)'\mathrm{T}}(t_{2g}) \longrightarrow \bar{\gamma}_{(\frac{4}{3})}^{(8)\mathrm{T}}(e_g)] = ^{1}/_{2}g_2 m_2$$

$$\mathfrak{X}[\bar{\gamma}_{(\frac{3}{4})}^{(8)'\mathrm{T}}(t_{2g}) \longrightarrow \bar{\gamma}_{(\frac{4}{3})}^{(8)\mathrm{T}}(e_g)] = ^{1}/_{2}g_2^{2}$$

$$\mathfrak{M}[\bar{\gamma}_{(\frac{3}{4})}^{(8)'\mathrm{T}}(t_{2g}) \longrightarrow \bar{\gamma}_{(\frac{4}{3})}^{(8)\mathrm{T}}(e_g)] = ^{1}/_{2}m_2^{2}$$

$$\mathfrak{W}[\bar{\gamma}_{(\frac{3}{4})}^{(7)\mathrm{T}}(t_{2g}) \longrightarrow \bar{\gamma}_{(\frac{3}{4})}^{(8)\mathrm{T}}(e_g)] = ^{1}/_{6}g_0 m_0$$

$$\mathfrak{X}[\bar{\gamma}_{(\frac{3}{4})}^{(7)\mathrm{T}}(t_{2g}) \longrightarrow \bar{\gamma}_{(\frac{3}{4})}^{(8)\mathrm{T}}(e_g)] = ^{1}/_{6}g_0^{2}$$

$$\mathfrak{M}[\bar{\gamma}_{(\frac{3}{4})}^{(7)\mathrm{T}}(t_{2g}) \longrightarrow \bar{\gamma}_{(\frac{3}{4})}^{(8)\mathrm{T}}(e_g)] = ^{1}/_{6}m_0^{2}$$

$$\mathfrak{W}[\bar{\gamma}_{(\frac{3}{4})}^{(7)\mathrm{T}}(t_{2g}) \longrightarrow \bar{\gamma}_{(\frac{4}{3})}^{(8)\mathrm{T}}(e_g)] = ^{1}/_{6}\{g_0 m_0 + 4g_1 m_1\}$$

$$\mathfrak{X}[\bar{\gamma}_{(\frac{3}{4})}^{(7)\mathrm{T}}(t_{2g}) \longrightarrow \bar{\gamma}_{(\frac{4}{3})}^{(8)\mathrm{T}}(e_g)] = ^{1}/_{6}\{g_0^{2} + 4g_1^{2}\}$$

$$\mathfrak{M}[\bar{\gamma}_{(\frac{3}{4})}^{(7)\mathrm{T}}(t_{2g}) \longrightarrow \bar{\gamma}_{(\frac{4}{3})}^{(8)\mathrm{T}}(e_g)] = ^{1}/_{6}\{m_0^{2} + 4m_1^{2}\}$$

$$\mathfrak{W}[\bar{\gamma}_{(\frac{3}{4})}^{(8)\mathrm{T}}(t_{2g}) \longrightarrow \bar{\gamma}_{(\frac{3}{4})}^{(8)\mathrm{T}}(e_g)] = ^{1}/_{3}g_0 m_0$$

$$\mathfrak{X}[\bar{\gamma}_{(\frac{3}{4})}^{(8)\mathrm{T}}(t_{2g}) \longrightarrow \bar{\gamma}_{(\frac{3}{4})}^{(8)\mathrm{T}}(e_g)] = ^{1}/_{3}g_0^{2}$$

$$\mathfrak{M}[\bar{\gamma}_{(\frac{3}{4})}^{(8)\mathrm{T}}(t_{2g}) \longrightarrow \bar{\gamma}_{(\frac{3}{4})}^{(8)\mathrm{T}}(e_g)] = ^{1}/_{3}m_0^{2}$$

$$\mathfrak{W}[\bar{\gamma}(^{3}_{4})^{(8)}{}^{T}(t_{2g}) \longrightarrow \bar{\gamma}(^{4}_{3})^{(8)}{}^{T}(e_g)] = {}^{1}/_{3}\{g_0 m_0 + g_1 m_1\}$$

$$\mathfrak{X}[\bar{\gamma}(^{3}_{4})^{(8)}{}^{T}(t_{2g}) \longrightarrow \bar{\gamma}(^{4}_{3})^{(8)}{}^{T}(e_g)] = {}^{1}/_{3}\{{g_0}^2 + {g_1}^2\}$$

$$\mathfrak{M}[\bar{\gamma}(^{3}_{4})^{(8)}{}^{T}(t_{2g}) \longrightarrow \bar{\gamma}(^{4}_{3})^{(8)}{}^{T}(e_g)] = {}^{1}/_{3}\{{m_0}^2 + {m_1}^2\}$$

$$\mathfrak{W}[\bar{\gamma}(^{3}_{4})^{(8)}{}'{}^{T}(e_g) \longrightarrow \bar{\gamma}(^{3}_{4})^{(8)}{}'{}^{T}(e_g)] = \mathfrak{X}[\bar{\gamma}(^{3}_{4})^{(8)}{}'{}^{T}(e_g) \longrightarrow \bar{\gamma}(^{3}_{4})^{(8)}{}'{}^{T}(e_g)] = \mathfrak{M}[\bar{\gamma}(^{3}_{4})^{(8)}{}'{}^{T}(e_g) \longrightarrow \bar{\gamma}(^{3}_{4})^{(8)}{}'{}^{T}(e_g)] = 0$$

$$\mathfrak{W}[\bar{\gamma}(^{3}_{4})^{(8)}{}'{}^{T}(e_g)] \longrightarrow \bar{\gamma}(^{4}_{3})^{(8)}{}'{}^{T}(e_g)] = \bar{g}_0{}^{\ddagger}(\bar{m}_0{}^{\ddagger} + \mu_B)$$

$$\mathfrak{X}[\bar{\gamma}(^{3}_{4})^{(8)}{}'{}^{T}(e_g) \longrightarrow \bar{\gamma}(^{4}_{3})^{(8)}{}'{}^{T}(e_g)] = \bar{g}_0{}^{\ddagger 2}$$

$$\mathfrak{M}[\bar{\gamma}(^{3}_{4})^{(8)}{}'{}^{T}(e_g) \longrightarrow \bar{\gamma}(^{4}_{3})^{(8)}{}'{}^{T}(e_g)] = (\bar{m}_0{}^{\ddagger} + \mu_B)^2$$

$$\mathfrak{W}[\bar{\gamma}(^{3}_{4})^{(8)}{}^{T}(e_g) \longrightarrow \bar{\gamma}(^{3}_{4})^{(8)}{}'{}^{T}(e_g)] = 0$$

$$\mathfrak{X}[\bar{\gamma}(^{3}_{4})^{(8)}{}^{T}(e_g) \longrightarrow \bar{\gamma}(^{3}_{4})^{(8)}{}'{}^{T}(e_g)] = {}^{1}/_{2}\bar{g}_0{}^2$$

$$\mathfrak{M}[\bar{\gamma}(^{3}_{4})^{(8)}{}^{T}(e_g) \longrightarrow \bar{\gamma}(^{3}_{4})^{(8)}{}'{}^{T}(e_g)] = {\mu_B}^2$$

$$\mathfrak{W}[\bar{\gamma}(^{3}_{4})^{(8)}{}^{T}(e_g) \longrightarrow \bar{\gamma}(^{4}_{3})^{(8)}{}'{}^{T}(e_g)] = 0$$

$$\mathfrak{X}[\bar{\gamma}(^{3}_{4})^{(8)}{}^{T}(e_g) \longrightarrow \bar{\gamma}(^{4}_{3})^{(8)}{}'{}^{T}(e_g)] = {}^{1}/_{2}\bar{g}_0{}^2$$

$$\mathfrak{M}[\bar{\gamma}(^{3}_{4})^{(8)}{}^{T}(e_g) \longrightarrow \bar{\gamma}(^{4}_{3})^{(8)}{}'{}^{T}(e_g)] = {\mu_B}^2$$

$$\mathfrak{W}[\bar{\gamma}(^{3}_{4})^{(8)}{}^{T}(e_g) \longrightarrow \bar{\gamma}(^{3}_{4})^{(8)}{}^{T}(e_g)] = \mathfrak{X}[\bar{\gamma}(^{3}_{4})^{(8)}{}^{T}(e_g) \longrightarrow \bar{\gamma}(^{3}_{4})^{(8)}{}^{T}(e_g)] = \mathfrak{M}[\bar{\gamma}(^{3}_{4})^{(8)}{}^{T}(e_g) \longrightarrow \bar{\gamma}(^{3}_{4})^{(8)}{}^{T}(e_g)] = 0$$

$$\mathfrak{W}[\bar{\gamma}(^{3}_{4})^{(8)}{}^{T}(e_g) \longrightarrow \bar{\gamma}(^{4}_{3})^{(8)}{}^{T}(e_g)] = \bar{g}_0{}^{\ddagger}(\bar{m}_0{}^{\ddagger} - \mu_B)$$

$$\mathfrak{X}[\bar{\gamma}(^{3}_{4})^{(8)}{}^{T}(e_g) \longrightarrow \bar{\gamma}(^{4}_{3})^{(8)}{}^{T}(e_g)] = \bar{g}_0{}^{\ddagger 2}$$

$$\mathfrak{M}[\bar{\gamma}(^{3}_{4})^{(8)}{}^{T}(e_g) \longrightarrow \bar{\gamma}(^{4}_{3})^{(8)}{}^{T}(e_g)] = (\bar{m}_0{}^{\ddagger} - \mu_B)^2$$

$$\mathfrak{W}[\bar{\gamma}(^{3}_{4})^{(7)}{}^{T}(t_{2g}) \longrightarrow \bar{\gamma}(^{3}_{4})^{(7)}{}^{T}(t_{2g})] = 0 \text{ or } -{}^{2}/_{9}\bar{p}_0(2\bar{m}_0 + \mu_B)$$

$$\mathfrak{X}[\bar{\gamma}(^{3}_{4})^{(7)}{}^{T}(t_{2g}) \longrightarrow \bar{\gamma}(^{3}_{4})^{(7)}{}^{T}(t_{2g})] = 0 \text{ or } {}^{4}/_{9}\bar{p}_0{}^2$$

$$\mathfrak{M}[\bar{\gamma}(^{3}_{4})^{(7)}{}^{T}(t_{2g}) \longrightarrow \bar{\gamma}(^{3}_{4})^{(7)}{}^{T}(t_{2g})] = {}^{1}/_{9}(2\bar{m}_0 + \mu_B)^2$$

$$\mathfrak{W}[\bar{\gamma}(^{3}_{4})^{(7)}{}^{T}(t_{2g}) \longrightarrow \bar{\gamma}(^{4}_{3})^{(7)}{}^{T}(t_{2g})] = (0 \text{ or } -{}^{2}/_{9}\bar{p}_0(2\bar{m}_0 + \mu_B)) + {}^{2}/_{9}\bar{g}_0{}^{\mp}(2\bar{m}_0{}^{\mp} + \mu_B)$$

$$\mathfrak{X}[\bar{\gamma}(^{3}_{4})^{(7)}{}^{T}(t_{2g}) \longrightarrow \bar{\gamma}(^{4}_{3})^{(7)}{}^{T}(t_{2g})] = (0 \text{ or } {}^{4}/_{9}\bar{p}_0{}^2) + {}^{4}/_{9}\bar{g}_0{}^{\mp 2}$$

$$\mathfrak{M}[\bar{\gamma}(^{3}_{4})^{(7)}{}^{T}(t_{2g}) \longrightarrow \bar{\gamma}(^{4}_{3})^{(7)}{}^{T}(t_{2g})] = {}^{1}/_{9}(2\bar{m}_0 + \mu_B)^2 + {}^{1}/_{9}(2\bar{m}_0{}^{\mp} + \mu_B)^2$$

$$\mathfrak{W}[\bar{\gamma}(^{3}_{4})^{(8)}{}^{T}(t_{2g}) \longrightarrow \bar{\gamma}(^{3}_{4})^{(8)}{}^{T}(t_{2g})] = 0 \text{ or } -{}^{4}/_{9}\bar{p}_0(\bar{m}_0 - \mu_B)$$

$$\mathfrak{X}[\bar{\gamma}(^{3}_{4})^{(8)}{}^{T}(t_{2g}) \longrightarrow \bar{\gamma}(^{3}_{4})^{(8)}{}^{T}(t_{2g})] = 0 \text{ or } {}^{4}/_{9}\bar{p}_0{}^2$$

$$\mathfrak{M}[\bar{\gamma}(^{3}_{4})^{(8)}{}^{T}(t_{2g}) \longrightarrow \bar{\gamma}(^{3}_{4})^{(8)}{}^{T}(t_{2g})] = {}^{4}/_{9}(\bar{m}_0 - \mu_B)^2$$

$$\mathfrak{W}[\bar{\gamma}(^{3}_{4})^{(8)}{}^{T}(t_{2g}) \longrightarrow \bar{\gamma}(^{4}_{3})^{(8)}{}^{T}(t_{2g})] = (0 \text{ or } -{}^{4}/_{9}\bar{p}_0(\bar{m}_0 - \mu_B)) + {}^{1}/_{9}\bar{g}_0{}^{\mp}(\bar{m}_0{}^{\mp} - \mu_B)$$

$$\mathfrak{X}[\bar{\gamma}(^{3}_{4})^{(8)}{}^{T}(t_{2g}) \longrightarrow \bar{\gamma}(^{4}_{3})^{(8)}{}^{T}(t_{2g})] = (0 \text{ or } {}^{4}/_{9}\bar{p}_0{}^2) + {}^{1}/_{9}\bar{g}_0{}^{\mp 2}$$

$$\mathfrak{M}[\bar{\gamma}(^{3}_{4})^{(8)}{}^{T}(t_{2g}) \longrightarrow \bar{\gamma}(^{4}_{3})^{(8)}{}^{T}(t_{2g})] = {}^{4}/_{9}(\bar{m}_0 - \mu_B)^2 + {}^{1}/_{9}(\bar{m}_0{}^{\mp} - \mu_B)^2$$

$$\mathfrak{W}[\bar{\gamma}(^{3}_{4})^{(8)}{}'{}^{T}(t_{2g}) \longrightarrow \bar{\gamma}(^{3}_{4})^{(8)}{}'{}^{T}(t_{2g})] = \mathfrak{X}[\bar{\gamma}(^{3}_{4})^{(8)}{}'{}^{T}(t_{2g}) \longrightarrow \bar{\gamma}(^{3}_{4})^{(8)}{}'{}^{T}(t_{2g})] = \mathfrak{M}[\bar{\gamma}(^{3}_{4})^{(8)}{}'{}^{T}(t_{2g}) \longrightarrow \bar{\gamma}(^{3}_{4})^{(8)}{}'{}^{T}(t_{2g})] = 0$$

$$\mathfrak{W}[\bar{\gamma}(^{3}_{4})^{(8)}{}'{}^{T}(t_{2g}) \longrightarrow \bar{\gamma}(^{4}_{3})^{(8)}{}'{}^{T}(t_{2g})] = \bar{g}_0{}^{\mp}(\bar{m}_0{}^{\mp} - \mu_B)$$

$$\mathfrak{X}[\bar{\gamma}(^{3}_{4})^{(8)}{}'{}^{T}(t_{2g}) \longrightarrow \bar{\gamma}(^{4}_{3})^{(8)}{}'{}^{T}(t_{2g})] = \bar{g}_0{}^{\mp 2}$$

$$\mathfrak{M}[\bar{\gamma}(^{3}_{4})^{(8)}{}'{}^{T}(t_{2g}) \longrightarrow \bar{\gamma}(^{4}_{3})^{(8)}{}'{}^{T}(t_{2g})] = (\bar{m}_0{}^{\mp} - \mu_B)^2 \quad (73)$$

Equation 70 has been constructed from eq. 20 and 69, [Division A, §3.1], eq. 71 and 73 from eq. 21 and 22, [Division A, §3.2], and eq. 72 from eq. A-22 [Appendix, §6.1]. The symbols $\mathfrak{W}$, $\mathfrak{X}$, $\mathfrak{M}$, l, g, r, p, and μ_B are as in Division A, §3 and the Appendix, §6. The redistribution of individual electric and magnetic dipole and spectral strength due to molecular spin-orbital functional reorientation in eq. 71 and 73 is a simple sample of what configurational interaction might be expected to accomplish. Indeed, this redistribution might be profitably thought as due to "orientational (symmetrizational) configurational interaction." Of course, as Kramers' pairs are not split on descent from digonal (D_2) and trigonal (D_3) dihedrality to unidigonal (D_1) dihedrality (except in the presence of magnetic fields; it would be exciting to measure their individual natural rotatory and spectral strengths in magnetic fields at low temperatures and thus to examine their actual polarizations and numerical valuations—the author sincerely hopes someone might attempt this task.), the full molecular spin-orbital rotational strengths derivable from eq. 71 and 73, in the absence of configuration, are coincident with those of eq. 26 [Division A, §3.2] and A-25 [Appendix, §6.2].

From eq. 57 through 73 and Tables IX and X, it is evident that numerous cross-relationships still exist in the unidigonal problem even though in many instances detailed assignations and polarizations have altered (these polarizations, although approximate in the off-axial directions due to neglect of true configuration interaction, are quite interesting and merit thorough and close experimental investigation and, hopefully, approximate confirmation[42]). This retention of cross-re-

(42) When true configuration interaction is small, as it may be for unidigonal dihedral aminated (and other) complexes in (cubically) isolated (and cubically degenerate) electronic states, such as the $^1T_{1g}$ state of cobalt(III) compounds, it may be actually possible to extract estimates of the magnitudes of the electric dipole strenghts g_0, g_1, and g_2 ($g = r$ or p) as well as their directions from polarized intensity and rotatory measurements on split triads and diads.

Table IX: The Spin-Free d^n (n = 1, 2, 3, 4, 5, 6, 7, 8, 9), Unidigonal Dihedral (Pseudo-Octahedral:Trigonal Orientation) Rotational and Spectral Strengths for Zero Spin-Orbit Forces[a]

n	Transitions	Rotational strengths	Spectral strengths: Electric	Spectral strengths: Magnetic
1 (s = 2)	$^2A(T_{2g}) \rightarrow {}^2E_{(B)}^{(A)}(T_{2g})$	$-\bar{g}_0\bar{m}_0$	$\bar{g}_0^2$	$\bar{m}_0^2$
and	$\rightarrow {}^2E_{(B)}^{(A)}(E_g)$	g_0m_0	g_0^2	m_0^2
6 (s = 5)	${}^2E_{(B)}^{(A)}(T_{2g}) \rightarrow {}^2E_{(A)}^{(B)}(T_{2g})$	$\bar{g}_0^{\mp}\bar{m}_0^{\mp}$	$^1/_2\bar{g}_0^{\pm 2} + \bar{g}_0^{\mp 2}$	$\bar{m}_0^{\mp 2}$
	$\rightarrow {}^2E_{(B)}^{(A)}(E_g)$	$^1/_2g_2m_2$	$^1/_2g_2^2$	$^1/_2m_2^2$
	$\rightarrow {}^2E_{(A)}^{(B)}(E_g)$	$g_1m_1 + {}^1/_2g_2m_2$	$g_1^2 + {}^1/_2g_2^2$	$m_1^2 + {}^1/_2m_2^2$
	${}^2E_{(B)}^{(A)}(E_g) \rightarrow {}^2E_{(A)}^{(B)}(E_g)$	$\bar{\bar{g}}_0^{\mp}\bar{\bar{m}}_0^{\mp}$	$^1/_2\bar{\bar{g}}_0^2 + \bar{\bar{g}}_0^{\mp 2}$	$\bar{\bar{m}}_0^{\pm 2}$
2 (s = 3)	$^2B(T_{1g}) \rightarrow {}^2E_{(A)}^{(B)}(T_{1g})$	$\bar{g}_0\bar{m}_0$	$\bar{g}_0^2$	$\bar{m}_0^2$
and	$\rightarrow {}^2A(T_{2g})$	$2g_1m_1$	$2g_1^2$	$2m_1^2$
7 (s = 4)	$\rightarrow {}^2E_{(B)}^{(A)}(T_{2g})$	$^1/_2g_2m_2$	$^1/_2g_2^2$	$^1/_2m_2^2$
	$\rightarrow {}^2B(T_{1g})$	0	0	0
	$\rightarrow {}^2E_{(A)}^{(B)}(T_{1g})$	$^1/_2g_2m_2$	$^1/_2g_2^2$	$^1/_2m_2^2$
	$\rightarrow {}^2B(A_{2g})$	0	0	0
	${}^2E_{(A)}^{(B)}(T_{1g}) \rightarrow {}^2E_{(B)}^{(A)}(T_{1g})$	$\bar{g}_0^{\mp}\bar{m}_0^{\mp}$	$^1/_2\bar{g}_0^{\pm 2} + \bar{g}_0^{\mp 2}$	$\bar{m}_0^{\mp 2}$
	$\rightarrow {}^2A(T_{2g})$	$^1/_2g_0m_0$	$^1/_2g_0^2$	$^1/_2m_0^2$
	$\rightarrow {}^2E_{(B)}^{(A)}(T_{2g})$	$^1/_4(g_0 + g_2)(m_0 + m_2) + {}^1/_2g_1m_1$	$^1/_4(g_0 + g_2)^2 + {}^1/_2g_1^2$	$^1/_4(m_0 + m_2)^2 + {}^1/_2m_1^2$
	$\rightarrow {}^2E_{(A)}^{(B)}(T_{2g})$	$^1/_4(g_0 + g_2)(m_0 + m_2)$	$^1/_4(g_0 + g_2)^2$	$^1/_4(m_0 + m_2)^2$
	$\rightarrow {}^2B(T_{1g})$	$^1/_2g_0m_0$	$^1/_2g_0^2$	$^1/_2m_0^2$
	$\rightarrow {}^2E_{(A)}^{(B)}(T_{1g})$	$^1/_4(g_0 - g_2)(m_0 - m_2)$	$^1/_4(g_0 - g_2)^2$	$^1/_4(m_0 - m_2)^2$
	$\rightarrow {}^2E_{(B)}^{(A)}(T_{1g})$	$^1/_4(g_0 - g_2)(m_0 - m_2) + {}^1/_2g_1m_1$	$^1/_4(g_0 - g_2)^2 + {}^1/_2g_1^2$	$^1/_4(m_0 - m_2)^2 + {}^1/_2m_1^2$
	$\rightarrow {}^2B(A_{2g})$	0	0	0
3 (s = 4)	$^2B(A_{2g}) \rightarrow {}^2A(T_{2g})$	$2g_1m_1$	$2g_1^2$	$2m_1^2$
and	$\rightarrow {}^2E_{(B)}^{(A)}(T_{2g})$	$^1/_2(g_0 + g_2)(m_0 + m_2)$	$^1/_2(g_0 + g_2)^2$	$^1/_2(m_0 + m_2)^2$
8 (s = 3)	$\rightarrow {}^2B(T_{1g})$	0	0	0
	$\rightarrow {}^2E_{(B)}^{(A)}(T_{1g})$	$^1/_2(g_0 - g_2)(m_0 - m_2)$	$^1/_2(g_0 - g_2)^2$	$^1/_2(m_0 - m_2)^2$
	$\rightarrow {}^2B(T_{1g})$	0	0	0
	$\rightarrow {}^2E_{(B)}^{(A)}(T_{1g})$	0	0	0
4 (s = 5)	${}^2E_{(B)}^{(A)}(E_g) \rightarrow {}^2E_{(A)}^{(B)}(E_g)$	$\bar{\bar{g}}_0^{\mp}\bar{\bar{m}}_0^{\mp}$	$^1/_2\bar{\bar{g}}_0^2 + \bar{\bar{g}}_0^{\mp 2}$	$\bar{\bar{m}}_0^{\pm 2}$
and	$\rightarrow {}^2A(T_{2g})$	g_0m_0	g_0^2	m_0^2
9 (s = 2)	$\rightarrow {}^2E_{(B)}^{(A)}(T_{2g})$	$^1/_2g_2m_2$	$^1/_2g_2^2$	$^1/_2m_2^2$
	$\rightarrow {}^2E_{(A)}^{(B)}(T_{2g})$	$g_1m_1 + {}^1/_2g_2m_2$	$g_1^2 + {}^1/_2g_2^2$	$m_1^2 + {}^1/_2m_2^2$
	$^2A(T_{2g}) \rightarrow {}^2E_{(B)}^{(A)}(T_{2g})$	$\bar{g}_0\bar{m}_0$	$\bar{g}_0^2$	$\bar{m}_0^2$
	${}^2E_{(B)}^{(A)}(T_{2g}) \rightarrow {}^2E_{(A)}^{(B)}(T_{2g})$	$\bar{g}_0^{\mp}\bar{m}_0^{\mp}$	$^1/_2\bar{g}_0^{\pm 2} + \bar{g}_0^{\mp 2}$	$\bar{m}_0^{\mp 2}$
5	$^6A(A_{1g}) \rightarrow {}^{2,4}B(T_{1g})$	0	0	0
	$\rightarrow {}^{2,4}E_{(A)}^{(B)}(T_{1g})$			
	$\rightarrow {}^{2,4}A(T_{2g})$			
	$\rightarrow {}^{2,4}E_{(B)}^{(A)}(T_{2g})$			
	$\rightarrow {}^2B(A_{2g})$			
	$\rightarrow {}^2A(A_{1g})$			
	$\rightarrow {}^2E_{(B)}^{(A)}(E_g)$			

[a] The quantities $\bar{g}_0$, $\bar{g}_0^{\pm}$, $\bar{g}_0^{\mp}$, $\bar{\bar{g}}_0$, $\bar{\bar{g}}_0^{\pm}$, $g_{0,1,2}$, $\bar{m}_0$, $\bar{m}_0^{\pm}$, $\bar{m}_0^{\mp}$, $\bar{\bar{m}}_0$, $\bar{\bar{m}}_0^{\pm}$, $m_{0,1,2}$ (g = r,p) are as defined generally and specially in ref. 6, footnote 49 and this paper, Appendix §6.1.

Table X: The Spin Paired d^n (n = 1, 2, 3, 4, 5, 6, 7, 8, 9), Unidigonal Dihedral (Pseudo-Octahedral:Trigonal Orientation) Rotational and Spectral Strengths for Zero Spin-Orbit Forces[a]

n	Transitions	Rotational strengths	Spectral strengths: Electric	Spectral strengths: Magnetic
4	$^3B(T_{1g}) \rightarrow {}^3E_{(B/A)}(T_{1g})$	$-\bar{g}_0\bar{m}_0$	$\bar{g}_0^2$	$\bar{m}_0^2$
	$\rightarrow {}^3E_{(A/B)}(E_g)$	$^4/_3 g_0 m_0$	$^4/_3 g_0^2$	$^4/_3 m_0^2$
	$\rightarrow {}^3B(T_{1g})$	0	0	0
	$\rightarrow {}^3E_{(B/A)}(T_{1g})$	$^1/_{12}(2g_0 + g_2)(2m_0 + m_2)$	$^1/_{12}(2g_0 + g_2)^2$	$^1/_{12}(2m_0 + m_2)^2$
	$\rightarrow {}^3A(T_{2g})$	$^1/_3 g_1 m_1$	$^1/_3 g_1^2$	$^1/_3 m_1^2$
	$\rightarrow {}^3E_{(A/B)}(T_{2g})$	$^1/_{12}(2g_0 - g_2)(2m_0 - m_2)$	$^1/_{12}(2g_0 - g_2)^2$	$^1/_{12}(2m_0 - m_2)^2$
	$\rightarrow {}^3A(A_{1g})$	$^2/_3 g_1 m_1$	$^2/_3 g_1^2$	$^2/_3 m_1^2$
	$\rightarrow {}^3E_{(A/B)}(E_g)$	$^1/_3 g_2 m_2$	$^1/_3 g_2^2$	$^1/_3 m_2^2$
	$\rightarrow {}^3B(A_{2g})$	0	0	0
	$\rightarrow {}^3A(T_{2g})$	$g_1 m_1$	g_1^2	m_1^2
	$\rightarrow {}^3E_{(A/B)}(T_{2g})$	$^1/_4 g_2 m_2$	$^1/_4 g_2^2$	$^1/_4 m_2^2$
	$\rightarrow {}^3B(T_{1g})$	0	0	0
	$\rightarrow {}^3E_{(B/A)}(T_{1g})$	$^1/_4 g_2 m_2$	$^1/_4 g_2^2$	$^1/_4 m_2^2$
	$^3E_{(B/A)}(T_{1g}) \rightarrow {}^3E_{(A/B)}(T_{1g})$	$\bar{g}_0^{\mp}\bar{m}_0^{\mp}$	$^1/_2\bar{g}_0^{\mp 2} + \bar{g}_0^{\mp 2}$	$\bar{m}_0^{\mp 2}$
	$\rightarrow {}^3E_{(A/B)}(E_g)$	$^4/_3 g_1 m_1 + {}^2/_3 g_2 m_2$	$^4/_3 g_1^2 + {}^2/_3 g_2^2$	$^4/_3 m_1^2 + {}^2/_3 m_2^2$
	$\rightarrow {}^3E_{(B/A)}(E_g)$	$^2/_3 g_2 m_2$	$^2/_3 g_2^2$	$^2/_3 m_2^2$
	$\rightarrow {}^3B(T_{1g})$	$^1/_{12}(g_0 + 2g_2)(m_0 + 2m_2)$	$^1/_{12}(g_0 + 2g_2)^2$	$^1/_{12}(m_0 + 2m_2)^2$
	$\rightarrow {}^3E_{(B/A)}(T_{1g})$	$^1/_{24}(g_0 - g_2)(m_0 - m_2)$	$^1/_{24}(g_0 - g_2)^2$	$^1/_{24}(m_0 - m_2)^2$
	$\rightarrow {}^3E_{(A/B)}(T_{1g})$	$^3/_4 g_1 m_1 + {}^1/_{24}(g_0 - g_2)(m_0 - m_2)$	$^3/_4 g_1^2 + {}^1/_{24}(g_0 - g_2)^2$	$^3/_4 m_1^2 + {}^1/_{24}(m_0 - m_2)^2$
	$\rightarrow {}^3A(T_{2g})$	$^1/_{12}(g_0 - 2g_2)(m_0 - 2m_2)$	$^1/_{12}(g_0 - 2g_2)^2$	$^1/_{12}(m_0 - 2m_2)^2$
	$\rightarrow {}^3E_{(A/B)}(T_{2g})$	$^1/_{24}(g_0 + g_2)(m_0 + m_2) + {}^1/_{12} g_1 m_1$	$^1/_{24}(g_0 + g_2)^2 + {}^1/_{12} g_1^2$	$^1/_{24}(m_0 + m_2)^2 + {}^1/_{12} m_1^2$
	$\rightarrow {}^3E_{(B/A)}(T_{2g})$	$^1/_{24}(g_0 + g_2)(m_0 + m_2)$	$^1/_{24}(g_0 + g_2)^2$	$^1/_{24}(m_0 + m_2)^2$
	$\rightarrow {}^3E_{(A/B)}(E_g)$	$^1/_6 g_0 m_0 + {}^1/_3 g_1 m_1$	$^1/_6 g_0^2 + {}^1/_3 g_1^2$	$^1/_6 m_0^2 + {}^1/_3 m_1^2$
	$\rightarrow {}^3E_{(B/A)}(E_g)$	$^1/_6 g_0 m_0$	$^1/_6 g_0^2$	$^1/_6 m_0^2$
	$\rightarrow {}^3A(A_{1g})$	$^1/_6(g_0 + g_2)(m_0 + m_2)$	$^1/_6(g_0 + g_2)^2$	$^1/_6(m_0 + m_2)^2$
	$\rightarrow {}^3B(A_{2g})$	$^1/_6(g_0 - g_2)(m_0 - m_2)$	$^1/_6(g_0 - g_2)^2$	$^1/_6(m_0 - m_2)^2$
	$\rightarrow {}^3A(T_{2g})$	$^1/_4 g_0 m_0$	$^1/_4 g_0^2$	$^1/_4 m_0^2$
	$\rightarrow {}^3E_{(A/B)}(T_{2g})$	$^1/_8(g_0 + g_2)(m_0 + m_2) + {}^1/_4 g_1 m_1$	$^1/_8(g_0 + g_2)^2 + {}^1/_4 g_1^2$	$^1/_8(m_0 + m_2)^2 + {}^1/_4 m_1^2$
	$\rightarrow {}^3E_{(B/A)}(T_{2g})$	$^1/_8(g_0 + g_2)(m_0 + m_2)$	$^1/_8(g_0 + g_2)^2$	$^1/_8(m_0 + m_2)^2$
	$\rightarrow {}^3B(T_{1g})$	$^1/_4 g_0 m_0$	$^1/_4 g_0^2$	$^1/_4 m_0^2$
	$\rightarrow {}^3E_{(B/A)}(T_{1g})$	$^1/_8(g_0 - g_2)(m_0 - m_2)$	$^1/_8(g_0 - g_2)^2$	$^1/_8(m_0 - m_2)^2$
	$\rightarrow {}^2E_{(A/B)}(T_{1g})$	$^1/_8(g_0 - g_2)(m_0 - m_2) + {}^1/_4 g_1 m_1$	$^1/_8(g_0 - g_2)^2 + {}^1/_4 g_1^2$	$^1/_8(m_0 - m_2)^2 + {}^1/_4 m_1^2$
5	$^2A(T_{2g}) \rightarrow {}^2E_{(A/B)}(T_{2g})$	$\bar{g}_0\bar{m}_0$	$\bar{g}_0^2$	$\bar{m}_0^2$
	$\rightarrow {}^2B(A_{2g})$	$^2/_3 g_1 m_1$	$^2/_3 g_1^2$	$^2/_3 m_1^2$
	$\rightarrow {}^2B(T_{1g})$	$3g_1 m_1$	$3g_1^2$	$3m_1^2$
	$\rightarrow {}^2E_{(B/A)}(T_{1g})$	$^3/_4 g_2 m_2$	$^3/_4 g_2^2$	$^3/_4 m_2^2$
	$\rightarrow {}^2A(T_{2g})$	0	0	0
	$\rightarrow {}^2E_{(A/B)}(T_{2g})$	$^1/_{12}(2g_0 + g_2)(2m_0 + m_2)$	$^1/_{12}(2g_0 + g_2)^2$	$^1/_{12}(2m_0 + m_2)^2$
	$\rightarrow {}^2E_{(A/B)}(E_g)$	$^1/_3 g_2 m_2$	$^1/_3 g_2^2$	$^1/_3 m_2^2$
	$\rightarrow {}^2A(T_{2g})$	0	0	0
	$\rightarrow {}^2E_{(A/B)}(T_{2g})$	$^3/_4 g_2 m_2$	$^3/_4 g_2^2$	$^3/_4 m_2^2$
	$\rightarrow {}^2B(T_{1g})$	$^1/_3 g_1 m_1$	$^1/_3 g_1^2$	$^1/_3 m_1^2$
	$\rightarrow {}^2E_{(B/A)}(T_{1g})$	$^1/_{12}(2g_0 - g_2)(2m_0 - m_2)$	$^1/_{12}(2g_0 - g_2)^2$	$^1/_{12}(2m_0 - m_2)^2$
	$\rightarrow {}^2A(A_{1g})$	0	0	0

Table X (*Continued*)

n	Transitions	Rotational strengths	Spectral strengths: Electric	Spectral strengths: Magnetic
	$\rightarrow {}^2E_{(\frac{A}{B})}(E_g)$	$^1/_3 g_0 m_0$	$^1/_8 g_0^2$	$^1/_3 m_0^2$
5	${}^2E_{(\frac{A}{B})}(T_{2g}) \rightarrow {}^2E_{(\frac{B}{A})}(T_{2g})$	$\bar{g}_0^{\mp}\bar{m}_0^{\mp}$	$^1/_2\bar{g}_0^{\mp 2} + \bar{g}_0^{\mp 2}$	$\bar{m}_0^{\mp 2}$
	$\rightarrow {}^2B(A_{2g})$	$^1/_6(g_0 + g_2)(m_0 + m_2)$	$^1/_6(g_0 + g_2)^2$	$^1/_6(m_0 + m_2)^2$
	$\rightarrow {}^2B(T_{1g})$	$^3/_4 g_0 m_0$	$^3/_4 g_0^2$	$^3/_4 m_0^2$
	$\rightarrow {}^2E_{(\frac{B}{A})}(T_{1g})$	$^3/_8(g_0 + g_2)(m_0 + m_2) + {}^3/_4 g_1 m_1$	$^3/_8(g_0 + g_2)^2 + {}^3/_4 g_1^2$	$^3/_8(m_0 + m_2)^2 + {}^3/_4 m_1^2$
	$\rightarrow {}^2E_{(\frac{A}{B})}(T_{1g})$	$^3/_8(g_0 + g_2)(m_0 + m_2)$	$^3/_8(g_0 + g_2)^2$	$^3/_8(m_0 + m_2)^2$
	$\rightarrow {}^2A(T_{2g})$	$^1/_{12}(g_0 + 2g_2)(m_0 + 2m_2)^2$	$^1/_{12}(g_0 + 2g_2)^2$	$^1/_{12}(m_0 + 2m_2)^2$
	$\rightarrow {}^2E_{(\frac{A}{B})}(T_{2g})$	$^1/_{24}(g_0 - g_2)(m_0 - m_2)$	$^1/_{24}(g_0 - g_2)^2$	$^1/_{24}(m_0 - m_2)^2$
	$\rightarrow {}^2E_{(\frac{B}{A})}(T_{2g})$	$^1/_{24}(g_0 - g_2)(m_0 - m_2) + {}^3/_4 g_1 m_1$	$^1/_{24}(g_0 - g_2)^2 + {}^3/_4 g_1^2$	$^1/_{24}(m_0 - m_2)^2 + {}^3/_4 m_1^2$
	$\rightarrow {}^2E_{(\frac{A}{B})}(E_g)$	$^1/_6 g_0 m_0$	$^1/_6 g_0^2$	$^1/_6 m_0^2$
	$\rightarrow {}^2E_{(\frac{B}{A})}(E_g)$	$^1/_6 g_0 m_0 + {}^1/_3 g_1 m_1$	$^1/_8 g_0^2 + {}^1/_3 g_1^2$	$^1/_6 m_0^2 + {}^1/_3 m_1^2$
	$\rightarrow {}^2A(T_{2g})$	$^3/_4 g_0 m_0$	$^3/_4 g_0^2$	$^3/_4 m_0^2$
	$\rightarrow {}^2E_{(\frac{A}{B})}(T_{2g})$	$^3/_8(g_0 - g_2)(m_0 - m_2)$	$^3/_8(g_0 - g_2)^2$	$^3/_8(m_0 - m_2)^2$
	$\rightarrow {}^2E_{(\frac{B}{A})}(T_{2g})$	$^3/_8(g_0 - g_2)(m_0 - m_2) + {}^3/_4 g_1 m_1$	$^3/_8(g_0 - g_2)^2 + {}^3/_4 g_1^2$	$^3/_8(m_0 - m_2)^2 + {}^3/_4 m_1^2$
	$\rightarrow {}^2B(T_{1g})$	$^1/_{12}(g_0 - 2g_2)(m_0 - 2m_2)$	$^1/_{12}(g_0 - 2g_2)^2$	$^1/_{12}(m_0 - 2m_2)^2$
	$\rightarrow {}^2E_{(\frac{B}{A})}(T_{1g})$	$^1/_{24}(g_0 + g_2)(m_0 + m_2) + {}^1/_{12} g_1 m_1$	$^1/_{24}(g_0 + g_2)^2 + {}^1/_{12} g_1^2$	$^1/_{24}(m_0 + m_2)^2 + {}^1/_{12} m_1^2$
	$\rightarrow {}^2E_{(\frac{A}{B})}(T_{1g})$	$^1/_{24}(g_0 + g_2)(m_0 + m_2)$	$^1/_{24}(g_0 + g_2)^2$	$^1/_{24}(m_0 + m_2)^2$
	$\rightarrow {}^2A(A_{1g})$	$^1/_6(g_0 - g_2)(m_0 - m_2)$	$^1/_6(g_0 - g_2)^2$	$^1/_8(m_0 - m_2)^2$
	$\rightarrow {}^2E_{(\frac{A}{B})}(E_g)$	$^1/_6 g_2 m_2$	$^1/_8 g_2^2$	$^1/_6 m_2^2$
	$\rightarrow {}^2E_{(\frac{B}{A})}(E_g)$	$^1/_3 g_1 m_1 + {}^1/_6 g_2 m_2$	$^1/_8 g_1^2 + {}^1/_6 g_2^2$	$^1/_3 m_2^2 + {}^1/_6 m_2^2$
6	${}^1A(A_{1g}) \rightarrow {}^1B(T_{1g})$	$4 g_1 m_1$	$4 g_1^2$	$4 m_1^2$
	$\rightarrow {}^1E_{(\frac{B}{A})}(T_{1g})$	$(g_0 + g_2)(m_0 + m_2)$	$(g_0 + g_2)^2$	$(m_0 + m_2)^2$
	$\rightarrow {}^1A(T_{2g})$	0	0	0
	$\rightarrow {}^1E(\frac{A}{B})(T_{2g})$	$(g_0 - g_2)(m_0 - m_2)$	$(g_0 - g_2)^2$	$(m_0 - m_2)^2$
7	${}^2E_{(\frac{A}{B})}(E_g) \rightarrow {}^2E_{(\frac{B}{A})}(E_g)$	$\bar{\bar{g}}_0^{\mp}\bar{\bar{m}}_0^{\mp}$	$^1/_2\bar{\bar{g}}_0^{\mp 2} + \bar{\bar{g}}_0^{\mp 2}$	$\bar{\bar{m}}_0^{\mp 2}$
	$\rightarrow {}^2B(T_{1g})$	$^3/_2 g_0 m_0$	$^3/_2 g_0^2$	$^3/_2 m_0^2$
	$\rightarrow {}^2E_{(\frac{B}{A})}(T_{1g})$	$^3/_2 g_1 m_1 + {}^3/_4 g_2 m_2$	$^3/_2 g_1^2 + {}^3/_4 g_2^2$	$^3/_2 m_2^2 + {}^3/_4 m_2^2$
	$\rightarrow {}^2E_{(\frac{A}{B})}(T_{1g})$	$^3/_4 g_2 m_2$	$^3/_4 g_2^2$	$^3/_4 m_2^2$
	$\rightarrow {}^2A(T_{2g})$	$^1/_2 g_2 m_2$	$^1/_2 g_2^2$	$^1/_2 m_2^2$
	$\rightarrow {}^2E_{(\frac{A}{B})}(T_{2g})$	$^1/_4 g_0 m_0$	$^1/_4 g_0^2$	$^1/_4 m_0^2$
	$\rightarrow {}^2E_{(\frac{B}{A})}(T_{2g})$	$^1/_4 g_0 m_0 + {}^1/_2 g_1 m_1$	$^1/_4 g_0^2 + {}^1/_2 g_1^2$	$^1/_4 m_0^2 + {}^1/_2 m_1^2$
	$\rightarrow {}^2B(T_{1g})$	$^1/_2 g_2 m_2$	$^1/_2 g_2^2$	$^1/_2 m_2^2$
	$\rightarrow {}^2E_{(\frac{B}{A})}(T_{1g})$	$^1/_4 g_0 m_0 + {}^1/_2 g_1 m_1$	$^1/_4 g_0^2 + {}^1/_2 g_1^2$	$^1/_4 m_0^2 + {}^1/_2 m_1^2$
	$\rightarrow {}^2E_{(\frac{A}{B})}(T_{1g})$	$^1/_4 g_0 m_0$	$^1/_4 g_0^2$	$^1/_4 m_0^2$
	$\rightarrow {}^2A(T_{2g})$	$^1/_2 g_0 m_0$	$^1/_2 g_0^2$	$^1/_2 m_0^2$
	$\rightarrow {}^2E(\frac{A}{B})(T_{2g})$	$^1/_4 g_2 m_2$	$^1/_4 g_2^2$	$^1/_4 m_2^2$
	$\rightarrow {}^2E_{(\frac{B}{A})}(T_{2g})$	$^1/_2 g_1 m_1 + {}^1/_4 g_2 m_2$	$^1/_2 g_1^2 + {}^1/_4 g_2^2$	$^1/_2 m_1^2 + {}^1/_4 m_2^2$

[a] The quantities $\bar{g}_0$, $\bar{g}_0^{\mp}$, $\bar{g}_0^{\mp}$, $\bar{\bar{g}}_0$, $\bar{\bar{g}}_0^{\mp}$, $g_{0,1,2}$, $\bar{m}_0$, $\bar{m}_0^{\mp}$, $\bar{m}_0^{\mp}$, $\bar{\bar{m}}_0$, $\bar{\bar{m}}_0^{\mp}$, $m_{0,1,2}$ ($g = r,p$) are as defined generally and specially in ref. 6, footnote 49 and this paper, Appendix, §6.1.

lations is, of course, not coincidental, but a direct consequent of our employment of the concept of pseudo-octahedrality. Measured deviations from these relations are sure indications of the import of intraconfigurational mixture.

The unidigonal dihedral polydentate wave functions,

Table XI: Specification of the Differential Angular Momentum Operations

	d_{xy}	d_{xz}	d_{yz}	$d_{x^2-y^2}$	$d_{3z^2-r^2}$	s	p_x	p_y	p_z
ℓ_x	$i\hbar d_{xz}$	$-i\hbar d_{xy}$	$i\hbar(\sqrt{3}d_{3z^2-r^2} + d_{x^2-y^2})$	$-i\hbar d_{yz}$	$-i\hbar\sqrt{3}d_{yz}$	0	0	$i\hbar p_z$	$-i\hbar p_y$
ℓ_y	$-i\hbar d_{yz}$	$-i\hbar(\sqrt{3}d_{3z^2-r^2} - d_{x^2-y^2})$	$i\hbar d_{xy}$	$-i\hbar d_{xz}$	$i\hbar\sqrt{3}d_{xz}$	0	$-i\hbar p_z$	0	$i\hbar p_x$
ℓ_z	$-i\hbar 2d_{x^2-y^2}$	$i\hbar d_{yz}$	$-i\hbar d_{xz}$	$i\hbar 2d_{xy}$	0	0	$i\hbar p_y$	$-i\hbar p_x$	0

matrix elements, and rotational and spectral strengths follow by similar means. We shall not produce these here, but leave their development to the future[43] [examine, however, section VII].

VII. Compounds of No Symmetry

Transition metal compounds of no symmetry (C_1) divide into four types: monodentate [Fig. 45], monobidentate [Fig. 46], dibidentate [Fig. 42], and polydentate [Fig. 43]. The unravelment of the transition metal monodentate problem [read Division C for the nontransition metal problem] is immediate—one need but take linear combinations of molecular orbitals of primary atom atomic-like kd, $(k + 1)$s, $(k + 1)$p and ligand atom atomic-like ns, np, nd orbitals, without regard to symmetry, and compute the requisite electric and magnetic dipole matrix arrays. Unfortunately, this immediacy is counterbalanced by ineradicable computational uncertainty. There is now no longer any simple way of fixing the signs and magnitudes of the covalency parameters thus introduced.[44] Hence, only long, protracted, tedious, and (presently) questionable calculation can solve the problem [view Division C].

The disentanglement of the asymmetrical monobidentate and dibidentate problems is easy. The wave functions, matrix elements, and rotational and spectral strengths of the unidigonal monobidentate and dibidentate problems of section VI apply directly. All that need be done is give all orbital electronic states the noncommital C_1 label A in place of the specific D_1 labels A and B and all molecular spin-orbital electronic states the common dual space $C_1\dagger$ label[41] γ_2 (or γ_2^A to indicate asymmetry) in place of the separate $D_1\dagger$ labels γ_3 and γ_4. Naturally, the authentic C_1 and $C_1\dagger$ wave functions, matrix elements, and rotational and spectral strengths depend critically upon the extent of interconfigurational interaction. However, those of the unidigonal circumstance should provide a good starting point.

Asymmetric polydentate complexes pose a more difficult proposition, primarily of a topological nature. As is visible from Fig. 42, 43, and 44, for such chemicals it is not clear without detailed X-ray evidence, which evidence is not yet extant, what their factual ligand internal geometrical conformations, and hence their

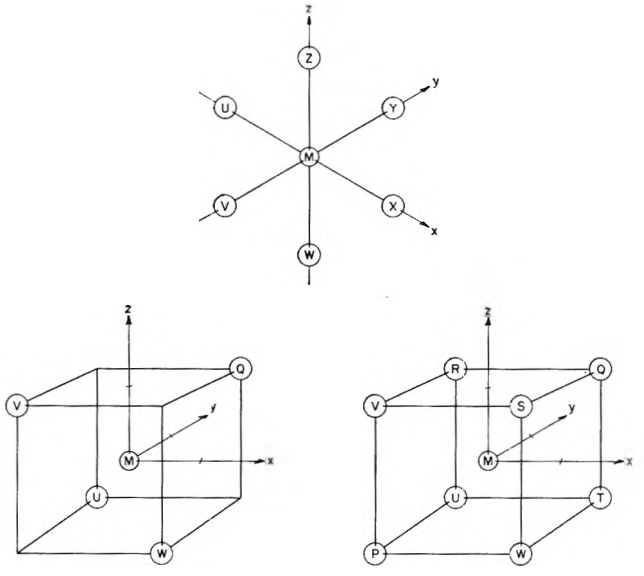

Figure 45. Some typical instances of possible optically active monodentate metallate architectures, the octahedrally hexacoordinate, the tetrahedrally tetracoordinate, and the hexahedrally octacoordinate. For a recount of their isomers, study ref. 46w.

localized lone-pair (or donor or acceptor) orbital conformations, will be. Without this vital information molecular orbitals cannot be formed and calculations cannot be made. Nonetheless, despite this critical drawback, some comment can still be voiced. The comment concerns the classification of their absolute nuclear configurations. Simply spoken, the comment is the following: a classification of the absolute nuclear configuration and a declaration of the rotatory sign should be founded solely on the detailed disposition of the ligand nuclear casements and of the localized ligand lone pair (or donor or acceptor) orbitals, which disposition can be (qualitatively) fixed by use of Dreiding or other directed orbital molecular models [witness Fig.

(43) A. D. Liehr, to be instituted.

(44) Overlap criteria cannot be used as those immixed functions which create electric dipole moments create no overlap. [This imbroglio is not new with the monodentate issue, but is quite general: it occurred also in the trigonal, digonal, and unidigonal bidentate situations. However, there an artful dodge was possible (but not necessarily factual!), which is not intelligibly extensible here (recall footnote 22).]

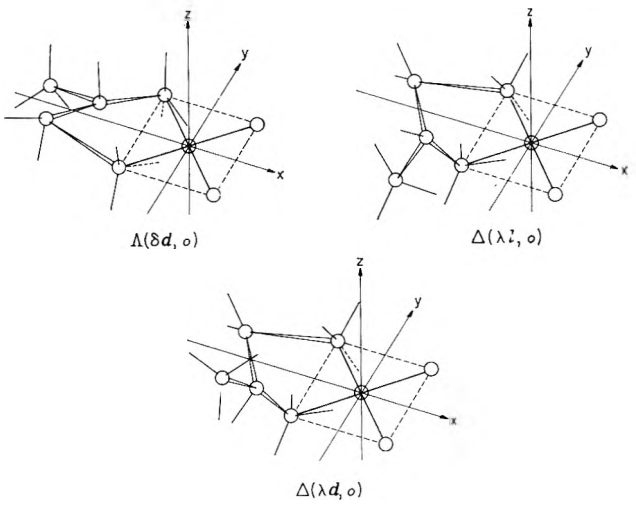

Figure 46. A prototype monobidentate asymmetric compound, the monopropylenediamine metallate aggregate. Exhibited is the $\Lambda(\delta d,o)$ optical isomer and its full and partial antipodes, $\Delta(\lambda l,o)$ and $\Delta(\lambda d,o)$, severally. [The adjective parenthesized *d* and *l* explicate the conformational condition of the bidentate propylenediamine addend.] Draftsman conventions are as in Fig. 36a,b. Slight differences in localized (nitrogen or other) lone-pair (or bond-pair) donor (or acceptor) orbital form due to methyl (or other) group inductive and steric effects prevent metallochromophoric rotational compensation in pseudo-racemic mixtures, $\Lambda(\delta d,o) + \Delta(\lambda d,o)$. Mark that these inductive and steric effects (so-called "vicinal effects") are additive to good approximation for electronic transitions which are either intrinsically electric dipole or magnetic dipole allowed [this declaration is quickly proved upon decomposition of the inductively and sterically altered localized orbital fractional contents into symmetrical and corrective forms, $a_{j\varsigma}'\lambda'_j$ equals $a_{j\varsigma}\lambda_j + (a_{j\varsigma}'\lambda_j' - a_{j\varsigma}\lambda_j)$, and substitution into eq. 3 through 12, 16, 17, 21, and 22. For electric or magnetic dipole-allowed transitions the corrective terms then appear linearly]. These theoretical anticipations and predictions are experimentally substantiated.[4,5,46g,n,t]

42, 43, and 44] in conjunction with the known (by X-ray crystallographic or other studies) internal and external ligand constellations, and should be made only with regard to a decomposition of this fixed ligand nuclear and lone-pair disposition into a set basis of elementary forms. The absolute molecular over-all configuration is then named in accord with the least contrived and contorted linear superposition of the basis forms which will precisely reproduce the given polydentate localized orbital structure. A suggested set of standard elementary orbital forms is pictured in Fig. 47, and sample decompositions and classifications with them are portrayed in Fig. 1 through 8, 14 through 17b, and 23 through 46.[45] Other examples should readily suggest themselves. The proof of this scheme will lie in its usefulness.

A compend of experimental fact of transition metal activity is attached.[46]

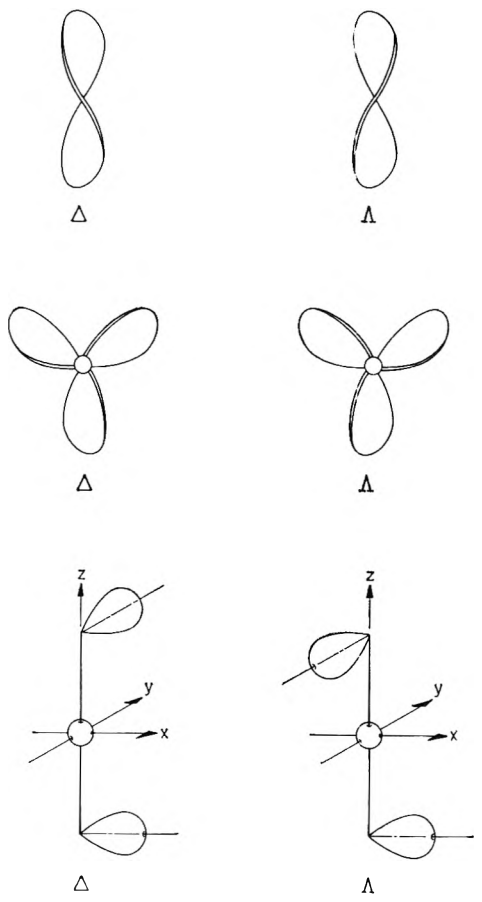

Figure 47. Standard orbital and structural dispositional basis forms and their advocated nomena.

(45) For a qualitative description of the interaction of electromagnetic radiation with elementary shapes of this sort consult (a) C. R. Noller, *J. Chem. Educ.*, 24, 600 (1947), and references 4b, p, q, x, y, z and 5s, bb, and cc. In particular, note the close similarity and strong analogy of the dissymmetric electron dispositions of the present work [*cf.* Fig. 1 through 8, 14 through 17b, and 23 through 46] with the skewed and spirated oscillator collocations (Drude, Oseen, Born, etc., Kuhn, and their followers[4,5]) and the torsed and crooked nuclear allocations (Fresnel, Pasteur, etc., Scheringa, and their successors[4,5]) of Fresnel, Pasteur, Drude, Oseen, Born, Kuhn, Scheringa, etc.[4,5] Our twisted electron arrangements are merely the quantal transcription and unification of their classical contention and perscription [in fact, they are simply the modernization and mathematization of Stark's qualitative valency electron theory[4,5]]. Note too that our notational innovation is readily extensible and straightly applicable to embrace and treat monodentate diversely coordinate and structurally irregulate allene- and spirane-like substitute situations also. All that be needed is the adoption of a sequence rule for chirality specification. If one adopts the presently popular atomic and mass number rule [read (b) R. S. Cahn, *ibid.*, 41, 116 (1964)] and views the groupment down its pseudo-threefold axis [*i.e.*, so as to point the lowest numbered group (pseudo-tetrahedral case) or groups (pseudo-octahedral or hexahedral case) *toward* the observer. A lone or bond pair, donor or acceptor is here counted as having atomic and mass number zero], then the monodentate situation is counted Δ (over-all designation) [or δ (sub-specification)] or Λ (over-all designation) [or λ (sub-specification)] according to whether a right-handed or left-handed screw advances toward the observer when turned from the group of highest number to that of next highest number [*i.e.*, so that a right-hand counterclockwise rotation or a left-hand clockwise rotation advances the right or left thumb toward the lowest numbered group, and so, toward the observer. *Cf.* Fig. 45 and 50]. If one stretches the now eminent atomic and mass number rule[45b] by the association of a vector

(dipole) run from the next lightest or heaviest to the lightest or heaviest groupment about a dissymmetric site and sights along the axis plumb to the groupment vector (dipole) pairs [for allene- and spirane-like aggregates this is the long primary atom (carbon, aluminum, cobalt, etc.)–primary atom (carbon, aluminum, cobalt, etc.) molecular axis. A lone or bond pair, donor or acceptor, is again reckoned to have atomic and mass number zero (the rare instance of two separate and distinct lone or bond pairs in the same aggregate requires but slight amendment)], then the allene- and spirane-like situations are reckoned Δ (over-all designation) [or δ (sub-specification)] or Λ (over-all designation) [or λ (sub-designation)] according as a right-handed or left-handed screw advances toward the observer when the hand is turned so that the palm side vector (dipole) is transplaced into ecliptic coincidence with the thumb side vector (dipole) [*i.e.*, so that a right-hand counterclockwise or left-hand clockwise rotation which advances the thumb (which is placed perpendicular to the directions of the skewed vector "dipoles") toward the observer sends the palm side vector (dipole) into eclipse with the thumb side vector (dipole). *Cf.* Fig. 49a, b, c. Mark that the vectorial prescription can also be applied to the varicoordinate monodentate situation and that it there yields stereochemical distinguishments identical with those of before. In truth, the vector (dipole) prescription actually yields them easier!]. These prescriptions are quickly transferred to more intricate chemical architectures. They lead to coincident stereochemical assignment with past usage where overlap exists [*e.g.*, our Δ, Λ (a catholicization of Piper's[5w] Δ and Λ) coincides with Cahn, Ingold, and Prelog's[4ib] R and S, without the latter's alphabetical disadvantage (remember that rotational and spectral strengths and that nuclear coordinate displacements and vectors are also customarily called R and S)], but are more ecumenical, not being fettered by the tyranny and magistery of the doctrine of the asymmetric carbon atom [read ref. 45a for an incisive and trenchant critique of the asymmetric carbon doctrine]. The author most sincerely hopes they will find favor.

(46) (a) F. M. Jaeger, "Spatial Arrangements of Atomic Systems and Optical Activity," The George Fisher Baker Non-Resident Lectureship in Chemistry, Cornell University, McGraw-Hill Book Co., Inc., New York, N. Y., 1930, pp. 23–234; (b) P. Pfeiffer, "Komplexverbindungen," Stereochemie, Buch 3, K. Freudenberg, Ed., F. Deuticke, Leipzig and Vienna, 1933, pp. 1200–1377; (c) M. Kobayashi, *J. Chem. Soc. Japan*, **64**, 648 (1943); (d) B. C. Kar, *J. Indian Chem. Soc.*, **24**, 117 (1947); (e) L. N. Essen and A. D. Gel'man, *Zh. Neorgan. Khim.*, **1**, 2475 (1956); L. N. Essen, F. A. Zakharova, and A. D. Gel'man, *ibid.*, **3**, 2654 (1958) [monodentate hexacoordinate platinum(IV) compounds]; (f) F. P. Dwyer, N. S. Gill, E. C. Gyarfas, and F. Lions, *J. Am. Chem. Soc.*, **79**, 1269 (1957) [sexadentate ligands]; F. Lions and K. V. Martin, *ibid.*, **79**, 1273 (1957) [possible optically active "tetrahedral" four-coordinate copper(II)]; F. P. Dwyer and F. L. Garvan, *ibid.*, **80**, 4480 (1958) [penta- and/or sexadentate ligands]; A. M. Sargeson, "Metal Chelates and Chelating Agents," D. P. Mellor and F. P. Dwyer, Ed., Academic Press, New York and London, 1964, Chapter 4; T. E. McDermott and A. M. Sargeson, ref. 29; (g) Y. Shimura, *Bull. Chem. Soc. Japan*, **31**, 315 (1958); J. Hidaka, S. Yamada, and R. Tsuchida, *ibid.*, **31**, 921 (1958); J. Hidaka, Y. Shimura, and R. Tsuchida, *ibid.*, **33**, 847 (1960); **35**, 567 (1962), Y. Shimura, *Bunko Kenkyu*, **9**, 127 (1961) [review of optical rotatory dispersion phenomena of metal complexes]; *Kagaku*, **16**, 529 (1961) [review of optical rotatory dispersion phenomena of d^6 complexes]; (h) F. Woldbye, "Optical Rotatory Dispersion of Transition Metal Complexes," Final Technical Research Report, European Research Office, U. S. Department of the Army, Frankfurt am Main, June 30, 1959, Contract No. DA-91-508-EUC-246; "Technique of Inorganic Chemistry," H. B. Jonassen, Ed., Interscience Publishers, Inc., New York and London, to be published; *Record Chem. Progr.*, **24**, 197 (1963); O. Kling and F. Woldbye, *Acta Chem. Scand.*, **15**, 704 (1961) [optical activity in the chromium(III) (spin-forbidden) "R bands." For theory read ref. 6 and C. J. Ballhausen, *Mol. Phys.*, **6**, 461 (1963)]; (i) M. Billardon, *Compt. rend.*, **251**, 2320 (1960); (j) E. Bunnenberg and C. Djerassi, *J. Am. Chem. Soc.*, **82**, 5953 (1960) [osmate esters]; B. Sjöberg and R. Backstrom, *Acta Chem. Scand.*, **16**, 786 (1962) [nickel xanthates]; (k) R. D. Archer and J. C. Bailar, Jr., *J. Am. Chem. Soc.*, **83**, 812 (1961); E. J. Corey and J. C. Bailar, Jr., ref. 28; (l) D. H. Busch, D. W. Cooke, K. Swaminathan, and Y. Ae Im, "Advances in the Chemistry of the Coordination Compounds," S. Kirschner, Ed., Macmillan, New York, N. Y., 1961, pp. 139–153; (m) S. F. Mason, *Proc. Chem. Soc.*, 137 (1962); R. E. Ballard, A. J. McCaffery, and S. F. Mason, *ibid.*, 331 (1962); A. J. McCaffery and S. F. Mason, *ibid.*, 388 (1962); *Trans. Faraday Soc.*, **59**, 1 (1963); *Mol. Phys.*, **6**, 359 (1963); *Proc. Chem. Soc.*, 211 (1963); A. J. McCaffery, S. F. Mason, and B. J. Norman, *ibid.*, 259 (1964); A. J. McCaffery, S. F. Mason, and R. E. Ballard, in press; S. F. Mason, ref. 5bb; (n) J. G. Brushmiller, E. L. Amma, and B. E. Douglas, *J. Am. Chem. Soc.*, **84**, 111, 3227 (1962), and to be published; B. E. Douglas, R. A. Haines, and J. G. Brushmiller, *Inorg. Chem.*, **2**, 1194 (1963); J. Hidaka and B. E. Douglas, *ibid.*, **3**, 1180, 1724 (1964); C. T. Liu and B. E. Douglas, *ibid.*, **3**, 1356, 1796 (1964); R. A. Maines and B. E. Douglas, *ibid.*, submitted; (o) Th. Bürer, *Helv. Chim. Acta*, **46**, 242, 2388 (1963); R. D. Gillard, *Nature*, **198**, 580 (1963); **201**, 989 (1964); *J. Inorg. Nucl. Chem.*, **26**, 657, 1455 (1964); *Spectrochim. Acta*, **20**, 1431 (1964); R. D. Gillard and G. Wilkinson, *J. Chem. Soc.*, 1368 (1964); J. H. Dunlop and R. D. Gillard, *Mol. Phys.*, **7**, 493 (1964); *J. Chem. Soc.*, 2822 (1964); J. H. Dunlop, R. D. Gillard, and G. Wilkinson, *ibid.*, 3160 (1964); and especially the classic works of Kuhn and Mathieu: (p) W. Kuhn and A. Szabo, *Z. physik. Chem.*, **15B**, 59 (1932); W. Kuhn and K. Bein, *Z. anorg. allgem. Chem.*, **216**, 321 (1934), and ref. 4; (q) J. P. Mathieu, *Compt. rend.*, **193**, 1079 (1931); **194**, 1727 (1932); **195**, 1017 (1932); **196**, 1222 (1933); **197**, 56 (1933); **198**, 251 (1934); *Bull. soc. chim. France*, **1**, 1713 (1934); *Ann. Phys.*, [11] **3**, 371 (1935) [metallo tartrates]; (r) J. P. Mathieu, *Compt. rend.*, **198**, 1598 (1934); **199**, 278 (1934); **201**, 1183 (1935); *J. chim. phys.*, **33**, 78 (1936); *Bull. soc. chim. France*, **3**, 463, 476 (1963); **4**, 687 (1937); **6**, 1258 (1939); "Contribution a l'Etude de la Structure Moleculaire," Volume Commemoratif Victor Henri, Desoer, Liege, 1947–1948, pp. 111–117; E. Drouard and J. P. Mathieu, *Compt. rend.*, **236**, 2395 (1953) [metallo amines and oxalates]; (s) J. P. Mathieu, *Bull. soc. chim. France*, **5**, 105 (1938) [binuclear metallates]; J. P. Mathieu, *ibid.*, **6**, 873 (1939); *Ann. Phys.*, **19**, 335 (1944) [metallochromophoric anomalous rotatory dispersion due to intrinsic free ligand dissymmetry. Confer also Shimura,[46k] Djerassi,[4k] Ranck,[5z] Liu and Douglas,[46n] and Dunlop and Gillard[46o]]; (u) J. P. Mathieu, *Compt. rend.*, **215**, 325 (1942) [critique of optical rotatory valence criteria]; (v) J. P. Mathieu, *Bull. soc. chim. France*, **5**, 725 (1938) [a marvelous review of inorganic optical activity and stereochemistry] and of A. Werner, F. M. Jaeger, and P. Pfeiffer [a literature search of their works is well worth the effort. Partial registers may be found in all of the references of this footnote. footnote 46]. The enumeration of optical isomers is reviewed in (w) B. A. Kennedy, D. A. McQuarrie, and C. H. Brubaker, Jr., *Inorg. Chem.*, **3**, 265 (1963). Some structures of biological interest [cobalamines and hemoproteins] are treated in (x) L. Velluz, M. Legrand, and R. Viennet, *Compt. rend.*, **255**, 15 (1962); M. Legrand and R. Viennet, *Bull. soc. chim. France*, 1435 (1962); G. L. Eichhorn and A. J. Osbahr, "Advances in the Chemistry of the Coordination Compounds," S. Kirschner, Ed., Macmillan, New York, N. Y., 1961, pp. 216–223; G. L. Eichhorn, ref. 4h, p. 208, among other places. Witness that our theory applies with equal force to systems such as these also [*cf.* Fig. 1 through 8, 14 through 17, 23 through 50].

NOTE ADDED IN PROOF.—In the course of their continued extremely important and fascinating studies on the effect of electrolytes and ion association on optical rotatory power [M. J. Albinak, D. C. Bhatnagar, S. Kirschner, and A. J. Sonnessa, "Advances in the Chemistry of the Coordination Compounds," S. Kirschner, Ed., The Macmillan Co., New York, N. Y., 1961, pp. 154–172; *Can. J. Chem.*, **39**, 2360 (1961), *et seq.*, see also the related work of H. L. Smith and B. E. Douglas, *J. Am. Chem. Soc.*, **86**, 3885 (1964)], Kirschner and his co-workers have recently discovered [S. Kirschner and D. C. Bhatnagar, Proceedings of the Symposium on the Structure and Properties of Coordination Compounds, Bratislava, Czechoslovakia, Sept. 2–4, 1964; Proceedings of the Symposium on Coordination Chemistry, Tihany, Lake Balaton, Hungary, Sept. 14–17, 1964] that a monodentively coordinated asymmetric ligand may induce a sizable optical rotivity in an over-all hexacoordinate transition metal compound [their example is $Co(NH_3)_5(d\text{-tartrate})^+$]. This finding apparently upsets the tentative suggestions of some [read, *e.g.*, E. Larsen and I. Olsen, *Acta Chem. Scand.*, **18**, 1025 (1964)] that chelation is necessary for such an (measurable) occurrence. However, it is difficult to envision how a freely (or but slightly hindered) rotating asymmetric ligand can induce metallochromophoric activity. Hence, perhaps, some secondary chelation [hydrogen-bond formation (?)], or other physicochemical steric hindrance ["pseudo" chelation (?)] takes place. Only time and further experimentation will tell. What is sure, though, is that, by some means, local metallochromophoric electronic dissymmetry must be established by a (average at least) fixation of the local metal–ligand charge density in a dissymmetric fashion, along the lines sketched in the text above. Reasonable van der Waals dissymmetric inductions

Division C

Nontransition Metal Compounds

VIII. Organic Compounds

Without doubt the richest lode of naturally optically active compounds is the organic cornucopia. However, also without doubt, it (and its inorganic obverse—see section IX) is the most difficult to treat theoretically. This difficulty obtains because of our current lack of a theory suitable for the fabrication of the needful wave functions, energy values, matrix elements, and for the prediction of the wanted rotational and spectral strengths. All latter day theories, be they Hückel or extended Hückel theories of unsaturated[47] or saturated[48] organic compounds, or sophisticated molecular orbital theories of intricate organic and inorganic (nontransition metal) systems,[47b,c,d,e,49] are woefully deficient so far as furnishing intimate *a priori* molecular information such as is needed for optical rotatory or intensiveness computations. All theories have furnished, in the whole, only *a posteriori* electronic rationalization. This situation is in stark contrast to that of the transition metals where prediction has been the rule rather than the exception; hence, the present line of the development.

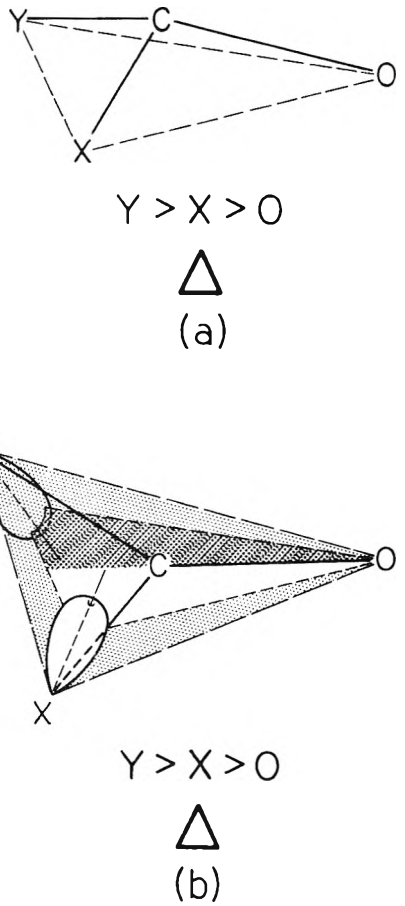

Figures 48a and 48b. Two intrigues by which the carbonyl chromophore may attain electronic dissymmetry, by nuclear (and consequently electronic) dissymmetry [Fig. 48a] and by electronic dissymmetry alone [Fig. 48b]. In Fig. 48b the nuclei OCXY are complanate but the local electron densities are not. The figure shows the plane of barycentric (local) bond densities of the OXY triad to be skewed with respect to that of the kernel (X,Y) and bond (OC) densities of the OCXY tetrad. [For conformational conventions, read footnote 45.]

It is most unlikely that the source of electronic optical rotatory power should differ dependent upon which nucleus the electron should find itself upon. This notion has guided the author's thoughts during his long years of rumination on the origin of optical rotivity. Therefore, to test the correctness of his beliefs he first tried their merit on systems for which *a priori* forecasts could be issued—the kd^n transition metal aggregates. Their merit there confirmed [read ref. 6 and Division A], he should like now to extend their range and apply them to other electron–nucleus unions, in a qualitative way, lending quantitative support when feasible.

In accord with our postulate of ref. 6 and Division A, we again attribute the existence of natural optical rotatory power to the presence of local chromophoric dissymmetry. This attribution is no more than a straightforward transcription of Pasteur's concepts[4d] to modern terms. We once more view this dissymmetry as arising from local orbital mismatch [Fig. 48], from molecular

would not give effects of the magnitude observed.

In other new work [C. Dijkgraaf, *Spectrochim. Acta*, **20**, 1227 (1964)] the (potential) power of combined single crystal polarized spectra and optical rotatory spectra has again been underscored, this time in connection with the metallochromophoric optical activity of bisbidentate α-amino acid copper(II) compounds. Also F. Woldbye [Proceedings of the Eighth International Conference on Coordination Chemistry, Vienna, Austria, Sept. 7-11, 1964, V. Gutmann, Ed., Springer-Verlag, Vienna and New York, 1964, pp. 103–107] has most elegantly demonstrated the potence of the rotatory technique to fix absolute configurations. [In this latter regard it is of great interest and consequence to note the potential of such conformational determinations in biology, once standards have been set by X-ray (and theoretical) analysis. View, as an instance, A. Zalkin, J. D. Forrester, and D. H. Templeton, *Science*, **146**, 261 (1964), and ref. 6.]

(47) Read, for example (a) E. Hückel, "Grundzüge der Theorie ungesättigter und aromatischer Verbindungen," Verlag Chemie, Berlin, 1938; (b) R. G. Parr, "The Quantum Theory of Molecular Electronic Structure," W. A. Benjamin, Inc., New York, N. Y., 1963; (c) W. T. Simpson, "Theories of Electrons in Molecules," Prentice-Hall, Englewood Cliffs, N. J., 1962; (d) J. C. Slater, "Quantum Theory of Molecules and Solids," Vol. 1, "Electronic Structure of Molecules," McGraw-Hill Book Co., Inc., New York, N. Y., 1963; (e) M. Kotani, K. Ohno, and K. Kayama, "Handbuch der Physik," S. Flügge, Ed., Band XXXVII/2, Moleküle II, Springer-Verlag, Berlin, 1961, pp. 1–172; (f) J. R. Platt, *ibid.*, pp. 173–281; (g) O. Sovers and W. Kauzmann, *J. Chem. Phys.*, **38**, 813 (1963) [*errata*, *ibid.*, **40**, 1165 (1964)].

(48) Study as current instances (a) H. Yoshizumi, *Trans. Faraday Soc.*, **53**, 125 (1957); R. Hoffmann, *J. Chem. Phys.*, **39**, 1397 (1963); **40**, 2474, 2480, 2745 (1964); (c) J. A. Pople and D. P. Santry, *Mol. Phys.*, **7**, 269 (1963).

(49) H. Conroy, *J. Chem. Phys.*, **40**, 603 (1964) [*errata*, **40**, 3121 (1964)]; **41**, 1327, 1331, 1336, 1341 (1964); and to be published.

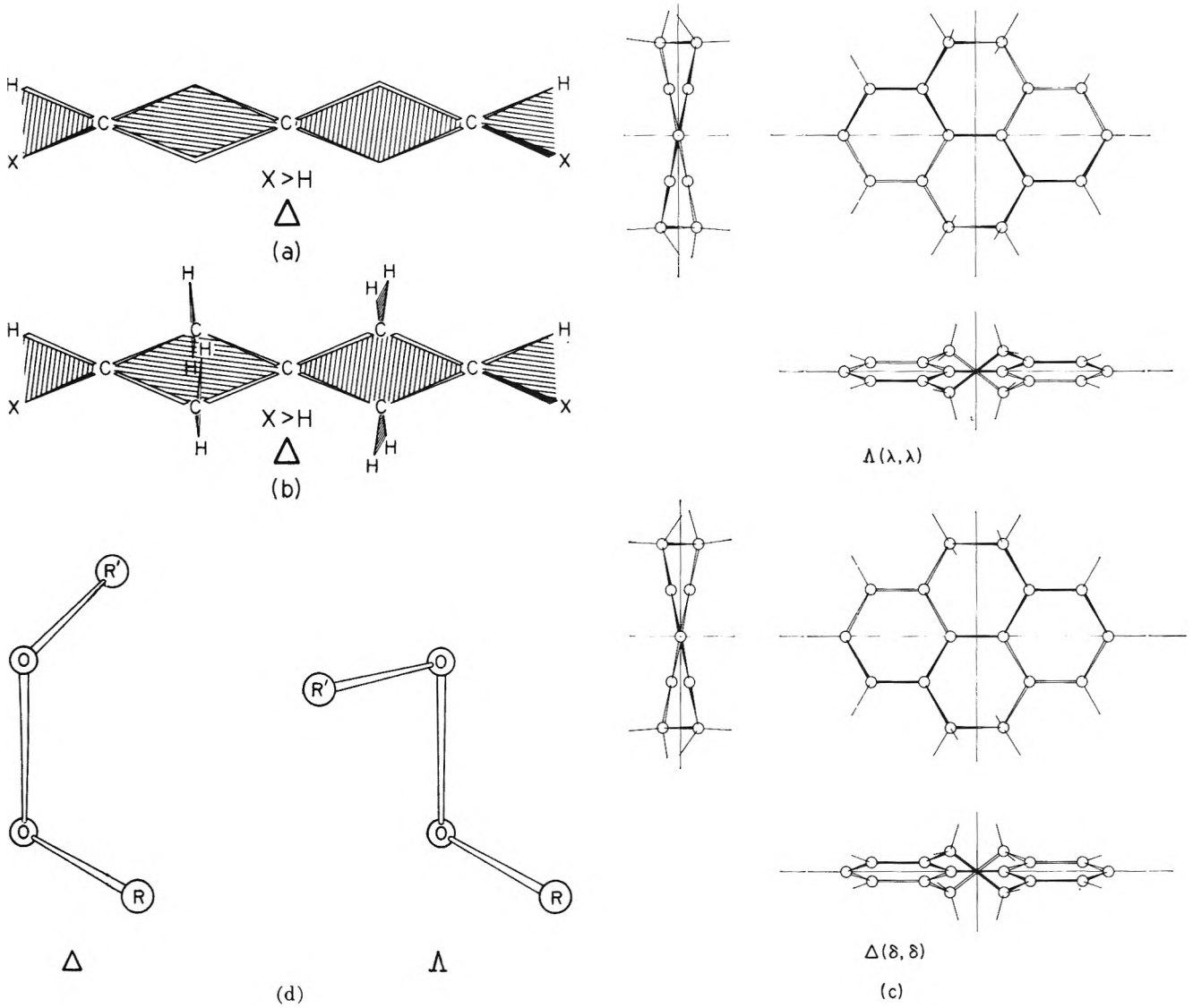

Figures 49a, b, c, and d. Four paradigms of over-all organic tectonic dissymmetry, the allenes [Fig. 49a], the spiranes [Fig. 49b], the hindered biphenyls [Fig. 49c], and the peroxides [Fig. 49d]. For conformational conventions, read footnote 45. [Note that the simplest dissymmetric peroxide is hydrogen peroxide itself, R = R′ = H.]

dissymmetry [Fig. 49], or from complete molecular asymmetry [Fig. 50]. Anew, the latter two situations can only be treated by full scale electronic computations.[5r,s,u,v,z,50] The former can be handled as before in ref. 6 and Division A. To manifest, consider the carbonyl dissymmetry. Figure 48 displays two modes by which the ordinarily planar conformation of the carbonyl chromophore may obtain optical rotatory power: (1) by aplanar geometrical distortion, and (2) by aplanar electronic distortion. The first mode needs little comment—it is the standard means by which optical rotativity is commonly attained. All that need be said is that the carbonyl tetrad is spectroscopically known[51] to have aplanar architectural tendencies and/or states, and, hence, that possible stereochemical capitalizations on these propensities are not completely unthinkable. The second requires more amplification.

In many structures, both simple and complex (*e.g.*, monocyclic ketone and steriodal forms), the electronic angular patterns required for maximum bond directiveness conflict greatly with those demanded by minimum

(50) The recent progress toward the erection of an internally self-constituent semiempirical electronic theory of saturated hydrocarbons by Yoshizumi,[48a] Hoffmann,[48b] and Pople and Santry[48c] lends hope that even such intractable systems may soon be rendered computationally accessible.

(51) For instruction, consult (a) S. E. Hodges, J. R. Henderson, and J. B. Coon, *J. Mol. Spectry.*, **2**, 99 (1958); (b) L. E. Giddings, Jr., and K. K. Innes, *ibid.*, **6**, 528 (1961).

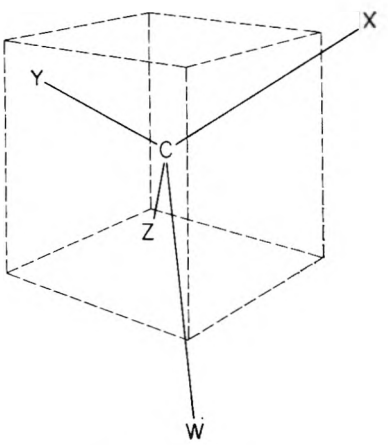

Z > Y > W > X

(a)

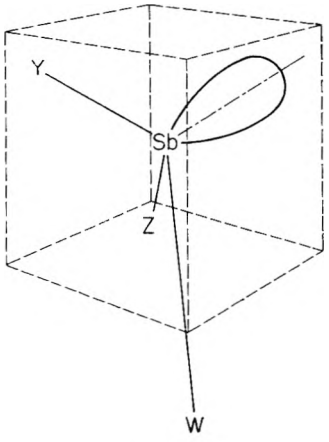

Z > Y > W

(b)

Figures 50a and 50b. Two paragons of total organic and inorganic edificial irregularity, asymmetrically substituted methane [Fig. 50a] and stibine [Fig. 50b]. For conformational conventions, read footnote 45.

Coulomb repulsiveness. Hence, electron–nuclear locational compromise must be reached. The easiest way this necessary compromise can be accomplished is by an electron–nuclear dispositional adjustment in which lines of maximum electron density do not quite match those of maximum nuclear density [*cf.* Fig. 48b]. This directional mismatch of the barycenters of negative and positive charge gives substance to sufficient electronic dissymmetry to engender observable optical rotativity. Before it be thought that this explanation is different from that of the past,[5m,n,r,z] hear assurance to the contrary.

We know from function theory that any well-behaved (*i.e.*, physical) mathematical function such as the one electron amplitude, Ψ, or its square, Ψ^2, the density, is expansible in an orthogonal series of spherical harmonics.

$$\Psi(\mathrm{r}, \vartheta, \varphi) = \sum_{l,m} \psi_l{}^m(\mathrm{r}) Y_l{}^m(\vartheta, \varphi) = \psi_0{}^0(\mathrm{r}) Y_0{}^0(\vartheta, \varphi) + \sum_{m=-1}^{1} \psi_1{}^m(\mathrm{r}) Y_1{}^m(\vartheta, \varphi) + \sum_{m=-2}^{2} \psi_2{}^m(\mathrm{r}) Y_2{}^m(\vartheta, \varphi) + \ldots . \quad (74)$$

Further, we know from this same theory that any function of radial distance such as $\psi_l{}^m(\mathrm{r})$ may be parsed so that it is printable as a sum of subfunctions, $\psi_{n,l}{}^m(\mathrm{r})$, each characterized by the property that they possess $n - 1$ radial nodes. From analogy with hydrogenic theory we may call these subfunctions 1s, 2s, 2p, 3d . . . . ., when $(n = 1, l = 0), (n = 2, l = 0), (n = 2, l = 1), (n = 3, l = 2), \ldots .$, and name their sum $\Psi(\mathrm{r}, \vartheta, \varphi)$ in eq. 74 a "valence hybrid" or a "hybrid orbital" and speak of the summation as "hybridization." It is common knowledge[5m,n,r,z] that the presence of a finite sub- (or atomic-like) function $\psi_{3,2}{}^m(\mathrm{r}) Y_2{}^m(\vartheta, \varphi)$ in the sum, eq. 74, in addition to the sub- (or atomic-like) function, $\psi_{2,1}{}^m(\mathrm{r}) Y_1{}^m(\vartheta, \varphi)$, will suffice to give measurable optical rotivity to an organic chromophore whose electrons are so governed (for inorganic chromophores the nodal index, n, may differ). Until now the relative $\psi_{3,2}{}^m(\mathrm{r}) Y_2{}^m(\vartheta, \varphi)$, $\psi_{2,1}{}^m(\mathrm{r}) Y_1{}^m(\vartheta, \varphi)$ content of eq. 74, mostly for carbon-like orbitals, has been estimated on an atomic perturbation method, the perturbation being the van der Waals (mutual) polarization forces of vicinal electron distributions.[4b,5m,n,r,z] To obtain relative contents of magnitude sufficient to yield rotational and spectral strengths in reasonable agreement with experiment, in spite of the smallness of the perturbant forces, quite unrealistic, or at least disconcerting, values of the Slater effective nuclear charges Z_{eff} were required. This fact has caused the present author to espouse and propose the alternate means of getting the requisite sized $\psi_{3,2}{}^m(\mathrm{r}) Y_2{}^m(\vartheta, \varphi)$, $\psi_{2,1}{}^m(\mathrm{r}) Y_1{}^m(\vartheta, \varphi)$ relative content mentioned earlier—that of assuming misaligned (*i.e.*, not aligned along the internuclear axis) molecular bond directivities [Fig. 48b]. It is actually not a new explanation, but rather a new interpretation, based on a rigorous mathematical formulation, eq. 74 and accompaniments, of an old observation.[52] It allows a more sensible view to be given to the mathematical exigencies.[53]

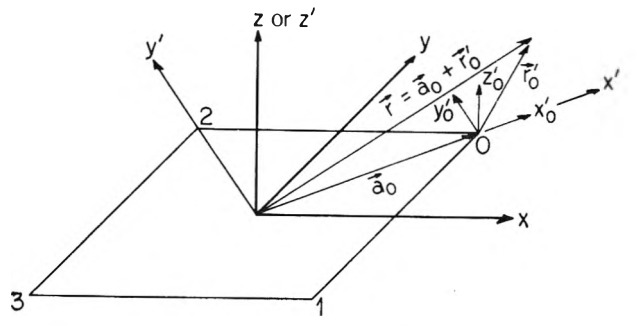

$$\vec{a}_0 \equiv a_{x_0}\hat{i} + a_{y_0}\hat{j} + a_{z_0}\hat{k} \equiv a_{x'_0}\hat{i}' + a_{y'_0}\hat{j}' + a_{z'_0}\hat{k}'$$

$$a_{x_0} = a\cos 45°, \quad a_{y_0} = a\sin 45°, \quad a_{z_0} = 0$$

$$a_{x'_0} = a, \quad a_{y'_0} = 0, \quad a_{z'_0} = 0$$

Figure 51. Trace of the local cartesian coordinate bases used in integral reductions and their translation kinships.

IX. Inorganic Compounds

Although inorganic chemistry is every bit as fertile a field as organic, with regard to optical rotatory phenomena, it has not been as thoroughly worked, this despite the fact that it was in the inorganic domain that optical rotatory power was first discovered.[4d] This situation should be rectified. Theoretically, the treatment follows that of section VIII quite closely as is evident from Fig. 45, 48, 49, 50, and 51 in which it is immaterial whether a carbon nucleus be present or not. However, it should be noted that the greater the ease of even–odd harmonic mixture in eq. 74, the greater the optical rotivity and intensity. Hence, joint experimental–theoretical studies of serially substituted inorganics in inorganic or organic molecules should bear much fruit.[54] The author most sincerely hopes that such research will be done.

Division D

X. Conclusion

The main outcomes of this pandect are compended below.

(1) The sign and magnitude of the optical rotation, the circular dichroism, and the dissymmetry of an arbitrary electronic system, inorganic or organic, for a set nuclear conformation, are directly determined by the sign and magnitude of the covalency and hybridization parameters, the localized metal–ligand electric and magnetic transition moments, the nuclear geometry, and, when extant, the angles of electronic cant.

(2) In general, stereochemically induced (through local chromophoric electronic dissymmetry) optical rotivity is predominant; polarization induced (through van der Waals vicinal interactions) is subservient.

(3) Dissymmetric descent destroys symmetric magnetic and electric selection principles.

(4) The optical rotatory and spectral powers of many electron systems are phrased as multiples and simple

(52) As this theory is but a new interpretation of an old observation, it naturally keeps whole all formal mathematical consequents of the older development [this fact is most readily recognized when it is realized that substituent and framework perturbations can induce, to first order, only those local geometric and electronic (bond) distortions of proportions consistent with initial symmetrical forms (*cf.* eq 74)]. To sample, the Kauzmann–Eyring Octant Rule,[5m] which has of late at long last been experimentally confirmed with great elegance by Moffitt, Woodward, Moscowitz, Klyne, and Djerassi,[6r] is retained inviolate.

(53) To sample the experimental literature and its current interpretation in this area look over the selection (a) B. Sjöberg, *Acta Chem. Scand.*, **14**, 273 (1960) [dissymmetric carboxylic acids]; (b) C. Djerassi, A. Fredga, and B. Sjöberg, *ibid.*, **15**, 417 (1961) [dissymmetric organic disulfides and diselenides]; (c) K. Mislow, *Ann. N. Y. Acad. Sci.*, **93**, 457 (1962); K. Mislow, M. A. W. Glass, R. E. O'Brien, P. Rutkin, D. H. Steinberg, J. Weiss, and C. Djerassi, *J. Am. Chem. Soc.*, **84**, 1455 (1962); K. Mislow and J. G. Berger, *ibid.*, **84**, 1956 (1962); K. Mislow and H. B. Hopps, *ibid.*, **84**, 3018 (1962); *Chem. Eng. News*, **41**, 44 (July 8, 1963); C. Djerassi and J. E. Gurst, *J. Am. Chem. Soc.*, **86**, 1755 (1964) [inherently dissymmetric organic molecular chromophores, hindered biphenyls and others]; (d) C. Djerassi, K. Mislow, and M. Shamma, *Experientia*, **18**, 53 (1962) [dissymmetric alkaloids]; (e) L. Velluz and M. Legrand, *Angew. Chem.*, **73**, 603 (1961); M. Legrand, A. Lacam, and R. Viennet, *Bull. soc. chim. France*, 792 (1961); H. Brockmann, Jr., and M. Legrand, *Tetrahedron*, **19**, 395 (1963); D. Bertin and M. Legrand, *Compt. rend.*, **256**, 960 (1963); D. Bertin and L. Nedelec, *Bull. soc. chim. France*, 406 (1963); M. Legrand and R. Viennet, *ibid.*, 713 (1964) [steroids and other complex organic molecules]; (f) H. P. Gervais and A. Rassat, *ibid.*, 743 (1961) [inherently dissymmetric carbonyls]; (g) S. F. Mason, *Mol. Phys.*, **5**, 343 (1962); *J. Chem. Soc.*, 3285 (1962); *Proc. Chem. Soc.*, 362 (1962); R. E. Ballard, S. F. Mason, and G. W. Vane, *Trans. Faraday Soc.*, **59**, 775 (1963) [see also A. J. Moscowitz, *Proc. Chem. Soc.*, 60 (1964); S. F. Mason, *ibid.*, 61 (1964)]; R. E. Ballard and S. F. Mason, *J. Chem. Soc.*, 1624 (1963); R. E. Ballard, S. F. Mason, and G. W. Vane, *Discussions Faraday Soc.*, **35**, 43 (1963) [inherently dissymmetric organic molecular chromophores, carbonyl and others]; (h) G. Snatzke, H. Pieper, and R. Tschesche, *Tetrahedron*, **20**, 107 (1964); R. C. Cambie, L. N. Mander, A. K. Bose, and M. S. Manhas, *ibid.*, **20**, 409 (1964); G. Snatzke and D. Becher, *ibid.*, **20**, 1921 (1964); Y. Tsuzuki, K. Tanaka, K. Tanabe, M. Akagi, and S. Tejima, *Bull. Chem. Soc. Japan*, **37**, 730 (1964); I. P. Dirkx and F. L. Sixma, *Rec. trav. chim.*, **83**, 522 (1964); I. P. Dirkx and Th. J. de Boer, *ibid.*, **83**, 535 (1964); N. Pace, C. Tanford, and E. A. Davidson, *J. Am. Chem. Soc.*, **86**, 3160 (1964); W. Gaffield, *Chem. Ind.* (London), 1460 (1964); as well as ref. 4, 5, and 46x. Be sure, however, not to miss the classical works of Kuhn[4] and Mathieu (i) J. P. Mathieu, *Compt. rend.*, **194**, 268 (1932); J. P. Mathieu and J. Perrichet, *ibid.*, **200**, 1583 (1935); *J. Phys. Radium*, **7**, 138 (1936); J. P. Mathieu and M. Ronayette, *Compt. rend.*, **208**, 1567 (1939); *Rev. Opt.*, **19**, 1 (1940) [inherently dissymmetric carbonyl optical rotatory dispersion, absorption and circular dichroism (compare also ref. 40)]; (g) A. Horeau, J. Jacques, J. P. Mathieu, and A. Petit, *Bull. soc. chim. France*, 130 (1955); J. P. Mathieu and A. Petit, "Constantes Selectionnes Pouvoir Rotatoire Naturel, Tome I, Steroides, Masson, Paris, 1956 [steroids].

(54) To illustrate, a study of the dependence of rotatory deportment as a function of substituent or framework metallicism (as, for example, a study of rotatory power as a function of atomic number in the series N, P, As, Sb, Bi and O, S, Se, Te, Po, where rotativity should increase in direct proportion to the import of second-order harmonics (the so-called "d" orbitals—recall eq. 74) in their (chromophoric) chemical bonds, that is, in direct connection with their atomic number), should be most gainful. Some steps have already been taken along this avenue [confer sources[4b,c,g] for reference].

NOTE ADDED IN PROOF.—A most recent and significant example of the harvests to be expected in this area may be found in W. R. Hertler, *J. Am. Chem. Soc.*, **86**, 2949 (1964).

sums of those derived from the correspondent one-electron transition densities.

(5) Optical rotatory and spectral intensity addition relations exist only for near cubic systems.

(6) In consequence of a general correspondence of spin-free transition metal electronic configurations and their spin-free half-shell supplements [n and $n + 5$ (scandanides, yttranides, and lutetanides) and n and $n + 7$ (lanthanides and actinides)] and of a special correspondence between these and other spin-free and spin-paired configurations for one-electron operators, there is a direct connection of their rotational and spectral powers.

(7) For nontransition metal systems only minute calculation, either nonempirical or semiemprical, can serve to foretell optical rotatory and spectral power.

(8) Rotational declination and absolute conformation is uniquely determined by the addend orbital (lone-pair, bond-pair, acceptor, or donor) disposition about the active center or chromophore.

(9) A singular classification of complex absolute nuclear and localized ligand orbital conformations as a sum of basic sub-conformations can be drafted.

(10) Similar nuclear conformations rotate oppositely when their local addend orbital (lone-pair, bond-pair, acceptor, or donor) efformations are apposed.

It is evident that a host of other kinships could be established and entered by amplifications and augmentations of the theory erected aloft. But, without substantiate particulate mensural experience such establishments appear a bit precipitate, at least at this instant. It is hoped that at a near moment circumstances will be such as to permit a greater unfoldment of the theory. Thoughts have been contemplated for its commencement.

Division E

XI. *Acknowledgments.* The multitude of friends and colleagues who so generously gave aid to the author's previous efforts in optical rotation (ref. 6) have likewise, unbeknownst to them, lent aid to the present attempt. The author wishes heartedly to extend his most sincere thanks to them again for all their actions on his behalf. Several friends, Drs. A. A. Bothner-By, B. E. Douglas, J. Hidaka, K. Mislow, A. J. Moscowitz, A. M. Sargeson, K. G. Untch, E. Wasserman, and F. Woldbye, have contributed quite specifically to the present work alone. It is with great gratification that the author can now give them special thanks. The author also wishes to thank Miss N. M. Morris, librarian, Bell Telephone Laboratories, Inc., for her assistance in select portions of the bibliography, and again to thank Mr. R. L. Kornegay, technical assistant, Bell Telephone Laboratories, Inc., for his help in checking certain integral forms and for the numerical evaluation of them. Inexpressible appreciation and thanks are once more due Mr. G. B. Arnold, Head, Mellon Institute Research Drafting Department, and his colleague, Mr. J. F. Benes (especially) for their indispensible and marvelous assistance in illustrating this article under rather arduous conditions.

Division F

XII. Appendix

§5. Evaluation of the Integrals

5.1 *Algebraic Reduction.* The algebraic reduction of the needed molecular and localized integrals to elementary forms is prompt: the simple application of the $\mathcal{C}_2(z)$, $\mathcal{C}_2(y)$, $\mathcal{C}_2(x)$ operations serves to show that all transitions are aligned singly along the twofold axes. For example

$$\left\langle \mathrm{a} \left| \frac{\vec{\mathrm{p}}}{\vec{\mathrm{m}}} \right| \mathrm{b}_1 \right\rangle = \hat{\mathrm{k}} \left\langle \mathrm{a} \left| \frac{\mathrm{p}_z}{\mathrm{m}_z} \right| \mathrm{b}_1 \right\rangle \qquad \text{(A-1)}$$

and so forth.

5.2 *Angular Momentum Integrals.* The angular momentum integrals divide themselves into three distinct types—metal–metal, metal–ligand, and ligand–ligand. The metal–metal and metal–ligand types are immediately evaluated by means of the differential operations of Table XI and matrix Hermiticity. To sample

$$\int \mathrm{d}_{xz}\ell_z\mathrm{d}_{yz}d\tau = -i\hbar\int \mathrm{d}_{xz}\mathrm{d}_{xz}d\tau = -i\hbar$$
$$\int \mathrm{d}_{xz}\ell_z\Lambda_-^{(+)}d\tau = \left\{\int \Lambda_-^{(+)}\ell_z\mathrm{d}_{xz}\mathrm{d}\tau\right\}^* = -i\hbar\int \Lambda_-^{(+)}\mathrm{d}_{yz}d\tau \quad \text{(A-2)}$$

The ligand–ligand types are somewhat less quickly evaluated by means of this same table (and matrix Hermiticity). The key to their disentanglement is the observation that [an identical vectorial relationship holds in the metal and ligand x, y, z coordinate basis of Fig. 1, 13, 16, and 51 also]

$$\vec{\ell}' = \vec{\mathrm{r}}' \times \frac{\hbar}{i}\vec{\nabla}' = (\vec{\mathrm{a}}_j + \vec{\mathrm{r}}_j') \times \frac{\hbar}{i}\vec{\nabla}_j' =$$
$$(\vec{\mathrm{a}}_j \times \frac{\hbar}{i}\vec{\nabla}_j') + \vec{\ell}_j',\ \ell_x = \sqrt{1/2}(l_{x'} - l_{y'}),$$
$$\ell_y = \sqrt{1/2}(\ell_{x'} + \ell_{y'}),\ l_z = \ell_{z'} \quad \text{(A-3)}$$

as $\vec{\mathrm{r}}'$ equals $\vec{\mathrm{a}}_j + \vec{\mathrm{r}}_j'$ and $\vec{\nabla}'$ equals $\vec{\nabla}_j'$, where $\vec{\ell}'$, $\vec{\mathrm{r}}'$, and $\vec{\nabla}'$ are the orbital angular momentum, coordinate, and gradient operators centered at the metal as origin in the x', y', z' coordinate basis; $\vec{\ell}_j'$, $\vec{\mathrm{r}}_j'$, and $\vec{\nabla}_j'$ are the orbital angular momentum, coordinate, and gradient operators

centered at ligand j as origin in the x', y', z' coordinate basis; and $\vec{a}_j$ is the metal to ligand directed bond length vector [view Fig. 51. The gradient operation is independent of origin since a derivative operation is translationally invariant, $\partial/\partial x'$ equals $\partial/\partial(a_{x'j} + x_j')$ equals $\partial/\partial x_j'$, where $a_{x'j}$ is the (constant) numerical value of the x' component of the metal to ligand j directed bond length vector, $\vec{a}_j$]. Hence, we have, as an instance [the other integrals, such as $\int \Sigma_-^{(-)c}\ell_z\tilde{\Pi}_-^{(+)s}$, vanish on the grounds of inversion (i) symmetry. See Table IV].

$$\int \Lambda_-^{(-)}\ell_z\Lambda_-^{(+)}d\tau = \int \Sigma_-^{(-)c}\ell_z\Sigma_-^{(+)c}d\tau + \int \Sigma_-^{(-)c}\ell_z\Pi_-^{(+)c}d\tau + \int \Pi_-^{(-)c}\ell_z\Sigma_-^{(+)c}d\tau + \int \Pi_-^{(-)c}\ell_z\Pi_-^{(+)c}d\tau + \int \tilde{\Pi}_-^{(-)s}\ell_z\tilde{\Pi}_-^{(+)s}d\tau \quad \text{(A-4)}$$

with

$$\int \Sigma_-^{(-)c}\ell_z\Sigma_-^{(+)c}d\tau = 8a_-^{\sigma-}a_-^{\sigma+}\int \sigma_0^c\ell_z\sigma_1^c d\tau$$

$$\int \Sigma_-^{(-)c}\ell_z\Pi_-^{(+)c}d\tau = 4a_-^{\sigma-}a_-^{\pi+} \times \{\int \sigma_0^c\ell_z\pi_0^c d\tau - \int \sigma_0^c\ell_z\pi_3^c d\tau\}$$

$$\int \Pi_-^{(-)c}\ell_z\Sigma_-^{(+)c}d\tau = -4a_-^{\pi-}a_-^{\sigma+}\{\int \sigma_0^c\ell_z\pi_0^c d\tau - \int \sigma_0^c\ell_z\pi_3^c d\tau\}$$

$$\int \Pi_-^{(-)c}\ell_z\Pi_-^{(+)c}d\tau = 8a_-^{\pi-}a_-^{\pi+}\int \pi_0^c\ell_z\pi_1^c d\tau$$

$$\int \tilde{\Pi}_-^{(-)s}\ell_z\tilde{\Pi}_-^{(+)s}d\tau = 8a_-^{\tilde{\pi}-}a_-^{\tilde{\pi}+}\int \tilde{\pi}_0^s\ell_z\tilde{\pi}_1^s d\tau \quad \text{(A-5)}$$

The nonappearance of integrals such as $\int \sigma_j^c\ell_z\sigma_j^c d\tau$, $\int \sigma_0^c\ell_z\sigma_2^c d\tau$, $\int \sigma_1^c\ell_z\sigma_3^c d\tau$, etc., is by virtue of the symmetry operations $C_2(x')$, $C_2(y')$, $C_2(x)$, $C_2(y)$, $C_2(z'$ or $z)$, i, $\sigma_v[x' - z']$, $C_4(z'$ or $z)$, etc., and of matrix Hermiticity: $C_2(x')\int \sigma_0^c\ell_z\sigma_0^c d\tau = -\int \sigma_0^c\ell_z\sigma_0^c d\tau$ or $\int \sigma_0^c\ell_z\sigma_0^c d\tau \equiv 0$; $C_2(z')\int \sigma_0^c\ell_z\sigma_2^c d\tau = \int \sigma_3\ell_z\sigma_1 d\tau = -C_2(y)\int \sigma_1^c\ell_z\sigma_3^c d\tau$, $C_4(z')\int \sigma_0^c\ell_z\sigma_1^c d\tau = \int \sigma_1^c\ell_z\sigma_3^c d\tau$, or $\int \sigma_0^c\ell_z\sigma_2^c d\tau = \int \sigma_3^c\ell_z\sigma_1 d\tau = -\int \sigma_1^c\ell_z\sigma_3^c d\tau = -\int \sigma_0^c\ell_z\sigma_1^c d\tau$; and so on. Whence, we can now invoke eq. A-3 and Tables V and XI to reduce eq. A-5 to a linear combination of the basic integrals[55]

$$M_{01}^{ss} = \int (2s)_{A_0}\frac{\partial}{\partial x_1'}(2s)_{A_1}d\tau,\ M_{01}^{p_\sigma p_\sigma} = \int (2p_{x'})_{A_0}\frac{\partial}{\partial x_1'}(2p_{y'})_{A_1}d\tau$$

$$M_{01}^{sp_\sigma} = \int (2s)_{A_0}\frac{\partial}{\partial x_1'}(2p_{y'})_{A_1}d\tau,\ M_{01}^{p_\sigma s} = \int (2p_{x'})_{A_0}\frac{\partial}{\partial x_1'}(2s)_{A_1}d\tau$$

$$M_{10}^{sp_\sigma} = \int (2s)_{A_1}\frac{\partial}{\partial x_0'}(2p_{x'})_{A_0}d\tau,\ M_{00}^{sp_\pi} = \int (2s)_{A_0}\frac{\partial}{\partial y_0'}(2p_{y'})_{A_0}d\tau$$

$$M_{03}^{sp_\pi} = \int (2s)_{A_0}\frac{\partial}{\partial y_3'}(2p_{y'})_{A_3}d\tau,\ M_{03}^{p_\sigma p_\pi} = \int (2p_{x'})_{A_0}\frac{\partial}{\partial y_3'}(2p_{y'})_{A_3}d\tau$$

$$M_{01}^{p_\pi p_\pi} = \int (2p_{y'})_{A_0}\frac{\partial}{\partial x_1'}(2p_{x'})_{A_1}d\tau,\ M_{01}^{p_{\tilde{\pi}}p_{\tilde{\pi}}} = \int (2p_{z'})_{A_0}\frac{\partial}{\partial x_1'}(2p_{z'})_{A_1}d\tau$$

$$M_{00}^{sp_{\tilde{\pi}}} = \int (2s)_{A_0}\frac{\partial}{\partial z_0'}(2p_{z'})_{A_0}d\tau,\ M_{03}^{sp_{\tilde{\pi}}} = \int (2s)_{A_0}\frac{\partial}{\partial z_3'}(2p_{z'})_{A_3}d\tau$$

$$M_{03}^{p_\sigma p_{\tilde{\pi}}} = \int (2p_{z'})_{A_0}\frac{\partial}{\partial z_3'}(2p_{z'})_{A_3}d\tau,\ M_{01}^{p_\pi p_{\tilde{\pi}}} = \int (2p_{y'})_{A_0}\frac{\partial}{\partial z_1'}(2p_{z'})_{A_1}d\tau$$

$$M_{01}^{sp_{\tilde{\pi}}} = \int (2s)_{A_0}\frac{\partial}{\partial z_1'}(2p_{z'})_{A_1}d\tau,\ M_{01}^{p_\sigma p_{\tilde{\pi}}} = \int (2p_{x'})_{A_0}\frac{\partial}{\partial z_1'}(2p_{z'})_{A_1}d\tau$$

$$M_{01}^{sp_\pi} = \int (2s)_{A_0}\frac{\partial}{\partial x_1'}(2p_{x'})_{A_1}d\tau,\ M_{01}^{p_\sigma p_\pi} = \int (2p_{x'})_{A_0}\frac{\partial}{\partial x_1'}(2p_{x'})_{A_1}d\tau \quad \text{(A-6)}$$

and of the local ligand–ligand overlap integrals listed in §5.4. All other integrals can be expressed in terms of these.[56]

The matrix elements of the magnetic transition moments, $\vec{m}$, are obtained from those of the angular momenta, $\vec{\ell}$, by multiplication by e/2mc, which converts the Planck constant, $\hbar$, of eq. A-2 through 5 and Table XI into the Bohr magneton, μ_B.

(55) Notice that the integrals of eq. A-6 convert to other forms of recognizable physical content (potential energies, overlaps, and angular averages) after differentiation. To demonstrate

$$\int (2s)_{A0}\frac{\partial}{\partial x_1'}(2s)_{A1}d\tau = \sqrt{1/3}\int (2s)_{A0}\left\{\frac{1}{r_1} - \frac{c}{a_0}\right\}(2p_{x'})_{A1}d\tau$$

$$\int (2p_{x'})_{A0}\frac{\partial}{\partial x_1'}(2p_{y'})_{A1}d\tau = -\frac{c}{a_0}\int (2p_{x'})_{A0}\frac{y_1'}{r_1}(2p_{x'})_{A1}d\tau, \text{ etc.,}$$

where a_0 is the Bohr radius and c is $Z_{2s\text{ or }2p}/2$.

(56) An illustration of this affirmation is to be found in the integral $M_{10}^{sp_\sigma}$ equals $\int (2s)_{A_1}\frac{\partial}{\partial x_0'}(2p_{x'})_{A0}d\tau$, which in light of the translational invariance and anti-Hermiticity of the derivative operator $\partial/\partial x_1'$, equals $-M_{01}^{p_\sigma s}$. More on this point will be given in §5.5, footnote 58.

5.3 *Local Electronic Transition Moment Integrals.* The localized electronic transition moment integrals are gauged in the self-same manner as those for the angular momentum. They again occur in three types, metal–metal (which vanish), metal–ligand, and ligand–ligand. Quadrate symmetry elements once more simplify the algebraic processes. The metal–ligand integrals are expressible as linear combinations of those of ref. 6, eq. A-4, 5, and 9, after transformation of the electric dipole moment components and the d-like orbitals from the x, y, z coordinate base to the x', y', z' base of Fig. 13 and 51.

$$x = \sqrt{1/2}(x' - y'); \; y = \sqrt{1/2}(x' + y'); \; z = z' \quad \text{(A-7)}$$

Nonetheless, there is one interesting integral relationship not mentioned in ref. 6

$$\sqrt{3}K_{4A_3} + K_{7A_3} = -\sqrt{2}[K_{2A_5} - K_{3A_3}] \quad \text{(A-8)}$$

which arises because $d_{x'z'}x'(2p_{z'})_{A_0} - d_{y'z'}y'(2p_{z'})_{A_0}$ equals $2d_{x'^2-y'^2}z'(2p_{z'})_{A_0}$ and two integral equations

$$\int (2p_z)_{A_0} z d_{x^2-y^2} d\tau = -\frac{\sqrt{6}}{4}\{\sqrt{3}K_{4A_3} + K_{7A_3}\}$$

$$\int (2p_z)_{A_0} z d_{3z^2-r^2} d\tau = -\frac{\sqrt{6}}{4}\{K_{4A_3} - \sqrt{3}K_{7A_3}\} \quad \text{(A-9)}$$

which arise because of new computations. [These latter two integral equations, eq. A-9, are derived by direct application of the trigonal dihedral $C_3(z')$ operation to K_{4A_1} and K_{7A_1} of ref. 6 and the later identification of K_{4A_1} and K_{7A_1} with K_{4A_3} and K_{7A_3}, each (recall §5.3 and 5.5, eq. A-5 and A-9 of ref. 6).]

The ligand–ligand types are new and are cataloged below.

$$L_{01}^{ss} = \int (2s)_{A_0} x_1'(2s)_{A_1} d\tau, \; L_{01}^{p_\sigma p_\sigma} = \int (2p_{x'})_{A_0} x_1'(2p_{y'})_{A_1} d\tau$$

$$L_{01}^{sp_\sigma} = \int (2s)_{A_0} x_1'(2p_{y'})_{A_1} d\tau, \; L_{01}^{p_\sigma s} = \int (2p_{x'})_{A_0} x_1'(2s)_{A_1} d\tau$$

$$L_{10}^{sp_\sigma} = \int (2s)_{A_1} x_1'(2p_{x'})_{A_0} d\tau, \; L_{00}^{sp_\pi} = \int (2s)_{A_0} x_0'(2p_{x'})_{A_0} d\tau$$

$$L_{03}^{sp_\pi} = \int (2s)_{A_0} y_3'(2p_{y'})_{A_3} d\tau, \; L_{03}^{p_\sigma p_\pi} = \int (2p_{z'})_{A_0} y_3'(2p_{y'})_{A_3} d\tau$$

$$L_{01}^{p_\pi p_\pi} = \int (2p_{y'})_{A_0} x_1'(2p_{x'})_{A_1} d\tau, \; L_{01}^{p_{\bar\pi} p_{\bar\pi}} = \int (2p_{z'})_{A_0} x_1'(2p_{z'})_{A_1} d\tau$$

$$L_{00}^{sp_{\bar\pi}} = \int (2s)_{A_0} z_0'(2p_{z'})_{A_0} d\tau, \; L_{03}^{sp_{\bar\pi}} = \int (2s)_{A_0} z_3'(2p_{z'})_{A_3} d\tau$$

$$L_{03}^{p_\sigma p_{\bar\pi}} = \int (2p_{x'})_{A_0} z_3'(2p_{z'})_{A_3} d\tau, \; L_{01}^{p_\pi p_{\bar\pi}} = \int (2p_{y'})_{A_0} z_1'(2p_{z'})_{A_1} d\tau$$

$$L_{01}^{sp_{\bar\pi}} = \int (2s)_{A_0} z_1'(2p_{z'})_{A_1} d\tau, \; L_{01}^{p_\sigma p_{\bar\pi}} = \int (2p_{x'})_{A_0} z_1'(2p_{z_1'}) d\tau$$

$$L_{01}^{sp_\pi} = \int (2s)_{A_0} x_1'(2p_{x'})_{A_1} d\tau, \; L_{01}^{p_\sigma p_\pi} = \int (2p_{x'})_{A_0} x_1'(2p_{x'})_{A_1} d\tau \quad \text{(A-10)}$$

All other integrals can be built from these basic ones.[57]

5.4 *Local Overlap Integrals.* The localized overlap integrals separate into two classes, metal–ligand and ligand–ligand. Those of the first class were censused in ref. 6, §5.4, eq. A-6. Those of the second class

$$s_{jk}^{d} = \int (2s)_{A_j}(2s)_{A_k} d\tau, \; \mathfrak{s}_{jk}^{d} = \int (2p_\sigma)_{A_j}(2p_\pi)_{A_k} d\tau$$

$$s_{jk}^{d} = \int (2s)_{A_j}(2p_\pi)_{A_k} d\tau, \; \bar{s}_{jk}^{d} = \int (2s)_{A_j}(2p_\sigma)_{A_k} d\tau$$

$$\mathfrak{f}_{jk}^{d} = \int (2p_\pi)_{A_j}(2p_\pi)_{A_k} d\tau, \; \bar{\mathfrak{f}}_{jk}^{d} = \int (2p_\sigma)_{A_j}(2p_\sigma)_{A_k} d\tau \quad \text{(A-11)}$$

are of the basic kinds inscribed below [the superscript d has been appended to distinguish the different atomic denumeration (the atom *trans* to 0 is now 3 rather than 5) of the equivalent, except for $\mathfrak{f}_{01}^{d}$ which equals $-\bar{\mathfrak{f}}_{01}^{t}$, digonal and trigonal localized ligand-ligand overlaps. The trigonal overlap will henceforth be scored with a superscript t].

$$s_{01}^{d} = \int (2s)_{A_0}(2s)_{A_1} d\tau, \; s_{03}^{d} = \int (2s)_{A_0}(2s)_{A_3} d\tau$$

$$s_{01}^{d} = \int (2s)_{A_0}(2p_{x'})_{A_1} d\tau$$

$$\bar{s}_{01}^{d} = \int (2s)_{A_0}(2p_{y'})_{A_1} d\tau, \; \bar{s}_{03}^{d} = \int (2s)_{A_0}(2p_{x'})_{A_3} d\tau$$

$$\mathfrak{f}_{01}^{d} = \int (2p_{z'})_{A_0}(2p_{z'})_{A_1} d\tau, \; \mathfrak{f}_{02}^{d} = \int (2p_{y'})_{A_0}(2p_{x'})_{A_2} d\tau$$

$$\mathfrak{f}_{03}^{d} = \int (2p_{z'})_{A_0}(2p_{z'})_{A_3} d\tau$$

$$\bar{\mathfrak{f}}_{01}^{d} = \int (2p_{x'})_{A_0}(2p_{y'})_{A_1} d\tau, \; \bar{\mathfrak{f}}_{03}^{d} = \int (2p_{x'})_{A_0}(2p_{x'})_{A_3} d\tau$$

$$\mathfrak{s}_{01}^{d} = \int (2p_{x'})_{A_0}(2p_{x'})_{A_1} d\tau \quad \text{(A-12)}$$

The correspondent integrals in the ligand x, y, z coordinate are easily extracted from those of eq. A-11 and A-12 with the workaday coordinate transformation, eq. A-7.

5.5 *Algebraic Evaluation of the Basic Integrals.* The basic integrals are reduced as in ref. 6, §5.5, after first being put into standard form [that is, the form in which all ligand p_σ and p_π orbitals are apportioned so as to be sequestered into fractions aligned parallel and perpendicular to the metal–ligand (for metal–ligand integrals) or ligand–ligand (for ligand–ligand integrals) internuclear axis. View Fig. 52]. The outcome is as docketed alow.

(57) As samples, $\int (2s)_{A_0} y_0'(2p_{y'})_{A_0} d\tau$ equals $\int (2s)_{A_0} x_0'(2p_{x'})_{A_0} d\tau$ $[L_{00}^{sp_\pi}]$ and $\int (2p_{x'})_{A_0} y_1'(2p_{x'})_{A_1} d\tau$ equals $\int (2p_{x'})_{A_0} x_1'(2p_{y'})_{A_1} d\tau$ $[L_{01}^{p_\sigma p_\sigma}]$.

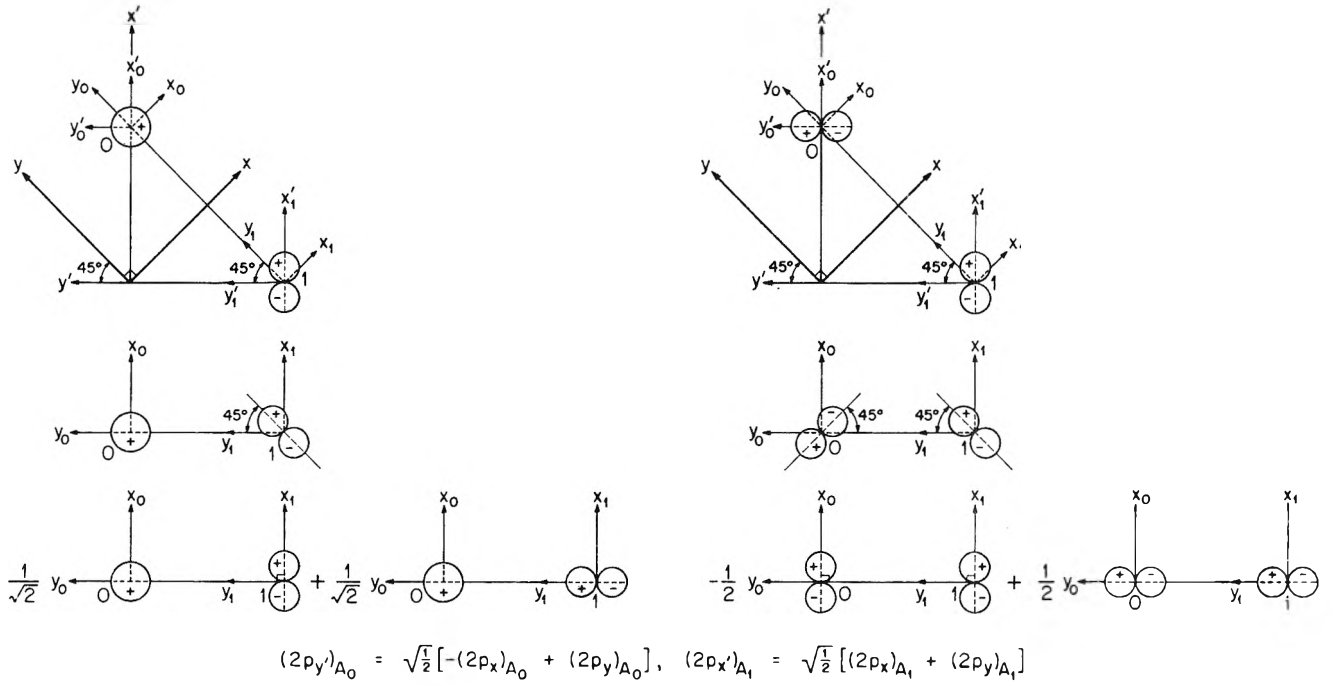

$$(2p_{y'})_{A_0} = \sqrt{\tfrac{1}{2}}[-(2p_x)_{A_0} + (2p_y)_{A_0}], \quad (2p_{x'})_{A_1} = \sqrt{\tfrac{1}{2}}[(2p_x)_{A_1} + (2p_y)_{A_1}]$$

Figure 52. Two representative decompositions of the localized ligand orbital cartesian base into its inter- and ortho-nuclearly collineated parts.

$$M_{01}^{ss} = \frac{(\bar{b}c)^5}{180\sqrt{2}b}\{5[A_2(\bar{b}c) + A_0(\bar{b}c)] - (\bar{b}c)[5A_3(\bar{b}c) - A_1(\bar{b}c)]\}$$

$$M_{01}^{p\sigma p\sigma} = -\frac{(\bar{b}c)^6}{30\sqrt{2}b}\{2A_1(\bar{b}c) - A_3(\bar{b}c)\}$$

$$M_{01}^{sp\sigma} = -\frac{(\bar{b}c)^6}{120\sqrt{3}b}\{A_2(\bar{b}c) + 3A_0(\bar{b}c)\}$$

$$M_{01}^{p\sigma s} = \frac{(\bar{b}c)^5}{120\sqrt{3}b}\{10[A_3(\bar{b}c) - 2A_1(\bar{b}c)] - (\bar{b}c)[5A_4(\bar{b}c) - 12A_2(\bar{b}c) + 3A_0(\bar{b}c)]\}$$

$$M_{00}^{sp\pi} = \frac{c}{2\sqrt{3}\,a_0} = M_{00}^{sp\bar{\pi}},\ M_{03}^{sp\pi} = M_{03}^{sp\bar{\pi}},\ M_{03}^{p\sigma p\pi} = M_{03}^{p\sigma p\bar{\pi}}$$

$$M_{03}^{sp\pi} = \frac{(\bar{d}c)^5}{120\sqrt{3}d}\{10[3A_3(\bar{d}c) - A_1(\bar{d}c)] - (\bar{d}c)[5A_4(\bar{d}c) - 4A_2(\bar{d}c) - A_0(\bar{d}c)]\}$$

$$M_{03}^{p\sigma p\pi} = -\frac{(\bar{d}c)^5}{60d}\{5[3A_2(\bar{d}c) - A_0(\bar{d}c)] - 3(\bar{d}c)[A_3(\bar{d}c) - A_1(\bar{d}c)]\}$$

$$M_{01}^{p\pi p\pi} = -\frac{(\bar{b}c)^5}{60\sqrt{2}b}\{5[3A_2(\bar{b}c) - A_0(\bar{b}c)] - (\bar{b}c)[3A_3(\bar{b}c) - A_1(\bar{b}c)]\}$$

$$M_{01}^{p\bar{\pi}p\bar{\pi}} = -\frac{(\bar{b}c)^5}{30\sqrt{2}b}\{A_3(\bar{b}c) - A_1(\bar{b}c)\}$$

$$M_{01}^{p\pi p\bar{\pi}} = -\frac{(\bar{b}c)^5}{60\sqrt{2}b}\{5[3A_2(\bar{b}c) - A_0(\bar{b}c)] - 3(\bar{b}c)[A_3(\bar{b}c) - A_1(\bar{b}c)]\}$$

$$M_{01}^{sp\bar{\pi}} = \frac{(\bar{b}c)^5}{120\sqrt{3}b}\{10[3A_3(\bar{b}c) - A_1(\bar{b}c)] - (\bar{b}c)[5A_4(\bar{b}c) - 4A_2(\bar{b}c) - A_0(\bar{b}c)]\}$$

$$M_{01}^{p\sigma p\bar{\pi}} = M_{01}^{p\pi p\bar{\pi}},\ M_{01}^{sp\pi} = M_{10}^{sp\sigma} = -M_{01}^{p\sigma s}$$

$$M_{01}^{p\sigma p\pi} = -\frac{(\bar{b}c)^5}{60\sqrt{2}b}\{5[3A_2(\bar{b}c) - A_0(\bar{b}c)] - (\bar{b}c)[3A_1(\bar{b}c) - A_3(\bar{b}c)]\}$$

$$L_{01}^{ss} = \frac{b}{2\sqrt{2}}s_{01}^{d},\ L_{01}^{sp\sigma} = \frac{b(\bar{b}c)^5}{60\sqrt{3}}A_3(\bar{b}c)$$

$$L_{01}^{p\sigma p\sigma} = \frac{b(\bar{b}c)^5}{240\sqrt{2}}\{5A_4(\bar{b}c) - 12A_2(\bar{b}c) + 3A_0(\bar{b}c)\}$$

$$L_{01}^{p\sigma s} = \frac{b(\bar{b}c)^5}{240\sqrt{3}}\{5A_5(\bar{b}c) - 12A_3(\bar{b}c) + 3A_1(\bar{b}c)\}$$

$$L_{00}^{sp\pi} = \frac{5a_0}{2\sqrt{3}c} = L_{00}^{sp\bar{\pi}},\ L_{03}^{sp\pi} = L_{03}^{sp\bar{\pi}},\ L_{03}^{p\sigma p\pi} = L_{03}^{p\sigma p\bar{\pi}}$$

$$L_{03}{}^{sp\pi} = \frac{d(\bar{d}c)^5}{240\sqrt{3}}\{5A_5(\bar{d}c) - 6A_3(\bar{d}c) + A_1(\bar{d}c)\}$$

$$L_{03}{}^{p\sigma p\pi} = -\frac{d(\bar{d}c)^5}{240}\{5A_4(\bar{d}c) - 6A_2(\bar{d}c) + A_0(\bar{d}c)\}$$

$$L_{01}{}^{p\pi p\pi} = \frac{b(\bar{b}c)}{240\sqrt{2}}\{A_0(\bar{b}c) - 5A_4(\bar{b}c)\}$$

$$L_{01}{}^{p\bar{\pi}p\bar{\pi}} = \frac{b}{2\sqrt{2}}\mathfrak{f}_{01}{}^{d}$$

$$L_{01}{}^{p\pi p\bar{\pi}} = -\frac{b(\bar{b}c)^5}{240}\{5A_4(\bar{b}c) - 6A_2(\bar{b}c) + A_0(\bar{b}c)\}$$

$$L_{01}{}^{sp\bar{\pi}} = \frac{b(\bar{b}c)^5}{240\sqrt{3}}\{5A_5(\bar{b}c) - 6A_3(\bar{b}c) + A_1(\bar{b}c)\}$$

$$L_{01}{}^{p\sigma p\bar{\pi}} = L_{01}{}^{p\pi p\bar{\pi}},\ L_{01}{}^{sp\pi} = L_{10}{}^{sp\sigma} = L_{01}{}^{p\sigma s} + a\bar{s}_{01}{}^{d}$$

$$L_{01}{}^{p\sigma p\pi} = L_{01}{}^{p\sigma p\sigma}$$

$$s_{01}{}^{d} = \frac{(\bar{b}c)^5}{360}\{15A_4(\bar{b}c) - 10A_2(\bar{b}c) + 3A_0(\bar{b}c)\}$$

$$s_{03}{}^{d} = \frac{(\bar{d}c)^5}{360}\{15A_4(\bar{d}c) - 10A_2(\bar{d}c) + 3A_0(\bar{d}c)\}$$

$$s_{01}{}^{d} = \frac{(\bar{b}c)^5}{60\sqrt{6}}\{5A_3(\bar{b}c) - A_1(\bar{b}c)\} = \bar{s}_{01}{}^{d}$$

$$\bar{s}_{03}{}^{d} = \frac{(\bar{d}c)^5}{60\sqrt{3}}\{5A_3(\bar{c}c) - A_1(\bar{d}c)\}$$

$$\mathfrak{f}_{01}{}^{d} = \frac{(\bar{b}c)^5}{120}\{5A_4(\bar{b}c) - 6A_2(\bar{b}c) + A_0(\bar{b}c)\}$$

$$\mathfrak{f}_{02}{}^{d} = \frac{(\bar{b}c)^5}{60}\{3A_2(\bar{b}c) - A_0(\bar{b}c)\} = -\bar{\mathfrak{f}}_{01}{}^{d}$$

$$\mathfrak{f}_{03}{}^{d} = \frac{(\bar{d}c)^5}{120}\{5A_4(\bar{d}c) - 6A_2(\bar{d}c) + A_0(\bar{d}c)\}$$

$$\bar{\mathfrak{f}}_{03}{}^{d} = \frac{(\bar{d}c)^5}{120}\{5A_4(\bar{d}c) - 18A_2(\bar{d}c) + 5A_0(\bar{d}c)\}$$

$$\mathfrak{s}_{01}{}^{d} = \frac{(\bar{b}c)^5}{120}\{5A_4(\bar{b}c) - 12A_2(\bar{b}c) + 3A_0(\bar{b}c)\} \quad \text{(A-13)}$$

In eq. A-13, a_0 is the Bohr radius, a is the metal–ligand bond distance, $\mathfrak{b}$ is $\sqrt{2}a$, $\mathfrak{d}$ is $2a$, $\bar{a}$, $\bar{\mathfrak{b}}$, and $\bar{\mathfrak{d}}$ are a/a_0, $\mathfrak{b}/a_0$, and $\mathfrak{d}/a_0$, c is $Z_{2s\text{ or }2p}/2$, and $A_n(v)$ are the integrals (mathematically known as incomplete gamma functions)

$$A_n(v) = \int_1^\infty \lambda^n e^{-v\lambda} d\lambda$$

defined in ref. 6, §5.5, eq. A-10, with arguments v of $\bar{b}c$ and $\bar{d}c$ as indicated above.[58]

5.6 *Group Electronic Transition Moment Integrals.* The group electronic transition moment integrals are straightforwardly set up as linear combinations of the localized integrals gathered in eq. A-13.

(*i*) *Group Magnetic Transition Moment Integrals*

$$M[\Lambda_-{}^{(-)};\ d_{yz}] = -i\mu_B S[\Lambda_-{}^{(-)};\ d_{xz}]$$

$$M[d_{xz};\ \Lambda_-{}^{(+)}] = -i\mu_B S[\Lambda_-{}^{(+)};\ d_{yz}]$$

$$M[\Lambda_-{}^{(-)};\ \Lambda_-{}^{(+)}] = M[\Sigma_-{}^{(-)c};\ \Sigma_-{}^{(+)c}] + M[\Sigma_-{}^{(-)c};\ \Pi_-{}^{(+)c}] + M[\Pi_-{}^{(-)c};\ \Sigma_-{}^{(+)c}] + M[\Pi_-{}^{(-)c};\ \Pi_-{}^{(+)c}] + M[\tilde{\Pi}_-{}^{(-)s};\ \tilde{\Pi}_-{}^{(+)s}]$$

$$M[d_{xz};\ \Lambda_+{}^{(+)}] = i\mu_B\{\sqrt{3}S[\Lambda_+{}^{(+)};\ d_{3z^2-r^2}] - S[\Lambda_+{}^{(+)};\ d_{x^2-y^2}]\}$$

$$M[\Lambda_-{}^{(-)};\ d_{x^2-y^2}] = -i\mu_B S[\Lambda_-{}^{(-)};\ d_{xz}]$$

$$M[\Lambda_-{}^{(-)};\ \Lambda_+{}^{(+)}] = M[\Sigma_-{}^{(-)c};\ \tilde{\Pi}_+{}^{(+)s}] + M[\Pi_-{}^{(-)c};\ \tilde{\Pi}_+{}^{(+)s}] + M[\tilde{\Pi}_-{}^{(-)s};\ \Sigma_+{}^{(+)c}] + M[\tilde{\Pi}_-{}^{(-)s};\ \Pi_+{}^{(+)c}]$$

$$M[\Lambda_-{}^{(-)};\ d_{3z^2-r^2}] = i\sqrt{3}\mu_B S[\Lambda_-{}^{(-)};\ d_{xz}]$$

$$M[d_{xz};\ \Lambda_+{}^{(-)}] = i\mu_B S[\Lambda_+{}^{(-)};\ d_{xy}]$$

$$M[\Lambda_-{}^{(-)};\ d_{xy}] = i\mu_B S[\Lambda_-{}^{(-)};\ d_{xz}]$$

$$M[\Lambda_-{}^{(-)};\ \Lambda_+{}^{(-)}] = M[\Sigma_-{}^{(-)c};\ \tilde{\Pi}_+{}^{(-)s}] + M[\Pi_-{}^{(-)c};\ \tilde{\Pi}_+{}^{(-)s}] + M[\tilde{\Pi}_-{}^{(-)s};\ \Sigma_+{}^{(-)c}] + M[\tilde{\Pi}_-{}^{(-)s};\ \Pi_+{}^{(-)c}]$$

$$M[d_{yz};\ \Lambda_+{}^{(+)}] = -i\mu_B\{\sqrt{3}S[\Lambda_+{}^{(+)};\ d_{3z^2-r^2}] + S[\Lambda_+{}^{(+)};\ d_{x^2-y^2}]\}$$

$$M[\Lambda_-{}^{(+)};\ d_{x^2-y^2}] = -i\mu_B S[\Lambda_-{}^{(+)};\ d_{yz}]$$

$$M[\Lambda_-{}^{(+)};\ \Lambda_+{}^{(+)}] = M[\Sigma_-{}^{(+)c};\ \tilde{\Pi}_+{}^{(+)s}] + M[\Pi_-{}^{(+)c};\ \tilde{\Pi}_+{}^{(+)s}] + M[\tilde{\Pi}_-{}^{(+)s};\ \Sigma_+{}^{(+)c}] + M[\tilde{\Pi}_-{}^{(+)s};\ \Pi_+{}^{(+)c}]$$

$$M[\Lambda_-{}^{(+)};\ d_{3z^2-r^2}] = -i\sqrt{3}\mu_B S[\Lambda_-{}^{(+)};\ d_{yz}]$$

$$M[d_{yz};\ \Lambda_+{}^{(-)}] = -i\mu_B S[\Lambda_+{}^{(-)};\ d_{xy}]$$

$$M[\Lambda_-{}^{(+)};\ d_{xy}] = -i\mu_B S[\Lambda_-{}^{(+)};\ d_{yz}]$$

(58) The equality of the integrals $M_{10}{}^{sp\sigma}$ and $-M_{01}{}^{p\sigma s}$ of eq. A-6 in eq. A-12 follows from the integral anti-Hermiticity of the translationally invariant derivative operator, $\partial/\partial x'$. Direct computation yields $M_{10}{}^{sp\sigma}$ equals $(\bar{b}c)^5/(120\sqrt{3}\mathfrak{b})\{10[3A_3(\bar{b}c) - A_1(\bar{b}c)] - (\bar{b}c)[5A_4(\bar{b}c) - 3A_2(\bar{b}c) + 2A_0(\bar{b}c)]\}$ which, although ostensibly different from the negative of $M_{01}{}^{p\sigma s}$ of eq. A-12, is nonetheless identical with it, as the iterant usage of the recurrence form $nA_{n-1}(v)$ equals $v(A_n(v) - A_0(v))$ shows. The equality of $L_{10}{}^{sp\sigma}$ and $L_{01}{}^{sp\sigma} + a\bar{s}_{01}{}^{d}$ follows from the integral Hermiticity of the nontranslationally invariant operator x_1' equals $x_0' + a$, where a is the metal–ligand bond length. The other equalities come from symmetry considerations or calculational happenstance.

$$M[\Lambda_-^{(+)};\ \Lambda_+^{(-)}] = M[\Sigma_-^{(+)c};\ \tilde{\Pi}_+^{(-)s}] + M[\Pi_-^{(+)c};\ \tilde{\Pi}_+^{(-)s}] + M[\tilde{\Pi}_-^{(+)s};\ \Sigma_+^{(-)c}] + M[\tilde{\Pi}_-^{(+)s};\ \Pi_+^{(-)c}]$$

$$M[\Lambda_+^{(+)};\ \mathrm{d}_{xy}] = -i2\mu_B S[\Lambda_+^{(+)};\ \mathrm{d}_{x^2-y^2}]$$

$$M[\mathrm{d}_{x^2-y^2};\ \Lambda_+^{(-)}] = -i2\mu_B S[\Lambda_+^{(-)};\ \mathrm{d}_{xy}]$$

$$M[\Lambda_+^{(+)};\ \Lambda_+^{(-)}] = M[\Pi_+^{(+)c};\ \Sigma_+^{(-)c}] + M[\Sigma_+^{(+)c};\ \Pi_+^{(-)c}]$$

$$M[\mathrm{d}_{3z^2-r^2};\ \Lambda_+^{(-)}] = 0 \qquad \text{(A-14)}$$

(ii) Group Electric Transition Moment Integrals

$$L[\Lambda_-^{(-)};\ \mathrm{d}_{yz}] = L[\Sigma_-^{(-)c};\ \mathrm{d}_{yz}] + L[\Pi_-^{(-)c};\ \mathrm{d}_{yz}]$$

$$L[\mathrm{d}_{xz};\ \Lambda_-^{(+)}] = L[\mathrm{d}_{xz};\ \Sigma_-^{(+)c}] + L[\mathrm{d}_{xz};\ \Pi_-^{(+)c}]$$

$$L[\Lambda_-^{(-)};\ \Lambda_-^{(+)}] = L[\Sigma_-^{(-)c};\ \tilde{\Pi}_-^{(+)s}] + L[\Pi_-^{(-)c};\ \tilde{\Pi}_-^{(+)s}] + L[\tilde{\Pi}_-^{(-)s};\ \Sigma_-^{(+)c}] + L[\tilde{\Pi}_-^{(-)s};\ \Pi_-^{(+)c}]$$

$$L[\mathrm{d}_{xz};\ \Lambda_+^{(+)}] = L[\mathrm{d}_{xz};\ \tilde{\Pi}_+^{(+)s}]$$

$$L[\Lambda_-^{(-)};\ \mathrm{d}_{x^2-y^2}] = L[\Sigma_-^{(-)c};\ \mathrm{d}_{x^2-y^2}] + L[\Pi_-^{(-)c};\ \mathrm{d}_{x^2-y^2}]$$

$$L[\Lambda_-^{(-)};\ \Lambda_+^{(+)}] = L[\Sigma_-^{(-)c};\ \Sigma_+^{(+)c}] + L[\Sigma_-^{(-)c};\ \Pi_+^{(+)c}] + L[\Pi_-^{(-)c};\ \Sigma_+^{(+)c}] + L[\Pi_-^{(-)c};\ \Pi_+^{(+)c}] + L[\tilde{\Pi}_-^{(-)s};\ \tilde{\Pi}_+^{(+)s}]$$

$$L[\Lambda_-^{(-)};\ \mathrm{d}_{3z^2-r^2}] = L[\Sigma_-^{(-)c};\ \mathrm{d}_{3z^2-r^2}] + L[\Pi_-^{(-)c};\ \mathrm{d}_{3z^2-r^2}]$$

$$L[\mathrm{d}_{xz};\ \Lambda_+^{(-)}] = L[\mathrm{d}_{xz};\ \tilde{\Pi}_+^{(-)s}]$$

$$L[\Lambda_-^{(-)};\ \mathrm{d}_{xy}] = L[\Sigma_-^{(-)c};\ \mathrm{d}_{xy}] + L[\Pi_-^{(-)c};\ \mathrm{d}_{xy}]$$

$$L[\Lambda_-^{(-)};\ \Lambda_+^{(-)}] = L[\Sigma_-^{(-)c};\ \Sigma_+^{(-)c}] + L[\Sigma_-^{(-)c};\ \Pi_+^{(-)c}] + L[\Pi_-^{(-)c};\ \Sigma_+^{(-)c}] + L[\Pi_-^{(-)c};\ \Pi_+^{(-)c}] + L[\tilde{\Pi}_-^{(-)s};\ \tilde{\Pi}_+^{(-)s}]$$

$$L[\mathrm{d}_{yz};\ \Lambda_+^{(+)}] = L[\mathrm{d}_{yz};\ \tilde{\Pi}_+^{(+)s}] = L[\mathrm{d}_{xz};\ \tilde{\Pi}_+^{(+)s}] = L[\mathrm{d}_{xz};\ \Lambda_+^{(+)}]$$

$$L[\Lambda_-^{(+)};\ \mathrm{d}_{x^2-y^2}] = L[\Sigma_-^{(+)c};\ \mathrm{d}_{x^2-y^2}] + L[\Pi_-^{(+)c};\ \mathrm{d}_{x^2-y^2}]$$

$$L[\Lambda_-^{(+)};\ \Lambda_+^{(+)}] = L[\Sigma_-^{(+)c};\ \Sigma_+^{(+)c}] + L[\Sigma_-^{(+)c};\ \Pi_+^{(+)c}] + L[\Pi_-^{(+)c};\ \Sigma_+^{(+)c}] + L[\Pi_-^{(+)c};\ \Pi_+^{(+)c}] + L[\tilde{\Pi}_-^{(+)s};\ \tilde{\Pi}_+^{(+)s}]$$

$$L[\Lambda_-^{(+)};\ \mathrm{d}_{3z^2-r^2}] = L[\Sigma_-^{(+)c};\ \mathrm{d}_{3z^2-r^2}] + L[\Pi_-^{(+)c};\ \mathrm{d}_{3z^2-r^2}]$$

$$L[\mathrm{d}_{yz};\ \Lambda_+^{(-)}] = L[\mathrm{d}_{yz};\ \tilde{\Pi}_+^{(-)s}]$$

$$L[\Lambda_-^{(+)};\ \mathrm{d}_{xy}] = L[\Sigma_-^{(+)c};\ \mathrm{d}_{xy}] + L[\Pi_-^{(+)c};\ \mathrm{d}_{xy}]$$

$$L[\Lambda_-^{(+)};\ \Lambda_+^{(-)}] = L[\Sigma_-^{(+)c};\ \Sigma_+^{(-)c}] + L[\Sigma_-^{(+)c};\ \Pi_+^{(-)c}] + L[\Pi_-^{(+)c};\ \Sigma_+^{(-)c}] + L[\Pi_-^{(+)c};\ \Pi_+^{(-)c}] + L[\tilde{\Pi}_-^{(+)s};\ \tilde{\Pi}_+^{(-)s}]$$

$$L[\Lambda_+^{(+)};\ \mathrm{d}_{xy}] = L[\tilde{\Pi}_+^{(+)s};\ \mathrm{d}_{xy}]$$

$$L[\mathrm{d}_{x^2-y^2};\ \Lambda_+^{(-)}] = 0$$

$$L[\Lambda_+^{(+)};\ \Lambda_+^{(-)}] = L[\Sigma_+^{(+)c};\ \tilde{\Pi}_+^{(-)s}] + L[\tilde{\Pi}_+^{(+)s};\ \Sigma_+^{(-)c}]$$

$$L[\mathrm{d}_{3z^2-r^2};\ \Lambda_+^{(-)}] = L[\mathrm{d}_{3z^2-r^2};\ \tilde{\Pi}_+^{(-)s}] \qquad \text{(A-15)}$$

(iii) Subgroup Magnetic Transition Moment Integrals

$$M[\Sigma_-^{(-)c};\ \Sigma_-^{(+)c}] = 8a_-^{\sigma-}a_-^{\sigma+}\int \sigma_0^c \mathrm{m}_z \sigma_1^c d\tau = -i\mu_B 8a_-^{\sigma-}a_-^{\sigma+}\{a[k_s^2 M_{01}^{ss} - k_p k_s \cos\alpha\cos\iota\,(M_{01}^{p_\sigma s} - M_{01}^{s p_\sigma}) - k_p^2\cos^2\alpha\cos^2\iota\, M_{01}^{p_\sigma p_\sigma} + k_p\cos\alpha\cos\iota\,[k_s s_{01}^d - k_p\cos\alpha\cos\iota\,\mathfrak{s}_{01}^d]\}$$

$$M[\Sigma_-^{(-)c};\ \Pi_-^{(+)c}] = 4a_-^{\sigma-}a_-^{\pi+}\{\int \sigma_0^c \mathrm{m}_z \pi_0^c d\tau - \int \sigma_0^c \mathrm{m}_z \pi_3^c d\tau\} = -i\mu_B 4a_-^{\sigma-}a_-^{\pi-}k_p\cos\iota\sin\alpha\times\{a[k_s(M_{00}^{s p_\pi} + M_{03}^{s p_\pi}) - k_p\cos\iota\cos\alpha\times(a^{-1}k_p\cos\iota\sin\alpha + M_{03}^{p_\sigma p_\pi})] - k_p\cos\iota\sin\alpha\,[k_s\bar{s}_{03}^d - k_p\cos\iota\cos\alpha\,\bar{\mathfrak{f}}_{03}^d]\}$$

$$M[\Pi_-^{(-)c};\ \Sigma_-^{(+)c}] = -(a_-^{\pi-}a_-^{\sigma+}/a_-^{\sigma-}a_-^{\pi+})M[\Sigma_-^{(-)c};\ \Pi_-^{(+)c}]$$

$$M[\Pi_-^{(-)c};\ \Pi_-^{(+)c}] = 8a_-^{\pi-}a_-^{\pi+}\int \pi_0^c \mathrm{m}_z \pi_1^c d\tau = i\mu_B 8a_-^{\pi-}a_-^{\pi+}k_p^2\cos^2\iota\sin^2\alpha\,\{aM_{01}^{p_\pi p_\pi} - \mathfrak{s}_{01}^d\}$$

$$M[\tilde{\Pi}_-^{(-)s};\ \tilde{\Pi}_-^{(+)s}] = 8a_-^{\tilde{\pi}-}a_-^{\tilde{\pi}+}\int \tilde{\pi}_0^s \mathrm{m}_z \tilde{\pi}_1^s d\tau = i\mu_B 8a_-^{\tilde{\pi}-}a_-^{\tilde{\pi}+}ak_p^2\sin^2\iota\, M_{01}^{p_{\tilde{\pi}} p_{\tilde{\pi}}}$$

$$M[\Sigma_-^{(-)c};\ \tilde{\Pi}_+^{(+)s}] = 2\sqrt{2}a_-^{\sigma-}a_+^{\tilde{\pi}+}\{\int \sigma_0^c \mathrm{m}_{y'} \tilde{\pi}_0^s d\tau + 2\int \sigma_0^c \mathrm{m}_{y'} \tilde{\pi}_1^s d\tau + \int \sigma_0^c \mathrm{m}_{y'} \tilde{\pi}_3^s d\tau\} = i\mu_B\, 2\sqrt{2}a_-^{\sigma-}a_+^{\tilde{\pi}+}k_p\sin\iota\,\{a[k_s(M_{00}^{s p_\pi} - M_{03}^{s p_\pi}) - k_p\cos\iota\cos\alpha\,(a^{-1} - M_{03}^{p_\sigma p_\pi})] - k_s(2s_{01}^d - \bar{s}_{03}^d) + k_p\cos\iota\cos\alpha\,(2\mathfrak{s}_{01}^d - \bar{\mathfrak{f}}_{03}^d)\}$$

$$M[\Pi_-^{(-)c};\ \tilde{\Pi}_+^{(+)s}] = 2\sqrt{2}a_-^{\pi-}a_+^{\tilde{\pi}+}\{\int \pi_0^c \mathrm{m}_{x'} \tilde{\pi}_0^s d\tau + 2\int \pi_0^c \mathrm{m}_{x'} \tilde{\pi}_1^s d\tau + \int \pi_0^c \mathrm{m}_{z'} \tilde{\pi}_3^s d\tau\} = -i\mu_B 2\sqrt{2}a_-^{\pi-}a_+^{\tilde{\pi}+}k_p^2\cos\iota\sin\iota\sin\alpha\times\{a(a^{-1} + 2M_{01}^{p_\pi p_{\tilde{\pi}}}) - (2\mathfrak{s}_{01}^d - \mathfrak{f}_{03}^d)\}$$

$$M[\tilde{\Pi}_-^{(-)s};\ \Sigma_+^{(+)c}] = -2\sqrt{2}a_-^{\bar{\pi}-}a_+^{\sigma+}\{\int\sigma_0^c m_{y'}\tilde{\pi}_0^s d\tau - 2\int\sigma_0^c m_{x'}\tilde{\pi}_1^s d\tau - \int\sigma_0^c m_{y'}\tilde{\pi}_3^s d\tau\} =$$
$$-i\mu_B 2\sqrt{2}a_-^{\bar{\pi}-}a_+^{\sigma+}k_p \sin\iota\{a[k_s(M_{00}^{sp_\pi} + 2M_{01}^{sp_{\bar{\pi}}} + M_{03}^{sp_\pi}) - k_p\cos\iota\cos\alpha\,(a^{-1} + 2M_{01}^{p_\pi p_{\bar{\pi}}} + M_{03}^{p_\sigma p_\pi})] -$$
$$k_s(2\bar{s}_{01}^{\ d} + \bar{s}_{03}^{\ d}) + k_p\cos\iota\cos\alpha\,(2\bar{\int}_{01}^{\ d} + \bar{\int}_{03}^{\ d})\}$$

$$M[\tilde{\Pi}_-^{(-)s};\ \Pi_+^{(+)c}] = -2\sqrt{2}a_-^{\bar{\pi}-}a_+^{\pi+}\{\int\pi_0^c m_{x'}\tilde{\pi}_0^s d\tau - 2\int\pi_0^c m_{y'}\tilde{\pi}_1^s d\tau - \int\pi_0^c m_{x'}\tilde{\pi}_3^s d\tau\} =$$
$$i\mu_B 2\sqrt{2}a_-^{\bar{\pi}-}a_+^{\pi+}k_p^2 \times \cos\iota\sin\iota\sin\alpha\,(1 - 2\bar{\int}_{01}^{\ d} - \int_{03}^{\ d})$$

$$M[\Sigma_-^{(-)c};\ \tilde{\Pi}_+^{(-)s}] = -2\sqrt{2}a_-^{\sigma-}a_+^{\bar{\pi}-} \times \{\int\sigma_0^c m_{y'}\tilde{\pi}_0^s d\tau - 2\int\sigma_0^c m_{y'}\tilde{\pi}_1^s d\tau + \int\sigma_0^c m_{y'}\tilde{\pi}_3^s d\tau\} =$$
$$-i\mu_B 2\sqrt{2}a_-^{\sigma-}a_+^{\bar{\pi}-}k_p \sin\iota \times \{a[k_s(M_{00}^{sp_\pi} - M_{03}^{sp_\pi}) - k_p\cos\iota\cos\alpha\,(a^{-1} - M_{03}^{p_\sigma p_\pi})] + k_s(2s_{01}^{\ d} + \bar{s}_{03}^{\ d}) - k_p\cos\iota \times \cos\alpha\,(2\bar{\mathfrak{s}}_{01}^{\ d} + \bar{\int}_{03}^{\ d})\}$$

$$M[\Pi_-^{(-)c};\ \tilde{\Pi}_+^{(-)s}] = 2\sqrt{2}a_-^{\pi-}a_+^{\bar{\pi}-} \times \{\int\pi_0^c m_{x'}\tilde{\pi}_0^s d\tau - 2\int\pi_0^c m_{x'}\tilde{\pi}_1^s d\tau + \int\pi_0^c m_{x'}\tilde{\pi}_3^s d\tau\} =$$
$$-i\mu_B 2\sqrt{2}a_-^{\pi-}a_+^{\bar{\pi}-}k_p^2\cos\iota \times \sin\iota\sin\alpha\,\{a(a^{-1} - 2M_{01}^{p_\pi p_{\bar{\pi}}}) + (2\bar{\mathfrak{s}}_{01}^{\ d} - \int_{03}^{\ d})\}$$

$$M[\tilde{\Pi}_-^{(-)s};\ \Sigma_+^{(-)c}] = 2\sqrt{2}a_-^{\bar{\pi}-}a_+^{\sigma-} \times \{\int\sigma_0^c m_{y'}\tilde{\pi}_0^s d\tau + 2\int\sigma_0^c m_{x'}\tilde{\pi}_1^s d\tau - \int\sigma_0^c m_{y'}\tilde{\pi}_3^s d\tau\} =$$
$$i\mu_B 2\sqrt{2}a_-^{\bar{\pi}-}a_+^{\sigma-}k_p \sin\iota \times \{a[k_s(M_{00}^{sp_\pi} - 2M_{01}^{sp_{\bar{\pi}}} + M_{03}^{sp_\pi}) - k_p\cos\iota \times \cos\alpha\,(a^{-1} - 2M_{01}^{p_\pi p_{\bar{\pi}}} + M_{03}^{p_\sigma p_\pi})] + k_s(2\bar{s}_{01}^{\ d} - \bar{s}_{03}^{\ d}) - k_p\cos\iota\cos\alpha\,(2\bar{\int}_{01}^{\ d} - \bar{\int}_{03}^{\ d})\}$$

$$M[\tilde{\Pi}_-^{(-)s};\ \Pi_+^{(-)c}] = -2\sqrt{2}a_-^{\bar{\pi}-}a_+^{\pi-}\{\int\pi_0^c m_{x'}\tilde{\pi}_0^s d\tau + 2\int\pi_0^c m_{y'}\tilde{\pi}_1^s d\tau - \int\pi_0^c m_{x'}\tilde{\pi}_3^s d\tau\} =$$
$$i\mu_B 2\sqrt{2}a_-^{\bar{\pi}-}a_+^{\pi-}k_p^2\cos\iota \times \sin\iota\sin\alpha\,\{1 + 2\bar{\int}_{01}^{\ d} - \int_{03}^{\ d}\}$$

$$M[\Sigma_-^{(+)c};\ \tilde{\Pi}_+^{(+)s}] = -(a_-^{\sigma+}/a_-^{\sigma-})M[\Sigma_-^{(-)c};\ \tilde{\Pi}_+^{(+)s}]$$
$$M[\Pi_-^{(+)c};\ \tilde{\Pi}_+^{(+)s}] = (a_-^{\pi+}/a_-^{\pi-})M[\Pi_-^{(-)c};\ \tilde{\Pi}_+^{(+)s}]$$
$$M[\tilde{\Pi}_-^{(+)s};\ \Sigma_+^{(+)c}] = -(a_-^{\bar{\pi}+}/a_-^{\bar{\pi}-})M[\tilde{\Pi}_-^{(-)s};\ \Sigma_+^{(+)c}]$$
$$M[\tilde{\Pi}_-^{(+)s};\ \Pi_+^{(+)c}] = (a_-^{\bar{\pi}+}/a_-^{\bar{\pi}-})M[\tilde{\Pi}_-^{(-)s};\ \Pi_+^{(+)c}]$$
$$M[\Sigma_-^{(-)c};\ \tilde{\Pi}_+^{(-)s}] = -(a_-^{\sigma+}/a_-^{\sigma-})M[\Sigma_-^{(-)c};\ \tilde{\Pi}_+^{(-)s}]$$
$$M[\Pi_-^{(+)c};\ \tilde{\Pi}_+^{(-)s}] = (a_-^{\pi+}/a_-^{\pi-})M[\Pi_-^{(-)c};\ \tilde{\Pi}_+^{(-)s}]$$
$$M[\tilde{\Pi}_-^{(+)s};\ \Sigma_+^{(-)c}] = -(a_-^{\bar{\pi}+}/a_-^{\bar{\pi}-})M[\tilde{\Pi}_-^{(-)s};\ \Sigma_+^{(-)c}]$$
$$M[\tilde{\Pi}_-^{(+)s};\ \Pi_+^{(-)c}] = (a_-^{\bar{\pi}+}/a_-^{\bar{\pi}-})M[\tilde{\Pi}_-^{(-)s};\ \Pi_+^{(-)c}]$$
$$M[\Pi_+^{(+)c};\ \Sigma_+^{(-)c}] = -4a_+^{\pi+}a_+^{\sigma-}\{\int\sigma_0^c m_z\pi_0^c d\tau + 2\int\sigma_0^c m_z\pi_1^c d\tau + \int\sigma_0^c m_z\pi_3^c d\tau\} = i\mu_B 4a_+^{\pi+}a_+^{\sigma-}k_p \times \cos\iota\sin\alpha\,\{a[k_s(M_{00}^{sp_\pi} + 2M_{01}^{p_\sigma s} + M_{03}^{sp_\pi}) - k_p\cos\iota\cos\alpha\,(a^{-1} - 2M_{01}^{p_\sigma p_\pi} + M_{03}^{p_\sigma p_\pi})] + k_s(2\bar{s}_{01}^{\ d} - \bar{s}_{03}^{\ d}) - k_p\cos\iota\cos\alpha\,(2\bar{\int}_{01}^{\ d} - \bar{\int}_{03}^{\ d})\}$$

$$M[\Sigma_+^{(+)c};\ \Pi_+^{(-)c}] = 4a_+^{\sigma+}a_+^{\pi-}\{\int\sigma_0^c m_z\pi_0^c d\tau - 2\int\sigma_0^c m_z\pi_1^c d\tau + \int\sigma_0^c m_z\pi_3^c d\tau\} = -i\mu_B 4a_+^{\sigma+}a_+^{\pi-}k_p \times \cos\iota\sin\alpha\,\{a[k_s(M_{00}^{sp_\pi} - 2M_{01}^{p_\sigma s} + M_{03}^{sp_\pi}) - k_p\cos\iota\cos\alpha\,(a^{-1} + 2M_{01}^{p_\sigma p_\pi} + M_{03}^{p_\sigma p_\pi})] - k_s(2\bar{s}_{01}^{\ d} + \bar{s}_{03}^{\ d}) + k_p\cos\iota\cos\alpha\,(2\bar{\int}_{01}^{\ d} + \bar{\int}_{03}^{\ d})\}$$

(A-16)

(iv) Subgroup Electric Transition Moment Integrals

$$L[\Sigma_-^{(-)c};\ d_{yz}] = 4a_-^{\sigma-}\int\sigma_0^c ez d_{yz}d\tau = -e2\sqrt{6}a_-^{\sigma-}\{k_s K_{0A_3} + k_p\cos\iota\cos\alpha\,K_{2A_3}\}$$
$$L[\Pi_-^{(-)c};\ d_{yz}] = 4a_-^{\pi-}\int\pi_0^c ez d_{yz}d\tau = e2\sqrt{6}a_-^{\pi-}k_p\cos\iota\sin\alpha\,K_{3A_3}$$
$$L[d_{xz};\ \Sigma_-^{(+)c}] = (a_-^{\sigma+}/a_-^{\sigma-})L[\Sigma_-^{(-)c};\ d_{yz}]$$
$$L[d_{xz};\ \Pi_-^{(+)c}] = -(a_-^{\pi+}/a_-^{\pi-})L[\Pi_-^{(-)c};\ d_{yz}]$$
$$L[d_{xz};\ \tilde{\Pi}_+^{(+)s}] = 4a_+^{\bar{\pi}+}\int d_{xz}ey\tilde{\pi}_0^s d\tau = e2\sqrt{3}a_+^{\bar{\pi}+}k_p\sin\iota\{K_{2A_3} - K_{3A_3}\}$$
$$L[\Sigma_-^{(-)c};\ d_{x^2-y^2}] = 4a_-^{\sigma-}\int\sigma_0^c ey d_{x^2-y^2}d\tau = e2\sqrt{6}a_-^{\sigma-}\{k_s K_{0A_3} + k_p\cos\iota\cos\alpha\,K_{2A_3}\}$$
$$L[\Pi_-^{(-)c};\ d_{x^2-y^2}] = 4a_-^{\pi-}\int\pi_0^c ey d_{x^2-y^2}d\tau = -e2\sqrt{6}a_-^{\pi-}k_p\cos\iota\sin\alpha\,K_{2A_3}$$
$$L[\Sigma_-^{(-)c};\ d_{3z^2-r^2}] = 4a_-^{\sigma-}\int\sigma_0^c ey d_{3z^2-r^2}d\tau = e2\sqrt{3}a_-^{\sigma-}\{k_s K_{14A_0} - k_p\cos\iota\cos\alpha\,K_{4A_0}\}$$
$$L[\Pi_-^{(-)c};\ d_{3z^2-r^2}] = 4a_-^{\pi-}\int\pi_0^c ey d_{3z^2-r^2}d\tau = e2\sqrt{3}a_-^{\pi-}k_p\cos\iota\sin\alpha\,K_{4A_3}$$
$$L[d_{xz};\ \tilde{\Pi}_+^{(-)s}] = 4a_+^{\bar{\pi}-}\int\tilde{\pi}_0^s ex d_{xz}d\tau = e2\sqrt{3}a_+^{\bar{\pi}-}k_p\sin\iota\{K_{2A_3} + K_{3A_3}\}$$
$$L[\Sigma_-^{(-)c};\ d_{xy}] = 4a_-^{\sigma-}\int\sigma_0^c ex d_{xy}d\tau = -e6a_-^{\sigma-}\{k_s K_{14A_0} - k_p\cos\iota\cos\alpha\,K_{4A_0}\}$$
$$L[\Pi_-^{(-)c};\ d_{xy}] = 4a_-^{\pi-}\int\pi_0^c ex d_{xy}d\tau = e2\sqrt{3}a_-^{\pi-}k_p\cos\iota\sin\alpha\,K_{7A_3}$$
$$L[d_{yz};\ \tilde{\Pi}_+^{(+)s}] = L[d_{xz};\ \tilde{\Pi}_+^{(+)s}]$$
$$L[\Sigma_-^{(+)c};\ d_{x^2-y^2}] = -L[\Sigma_-^{(-)c};\ d_{x^2-y^2}]$$

$$L[\Pi_-^{(+)c};\ d_{x^2-y^2}] = L[\Pi_-^{(-)c};\ d_{x^2-y^2}]$$

$$L[\Sigma_-^{(+)c};\ d_{3z^2-r^2}] = L[\Sigma_-^{(-)c};\ d_{3z^2-r^2}]$$

$$L[\Pi_-^{(+)c};\ d_{3z^2-r^2}] = -L[\Pi_-^{(-)c};\ d_{3z^2-r^2}]$$

$$L[d_{yz};\ \tilde{\Pi}_+^{(-)s}] = L[d_{xz};\ \tilde{\Pi}_+^{(-)s}]$$

$$L[\Sigma_-^{(+)c};\ d_{xy}] = L[\Sigma_-^{(-)c};\ d_{xy}]$$

$$L[\Pi_-^{(+)c};\ d_{xy}] = -L[\Pi_-^{(-)c};\ d_{xy}]$$

$$L[\tilde{\Pi}_+^{(+)s};\ d_{xy}] = 4a_+^{\tilde{\pi}+}\int\tilde{\pi}_0^{s}ezd_{xy}d\tau = -e\sqrt{6}a_+^{\tilde{\pi}+}k_p\sin\iota\left\{\sqrt{3}K_{4A_2}+K_{7A_2}\right\}$$

$$L[d_{3z^2-r^2};\ \tilde{\Pi}_+^{(-)s}] = 4a_+^{\tilde{\pi}-}\int\tilde{\pi}_0^{s}ezd_{3z^2-r^2}d\tau = -e\sqrt{6}a_+^{\tilde{\pi}-}k_p\sin\iota\left\{K_{4A_2}-\sqrt{3}K_{7A_2}\right\}$$

$$L[\Sigma_-^{(-)c};\ \tilde{\Pi}_-^{(+)s}] = 4a_-^{\sigma-}a_-^{\tilde{\pi}+}\left\{\int\sigma_0^{c}ez\tilde{\pi}_0^{s}d\tau - \int\sigma_0^{c}ez\tilde{\pi}_3^{s}d\tau\right\} = e4a_-^{\sigma-}a_-^{\tilde{\pi}+}k_p\sin\iota\times\left\{k_s(L_{00}^{sp_\pi}-L_{03}^{sp_\pi})+k_p\cos\iota\cos\alpha\,L_{03}^{p_\sigma p_\pi}\right\}$$

$$L[\Pi_-^{(-)c};\ \tilde{\Pi}_-^{(+)s}] = 8a_-^{\pi-}a_-^{\tilde{\pi}+}\int\pi_0^{c}ez\tilde{\pi}_1^{s}d\tau = -e8a_-^{\pi-}a_-^{\tilde{\pi}+}k_p^{2}\cos\iota\sin\iota\sin\alpha\,L_{01}^{p_\pi p_{\tilde{\pi}}}$$

$$L[\tilde{\Pi}_-^{(-)s};\ \Sigma_-^{(+)c}] = (a_-^{\tilde{\pi}-}a_-^{\sigma+}/a_-^{\sigma-}a_-^{\tilde{\pi}+})L[\Sigma_-^{(-)c};\ \tilde{\Pi}_-^{(+)s}]$$

$$L[\tilde{\Pi}_-^{(-)s};\ \Pi_-^{(+)c}] = -(a_-^{\tilde{\pi}-}a_-^{\pi+}/a_-^{\pi-}a_-^{\tilde{\pi}+})L[\Pi_-^{(-)c};\ \tilde{\Pi}_-^{(+)s}]$$

$$L[\Sigma_-^{(-)c};\ \Sigma_+^{(+)c}] = 2\sqrt{2}a_-^{\sigma-}a_+^{\sigma+}\left\{\int\sigma_0^{c}ex'\sigma_0^{c}d\tau + 2\int\sigma_0^{c}ex'\sigma_1^{c}d\tau\right\} = e2\sqrt{2}a_-^{\sigma-}a_+^{\sigma+}\left\{k_s^{2}(a+2L_{01}^{ss}) - 2k_sk_p\cos\iota\cos\alpha\,(L_{00}^{sp_\pi}-L_{01}^{sp_\sigma}+L_{01}^{p_\sigma s}) + k_p^{2}\cos^2\iota\cos^2\alpha\,(a-2L_{01}^{p_\sigma p_\sigma})\right\}$$

$$L[\Sigma_-^{(-)c};\ \Pi_+^{(+)c}] = 2\sqrt{2}a_-^{\sigma-}a_+^{\pi+}\left\{\int\sigma_0^{c}ey'\pi_0^{c}d\tau + 2\int\sigma_0^{c}ey'\pi_1^{c}d\tau + \int\sigma_0^{c}ey'\pi_3^{c}d\tau\right\} = e2\sqrt{2}a_-^{\sigma-}a_+^{\pi+}k_p\cos\iota\sin\alpha\times\left\{k_s(L_{00}^{sp_\pi}+2as_{01}^{d}-2L_{01}^{sp_\sigma}-L_{03}^{sp_\pi}) + k_p\cos\iota\cos\alpha\,(as_{01}^{d}+L_{01}^{p_\sigma p_\sigma}+L_{03}^{p_\sigma p_\pi})\right\}$$

$$L[\Pi_-^{(-)c};\ \Sigma_+^{(+)c}] = 2\sqrt{2}a_-^{\pi-}a_+^{\sigma+}\left\{\int\sigma_0^{c}ey'\pi_0^{c}d\tau - 2\int\sigma_0^{c}ex'\pi_1^{c}d\tau - \int\sigma_0^{c}ey'\pi_3^{c}d\tau\right\} = e2\sqrt{2}a_-^{\pi-}a_+^{\sigma+}k_p\cos\iota\sin\alpha\times\left\{k_s(L_{00}^{sp_\pi}+2L_{01}^{p_\sigma s}+2as_{01}^{d}+L_{03}^{sp_\pi}) - k_p\cos\iota\cos\alpha\,(2L_{01}^{p_\sigma p_\sigma}+L_{03}^{p_\sigma p_\pi})\right\}$$

$$L[\Pi_-^{(-)c};\ \Pi_+^{(+)c}] = 4a_-^{\pi-}a_+^{\pi+}\left\{\int\pi_0^{c}ex'\pi_0^{c}d\tau + 2\int\pi_0^{c}ex'\pi_1^{c}d\tau\right\} = e4a_-^{\pi-}a_+^{\pi+}k_p^{2}\cos^2\iota\sin^2\alpha\left\{a-2L_{01}^{p_\pi p_\pi}\right\}$$

$$L[\tilde{\Pi}_-^{(-)s};\ \Pi_+^{(+)s}] = 2\sqrt{2}a_-^{\tilde{\pi}-}a_+^{\tilde{\pi}+}\left\{\int\tilde{\pi}_0^{s}ex'\tilde{\pi}_0^{s}d\tau + 2\int\tilde{\pi}_0^{s}ex'\tilde{\pi}_1^{s}d\tau\right\} = e2\sqrt{2}a_-^{\tilde{\pi}-}a_+^{\tilde{\pi}+}k_p^{2}\sin^2\iota\left\{a-2L_{01}^{p_{\tilde{\pi}}p_{\tilde{\pi}}}\right\}$$

$$L[\Sigma_-^{(-)c};\ \Sigma_+^{(-)c}] = 2\sqrt{2}a_-^{\sigma-}a_+^{\sigma-}\left\{\int\sigma_0^{c}ex'\sigma_0^{c}d\tau - 2\int\sigma_0^{c}ex'\sigma_1^{c}d\tau\right\} = e2\sqrt{2}a_-^{\sigma-}a_+^{\sigma-}\left\{k_s^{2}(a-2L_{01}^{ss}) - 2k_sk_p\cos\iota\cos\alpha\times(L_{00}^{sp_\pi}+L_{01}^{sp_\sigma}-L_{01}^{p_\sigma s}) + k_p^{2}\cos^2\iota\cos^2\alpha\times(a+2L_{01}^{p_\sigma p_\sigma})\right\}$$

$$L[\Sigma_-^{(-)c};\ \Pi_+^{(-)c}] = -2\sqrt{2}a_-^{\sigma-}a_+^{\pi-}\left\{\int\sigma_0^{c}ey'\pi_0^{c}d\tau - 2\int\sigma_0^{c}ey'\pi_1^{c}d\tau + \int\sigma_0^{c}ey'\pi_3^{c}d\tau\right\} = -e2\sqrt{2}a_-^{\sigma-}a_+^{\pi-}k_p\cos\iota\sin\alpha\times\left\{k_s(L_{00}^{sp_\pi}-2as_{01}^{d}+2L_{01}^{sp_\sigma}-L_{03}^{sp_\pi}) - k_p\cos\iota\cos\alpha\,(2as_{01}^{d}+2L_{01}^{p_\sigma p_\sigma}-L_{03}^{p_\sigma p_\pi})\right\}$$

$$L[\Pi_-^{(-)c};\ \Sigma_+^{(-)c}] = -2\sqrt{2}a_-^{\pi-}a_+^{\sigma-}\left\{\int\sigma_0^{c}ey'\pi_0^{c}d\tau + 2\int\sigma_0^{c}ex'\pi_1^{c}d\tau - \int\sigma_0^{c}ey'\pi_3^{c}d\tau\right\} = -e2\sqrt{2}a_-^{\pi-}a_+^{\sigma-}k_p\cos\iota\sin\alpha\times\left\{k_s(L_{00}^{sp_\pi}-2L_{01}^{p_\sigma s}-2a\bar{s}_{01}^{d}+L_{03}^{sp_\pi}) + k_p\cos\iota\cos\alpha\,(2L_{01}^{p_\sigma p_\sigma}-L_{03}^{p_\sigma p_\pi})\right\}$$

$$L[\Pi_-^{(-)c};\ \Pi_+^{(-)c}] = 2\sqrt{2}a_-^{\pi-}a_+^{\pi-}\left\{\int\pi_0^{c}ex'\pi_0^{c}d\tau - 2\int\pi_0^{c}ex'\pi_1^{c}d\tau\right\} = e2\sqrt{2}a_-^{\pi-}a_+^{\pi-}k_p^{2}\cos^2\iota\sin^2\alpha\,(a+2L_{01}^{p_\pi p_\pi})$$

$$L[\tilde{\Pi}_-^{(-)s};\ \tilde{\Pi}_+^{(-)s}] = 2\sqrt{2}a_-^{\tilde{\pi}-}a_+^{\tilde{\pi}-}\left\{\int\tilde{\pi}_0^{s}ex'\tilde{\pi}_0^{s}d\tau - 2\int\tilde{\pi}_0^{s}ex'\tilde{\pi}_1^{s}d\tau\right\} = e2\sqrt{2}a_-^{\tilde{\pi}-}a_+^{\tilde{\pi}-}k_p^{2}\sin^2\iota\,(a+2L_{01}^{p_{\tilde{\pi}}p_{\tilde{\pi}}})$$

$$L[\Sigma_-^{(+)c};\ \Sigma_+^{(+)c}] = (a_-^{\sigma+}/a_-^{\sigma-})L[\Sigma_-^{(-)c};\ \Sigma_+^{(+)c}]$$

$$L[\Sigma_-^{(+)c};\ \Pi_+^{(+)c}] = -(a_-^{\sigma+}/a_-^{\sigma-})L[\Sigma_-^{(-)c};\ \Pi_+^{(+)c}]$$

$$L[\Pi_-^{(+)c};\ \Sigma_+^{(+)c}] = -(a_-^{\pi+}/a_-^{\pi-})L[\Pi_-^{(-)c};\ \Sigma_+^{(+)c}]$$

$$L[\Pi_-^{(+)c};\ \Pi_+^{(+)c}] = (a_-^{\pi+}/a_-^{\pi-})L[\Pi_-^{(-)c};\ \Pi_+^{(+)c}]$$

$$L(\tilde{\Pi}_-^{(+)s};\ \tilde{\Pi}_+^{(+)s}] = (a_-^{\tilde{\pi}+}/a_-^{\tilde{\pi}-})L[\tilde{\Pi}_-^{(-)s};\ \tilde{\Pi}_+^{(+)s}]$$

$$L[\Sigma_-^{(+)c};\ \Sigma_+^{(-)c}] = (a_-^{\sigma+}/a_-^{\sigma-})L[\Sigma_-^{(-)c};\ \Sigma_+^{(-)c}]$$

$$L[\Sigma_-^{(+)c};\ \Pi_+^{(-)c}] = -(a_-^{\sigma+}/a_-^{\sigma-})L[\Sigma_-^{(-)c};\ \Pi_+^{(-)c}]$$

$$L[\Pi_-^{(+)c};\ \Sigma_+^{(-)c}] = -(a_-^{\pi+}/a_-^{\pi-})L[\Pi_-^{(-)c};\ \Sigma_+^{(-)c}]$$

$$L[\Pi_-^{(+)c};\ \Pi_+^{(-)c}] = (a_-^{\pi+}/a_-^{\pi-})L[\Pi_-^{(-)c};\ \Pi_+^{(-)c}]$$

$$L[\tilde{\Pi}_-^{(+)s};\ \tilde{\Pi}_+^{(-)s}] = (a_-^{\tilde{\pi}-}/a_+^{\tilde{\pi}-})L[\tilde{\Pi}_-^{(-)s};\ \tilde{\Pi}_+^{(-)s}]$$

$$L[\Sigma_+^{(+)c};\ \tilde{\Pi}_+^{(-)s}] = 4a_+^{\sigma+}a_+^{\tilde{\pi}-}\{\int\sigma_0^c ez\tilde{\pi}_0^s d\tau - 2\int\sigma_0^c ez\tilde{\pi}_1^s d\tau + \int\sigma_0^c ez\tilde{\pi}_3^s d\tau\} = e4a_+^{\sigma+}a_+^{\tilde{\pi}-}k_p \sin\iota \times \{k_s(L_{00}^{sp_\pi} + 2L_{01}^{sp_{\tilde{\pi}}} + L_{03}^{sp_\pi}) - k_p\cos\iota\cos\alpha\,(2L_{01}^{p_\pi p_{\tilde{\pi}}} + L_{03}^{p_\sigma p_\pi})\}$$

$$L[\tilde{\Pi}_+^{(+)s};\ \Sigma_+^{(-)c}] = 4a_+^{\tilde{\pi}+}a_+^{\sigma-}\{\int\sigma_0^c ez\tilde{\pi}_0^s d\tau + 2\int\sigma_0^c ez\tilde{\pi}_1^s d\tau + \int\sigma_0^c ez\tilde{\pi}_3^s d\tau\} = e4a_+^{\tilde{\pi}+}a_+^{\sigma-}k_p \sin\iota \times \{k_s(L_{00}^{sp_\pi} - 2L_{01}^{sp_{\tilde{\pi}}} + L_{03}^{sp_\pi}) + k_p\cos\iota\cos\alpha\,(2L_{01}^{p_\pi p_{\tilde{\pi}}} - L_{03}^{p_\sigma p_\pi})\} \quad \text{(A-17)}$$

In eq. A-14 through 17, the symbols $M[\chi_1;\chi_2]$ and $L[\chi_1;\chi_2]$ are stand-ins for $\int\chi_1{}^*m_w\chi_2 d\tau$ and $\int\chi_1{}^*p_w\chi_2 d\tau$, where w equals x, y, or z as digonal symmetry dictates [*cf.* § 3, eq. 17 and § 5.1, eq. A-1]. The sundry integral interrelationships noted aloft arise from pseudo-quadrate ligand molecular orbital regularity [see Table IV]. The functions $\Lambda_{s_z}{}^{(s_z)}$, $\Sigma_{s_z}{}^{(s_z)c}$, $\Pi_{s_z}{}^{(s_z)}{}_c$, $\tilde{\Pi}_{s_z}{}^{(s_z)}{}_s$, ($s_z$, $s_z = \pm$), are defined in § 1.1, eq. 9 and 10. Integrals not appearing in eq. A-14 through 17 are zero for reasons of digonal or pseudo-quadrate symmetry.

5.7 *Group Overlap Integrals.* The group overlap integrals are readily determined as linear combinations of the localized overlap integrals collected earlier. As priorly, they are of two types, metal–ligand and ligand–ligand.

(*i*) *Group Metal–Ligand Overlap Integrals*

$$S[\Lambda_-^{(-)};\ d_{xz}] = S[\tilde{\Pi}_-^{(-)s};\ d_{xz}]$$

$$S[\Lambda_-^{(+)};\ d_{yz}] = S[\tilde{\Pi}_-^{(+)s};\ d_{yz}] = (a_-^{\tilde{\pi}+}/a_-^{\tilde{\pi}-})S[\Lambda_-^{(-)};\ d_{xz}]$$

$$S[\Lambda_+^{(+)};\ d_{3z^2-r^2}] = S[\Sigma_+^{(+)c};\ d_{3z^2-r^2}]$$

$$S[\Lambda_+^{(+)};\ d_{x^2-y^2}] = S[\Pi_+^{(+)c};\ d_{x^2-y^2}]$$

$$S[\Lambda_+^{(-)};\ d_{xy}] = S[\Sigma_+^{(-)c};\ d_{xy}] = -\sqrt{3}(a_+^{\sigma-}/a_+^{\sigma+})S[\Lambda_+^{(+)};\ d_{3z^2-r^2}] \quad \text{(A-18)}$$

(*ii*) *Group Ligand–Ligand Overlap Integrals*

$$S[\Lambda_+^{(+)};\ \Lambda_+^{(+)}] = S[\Sigma_+^{(+)c};\ \Sigma_+^{(+)c}] + S[\Pi_+^{(+)c};\ \Pi_+^{(+)c}] + S[\tilde{\Pi}_+^{(+)s};\ \tilde{\Pi}_+^{(+)s}]$$

$$S[\Lambda_+^{(-)};\ \Lambda_+^{(-)}] = S[\Sigma_+^{(-)c};\ \Sigma_+^{(-)c}] + S[\Pi_+^{(-)c};\ \Pi_+^{(-)c}] + S[\tilde{\Pi}_+^{(-)s};\ \Pi_+^{(-)s}]$$

$$S[\Lambda_-^{(-)};\ \Lambda_-^{(-)}] = S[\Sigma_-^{(-)c};\ \Sigma_-^{(-)c}] + 2S[\Sigma_-^{(-)c};\ \Pi_-^{(-)c}] + S[\Pi_-^{(-)c};\ \Pi_-^{(-)c}] + S[\tilde{\Pi}_-^{(-)s};\ \tilde{\Pi}_-^{(-)s}]$$

$$S[\Lambda_-^{(+)};\ \Lambda_-^{(+)}] = S[\Sigma_-^{(+)c};\ \Sigma_-^{(+)c}] + 2S[\Sigma_-^{(+)c};\ \Pi_-^{(+)c}] + S[\Pi_-^{(+)c};\ \Pi_-^{(+)c}] + S[\tilde{\Pi}_-^{(+)s};\ \tilde{\Pi}_-^{(+)s}] \quad \text{(A-19)}$$

(*iii*) *Subgroup Metal–Ligand Overlap Integrals*

$$S[\tilde{\Pi}_-^{(-)s};\ d_{xz}] = 4a_-^{\tilde{\pi}-}\int\tilde{\pi}_0^s d_{xz} d\tau = 2\sqrt{6}a_-^{\tilde{\pi}-}k_p \sin\iota\, K_{26A_4}$$

$$S[\tilde{\Pi}_-^{(+)s};\ d_{yz}] = (a_-^{\tilde{\pi}+}/a_-^{\tilde{\pi}-})S[\tilde{\Pi}_-^{(-)s};\ d_{xz}] = (a_-^{\tilde{\pi}+}/a_-^{\tilde{\pi}-})S[\Lambda_-^{(-)};\ d_{xz}]$$

$$S[\Sigma_+^{(+)c};\ d_{3z^2-r^2}] = 4a_+^{\sigma+}\int\sigma_0^c d_{3z^2-r^2} d\tau = -\sqrt{6}a_+^{\sigma+}\{k_s K_{24A_4} - 2k_p\cos\iota\cos\alpha\, K_{32A_5}\}$$

$$S[\Pi_+^{(+)c};\ d_{x^2-y^2}] = 4a_+^{\pi+}\int\pi_0^c d_{x^2-y^2} d\tau = 4\sqrt{3}a_+^{\pi+}k_p\cos\iota\sin\alpha\, K_{26A_4}$$

$$S[\Sigma_+^{(-)c};\ d_{xy}] = 4a_+^{\sigma-}\int\sigma_0^c d_{xy} d\tau = -\sqrt{3}(a_+^{\sigma-}/a_+^{\sigma+})S[\Sigma_+^{(+)c};\ d_{3z^2-r^2}] \quad \text{(A-20)}$$

(*iv*) *Subgroup Ligand–Ligand Overlap Integrals*

$$S[\Sigma_+^{(+)c};\ \Sigma_+^{(+)c}] = 4a_+^{\sigma+}a_+^{\sigma+}\{\int\sigma_0^c\sigma_0^c d\tau + 2\int\sigma_0^c\sigma_1^c d\tau + \int\sigma_0^c\sigma_3 d\tau\} = 4a_+^{\sigma+}a_+^{\sigma+} \times \{k_s^2(1 + 2s_{01}^d + s_{03}^d) + 2k_sk_p\cos\iota\cos\alpha\,(2\bar{s}_{01}^d + \bar{s}_{03}^d) + k_p^2\cos^2\iota\cos^2\alpha\,(1 - 2\bar{f}_{01}^d - \bar{f}_{03}^d)\}$$

$$S[\Pi_+^{(+)c};\ \Pi_+^{(+)c}] = 4a_+^{\pi+}a_+^{\pi+}\{\int\pi_0^c\pi_0^c d\tau + 2\int\pi_0^c\pi_1^c d\tau + \int\pi_0^c\pi_3^c d\tau\} = 4a_+^{\pi+}a_+^{\pi+}k_p^2\cos^2\iota\sin^2\alpha\,\{1 - 2\bar{f}_{01}^d - \bar{f}_{03}\}$$

$$S[\tilde{\Pi}_+^{(+)s};\ \tilde{\Pi}_+^{(+)s}] = 4a_+^{\tilde{\pi}+}a_+^{\tilde{\pi}+}\{\int\tilde{\pi}_0^s\tilde{\pi}_0^s d\tau + 2\int\tilde{\pi}_0^s\tilde{\pi}_1^s d\tau + \int\tilde{\pi}_0^s\tilde{\pi}_3^s d\tau\} = 4c_+^{\tilde{\pi}+}a_+^{\tilde{\pi}+}k_p^2\sin^2\iota\,\{1 - 2\bar{f}_{01}^d + \bar{f}_{03}^d\}$$

$$S[\Sigma_+^{(-)c};\ \Sigma_+^{(-)c}] = 4a_+^{\sigma-}a_+^{\sigma-}\{\int\sigma_0^c\sigma_0^c d\tau - 2\int\sigma_0^c\sigma_1^c d\tau + \int\sigma_0^c\sigma_3^c d\tau\} = 4a_+^{\sigma-}a_+^{\sigma-} \times \{k_s^2(1 - 2s_{01}^d + s_{03}^d) - 2k_sk_p\cos\iota\cos\alpha\,(2\bar{s}_{01}^d - \bar{s}_{03}^d) + k_p^2\cos^2\iota\cos^2\alpha\,(1 + 2\bar{f}_{01}^d - \bar{f}_{03}^d)\}$$

$$S[\Pi_+^{(-)c};\ \Pi_+^{(-)c}] = 4a_+^{\pi-}a_+^{\pi-}\{\int\pi_0^c\pi_0^c d\tau - 2\int\pi_0^c\pi_1^c d\tau + \int\pi_0^c\pi_3^c d\tau\} = 4a_+^{\pi-}a_+^{\pi-}k_p^2\cos^2\iota\sin^2\alpha\,\{1 + 2\bar{f}_{01}^d - \bar{f}_{03}^d\}$$

$$S[\tilde{\Pi}_+^{(-)s};\ \tilde{\Pi}_+^{(-)s}] = 4a_+^{\tilde{\pi}-}a_+^{\tilde{\pi}-}\{\int\tilde{\pi}_0^s\tilde{\pi}_0^s d\tau - 2\int\tilde{\pi}_0^s\tilde{\pi}_1^s d\tau + \int\tilde{\pi}_0^s\tilde{\pi}_3^s d\tau\} = 4a_+^{\tilde{\pi}-}a_+^{\tilde{\pi}-}k_p^2\sin^2\iota\,\{1 + 2\bar{f}_{01}^d + \bar{f}_{03}^d\}$$

$$S[\Sigma_-^{(-)c};\ \Sigma_-^{(-)c}] = 4a_-^{\sigma-}a_-^{\sigma-}\{\int\sigma_0^c\sigma_0^c d\tau - \int\sigma_0^c\sigma_3^c d\tau\} = 4a_-^{\sigma-}a_-^{\sigma-}\{k_s^2(1 - s_{03}^d) - 2k_sk_p\cos\iota\cos\alpha\,\bar{s}_{03}^d + k_p^2\cos^2\iota\cos^2\alpha\,(1 + \bar{f}_{03}^d)\}$$

$$S[\Sigma_-^{(-)c};\ \Pi_-^{(-)c}] = -8a_-^{\sigma-}a_-^{\pi-}\int\sigma_0^c\pi_1^c d\tau = 8a_-^{\sigma-}a_-^{\pi-}k_p\cos\iota\cos\alpha\,\{k_s s_{01}^d - k_p\cos\iota\cos\alpha\,s_{01}^d\}$$

$$S[\Pi_-^{(-)c};\ \Pi_-^{(-)c}] = 4a_-^{\pi-}a_-^{\pi-}\{\int \pi_0^c\pi_0^c d\tau - \int \pi_0^c\pi_3^c d\tau\} = 4a_-^{\pi-}a_-^{\pi-}k_p^2\cos^2\iota\sin^2\alpha\{1 + [_{03}^{d}]\}$$

$$S[\tilde{\Pi}_-^{(-)s};\ \tilde{\Pi}_-^{(-)s}] = 4a_-^{\tilde{\pi}-}a_-^{\tilde{\pi}-}\{\int \tilde{\pi}_0^s\tilde{\pi}_0^s d\tau - \int \tilde{\pi}_0^s\tilde{\pi}_3^s d\tau\} = 4a_-^{\tilde{\pi}-}a_-^{\tilde{\pi}-}k_p^2\sin^2\iota\{1 - [_{03}^{d}]\}$$

$$S[\Sigma_-^{(+)c};\ \Sigma_-^{(+)c}] = (a_-^{\sigma+}a_-^{\sigma+}/a_-^{\sigma-}a_-^{\sigma-})S[\Sigma_-^{(-)c};\ \Sigma_-^{(-)c}]$$

$$S[\Sigma_-^{(+)c};\ \Pi_-^{(+)c}] = -(a_-^{\sigma+}a_-^{\pi+}/a_-^{\sigma-}a_-^{\pi-})S[\Sigma_-^{(-)c};\ \Pi_-^{(-)c}]$$

$$S[\Pi_-^{(+)c};\ \Pi_-^{(+)c}] = (a_-^{\pi+}a_-^{\pi+}/a_-^{\pi-}a_-^{\pi-})S[\Pi_-^{(-)c};\ \Pi_-^{(-)c}]$$

$$S[\tilde{\Pi}_-^{(+)s};\ \tilde{\Pi}_-^{(+)s}] = (a_-^{\tilde{\pi}+}a_-^{\tilde{\pi}+}/a_-^{\tilde{\pi}-}a_-^{\tilde{\pi}-})S[\tilde{\Pi}_-^{(-)s};\ \tilde{\Pi}_-^{(-)s}] \quad \text{(A-21)}$$

As in ref. 6, the symbol $S[\chi_1;\chi_2]$ substitutes for $\int\chi_1^*\chi_2 d\tau$.

5.8 *Auxiliary Integrals.* A few auxiliary integrals occurrent in the theory are of wide interest. We slate these beneath.

$$\int(2s)_{A_0}\frac{1}{r_1}(2p_y)_{A_1}d\tau = \frac{(\bar{bc})^5}{12\sqrt{3b}}\{A_2(\bar{bc}) + A_0(\bar{bc})\}$$

$$\int(2p_x)_{A_0}\frac{y_1}{r_1}(2p_x)_{A_1}d\tau = \frac{(\bar{bc})^5}{30}\{A_3(\bar{bc}) - A_1(\bar{bc})\} = \int(2p_x)_{A_0}\frac{x_1}{r_1}(2p_y)_{A_1}d\tau$$

$$\int(2p_y)_{A_0}\frac{x_1}{r_1}(2p_x)_{A_1}d\tau = -\frac{(\bar{bc})^5}{20}\{A_3(\bar{bc}) - A_1(\bar{bc})\}$$

$$\int(2p_y)_{A_0}\frac{y_1}{r_1}(2p_y)_{A_1}d\tau = \frac{(\bar{bc})^5}{60}\{A_3(\bar{bc}) - 5A_1(\bar{bc})\}$$

$$\int(2s)_{A_0}\frac{x_1}{r_1}(2p_x)_{A_1}d\tau = \frac{(\bar{bc})^5}{120\sqrt{3}}\{5A_4(\bar{bc}) - 4A_2(\bar{bc}) - A_0(\bar{bc})\}$$

$$\int(2s)_{A_0}\frac{y_1}{r_1}(2p_y)_{A_1}d\tau = \frac{(\bar{bc})^5}{120\sqrt{3}}\{5A_4(\bar{bc}) - 2A_2(\bar{bc}) + 5A_0(\bar{bc})\}$$

$$\int(2p_x)_{A_0}\frac{1}{r_1}(2p_x)_{A_1}d\tau = \frac{(\bar{bc})^5}{12b}\{A_3(\bar{bc}) - A_1(\bar{bc})\}$$

$$\int(2p_y)_{A_0}\frac{1}{r_1}(2p_y)_{A_1}d\tau = \frac{(\bar{bc})^5}{12b}\{A_3(\bar{bc}) - 3A_1(\bar{bc})\}$$

$$\int(2s)_{A_0}\frac{1}{r_1}(2s)_{A_1}d\tau = \frac{(\bar{bc})^5}{36b}\{3A_3(\bar{bc}) - A_1(\bar{bc})\}$$

$$\int(2s)_{A_0}\frac{1}{r_0}(2s)_{A_0}d\tau = \frac{c}{2}$$

$$\int(2s)_{A_0}\frac{y_0}{r_0}(2p_y)_{A_0}d\tau = \sqrt{1/3}$$

$$\int(2p_{x'})_{A_0}\frac{1}{r_3}(2s)_{A_3}d\tau = -\frac{(\bar{dc})^5}{12\sqrt{3d}}\{3A_2(\bar{dc}) - A_0(\bar{dc})\}$$

$$\int(2p_{x'})_{A_0}\frac{y_3'}{r_3}(2p_{y'})_{A_3}d\tau = -\frac{(\bar{dc})^5}{20}\{A_3(\bar{dc}) - A_1(\bar{dc})\}$$

$$\int(2p_y)_{A_0}\frac{1}{r_1}(2s)_{A_1}d\tau = -\frac{(\bar{bc})^5}{12\sqrt{3b}}\{3A_2(\bar{bc}) - A_0(\bar{bc})\}$$

$$\int(2s)_{A_0}x_1(2p_x)_{A_1}d\tau = \frac{b(\bar{bc})^5}{240\sqrt{3}}\{5A_5(\bar{bc}) - 6A_3(\bar{bc}) + A_1(\bar{bc})\}$$

$$\int(2s)_{A_0}y_1(2p_y)_{A_1}d\tau = \frac{b(\bar{bc})^5}{240\sqrt{3}}\{5A_5(\bar{bc}) + 2A_3(\bar{bc}) + A_1(\bar{bc})\}$$

$$\int(2p_x)_{A_0}x_1(2p_y)_{A_1}d\tau = \frac{(b\bar{bc})^5}{240}\{5A_4(\bar{bc}) - 6A_2(\bar{bc}) + A_0(\bar{bc})\} = -\int(2p_y)_{A_0}x_1(2p_x)_{A_1}d\tau$$

$$\int(2p_y)_{A_0}y_1(2p_y)_{A_1}d\tau = \frac{b(\bar{bc})^5}{240}\{5A_4(\bar{bc}) - 18A_2(\bar{bc}) + 5A_0(\bar{bc})\} \quad \text{(A-22)}$$

Mark the error in Kotani, Amemiya, Ishiguro, and Kimura[59] with regard to the first integral printed in eq. A-22.

§6. Trigonal Dihedral Spin-Orbital Generalized Matrix Elements and Rotational and Spectral Strengths

6.1 *Matrix Elements.* As an aid in the practical employment of the results of eq. 49, 54, and 55 of ref. 6, we here transcribe them to the simpler and more ecumenical notation of ref. 6, footnote 49.

$$\left\langle \gamma_{6a}^{(8)}(t_{2g}) \left| \begin{matrix}\vec{p}\\ \vec{m}\end{matrix} \right| \gamma_{6a}^{(7)}(t_{2g}) \right\rangle = \begin{bmatrix} 0 \text{ or } \frac{\sqrt{2}}{3}p_0^{\mp} \\ \frac{\sqrt{2}}{3}(2\mu_B + \bar{m}_0^{\mp}) \end{bmatrix} \hat{k}_0'$$

$$\left\langle \gamma_{6a}^{(8)}(t_{2g}) \left| \begin{matrix}\vec{p}\\ \vec{m}\end{matrix} \right| \gamma_{5b}^{(7)}(t_{2g}) \right\rangle = \begin{bmatrix} -i\bar{r}_0 \\ 1/3(2\mu_B + \bar{m}_0) \end{bmatrix} \hat{k}_+'$$

(59) M. Kotani, A. Amemiya, E. Ishiguro, and T. Kimura, "Tables of Molecular Integrals," Maruzen Co., Ltd., Tokyo, 1955, p. 82. Page 87 of this book contains another misprint as $(X \pm iY)_{2\sigma\mp}$ should equal $-(X \pm iY)_{\pm 2\sigma}$ by Fig. 9, p. 30 of the book.

$$\left\langle \gamma_{6a}^{(8)}(t_{2g}) \left| \begin{matrix}\vec{p}\\ \vec{m}\end{matrix} \right| \gamma_4(t_{2g}) \right\rangle = \frac{e^{i\beta/4}}{\sqrt{2}} \begin{bmatrix} -\sqrt{1/3}(\sqrt{2}\bar{r}_0 + i\bar{r}_0^{+}) \\ i\sqrt{2/3}(\mu_B - \bar{m}_0) \end{bmatrix} \hat{k}_-'$$

$$\left\langle \gamma_{6a}^{(8)}(t_{2g}) \left| \begin{matrix}\vec{p}\\ \vec{m}\end{matrix} \right| \gamma_5(t_{2g}) \right\rangle = \frac{e^{-i\beta/4}}{\sqrt{2}} \begin{bmatrix} \sqrt{1/3}(\sqrt{2}\bar{r}_0 - i\bar{r}_0^{+}) \\ -i\sqrt{2/3}(\mu_B - \bar{m}_0) \end{bmatrix} \hat{k}_-'$$

$$\left\langle \gamma_{6a}^{(7)}(t_{2g}) \left| \begin{matrix}\vec{p}\\ \vec{m}\end{matrix} \right| \gamma_4(t_{2g}) \right\rangle = \frac{e^{i\beta/4}}{\sqrt{2}} \begin{bmatrix} \sqrt{1/3}(\bar{r}_0 - i\sqrt{2}\bar{r}_0^{+}) \\ i\sqrt{1/3}(2\mu_B + \bar{m}_0) \end{bmatrix} \hat{k}_-'$$

$$\left\langle \gamma_{6a}^{(7)}(t_{2g}) \left| \begin{matrix}\vec{p}\\ \vec{m}\end{matrix} \right| \gamma_5(t_{2g}) \right\rangle = \frac{e^{-i\beta/4}}{\sqrt{2}} \begin{bmatrix} -\sqrt{1/3}(\bar{r}_0 + i\sqrt{2}\bar{r}_0^{+}) \\ -i\sqrt{1/3}(2\mu_B + \bar{m}_0) \end{bmatrix} \hat{k}_-'$$

$$\left\langle \gamma_4(t_{2g}) \left| \begin{matrix}\vec{p}\\ \vec{m}\end{matrix} \right| \gamma_4(e_g) \right\rangle \equiv 0$$

$$\left\langle \gamma_5(t_{2g}) \left| \begin{matrix}\vec{p}\\ \vec{m}\end{matrix} \right| \gamma_4(e_g) \right\rangle = \begin{bmatrix} ir_1 \\ m_1 \end{bmatrix} \hat{k}_0'$$

$$\left\langle \gamma_{6a}^{(7)}(t_{2g}) \left| \begin{matrix}\vec{p}\\ \vec{m}\end{matrix} \right| \gamma_4(e_g) \right\rangle = \frac{e^{-i\beta/4}}{\sqrt{2}} \begin{bmatrix} -\sqrt{1/3}(r_0 + i\sqrt{2}r_2) \\ i\sqrt{1/3}(m_0 + i\sqrt{2}m_2) \end{bmatrix} \hat{k}_-'$$

$$\left\langle \gamma_{6b}^{(7)}(t_{2g}) \left| \begin{matrix}\vec{p}\\ \vec{m}\end{matrix} \right| \gamma_4(e_g) \right\rangle = \frac{e^{-i\beta/4}}{\sqrt{2}} \begin{bmatrix} -i\sqrt{1/3}(r_0 + i\sqrt{2}r_2) \\ -\sqrt{1/3}(m_0 + i\sqrt{2}m_2) \end{bmatrix} \hat{k}_+'$$

$$\left\langle \gamma_{6a}^{(8)}(t_{2g}) \left| \begin{matrix}\vec{p}\\ \vec{m}\end{matrix} \right| \gamma_4(e_g) \right\rangle = \frac{e^{-i\beta/4}}{\sqrt{2}} \begin{bmatrix} \sqrt{1/3}(\sqrt{2}r_0 - ir_2) \\ -i\sqrt{1/3}(\sqrt{2}m_0 - im_2) \end{bmatrix} \hat{k}_-'$$

$$\left\langle \gamma_{6b}^{(8)}(t_{2g}) \left| \begin{matrix}\vec{p}\\ \vec{m}\end{matrix} \right| \gamma_4(e_g) \right\rangle = \frac{e^{-i\beta/4}}{\sqrt{2}} \begin{bmatrix} i\sqrt{1/3}(\sqrt{2}r_0 - ir_2) \\ \sqrt{1/3}(\sqrt{2}m_0 - im_2) \end{bmatrix} \hat{k}_+'$$

$$\left\langle \gamma_4(t_{2g}) \left| \begin{matrix}\vec{p}\\ \vec{m}\end{matrix} \right| \gamma_{6b}(e_g) \right\rangle = \frac{e^{-i\beta/4}}{\sqrt{2}} \begin{bmatrix} -r_2 \\ im_2 \end{bmatrix} \hat{k}_-'$$

$$\left\langle \gamma_5(t_{2g}) \left| \begin{matrix}\vec{p}\\ \vec{m}\end{matrix} \right| \gamma_{6b}(e_g) \right\rangle = \frac{e^{i\beta/4}}{\sqrt{2}} \begin{bmatrix} r_2 \\ -im_2 \end{bmatrix} \hat{k}_-'$$

$$\left\langle \gamma_{6a}^{(7)}(t_{2g}) \left| \begin{matrix}\vec{p}\\ \vec{m}\end{matrix} \right| \gamma_{6b}(e_g) \right\rangle = \sqrt{1/3} \begin{bmatrix} ir_0 \\ m_0 \end{bmatrix} \hat{k}_+'$$

$$\left\langle \gamma_{6b}^{(7)}(t_{2g}) \left| \begin{matrix}\vec{p}\\ \vec{m}\end{matrix} \right| \gamma_{6t}(e_g) \right\rangle = \sqrt{2/3} \begin{bmatrix} -ir_1 \\ -m_1 \end{bmatrix} \hat{k}_0'$$

$$\left\langle \gamma_{6a}^{(8)}(t_{2g}) \left| \begin{matrix}\vec{p}\\ \vec{m}\end{matrix} \right| \gamma_{6b}(e_g) \right\rangle = \sqrt{2/3} \begin{bmatrix} -ir_0 \\ -m_0 \end{bmatrix} \hat{k}_+'$$

$$\left\langle \gamma_{6b}^{(8)}(t_{2g}) \left| \begin{matrix}\vec{p}\\ \vec{m}\end{matrix} \right| \gamma_{6t}(e_g) \right\rangle = \sqrt{1/3} \begin{bmatrix} -ir_1 \\ -m_1 \end{bmatrix} \hat{k}_0'$$

$$\left\langle \gamma_4(e_g) \left| \begin{matrix}\vec{p}\\ \vec{m}\end{matrix} \right| \gamma_4(e_g) \right\rangle \equiv 0$$

$$\left\langle \gamma_5(e_g) \left| \begin{matrix}\vec{p}\\ \vec{m}\end{matrix} \right| \gamma_4(e_g) \right\rangle = e^{-i\beta/2} \begin{bmatrix} 0 \text{ or } \bar{\bar{p}}_0^{\ddagger} \\ (\mu_B + \bar{\bar{m}}_0^{+}) \end{bmatrix} \hat{k}_0'$$

$$\left\langle \gamma_{6a}(e_g) \left| \begin{matrix}\vec{p}\\ \vec{m}\end{matrix} \right| \gamma_4(e_g) \right\rangle = \frac{e^{-i\beta/4}}{\sqrt{2}} \begin{bmatrix} i\bar{\bar{r}}_0 \text{ or } 0 \\ -i\sqrt{2}\mu_B \end{bmatrix} \hat{k}_-'$$

$$\left\langle \gamma_{6b}(e_g) \left| \begin{matrix}\vec{p}\\ \vec{m}\end{matrix} \right| \gamma_4(e_g) \right\rangle = \frac{e^{-i\beta/4}}{\sqrt{2}} \begin{bmatrix} -\bar{\bar{r}}_0 \text{ or } 0 \\ \sqrt{2}\mu_B \end{bmatrix} \hat{k}_+'$$

$$\left\langle \gamma_{6a}(e_g) \left| \begin{matrix}\vec{p}\\ \vec{m}\end{matrix} \right| \gamma_{6a}(e_g) \right\rangle = \begin{bmatrix} 0 \text{ or } -\bar{\bar{p}}_0^{\ddagger} \\ (\mu_B - \bar{\bar{m}}_0^{+}) \end{bmatrix} \hat{k}_0'$$

$$\left\langle \gamma_{6a}(e_g) \left| \begin{matrix}\vec{p}\\ \vec{m}\end{matrix} \right| \gamma_{6b}(e_g) \right\rangle = 0$$

$$\left\langle \gamma_{6a}^{(7)}(t_{2g}) \left| \begin{matrix}\vec{p}\\ \vec{m}\end{matrix} \right| \gamma_{6a}^{(7)}(t_{2g}) \right\rangle = 1/3 \begin{bmatrix} 0 \text{ or } 2\bar{p}_0^{\mp} \\ (\mu_B + 2\bar{m}_0^{\mp}) \end{bmatrix} \hat{k}_0'$$

$$\left\langle \gamma_{6a}^{(7)}(t_{2g}) \left| \begin{matrix}\vec{p}\\ \vec{m}\end{matrix} \right| \gamma_{6b}^{(7)}(t_{2g}) \right\rangle = \frac{\sqrt{2}}{3} \begin{bmatrix} 0 \text{ or } 2\bar{p}_0 \\ -(\mu_B + 2\bar{m}_0) \end{bmatrix} \hat{k}_+'$$

$$\left\langle \gamma_{6a}^{(8)}(t_{2g}) \left| \begin{matrix}\vec{p}\\ \vec{m}\end{matrix} \right| \gamma_{6a}^{(8)}(t_{2g}) \right\rangle = 1/3 \begin{bmatrix} 0 \text{ or } \bar{p}_0^{\mp} \\ -(\mu_B - \bar{m}_0^{\mp}) \end{bmatrix} \hat{k}_0'$$

$$\left\langle \gamma_{6a}^{(8)}(t_{2g}) \left| \begin{matrix}\vec{p}\\ \vec{m}\end{matrix} \right| \gamma_{6b}^{(8)}(t_{2g}) \right\rangle = \frac{2\sqrt{2}}{3} \begin{bmatrix} 0 \text{ or } -\bar{p}_0 \\ -(\mu_B - \bar{m}_0) \end{bmatrix} \hat{k}_+'$$

$$\left\langle \gamma_4(t_{2g}) \left| \begin{matrix}\vec{p}\\ \vec{m}\end{matrix} \right| \gamma_4(t_{2g}) \right\rangle \equiv 0$$

$$\left\langle \gamma_5(t_{2g}) \left| \begin{matrix}\vec{p}\\ \vec{m}\end{matrix} \right| \gamma_4(t_{2g}) \right\rangle = e^{i\beta/2} \begin{bmatrix} 0 \text{ or } -\bar{p}_0^{\mp} \\ (\mu_B - \bar{m}_0^{\mp}) \end{bmatrix} \hat{k}_0' \quad \text{(A-23)}$$

The new emblems $\bar{g}_0^{\ddagger}$, $\bar{m}_0^{\ddagger}$, $\bar{g}_0^{\mp}$, $\bar{m}_0^{\mp}$, $\bar{\bar{g}}_0$, $\bar{\bar{m}}_0$, $\bar{\bar{g}}_0^{\ddagger}$, and $\bar{\bar{m}}_0^{\ddagger}$ ($g = r, p$) of eq. A-23 are labels for

$$\left\langle e_{\mp}(t_{2g}) \left| \begin{matrix}\vec{p}\\ \vec{m}\end{matrix} \right| e_{\mp}(t_{2g}) \right\rangle = \mp \begin{bmatrix} i\bar{g}_0^{\ddagger} \\ \bar{m}_0^{\ddagger} \end{bmatrix} \hat{k}_{\pm}'$$

$$\left\langle e_{\pm}(t_{2g}) \left| \begin{matrix}\vec{p}\\ \vec{m}\end{matrix} \right| e_{\pm}(t_{2g}) \right\rangle = \mp \begin{bmatrix} \bar{g}_0^{\mp} \\ \bar{m}_0^{\mp} \end{bmatrix} \hat{k}_0'$$

$$\left\langle e_{\pm}(e_g) \left| \begin{matrix}\vec{p}\\ \vec{m}\end{matrix} \right| e_{\mp}(e_g) \right\rangle = \mp \begin{bmatrix} i\bar{\bar{g}}_0 \\ \bar{\bar{m}}_0 \end{bmatrix} \hat{k}_{\pm}'$$

and

$$\left\langle e_\pm(e_g)\left|\begin{matrix}\vec{p}\\ \vec{m}\end{matrix}\right|e_\pm(e_g)\right\rangle = \pm\begin{bmatrix}\bar{\bar{g}}_0^{\ddagger}\\ \bar{\bar{m}}_0^{\ddagger}\end{bmatrix}\hat{k}_0'$$

When $\vec{p}$ equals $\vec{er}$, and hence g equals r, the quantities $\bar{r}_0^{\ddagger}$ and $\bar{\bar{r}}_0^{\ddagger}$ vanish identically; when $\vec{p}$ equals $(\hbar/i)\vec{\nabla}$, and hence g equals p, the quantities $\bar{p}_0^{\ddagger}$ and $\bar{\bar{p}}_0$ vanish identically; and when $\vec{m}$ equals $\mu_B(\vec{\ell} + 2\vec{s})$, the quantities $\bar{m}_0^{\ddagger}$ and $\bar{\bar{m}}_0$ vanish identically.[60] The zero in the third and fifth entries from the bottom of eq. A-23 arise from additive cancellation and not because $\bar{r}_0$ is zero. The cancellation is a consequence of the nonexactness of our wave functions (see section IV). To transfer the coordinate electric dipole representatives, $\bar{r}_0$, r_0, r_1, and r_2 to the gradient electric dipole representative, $\bar{p}_0$, p_0, p_1, and p_2 in eq. A-23 just replace $i\bar{r}_0$, ir_0, ir_1, and ir_2 everywhere by $\bar{p}_0$, p_0, p_1, and p_2, individually.[61]

6.2 *Rotational and Spectral Strengths.* The rotational and spectral strengths dictated by the electric and magnetic dipole matrix contents of eq. A-23 are blocked [$\mathfrak{W}$ equals $\mathfrak{R}$ or $\mathfrak{P}$, $\mathfrak{X}$ equals $\mathfrak{S}$ or $\mathfrak{O}$, and g equals r or p, severally].

$$\mathfrak{W}[\gamma_{6(\substack{a\\b})}^{(8)}(t_{2g}) \longrightarrow \gamma_{6(\substack{b\\a})}^{(7)}(t_{2g})] = 0 \text{ or } {}^2/_9\bar{p}_0^{\mp}(2\mu_B + \bar{m}_0^{\mp})$$

$$\mathfrak{X}[\gamma_{6(\substack{a\\b})}^{(8)}(t_{2g}) \longrightarrow \gamma_{6(\substack{b\\a})}^{(7)}(t_{2g})] = 0 \text{ or } {}^2/_9\bar{p}_0^{\mp 2}$$

$$\mathfrak{M}[\gamma_{6(\substack{a\\b})}^{(8)}(t_{2g}) \longrightarrow \gamma_{6(\substack{a\\b})}^{(7)}(t_{2g})] = {}^2/_9(2\mu_B + \bar{m}_0^{\mp})^2$$

$$\mathfrak{W}[\gamma_{6(\substack{a\\b})}^{(8)}(t_{2g}) \longrightarrow \gamma_{6(\substack{b\\a})}^{(7)}(t_{2g})] = -{}^1/_3\bar{g}_0(2\mu_B + \bar{m}_0)$$

$$\mathfrak{X}[\gamma_{6(\substack{a\\b})}^{(8)}(t_{2g}) \longrightarrow \gamma_{6(\substack{b\\a})}^{(7)}(t_{2g})] = \bar{g}_0^2$$

$$\mathfrak{M}[\gamma_{6(\substack{a\\b})}^{(8)}(t_{2g}) \longrightarrow \gamma_{6(\substack{b\\a})}^{(7)}(t_{2g})] = {}^1/_9(2\mu_B + \bar{m}_0)^2$$

$$\mathfrak{W}[\gamma_{6(\substack{a\\b})}^{(8)}(t_{2g}) \longrightarrow \gamma_{4 \text{ or } 5}(t_{2g})] = {}^1/_3\bar{g}_0(\mu_B - \bar{m}_0)$$

$$\mathfrak{X}[\gamma_{6(\substack{a\\b})}^{(8)}(t_{2g}) \longrightarrow \gamma_{4 \text{ or } 5}(t_{2g})] = {}^1/_6\{2\bar{g}_0^2 + \bar{g}_0^{\ddagger 2}\}$$

$$\mathfrak{M}[\gamma_{6(\substack{a\\b})}^{(8)}(t_{2g}) \longrightarrow \gamma_{4 \text{ or } 5}(t_{2g})] = {}^1/_3(\mu_B - \bar{m}_0)^2$$

$$\mathfrak{W}[\gamma_{6(\substack{a\\b})}^{(7)}(t_{2g}) \longrightarrow \gamma_{4 \text{ or } 5}(t_{2g})] = -{}^1/_6\bar{g}_0(2\mu_B + \bar{m}_0)$$

$$\mathfrak{X}[\gamma_{6(\substack{a\\b})}^{(7)}(t_{2g}) \longrightarrow \gamma_{4 \text{ or } 5}(t_{2g})] = {}^1/_6\{\bar{g}_0^2 + 2\bar{g}_0^{\ddagger 2}\}$$

$$\mathfrak{M}[\gamma_{6(\substack{a\\b})}^{(7)}(t_{2g}) \longrightarrow \gamma_{4 \text{ or } 5}(t_{2g})] = {}^1/_6(2\mu_B + \bar{m}_0)^2$$

$$\mathfrak{W}[\gamma_{(\substack{4\\5})}(t_{2g}) \longrightarrow \gamma_{(\substack{4\\5})}(t_{2g})] \equiv \mathfrak{X}[\gamma_{(\substack{4\\5})}(t_{2g}) \longrightarrow \gamma_{(\substack{4\\5})}(t_{2g})] \equiv \mathfrak{M}[\gamma_{(\substack{4\\5})}(t_{2g}) \longrightarrow \gamma_{(\substack{4\\5})}(t_{2g})] \equiv 0$$

$$\mathfrak{W}[\gamma_{(\substack{5\\4})}(t_{2g}) \longrightarrow \gamma_{(\substack{4\\5})}(e_g)] = g_1m_1$$

$$\mathfrak{X}[\gamma_{(\substack{5\\4})}(t_{2g}) \longrightarrow \gamma_{(\substack{4\\5})}(e_g)] = g_1^2$$

$$\mathfrak{M}[\gamma_{(\substack{5\\4})}(t_{2g}) \longrightarrow \gamma_{(\substack{4\\5})}(e_g)] = m_1^2$$

$$\mathfrak{W}[\gamma_{6(\substack{a\\b})}^{(7)}(t_{2g}) \longrightarrow \gamma_{4 \text{ or } 5}(e_g)] = {}^1/_6\{g_0m_0 + 2g_2m_2\}$$

$$\mathfrak{X}[\gamma_{6(\substack{a\\b})}^{(7)}(t_{2g}) \longrightarrow \gamma_{4 \text{ or } 5}(e_g)] = {}^1/_6\{g_0^2 + 2g_2^2\}$$

$$\mathfrak{M}[\gamma_{6(\substack{a\\b})}^{(7)}(t_{2g}) \longrightarrow \gamma_{4 \text{ or } 5}(e_g)] = {}^1/_6\{m_0^2 + 2m_2^2\}$$

$$\mathfrak{W}[\gamma_{6(\substack{a\\b})}^{(8)}(t_{2g}) \longrightarrow \gamma_{4 \text{ or } 5}(e_g)] = {}^1/_6\{2g_0m_0 + g_2m_2\}$$

$$\mathfrak{X}[\gamma_{6(\substack{a\\b})}^{(8)}(t_{2g}) \longrightarrow \gamma_{4 \text{ or } 5}(e_g)] = {}^1/_6\{2g_0^2 + g_2^2\}$$

(60) These statements are swiftly proved by use of integral Hermiticity and rotational symmetry. For trigonal dihedral complex conjugate wave functions $e_\pm(t_{2g})$ or $e_\pm(e_g)$, separately, we have, ($\vec{v} = \vec{p}, \vec{m}$)

$$\langle e_\pm|\vec{v}|e_\pm\rangle = \langle e_\pm|\vec{v}|e_\pm\rangle^* = \langle e_\mp|\vec{v}^*|e_\mp\rangle \text{ and}$$

$$\langle e_\pm|\vec{v}|e_\pm\rangle = \mathcal{C}_2(y')\langle e_\pm|\vec{v}|e_\pm\rangle = \langle e_\mp| - v_x'\hat{i}' + v_y'\hat{j}' - v_z'\hat{k}'|e_\mp\rangle$$

so that if $\vec{v}$ equals $\vec{er}$, $\langle v_x'\rangle$ and $\langle v_z'\rangle$ must be naught and if $\vec{v}$ equals $(\hbar/i)\vec{\nabla}$ or $\vec{m}$, $\langle v_y'\rangle$ must be naught. But as $\langle e_\pm|v_x'|e_\pm\rangle = \mathcal{C}_3(z')\langle e_\pm|v_x'|e_\pm\rangle = \cos 2\pi/3\langle e_\pm|v_x'|e_\pm\rangle - \sin 2\pi/3\langle e_\pm|v_y'|e_\pm\rangle$, we must also have $\langle v_y'\rangle$ be naught if $\vec{v}$ equals $\vec{er}$ and $\langle v_x'\rangle$ be naught if $\vec{v}$ equals $\vec{m}$. Hence, $\langle e_\pm|\vec{er}|e_\pm\rangle$ is null and $\langle e_\pm|(\hbar/i)\vec{\nabla}$ or $\vec{m}|e_\pm\rangle$ is coincident with $\hat{k}'$ equals $\hat{k}_0'$ and real [The diagonal matrix elements of a Hermitian operator are always real. The proof follows upon division of $e_\pm$ into its real and imaginary parts]. Similarly, because $\langle e_\pm|\vec{v}|e_\mp\rangle = \langle e_\mp|\vec{v}|e_\pm\rangle^* = \langle e_\pm|\vec{v}^*|e_\mp\rangle$, we have that $\langle\vec{v}\rangle$ is null if $\vec{v}$ equals $(\hbar/i)\vec{\nabla}$ or $\vec{m}$; and because [recall ref. 6, footnote 25] $\langle e_\pm|\vec{v}|e_\mp\rangle = \mathcal{C}_3(z')\langle e_\pm|\vec{v}_+'\hat{k}'_- + v_-'\hat{k}_+' + v_0'\hat{k}_0'|e_\mp\rangle = \omega^{\mp 2}\langle e_\pm|\omega v_+'\hat{k}_-' + \omega^{-1}v_-'\hat{k}_+' + v_0'\hat{k}_0'|e_\mp\rangle$, we have that $\langle e_\pm|\vec{er}|e_\mp\rangle$ is coincident with $\hat{k}_\pm'$. The factors $\mp i$ and $\mp$ or $\pm$ in the definitions of the matrix substitutes of the text occur since by this footnote s development $\langle e_+|v_z'|e_+\rangle = \langle e_+|v_z'|e_+\rangle^* = \langle e_-|v_z'^*|e_-\rangle$ demands that $\langle e_+|v_z'|e_+\rangle$ be real and equal to $-\langle e_-|v_z'|e_-\rangle$ for $\vec{v}$ equals $(\hbar/i)\vec{\nabla}$ and $\vec{m}$; and $\langle e_+|\vec{v}|e_-\rangle = \mathcal{C}_2(y')\langle e_+|\vec{v}|e_-\rangle = \langle e_-| - v_x'\hat{i}' + v_y'\hat{j}' - v_z'\hat{k}'|e_+\rangle = \langle e_+| - v_x'\hat{i}' + v_y'\hat{j}' - v_z'\hat{k}'|e_-\rangle^*$ for $\vec{v}$ equals $\vec{er}$, demands that $\langle v_x'\rangle^* = -\langle v_x'\rangle$, $\langle v_y'\rangle^* = \langle v_y'\rangle$, and $\langle v_z'\rangle^* = -\langle v_z'\rangle$ [remember v_0' equals v_z', thus $\langle v_z'\rangle$ equals zero by our previous $\mathcal{C}_3(z')$ argument], and so the matrix element $\langle e_+|v_-'|e_-\rangle$ which equals $\langle e_-|v_+'|e_+\rangle^*$, where $v_\pm' = \sqrt{1/2}(v_x' \pm iv_y')$ by ref. 6, footnote 25, must be pure imaginary, as $\langle e_+|v_-'|e_-\rangle = \langle v_x'\rangle - i\langle v_y'\rangle = -\langle v_x'\rangle^* - i\langle v_y'\rangle^* = -(\langle v_x'\rangle - i\langle v_y'\rangle)^* = -\langle e_+|v_-'|e_-\rangle^*$, and hence, $\langle e_+|\vec{v}|e_-\rangle$ equals $-\langle e_-|\vec{v}|e_+\rangle$ for $\vec{v}$ equals $\vec{er}$ [the opposed phase of the matrix component pairs $\langle e_\pm|\vec{v}|e_\pm\rangle$ and $\langle e_\pm|\vec{v}|e_\mp\rangle$ here discussed can also be derived from consideration of the fact that $\langle\gamma_{(\substack{4\\5})}(t_{2g}$ or $e_g)|\vec{v}|\gamma_{(\substack{4\\5})}(t_{2g}$ or $e_g)\rangle$ must (algebraically) vanish *identically*, or, from a division of $e_\pm$ into its real and imaginary parts, the invocation of operator Hermiteness, the recognition of operator reality or nonreality, and the imposition of symmetry operations]. Analogous logistics yield similar connections for the reduced matrix members of ref. 6, footnote 49 [read A. D. Liehr, *Progr. Transition Metal Chem.*, in press, for example].

Under the special assumptions of ref. 6, the non-null quantities $\bar{r}_0^{\ddagger}$, $\bar{m}_0^{\ddagger}$, $\bar{r}_0$, and $\bar{\bar{m}}_0^{\ddagger}$ take on the magnitudes

$$\bar{r}_0^{\ddagger} = e\xi\sqrt{6}\,k_p \sin\alpha\,(K_{3A_3} + K_{2A_6})N_{e(t)}^2, \quad \bar{\bar{r}} = 0$$

$$\bar{\bar{m}}_0^{\mp} = \mu_B N_{e(t)}^2, \; \bar{m}_0^{\ddagger} = 0$$

The zero values of $\bar{r}_0$ and $\bar{\bar{m}}_0^{\ddagger}$ are only valid so long as pseudo-octahedrality is maintained [the cubic e_g species character then banishes all electric and magnetic molecular orbital dipole contributions as the direct product $e_g \times e_\epsilon$ does not contain the t_{1u} (electric dipole) or t_{1g} (magnetic dipole) species]. When pseudo-octahedrality is dropped and odd σ- and π-ligand and even π-ligand contributions are added, $\bar{r}_0$ and $\bar{\bar{m}}_0^{\ddagger}$ attain substance.

(61) This replacement procedure ensues because $(\hbar/i)\vec{\nabla}$, being an imaginary operator like $\vec{m}$, generates matrix fragments of the same structure as $\vec{m}$. The proof of this fact emerges upon slight alteration of the development of the previous footnote, footnote 60. The $\mathcal{C}_3(z')$ argument again demonstrates the directions of the matrix vectors, $\hat{k}_0'$ and $\hat{k}_\pm'$, of $\vec{er}$, $(\hbar/i)\vec{\nabla}$, and $\vec{m}$ for the coupled pairs of molecular orbitals $a_1(t_{2g})$, $e_\pm(t_{2g})$, and $e_\pm(e_g)$ are tangent. The $\mathcal{C}_3(z')$, $\mathcal{C}_2(y')$, and complex conjugation arguments show that $\langle a_1(t_{2g})|\vec{v}|e_+(t_{2g}$ or $e_g)\rangle$ and $\langle e_+(t_{2g})|\vec{v}|e_\pm(e_g)\rangle$ equal $-\langle a_1(t_{2g})|\vec{v}|e_-(t_{2g}$ or $e_g)\rangle$ and $-\langle e_-(t_{2g})|\vec{v}|e_\mp(e_g)$ for $\vec{v}$ equals $\vec{er}$, $(\hbar/i)\vec{\nabla}$, or $\vec{m}$ and that they are pure imaginary for $\vec{v}$ equals $\vec{er}$ and real for $\vec{v}$ equals $(\hbar/i)\vec{\nabla}$ or $\vec{m}$ [as then $\langle v_x'\rangle^* = \langle v_x'\rangle$, $\langle v_y'\rangle^* = -\langle v_y'\rangle$, and $\langle v_z'\rangle^* = \langle v_z'\rangle$ for $\vec{v}$ equals $(\hbar/i)\vec{\nabla}$ or $\vec{m}$, in the condensed shorthand of footnote 60].

$$\mathfrak{M}[\gamma_{6(^{a}_{b})}{}^{(8)}(t_{2g}) \longrightarrow \gamma_{4\text{ or }5}(e_g)] = {}^{1}/_{6}\{2m_0^2 + m_2^2\}$$

$$\mathfrak{W}[\gamma_{4\text{ or }5}(t_{2g}) \longrightarrow \gamma_{6(^{a}_{b})}(e_g)] = {}^{1}/_{2}g_2m_2$$

$$\mathfrak{X}[\gamma_{4\text{ or }5}(t_{2g}) \longrightarrow \gamma_{6(^{a}_{b})}(e_g)] = {}^{1}/_{2}g_2^2$$

$$\mathfrak{M}[\gamma_{4\text{ or }5}(t_{2g}) \longrightarrow \gamma_{6(^{a}_{b})}(e_g)] = {}^{1}/_{2}m_2^2$$

$$\mathfrak{W}[\gamma_{6(^{a}_{b})}{}^{(7)}(t_{2g}) \longrightarrow \gamma_{6(^{a}_{b})}(e_g)] = {}^{2}/_{3}g_1m_1$$

$$\mathfrak{X}[\gamma_{6(^{a}_{b})}{}^{(7)}(t_{2g}) \longrightarrow \gamma_{6(^{a}_{b})}(e_g)] = {}^{2}/_{3}g_1^2$$

$$\mathfrak{M}[\gamma_{6(^{a}_{b})}{}^{(7)}(t_{2g}) \longrightarrow \gamma_{6(^{a}_{b})}(e_g)] = {}^{2}/_{3}m_1^2$$

$$\mathfrak{W}[\gamma_{6(^{a}_{b})}{}^{(7)}(t_{2g}) \longrightarrow \gamma_{6(^{b}_{a})}(e_g)] = {}^{1}/_{3}g_0m_0$$

$$\mathfrak{X}[\gamma_{6(^{a}_{b})}{}^{(7)}(t_{2g}) \longrightarrow \gamma_{6(^{b}_{a})}(e_g)] = {}^{1}/_{3}g_0^2$$

$$\mathfrak{M}[\gamma_{6(^{a}_{b})}{}^{(7)}(t_{2g}) \longrightarrow \gamma_{6(^{b}_{a})}(e_g)] = {}^{1}/_{3}m_0^2$$

$$\mathfrak{W}[\gamma_{6(^{a}_{b})}{}^{(8)}(t_{2g}) \longrightarrow \gamma_{6(^{a}_{b})}(e_g)] = {}^{1}/_{3}g_1m_1$$

$$\mathfrak{X}[\gamma_{6(^{a}_{b})}{}^{(8)}(t_{2g}) \longrightarrow \gamma_{6(^{a}_{b})}(e_g)] = {}^{1}/_{3}g_1^2$$

$$\mathfrak{M}[\gamma_{6(^{a}_{b})}{}^{(8)}(t_{2g}) \longrightarrow \gamma_{6(^{a}_{b})}(e_g)] = {}^{1}/_{3}m_1^2$$

$$\mathfrak{W}[\gamma_{6(^{a}_{b})}{}^{(8)}(t_{2g}) \longrightarrow \gamma_{6(^{b}_{a})}(e_g)] = {}^{2}/_{3}g_0m_0$$

$$\mathfrak{X}[\gamma_{6(^{a}_{b})}{}^{(8)}(t_{2g}) \longrightarrow \gamma_{6(^{b}_{a})}(e_g)] = {}^{2}/_{3}g_0^2$$

$$\mathfrak{M}[\gamma_{6(^{a}_{b})}{}^{(8)}(t_{2g}) \longrightarrow \gamma_{6(^{b}_{a})}(e_g)] = {}^{2}/_{3}m_0^2$$

$$\mathfrak{W}[\gamma_{(^{4}_{5})}(e_g) \longrightarrow \gamma_{(^{4}_{5})}(e_g)] \equiv \mathfrak{X}[\gamma_{(^{4}_{5})}(e_g) \longrightarrow \gamma_{(^{4}_{5})}(e_g)] \equiv \mathfrak{M}[\gamma_{(^{4}_{5})}(e_g) \longrightarrow \gamma_{(^{4}_{5})}(e_g)] \equiv 0$$

$$\mathfrak{W}[\gamma_{(^{5}_{4})}(e_g) \longrightarrow \gamma_{(^{4}_{5})}(e_g)] = 0 \text{ or } \bar{\bar{p}}_0^{\mp}(\mu_B + \bar{\bar{m}}_0^{\mp})$$

$$\mathfrak{X}[\gamma_{(^{5}_{4})}(e_g) \longrightarrow \gamma_{(^{4}_{5})}(e_g)] = 0 \text{ or } \bar{\bar{p}}_0^{\mp 2}$$

$$\mathfrak{M}[\gamma_{(^{5}_{4})}(e_g) \longrightarrow \gamma_{(^{4}_{5})}(e_g)] = (\mu_B + \bar{\bar{m}}_0^{\mp})^2$$

$$\mathfrak{W}[\gamma_{6(^{a}_{b})}(e_g) \longrightarrow \gamma_{4\text{ or }5}(e_g)] = 0$$

$$\mathfrak{X}[\gamma_{6(^{a}_{b})}(e_g) \longrightarrow \gamma_{4\text{ or }5}(e_g)] = {}^{1}/_{2}\bar{\bar{r}}_0^2 \text{ or } 0$$

$$\mathfrak{M}[\gamma_{6(^{a}_{b})}(e_g) \longrightarrow \gamma_{4\text{ or }5}(e_g)] = \mu_B^2$$

$$\mathfrak{W}[\gamma_{6(^{a}_{b})}(e_g) \longrightarrow \gamma_{6(^{a}_{b})}(e_g)] = 0 \text{ or } -\bar{\bar{p}}_0^{\mp}(\mu_B - \bar{\bar{m}}_0^{\mp})$$

$$\mathfrak{X}[\gamma_{6(^{a}_{b})}(e_g) \longrightarrow \gamma_{6(^{a}_{b})}(e_g)] = 0 \text{ or } \bar{\bar{p}}_0^{\mp 2}$$

$$\mathfrak{M}[\gamma_{6(^{a}_{b})}(e_g) \longrightarrow \gamma_{6(^{b}_{a})}(e_g)] = (\mu_B - \bar{\bar{m}}_0^{\mp})^2$$

$$\mathfrak{W}[\gamma_{6(^{a}_{b})}(e_g) \longrightarrow \gamma_{6(^{b}_{a})}(e_g)] = \mathfrak{X}[\gamma_{6(^{a}_{b})}(e_g) \longrightarrow \gamma_{6(^{b}_{a})}(e_g)] = \mathfrak{M}[\gamma_{6(^{a}_{b})}(e_g) \longrightarrow \gamma_{6(^{b}_{a})}(e_g)] = 0$$

$$\mathfrak{W}[\gamma_{6(^{a}_{b})}{}^{(7)}(t_{2g}) \longrightarrow \gamma_{6(^{a}_{b})}{}^{(7)}(t_{2g})] = 0 \text{ or } {}^{2}/_{9}\bar{p}_0^{\mp}(\mu_B + 2\bar{m}_0^{\mp})$$

$$\mathfrak{X}[\gamma_{6(^{a}_{b})}{}^{(7)}(t_{2g}) \longrightarrow \gamma_{6(^{a}_{b})}{}^{(7)}(t_{2g})] = 0 \text{ or } {}^{4}/_{9}\bar{p}_0^{\mp 2}$$

$$\mathfrak{M}[\gamma_{6(^{a}_{b})}{}^{(7)}(t_{2g}) \longrightarrow \gamma_{6(^{a}_{b})}{}^{(7)}(t_{2g})] = {}^{1}/_{9}(\mu_B + 2\bar{m}_0^{\mp})^2$$

$$\mathfrak{W}[\gamma_{6(^{a}_{b})}{}^{(7)}(t_{2g}) \longrightarrow \gamma_{6(^{b}_{a})}{}^{(7)}(t_{2g})] = 0 \text{ or } -{}^{4}/_{9}\bar{p}_0(\mu_B + 2\bar{m}_0)$$

$$\mathfrak{X}[\gamma_{6(^{a}_{b})}{}^{(7)}(t_{2g}) \longrightarrow \gamma_{6(^{b}_{a})}{}^{(7)}(t_{2g})] = 0 \text{ or } {}^{8}/_{9}\bar{p}_0^2$$

$$\mathfrak{M}[\gamma_{6(^{a}_{b})}{}^{(7)}(t_{2g}) \longrightarrow \gamma_{6(^{b}_{a})}{}^{(7)}(t_{2g})] = {}^{2}/_{9}(\mu_B + 2\bar{m}_0)^2$$

$$\mathfrak{W}[\gamma_{6(^{a}_{b})}{}^{(8)}(t_{2g}) \longrightarrow \gamma_{6(^{a}_{b})}{}^{(8)}(t_{2g})] = 0 \text{ or } -{}^{1}/_{9}\bar{p}_0^{\mp}(\mu_B - \bar{m}_0^{\mp})$$

$$\mathfrak{X}[\gamma_{6(^{a}_{b})}{}^{(8)}(t_{2g}) \longrightarrow \gamma_{6(^{a}_{b})}{}^{(8)}(t_{2g})] = 0 \text{ or } {}^{1}/_{9}\bar{p}_0^{\mp 2}$$

$$\mathfrak{M}[\gamma_{6(^{a}_{b})}{}^{(8)}(t_{2g}) \longrightarrow \gamma_{6(^{a}_{b})}{}^{(8)}(t_{2g})] = {}^{1}/_{9}(\mu_B - \bar{m}_0^{\mp})^2$$

$$\mathfrak{W}[\gamma_{6(^{a}_{b})}{}^{(8)}(t_{2g}) \longrightarrow \gamma_{6(^{b}_{a})}{}^{(8)}(t_{2g})] = 0 \text{ or } {}^{8}/_{9}\bar{p}_0(\mu_B - \bar{m}_0)$$

$$\mathfrak{X}[\gamma_{6(^{a}_{b})}{}^{(8)}(t_{2g}) \longrightarrow \gamma_{6(^{b}_{a})}{}^{(8)}(t_{2g})] = 0 \text{ or } {}^{8}/_{9}\bar{p}_0^2$$

$$\mathfrak{M}[\gamma_{6(^{a}_{b})}{}^{(8)}(t_{2g}) \longrightarrow \gamma_{6(^{b}_{a})}{}^{(8)}(t_{2g})] = {}^{8}/_{9}(\mu_B - \bar{m}_0)^2$$

$$\mathfrak{W}[\gamma_{(^{4}_{5})}(t_{2g}) \longrightarrow \gamma_{(^{4}_{5})}(t_{2g})] \equiv \mathfrak{X}[\gamma_{(^{4}_{5})}(t_{2g}) \longrightarrow \gamma_{(^{4}_{5})}(t_{2g})] \equiv \mathfrak{M}[\gamma_{(^{4}_{5})}(t_{2g}) \longrightarrow \gamma_{(^{4}_{5})}(t_{2g})] \equiv 0$$

$$\mathfrak{W}[\gamma_{(^{5}_{4})}(t_{2g}) \longrightarrow \gamma_{(^{4}_{5})}(t_{2g})] = 0 \text{ or } -\bar{p}_0^{\mp}(\mu_B - \bar{m}_0^{\mp})$$

$$\mathfrak{X}[\gamma_{(^{5}_{4})}(t_{2g}) \longrightarrow \gamma_{(^{4}_{5})}(t_{2g})] = 0 \text{ or } \bar{p}_0^{\mp 2}$$

$$\mathfrak{M}[\gamma_{(^{5}_{4})}(t_{2g}) \longrightarrow \gamma_{(^{4}_{5})}(t_{2g})] = (\mu_B - \bar{m}_0^{\mp})^2 \qquad \text{(A-24)}$$

These portionate rotational and spectral strengths sum to the total rotational and spectral strengths lodged downward.

$$\mathfrak{W}[\gamma_6{}^{(8)}(t_{2g}) \longrightarrow \gamma_6{}^{(7)}(t_{2g})] = (0 \text{ or } {}^{2}/_{9}\bar{p}_0^{\mp}(2\mu_B + \bar{m}_0^{\mp})) - {}^{1}/_{3}\bar{g}_0(2\mu_B + \bar{m}_0)$$

$$\mathfrak{X}[\gamma_6{}^{(8)}(t_{2g}) \longrightarrow \gamma_6{}^{(7)}(t_{2g})] = (0 \text{ or } {}^{2}/_{9}\bar{p}_0^{\mp 2}) + \bar{g}_0^2$$

$$\mathfrak{M}[\gamma_6{}^{(8)}(t_{2g}) \longrightarrow \gamma_6{}^{(7)}(t_{2g})] = {}^{2}/_{9}(2\mu_B + \bar{m}_0^{\mp})^2 + {}^{1}/_{9}(2\mu_B + \bar{m}_0)^2$$

$$\mathfrak{W}[\gamma_6{}^{(8)}(t_{2g}) \longrightarrow \gamma_{4\text{ or }5}(t_{2g})] = {}^{1}/_{3}\bar{g}_0(\mu_B - \bar{m}_0)$$

$$\mathfrak{X}[\gamma_6{}^{(8)}(t_{2g}) \longrightarrow \gamma_{4\text{ or }5}(t_{2g})] = {}^{1}/_{6}\{2\bar{g}_0^2 + \bar{g}_0^{\mp 2}\}$$

$$\mathfrak{M}[\gamma_6{}^{(8)}(t_{2g}) \longrightarrow \gamma_{4\text{ or }5}(t_{2g})] = {}^{1}/_{3}(\mu_B - \bar{m}_0)^2$$

$$\mathfrak{W}[\gamma_6{}^{(7)}(t_{2g}) \longrightarrow \gamma_{4\text{ or }5}(t_{2g})] = -{}^{1}/_{6}\bar{g}_0(2\mu_B + \bar{m}_0)$$

$$\mathfrak{X}[\gamma_6{}^{(7)}(t_{2g}) \longrightarrow \gamma_{4\text{ or }5}(t_{2g})] = {}^{1}/_{6}\{\bar{g}_0^2 + 2\bar{g}_0^{\mp 2}\}$$

$$\mathfrak{M}[\gamma_6{}^{(7)}(t_{2g}) \longrightarrow \gamma_{4\text{ or }5}(t_{2g})] = {}^{1}/_{6}(2\mu_B + \bar{m}_0)^2$$

$$\mathfrak{W}[\gamma_{(^{4}_{5})}(t_{2g}) \longrightarrow \gamma_{(^{4}_{5})}(t_{2g})] \equiv \mathfrak{X}[\gamma_{(^{4}_{5})}(t_{2g}) \longrightarrow \gamma_{(^{4}_{5})}(t_{2g})] \equiv \mathfrak{M}[\gamma_{(^{4}_{5})}(t_{2g}) \longrightarrow \gamma_{(^{4}_{5})}(t_{2g})] \equiv 0$$

$$\mathfrak{W}[\gamma_{(^{5}_{4})}(t_{2g}) \longrightarrow \gamma_{(^{4}_{5})}(e_g)] = g_1m_1$$

$$\mathfrak{X}[\gamma_{(^{5}_{4})}(t_{2g}) \longrightarrow \gamma_{(^{4}_{5})}(e_g)] = g_1^2$$

$$\mathfrak{M}[\gamma_{(^{5}_{4})}(t_{2g}) \longrightarrow \gamma_{(^{4}_{5})}(e_g)] = m_1^2$$

$$\mathfrak{W}[\gamma_6{}^{(7)}(t_{2g}) \longrightarrow \gamma_{4\text{ or }5}(e_g)] = {}^{1}/_{6}\{g_0m_0 + 2g_2m_2\}$$

$$\mathfrak{X}[\gamma_6{}^{(7)}(t_{2g}) \longrightarrow \gamma_{4\text{ or }5}(e_g)] = {}^{1}/_{6}\{g_0^2 + 2g_2^2\}$$

$$\mathfrak{M}[\gamma_6^{(7)}(t_{2g}) \longrightarrow \gamma_{4\text{ or }5}(e_g)] = {}^1/_6\{m_0^2 + 2m_2^2\}$$

$$\mathfrak{W}[\gamma_6^{(8)}(t_{2g}) \longrightarrow \gamma_{4\text{ or }5}(e_g)] = {}^1/_6\{2g_0m_0 + g_2m_2\}$$

$$\mathfrak{X}[\gamma_6^{(8)}(t_{2g}) \longrightarrow \gamma_{4\text{ or }5}(e_g)] = {}^1/_6\{2g_0^2 + g_2^2\}$$

$$\mathfrak{M}[\gamma_6^{(8)}(t_{2g}) \longrightarrow \gamma_{4\text{ or }5}(e_g)] = {}^1/_6\{2m_0^2 + m_2^2\}$$

$$\mathfrak{W}[\gamma_{4\text{ or }5}(t_{2g}) \longrightarrow \gamma_6(e_g)] = g_2m_2$$

$$\mathfrak{X}[\gamma_{4\text{ or }5}(t_{2g}) \longrightarrow \gamma_6(e_g)] = g_2^2$$

$$\mathfrak{M}[\gamma_{4\text{ or }5}(t_{2g}) \longrightarrow \gamma_6(e_g)] = m_2^2$$

$$\mathfrak{W}[\gamma_6^{(7)}(t_{2g}) \longrightarrow \gamma_6(e_g)] = {}^1/_3\{g_0m_0 + 2g_1m_1\}$$

$$\mathfrak{X}[\gamma_6^{(7)}(t_{2g}) \longrightarrow \gamma_6(e_g)] = {}^1/_3\{g_0^2 + 2g_1^2\}$$

$$\mathfrak{M}[\gamma_6^{(7)}(t_{2g}) \longrightarrow \gamma_6(e_g)] = {}^1/_3\{m_0^2 + 2m_1^2\}$$

$$\mathfrak{W}[\gamma_6^{(8)}(t_{2g}) \longrightarrow \gamma_6(e_g)] = {}^1/_3\{2g_0m_0 + g_1m_1\}$$

$$\mathfrak{X}[\gamma_6^{(8)}(t_{2g}) \longrightarrow \gamma_6(e_g)] = {}^1/_3\{2g_0^2 + g_1^2\}$$

$$\mathfrak{M}[\gamma_6^{(8)}(t_{2g}) \longrightarrow \gamma_6(e_g)] = {}^1/_3\{2m_0^2 + m_1^2\}$$

$$\mathfrak{W}[\gamma_{(\frac{4}{5})}(e_g) \longrightarrow \gamma_{(\frac{4}{5})}(e_g)] \equiv \mathfrak{X}[\gamma_{(\frac{4}{5})}(e_g) \longrightarrow \gamma_{(\frac{4}{5})}(e_g)] \equiv \mathfrak{M}[\gamma_{(\frac{4}{5})}(e_g) \longrightarrow \gamma_{(\frac{4}{5})}(e_g)] \equiv 0$$

$$\mathfrak{W}[\gamma_{(\frac{5}{4})}(e_g) \longrightarrow \gamma_{(\frac{4}{5})}(e_g)] = 0 \text{ or } \bar{\bar{p}}_0^{\mp}(\mu_B + \bar{\bar{m}}_0^{\mp})$$

$$\mathfrak{X}[\gamma_{(\frac{5}{4})}(e_g) \longrightarrow \gamma_{(\frac{4}{5})}(e_g)] = 0 \text{ or } \bar{\bar{p}}_0^{\mp 2}$$

$$\mathfrak{M}[\gamma_{(\frac{5}{4})}(e_g) \longrightarrow \gamma_{(\frac{4}{5})}(e_g)] = (\mu_B + \bar{\bar{m}}_0^{\mp})^2$$

$$\mathfrak{W}[\gamma_6(e_g) \longrightarrow \gamma_{4\text{ or }5}(e_g)] = 0$$

$$\mathfrak{X}[\gamma_6(e_g) \longrightarrow \gamma_{4\text{ or }5}(e_g)] = {}^1/_2\bar{r}_0^2 \text{ or } 0$$

$$\mathfrak{M}[\gamma_6(e_g) \longrightarrow \gamma_{4\text{ or }5}(e_g)] = \mu_B^2$$

$$\mathfrak{W}[\gamma_6(e_g) \longrightarrow \gamma_6(e_g)] = 0 \text{ or } -\bar{\bar{p}}_0^{\mp}(\mu_B - \bar{\bar{m}}_0^{\mp})$$

$$\mathfrak{X}[\gamma_6(e_g) \longrightarrow \gamma_6(e_g)] = 0 \text{ or } \bar{\bar{p}}_0^{\mp 2}$$

$$\mathfrak{M}[\gamma_6(e_g) \longrightarrow \gamma_6(e_g)] = (\mu_B - \bar{\bar{m}}_0^{\mp})^2$$

$$\mathfrak{W}[\gamma_6^{(7)}(t_{2g}) \longrightarrow \gamma_6^{(7)}(t_{2g})] = 0 \text{ or } {}^2/_9\{\bar{p}_0^{\mp}(\mu_B + 2\bar{m}_0^{\mp}) - 2\bar{p}_0(\mu_B + 2\bar{m}_0)\}$$

$$\mathfrak{X}[\gamma_6^{(7)}(t_{2g}) \longrightarrow \gamma_6^{(7)}(t_{2g})] = 0 \text{ or } {}^4/_9\{\bar{p}_0^{\mp 2} + 2\bar{p}_0^2\}$$

$$\mathfrak{M}[\gamma_6^{(7)}(t_{2g}) \longrightarrow \gamma_6^{(7)}(t_{2g})] = {}^1/_9\{(\mu_B + 2\bar{m}_0^{\mp})^2 + 2(\mu_B + 2\bar{m}_0)^2\}$$

$$\mathfrak{W}[\gamma^{(8)}(t_{2g}) \longrightarrow \gamma_6^{(8)}(t_{2g})] = 0 \text{ or } -{}^1/_9\{\bar{p}_0^{\mp}(\mu_B - \bar{m}_0^{\mp}) - 8\bar{p}_0(\mu_B - \bar{m}_0)\}$$

$$\mathfrak{X}[\gamma_6^{(8)}(t_{2g}) \longrightarrow \gamma_6^{(8)}(t_{2g})] = 0 \text{ or } {}^1/_9\{p_0^{\mp 2} + 8\bar{p}_0^2\}$$

$$\mathfrak{M}[\gamma_6^{(8)}(t_{2g}) \longrightarrow \gamma_6^{(8)}(t_{2g})] = {}^1/_9\{(\mu_B - \bar{m}_0^{\mp})^2 + 8(\mu_B - \bar{m}_0)^2\}$$

$$\mathfrak{W}[\gamma_{(\frac{4}{5})}(t_{2g}) \longrightarrow \gamma_{(\frac{4}{5})}(t_{2g})] \equiv \mathfrak{X}[\gamma_{(\frac{4}{5})}(t_{2g}) \longrightarrow \gamma_{(\frac{4}{5})}(t_{2g})] \equiv \mathfrak{M}[\gamma_{(\frac{4}{5})}(t_{2g}) \longrightarrow \gamma_{(\frac{4}{5})}(t_{2g})] \equiv 0$$

$$\mathfrak{W}[\gamma_{(\frac{5}{4})}(t_{2g}) \longrightarrow \gamma_{(\frac{4}{5})}(t_{2g})] = 0 \text{ or } -\bar{p}_0^{\mp}(\mu_B - \bar{m}_0^{\mp})$$

$$\mathfrak{X}[\gamma_{(\frac{5}{4})}(t_{2g}) \longrightarrow \gamma_{(\frac{4}{5})}(t_{2g})] = 0 \text{ or } \bar{p}_0^{\mp 2}$$

$$\mathfrak{M}[\gamma_{(\frac{5}{4})}(t_{2g}) \longrightarrow \gamma_{(\frac{4}{5})}(t_{2g})] = (\mu_B - \bar{m}_0^{\mp})^2 \qquad \text{(A-25)}$$

Witness that spin magnetic moments alone produce sizable contributions to both the rotational and (magnetic) spectral strengths. The internal (Kramers') degenerate transitions stenciled above contribute nothing to the optical rotatory power as they cancel against their own inverses [in the gradient representation of the electric dipole operator this cancellation occurs because of the energy reversal in the pirouettory power multiplicative factor $(E_b - E_a)^{-1}$ and in the coordinate representation of the electric dipole operator it occurs because of the functional reversal in the rotatory power functional arguments].

The Sorption of Halogens from Aqueous Solution by Collagen[1]

by Christopher Earland and David J. Raven

Department of Textile Industries, Institute of Technology, Bradford, England *(Received December 16, 1963)*

It is shown that the sorption of chlorine, bromine, and iodine from aqueous solution by collagen, which is always endothermic, obeys the Freundlich isotherm and in some cases this reduces to the distribution law. Maximum values are too great to be ascribed solely to the formation of either a monomolecular adsorption layer or chemisorption, although it is shown that the latter occurs to some extent in the case of chlorine. Iodine is sorbed only as the triiodide anion. The most probable mechanism for the sorption of Br_3^- is an ion-exchange process, which is supported by its zero heat of sorption.

Introduction

The main reaction between halogens in aqueous solution and keratin is the oxidation of cystine residues to sulfonic acid groups in the case of chlorine and bromine[2] and substitution in the 3,5 positions of the tyrosine residues with iodine, although with the latter halogen sorption also occurs.[3] Silk fibroin, which is devoid of cystine residues, undergoes chiefly substitution with all three halogens. No comparable studies have, however, been made of the uptake of halogens from aqueous solution by the fibrous protein collagen. Since collagen, which is practically devoid of both cystine and tyrosine residues, has a comparable water uptake and surface area, as measured by nitrogen or water vapor adsorption, to keratin and fibroin,[4] it should lend itself particularly well to a study of the physical processes which occur when halogens are taken up from aqueous solution by fibrous proteins, but which may be masked by subsequent chemical reaction.

Experimental

Materials. The collagen used was "Standard Hide Powder," an official hide powder of the Society of Leather Trades Chemists. It was prepared by Baird and Tatlock, London, and had the following specification: moisture, 13.5%; ash, 0.25%; pH 5.25. Prior to weighing, the powder was dried overnight under vacuum over silica gel, and then at atmospheric pressure over P_2O_5 for 2 days.

All reagents, including bromine and iodine, were of Analar quality, except chlorine which was obtained as laboratory reagent sodium hypochlorite solution.

Determination of Sorption. Unless stated otherwise all determinations were carried out at 20.0 ± 0.1°.

A solution of the halogen, adjusted to the requisite pH, was prepared and the concentration of halogen was determined iodometrically. Then 100 ml. of this solution was allowed to stand with a known weight (about 0.5 g.) of hide powder in a closed flask immersed in a thermostat tank, with occasional agitation, until equilibrium was attained. After allowing the collagen to settle, 10.0 ml. of the supernatant liquid was titrated with potassium iodide and 0.100 *N* $Na_2S_2O_3$ solution to determine the equilibrium concentration of halogen in solution. Potassium iodide was then added to the remainder of the reaction mixture and the whole was titrated iodometrically. The time taken for this titration could be reduced by titrating the liquid separately and then the solid in the presence of 50 ml. of methanol. It was established that equilibrium was usually attained within 30 min. and, unless stated to the contrary, this reaction time was adhered to throughout the investigation. It was confirmed that well-defined equilibria were established under the experimental conditions used.[5]

(1) This work was supported by a grant from the Wool Textile Research Council, Bradford, England.

(2) (a) R. Consden, A. H. Gorden, and A. J. P. Martin, *Biochim. J.*, **40**, 580 (1946); (b) G. J. Weston, *Biochim. Biophys. Acta*, **17**, 462 (1955).

(3) S. Blackburn and H. Phillips, *J. Soc. Dyers Colourists*, **61**, 100 (1945).

(4) J. W. Rowen and R. L. Blaine, *Ind. Eng. Chem.*, **39**, 1659 (1947); A. C. Zettlemoyer, A. Chand, and E. Gamble, *J. Am. Chem. Soc.*, **72**, 2752 (1950); J. R. Kanagy, *J. Am. Leather Chemists' Assoc.*, **42**, 98 (1947); H. B. Bull, *J. Am. Chem. Soc.*, **66**, 1499 (1944).

Calculation of Sorption. Depending on the pH, halogens may be present in aqueous solutions as molecules, hypohalous acid, or hypohalite ions, *i.e.*, as X_2, HOX, or OX^-, where X = halogen, and in the presence of halide ions, as X_3^-.

To avoid confusion, all concentrations in this work are given in terms of "available" or "positive" halogen, calculated from the relationship: 1 l. of 1 *N* $Na_2S_2O_3$ solution $\equiv$ 0.5 mole of halogen. Using this method for expressing halogen concentration, $X_2 \equiv HOX \equiv OX^- \equiv X_3^-$. The actual form of the halogen may be calculated from the appropriate equilibrium constant. Thus, chlorine in aqueous solution is nearly exclusively Cl_2 at pH 1, HOCl at pH 4, and OCl^- at pH 9.

The usual method for determining sorption from solution is to measure the change in concentration of the solution after equilibrium with the solid. This method was unsuitable for this investigation, however, because a small quantity of halogen is lost by oxidizing the collagen, and in the case of chlorine its low solubility in water precluded high values for the absorption from being obtained. The latter were determined by passing chlorine gas through the solution as sorption proceeded. The halogen sorbed was, therefore, calculated solely from data obtained from the reaction at equilibrium, although the concentration of the solution was determined prior to the introduction of the collagen, as it provided a useful check on the accuracy of the run and enabled the quantity of halogen that had reacted to be calculated. The details of the calculations follow.

If 10.0 ml. of halogen solution before the introduction of collagen requires x ml. of 0.100 *N* $Na_2S_2O_3$ solution and 10.0 ml. of the solution (100 ml.) in equilibrium with w g. of collagen requires y ml. of 0.100 *N* $Na_2S_2O_3$ solution, and the remainder of the reaction mixture (90 ml. of solution + w g. of collagen) requires z ml. of 0.100 *N* $Na_2S_2O_3$ solution, then: the equilibrium concentration of halogen in solution (c) = $5y$ mmoles/l.; the halogen sorbed (a) = $5(z - 9y)/w$ mmoles/100 g.; and the halogen reacted = $5(10x - y - z)/w$ mmoles/100 g.

Determination of Protons Liberated during Sorption. Positive halogen formation can be distinguished from simple sorption by the fact that in the former case each molecule of halogen taken up liberates one proton

$$PNH_2 + X_2 \rightleftharpoons PNHX + X^- + H^+$$

where P = protein, although iodometrically the two are identical.

The protons liberated were determined by measuring the fall in pH of the solution using a glass electrode against a standard calomel cell, the actual concentrations being obtained from plots of pH *vs.* acid concentration of solutions containing known amounts of HCl or HBr. To this value was added 80 mequiv./100 g. of collagen to allow for the uptake of protons by the collagen.

$$PNH_2 + H^+X^- \longrightarrow PNH_3^+X^-$$

Each molecule of halogen that oxidizes collagen, on the other hand, liberates two protons.

$$P + X_2 + H_2O \longrightarrow PO + 2H^+ + 2X^-$$

It was essential, therefore, to know the quantity that had reacted in addition to that sorbed. After reaction with chlorine or bromine, followed by removal of positive halogen, collagen contains negligible combined halogen and therefore the substitution reaction

$$PH + X_2 \longrightarrow PX + H^+ + X^-$$

may be disregarded.

In order to produce an appreciable fall in pH with increase in acidity, these experiments were carried out at pH 2 instead of pH 1, and in the case of chlorine, the solution was made 1.0 *M* with respect to KCl to suppress the formation of HOCl which could exert a buffering effect.

$$HOCl + H^+ + Cl^- \longrightarrow Cl_2 + H_2O$$

Results

Isotherms—Sorption of Halogens at pH 0.7. The isotherms for the sorption of chlorine and bromine which exist in the free state at pH 0.7 and iodine are shown in Fig. 1. The pH was adjusted to the required value with H_2SO_4, and the solutions of iodine were prepared by diluting the requisite quantity of a solu-

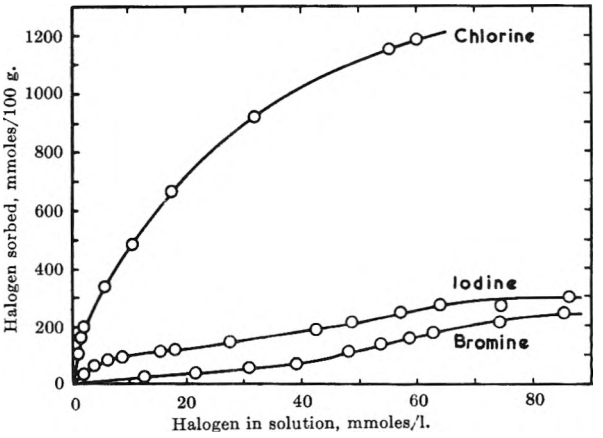

Figure 1. Sorption of halogens on collagen at pH 0.7 and 20°.

(5) H. Freundlich, "Colloid and Capillary Chemistry," Methuen and Co., London, 1926, p. 174.

tion containing 5 g. of I_2 and 10 g. of KI in 100 g. of water. It is seen from Fig. 1 that only bromine obeys the distribution law and this is limited to the initial sorption; but log–log plots of the amount sorbed (a) against the equilibrium concentration in solution (c) (Fig. 2) showed that in all cases the sorption obeyed approximately the Freundlich adsorption isotherm, $a = kc^{1/n}$, where k and n are constants. The distinct break in the curve, however, for the sorption of bromine at a solution concentration of 45 mmoles/l. (Fig. 1) emphasizes that for this halogen the data can be represented only approximately by the Freundlich isotherm. No sorption of iodine occurred from solution in 7:3 alcohol–water mixtures.

Isotherms—Sorption of Chlorine and Bromine at pH 0.7 in Presence of Anions. Since chlorine and bromine were sorbed on collagen as Cl_2 or Br_2, whereas iodine was sorbed only as I_3^-, the sorption isotherms for the two former halogens were redetermined in the presence of 1.0 *M* KCl or 1.0 *M* KBr, respectively. The sorption was determined also in the presence of 1.0 *M* KNO_3 to confirm that any change in sorption was due to the formation of the trihalide anion and not to a general anion effect. The sorption isotherm for chlorine at pH 0.7 was unchanged by the presence of KCl or KNO_3. The effect of 1.0 *M* KBr on the sorption of bromine was, however, most marked and in the presence of this salt a maximum value of 75 mmoles/100 g. only could be sorbed (see Fig. 3), whereas in the absence of bromide ions, values in excess of 250 mmoles/100 g. were obtained. KNO_3 had no effect on the sorption.

Sorption of Chlorine at pH 4 and 7. The determination of the sorption isotherm for chlorine in solution of pH 0.7 presented no difficulty since well-defined equilibria were attained after 30 min., and the amount

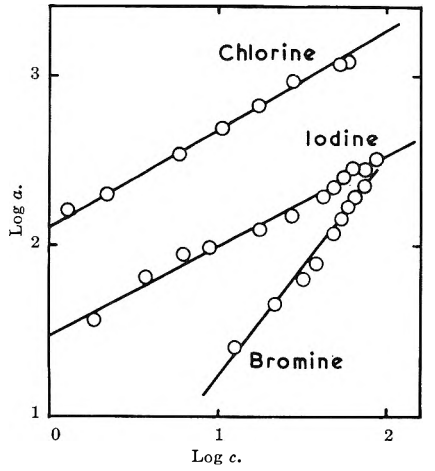

Figure 2. Graphs of log a *vs.* log c for the sorption of halogens on collagen at pH 0.7 and 20°.

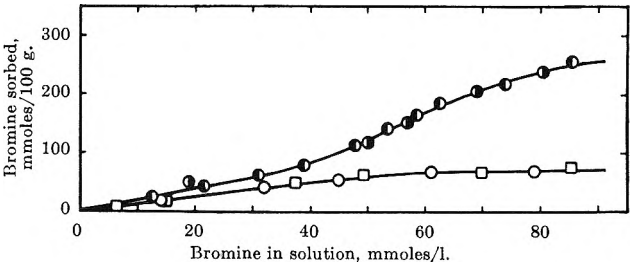

Figure 3. Effect of KBr and KNO_3 on the sorption of bromine at pH 0.7: ◐, bromine at 20°; ◑, bromine + 1.0 *M* KNO_3 at 20°; ○, bromine + 1.0 *M* KBr at 10°; □, bromine + 1.0 *M* KBr at 20°.

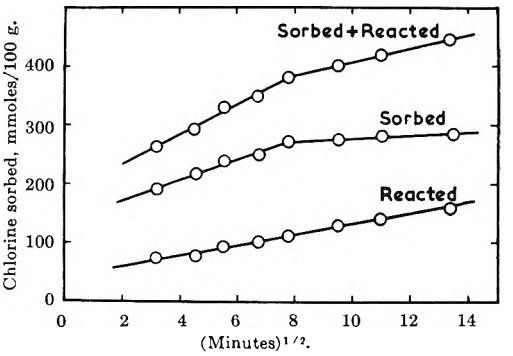

Figure 4. Rate of sorption of chlorine at pH 4 and 20°.

of chlorine that reacted was only 10 to 20% of that sorbed. At pH 4, however, the hypochlorous acid reacted with the collagen to the extent of 50% of that sorbed and continued reaction masked the equilibrium point of sorption. However, because a stirring rate of 200 r.p.m. was fast enough to make the rate of uptake controlled by diffusion within the solid,[6] plots of the amounts of chlorine sorbed and reacted *vs.* $(\text{time})^{1/2}$ gave straight lines (see Fig. 4) from which it was possible to determine the equilibrium values for the chlorine sorbed and in solution. Thus, it is seen from Fig. 4, which refers to a solution containing 31 mmoles of chlorine/l. before the introduction of the collagen, that equilibrium was attained after 60 min. when 271 mmoles/100 g. of collagen was sorbed, the solution in equilibrium containing 12.7 mmoles of chlorine/l. The amount sorbed was only half that at pH 0.7.

At pH 7, from a chlorine solution of initial concentration of 31 mmoles/l., after 10 min. 145 mmoles/100 g. was sorbed and 143 mmoles/100 g. reacted. After 90 min., the corresponding values were 176 and 357 which indicated that the absorbent was being oxidized to such an extent that the values for the sorption have little significance.

(6) A. V. Hill, *Proc. Roy. Soc.* (London), **B104**, 39 (1929).

Sorption of Bromine and Iodine at Different pH Values. When the isotherm for the sorption of bromine at pH 4 is compared with that at pH 0.7 (Fig. 5), it is seen that the maximum amount sorbed is approximately doubled at the higher pH value. Equilibrium was attained in 30 min. and the amount reacted was approximately equal to that sorbed. Sorption at pH 7 was considerably slower and equilibrium was not achieved after 105 min.

The sorption of iodine over the pH range 0.7 to 7, obtained by diluting a solution in KI with appropriate buffer solutions, varied but little and gave typical isotherms (see Fig. 6). At pH 9.2, however, the sorption halved and obeyed the distribution law. This pH was obtained by the use of 0.05 *M* borax solution, but in other cases sodium phosphate was used. In none of these experiments did more than 50 mmoles/100 g. react.

Liberation of Protons during Sorption. It is seen from Fig. 7 that the sorption of chlorine is accompanied by the liberation of protons in excess of those produced by reaction, and approximately one-half of the sorbed chlorine liberates protons. In the case of bromine, however, the correlation between the protons liberated and halogen reacted is complete and, therefore, the sorption process does not involve the liberation of protons.

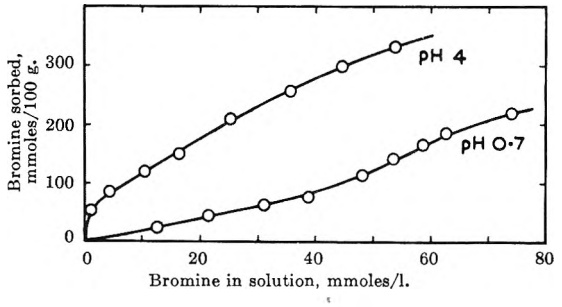

Figure 5. Sorption of bromine at pH 4 and 20°.

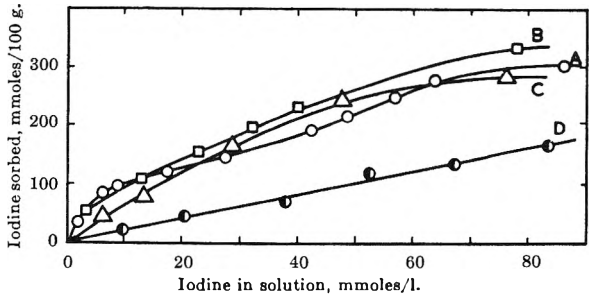

Figure 6. Sorption of iodine from solutions of different pH at 20°: A, pH 0.7; B, pH 4.0; C, pH 7.0; D, pH 9.2.

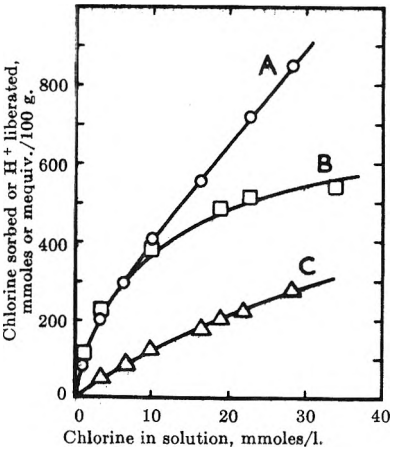

Figure 7. Liberation of protons during sorption of chlorine at pH 2 and 20°: A, sorption of chlorine at pH 2; B, actual liberation of protons; C, theoretical curve of protons liberated from chlorine reacted.

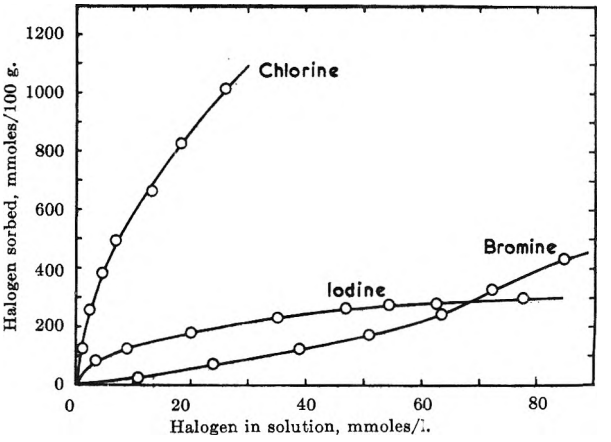

Figure 8. Sorption of halogens on collagen at pH 0.7 and 30°.

Effect of Temperature on Sorption. From Fig. 3 it is seen that the sorption of Br_3^- is the same at 10° as at 20°, whereas in the case of chlorine, bromine, and iodine there is a considerable temperature effect, the isotherms at 30° being shown in Fig. 8. It was not possible to determine the sorption of Br_3^- at 30° since the potassium bromide induced hydrothermal shrinkage of the collagen.

Discussion

It is shown that collagen can sorb large quantities of halogens from aqueous solution. Isotherms indicate that approximate maximum values (mmoles/100 g.) are 1200 for chlorine (from solution of pH 0.7), *i.e.*, nearly its own weight, and 350 for bromine or iodine (from solution of pH 4). In all cases the sorption obeys approximately the Freundlich adsorption isotherm and with bromine and iodine under certain

conditions this reduces to the distribution law. Sorption occurs over a wide range of pH values of the halogen solution, but with chlorine and bromine above pH 4 considerable reaction occurs in addition to sorption. Thus sorption, as opposed to reaction, is favored when these halogens are in the elemental form and not as oxy acids. Iodine, however, sorbs only in the presence of iodide ions, showing that the sorbing species is the triiodide anion. This effect is known for other absorbents.[7]

With bromine, on the other hand, the presence of sufficient bromide ions to convert all the free bromine to tribromide ions reduces the sorption to a maximum value of 75 mmoles/100 g. The latter is very close to the acid-combining value of collagen and suggests that the mechanism of the sorption is the ion-exchange process

$$-NH_3^+X^- + Br_3^- \rightleftharpoons -NH_3^+Br_3^- + X^-$$

It has been proposed by Blackburn and Phillips[3] that iodine sorbs on wool by a similar mechanism. Although iodine is sorbed by collagen greatly in excess of 80 mmoles/100 g., this is not surprising since iodine is sorbed from potassium iodide solution by many substances[8] where an ion-exchange mechanism cannot operate.

The fact that the sorption of bromine from solution at pH 2 is unaccompanied by the liberation of protons shows that positive halogen formation does not occur. The inability of free bromine to form >N–Br compounds with simple amides and amines in acid solution supports this view. In the case of chlorine, however, about 250 mequiv./100 g. of collagen of protons are evolved in excess of those liberated by oxidation and this corresponds to positive halogen formation on free amine, amide, and guanidine groups.[9] The ease with which free chlorine reacts with such groups in simple compounds makes it virtually certain that similar reactions will occur with collagen.

The total surface area of hide powder available for adsorption is about 300 m.^{2}/g.,[4] when the material is swollen in water. This value would allow 170 mmoles of Cl_2/100 g. of collagen to be adsorbed as a monomolecular layer (assuming each molecule of chlorine occupies 30 Å.^{2}), the corresponding figure for bromine being 140. It is clear, therefore, that the sorption of these large quantities of halogens by collagen cannot be accounted for solely either as a monomolecular layer or by chemisorption involving proton liberation.

The isotherms shown in Fig. 1 and 8 indicate that the sorption is endothermic, which although not unknown from solution, is unusual. It was unsatisfactory to calculate the heats of sorption from these data, however, because the value derived is an over-all figure involving both the removal of halogen from solution and its subsequent sorption by the collagen. Furthermore, at very low surface coverage, the concentration of halogen in solution is so small that hydrolysis to hypochlorous acid cannot be neglected. The zero over-all heat of sorption of Br_3^- is, however, in accordance with the ion-exchange mechanism proposed, since the heat of reaction of simple anions with proteins is very small or zero[10] and therefore no appreciable heat transfer would be involved in the replacement of one anion by another of similar size.

(7) F. Mylius, *Ber.*, **20**, 689 (1887).

(8) F. W. Kuster, *Ann.*, **283**, 360 (1894).

(9) J. H. Bowes and R. H. Kenten, *Biochem. J.*, **43**, 358 (1948).

(10) T. Vickerstaff, "The Physical Chemistry of Dyeing," Oliver and Boyd, London, 1954, p. 375.

Mechanisms of Photoreactions in Solution. XX.[1] Quenching of Excited States of Benzophenone by Metal Chelates

by George S. Hammond and Robert P. Foss

Contribution No. 3064 from the Gates and Crellin Laboratories of Chemistry, California Institute of Technology, Pasadena, California *(Received February 14, 1964)*

Metal chelate compounds containing ligands derived from β-diketones show variable reactivity as quenchers in the photoreduction of benzophenone by benzhydrol. Reactivity varies both as a function of the nature of the central metal atom and of the ligand. There is no correlation between quenching activity and the magnetic properties of the ground states of the chelates. Two possible mechanisms for quenching are discussed but no selection between them is attempted.

Introduction

In recent years there have been a number of reports that compounds of transition metals have marked activity as quenchers for the triplet states of organic molecules in solution.[2-7] A possible mechanism for quenching was discussed in detail by Porter and Wright.[4] They were struck by the fact that in aqueous and alcoholic solutions only paramagnetic metallic ions were effective as quenchers. Consequently, they suggested that the quenching process was essentially the same as that suggested by McConnell[8] for catalysis of *cis–trans* isomerization, *via* triplet transition states, by nitric oxide. In this process the paramagnetic quencher serves as a catalyst for nonradiative decay of triplets. The catalytic effect arises from the fact that complexes between triplet and quencher can undergo spin-allowed transitions producing complexes between the singlet ground state and the quencher in its original spin state. Factors influencing the efficiencies of various quenchers would be (1) the statistics of spin combination in complex formation,[9] (2) the extent of spin–spin coupling between triplet and quencher in the complex, and (3) the lifetime of the complex relative to its nonradiative decay time. Porter and Wright attributed the relatively weak quenching activity of rare earth cations to the weakness of coupling between the spin of the triplet and the spins of the metallic ions because of large shielding of the unpaired f-electrons from the external environment.

Linschitz and co-workers[3,5,7] have recently shown that other factors are involved. Using copper(II) chloride in pyridine solution, they have demonstrated the existence of large ligand effects on quencher activity. A saturated ligand, ethylenediamine, decreased reactivity, and an unsaturated ligand, *o*-phenanthroline, increased reactivity in quenching of anthracene triplets. They concluded that the properties of the ligand as "electron conductors" were important in establishing contact between the spin of the triplet and that of the metal. They have also introduced the notion that charge-transfer interaction may be an important factor in prolonging the lifetime of the complex and increasing the rate of decay directly from the excited complex to its ground state.

We have followed the same line of thought in interpreting our own early studies of the quenching of benzo-

(1) Part XIX is J. Bradshaw and G. S. Hammond, *J. Am. Chem Soc.*, **85**, 3953 (1963).

(2) G. Porter and M. P. Wright, *J. chim. phys.*, **55**, 705 (1958).

(3) H. Linschitz and K. Sarkanen, *J. Am. Chem. Soc.*, **80**, 4826 (1958).

(4) G. Porter and M. P. Wright, *Discussions Faraday Soc.*, **27**, 18 (1959).

(5) H. Linschitz and L. Pekkarieneu, *J. Am. Chem. Soc.*, **82**, 2411 (1960).

(6) W. M. Moore, G. S. Hammond, and R. P. Foss, *J. Chem. Phys.*, **32**, 1594 (1960); *J. Am. Chem. Soc.*, **83**, 2789 (1961).

(7) J. A. Bell and H. Linschitz, *ibid.*, **85**, 528 (1963).

(8) H. McConnell, *J. Chem. Phys.*, **20**, 1043 (1952).

(9) The triplet has $S = 1$ and the quencher has $S = x$ with $x > 0$. Only those complexes having $S = x$ can decay with spin conservation to give the quenched product.

phenone triplets[6] by metallic compounds. However, one rather sticky point was ignored. The reactivity of tris(dipivaloylmethanato)iron(III), $Fe(DPM)_3$, as a quencher was found to be similar to that of oxygen. This relationship is in strong contrast to the results of Porter and Wright,[4] who found that solvated ferric ion was two orders of magnitude less active than oxygen or nitric oxide. The high reactivity of $Fe(DPM)_3$ could be attributed to a ligand effect of the type discussed by Linschitz, or it could indicate that a different mechanism of quenching is involved. The work reported in this paper was undertaken in an attempt to elucidate the problem further.

Results

The method of study was observation of the effects of quenchers on the reduction of benzophenone by benzhydrol.

$$\underset{\text{B}}{(C_6H_5)_2CO} + \underset{BH_2}{(C_6H_5)CHOH} \xrightarrow{h\nu} 2(C_6H_5)_2C(OH)C(OH)(C_6H_5)_2 \quad (1)$$
$$\text{HB–BH}$$

The reactions were monitored by spectrophotometric analysis for residual benzophenone. Light from a high-pressure mercury lamp was filtered to exclude virtually all emission other than the 3600-Å. band. The mechanism[6] of the reduction is believed to be given by eq. 2–9.

$$B \xrightarrow{h\nu} B_{s_1} \quad (2)$$

$$B_{s_1} \xrightarrow{k_{is}} B_{t_1} \quad (3)$$

$$B_{s_1} \xrightarrow{k_{ds}} B_{s_0} + E \quad (4)$$

$$B_{s_1} + Q \xrightarrow{k_{sq}} B_{s_0} + Q^* \quad (5)$$

$$B_{t_1} + BH_2 \xrightarrow{k_r} 2BH \quad (6)$$

$$B_{t_1} \xrightarrow{k_d} B_{s_0} + E \quad (7)$$

$$B_{t_1} + Q \xrightarrow{k_q} B_{s_0} + Q^* \quad (8)$$

$$2BH \xrightarrow{k_c} HB\text{–}BH \quad (9)$$

Quenching of singlets, reaction 5, is included although evidence for the process is discussed in the accompanying paper.[10] Reaction 7 represents all first-order decay processes of triplets. Reaction 8 is formulated as an energy transfer although it may include catalytic quenching mechanism such as that discussed in the Introduction.

Actinometry. Actinometric procedures have been revised so as to minimize dependence of the results on presumptions concerning the efficiency of intersystem crossing, reaction 3. Equation 10 has previously been used for analysis of experimental data.

$$\frac{1}{\Phi} = \frac{1}{a} + \frac{k_d}{ak_r[BH_2]} \quad (10)$$

where Φ is the quantum yield for disappearance of either B or BH_2, a is the quantum yield of triplets, and $k_{is}/k_{is} + k_{ds} + k_{sq}[Q]$.

A different equation can be developed as follows by making the steady-state approximation for the concentration of B triplets.

$$-\frac{d[BH_2]}{dt} = \frac{k_r[BH_2]aI_{abs}}{k_d + k_r[BH_2]}$$

$$aI_{abs}t = [BH_2]_0 - [BH_2]_f + \frac{k_d}{k_r}\ln\frac{[BH_2]_0}{[BH_2]_f} \quad (11)$$

where I_{abs} is the light absorbed in einsteins $l.^{-1}$ $sec.^{-1}$, t is the irradiation time, $[BH_2]_0$ is the initial concentration of BH_2, and $[BH_2]_f$ is the final concentration of BH_2.

Data from pairs of runs can be used to determine both aI_{abs}, the *effective light intensity*, and the ratio k_d/k_r. Solutions were obtained by making the substitutions

$$z = \frac{k_d}{k_r} \quad (12)$$

$$b = 2.303 \log\frac{[BH_2]_0}{[BH_2]_f} \quad (13)$$

$$c = [BH_2]_0 - [BH_2]_f \quad (14)$$

Equation 11 may be rewritten

$$aI_{abs} - \frac{c}{t} = z\frac{b}{t} \quad (15)$$

Table I gives data for a group of four samples which were irradiated simultaneously. Figure 1 shows a plot of c/t against b/t. The line drawn through the figure is the best straight line calculated by the method of least squares. The calculated best value of k_d/k_r is 0.0326 mole $l.^{-1}$ and the calculated value of aI_{abs} is 3.19×10^{-6} einstein $l.^{-1}$ $sec.^{-1}$.[11] Although the *effective light intensity* may be used directly for calculation of the numbers of interest in the experiment with quenchers, it is of interest to see how the results compare with measurements of the intensity determined by the use of the uranyl oxalate actinometer.[12] The intensity of the

(10) R. P. Foss, D. O. Cowan, and G. S. Hammond, *J. Phys. Chem.*, **68**, 3747 (1964).

(11) Since 4-ml. samples were irradiated, the actual intensity of the beam was considerably smaller than this value.

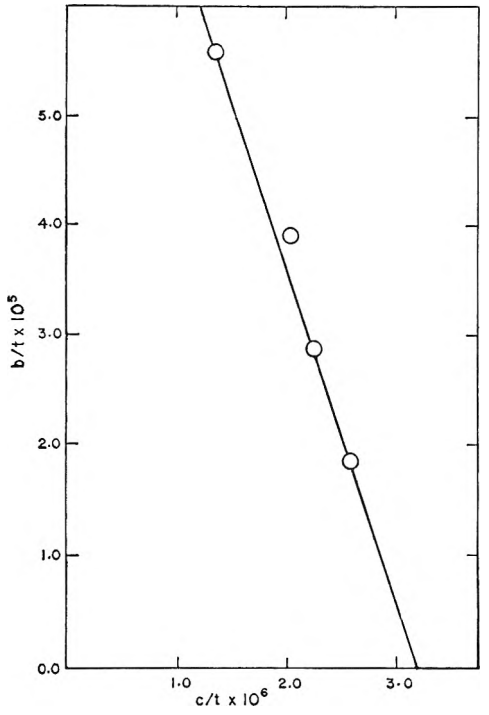

Figure 1. Plot of eq. 15.

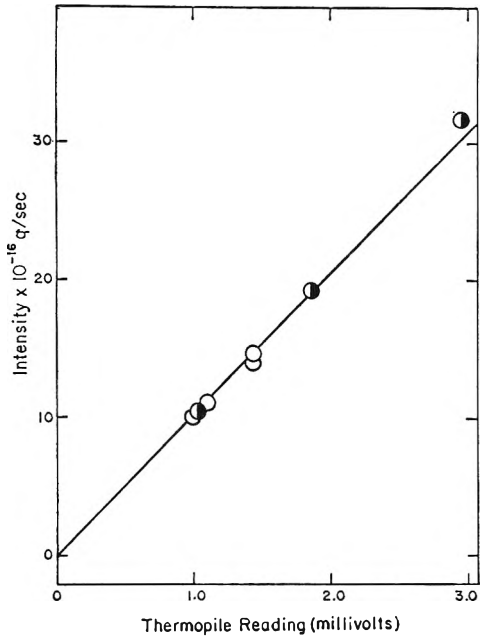

Figure 2. Correlation of actinometric measurements with thermopile readings: O, benzophenone–benzhydrol; ◑, uranyl oxalate.

lamps decreased with time, and data comparable to those shown in Table I were collected at various times and compared with the values of the absolute intensity calculated from results obtained with the uranyl oxalate actinometer. The comparison involves some uncertainty for two reasons: (1) the light transmitted by the filter system covers a range of values of quantum yields as determined by Leighton and Forbes and (2) if the concentrations recommended for uranyl oxalate actinometry are used, only about 10% of the incident light is absorbed, necessitating imprecise corrections for losses due to reflection from the cell faces and other distortions. In Fig. 2 the values of aI_{abs} determined with the benzophenone–benzhydrol system are plotted against thermopile readings; the values of absolute intensity calculated from measurements with uranyl oxalate are plotted in the same figure using a value of 0.53 for the quantum yield of uranyl oxalate decomposition. The fact that the two values seem to lie on the same line indicates that the value of a is indistinguishable from unity. Apparently nearly all excited singlets of benzophenone undergo intersystem crossing to triplets.

Table I: Data from Actinometric Measurements

Sample no.	t, sec.	$[BH_2]_0$, mole l.$^{-1}$	$[BH_2]_f$, mole l.$^{-1}$
1	7200	0.1500	0.1314
2	7200	0.0600	0.0453
3	8000	0.0300	0.0192
4	9000	0.0900	0.0696

Quenching Experiments. Quenchers are substances which decrease the quantum yield of the photoreduction of benzophenone by benzhydrol. Inclusion of reaction 8, quenching of benzophenone triplets, leads to the modification of eq. 10 to 16.

$$\frac{1}{\Phi} = \frac{1}{a} + \frac{k_d + k_q[Q]}{ak_r[BH_2]} \qquad (16)$$

The "true" quantum yields are replaced by *effective quantum yields*, Φ', defined in eq. 17.

$$\Phi' = \frac{\Phi}{a} \qquad (17)$$

Substitution in eq. 16 gives eq. 18.

$$\frac{1}{\Phi'} = 1 + \frac{k_d}{k_r[BH_2]_{av}} + \frac{k_q[Q]}{k_r[BH_2]_{av}} \qquad (18)$$

The *effective quantum yields* are calculated using the values of aI_{abs} determined from blank experiments run in parallel with the experiments with quenchers. In fitting data, the value of $[BH_2]$ was considered to be

(12) P. A. Leighton and G. S. Forbes, *J. Am. Chem. Soc.*, 52, 3139 (1930).

Table II: Experimental Data Concerning the Quenching of Triplet Benzophenone by Transition Metal Chelates[a,b]

No.	Quencher[c]	Quencher concn., $[Q] \times 10^4$	$\frac{1}{\Phi'}$	$\frac{1}{\Phi'} - \frac{0.033}{[BH_2]_{av}}$	$\frac{[Q] \times 10^4}{[BH_2]}$	$[\Phi_2CHOH]_{av}$, mole/l.
1	$Fe(DPM)_3$	1.107	1.594	1.120	15.91	0.080
2	$Fe(DPM)_3$	1.165	1.890	1.236	23.07	0.060
3	$Fe(DPM)_3$	1.132	1.500	1.147	12.11	0.100
4	$Fe(DPM)_3$	1.132	1.634	1.174	15.80	0.080
5	$Cr(DPM)_3$	1.329	1.579	1.104	19.12	0.080
6	$Cr(DPM)_3$	1.329	1.769	1.104	26.66	0.060
7	$Cr(DPM)_3$	1.124	1.560	1.096	15.80	0.080
8	$Cr(DPM)_3$	1.130	1.420	1.019	13.73	0.090
9	$Fe(AA)_3$	1.020	2.225	1.770	14.06	0.080
10	$Fe(AA)_3$	1.700	2.298	1.951	17.84	0.100
11	$Fe(AA)_3$	1.700	3.253	2.662	30.47	0.060
12	$Fe(AA)_3$	1.000	1.950	1.505	10.44	0.100
13	$Cr(AA)_3$	1.529	2.302	1.849	21.01	0.080
14	$Cr(AA)_3$	1.529	2.601	1.980	28.79	0.060
15	$Cr(AA)_3$	1.349	1.904	1.553	14.35	0.100
16	$Cr(AA)_3$	1.349	2.558	1.956	24.62	0.060
17	$Co(DPM)_3$	1.00	1.243	1.008	7.110	0.150
18	$Co(DPM)_3$	0.987	1.530	0.936	17.78	0.060
19	$Co(DPM)_3$	1.033	1.440	0.983	14.84	0.080
20	$Co(DPM)_3$	2.066	1.420	0.958	28.90	0.080
21	$Co(AA)_3$	1.222	1.500	1.035	17.21	0.080
22	$Co(AA)_3$	2.444	1.640	1.188	33.50	0.080
23	$Co(AA)_3$	1.222	1.418	1.066	13.18	0.100
24	$Al(DPM)_3$	1.014	1.441	0.970	14.45	0.080
25	$Al(DPM)_3$	2.028	1.533	1.070	28.50	0.080
26	$Al(DPM)_3$	1.014	1.350	0.998	13.18	0.090
27	$Al(AA)_3$	1.454	1.698	0.984	24.16	0.080
28	$Al(AA)_3$	1.454	3.395	0.990	47.35	0.040
29	$Al(AA)_3$	1.454	1.354	1.002	13.20	0.120
30	$Fe(MAA)_3$	1.190	2.385	1.933	16.29	0.08
31	$Fe(MAA)_3$	1.190	2.805	2.189	22.20	0.06
32	$Fe(MAA)_3$	1.448	2.398	2.054	15.08	0.10
33	$Fe(MAA)_3$	1.122	1.979	1.520	15.60	0.08
34	$Fe(AC)_3$	1.057	2.960	2.516	14.20	0.08
35	$Fe(AC)_3$	1.057	3.590	2.990	19.21	0.06
36	$Fe(AC)_3$	0.547	1.653	1.310	5.68	0.100
37	$Fe(AC)_3$	1.093	2.140	1.801	11.25	0.100
38	$Fe(AC)_3$	1.640	2.520	2.181	16.80	0.100
39	$Gd(DPM)_3$	1.028	1.440	1.039	12.49	0.09
40	$La(DPM)_3$	1.087	2.326	1.026	42.83	0.04
41	$La(DPM)_3$	1.00	2.500	1.206	39.20	0.03
42	$La(DPM)_3$	2.00	1.462	1.116	21.00	0.10
43	$La(DPM)_3$	2.00	1.772	1.040	44.34	0.05
44	$La(DPM)_3$	0.913	1.500	1.114	10.67	0.10
45	$Er(DPM)_3$	1.085	1.433	1.032	13.18	0.09
46	$Er(DPM)_3$	1.00	1.430	1.027	12.20	0.09
47	$Er(DPM)_3$	1.00	2.430	1.136	39.20	0.03
48	$Mn(DPM)_3$	1.00	1.690	1.071	18.75	0.06
49	$Mn(DPM)_3$	1.00	1.418	1.015	12.20	0.09

Table II (*Continued*)

No.	Quencher[c]	Quencher concn., $[Q] \times 10^4$	$\frac{1}{\Phi'}$	$\frac{1}{\Phi'} - \frac{0.033}{[BH_2]_{av}}$	$\frac{[Q] \times 10^4}{[BH_2]}$	$[\Phi_2CHOH]_{av}$, mole/l.
50	$Co(DPM)_2$	1.00	1.720	1.323	11.72	0.09
51	$Co(DPM)_2$	1.07	2.190	1.606	18.94	0.06
52	$Co(DPM)_2$	1.00	1.718	1.322	12.00	0.09
53	$Ni(DPM)_2$	1.00	2.063	1.458	18.35	0.06
54	$Ni(DPM)_2$	2.00	1.995	1.598	24.06	0.09
55	$Ni(DPM)_2$	2.00	2.374	1.765	36.90	0.06
56	$Ni(DPM)_2$	1.00	1.700	1.309	11.85	0.09
57	$Ni(DPM)_2$	1.00	1.637	1.288	10.57	0.100
58	$Ni(DPM)_2$	1.00	2.286	1.560	22.00	0.05
59	$Cu(DPM)_2$	1.116	1.610	1.225	13.01	0.09
60	$Cu(DPM)_2$	1.163	1.445	1.098	12.25	0.10
61	$FeCl_3$	1.231	1.694	0.972	13.97	0.10[d]
62	$FeCl_3$	1.231	2.327	0.890	28.73	0.050[d]
63	$FeCl_3$	1.231	1.956	1.027	18.55	0.075[d]
64	$Fe(DPM)_3$	1.041	1.937	1.250	11.62	0.10[d]
65	$Fe(DPM)_3$	1.041	2.400	1.493	15.32	0.075[d]
66	$Fe(DPM)_3$	1.041	2.869	1.476	23.55	0.050[d]
67	HDPM	1.876	1.587	1.125	26.24	0.080
68	HDPM	4.690	1.606	1.145	65.50	0.080
69	HAA	2.080	1.524	1.060	29.23	0.080
70	HAA	4.160	1.650	1.185	57.94	0.080
71	HDPM	1.295	2.326	1.881	17.45	0.080
72	HDPM	2.590	3.457	3.030	33.46	0.080
73	HAC	1.601	2.091	1.643	21.77	0.080
74	HAC	3.203	2.846	2.407	42.56	0.080
75	HMAA	1.754	1.895	1.350	23.70	0.080
76	HMAA	3.509	2.028	1.578	87.84	0.080

[a] The initial benzophenone concentration in all of the experiments was 0.10 *M*. [b] The solvent used for all experiments listed here was benzene unless indicated otherwise. [c] DPM is dipivaloylmethanate; AA is acetylacetonate; MAA is 3-methylacetylacetonate; AC is 2-acetylcyclohexanonate. [d] The solvent was *t*-butyl alcohol.

equal to the average concentration of benzhydrol $([BH_2]_0 + [BH_2]_f)/2$. This approximation is reasonably accurate if the reaction is not carried to high conversion. Since the value of k_d/k_r is known, the quantity $(1/\Phi') - (0.033/[BH_2]_{av})$ was plotted against $[Q]/[BH_2]_{av}$. Treatment of data in this manner permits direct correlation of results obtained from runs in which both $[BH_2]$ and [Q] are varied. Good fits to the expected linear relationship were obtained except for experiments with dibenzoylmethanato chelates. The slopes of the straight lines are equal to the relative quenching constants, k_q/k_r. Figure 3 shows the plot of data obtained in a typical series of experiments with tris(acetylacetanato)iron(III) and tris(dipivaloylmethanato)iron(III). Table II contains data for all quenching experiments and Table III contains a summary of the values of k_q/k_r derived from the data.

No real significance can be attached to values of k_q/k_r less than 30. All of the good quenchers underwent photodecomposition at rates which, however, varied considerably from case to case. Values derived from runs in which decomposition was extensive are indicated in Table III as approximate ($\sim$) or lower limits ($>$).

Discussion

Triplet Quenching by Chelates. The results shown in Table III show two important facts: first, the quenching efficiency of chelates does not show any significant correlation with their magnetic properties; second, the nature of both the central metal atoms and the ligands is of importance in determination of the activity. The first point is illustrated by the fact that $Ni(DPM)_2$, which is known to be diamagnetic,[13] is an excellent quencher. In contrast, $Cr(DPM)_3$, which probably has a

Table III: Relative Quenching Constants for β-Diketone Chelates

Quencher[a]	k_q/k_r, moles l.$^{-1}$
$Fe(AA)_3$	540
$Fe(DPM)_3$	100
$Fe(MAA)_3$	~550
$Fe(AC)_3$	~860
$Cr(AA)_3$	380
$Cr(DPM)_3$	45
$Co(AA)_3$	47
$Co(DPM)_3$	0
$Co(DPM)_2$	296
$Mn(DPM)_3$	>32
$La(DPM)_3$	~28
$Er(DPM)_3$	30
$Gd(DPM)_3$	31
$Ni(DPM)_2$	246
$Co(DPM)_2$	>130
HDBM	577
HAC	320
HMAA	128
HDPM	27
HAA	27
$FeCl_3$ (in t-C_4H_9OH)	0

[a] AA = acetylacetonate; DPM = dipivaloylmethanate; MAA = 3-methylacetylacetonate; AC = 2-acetylcyclohexanonate; DBM = dibenzoylmethanate.

spin of $^3/_2$, is not highly reactive. Actually, all of our results contrast with those reported by Porter and Wright,[2] who found that paramagnetic metal ions of the first transition series were two orders of magnitude less reactive than oxygen and nitrous oxide as quenchers for anthracene triplets. A spread of reactivity of this order of magnitude would be undetectable by our techniques.[14] Further evidence is provided by the fact that a solution of ferric chloride in t-butyl alcohol has no detectable activity. Obviously the presence of an unsaturated ligand is required for efficient quenching activity.

There are two reasonable models to account for the ligand effects on quenching activity. First, one can merely say that triplet benzophenone forms a complex with the quencher and that internal conversion occurs within the lifetime of the complex so that it dissociates to give back ground-state benzophenone. In such a model it is implied that the excitation has been converted to thermal energy during the lifetime of the complex. The second model describes the excitation as becoming localized in the quencher *as electronic excitation* before thermalization, *i.e.*, quenching involves transfer of electronic energy. The two mechanisms are not easily distinguished experimentally and may actually

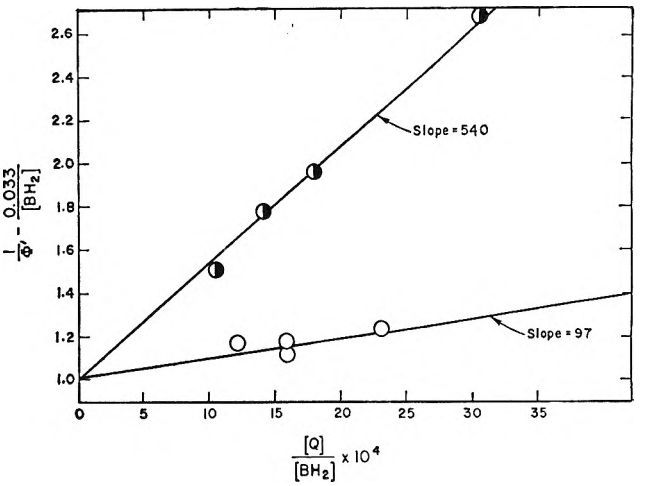

Figure 3. Quenching by tris(acetylacetonato)iron(III), ◑, and tris(dipivaloylmethanato)iron(III), ○.

represent extremes in a mechanistic continuum. Since many of the chelates undergo decomposition during the experiments, it is certain that large amounts of energy must be concentrated in them at times. However, the quantum yields for the decomposition reactions are very small in all cases so decomposition may not be relevant to the principal quenching processes.

The largest values of k_q/k_r found for chelates are of the same order of magnitude (700–800) as have been observed with organic compounds believed to quench benzophenone by energy transfer.[15] In the latter cases, quenching is believed to be diffusion controlled.[16,17] Consequently, we conclude that quenching must occur on nearly every collision with many of the chelate compounds. However, the precision of the measurements is sufficient to guarantee that quenching efficiencies are not really constant. The data suggest that two factors related to the structures of the ligands may be important. First, the iron(III) chelates of 2-acetylcyclohexanone and 3-methylacetylacetone appear to be very reactive although results with these compounds are somewhat imprecise because of photodecomposition. Since both the parent enols are good quenchers, we would anticipate that these chelates should be very reactive; they obviously should be capable of functioning by the energy-transfer mecha-

(13) F. A. Cotton and J. P. Fackler, *J. Am. Chem. Soc.*, **83**, 2818 (1961).

(14) It is not feasible to use high concentrations of quenchers because the results would be complicated by internal filtering effects.

(15) G. S. Hammond and P. A. Leermakers, *J. Phys. Chem.*, **66**, 1148 (1962).

(16) G. Porter and F. Wilkinson, *Proc. Roy. Soc.* (London), **A264**, 1 (1961).

(17) K. Sandros and H. L. J. Bäckstrom, *Acta Chem. Scand.*, **16**, 958 (1962).

nism. Since acetylacetone and dipivaloylmethane are not themselves very efficient quenchers, the energy-transfer mechanism is not necessarily applicable to their chelates. However, it is possible that interaction with the metal would lower the energy of transitions essentially localized in the ligands sufficiently to allow transfer to occur. Furthermore, it is always conceivable that transfer may cause excitation of ligand field transitions in the metal. The difference between the reactivity of dipivaloylmethanates and acetylacetonates may be due to steric shielding of the unsaturated ligands by the *t*-butyl groups of the former. If so, this is the first observation of such an effect to our knowledge.

Comparison of compounds containing the same ligands, but different metal atoms, are also interesting, but we will refrain from interpretation at this time since further studies of the problem will hopefully produce a sounder basis for speculation. We will only note that consideration of spin statistical factors does not alone provide entirely satisfactory answers. Pertinent examples are $Co(DPM)_3$ and $Ni(DPM)_2$, which have singlet ground states but are less efficient as quenchers than analogous high-spin compounds.

Experimental

Benzophenone. Benzophenone (Matheson Coleman and Bell, reagent grade) was recrystallized from a mixture of hot benzene and ligroin. The plates melted sharply at 50°.

Benzhydrol. Benzhydrol (Matheson Coleman and Bell, reagent grade) was recrystallized twice from a mixture of hot benzene and ligroin. Slow cooling yielded colorless, fine, light needles, m.p. 68°.

Benzene. Benzene (Mallinckrodt, analytic reagent grade) was used without further purification after it was found that there was no effect upon experimental results after the benzene had been subjected to further purification. The purification consisted of washing the benzene with concentrated sulfuric acid, then distilling it over sodium. No darkening was observed upon addition of sulfuric acid.

t-Butyl Alcohol. *t*-Butyl alcohol (Matheson Coleman and Bell, reagent grade) was redistilled; the fraction boiling from 82 to 83° was collected for use.

3-Methyl-2,4-pentanedione. 3-Methyl-2,4-pentanedione was prepared by the method of Hauser and Adams.[18] Acetic anhydride was treated with 2-butanone using boron trifluoride as a catalyst. The product was distilled at 30 mm., and the fraction boiling in the range between 73 and 77° was collected for further use.

2-Acetylcyclohexanone. 2-Acetylcyclohexanone (Eastman Kodak, White Label) was used directly without further purification.

Dibenzoylmethane. Dibenzoylmethane was obtained from Dr. Karl Kopecky. The compound melted at 79° and was used without further purification.

Chelates. Ferric dipivaloylmethide, chromium dipivaloylmethide, cobalt(III) dipivaloylmethide, aluminum dipivaloylmethide, ferric acetylacetonate, chromium acetylacetonate, cobalt acetylacetonate, aluminum acetylacetonate, cobalt(II) dipivaloylmethide, copper dipivaloylmethide, nickel(II) dipivaloylmethide, manganese dipivaloylmethide, lanthanum dipivaloylmethide, erbium dipivaloylmethide, and gadolinium dipivaloylmethide were obtained pure from Dr. Chin-Hua Wu. The details of the synthesis of these chelates are given elsewhere.[19] The chelates were freshly sublimed before use in quenching experiments.

Tris(acetylacetonato)iron(III), tris(acetylacetonato)chromium(III), tris(2-acetylcyclohexanato)iron(III), and tris(2-acetylcyclohexanato)chromium(III) were prepared using the following general procedure. This method was also used for preparation of the previously described chelates and found equally effective for all. Higher yields of the chromium chelates were generally obtained than are normally obtained by other procedures.

Metal chloride hexahydrate was dissolved in N,N-dimethylformamide. A slight excess of ligand was dissolved in additional N,N-dimethylformamide, and the two solutions were mixed. Excess sodium bicarbonate was added, and the flask was swirled until the mixture became homogeneous. The mixture was placed on a steam bath for a few minutes, removed, and allowed to stand until cool. Benzene was added and the resulting solution was extracted with water. A small amount of ethyl ether had to be added in some instances to assist in the separation of the aqueous and organic layers. The organic layer containing the chelate was dried over anhydrous calcium chloride and evaporated to dryness. The crystalline residue was recrystallized twice from a benzene–ligroin mixture and sublimed if the melting point was sufficiently low. The new compounds are listed below.

$Fe(AC)_3$, m.p. 150°. *Anal.* Calcd. for $C_{36}H_{33}O_6Fe$: C, 61.03; H, 6.99. Found: C, 61.32; H, 6.99.

$Fe(MAA)_3$, m.p. 145–148°. *Anal.* Calcd. for $C_{18}H_{27}O_6Fe$: C, 54.70; H, 6.84. Found: C, 54.40; H, 6.75.

(18) C. Hauser and J. Adams, *J. Am. Chem. Soc.*, 66, 347 (1944).

(19) G. S. Hammond, D. C. Nonhebel, and C.-H. S. Wu, *Inorg. Chem.*, 2, 73 (1963).

$Cr(AC)_3$, m.p. 187°. *Anal.* Calcd. for $C_{36}H_{33}O_6Cr$: C, 55.1; H, 6.89. Found: C, 61.00; H, 7.38.

$Cr(MAA)_3$, m.p. 156° *Anal.* Calcd. for $C_{18}H_{27}O_6Cr$: C, 55.26; H, 6.90. Found: C, 55.47; H, 6.80.

Apparatus. The apparatus used for these experiments has been described previously.[6] Two types of cells were used in this investigation. Early experiments were carried out in quartz cells of Type I which have been described in detail.[6] They were mounted in the apparatus by means of a cell holder set in a V-block and fitted with 25.52-cm.^{2} diaphragm to ensure a constant, incident light beam cross section. The second type of cell was formed by sealing a 14/38 ground glass joint to the top of a 15-mm. diameter Pyrex test tube. The test tubes were matched for diameter and light transmission before use.

The filter system that was used in this work consisted of a combination of Corning glass filters 0-52 and 7-60. This filter combination transmitted a narrow spectral band with a maximum transmission at 3700 Å. and a half-height width of 300 Å. This completely eliminated the 3130-Å. mercury line and passed less than 2% of the 3450- and 4050-Å. lines. The transmission at the maximum was 42%.

Procedure. All quenching experiments were conducted by the same general procedure. Stock solutions of benzophenone, benzhydrol, and quencher were prepared. Samples consisting of the proper amount of each stock solution were placed in a flask and diluted with solvent. The cells were filled and degassed three times to 1 μ using a freeze–thaw cycle. After the final degassing cycle, the cells were sealed by torch. The large quartz cells (Type I) held 75 ml. of solution. The small quartz cells (Type II) and the Pyrex tubes (Type III) each held 4 ml. of solution. The smaller cells were filled with an automatic syringe set for the required volume. Precision in filling cells by this technique was found to be better than one part per thousand.

One large cell or four small cells could be placed in the light beam for each irradiation period. In every case in which small cells were used, one of the four contained only benzophenone and benzhydrol and was used for monitoring the light intensity. In all instances the initial benzophenone and benzhydrol concentrations in each of the four cells irradiated simultaneously were the same. In most cases, at regular intervals of 500 to 600 sec. during a run, the cells were mixed and rotated in their positions so that each cell spent an identical period of time in each cell location in the light beam. This ensured an over-all constant light intensity on each cell and sufficient mixing of the sample during the irradiation. It was found, however that the cross-section intensity of the light beam was very constant.

The amount of benzophenone reacted was measured spectrophotometrically by dilution and measurement of absorption at five wave lengths from 3450 to 3650 Å. The quantity of chelate destroyed during irradiation was determined by measuring the optical density of undiluted samples of irradiated and nonirradiated solutions, if possible, in regions where the chelate had a visible absorption not interfered with by benzophenone absorption. A Beckman DU and Cary Model 11 and Model 14 spectrophotometers were used for the measurements.

Acknowledgment. This study was supported by a grant from the Atomic Energy Commission. R. P. F. is also grateful to the California Research Corp. for a summer research stipend.

Mechanisms of Photoreactions in Solution. XXI.[1] Quenching of Excited Singlet States of Benzophenone

by Robert P. Foss, Dwaine O. Cowan, and George S. Hammond

Contribution No. 3080 from the Gates and Crellin Laboratories of Chemistry, California Institute of Technology, Pasadena, California *(Received February 14, 1964)*

Tris(dibenzoylmethanato)iron(III) and tris(dibenzoylmethanato)chromium(III) show exceptionally high reactivity as quenchers in the photoreduction of benzophenone by benzhydrol. The dependence of the effect on the concentrations of the quenchers suggests that, in addition to benzophenone triplets, excited singlet states of the ketone are deactivated by the chelates. Study of the effects of the two chelates on the benzophenone-sensitized isomerization confirms the singlet quenching. Singlet quenching occurs at lower concentrations than would have been predicted by approximate theories.

Introduction

Transfer of singlet electronic excitation in solution has been detected by observation of induced fluorescence.[2] Dexter[3] and Förster[4] have formulated a theory to account for the variation of transfer efficiency with concentration of acceptors. The theory has been criticized by Robinson and Frosch,[5] who have developed a theory that is more exact in principle but not readily amenable to quantitative calculations of an *ab initio* nature.

The work reported in this paper originated as part of a program to evaluate the relative reactivities of metal chelates as acceptors of triplet excitation.[1] The reactivity of tris(dibenzoylmethanato)iron(III) and tris(dibenzoylmethanato)chromium(III) appeared to be anomalously high; more detailed study indicated that the chelates are capable of intercepting excited singlets of benzophenone before they undergo intersystem crossing.

Results

The mechanism for the photoreduction reaction was presented in the accompanying paper.[1] The same rate constants are used in this report. Measurements made in the presence of the iron(III) and chromium(III) chelates of dibenzoylmethane, **1** and **2**, respectively, showed that these compounds are remarkably efficient quenchers of the photoreduction reaction. The data are summarized in Table I.

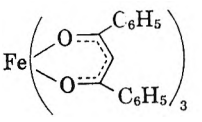

1
Tris(dibenzoylmethanato)-iron(III)

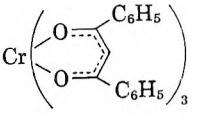

2
Tris(dibenzoylmethanato)-chromium(III)

Attempts to fit the data to eq. 18 of the previous paper gave widely scattered results as is shown by Fig. 1. The straight lines drawn arbitrarily in the vicinity of the various experimental points have slopes several times larger than any encountered in other studies of quenchers for excited states of benzophenone. The values of k_q/k_r calculated on the basis of the best slopes are 3400 for $Fe(DBM)_3$ and 1520 for $Cr(DBM)_3$. A large number of organic quenchers[6] have values falling between 580 and 650. This level of activity has

(1) Part XX is G. S. Hammond and R. P. Foss, *J. Phys. Chem.*, **68**, 3739 (1964).

(2) See ref. 4 for leading references on this subject.

(3) D. L. Dexter, *J. Chem. Phys.*, **21**, 836 (1953).

(4) Th. Förster, *Discussions Faraday Soc.*, **27**, 7 (1959).

(5) G. W. Robinson and R. P. Frosch, *J. Chem. Phys.*, **38**, 1187 (1963).

(6) More than 70 compounds having quenching constants falling between these limits have been studied.[7] Only azulene has a higher value, ~1000. Note that re-evaluation of data for the quantum yields in the absence of quenchers leads to slightly lower values than were previously reported.[8]

(7) T. D. Walsh, unpublished results.

(8) G. S. Hammond and P. A. Leermakers, *J. Phys. Chem.*, **66**, 1144 (1962).

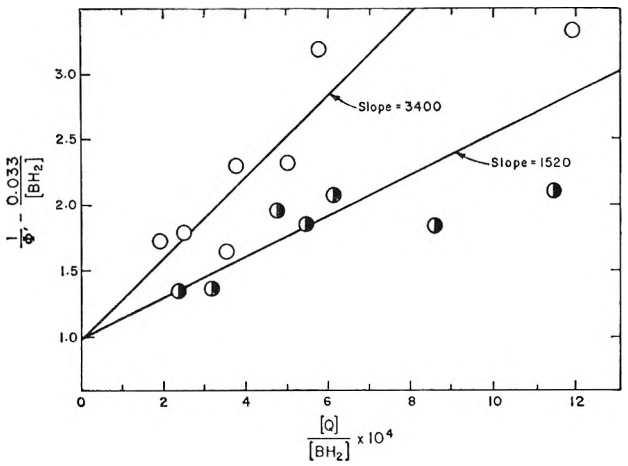

Figure 1. Quenching of the photoreduction of benzophenone by benzhydrol in benzene solution: O, $Fe(DBM)_3$; ◑, $Cr(DBM)_3$.

been associated with diffusion-controlled quenching. The implication is strong that the two chelates in question either quench benzophenone triplets from positions more remote than nearest neighbor sites in solution or that some other deactivation mechanism is operative. Although the former possibility would be interesting, we favor the latter alternative.

Table I: Quenching of the Photoreaction of Benzophenone with Benzhydrol by Dibenzoylmethanates of Iron(III) and Chromium(III)[a]

Run no.	Quencher	$[Q] \times 10^5$	$1/\Phi$	$\frac{1}{[BH_2]_{av}}$[b]
77	$Fe(DBM)_3$	1.81	2.24	13.8
78	$Fe(DBM)_3$	2.72	2.75	13.4
79	$Fe(DBM)_3$	1.81	2.29	19.2
80	$Fe(DBM)_3$	2.72	2.94	18.6
81	$Fe(DBM)_3$	5.54	3.53	10.4
82	$Fe(DBM)_3$	5.54	4.04	21.5
83	$Fe(DBM)_3$	1.81	2.08	10.5
84	$Cr(DBM)_3$	4.52	2.55	13.6
85	$Cr(DBM)_3$	4.52	2.46	19.0
86	$Cr(DBM)_3$	2.26	1.70	10.4
87	$Cr(DBM)_3$	2.26	1.83	14.0
88	$Cr(DBM)_3$	5.15	2.21	10.6
89	$Cr(DBM)_3$	5.15	2.83	22.2
90	$Cr(DBM)_3$	4.52	2.31	10.5

[a] Initial concentration of benzophenone was 0.10 *M*; benzene was the solvent. [b] BH_2 is benzhydrol.

Closer scrutiny of the data suggests that the chelates function by two mechanisms, one that is directly competitive with attack on benzohydrol and one that is not. As is shown by Fig. 2 and 3, plots of $1/\Phi$ against $1/[BH_2]$ indicate that the maximum number of benzophenone triplets available for reaction with benzhydrol is an inverse function of the chelate concentrations. This suggests that the chelates are quenching excited singlets as well as triplets. The appropriate equation for description of this mechanism is

$$\frac{1}{\Phi} = \left(1 + \frac{k_{ds} + k_{sq}[Q]}{k_{is}}\right)\left(1 + \frac{k_d + k_q[Q]}{k_r[BH_2]}\right) \quad (1)$$

Plots of $1/\Phi$ against $[BH_2]$ should yield straight lines, for any given value of $[Q]$, with intercepts equal to $0.95 + k_{sq}[Q]/k_{is}$.[9,10] The slopes of the lines should increase with increasing $[Q]$ so no crossing, such as appears in Fig. 3, should occur. The data are obviously insufficient to establish thoroughly the law of eq. 1 but,

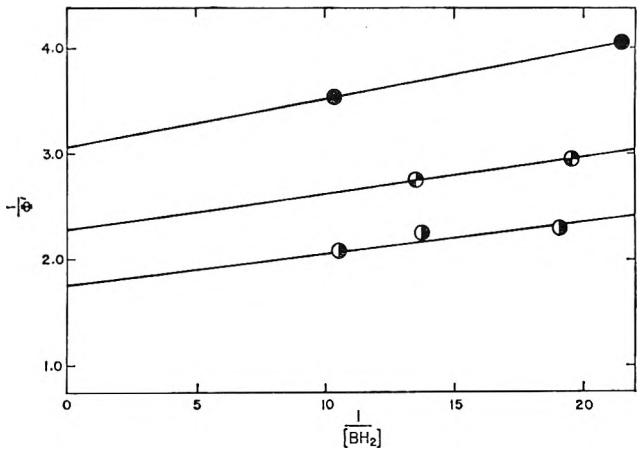

Figure 2. Quenching by $Fe(DBM)_3$: ●, 5.54×10^{-5} *M*; ◒, 2.72×10^{-5} *M*; ◑, 1.81×10^{-5} *M*.

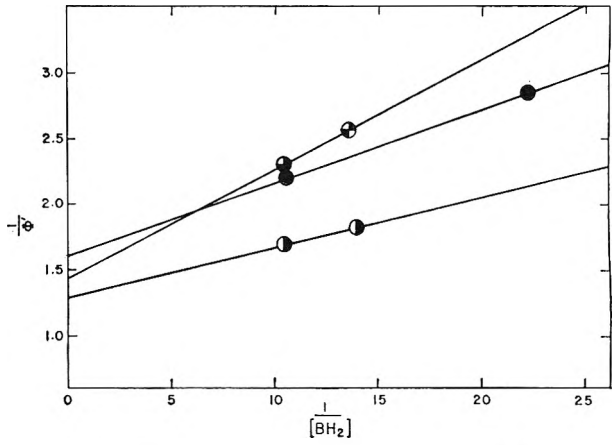

Figure 3. Quenching by $Cr(DBM)_3$: ●, 5.15×10^{-5} *M*; ◒, 4.52×10^{-5} *M*; ◑, 2.26×10^{-5} *M*.

(9) The intersystem crossing efficiency in the absence of quenchers is 0.95.[10]

(10) A. A. Lamola and D. O. Cowan, unpublished results.

with the single exception noted, semiquantitative agreement is observed. Because the chelates absorb the exciting light rather strongly, it is not possible to carry out experiments using higher concentrations of the chelates.[11] Consequently, confirmation of the singlet quenching mechanism was sought in another type of experiment.

It has been shown that benzophenone acts as a sensitizer for the *cis–trans* photoisomerization of the stilbenes.[12,13] Benzophenone is among the group of compounds that are classified as "high-energy" sensitizers.[14] With such a sensitizer the mechanism of isomerization can be simplified to the following scheme in which **T** represents the triplet group that decays to ground-state molecules.[13]

$$(C_6H_5)_2CO^{*(3)} + \textit{cis}\text{-}C_{14}H_{12} \xrightarrow{k_t} (C_6H_5)_2CO + \mathbf{T}$$

$$(C_6H_5)_2CO^{*(3)} + \textit{trans}\text{-}C_{14}H_{12} \xrightarrow{k_t} (C_6H_5)_2CO + \mathbf{T}$$

$$\mathbf{T} \xrightarrow{k_1} \textit{cis}\text{-}C_{14}H_{12}$$

$$\mathbf{T} \xrightarrow{k_2} \textit{trans}\text{-}C_{14}H_{12}$$

The ratio of the isomers present at the photostationary state is given by eq. 2

$$\frac{[cis]_s}{[trans]_s} = \frac{k_1}{k_2} \qquad (2)$$

Solutions initially containing *trans*-stilbene, benzophenone, and various iron(III) chelates were irradiated until stationary states were established. As is shown by the data in Table II, none of the chelates has any influence on the composition of the systems in the stationary states. The result clearly demonstrates that the chelates do not influence the decay of stilbene triplets; *i.e.*, **T** is not quenched by the chelates.

Table II: Stationary States of Photosensitized Isomerization of *trans*-Stilbene[a]

Quencher[b]	$[cis]_s/[trans]_s$
None	1.51
$Fe(DPM)_3$[c]	1.50
$Fe(DBM)_3$	1.52
$Fe(AA)_3$[d]	1.52

[a] Benzene solution; $[trans\text{-stilbene}]_0 = 0.05\ M$; [benzophenone] = 0.1 *M*. [b] [Quencher] = $2.2 \times 10^{-5}\ M$. [c] DPM = dipivaloylmethanate. [d] AA = acetylacetonate.

The relative rates of the *trans* → *cis* process were then measured in the presence of several chelates. Rates measured at low conversion are proportional to quantum yields. The results, which are entered in Table III, show that the quantum yields are lowered by $Fe(DBM)_3$ and $Cr(DBM)_3$ although tris(acetylacetonato)iron(III) and tris(dipivaloylmethanato)iron(III) have no significant effect on the rates of conversion.

Table III: Rates of *trans–cis* Reaction[a]

Quencher	% conversion — 400 min.	% conversion — 900 min.
None	1.70	3.30
$Fe(DPM)_3$	1.70	3.29
$Fe(AA)_3$	1.66	3.26
$Fe(DBM)_3$	1.58	2.99
$Cr(DBM)_3$	1.59	3.02

[a] Benzene solution; $[trans\text{-stilbene}]_0 = 0.05\ M$; [benzophenone] = 0.1 *M*.

Similar measurements were made with *cis*-stilbene as the substrate with varying amounts of $Cr(DBM)_3$ and $Fe(DBM)_3$. The results are summarized in Table IV in terms of per cent *trans*-stilbene produced during a fixed period of irradiation chosen to produce a sufficient amount of the *trans* isomer to be compatible with accurate analysis but still maintain the low conversion approximation. Since the photostationary states contain 40% *trans*-stilbene, conversions in the 6–7% range represent ~15% of the final conversion so correction for back-reaction can be neglected in a first approximation. The initial rates of conversion can be conveniently expressed in the form of eq. 3 if it is assumed that triplets are deactivated only by energy transfer to *cis*-stilbene. The assumption is reasonable in view of the high concentration of the substrate.[13] The data are plotted in Fig. 4.

$$\frac{1}{R_{c\to t}} = \frac{k_{is} + k_{ds}}{k_{is}\alpha} + \frac{k_{sq}[Q]}{k_{is}\alpha} \qquad (3)$$

(11) Throughout the study we have maintained concentrations of quenchers low enough to keep internal filtering effects very small. Unless pure monochromatic light is used for excitation, precise correction for competitive absorption cannot be made. Careful measurement of the absorption spectra of solutions of the chelates and benzophenone showed no departure from additivity of absorption. With concentrations of the order of those used in the experiments, only the long wave length tail of the benzophenone absorption could be studied, but the visible absorption bands of the chelates showed no perturbation at all from the rather high concentration of the chelates.

(12) G. S. Hammond and J. Saltiel, *J. Am. Chem. Soc.*, **85**, 2515 (1963).

(13) G. S. Hammond, *et al.*, *ibid.*, **86**, 3197 (1964).

(14) A high-energy sensitizer has a triplet excitation energy substantially above that required to excite either of the isomeric stilbenes to triplet states by Franck–Condon processes.

$$\alpha = \frac{I_{abs}k_2}{k_1 + k_2}$$

where I_{abs} is the intensity of light absorbed in einsteins $l.^{-1}$ $sec.^{-1}$.

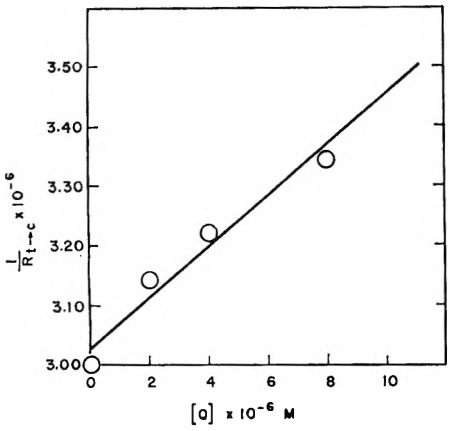

Figure 4. Plot of eq. 3.

Table IV: Rates of Sensitized Conversion of *cis*-Stilbene to *trans*-Stilbene in the Presence of Chelates

Chelate	[Chelate] × 10 M	% *trans*-stilbene	$1/R$, mole^{-1} l. sec. × 10^{-6}
None	...	6.67	3.00
Fe(DBM)$_3$	2.0	6.36	3.14
Fe(DBM)$_3$	4.0	6.20	3.22
Fe(DBM)$_3$	8.0	5.99	3.34
Cr(DBM)$_3$	2.0	6.41	3.12
Cr(DBM)$_3$	4.0	6.22	3.22
Cr(DBM)$_3$	8.0	6.00	3.34

Whether or not eq. 3 is really an appropriate form is a moot question. The data available are too few to serve as an appropriate test of the functional form of the dependence of the quenching effect on the concentrations of the chelates. It is clear that data could not be fitted any better by the equations of Förster[4] which require a second-order dependence of the rate of transfer on the concentrations of acceptor at low concentrations of the latter.

The results can only be reasonably accounted for by the hypothesis that Fe(DBM)$_3$ and Cr(DBM)$_3$ prevent formation of benzophenone triplets. There is very strong evidence that excitation transfer from benzophenone triplets to *trans*-stilbene is diffusion controlled.[13] Since the concentration of *trans*-stilbene is 2.3×10^3 times as large as the concentration of the chelates, the results would require that quenching rate constants be at least 100 times greater than the diffusion-controlled rate. This conclusion is rejected as clearly untenable. The alternative hypothesis that quenching of excited benzophenone singlets occurs is again much more attractive.

Comparison of the two studies provides information that could have been supplied by neither alone. In the photoreduction reaction, competition for triplets involves quenching and a relatively slow process, hydrogen abstraction from benzhydrol; in the isomerization reaction, triplet quenching is pitted against the diffusion-controlled process of energy transfer. Semiquantitative comparison shows that the inhibitory effect of 2×10^{-5} M Fe(DBM)$_3$ on the two reactions is very similar. The result is clearly incompatible with any mechanism which attributes quenching exclusively to reaction with triplets. If it were, a concentration sufficient to give a measurable effect on the rate of stilbene isomerization would, of necessity, essentially eliminate photoreduction completely. The implication that the quencher must intercept a precursor of the triplets easily accounts for the observations. The only likely candidate for a mechanism seems to be quenching of singlets.

Examples of very efficient singlet quenching have been observed before in studies of solutions of fluorescent dyes, and the results have usually been treated by eq. 4, the Förster equation.

$$k_0 = \frac{1}{\tau_s}\left(\frac{R_0}{R}\right)^6 \qquad (4)$$

where k_0 is the pseudo-first-order rate constant for decay of excited singlet donors by energy transfer; τ_s is the actual mean lifetime of the excited donor, taking into account all modes of deactivation; R_0 is the "critical" distance separating donor and acceptor, at which the rate of transfer becomes equal to the rates of unimolecular decay of the donor; in the present case, the principal competing process must be intersystem crossing; and R is the average distance between donor and acceptor in the system under observation. Although our data do not fit eq. 4, and probably should not (*vide infra*), we can make a comparison of the efficiency of the quenching process that we have observed with that studied by induced fluorescence. Equation 4 may be rewritten as eq. 5 for the case in which the principal unimolecular process is intersystem crossing.

$$k_{sq}[Q] = (k_{is} + k_{sq}[Q])\left(\frac{R_0}{R}\right)^6 \qquad (5)$$

The value of R_0 is easily estimated from a knowledge of the concentration of acceptor sufficient to deactivate

half the excited donor singlets by energy transfer. At this point $k_{is} = k_{sq}[Q]$, and eq. 5 becomes

$$\frac{1}{2} = \left(\frac{R_0}{R}\right)^6 \qquad (6)$$

Examination of the intercepts in Fig. 2 indicates that a concentration of $Fe(DBM)_3$ of $\sim 3 \times 10^{-5}$ M is sufficient to reduce the yield of benzophenone triplets by half. Assuming a random distribution of quencher molecules throughout the solution, this gives a value of 5.6×10^7 Å.^{3} as the average volume of the chelate molecules and makes the average distance from a benzophenone molecule to the nearest quencher molecule about 190 Å. Substitution of this value for R in eq. 6 gives a value of R_0 of 171 Å. Since the values of R_0 estimated from studies of induced fluorescence are of the order of 50–100 Å. as a maximum, the phenomena which we are observing are obviously of relatively high efficiency. Another tentative measure of efficiency may be obtained from the slope of the straight line drawn tentatively in Fig. 4. The indicated value of k_{sq}/k_{is} is 1.26×10^4 l. mole^{-1}. The rate constant for intersystem crossing is not known, but it must be 10^9 sec.$^{-1}$ or greater since most of the excited singlets of benzophenone become triplets, despite the fact that they are too short-lived to give detectable fluorescence. This leads to an estimated value of $>10^{11}$ l. mole^{-1} sec.$^{-1}$ for k_{sq}, a value far in excess of diffusion-controlled bimolecular reactions.

Experimental

Tris(dibenzoylmethanato)iron(III), $Fe(DBM)_3$, and tris(dibenzoylmethanato)chromium(III), $Cr(DBM)_3$, were prepared by the same procedure. The metallic chloride hexahydrate was dissolved in varying (not critical) volumes of 50:50 ethanol–water containing excess sodium acetate. A solution of dibenzoylmethane in the minimum volume of absolute ethanol was then added, and the chelates were precipitated. After a short period of warming on the steam bath, benzene was added and the layers were separated. The organic layer was dried, first with anhydrous calcium chloride and then with anhydrous magnesium sulfate, and the residual mixtures were then evaporated to dryness. The chelates could be recrystallized from petroleum ether. $Fe(DBM)_3$, dark red, m.p. 275°. *Anal.* Calcd. for $C_{45}H_{33}O_6Fe$: C, 74.47; H, 4.59. Found: C, 73.85; H, 4.50. $Cr(DBM)_3$, yellowish green, m.p. 316°. *Anal.* Calcd. for $C_{45}H_{33}O_6Cr$: C, 74.77; H, 4.60. Found: C, 74.20; H, 4.49.

Quenching of Reaction of Benzophenone with Benzhydrol. The apparatus has been described previously.[15] The procedure was the same as is described in the accompanying paper. The lines in the 3650-Å. region of the emission from the high-pressure mercury arc were isolated by a combination of Corning glass filters 0-52 and 7-60. The extinction coefficient of $Fe(DBM)_3$ at 3650 Å. is 4.04×10^3 times as large as that of benzophenone. Consequently, only 4% of the 3650-Å. radiation is absorbed by the chelate in a solution containing 0.1 M benzophenone and 10^{-5} M chelate. The ratio of the extinction coefficients of $Cr(DBM)_3$ and benzophenone is 3.97×10^3 at the same wave length. Although the internal filtering effect due to competitive absorption by the chelates is significant, it is insufficient to account for more than 20% of the measured quenching effects. Since the source is not monochromatic, it was necessary to investigate the possibility that competitive absorption by the chelates at the edges of the filter window could account for the measured effects. Figure 5 shows a comparison of the absorption by benzophenone and $Fe(DBM)_3$ with the profile of the exciting beam. A prism spectrograph was placed at the focus of the parabolic mirror which terminates the optical bench.

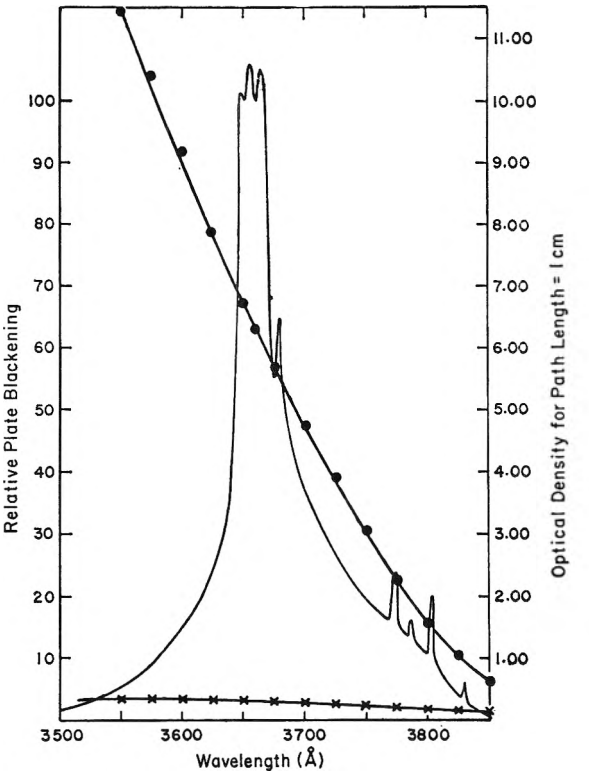

Figure 5. Comparison of absorption by $Fe(DBM)_3$ and benzophenone with light transmitted by the filter system.

(15) W. M. Moore, G. S. Hammond, and R. P. Foss, *J. Am. Chem. Soc.*, **83**, 2789 (1961).

The curve shown is a densitometer trace of the photographic plate. The response of the film is not perfectly linear, but the relative intensities indicated by the trace should be sufficiently accurate to guarantee that competitive absorption cannot account for the effect of the chelate on the photoreactions.

Acknowledgment. This work was supported by the U. S. Atomic Energy Commission.

Kinetic Order Determination in the Thermal Decomposition of Dimethylmercury

by K. B. Yerrick and M. E. Russell

Department of Chemistry, Michigan State University, East Lansing, Michigan *(Received February 28, 1964)*

A kinetic order determination was made of the thermal decomposition of dimethylmercury in the temperature range from 275 to 330°. The rate expression used to fit the experimental data is $-\mathrm{d(DMM)}/\mathrm{d}t = k_a\mathrm{(DMM)} + k_b\mathrm{(DMM)}^2$. The temperature dependence of the rate constants is $k_a = 2.6 \times 10^9 \exp(-39{,}000/RT)$ sec.$^{-1}$ and $k_b = 9.5 \times 10^{26} \exp(-71{,}000/RT)$ cc. mole^{-1} sec.$^{-1}$.

Introduction

The kinetics of the thermal decomposition of dimethylmercury has been examined by a number of workers.[1-14] However, the kinetic order of this decomposition in the vicinity of 300° has not been studied in much detail, and the few determinations which have been done conflict with one another. Laurie and Long[4] reported first-order kinetics in the temperature range 294 to 333° whereas Yeddanapalli, *et al.*,[3] in the temperature range 305 to 342°, found their data were best correlated by using a three-halves-order expression for the decomposition. The work of Russell and Bernstein[8] yielded first-order kinetics for the cyclopentane-inhibited reaction (290 to 375°), but they did not perform an order determination for the uninhibited reaction. Since the mechanisms proposed[3,5,8,11,14,15] for the reaction depend upon the order, it seemed necessary to re-examine the kinetics over a wider concentration range than had been used previously. Accordingly, the initial concentration was varied about 10-fold at each of five temperatures in the range 275 to 330°. The results of this study are consistent with neither first- nor three-halves-order kinetics but can be well correlated using a two-term rate expression.

Experimental

A conventional high-vacuum system was used. The decompositions (static) took place in a Vycor vessel whose volume was 870 cc. and whose surface-to-volume ratio was 0.73 cm.$^{-1}$. In certain runs the surface-

(1) J. P. Cunningham and H. S. Taylor, *J. Chem. Phys.*, **6**, 359 (1938).

(2) B. G. Gowenlock, J. C. Polanyi, and E. Warhurst, *Proc. Roy. Soc.* (London), **A218**, 269 (1953).

(3) L. M. Yeddanapalli, R. Srinivasan, and V. J. Paul, *J. Sci. Ind. Res.* (India), **13B**, 232 (1954).

(4) C. M. Laurie and L. H. Long, *Trans. Faraday Soc.*, **51**, 665 (1955).

(5) L. H. Long, *ibid.*, **51**, 673 (1955).

(6) S. J. W. Price and A. F. Trotman-Dickinson, *ibid.*, **53**, 939 (1957).

(7) R. Srinivasan, *J. Chem. Phys.*, **28**, 895 (1958).

(8) M. E. Russell and R. B. Bernstein, *ibid.*, **30**, 607, 613 (1959).

(9) J. Cattanach and L. H. Long, *Trans. Faraday Soc.*, **56**, 1286 (1960).

(10) R. Ganesan, *J. Sci. Ind. Res.* (India), **20B**, 228 (1961).

(11) R. Ganesan, *Z. physik. Chem.* (Frankfurt), **31**, 328 (1962).

(12) R. E. Weston, Jr., and S. Seltzer, *J. Phys. Chem.*, **66**, 2192 (1962).

(13) M. Krech and S. J. Price, *Can. J. Chem.*, **41**, 224 (1963).

(14) A. S. Kallend and J. H. Purnell, *Trans. Faraday Soc.*, **60**, 93, 103 (1964).

(15) L. H. Long, *J. Chem. Soc.*, 3410 (1956).

to-volume ratio of the vessel was increased to 10.1 cm.$^{-1}$ by packing it with short lengths of Vycor tubing. The reactor was conditioned to a reproducible state[7] by performing a large number of preliminary decompositions prior to making the kinetic measurements. The temperature in the vessel was measured using eight thermocouples placed next to the vessel at various points; the mean of these eight readings was designated as the temperature of the run. The average deviation from the mean of these readings was typically $\pm 0.1°$. The drift of any thermocouple with time was less than 0.4° for the longest reaction times used. The average deviation of a single run temperature about the mean of all runs at that temperature was less than $\pm 0.2°$.

Samples of dimethylmercury (DMM) were kindly furnished by C. H. Brubaker, Jr., and R. B. Bernstein; each sample was prepared by the method of Gilman and Brown.[16] The Brubaker sample was fractionated in an efficient column, mixed with the Bernstein sample, and this mixture was fractionated in the same column. The fraction boiling between 91.5 and 92.0° (740 mm.) was collected, passed over P_2O_5, distilled *in vacuo*, and stored in the dark at −78°. The infrared spectrum of this material agreed with the literature.[17]

A weighed amount of DMM was introduced into the reaction vessel, and the reaction was allowed to proceed until approximately 15% of the reactant had decomposed. The reactor contents were passed through two traps at −194°, and the product volatile at this temperature (pure CH_4) was discarded. The remaining substances were warmed to −97°, and the products volatile at this temperature (hydrocarbons containing two to four carbon atoms) were also discarded. The residual material was warmed up, distilled into a weighing bulb, and weighed as DMM. The infrared spectrum of this residual material was identical with the spectrum of DMM. In separate experiments, performed at 230°, it was shown that less than 0.3% of the DMM was lost using the above technique. In certain experiments the total pressure was increased by the addition of CO_2 (Matheson Chemical Co., Bone Dry grade, stated purity >99.9%) shortly after the DMM had been introduced into the reaction vessel.

Results and Discussion

Table I gives typical experimental data obtained at the two extreme temperatures used in this study. (All of the points are included for 275.5°, and half of the points are included for 330.2°. At 330.2° the selection was done by choosing every other point in the order of increasing concentration.) The calculated rate constants assuming first order (k_1*) and three-halves order ($k_{3/2}$*) are given for each of the experimental points. The systematic drift in the calculated first- and three-halves-order constants shows that neither order is very satisfactory. Other one-term rate expressions, such as second-order, yield rate constants which are also functions of the concentration.

Table I: Effect of Concentration on the Thermal Decomposition of Dimethylmercury

$(DMM)_0 \times 10^6$, moles/cc.[a]	reaction time $\times 10^{-3}$, sec.	f fraction decomposed	$k_1^* \times 10^6$, sec.$^{-1}$	$k_{3/2}^* \times 10^3$, (cc./mole)$^{1/2}$ sec.$^{-1}$
		Temp. 275.5°		
0.526	313.7	0.170	0.60	0.86
1.636	217.6	0.122	0.60	0.48
3.848	220.7	0.163	0.81	0.43
5.454	187.2	0.149	0.86	0.38
6.786	185.8	0.160	0.94	0.38
		Temp. 330.2°		
0.220	11.16	0.149	15	32
0.270	8.44	0.122	16	31
0.434	7.44	0.163	24	38
0.845	5.82	0.153	29	32
1.792	4.20	0.162	42	33
2.821	2.94	0.165	62	38
3.401	2.22	0.146	71	40
3.917	2.04	0.147	78	41
4.942	1.74	0.149	93	43
5.907	1.44	0.150	113	48
6.436	1.44	0.162	123	51

[a] $(DMM)_0$ = initial concentration of the dimethylmercury.

The rate expression which was used to correlate the experimental data in this study is

$$-\frac{d(DMM)}{dt} = k_a(DMM) + k_b(DMM)^2 \quad (1)$$

Equation 1 can be approximated, at small values of f (fraction decomposed), by

$$\frac{-\Delta(DMM)}{\Delta t} = \frac{(DMM)_0 - (DMM)}{t} = k_a\overline{(DMM)} + k_b\overline{(DMM)^2} \quad (2)$$

where $\overline{(DMM)} = [(DMM)_0 + (DMM)]/2$. By substituting in eq. 2 the relation

$$(DMM) = (1 - f)(DMM)_0$$

and noting that $f/(1 - f/2)$ is approximately equal to $f(1 + f/2)$, we obtain

(16) H. Gilman and R. E. Brown, *J. Am. Chem. Soc.*, **52**, 3314 (1930).

(17) H. S. Gutowsky, *J. Chem. Phys.*, **17**, 128 (1949).

$$f(1 + f/2) = [k_a + k_b(1 - f/2)(\mathrm{DMM})_0]t \quad (3)$$

The first-order rate expression

$$k_1{}^*t = -\ln(1 - f) \quad (4)$$

can be approximated, for small f, by

$$k_1{}^*t = f(1 + f/2) \quad (5)$$

Combining (3) and (5) gives

$$k_1{}^* = k_a + k_b(1 - f/2)(\mathrm{DMM})_0 \quad (6)$$

Thus, if f is small and constant, a plot of a pseudo-first-order rate constant (*i.e.*, one calculated using eq. 4) *vs.* the initial concentration of dimethylmercury will yield a straight line. Figures 1 and 2 are plots of the data[18] at each of the five temperatures studied. The linear nature of these plots is evident.

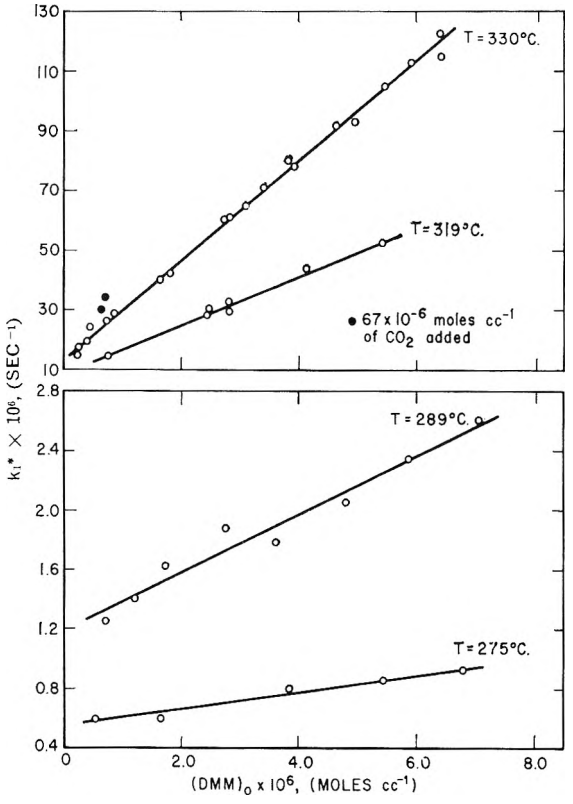

Figure 1. Pseudo-first-order rate constants as a function of initial DMM concentration at 275.5, 289.2, 319.2, and 330.2°.

The method used to evaluate the rate constants k_a and k_b was to rearrange the integrated form of eq. 1 into an equation which yielded k_a and k_b by an iterative procedure. Integration of (1) gives

$$\ln\left\{\frac{(\mathrm{DMM})_0[k_a + k_b(\mathrm{DMM})]}{(\mathrm{DMM})[k_a + k_b(\mathrm{DMM})_0]}\right\} = k_a t \quad (7)$$

or

$$\frac{(\mathrm{DMM})[k_a + k_b(\mathrm{DMM})_0]}{(\mathrm{DMM})_0[k_a + k_b(\mathrm{DMM})]} = e^{-k_a t} \quad (8)$$

Letting $\alpha = (\mathrm{DMM})_0/(\mathrm{DMM})$ and expanding the exponential gives

$$\frac{k_a + k_b(\mathrm{DMM})_0}{\alpha k_a + k_b(\mathrm{DMM})_0} = 1 - k_a t + \frac{(k_a t)^2}{2!} - \frac{(k_a t)^3}{3!} + \ldots \quad (9)$$

Equation 9 can be rearranged in the form

$$(\mathrm{DMM})_0 = \frac{\alpha - 1}{k_b t[1 - k_a t/2! + (k_a t)^2/3! - \ldots]} - \alpha k_a/k_b \quad (10)$$

Since $(1 - k_a t/2! + (k_a t)^2/3! - \ldots)$ is approximately equal to 1, eq. 10 was used to evaluate k_a and k_1, by an iterative procedure. These values were then used to correct the experimental data to constant α, and the iteration was repeated. The values of k_a and k_b obtained by this procedure (unpacked vessel) are plotted

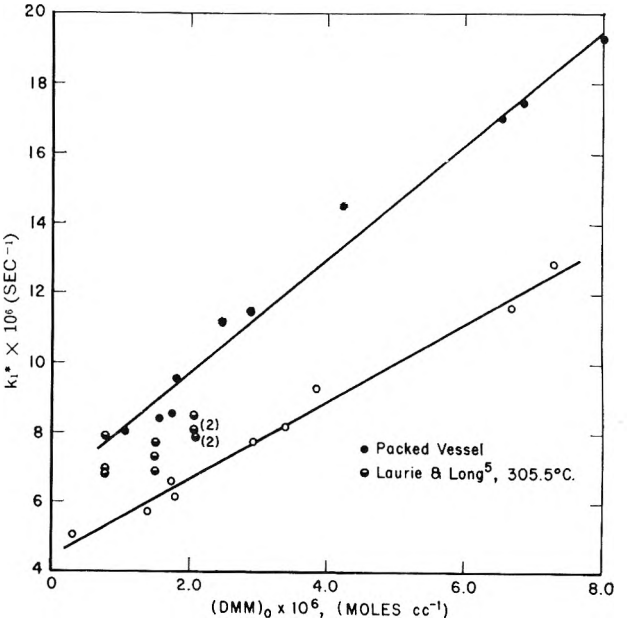

Figure 2. A comparison of pseudo-first-order rate constants as a function of initial DMM concentration for the packed and unpacked (open circles) vessel at 303.7°.

(18) The data plotted are uncorrected for variations in f. However, the maximum variation in f was from 0.122 to 0.185. The variation of $1 - f/2$ is then from 0.91 to 0.94, which will not affect the slopes significantly.

in Fig. 3. A least-squares treatment of these points gives the Arrhenius equations

$$k_a = 2.6 \times 10^9 \exp(-39{,}000/RT) \text{ sec.}^{-1} \quad (11)$$

$$k_b = 9.5 \times 10^{26} \exp(-71{,}000/RT) \text{ cc. mole}^{-1} \text{ sec.}^{-1} \quad (12)$$

The effect of surface on the reaction was examined by making runs in a packed vessel at 304° and comparing them with runs made in the unpacked vessel at the same temperature. The results are plotted in Fig. 2. Calculation of k_a and k_b from these data shows that each increased 40% over its value for the unpacked vessel whereas the surface-to-volume ratio increased by a factor of 14. From this we can conclude that the heterogeneous component in the unpacked reactor is less than 5% of the total.

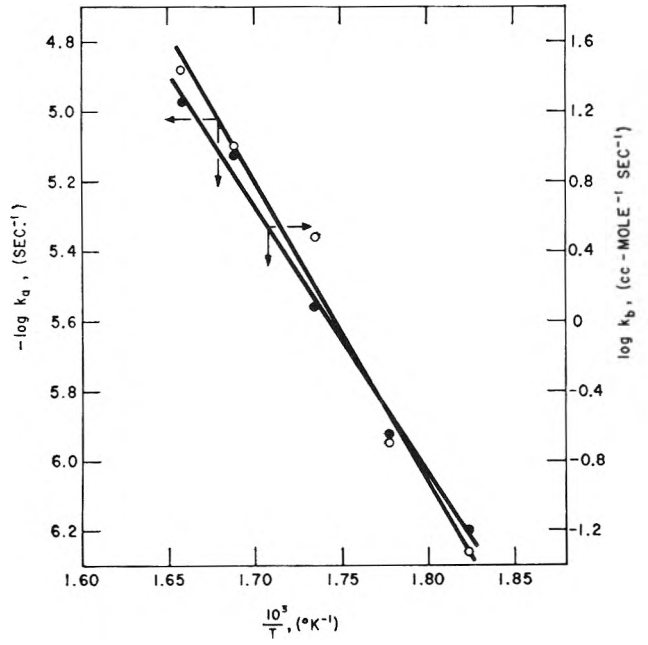

Figure 3. Arrhenius plots for k_a (open circles) and k_b (full circles).

A possibility exists that the increase in k_1* as concentration increases might be attributed to the falling-off region of unimolecular reactions. However, this can be refuted by examining the two points at 330° in Fig. 1 in which the pressure was increased approximately 100-fold by the addition of CO_2. The increase in k_1* is small and within the scatter of the data. Moreover, the large number of atoms in DMM would seem to preclude such a large effect at this temperature and pressure,[19] and the shape of the curve is not what one would expect for a unimolecular fall-off.

The data used by Laurie and Long[4] for their order determination are compared with our data in Fig. 2. Extrapolation of their points (mean temperature 305.5°) to 303.7° gives agreement with our data within the experimental error of both sets of data. The determination of order by Yeddanapalli, *et al.*,[3] was conducted at a temperature higher (342°) than that used in the present study, but using k_a and k_b (calculated at 342° from eq. 11 and 12) in eq. 7 yields calculated values of $(DMM)_0/(DMM)$ which deviate by less than 2% from the experimental values of ref. 3.

It is of some interest to note the observations of previous investigators with respect to the effect of temperature on the kinetic order of the reaction. Yeddanapalli, *et al.*,[3] reported that at 305 and 323° there was little to choose between first- and three-halves-order kinetics. On the other hand, at 342° the three-halves-order constants were decidedly more consistent than first-order constants. Laurie and Long[4] observed that the reaction appeared to be first order in the range 294–332°, but at 343° the order appeared to increase to nearly three-halves. These observations are qualitatively consistent with eq. 1. At low temperatures the first term in this expression would predominate because k_a has a much lower activation energy than k_b. Thus, the data would appear to correlate better with a first-order expression rather than a higher order. At higher temperatures, however, the contribution of the second term in eq. 1 increases, and, thereby, the apparent order of the reaction increases. These effects can be seen also from the calculated first- and three-halves-order rate constants in Table I.

Since the submission of this study for publication, a comprehensive study of the decomposition in the vicinity of 400° has been published by Kallend and Purnell.[14] Their proposed mechanism gives the rate equation

$$\frac{-\mathrm{d(DMM)}}{\mathrm{d}t} = 2k_1[\mathrm{DMM}] + B[\mathrm{DMM}]^{3/2} \quad (13)$$

where k_1 is the rate constant for the elementary reaction

$$(CH_3)_2Hg \longrightarrow CH_3 + CH_3Hg$$

and B is a combination of several rate constants in their postulated mechanism. Their data are found to fit this expression rather well.

The results of the present study differ from those of Kallend and Purnell in several respects. They ob-

(19) A. F. Trotman-Dickinson, "Gas Kinetics," Butterworths Scientific Publications, London, 1955, p. 69.

tained good material balances on carbon and hydrogen whereas data near 300°, even at low extents of reaction, show poor material balances (*e.g.*, in a run[20] for which f was 0.066, the amount of carbon and hydrogen in the recovered products was approximately 60% of the total in the decomposed dimethylmercury). Our rate expression also differs from eq. 13. A plot of k_1* *vs.* $(DMM)_0^{1/2}$ does not yield a straight line as it should if their expression is valid at 300°. Furthermore, k_a should equal $2k_1$ if the results of ref. 14 were applicable in the temperature range of this study. The difference between k_a and $2k_1$ is quite large (*e.g.*, at 305°, $2k_1$ is equal to 3×10^{-7} sec.$^{-1}$ and $k_a = 4.4 \times 10^{-6}$ sec.$^{-1}$). We feel the differences cited above are probably due to the two different temperature ranges examined in these two studies.

The nature of the hydrogen and carbon "lost" has been the subject of some speculation. Several workers[1,3,4] have assumed that a hydrocarbon polymer deposits on the walls of the reaction vessel. Some experiments by one of us[21] indicate another possibility. A calculation of the empirical formula of the "lost" carbon and hydrogen was made from the results of two runs carried out at low f (0.066 and 0.074). The values obtained were $CH_{2.47}$ and $CH_{2.54}$. In another series of experiments a material balance on the mercury was made, and it was found that about half of the mercury from the decomposed dimethylmercury was not recovered. This indicates that the "polymer" contains mercury. A substance which has been proposed as a possible product[2,14] in the pyrolysis is $(CH_3HgCH_2)_2$. This substance has a carbon–hydrogen empirical formula of $CH_{2.5}$ and also contains mercury. If this compound were relatively nonvolatile the loss of carbon, hydrogen, and mercury could be explained. However, attempts by us to isolate $(CH_3HgCH_2)_2$ have not been successful. The "polymer" may well be a complex mixture which gave the empirical formula of $CH_{2.5}$ by coincidence for the two runs mentioned.

We are unable to postulate a mechanism which is consistent with our data. The very large pre-exponential factor of k_b suggests that it is at least the product of two elementary rate constants. It also should be noted that the Arrhenius plots of k_a and k_b show considerable scatter. This may indicate that k_a and k_b are each a collection of elementary rate constants and their Arrhenius plots might well be curved. A situation like this was found by Palmer and Dormish[22] in their examination of the kinetics of ethylene decomposition.

Acknowledgment. We wish to thank Professors R. B. Bernstein and C. H. Brubaker, Jr., for furnishing the dimethylmercury used in this study.

(20) M. E. Russell, Ph.D. Thesis, University of Michigan, 1958.

(21) M. E. Russell, unpublished work, University of Michigan.

(22) H. P. Palmer and F. L. Dormish, *J. Phys. Chem.*, 68, 1553 (1964).

Electrode Potentials in Fused Systems. VIII. Oxidation Kinetics of Silver in Sodium Chloride

by Kurt H. Stern and Walter E. Reid, Jr.

Electrochemistry Section, National Bureau of Standards, Washington, D. C. *(Received April 17, 1964)*

The oxidation rate of metallic silver in molten sodium chloride has been studied as a function of oxygen partial pressure and temperature (800–900°). The rate of appearance of silver ions was followed by an e.m.f. method. These ions are formed by: (A) the reaction of O_2 with silver and (B) the reaction $Ag + Na^+ = Ag^+ + Na$. The rate of (A) is a linear function of p_{O_2} in the range $0 < p_{O_2} \leq 1$ atm. For $p_{O_2} = 1$ at 870°, $r_A = 11.9 \times 10^{15}$, $r_B = 0.35 \times 10^{15}$ atoms cm.$^{-2}$ sec.$^{-1}$. With increasing time $d[Ag^+]/dt$ decreases because of the reverse of reaction A—the formation of metallic silver from Ag^+ and O^{-2} ions—for which $r_A^{-1} = (r_A + r_B)/K_A p_{O_2}^{1/2}$, where K_A, the equilibrium constant for (A), is 8.3×10^{-7} on the mole fraction scale. The general differential equation for this system is derived and numerically integrated. It is concluded that the rate-determining step for (A) is the chemisorption of O_2, which is hindered by an adsorbed layer of chloride ions, and that for (B) charge transfer is rate-determining.

Introduction

As the result of previous studies[1,2] the general features of the oxidation of metallic silver in molten sodium chloride in the presence of oxygen are fairly well established. The appearance of silver and oxide ions is accounted for by the following two reactions occurring on the metal surface

$$2Ag(s) + {}^1/_2O_2 = (2Ag^+ + O^{-2}) \quad \text{(in NaCl)} \quad \text{(A)}$$

$$Ag(s) + Na^+(l) = Ag^+ + Na \quad \text{(in Ag)} \quad \text{(B)}$$

Most or all of the sodium metal formed in reaction B diffuses into the silver.[1b] Reaction A was found to be reversible, however, so that when $[Ag^+]^2[O^{-2}]$ becomes large, the formation of metallic silver occurs throughout the melt from the reaction

$$2Ag^+ + O^{-2} = 2Ag(s) + {}^1/_2O_2 \quad \text{(C)}$$

Since (B), in general, does not come to equilibrium (the solubility of sodium in silver is usually not exceeded), it follows that when $[Ag^+]^2[O^{-2}] = K_A p_{O_2}^{1/2}$ the oxide ion concentration decreases as $[Ag^+]$ increases by reaction B. For a high metal surface–salt ratio this has been observed.[1b] The relative rates of (A) and (B) depend on the partial pressure of oxygen. When p_{O_2} is high, (A) predominates, when it is low, (B) does.

Previous rate measurements[1b] have shown that oxygen partial pressure has considerable effect on the rate although the thermodynamic equilibrium concentration of silver ion depends only on $p_{O_2}^{1/6}$.

An additional complication discovered during this work (see Experimental part) is that the passage of O_2 gas through NaCl displaces the equilibrium ($K_{eq} = 4.5 \times 10^{-5}$)

$$2NaCl(l) + {}^1/_2O_2(g) = Na_2O(l) + Cl_2(g) \quad \text{(D)}$$

to the right. The chlorine thus produced may react with the silver according to

$$Ag + {}^1/_2Cl_2 = Ag^+ + Cl^- \quad \text{(E)}$$

However, since the partial pressure of Cl_2 in the effluent gas was found to be approximately 1 part in 10^5 of O_2, its effect on the rate of formation of Ag^+ compared to that of O_2, its effect on the rate of formation of Ag^+ compared to that of O_2 is negligible. Reaction E has therefore been neglected in the kinetic analysis.

The purpose of the present work was to study certain kinetic aspects of this system, in particular the

(1) (a) K. H. Stern, *J. Phys. Chem.*, 62, 385 (1958); (b) *ibid.*, 66, 1311 (1962).

(2) J. Kruger and K. H. Stern, *J. Electrochem. Soc.*, 109, 889 (1962).

dependence of the rate of appearance of Ag^+ on the oxygen partial pressure in reaction A, the rates of reactions B and C, and the over-all kinetic behavior of the system, and also to determine the mechanism of reactions A and B. In order to gain more insight into the mechanism of (A) and (B), it proved useful to study the initial stages of the reaction where (C) does not occur.

Principle of the Experimental Method. The general experimental procedure consisted of placing a silver rod into molten NaCl at various fixed temperatures and measuring the rate of appearance of Ag^+ ions for various environmental conditions.

Since previous studies with radioactive silver[1a] had shown that silver ions appear in the melt almost immediately after immersion of the Ag specimen it was necessary to use a simple method to follow the very low silver ion concentrations accurately and continuously without disturbing the system, as it would be by sampling.

Assuming only that silver is reversible to its ions at very low concentrations in AgCl–NaCl melts, some form of concentration cell appeared to be ideally suited to this method. After preliminary experiments[3] with simple concentration cells had established such reversibility and the feasibility of carrying out kinetic studies by this method, it was found that membrane reference electrodes[4] permitted a considerable simplification of the experimental arrangement. In this method the unknown concentration (strictly, the activity) is directly calculable from a cell e.m.f.

For the system under study we used the cell

$$\mathrm{Ag}|\mathrm{AgCl}(X_\mathrm{R}),\ \mathrm{NaCl}(1 - X_\mathrm{R})|\mathrm{Vycor}|\mathrm{AgCl}(X),\ \mathrm{NaCl}(1 - X)|\mathrm{Ag} \quad \text{(F)}$$

where the left compartment represents the reference electrode. The e.m.f. of this cell is[4]

$$E = (RT/F)t_{\mathrm{Na}^+} \ln\left[\left(\frac{X}{X_\mathrm{R}}\right)\left(\frac{1 - X_\mathrm{R}}{1 - X}\right)\right] \quad \text{(1a)}$$

t_{Na^+}, the sodium ion transport number in the glass, is 0.95, independent of temperature in the range of this study (800–900°). To determine the unknown silver concentration X, eq. 1a is more conveniently written

$$\log X \simeq \log\left(\frac{X}{1 - X}\right) = \frac{E}{2.303t_{\mathrm{Na}^+}(RT/F)} - \log\left(\frac{1 - X_\mathrm{R}}{X_\mathrm{R}}\right) \quad \text{(1b)}$$

where the approximate equality sign holds for low concentrations, and the last term on the right is a constant for a fixed reference composition. Since e.m.f. measurements can easily be made to ±0.1 mv., concentrations can be calculated to three significant figures even near $X = 10^{-5}$. It should also be noted that because of the form of eq. 1 a given change in e.m.f. corresponds to a relatively larger concentration change when X is small, so that the method is particularly sensitive in very dilute solutions.

Reference Electrode Preparation. A batch of a suitable AgCl–NaCl mixture ($X_\mathrm{R} = 0.0720$) was prepared by melting together the appropriate quantities of AgCl and NaCl. The cold melt was ground, analyzed several times by electrodeposition, and stored in a dark bottle in a desiccator. In each run 2–3 g. of this material was placed in fresh 9-mm. o.d., 20-cm. long Vycor tube. These tubes had previously been cleaned by soaking both their inside and outside surfaces in concentrated nitric or chromic acid and distilled water; they were dried at 130°.

To test the applicability of eq. 1 to cell F these reference electrodes were placed in synthetic AgCl–NaCl mixtures. In the concentration range of this study ($10^{-5} < X < 10^{-3}$), calculated X values were within 1.5% of prepared ones.

Cell Construction and Procedure. A heavy-walled 3.4-cm. i.d., 20-cm. long alumina crucible, placed into the outer alumina crucible, constituted the cell container. The hot junction of the measuring chromel–alumel thermocouple was placed in a Vycor protection tube inside the container. The reference electrode and 75 g. of dried NaCl were placed in the cell. A tight-fitting Vycor tube with a standard taper, ground female joint at its upper end was slipped over the crucible. In this position the top of the crucible was even with the top of the furnace, and the joint protruded above it. The upper part of the cell, consisting of the male joint and a length of tubing terminating in four narrow tubes accommodating the two silver electrodes, gas flow tube, and thermocouple, was placed into the lower joint. The Ag specimen, a mint silver cylinder, 3 cm. long and 1 cm. in diameter (area = 10.99 cm.^{2}), attached to a heavy silver wire sheathed in a ceramic tube, was positioned by a clamp above the furnace inside the glass envelope. A thinner silver wire, also sheathed in ceramic for mechanical rigidity, was lowered into the reference electrode. Heating was started. When the NaCl had melted, a ceramic two-hole gas flow tube (hole diameter 1 mm.) was lowered into the melt. The de-

(3) K. H. Stern and E. A. Richardson, presented at the 142nd National Meeting of the American Chemical Society, Atlantic City, N. J., September, 1962. Part of this work was done at the University of Arkansas, supported by the U. S. Air Force Research and Development Command under Contract AF 49(638)-653.

(4) K. H. Stern, *J. Phys. Chem.*, **67**, 893 (1963).

sired gas ($He–O_2$ mixtures were obtained in tanks) was passed through a calibrated flow meter, $CaSO_4$ and Ascarite, and through the tube into the melt. After the gas had bubbled through the melt for 5–10 min., the Ag specimen was lowered into the melt and positioned with the bottom of the cylinder 1–2 cm. from the crucible bottom.

For approximately the first 5 min. the e.m.f. was usually steady or increased slightly, after which a regular decrease began. The time at which the decrease began was taken to be t_0. Each run was continued for 1–3 hr. Potentials were read on either a Leeds and Northrup Type K-3 potentiometer or on a Sargent recording potentiometer. In some cases data at more than one temperature and/or flow rate were obtained from the same run. The silver specimens could be used a number of times since their dimensions remained virtually unchanged during any experiment. They were cleaned before each run by washing in NH_4OH, concentrated HNO_3, and distilled water. Although this etching procedure revealed an increase in grain size with time, the reaction rate was independent of grain size, as expected.[2]

The Reaction of NaCl with O_2 and NaCl Thermal Decomposition. Separate experiments were carried out to assess the importance of reaction D and of direct thermal decomposition, $NaCl = Na^0 + {}^1/_2Cl_2$. The equilibrium constant of the latter is very small ($K = 8 \times 10^{-13}$ at 850°), but it is conceivable that, when a carrier gas is bubbled through the melt, the equilibrium is significantly displaced to the right. To study these reactions, a test tube filled with NaCl was heated to 870° in the Vycor apparatus described previously.[1b] The desired gas mixture was bubbled through the melt and the effluent gas was passed through a gas wash bottle containing 200 ml. of *o*-toluidine solution to absorb Cl_2 and was collected over water for ameasurement of gas volume. Thus, the amount of Cl_2 produced by the NaCl per liter of gas could be determined. This experimental method is sensitive to 0.1 p.p.m. Cl_2 in solution.

When helium, passed over hot copper to remove residual oxygen, was passed through the melt, no Cl_2 was detected. Hence, direct thermal decomposition is insignificant. When various O_2–He mixtures were used, however, Cl_2 was evolved, p_{Cl_2} increasing with oxygen content. For $0.007 \leq p \leq 1$ atm., the ratio p_{Cl_2}/p_{O_2} remained constant at $\sim 10^{-5}$.

If we assume that every molecule of O_2 and Cl_2 adsorbed on silver reacts, the correction to reaction A due to (D) is 1 part in 10^5 and, therefore, negligible.

Results

In all the experiments no silver ion concentration $<10^{-5}$ mole fraction (m.f.) was ever observed. This is apparently the concentration which is established initially near the silver surface. Since this same numerical result was also obtained when deoxygenated helium was used, it is attributable to reaction B.

The rate of this reaction was determined separately by outgassing the melt for more than an hour with helium (initial O_2 content 5×10^{-5} atm.) which had been passed through a long tube filled with copper wool at 500° to remove residual oxygen. Four separate runs were carried out, each consisting of rate measurements at three temperatures in random sequence. Since the silver surface area and melt volume are constant during the experiment and since, in the very dilute melts, the sodium ion concentration remains virtually constant, zero-order behavior would be expected and was found; *i.e.*

$$(d[Ag^+]/dt)_B = k_2 \qquad (2)$$

At 870° $k_2 = 3.0 \times 10^{-7}$ m.f. min.$^{-1}$, and the Arrhenius activation energy $E_2 = 45.4 \pm 11.4$ kcal. (1 cal. = 4.1840 joules).

In studying reaction A with $He–O_2$ mixtures, it was found that, particularly at high p_{O_2} values, $d[Ag^+]/dt$ was quite dependent on the gas flow rate. Consequently a number of runs were carried out to determine

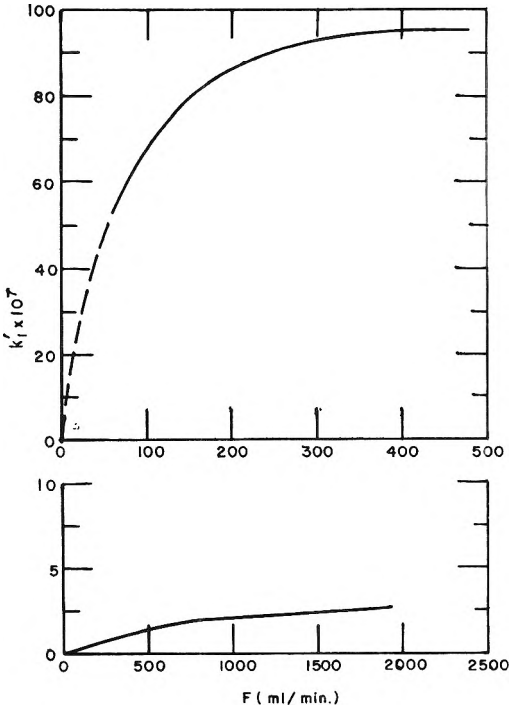

Figure 1. Dependence of k_1' on flow rate: upper curve, $p_{O_2} = 1.00$; lower curve, $p_{O_2} = 0.0228$ atm. at 870°.

this rate dependence for p_{O_2} values of 1.00 and 0.0228. The results are shown in Fig. 1 where $d[Ag^+]/dt$ has been plotted as a function of flow rate F. Since reaction B occurs simultaneously and independently of (A) the rate shown is the sum of the two reactions. The dependence on F is clearly due to (A) alone since the rate of (B) is very small and independent of F. At both pressures there is a flow rate F_{max} above which $d[Ag^+]/dt$ depends only on p_{O_2}, *i.e.*, is independent of flow rate, but F_{max} increases with decreasing p_{O_2}. Consequently the pressure dependence of the rate was studied at flow rates $>F_{max}$.

In all the experiments the silver ion concentration was a linear function of time, *i.e.*, reactions A and B are zero order at constant p_{O_2}. We therefore write for these reactions

$$d[Ag^+]/dt = k_1'(p_{O_2}) + k_2 = k' \qquad (3)$$

$k_1'(p_{O_2})$ represents the pressure-dependent rate of reaction A and was determined from eq. 3 in two ways: (a) k_2 was determined in a separate experiment in the absence of O_2 (see above) and subtracted from the experimental rate k' measured in the presence of O_2; (b) k' was measured at a number of p_{O_2} values (*cf.* Table I) and extrapolated to $p_{O_2} = 0$. The extrapolated value is k_2. Both methods give the same result for $k_1'(p_{O_2})$. Moreover, the value of k_2 obtained from method b is the same as that determined separately in the absence of O_2, showing that reactions A and B occur independently. This implies either that the diffusion of sodium into silver is rapid compared to the rate of arrival of O_2 molecules at the surface or that the two reactions occur at fairly widely separated sites on the surface.

The dependence of $k_1'(p_{O_2})$ and k' on p_{O_2} is shown in Fig. 2 on a logarithmic plot. The dashed lines for n values of 0.5, 1, and 2 represent possible dependences of these rate constants on p_{O_2} in the equation

$$k_1'(p_{O_2}) \text{ and } k' = (\text{const.})(p_{O_2}^n) \qquad (4)$$

The determination of n is of course a useful tool for determining the mechanism of reaction A. It is clear from the plot that the data for $k_1'(p_{O_2})$ (filled circles) are best fitted to the $n = 1$ line and $k_1'(p_{O_2})$ is therefore a linear function of p_{O_2} as written in eq. 3.

In Table I are listed the values obtained. These rate constants represent the actual change per minute in the ion fraction of silver in the particular melt used. To convert these to the more significant units of g.-atoms of Ag cm.$^{-2}$ min.$^{-1}$, these values must be multiplied by $75.0/(58.5)(10.99) = 0.117$.

Some idea of the reaction velocity on the atomic level can be gained by a simple calculation. The highest rate measured, at $p_{O_2} = 1$, is 67.2×10^{16} atoms cm.$^{-2}$ min.$^{-1}$. Since there are 1.2×10^{15} atoms/cm.^{2}, the number of atomic layers disappearing is $67.2 \times 10^{16}/1.2 \times 10^{15} = 562$, or one layer disappearing every 0.11 sec. This corresponds to a change in thickness of 0.1 mm. in 10.3 hr.

The rate constant for reaction C cannot conveniently be obtained experimentally because (a) it is very large, and (b) the deposition of silver occurs in the form of fine crystals[1,2] so that the surface area changes greatly. It was therefore assumed that, when the solubility product $[Ag^+]^2[O^{-2}] = K_A p_{O_2}^{1/2}$ is reached, the driving force is represented by $k_3[Ag^+]^2[O^{-2}]$. This assumption is valid, independent of the mechanism of formation of metallic silver by reaction C. k_3 can then be calculated from the rate equations for reactions A, B, and C, *viz.*

$$d[Ag^+]/dt = k_1'(p_{O_2}) + k_2 - k_3[Ag^+]^2[O^{-2}] \qquad (5)$$

and the steady-state condition $d[Ag^+]/dt = 0$. Then

$$k_3 = \frac{k_1'(p_{O_2}) + k_2}{K_A p_{O_2}^{1/2}} \qquad (6)$$

At 870° $K_A = 8.3 \times 10^{-7}$.[1b]

k_3 values calculated from eq. 6 are given in Table I.

Table I: Rate Constants for Reactions A–C at 870°

p_{O_2}	$k' \times 10^7$, m.f. min.$^{-1}$[a]	$k_1' \times 10^7$ (p_{O_2}), m.f. min.$^{-1}$[a]	k_3
1.00	98.5	95.5	11.9
0.65	45.0	42.0	6.8
0.21 (Air)	31.8	28.0	8.4
0.10	15.2	12.2	5.8
0.0547	8.74	5.74	4.5
0.0228	5.70	2.70	4.9
0.007	3.60	0.60	5.2
<0.00005	3.00	...	...

[a] To convert these values to atoms cm.$^{-2}$ sec.$^{-1}$ multiply by 1.172×10^{21}.

For a change in p_{O_2} over more than two orders of magnitude k_3 is virtually constant, as expected, since the rate of reaction C should be independent of p_{O_2}. The last line in Table I represents $d[Ag^+]/dt$ in the absence of O_2, *i.e.*, it is the rate of reaction B ($k_2 = 3.00 \times 10^{-7}$ m.f. min.$^{-1}$ at 870°).

k' values were also determined for four p_{O_2} values at 830°. From these and from the data in Table I, the Arrhenius activation energy for reaction A could be calculated. The results of two methods of calculation are shown in Fig. 3. In the first method (closed circles) $k_1'(p_{O_2})$ values are calculated from eq. 3 at both 870 and 830°, and E_1 is determined in the usual way. In

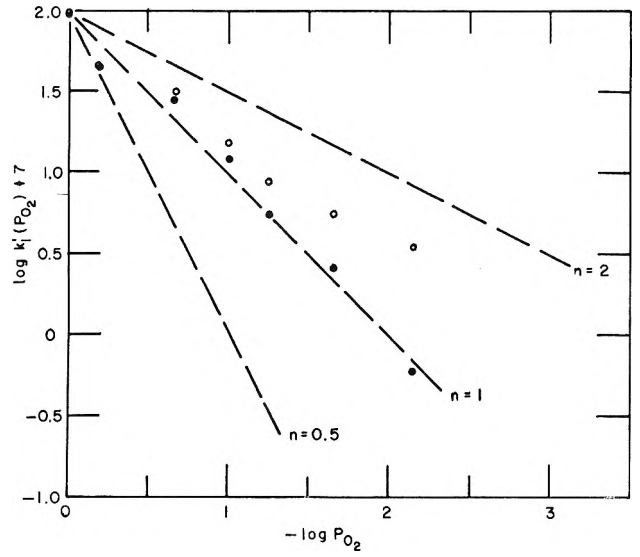

Figure 2. Test for the pressure dependence of the rate constants at 870°: ●, $k_1'(p_{O_2})$; O, $k' = k_1'(p_{O_2}) + k_2$. Dashed lines represent theoretical slopes for log k = constant + n log p_{O_2}.

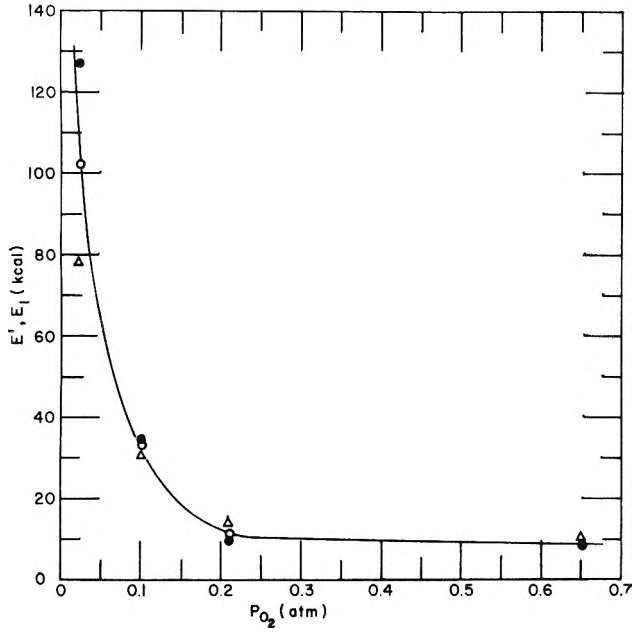

Figure 3. Activation energy as a function of oxygen pressure. Δ, E'; ● and O, E_1. For method of calculation see text.

the second method (open circles) E_1 is calculated from E' (which is obtained from k' values at 870 and 830°) using the relation[5]

$$E' = \frac{E_1 k_1'(p_{O_2})}{k'} + \frac{E_2 k_2}{k'} \qquad (7)$$

Both methods of calculation give essentially the same results for E_1. The E_1 value at the lowest pressure (p_{O_2} = 0.023 atm.) is subject to the greatest uncertainty since a small error in k_2 could greatly affect $k_1'(p_{O_2})$.

The increase in E_1 at low pressure is similar to the behavior of heats of chemisorption and is associated with a variety of surface sites. This will be discussed in the next section.

Discussion

In the previous section the expression for the rate of appearance of Ag^+ was deduced (eq. 5). From this, reactions A, B, C, and the experimental results it also follows that

$$d[O^{-2}]/dt = k_1'(p_{O_2}) - k_3[Ag^+]^2[O^{-2}] \qquad (8)$$

$$d[Na^0]/dt = k_2 \qquad (9)$$

By combining eq. 8 and 9 with (5), the over-all corrosion rate of the silver can be expressed in terms of $[Ag^+]$ alone. In this form $[Ag^+]$ can be predicted for large t from our own measurements on relatively short time intervals at the beginning of the reaction. If the concentrations are given in terms of equivalents

$$d[Ag^+]/dt - d[O^{-2}]/dt = k_2 \qquad (10)$$

from which

$$[O^{-2}] = [Ag^+] - k_2 t \qquad (11)$$

Substitution of (11) into (5) gives

$$d[Ag^+]/dt = k_1'(p_{O_2}) + k_2 - k_3[Ag^+]^3 + k_3 k_2 [Ag^+]^2 t \qquad (12)$$

Equation 12 is the general differential equation which applies to the over-all rate of formation of silver ion in solution.

Equation 12 is in general agreement with experimental observations: (a) the initial kinetics (small $[Ag^+]$, t) are zero order; (b) for larger t $d[Ag^+]/dt$ decreases as the negative term becomes more important, but does not become zero, as long as reaction B continues—the rate does, however, go through a minimum; (c) eq. 11 implies that $[O^{-2}]$ goes through a maximum. Although eq. 12 cannot yet be integrated explicitly, the results of a numerical integration for the rate constants in Table I carried out on an IBM 7094 computer are shown in Fig. 4 for 10^5 min.; in Fig. 5 the first 10^4 min. have been shown on an expanded scale. One-half of the average value of k_3 in Table I (3.4) was used since $[O^{-2}]$ is expressed in equivalents. Figure 5 is in good agreement with the general results previously obtained for much higher metal surface area–salt ratios.[1b] A

(5) *Cf.* A. A. Frost and R. G. Pearson, "Kinetics and Mechanism," 2nd Ed., John Wiley and Sons, Inc., New York, N. Y., 1962, p. 375.

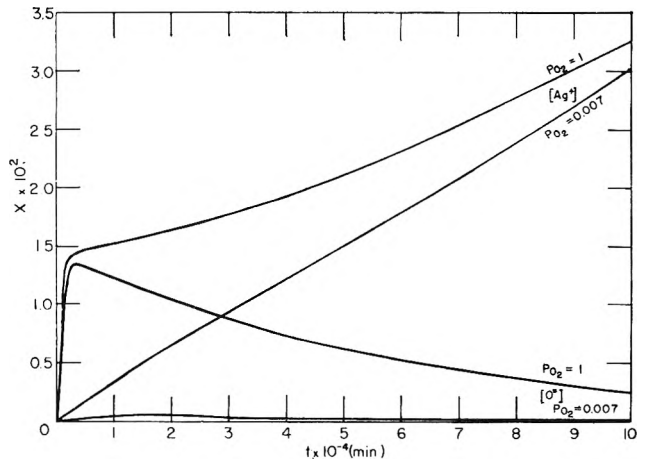

Figure 4. $[Ag^+]$ and $[O^{-2}]$ concentrations for p_{O_2} = 1.0 and 0.007 calculated from eq. 4 and 5 and the rate constants in Table I.

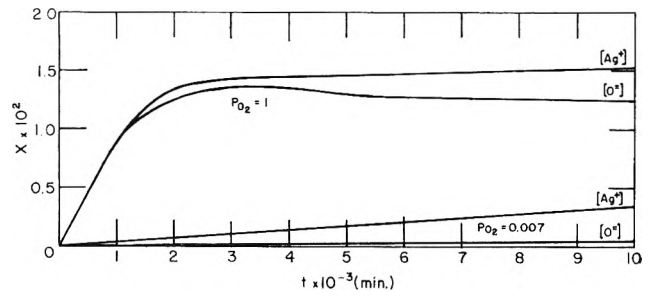

Figure 5. $[Ag^+]$ and $[O^{-2}]$ concentrations for p_{O_2} = 1.0 and 0.007 calculated from eq. 4 and 5 and the rate constants in Table I.

previous interpretation for rates at $p_{O_2} = 1$, in terms of a diffusion-controlled process,[1b] is, thus, in error. The decrease in the rate at higher $[Ag^+]$ is merely the result of reaction C. Although the initial rate of silver ion formation is very strongly dependent on oxygen pressure, the silver ion concentrations for large t become nearly equal at all pressures (*cf.* Fig. 4). This is because, at large t, $[O^{-2}]$ is nearly zero at both high and low p_{O_2}, and the rate of reaction is primarily due to (B). Thus, at high p_{O_2} reaction A comes to equilibrium at long times, and the subsequent rate is due to (B) alone; at low p_{O2} the rate of (A) is small and (C) is negligible, and the over-all rate is again primarily due to (B). At higher pressures the $[O^{-2}]$ maximum occurs sooner, and, of course, at much higher values.

We consider next reactions A and B from a more mechanistic viewpoint.

Reaction A. The general course of this reaction, as of any heterogeneous reaction, can be discussed in terms of a number of consecutive steps, *viz.*

A_1 transport of O_2 molecules to the surface
A_2 O_2 adsorption
A_3 $O_2 \rightarrow 2O$ possible rearrangements on the surface
A_4 $O + 2Ag \rightarrow 2Ag^+ + O^{-2}$ (surface)
A_5 desorption of products
A_6 transport of products into the bulk liquid

Since the rate constant $k_1'(p_{O_2})$ is a linear function of p_{O_2}, *i.e.*, $k_1'(p_{O_2}) = ap_{O_2}$, it follows from simple considerations, based on the Langmuir adsorption theory,[6,7] that A_2, adsorption of molecular oxygen, is the rate-determining step in the sequence. Moreover, even at the highest pressure studied, 1 atm., the metal surface is only sparsely covered with O_2. The flow rate experiments indicate that, at F_{max} values or above, the O_2 in the melt and on the surface are in a steady-state condition since one would expect the fraction of the surface covered by O_2, θ, to be proportional to the pressure. Under these conditions the rate of O_2 transport to the surface (A_1) equals the rate of the slowest step subsequent to A_2. At lower flow rates, A_1 decreases relative to these steps so that the steady-state concentration is no longer maintained on the surface. The increase of F_{max} with decreasing partial pressure is consistent with this mechanism. Rates of A_3–A_6 are independent of partial pressure and flow rate whereas A_1 and A_2 depend on both. Therefore, at the lower pressures an increased flow rate is the only mechanism whereby A_1 can be sufficient to maintain a steady-state concentration of the surface. The effect is rather small (a change in p_{O_2} by a factor of 50 changes F_{max} by a factor of 3) because the steady-state coverage θ is much less at lower pressures, and, thus, $d[Ag^+]/dt$ is limited primarily by low θ rather than low F. It is quite possible that the melt may be supersaturated with O_2 (entrapment), but in any case, since the solubility (or supersolubility) is proportional to p_{O_2}, it follows that at any particular partial pressure when $F < F_{max}$ the melt does not hold the maximum possible concentration of O_2, and $\theta < \theta_{max}$.

Since the magnitude of the activation energy of reaction A exceeds 5 kcal. (*cf.* Fig. 3) and increases with decreasing pressure, it is clear that the adsorption of O_2 is chemical rather than physical. This conclusion is also supported by a number of studies[8-11] of oxygen adsorp-

(6) I. Langmuir, *J. Am. Chem. Soc.*, **38**, 2221 (1916).

(7) S. Glasstone, "Textbook of Physical Chemistry," 2nd Ed., D. Van Nostrand Co., Inc., New York, N. Y., 1946, p. 1200.

(8) F. H. Buttner, E. R. Funk, and V. Hilldin, *J. Phys. Chem.*, **56**, 657 (1952).

(9) A. F. Benton and L. C. Drake, *J. Am. Chem. Soc.*, **56**, 255 (1934).

(10) W. W. Smeltzer, E. L. Tollefson, and A. Cambron, *Can. J. Chem.*, **34**, 1046 (1956).

tion on silver. Although only one of these[8] lies in the temperature range of this work, all of the cited results above 200° are consistent with chemisorption; also, the properties of the adsorbed film are different from those of bulk Ag_2O. Near 200° two consecutive rates of adsorption, rapid and slow, have been found[10] and interpreted in terms of two kinds of adsorption sites, but no relevant data exist at high temperatures. Surface tension measurements of silver[8] in helium–oxygen mixtures at 930° in the range $10^{-4} \leq p_{O_2} \leq 0.2$ give a surface concentration of 1.98×10^{15} atoms of oxygen/cm.^{2}. Since the number of silver atoms is approximately (r_{Ag} = 1.44 Å.) 1.2×10^{15}, this gives 1.65 atoms of O/atom of Ag.

As seen in Fig. 2, the rate of reaction is still increasing at $p_{O_2} = 1$. Hence, θ must be considerably less than unity, even at this pressure and for all $p_{O_2} \leq 1$ since the surface coverage of O_2 on the metal surface is controlled by the solubility of O_2 in the molten salt (and by the possible preferential adsorption of chloride ions) and is proportional to the pressure through Henry's law.

This conclusion is also consistent with steps A_2, A_3, and A_4 of the proposed mechanism. Each adsorbed O_2 molecule is adsorbed on two surface Ag sites. After its dissociation each resulting oxygen atom must exchange electrons with two adjacent Ag atoms. This requires that the surface be only sparsely covered with oxygen.

To gain some insight into possible reasons for the slowness of this reaction we write, from absolute reaction-rate theory

$$k_R = \frac{kT}{h} c_{Ag} c_{O_2} e^{\Delta S^*/R} e^{-\Delta H^*/RT} \qquad (13)$$

If the rate-determining step is the chemisorption of O_2 on silver, ΔS^* in eq. 13 should then correspond to the entropy of chemisorption. The maximum value of ΔS^* would be obtained for complete coverage, *i.e.*, $c_{O_2} = 10^{15}$ molecules cm.$^{-2}$. k_R is the rate constant at 870° in atoms cm.$^{-2}$ sec.$^{-1}$, and $c_{Ag} = 1.2 \times 10^{15}$ atoms cm.$^{-2}$. Changes of an order of magnitude in these concentrations hardly affect ΔS^*. The results of the calculation of ΔS^* are shown in Table II, where the Arrhenius activation E_1 (*cf.* Fig. 3) energy has been identified with ΔH^* since $\Delta H^* \approx E_1$ for reaction A.

It is immediately apparent that these entropies are impossibly large. The total molar entropy of O_2 at 870° is 53 e.u. The translational part of this is 43 e.u., and, normally, the loss of translational entropy is less, typically 30–35 e.u., because, even in immobile layers, the molecules possess configurational entropy.[12] The above model, together with the values of Table II, implies that reasonable entropy values can only be obtained if the concentration terms are drastically reduced. Even if we assume that the entire translational entropy is lost on chemisorption, we obtain from eq. 13 the product $c_{Ag}c_{O_2} = 10^{21}$, or, assuming equal concentrations, 3×10^{10} sites/cm.^{2}, covered with $p_{O_2} = 0.65$, *i.e.*, $\theta = 2.5 \times 10^{-5}$. Such an extremely small coverage suggests that the chloride ions in the system undoubtedly are strongly adsorbed and thus interfere with the adsorption of oxygen.

Table II: Activation Entropies for Reaction A at 870°

p_{O_2}, atm.	$k_1 \times 10^{-15}$, atoms cm.$^{-2}$ sec.$^{-1}$	ΔS^* (e.u.)[a]
0.65	4.92	−134
0.21	3.37	−137
0.10	1.43	−158
0.0228	0.316	−222

[a] 1 e.u. = 4.1840 joules/°K./mole.

Reaction B. By analogy with reaction A we write reaction B as a sequence of steps, *viz.*

- B_1 transport of Na^+ to surface
- B_2 adsorption
- B_3 electron exchange
- B_4 desorption of Ag^+
- B_5 removal of Na atoms from the surface, *e.g.*, by diffusion into silver

The magnitude of $E_2 \simeq \Delta H^* = 45.4$ kcal. rules out adsorption of sodium metal or diffusion of sodium into silver as rate-determining steps. For the latter process activation energies would be expected to be 2–5 kcal.[13] Assuming that a lattice of NaCl is laid down on the silver, ΔS^* can be estimated from eq. 13. We obtain $c_{Na^+} = 7.6 \times 10^{14}$ ions/cm.^{2}. Again taking $c_{Ag} = 10^{15}$ atoms/cm.^{2} gives, for $\Delta H^* = 45.4$ kcal., $\Delta S^* = -92$ e.u., a very large negative value.

The large values of ΔH^* seem to rule out any step except B_3 as rate-determining. The work function of clean silver is 4.3 e.u. = 99 kcal., but this value decreases on adsorption of foreign species on the metal surface.[14,15] The large negative ΔS^* indicates that the same process

(11) R. G. Meisenheimer, A. W. Ritchie, D. O. Schissler, D. B. Stevenson, H. H. Voge, and J. N. Wilson, "Second International Congress of Surface Activity," Vol. II, Academic Press, New York, N. Y., 1957, pp. 299–308.

(12) *Cf.* B. M. W. Trapnell in "Chemisorption," W. E. Garner, Ed., Butterworth Scientific Publications, London, 1955, pp. 209–213.

(13) D. Lazarus in "Metallic Solid Solutions," J. Friedel and A. Guinier, Ed., W. A. Benjamin, New York, N. Y., 1963; pp. xxxiv–7.

(14) M. Boudart, *J. Am. Chem. Soc.*, **74**, 3556 (1952).

(15) J. H. de Boer in "Chemisorption," W. E. Garner, Ed., Butterworth Scientific Publications, London, 1955, pp. 209–213.

which accounts for the slowness of reaction A also affects (B) in a similar manner. Thus, if a layer of chloride ions is preferentially adsorbed on the metal, the concentration product $c_{Ag}c_{Na}$, will be considerably less than for complete coverage.

From this viewpoint both reactions A and B must be characterized as slow; *i.e.*, they would go much faster if the reactants could come into contact. In this model we then have a charged double layer on the surface, with sodium ions largely excluded from the metal side. This view is also consistent with the observation that when silver is briefly immersed in NaCl and withdrawn, the adherent salt is high in AgCl.

We next examine the reaction in more detail, particularly with respect to events occurring in the double layer. Initially the electrochemical potential of the silver ($\mathcal{E}_1$) is greater than that of the sodium chloride ($\mathcal{E}_2$). When the two are placed in contact, the difference $\mathcal{E}_1 - \mathcal{E}_2$ decreases. This decrease occurs most easily through the formation of a charged double layer at the surface of the silver which is positive on the metal and negative on the sodium chloride side. As electrons are transferred from the silver to the sodium ions to establish equal electrochemical potentials for the two phases, the silver surface becomes positively charged, and sodium ions are reduced to metallic sodium. If the system remained in this condition, reaction B would cease after the initial formation of the double layer. A driving force for the experimentally observed continuation of the reaction is provided for by the formation of AgCl ion pairs, *i.e.*, the reaction, $Ag^+ + Cl^- \rightleftarrows AgCl$, continues until this equilibrium is reached. The equilibrium constant for this reaction in NaCl has not been measured, but values are available in KNO_3 solvent.[16] At 402°, $K = [AgCl]/[Ag^+][Cl^-] = 396$; K values for AgBr and AgI in this solvent are 932 and 5420, respectively. The addition of the ion-pair formation reaction to reactions A–C would require a modification of eq. 5. The net effect is to decrease $d[Ag^+]/dt$ at large $[Ag^+]$. Previous studies[1b] of reaction B over long periods of time showed that the concentration of Na in the silver is, at most, only a small fraction of that possible under equilibrium conditions.[17] This indicates that alloy formation is, thus, only a secondary effect and that the ion-pair equilibrium is the factor which determines the eventual equilibrium state of this system.

The kinetic model used here predicts that $[Ag^+]$ increases indefinitely after reactions A and C have come to equilibrium due to the continuation of reaction B. It is known, however, that silver electrodes are quite stable in AgCl–NaCl melts containing more than 7–8% AgCl.[1a] The rate of appearance of $[Ag^+]$, after reactions A and C have reached equilibrium and $[O^{-2}]$ has reached an approximately constant low value, would be of the form

$$d[Ag^+]/dt = k/[AgCl] = k/K[Ag^+][Cl^-] = k'/K[Ag^+] \quad (14)$$

where k is the rate constant for reaction B and K is the ion-pair formation constant for AgCl. Equation 14 indicates a gradual decrease of $d[Ag^+]/dt$ through (B) as $[Ag^+]$ increases. In the absence of oxygen the initial rate is approximately 10^{-7} m.f. min.$^{-1}$ (Table I) for $[Ag^+] \simeq 10^{-5}$. This gives for $k_2/K \simeq 10^{-12}$. Thus, when $[Ag^+]$ is increased to 10^{-2}, $d[Ag^+]/dt$ is decreased by a factor of 10^3, *e.g.*, a change in $[Ag^+]$ which initially takes 1 min. will then require 16 hr. This undoubtedly accounts for the stability of Ag–AgCl reference electrodes.

Unfortunately, it is not yet possible to determine K separately since it cannot be assumed that its value is the same in a pure chloride as in a nitrate environment. In any case, however, the k_2 values given earlier in the paper should be regarded as rates $(d[Ag^+]/dt)$ in the absence of oxygen which include an ion-pair equilibrium constant.

Ion-pair formation provides a plausible mechanism for the removal of positively charged silver formed on the silver side of the double layer. It implies that initial rates of both reactions A and B should increase with increasing covalent character of the silver–anion pair, *i.e.*, with increasing ion-pair formation constants. For example, rates should be greater in bromide and iodide melts and less in sulfates. Experimental tests of this conclusion are in progress.

Acknowledgments. We wish to thank Dr. H. Oser and Mr. J. D. Waggoner for the numerical integration of eq. 12 and for other mathematical assistance, and Mrs. J. L. Stiff for various analytical determinations. We are grateful to Drs. Margaret A. Reid and Jerome Kruger for helpful discussions.

(16) A. Alvarez-Funes, J. Braunstein, and M. Blander, *J. Am. Chem. Soc.*, **84**, 1539 (1962).

(17) E. Quercigh, *Z. anorg. Chem.*, **68**, 301 (1910).

Transient Ionic Species Resulting from Gas–Solid Interactions: Oxygen Adsorption on Nickel Monoxide[1a]

by H. Saltsburg, D. P. Snowden, and M. C. Garrison

General Atomic Division of General Dynamics Corporation, John Jay Hopkins Laboratory for Pure and Applied Science, San Diego, California *(Received April 30, 1964)*

The effect of the pulsed adsorption of oxygen on the conductivity of powdered NiO has been investigated over a frequency range from 10^3 to 10^{10} c.p.s. From a study of the magnitude of the relative conductivity change as a function of frequency it is possible to identify the frequency range over which surface effects dominate the conductivity. At all frequencies, however, after a sharp conductivity increase caused by oxygen adsorption, the conductivity decays very slowly and nonexponentially back toward its initial value. This decay is shown to be due neither to desorption of adsorbed oxygen nor to lattice incorporation. Since at 400° the fraction of the adsorbed species ionized is found to be 5×10^{-5} and since the conductivity decay is nonexponential, it is suggested that the decay is caused by multiple electronic transitions of the adsorbed oxygen between an ionized and an un-ionized excited state before final de-excitation to a neutral adsorbed species. Such transitions provide for conductivity reversal with an effective lifetime of the ionized species many times greater than the relevant transition times between states without requiring extensive ionization. Qualitatively similar transient conductivity decays generated by pulsed gas adsorption have been observed in ZnO, α-Fe_2O_3, and Cr_2O_3.

Introduction

Studies of chemisorptive charge-transfer reactions utilizing electrical techniques have been extremely useful in the elucidation of reaction mechanisms.[1b] Development of these techniques to yield quantitative information, however, has been limited by the availability of good single crystals upon which careful adsorption studies may be carried out simultaneously with conductivity measurements.

Since polycrystalline adsorbents are readily available, it is worthwhile to examine electrical techniques which could lead to quantitative or semiquantitative interpretation. In the work reported here, frequency-dependent conductivity measurements have been combined with pulsed gas adsorption (so as to emphasize primary surface reaction processes) in a study of O_2 adsorption by NiO. In the course of this study, evidence has been obtained for the existence of transient but long-lived adsorbed ionic species resulting from this pulsed interaction.

Similar observations involving transient "slow states" in chemisorption have recently been reported by Glemza and Kokes[2] and by Belenkii and Alkhazov,[3] and in an earlier sulfide oxidation study Anderson[4] reported a related observation, although all of these experiments involved measurements of d.c. conductivity and static gas adsorption.

Experimental

Difficulties in the interpretation of d.c. conductivity measurements on powdered or sintered specimens are due to the inability of a d.c. measurement to see any but the limiting resistance path, which, in the worst case in a powder, could be some "contact resistance."

(1) (a) This work was supported by the U. S. Army Research and Development Laboratories under Contract DA-44-009-ENG-4832. It was presented in part at the 142nd National Meeting of the American Chemical Society, Atlantic City, N. J., September, 1962; (b) F. S. Stone, in "Chemisorption," W. E. Garner, Ed., Academic Press, Inc., New York, N. Y., 1957, p. 181 ff.

(2) R. Glemza and R. J. Kokes, *J. Phys. Chem.*, **66**, 566 (1962).

(3) M. S. Belenkii and T. G. Alkhazov, *Kinetika i Kataliz*, **2**, 368 (1961).

(4) J. S. Anderson, *Discussions Faraday Soc.*, **4**, 163 (1948).

Since the primary interest is in the study of all regions which are directly affected by the gas during adsorption (primarily the surface) one could be misled by d.c. measurements not only quantitatively but, in some cases, qualitatively as well. For example, the contact between particles could be an inversion region. Since resistive inhomogeneities are not distinguishable in a d.c. measurement, a.c. techniques have been employed, the theory of which has been discussed in detail elsewhere.[5] It is sufficient to say that, in principle, one should obtain regional discrimination (between contacts, surface, bulk) by varying the frequency, and thus one should be able to locate the surface region (in terms of frequency) and confine the study to that part of the frequency spectrum where surface effects predominate.

Many techniques for making a.c. conductivity measurements have been described.[6] For the present study a Q-meter was employed at frequencies below 10^8 c.p.s., and transmission line measurements using a slotted line were used at higher frequencies. The details of the experimental procedures have been presented previously.[5] For transient studies, provision was made to sweep the Q-meter through resonance continually and similarly to sweep the slotted line through the voltage minimum. The outputs of these devices were then displayed on a chart recorder, from which record the circuit Q or voltage minimum could be obtained as a function of time, and from which, in turn, the time-dependent sample conductivity was determined.

In the adsorption measurements, in order to minimize secondary effects not directly involving the primary gas–solid interaction (as for example diffusion into the solid during adsorption), the adsorption studies reported here were carried out in a flow system in which the powdered specimen was placed in a conductivity cell in the carrier gas stream of a gas chromatograph, the conductivity cell being located between the gas sample injection valve and the columns. In this manner, pulses of reactive gas can be transported in plug flow to the solid and the adsorption or reaction studied by the usual techniques of gas chromatography.[7] The contact times therefore can be limited and, in addition, both qualitative and quantitative analyses relating to the gas adsorption or reaction are obtained. The carrier gas atmosphere in which the solid resides is helium (purified by sequential passage through traps containing Linde Molecular Sieve 5A and charcoal at 77°K.). The contact time for the gas–solid reaction is of the order of a few seconds (depending on the gas sample volume injected).

The NiO powders are prepared by decomposition of the carbonate at 900 to 1100° in alumina or silica vessels. They are then quenched in air, sieved to remove excessive fines, loaded into the coaxial conductivity cell,[8] outgassed in flowing helium at 700 to 750° for a few hours, and cooled to the desired temperature.

ZnO is prepared by decomposition of ZnC_2O_4 at 700° in a silica vessel and quenched in air. α-Fe_2O_3 is a commercially available oxide (IRN-130, C. K. Williams and Co.). Cr_2O_3 is made by decomposition of ammonium chromate. Sieving and outgassing are as described for NiO, except that ZnO is heated to only 450°.

Gases which are to be reacted with the solid are prepared at various partial pressures as mixtures with helium. Injection into the gas chromatograph carrier gas stream then occurs with minimal flow disruption.

The experiment consists of the injection of a known volume of reactive gas at some known partial pressure into the carrier stream while the a.c. conductivity of the powder at a given frequency is simultaneously monitored. In this way a continuous record is obtained of the sample conductivity before, during, and after the reactive gas plug has made contact with the solid. The quantity of reactive gas which can conveniently react with the solid can be readily controlled so that the solid can be kept well below any saturation limit. On the other hand, complete adsorption or reaction of the injected pulse must be avoided, or nonuniform exposure along the cylindrical adsorbent column will result.

The extent of adsorption or reaction during the pulse contact is measured by the usual techniques of gas chromatography applied to the unadsorbed gas and/or to the gaseous reaction products which emerge from the conductivity cell.

1. Pulsed Gas Adsorption and Conductivity: NiO. The injection of O_2 (3.7 cc. (NTP), O_2 partial pressure: 7.6 to 76 mm.) into NiO at 300 to 700° results in the expected large increase in conductivity which occurs within a few seconds. Following this, however, the conductivity begins to decrease toward the initial value, and, further, this decay in conductivity is strikingly slow by comparison with the initial change. Figure 1 shows a typical rise and decay of the circuit

(5) D. P. Snowden, H. Saltsburg, and J. H. Pereue, Jr., *J. Phys. Chem. Solids*, **25**, 1099 (1964).

(6) See for example "Dielectric Materials and Applications," A. von Hipple, Ed., Technology Press of Massachusetts Institute of Technology and John Wiley and Sons, Inc., New York, N. Y., 1954, Chapter II.

(7) R. J. Kokes, *J. Phys. Chem. Solids*, **14**, 51 (1960).

(8) D. P. Snowden and H. Saltsburg, *Rev. Sci. Instr.*, **34**, 1263 (1963).

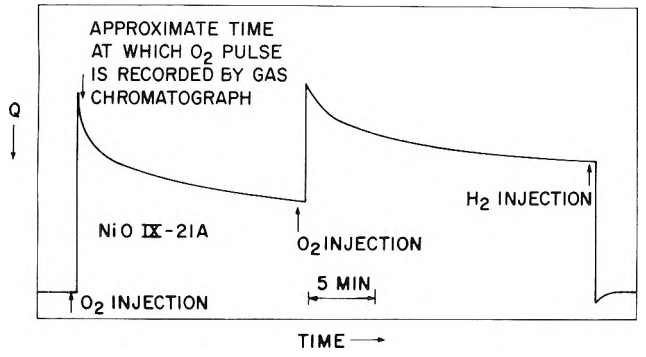

Figure 1. Tracing of circuit Q as a function of time for pulse injection of O_2 and H_2 to NiO; $f = 3.5 \times 10^4$ c.p.s.; 400°.

Q for NiO at 400° at a frequency of 3.5×10^4 c.p.s. Qualitatively similar behavior (a sharp increase followed by a slow decay) is observed at all frequencies (10^3 to 10^{10} c.p.s.), but the magnitude of the initial change is less at higher frequencies. The measured conductivity, σ, is a volume average value, uncorrected for density, and is computed from the circuit Q by the relation

$$\sigma = K_1\left(\frac{1}{Q} - \frac{1}{Q_0}\right)$$

where K_1 and Q_0 are constants at any given frequency, and thus an increase in Q indicates a decrease in σ. The scale for Q in Fig. 1 is nonlinear.

The major portion of the decay occurs after the unadsorbed O_2 in the pulse has passed the sample and thus occurs in the absence of a substantial O_2 pressure (other than background, which was less than 1 p.p.m.) in the helium stream.

It has been found that both H_2 and CO will quench this O_2-induced transient decay quite sharply at all frequencies of measurement. A qualitative sequence of O_2 adsorption and H_2 quenching (and cycling) is also shown in Fig. 1.

Using pulsed H_2 reaction, one is able to restore the initial (*i.e.*, prior to O_2 adsorption) conductivity. This conductivity is a stable end point, and thus a cyclic process of oxidation and reduction can be carried out with both the conductivity and the gas adsorption (or reaction) being reproducible from cycle to cycle. In this manner, transient studies at various frequencies may be compared. In the following discussion the stable surface produced by pulsed H_2 reaction is called "reduced."[9] The frequency-dependent conductivity of NiO is shown in Fig. 2, where the observed conductivity of the sample after initial outgassing is compared with that of the reduced surface obtained in the course of O_2–H_2 reactions on the NiO at various

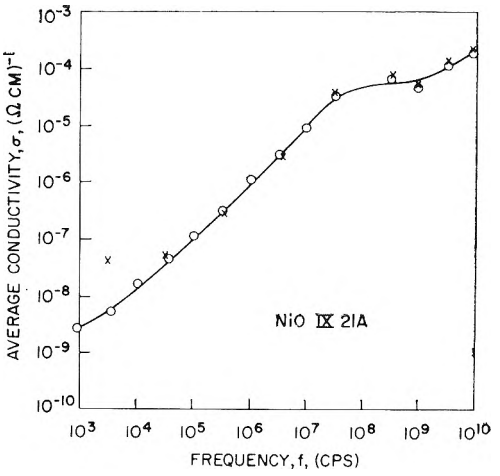

Figure 2. Frequency dependence of NiO conductivity and effects of O_2–H_2 cycling: O, initially outgassed; ×, reduced surface; 400°.

frequencies. The reproducibility is very good. Pulsed H_2 reaction was more convenient than high-temperature outgassing and was used throughout this work to produce a fiducial surface.[10] Once the stable fiducial surface has been formed, further H_2 pulses resulted in a small conductivity overshoot and decay, but no examination of this decay has been carried out.

A second pulse of O_2 during the transient decay causes another increase and decay (of comparable magnitude), but much less O_2 is adsorbed. The quantity of O_2 adsorbed in a second pulse, however, is independent of when during the decay the adsorption occurs. Similarly, the extent of H_2 and CO reaction during the O_2-induced decay is independent of the degree to which the decay has progressed. The reaction between H_2 and adsorbed O_2 appears to be stoichiometric, H_2 removing O_2 as water. Further O_2 removal beyond that initially adsorbed is more difficult, the quantity of O_2 removed per H_2 pulse decreasing sharply once this initial amount has been removed.

The rate of the decay is temperature dependent, increasing with increasing temperature, but the conductivity decay is not a simple function of time such as an exponential. Typical data are shown in Fig. 3a,b,c for NiO at 400 and 600°, at frequencies of 10^5, 10^7, and 3×10^9 c.p.s. (The data shown are for the same NiO sample.) The uncorrected Elovitch representation of the data has been chosen for convenience and is not meant to imply any mechanism for the

(9) The presence of metallic Ni is not implied. No evidence was found that metal formation had occurred.

(10) H. B. Charman, R. M. Dell, and S. S. Teale, *Trans. Faraday Soc.*, **59**, 453 (1963).

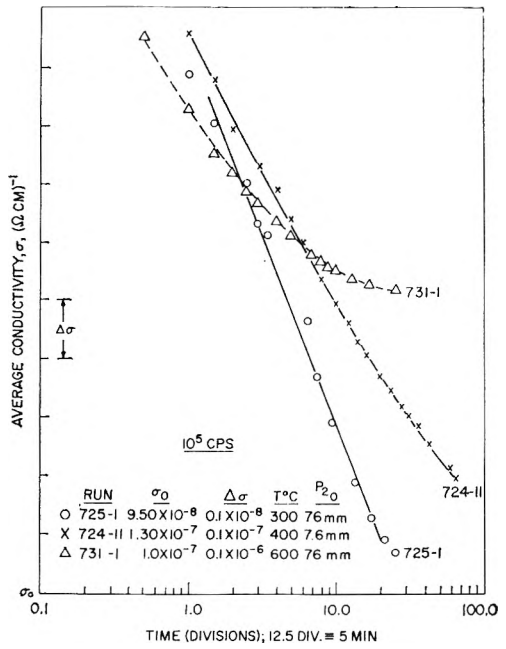

Figure 3a. Conductivity decay following pulsed O_2 adsorption on "reduced" surface; 10^5 c.p.s. (Note conductivity scale shift with temperature.)

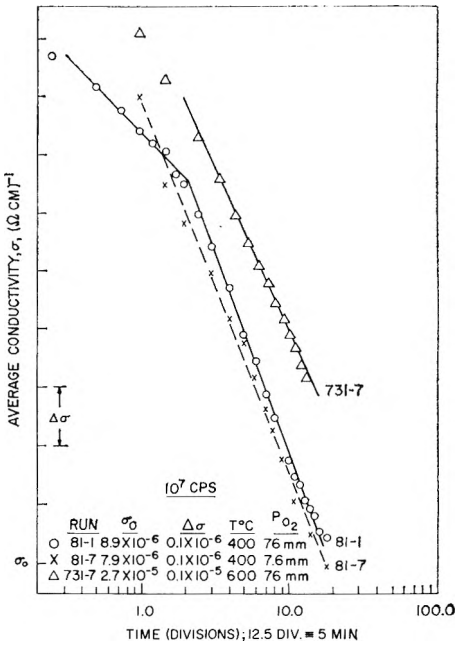

Figure 3b. Conductivity decay following pulsed O_2 adsorption on "reduced" surface; 10^7 c.p.s. (Note conductivity scale shift with temperature.)

process.[11] The decay observed at these various frequencies is the same process following the same kinetic pattern. One can further compare the slopes $d\sigma/d(\ln t)$ in the mid-range of the decay and calculate an energy parameter. One finds 12.3 kcal. (10^5 c.p.s.), 12.2 kcal. (10^7 c.p.s.), and 10.5 kcal. (3×10^9 c.p.s.), which indicates a similar temperature coefficient and again implies that the processes observed are the same. It should also be noted that first and second O_2 pulses and variations in O_2 pulse pressure seem not to affect the decay (except as changes in initial conditions affect the quantitative aspects of the decay).

The magnitude of the initial conductivity change is pressure dependent and increases with increasing pressure. It has been found, however, that if the total number of moles reacted is kept constant in a given series of pulsed adsorptions (where contact time is varied), the decay is essentially unaltered. Figure 4 illustrates the decays produced by 1.1 cc. (NTP) of O_2 (partial pressure = 76 mm.) and 10.4 cc. (NTP) of O_2 (partial pressure = 7.6 mm.) on NiO at 400°; the slight difference is probably due to the inequality in total oxygen content of the pulses. The change may be described by $(\Delta\sigma)_{\text{initial}} \cong \text{const.}[(O_2)(t_c)]^{1/3.5}$ where O_2 is the oxygen partial pressure and t_c is the contact time (t_c = gas sample volume/flow rate).

2. Pulsed Gas Adsorption and Conductivity: α-Fe_2O_3, Cr_2O_3, and ZnO. Preliminary measurements were made of pulsed O_2 and H_2 adsorption on α-Fe_2O_3, Cr_2O_3, and ZnO. In each case the same large initial fast change was followed by a long, slow decay. H_2 and O_2 acted to cause opposite conductivity changes, and the n-type conductors α-Fe_2O_3 and ZnO behaved in accord with this assignment of majority carrier sign, H_2 causing conductivity to increase. Cr_2O_3 behaved as NiO, in accord with its p-type character. A typical response of α-Fe_2O_3 is illustrated in Fig. 5.

In all cases, the magnitude of the effect is more pronounced, and the decay is more rapid as the temperature of the solid is increased.

3. Pulsed Gas Adsorption and Carrier Mobility: NiO. In order to determine the number of charge carriers generated by the pulse-adsorption reaction, the mobility of the charge carriers in the solid must be determined. Reasons akin to those limiting the utility of a.c. conductivity measurements limit the d.c. measurement of carrier mobilities in powders and a.c. techniques (microwave Faraday rotation) must be employed.[12]

Assuming that the mobility of a semiconductor such as NiO may be obtained from a microwave Faraday rotation measurement in the same manner as the mo-

(11) No attempt to linearize the data *via* a "t_0" has been made. The use of the simple temperature dependence of the slope assumes "t_0" to be independent of temperature.

(12) D. P. Snowden, *IRE Trans. Instr.*, 11, 156 (1962).

bility of a band-type semiconductor (where Hall and drift mobilities are similar in magnitude), the Hall mobility for NiO in principle can be determined. Measurements at 400° on the powdered samples described above yield only a limiting value, $\mu \leq 1$ cm.^{2}/v. sec. A similar sensitivity limit has been found for carriers injected by pulsed oxygen adsorption.

Discussion

1. Relative Change in Conductivity with O_2 Adsorption. Although the a.c. conductivity of NiO is not describable by any simple model which permits one to identify separate regions of conductivity, probably because of inherent frequency-dependent losses in NiO,[5] one might expect to see some regional discrimination result from an examination of the relative change in conductivity since the region of primary gas–solid reaction is the exterior of the solid. This relative change is shown in Fig. 6 as a function of frequency for two different NiO samples at 400°. Three frequency regions are observed, 3×10^3 to 10^6, 10^6 to 10^8, and above 10^8 c.p.s., which suggest the presence of different physical regions in the system (contact, surface, and bulk).

The exterior regions would be expected to be emphasized by pulsed gas adsorption since, owing to space charge limitations, extensive free motion of one sign of carrier toward the interior is not expected.

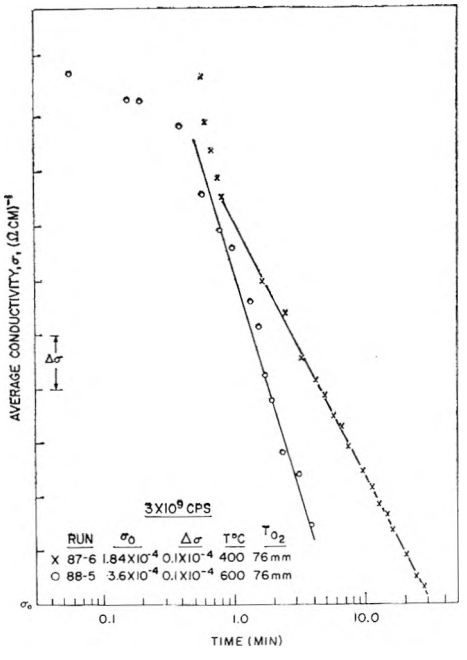

Figure 3c. Conductivity decay following pulsed O_2 adsorption on "reduced" surface; 3×10^9 c.p.s. (Note conductivity scale shift with temperature.)

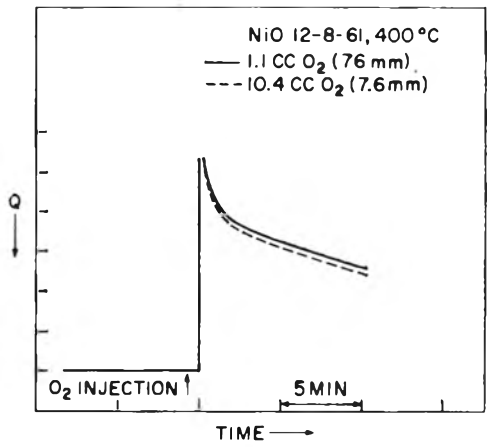

Figure 4. Circuit Q as a function of time for pulsed O_2 adsorption on NiO when total moles are constant and contact time is varied.

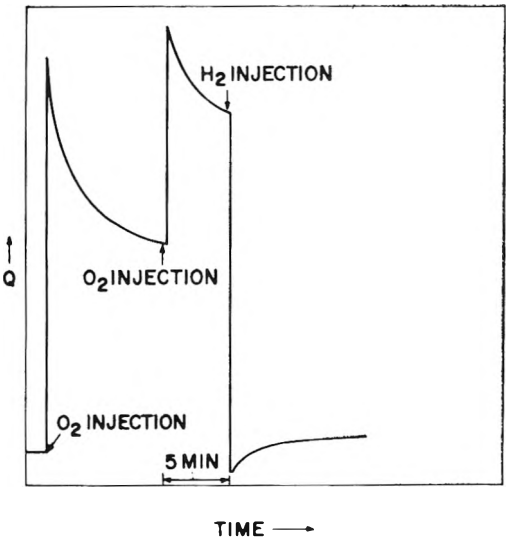

Figure 5. Circuit Q as a function of time following pulsed adsorption of O_2 and H_2 on α-Fe_2O_3; $f = 10^6$ c.p.s.; 400°.

Therefore, both the contacts between particles and the surface region should show relatively large conductivity changes compared to those generated in the bulk. As frequency is increased, the relative change should therefore decrease since a greater portion of the volume of the solid is being examined electrically.[5] It has been found that mechanical vibration of the conductivity cell causes a small, transient conductivity change,[13] the decay of which is weakly temperature dependent. However, this change can only be observed *below* 10^6 c.p.s. if the sample packing is stable. This vibration sensitivity may be interpreted as an

(13) This change is an order of magnitude smaller than that produced by O_2.

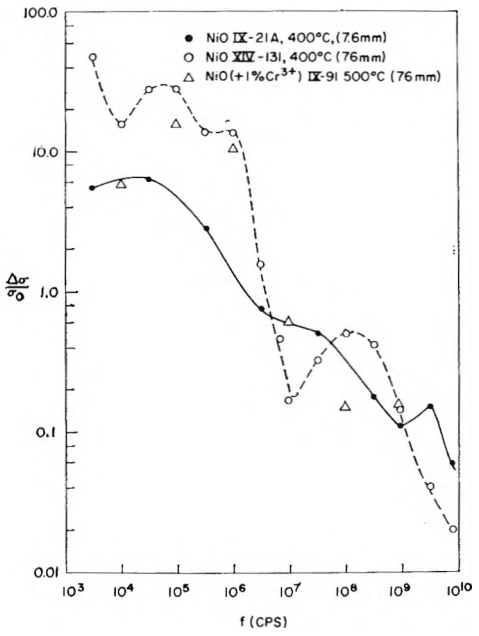

Figure 6. Relative changes in conductivity on "reduced" NiO surfaces following pulsed O_2 adsorption.

indication of participation by particle-to-particle contacts in the observed conductivity. Vibration breaks these contacts and the transient conductivity change is due to a resintering of the contacts. It appears, therefore, that only when conductivity is measured at frequencies of $>10^6$ c.p.s., is the surface contribution (uninfluenced by interparticle contacts) prominent, with changes in other external regions not predominant. Beyond 10^8 c.p.s. it can be inferred that the region of bulk conductivity is being observed, since the relative change drops again. At frequencies below 10^6 c.p.s., the contacts or grain boundaries, which are quite sensitive to O_2, may be observed. The dispersion in Cr^{3+}-doped NiO, which, unlike undoped NiO, exhibits a frequency-independent region,[5] is consistent with these interpretations of the location of the relevant surface region in the frequency domain. The relative conductivity change following pulsed O_2 adsorption is shown for Cr^{3+}-doped NiO (Fig. 6) and the agreement with undoped NiO is quite satisfactory.

Although the relevant region of frequency can be located for examination of predominantly surface effects, it is important to note that the observation of the long transient conductivity decay following pulsed adsorption is seen over a wide frequency range, so that only for quantitative use of the decay phenomena is this specific location relevant to the discussion to follow in the next section.

Before proceeding to a discussion of the nature of the transient decay, the results of the conductivity measurements must be examined in the light of recent determinations of the spatial distribution of excess oxygen ions intrinsically bound in NiO powders. Gossel[14] has performed iodometric titration measurements which have been interpreted to show that most of these oxygen ions appear to be on the outside of the particle. For such a situation the skin would be highly conductive, and little frequency dependence would result since the outside would provide a low-resistance path at all frequencies, in contrast to the observed conductivity which is strongly frequency dependent. It is possible however that as a result of the titration charge carriers are pumped from the interior to the surface so that the total excess oxygen is measured without being on the surface. Further, as will be shown below, most of the oxygen adsorbed in a pulsed adsorption experiment is bound on the surface and not ionized, and therefore may not be detectable by the titration technique. Thus, the distribution of oxygen is by no means well defined even though the total excess quantity of oxygen can be determined.

2. Nature of Transient Decay. At the outset, the fact that a conductivity reversal occurs implies that the O_2 which is adsorbed is not subsequently taken up by the bulk lattice as O^{-2}; this would require either no reversal or a slow increase in conductivity. Note, too, that since the same qualitative changes (increase and reversal in conductivity) are seen at all frequencies, it cannot be assumed that the ions formed "outside" leave and drift into the "interior." In that case, the low-frequency reversal would be accompanied by a high-frequency drift in the opposite direction; this is not observed.

Since lattice incorporation cannot be the cause of the conductivity reversal, extensive oxygen desorption must be considered. The evidence against the desorption mechanism is summarized below.

a. The observed decay is completely independent of helium carrier gas flow, including complete isolation of the cell from the stream during the decay.

b. No drift is observed in the gas chromatograph bridge output, indicating no slow desorption following the main pulse, and trapping of the cell effluent during the decay, using glass wool at 4.2°K., yields O_2 only in amounts attributable to the normal background in the helium carrier (<1 p.p.m. at STP).

c. Injection of a mixture of argon and O_2 shows no indication of any separation between these gases on NiO. Therefore, no reversible adsorption–desorption step is so slow as to hold back the O_2 relative to the argon.[15]

(14) H. Gossel, *Z. Elektrochem.*, 65, 98 (1961).

d. Extensive desorption (or chemical transitions of adsorbed species) might be expected to lead to time-dependent chemical effects. In adsorption or reaction of H_2, O_2, and CO, no difference in the amount adsorbed or reacted can be detected as a function of time following pulsed O_2 adsorption, and thus no gross chemical changes occur during the decay. The fact that H_2 reacts primarily with the quantity of O_2 adsorbed shows that newly adsorbed O_2 is considerably less tightly bound than lattice oxygen.

Local temperature changes resulting from O_2 adsorption do not create the time-dependent decay, since reaction during the decay with H_2 or CO causes the conductivity to change abruptly in the opposite direction (with respect to O_2). The sign of the initial change clearly is in agreement with the usual conception of NiO as having p-type charge carriers[16] with O_2 acting as an acceptor and H_2 and CO as donors. Preliminary examination of n-type oxides (α-Fe_2O_3[17] and ZnO[18]) described above reveals a similar electronic pattern. One would expect, however, to see unidirectional thermal effects since all these reactions are exothermal.[19]

Gaseous diffusional effects due to the presence of a helium atmosphere and the powdered nature of the specimen must be considered, but the data show no indication of such effects. Measurement of the extent of irreversible adsorption from the pulse on the reduced surface indicates a surface coverage of the order of magnitude observed in equilibrium studies[10] and thus indicates complete physical accessibility of the surface to the O_2.

Consequently, the transient decay, which implies the loss of the carriers generated by O_2 adsorption, is not due to extensive desorption of the adsorbed O_2, nor to local heating, nor to gaseous diffusion effects.

Next it is relevant to inquire into the number of charge carriers generated on the freshly reduced surface. In a typical pulse (O_2 on NiO at 400°) on a reduced surface, the largest change in conductivity is observed at 8500 Mc.p.s. where $\Delta\sigma$ is approximately 10^{-5} (ohm cm.)$^{-1}$.[20] Assuming the upper limit for the mobility, 1 cm.^{2}/v. sec., the increase in the number of carriers is 10^{14}/cm.^{3}. The NiO sample (0.25 cm.^{3}) adsorbed (irreversibly) 5×10^{17} molecules and had a B.E.T. area of $\sim$1 m.^{2}. The surface coverage is thus $\sim 5 \times 10^{13}$/cm.^{2}; the ratio of ions remaining (which participate in the conductivity decay) to molecules adsorbed is $\leq 5 \times 10^{-5}$. It should be noted that even if the Hall mobility is as small as the lowest value deduced for NiO at 400° by Morin[16] ($\mu \approx 10^{-2}$ cm.^{2}/v. sec.) from conductivity and Seebeck coefficient data, the ion-to-molecule ratio will be much smaller than unity.[21] Such low ion–molecule ratios have also been reported for ZnO[22] and Cu_2O.[23] Because of the uncertainties in interpretation, however, extensive quantitative measurements of carrier concentration in NiO seem premature, and only the order of magnitude of the ratio can be considered meaningful.

That this ratio is so small in NiO is consistent with other recent studies. Maxim and Braun[24] have proposed that most of the O_2 that is chemisorbed on NiO is present as a neutral species, so that when O_2 preadsorbed on NiO is irradiated with neutrons, the O_2 neutral can act as an acceptor and trap an electron, thus altering the ratio of ionized to neutral oxygens without altering the gross concentration of adsorbed oxygen. This suggestion is based on discrepancies between gravimetric and iodometric titration measurements of excess oxygen, the former always showing much larger quantities of oxygen to be present and the latter showing increasing quantities after irradiation. Haber and Stone[25] have observed photodesorption of O_2 from NiO despite the fact that NiO is not a photoconductor[26,27]; again a stable neutral chemisorbed species is implied. Possible photodesorptive contributions from Ni^{3+} are ignored by assuming that Ni^{3+} is not concentrated on the surface; however, the measurements described above imply that the total number of Ni^{3+} ions is too small to be relevant.

The use of powdered specimens might imply that some kind of special sites peculiar to powders are involved in the decay, but experiments have been carried out on single crystals of NiO (where d.c. measurements suffice), and the slow, flow-independent decays similar to those obtained with powders are still observed.[28]

(15) P. E. Eberly, Jr., *J. Phys. Chem.*, 65, 68 (1961).

(16) F. J. Morin, *Phys. Rev.*, 93, 1199 (1954).

(17) F. J. Morin, *ibid.*, 93, 1195 (1954).

(18) A. R. Hutson, *ibid.*, 108, 222 (1957).

(19) R. M. Dell and F. S. Stone, *Trans. Faraday Soc.*, 50, 501 (1954).

(20) This change may not even represent a d.c. conductivity; it may be merely an upper limit on the magnitude. It is not corrected for density.

(21) The conductivity used is an average value and would be expected to be lower than actual material conductivity, but this factor would not be sufficient to alter the qualitative conclusion.

(22) G. Heiland, E. Mollwo, and F. Stockmann in "Solid State Physics," Vol. 8, F. Seitz and D. Turnbull, Ed., Academic Press, New York, N. Y., 1959, p. 277.

(23) T. J. Gray and S. D. Savage, *Discussions Faraday Soc.*, 28, 159 (1959).

(24) I. Maxim and T. Braun, *J. Phys. Chem. Solids*, 24, 537 (1963).

(25) J. Haber and F. S. Stone, *Trans. Faraday Soc.*, 59, 192 (1963).

(26) J. H. De Boer and E. W. J. Verwey, *Proc. Phys. Soc. Suppl.* (London), 49, 59 (1937).

(27) Recent measurements in this laboratory on both powders and single crystals have confirmed that NiO is not a photoconductor.

All of the available evidence then points to the origin of the conductivity reversal following O_2 adsorption on NiO as being the removal of the gross reactive gas phase (O_2), and this in turn implies, with no desorption, no lattice incorporation, and other artifacts ruled out, that the apparently limited numbers of ions initially formed revert slowly to some neutral but stable adsorbed species. Since the decay is not a simple function of time, it cannot be described in terms of a simple reverse reaction sequence. A more complicated model involving multiple trapping of the charge carrier must be invoked to describe these decays. In this model ions are formed to a limited extent, with the major portion of the adsorbed species being formed in some neutral but excited state. Multiple transitions between excited neutral oxygen and the ion, which involve only the motion of a charge carrier, occur many times prior to a transition of the excited neutral to an unexcited neutral. The excited neutrals are thus slowly removed from the electrical system. In this type of mechanism a limited number of the adsorbed species are ionized at any given time, but all are capable of becoming ionized. Such processes are well known in photoactive semiconductors,[29] but have received scant attention in chemical reaction studies. Calculations based on this model have been performed to describe the form of the decay observed on single crystals.[28] It is found that the analytic expression for the decay thus obtained also describes the results on powders presented here. Maxim and Braun, as noted above, have independently invoked the consequences of such a mechanism to explain a shift in equilibrium adsorption of O_2 on NiO following neutron irradiation.

The connection between these transient decay experiments and those of Glemza and Kokes[2] and Belenkii and Alkhazov[3] seems clear: all these workers observed conductivity reversals when the O_2 pressure in the static system became very small or vanished. Anderson[4] observed a related effect, and in all three studies the necessity of avoiding large quantities of reactive gas in order to observe the effect clearly was noted.

Belenkii and Alkhazov assume that the d.c. conductivity which they measure in Fe_2O_3 is characteristic of the powder surface, and hence the reversals observed must be due to the motion of oxygen ions to and from the surface. Measurements on α-Fe_2O_3 powder using a.c. techniques do not show any difference in the sign of the conductivity change as a function of the frequency. Consequently, since it seems unlikely that ions could move in and out of the bulk without causing one regional conductivity to change in one direction while another undergoes the opposite change, this mechanism seems unlikely. Similar results were found for ZnO.[30]

The multiple trapping concept presented for the O_2–NiO system does not require the motion of ions but only of charge carriers between various trapping sites. Further, the long life associated with these carriers does not require very slow elementary molecular reaction rates (*i.e.*, diffusion steps) but rather a long average lifetime resulting from competitive reactions in which the rate-determining step is not electrically active.

Finally, the existence of these decay phenomena bears strongly on interpretations of desorption experiments, particularly when monitored by electrical conductivity. In particular, the reversal of the conductivity upon pumping out the adsorbing gas does not necessarily imply desorption. Thus, a conductivity reversal of the type discussed above could easily account for the observation of an Elovitch-type decay reported by Gray on the O_2–NiO system,[31] and no slow desorption need ever have occurred. A similar problem exists in the photodesorption studies of Haber and Stone,[25] where the transient nature of the excited neutrals postulated here, if involved, could play a role in the observed inverse relationship between photodesorbed O_2 and O_2 content of NiO.

Summary and Conclusions

1. A technique for simultaneously carrying out pulsed gas adsorption and frequency-dependent conductivity measurements has been described.

2. The utility of pulsed gas adsorption in the study of structural inhomogeneities by a.c. conductivity techniques has been demonstrated.

3. The existence of a transient but long-lived adsorbed ionic species resulting from the adsorption of O_2 on NiO has been demonstrated.

4. The fraction of these transient ions formed that survive long enough to be observed, relative to the number of O_2 molecules initially adsorbed on NiO, has been shown to be $<<1$.

5. The mechanism of the conductivity decay has been postulated to involve the multiple trapping of the carrier by the adsorbed species, leading to a prolonged effective life for the ion involved. Lattice

(28) H. Saltsburg and D. P. Snowden. These results have been presented at the International Conference on the Physics and Chemistry of Solid Surfaces, Brown University, June, 1964. To be published in the proceedings of that conference in "Surface Science."

(29) J. A. Hornbeck and J. R. Haynes, *Phys. Rev.*, **97**, 311 (1955).

(30) H. Saltsburg and D. P. Snowden, *J. Phys. Chem.*, **68**, 2734 (1964).

(31) T. J. Gray and P. W. Darby, *ibid.*, **60**, 209 (1956).

incorporation and desorption have been shown not to occur.

6. The existence of a qualitatively similar effect in Fe_2O_3, Cr_2O_3, and ZnO has been demonstrated.

Potentiometric Studies in Mixed Solvents. I. The Determination of Activity Coefficients and Junction Potentials Using Modified Gran Plots

by F. J. C. Rossotti and Hazel Rossotti

Inorganic Chemistry Laboratory, Oxford University, Oxford, England *(Received May 26, 1964)*

The suitability of various mixed aqueous–organic electrolyte solutions for use as media in potentiometric studies of equilibria was investigated. For systems of 0.5 *M* MX (M = Li^+ or Na^+ and X = ClO_4^- or NO_3^-) in water and 50% v./v. organic solvent (methanol, ethanol, or dioxane), M^+ was gradually replaced by H^+. The resulting changes in activity coefficients and liquid junction potentials are discussed.

Complexes formed in aqueous solution between metal ions and ligands, which are conjugate bases of weak acids, are frequently studied by measuring the concentration, h, of free hydrogen ions, using a suitable galvanic cell.[1,2]

The results are best interpreted if activity coefficients of species participating in the cell reaction, and the potentials at any liquid–liquid junctions, can be kept constant throughout the measurements. Mixed aqueous–organic solvent media are often used to increase the solubility of many metal complexes and also because of their intrinsic interest. Many authors have combined an aqueous reference half-cell with a mixed solvent half-cell and thus have introduced large liquid junction potentials.

In the present work, liquid junctions between aqueous solutions and mixed solvents have been avoided. As a preliminary to studying metal complex formation in mixed aqueous–organic solvents, two series of measurements were made at 25° and ionic strength 0.5 *M* in each of the possible combinations of solvent S (water, 50% v./v. methanol, 50% v./v. ethanol, and 50% v./v. dioxane), background cation M^+ (lithium, sodium), and background anion X^- (perchlorate, nitrate).

Series I. The mean stoichiometric activity coefficient $(\gamma_H\gamma_{Cl})^{1/2}$ was measured as a function of h using the cells

– glass electrode

$$\left|\begin{array}{l}H^+, M^+, Cl^-, X^- \text{ in S}\\ [M^+] + h \sim 0.5\ M\end{array}\right| AgCl(s), Ag(s) + (I)$$

The activity coefficient product $\gamma_H\gamma_{Cl}$ is defined so that $\gamma_H\gamma_{Cl} \rightarrow 1$ as $(h + [Cl^-]) \rightarrow 0$ in each MX–S medium. A stoichiometric activity coefficient is obtained[3] by dividing activity by total as opposed to free concentration and will accordingly differ from the true activity coefficient if the ion under consideration is partially associated.

Series II. The dependence of

$$E_j = E_{j\gamma} - RT/F \ln \gamma_H$$

on h was determined using the cells

(1) F. J. C. Rossotti and H. Rossotti, "The Determination of Stability Constants," McGraw-Hill Book Co., Inc., New York, N. Y., 1961, Sections 4-1, 7-3-A.

(2) J. Bjerrum, G. Schwarzenbach, and L. G. Sillén, Ed., "Stability Constants," The Chemical Society, London, 1957 and 1958.

(3) See ref. 1, Section 2-2-C.

– glass electrode

M^+ (0.5 – h) M H^+ h M X^- 0.5 M in S	MX 0.5 M in S	M^+ 0.49 M Ag^+ 0.01 M X^- 0.5 M in S
(a)		(b)

AgCl(s), Ag(s) + (II)

The term E_j is the potential at the boundary (a); the potential at (b) remains constant and is included in the appropriate formal potential.

Method

Series I. The measurements were carried out as potentiometric acid–base titrations using cell I. A mixture of V ml. of aqueous acid ((1 – Y) M HX + Y M HCl) and V ml. of water or pure organic solvent was titrated with v ml. of aqueous alkali (B M MOH + 1 M MX) together with v ml. of water or pure organic solvent.

The e.m.f. of cell I is given by

$$E = E_0 - \frac{RT}{F} \ln \{H^+\}\{Cl^-\} \qquad (1)$$

where the parameter E_0 contains the formal potentials of both half-cells and the asymmetry potential of the glass electrode. If HX and HCl are completely dissociated

$$h = \frac{VH - vB}{2r(V + v)} = \frac{VH(v_e - v)}{2v_e r(V + v)} \qquad (2)$$

and if HCl and MCl are completely dissociated

$$[Cl^-] = \frac{VY}{2r(V + v)} \qquad (3)$$

where H (1 M in this work) is the initial concentration of aqueous acid, v_e is the equivalence point, and $r = V/2v$ is the contraction factor for the addition of v ml. of aqueous 1 M MX to v ml. of pure solvent to give V ml. of mixture (*cf.* Table I). The ionic strength was kept at a constant value of $\mu = 0.5r^{-1}$ M for each MX–S pair.

Table I: Contraction Factor, r, for Solvent Mixtures

	Water	50% MeOH	50% EtOH	50% dioxane
$LiNO_3$	1.00	0.97	0.97	0.98
$LiClO_4$	1.00	0.96	0.97	0.99
$NaNO_3$	1.00	0.97	0.97	0.98
$NaClO_4$	1.00	0.97	0.97	0.99

From eq. 1, 2, and 3

$$E = E_0 - \frac{RT}{F} \ln \frac{VY(VH - vB)}{4r^2(V + v)^2} - \frac{RT}{F} \ln \gamma_H\gamma_{Cl} \qquad (4)$$

whence

$$E_v = E - \frac{RT}{F} \ln (V + v) = E_0' - \frac{RT}{F} \ln \frac{VH - vB}{V + v} - \frac{RT}{F} \ln \gamma_H\gamma_{Cl} \qquad (5)$$

where the term

$$E_0' = E_0 - \frac{RT}{F} \ln \frac{VY}{4r^2}$$

is constant throughout a titration.

The equivalence point may readily be obtained by a modification of Gran's method.[4] The present procedure also gives values of $\gamma_H\gamma_{Cl}$. The quantity

$$\psi = (V + v) \times 10^{-E.F/2.303RT} \qquad (6)$$

is plotted against v. From eq. 5 and 6

$$\psi = 10^{-E_0'F/2.303RT}(VH - vB)\gamma_H\gamma_{Cl} \qquad (7)$$

Whence, $\psi = 0$ when $VH = v_eB$ and ψ is a linear function of v, provided that $\gamma_H\gamma_{Cl} = 1$. If $\gamma_H\gamma_{Cl} = 1$ only at low values of h, then a straight line drawn through the points $\psi(v)$ at low h can be extrapolated to give values of

$$\psi_1 = 10^{-E_0'F/2.303RT}(VH - vB) \qquad (8)$$

Then from eq. 7 and 8

$$\left(\frac{\psi}{\psi_1}\right)_v = \gamma_H\gamma_{Cl} \qquad (9)$$

Series II. Two sets of measurements were carried out as potentiometric titrations using cell II.

(1) Values of $E_{j\gamma}$ in the region $h \lesssim 0.2$ M were obtained by titrating a mixture of V ml. of aqueous 1 M MX and V ml. of pure solvent with v ml. of aqueous 1 M HX and v ml. of pure solvent. For cell II

$$E = E_0 + E_{j\gamma} - \frac{RT}{F} \ln h \qquad (10)$$

where, provided that HX is completely dissociated

$$h = \frac{vH}{2r(V + v)} \qquad (11)$$

(4) G. Gran, *Analyst*, **77**, 661 (1952).

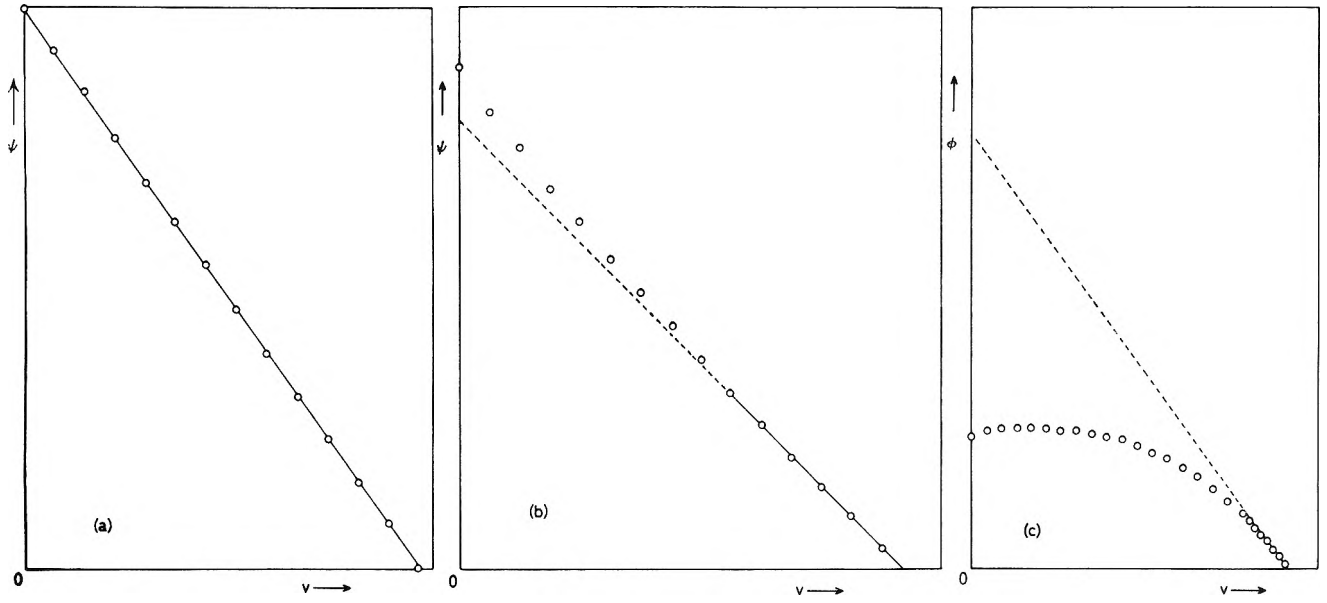

Figure 1. Gran plots $\psi(v)$ and $\phi(v)$, *cf.* eq. 6 and 13: (a) $LiNO_3$–EtOH in cell I, $\gamma_H\gamma_{Cl} = 1$; (b) $NaNO_3$–dioxane in cell I, $\gamma_H\gamma_{Cl} \gtrsim 1$; (c) $NaClO_4$–MeOH in cell II, $E_j \gtrsim 0$. The dotted lines represent $\psi_1(v)$ and $\phi_1(v)$, *cf.* eq. 8 and 14.

The value of E_0 was obtained as the value of $E + RT/F \ln h$ at low values of h and was found to be constant for values of h up to at least 0.01 M.

(2) Values of E_j over the whole range $h \lesssim 0.5$ M were obtained by titrating a mixture of V ml. of aqueous 1 M HX and V ml. of pure solvent with v ml. of aqueous alkali (B M MOH and 1 M MX) together with v ml. of pure solvent. The value of $E_{j\gamma}$ was calculated by an extension of Gran's method.[4]

Since h is again given by eq. 2, combination with eq. 10 gives

$$E = E_0 + E_j - \frac{RT}{F} \ln \frac{VH - vB}{2r(V + v)} \qquad (12)$$

Thus

$$\phi = (V + v) \times 10^{-EF/2.303RT} = 10^{-(E_0 + E_{j\gamma})F/2.303RT} \left(\frac{VH - vB}{2r}\right) \qquad (13)$$

As $h \to 0$, $E_{j\gamma} \to 0$ and ϕ becomes a linear function of v such that $\phi = 0$ when $v = v_e$. Extrapolation of the linear part of the function $\phi(v)$ gives values of

$$\phi_1 = 10^{-E_0F/2.303RT}\left(\frac{VH - vB}{2r}\right) \qquad (14)$$

whence

$$E_{j\gamma} = \frac{2.303RT}{F} \log \left(\frac{\phi}{\phi_1}\right)_v \qquad (15)$$

Experimental

Chemicals. Lithium perchlorate was prepared by neutralizing Analar grade perchloric acid with lithium carbonate and recrystallizing the product from water. Hopkins and Williams G.P.R. grade lithium hydroxide was found to be free from sodium and halide ions and was used without further purification. All other chemicals were of Analar grade.

Apparatus. Grade A glassware was used for all volumetric work. Solutions were prepared and measurements were made in a room kept at 25 ± 1°. Titrations were carried out in a five-necked flask in a water bath thermostated at 25 ± 0.1°. Stirring was carried out by a stream of nitrogen presaturated with the appropriate MX–S mixture. Potentials were measured to ±0.2 mv. with a Radiometer pHM4 which had been calibrated against a Pye precision potentiometer. The Radiometer glass electrode, Type 202A, was stored in water when not in use. Silver and silver–silver chloride electrodes were prepared as described by Brown[5] and were soaked overnight in water before use. For cell I, it was necessary to use a new silver–silver chloride electrode for each titration. A Wilhelm-type reference half-cell and liquid junction[6] was used in cell II. For both cells, attainment of equilibrium was somewhat slow in ethanolic solutions, but it was rapid and repro-

(5) A. S. Brown, *J. Am. Chem. Soc.*, **56**, 646 (1934).

(6) W. Forsling, S. Hietanen, and L. G. Sillén, *Acta Chem. Scand.*, **6**, 901 (1952).

Table II: The Stoichiometric Activity Coefficient Product $\gamma_H\gamma_{Cl}$ as a Function of h for $[Cl^-] = 2 \pm 0.5$ mM

	h, M	0.449	0.392	0.342	0.297	0.257	0.221	0.189	0.159	
$NaNO_3$–EtOH	$\gamma_H\gamma_{Cl}$	(1.085)	1.096	1.078	1.072	1.052	1.041	1.023	1.012	
$NaNO_3$–dioxane	$\gamma_H\gamma_{Cl}$	1.090	1.075	1.063	1.041	1.037	1.025	1.015	1.003	
	h, M	0.482	0.420	0.365	0.316	0.272	0.233	0.197	0.165	0.135
$NaClO_4$–EtOH	$\gamma_H\gamma_{Cl}$	1.105	1.088	1.074	1.059	1.044	1.035	1.026	1.019	1.002
$NaClO_4$–dioxane	$\gamma_H\gamma_{Cl}$	1.103	1.082	1.065	1.044	1.035	1.028	1.024	1.013	1.006

ducible in the other three solvents. All titrations were carried out in duplicate.

Contraction Factors. Densities ρ_A, ρ_B, and ρ_{AB} of aqueous 1 M MX (A), of pure solvents (B), and of 50% v./v. mixtures of A and B were determined by weighing volumes measured by buret. Values of the contraction factors $\gamma = (\rho_A + \rho_B)/2\rho_{AB}$ are given in Table I.

Results

Series I. Measurements were first carried out in the range of chloride ion concentration 1.25 m$M \leqslant [Cl^-] \leqslant 2.5$ mM. Linear plots $\psi(v)$ (see Fig. 1a) were obtained for all systems in which $M^+ = Li^+$ and for the two sodium salts in water and in aqueous methanol. Thus, for all these systems, $\gamma_H\gamma_{Cl} = 1$ over the whole range of acidity 0.5 $M \leqslant h \leqslant 0$ studied. Deviations of $\psi(v)$ from linearity for sodium nitrate and perchlorate in aqueous ethanol and aqueous dioxane are consistent with values of $\gamma_H\gamma_{Cl} > 1$ for $h \gtrsim 0.08$ M (see Fig. 1b and Table II). Plots $\psi(v)$ for the systems $NaNO_3$–dioxane, $NaClO_4$–ethanol, and $NaClO_4$–dioxane were linear at lower chloride ion concentrations, 1 m$M \geqslant [Cl^-] \geqslant 0.5$ mM, indicating that $\gamma_H\gamma_{Cl} = 1$ under these conditions and hence presumably that $\lim_{[Cl^-]\to 0} \gamma_H = 1$. The less reliable functions $\psi(v)$ for the $NaNO_3$–ethanol system were similar for the two chloride ion concentrations studied.

Series II. Deviations of the plots $\phi(v)$ from linearity (see Fig. 1c) in the region $h \gtrsim 0.01$ M indicated that, for all sixteen systems studied, $E_{j\gamma} > 0$. There was usually excellent agreement between the functions $E_{j\gamma}(h)$ obtained using eq. 10 and 11, and those obtained using large-scale Gran plots (eq. 2 and 15). However, for a few systems (*cf.* Fig. 1c), the linear extrapolation of $\phi(v)$ was not unequivocal. In these cases, values of $E_{j\gamma}$ obtained from eq. 10 and 11 at moderate values of h were inserted into eq. 15 to obtain values of $E_{j\gamma}$ at higher values of h. Plots of $E_{j\gamma}$ against h are shown in Fig. 2.

Discussion

Series I. The linearity of the plots $\psi(v)$ for all eight lithium systems and for the two sodium systems in both water and in aqueous methanol supports the assumptions made in deriving eq. 2, 3, and 11 that $HClO_4$, HNO_3, HCl, and MCl are all completely dissociated. Since the stoichiometric activity coefficient product $\gamma_H\gamma_{Cl}$ is unity over the whole range of replacement of M^+ by H^+, the true activity coefficient product must also be unity. The direction of curvature of $\psi(v)$ for the two sodium systems in aqueous ethanol and aqueous dioxane is consistent with a greater association of chloride ions with sodium ions than with protons. Indeed, since HCl is completely dissociated in the lithium media, it is unlikely to be appreciably associated in the analogous sodium media. If sodium and chloride ions do associate, the values of the stoichiometric activity coefficient products $\gamma_H\gamma_{Cl}$ given in Table II will differ from those of the true activity coefficient products.

There is independent evidence that $HClO_4$ is completely dissociated in 80% v./v. acetone.[7]

On the other hand, there are indications[8-10] that HCl, LiCl, and NaCl are incompletely dissociated in 50% v./v. dioxane. Unfortunately, the values of the dissociation constants, which are mainly derived from conductivity measurements, are so sensitive to the method of computation that it is not clear what reliance should be placed upon the data. However, such association as might occur would certainly be expected to increase in the sequences $H^+ < Li^+ < Na^+$ (*cf.* ref. 9 and 10), $ClO_4^- < NO_3^- < Cl^-$ (*cf.* ref. 2 and 11), and water < methanol < ethanol < dioxane. Our results are compatible with these sequences.

No activity coefficients of acids in $HClO_4$–$MClO_4$ or HNO_3–MNO_3 media seem to have been reported. Biedermann and Sillén's measurements[12] of the potentials of several half-cells in mixtures of H^+ and Na^+ in aqueous ClO_4^- could best be explained by assuming

(7) V. M. Atkins and C. B. Monk, *J. Chem. Soc.*, 1817 (1961).

(8) H. P. Marshall and E. Grunwald, *J. Chem. Phys.*, **21**, 2143 (1953).

(9) G. R. Nash and C. B. Monk, *Trans. Faraday Soc.*, **54**, 1650 (1958).

(10) T. L. Fabry and R. M. Fuoss, *J. Phys. Chem.*, **68**, 971 (1964).

(11) L. G. Van Uitert, W. C. Fernelius, and B. E. Douglas, *J. Am. Chem. Soc.*, **75**, 2739 (1953).

(12) G. Biedermann and L. G. Sillén, *Arkiv Kemi*, **5**, 425 (1953).

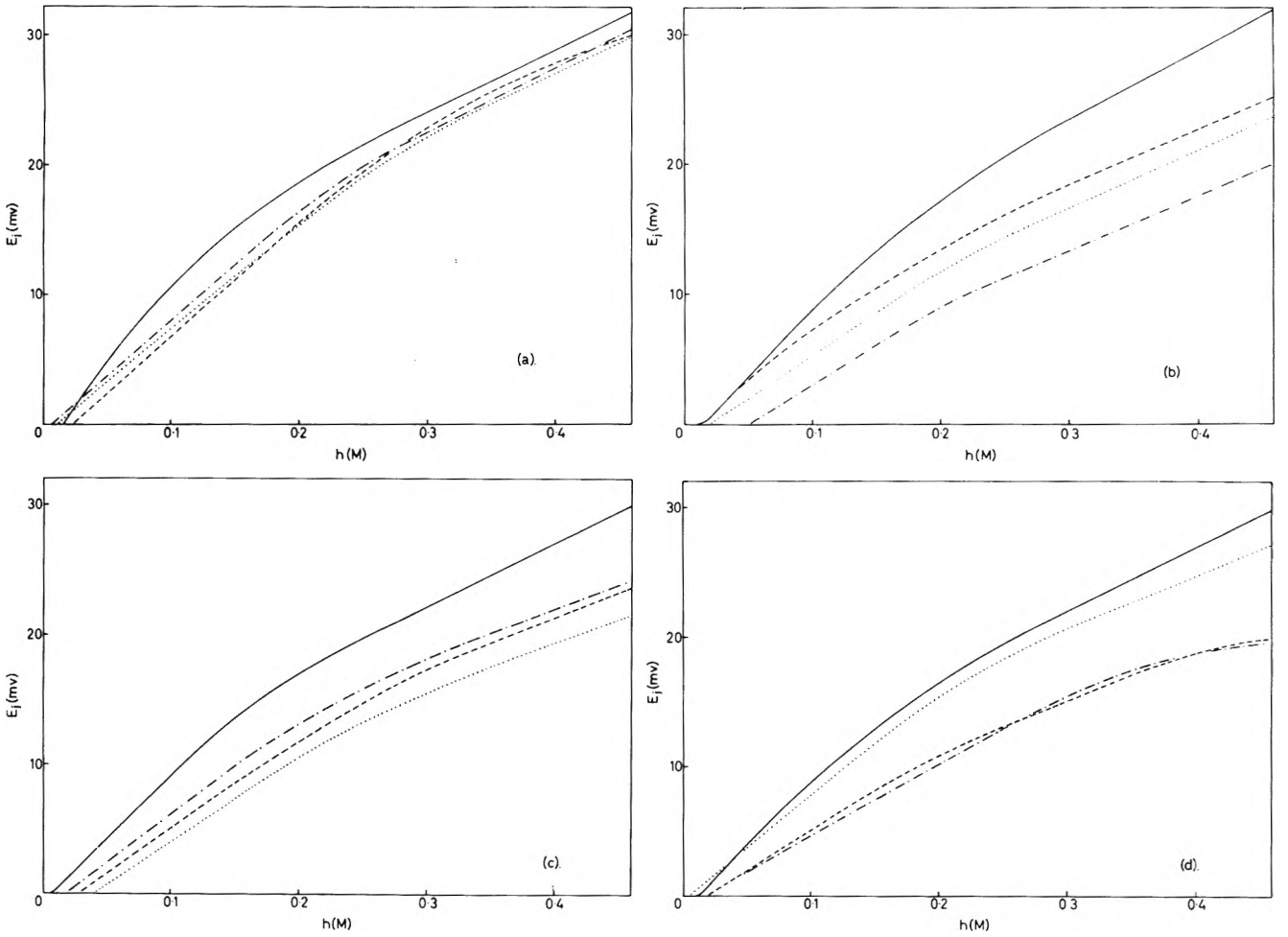

Figure 2. Liquid junction potentials E_j as function of h: (a) $LiNO_3$, (b) $LiClO_4$, (c) $NaNO_3$, (d) $NaClO_4$. Full lines represent water, dotted lines 50% methanol, dot-dashed lines 50% ethanol, and dashed lines 50% dioxane.

that the activity coefficients of the participating cations were independent of h in the range 50 m$M \leqslant h \leqslant$ 600 mM. However, Zielen and Sullivan[13] found that the formal potentials of some couples involving metal ions in 2 M aqueous $HClO_4$–$MClO_4$ mixtures were linear functions of h, indicating a Harned rule relationship[14] between the activity coefficients of the cations and the composition of the medium. Biedermann and Sillén[12] observed similar behavior of γ_{Cl} and γ_{Br} in 3 M ($H^+ + Na^+$) mixtures containing ~10 mM halide ions in a perchlorate medium. Thus the present observation that, as $[Cl^-] \rightarrow 0$, $\gamma_H\gamma_{Cl} \rightarrow 1$, is in agreement with Brønsted's principle of specific ionic interaction[15,16] and with Biedermann and Sillén's conclusion[12] that, at constant ionic strength, change in h affects γ_{Cl} but not γ_H. The effect of h on $\gamma_H\gamma_{Cl}$ for the low concentrations, 0.5 m$M \leqslant [Cl^-] \leqslant$ 1 mM, of chloride ions used in this work is much smaller than the effect of h on γ_{Cl} and γ_{Br} for halide ion concentrations of about 10 mM. The fact that $\gamma_H\gamma_{Cl}$ deviates from unity when Na^+, but not Li^+, replaces H^+ is in agreement with Zielen and Sullivan's observation[13] that dE/dh for the formal potential E of the Np(V)–(VI) couple is −4.78 mv. in 2 M $NaClO_4$ but is only −1.51 mv. in 2 M $LiClO_4$.

Values of $\gamma_H\gamma_{Cl}$ do not show a Harned rule dependence on h over the whole range of acidities studied. Thus for $NaNO_3$ and $NaClO_4$ in aqueous ethanol and dioxane, log $\gamma_H\gamma_{Cl} \sim 0$ in the range $0 < h \lesssim 0.1$ M, but it is an approximately linear function of h when $0.1 \lesssim h \lesssim 0.5$ M.

Series II. For all systems except $NaNO_3$–EtOH, it can be assumed that $\gamma_H = 1$ and hence that the term $E_{j\gamma}$ represents only the liquid junction potential, E_j.

(13) A. J. Zielen and J. C. Sullivan, *J. Phys. Chem.*, **66**, 1065 (1962).

(14) H. S. Harned, *J. Am. Chem. Soc.*, **57**, 1865 (1935); K. S. Pitzer and L. Brewer, "Thermodynamics," McGraw-Hill Book Co., Inc., New York, N. Y., 1961, p. 568.

(15) See ref. 1, Section 2-1.

(16) J. N. Brønsted, *J. Am. Chem. Soc.*, **44**, 877 (1922); **45**, 2898 (1923).

The theoretical value of E_j for a given liquid–liquid junction could only be calculated if the exact structure of the boundary[17] and the mobilities of all ions present were known under the conditions used. For a continuous boundary junction between an aqueous solution of MX and aqueous HX–MX mixtures at constant ionic strength, an approximate form[12] of Henderson's equation gives

$$E_j = \frac{RT}{F} \ln\left(1 + \frac{dh}{\mu}\right) \qquad (16)$$

The experimental value of the parameter d in some perchlorate and nitrate mixtures was found[12] to be considerably lower than the predicted value

$$d_{\text{calcd}} = (\Lambda_{HX} - \Lambda_{MX})/\Lambda_{MX} \qquad (17)$$

where Λ_{HX} and Λ_{MX} are the conductivities of μM HX and μM MX.

Plots of the present measurements of $y = (10^{E_jF/2.303RT} - 1)$ are markedly curved showing that d is not independent of h over the whole range of acidities studied. The dependence of d on h has also been observed for 0.1 M HNO_3–$AgNO_3$ mixtures.[18]

Although there are no available conductivity data obtained under conditions even approaching those used in the present work, values of $d^\circ_{\text{calcd}} = (\Lambda^\circ_{HX} - \Lambda^\circ_{MX})/\Lambda^\circ_{HX}$ have been calculated from limiting conductivities[19] in pure water, pure methanol, and pure ethanol (see Table III). These values of d°_{calcd} must differ considerably from values of d_{calcd} for 0.5 M electrolytes in mixed solvents. However, the high values of d°_{calcd} for water, compared with those for the alcohols, are consistent with the observation that, for a given electrolyte, $(E_j)_h$ is higher in water than for that in mixed solvents. The differences between d°_{calcd} for the various electrolytes in a given solvent and for the same electrolyte in methanol and ethanol are too small to predict any other trend in E_j. The expected similarity between the plots $E_j(h)$ for different electrolytes in the same solvent is in agreement with Biedermann and Ciavatta's observation[20] that the values of dE_j/dh for 3 M $HClO_4$–$NaClO_4$ and 3 M $HClO_4$–$LiClO_4$ differ by only $\sim$1 mv. M^{-1}.

Table III: Values of d°_{calcd}

	Water	50% MeOH	50% EtOH
$LiNO_3$	2.80	1.03	1.05
$LiClO_4$	2.93	0.83	0.96
$NaNO_3$	2.42	0.91	...
$NaClO_4$	2.79	0.86	0.82

It has been seen that for all systems studied (except $NaNO_3$–EtOH), $\gamma_H \rightarrow 1$ as $[Cl^-] \rightarrow 0$. Moreover, the functions $E_j(h)$ for a given solvent do not vary grossly with the nature of the salt medium. Thus, with regard to activity coefficients and junction potentials, there is little to choose between Li^+ and Na^+, or between NO_3^- and ClO_4^- as background ions.

(17) R. G. Bates, "Determination of pH," John Wiley and Sons, Inc., New York, N. Y., 1964, pp. 36, 268.

(18) E. Ekedahl, unpublished work referred to in ref. 12.

(19) Landolt-Bornstein, II (7), Sections 276311, 276411 (1960).

(20) G. Biedermann and L. Ciavatta, *Acta Chem. Scand.*, 15, 1347 (1961).

Spectral Evidence on Rare Earth Covalent Binding[1a]

by Leonard I. Katzin and M. Louise Barnett[1b]

Chemistry Division, Argonne National Laboratory, Argonne, Illinois *(Received May 28, 1964)*

It is shown that under conditions which satisfy chemical criteria for covalent interaction—dissolution of precipitates by complexing agents, alteration of vibrational spectra of donors, and changes in coordination number—the absorption spectra of Pr(III), Nd(III), and Er(III) are altered by small wave length shifts in some absorption peaks, large differential shifts in intensities, and differential changes in splittings. The alterations are rather individual for the different ligands. The conclusion is drawn that hybrid orbitals with 4f contribution are involved in even the crystal and hydrate systems for which the spectrum is "normal."

I. Introduction

A statement of the structural basis for the chemical similarities of the rare earths made in 1947 by Yost, Russell, and Garner,[2] "... the marked similarity in chemical behavior results from the existence of the seven 4f states with a capacity for fourteen electrons ... (in the normal trivalent state) the 4f electrons are not involved in the formation of chemical bonds, and the electrons remaining in these states are perturbed only slightly by the fields due to neighboring atoms," would probably still be considered acceptable by most chemists and physicists.

As can be seen, if the 4f orbitals are not involved in bonding, the rare earth ions must present a noble gas configuration to the environment. As with the alkali metals and alkaline earths, it has therefore been the practice to treat these ions as simple, electrostatically charged spheres in their chemical relations. In recent years, this has been refined to the crystal field description of the alterations in the properties, particularly of the spectrum.

Spectral studies in 1928[3] showed that even in aqueous solution, nitrate ion and nitric acid affected some rare earth spectra differently than did HCl and chloride (see also Oetjen[4]). Moeller and Jackson[5a] were able to form soluble compounds of rare earths with substituted 8-quinolinols in alkaline solutions from which they would otherwise be precipitated (Moeller and Ulrich[5b] did similarly with acetylacetone) and to extract these chelates into chloroform. Anionic complexes were formed in alkaline solutions of ethylenediaminetetraacetate, and marked spectral changes were exhibited.[6] With the distinction still current between robust complexes of the sort involved with, for example, nonmagnetic Co(III) compounds, square-planar nickel cyanide, etc.,[7] and the rapidly reacting, fugitive sorts of complexes formed by most cations, and with the absorption spectra of the salts not yet well analyzed and understood, such findings were interesting but not presented as direct challenges to the current dogma.

The liquid, tributyl phosphate (TBP), as well as related compounds possessing the phosphoryl group, is a very strong electron donor. This enables it to dissolve many metal salts, by forming a liquid, water-insoluble solvate complex, soluble even in alkyl hydrocarbon solvents. In particular, it will dissolve rare earth salts, and the infrared absorption spectrum of such solutions[8] shows not only that the vibrational fre-

(1) (a) Based on work performed under the auspices of the U. S. Atomic Energy Commission; presented at 4th Rare Earth Research Conference, Phoenix, Ariz., April 22–25, 1964; (b) Student Aide (Knox College), Argonne-ACM Program, Fall, 1963.

(2) D. M. Yost, H. Russell, Jr., and C. S. Garner, "The Rare Earth Elements and Their Compounds," John Wiley and Sons, Inc., New York, N. Y., 1947, p. 4.

(3) L. L. Quill, P. W. Selwood, and B. S. Hopkins, *J. Am. Chem. Soc.*, **50**, 2929 (1928).

(4) G. W. Oetjen, *Z. Naturforsch.*, **4a**, 1 (1949).

(5) (a) T. Moeller and D. E. Jackson, *Anal. Chem.*, **22**, 1393 (1950); (b) T. Moeller and W. F. Ulrich, *J. Inorg. Nucl. Chem.*, **2**, 164 (1956).

(6) T. Moeller and J. C. Brantley, *J. Am. Chem. Soc.*, **72**, 5447 (1950).

(7) L. Pauling, "The Nature of the Chemical Bond," 3rd Ed., Cornell University Press, Ithaca, N. Y., 1960, Chapter 5.

quency of the phosphoryl group has changed by virtue of being bonded to the metal ion, but if the salt is a nitrate, the vibrational spectrum of the nitrate ion is altered to show that it also is bonded to the cation. It therefore seems essential to consider the implications and consequences of covalent bonding in the rare earths.

This paper will present data on absorption spectral changes for Pr^{3+}, Eu^{3+}, and Er^{3+} systems for which covalency is adduced on chemical grounds. The term assignments recently made for the absorption bands[9-13] furnish a necessary background to the discussion of these data. Inasmuch as it has been observed that alkaline solutions of hydroxylic organic acids, such as tartaric acid, not only give chemical evidence for strong complexes with rare earths, but also show Cotton effects in the absorption region[14] which are evidence for covalent relations, our studies include TBP solutions, alkaline solutions of hydroxylic acids, and simple nonaqueous solutions, as in ethyl alcohol.

II. Experimental Findings

a. Pr^{3+} Salts. The spectrum of a $PrCl_3$ solution in water (*ca.* 0.1 *M*) is shown in Fig. 1a. The assigned ground state[9,10] is $^3H_4$, and the upper levels of the transitions are indicated on the respective absorption peaks. The asymmetry on the short wave length side of the $^3P_1$ peak base presumably reflects the absorption to the $^1I_6$ state. Dissolving the chloride in ethyl alcohol (Fig. 1b) or the bromide in tributyl phosphate (TBP) (Fig. 1c) decreases the $^3P_2$ intensity relative to the $^3P_1$ peak and raises the intensity of the $^3P_0$ relative to the same standard. There also are obvious broadenings and wave length shifts of all the peaks in the spectrum.

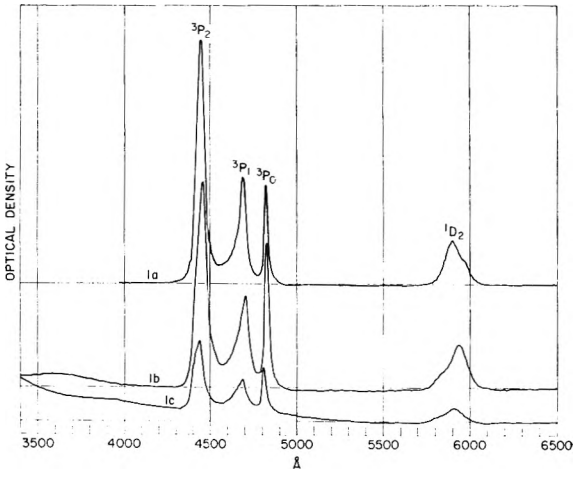

Figure 1. Pr(III) spectra: a, chloride in water; b, chloride in EtOH; c, bromide in TBP. Broad absorption at 3700 Å. in (b) and 3900 Å. in (c) due to $^{tet}Fe(III)$.

The chloride in TBP shows a spectrum very like the bromide, with respect to the Pr(III) peaks, but there are differences.

The spectrum of $Pr(NO_3)_3$ in TBP, in contrast (Fig. 2), shows a very marked intensification of the $^3P_2$ peak relative to the others in the spectrum, the $^3P_1$ absorption is markedly broadened, and the $^3P_0$ shows a definite fine structure. The $^1D_2$ also shows very marked change.

b. Pr(III) and Hydroxy Acids. If, to an aqueous solution of a Pr(III) salt and tartaric acid, alkali is slowly added, a precipitate forms as the acid is progressively neutralized with alkali. If alkali is added to

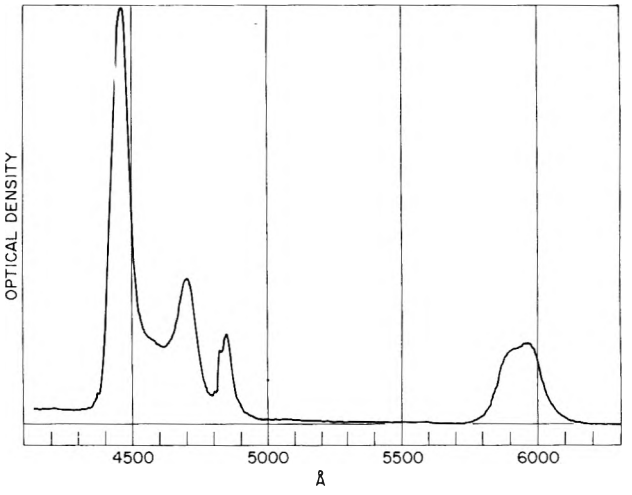

Figure 2. $Pr(NO_3)_3$ in TBP.

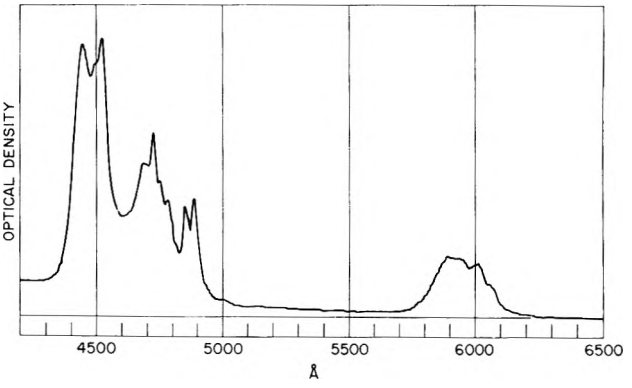

Figure 3. Pr(III) in tartrate, 1:1, pH 9.

(8) L. I. Katzin, Report AERE-R 3031 (1959); *J. Inorg. Nucl. Chem.*, **20**, 300 (1961); **24**, 245 (1962).
(9) G. H. Dieke and R. Sarup, *J. Chem. Phys.*, **29**, 741 (1958).
(10) J. B. Gruber, *ibid.*, **38**, 946 (1963).
(11) B. G. Wybourne, *ibid.*, **32**, 639 (1960).
(12) J. C. Eisenstein, *ibid.*, **39**, 2128 (1963).
(13) J. C. Eisenstein, *ibid.*, **39**, 2134 (1963).
(14) L. I. Katzin and R. W. Anderson, unpublished.

about pH 7, the solid redissolves and the solution remains clear until past pH 11. Further alkali may reprecipitate praeseodymium. As low a tartrate:Pr mole ratio as 1:1 is just sufficient to allow full solution of the precipitate above pH 7. Higher ratios of tartrate do not affect the spectrum shown in Fig. 3, although there is a slight alteration perceived between ratios of, say, 1.0 and 1.1, presumably due to a mass action effect. The spectrum shown was taken at about pH 9. From about pH 10 up, the spectrum commences to deteriorate and alter, presumably reflecting changes which finally give precipitation. A solution of the complex, placed on a cation-exchange resin column and eluted with alkaline tartrate, shows no sign of lag in removal, showing lack of positive charge. A similar experiment with an anion-exchange column shows perhaps a slight lag, of one column volume. This suggests that the complex is either neutral or of a negative charge which does not compete well with tartrate ion (*e.g.*, -1).

One mole of citric acid per mole of Pr(III) gives a precipitate which dissolves on addition of excess alkali. With three to six moles of citric acid per Pr, no precipitate is seen. If one follows the spectrum of the solution with six moles citric acid per Pr through pH 7, no appreciable change from that of a salt in water is seen. However, the spectra at pH 9 and 11 are shown in Fig. 4. If one keeps the pH at which the spectra are read approximately constant, say pH 10–11, and varies the ratio of citrate to Pr(III) from 1 to 6, and higher, one sees the spectra given in Fig. 5. The spectra seem to indicate that there may be two soluble complexes in the alkaline region that do not occur at lower pH, and the equilibria between these depend both on the stoichiometry (two different citrate:Pr ratios are involved) and on the competition of the hydroxyl.

Malic acid, at ratios of 3:1 and 7:1, prevents Pr(III) from being precipitated at pH 9–11. The spectra are

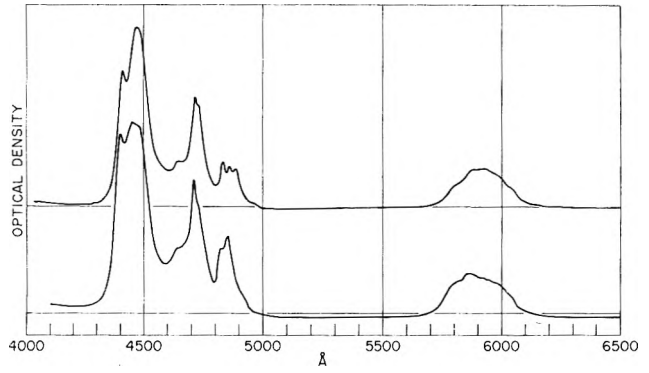

Figure 4. Pr(III) and citrate, 1:6: (from top) pH 9; pH 11.

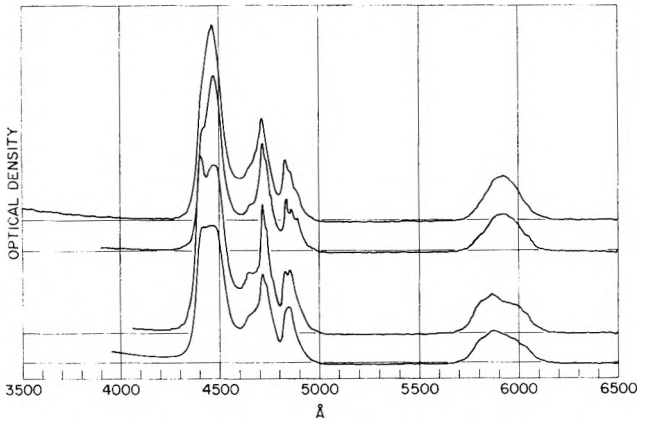

Figure 5. Pr(III) and citrate, pH 11: (from top) 1:1; 1:3; 1:6; 1:saturated.

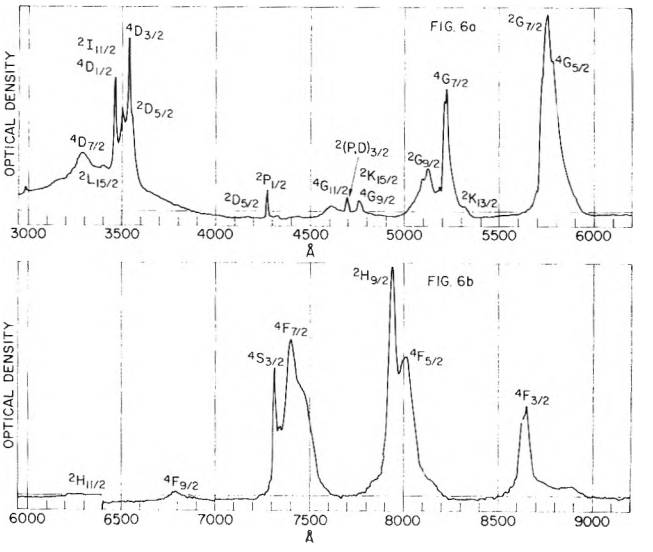

Figure 6. Nd(III) in water.

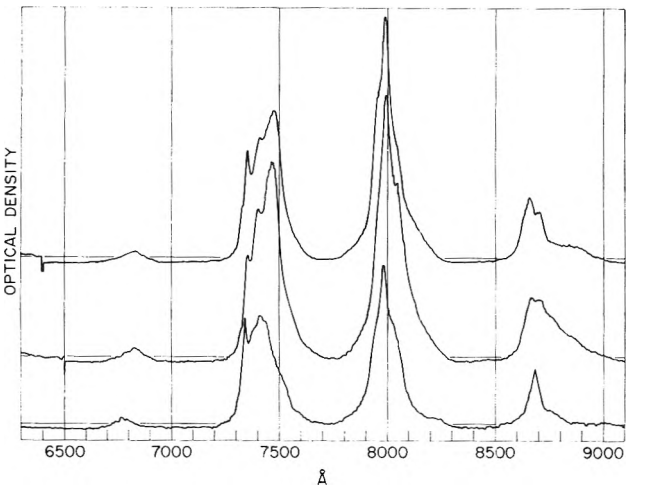

Figure 7. Neodymium salts in TBP: (from top) $NdBr_3$; $NdCl_3$; $Nd(NO_3)_3$.

slightly broadened and shifted to longer wave length, so that the $^1I_6$ absorption is more separated from the $^3P_1$ peak. At the highest concentration ratio and pH, there are indications of a distinct doubling in the $^3P_2$ absorption, with probable peaks at roughly 4425 and 4465 Å. Gluconic acid (prepared by hydrolyzing the lactone in alkali) showed a very similar pattern of behavior, the splitting of $^3P_2$ (at a ratio of 6:1 and pH 11) showing peaks at 4450 and 4485 Å. γ-Hydroxybutyric acid, similarly prepared from the lactone, also maintained Pr(III) in solution, but showed no spectral alterations. Ethylenediaminetetracetic acid, at pH 11, showed only slight shifts and broadenings of the ^3P absorptions.

c. Nd^{3+} Salts. The aqueous spectrum of a solution of $NdCl_3$ is shown in Fig. 6, with the upper-state levels[13] for the absorption bands marked. The ground state is $^4I_{9/2}$. The nitrate, bromide, and chloride dissolved in TBP show distinctive spectra, as illustrated in Fig. 7 and 8. There is a small systematic shift of the bands to longer wave length, presumably related to a shift in the ground-state level. In addition, certain of the transitions are markedly affected in all three spectra, though to different degrees. These are the members of the ^4F bands ($^4F_{3/2}$, $^4F_{5/2}$, $^4F_{7/2}$; changes in the $^4F_{9/2}$ peak are not obvious, perhaps due to its low intensity) and of the ^4G bands ($^4G_{5/2}$, $^4G_{7/2}$, and $^4G_{9/2}$).

d. Nd(III) and Hydroxy Acids. The chemical evidence for strong complex formation is similar to that for Pr(III)—color change and redissolution of a precipitate in going from acid to alkaline solutions. The spectra for the Nd(III)–tartrate system are shown in Fig. 9 and 10, for approximately constant pH 11, and tartrate:Nd ratios from about 1.5 to 4. There may

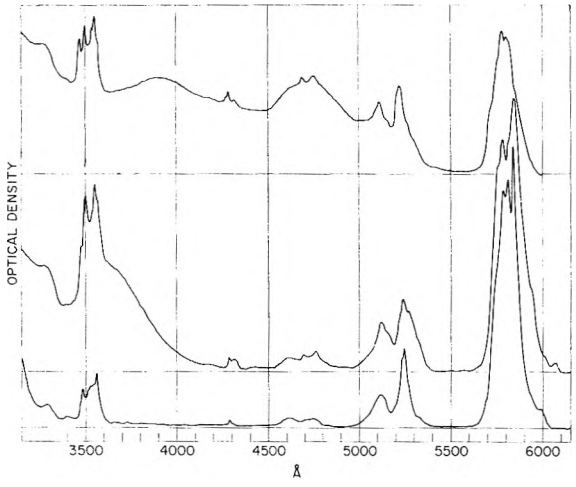

Figure 8. Neodymium salts in TBP: (from top) $NdBr_3$; $NdCl_3$; $Nd(NO_3)_3$. Broad absorptions at 3900 and 4700 Å. in bromide, 3700 Å. in chloride, due to $^{tet}Fe(III)$.

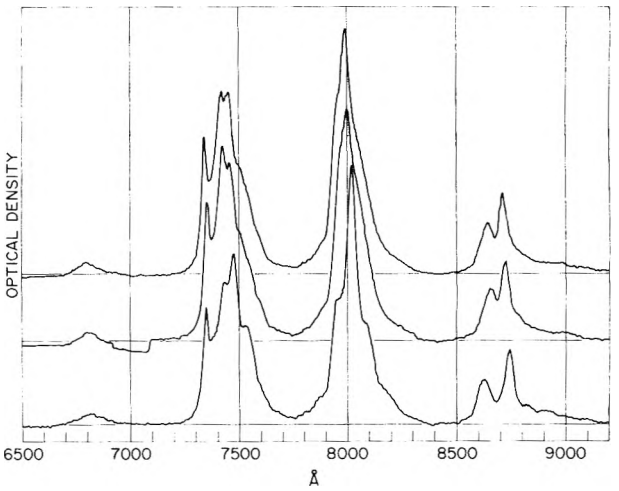

Figure 9. Nd(III)–tartrate solutions, pH ~11: (from bottom) 1:1.5; 1:3; 1:4.

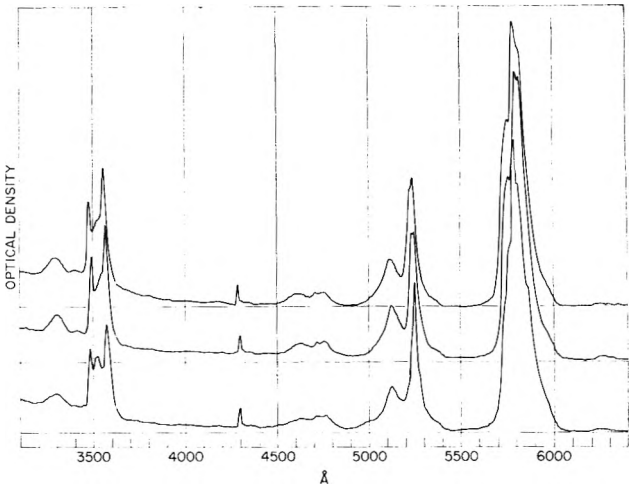

Figure 10. (See Fig. 9).

have been an inconstancy of pH which may cloud fine details of the results slightly. Again the ^4F and ^4G terms seem to show the most of the alterations, the $^4F_{3/2}$ in particular showing a very wide splitting. Either the $^2D_{5/2}$ or the $^4D_{3/2}$ contributor to the 3500-Å. band also is affected. In contrast to the situation with Pr(III), there may be evidence for more than a sole 1:1 complex.

Citric acid, even at pH 3, shows a considerable alteration of the Nd(III) spectrum, which is rather reminiscent of the spectrum in alkaline tartrate above. This spectrum remains unaltered to pH 7 (Fig. 11, 12), in a solution with 6 moles of citrate per Nd. At pH 9 and 11, marked additional charges are seen, *e.g.*, further splitting of the ^4F levels, etc. Many of these changes can be seen with a ratio of citrate to rare earth of only 1:1 (see figures) in alkaline solution.

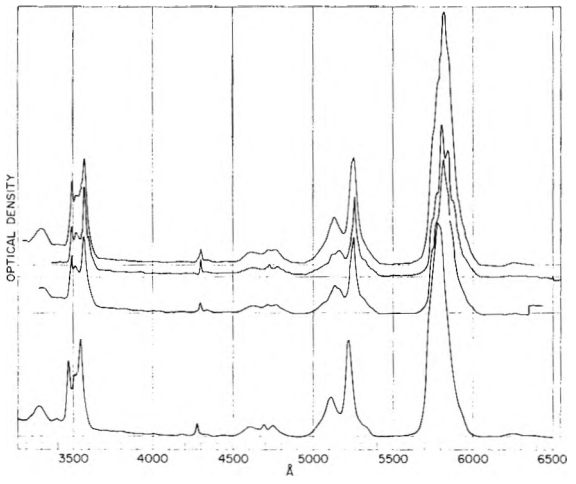

Figure 11. Nd(III)–citrate: (from bottom) 1:6 ratio, pH 3; pH 9; pH 11; 1:1 at pH 11.

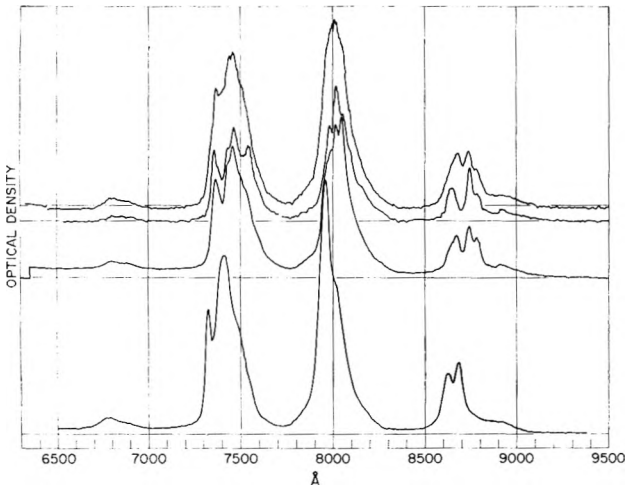

Figure 12. (See Fig. 11.)

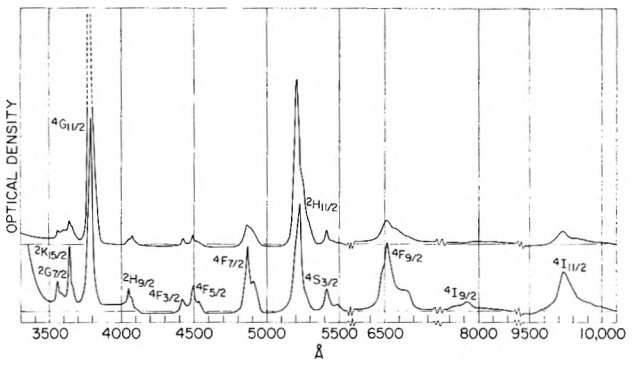

Figure 13. $Er(NO_3)_3$: (lower) in water; (upper) in TBP.

e. Er^{3+} Salts. While Nd^{3+} has an f^3 configuration, Er^{3+} is three electrons shy of a full f^{14} configuration. The terms are therefore the same, with an inversion of the order of multiplets. As seen in the aqueous spectrum of the nitrate (Fig. 13), the various levels are rather more separated than for Nd, simplifying the spectrum somewhat. In the absence of the nitrate absorption below 3500 Å., as in a chloride solution, small absorptions at about 3355 Å. ($^2P_{3/2}$) and at 3160 Å. ($^2K_{13/2}$) may also be given. The ground state is given as $^4I_{15/2}$.

Erbium nitrate, dissolved in TBP, shows an enhancement of two bands—the $^4G_{11/2}$ and the $^2H_{11/2}$ bands—relative to the others in the spectrum (Fig. 13). There is also a change in the relative intensities of the components, giving a small shift of the maxima to lower wave lengths. The bromide salt shows an effect in the same two bands, but because the two components in each are now clearly resolved, the relative intensification in the bands is less noticeable (Fig. 14). Similarly, $ErCl_3$ in TBP shows intensification and considerable splitting of the $^4G_{11/2}$ and the $^2H_{11/2}$ bands. To see if these changes are absolute or relative, a volume of the TBP solution was equilibrated with an equal volume of water and the spectrum of the water solution compared with that of the TBP solution which had originally contained the rare earth. The comparison (Fig. 15) shows clearly that (in the TBP) not only is there enhancement and modification in the two bands as noted, but concomitantly there is a gross loss in intensity in all the other bands. This behavior is presumably true for the spectra of the other salts also.

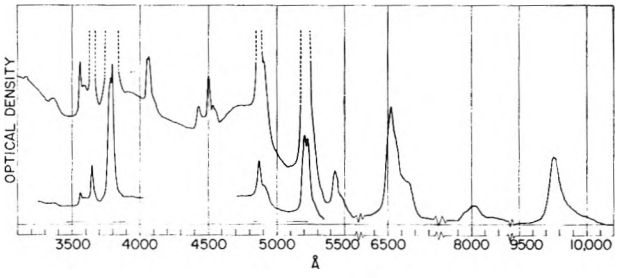

Figure 14. $ErBr_3$ in TBP: inserts, 0.3-cm. path, same solution. Broad absorptions at 3900 and 4700 Å. due to $^{tet}Fe(III)$.

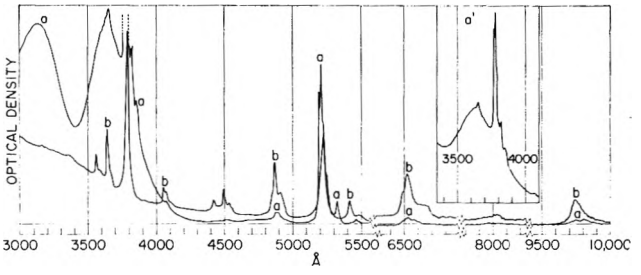

Figure 15. $ErCl_3$: a, TBP solution; b, water extract of TBP solution; c, TBP solution, 0.3-cm. path. Broad absorptions at 3100 and 3700 Å. in (a) due to $^{tet}Fe(III)$.

f. Er(III) and Hydroxy Acids. The chemical relations of the erbium with tartrate and with citrate are as with the other rare earths, as already described. As with the others, approximately pH 9 gives the maximal spectral effect with tartrate, and pH 11 is the most effective pH with citrate. The spectra for varied ratios of reagent and cation, and for different pH values are shown in Fig. 16 and 17. As with the solutions of the salts in nonaqueous solvents, the bands with the $^2H_{11/2}$ and $^4G_{11/2}$ upper states show alterations, although they are of different character than in the organic solvents. In addition to these changes, however, there are definite systematic alterations also in the $^2H_{9/2}$ band, in the several ^4F bands ($J = {}^9/_2$ through $J = {}^3/_2$), in the $^4S_{3/2}$ band, and apparently, even in the two members of the ^4I system visible in the spectral range studied. The ^2G and ^2P bands do not seem to be altered, however.

III. Discussion

The coordination number 9 is common for rare earths in many solid systems, both with oxygen coordinated (water, bromate, ethyl sulfate, etc.) and with halide. Coordination number 8 is also known in some fluorides. The correspondence of spectra suggests that in dilute aqueous solution a coordination number of 9 is a good first approximation. In tributyl phosphate, the consensus of evidence seems to be that there are three TBP groups coordinated through a single point each (the phosphoryl oxygen) and that there probably is no water left in the coordination sphere.[15,16] This leaves a coordination number of 6. One may, therefore, look for spectral evidence[17] of this change in coordination number, which should be more than a minor one; indeed the data for all three rare earths studied in this work furnishes such evidence.

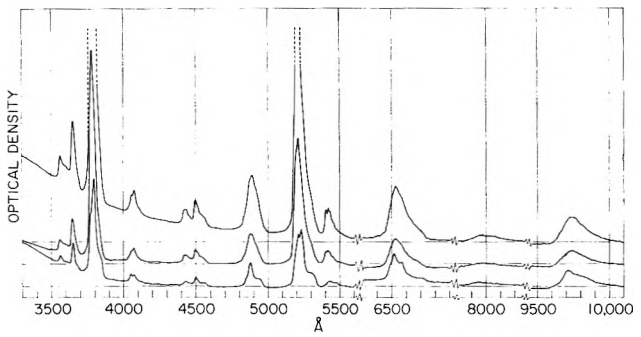

Figure 16. Er(III)–tartrate: (from bottom) 1:6, pH 9; 1:6, pH 11; 1:3, pH 11.

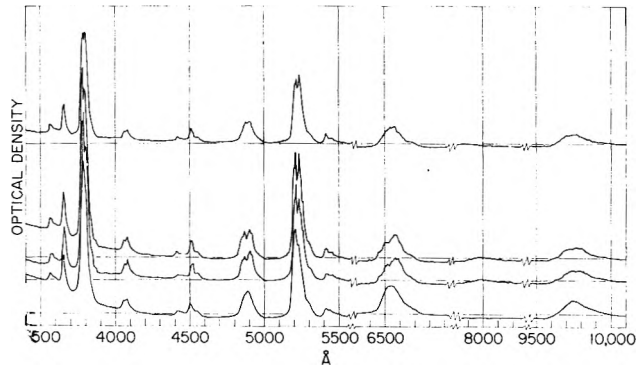

Figure 17. Er(III)–citrate: (from bottom) 1:6, pH 9; 1:6, pH 11; 1:3, pH 11; 1:1, pH 11.

Not only is there a general change between the dilute aqueous spectrum and the spectrum in TBP, but each of the salts has a distinctive variation on the over-all change, indicating the role of the difference in specific bonding relations of the rare earth central atom and the different anions. The specific nitrate absorption, below 3500 Å., shows a shift between the aqueous solution where it is ionized free and the TBP solution where it is coordinated to rare earth ion.

The behavior of the rare earths with the hydroxylic acids is clearly to be described in the following fashion. In neutral or acid solution a solid precipitates which may represent a partially hydrolyzed rare earth, but in any case is a compound in which the hydroxyl group of the organic anion, with its constituent proton, is probably coordinated to the cation. In some instances, with the proper stoichiometry or with a given organic acid, the complex may be soluble. When the solution is made sufficiently alkaline, pH ~7 and higher for tartrates and nearer pH 9–11 for citrates, the deprotonation of the hydroxyl group is forced, and a coordinate bond of a different sort is formed between the rare earth cation and the (now) negatively charged oxygen. This alkaline compound is stable with only one tartrate or citrate per metal ion. With Pr(III) there seems to be no evidence for more than one tartrate complex; with Nd(III) and Er(III) the situation is less clear-cut. There is a similar uncertainty with the citrate complexes. There is also no clear evidence as to whether there are hydroxyl groups associated with the metal central ion. If the resin evidence with the Pr(III) is taken at face value, the tartrate is probably neutral, and the metal charge is balanced by the ionized carboxyls and ionized hydroxylate. It may be that the citrate

(15) E. Glueckauf, *Ind. Chim. Belge*, **23**, 1215 (1957).

(16) L. I. Katzin, *J. Inorg. Nucl. Chem.*, **20**, 300 (1961).

(17) The pyramid of assumptions needed to cling to a purely electrostatic picture of the relations between the trivalent rare earths and neutral molecular addends, as well as anions, is so artificial that no further argumentation about the covalent nature of the interactions seems called for. The solid state seems to be no exception, as *e.g.*, the vibrational pattern of solid nitrates.[8]

also has only two carboxyls directly involved with the cation, in addition to the hydroxylate.

The assignment of coordination number and configuration in these complexes is open—at least there is no direct evidence on what groups are coordinated to the rare earth other than the complexing group. The nonalkaline solutions of Pr(III) and citrate fail to show any distinct spectral modifications, although certainly complexes of rare earths and both tartrate and citrate can be shown to exist, by a variety of techniques. In the citrate solutions of Nd(III), however, even at pH 3, there is a distinct alteration of the spectrum which is not too much different from that seen in the alkaline tartrate solutions. In alkaline solution, further change takes place. At present, the exact meaning of these in terms of coordination number and configuration must remain purely speculative. It is reasonably certain, however, that there has been a change from the simple water solution situation with its *presumed* C_{3v} symmetry and ninefold coordination.

A relationship between spectral theory and experimental results of the sort indicated above clearly cannot rest on the parameters of crystal field theory alone. Even for complete description of the spectra of rare earths in crystals, it is necessary to assume varying degrees of covalency.[18] It has further been shown[19] that where discrepancies remain it cannot be assumed that they will be taken care of with considerations of configuration and electron interaction as further refinements. These are predetermined by the symmetry assumptions which are made.

One must, therefore, look at the rare earth system afresh, without the assumption of noninvolvement of f electrons in bonding and orbital formation. A good starting point would seem to be two apparently neglected papers by Van Vleck[20] and by Eisenstein,[21] in which the irreducible representations for the hybrid orbitals of a number of geometric bond arrangements have been worked out. A recent paper by Jørgensen, Pappalardo, and Schmidtke[22] may represent a first step toward a formal treatment.

IV. Spectral Measurements

Spectra were recorded with a Cary recording spectrophotometer, Model 14. Path lengths were most often 1 cm., but 0.1 and 2.0 cm. were also used. Appropriate blanks were used in all cases. The curves in the figures are tracings from the originals which were then inked. There may therefore be some small losses in quality.

(18) E. Y. Wong, O. M. Stafsudd, and D. R. Johnston, *J. Chem. Phys.*, **39**, 786 (1963).

(19) K. Rajnak and B. G. Wybourne, *ibid.*, **41**, 565 (1964).

(20) J. H. Van Vleck, *ibid.*, **3**, 803 (1935).

(21) J. C. Eisenstein, *ibid.*, **25**, 142 (1956).

(22) C. K. Jørgensen, R. Pappalardo, and H. H. Schmidtke, *ibid.*, **39**, 1422 (1963).

Oxygen Stoichiometry in the Compound $BaFeO_{3-x}$

by H. J. Van Hook

Raytheon Research Division, Waltham, Massachusetts *(Received June 12, 1964)*

The compound $BaFeO_{3-x}$ has been prepared from several different starting materials. At least two crystallographic forms have been observed: (1) a high-temperature form of unidentified crystal structure with a limited range in oxygen stoichiometry near the composition $BaFeO_{2.50}$; this phase melts congruently at 1370° in air; (2) a low-temperature phase similar to hexagonal α-$BaTiO_3$. This phase has an extraordinary range in oxygen content with no detectable change in crystal structure between $BaFeO_{2.47}$ and $BaFeO_{2.92}$. The thermal stability of the hexagonal phase is increased by oxygen pressure; decomposition to the high form occurs at 915° in air, at 1250° under 10 atm. of oxygen pressure. At 50 atm. the hexagonal (low) phase melts at 1412° without transforming to high $BaFeO_{3-x}$. Density measurements on hexagonal $BaFeO_{3-x}$ indicate a linear decrease with increasing oxygen deficiency from ρ = 6.11 g./cc. at x = 0.10 to ρ = 5.71 g./cc. at x = 0.50.

I. Introduction

The oxidation states of iron normally encountered in the synthesis of oxide compounds at elevated temperatures are the divalent and trivalent states. The existence of higher valence states of iron in certain oxide compounds, however, was postulated some time ago. In 1715 Stahl[1] first prepared potassium orthoferrate (K_2FeO_4) which he obtained by reaction of powdered iron and potassium nitrate. To account for the indicated oxygen fraction, Stahl assumed the iron was hexavalent. In more recent times Scholder and coworkers[2-4] have synthesized ferrates containing all of the alkali and alkaline earth elements except calcium and magnesium. Each alkali–iron oxide combination may yield several ferrate phases, for example, Na_2FeO_3, Na_2FeO_4, and Na_3FeO_4. The ferrates are very soluble in dilute acid solution. They tend to react with the H_2O and CO_2 in normal atmospheres at room temperature and thus require special handling. The thermal stability increases generally with atomic number of the alkaline element. Chemical analysis for "active oxygen" in the powdered material by the thiosulfate–iodide reaction has indicated oxidation states of Fe^{4+}, Fe^{5+}, and Fe^{6+}, assuming that oxygen and the alkaline element maintain their customary valence.

Barium orthoferrate is among the more stable of the alkali ferrates; its preparation and physical properties were first reported by Erchak, *et al.*,[5] in 1946. X-Ray diffraction studies indicated a cubic perovskite-type structure, and weight loss experiments indicated a composition $BaFeO_{2.62}$ in a phase produced by reaction of $BaCO_3$ and Fe_2O_3 above 900° in oxygen. Several weak diffraction lines were noted which led the authors to adopt a unit cell twice the length of the elementary perovskite cell. The larger unit cell (a_0 = 8.06 Å.) contains three oxygen vacancies per formula unit $Ba_8Fe_8O_{21}$. Malinofsky and Kedesdy[6] prepared barium orthoferrate by similar methods; they found a better fit between their diffraction patterns and one corresponding to the hexagonal, high-temperature form of barium titanate. The authors related the cubic and tetragonal polymorphs of $BaTiO_3$ with high temperature $BaFeO_{3-x}$ phases. Prokopalo, *et al.*,[7] also noted

(1) G. E. Stahl, "Opusculum Chymico-Physico-Medicum," Hatae-Magdeburgiae, 1715.

(2) R. Scholder, H. v. Bunsen, F. Kindervater, and W. Zeiss, *Z. anorg. allgem. Chem.*, **282**, 268 (1955).

(3) R. Scholder, H. v. Bunsen, and W. Zeiss, *ibid.*, **283**, 330 (1956).

(4) R. Scholder, F. Kindervater, and W. Zeiss, *ibid.*, **283**, 338 (1956).

(5) M. Erchak, I. Fankuchen, and R. Ward, *J. Am. Chem. Soc.*, **68**, 2085 (1946).

(6) W. W. Malinofsky and H. Kedesdy, *ibid.*, **76**, 3090 (1954).

structural similarities between barium orthoferrate and barium titanate and prepared solid solutions between these compounds. Cubic perovskite solid solutions were also investigated recently in the series $LaFeO_3$–$SrFeO_{3-x}$[8] and $SrTiO_3$–$SrFeO_{3-x}$.[9,10] The data obtained on electrical and magnetic properties of these phases are consistent with the view that positive carriers, probably Fe^{4+} ions, are produced.

There is, however, some reluctance to assume Fe^{4+}, or higher, oxidation states of iron in the alkali ferrates since no concrete evidence for this valence is found in the many ferrites presently known. White and Roy[11] have synthesized compositions in the series CrO_2–"FeO_2" from CrO_2 to $Cr_{0.5}Fe_{0.5}O_2$ at high oxygen pressures (50,000 bars) and low temperatures, but the existence of Fe^{4+} is ambiguous since Cr^{6+} is quite stable, at least in pure CrO_3, under these pressure–temperature conditions and could account for the oxygen content. The same uncertainty in iron valence exists in the solid solution series $Mn_{1-x}Fe_xO_2$ owing to the variable valence of manganese.

The alkali and alkaline earth ferrates are unique in that a high oxygen content is produced in compounds with a single transition metal element. Therefore, it may be possible to determine, without ambiguity, whether the postulated Fe^{4+} ion is stable in the crystalline state. Since the thermal stability of the ferrates parallels the increase in stability of the corresponding alkali and alkaline earth peroxides, it is necessary to establish whether peroxide-type bonding, either in the crystal structure or by surface adsorption, could account for the high oxygen content. Since all previous studies were made using powdered material with high surface area, the possibility of adsorption cannot be discounted until single crystals are available for study.

The purpose of this investigation has been to prepare barium orthoferrate in single crystal and polycrystalline form and to study the range of oxygen stoichiometry in the phase and its effect on certain physical properties.

II. Experimental Procedure

$BaFeO_{3-x}$ was prepared by the reaction of C.P. Fe_2O_3 with $BaCO_3$, BaO_2, or $Ba(OH)_2 \cdot 8H_2O$ in the proper molar proportions at 1100° in air. Ingots of single crystalline $BaFeO_{3-x}$ 1.2 cm. in diameter × 10 cm. were grown in air in platinum crucibles by the Bridgmann method. The temperature gradient at the growth zone was approximately 100°/cm., and the growth rate was 0.254 cm./hr.

The single crystals and polycrystalline material were identified by X-ray powder diffraction techniques using Co $K\alpha$ radiation. The oxygen fraction in $BaFeO_{3-x}$ was determined by weight changes on the reaction of the starting materials by quenching in argon and by weighing at high temperature using a Mauer thermobalance. The precision in weighing, in both cases, was ±0.1 mg. on samples ranging from 20 to 100 g. The density of single crystals weighing about 10 g. was obtained by displacement of toluene at a known temperature (±0.1°). Volume was determined simultaneously on a 1.6-cc. cube of single crystalline germanium assuming a density of 5.327 g./cc. A comparison of measured dimensions and displacement volume of the germanium cube gave excellent agreement with the reported density[12] of toluene at different temperatures. By comparison with the germanium standard, the density of the $BaFeO_{3-x}$ ingots is believed accurate to within 0.1%.

III. Experimental Results

Barium orthoferrite has been synthesized by firing above 900° an intimate mixture of Fe_2O_3 with the proper molar ratio of either $BaCO_3$, BaO_{2-x}, or $Ba(OH)_2 \cdot 8H_2O$ to yield $BaFeO_{3-x}$. Deviations from the cation ratio, Ba:Fe = 1, within the limits of accuracy in mixing and weighing (±0.1%), result in either barium oxide or $BaFe_2O_4$ as a second phase. The loss in weight which occurs during the reaction of iron oxide and barium carbonate at 1300° in air or in a pure oxygen atmosphere corresponds exactly to the calculated amount of CO_2 evolved in the reaction: $\frac{1}{2}Fe_2O_3 + BaCO_3 \rightarrow BaFeO_{2.50} + CO_2$. The weight change at 1300° was determined using a recording thermobalance and was further confirmed by quenching samples from 1300° in a neutral (N_2–Ar) atmosphere before room temperature weighing. The composition $BaFeO_{2.50}$ melts congruently at 1370° in air with no apparent change in oxygen content.

Although the atomic proportions of barium and iron in the phase are essentially invariant, there appears to be a considerable range in oxygen fraction, especially at lower temperatures. Upon slow cooling in air below 1370°, the compound gradually gains weight to 915° at which point a discontinuous gain occurs (Fig. 1). Below 915° the gain in weight is again continuous

(7) I. Prokopalo and I. G. Fesenko, *Izv. Akad. Nauk SSSR, Ser. Fiz.*, **22**, 1488 (1958).

(8) J. S. Waugh, MIT Technical Report 152, August, 1960.

(9) J. R. Clevenger, *J. Am. Ceram. Soc.*, **46**, 207 (1963).

(10) J. B. MacChesney and J. F. Potter, paper BE8 presented at the Physical Society Meeting, Philadelphia, Pa., March 23, 1964.

(11) W. B. White and R. Roy, paper 52-B-63 presented at the Ceramic Society Annual Meeting, Pittsburgh, Pa., April 28, 1963.

(12) "International Critical Tables," Vol. 3, E. W. Washburn, Ed., McGraw-Hill Book Co., Inc., New York, N. Y., 1929, p. 29.

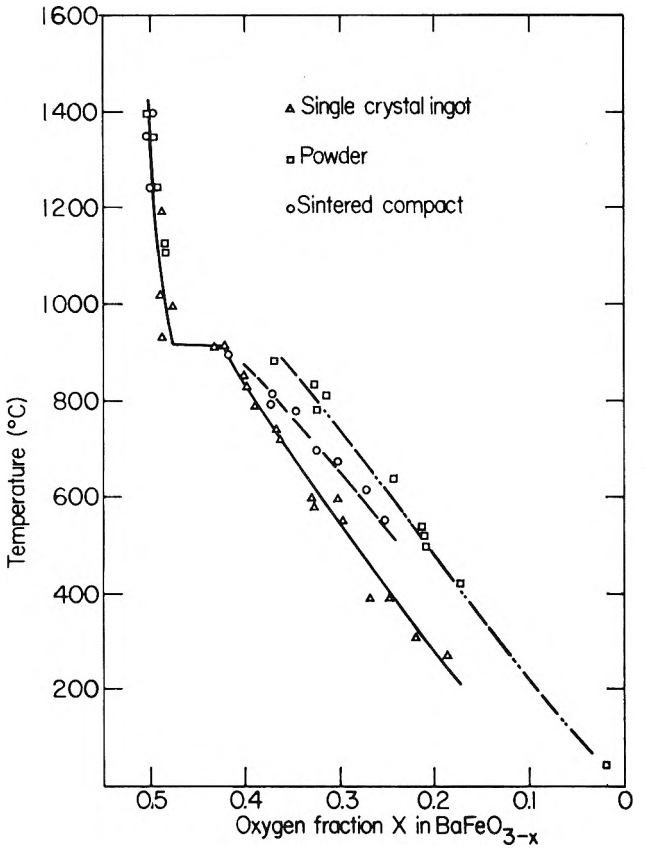

Figure 1. Oxygen fraction of hexagonal $BaFeO_{3-x}$ as a function of temperature and surface area.

down to the lowest temperatures investigated. A similar curve, with somewhat larger values of weight gain with temperature, was obtained in an atmosphere of pure oxygen gas. X-Ray diffraction patterns of samples quenched from below 915° indicate a single-phase material identical with patterns of hexagonal α-$BaTiO_3$, a similarity first noted by Malinofsky and Kedesdy.[6] Diffraction traces of material quenched between 915° and the melting point indicated a change in phase to a more complex crystallographic form had occurred. This high-temperature phase has not yet been identified. It is apparently unrelated to the cubic and tetragonal $BaTiO_3$ polymorphs.[13]

To determine whether the weight changes were, in fact, due to incorporation of oxygen, a sample equilibrated in air at 400° was heated above this temperature within the vacuum system of a mass spectrometer. The spectrographic analysis of the gas evolved in this experiment was 91% O_2, 7.5% CO_2, and 1.5% N_2; the latter two gases probably adsorbed on transferring the sample. We have assumed, therefore, that the gains and losses in weight recorded are due to variations in oxygen content in the sample. These findings are in accord with the results of chemical analyses performed on similar compositions by Scholder, *et al.*

Because of the rapidity of oxidation and reduction of the orthoferrate, it seemed desirable to determine whether the observed oxygen exchange is due to a surface adsorption or to incorporation of oxygen in the bulk of the phase. To test the effect of surface area, three samples were prepared for thermobalance measurements: (1) a loose powder of calcined material, average grain size ~5 μ, (2) a sintered compact of the same material with ~25% porosity, and (3) a single crystalline ingot of $BaFeO_{3-x}$ grown from the melt by the Bridgmann technique. Changes in weight were recorded for each of the three starting materials at a series of temperatures (Fig. 1). The values were obtained at both successively increasing and decreasing temperatures. Each measurement was made after apparent equilibration, *i.e.*, after no change in weight with time. It is apparent from the figure that the degree of oxidation does depend somewhat on surface area, especially at lower temperatures, although adsorption is evidently a minor factor in view of the small differences observed for large variations in available surface area. However, since some adsorption apparently does take place, all subsequent composition determinations were made on single crystalline ingots of melt-grown $BaFeO_{3-x}$.

In addition to experiments in air (P_{O_2} = 0.21 atm.), runs were made in an atmosphere of oxygen gas and in a 95% N_2–5% H_2 ambient. The partial oxygen pressure of the N_2–H_2 mixture, estimated from the dew point (−70°), was approximately 10^{-25} atm. P_{O_2} at 800°. The data are plotted in Fig. 2 as isobars on the composition–temperature phase diagram. Samples of $BaFeO_{3-x}$ were also fired over a range of temperatures in a platinum-wound furnace enclosed in a pressure vessel at oxygen pressures up to 50 atm. The determination of oxygen content of samples fired under pressure was made by weight changes after quenching the samples to room temperature. These data are somewhat less accurate than the results obtained on samples at atmospheric total pressure, primarily because of the limitations in sample size. The high pressure results are also plotted in Fig. 2.

Density measurements were made on four single crystal samples of the hexagonal phase using toluene as the displacement medium. Several density values for different oxygen fractions were obtained with each sample, establishing the reversibility of the linear density–composition relation shown in Fig. 3.

(13) Diffraction data on the two crystallographic forms may be obtained from the author on request. A more detailed X-ray study of these materials is now in progress.

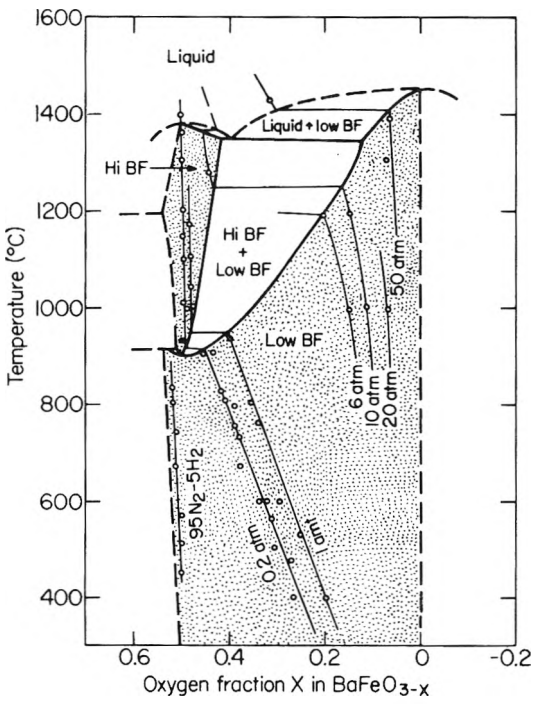

Figure 2. Phase relations involving $BaFeO_{3-x}$. Stippled areas are single-phase regions for high- and low-temperature forms of $BaFeO_{3-x}$. Oxygen isobars are shown as light lines with experimental points as open circles. Dashed lines indicate inferred relations.

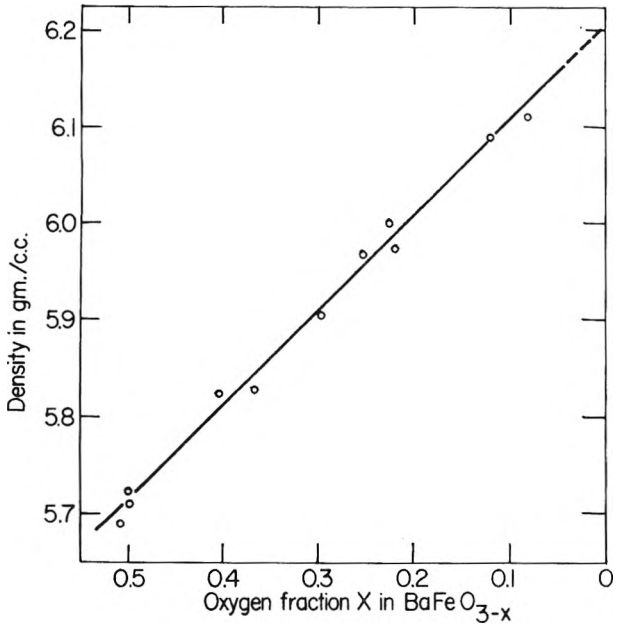

Figure 3. Density of $BaFeO_{3-x}$ *vs.* composition.

IV. Discussion

Barium orthoferrite can be prepared by reaction of any of a number of different starting materials above about 1000°. As the compound is cooled in an oxidizing environment, a gain in weight occurs. The amount of weight gain is found to be primarily dependent on the mass of the sample although some dependence on surface area was observed. Spectrographic analysis of oxidized compositions indicates further that the weight gains are due to the incorporation of oxygen in the sample from the surrounding atmosphere. Weight change *vs.* temperature curves show an abrupt change in composition at a temperature which depends on the oxygen content of the surrounding atmosphere. In air (P_{O_2} = 0.2 atm.) the composition–temperature discontinuity occurs at 915° whereas, at 10 atm. oxygen pressure (147 p.s.i.), the corresponding point is 1250°. The existence of the temperature–pressure dependent composition change has been correlated with a phase change from a hexagonal low-temperature form to a high form with an unidentified structure as shown by powder diffraction scans of these materials. The relationship of the barium orthoferrate phases is indicated in a phase equilibrium diagram in which two condensed phases plus vapor represent a univariant situation, *i.e.*, a binary noncondensed system.

The range in composition of the solid phases has been determined gravimetrically using single crystalline ingots grown from the melt. The hexagonal phase is seen to have an extraordinary range in oxygen stoichiometry from compositions approaching $BaFeO_3$ to oxygen-deficient compositions which may reach proportions as high as 17 mole %, *i.e.*, one oxygen vacancy per six normally occupied positions in the composition $BaFeO_{2.50}$.

Density measurements were made on single crystals to determine how such large deviations from stoichiometry might be accommodated. The results show a linear decrease in density with oxygen deficiency which is consistent with an oxygen vacancy model. X-Ray studies are planned to investigate the structural characteristics of the oxygen-deficient compositions. It has been observed that high-temperature orthoferrate crystals grown from the melt cannot be converted directly to the hexagonal low-temperature form without an intermediate step in which the phase is oxidized. Oxidation apparently catalyzes the transformation at temperatures as low as 400° whereas the phase change does not occur in several days at 800° at constant composition ($BaFeO_{2.50}$). The necessity for an indirect path to produce hexagonal $BaFeO_{2.50}$ raises some doubt concerning the true stability relations of the maximum defect compositions of the hexagonal phase.

Acknowledgment. The writer is indebted to C. R. Snider for his assistance in the experimental work and to W. Bekebrede and S. Cvikevich (all from Raytheon) for X-ray identification of the material.

Mutual Diffusion in Nonideal, Nonassociating Liquid Systems

by D. L. Bidlack and D. K. Anderson

Department of Chemical Engineering, Michigan State University, East Lansing, Michigan *(Received June 18, 1964)*

Mutual diffusion coefficients and viscosities were measured over the entire concentration range for the nonideal, nonassociating systems, heptane–hexadecane, hexane–dodecane, and hexane–carbon tetrachloride. According to existing theories for diffusion of nonideal systems, the diffusivity–viscosity product, divided by an activity correction, $D\eta/(\mathrm{d}\ln a/\mathrm{d}\ln X)$, should be a linear function with mole fraction. This study shows that, like associating systems, the activity correction tends to overcorrect in nonassociating systems, sometimes by more than the original deviation from Raoult's law.

In recent years many papers have appeared concerning diffusion in binary liquid mixtures. Most of these papers have dealt with ideal mixtures[1] or nonideal, associating mixtures.[2] It is hoped that some useful insight into the diffusion mechanism can be gained from a study of nonideal, nonassociating systems.

According to Hartley and Crank,[3] the dependence of the mutual diffusion coefficient, D_{AB}, on concentration at constant temperature may be described by

$$D_{AB} = \frac{RT}{N\eta}\left[\frac{X_A}{f_B} + \frac{X_B}{f_A}\right]\frac{\mathrm{d}\ln a_A}{\mathrm{d}\ln X_A} \qquad (1)$$

where X_A and X_B are the mole fractions of the two components of the system; a_A is the activity of component A; f_A and f_B are resistance coefficients which depend on molecular size; and η is the solution viscosity. R, T, and N are the gas constant, temperature, and Avogadro's constant, respectively. Other authors disagree with the derivation of the Hartley and Crank equation[4,5]; however, the absolute rate theory[6] and statistical mechanics[5,7] also predict that $D\eta/(\mathrm{d}\ln a/\mathrm{d}\ln X)$ will be a linear function of mole fraction, and this dependency is tested here.

Mutual diffusion coefficients for ideal solutions have been shown by Caldwell and Babb[1] to vary linearly with mole fraction. This is to be expected since the activity term of eq. 1 is unity for ideal solutions. However, for nonideal solutions in which the components associate, $D\eta/(\mathrm{d}\ln a/\mathrm{d}\ln X)$ is found not to be linear.[2,8] In fact, when $D\eta$ is divided by the activity term, it is overcorrected. This overcorrection is as much as several hundred per cent in some cases.[3] The tendency to overcorrect is common to both negatively deviating $(\mathrm{d}\ln a/\mathrm{d}\ln X) > 1$ and positively deviating $(\mathrm{d}\ln a/\mathrm{d}\ln X) < 1$ systems from Raoult's law.

It has been suggested,[8,9] since ideal solutions follow theory and associating systems do not, that association inhibits movement of the molecules and causes the deviation from theory. By investigating a group of nonideal solutions that do not associate, the effect of nonideality can be determined when the diffusion mechanism is not complicated by association.

Experimental

Method and Materials. The diffusion data were obtained using a diffusiometer similar to the one described by Caldwell, Hall, and Babb.[10] Although the

(1) C. S. Caldwell and A. L. Babb, *J. Phys. Chem.*, **60**, 51 (1956).

(2) See P. A. Johnson and A. L. Babb, *Chem. Rev.*, **56**, 387 (1956); A. P. Hardt, D. K. Anderson, R. Rathbun, B. W. Mar, and A. L. Babb, *J. Phys. Chem.*, **63**, 2059 (1959); P. C. Carman and L. Miller, *Trans. Faraday Soc.*, **55**, 1838 (1959); D. K. Anderson, J. R. Hall, and A. L. Babb, *J. Phys. Chem.*, **62**, 404 (1958); and ref. 8 and 9 for discussion and further references to associating systems.

(3) G. S. Hartley and J. Crank, *Trans. Faraday Soc.*, **45**, 801 (1949).

(4) R. Mills, *J. Phys. Chem.*, **67**, 600 (1963).

(5) R. J. Bearman, *ibid.*, **65**, 1961 (1961).

(6) S. Glasstone, K. J. Laidler, and H. Eyring, "The Theory of Rate Processes," McGraw-Hill Book Co., Inc., New York, N. Y., 1941, Chapter IX.

(7) R. J. Bearman and P. F. Jones, *J. Chem. Phys.*, **33**, 1432 (1960).

(8) B. R. Hammond and R. H. Stokes, *Trans. Faraday Soc.*, **52**, 781 (1956).

(9) D. K. Anderson and A. L. Babb, *J. Phys. Chem.*, **65**, 1281 (1961).

(10) C. S. Caldwell, J. R. Hall, and A. L. Babb, *Rev. Sci. Instr.*, **28**, 816 (1957).

Table I: Summary of Experimental Data

			Mutual diffusion coefficients				
			Heptane–hexadecane				
Av. mole fraction of hexadecane	0.0056	0.1064	0.2024	0.3934	0.5821	0.7920	0.9761
Difference in mole fraction between upper and lower level in cell	0.0112	0.0124	0.0172	0.0161	0.0362	0.0343	0.0478
$D_{AB} \times 10^{-5}$, cm.²/sec.	1.775	1.586	1.451	1.238	1.065	0.895	0.760
			Hexane–dodecane				
Av. mole fraction of dodecane	0.0058	0.1013	0.1989	0.3623	0.5981	0.7909	0.9755
Difference in mole fraction between upper and lower level in cell	0.0116	0.0115	0.0160	0.0253	0.0317	0.0336	0.0491
$D_{AB} \times 10^{-5}$, cm.²/sec.	2.729	2.533	2.327	2.066	1.799	1.618	1.450
			Hexane–carbon tetrachloride				
Av. mole fraction of CCl_4	0.0042	0.1489	0.3234	0.5454	0.7497	0.9893	
Difference in mole fraction between upper and lower level in cell	0.0084	0.0112	0.0102	0.0097	0.0098	0.0215	
$D_{AB} \times 10^{-5}$, cm.²/sec.	3.858	3.388	2.938	2.368	1.943	1.487	
			Solution viscosities and densities				
			Heptane–hexadecane				
Mole fraction of hexadecane	0	0.2110	0.4067	0.5795	0.7867	1.000	
η, cp.	0.3893	0.7064	1.1020	1.5520	2.2020	3.0306	
Density, g./cm.³	0.6796	0.7117	0.7315	0.7463	0.7596	0.7698	
			Hexane–dodecane				
Mole fraction of dodecane	0	0.1924	0.4248	0.6050	0.8064	1.000	
η, cp.	0.2958	0.4343	0.6351	0.8243	1.0673	1.3379	
Density, g./cm.³	0.6550	0.6818	0.7059	0.7205	0.7340	0.7450	
			Hexane–carbon tetrachloride				
Mole fraction of CCl_4	0	0.1729	0.3869	0.5869	0.7906	1.000	
η, cp.	0.2958	0.3422	0.4102	0.5067	0.6461	0.8963	
Density, g./cm.³	0.6550	0.7803	0.9514	1.1318	1.3385	1.5842	

exact details differ somewhat from their apparatus, the optical quality and experimental methods involved are essentially the same. That paper describes both the apparatus and method in great detail and will not be repeated here. The experimental diffusivities were obtained by measuring the interdiffusion of two solutions of slightly different concentration. The diffusion coefficient is taken as that of a solution with a concentration equal to the average of the two solutions.

The accuracy of the diffusiometer was determined by comparing diffusivities of seven sucrose solutions with data of Gosting and Morris.[11] The values in all cases deviated by less than 1% and had an average deviation of 0.5%.

Viscosities were obtained with an Ostwald–Fenske type viscosimeter, and densities were obtained with a 10-cc. glass specific gravity bottle.

The results of this work are recorded in Table I. The mutual diffusion coefficients were measured at a temperature of 25.1 ± 0.05°, viscosities at 25.0 ± 0.05°, and densities at 25 ± 1°.

The hexane, heptane, dodecane, and hexadecane were purchased from Matheson Coleman and Bell Co. The hexane was Spectroquality grade, the heptane Chromatoquality, and the dodecane and hexadecane were 99+% (olefin free) pure. Spectro grade carbon tetrachloride was purchased from Eastman Organic Chemical Co. The purity of the chemicals were further confirmed by comparing their densities and refractive indices with values given by Timmermans.[12] See Table II.

Table II: Comparison of Physical Constants with Previous Data

	Density at 25°		Refractive index, $n^{25}D$	
	This work	Ref. 12	This work	Ref. 12
Hexane	0.6550	0.6549[a]	1.3720	1.3723[a]
Heptane	0.6796	0.6795[a]	1.3855	1.3852[a]
Dodecane	0.7450	0.7451	1.4193	1.4195
Hexadecane	0.7698	0.7699	1.4319	1.4325
Carbon tetrachloride	1.5842	1.5845[a]	1.4570	1.4576[a]

[a] Average of several recorded data.

(11) L. J. Gosting and M. S. Morris, *J. Am. Chem. Soc.*, 71, 1998 (1949).

(12) J. Timmermans, "Physico-Chemical Constants of Pure Organic Compounds," Elsevier Publishing Co., Inc., New York, N. Y., 1950.

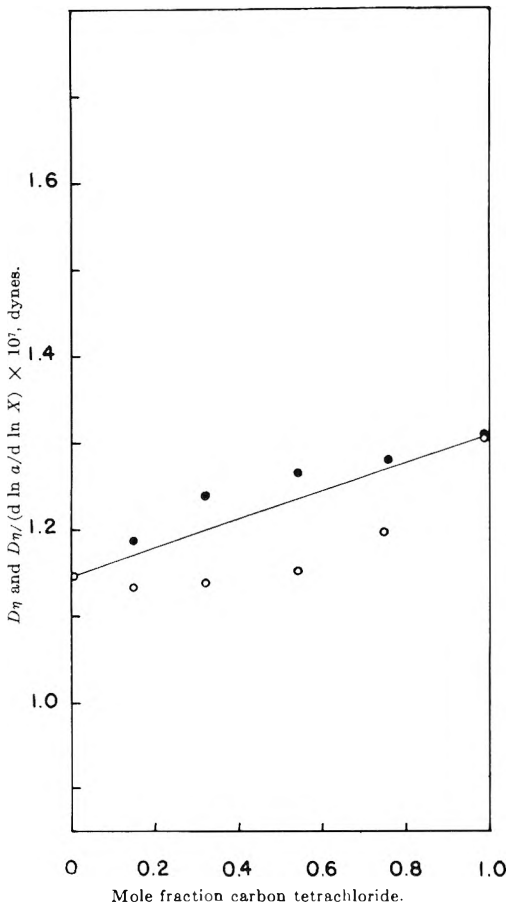

Figure 1. $D\eta$ and $D\eta/(\mathrm{d}\ln a/\mathrm{d}\ln X)$ as a function of mole fraction for the system hexane–carbon tetrachloride: ———, linear or ideal behavior; O, $D\eta$; ●, $D\eta/(\mathrm{d}\ln a/\mathrm{d}\ln X)$.

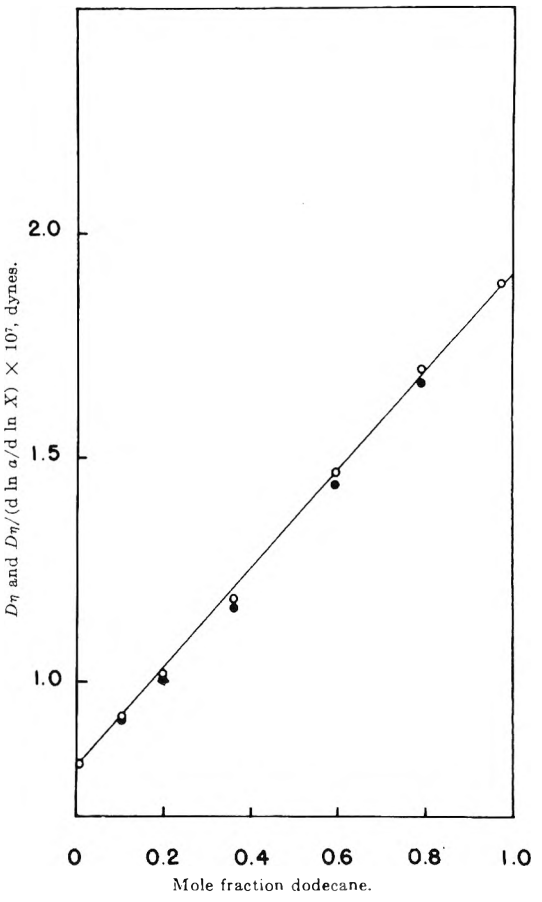

Figure 2. $D\eta$ and $D\eta/(\mathrm{d}\ln a/\mathrm{d}\ln X)$ as a function of mole fraction for the system hexane–dodecane: ———, linear or ideal behavior; O, $D\eta$; ●, $D\eta/(\mathrm{d}\ln a/\mathrm{d}\ln X)$.

Activity Data. There are probably many nonideal binary liquid systems which are not associative but few whose activity data have been fully investigated. Thus, since activity data are required for the theory comparison, their availability became a factor in the selection of the systems for study.

The activities for the systems heptane–hexadecane and hexane–dodecane were obtained by Brønsted and Koefoed,[13] and the system hexane–carbon tetrachloride by Christian, Naparko, and Affsprung.[14] The data for all three systems were at 20°. The activity coefficient, f, for each of the three systems was found to follow the equation

$$\ln f_A = KX_B^2 \qquad (2)$$

where X is the mole fraction, K is a constant depending on the particular system, and A and B refer to the two components of the system. Because the systems chosen for this study exhibit no association, they can be classified as "regular" or nearly regular, in which case the constant K depends on the temperature according to

$$K = K'/T \qquad (3)$$

where K' is a constant independent of temperature. Therefore, activities for these systems may be converted to other temperatures by means of eq. 3. The values of K for the three systems are given in Table III for 20°.

Table III: Values for the Constant K of Equation 2 at 20°

System	K	Reference
Heptane–hexadecane	−0.0921	13
Hexane–dodecane	−0.0403	13
Hexane–carbon tetrachloride	0.180	14

(13) J. N. Brønsted and J. Koefoed, *Kgl. Danske Videnskab. Selskab. Met.-Fis. Medd.*, **22**, 1 (1946).

(14) S. D. Christian, E. Naparko, and H. E. Affsprung, *J. Phys. Chem.*, **64**, 442 (1960).

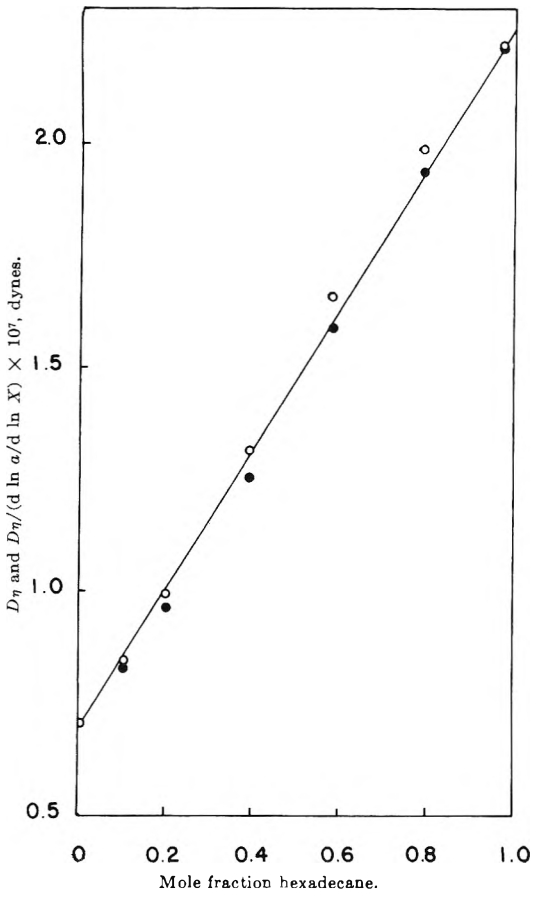

Figure 3. $D\eta$ and $D\eta/(\mathrm{d}\ln a/\mathrm{d}\ln X)$ as a function of mole fraction for the system heptane–hexadecane: ———, linear or ideal behavior; O, $D\eta$; ●, $D\eta/(\mathrm{d}\ln a/\mathrm{d}\ln X)$.

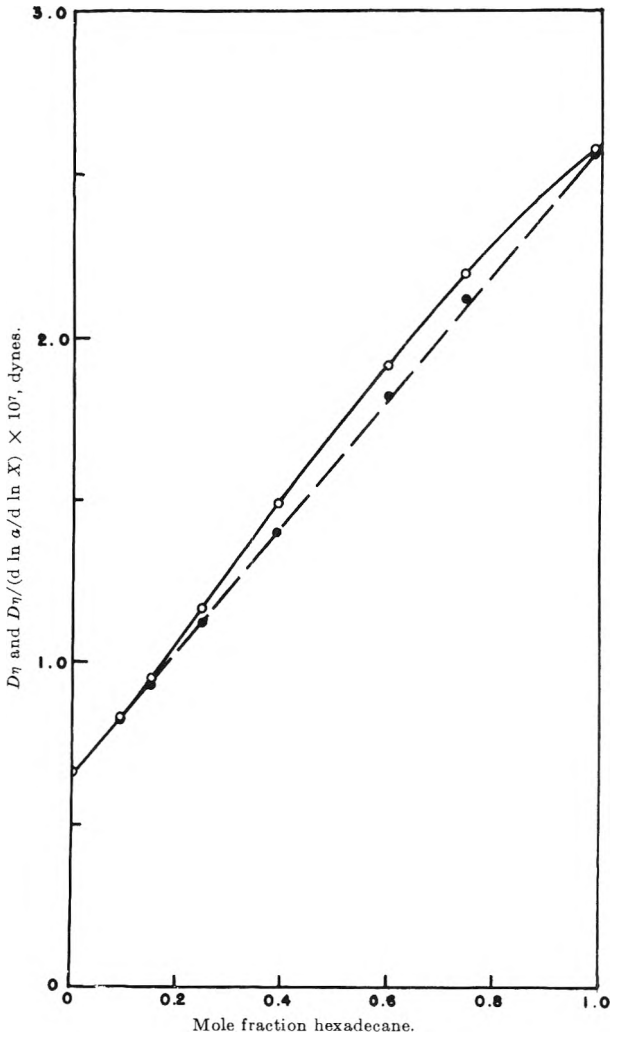

Figure 4. $D\eta$ and $D\eta/(\mathrm{d}\ln a/\mathrm{d}\ln X)$ as a function of mole fraction for the system hexane–hexadecane: ———, ideal or linear behavior; —O— —, $D\eta$; —●—, $D\eta/(\mathrm{d}\ln a/\mathrm{d}\ln X)$.

Brønsted and Koefoed used a highly accurate method for determining their activity data. A later paper by McGlashan and Williamson[15] on hexane–hexadecane, another system studied by Brønsted and Koefoed, showed that ln a differed by 0.15% at 0.5 mole fraction between the two sets of data. Christian, Naparko, and Affsprung tested their method by comparing their data for benzene–carbon tetrachloride with those of Scatchard, Wood, and Mochel[16] and found agreement within 0.4%. These accuracies are well within the accuracy required for the present study.

Using eq. 2 and 3, the activity correction is

$$\frac{\mathrm{d}\ln a_A}{\mathrm{d}\ln X_A} = \frac{\mathrm{d}\ln a_B}{\mathrm{d}\ln X_B} = 1 + \frac{\mathrm{d}\ln f_B}{\mathrm{d}\ln X_A}$$

$$= 1 - 2KX_AX_B = 1 - \frac{2K'}{T} X_AX_B \quad (4)$$

Discussion

In Fig. 1, 2, and 3, $D\eta$ and $D\eta/(\mathrm{d}\ln a/\mathrm{d}\ln X)$ for the systems, heptane–hexadecane, hexane–dodecane, and hexane–carbon tetrachloride, are shown as functions of mole fraction along with the predicted linear behavior of $D\eta/(\mathrm{d}\ln a/\mathrm{d}\ln X)$. All three cases show that the activity overcorrects the diffusivity–viscosity product. In one case, hexane–dodecane, $D\eta$ was nearly linear with mole fraction but was overcorrected by as much as 4%. The overcorrection for heptane–hexadecane was also about 4%. This same overcorrection occurs in the system cyclohexane–carbon tetrachloride, which was investigated by Hammond and Stokes.[8] The maximum overcorrection

(15) M. L. McGlashan and A. G. Williamson, *Trans. Faraday Soc.*, 57, 588 (1961).

(16) G. Scatchard, S. E. Wood, and J. M. Mochel, *J. Am. Chem. Soc.*, 62, 712 (1940).

in this system is 4% from a deviation from Raoult's law of 5.6%.

It should be noted that in two of these systems, heptane–hexadecane and hexane–dodecane, the deviation from Raoult's law is negative while, in the other two, hexane–carbon tetrachloride and cyclohexane–carbon tetrachloride, the deviation is positive.

Figure 4 shows the system hexane–hexadecane, from data reported previously by the authors.[17] In this case, the activity term appears to correct the $D\eta$ curve for nonideality; however, from the results of the other four systems, it is apparent that this agreement is fortuitous. It may be that with deviations from ideality this small, the effect of size and shape of the diffusing molecule on the hydrodynamic resistance of the molecule is greater than that of solution nonideality.

In any case, it is apparent that the term (d ln a/d ln X) does not account for nonideal diffusion behavior whether the system is associative or not.

Acknowledgment. This work was supported by a grant from the Petroleum Research Fund, administered by the American Chemical Society. Grateful acknowledgment is hereby made to the donors of the fund.

(17) D. L. Bidlack and D. K. Anderson, *J. Phys. Chem.*, **68**, 206 (1964).

The Vapor Pressures of Some Polynuclear Aromatic Hydrocarbons[1]

by J. Daniel Kelley[2] and Francis Owen Rice

Department of Chemistry, Georgetown University, Washington, D. C. *(Received June 22, 1964)*

The vapor pressures of anthracene, 1,2-benzanthracene, 9,10-dimethyl-1,2-benzanthracene, and 20-methylcholanthrene have been measured over the following temperature ranges, respectively: 69 to 86°, 104 to 127°, 106 to 135°, and 128 to 152°. The results are expressed in the form log $P_{mm} = A - B/T$°K. where A and B are 12.068 and 5145 for anthracene, 11.528 and 5461 for 1,2-benzanthracene, 13.168 and 6643 for 20-methylcholanthrene, 15.108 and 7051 for solid 9,10-dimethyl-1,2-benzanthracene, and 12.232 and 5897 for liquid dimethylbenzanthracene. The average heats of sublimation over the experimental temperature ranges are obtained, and the results for anthracene are compared to previous work.

The vapor pressures of anthracene, 1,2-benzanthracene, 9,10-dimethyl-1,2-benzanthracene, and 20-methylcholanthrene have been measured in the pressure regions 0.001–0.01 mm. for the former two compounds and 0.0004–0.006 mm. for the latter two. The vapor pressure of anthracene has been previously studied in higher pressure regions.[3-7] The vapor pressures of the other three compounds have apparently not been investigated in any pressure region.

Experimental

Compounds. The compounds used in these vapor pressure studies were of the highest purity commercially available. Each was further purified by vacuum sublimation, and the melting point ranges of the samples

(1) This work is taken from the dissertation submitted by J. D. Kelley to the Graduate School of Georgetown University for the degree of Doctor of Philosophy. This work was supported in part by the National Institutes of Health, NIH Grant No. C-5411.

(2) Brookhaven National Laboratory, Upton, N. Y.

(3) C. A. Nelson and C. E. Senseman, *Ind. Eng. Chem.*, **14**, 58 (1922).

(4) F. S. Mortimer and R. V. Murphy, *ibid.*, **15**, 1140 (1923).

(5) G. W. Sears and E. R. Hopke, *J. Am. Chem. Soc.*, **71**, 1632 (1949).

(6) B. Stevens, *J. Chem. Soc.*, 2973 (1953).

(7) V. P. Klochkov, *Zh. Fiz. Khim.*, **32**, 1177 (1958).

actually employed were: anthracene, 217.0 to 217.5°; 1,2-benzanthracene, 161.0 to 161.5°; 9,10-dimethyl-1,2-benzanthracene, 122.9 to 123.5°; and 20-methylcholanthrene, 179.0 to 179.5°.

Apparatus. These vapor pressure data were obtained by a dynamic method, in which the vapor at its equilibrium pressure above the sample was allowed to effuse through a small orifice and condense on a liquid nitrogen cooled cold finger above the orifice. This apparatus was similar to that employed by Verhoek and Marshall[8] to measure vapor pressures of nonvolatile esters.

The sample chamber was a 25-ml. Pyrex bulb with an arm sealed to a short section of Kovar tubing, about 2.0 cm. in diameter and 1.5 cm. long; a disk of copper foil 0.013 cm. thick with an orifice of area 0.0615 cm.^{2} was soldered across the top of this tubing, and another short section of Kovar tubing was attached. The top portion of the apparatus was sealed to the free end of this tubing section. During a run this apparatus was immersed up to the vacuum side arm in an oil bath kept at temperatures constant to 0.1°.

Procedure. To begin a typical set of determinations, the small arm on the sample bulb was opened and approximately 1 g. of sample was introduced; since the compounds were all in the form of fine, loosely packed crystals, a large evaporating surface was assured. The arm was then closed and the apparatus immersed in the oil bath and connected to the vacuum line through a two-channel stopcock which could be closed, opened to vacuum, or opened to a tank of dry nitrogen gas for subsequent breaking of vacuum. The fresh sample was then pumped at room temperature for at least 2 hr.; the temperature of the bath was then slowly raised to 60°, the cold finger filled with liquid nitrogen, and pumping continued at that temperature for about 30 min. At this point vacuum was broken by admitting nitrogen gas, the cold finger was removed, and a clean cold finger substituted. The oil bath was then allowed to warm to the temperature desired for a vapor pressure determination. When the oil bath had stabilized at this temperature, which was read on a calibrated mercury-in-glass thermometer to the nearest 0.1° including the emergent stem correction, the apparatus was quickly evacuated and, when the pressure had fallen to 0.1 mm., the cold finger was filled with liquid nitrogen. Timing of the run was started as the cold finger was filled. When a sufficient amount of sample, 20–30 mg., had condensed on the finger, vacuum was broken by admitting nitrogen and the timing of the run stopped.

The condensed sample was then carefully washed from the finger with a minimum amount of spectral grade acetone into a preweighed weighing bottle. The bottle with sample was placed in a vacuum desiccator and carefully dried and weighed. All weights were obtained on a Mettler Type H one-pan balance read to the nearest 0.1 mg.

The determinations were not carried out in any particular order with regard to temperature; 30 to 40 points were used in the determination of each vapor pressure curve. During the course of the investigation of a compound, the melting points of the charged samples and condensates were periodically checked to ensure that no change in the nature of the material had occurred.

Calculations. From kinetic theory,[9] the number of gas molecules, Z, entering an orifice of area a in time t is given by

$$Z = (nu/4)at \qquad (1)$$

where n is the number of molecules per unit volume and u is the average velocity of the molecules. Substituting for n and u their values in terms of pressure, p, temperature, T, molecular mass m, and Boltzmann's constant, k, one obtains from (1)

$$Z = atp(1/2\pi mkT)^{1/2} \qquad (2)$$

The mass of material entering the orifice, G, may be obtained by multiplying (2) by M/N_0, where N_0 is Avogadro's number. Remembering that N_0k is equal to R, the gas constant, we obtain for G

$$G = atp(M/2\pi RT)^{1/2} \qquad (3)$$

Since the orifice has a finite thickness, not every molecule which enters passes through, so that (3) must be multiplied by W, the probability that an entering molecule leaves the orifice. Values of W for channels of various dimensions have been tabulated by Clausing[10]; W proved to be 0.978 for this orifice.

Rearranging (3), the equilibrium vapor pressure is given by

$$p = G'T^{1/2}[(1/aW)(2\pi R/M)^{1/2}] \qquad (4)$$

where the quantity in brackets is constant for a given compound in a given apparatus, and G' is equal to G/t.

Results

The vapor pressures of the four substances investigated were measured over the following temperature ranges: anthracene, 69 to 86°; 1,2-benzanthracene,

(8) F. H. Verhoek and A. L. Marshall, *J. Am. Chem. Soc.*, 61, 2737 (1939).

(9) R. D. Present, "Kinetic Theory of Gases," McGraw-Hill Book Co., Inc., New York, N. Y., 1958, Chapter 2.

(10) P. Clausing, *Ann. Physik*, 12, 961 (1932).

104 to 127°; 9,10-dimethyl-1,2-benzanthracene, 106 to 135°; and 20-methylcholanthrene, 128 to 152°.

The data for anthracene are represented by the equation

$$\log p_{mm} = 12.068 - 5145/T \qquad (L_s = 23.54 \text{ kcal./mole}) \quad (5)$$

where L_s is the average heat of sublimation over the experimental temperature range.

The data for 1,2-benzanthracene are represented by

$$\log p_{mm} = 11.528 - 5461/T \qquad (L_s = 24.99 \text{ kcal./mole}) \quad (6)$$

The data for 20-methylcholanthrene are represented by

$$\log p_{mm} = 13.168 - 6643/T \qquad (L_s = 30.40 \text{ kcal./mole}) \quad (7)$$

The temperature range over which 9,10-dimethyl-1,2-benzanthracene was studied included the melting temperature, so that a discontinuity appeared in the slope of the log p_{mm} *vs.* $1/T$ plot corresponding to the heat of fusion, L_f. The data for the sublimation of solid dimethylbenzanthracene and the evaporation of liquid dimethylbenzanthracene are represented, respectively, by the two equations

$$\log p_{mm} = 15.108 - 7051/T \qquad (L_s = 32.26 \text{ kcal./mole}) \quad (8)$$

and

$$\log p_{mm} = 12.232 - 5897/T \qquad (L_e = 26.98 \text{ kcal./mole}) \quad (9)$$

where L_e is the average heat of vaporization over the experimental temperature range. The heat of fusion is given to a good approximation by $L_s - L_e$ and was found to be 5.28 kcal./mole.

The above equations were obtained by obtaining the best straight line through the experimental points by the method of least squares. The mean percentage errors were 2.3, 4.4, 1.9, 1.8, and 1.0% for anthracene, 1,2-benzanthracene, 20-methylcholanthrene, and solid and liquid 9,10-dimethyl-1,2-benzanthracene, respectively.

Discussion

The vapor pressure of anthracene has been studied over several temperature ranges,[3-7] all above the range covered in this work. Sears and Hopke,[5] and Klochkov,[7] have made measurements in the range 105 to 125°. The agreement between these experimenters was only fair, Klochkov's results being about 15% higher on the average over the experimental range.

Table I shows a comparison of these two determinations with the present one for vapor pressures, given in microns, calculated at three temperatures intermediate between the two experimental ranges; the average heats of sublimation in kcal./mole for the three determinations are shown as well.

Table I

T, °C.	P, μ[a]	P, μ[b]	P, μ[c]
95	15.0	11.9	12.5
100	21.4	18.5	19.1
105	32.5	28.3	29.1
	L_s	L_s	L_s
	23.35	23.90	23.45

[a] Data of Sears and Hopke.[5] [b] Data of Klochkov.[7] [c] Present study.

As the table shows, the pressures calculated from Klochkov's vapor pressure equation agree with those calculated from eq. 5 to within a few per cent for these intermediate temperatures; the pressures calculated from the equation of Sears and Hopke are about 10% higher.

The average heat of sublimation calculated from these data is close to that obtained from the data of Sears and Hopke, and slightly higher, as would be expected from the fact that the heat of sublimation is not constant but in general increases with decreasing temperature. The heat of sublimation obtained by Klochkov is higher than that found here, although Klochkov's experimental temperature range was, as was that of Sears and Hopke, 35° higher on the average than that of the present investigation.

The heat of fusion calculated from the data on 9,10-dimethyl-1,2-benzanthracene, 5.28 kcal./mole, leads to a value for the entropy of fusion ($L_f/T_{melting}$) of 13.1 cal./deg.-mole. Mortimer[11] noticed that the entropies of fusion for a number of aromatic hydrocarbons related to anthracene and phenanthrene were close to 12.8 cal./deg.-mole. The above value for 9,10-dimethyl-1,2-benzanthracene seems to be in good agreement with this empirical observation.

(11) F. S. Mortimer, *J. Am. Chem. Soc.*, **44**, 1429 (1922).

Notes on the Rapid Computation of Chemical Equilibria

by D. R. Cruise

Propulsion Development Department, U. S. Naval Ordnance Test Station, China Lake, California *(Received June 22, 1964)*

Two previously published techniques used in the computation of chemical equilibria were combined in such a way as to achieve an appreciable reduction in computer time and computer memory requirements. A method of approximation is described which (1) at all times expresses the chemical reactions in terms of optimum reaction components, and (2) successively establishes the proper equilibrium relationship for each individual reaction by a stoichiometric change in composition. Also described are procedures with condensed phases which lead to correct solutions even in cases previously considered difficult or impossible.

Introduction

In the past 5 years the computation by high-speed digital computers of high-temperature chemical equilibria has become an increasingly significant application of these computers. It has also become one of their most challenging applications because of the large sets of nonlinear algebraic equations which must be simultaneously solved and because of the necessity of devising computer codes general enough to handle any particular chemical system.[1] Two numerical approaches to the solution of nonlinear algebraic equations are widely used.

One approach, presented by White, *et al.*,[2] is directly motivated by the free energy criterion for chemical equilibrium. The resulting procedure, however, is the method of steepest descent, which is a general method for the numerical solution of nonlinear algebraic equations.

The other approach, presented by Brinkley,[3] uses "equilibrium constants" and for purposes of background will be described in some detail. First, a "basis" is chosen. A basis is a subset of molecular species (also called "components"[4]). It contains as many species as there are chemical elements, and from it all other species may be formed by chemical reaction. A set of equations then establishes the equilibrium relationship of each nonbasis species to the basis. Another set of equations establishes the gram-atom amount of each chemical element. Both sets of equations are solved simultaneously by the Newton–Raphson method, which is also a general method for the numerical solution of nonlinear algebraic equations.

Interesting variations in the latter method are presented by Huff, *et al.*,[5] and Browne.[6] The latter, in particular, introduces the concept of the "optimized" basis, in which the components are present in the greatest possible molar amounts. Browne's computer code for the equilibrium-constant approach has been very successfully used for 3 years by the U. S. Naval Ordnance Test Station (NOTS) in the theoretical evaluation of rocket propellants.

Recently a number of physicochemical problems have arisen that are considerably more complex than the propellant evaluation problem. In these cases chemical compositions have to be computed for a much larger number of pressures and temperatures. For this reason, and because advances in the state of the art are always desirable, it was decided to review all computa-

(1) "Proceedings of the First Conference on Kinetics, Equilibria and Performance of High Temperature Systems," Western States Section of the Combustion Institute, G. Bahn and E. Zuckowsky, Ed., Butterworths Scientific Publications, Washington, D. C., 1960.

(2) W. White, *et al.*, *J. Chem. Phys.*, **28**, 751 (1958).

(3) S. Brinkley, Jr., *ibid.*, **15**, 107 (1947).

(4) H. Kandiner and S. Brinkley, *Ind. Eng. Chem.*, **42**, 850 (1950).

(5) V. Huff, *et al.*, "General Method of Thermodynamic Tables for Computation of Equilibrium Composition and Temperature of Chemical Reactions," NACA Report 1037 (1951).

(6) U. S. Naval Ordnance Test Station. H. Browne, Jr., *et al.*, "The Theoretical Computation of Equilibrium Compositions, Thermodynamic Properties and Performance Characteristics of Propellant Systems," China Lake, Calif., NOTS, 1960. (NAVWEPS Report 7043; NOTS TP 2434.)

tional procedures to see whether any progress could be made in the speed and certainty of convergence.

The two methods in current use were quickly eliminated. These are very general numerical methods for the solution of nonlinear, algebraic equations and are slowed down by the peculiarities of the particular problem. Older hand-computational methods were also eliminated, for they depend a great deal for convergence on the intuition of the chemist.

The method of Villars[7] was also reviewed. This too was a method suggested early in the development of computer codes but not widely used. It has some very desirable features. It is a particular method designed for a particular problem. Its theory is simple: The chemical system is divided into a number of subsystems, each relating a nonbasis species to the basis. The subsystem with the greatest discrepancy in its equilibrium relationship is corrected stoichiometrically. In this way the gram-atom amounts (chosen correctly at the start) do not change. The reason for convergence is clear: each iteration is equivalent to arresting all possible reactions but one and allowing that one to proceed according to the law of mass action. This possible (though not plausible) kinetic model can lead only in the direction of equilibrium.

In its computational aspects the method presented by Villars has both advantages and disadvantages. Unlike the widely used methods, it does not require the inversion of large matrices. This simplifies the coding and reduces the required computer memory. On the other hand, the speed of the method is greatly dependent on the choice of the basis. It is admittedly quite slow when components are chosen which are present only in small molar amounts.

It was decided to try Villars' method and to choose the optimum basis by Browne's method. The automatic choosing of the largest possible basis is not difficult to code and serves two purposes: it greatly speeds convergence, and it relieves the user of the burden of choosing the basis himself.

The rest of this paper will describe the combination of methods for computing a chemical composition at a given pressure and temperature. This description will be divided into three parts. The first part presents, in detail, the basis optimization technique used, which differs only slightly from that reported by Browne. The second part presents the procedures for determining equilibrium, which follow essentially the method of Villars, except for some suitable modifications to increase computing speed. The third part presents certain manipulations with condensed phases which increase the generality of the method.

For a concise presentation, the procedures are described in the notation of linear algebra. Numerical examples are available, upon request, from the author.

Basis Optimization

Consider a system which contains S chemical elements and N molecular species such that N is greater than S. Relating the species to the elements is a molecular composition matrix C. Here the individual elements c_{ik} state how many atoms of the kth element are contained in a molecule of the ith species.

Let any arbitrary choice of S molecular species be denoted

$$i(j) \qquad 1 \leq j \leq S$$

where the subset of i values chosen is considered to be a function of a dummy index j. A basis is formed by $i(j)$ if, and only if, the following relationship exists

$$|B| \neq 0 \tag{1}$$

where the vertical bars denote the determinant of the matrix B and where the elements of B are defined as

$$b_{jk} = c_{i(j),k} \qquad \begin{matrix} 1 \leq j \leq S \\ 1 \leq k \leq S \end{matrix} \tag{2}$$

Equation 2 involves three indexes, i, j, and k, where i is not independent because of its functional relationship to j. This equation describes the formation of the square basis matrix B by extracting some of the rows of the larger composition matrix C, namely, those rows corresponding to the chosen species.

The optimization problem requires that $i(j)$ be chosen to form a basis and that the corresponding molar amounts $n_{i(j)}$ be as large as possible. This can be done by a process of trial and error, but first the molecular species must be so sorted that the molar amounts are in descending order. Here the species subscript i becomes itself a function of a subscript m, such that

$$n_{i_1} \geq n_{i_2} \geq \ldots \geq n_{i_m} \geq n_{i_{m+1}} \geq \ldots \geq n_{i_N} \tag{3}$$

The basis is now found as follows. First i_1 is chosen to be the first basis species and the i_1st row of the C matrix is put into the first row of the B matrix. Next the j and m indexes are set to the value 2. The third step is to test i_m as an acceptable basis species. This is done by inserting the i_mth row of the C matrix into the jth row of the thus far incomplete B matrix. If there is linear dependence among the rows of the incomplete B matrix, the test fails, and the m index is increased by unity. If there is no linear dependence, i_m becomes the jth basis species, which is to say, $i(j)$, and both the j and

(7) D. Villars, *J. Phys. Chem.*, **63**, 521 (1959). Also see Villars' paper, pp. 141–151, in ref. 1.

m indexes are increased by unity. From here the process returns to the third step until $i(S)$ is determined.

Linear dependence was established by Browne using the relationship

$$|(B^{inc})(B^{inc})^T| = 0 \qquad (4)$$

where T denotes transposition and B^{inc} is the incomplete B matrix. However, it was found that the test could be performed much faster by using the Gram–Schmidt construction. This construction may be expressed as

$$b_{lk}' = b_{lk} - \left(\sum_{h=1}^{S} b_{lh}b_{nh} \Big/ \sum_{h=1}^{S} b_{lh}^2\right) b_{nk} \begin{cases} 2 \le l \le j \\ 1 \le n \le l-1 \\ 1 \le k \le S \end{cases} \qquad (5)$$

where b_{lk}' replaces the element b_{lk}, and n and l are dummy indexes. If all elements of the jth row are zero after the construction, there is linear dependence, and the test fails. The underlying theory of linear dependence and the Gram–Schmidt construction are presented by Stoll[8] and other texts on linear algebra.

The complete B matrix is determined at the end of the optimization process, and the ν-matrix of reaction coefficients may be expressed as

$$\nu = CB^{-1} \qquad (6)$$

Equilibrium constants may then be computed from the elements of the ν-matrix as

$$\ln K_i = \frac{1}{R}\left[g_i - \sum_{j=1}^{S} \nu_{ij} g_{i(j)}\right] \qquad (7)$$

where g_i is the standard Gibbs free energy of the ith species at the given temperature T.

Procedures for Determining Equilibrium

The equilibrium procedure requires that a first estimate of the equilibrium composition be given. This estimate need not closely approximate the final solution, but it must express the desired gram-atom amount of each chemical element. This can be accomplished in many ways. One way, easy to code, is to set the molar amount of one monatomic species of each chemical element to the desired gram-atom amount; then set the molar amounts of the rest of the species at zero (or at negligibly small values). This particular way requires that the monatomic species appear in the formulation.

The general iterative procedure assumes that the gram-atom amounts are correct and that the optimum basis has been chosen for the current estimate of the molar amounts. The reaction coefficient matrix, ν, and the array of equilibrium constants, K_i, are therefore available from eq. 6 and 7. A pass is made through the reaction (nonbasis) species to determine whether the proper equilibrium relationships are met. If not, the molar amounts, n_i, are stoichiometrically corrected. Before beginning another pass, the basis is again optimized whenever the current basis is no longer optimum. The details are described below using the conventions of Prigogine.[9]

The chemical reaction which forms the ith reaction species from the basis may be written as

$$\sum_{j=1}^{S} \nu_{ij} i(j) \longrightarrow i \qquad (8)$$

therefore, a stoichiometric change in the extent of reaction, $\Delta\xi$, causes the following alterations in composition

$$n_i' = n_i + \Delta\xi \qquad (9)$$

$$n_{i(j)}' = n_{i(j)} - \nu_{ij}\Delta\xi \qquad 1 \le j \le S \qquad (10)$$

where the primed n_i denotes the molar amounts after the change. This change, by definition, does not alter the gram-atom amount of any chemical element.

Basis optimization guarantees that n_i is smaller than any of the $n_{i(j)}$ in the basis for which $\nu_{ij} \neq 0$. (If this condition does not hold, the basis must again be optimized before the next iteration pass.) In the problems that the author encounters, most reaction species are smaller in molar amount by many orders of magnitude than the basis species from which they are formed. The gaseous species, more than two orders of magnitude smaller, are arbitrarily classified as *minor* species, and the rest of the nonbasis species, including condensed species of any molar amount, are classified as *major* species.

The correct equilibrium relationship for the ith reaction is expressed as

$$\sum_{j=1}^{S} \gamma_{i(j)}\nu_{ij} \ln (An_{i(j)}) - \gamma_i \ln (An_i) = \ln K_i \qquad (11)$$

where the phase parameter γ_i takes the value unity if the ith species is a gas and the value zero if it is condensed, and A is equal to $P/\sum_{i=1}^{N} \gamma_i n_i$, where P is the given pressure. If the current molar guesses are incorrect, the terms on the left will equal some value other than $\ln K_i$, denoted $\ln Q_i$. The iterative procedure obviously must adjust the values of n_i until the values

(8) R. Stoll, "Linear Algebra and Matrix Theory," McGraw-Hill Book Co., Inc., New York, N. Y., 1952, Chapter 8, especially Section 8.7.

(9) I. Prigogine, "Chemical Thermodynamics," translated by D. Everett, Longmans Green and Co., London, 1954.

of Q_i approach those of K_i within a specified tolerance. The log of the equilibrium constant may be differentiated with respect to the reaction parameter ξ (assuming A to be constant), yielding

$$\left(\sum_{j=1}^{S} \gamma_{i(j)}\nu_{ij}^2/n_{i(j)} - \gamma_i/n_i\right)d\xi = d(\ln K_i) \quad (12)$$

An estimate of the stoichiometric correction for a major species is obtained by applying Newton's method of locating roots, which is expressed by the approximate form of eq. 12

$$\Delta\xi \cong (\ln K_i - \ln Q_i)/(\sum\gamma_i\nu_{ij}^2/n_{i(j)} - \gamma_i/n_i) \quad (13)$$

Equations 9 and 10 are then applied. (In practice, $\Delta\xi$ is not allowed to take values leading to negative n_i.) All major species are corrected by this method during the iteration pass. This differs from the method used by Villars, who applied the correction only where the discrepancy $|\ln K_i - \ln Q_i|$ was greatest. The modification is justified for two reasons: very little additional computing time is required to make the correction after the discrepancy is determined, and basis optimization has minimized the interaction effect that a given correction has on the other equilibrium relationships.

An estimate of the stoichiometric correction for minor species is obtained as

$$n_i' \cong n_i(K_i/Q_i) \quad (14)$$

$$\Delta\xi = n_i' - n_i \quad (15)$$

Equation 10 is then applied. This approach assumes that the error in K_i is contained entirely in the value of n_i. This is nearly true for minor species, because a large relative change in n_i is accomplished by a small $\Delta\xi$, and there is no appreciable change in the basis. This separate analysis of minor species also differs from that of Villars. Again there are advantages. Equations 14 and 15 require less computing time than eq. 13. Then too, the former equations compute the molar amounts of the minor species to a high degree of accuracy (four or more significant decimal places) even when the relative molar amounts are quite small (*e.g.*, 10^{-10} or 10^{-20}). (This is useful in some applications involving ionic species.) It was also found that computer time is saved by correcting the minor species only on every fourth iteration pass, unless convergence is attained among the major species in the meantime. The variable A, defined above, is computed once at the start of every iteration pass.

Convergence was considered to be attained when all *binding* equilibrium relationships passed the following tests

$$\text{(major species)}\ |(1 - K_i/Q_i)| \leq 10^{-5} \quad (16)$$

$$\text{(minor species)}\ |(1 - K_i/Q_i)| \leq 10^{-4} \quad (17)$$

However, not all equilibrium relationships are binding; this is discussed in the following section.

Deletion of Condensed Phases

The formulation of the chemical equilibrium problem, as usually presented, is not general enough to describe completely the behavior of condensed phases. To overcome this weakness special procedures must be used. The following two procedures are particularly suited to the method of determining equilibrium presented above.

When the molar amount of a condensed species becomes negligibly small (say, 10^{-6}) and $\ln K_i - \ln Q_i$ is negative, no correction is applied, and the equilibrium relationship is no longer binding. In this way a phase is deleted, and a degree of freedom is gained in accordance with the phase rule.[10]

When a reaction occurs entirely among condensed species, the denominator in eq. 13 is zero. In this situation the phase rule states that at least one of the involved species cannot be present in any molar amount (if we are free to specify pressure and temperature). The situation is handled by ignoring eq. 13 and by determining a value of $\Delta\xi$ that takes the sign of $\ln K_i - \ln Q_i$ and that has a magnitude not leading to negative molar amounts when eq. 9 and 10 are applied. This is symbolically expressed as

$$\Delta\xi = \text{sign}(\ln K_i - \ln Q_i) \times \min[n_i, n_{i(1)}/|\nu_{i1}|, n_{i(2)}/|\nu_{i2}|, \ldots, n_{i(S)}/|\nu_{iS}|] \quad (18)$$

In this manner the molar amount of at least one condensed species is reduced to zero.

When these procedures were included in the computer code, correct solutions were obtained even in extremely difficult cases. In fact, correct solutions can be obtained where no gas phase is postulated.

Results and Comments

A computer code devised to use the foregoing combination of procedures was incorporated in the present propellant evaluation program at NOTS. Figure 1 is an idealized flow chart that shows the logical relationship of the various procedures to one another.

Computer time (averaged over 3 months and 2000 runs) was reduced by a factor of five. No convergence failures were noted. Other timing tests indicated that pressure–temperature points for systems containing seven and eight elements and 40 or 50 species can be computed in less than 1 sec. on the IBM 7094 elec-

(10) A. Findlay, "Phase Rule," Dover Publications, Inc., New York, N. Y., 1951.

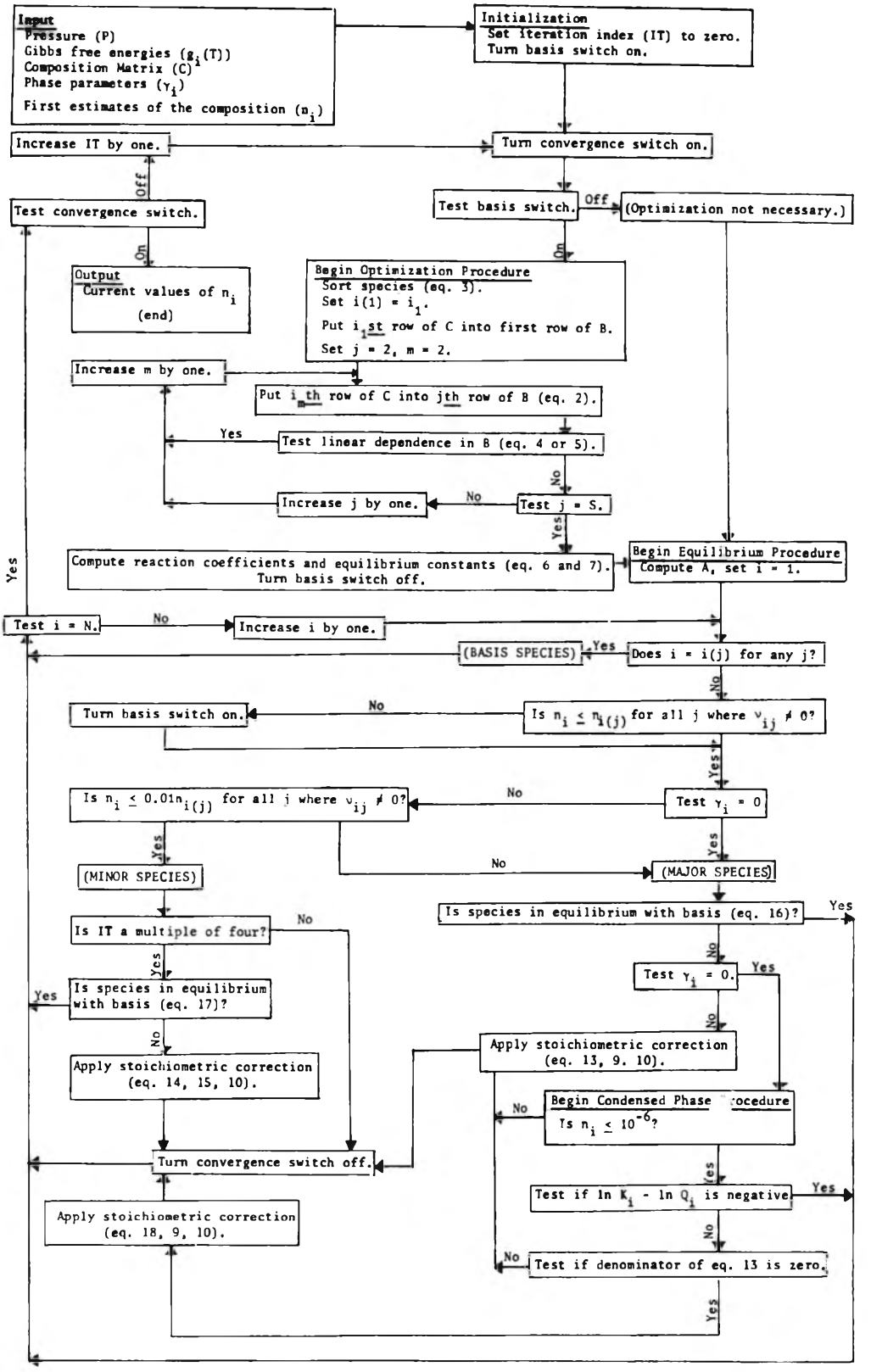

Figure 1. Flow chart for computation procedures.

tronic data processing machine. Compositions for a given pressure and enthalpy (involving the calculation of several pressure–temperature points) were clocked at 4 sec. for several six-element systems. The propellant evaluation program with unbuffered input and output averaged less than 0.0025 hr./run.

The times indicated above were obtained without extreme measures, such as converting the Fortran coding to machine language, and can probably be reduced. One untried suggestion is to code a logarithm routine which is faster, but is at the expense of the computer memory. This would speed computations because a great portion of time is used by the computer in computing logarithms.

The combination of procedures described in this report is being considered for future applications involving gas imperfection, where, because it still requires no matrix inversion, it will gain a further advantage over the two most widely used methods, which must handle even larger matrices than required in the study of perfect-gas mixtures.[11]

(11) F. Boynton, III, "Computation of Equilibrium Compositions and Properties in a Gas Obeying the Virial Equation of State," presented at the Second Conference on Kinetics, Equilibria, and Performance of High Temperature Systems, Western States Section of the Combustion Institute, Los Angeles, Calif., April, 1962.

Mass Spectrometry-Knudsen Cell Studies of the Vaporization of Uranium Dicarbide*

by J. H. Norman and P. Winchell

General Atomic Division of General Dynamics Corporation, John Jay Hopkins Laboratory for Pure and Applied Science, San Diego, California *(Received June 23, 1964)*

The presence of $UC_2(g)$ is important in the vaporization of uranium dicarbide. In the presence of excess carbon, the vaporization of uranium dicarbide as $UC_2(g)$ can be represented by a heat of vaporization of 185 kcal./mole and an entropy of 38.3 cal./°K. mole in the temperature range 2350 to 2700°K. Good thermodynamic agreement between this work and previous studies of vaporization of uranium dicarbide to U(g) + 2C(s) has been obtained. The values obtained in this study are $\Delta H = 127.3$ kcal./mole and $\Delta S = 18.6$ cal./°K. mole in the temperature range 2150 to 2700°K.

Introduction

During the past few years interest in uranium dicarbide as a high-temperature reactor fuel has prompted several investigators to study the vaporization of this material.[1-5] In these studies U(g) was assumed to be the only form in which uranium vaporizes. Several studies have shown, however, that in some systems gaseous carbide species are important.[6,7] Of relevance to this study is the fact that a species UC_2^+ has been identified in mass spectrometric surface ionization

* This research was carried out under a joint program of General Atomic and Empire State Atomic Development Associates, Inc.

(1) H. K. Lonsdale and J. N. Graves, "Thermodynamics of Nuclear Materials," International Atomic Energy Agency, Vienna, 1962, p. 601.

(2) J. M. Leitnaker and W. G. Witteman, *J. Chem. Phys.*, **36**, 1443 (1962).

studies with carbon and uranium,[8] and $UC_2(g)$ has been identified as a gas-phase species over the carbide.[5] In this vapor pressure study a species $UC_2(g)$ has also been observed, and the uranium vapor pressures in terms of U(g) and $UC_2(g)$ over UC_x in the presence of excess carbon have been measured using combined Knudsen cell–mass spectrometry techniques.

Experimental

The amount of material effusing from a Knudsen cell as a particular uranium gaseous species was investigated by observing the quantity and type of ions produced by crossing an electron beam with the effusate beam. Figure 1 is a representation of the apparatus used in this study; the apparatus is similar to that used by Inghram and Drowart[9] to study high-temperature vaporization processes. A graphite Knudsen cell was used to contain the uranium dicarbide sample. This cell consisted of overlapping cups machined for close fit, with the covering cup having a centered orifice of 0.037-cm.^{2} area. The ratio of the cell cross-sectional area to orifice area was 40:1, and, since powdered uranium dicarbide was used, the ratio of sample evaporating area to orifice area was larger than this. The Knudsen cell was mounted in a tantalum cup, which in turn was mounted on the furnace base by 0.159-cm. tungsten rods. The cell was surrounded by seven layers of 5-mil tantalum as heat shielding except directly above the orifice, where the first of the seven layers was tungsten. This tungsten shield sagged much less than did tantalum shields used in the same position.

Working temperatures were obtained by electron bombardment heating. The cell was operated at 300 to 500 v. positive with respect to its surroundings, and 600 to 1200 w. was dissipated at the cell. Bombardment was begun by electron emission from a heated filament surrounding the cell; however, when the temperature reached 2000°K., electron emission from the heat shields far exceeded the filament emission, and the filament was not used above this temperature. The power dissipation in the furnace was regulated by dropping the bombarding current through a resistor in series with the furnace. The furnace resistance and the external resistor resistance were made similar for this purpose. Under these conditions, at most applied voltages no fluctuation in the cell temperature was detected. At the highest temperatures (2700°K.), however, a slight drift toward lower temperatures was noted.

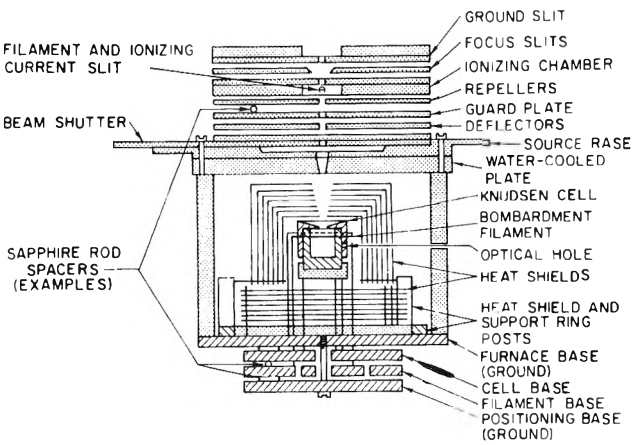

Figure 1. Ion source and furnace arrangement.

Temperature measurements were made by using a Leeds and Northrup optical pyrometer No. 8626-C. This pyrometer was calibrated against a U. S. National Bureau of Standards standard lamp. These calibrations were performed by each of the investigators, as measured temperatures varied significantly with the observer. Window corrections were measured and applied to the optical pyrometer readings. Sightings were made into a hole 0.318 cm. deep by 0.159 cm. in diameter in the side of the crucible. At working temperatures the hole was barely perceptible.

The mass spectrometer was constructed at General Atomic. This mass spectrometer has a 7.62-cm. radius and a measured resolving power of 40 (mass 41 contributes 1% of its height to mass 40). This resolution is sufficient for the UC_2 studies since uranium is essentially monoisotopic, and the observed peaks (U^+, UO^+, UC_2^+, and UO_2^+) were no closer than 8 mass units at 260. This mass spectrometer and its mode of operation are described by Norman, Winchell, and Staley.[10]

An investigation of the appearance potentials of the two major species observed in these studies showed that the appearance potentials of U^+ and UC_2^+ do not differ greatly; thus the appearance potential of UC_2^+ was taken as equal to the 5.4 v. reported by DeMaria, *et al.*,[11] for U^+. The accuracy in the appearance po-

(3) S. Fujishiro, *J. At. Energy Soc. Japan*, 3, 913 (1961).

(4) C. B. Alcock and P. Greiveson in "Thermodynamics of Nuclear Materials," International Atomic Energy Agency, Vienna, 1962, p. 563.

(5) H. A. Eick, E. G. Rauh, and R. J. Thorn, *ibid.*, p. 549.

(6) W. A. Chupka, J. Berkowitz, C. F. Giese, and M. G. Inghram, *J. Phys. Chem.*, 62, 611 (1958).

(7) D. D. Jackson, G. W. Barton, O. H. Krikorian, and R. S. Newberry in "Thermodynamics of Nuclear Materials," International Atomic Energy Agency, Vienna, 1962, p. 529.

(8) M. H. Studier, E. N. Sloth, and L. E. Moore, *J. Phys. Chem.*, 66, 133 (1962).

(9) M. G. Inghram and J. Drowart, *Proc. Intern. Symp. High Temp. Technol., Asilomar Conf. Grounds, Calif.*, 219 (1960).

(10) J. H. Norman, P. Winchell, and H. G. Staley, *J. Chem. Phys.*, 41, 60 (1964).

(11) G. DeMaria, R. P. Burns, J. Drowart, and M. G. Inghram, *ibid.*, 32, 1373 (1960).

tential determinations in the present measurements is rather poor because of inadequate source operation at very low voltages.

Observations of U^+ and UC_2^+ were made using a nominal ionizing electron energy of 8 e.v. This voltage was low enough so that the fragmentation of UC_2 on electron impact to give U^+ was negligible.

Uranium dicarbide in excess carbon was prepared by slowly heating UO_2 with excess carbon to 2200° until the system pressure fell to less than 10^{-5} torr. The samples were ground in an inert atmosphere and placed in the Knudsen cell, which was protected from air exposure during installation and pumpdown of the cell in the mass spectrometer furnace. Three cell charges were used to collect the data. The composition of the UC_2 phase in a similarly prepared sample was investigated by Lonsdale and Graves[1] in this laboratory. The actual carbon–uranium ratio of uranium carbide has been shown to be somewhat less than 2. This has also been discussed by Kubaschewski.[12]

A silver calibration experiment was performed prior to one of the observations of U^+ and UC_2^+ signals to obtain uranium pressures according to the method described by Drowart and Inghram.[9] The cross sections for silver and carbon of Ötvos and Stevenson,[13] the cross section for uranium of DeMaria, *et al.*,[11] and multiplier gains inversely proportional to molecular weight, as suggested by Inghram, Hayden, and Hess,[14] were assumed. The pressure of U at 2277°K. was estimated at 7.1×10^{-9} atm. Similarly, a factor of 0.90 was estimated for conversion of the ratio of ion signals to a ratio of cell pressures of UC_2 and U.

The basic data of this study are the U^+ and UC_2^+ ion intensity measurements made at temperatures between 2150 and 2700°K. The upper temperature limit was dictated by the furnace design, and the lower limit by signal detection ability. The ion intensities were compared with a beam-shuttered background. The U^+ and UC_2^+ peaks were, thus, proved to originate solely in the ion source. Both UO^+ and UO_2^+ peaks were observed in these experiments; however, they had a wider shutter profile than the U^+ and UC_2^+ peaks. It is believed that these oxide peaks emanated from heat shields where the oxide could be produced by exposure of condensed uranium to residual mass spectrometric gases, and they were discounted on this basis.

Results and Discussion

In this investigation uranium was found to evaporate from uranium dicarbide both as monatomic U and as UC_2. A representative set of ion signals for these two species over uranium dicarbide in excess carbon is presented in Fig. 2. The thermodynamic behavior of these species can be described according to the equations

$$UC_2(s) \rightleftarrows U(g) + 2C(s) \quad (1)$$

$$U(g) + 2C(s) \rightleftarrows UC_2(g) \quad (2)$$

Equation 2 was used in place of a vaporization of $UC_2(s)$ because using a ratio of ion signals reduced inaccuracies resulting from ion source instability and also because this equation is not dependent on the composition of the UC_2 phase. The experimental data can be represented by heats of reaction between 2150 and 2700°K. for eq. 1 and 2 of 127.3 ± 3.5 and 57.4 ± 3.3 kcal./mole and entropies of reaction of 18.6 and 19.7 cal./°K. mole, respectively, in seven and five sets of measurements where the error estimates are reported as standard deviations of the mean. Also, this thermodynamic information can be expressed in terms of equations representing the vapor pressures, P_U and P_{UC_2}, of U(g) and UC_2(g) over UC_2(s) and excess carbon as

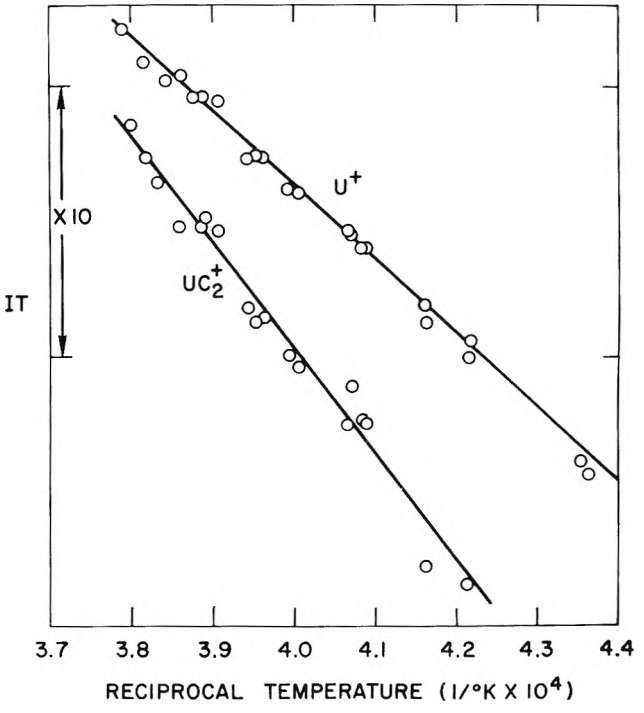

Figure 2. U^+ and UC_2^+ intensity–temperature products as a function of reciprocal temperature.

(12) O. Kubaschewski, *et al.*, "The Uranium–Carbon and Plutonium–Carbon Systems," International Atomic Energy Agency, Technical Report Series No. 14, Vienna, 1963.

(13) J. W. Ötvos and D. P. Stevenson, *J. Am. Chem. Soc.*, 78, 546 (1956).

(14) M. G. Inghram, R. J. Hayden, and D. C. Hess, U. S. National Bureau of Standards Circular 522, U. S. Govt. Printing Office, Washington, D. C., 1953, p. 257.

$$\log P_U = -\frac{27{,}800}{T} + 4.07 \qquad (3)$$

$$\log P_{UC_2} = -\frac{40{,}400}{T} + 8.38 \qquad (4)$$

The accuracy of the measured vapor pressures is associated with the reliability of the silver calibration, the measurement of the size of the effusion orifice, and the mass spectrometric sensitivity estimations. The authors estimate that eq. 3 and 4 give vapor pressures reliable to a factor of two or three. As previously stated, the cell charge was taken to be as described by earlier work from this laboratory. It is true that data on different cell charges appeared to be slightly different, but not so much so that combining the data was not deemed reasonable.

A comparison of these data with the other measured uranium dicarbide vapor pressures is shown in Fig. 3. Total uranium pressures ($P_U + P_{UC_2}$) corrected for effusion rates are presented for this work in the curve called "present studies" (curvature is apparent in the dotted extrapolation of the curve to higher temperatures where P_{UC_2} becomes important). This figure demonstrates the agreement between the data of this study and other reported data shown in this figure, particularly those of Leitnaker and Witteman,[2] L + W, and Lonsdale and Graves,[1] L + G. Another point of interest is that the heat of vaporization determined by Fujishiro,[3] F, is in very good agreement with a heat determined from present studies that were conducted in the temperature range of his experiments. The increasing importance of $UC_2(g)$ with increasing temperature leads to a noticeably higher experimental heat of vaporization of uranium above 2400°K. Previously, Fujishiro's heat was inexplicably higher than generally accepted values. This report does not agree with the somewhat higher vapor pressures he reported. The vapor pressure estimated from thermochemical data compiled by Kubaschewski, *et al.*,[12] K, also appears to be somewhat higher than a consensus of the reported vapor pressures, including this work.

Estimating an entropy at 2500°K. of $UC_2(g)$ from statistical mechanical considerations is very nebulous. Entropy calculations for a linear asymmetric molecule

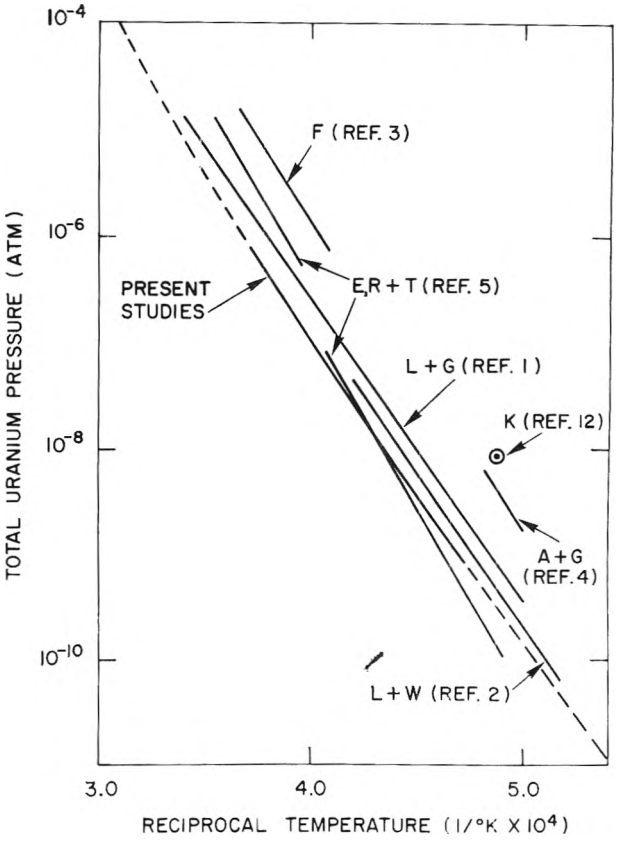

Figure 3. Comparison of present studies with other reported uranium vapor pressures.

(approximated U–C = 2.04 Å., C–C = 1.17 Å.) such as were done, for example, by Chupka, *et al.*,[6] for LaC_2 give a value that is only a few calories/degree mole smaller than that derived from the experimental data. It is worthwhile, however, to point out that any structure used in these calculations is tenuous. For instance, even though a symmetrical triangular molecular form of UC_2 would probably have a lower entropy, this structure is appealing to consider as representing the gaseous molecule.

Acknowledgments. We extend our gratitude to F. Kester and J. Graves for preparing $UC_2(s)$ samples. We are particularly indebted to Drs. H. Lonsdale, S. Langer, U. Merten, and A. Searcy for many helpful discussions concerning these studies.

Second Dissociation Constant of Deuteriophosphoric Acid in Deuterium Oxide from 5 to 50°. Standardization of a pD Scale

by Robert Gary, Roger G. Bates, and R. A. Robinson

National Bureau of Standards, Washington, D. C. *(Received June 25, 1964)*

The second dissociation constant of deuteriophosphoric acid in deuterium oxide has been determined from electromotive force measurements of a cell without liquid junction from 5 to 50°. Thermodynamic quantities for the second dissociation process of this acid have been calculated. Values of $-\log (a_{D^+}\gamma_{Cl^-})$ and the conventional pa_D values for the equimolal (0.025 *m*) KD_2PO_4–Na_2DPO_4 buffer solutions have been established.

Introduction

In a previous paper,[1] we reported the standard electromotive force of the deuterium–silver, silver chloride cell from 5 to 50° with deuterium chloride in deuterium oxide as electrolyte. Continuing a program of work on the thermodynamics of electrolytes in deuterium oxide, we now present e.m.f. measurements for the cell

$$\text{Pt; } D_2(g) \text{ at 1 atm., } KD_2PO_4(m), Na_2DPO_4(m), NaCl(m'), AgCl; Ag \quad (I)$$

at 5° intervals from 5 to 50°. From these data we have derived the second dissociation constant of deuteriophosphoric acid over this range of temperature, as well as the partial molal enthalpy, entropy, and heat capacity changes on dissociation. These are compared with the corresponding quantities for the dissociation of the $H_2PO_4^-$ ion in ordinary water.

In addition, values of $p(a_D\gamma_{Cl})$ [$\equiv -\log (a_{D^+}\gamma_{Cl^-})$] have been calculated and tabulated for three buffer solutions of equimolal (0.025 *m*) potassium dideuteriophosphate and disodium deuteriophosphate in solutions of sodium chloride of molalities 0.025, 0.015, and 0.005. A linear extrapolation gave values of $p(a_D\gamma_{Cl})^\circ$ for a solution 0.025 *m* in each of the phosphates but without added chloride. Values of the conventional pa_D [$\equiv -\log a_{D^+}$] were calculated with the aid of a convention for the chloride ion activity coefficient analogous to that proposed by Bates and Guggenheim[2] for solutions in ordinary water.

Experimental Results

Deuterium gas was taken from commercial cylinders; mass spectrometric analysis[3] gave a hydrogen content not greater than 0.5 atom %. The phosphates were NBS Standard Samples 186 Ib and 186 IIb. Sodium chloride was a bromide-free preparation used in previous work.[4] The deuterium oxide had an isotopic purity of 99.65%; this was reduced by a further 0.075% on the dissolution of the two phosphates, each at a concentration of 0.025 *m*. The solutions made by dilution of this stock solution with 99.65% deuterium oxide were proportionally closer to 99.65% in isotopic purity.

The cells have already been described.[1] The measured values of the e.m.f., corrected to 1 atm. of the gas used, are recorded in Table I. Each entry is the mean value given by two cells. The average difference between the e.m.f. of duplicate cells at all ten temperatures was 0.04 mv. The e.m.f. of each cell was measured in ascending order of temperature at 5° intervals from 5 to 50°. In three instances a final measurement at 25° was made. For the solutions with $m = m' = 0.025$, $m = m' = 0.020$, and $m = 5m' = 0.025$, the final e.m.f. at 25° was lower by 0.03, 0.05, and 0.04 mv., respectively, than that measured at 25° in the course of raising the temperature from 5 to 50°.

(1) R. Gary, R. G. Bates, and R. A. Robinson, *J. Phys. Chem.*, 68, 1186 (1964).

(2) R. G. Bates and E. A. Guggenheim, *Pure Appl. Chem.*, 1, 163 (1960).

(3) Analyses by E. E. Hughes, Analysis and Purification Section.

(4) V. E. Bower and R. A. Robinson, *J. Phys. Chem.*, 67, 1524 (1963).

Table I: Electromotive Force of the Cell Pt; D_2(g) at 1 atm., KD_2PO_4(m), Na_2DPO_4(m), NaCl(m'), AgCl; Ag (in volts) from 5 to 50°

m	m'	5°	10°	15°	20°	25°	30°	35°	40°	45°	50°
0.005004	0.005004	0.77971	0.78481	0.79004	0.79527	0.80054	0.80590	0.81128	0.81675	0.82209	0.82757
.010004	.010004	.76060	.76535	.77021	.77506	.77998	.78497	.78999	.79504	.80011	.80520
.01500	.01500	.74897	.75353	.75809	.76276	.76751	.77229	.77699	.78184	.78670	.79156
.02002	.02002	.74067	.74510	.74964	.75408	.75868	.76326	.76790	.77261	.77729	.78197
.02502	.02502	.73406	.73838	.74276	.74718	.75162	.75606	.76064	.76518	.76977	.77432
.02500	.01499	.74672	.75135	.75610	.76076	.76540	.77015	.77484	.77969	.78453	.78916
.02500	.004994	.77415	.77920	.78422	.78944	.79458	.79975	.80504	.81032	.81557	.82087

Discussion

Values of $p(a_D\gamma_{Cl})$ were calculated from

$$(E - E^\circ)/k + \log m_{Cl^-} = -\log (a_{D^+}\gamma_{Cl^-}) \quad (1)$$

where k is written for $(RT \ln 10)/F$. By combining eq. 1 with the equation for the second dissociation constant of deuteriophosphoric acid

$$K_2 = \frac{m_{D^+} m_{DPO_4^{-2}}}{m_{D_2PO_4^-}} \times \frac{\gamma_{D^+}\gamma_{DPO_4^{-2}}}{\gamma_{D_2PO_4^-}} \quad (2)$$

there results

$$pK_2 = -\log (a_{D^+}\gamma_{Cl^-}) - \log \frac{m_{DPO_4^{-2}}}{m_{D_2PO_4^-}} - \log \frac{\gamma_{DPO_4^{-2}}}{\gamma_{D_2PO_4^-}\gamma_{Cl^-}} \quad (3)$$

Since the two phosphates were present at equal molalities and since the last term of eq. 3 can be written[5]

$$-\log \frac{\gamma_{DPO_4^{-2}}}{\gamma_{D_2PO_4^-}\gamma_{Cl^-}} = \frac{2A(Id_0)^{1/2}}{1 + B\mathring{a}(Id_0)^{1/2}} - \beta I \quad (4)$$

eq. 3 becomes

$$pK_2 + \beta I = -\log (a_{D^+}\gamma_{Cl^-}) + \frac{2A(Id_0)^{1/2}}{1 + B\mathring{a}(Id_0)^{1/2}} \quad (5)$$

Bates and Acree[5,6] used the value $\mathring{a} = 4.4$ Å. for the "distance of closest approach" in aqueous solutions. This value was also used in the present work, and good linear extrapolations were obtained. Values of the intercept (pK_2) are given in Table II along with the standard deviations (σ_i).

The data have been fitted by the method of least squares to the equation[7]

$$pK_2 = A_1/T - A_2 + A_3T \quad (6)$$

where T is the temperature in °K. The values of A_1, A_2, and A_3 are given at the bottom of Table II. The pK_2 values calculated by eq. 6 are given in column 4. For comparison, values of pK_2 for phosphoric acid in ordinary water are given in column 5 of Table II.

Table II: Second Dissociation Constant of Deuteriophosphoric Acid in Deuterium Oxide from 5 to 50°

t, °C.	pK_2 (obsd.)	σ_i	pK_2 (calcd.)[a]	pK_2 (in H_2O)	Δ[b]
5	7.8846	0.0008	7.8837	7.2810	0.6027
10	7.8499	.0007	7.8508	7.2545	.5963
15	7.8233	.0018	7.8229	7.2324	.5905
20	7.7986	.0014	7.7994	7.2145	.5849
25	7.7796	.0010	7.7804	7.2005	.5799
30	7.7667	.0009	7.7655	7.1902	.5753
35	7.7547	.0018	7.7546	7.1834	.5712
40	7.7484	.0018	7.7475	7.1800	.5675
45	7.7433	.0015	7.7439	7.1799	.5640
50	7.7435	.0015	7.7437	7.1828	.5609

[a] pK_2 (calcd.) $= A_1/T - A_2 + A_3T = 2202.11/T - 5.9823 + 0.021388T$. [b] $\Delta = pK_2$ (calcd.) in D_2O − pK_2 in H_2O.

They are averaged values from three sets of data[5,8,9] which agree well among themselves. The differences (Δ) between pK_2 in heavy water and in ordinary water, shown in the last column, give the logarithm of the ratio of K_2 in ordinary water to K_2 in deuterium oxide. Rule and La Mer[10] give this ratio as 3.62 at 25°. Our value is 3.80.

Thermodynamic Quantities

From eq. 6 it follows that $\Delta H^\circ = 2.3026R(A_1 - A_3T^2)$, $\Delta S^\circ = 2.3026R(A_2 - 2A_3T)$, and $\Delta C_p^\circ = 2.3026R(-2A_3T)$. Moreover, the temperature at which the dissociation constant will have a maximum value is given by

(5) R. G. Bates and S. F. Acree, *J. Res. Natl. Bur. Std.*, **34**, 373 (1945).

(6) R. G. Bates, *ibid.*, **39**, 411 (1947).

(7) H. S. Harned and R. A. Robinson, *Trans. Faraday Soc.*, **36**, 973 (1940).

(8) A. K. Grzybowski, *J. Phys. Chem.*, **62**, 555 (1958).

(9) F. Ender, W. Teltschik, and K. Schäfer, *Z. Elektrochem.*, **61**, 775 (1957).

(10) C. K. Rule and V. K. La Mer, *J. Am. Chem. Soc.*, **60**, 1974 (1938).

$$T_{max} = \sqrt{A_1/A_3}$$

At this temperature the value of the dissociation constant is

$$-\log K_{max} = 2\sqrt{A_1 A_3} - A_2$$

A few values for the enthalpy and entropy changes on dissociation are as follows, corresponding values for ordinary water as solvent being given in parentheses

t, °C.	$\Delta H°$, cal. mole^{-1}	$\Delta S°$, cal. deg.$^{-1}$ mole^{-1}
0	2504 (2034)	−27.1 (−26.0)
25	1376 (987)	−31.0 (−29.6)
50	−144 (−423)	−35.9 (−34.2)

At 25° $\Delta C_p° = -58.4$ cal. deg.$^{-1}$ mole^{-1} compared with −54.1 cal. deg.$^{-1}$ mole^{-1} for ordinary water as solvent. T_{max} is 47.7° (42.7° for ordinary water) at which temperature $-\log K_{max} = 7.7436$ compared with 7.1796 at 42.7° when the solvent is water.

Establishment of a pD Scale

Table III gives values of $p(a_D\gamma_{Cl})$, calculated from the e.m.f. data (Table I) and eq. 1, for three solutions, all containing 0.025 m KD_2PO_4 and 0.025 m Na_2DPO_4 but different concentrations of sodium chloride—namely, 0.025, 0.015, and 0.005 m. Extrapolation to zero chloride molality by the method of least squares gave the values recorded in the fifth column of Table III.

Table III: Standard Reference Values of pa_D for the Buffer Solutions KD_2PO_4 (0.025 m) and Na_2DPO_4 (0.025 m) in Deuterium Oxide

	$p(a_D\gamma_{Cl})$[a]					
t, °C.	0.025 m'	0.015 m'	0.005 m'	0 m'	pa_D	pa_D (calcd.)
5	7.618	7.624	7.644	7.648	7.537	7.537
10	7.583	7.591	7.610	7.615	7.504	7.504
15	7.554	7.565	7.580	7.586	7.474	7.475
20	7.530	7.541	7.557	7.563	7.450	7.450
25	7.509	7.520	7.536	7.542	7.428	7.429
30	7.493	7.504	7.519	7.525	7.410	7.411
35	7.481	7.491	7.508	7.513	7.397	7.397
40	7.472	7.483	7.499	7.505	7.388	7.386
45	7.467	7.478	7.492	7.498	7.380	7.380
50	7.464	7.473	7.490	7.495	7.376	7.377

[a] Values in these four columns are for the respective values of m' (NaCl).

Bates and Guggenheim[2] used the convention

$$-\log \gamma_{Cl^-} = \frac{A(Id_0)^{1/2}}{1 + 1.5I^{1/2}} \qquad (7)$$

to eliminate the $\log \gamma_{Cl^-}$ term and convert values of $-\log (a_H\gamma_{Cl^-})$ into pa_H values. This is equivalent to assigning a value of 4.565 Å. to the ion-size parameter $\mathring{a}$ in the Debye–Hückel equation at 25°. We have used a similar convention to convert the $p(a_D\gamma_{Cl})$ values (Table III, column 5) into pa_D values. In this procedure, the equation

$$-\log \gamma_{Cl^-} = \frac{A(Id_0)^{1/2}}{1 + B\mathring{a}(Id_0)^{1/2}} \qquad (8)$$

is used with $\mathring{a} = 4.565$ Å.; appropriate values of T and ϵ were used to obtain the constants A and B. Values of pa_D calculated in this way are given in column 6 of Table III. These values have been smoothed by fitting them to the equation

$$pa_D \text{ (calcd.)} = 7.573 - 0.00764t + 0.0000744t^2 \qquad (9)$$

where t is the temperature in °C. Values calculated in this way are given in the last column of Table III. From a consideration of the standard deviation of the data on which the determination of $E°$ was based,[1] as well as the reproducibility of the e.m.f. data given in Table I, the values of pa_D are estimated to have an uncertainty of about 0.003 unit.

Finally, we have studied the response of the glass electrode to solutions in deuterium oxide at 25°. The customary pH cell with a liquid junction (indicated by the vertical line)

glass electrode, solution | concentrated KCl(aq); calomel electrode

was standardized at 25° by means of the aqueous equimolal (0.025 m) KH_2PO_4–Na_2HPO_4 buffer solution[11] [pH(S) 6.865]. The standardization was checked with a second reference solution,[11] 0.008695 m with respect to KH_2PO_4 and 0.03043 m with respect to Na_2HPO_4 [pH(S) = 7.413]. The equimolal (0.025 m) phosphate buffer solution in deuterium oxide then gave a meter reading of 6.982, constant for at least 3 hr. The pa_D value of this solution, determined by means of cells without liquid junction with the aid of the convention for $-\log \gamma_{Cl^-}$ described above, is 7.429. It appears, therefore, that meter readings (*i.e.*, the operational pH) should be increased by 0.447 to yield values of pa_D. This is somewhat more than the value of 0.408 which has been recommended recently.[12,13]

It should be noted, however, that the correction recommended by Long and co-workers was based on

(11) R. G. Bates, *J. Res. Natl. Bur. Std.*, **66A**, 179 (1962).

(12) P. K. Glasoe and F. A. Long, *J. Phys. Chem.*, **64**, 188 (1960).

(13) P. Salomaa, L. L. Schaleger, and F. A. Long, *J. Am. Chem. Soc.* **86**, 1 (1964).

hydrogen ion concentrations expressed in molarity units, whereas our pa_D value is referred to molality units. The two scales of pa_D differ by log d_0, where d_0 is the density of the solvent. In deuterium oxide, therefore, pa_D on the molality scale is 0.043 unit higher than that on the molarity scale, and the appropriate correction[13] becomes 0.451, in excellent agreement with 0.447 unit which we have found.

There is evidence that the glass electrode responds to deuterium ion as efficiently as it responds to hydrogen ion.[12,14] It is appropriate, therefore, to define the operational pD of a solution X in the same way as the operational pH is defined

$$\mathrm{pD} = \mathrm{pD(S)} + \frac{E_X - E_S}{(RT \ln 10)/F} \qquad (10)$$

where E_X and E_S are the e.m.f. values of the pH cell containing the "unknown" and the pD standard, respectively. The conventional pa_D values of *selected* reference solutions are identified with pD(S)

$$\mathrm{pD(S)} \equiv pa_D \qquad (11)$$

for the experimental determination of pD by eq. 10.

(14) P. R. Hammond, *Chem. Ind.* (London), 311 (1962).

Radiolysis of Crystalline Lithium Bromate by Lithium-6 Fission Recoil Particles[1]

by G. E. Boyd and T. G. Ward, Jr.

Oak Ridge National Laboratory, Oak Ridge, Tennessee *(Received June 29, 1964)*

Measurements were made of the decomposition of BrO_3^- ion and the production of oxidizing fragments in crystalline $LiBrO_3$ by energetic tritons and α-particles released following neutron capture by ^6Li in the Oak Ridge graphite reactor. A strong dependence of the radiolysis on the linear energy transfer (LET) was indicated by the initial 100-e.v. yield for bromate decomposition, $G_0(-BrO_3^-) = 1.48$, which was five times larger than that obtained with ^{60}Co γ-rays. A correspondingly large yield of oxidizing fragments also was observed; this yield and the ease with which these fragments could be removed from the crystals by mild thermal annealing was interpreted as being inconsistent with a "thermal spike" radiolysis mechanism. The observation that the yields, $G_0(-BrO_3^-)$, G_0("Ox"), and $G_0(Br^-)$, all were approximately five times those observed with γ-rays also suggested that the mechanism for the radiolysis did not change with increasing LET. A tenfold increase in the dose rate caused no change in the yields either for bromate decomposition or oxidizing fragment production.

The dependence of radiolytic yields on the linear energy transfer (LET) is well known for liquids and gases although, as yet, there is comparatively little information on track effects in crystalline, inorganic solids. The alkali metal nitrates have been studied most extensively in this connection, and yields have

(1) Presented before the Division of Physical Chemistry, 146th National Meeting of the American Chemical Society, Denver, Colo., Jan. 19–24, 1964. Research sponsored by the U. S. Atomic Energy Commission under contract with Union Carbide Corp.

been reported for the production of nitrite by the action of ^{60}Co γ-rays (~0.06 e.v./Å.), 44.5-ke.v. X-rays (~0.8 e.v./Å.), 3.4-Mc.v. α-particles (~34 e.v./Å.), and uranium fission recoil particles (~730 e.v./Å.).[2] The initial 100-e.v. yields of nitrite, G_0 (NO_2^-), in KNO_3 at 25°, for example, were 1.5, 2.0, 2.2, and 6.0, respectively. The increase in nitrite ion yield with the LET is roughly parallel to the increase produced when the temperature is raised in the radiolysis with low LET radiations. This analogy was led to the suggestion that the high temperature in heavy particle tracks may be an important factor in the dependence of yield on LET.[2] Observations on the chloride ion yields in the radiolysis of $NaClO_3$ by γ-rays and α-particles also have been interpreted in terms of the "thermal spike" hypothesis.[3]

An LET dependence has been noted[4] in our own recent work on the radiolysis of $LiBrO_3$ in the Oak Ridge graphite reactor (ORGR). The yield for bromate decomposition by energetic tritons and α-particles from the thermal neutron fission of ^6Li was $G_0(-BrO_3^-) \approx 1.4$, which is significantly larger than the yield (0.31) observed with ^{60}Co γ-rays.[5] To study this effect further, a series of neutron-irradiated crystalline $LiBrO_3$ preparations containing small, predetermined amounts of ^6Li was examined. An estimate of the decomposition caused by reactor γ-rays, energetic neutrons, and thermal neutron capture in bromine was obtained by extrapolating the observed bromate decompositions to zero ^6Li content. The gross radiolysis therefore could be corrected to give the decomposition by the $^6Li(n,\alpha)^3H$ reaction. Actually, most of the bromate radiolysis resulted from this reaction because of its large cross section and the large energy release per ^6Li fission (4.787 Mev.) and the fact that the energetic triton and α-particles were stopped entirely within the crystals. The use of isotopically labeled $LiBrO_3$ crystals also permitted an investigation of the role of the dose rate.

Experimental

Preparation of Anhydrous Compounds. Crystalline $LiBrO_3$ preparations with 0.01 to 1.0 atomic % ^6Li were synthesized by mixing aqueous solutions of $^6LiBrO_3$ (99.3% ^6Li) and $^7LiBrO_3$ (99.99% ^7Li) and evaporating them to dryness at 60–70° under vacuum to give the anhydrous salt. These preparations were stored away from light over P_2O_5 in a vacuum desiccator.

The $^6LiBrO_3$ solution was prepared by dissolving ^6Li metal in water to form LiOH which was neutralized to *ca.* pH 4 with $HBrO_3$ prepared from reagent grade $KBrO_3$ by cation exchange. A slightly acid solution was employed to permit the reaction: $5Br^- + BrO_3^- + 6H^+ \rightarrow 3Br_2, + 3H_2O$. Subsequent evaporation of the solution removed excess Br^- from the system. A $^6LiBrO_3$ preparation containing *ca.* 7 p.p.m. of Br^- was separated by crystallization and made anhydrous by heating at 60° under vacuum. An accurately weighed quantity of this salt was dissolved in a weighed amount of water to give a solution of known concentration.

The $^7LiBrO_3$ solution was prepared from ^7Li metal as before, except that the initial solution was not evaporated and the $^7LiBrO_3$ crystallized from it; instead, its concentration was determined by evaporating aliquots of known volume to dryness. This more expedient method was followed because the atomic percent of ^6Li in the desired isotopic preparations was insensitive to slight variations or inaccuracies in the concentration of the $^7LiBrO_3$ solution. The $^7LiBrO_3$ contained 48 p.p.m. of Br^- ion.

Flame spectrophotometric analyses on the $^6LiBrO_3$ and $^7LiBrO_3$ solutions showed less than 20 p.p.m. of the other alkali metals, except with the former where 297 p.p.m. of Na^+ was found.

Irradiation of Samples. Aliquots (3 g.) of each of the ten isotopic $LiBrO_3$ mixtures were irradiated in the active lattice of the ORGR for 2-, 4-, and 6-hr. periods, respectively. These samples were placed in sealed, 12 × 20 mm., cylindrical, polystyrene capsules of 1-mm. wall thickness and were irradiated together with thermal and fast neutron flux monitors. The thermal and fast fluxes were $\phi_{th} = 6.75 \times 10^{11}$, 6.72×10^{11}, and 6.97×10^{11} and $\phi_f = 9.5 \times 10^9$, 10.0×10^9, and 9.2×10^9 cm.$^{-2}$ sec.$^{-1}$, respectively. The methods for flux estimation and the irradiation facility are described elsewhere.[4]

Analytical Methods for Radiolytic Products. The irradiated salts were analyzed first for their oxidizing power. A dilute, alkaline solution of sodium arsenite was employed because it does not reduce bromate. The complete reduction of the oxidizing fragments was slow, and it was necessary to adopt a standardized procedure to obtain reproducible results. Enough salt to contain *ca.* 0.01 mequiv. of oxidizing power was weighed into 9 ml. of 0.2 *M* $NaHCO_3$ containing 0.5 ml. of 0.1 *N* $NaAsO_2$ solution. After a time (*ca.* 6 hr.) sufficient for complete reaction, this mixture was back-titrated with standardized I_2 solution. Spectrophotometric studies of the kinetics of

(2) For a summary of these investigations, see C. J. Hochanadel, *Radiation Res.*, **16**, 286 (1962).

(3) C. J. Hochanadel, *J. Phys. Chem.*, **67**, 2229 (1963).

(4) G. E. Boyd and Q. V. Larson, *ibid.*, **68**, 2627 (1964).

(5) G. E. Boyd, E. W. Graham, and Q. V. Larson, *ibid.*, **66**, 300 (1962).

the oxidation–reduction reactions indicated that the reduction of BrO^- and BrO_2^- was first order and pH dependent.

The irradiated crystals also were analyzed for total bromate decomposition by weighing out 0.2–0.5-g. amounts and dissolving them in water containing bicarbonate and excess (20%) arsenite. Aliquots of these solutions were titrated with 0.01 N $AgNO_3$ solution 12–18 hr. after preparation. Blank corrections determined by bromide ion titrations on aliquots of the unirradiated salts were applied to the foregoing results. It was assumed that the net Br^- ion found was equivalent to the number of BrO_3^- ions decomposed by radiation. Significant quantities of gas (presumably oxygen) were evolved when the irradiated crystals were dissolved prior to analysis.

Dosimetry. The radiation dose per mole of BrO_3^- ions imparted by the ^6Li fission recoil particles was estimated from

$$D_r \text{ (e.v. mole}^{-1}) = \phi_{th} t \sigma_{eff} N_A E_r \theta_r f c \qquad (1)$$

where ϕ_{th} is the thermal neutron flux, t is the time in seconds, σ_{eff} is the "effective" neutron capture cross section of ^6Li, N_A is the Avogadro number, E_r is the energy release per fission (4.787 Mev.), and θ_r is the fraction of the energy of the recoil particles absorbed by the crystals. The quantity f is a self-shielding factor to correct for the flux depression in the interior of the samples by the strong absorption of neutrons at the surface, and c is the atomic per cent of ^6Li in the preparations. Because of the very short range of the tritons (29.2 μ) and α-particles (5.8 μ), it was assumed that $\theta_r = 1.0$.

The "effective" neutron capture cross section of ^6Li for the energy spectrum of neutrons existing in the ORGR was estimated with

$$\sigma_{eff} = g\sigma_0 + \frac{\phi_r}{\phi_{th}} I_0' \qquad (2)$$

where σ_0 is the 2200-m. sec.$^{-1}$ cross section (945 barns), ϕ_r/ϕ_{th} is the ratio of the resonance neutron flux, ϕ_r, to the thermal flux, ϕ_{th}, and I_0' is the resonance integral defined by

$$I_0' = \int_{5E_m}^{1\,\text{Mev.}} \frac{\sigma(E)\mathrm{d}E}{E} \qquad (3)$$

where $E_m = 0.0431$ e.v. for the ORGR. When $\sigma(E)$ varies as $1/v$, as is the case for ^6Li, $I_0' = 0.90\sigma_0$ and $g = 1$.[6]

The ratio ϕ_r/ϕ_{th} may be estimated from cadmium ratio (Cd R) measurements on the thermal neutron flux monitor: using Cd $R = 9.8$, $\sigma_0 = 37$ barns, and $I_0 = 75$ barns for Co when present at high dilution in pure aluminum, we find $\phi_r/\phi_{th} = 0.057$; accordingly, $\sigma_{eff} = 993$ barns for ^6Li.

Neutron self-shielding corrections were estimated with equations derived from neutron diffusion theory.[7] These were small; their maximum value was only 6.8% for the most highly enriched $LiBrO_3$ preparation employed.

Thermal Decomposition of $LiBrO_3$ during Reactor Irradiation. The possibility that part of the bromate decomposition was caused by generalized heating of the $LiBrO_3$ preparations by the ^6Li fission process was examined. Crystalline $LiBrO_3$ (m.p. 254°) showed decomposition rates of 3.1 and 10.2 p.p.m. hr.$^{-1}$ when heated for extended periods at 175 and 203°, respectively. The maximum temperature rise possible, that for adiabatic conditions, was calculated for the greatest dose received by any sample employed (*i.e.*, the 1% ^2Li sample irradiated for 6 hr.). Assuming the specific heat of $LiBrO_3$ to be independent of temperature and the same as for $LiNO_3$ (0.387 cal. deg.$^{-1}$ g.$^{-1}$), an increase of only 28° was estimated from the energy balance. The temperature at the irradiation position was approximately 40°, so that the highest temperature reached would not have exceeded 70°. Thermal decomposition of $LiBrO_3$ during irradiation, therefore, was considered as negligible.

Thermal Annealing of Irradiated $LiBrO_3$. Measurements also were made of the changes in the oxidizing power of the irradiated $LiBrO_3$ crystals brought about by heating them for periods up to 24 hr. at temperatures as high as 228°. In these experiments, aliquots of a preparation containing 3.78 atom % ^6Li which had been irradiated for 1 hr. were placed in a porcelain boat located at the center of an electric tube furnace whose temperature was controlled to ±2°. Periodically, small samples were withdrawn and analyzed. The fraction of oxidizing power removed, ϕ_t, for a given time was computed from

$$\phi_t = [(Ox)_i - (Ox)_t]/(Ox)_i \qquad (4)$$

where $(Ox)_i$ and $(Ox)_t$ are the oxidizing powers in mequiv./g. initially and after heating for time t.

Results and Discussion

The observed gross bromate decompositions and oxidizing power yields are plotted as a function of the atom per cent of ^6Li for each of the three reactor bombardments in Fig. 1 and 2, respectively. Extrapolation of the yields to zero ^6Li content gives the contribution of the generalized reactor radiations (*i.e.*, γ-

(6) R. W. Stoughton and J. Halperin, *Nucl. Sci. Eng.*, 6, 100 (1959).
(7) P. F. Zweifel, *Nucleonics*, 18, 174 (1960).

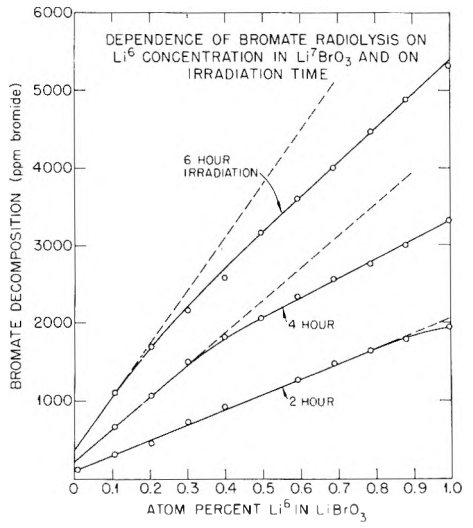

Figure 1. Dependence of bromate radiolysis on ^{6}Li concentration in $^7LiBrO_3$ and on irradiation time.

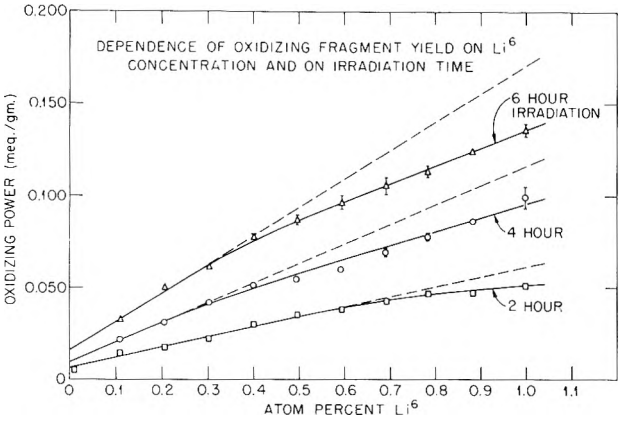

Figure 2. Dependence of oxidizing fragment yield on ^{6}Li concentration and on irradiation time.

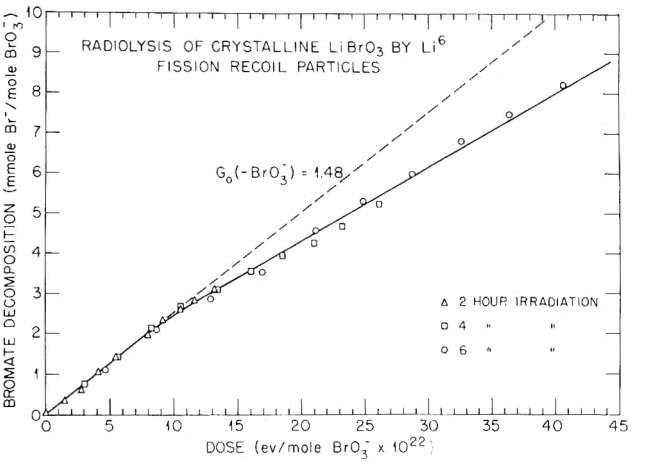

Figure 3. Radiolysis of crystalline $LiBrO_3$ by ^{6}Li fission recoil particles.

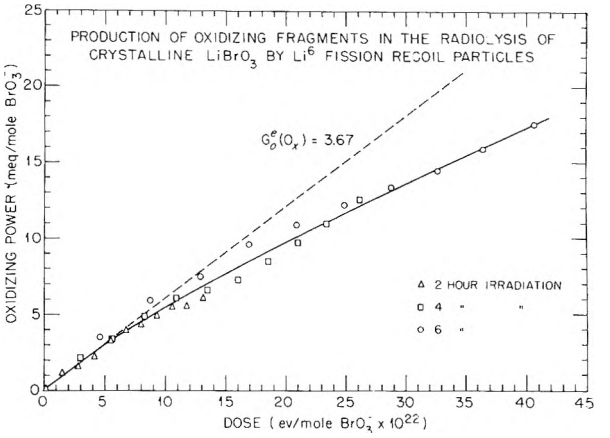

Figure 4. Production of oxidizing fragments in the radiolysis of crystalline $LiBrO_3$ by ^{6}Li fission recoil particles.

rays, fast neutrons, and neutron capture in bromine); the net decomposition or oxidizing power yield may be identified with that caused by the $^6Li(n,\alpha)^3H$ reaction. The linearity of the decomposition with ^{6}Li content up to 0.9 atom % for the 2-hr. irradiation (Fig. 1) showed that the radiolysis was independent of the dose rate; the fact that all of the data of Fig. 1 may be plotted against the dose absorbed, estimated with eq. 1, to give a single curve (Fig. 3) suggests that the decomposition was dose rate independent. The yields of oxidizing power (Fig. 2) when plotted against dose also gave a single curve (Fig. 4). This latter result may indicate that the oxidizing fragments themselves were not radiolyzed perceptibly. Support for this view was given by the observation that the oxidizing power yields, y, were related to the bromate decompositions, x, by the simple relation: $y = 2.179x + 0.274$.

The slopes of the initial parts of the curves in Fig. 3 and 4 were employed to compute 100-e.v. yields for bromate decomposition, $G_0(-BrO_3^-) = 1.48$, and oxidizing power, G_0^e("Ox") = 3.7. Earlier work[4] has shown that the initial average oxidation number of the fragments in $LiBrO_3$ was 2.5. If this number is assumed to apply to the results from this investigation, as seems reasonable, a value of G_0("Ox") = 1.1 may be computed for the initial oxidizing fragment yield. The yield for bromide ion production is then $G_0(Br^-) = 0.38$. The values for $G_0(-BrO_3^-)$, G_c("Ox"), and $G_0(Br^-)$ found with ^{60}Co γ-rays,[5] whose LET is *ca.* 0.06 e.v./Å., were 0.31, 0.21, and 0.10, respectively. These values are approximately one-fifth as large as those obtained with ^{6}Li fission recoil particles whose LET values are 9.4 e.v./Å. (tritons) and 34.7 e.v./Å. (α-particles), respectively. Clearly a pronounced LET

dependence exists for the radiolysis of bromate ion; however, the observation that all the G_0 values were approximately five times those for γ-rays suggests that the initial decomposition mechanism did not change with increasing LET.

As noted earlier in this paper, increases in G_0 with LET have been interpreted in terms of the "thermal spike" hypothesis which assumed that the high temperature in heavy particle tracks may be an important factor. Accordingly, the thermal annealing experiments are of particular interest (Fig. 5), because they reveal that most of the oxidizing power of the radiolyzed $LiBrO_3$ crystals was removed quite readily by heating them at relatively low temperatures. The oxidizing fragments produced by ^{60}Co γ-rays in $LiBrO_3$ also have been found to show changes on heating quite similar to those in Fig. 5. The production of large yields of decomposition products which can be removed by mild thermal treatment is difficult to reconcile with the hypothesis that a "thermal spike" is produced during the passage of the energetically charged particles through crystalline $LiBrO_3$. Tracks with intense local heating would be expected to give only relatively stable end products which would not decompose on heating at temperatures well below the melting point (254°).

The formation of thermally unstable products also has been observed in the γ-radiolysis of crystalline $XClO_3$.[8] Values of $G(ClO_2^-) = 1.2$ were found which could be reduced to 0.8 on heating the irradiated salt at 200°; the reduction in chlorite ion yield was attributed to decomposition to give chloride and oxygen gas. Moreover, later work[9] with $NaClO_3$ has shown that $G(Cl^-)$ increased on heating the salt at various temperatures up to 210° after irradiation. After the same compound was irradiated with 3.3-Mev. α-particles, however, $G(Cl^-)$ was reported[3] to have remained unchanged on heating at 185°. This result has been interpreted as supporting the view that thermal effects in α-particle tracks are a significant factor in the radiolysis of molecular ions in crystals. We would point out, however, that the manner in which energy was deposited in the crystals was radically different than in our work where fission tracks were produced at random throughout the body of the solid. In the former experiments α-particles impinged on the external surfaces of the $NaClO_3$ crystals and penetrated to a depth of ≤ 10 μ; accordingly, only the surface region was affected, and this was decomposed extensively (*i.e.*, 18%). Under these circumstances the unstable intermediates (ClO_2^-, ClO_2, ClO^-, etc.) would have reached a steady-state concentration which was quite small compared with the amounts of Cl^- ion formed. Accordingly, only a very small increase in $G(Cl^-)$ would have been produced by heating after the irradiation.

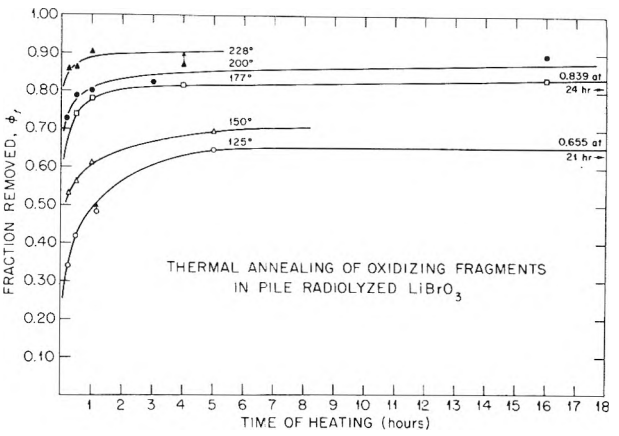

Figure 5. Thermal annealing of oxidizing fragments in pile radiolyzed $LiBrO_3$.

Differences in the rapidity of distribution of the ionization and excitation energy deposited in the crystals by γ-rays or by tritons and α-particles, respectively, may explain the large LET dependence observed in this research. With γ-rays the energy will be dissipated by diffusion from widely separated, essentially spherical regions of excitation; with ^6Li fission recoil particles, energy is deposited along a cylindrical track extending through many unit cells in the crystal lattice. The energy density in the ^6Li fission track is several hundred times greater than for γ-rays, and this energy will be dissipated less rapidly because of the smaller surface-to-volume ratio for the track. The critical excitation or dissociation energy of a bromate ion therefore is exceeded for a longer time resulting in a localization of radiolytic products along the track.

Back reactions reconstituting BrO_3^- ion are expected to be more important than those with γ-rays because of the higher density of decomposition products. The evidence for a back reaction, however, is only indirect: with ^6Li fission fragments the decomposition became nonlinear after *ca.* 0.2% radiolysis of BrO_3^- (Fig. 3); with ^{60}Co γ-rays,[5] in contrast, the radiolysis increased linearly with dose up to the highest decompositions which were above 0.4%. If a back reaction is assumed in the mechanism for BrO_3^- ion radiolysis, a quantitative treatment of the data of Fig. 3 may be obtained. Thus, formally

(8) A. S. Baberkin, "The Action of Ionizing Radiation on Inorganic and Organic Systems," Academy of Science of the USSR Press, Moscow, 1958, p. 187.

(9) P. F. Patrick and K. J. McCallum, *Nature*, 194, 766 (1962).

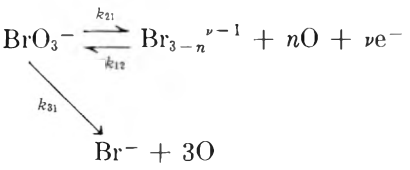

where n is an integer with values 0, 1, or 2, and $\nu \geq 0$. The species $Br_{3-n}^{\nu-1}$ represents the oxidizing fragments which may be either free radicals and/or bromite plus hypobromite and/or positively charged bromine-containing ions. A least-squares fit of the data of Fig. 3 to the equation for the decomposition of BrO_3^- gives: $k_{12} = (1.96 \pm 0.84) \times 10^{-23}$ mole e.v.$^{-1}$, $k_{21} = (1.11 \pm 0.26) \times 10^{-26}$ mole e.v.$^{-1}$, and $k_{31} = (1.88 \pm 0.05) \times 10^{-26}$ mole e.v.$^{-1}$. To reproduce the nonlinearity of the radiolysis with dose which sets in at *ca.* 0.2% decomposition, therefore, a relatively important reverse reaction ($k_{12} \approx 1000k_{21}$) would seem to be required.

The Volume of Activation in the Alkylation of Ambident Anions

by K. R. Brower, Robert L. Ernst, and Jean S. Chen

Department of Chemistry, New Mexico Institute of Mining and Technology, Socorro, New Mexico
(Received July 1, 1964)

Determinations of relative and absolute volumes of activation were performed on several alkylation reactions of sodium nitrite and the sodium salts of 2,4-pentanedione, methyl acetoacetate, phenol, and 2-pyridinol. In all reactions but one, the application of pressure up to 1360 atm. has no effect on the proportions of isomeric products, and the isomeric transition states therefore have nearly identical molar volumes. Since the products usually differ in volume by several ml./mole, it is inferred that the branching of the reaction pathways occurs at or beyond the transition state. In the benzylation of phenol the activation volumes for the three major products differ substantially, and a special explanation is given.

Introduction

In recent years the alkylation of ambident anions has been intensively studied in order to discover and explain the effects of reactant structure and reaction conditions on the proportions of isomeric products. The practical result of this work is that syntheses which utilize such reactions can be designed to increase the yield of the desired isomer, but it also has theoretical importance insofar as the ratio of isomers is a clue to certain mechanistic details of nucleophilic substitution reactions. The measurement of product proportions has been applied to many classes of reactions in order to find the difference in free energy of isomeric transition states formed from identical reactants under identical conditions. In most of such studies the isomerism has been positional, but the alkylation of ambident anions involves the more interesting case in which different elements are being bonded.

Aside from gross constitutional variations, the factors which are reported to affect the proportions of products are solvent polarity,[1,2] heterogeneity,[3,4] steric hindrance,[5] and hydrostatic pressure.[6] All of these

(1) N. Kornblum, P. Berrigan, and W. le Noble, *J. Am. Chem. Soc.*, 85, 1141 (1963).

(2) N. Kornblum, R. Seltzer, and P. Haberfeld, *ibid.*, 85, 1148 (1963).

(3) N. Kornblum and A. P. Lurie, *ibid.*, 81, 2705 (1959).

(4) D. Curtin and D. Dybvig, *ibid.*, 84, 225 (1962).

(5) N. Kornblum and R. Seltzer, *ibid.*, 83, 3668 (1961).

effects have received mechanistic interpretations. The present study, like that of le Noble,[6] was designed to determine whether the isomeric transition states have significantly different volumes. A difference of activation volume could be expected to indicate a difference in the lengths of bonds being formed since the activated complexes under comparison should be very similar in most other respects.

Results and Discussion

Although the kinetic order has not been demonstrated for every combination of alkylating agent, substrate, and solvent, the studies which have been made indicate second-order kinetics. Examples are the alkylation of phenols,[1] the alkylation of sodium nitrite with 1- and 2-bromooctane in DMF,[7] and the reaction of ethyl bromide with the sodium salt of methyl acetoacetate in dimethyl sulfoxide (Table III). The rate law is given by eq. 1 in which the subscripts a and b denote the reactants, and the numerical subscripts denote the isomeric products. The symbol k is thus the sum of the specific rate constants for the

$$dC_a/dt = -C_aC_b(k_1 + k_2 \cdots) = -kC_aC_b \quad (1)$$

various isomers. If the product fractions, x_1, $x_2 \cdots x_t$, are known and k is known, then k_t is given by kx_t. From this datum one may calculate the volume of activation for each isomer with the aid of eq. 2.[8] If k is too large for accurate measurement, the difference in

$$RT(\partial \ln k_t/\partial P)_T = -\Delta V_t^* \quad (2)$$

activation volume for a pair of isomers may be calculated from the product ratio, $X = x_1/x_2$, by

$$RT(\partial \ln X/\partial P)_T = -\Delta\Delta V^* \quad (3)$$

The range of pressures was 1–1360 atm. which is not so broad as to cause serious curvature in the plot of ln k or ln X *vs.* P for the class of reactions and solvents used here. Curvature was shown to be absent in a few test cases, and, thereafter, the middle range of pressures was not explored. Figure 1 illustrates one of these cases.

It is noteworthy that the alkylation of enolate ions in dimethyl sulfoxide produced substantial amounts of the O-alkyl derivatives whereas the usual alcoholic medium yields only C-alkyl products. The incursion of O-alkylation is explained by Kornblum's hypothesis of differential solvation,[1] according to which the reaction at the strongly negative oxygen atom is suppressed relative to reaction at carbon by solvents which form strong hydrogen bonds. In dimethyl sulfoxide the suppression by hydrogen bonding is absent, and both reactions proceed very much faster

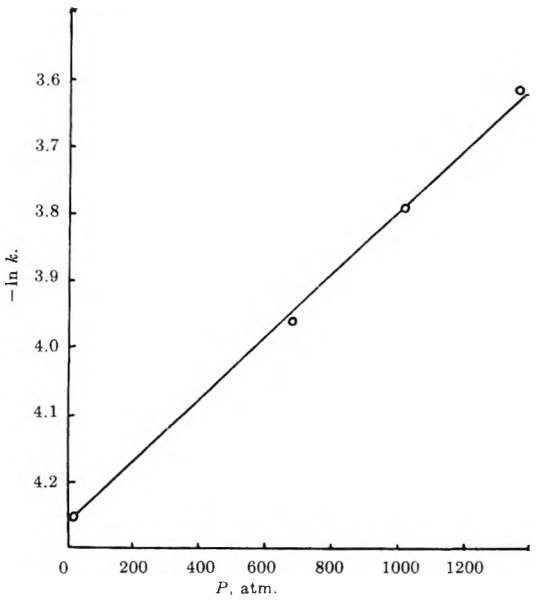

Figure 1. Benzylation of phenol; plot of −ln k *vs.* P (atm.).

than in alcohol. Surprisingly high rates for nucleophilic reactions in dimethyl sulfoxide have been noted elsewhere.[9] The alkylation of 2-pyridone is similarly affected by changing the solvent, but to a smaller degree. In ethanol the proportion of 2-*n*-butoxypyridine to N-*n*-butyl-2-pyridone is 11:89, whereas in dimethyl sulfoxide it is 70:30. Since the electronegativities of nitrogen and oxygen differ less than those of carbon and oxygen, it is understandable that N-alkylation might persist in dimethyl sulfoxide.

A list of the reactions chosen for this study and data concerning their activation volumes are given in Table I. With the exception of the benzylphenols, the proportions of isomeric products are not appreciably affected by pressure. It therefore appears that the isomeric transition states normally have equal volumes within 1 ml./mole. The products, on the other hand, usually have volumes which are different by several milliliters; for example, butyl nitrite is 6.0 ml. larger than 1-nitrobutane, 2-*n*-butoxypyridine is 8.8 ml. larger than N-*n*-butyl-2-pyridone, and anisole is 4.8–6.3 ml. larger than the cresols. It is barely possible that the transition states have quite different structures and that the equality of volume is due to fortuitous compensation of differences in (1) the effective cross-

(6) W. J. le Noble, *J. Am. Chem. Soc.*, **85**, 1470 (1963).
(7) N. Kornblum, *et al.*, *J. Am. Chem. Soc.*, **78**, 1497 (1956).
(8) A. E. Stearn and H. Eyring, *Chem. Rev.*, **29**, 509 (1941).
(9) J. Miller and A. J. Parker, *J. Am. Chem. Soc.*, **83**, 117 (1961); D. Cram, B. Rickborn, and G. Knox, *ibid.*, **82**, 6412 (1960).

Table I: Absolute and Relative Volumes of Activation

Reagents	Solvent	ΔV^*, ml./mole	$\Delta\Delta V^*$, ml./mole
Benzyl chloride and sodium phenoxide	Phenol	0 (ether)	..
		−11 (*o*-Bz)	11
		−16 (*p*-Bz)	16
Ethyl bromide and sodioacetoacetic ester	Methanol	−13	*a*
	DMSO	*b*	0
Ethyl bromide and sodioacetylacetone	DMSO	*b*	0
n-Butyl bromide and sodium nitrite	DMSO	*b*	0
sec-Butyl bromide and sodium nitrite	DMSO	−12	*c*
n-Butyl bromide and sodium 2-pyridoxide	Ethanol–water	−7	*c*
	DMSO	*b*	0
n-Butyl bromide and potassium 2-pyridoxide	Ethanol–water	−8	*c*
	Ethanol	−12	*c*
Benzyl chloride and potassium 2-pyridoxide	Ethanol–water	−9	0

[a] The extent of O-alkylation is immeasurably small. [b] The reaction is too rapid for accurate measurement of k. [c] These quantities were not measured.

sectional areas of the reactant molecules which are dependent on the direction of approach, (2) the lengths of the bonds being formed, and (3) the degree of desolvation of the nucleophilic atoms. It is more credible, however, that the volumes are equal because the structures are virtually the same. In the four ambident anions which show no pressure effect, the nucleophilic centers are either adjacent or have one atom intervening. It would therefore be possible for the two centers to contribute to the bonding in the isomeric transition states as shown below.

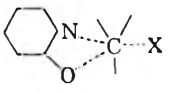

The choice of reaction by one or the other pathway would be determined by minor differences in the conformation or the distribution of energy, neither of which would appreciably affect the molar volume.

The benzylation of phenoxide ion in phenol is reported to yield phenyl benzyl ether, *o*-benzylphenol, and *p*-benzylphenol in the proportions 28:35:37, respectively.[1] At ordinary pressure and a slightly higher temperature (75° instead of 43°) we obtained the proportions 13:52:35. It should be noted that the proportions are very sensitive to traces of water. When phenol containing 2% admixture of water was used as the solvent, the proportions became 62:24:14. It was also noted that the solubility of sodium phenoxide in phenol increased sharply when small amounts of water were added. We were unable to dissolve as much as 1.0 g. of sodium phenoxide in 20 g. of phenol at 43° as reported by Kornblum, *et al.*,[1] and suspect, therefore, that the discrepancy in quantitative results is due to the fact that our mixture was more nearly anhydrous.

While the present work was in progress, le Noble[6] published a study of the effect of pressure on the distribution of isomers in the allylation of phenol in water. He found that the transition states for *ortho* and *para* allylation were 2.2 and 7.6 ml./mole smaller than for ether formation. We find that in benzylation the *ortho* transition state is 11 ml. smaller, and the *para* transition state is 16 ml. smaller. Figure 2

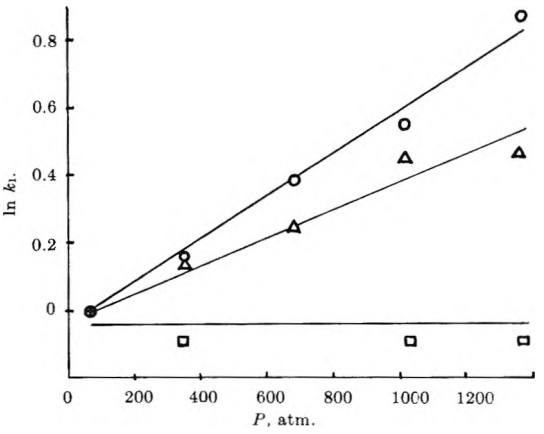

Figure 2. Benzylation of phenol; plot of ln k_1 *vs.* P (atm.): □, benzyl phenyl ether; △, *o*-benzylphenol; ○, *p*-benzylphenol.

illustrates the data from which these values were obtained. For ease of comparison the rate constant for each isomer has been reduced to unity at zero pressure.

We subscribe to le Noble's interpretation which is that the C-alkyl transition states are strongly solvated at oxygen and, hence, are smaller than the O-alkyl transition state which must be largely desolvated at oxygen in order to permit formation of the new bond. The greater magnitude of the effects which we observe is consistent with the observation that the electrostriction of water by ionic transition states is less than that of polar organic solvents.[10]

(10) K. R. Brower, *J. Am. Chem. Soc.*, **85**, 1401 (1963).

Table II: Summary of Reaction Conditions and Rate Constants

Reactants	Solvent	Temp., °C.	k at 1 atm., l. mole^{-1} min.$^{-1}$	k at 1360 atm., l. mole^{-1} min.$^{-1}$
0.5 *M* Benzyl chloride + 0.5 *M* sodium phenoxide	Phenol	52	0.0143	0.0270
0.6 *M* Ethyl bromide + 0.6 *M* methyl sodioacetoacetate	Methanol	49.6	0.00665	0.0129
0.3 *M* *sec*-Butyl bromide + 0.3 *M* sodium nitrite	DMSO	20	0.00582	0.0104
0.4 *M* *n*-Butyl bromide + 0.4 *M* sodium 2-pyridoxide	Ethanol–water[a]	25	0.00984	0.0144
0.2 *M* *n*-Butyl bromide + 0.2 *M* potassium 2-pyridoxide	Ethanol–water	25	0.00945	0.0148
0.4 *M* *n*-Butyl bromide + 0.4 *M* potassium 2-pyridoxide	Ethanol	70.9	0.0108	0.0208
0.25 *M* Benzyl chloride + 0.25 *M* potassium 2-pyridoxide	Ethanol	15	0.0143	0.0241

[a] The ethanol–water contains 0.33 mole fraction of ethanol.

The alkylation of 2-pyridone contrasts sharply with that of its isoelectronic relative, phenol, in that pressure does not influence the product ratio. This result would be disturbing except for the fact that the product ratio is also much less sensitive to the nature of the solvent. Evidently, differential solvation plays a small role because the electronegativities of oxygen and nitrogen are only slightly different.

The volumes of activation may be divided into two classes, according to the polarity of the solvent. The three alkylations of 2-pyridone in aqueous alcohol as listed in Table I and the butylation of phenol in the same medium[10] show an average ΔV^* of -8 ml./mole with a mean deviation of 1 ml. The less polar solvents —dimethyl sulfoxide, methanol, ethanol, and phenol— which were used for the remaining reactions of Table I and the butylation of phenol[10] cause an increase of the average ΔV^* to -12.5 ml./mole with a mean deviation of 1 ml. These reactions belong to the class involving no change of charge type and, on that account, should not show a variation of ΔV^* with solvent.[10] An explanation can be constructed on the supposition that the ambident anion, owing to its bulkiness and delocalization of charge, constricts a smaller volume of solvent than the halide ion. If the transition state shares in the over-all tendency to increasing electrostriction of solvent, then ΔV^* would be more negative in the less polar solvent, just as it is for reactions which produce ions from neutral reactants.

Experimental

Rate Measurements. The high-pressure equipment, sampling technique, and general approach to the measurement of second-order rate constants have been described before.[10,11] Total rates were based on the determination of halide ion by titration with silver nitrate solution, and rates for the individual isomers were obtained by multiplying the total rate by the product fractions.

Table III: Determination of Rate Constant for Ethyl Bromide and Methyl Sodioacetoacetate in DMSO at 27°

t, min.	Concn. of Br^-	k, l. mole^{-1} min.$^{-1}$
0.2 *M* ethyl bromide + 0.2 *M* methyl sodioacetoacetate		
9.0	0.0313	0.105
14.0	0.0437	0.100
20.0	0.0555	0.098
30.0	0.0700	0.090
40.0	0.0828	0.088
0.8 *M* ethyl bromide + 0.2 *M* methyl sodioacetoacetate		
4.0	0.0240	0.088
10.0	0.0455	0.082
14.0	0.0527	0.073
22.0	0.0682	0.072

Errors. The mean deviation of duplicate rate measurements is about 3%. The error in the volume of activation is 1 ml./mole, and it arises almost entirely from the 6% uncertainty in $\ln (k_p/k_o)$. Temperatures were controlled within 0.05° and pressures within 7 atm. In all cases, the high-pressure vessel was preheated to the setting temperature so that the time required for pressurization and thermal equilibration did not exceed 2 min. out of a reaction time of 2 hr. Even though the uncertainty in reaction time affects the absolute accuracy of the rate constant, it is largely canceled in the term $\ln (k_p/k_o)$.

Materials. Ethyl bromide, *n*-butyl bromide, *sec*-butyl bromide, *n*-butyl chloride, methyl acetoacetate, 2,4-pentanedione, methanol, 2-aminopyridine, and dimethyl sulfoxide were obtained from Distillation Products Industries and used without further purification. Phenol was purified by vacuum distillation; m.p. 41.3–41.4°; lit. 41.8°. The ethanol was anhydrous U.S.P. reagent quality.

(11) K. R. Brower, *J. Am. Chem. Soc.*, **80**, 2105 (1958).

Preparation of Sodium Phenoxide.—A solution of 44.6 g. (0.476 mole) of phenol in 49.6 ml. of 9.60 *N* sodium hydroxide solution was evaporated to dryness under vacuum at room temperature. The product was stored in a vacuum desiccator containing concentrated sulfuric acid as desiccant. After standing 4 days the neutralization equivalent declined from 163 to 117 (calcd. 116).

Preparation of 2-Pyridinol. A mixture of 100 g. (1.06 moles) of 2-aminopyridine and 100 ml. of water in a 5-l. beaker was acidified by addition of 250 ml. of 50% sulfuric acid solution. Ice was added in order to maintain the temperature at 5° during the addition of a solution of 80 g. (1.15 moles) of sodium nitrite in 200 ml. of water. The diazotization process was completed in approximately 1 min. The mixture was heated to boiling to complete the expulsion of nitrogen, evaporated to a volume of 500 ml., and neutralized to a pH near 7 by careful addition of 40% sodium hydroxide solution. The resulting mixture was evaporated to dryness on a steam bath, and the residue was triturated with acetone until the washings were colorless. The acetone solution was concentrated on the steam bath and distilled at 1–2 mm. 2-Pyridinol was collected in the range 130–140°, and the yield was 83.5 g. (83%).

Preparation of the Sodium Salts of 2-Pyridinol, 2,4-Pentanedione, and Methyl Acetoacetate. A solution of 0.05 mole of the appropriate conjugate acid in 20 ml. of freshly prepared 2.5 *M* methanolic sodium methoxide was evaporated to dryness under reduced pressure. The residue was stored over concentrated sulfuric acid in a vacuum desiccator.

Preparation of Benzyl Phenyl Ether and p-Benzylphenol. This was accomplished by the method of Kornblum, Berrigan, and le Noble[1] which involves the benzylation of phenol and separation of products on a chromatographic column of basic alumina. *o*-Benzylphenol was obtained in impure condition and was further purified in amounts sufficient for infrared spectrum analysis by gas chromatography.

Preparation of Methyl Ethylacetoacetate. Ethyl bromide was substituted for ethyl iodide in the method of Büchi, *et al.*[12] A 65% yield was obtained; b.p. 170–175° (650 mm.).

Preparation of Methyl Diethylacetoacetate. Methyl ethylacetoacetate was ethylated again by the procedure above. Using 10 g. of starting material yielded 6.0 g. (49%) of product, b.p. 180–190° (650 mm.).

Preparation of Ethyl 3-Methoxycrotonate. Ethyl acetoacetate was treated with diazomethane.[13]

Preparation of 3-Ethyl-2,4-pentanedione. Ethyl bromide was substituted for ethyl iodide in the method of Johnson, *et al.*[14]; a 58% yield was obtained, b.p. 170–174° (650 mm.).

Preparation of 3,3-Diethyl-2,4-pentanedione. A mixture of 4.0 g. of the sodium salt of 3-ethyl-2,4-pentanedione, 10 ml. of dimethyl sulfoxide, and 4.0 ml. of ethyl bromide was allowed to react at room temperature for 3 hr. The organic products were removed by shaking with 20 ml. of water and 10 ml. of ether. After being washed with water, extracted with aqueous sodium hydroxide, and dried with magnesium sulfate, the ether layer was distilled. The yield was 4.0 g. (82%), b.p. 175–185° (650 mm.).

The structure of the product was proved by cleavage with alkali to 3-ethyl-2-pentanone. A 1.0-g. portion was dissolved in 5 ml. of 10% aqueous alcoholic sodium hydroxide and heated to boiling for 3 min. The product was extracted into ether as described above, and the ether was evaporated on a water bath. The residue was identified as 3-ethyl-2-pentanone by conversion to the semicarbazone; m.p. 97–98°; lit. 99°.

Preparation of 1-Nitrobutane. This was accomplished by the general method of Kornblum, *et al.*,[7] with substitution of dimethyl sulfoxide for dimethylformamide as solvent.

Preparation of n-Butyl Nitrite. The method of Noyes[15] was used.

Preparation of 2-n-Butoxypyridine and N-n-Butyl-2-pyridone. A mixture of 0.1 mole of sodium 2-pyridoxide and 0.1 mole of *n*-butyl bromide in 60 ml. of 95% alcohol was refluxed with stirring for 16 hr. After evaporation of most of the alcohol the mixture was shaken with 20 ml. of water and 20 ml. of ether. The water layer was analyzed for bromide ion, and 98.5% of the theoretical amount was found. A small portion of the ether solution was removed for gas chromatographic analysis by the method described below, and the proportion of the O-butyl and N-butyl isomers was 11:89. The bulk of the ether layer was evaporated, and the residue was steam distilled to remove 2-*n*-butoxypyridine. The steam distillate was combined with the distillate from two parallel experiments and extracted with ether. The ether layer was dried, concentrated, and distilled to yield 2.5 g. (6%) of 2-*n*-butoxypyridine; b.p. 194–198° (650 mm.); d^{25}_4 0.968. The residue from the steam distillation

(12) J. Büchi, P. Schneeberger, and R. Lieberherr, *Helv. Chim. Acta*, **36**, 1402 (1953).

(13) F. Arndt, L. Loewe, T. Severge, and I. Turegur, *Ber.*, **71B**, 1640 (1938).

(14) A. W. Johnson, E. Markham, R. Price, and K. B. Shaw, *J. Chem. Soc.*, 4254 (1958).

(15) W. A. Noyes, "Organic Syntheses," Coll. Vol. II, John Wiley and Sons, Inc., New York, N. Y., 1943, p. 108.

was distilled at reduced pressure to yield 5.0 g. (36%) of N-*n*-butyl-2-pyridone, b.p. 172–174° (33 mm.); d^{25}_4 1.058.

Preparation of N-Benzyl-2-pyridone. A solution containing 20 ml. of water, 35 ml. of ethanol, 3.3 g. of sodium hydroxide, 7.0 g. of 2-pyridinol, and 10.2 ml. of benzyl chloride was allowed to react for 15 hr. at 25°. The mixture was steam-distilled until the distillate was clear, and the residue was recrystallized from petroleum ether, b.p. 90–110°, to yield 7.3 g. (53%), m.p. 75–76°; lit. 75–76°.

Preparation of 2-Benzyloxypyridine. A mixture of 12 g. of 2-pyridinol and 25 g. of phosphorus pentachloride was placed in a flask fitted with a reflux condenser and heated on an oil bath which was maintained at 145°. After the evolution of hydrogen chloride ceased, the mixture was poured over cracked ice and neutralized with solid sodium carbonate. The organic layer was taken up in ether, dried with magnesium sulfate, and distilled. The yield of 2-chloropyridine was 10 g. (70%), b.p. 160–164° (650 mm.). The 2-chloropyridine was added to a preparation of sodium benzyloxide which was obtained by dissolving 2.1 g. of sodium metal in 40 ml. of hot benzyl alcohol. The mixture was maintained at 116° for 16 hr. and then partitioned between 50 ml. of water and 50 ml. of ether. The ether layer was washed with water and extracted with 100 ml. of 8% hydrochloric acid. The acid layer was made basic with sodium hydroxide, and the oil which separated was taken up in 30 ml. of benzene. After being dried with magnesium sulfate the benzene solution was distilled under reduced pressure. The yield of 2-benzyloxypyridine was 9.8 g. (60%), b.p. 110–114° (3 mm.).

Gas Chromatographic Analyses. The analysis of the products of benzylation of phenol is typical of the method. The reaction mixture, which contained roughly 1.5 g. of mixed benzyl derivatives of phenol in 10 g. of phenol, was poured into 100 ml. of water and acidified with acetic acid. The mixture was shaken with 5 ml. of ether in a separatory funnel, and the aqueous layer was removed for determination of chloride ion. A small portion of the organic layer was injected into a Beckman GC-2 gas chromatograph which was fitted with a 0.64 cm. × 1.8 m. silicone grease column at 254°, and the flow of helium gas was adjusted to give a retention time of 40 min. for the final peak (*p*-benzylphenol). A calibration curve was constructed by analyzing known solutions of benzyl phenyl ether and *p*-benzylphenol in phenol over the expected range of proportions. The data in Table IV were collected.

It can be seen that the mean deviation is 1–2%.

Table IV: Proportion of Benzyl Phenyl Ether to *p*-Benzylphenol

By weight	By g. c. peak area
28.5:71.5	35:65, 35:65, 38:62
33:67	39:61
43:57	45:55, 48:52, 47:53, 49:51
54.5:45.5	57:43, 59:41

Since pure *o*-benzylphenol was not available in amounts sufficient for preparing synthetic mixtures, it was assumed that its calibration would be identical with that of *p*-benzylphenol. Although the absolute accuracy of the k_i is dependent on the reliability of this assumption, the accuracy of the ΔV^* is not since it is calculated from a ratio of rates. It was established that the order of elution is (1) phenyl benzyl ether, (2) *o*-benzylphenol, and (3) *p*-benzylphenol by comparison of the infrared spectra of the three fractions with those of authentic specimens.

Effect of Pressure on the Benzylation of Phenol. To a suspension of 1.0 g. of sodium phenoxide in 10.0 g. of phenol was added 1.0 g. of benzyl chloride. The mixture was divided into two portions for reaction at 70 and 1360 atm. at 75° for 5 hr. Titration of the liberated chloride ion indicated 82% reaction. Analytical results by gas chromatography for this reaction and others at different pressures are shown in Table V.

Table V

P, atm.	Ether:*o*-benzyl:*p*-benzyl
70	14:50:36, 13:53:34
340	11:55:35, 11:54:36
680	8.3:51:41, 8.7:54:38
1020	8.6:52:39, 7.5:53:39
1360	7.2:44:48

Effect of Pressure on the Ethylation of Methyl Acetoacetate. A solution of 2.76 g. of the sodium derivative of methyl acetoacetate and 2.20 g. of ethyl bromide in dimethyl sulfoxide was made up to 20 ml. After division in half, the solution was allowed to react at 1 and 1360 atm. for 2 hr. at 47°. The mixture was worked up and analyzed by the procedure used for the benzylated phenols. The liberation of bromide ion was 95% of theoretical. The gas chromatogram at 160° had three peaks which were identified as methyl ethylacetoacetate, methyl 3-ethoxycrotonate, and methyl diethylacetoacetate, in that order of appearance. The

first was characterized by the indistinguishability of its retention time and infrared spectrum from those of an authentic specimen. The second was identified by its insolubility in alkali and the near-identity of its infrared spectrum with that of ethyl 3-methoxycrotonate. A strong band at 1620 cm.$^{-1}$, which is probably due to the olefinic linkage, is characteristic of these compounds. The third fraction was shown to be methyl diethylacetoacetate by its insolubility in alkali and the indistinguishability of its retention time and infrared spectrum from that of an authentic sample. The proportions of C-ethyl, O-ethyl, and C,C-diethyl products by calculation from the gas chromatograms were 71.5:18.5:10 at 1 atm. and 71.5:18:10.5 at 1360 atm.

Effect of Pressure on the Ethylation of 2,4-Pentanedione. A solution of 2.0 g. of the sodium derivative of 2,4-pentanedione in 20 ml. of dimethyl sulfoxide was filtered and partly frozen by cooling with ice. After addition of 4.0 ml. of ethyl bromide, two 10-ml. portions were removed and allowed to react at 36° for 1 hr. at 1 and 1360 atm. Since the O-ethyl product is sensitive to acid hydrolysis, the reaction mixture was acidified by pouring it into 15 ml. of buffer solution which was 0.5 *M* in acetic acid and sodium acetate. Analysis was then performed by the method used for the benzylated phenols. The gas chromatogram at 160° showed three fractions which were identified as 3-ethyl-2,4-pentanedione, 4-ethoxy-3-penten-2-one, and 3,3-diethyl-2,4-pentanedione, in that order of appearance. The first was characterized by identity of its retention time and infrared spectrum with that of an authentic sample. The second was identified by its insolubility in alkali and the indistinguishability of its infrared spectrum from a published spectrum.[16] The third was identical in retention time and infrared spectrum with an authentic specimen. The proportions of C-ethyl, O-ethyl, and C,C-diethyl products were 69.5:17.7:12.8 both at 1 and 1360 atm.

Effect of Pressure on the Butylation of Sodium Nitrite. A solution of 7.3 g. of sodium nitrite and 6.0 ml. of *n*-butyl bromide in 46 ml. of dimethyl sulfoxide was chilled to the freezing point as quickly as possible. The mixture was divided in halves for reaction at 30° for 100 min. at 1 and 1360 atm. Analysis of the products was performed by the method applied to the benzylated phenols. Liberation of bromide ion was nearly quantitative. The gas chromatogram at 130° had two peaks due to *n*-butyl nitrite and 1-nitrobutane, respectively, as shown by comparison with authentic specimens. The proportion of nitro compound to nitrite was 83.2:16.8 at 1360 atm. and 83.0:17.0 at 1 atm.

Effect of Pressure on the Butylation of 2-Pyridinol. A solution of 3.0 g. of sodium 2-pyridoxide in 20 ml. of dimethyl sulfoxide was chilled to the freezing point, and 2.1 ml. of *n*-butyl bromide was added. It was found by analysis of an aliquot that 15% of the reaction occurred during the 2 min. required to fill and pressurize the high-pressure sample cell. Two portions were allowed to react at 1 and 1360 atm. at 27° for 2 hr. and analyzed in the usual way. The gas chromatogram at 220° showed peaks due to 2-*n*-butoxypyridine and N-*n*-butyl-2-pyridone in the proportion 70:30, at both pressures.

Effect of Pressure on the Benzylation of 2-Pyridinol. A solution containing 0.95 g. of 2-pyridinol, 10 ml. of 1.31 *N* potassium hydroxide solution, 35 ml. of ethanol, and 1.38 ml. of benzyl chloride was diluted with water to 50 ml. Duplicate 3-ml. portions were allowed to react for 20 hr. at 30° under pressures of 1 and 1360 atm. Liberation of chloride ion was nearly quantitative. The reaction mixture was evaporated in the open to dryness, and the organic part was taken up in 3.00 ml. of carbon tetrachloride. The infrared optical densities at 1430 cm.$^{-1}$, which measure the minor ingredient, 2-benzyloxypyridine, were identical for the two reaction pressures. In order to determine the composition, the behavior of this peak and the stronger 1660-cm.$^{-1}$ peak of N-benzyl-2-pyridone was observed through a series of dilutions and compared with that of known synthetic mixtures. A close match was obtained with a mixture of O-benzyl and N-benzyl compounds in the proportion 10:90.

Analytical Instruments. The benzylated pyridones were analyzed with a Beckman IR-5, and all other infrared spectra were obtained with a Perkin-Elmer Model 421. Carbon tetrachloride solutions in liquid sample cells were used in every case. The gas chromatograph is a Beckman GC-2 fitted with a silicone grease column, No. 70158.

Acknowledgment. The authors are indebted to the National Science Foundation, which supported this work through Grant G-19144 and the Undergraduate Research Participation Program.

(16) R. West, *J. Am. Chem. Soc.*, **80**, 3246 (1958).

Derivation of the Chronoamperometric Constant for Unshielded, Circular, Planar Electrodes[1]

by Zoltán G. Soos and Peter James Lingane

Division of Chemistry and Chemical Engineering, California Institute of Technology, Pasadena, California *(Received July 6, 1964)*

We have calculated the chronoamperometric constant for a circular electrode of finite size and have shown that it can be expanded as a power series in $\sqrt{Dt}/\rho_0$. The coefficient of the term in $\sqrt{Dt}/\rho_0$ is 2.26 and is in agreement with experiment. This coefficient is calculated by exploiting the equivalence between this problem and the corresponding heat conduction problem.

I. Introduction

The familar Cottrell equation[2]

$$\frac{it^{1/2}}{AC} = \frac{n\mathfrak{F}D^{1/2}}{\pi^{1/2}} \qquad (1.1)$$

does not adequately describe the current–time behavior observed with electrodes of finite size at times longer than a few seconds.[3] Therefore, we have calculated the current–time behavior for a circular electrode of radius ρ_0 and have shown that the chronoamperometric constant can be expanded as a power series in $\sqrt{Dt}/\rho_0$; the coefficient of the term in $\sqrt{Dt}/\rho_0$ is calculated. To do this, we have exploited the similarity between this problem and analogous heat conduction problems by adding current sources in direct analogy to the heat sources added in heat conduction problems. We discuss only the mixed boundary condition problem in which the concentration is fixed at the surface of the electrode; the solution to the Neumann problem (chronopotentiometry) may be obtained analogously.

If we neglect the effect of turbulence and of convective stirring, then the current passing through the area $\vec{A}$ is simply

$$i = n\mathfrak{F}\frac{d\vec{N}}{dt}\cdot\vec{A} = n\mathfrak{F}D\nabla\bar{\mu}\cdot\vec{A} \qquad (1.2)$$

where i is the current in amperes, n is the number of equivalents per mole, D is the diffusion coefficient in cm.^{2}/sec., and $\bar{\mu}$ is the electrochemical potential. If the solution contains a large concentration of supporting electrolyte, the transference number of the electroactive species is essentially zero. Under these conditions,[4] the diffusion equation reduces to

$$\frac{\partial C_i}{\partial t} = D_i\nabla^2 C_i \qquad (1.3)$$

where C_i is the concentration in moles/cc. of the ith electroactive species.

In the presence of excess supporting electrolyte, the compact double layer[5,6] can be approximated by a parallel plate condenser whose plates are separated by one or two molecular diameters. Therefore, the charge on the double layer for a circular electrode of radius ρ_0 will be uniform until $\rho - \rho_0$ approaches the thickness of the compact double layer (*cf.* Fig. 1). Since the metallic electrode is an equipotential surface, the uniformity of the double-layer charge requires that the potential at the outer Helmholtz plane also be uniform until $\rho - \rho_0$ approaches the thickness of the compact double layer. Very close to the edge, the potential at the outer Helmholtz plane will decrease with respect to the solution potential.

Therefore, it is very reasonable to assume that the concentration of the electroactive species will be uni-

(1) Contribution No. 3141 from the Gates and Crellin Laboratories of Chemistry.

(2) F. G. Cottrell, *Z. physik. Chem.*, **42**, 385 (1902).

(3) P. J. Lingane, *Anal. Chem.*, **36**, 1723 (1964).

(4) H. L. Kies, *J. Electroanal. Chem.*, **4**, 156 (1962).

(5) D. C. Grahame, *Chem. Rev.*, **41**, 441 (1947).

(6) R. Parsons, "Advances in Electrochemistry and Electrochemical Engineering," Vol. 1, P. Delahay and C. W. Tobias, Ed., Interscience Publishers, Inc., New York, N. Y., 1961, Chapter I.

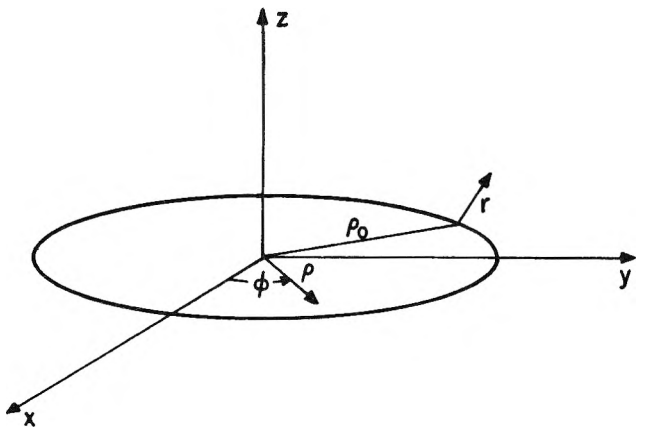

Figure 1. Model for the circular disk electrode.

form at the outer Helmholtz plane of metallic electrodes of finite size and in the presence of excess supporting electrolyte if the concentration is governed by the Nernst equation.

II. Formal Solution

We will first consider the oxidation of a single insoluble species to give a soluble product, *e.g.*, the generation of silver ion into a solution initially free of silver. Our electrode is a circular planar disk of radius ρ_0 situated in the $z = 0$ plane (*cf.* Fig. 1). This electrode is potentiostated at a fixed potential E, and it is assumed that the Nernst equation is obeyed. This guarantees that diffusion and not the electron-transfer step will control the current. Observe that under these conditions, the concentration at the surface of the electrode will continuously increase with potential and no limiting current will be achieved. This approach is purely one of convenience and is taken to achieve greater generality as will become evident in the Discussion section.

The cylindrical symmetry enables us to write the concentration as $C(\rho,z,t)$. The boundary conditions for $C(\rho,z,t)$ are

$$C(\rho,0,t) = \begin{cases} C^0(E) & \rho \leq \rho_0 \quad t \geq 0^+ \\ 0 & \rho > \rho_0 \quad t = 0^+ \end{cases}$$

$$\frac{\partial C}{\partial z}(\rho,0,t) = 0 \qquad \rho > \rho_0 \quad t \geq 0^+ \qquad (2.1)$$

$$C(\rho,z,0) = 0 \qquad z > 0$$

$$\lim_{\rho \to \infty} C(\rho,z,t) = \lim_{z \to \infty} C(\rho,z,t) = 0 \qquad (2.2)$$

$$\lim_{t \to \infty} C(\rho,z,t) = C^0(E)$$

We use the superposition theorem and write

$$C(\rho,z,t) = C^{\mathrm{I}}(\rho,z,t) + C^{\mathrm{II}}(\rho,z,t) \qquad (2.3)$$

In general, the surface of an electrode can be represented by a continuum of current sources whose distribution and strengths are time dependent. The source distribution for an infinite planar electrode is time independent and is uniform over the surface of the electrode. The time-dependent sources of $C^{\mathrm{I}}(\rho,z,t)$ are chosen to be equivalent to such a uniform distribution for $\rho \leq \rho_0$ at $t = 0^+$. Therefore, $C^{\mathrm{I}}(\rho,z,t)$ is equivalent, initially, to the concentration distribution at a circular section of an infinite electrode. At later times, radial diffusion causes the sources of $C^{\mathrm{I}}(\rho,z,t)$ to decrease near the edge of the electrode and apparent sources to appear at $\rho > \rho_0$. The sources of $C^{\mathrm{II}}(\rho,z,t)$ could be chosen so that the boundary condition (2.1) is satisfied at all times. Alternatively, the sources of $C^{\mathrm{II}}(\rho,z,t)$ might be chosen so that the total flux from the finite electrode into the region $\rho \leq \rho_0$ is the same as from the infinite electrode. We shall adopt the second condition because we wish to approximate the sources for $C^{\mathrm{II}}(\rho,z,t)$ by a line source. Such an approximation gives a nonuniform concentration at the surface of the electrode. Obviously, an exact solution must satisfy both conditions simultaneously.

The analogous heat conduction problem is that of a circular hot plate whose sources are chosen so as to keep the heat flux from the plate into the region $\rho \leq \rho_0$ the same as the flux from a circular section of an infinite hot plate whose temperature is uniform and time independent.

The initial conditions for $C^{\mathrm{I}}(\rho,z,t)$ are

$$C^{\mathrm{I}}(\rho,0,0^+) = \begin{cases} C^0(E) & \rho \leq \rho_0 \\ 0 & \rho > \rho_0 \end{cases} \qquad (2.4)$$

Since the diffusion equation contains only a first derivative with respect to time, it is convenient to make the partial separation

$$C^{\mathrm{I}}(\rho,z,t) = C^0 g(\rho,t) f(z,t) \qquad (2.5)$$

where $C^0(E)$ is the concentration at the outer Helmholtz plane and $f(z,t)$ and $g(\rho,t)$ are dimensionless functions to be determined. It is evident that under certain conditions, such as $t \to 0$ or $\rho \to 0$, the solution must reduce to the solution for the infinite planar electrode. Hence, $f(z,t)$ corresponds to the well-known solution for the infinite planar electrode[7]

$$f(z,t) = 1 - \mathrm{erf}\left(\frac{z}{2\sqrt{Dt}}\right) \qquad (2.6)$$

and $g(\rho,t)$ represents the effect of diffusion in the radial direction. Furthermore, the initial condition for $g(\rho,t)$ is

(7) P. Delahay, "New Instrumental Methods in Electrochemistry," Interscience Publishers, Inc., New York, N. Y., 1954, Chapter 3.

$$g(\rho,0^+) = \begin{cases} 1 & \rho \leq \rho_0 \\ 0 & \rho > \rho_0 \end{cases} \quad (2.7)$$

$g(\rho,t)$ must satisfy the radial portion of the diffusion equation.

$g(\rho,t)$ may be obtained *via* a Hankel transform.[8] Only zeroth-order Bessel functions appear because of the cylindrical symmetry. The integrand is a solution to the diffusion equation for each value of k, and hence $g(\rho,t)$ is a solution.

$$g(\rho,t) = \int_0^\infty k\mathrm{d}k\, f(k)e^{-Dk^2t}J_0(k\rho)$$
$$f(k) = \int_0^\infty \rho\mathrm{d}\rho\, g(\rho,0^+)J_0(k\rho) \quad (2.8)$$

As is shown in Fig. 2, $g(\rho,t)$ is a step function at $t = 0^+$; at later times, the time dependence of (2.8) gives different superpositions of the Bessel functions and the step-function decays. This decay expresses the fact that there is radial diffusion.

Since $C^{\mathrm{I}}(\rho,z,t)$ satisfies the boundary conditions only at $t = 0^+$, it is evident that a current source must be added toward the edge of the electrode to maintain a uniform concentration distribution. This current source will produce the concentration $C^{\mathrm{II}}(\rho,z,t)$. Once we have calculated $C^{\mathrm{I}}(\rho,z,t)$, we will be able to determine the position and the strength of the current sources that produce $C^{\mathrm{II}}(\rho,z,t)$.

The current flowing through the electrode is given rigorously by the gradient with respect to z of the concentration evaluated at $z = 0$, $\rho \leq \rho_0$. Therefore, the current density corresponding to $C^{\mathrm{I}}(\rho,z,t)$ is

$$\frac{i}{\pi\rho_0^2} = n\mathfrak{F}D\frac{2}{\rho_0^2}\int_0^{\rho_0}\left(\frac{\partial C^{\mathrm{I}}}{\partial z}\right)_{z=0}\rho\mathrm{d}\rho = -\frac{n\mathfrak{F}DC^0}{\sqrt{\pi Dt}}\int_0^{\rho_0}\rho\mathrm{d}\rho g(\rho,t) \quad t > 0 \quad (2.9)$$

$$g(\rho,t) = \int_0^\infty k\mathrm{d}k e^{-Dk^2t}J_0(k\rho) \times \int_0^\infty \rho'\mathrm{d}\rho' g(\rho',0^+)J_0(k\rho') \quad (2.10)$$

By reversing the orders of integration freely, it is possible to show that for an arbitrary $g(\rho,0^+)$ the current density is an expansion in powers of $\sqrt{Dt}/\rho_0$.

III. Special Case: One-Component System

A. Expressions for $g(\rho,t)$. We now consider in detail the properties of $C^{\mathrm{I}}(\rho,z,t)$. The initial conditions are fixed by (2.4); $f(z,t)$ is given by (2.6); $g(\rho,0^+)$ is the step function defined by (2.8). We integrate (2.8) to obtain

$$f(k) = \int_0^\infty \rho'\mathrm{d}\rho' g(\rho',0^+)J_0(k\rho') = \rho_0\frac{J_1(k\rho_0)}{k} \quad (3.1)$$

The exponential in (2.10) is now expanded in a Hankel transform. Only zeroth-order Bessel functions appear because of the symmetry in the k-plane. The inverse transformation reduces to a Laplace transform.[9]

$$e^{-Dk^2t} = \int_0^\infty q\mathrm{d}q J_0(kq)f(q) \quad (3.2)$$

$$f(q) = \int_0^\infty k\mathrm{d}k e^{-Dk^2t}J_0(kq) = \frac{1}{2Dt}\int_0^\infty \mathrm{d}y e^{-y}J_0\left(\frac{q}{\sqrt{Dt}}\sqrt{y}\right) = \frac{1}{2Dt}e^{-\frac{q^2}{4Dt}} \quad (3.3)$$

Combining (2.9), (2.10), (3.2), and (3.3), we obtain

$$g(\rho,t) = \frac{\rho_0}{2Dt}\int_0^\infty q\mathrm{d}q e^{-\frac{q^2}{4Dt}} \times \int_0^\infty J_0(kq)J_0(k\rho)J_1(k\rho_0)\mathrm{d}k \quad (3.4)$$

The integral over the Bessel functions is a special case of the formula of Sonine and Dougall.[10]

$$g(\rho,t) = \frac{1}{2\pi Dt}\int_0^\infty q\mathrm{d}q e^{-q^2/4Dt}A(\rho,\rho_0,q) \quad (3.5)$$

$$A(\rho,\rho_0,q) = \begin{cases} \pi & \rho_0^2 > (\rho+q)^2 \\ \cos^{-1}\left(\dfrac{\rho^2+q^2-\rho_0^2}{2q\rho}\right) & (\rho+q)^2 > \rho_0^2 > (\rho-q)^2 \\ 0 & (\rho-q)^2 > \rho_0^2 \end{cases} \quad (3.6)$$

Hence

$$\rho \leq \rho_0 \quad g(\rho,t) = 1 + \frac{1}{\pi}\int_{\rho_0-\rho}^{\rho_0+\rho}\mathrm{d}q e^{-\frac{q^2}{4Dt}} \times \frac{\partial}{\partial q}\left(\cos^{-1}\left(\frac{\rho^2+q^2-\rho_0^2}{2q\rho}\right)\right) \quad (3.7)$$

$$\rho > \rho_0 \quad g(\rho,t) = \frac{1}{\pi}\int_{\rho-\rho_0}^{\rho+\rho_0}\mathrm{d}q e^{-\frac{q^2}{4Dt}} \times \frac{\partial}{\partial q}\left(\cos^{-1}\left(\frac{\rho^2+q^2-\rho_0^2}{2q\rho}\right)\right) \quad (3.8)$$

(8) P. M. Morse and H. Feshbach, "Methods of Theoretical Physics," McGraw-Hill Book Co., New York, N. Y., 1953.

(9) W. Magnus and F. Oberhettinger, "Formulas and Theorems for the Functions of Mathematical Physics," Chelsea Publishing Co., New York, N. Y., 1949, p 132.

(10) W. Magnus and F. Oberhettinger, *ibid.*, p. 37

In order to evaluate the integrals in (3.7) and (3.8), we first evaluate $\partial g/\partial\rho(\rho,t)$. We can easily verify (or observe from the boundary conditions) that $\partial g/\partial\rho(\rho,0^+)$ is a δ-function of unit strength.

$$t = 0^+ \quad \frac{\partial g}{\partial \rho}(\rho,0^+) = -\rho_0 \int_0^\infty k\mathrm{d}k J_1(k\rho)J_1(k\rho_0) = -\delta(\rho - \rho_0) \tag{3.9}$$

$$t > 0^+ \quad \frac{\partial g}{\partial \rho}(\rho,t) = -\frac{\rho_0}{2}\int_0^\infty \mathrm{d}y e^{-Dty} J_1(\rho\sqrt{y})J_1(\rho_0\sqrt{y}) = -\frac{\rho_0}{2Dt} I_1\left(\frac{\rho\rho_0}{2Dt}\right) e^{-\frac{\rho^2+\rho_0^2}{4Dt}} \tag{3.10}$$

The Laplace transform[10] in (3.10) gives the modified Bessel function of the first order.

We define $\Delta g(\rho,t)$ to be the deviation of $g(\rho,t)$ from the step function $g(\rho,0^+)$.

$$\begin{aligned} \Delta g(\rho,t) &= g(\rho,t) - 1 && \rho \le \rho_0 \\ &= g(\rho,t) && \rho > \rho_0 \end{aligned} \tag{3.11}$$

We now obtain an expression for $\Delta g(\rho,t)$, $\rho \le \rho_0$. It is evident from (3.7) that $g(0,t) = 1$ for all $t > 0$. Equation 3.10 then gives

$$\Delta g(\rho,t) = g(\rho,t) - g(0,t) = \int_0^\rho \frac{\partial g}{\partial \rho'}(\rho',t)\mathrm{d}\rho' = -\frac{\rho_0}{2Dt}\int_0^\rho I_1\left(\frac{\rho'\rho_0}{2Dt}\right) e^{\frac{-(\rho')^2+\rho_0^2}{4Dt}}\mathrm{d}\rho' \qquad \rho \le \rho_0 \tag{3.12}$$

If we set $\chi = \rho\rho_0/2Dt$, $\chi_0 = \rho_0^2/2Dt$, and $\beta = Dt/\rho_0^2 = 1/2\chi_0$, we find

$$\Delta g(\chi,t) = -e^{-\chi_0/2}\int_0^\chi I_1(x)e^{-\beta x^2}\mathrm{d}x \tag{3.13}$$

We use the properties of the modified Bessel functions[11] and integrate (3.13) by parts repeatedly.

$$\Delta g(\chi,t) = -e^{-\chi_0/2}\left\{\sum_{\nu=0}^\infty (2\beta\chi)^\nu I_\nu(\chi)e^{-\beta\chi^2} - 1\right\} = e^{-\chi_0/2}\left\{1 - e^{-\rho^2/4Dt}\sum_{\nu=0}^\infty \left(\frac{\rho}{\rho_0}\right)^\nu I_\nu\left(\frac{\rho\rho_0}{2Dt}\right)\right\}, \qquad \rho \le \rho_0 \tag{3.14}$$

where I_ν is the modified Bessel function of order ν.

B. Correction to the Current Density. Expressions 3.13 and 3.14 will be used to evaluate $g(\rho,t)$. Before we perform this calculation, which requires a variety of special conditions, we will evaluate the decay in the current density *at the electrode* due to the apparent motion of the current sources for $C^I(\rho,z,t)$ to $\rho > \rho_0$ in the $z = 0$ plane. We replace $g(\rho,t)$ in (2.9) by $\Delta g(\rho,t)$; except for constants, we have

$$\int_0^{\rho_0}\rho\mathrm{d}\rho\Delta g(\rho,t) = \frac{\rho_0^2}{2}e^{-\frac{\chi_0}{2}} - \int_0^{\rho_0}\rho\mathrm{d}\rho e^{-\frac{\rho_0^2+\rho^2}{4Dt}}\sum_{\nu=0}^\infty\left(\frac{\rho}{\rho_0}\right)^\nu I_\nu\left(\frac{\rho\rho_0}{2Dt}\right) = e^{-\frac{\chi_0}{2}}\left\{\frac{\rho_0^2}{2} - \left(\frac{2Dt}{\rho_0}\right)^2\sum_{\nu=0}^\infty\int_0^{\chi_0}(2\beta x)^\nu e^{-\beta x^2}I_\nu(x)x\mathrm{d}x\right\} \tag{3.15}$$

We integrate by parts repeatedly to obtain

$$\int_0^{\chi_0} x^{\nu+1}e^{-\beta x^2}I_\nu(x)\mathrm{d}x = \sum_{\mu=\nu+1}^\infty \frac{(2\beta\chi_0)^\mu}{2\beta^{\nu+1}}I_\mu(\chi_0)e^{-\beta\chi_0^2} \tag{3.16}$$

Substituting (3.16) in (3.15), we have

$$\int_0^{\chi_0}\rho\mathrm{d}\rho\Delta g(\rho,t) = e^{-\frac{\rho_0^2}{4Dt}}\times\left\{\frac{\rho_0^2}{2} - 2Dte^{-\frac{4Dt}{\rho_0^2}}\sum_{\nu=0}^\infty \nu I_\nu\left(\frac{\rho_0^2}{2Dt}\right)\right\} \tag{3.17}$$

Using the recursion relations for the modified Bessel functions, we find

$$\frac{1}{2x}\sum_{\nu=1}^\infty \nu I_\nu(x) = {}^1/_2\sum_{\nu=1}^\infty\{I_{\nu-1}(x) - I_{\nu+1}(x)\} = {}^1/_2\{I_0(x) + I_1(x)\} \tag{3.18}$$

Substituting (3.18) in (3.17), we obtain

$$\int_0^{\chi_0}\Delta g(\rho,t)\rho\mathrm{d}\rho = -\frac{\rho_0^2}{2}e^{-\frac{\rho_0^2}{2Dt}}\times\left\{I_0\left(\frac{\rho_0^2}{2Dt}\right) + I_1\left(\frac{\rho_0^2}{2Dt}\right) - e^{+\rho_0^2/4Dt}\right\} \tag{3.19}$$

Hence

$$\frac{\Delta i}{\pi\rho_0^2} = \frac{n\mathfrak{F}DC^0}{\sqrt{\pi Dt}}e^{-\frac{\rho_0^2}{2Dt}}\left\{I_0\left(\frac{\rho_0^2}{2Dt}\right) + I_1\left(\frac{\rho_0^2}{2Dt}\right) - e^{+\rho_0^2/4Dt}\right\} \tag{3.20}$$

Equation 3.20 is an exact expression. The current sources for $C^I(\rho,z,t)$ have an initial uniform distribution over the surface of the electrode that is identical with the time-independent distribution of the current sources

(11) H. B. Dwight, "Tables of Integrals and Other Mathematical Data," The Macmillan Co., New York, N. Y., 1961.

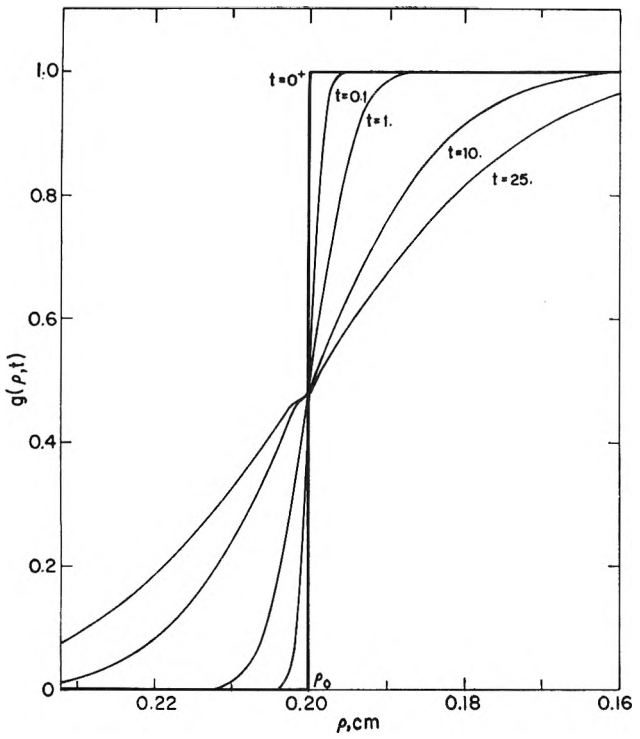

Figure 2. Plot of $g(\rho,t)$ as a function of ρ illustrating the redistribution of the sources of $C^{I}(\rho,z,t)$. $\rho_0 = 0.2$ cm., $D = 1 \times 10^{-5}$ cm.^{2}/sec.

for the infinite planar electrode. However, the current sources for $C^{I}(\rho,z,t)$ are redistributed in time because of radial diffusion; the sources near the edge of the electrode decay, and apparent sources are found outside the electrode ($\rho > \rho_0$). $g(\rho,t)$ is identically unity for the infinite planar electrode since there is no radial diffusion in that case.

C. Evaluation of $g(\rho,t)$ for Experimental Conditions. In order to find $g(\rho,t)$, $\rho < \rho_0$, and thus determine the position of the sources that we shall use for $C^{II}(\rho,z,t)$, it is convenient to specialize the experimental conditions, *i.e.*, $\rho_0 \gtrsim 0.2$ cm., $D \sim 10^{-5}$ cm.^{2}/sec., $t \lesssim 100$ sec. Under these conditions, $\rho_0^2/4Dt = \chi_0/2 > 10$. From the definition of $I_\nu(x)$, it is evident that $I_{\nu-1}(x) < I_\nu(x)$ for all ν when $x > 0$. Hence, we have from (3.14)

$$|\Delta g(\rho,t)| < e^{-\frac{\rho_0^2+\rho^2}{4Dt}} I_0\left(\frac{\rho\rho_0}{2Dt}\right) \sum_{\nu=0}^{\infty} \left(\frac{\rho}{\rho_0}\right)^{\nu} = e^{-\frac{\rho_0^2+\rho^2}{4Dt}} I_0\left(\frac{\rho\rho_0}{2Dt}\right) \frac{1}{1-\rho/\rho_0}, \quad \rho \leq \rho_0 \quad (3.21)$$

For $\rho = \rho_0/4$, $\chi_0/4 \gtrsim 5$, and we may use the large argument expansion of I_0.[11] We then have, for $0 < \rho \leq \rho_0/4$

$$|\Delta g(\rho,t)| < |\Delta g(\rho_0/4,t)| \approx {}^4/_3 \frac{e^{-\frac{9\chi_0}{32}}}{\sqrt{\frac{\pi\chi_0}{2}}}\left[1 + \frac{1}{2\chi_0} \cdots\right] \sim e^{-7} \quad (3.22)$$

Hence we observe that $\Delta g(\rho,t)$ is negligible for $\rho \leq \rho_0/4$. Equation 3.21 is an upper bound for $|\Delta g(\rho,t)|$, since, in it, we have replaced all of the modified Bessel functions by I_0. For example, eq. 3.21 gives $|\Delta g(0,t)| \lesssim e^{-10}$ while $\Delta g(0,t) \equiv 0$ (for all t) from eq. 3.14. For $\rho_0/4 < \rho \leq \rho_0$, we may use the large argument expansion of the modified Bessel functions in eq. 3.12 throughout the entire range of the integration.

$$\Delta g(\chi,t) = -e^{-\beta\chi_0^2} \int_{\chi_0/4}^{\chi} e^{-\beta y^2} e^{y} \frac{dy}{\sqrt{2\pi y}}\left(1 - \frac{3}{8y} \cdots\right) \quad (3.23)$$

$$= -\int_{\chi_0/4}^{\chi} e^{-\beta(\chi_0 - y)^2} \frac{dy}{\sqrt{2\pi y}}\left(1 - \frac{3}{8y} \cdots\right)$$

Since $\chi_0/4 > 5$, it is straightforward to integrate (3.23). Hence

$$\Delta g(\rho,t) = \begin{cases} -{}^1/_2\left(1 - \operatorname{erf}\left(\frac{\rho_0 - \rho}{2\sqrt{Dt}}\right)\right) - \frac{1}{2\sqrt{\pi}} \frac{\sqrt{Dt}}{\rho_0} \times e^{-\frac{(\rho_0-\rho)^2}{4Dt}} + 0\left(\left(\frac{\sqrt{Dt}}{\rho_0}\right)^3\right) & \frac{\rho_0}{4} < \rho \leq \rho_0 \\ 0 & \rho \leq \frac{\rho_0}{4} \end{cases} \quad (3.24)$$

Expression 3.24, which has the expected form, may be obtained directly from (3.7) by taking $\rho = \rho_0 - \Delta$ and letting $\Delta \to 0$ *after* the integration. If we set $\rho = \rho_0$ in (3.7), the integrand is indeterminate at $q = 0$; when the integration is now performed, only the second term of (3.24), evaluated at $\rho = \rho_0$, is obtained.

Since the derivative of $g(\rho,t)$ is continuous for $t > 0$, we may use an expression similar to (3.12) to evaluate $g(\rho,t)$ for $\rho > \rho_0$.

$$\Delta g(\rho,t) = 1 + \Delta g(\rho_0,t) - \frac{\rho_0}{2Dt} \int_{\rho_0}^{\rho} I_1\left(\frac{\rho'\rho_0}{2Dt}\right) \times e^{-\frac{(\rho')+\rho_0^2}{4Dt}} d\rho' \qquad \rho > \rho_0 \quad (3.25)$$

$$= {}^1/_2\left(1 - \operatorname{erf}\left(\frac{\rho - \rho_0}{2\sqrt{Dt}}\right)\right) - \frac{1}{2\sqrt{\pi}} \frac{\sqrt{Dt}}{\rho_0} \times e^{-\frac{(\rho-\rho_0)^2}{4Dt}} + 0\left(\left(\frac{\sqrt{Dt}}{\rho_0}\right)^3\right)$$

The next term in eq. 3.24 or 3.25 is negligible for the times of interest. Since $f(0,t) = 1$, the deviation of $C^{I}(\rho,0,t)$ from C^0 for $\rho \leq \rho_0$ is C^0 times expression 3.24.

D. Sources for and Calculation of $C^{II}(\rho,z,t)$. $g(\rho,t)$ is plotted as a function of ρ for various values of t in Fig. 2. It is evident that, for $t \lesssim 25$ sec., deviations from the step-function initial condition are important only within 0.02 to 0.03 cm. of the edge of the electrode. Of course, this is precisely what is expected, especially if the analogous heat problem is considered. Therefore, we need a current source of radius of about 0.01 cm. at the perimeter of the electrode, placed so that the outer edge of the source is at $\rho = \rho_0$ if the boundary condition (2.4) is to be satisfied for all times. Such a time-dependent source, which arises from the decomposition of the concentration in (2.3), defines the diffusion problem for $C^{II}(\rho,z,t)$.

As a first approximation, we consider a time-independent source at $\rho = \rho_0$. This should be a good approximation for short times since, for short times, (3.24) shows that the source is essentially at the edge and, as is evident from the large argument expansion of the modified Bessel functions, (3.20) shows that $\Delta i/\pi\rho_0^2$ is essentially time independent.

$$\frac{\Delta i}{A} = \frac{n\mathfrak{F}D2C^0}{\pi\rho_0^2}\left\{1 + 0\left(\frac{Dt}{\rho_0^2}\right)\right\} \qquad (3.26)$$

In the same spirit, we may, for short times, approximate the source by an infinitely long, straight wire and express the concentration at a distance r from the wire as

$$C^{II}(r,t) = \frac{C^0\alpha}{2\pi}\int_{r/2\sqrt{Dt}}^{\infty}\frac{dx}{x}e^{-x^2} = -\frac{C^0\alpha}{4\pi}Ei\left(-\frac{r^2}{4Dt}\right) \qquad (3.27)$$

where $Ei(x)$ is the exponential integral. α is the strength of the source and will be evaluated below. This solution is borrowed from the analogous heat conduction problem.[12]

It is not convenient to satisfy the boundary condition (2.1) by requiring that the sum of $C^{I}(\rho,z,t)$ and $C^{II}(\rho,z,t)$ be uniform and time independent at the face of the electrode, since, by lumping the corrections into a line source, we have introduced a singularity. We may, however, as an alternative condition, match fluxes. Since the exact sources of $C^{II}(p,z,t)$ have "radii" of about 0.01 cm. for $t \lesssim 25$ sec., the approximation of a line source should be excellent for $r \gtrsim 0.01$ cm. (*cf.* Fig. 2). Once outside the source distribution, its detailed composition becomes unimportant; as in a multipole expansion, the major effect is found by putting a point source at the center of the distribution. We will approximate even further and place the source at the edge of the electrode instead of near the edge.

The current flowing from a straight wire is radial by symmetry. At a line source of strength α, the current per unit length is

$$i_s = n\mathfrak{F}D2\pi r\frac{\partial}{\partial r}C^{II}(r,t)|_{r=0} = -n\mathfrak{F}DC^0\alpha \qquad (3.28)$$

It is evident from Fig. 1 that the symmetry in the $z = 0$ plane requires that the flux flowing into the region where $z > 0$ is just half the total flux from a source whose intensity is twice the intensity of the actual source. Thus (3.28) will be correct if α is taken to be the actual intensity per unit length of the line source. Furthermore, at least for short times, the flux into the region $\rho < \rho_0$ is the same, by symmetry, as the flux into the region $\rho > \rho_0$. The total flux from a line source of length $2\pi\rho_0$ is

$$\frac{i_s}{\pi\rho_0^2} = -\frac{2}{\rho_0}n\mathfrak{F}DC^0\alpha \qquad (3.29)$$

Half of this current will flow into the region $z > 0$, $\rho < \rho_0$. Hence

$$^1/_2 i_s = -\Delta i \qquad (3.30)$$

where Δi is given by (3.20). These two currents have opposite signs since the source for $C^{II}(\rho,z,t)$ is to correct for the effects of radial diffusion. Thus we obtain

$$\alpha = \frac{2}{\pi} \qquad (3.31)$$

The correction current density is therefore

$$\frac{i_s}{\pi\rho_0^2} = -\frac{n\mathfrak{F}DC^0}{\sqrt{\pi Dt}}\frac{4}{\sqrt{\pi}}\frac{\sqrt{Dt}}{\rho_0} \qquad (3.32)$$

E. Total Current Density and Concentration Profiles. The total current density is the sum of the current sources for $C^{I}(\rho,z,t)$ and eq. 3.32. The *total* current density due to the sources of $C^{I}(\rho,z,t)$ is (*cf.* eq. 2.9)

$$\frac{i_1}{\pi\rho_0^2} = -n\mathfrak{F}C^0\sqrt{\frac{D}{\pi t}}\int_0^{\infty}g(\rho,t)\rho d\rho = -n\mathfrak{F}C^0\sqrt{\frac{D}{\pi t}}\left\{1 + 0\left(\frac{Dt}{\rho_0^2}\right)\right\} \qquad (3.33)$$

Therefore, the total current is

(12) L. R. Ingersoll, O. J. Zobel, and A. C. Ingersol, "Heat Conduction," McGraw-Hill Book Co., New York, N. Y., 1948, p. 146.

$$\frac{i}{\pi\rho_0^2} = -\frac{n\mathfrak{F}DC^0}{\sqrt{\pi Dt}}\left\{1 + \frac{4}{\sqrt{\pi}}\frac{\sqrt{Dt}}{\rho_0} + 0\left(\frac{Dt}{\rho_0^2}\right)\right\} \tag{3.34}$$

Although the boundary condition (2.1) is not satisfied in detail on the electrode, it is evident that, if the line charge is redistributed near the edge, the concentration could be calculated even at the face of the electrode. The current correction would, however, be very nearly the same since the flux from a source distribution may be found by calculating the flux from the equivalent point source.

We have overestimated the correction in (3.30) since the center of the correction source is actually at $\rho < \rho_0$ rather than at $\rho = \rho_0$. Thus slightly more than half of the flux goes into the region $\rho < \rho_0$. This effect is only of the order of a few per cent for $t \lesssim 25$ sec. At longer times, when this effect becomes larger, the assumption that the added current is a line source approximated by a straight wire also becomes untenable.

$C^{\mathrm{I}}(\rho,z,t)$ and $C^{\mathrm{II}}(\rho,z,t)$ are given by (2.4), (2.6), (3.24), (3.25), and (3.27). As discussed above, $C^{\mathrm{II}}(\rho,z,t)$ is a poor approximation for distances smaller than the dimensions of the sources of $C^{\mathrm{II}}(\rho,z,t)$. The dimensions of the sources of $C^{\mathrm{II}}(\rho,z,t)$ may be estimated from Fig. 2 which shows the region for $\rho < \rho_0$ where $\Delta g(\rho,t)$ is appreciably different from zero. For $t \lesssim 25$ sec., a distance of about 0.01 cm. from the edge of the electrode is sufficient to ensure being outside the source. We therefore have, for $t \lesssim 25$ sec. and $r \gtrsim 0.01$ cm.

$$C(\rho,z,t) = C^{\mathrm{I}}(\rho,z,t) + C^{\mathrm{II}}(\rho,z,t)$$

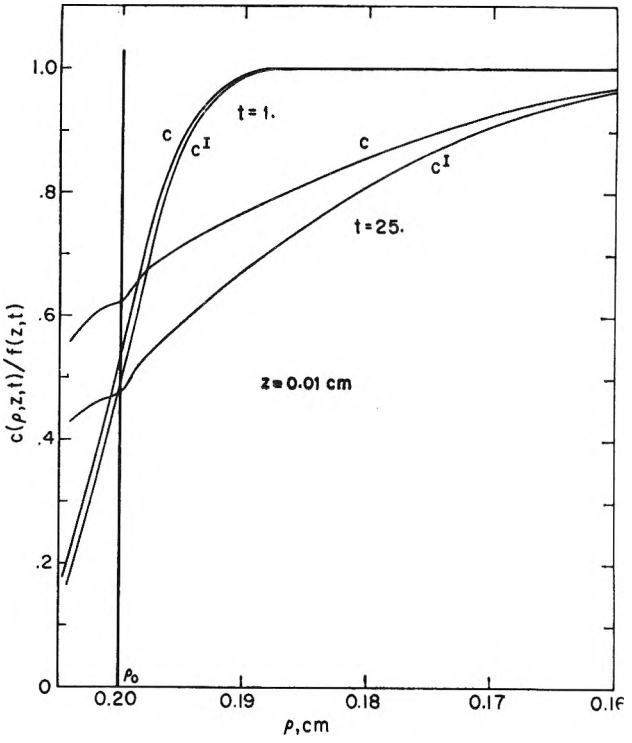

Figure 3. Typical concentration profiles for $C(\rho,z,t)$ and $C^{\mathrm{I}}(\rho,z,t)$: $z = 0.01$ cm., $\rho_0 = 0.2$ cm., $D = 1 \times 10^{-5}$ cm.^{2}/sec.

of line sources and then replacing each line source by a finite source. The strength of such sources is still determined by $\Delta g(\rho,t)$. As is evident, such a procedure approximates the exact solution more and more accurately. However, in order to obtain the exact solution, both the location and the strength of the sources

$$C^{\mathrm{I}}(\rho,z,t) = C^0\begin{cases} 1 - \operatorname{erf}\left(\dfrac{z}{2\sqrt{Dt}}\right) & 0 \le \rho < \dfrac{\rho_0}{4} \\ \left[\tfrac{1}{2}\left(1 + \operatorname{erf}\left(\dfrac{\rho_0 - \rho}{2\sqrt{Dt}}\right)\right) - \dfrac{1}{2\sqrt{\pi}}\dfrac{\sqrt{Dt}}{\rho_0}e^{-\left(\frac{\rho_0-\rho}{4Dt}\right)^2}\right]\left(1 - \operatorname{erf}\left(\dfrac{z}{2\sqrt{Dt}}\right)\right) & \dfrac{\rho_0}{4} \le \rho \le \rho_0 \\ \left[\tfrac{1}{2}\left(1 - \operatorname{erf}\left(\dfrac{\rho - \rho_0}{2\sqrt{Dt}}\right)\right) - \dfrac{1}{2\sqrt{\pi}}\dfrac{\sqrt{Dt}}{\rho_0}e^{-\left(\frac{\rho-\rho_0}{4Dt}\right)^2}\right]\left(1 - \operatorname{erf}\left(\dfrac{z}{2\sqrt{Dt}}\right)\right) & \rho_0 < \rho \le \infty \end{cases} \tag{3.35}$$

$$C^{\mathrm{II}}(\rho,z,t) = C^0\begin{cases} -\dfrac{1}{2\pi^2}Ei\left(-\dfrac{r^2}{4Dt}\right) & 0 < r < \dfrac{\rho_0}{2} \\ 0 & \dfrac{\rho_0}{2} \le r < \infty \end{cases} \tag{3.36}$$

where $r = [z^2 + (\rho - \rho_0)^2]^{1/2}$.

Near the electrode, the concentration may be found more accurately by replacing our line source by a series

for $C^{\mathrm{II}}(\rho,z,t)$ must be time dependent. Thus, the mathematics becomes considerably less tractable. The simple model discussed in this paper is therefore useful in that it provides an accurate value of the total current density and, except very near the electrode, accurate concentration profiles.

IV. Discussion

A. Generalization. Our solution can be readily converted into the more usual situation where the solu-

tion originally contains the electroactive species at concentration C^0 and the product is insoluble. This is done by the simple transformation

$$C'(\rho,z,t) = C^0 - C(\rho,z,t) \qquad (4.1)$$

where $C'(\rho,z,t)$ is the transformed concentration and $C(\rho,z,t)$ is given by (2.3). Under these conditions, eq. 3.34 will be valid at all points on the i–E curve if C^0 is replaced by $C^0 - C(\rho,0,t,E)$.

This treatment can be extended to include the more general system where both the oxidized and reduced species are soluble and the solution is initially free of the reduced species. We decompose the concentration of both the oxidized and reduced species into the two components $C_i^{\mathrm{I}}(\rho,z,t)$ and $C_i^{\mathrm{II}}(\rho,z,t)$. We require the additional boundary conditions that the ratio of the concentrations of the two components at the outer Helmholtz plane is fixed by the Nernst equation and that the sum of their fluxes is zero at the electrode.[7] The current on the diffusion plateau will be independent of the reduced species and will again be given by eq. 3.34.

It is evident that an analogous approach can be used to obtain a solution under different boundary conditions, such as a constant concentration gradient at $z = 0$.

B. Comparison with Experiment. The theoretical value of the chronoamperometric constant is obtained by rearranging eq. 3.34.

$$\frac{it^{1/2}}{AC^0} = n\mathfrak{F}\sqrt{\frac{D}{\pi}}\left\{1 + \frac{4}{\sqrt{\pi}}\frac{\sqrt{Dt}}{\rho_0} + 0\left(\frac{Dt}{\rho_0^2}\right)\right\} \qquad (4.2)$$

The coefficient of the first term has been evaluated experimentally for $\rho_0 = 0.258$ cm. and $0.01 < \sqrt{Dt}/\rho_0 < 0.08$ for a variety of systems.[3] The experimental value of this coefficient is 2.12 ± 0.11 (95% confidence level) and is in agreement with the theoretical value of 2.26; the agreement is especially good since the latter is a slight overestimate.

Acknowledgment. It is a pleasure to acknowledge helpful discussions with James N. Foster, L. Gierst, H. Hurwitz, and G. N. Richter. We are indebted to the National Science Foundation and to the Public Health Service, Division of General Medical Sciences, for predoctoral fellowships.

Pulse Radiolysis Studies of Aqueous Sodium Chloride Solutions[1]

by M. Anbar[2] and J. K. Thomas

Chemistry Division, Argonne National Laboratory, Argonne, Illinois *(Received June 11, 1964)*

The reaction of OH radicals with chloride ions has been studied by the pulse radiolysis technique. The product of the reaction was identified as Cl_2^-, and its rate of formation was studied. The effect of OH radical and solvated electron scavengers on the Cl_2^- yield indicated that the former radicals produced the Cl_2^-. The rate of production of the Cl_2^- was independent of oxygen concentration, first order in $[H^+]$ from pH 3 to 0, and first order in chloride ion and hydroxyl radical concentrations. At pH <3, $G(Cl_2^-)$ was independent of pH and of $[Cl^-]$ and corresponded to $G(OH)$. However, at pH 7 $G(Cl_2^-)$ depended on $[Cl^-]$ up to 3 M and was less than that in acid solution. The results demonstrate the importance of hydrogen ions in the formation of Cl_2^- and suggest that in neutral solution Cl_2^- may be formed in the "spur" regions. The mechanisms of Cl_2^- formation are discussed.

Introduction

Grossweiner and Matheson[3] have observed a transient with a maximum at 350 mμ in the flash photolysis of sodium chloride solutions. They proposed that this transient was due to Cl_2^- formed in the following manner

$$Cl^- \xrightarrow{h\nu} Cl + e_{aq}^-$$

$$Cl + Cl^- \longrightarrow Cl_2^- \qquad (1)$$

Delbecq, Smaller, and Yuster[4] have identified the species Cl_2^- in the X-radiolysis of potassium chloride crystals at liquid nitrogen temperatures. They found that it had a strong optical absorption with maxima at 365 and 750 mμ.

Some workers[5a,6] have indicated that the reaction $OH + Cl^- \rightarrow Cl + OH^-$ is pH dependent. Most of the evidence[7] for this statement was obtained from studying the effect of chloride ion on the dimerization of OH radicals in the radiolysis of aqueous solutions. This pH dependence may be expressed accordingly

$$OH + Cl^- + H_3O^+ \longrightarrow Cl + 2H_2O \qquad (2)$$

In the absence of other solutes, the Cl atom is expected to combine with Cl^- to form Cl_2^-. The formation of the transient Cl_2^- could therefore be used as an indication for the progress of reaction 2.

In the present work a transient species with a maximum at 340 mμ was observed in the pulse radiolysis of sodium chloride solutions. The spectrum of this transient was similar to that reported for Cl_2^- in ref. 3. We believe that this transient is Cl_2^- formed by reactions 1 and 2. The inhibition of this transient by the addition of typical OH scavengers such as methanol and potassium ferrocyanide supports this mechanism. The rate of formation of the Cl_2^- was studied at different pH and different chloride ion concentrations.

Experimental

The water was triply distilled from alkaline potassium permanganate and acid potassium dichromate under an oxygen atmosphere. The solutes used were all of A.R. grade.

The solutions were deoxygenated in the following manner. In a 100-ml. glass syringe with no air space

(1) Based on work performed under the auspices of the U. S. Atomic Energy Commission.

(2) On Sabbatical leave from the Weizmann Institute of Science, Rehovoth, Israel.

(3) L. I. Grossweiner and M. S. Matheson, *J. Phys. Chem.*, **61**, 1089 (1957).

(4) C. J. Delbecq, B. Smaller, and P. H. Yuster, *Phys. Rev.*, **111**, 1235 (1958).

(5) (a) A. O. Allen, "The Radiation Chemistry of Water and Aqueous Solutions," D. Van Nostrand and Company, Inc., New York, N. Y., 1961, p. 63; (b) p. 47; (c) p. 62.

(6) J. K. Thomas, *Discussions Faraday Soc.*, **36**, 319 (1963).

(7) T. J. Sworski, *Radiation Res.*, **2**, 26 (1955); *J. Am. Chem. Soc.*, **76**, 4687 (1954).

was placed 50 ml. of the solution. Helium or argon gas (50 ml.) was forced into the syringe *via* the nozzle. The nozzle was closed off, and the syringe was shaken vigorously for 3 min. The mixture of inert gas and air was then forced out of the nozzle by depressing the plunger. This procedure was repeated three times, and subsequent analysis of the solution on a gas chromatograph indicated that the oxygen concentration was less than 1 μM. Hydrated electrons, e_{aq}^-, have an appreciable absorption between 300 to 400 mμ. In most experiments, especially at neutral pH, oxygenated solutions were used to remove the e_{aq}^- as O_2^-.

The pulse radiolysis apparatus for some of these experiments was the same as that used in previous work.[8,9]

Figure 1 illustrates typical oscilloscope photographs of the appearance of the Cl_2^- transient in acid and neutral solution taken at 350 mμ. In the neutral 1 M sodium chloride solution the transient was formed in a time that was short compared to the pulse length, *i.e.*, it was formed in less than 10^{-7} sec.

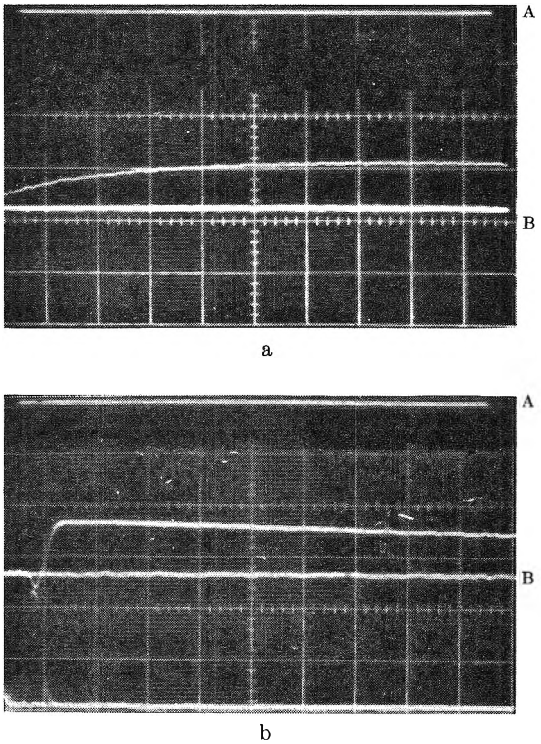

Figure 1. (a) Radiolysis of 10^{-2} M sodium chloride + 10^{-3} N perchloric acid in aerated solution. Sweep rate, 2 μsec. for each small square; optical path length, 16 cm.; radiation intensity ~1 μM OH radicals/pulse; wave length of analyzing light, 350 mμ. (b) Radiolysis of aerated 1.0 M sodium chloride at neutral pH. Sweep rate, 1.0 μsec. for each small square; optical path length, 8 cm.; radiation intensity, ~5 μM OH radicals/pulse.

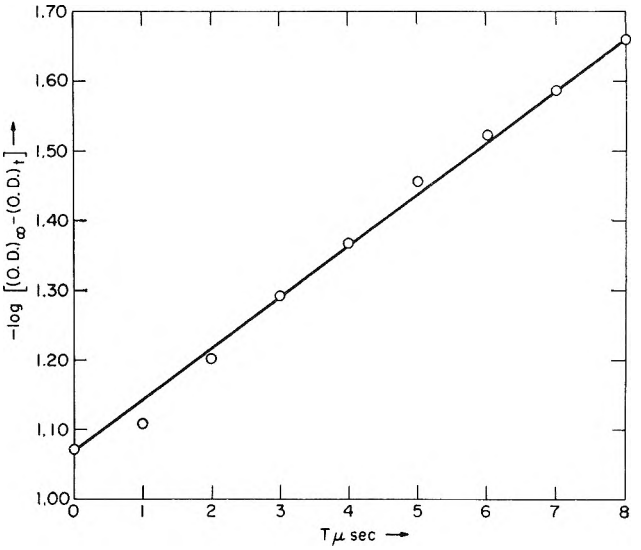

Figure 2. Kinetic plot of the results from Fig. 1a; $k = 1.66 \times 10^{10}$ M^{-2} sec.$^{-1}$.

In the acid solutions the rate of appearance of the Cl_2^- could be followed. The smooth straight trace A at the top of the picture corresponds to the condition where no light falls on the photomultiplier. The straight trace B at the bottom corresponds to maximum light falling on the photomultiplier. The distance between these lines A and B is I_0. The curve between the two lines corresponds to the absorption of light by the Cl_2^-. The distance from A to this line is I_t. Hence the optical density at any time could be calculated from optical density = $\log I_0/I_t$.

If a radical R reacts with a solute S to give an optically observable transient T then

$$\frac{d[T]}{dt} = k[R][S]$$

where k is the rate constant for the reaction. If we denote the concentration of T at time infinity and t as $[T_\infty]$ and $[T_t]$ respectively then

$$[R] = [T_\infty] - [T_t]$$

so

$$\int_0^t \frac{d[T]}{[T_\infty] - [T_t]} = \int_0^t k[S]dt$$

i.e.

$$\ln\left(\frac{[T_\infty]}{[T_\infty] - [T_t]}\right) = kt[S]$$

(8) S. Gordon, E. J. Hart, and J. K. Thomas, *J. Phys. Chem.*, **68**, 1262 (1964).

(9) S. Gordon, E. J. Hart, M. Matheson, J. Rabani, and J. K. Thomas, *Discussions Faraday Soc.*, **36**, 193 (1964).

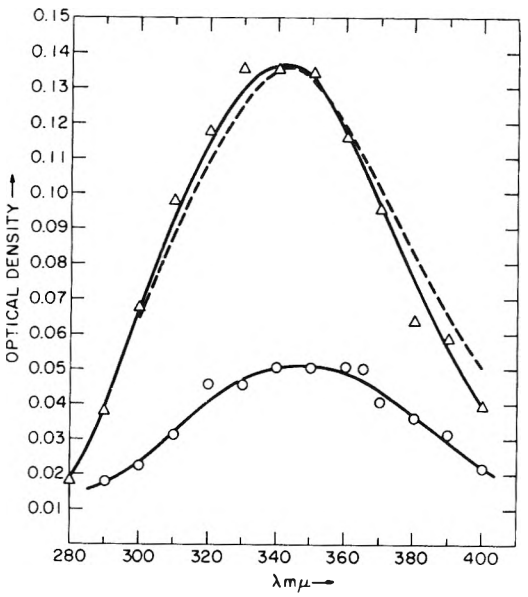

Figure 3. Spectra of Cl_2^-: △, 10 *M* sodium chloride + 0.1 *N* sulfuric acid, aerated solution; ○, 1 *M* sodium chloride aerated solution; - - -, results of Grossweiner and Matheson.

The concentration of S is not changed during the transient lifetimes. Hence a plot of $-\ln([T_\infty] - [T_t])$ *vs.* *t* should be linear. In the present work the optical density of the transient was substituted for its concentration in the latter expression.

Figure 2 illustrates that the results from Fig. 1a are first order. The symbols $(O.D.)_\infty$ and $(O.D.)_t$ represent the optical density of the Cl_2^- at time infinity and time *t*, respectively. Time infinity was defined as the plateau region on the Cl_2^- appearance curve.

Dosimetry. The dosimetry was carried out by irradiating the Fricke dosimeter (aerated solution of 10^{-3} *M* ferrous sulfate and 0.8 *N* sulfuric acid) and measuring the ferric ion formed at 303 mμ.

The reproducibility of the pulses was monitored by a sensor device designed by Johnson, *et al.*[10]

Results

A transient absorption was observed in the radiolysis of dilute sodium chloride solutions (in the range 0.2–10 m*M*) provided the pH was less than 3. In neutral solution transient absorption was observed only if the sodium chloride concentration was greater than 0.1 *M*. This absorption was unaffected by oxygen concentrations up to 1.1×10^{-3} *M*.

Figure 3 shows the absorption spectra obtained by irradiating aerated 10 m*M* sodium chloride in 0.1 *N* sulfuric acid and an aerated 1 *M* sodium chloride at neutral pH. The optical path length was 8 cm., and 1.31 μ*M* OH radicals were produced per pulse. (G(OH) = 2.8, ref. 5b) It was assumed that $G(Cl_2^-) = G$(OH) so the extinction coefficient at 340 mμ was measured as 12,500 ± 1000 in the acid solution.

From the similarity in spectra obtained by pulse radiolysis and flash photolysis we conclude that the species observed in radiolysis is Cl_2^- both in acid and in neutral solutions.

The Formation of Cl_2^- in Acid Solution. Table I shows how the optical density at infinite time varied with pH and chloride ion concentration, as well as the effect of the addition of methanol and potassium ferrocyanide to these solutions. These solutes reduced the optical density of the Cl_2^-, the potassium ferrocyanide being fivefold more efficient than methanol. The decreased yield of Cl_2^- could not be accounted for in terms of reaction of the Cl_2^- with the added solutes, as the slow decay of the Cl_2^- was not affected by these solutes. It is possible that the Cl atoms may have reacted with the solutes and lowered the Cl_2^- yield. However, the fivefold difference in reactivity of the methanol and potassium ferrocyanide is analogous to the reactivity of these two compounds with OH radicals where a value of 14:1 was obtained.[11,12]

Table I: Optical Density of Cl_2^- Transient at 3650 Å. in Pulse-Radiolyzed Chloride Solutions in the Acid Region

pH	NaCl, m*M*	S[a]	[S], m*M*	[Cl⁻]/[S]	O.D.$_{3650}$	k_{OH+Cl^-}/k_{OH+S}[b]
0.1	1	...	...	...	0.18	...
0.1	10	...	...	...	0.19	...
1.0	5	...	...	...	0.19	...
2.0	10	...	...	...	0.17	...
3.0	10	...	...	...	0.18	...
3.0	50	...	...	...	0.17	...
7.0	50	...	...	...	<0.01	...
2.7	10	$Fe(CN)_6^{-4}$	0.1	100	0.077	0.725×10^{-2}
2.5	5	$Fe(CN)_6^{-4}$	0.1	50	0.062	1.05×10^{-2}
2.0	1	$Fe(CN)_6^{-4}$	0.1	10	0.060	5.00×10^{-2}
1.5	1	$Fe(CN)_6^{-4}$	0.1	10	0.102	13.2×10^{-2}
1.0	1	$Fe(CN)_6^{-4}$	0.5	2	0.045	16.9×10^{-2}
2.5	10	MeOH	1.0	10	0.086	9.9×10^{-2}
2.0	5	MeOH	1.0	5	0.105	27.8×10^{-2}
1.5	1	MeOH	1.0	1	0.055	43.5×10^{-2}
1.0	1	MeOH	1.0	1	0.075	71.5×10^{-2}

[a] Added scavenger. [b] The optical density in the absence of scavenger was 0.18.

(10) K. Johnson, T. Klippert, and W. J. Ramler, *Nucl. Instr. Methods*, **14**, 125 (1962).

(11) J. Rabani and G. Stein, *Trans. Faraday Soc.*, **58**, 7156 (1962).

(12) A. J. Swallow, "Radiation Chemistry of Organic Compounds," Pergamon Press, Ltd., London, 1960, pp. 55 and 56.

Other work[13] has illustrated that the addition of hydrogen peroxide to acidified sodium chloride solutions results in a twofold enhancement of the Cl_2^- absorption. Here the H atoms produce more OH radicals *via* $H + H_2O_2 \rightarrow H_2O + OH$. From the above evidence we conclude that the OH radicals react with chloride ions in the presence of H^+ to produce Cl_2^-.

The rate constant ratios for the OH radical reactions with chloride ions and added solute are derived from the following equation and are given in Table I.

$$\frac{k_{OH+solute}}{k_{OH+chloride}} = \frac{(O.D.)_0 - (O.D.)_s}{(O.D.)_s} \frac{[Cl^-]}{[solute]}$$

The optical density of the sodium chloride was $(O.D.)_0$, and that obtained after adding a solute at concentration [S] was $(O.D.)_s$.

A point of interest in Table I is that the above rate constant ratio decreases as the pH decreases. To investigate this phenomenon further, the rate of appearance of Cl_2^- was measured at different acid concentrations. The results are summarized in Table II.

Table II: The Rate of Formation of Cl_2^- in Radiolyzed Aqueous Solutions

$HClO_4$, mM	NaCl, mM	R,[a] sec.$^{-1}$ × 10^{-5}	k,[b] M^{-2} sec.$^{-1}$ × 10^{-10}	O.D.$_{3660}$[c]
1	5	1.08	2.16	0.15
1	10	1.66	1.66	0.16
1	20	3.56	1.78	0.18
2[d]	10	3.46	1.73	0.17
8.9	10	15.4	1.73	
8.9[e]	10	14.8	1.67	
10	2	3.8	1.90	0.16
10[e]	3	4.28	1.43	
10[d]	5	8.90	1.78	0.20
10	10	13.9	1.39	0.19
30[e]	1	4.60	1.54	0.18
45	2	13.9	1.54	0.17
45[e]	2	13.0	1.45	
100	1	13.7	1.37	0.20
100[d]	2	22.3	1.12	0.19
100	5	58.0	1.16	0.20

[a] $R = \log \left[\frac{(O.D.)_t}{(O.D.)_0}\right]/t$. [b] $k = R/[Cl^-][H^+]$. [c] See note *b*, Table I. [d] H_2SO_4 $M/2$. [e] In 98% D_2O.

The rate of appearance of the Cl_2^- depends directly on the chloride ion concentration and also on the acid concentration. In column 4 the rate constant calculated from the rate of formation of Cl_2^- divided by the chloride and hydrogen ion concentrations decreased only slightly from 10^{-3} to 1 M perchloric acid. Thus the decrease in Table I in the rate constant ratio for reaction of the OH radical with methanol and potassium ferrocyanide and chloride ion may be accounted for in terms of the increased rate of the reaction of the OH radical with the chloride ion.

The effect of ionic strength on the rate of formation of Cl_2^- is shown in Table III. A negative salt effect was obtained. At pH 2.065 the rate constant k decreased nearly twofold in increasing the ionic strength from 0.012 to 1.00. We conclude that the rate-determining step involves reacting ions of opposite charge. There was no isotope effect, on the rate of Cl_2^- formation, from substituting D_2O for H_2O.

Table III: The Effect of Ionic Strength and Higher Acidity on the Rate of Formation of Cl_2^-

$HClO_4$, mM	NaCl, mM	μ[a]	pH[b,c]	k,[d] M^{-2} sec.$^{-1}$ × 10^{-10}
1	20	0.02		1.78
10	2	0.012	2.065	1.84
10	2	0.05	2.005	1.67
10	2	1.00	1.925	1.10
20	2	1.00	1.61	1.00
50	1	1.00	1.27	0.91
100	0.5	0.10	1.10	1.12
100	0.5	0.50	1.045	0.97
100	0.5	1.00	0.960	0.87
100	1.0	1.00	0.965	0.82
200	0.5	1.00		0.72
200	1.0	1.00		0.70
500	0.5	1.00		0.48
1000	0.5	1.00		0.32
1000	0.2	1.00		0.38

[a] $\mu = {}^1/_2 \sum_i c_i z_i^2$ maintained by the addition of $NaClO_4$. [b] Determined by a glass electrode with a radiometer pH meter model. [c] Burton and Kurien give $k_{OH + Cl^-} = 4 \times 10^9$ in 0.8 N H_2SO_4 [M. Burton and K. C. Kurien, *J. Phys. Chem.*, **63**, 899 (1959)]. [d] k defined in Table II.

The Formation of Cl_2^- in Neutral and Alkaline Solutions. In neutral solution the Cl_2^- transient was only observed at chloride ion concentrations of 0.1 M or greater. It is apparent from Fig. 1 that the rate of formation of the Cl_2^- is extremely fast and that the Cl_2^- was formed in a time that was considerably less than 0.4 μsec., the length of the electron pulse. Table IV summarizes the results that were obtained.

In aerated solution at pH 7 the optical density, or yield of the Cl_2^-, increased up to 3 M chloride ion. At 1 M chloride the yield of Cl_2^- was about one-third that obtained in acid solution (see Fig. 1). Even in 3 M

(13) J. Sweet and J. K. Thomas, *J. Phys. Chem.*, **68**, 1363 (1964).

Table IV: Optical Density of Cl_2^- Transient at 3650 Å. in Neutral and Alkaline Solutions

pH	NaCl, *M*	S	[S], *M*	O.D.$_{3650}$[a]	$[S]^{1/3}$
7.0	0.050	...	...	<0.01	
7.0	0.10	...	...	<0.01	0.465
7.0	0.3	...	...	0.026	0.670
7.0	0.7	...	...	0.055	0.89
7.0	1.0	...	...	0.074	1.00
7.0	1.4	...	...	0.096	1.12
7.0	2.0	...	...	0.115	1.26
7.0	3.0	...	...	0.128	1.44
7.0	1.0	H_2O_2[b]	0.001	0.075	
7.0	1.0	H_2O_2[c]	0.001	0.073	
7.0	1.0	Phosphate	0.3	0.072	
7.0	1.0[d]	KF	0.5	0.074	
9.9	2.0	NaOH	0.0001	0.113	
10.9	2.0	NaOH	0.001	0.119	0.100
12.0	2.0	NaOH	0.01	0.108	0.216
13.0[e]	2.0	NaOH	0.1	0.045	0.465
14.0[e]	2.0	NaOH	1.0	0.023	1.00

[a] See note *b*, Table I. [b] Aerated solution. [c] Deaerated solution. [d] KCl. [e] 0.1–1.0 *M* NaOH pH values given by definitions.

chloride ion, the yield at pH 7 was less than that obtained at lower chloride ion concentrations in acid solution. The yield of Cl_2^- depended on the third root of the chloride ion concentration.

Solutions 10^{-3} *M* in hydrogen peroxide produced no change in the yield of Cl_2^-. At this hydrogen peroxide concentration all the hydrated electrons should have reacted to produce OH radicals.

$$e_{aq}^- + H_2O_2 \longrightarrow OH^- + OH$$

where $k = 1.1 \times 10^{10}$ M^{-1} sec.$^{-1}$ (ref. 9) and half-life $< 10^{-7}$ sec. It would appear that, at pH 7, OH radicals formed in the bulk of the solution do not produce Cl_2^-.

The yield of Cl_2^- was decreased by progressively adding sodium hydroxide to the solution. Above pH 12 increasing the hydroxyl ion concentration tenfold produced a twofold decrease in the yield of Cl_2^-. The results illustrate that the scavenging action of the OH^- depends on $[OH^-]^{1/3}$.

Discussion

In acid solution the results in Table I indicate that the Cl_2^- was produced by a reaction of OH radicals with chloride ions, and that the rate of reaction depended on the H^+ concentration.

At pH 7 the results indicated (1) that OH radicals produced in the bulk of the solution *via* the reaction $e_{aq}^- + H_2O_2 \rightarrow OH^- + OH$ did not react with Cl^-,

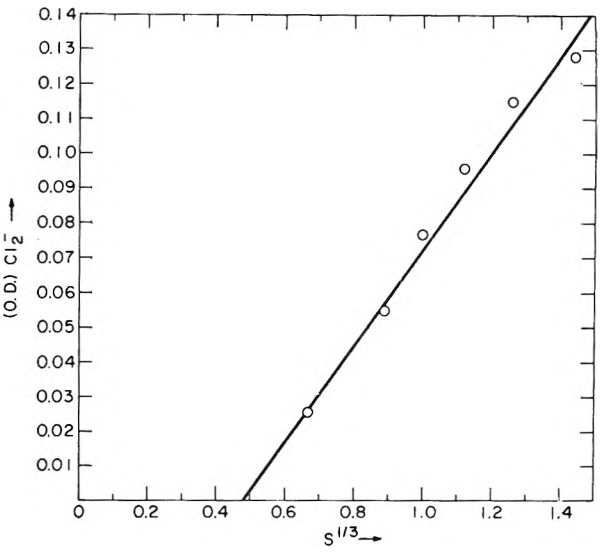

Figure 4. Cube root plot of the increasing Cl_2^- yield with increasing sodium chloride concentration in aerated solution at neutral pH.

(2) that Cl_2^- was only observed at chloride ion concentrations greater than 0.1 *M*, (3) that the yield of Cl_2^- increased with increasing chloride ion, and (4) that hydroxyl ions decreased the Cl_2^-. The above facts suggest that the origin of the Cl_2^- at neutral pH is in the "spur regions."

Because of the diffusion of the radicals out of the spur, the scavenging effect of any solute on a spur product should follow a cube root relationship. This has been demonstrated for various solutes.[5c] The results in Table IV have been plotted in Fig. 4 for the increasing yield of Cl_2^- with chloride ion concentration and bear out the previous cube root relationship.

In the spur regions the initial products of the radiolysis, *i.e.*, OH radicals, hydrated electrons, and hydrogen ions, exist for a short period of time, usually less than 10^{-8} sec. The initial concentrations of these products are probably in excess of 1 *M*. In 1 *M* acid the rate constant for reaction of OH radicals with chloride ions was about 10^{10} M^{-1} sec.$^{-1}$. The half-life of the reaction in 0.1 *M* chloride ion would be about 10^{-9} sec. It is generally considered[14,15] that the spur reactions are essentially complete in 10^{-8} sec., so at concentrations of chloride greater than 0.1 *M* a distinct possibility exists that the chloride ions will encounter appreciable concentrations of hydrogen ions and OH radicals to form Cl atoms.

Under these conditions Cl_2^- may be formed in times of about 10^{-9} to 10^{-8} sec., *i.e.*, times that are very

(14) P. J. Dyne and J. M. Kennedy, *Can. J. Chem.*, 35, 1518 (1958).
(15) D. A. Flanders and H. Fricke, *J. Chem. Phys.*, 28, 1126 (1958).

much shorter than the duration of the electron pulse. The OH radicals produced *via* the reaction of e_{aq}^- with hydrogen peroxide have a half-life of appearance of about 10^{-7} sec. This is considerably longer than the time region when all the hydrogen ions have disappeared, and so no Cl_2^- should result from these OH radicals. This is precisely what was observed.

The addition of OH^- ions to the solution leads to a removal of H^+ ions *via* $H^+ + OH^- \rightarrow H_2O$, where $k = 1.5 \times 10^{11}$,[16] and, hence, to a decrease in the Cl_2^- yield. The initial hydrogen ion concentration in a spur is considered to be about 1 M. Hence, we may to a first approximation use the rate constant of $\sim 10^{10}$ determined in 1 M acid to discuss the spur reactions. In 2 M chloride ion the half-life of the appearance of the Cl_2^- is about 5×10^{-11} sec. In order to affect he Cl_2^- yield, the $OH^- + H^+$ reaction should have a half-life that is comparable to 5×10^{-11} sec. This will occur in 0.1 N sodium hydroxide. In Table IV, the Cl_2^- yield was halved in 0.1 N sodium hydroxide.

The yields of Cl_2^- in neutral solution and in acid solution seem to arise from a similar mechanism. The reaction of the OH radical with chloride ions requires the presence of hydrogen ions to facilitate the formation of the chlorine atom and subsequently the Cl_2^- molecule.

Several mechanisms may be written to follow the above dependency on H_3O^+. The first one is

$$Cl^- + OH \rightleftarrows Cl + OH^- \qquad (a)$$

This reaction is moved to the right by removal of OH^- by H_3O^+ and also by removal of Cl by Cl^- to give Cl_2^-. However, this mechanism predicts a second-order dependence on the chloride ion concentration.

It is unlikely that an activated complex of the composition $Cl^- \cdots OH \cdots H_3O^+$ can be formed at a high enough rate by a random three-body collision to explain the rapid Cl_2^- formation that was observed. Hence a pre-equilibrium of some kind between two of the reactants has to be assumed.

Three pre-equilibria can be conceived.

$$H_3O^+ + Cl^- \rightleftarrows HCl + H_2O$$
$$HCl + OH \longrightarrow Cl + H_2O \qquad (b)$$

$$OH + Cl^- \rightleftarrows HOCl^-$$
$$HOCl^- + H^+ \longrightarrow Cl + H_2O \qquad (c)$$

$$OH + H_3O^+ \rightleftarrows H_2O^+ + H_2O$$
$$H_2O^+ + Cl^- \longrightarrow Cl + H_2O \qquad (d)$$

There are arguments for and against each of these mechanisms.

In mechanism b the reaction of OH radicals with HCl may proceed faster than with Cl^- in analogy to the behavior of iodide ion and hydriodic acid in oxidation–reduction reactions. The observed salt effect does not exclude this mechanism, as it may be a secondary salt effect resulting in an increased dissociation of HCl. In 1 N acid the extrapolated rate constant for the reactions $OH + Cl^-$ or OH + chloride ion intermediate was 2×10^{10}. The reported value for the dissociation constant for the process $HCl \rightleftarrows H^+ + Cl^-$ is $\sim 10^7$.[17] This implies that the rate constant for the reaction $OH + HCl \rightarrow Cl + H_2O$ would have to be very much larger than 10^{11}. This is larger than the upper limit for diffusion-controlled processes and eliminates this mechanism.

The formation of $HOCl^-$ in a pre-equilibrium is analogous to the formation of Cl_2^- and may have a diffusion-controlled rate constant of 2×10^{10} M^{-1} sec.$^{-1}$. This would indicate that in 10 mM chloride ion an appreciable percentage of the OH radicals would exist as $HOCl^-$. This possibility was investigated by observing the effect of chloride ions up to 10 mM on the rate and yield of the reaction of OH radicals with benzene and ferrocyanide. No effect whatsoever was found, and the experiments indicate the absence of a complex $HOCl^-$, unless it is assumed that the chemical and kinetic behavior of $HOCl^-$ is equal to that of OH radicals. The absence of an appreciable D_2O isotope effect makes a proton-transfer reaction such as (c) less likely.

The formation of H_2O^+ in a pre-equilibrium has been suggested by Sworski.[7] In 1 N acid the rate of formation of Cl_2^- was 10^{10} M^{-1} sec.$^{-1}$. If the rate constant of the reaction $H_2O^+ + Cl^- \rightarrow Cl$ was as high as 10^{11}, then the dissociation constant of H_2O^+ *via* $H_2O^+ + H_2O \rightleftarrows H_3O^+ + OH$ would have to be less than 0.1. Tal'roze and Frankevich have found that the rate constant for reaction d, $H_2O + H_2O^+ \rightarrow H_3O^+ + OH$, is 5.1×10^{11} M^{-1} sec.$^{-1}$ in the gas phase at 410°K. The dissociation constant for H_2O^+ of less than 0.1 would indicate that the rate constant for the preceding reaction d in aqueous solution is less than 10^{10} M^{-1} sec.$^{-1}$; otherwise the reaction $H_3O^+ + OH \rightarrow H_2O^+ + H_2O$ would have too large a rate constant. The effect of solvation on (d) might cause such a lowering in the rate constant. The work of Hochanadel[18] has illustrated that there was no effect of acidity up to 0.4 M acid on the ratio $k_{OH+H_2}/k_{OH+H_2O_2}$. This result argues strongly against the formation of H_2O^+ under our experimental conditions.

(16) M. Eigen and L. De Maeyer, *Z. Elektrochem.*, **59**, 986 (1955).
(17) W. F. K. Wynne-Jones, *J. Chem. Soc.*, 1064 (1930).
(18) C. J. Hochanadel, *Radiation Res.*, **17**, 286 (1962).

In conclusion, it may be stated that none of the above three mechanisms is free from objections, and only further experiments may help to achieve a final decisive answer.

Acknowledgments. We express thanks to Dr. E. J. Hart for many useful discussions and for advice in the work. We also thank Miss P. Walsh, Mr. E. Backstrom, and Mr. B. E. Clifft, who helped with the work.

Thermodynamics of Vaporization of Liquid Thallous Bromide and Its Gaseous Dimerization[1]

by Daniel Cubicciotti

Stanford Research Institute, Menlo Park, California 94025 *(Received July 15, 1964)*

The vapor pressure of liquid thallous bromide was measured by a quasi-static method from the melting point to the boiling point. The results can be represented by the equation: $\log p = -7324/T + 22.874 - 4.38 \log T$. The species in the vapor were found to be mainly monomer (TlBr) and some dimer (Tl_2Br_2). The partial pressures of these species were established by combining transpiration measurements with the vapor pressure measurements. Extrapolation of the data indicated that the dimer would constitute about 25% of the vapor at the normal boiling point and about 0.05% at the melting point. The heats of evaporation at 1000°K. were 24.3 kcal. to monomer and 50 to dimer. The corresponding entropies were 22.0 and 42 e.u.

Introduction

Vapor saturated with liquid thallous chloride has been found[2] to contain some dimer in addition to the predominant monomeric species. Comparison of the behaviors of the thallous halides and the alkali halides should provide some understanding of the binding in such molecules; thus, our study was extended to thallous bromide.

A qualitative examination of the vapors produced from liquid thallous bromide was made using a Bendix time-of-flight mass spectrometer. In this experiment the sample was contained in a graphite cell having a narrow slit orifice. With the sample above its melting point the shutter-dependent peaks observed were Tl^+ (relative intensity unknown because of interference by Hg^+ peaks), $TlBr^+$ (very strong), Tl_2^+ (weak), Tl_2Br^+ (strong), and $Tl_2Br_2^+$ (medium). No higher molecular weight species were observed. These results were interpreted as indicating that dimers existed in the vapors, but higher polymers were not important. Also, it appeared that the dimer to monomer ratio was smaller for the bromide than for the chloride. This was borne out by the more quantitative measurements reported below.

Experimental

The composition of the saturated vapor was determined from measurements of the vapor pressure and transpiration pressure. These data, together with the indication from the mass spectrometer results that higher polymers were unimportant, permitted a calculation of the partial pressures of monomer and

(1) This work was made possible by the support of the Research Division of the U. S. Atomic Energy Commission under Contract No. AT(04-3)-106.

(2) D. Cubicciotti, *J. Phys. Chem.*, **68**, 1528 (1964).

dimer in the equilibrium vapor as a function of temperature.

The vapor pressure was measured by the quasi-static method of Rodebush, *et al.* The details of our apparatus for this measurement have been described elsewhere.[2,3] For the present work the cell was made of fused quartz and required about 200 g. of TlBr. The inert gas used was high-purity, dry nitrogen. The transpiration apparatus has also been described in ref. 3. In the present work high-purity, dry nitrogen was again used as a carrier gas.

Thallous bromide was made by dissolving pure thallium (99.95% from American Smelting and Refining Co.) in dilute HNO_3 and adding sufficient dilute HBr to precipitate TlBr. The precipitate was collected on a sintered glass filter and air-dried. A sample of this material was prepared for analysis by fuming in concentrated H_2SO_4, diluting, and reducing with SO_2. The resulting solution was analyzed for thallium by the chromate method.[4] It was found necessary to perform the chromate precipitations at 0° because samples precipitated at room temperature gave values that were low by a few tenths of 1%. The analysis indicated 71.89% of Tl in the TlBr compared with 71.89% theoretical for TlBr. The freezing point of this material was found to be 460.0 ± 0.5°.

Temperatures in both sets of measurements were determined with a platinum–10% rhodium thermocouple that had been checked against a similar NBS-calibrated themocouple.

Results

Vapor pressures were obtained over the range from a few millimeters to slightly more than 1 atm. The results are shown in Fig. 1. The quasi-static results which represent the total vapor pressure of all thallous bromide species can be represented by

$$\log p \text{ (mm.)} = \left[-\frac{7324}{T} + 22.874 - 4.38 \log T \right] \pm 1\%$$

from 500 to 850°. These results should be comparable with the boiling point data obtained by von Wartenberg and Bosse.[5] Their data have almost the same slope as the present data, but their curve is displaced toward lower temperatures by a few degrees. A similar difference, observed between our results and those of von Wartenberg and Bosse for TlCl, was presumed to be due to a correction they applied for superheating. The same presumption holds for TlBr.

The results of the transpiration measurements were reduced to the pressure of TlBr using 284 for the molecular weight of the gaseous species. When calculated in this way, the transpiration pressures are greater than the vapor pressures by approximately the partial pressure of dimer. The results of the transpiration study are also shown in Fig. 1. Multiple points at a given temperature were obtained at different flow rates of carrier gas, usually over a five- or tenfold range. The results at different flow rates were within a 5% range, thus indicating that for our experimental arrangement the gas stream was saturated with thallium chloride. These data are compared in Fig. 1 with the transpiration results of Volmer.[6] His data are higher than the present results and have a greater slope.

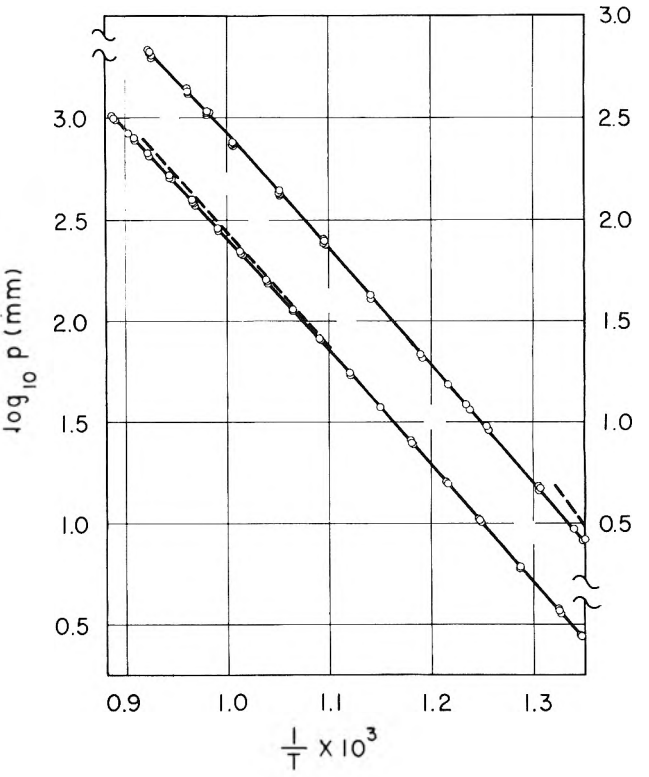

Figure 1. Vapor pressure of TlBr. Lower set of curves from quasi-static or boiling point method. Full line and points, present data; dashed line, data of von Wartenberg and Bosse. Upper set of curves from transpiration. Full line, present data; dashed line, data of Volmer.

The vapor pressures were combined with the transpiration results to calculate partial pressures of mono-

(3) F. J. Keneshea and D. Cubicciotti, *J. Chem. Phys.*, **40**, 191 (1964).

(4) O. L. Forchheimer and R. P. Epple, *Anal. Chem.*, **23**, 1445 (1951).

(5) H. von Wartenberg and O. Bosse, *Z. Elektrochem.*, **28**, 384 (1922); see also H. von Wartenberg and P. Albrecht, *ibid.*, **27**, 162 (1921), for technique.

(6) F. Volmer, *Physik. Z.*, **30**, 590 (1929).

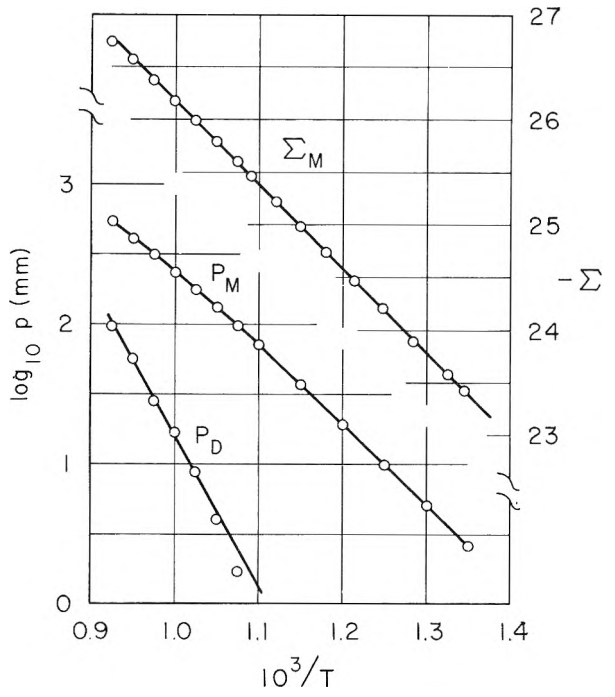

Figure 2. Partial pressures of monomer (P_M) and dimer (P_D) and Σ plot for monomer.

mer and dimer by the same method used for the analysis of the thallium chloride data since the mass spectrometer indicated only two important vapor species—monomer and dimer. The partial pressures of monomer and dimer calculated in this way are shown as the points in Fig. 2. The monomer data showed a small curvature, which was presumed to be due to the effect of the difference in heat capacities of the monomer and the liquid. Accordingly, a Σ plot treatment[7] of the data was applied. The heat capacity of gaseous TlBr was calculated from molecular constant data.[8] In the temperature range of interest it was found to be essentially constant and equal to 8.9 cal./mole/deg. The heat capacity of the liquid was remeasured for this work.[9] It was found to have a value of $25.3 - 9.04 \times 10^{-3}T$ °K. cal./mole/deg. The expression for Σ therefore becomes

$$\Sigma_M = -\log P_M \text{ (mm.)} - 8.27 \log T \text{ (°K.)} + 0.99 \times 10^{-3}T \text{ (°K.)}$$

The Σ plot for the monomer data is shown in Fig. 2. All the points except that at the highest temperature fall quite well on a straight line indicating that the curvature of the pressure data did arise from heat capacity effects. At the highest temperature the low value for P_M probably arises from errors in the transpiration measurements. An equation for the partial pressure of monomer derived from the Σ plot is

$$\log P_M \text{ (mm.)} = \left[-\frac{7895}{T} - 8.27 \log T + 0.99 \times 10^{-3}T + 34.090 \right] \pm 2\%$$

The partial pressures of the dimer (P_D) as calculated from the vapor pressure and transpiration measurements are given in Fig. 2. Those data also show some curvature; however, since the pressures, being relatively small differences of experimental quantities, are not known too well, it was felt they were well enough represented by a straight line. The equation for that line is

$$\log P_D \text{ (mm.)} = -\frac{10800}{T} + 12.012$$

The equation represents the dimer pressures to within 20%, except for the lowest pressure calculated.

The vapor pressure over solid thallous bromide has been measured by Barrow, *et al.*[10] (from 220 to 340°), by Volmer[6] (335 to 460°), and Niwa[11] (270 to 340°). Linear extrapolations of their data are represented in Fig. 3. The present data join quite well with those of Barrow, *et al.*, and of Volmer.

The partial pressure of dimer over solid thallous bromide was calculated from the present values over the liquid. The heat of evaporation to dimer from the solid must be larger than that from the liquid by twice the heat of fusion and, of course, the dimer pressure curves must join at the melting point. The partial pressure of dimer is less than 0.1 of 1% of that of the monomer over the solid. Therefore, pressure measurements over the solid can be assumed to be monomer pressures, within experimental accuracy.

Discussion

The thermodynamic quantities for the evaporation processes were evaluated from the partial pressure

(7) (a) K. K. Kellev, U. S. Bureau of Mines Bulletin 383 (1935), reprinted in U. S. Bureau of Mines Bulletin 601 U. S. Govt. Printing Office, Washington, D. C., 1962; (b) G. N. Lewis and M. Randall, "Thermodynamics," revised by K. S. Pitzer and L. Brewer, McGraw-Hill Book Co., Inc., New York, N. Y., 1961, p. 175 ff.

(8) Internuclear distance from M. Mandel and A. H. Barrett, *Phys. Rev.*, 98, 1159 (1955); vibration frequencies from G. Herzberg, "Molecular Spectra and Molecular Structure," Vol. I, 2nd Ed., D. Van Nostrand Co., Inc., New York, N. Y., 1950.

(9) D. Cubicciotti and H. Eding, "Heat Contents of Thallous Halides," to be published.

(10) R. F. Barrow, E. A. N. S. Jeffries, and J. M. Swinstead, *Trans. Faraday Soc.*, 51, 1650 (1955).

(11) K. Niwa, *J. Fac. Sci., Hokkaido Imp. Univ., Ser. III*, 3, 17 (1940).

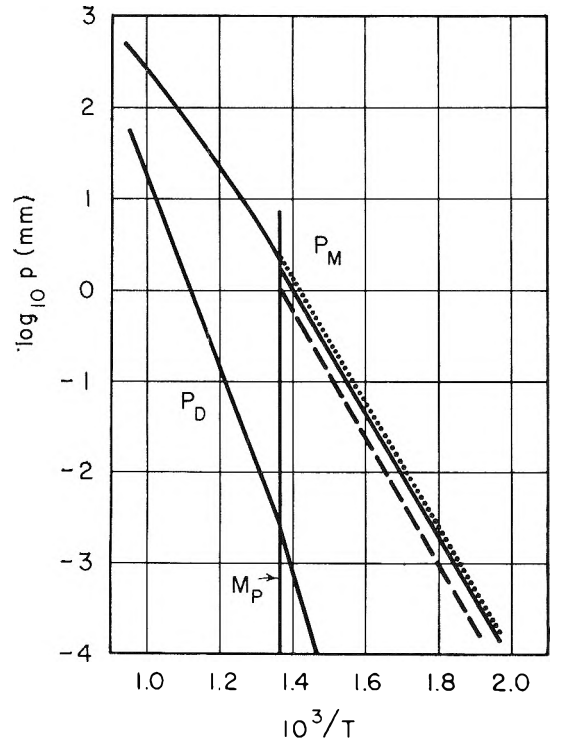

Figure 3. Pressures of species above and below melting point. P_M = partial pressure of monomer; above melting point—present data; below melting point—dotted line from Volmer, full line from Barrow, *et al.*, dashed line from Niwa. P_D = partial pressure of dimer; above melting point—present data; below melting point—extrapolation of present data.

data. For the monomer the heat of evaporation derived from the Σ plot is given by

$$\Delta H_T \text{ (kcal./mole of monomer)} = [36.13 - 16.4 \times 10^{-3}T + 4.52 \times 10^{-6}T^2] \pm 0.1$$

with T in °K. At 1000°K. ΔH of evaporation is 24.25 kcal./mole. For gaseous TlBr the quantity ($H_{1000} - H_{298}$) was calculated from molecular constant data[7] to be 6.25 kcal./mole and ($H_{1000} - H_{298}$) for thallous bromide has been measured in our laboratory[9] to be 14.49 kcal./mole. Therefore, the heat of sublimation to the monomer at 298°K. is 32.50 ± 0.1 kcal./mole. We have slightly revised the data of Barrow, *et al.*, and their treatment of Volmer's data in the light of our new measurements of the heat content of the solid and find their second-law values to be 32.40 ± 0.05 and 32.33 ± 0.4 kcal./mole, respectively. Thus, the heats of sublimation (as well as the pressure of monomer at the melting point) are in good agreement. The absolute entropy of solid thallous bromide has not been measured calorimetrically, so a precise third-law treatment of the data is not possible.

The standard thermodynamic quantities for vaporization of liquid thallous bromide are given in Table I. It is interesting to note that the thermodynamic quantities for evaporation to the monomer are essentially the same as those for the chloride as, in fact, they must be because the monomer partial pressure curves for these two substances are almost identical. The values for the dimer are much less precisely known because the dimer pressures were obtained as differences of large numbers. Both the entropy and heat of vaporization to the bromide dimer are substantially larger than the corresponding values for thallous chloride. At 1000°K. these quantities combine so that the resultant ratio of dimer to monomer pressures is smaller for the bromide than for the chloride; however, above about 1150°K. the situation is reversed and the bromide should have a larger dimer to monomer ratio. The behavior of the bromide compared to the chloride for thallium is different from that for potassium.[12] With potassium, which may be considered as representative of the alkali halides, the thermodynamic quantities of vaporization of the bromide are almost the same as those for the chloride. The fact that the change from chloride to bromide has a significantly different effect in the thallium case from that in the potassium case indicates that the nature of the binding in the liquid, or the gas, or both is different in the two cases.

Table I: Thermodynamic Data for Vaporization of Liquid TlBr Compared to Other Liquid Halides

	T, °K.	$\Delta H°$ monomer, kcal./mole	$\Delta H°$ dimer, kcal./mole	$\Delta S°$ monomer, cal./mole/deg.	$\Delta S°$ dimer, cal./mole/deg.	P_D/P_M in saturated vapor
TlBr	1000	24.3 ± 0.1	50 ± 5	22.0 ± 0.2	42 ± 4	0.067
TlCl	1000	24.4	31.8	22.0	25.7	0.15
KBr	1100	41.1	42.6	24.9	23.4	0.24
KCl	1100	42.5	41.0	25.1	22.6	0.6

The standard thermodynamic functions for dissociation of the dimer, $Tl_2Br_2(g) = 2TlBr(g)$, at 1000°K. are $\Delta H° = -2 \pm 5$ kcal. and $\Delta S° = 2 \pm 4$ e.u. These values are smaller than the corresponding ones for the chloride (17 kcal. and 18 e.u., respectively).

The absolute entropy of the dimer is equal to that of two monomers minus its dissociation entropy. At 1000°K. the absolute entropy of the gaseous mono-

(12) "JANAF Thermochemical Tables," The Dow Chemical Co., Midland, Mich., revised as of December, 1963.

mer is 74.67 e.u.; thus, the absolute entropy of the dimer is 147 e.u. The translational entropy of the dimer was calculated to be 51 e.u. On the assumption of a square-planar molecule (in analogy with Li_2Cl_2[13]) of side 2.65 Å. (slightly larger than the monomer internuclear distance) the entropy of rotation is 35 e.u. Thus, on a square-planar model the vibrational entropy should be 61 e.u. at 1000°K. An estimate of the vibrational entropy of the square-planar molecule can be made as follows. Berkowitz[14] has calculated the vibration frequencies expected for the alkali halide dimers on an ionic model. For the heavier alkali chlorides one can roughly summarize the frequencies he obtained: four frequencies with values about two-thirds that of monomer, and two frequencies about one-third that of monomer. Using this approximation, one calculates the vibrational entropy of the square-planar Tl_2Br_2 at 1000°K. to be 35 e.u., about 26 e.u. smaller than the experimental value deduced above.

A linear model for the dimer molecule would have a larger absolute entropy than the square-planar. For instance, the linear molecule BrTlTlBr would have 51 e.u. translational and 25 e.u. rotational entropy (assuming TlBr distance = 2.6 Å. and TlTl distance = 2.4 Å.), and the vibrational entropy, arising largely from the four very low-frequency bending modes of such a flexible linear molecule, would be quite large. In order to fit the experimental entropy, the vibrational entropy would have to be about 70 e.u. This is possible if the bending vibrations have frequencies of the order of a few wave numbers.

The dissociation energy of the gaseous molecule TlBr was calculated from the heat of formation of the solid and the heat of sublimation as shown in Table II. This thermochemical value is about 0.2 e.v. larger than the spectroscopic value (3.2 e.v.[15]).

Table II: Thermochemical Calculation of TlBr Dissociation Energy

Reaction	ΔH, kcal.	Ref.
$Tl(s) + {}^1/_2Br_2(l) = TlBr(s)$ [298°K.]	−41.9	[a]
$TlBr(s) = TlBr(g)$ [298°K.]	32.5	This work
$Tl(s) = Tl(g)$ [298°K.]	43.6	[b]
$^1/_2Br_2(l) = Br(g)$ [298°K.]	26.8	[a]
$TlBr(g)$ [0°] = $TlBr(g)$ [298°K.]	2.4	[c]
$Tl(g)$ [0°] = $Tl(g)$ [298°K.]	1.5	[a]
$Br(g)$ [0°] = $Br(g)$ [298°K.]	1.5	[a]
$TlBr(g) = Tl(g) + Br(g)$ [0°K.]	79.2 (= 3.43 e.v.)	

[a] See ref. 7b, Appendix 7. [b] R. Hultgren, R. L. Orr, P. D. Anderson, and K. K. Kelley, "Thermodynamic Properties of Metals and Alloys," John Wiley and Sons, New York, N. Y., 1963, p. 290. [c] Calculated from molecular constant data.

Acknowledgment. The author is indebted to Mr. W. E. Robbins, who carried out much of the experimental work.

(13) See S. H. Bauer and R. F. Porter in "Molten Salt Chemistry," M. Blander, Ed., Interscience Publishers, Inc., New York, N. Y., 1964, p. 652.

(14) J. Berkowitz, *J. Chem. Phys.*, **32**, 1519 (1960).

(15) See T. L. Cottrell, "The Strengths of Chemical Bonds," 2nd Ed., Butterworths, London, 1958, p. 232.

A Thermochemical Study of Some Reciprocal Fused-Salt Systems Involving the Monovalent Liquid Nitrates

by S. V. Meschel and O. J. Kleppa

Department of Chemistry and Institute for the Study of Metals, The University of Chicago, Chicago, Illinois 60637 *(Received July 17, 1964)*

The enthalpies of solution in liquid monovalent nitrates of some solid alkali and alkaline earth chlorides and bromides have been measured. The results have been analyzed as the sum of two binary steps, $BX(s) + BNO_3(l)$ = dilute solution and $ANO_3(l) + BNO_3(l)$ = dilute solution, plus a metathetical step, $AX(s) + BNO_3(l) = ANO_3(l) + BX(s)$. The energy changes obtained for the latter step have been compared with literature data and discussed in terms of a simple ionic model and departures from this model.

Introduction

Mixtures of fused salts may be classified into four basic types according to the following scheme: (I) systems with symmetrical charge structure containing a common ion; this ion may be either (a) the anion, as in $(Na–K)NO_3$, or (b) the cation, as in $Na(Cl–NO_3)$; (II) systems with asymmetrical charge structure, but containing a common ion; again this ion may be (a) the anion, as in $(Ca–Na)NO_3$, or (b) the cation, as in $Na(MoO_4–NO_3)$; (III) systems with symmetrical charge structure, but containing no common ion, for example $KCl–NaNO_3$; (IV) systems which possess neither charge symmetry nor a common ion, such as $CaBr_2–NaNO_3$.

This list outlines, in the order of increasing complexity, a series of basic problems in the solution chemistry of fused salts: How do the solution properties of each class of mixed system depend on such parameters as the size, charge, and structure of the participating ions?

Through systematic calorimetric investigations carried out in this laboratory during recent years, we have attempted to provide answers to these questions. Thus, Kleppa and Hersh[1] found that all the binary liquid alkali nitrate mixtures (type Ia) have *negative* enthalpies of mixing with the magnitude increasing in a regular manner with increasing difference in size between the two participating cations. This has been attributed, in the main, to the reduction in coulombic repulsion between second nearest neighbor cations, as proposed by Førland.[2]

The alkali chloride–nitrate and bromide–nitrate systems (I(b)), on the other hand, all show small *positive* enthalpies of mixing.[3] We believe that this change in sign may be related to the radius-ratio effect, *i.e.*, to the importance of the core repulsion between the large anions.

In most cases the alkaline earth–alkali nitrate mixtures (IIa) exhibit negative enthalpies of mixing, which are comparable in magnitude or somewhat larger than those found for the binary alkali nitrates.[4] On the other hand, charge-unsymmetrical anion systems (IIb) appear to be more complex.[5] So far it has proved difficult to rationalize the solution behavior of such systems in terms of the simple physical ideas outlined above.

In the present work, our systematic study of the solution properties of fused-salt mixtures is extended to simple reciprocal mixtures (III and IV). Presently, we shall restrict our attention to solutions in the liquid monovalent nitrates. We report below the results obtained in a calorimetric investigation of the heats of solution of simple alkali and alkaline earth halides (AX and AX_2) in solvents such as $NaNO_3$, KNO_3, $TlNO_3$, and $AgNO_3$.

(1) O. J. Kleppa and L. S. Hersh, *J. Chem. Phys.*, **34**, 351 (1961).

(2) T. Førland, "On the Properties of Some Mixtures of Fused Salts," N. T. H. Trykk, Trondheim, Norway, 1958.

(3) O. J. Kleppa and S. V. Meschel, *J. Phys. Chem.*, **67**, 668 (1963).

(4) O. J. Kleppa, *ibid.*, **66**, 1668 (1962).

(5) O. J. Kleppa and S. V. Meschel, *ibid.*, **67**, 2750 (1963).

In the course of the present study we have determined experimentally the molar changes in enthalpy, ΔH_A, associated with reactions of the type

$$AX(s) + BNO_3(l) = \text{dilute solution of } A^+ \text{ and } X^- \text{ in } BNO_3 \quad (A)$$

If the solution of A^+ and X^- in BNO_3 is quite dilute, interaction between A^+ and X^- in the dilute solution may be neglected. Under these conditions process A, through a thermodynamic argument related to that used by Flood, Førland, and Grjotheim[6,7] in their theory of simple reciprocal fused-salt mixtures, may be considered to represent the sum of three part processes

$$AX(s) + BNO_3(l) = BX(s) + ANO_3(l); \ \Delta H_B \quad (B)$$

$$BX(s) + BNO_3(l) = \text{dilute solution of } X^- \text{ in } BNO_3(l); \ \Delta H_C \quad (C)$$

$$ANO_3(l) + BNO_3(l) = \text{dilute solution of } A^+ \text{ in } BNO_3(l); \ \Delta H_D \quad (D)$$

Under the stated assumption we have

$$\Delta H_A = \Delta H_B + \Delta H_C + \Delta H_D$$

The significance of this relation is that it reduces the problem of describing the reciprocal solution process A to the sum of a *metathetical* or *exchange* step B, plus two simple binary steps C and D.

The present investigation, which is concerned with dilute solutions of AX in BNO_3 only, does not address itself to the more basic question of to what extent a reciprocal fused salt mixture of *arbitrary composition* also can be described fully in terms of binary steps plus a metathetical step.[8] We propose to return to this problem in future work.

For the various solutes (AX and AX_2) considered in the present work, the quantities ΔH_C and ΔH_D already have been reported in earlier communications from this laboratory.[1,3-5] In principle, the quantities ΔH_B may be calculated from the standard heats of formation of the four substances involved, suitably corrected for the difference in enthalpy between 25° and our experimental temperature. Thus, one should, at least in some cases, be able to calculate ΔH_A from already published information.

In attempting to check this point experimentally we found a number of discrepancies between our own experimental results and the values which we calculated on the basis of literature data. While some of these discrepancies may be due to our neglect of the interaction between A^- and X^-, most of them probably arise from uncertainties in the heat contents. For this reason and also in order to check the internal consistency of own thermochemical data (ΔH_C and ΔH_D), we report in the present work the results of a survey of the heats of solution of various simple halides in the monovalent nitrates. The results will be discussed in terms of a simple ionic model.

Experimental and Chemicals

The calorimeter used in the present investigation has been described previously.[9] Most experiments were performed at 450 ± 1°. However, in order to avoid thermal decomposition, all work involving the salts of calcium, thallium, and silver was carried out at 350 ± 1°.

Calibrations were generally by the "gold-drop" method, *i.e.*, based on the heat content equation for pure gold as given by Kelley.[10] In experiments where silver nitrate was the solvent, we used an electrical calibration method. This was done in order to avoid the small spurious heat effect which results from a slight deposition of silver on the surface of the gold, as noted by Kleppa, Clarke, and Hersh.[11]

The sodium and potassium halides and nitrates and the alkaline earth halides were Mallinckrodt A.R. grade reagents. The rubidium, cesium, and thallium halides and thallium nitrate were purchased from Millmaster Chemical Corp. as "99.9% pure." The silver salts were of analytical grade and furnished by Goldsmith Brothers. Thallium nitrate was recrystallized twice from distilled water before use. The remaining salts were used without further purification.

With the exception of lithium chloride and bromide, which were dried by heating under vacuum, the salts were dried as required in the atmosphere. After drying, the lithium salts were tested for alkalinity by dissolution in distilled water. These solutions were neutral with respect to phenolphthalein.

All the experiments carried out in the present study involved the solution of a small amount of a solid salt in a large surplus of solvent. The final concentrations always were below 1 mole % of solute. Thus, the assumption discussed in the Introduction, that the interaction between the two solute ions may be neglected, is a reasonable one.

(6) H. Flood, T. Førland, and K. Grjotheim, *Z. anorg. allgem. Chem.*, **276**, 289 (1954).

(7) M. Blander and E. B. Luchsinger, *J. Am. Chem. Soc.*, **86**, 319 (1964).

(8) M. Blander and S. J. Yosim, *J. Chem. Phys.*, **39**, 2610 (1963).

(9) O. J. Kleppa, *J. Phys. Chem.*, **64**, 1937 (1960).

(10) K. K. Kelley, U. S. Bureau of Mines Bulletin No. 584, U. S. Govt. Printing Office, Washington, D. C., 1960.

(11) O. J. Kleppa, R. B. Clarke, and L. S. Hersh, *J. Chem. Phys.*, **35**, 175 (1961).

Table I: Summary of Thermochemical Data (in kcal./mole) for Mono-monovalent Reciprocal Halide–Nitrate Systems. (Unless otherwise stated, experimental uncertainty in ΔH_A is about ±0.03 kcal., the mean deviation of four experiments)

System solute–solvent	t, °C.	ΔH_A, measured	ΔH_C[a]	ΔH_D[b]	$\Delta H_B = \Delta H_A - \Delta H_C - \Delta H_D$	ΔH_B (lit.) $s_1 + l_2 = s_3 + l_4$
LiCl–$NaNO_3$	450	+2.64	6.40	−0.46[d]	−3.30	−2.72
LiBr–$NaNO_3$	450	+0.43[c]	6.10	−0.46[d]	−5.21	−4.49
LiCl–KNO_3	450	+1.64	5.43	−1.76[d]	−2.03	−1.63
LiBr–KNO_3	450	−1.85	5.42	−1.76[d]	−5.51	−5.17
KCl–$NaNO_3$	450	+4.71	6.40	−0.48	−1.21	−1.09
KBr–$NaNO_3$	450	+5.92	6.10	−0.48	+0.30	+0.67
RbCl–$NaNO_3$	450	+3.53	6.40	−1.01[d]	−1.86	−2.20
RbBr–$NaNO_3$	450	+5.49	6.10	−1.01[d]	+0.40	+0.12
RbCl–KNO_3	450	+4.77	5.43	−0.06[d]	−0.60	−1.12
RbBr–KNO_3	450	+5.28	5.42	−0.06[d]	−0.08	−0.55
CsCl–$NaNO_3$	450	+2.93[e]	6.40	−1.48	−1.99	−1.53
CsBr–$NaNO_3$	450	+5.90	6.10	−1.48	+1.28	+1.47
TlCl–$NaNO_3$	350	+9.12	5.91[f]	+0.13	+3.08	+3.28
NaBr–$TlNO_3$	350	−2.67	4.75	+0.37	−7.79	−7.69
KCl–$TlNO_3$	350	+0.23	4.22	+0.43	−4.42	−4.37
KBr–$TlNO_3$	350	−2.08	4.75	+0.43	−7.26	−7.02
RbCl–$TlNO_3$	350	−0.65	4.22	+0.23	−5.10	−5.48
RbBr–$TlNO_3$	350	−2.37	4.75	+0.23	−7.35	−7.57
NaCl–$AgNO_3$	350	−9.72	2.72[f]	+0.52	−12.96	−13.31
NaBr–$AgNO_3$	350	−16.46	1.46[f]	+0.52	−18.44	−18.93
KCl–$AgNO_3$	350	−12.01	2.72[f]	−0.60	−14.13	−14.40
KBr–$AgNO_3$	350	−16.88	1.46[f]	−0.60	−17.74	−18.26
RbCl–$AgNO_3$	350	−13.55	2.72[f]	−1.28	−14.99	−15.51
RbBr–$AgNO_3$	350	−17.75	1.46[f]	−1.28	−17.93	−18.81

[a] See ref. 3. [b] See ref. 1, 11, and O. J. Kleppa and L. S. Hersh, *J. Chem. Phys.*, **36**, 544 (1962). [c] Experimental uncertainty ±0.1 kcal. [d] Measured at 345°. [e] Experimental uncertainty ±0.06 kcal. [f] Measured in this investigation.

The actually measured heat effects ranged from as little as 0.2 cal. (for KCl in $TlNO_3$) to as much as 30 cal. (for alkali bromides and chlorides in $AgNO_3$). In the tables below we report only the calculated molar enthalpies of solution, usually as the average of four separate determinations which agreed to 1% or better. The accuracy of the reported data for the enthalpy of exchange (ΔH_B) is estimated to be of the order of ±0.1 kcal./mole.

Results and Discussion

1. Monovalent Halides in Nitrate (Type III). The experimental heats of solution, ΔH_A, obtained in the course of the present study are recorded in Table I. This table also contains data on ΔH_C and ΔH_D, based on recent publications from this laboratory. From these quantities we have calculated the experimental exchange terms, ΔH_B, which also are given in the table.

These values may be compared with corresponding data calculated from standard heat of formation information. Since the standard heats of formation all are referred to the solid state and 25°, these must be corrected for the heat content of all species at the working temperature of the calorimeter. In general, detailed and reliable heat content data are not available for most of the substances used. However, as shown by Blander and Luchsinger,[7] a good approximation to the heat content difference can be made by taking into account only the sum of the heats of transformation and of fusion of the nitrates. Apart from this, the heat content correction appears to be quite small in these charge-symmetrical systems. Using the standard heats of formation[12] and in each case what we considered to be the most reliable data in the literature on the heats of fusion and heats of transformation of the nitrates, we calculated the values of ΔH_B (lit.) given in the last column of Table I. While there is no quantitative agreement between our own exchange data and the literature values, the discrepancies, on the whole, fall within the range of ±1 kcal./mole. The major part of these discrepancies undoubtedly must be attributed to the heat content corrections.

We noted, by way of introduction, that in binary

(12) National Bureau of Standards Circular 500, U. S. Govt. Printing Office, Washington, D. C., 1952.

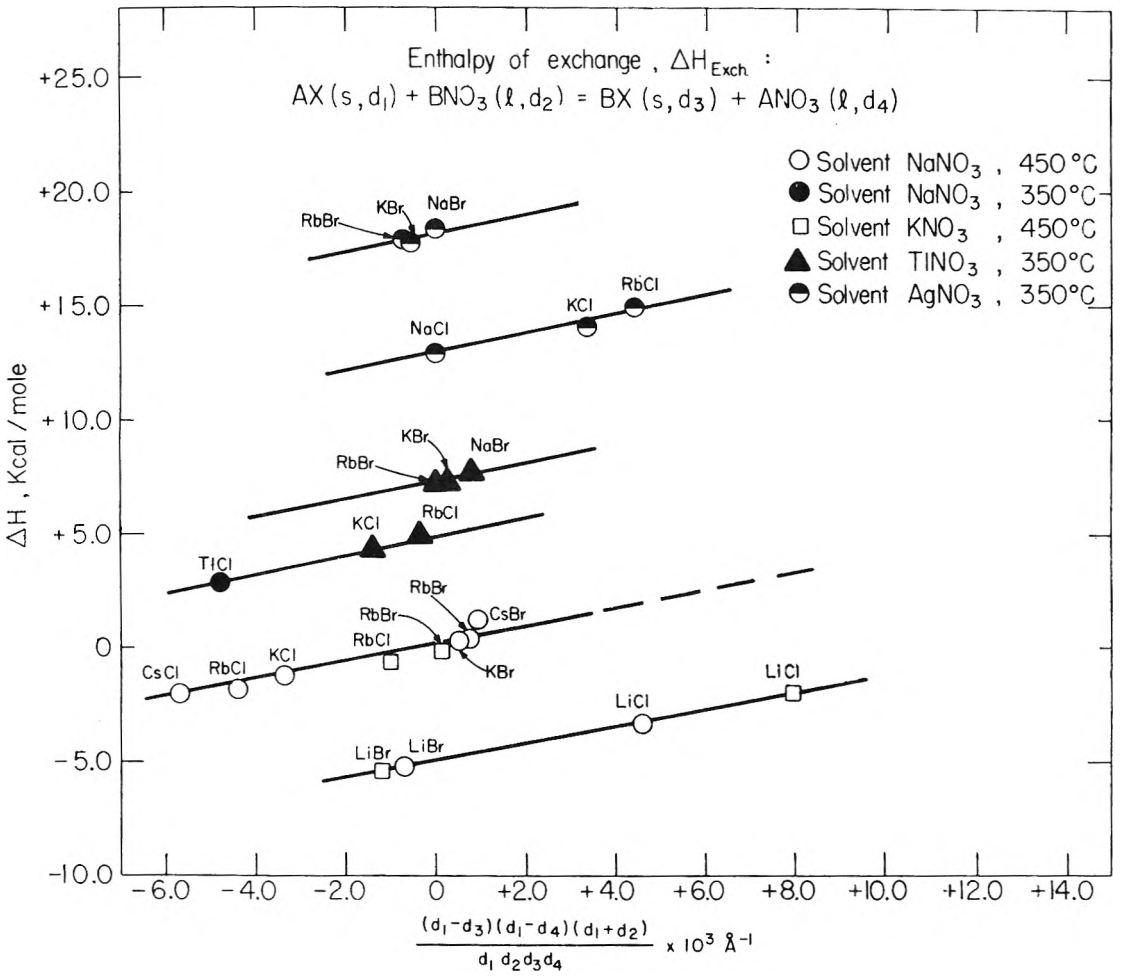

Figure 1. Plot of enthalpies of exchange for monovalent halide–nitrate systems ($\Delta H_{exch} = \Delta H_B$) *vs.* size parameter $(d_1 - d_3)(d_1 - d_2)(d_1 + d_4)/d_1d_2d_3d_4$.

fused-salt mixtures containing a common ion it is possible to relate the enthalpy of mixing to the changes in second nearest neighbor populations. In general, the enthalpy changes associated with reciprocal systems tend to be considerably larger since here changes occur even in the nearest neighbor ionic populations. The dominant term often will be the enthalpy of exchange, ΔH_B.

If all four species in (B) were in the solid state, we should in principle be able to relate ΔH_B to the "lattice enthalpies" of the participating species as follows: Let H_{AX} be the enthalpy of formation of AX(s) from $A^+(g)$ and $X^-(g)$. Similarly, let H_{BNO_3} be the enthalpy of formation of $BNO_3(s)$ from $B^+(g)$ and $NO_3^-(g)$. For the exchange process, with all species solid, we accordingly have

$$\Delta H_B' = H_{BX(s)} + H_{ANO_3(s)} - H_{AX(s)} - H_{BNO_3(s)}$$

In the ionic approximation we may set

$$H_{AX} = C/d_{AX}$$

where d_{AX} is the interionic distance in the compound AX, while the proportionality constant, C, includes the Madelung constant, the correction for repulsion, etc. Similar relationships hold for the other species. To a first approximation, C may be assumed to have the same value for each species. Thus, we obtained

$$\Delta H_B' = C\left[\frac{1}{d_{BX}} + \frac{1}{d_{ANO_3}} - \frac{1}{d_{AX}} - \frac{1}{d_{BNO_3}}\right] = C(d_{AX} - d_{EX})(d_{AX} - d_{ANO_3})(d_{AX} + d_{BNO_3})/d_{BX}d_{ANO_3}d_{AX}d_{BNO_3}$$

The latter expression arises from the additivity of the ionic radii. Also, since the heats of fusion of ANO_3 and BNO_3 are of comparable magnitude and are very small compared to the lattice enthalpy, we have $\Delta H_B \cong \Delta H_B'$.

We have in Fig. 1 plotted our experimentally determined values of ΔH_B *vs.* the parameter $(d_1 - d_3)(d_1 - d_2)(d_1 + d_4)/d_1d_2d_3d_4$ where $d_1 = d_{AX}$, etc. In calculating this parameter we have, as usual, set $d = r_+ + r_-$, where r_+ and r_- are the ionic radii of cation and anion, respectively. For the alkali metals, thallium, and the chloride and bromide ions we have used the Pauling radii, while for silver we have adopted the value r_{Ag^+} = 0.95 Å. This choice was dictated by the fact that the lattice parameters of AgCl and NaCl are very similar, suggesting that the "ionic" radius of silver must be very nearly the same as that of sodium.

Somewhat greater uncertainty is associated with the proper choice of an ionic radius for the nitrate ion. For this ion Janz[13] lists 2.3 Å. while Kleppa and Hersh,[1] on the basis of crystal chemical data, adopted the value 2.19 Å. On the other hand, the "thermochemical radius" of Kapustinskii,[14] which is based on arguments related to those presented previously in the calculation of ΔH_B, is 1.89 Å. In the course of the present study we noted that ΔH_B for potassium chloride + sodium nitrate is negative (−1.21 kcal.) while the value for potassium bromide + sodium nitrate is positive (+0.30 kcal.). Since, according to the expression for ΔH_B given previously, the enthalpy of exchange should change sign for $r_{X^-} = r_{NO_3^-}$, these results suggested strongly that the effective radius of the nitrate ion in a fused-nitrate medium should be intermediate between that of Cl^- (1.81 Å.) and Br^- (1.96 Å.). Interpolation gave $r_{NO_3^-}$ = 1.93 Å. This value was confirmed by other data on ΔH_B and has been adopted in the present work. As might be expected, this value is close to Kapustinskii's thermochemical radius of 1.89 Å.

Let us now examine Fig. 1 in somewhat greater detail. Note first that most of the values for the alkali chlorides and bromides in sodium and potassium nitrate fall on a single straight line. The slope of this line is about 400 kcal./Å., *i.e.*, of an order of magnitude consistent with the lattice enthalpies of simple ionic salts. However, even among the considered alkali halides, there are some that do not fall on this line. Most important among these are lithium chloride and bromide, which show a negative deviation of about 5 kcal./mole. This exothermic shift may be attributed either to an abnormally *low* cohesive energy of the *solid* lithium halides or to an abnormally *high* cohesive energy of *liquid* lithium nitrate. Here it is recalled that lithium chloride and bromide, in spite of an unfavorable radius ratio, both crystallize with the sodium chloride structure. Also, since the lithium ion is very small, it may be able to approach the nonspherical nitrate ion somewhat more closely than do the other alkali metal ions. Both of these effects may contribute to the negative shift. On the other hand, since the shift appears to be the same for bromide and chloride, we consider it probable that it is caused by added stability of the liquid lithium nitrate. On this basis, using arguments related to those given above for the radius of the nitrate ion in more typical alkali nitrates, we estimate an "effective ionic radius" of about 1.85 Å. for NO_3^- in combination with the lithium ion.

Among the other alkali halides studied we also find a small *positive* shift for cesium bromide. Probably, this is due to the added stability of solid cesium bromide, which exists at 450° in the cesium chloride modification. Cesium chloride itself, on the other hand, at this temperature has the sodium chloride structure and shows no anomaly.

The reciprocal mixtures of the typical alkali halides with thallium nitrate again exhibit the same linear dependence of ΔH_B on the size parameter, as do the alkali systems. However, now the line is shifted in the positive direction by about 5 kcal./mole for the chlorides and by an additional 2 kcal./mole for the bromides. We attribute these shifts to the extra cohesive energy of the thallium salts, compared to the alkali salts of the same interionic separation, which contributions presumably increase in the sequence, nitrate < chloride < bromide. Here it is of interest to correlate our results with those found in a recent n.m.r. study of solid and liquid thallium salts. This study, by Hafner and Nachtrieb,[15] shows an increasing chemical shift of the thallium resonance, *i.e.*, increasing "covalency," in the sequence, $TlNO_3 < TlCl < TlBr$.

Finally, we see from Fig. 1 that the alkali halide–silver nitrate systems also show a linear dependence of the enthalpy of exchange on the size parameter, and again the slope is of the same magnitude as that for the alkali halide–alkali nitrates. However, now the positive shift is quite large, roughly three times as large as for the thallium systems, about +15 kcal./mole for chloride–nitrate and +18 kcal./mole for bromide–nitrate. These larger endothermic shifts clearly reflect the larger nonionic contributions to cohesion in the silver salts. Of particular significance is the very considerable difference between silver nitrate, on the one hand, and chloride and bromide, on the other.

2. Alkaline Earth Halides–Sodium Nitrate (Type IV). The experimental heats of solution (ΔH_A) are recorded in Table II. Other columns in this table give ΔH_C, ΔH_D, and the enthalpy of exchange, $\Delta H_B'' =$

(13) G. J. Janz and D. W. James, *Electrochim. Acta*, **7**, 427 (1962).

(14) A. F. Kapustinskii, *Quart. Rev.* (London), **10**, 283 (1956).

(15) S. Hafner and N. H. Nachtrieb, *J. Chem. Phys.*, **40**, 2891 (1964).

Table II: Summary of Thermochemical Data (in kcal./mole) for Alkaline Earth Halide–Sodium Nitrate Reciprocal Systems. (Quoted experimental uncertainties are mean deviations of four experiments)

System solute–solvent	t, °C.	ΔH_A, measured	ΔH_C[a]	ΔH_D[b]	$\Delta H_B'' = \Delta H_A - 2\Delta H_C - \Delta H_D$	$\Delta H_B''$ (lit.) $s_1 + 2l_2 = 2s_3 + l_4$
$CaCl_2$–$NaNO_3$	350	-2.06 ± 0.15	5.91[c]	−0.9	−13.0	−10.50
$CaBr_2$–$NaNO_3$	350	(-6.0 ± 0.3)[d]	5.54[c]	−0.9	(−16.2)	−14.80
$SrCl_2$–$NaNO_3$	450	$+2.28 \pm 0.03$	6.40	−0.25	−10.27	−6.80
$SrBr_2$–$NaNO_3$	450	-1.31 ± 0.02	6.10	−0.25	−13.26	−9.30
$BaCl_2$–$NaNO_3$	450	$+6.15 \pm 0.02$	6.40	+0.40	−7.05	−3.75
$BaBr_2$–$NaNO_3$	450	$+4.90 \pm 0.02$	6.10	+0.40	−7.70	−4.51

[a] Unless otherwise stated, see ref. 3. [b] From Kleppa, *et al.*, *Discussions Faraday Soc.*, **32**, 99 (1961); see also ref. 4. [c] Measured in this investigation. [d] Approximate value only.

$\Delta H_A - 2\Delta H_C - \Delta H_D$. In this case the exchange process is

$$CaX_2(s) + NaNO_3(l) = 2NaCl(s) + Ca(NO_3)_2(l)$$

This accounts for the coefficient which is applied to ΔH_C in the calculation of $\Delta H_B''$. Otherwise, the calculation is analogous to the one for the monovalent halides, with the exception that, since the alkaline earth nitrates are solid at the temperature of the experiments, the values for ΔH_D have been corrected for the heats of fusion of these compounds.[4] Note also that in the calcium halide–sodium nitrate systems, because of a slight decomposition of the melt, the values for ΔH_A are not as precise as in most of the other experiments. We estimate the errors to be about ±0.15 kcal./mole for calcium chloride in sodium nitrate and ±0.3 kcal./mole for calcium bromide.

In the last column of Table II we finally give values of $\Delta H_B''$ (lit.) calculated as given previously from literature data on the enthalpies of formation, fusion, and transformation. It will be noted that for the alkaline earth–sodium nitrate systems there is a much larger discrepancy between our own data and the literature values. In all cases our experiments give significantly more negative values of $\Delta H_B''$ than calculated. We attribute this to the unsymmetrical character of the metathetical step, which presumably prevents the extensive cancellation of the heat contents noted for the charge-symmetrical systems. Unfortunately, reliable heat content data are not available to throw further light on this.

Acknowledgments. This work has been supported by the National Science Foundation (GP-1993) and by the Office of Naval Research (Nonr-2121(11)). General support of the Institute for the Study of Metals by the Advanced Research Projects Agency is also acknowledged.

Thermochemistry of the Alkali Chloride–Lead Chloride Liquid Mixtures

by F. G. McCarty and O. J. Kleppa

Institute for the Study of Metals and Department of Chemistry, The University of Chicago, Chicago, Illinois 60637 *(Received July 31, 1964)*

The enthalpies of mixing of the five lead chloride–alkali chloride mixtures have been determined calorimetrically. (Pb–Li)Cl is endothermic with a maximum value of the enthalpy of mixing near the 50:50 composition of +0.30 kcal./mole. The remaining systems are exothermic with corresponding values of about −0.10 for (Pb–Na)Cl, −1.3 for (Pb–K)Cl, −1.8 for (Pb–Rb)Cl, and −2.25 kcal./mole for (Pb–Cs)Cl. The results are discussed with respect to the following points: (1) comparison with data for related fused nitrate mixtures; (2) evidence for the formation of complex, anionic species; (3) comparison with excess free energies derived from e.m.f. investigations. Through the last comparison we have obtained some new reliable information on the entropy of mixing. The excess entropy appears to be near zero for lead–lithium and to assume increasingly positive values as the alkali metal cation becomes larger. A correlation between the excess entropies and the excess volumes has been established.

Introduction

Recently, we have developed a new, precision reaction calorimeter suitable for temperatures up to about 800°.[1] This apparatus makes possible, in the temperature range 500 to 800°, detailed calorimetric investigations of fused-salt mixtures of the type initiated below 500° by Kleppa and Hersh.[2] The present paper reports the results of an investigation of the binary liquid mixtures of lead chloride with the alkali chlorides.

These systems have already been explored by a variety of different physicochemical techniques. Thus, for several of them, experimental information is available in the literature on such topics as the phase diagram, molar volume, electrical conductivity, surface tension, and vapor pressure.[3] Also, which is of particular interest from the point of view of the present investigation, with the exception of $PbCl_2$–CsCl, these mixtures have been explored in some detail by means of e.m.f. formation and decomposition cells.[4–6] Unfortunately, in such studies the partial thermodynamic quantities relating to the liquid solutions occur as differences between two large numbers. As a consequence they are associated with considerable experimental uncertainty. This is smallest for the Gibbs free energy, which is directly proportional to the difference between two e.m.f. values, and more significant for the derived quantities, enthalpy and entropy, which depend on the temperature coefficient of the e.m.f. values for their determination.

The problem of the entropy of mixing in charge-unsymmetrical fused-salt systems has been the subject of a considerable amount of attention during recent years. For example, for such mixtures Førland[7] calculated the entropy of mixing on the basis of several different quasi-lattice models. However, when he attempted to compare his theoretical values with entropies derived from equilibrium information alone, he was unable to reach very firm conclusions. In the present communication we give a direct comparison between calorimetric enthalpies and corresponding free energy information. This will permit a fresh look at the entropy problem.

(1) O. J. Kleppa, to be published.

(2) O. J. Kleppa and L. S. Hersh, *J. Chem. Phys.*, **34**, 351 (1961).

(3) Some of this information is reviewed by H. Bloom, *Pure Appl. Chem.*, **7**, 389 (1963).

(4) J. H. Hildebrand and G. Ruhle, *J. Am. Chem. Soc.*, **49**, 722 (1927).

(5) M. F. Lantratov and A. F. Alabyshev, *Zh. Prikl. Khim.*, **26**, 263 (1953).

(6) B. F. Markov, IU. K. Delimarskii, and I. D. Panchenko, *Zh. Fiz. Khim.*, **28**, 1987 (1954).

(7) T. Førland, "On the Properties of Some Mixtures of Fused Salts," N. T. H. Trykk, Trondheim, Norway, 1958.

Experimental and Materials

The calorimetric mixing experiments were all carried out at 655 to 665°. The choice of this temperature range was dictated by considerations relating to the melting points of the alkali halides and the volatility of lead chloride. Lead chloride melts at 501° and has a vapor pressure at 660° of about 10 mm. This is sufficiently low so that losses and other errors arising from evaporation are small. Among the alkali chlorides only lithium chloride (m.p. 613°) and cesium chloride (m.p. 646°) are liquid at this temperature. However, the melting points of the other salts (NaCl, 801°; KCl, 776°; RbCl, 715°) are low enough so that a considerable range of liquid compositions can be explored near 660°.

Two different types of calorimetric experiments were performed. In the case of lithium chloride–lead chloride and cesium chloride–lead chloride, we carried out direct liquid–liquid mixing experiments. For the remaining three systems, where one component was solid, the calorimetric experiments involved the dissolution of the high-melting solid component in liquid lead chloride to form solutions containing up to 50 mole % alkali chloride.

Most chemicals were used as received, after appropriate drying. The lithium, sodium, and potassium chlorides were Mallinckrodt A.R. grade salts. The hygroscopic lithium chloride was dried, melted, and cast into 8-mm. diameter sticks under vacuum and stored in a vacuum desiccator. Basicity tests showed negligible hydrolysis during drying. The lead chloride was "Baker analyzed" reagent. The rubidium and cesium chlorides were purchased from Millmaster Chemical Co. as "99.9% pure." However, a semiquantitative spectrographic analysis of these salts gave the results in Table I. Since the heat of mixing for potassium–lead chloride is roughly comparable to that of rubidium–lead chloride (see below), no correction was made for the potassium impurity in rubidium chloride. The error introduced through about 0.5% Ba in CsCl may be more significant. However, as no data are available on the barium chloride–lead chloride liquid system, we have no basis for making a quantitative estimate of this error. Presumably, it will be of the same order of magnitude as the experimental scatter of about ±1%.

Table I

	Approximate impurity content, %				
Salt	Cs	Rb	K	Ba	Total
CsCl	...	0.1	0.01	0.5	0.6
RbCl	0.1	...	1.0	0.1	1.2

The details of the new calorimeter will be given elsewhere.[1] Basically, it is similar to a previously described twin unit for work up to 500°.[8] However, the following significant modifications were made. (1) The aluminum jacket of the earlier calorimeter was replaced by a cylindrical, 25-cm. diameter nickel block of about 300 lb. weight, but otherwise of comparable construction. (2) The diameter of each calorimeter was increased from 1.90 to 2.54 cm. while the length was kept at 12.7 cm. The larger diameter gives a somewhat larger "time constant," partly offset by the higher operating temperatures. (3) The number of thermocouples in each twin calorimeter was reduced from 96 to 48. The corresponding reduction in temperature sensitivity was not very significant for the relatively large heat effects involved in the present work.

The output from the thermopile system was amplified by means of a Leeds and Northrup d.c. amplifier and recorded on a Leeds and Northrup Type G-AZAR recorder. The e.m.f. *vs.* time curves were integrated by means of an Ott precision planimeter. In this way the area between curve and base line, which is proportional to the total heat effect, could be determined with a precision of about 0.3%. All calibrations were made by the "gold-drop method," and based on Kelley's equation for the heat content of gold.[9] A correction of about 1% was made for the heat pickup of the calibrating 2-mm. gold wire during the drop from room temperature into the calorimeter. Similarly, an exothermic correction of 0.15 ± 0.07 cal. was made for the heat effect associated with the shattering of the tip of the "break-off tube," which, prior to the mixing operation, contained one of the two components.

The furnace surrounding the calorimeter assembly was maintained at its operating temperature by means of a simple proportional controller. The temperature of the calorimeter proper was measured daily by means of a chromel–alumel thermocouple which was calibrated about every 2 weeks against a NBS standard Pt—Pt–10%Rh couple. The day-to-day variation of temperature was of the order of ±0.5°, while the drift in temperature from the beginning to the end of a 1-day run usually was less than 0.2°.

Considering all possible sources of error (evaporation of lead chloride, impurities, calibration, amplification, recording, integration, etc.), it is estimated that the reported heat data probably are correct to 2% or better.

(8) O. J. Kleppa, *J. Phys. Chem.*, **64**, 1937 (1960).

(9) K. K. Kelley, U. S. Bureau of Mines Bulletin 584, U. S. Govt. Printing Office, Washington, D. C., 1960.

Results

All experimental data obtained in the course of the present investigation are recorded in Tables II and III. Table II gives the results for the liquid–liquid mixing experiments. The columns of this table are (1) mole fraction of alkali chloride in the liquid mixture; (2) total number of moles in each experiment; (3) molar enthalpy of mixing, ΔH^{M}_{l-l}. Similarly, Table III gives the results for the solid–liquid experiments. The four columns are (1) and (2), as above; (3) molar enthalpy of solution, $\Delta H^{M}_{s-l}/X_{ACl}$, where X_{ACl} is the mole fraction of alkali chloride in the liquid mixture; (4) molar enthalpy of mixing of liquid, undercooled alkali chloride + lead chlorde, ΔH^{M}_{l-l}. In calculating these values we adopted the measured heats of fusion of Dworkin and Bredig[10] and the values of ΔC_p for the process of fusion given by Kleppa and Meschel.[11]

Table II: Enthalpies of Mixing from Liquid–Liquid Mixing Experiments

$PbCl_2$–LiCl at 665°

Composition, X_{LiCl}	Total moles	ΔH^{M}_{l-l}, cal./mole
0.2387	0.1043	189
.2584	.1064	201
.4067	.1123	277
.4287	.1136	292
.5112	.1016	296
.5275	.1031	301
.6438	.1015	296
.6543	.1016	297
.8039	.1018	228
.8046	.1022	227

$PbCl_2$–CsCl at 665°

Composition, X_{CsCl}	Total moles	ΔH^{M}_{l-l}, kcal./mole
0.0866	0.1091	−0.569
.0895	.1114	−0.588
.1669	.0601	−1.04
.1675	.0602	−1.02
.3483	.0500	−1.86
.3497	.0500	−1.86
.3503	.0500	−1.87
.3508	.0501	−1.86
.4994	.0601	−2.22
.4995	.0600	−2.26
.5000	.0599	−2.24
.6490	.0499	−2.22
.6494	.0500	−2.26
.7081	.1259	−2.09
.7824	.1317	−1.76
.8332	.0601	−1.40
.8334	.0600	−1.41
.8589	.1038	−1.22
.9126	.1129	−0.796
.9421	.1261	−0.546

Table III: Enthalpies of Mixing from Solid–Liquid Mixing Experiments

$PbCl_2$–NaCl at 665°
ΔH_f (NaCl) at 665° = 6.41 kcal./mole

Composition, X_{NaCl}	Total moles	$\Delta H^{M}_{s-l}/X_{NaCl}$, kcal./mole	ΔH^{M}_{l-l}, cal./mole (calcd.)
0.150	0.136	6.00	−62
.156	.133	6.03	−59
.200	.108	6.02	−78
.200	.107	6.05	−72
.264	.0721	6.15	−69
.266	.0720	6.03	−101
.333	.0591	6.10	−103
.337	.0597	6.15	−88
.415	.0499	6.16	−104
.417	.0494	6.17	−100
.487	.0391	6.28	−63
.488	.0392	6.16	−122

$PbCl_2$–KCl at 655°
ΔH_f (KCl) at 655° = 5.94 kcal./mole

Composition, X_{KCl}	Total moles	$\Delta H^{M}_{s-l}/X_{KCl}$, kcal./mole	ΔH^{M}_{l-l}, kcal./mole (calcd.)
0.151	0.132	2.22	−0.562
.153	.132	2.37	−0.546
.194	.110	2.51	−0.665
.198	.108	2.42	−0.697
.200	.107	2.49	−0.690
.277	.0730	2.70	−0.897
.281	.0713	2.67	−0.919
.337	.0593	2.84	−1.04
.343	.0589	2.97	−1.02
.423	.0502	3.21	−1.15
.425	.0507	3.14	−1.19
.428	.0502	3.20	−1.17
.511	.0395	3.44	−1.28
.526	.0381	3.40	−1.34

$PbCl_2$–RbCl at 660°
ΔH_f (RbCl) at 660° = 5.50 kcal./mole

Composition X_{RbCl}	Total moles	$\Delta H^{M}_{s-l}/X_{RbCl}$, kcal./mole	ΔH^{M}_{l-l}, kcal./mole (calcd.)
0.156	0.133	0.476	−0.783
.191	.107	0.634	−0.930
.192	.107	0.613	−0.939
.260	.0721	1.06	−1.15
.263	.0730	0.928	−1.20
.343	.0603	1.28	−1.45
.415	.0494	1.56	−1.64
.416	.0494	1.49	−1.67
.489	.0388	1.95	−1.74
.491	.0394	1.89	−1.77

In Fig. 1 we compare the enthalpies of mixing for all the five systems studied. For this purpose we plot the

(10) A. S. Dworkin and M. A. Bredig, *J. Phys. Chem.*, 64, 269 (1960).
(11) O. J. Kleppa and S. V. Meschel, *ibid.*, 67, 668 (1963).

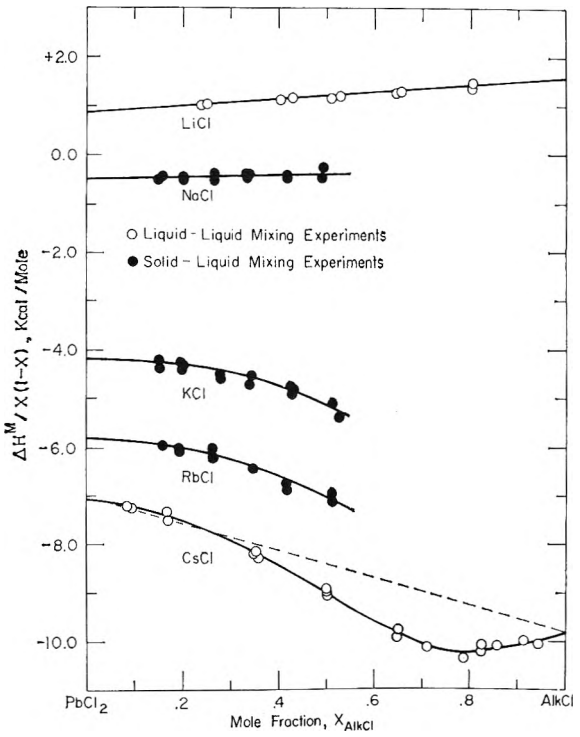

Figure 1. Plots of the interaction parameter, $(\Delta H^{M}{}_{1-1}/X(1 - X)$, *vs.* mole fraction for lead chloride–alkali chloride liquid mixtures.

"interaction parameter," $\Delta H^{M}{}_{1-1}/X(1 - X)$, *vs.* the mole fraction X.

The data show the expected trend toward more exothermic heats of mixing as the alkali metal cation becomes larger (see below). Thus, the interaction parameter changes from about +1.2 kcal./mole for lithium–lead chloride to −7 to −10 kcal./mole for cesium–lead chloride. We shall consider the significance of these results below.

Discussion

We shall discuss the new enthalpy data from two different points of view. On the one hand we want to compare our results with similar data previously reported for charge-unsymmetrical fused-salt mixtures. On the other hand we shall discuss the new data as they relate to the already available information on the lead chloride–alkali chloride systems. In particular, we shall attempt to find answers to the following two questions. (1) Do the new enthalpy data throw any further light on the nature of the complex species present in some of these liquid systems? (2) How do our enthalpies of mixing compare with the corresponding free energies? What new insights, if any, do they give regarding the entropy of mixing in these charge-unsymmetrical systems?

Comparison with Nitrates. Ideally, we should have preferred to compare the lead chloride–alkali chloride liquid systems with the corresponding nitrates; but, due to the well-known thermal instability of lead nitrate, these solutions cannot be investigated in the liquid state. Now, we know that the lead ion (r = 1.21 Å.) is very similar in size to the strontium ion (r = 1.13 Å.). Therefore, although the higher polarizability of the lead ion might be expected to give some additional positive contribution to the enthalpies of mixing, we shall compare our results with those for the strontium nitrate–alkali nitrate systems.[12] Such a comparison is given in Table IV.

Table IV: Limiting Enthalpies of Solution in Liquid Alkali Chloride–Lead Chloride Systems, Compared with Values for Undercooled Strontium Nitrate in the Alkali Nitrates (from ref. 12)[a]

Chlorides	Enthalpy of solution (655–665°) $PbCl_2$ in Alk-Cl	Alk-Cl in $PbCl_2$	Nitrates	Enthalpy of solution (450°) $Sr(NO_3)_2$ in Alk-NO_3
Li–Pb	+1.6	+0.8	Li–Sr	>0
Na–Pb	(−0.25)	−0.5	Na–Sr	−0.25
K–Pb	(−5)	−4.2	K–Sr	−2.25
Rb–Pb	(−8)	−5.8	Rb–Sr	−3.50
Cs–Pb	−9.8	−7.1	Cs–Sr	−4.85

[a] Data in kcal./mole; values in parentheses are estimated.

The table shows that there is, indeed, a high degree of analogy between the two sets of data. For example, in both sets the lithium systems have positive enthalpies of mixing, the sodium systems are slightly negative, and there is a clear trend toward more negative values as the size of the alkali ion is increased. On the other hand, numerically the new chloride data are larger than the nitrate values by a factor of the order of 2. Interestingly enough, a ratio of this magnitude is found also between the enthalpies of mixing in most of the recently investigated alkali chloride systems[13] when compared with the corresponding nitrates.[2]

In the case of the alkali nitrate–alkaline earth nitrates, it is found that the limiting heats of solution vary in a nearly linear manner with two nondimensional size parameters, namely, $[(r^+ - r^{+2}/2)/(d_1 + d_2)]^2$ [12] and $[(r^+ - r^{+2})/(d_1 + d_2)]$.[14] Here, r^+ and r^{+2}

(12) O. J. Kleppa, *J. Phys. Chem.* **66**, 1668 (1962).

(13) L. S. Hersh and O. J. Kleppa, to be published.

(14) F. G. McCarty, L. S. Hersh, and O. J. Kleppa, *J. Chem. Phys.*, **41**, 1522 (1964).

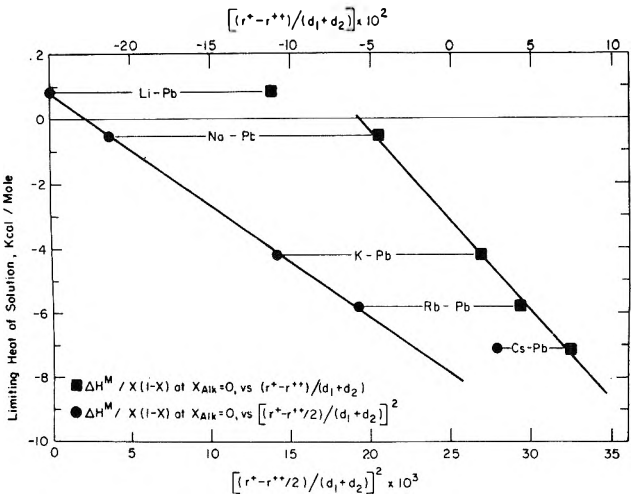

Figure 2. Plots of the limiting heats of solution of liquid alkali chlorides in lead chloride *vs.*: (1) the size parameter $(r^+ - r^{2+})/(d_1 + d_2)$; (2) the size-charge parameter $[(r^+ - r^{2+}/2)/(d_1 + d_2)]^2$.

are the ionic radii of the cations of charge 1 and 2, respectively, while d_1 and d_2 are the sums of the radii of anion and cation. To a first approximation similar relationships appear to apply for the lead chloride–alkali chloride systems, as is illustrated in Fig. 2. Note, however, that the observed linear relationships tend to break down for extreme values of the size parameters, *i.e.*, in one case for lithium–lead and in the other for cesium–lead. At the present time our use of these parameters is completely empirical in nature. It appears that recent, unpublished theoretical work by Davis[15] may provide a theoretical justification for the parameter $[(r^+ - r^{+2})/(d_1 + d_2)]$.

Complex Species. We mentioned by way of introduction that the lead chloride–alkali chloride liquid systems have been explored in the past by a wide range of different physicochemical methods. Many of these earlier investigations have been devoted to the problem of the presence or nonpresence of complex ionic species in the melts. In the course of time the presence of one or more of the following ions have all been postulated: $PbCl^+$, $Pb_2Cl_6^-$, $PbCl_3^-$, $PbCl_4^{-2}$, $PbCl_5^{-3}$, $PbCl_6^{-4}$. We want to re-examine this problem briefly in the light of our new enthalpy data, and refer for this purpose again to Fig. 1. This figure shows that the enthalpies of mixing for the five systems covered in the present work fall into two distinct groups. On the one hand we have the lithium–lead chloride and sodium–lead chloride systems. These have relatively small enthalpies of mixing, lithium–lead being positive and sodium–lead slightly negative. In both cases the interaction parameter is a slowly varying linear function of composition. On the other hand we have the remaining three systems for which the enthalpies of mixing are fairly strongly negative. For these the plot of the interaction parameter *vs.* composition shows a noticeable departure from linearity. This behavior is particularly evident for cesium–lead chloride, for which our results cover the complete range in composition. In this case the interaction parameter appears to have a shallow minimum near 75 mole % cesium chloride.

The two groups of systems correlate with the character of the equilibrium phase diagram. Thus, the phase diagrams for lithium–lead chloride and sodium–lead chloride are of the simple eutectic type, while the remaining three systems have several "interionic compounds."[3] These are the systems most likely to contain complex ionic species even in the liquid state. This tendency undoubtedly will be most pronounced for cesium–lead chloride, which has the largest negative enthalpy of mixing.

In their calorimetric study of the binary alkali nitrates, Kleppa and Hersh[2] noted a correlation between the magnitude of the interaction parameter and its deviation from linearity. This was interpreted, in terms of the quasi-chemical theory of solutions, to indicate "short range order" among the two different cations. For lead chloride–cesium chloride both the (negative) interaction parameter and the deviation from linearity are substantially larger than for the binary nitrates. Furthermore, the deviation is no longer, as in the nitrates, centered around the 50:50 composition but is shifted toward the cesium-rich side, with a maximum near 70 mole % cesium chloride.

For mixtures with strong interaction it is difficult to make a clear distinction between the concepts of "short range order" and of "complex formation." We propose that the departures of the interaction parameter in the potassium–lead, rubidium–lead, and cesium–lead chloride systems from linear behavior may in fact be related to the formation of complex, anionic species in these mixtures. If this interpretation is correct, the location of the maximum deviation near 70 mole % cesium chloride may be significant and may point toward the existence of species such as $PbCl_4^{-2}$ (67% CsCl), $PbCl_5^{-3}$ (75%), and/or possibly even $PbCl_6^{-4}$ (80% CsCl). On the other hand, it seems difficult to reconcile our enthalpy data with species containing less than four chlorides per lead ion, such as, *e.g.*, $PbCl_3^-$. It is believed that the uncertainty in the location of the maximum reflects the

(15) H. T. Davis, *J. Chem. Phys.*, in press.

relatively low stability of the lead chloride complex(es), and it would be of interest to investigate, by the calorimetric method, other mixtures in which the complex species has greater stability. For this reason we have recently initiated a study of the magnesium chloride–alkali chloride liquid systems.

Entropy of Mixing. Unfortunately, the published literature contains no detailed thermodynamic data on the cesium chloride–lead chloride liquid mixtures. However, for the remaining four systems, free energy data have been published in recent years. These were obtained in vapor pressure work by Barton and Bloom[16] (potassium–lead only), and in the mentioned e.m.f. studies by Lantratov and Alabyshev,[5] and by Markov, Delimarskii, and Panchenko.[6] The vapor pressure results are in qualitative agreement with the e.m.f. data. However, since the former were obtained near 900° while the latter were determined in the 600–700° region, we shall here compare our results with the e.m.f. values only.

In the two e.m.f. investigations related, but still somewhat different, experimental methods were applied. Thus, Lantratov and Alabyshev used a formation cell, similar to the one adopted by Hildebrand and Salstrom in their classical study of the silver bromide–alkali bromide systems.[17] Markov, Delimarskii, and Panchenko, on the other hand, used the decomposition potential method. This appears to be quite reliable for the study of pure salts. However, due to polarization effects, it tends to be associated with some error in mixed systems. We give in Fig. 3 excess free energy data for lead chloride, $\bar{G}^{E}_{PbCl_2}$, derived from the two e.m.f. investigations. As expected, the data of Markov, Delimarskii, and Panchenko show somewhat greater experimental scatter than those of Lantratov and Alabyshev. But, on the whole, there is reasonable agreement between the two studies. We have not included in Fig. 3 the earlier e.m.f. data for lead–potassium chloride of Hildebrand and Ruhle,[4] whose values of the excess free energy are significantly more negative than those found in the more recent Russian investigations.

In the same figure we have included curves for the partial excess enthalpies of lead chloride, $\bar{H}^{E}_{PbCl_2}$, calculated from our own integral data. While some uncertainty tends to be associated with partial heats derived from integral data, we estimate that the errors in our partial enthalpies probably are less than 10%. The figure illustrates the extensive analogy between the excess free energies and the excess enthalpies, and it is noteworthy that in all cases the enthalpies are more positive than the excess free energies, *i.e.*, the excess entropies are *positive*. This is of very considerable interest, in view of the fact that four of the five systems have *negative* enthalpies of mixing. In this respect the considered systems differ from most simple mixtures of nonelectrolytes, for which the excess thermodynamic quantities usually have the same sign.

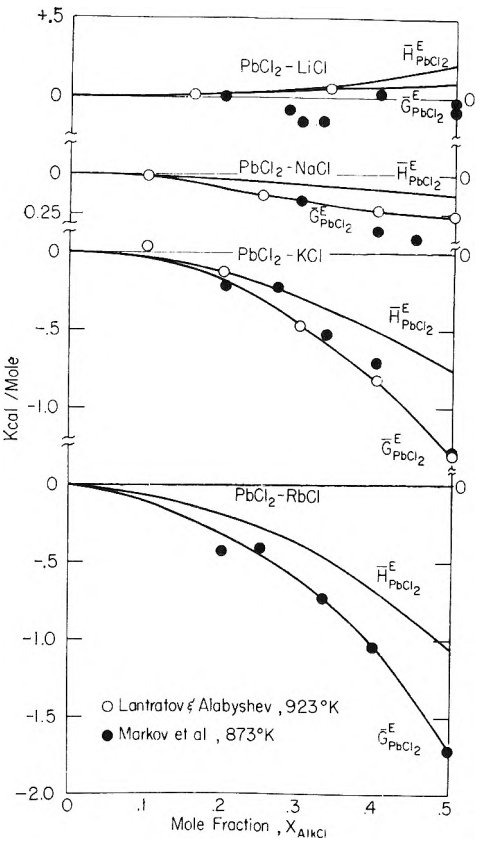

Figure 3. Partial excess enthalpies of lead chloride ($\bar{H}^{E}_{PbCl_2}$) from the present work compared with excess free energies ($\bar{G}^{E}_{PbCl_2}$) from e.m.f. investigations.

From the data given in Fig. 3 we have calculated the partial excess entropies of lead chloride, $\bar{S}^{E}_{PbCl_2}$, which are plotted against composition in Fig. 4. In constructing this figure we have, where data were available, preferred the free energies of Lantratov and Alabyshev. Again, the mixtures fall into two distinct groups. Let us first consider the weak interaction systems, lead–lithium chloride and lead–sodium chloride. For these the excess entropies are quite small, the values of $\bar{S}^{E}_{PbCl_2}$ at $X = 0.5$ being about +0.1 (±0.1?) and +0.2 cal./deg./mole, respectively. To a first approximation these mixtures, accordingly, may be considered to be "Hildebrand regular solutions,"

(16) J. L. Barton and H. Bloom, *Trans. Faraday Soc.*, **55**, 1792 (1955).

(17) J. H. Hildebrand and E. J. Salstrom, *J. Am. Chem. Soc.*, **54**, 4257 (1932).

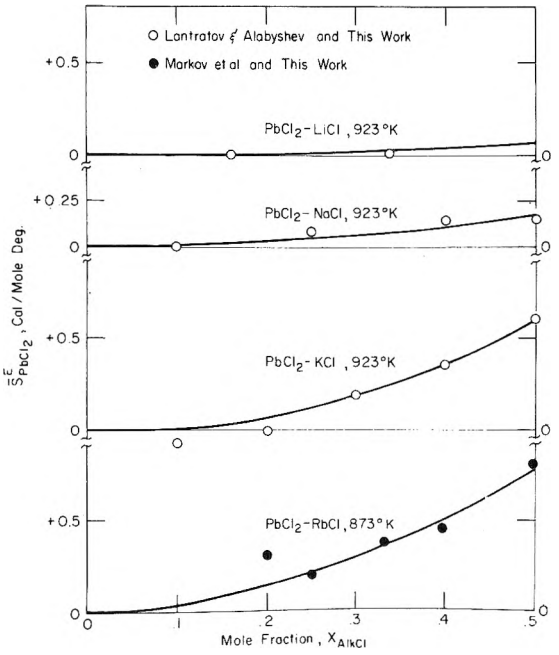

Figure 4. Partial excess entropies of lead chloride ($\bar{S}^{E}_{PbCl_2}$) plotted against mole fraction.

or, from the point of view of fused-salt solution chemistry, to conform to the Temkin model.[18] In this model the process of mixing is visualized as a randomization of the two types of cations, independent of the charge on the two ions. Our conclusion regarding the entropy of mixing for these two systems parallels that previously reached by Førland for liquid AgBr–$PbBr_2$ and for $CaCO_3$–Na_2CO_3.[7]

When we go on to consider the strong interaction systems, lead–potassium and lead–rubidium chloride, the situation is different. In these mixtures the values of $\bar{S}^{E}_{PbCl_2}$ at $X = 0.5$ are about +0.6 and +0.8 cal./deg./mole, respectively, *i.e.*, substantially *larger* than predicted by the simple Temkin model. It is noteworthy that these are systems in which the tendency toward complex formation presumably is fairly pronounced. Thus, one might intuitively have anticipated departures from random mixing and *negative* excess entropies.

In solutions of nonelectrolytes and of metals it is commonly found that positive excess entropies are associated with positive excess volumes. According to Scatchard, who was the first investigator to consider this problem in some detail,[19] the volume change on mixing should contribute to the (excess) entropy a term of the order of $(\alpha/\beta)V^{E}$. Here α denotes the thermal coefficient of expansion for the mixture and β is the isothermal compressibility. Detailed information is not available which permits a precise evaluation of α/β for the considered mixtures. However, for ionic liquids this ratio commonly is of the order of 0.1–0.3 cal./deg./cm.^{3}.

For the lead chloride–alkali chloride liquid mixtures, approximate excess volumes can be read from a graph recently published by Bloom.[3] The graph gives the molar volumes at 720°, and we estimate the following values of V^{E} (cm.^{3}/mole) at the 50:50 composition: Pb–Na, 0.3; Pb–K, 0.8; Pb–Rb, 1.5; Pb–Cs, 2.0. Since the data are referred to a temperature well below the melting points of sodium chloride and potassium chloride, the first two values must be considered to be quite uncertain. Nevertheless, it is unmistakable that the signs are positive and that the trend of the excess volumes parallels that of the excess entropies. It seems highly desirable to give further attention to this correlation in the future.

Finally, we want to comment briefly on entropy calculations based on quasi-lattice models. It is well known that in the solid state impurity "molecules" (say $PbCl_2$) of charge structure different from that of the host lattice (say NaCl) will give rise to local departures from electroneutrality. However, electroneutrality can be restored through the creation of vacancies. Førland carried the notion of distinct vacancies into the liquid state and made use of them in statistical calculations based on solid-like models.[7] Our entropy data for the lead chloride–alkali chloride liquid mixtures cannot be reconciled with the mentioned models.

Acknowledgments. We want to acknowledge that the spectrochemical analyses were performed by Miss M. C. Batchelder. This work has been supported by the National Science Foundation (GP-1993) and by the Office of Naval Research (Nonr-2121 (11)). General support of the Institute for the Study of Metals by the Advanced Research Projects Agency also is acknowledged.

(18) M. Temkin, *Acta Physicochim. URSS*, **20**, 411 (1945).
(19) G. Scatchard, *Trans. Faraday Soc.*, **33**, 160 (1937).

Fluorocarbon Solutions at Low Temperatures. IV. The Liquid Mixtures $CH_4 + CClF_3$, $CH_2F_2 + CClF_3$, $CHF_3 + CClF_3$, $CF_4 + CClF_3$, $C_2H_6 + CClF_3$, $C_2H_6 + CF_4$, and $CHF_3 + CF_4$

by Ian M. Croll and Robert L. Scott

Contribution No. 1711 from the Department of Chemistry, University of California, Los Angeles, California 90024 *(Received July 25, 1964)*

Total vapor pressures have been measured for seven binary liquid mixtures, and from these measurements equations for the excess Gibbs free energy have been derived, yielding the following values for G^E/cal. at $x = 0.5$: $CH_4 + CClF_3$ at 105.1°K., 62; $CH_2F_2 + CClF_3$ at 178.7°K., 204; $CHF_3 + CClF_3$ at 178.2°K., 123; $CF_4 + CClF_3$ at 145.2°K., 26; $C_2H_6 + CClF_3$ at 178.7°K., 67; $C_2H_6 + CF_4$ at 150.6°K., 169; and $CHF_3 + CF_4$ at 145.2°K., 140. The liquid–liquid miscibility diagram for $C_2H_6 + CF_4$ has been measured; the critical solution point is at $T_c = 150.1$°K., $x_c = 0.50$. The theoretical significance of these results is discussed.

Introduction

The work reported in this paper is part of a continuing research program on fluorocarbon solutions; previously we have reported[1,2] vapor pressures and phase diagrams for the liquid binary systems $CH_4 + CF_4$, $CH_4 + Kr$, $CHF_3 + CF_4$, $CH_2F_2 + CHF_3$, $Xe + CHF_3$, $C_2H_6 + C_2F_6$, $C_2H_6 + CHF_3$, and $CHF_3 + C_2F_6$. In this paper we report similar work on the additional systems $CF_4 + CClF_3$, $CHF_3 + CClF_3$, $CH_2F_2 + CClF_3$, $CH_4 + CClF_3$, and $C_2H_6 + CClF_3$, together with additional studies on the systems $CHF_3 + CF_4$ and $C_2H_6 + CF_4$. Moreover, these vapor pressure data, together with those of the earlier papers, have all been processed using the computer programs recently developed by Myers and Scott.[3]

Experimental

Materials. Experimental samples of CF_4 (perfluoromethane), CHF_3 (trifluoromethane), CH_2F_2 (difluoromethane), and $CClF_3$ (chlorotrifluoromethane) were donated by the Jackson Laboratories of E. I. du Pont de Nemours and Co. The samples of CF_4 were purified by repeated passage over activated charcoal held at solid CO_2 temperatures. The samples of CHF_3, CH_2F_2, and $CClF_3$ were further purified by partial distillation, the distillate being rejected. Phillips research grade methane and ethane were used without further purification. The last traces of air were removed from all samples just prior to use by pumping while alternately freezing and melting. Liquids for low temperature baths were laboratory grade materials without further purification.

Apparatus and Experimental Procedure. The vacuum system used was essentially that described by Thorp and Scott.[1] The system was evacuated by a Welch Duo-seal oil pump in conjunction with a two-stage mercury diffusion pump. The manifold pressure was determined by means of a McLeod gauge.

Gas samples were introduced into storage bulbs through a gas purification train. A Toepler pump, equipped with a 0.5-l. cylinder whose volume was calibrated to a reference mark and a side arm for measuring the pressure of its contents, was provided to transfer samples of gases from storage to the experimental vessels and for the measurement of the amount of material transferred.

An eight-junction copper–constantan thermopile, referred to a bath of melting ice, was used for tempera-

(1) N. Thorp and R. L. Scott, *J. Phys. Chem.*, 60, 670, 1441 (1956).
(2) I. M. Croll and R. L. Scott, *ibid.*, 62, 954 (1958).
(3) D. B. Myers and R. L. Scott, *Ind. Eng. Chem.*, 55, 43 (1963).

ture measurement. The bulk of the thermoelectric e.m.f. was balanced by a calibrated variable voltage supply, and the residual e.m.f. was measured with a 2.5-mv. range Brown recording potentiometer. The temperature scale was calibrated against the triple point of methane and the vapor pressures of oxygen, methane, and ethane. Temperatures could be measured to a precision of 0.02°, and were considered accurate to 0.1°.

Temperature control for the determination of the mutual solubility of the C_2H_6–CF_4 system was obtained by refluxing mixtures of methane and propane. The refluxing bath was held in a dewar flask whose main features were a relatively long neck (30 cm.), which reduced end effects and thus allowed clear vision through the vessel by minimizing moisture condensation on the exterior, and a side arm leading to a cold finger filled with liquid nitrogen which acted as a condenser.

The bath was magnetically stirred, and small reductions in temperature were achieved by reducing the pressure above the bath with an aspirator. Large temperature changes were obtained by varying the composition of the refluxing mixtures. The temperature control achieved in this manner was adequate for short periods of time, but a slight drift in composition due to loss of methane from the system required periodic additions of methane.

The method of changing temperature by varying bath composition was time consuming, and temperature control for solubility measurements of subsequent systems was achieved in another manner. A Pyrex inner container with a surrounding jacket which could be evacuated through a stopcock was placed in a flat-bottomed dewar flask which had a pair of diametrically opposed unsilvered strips down its sides to allow vision through the apparatus. The dewar flask was filled with liquid nitrogen as a refrigerant. A small nichrome wire heater was placed in the bottom of the inner container which held the $CClF_3$ (Freon 13) used as the liquid bath. $CClF_3$ was chosen because of its wide liquid range (92–192°K.), its relatively low viscosity near the freezing point, and its inert chemical nature. To make up the liquid bath, a small amount of dry air was allowed into the jacket of the inner container to increase the rate of heat flow to the liquid nitrogen bath. $CClF_3$ was then passed into the inner container where it condensed. The jacket was then evacuated.

The mechanical action of the moving carriage of the recording potentiometer was utilized to open and close the primary circuit of an electronic relay at preselected temperatures in order to activate the heater circuit. By use of this procedure, a preselected bath temperature could be easily obtained and could be maintained indefinitely to ±0.05°.

Temperature control for vapor pressure measurements was obtained by a modification of the refluxing bath method. The pressure of the bath was controlled by a conventional distillation manostat which was connected through a cold trap to a vacuum pump. A ballast tank was provided to damp out minor pressure fluctuations in the system. One-component baths were used so that temperature control would not be affected by loss of material. Methane was used at the lowest temperatures, ethylene at intermediate temperatures, and propane at the highest temperatures. By use of this method the temperature could be controlled to ±0.05° for an indefinite period of time, and to ±0.02° for shorter periods.

The experimental vessel of Thorp and Scott[1] was used to investigate mutual solubilities. It consisted of a capillary stem leading to a sample-holding bulb of about 2 cm.^{3} volume. During operation the bulb was immersed in the low temperature bath, and a sample of gas was withdrawn from storage into a Toepler pump where its pressure (always below 20 cm.) was measured at a known volume. The sample was then transferred to the experimental vessel, where it condensed. Small amounts of the second component were added in a similar manner. Mixtures were allowed to evaporate back into the Toepler pump and were recondensed into the experimental vessel before making observations.

The mole fraction composition of the liquid mixture was taken to be the ratio of the gas pressures as measured in the Toepler pump. The volume of the experimental vessel was less than 10% of the volume of the Toepler pump. The precision of the composition was approximately ±0.005 mole fraction. Liquid–liquid solubility data were obtained by varying the temperature of the bath until two phases were observed to appear on cooling and disappear on warming.

The method of measuring vapor pressure was that described by Thorp and Scott.[1] The sample holder volume was about 2 cm.^{3}, and it was closed by a thin, slightly concave, glass membrane. At a reproducible pressure differential, the membrane clicked audibly, and a sudden displacement could be observed visually. The click gauge was calibrated at each working temperature, since the calibration was found to change with temperature (by 2 mm. in 100°).

The experimental vessel was loaded in the same manner as in the solubility measurements. The pressure on the upper side of the click gauge was varied until it operated, and the applied pressure read on a mercury manometer to the nearest millimeter. Several read-

ings were made, with both increasing and decreasing applied pressure. From the calibration of the click gauge the vapor pressure could be calculated with an estimated accuracy of 2 mm.

The mixtures were made up, with a precision of ±0.005 mole fraction, in the same manner as for solubility measurements. For systems with large differences in vapor pressure of the pure components, practically all of the vapor was of the lower boiling component. Although the vapor space above the liquid was small, this results in a deviation of the liquid composition from that calculated. This composition error is greatest when the amount of the lower boiling component is smallest. The magnitude of this effect is somewhat reduced by the fact that the vapor pressure above the liquid is generally low in this region. However, when the vapor pressure of mixtures containing small amounts of the lower boiling component is considerably higher than the vapor pressure of the pure high boiling constituent (as in the C_2H_6 + CF_4, CHF_3 + CF_4, and CH_2F_2 + $CClF_3$ systems), this error can be as large as 0.01 mole fraction.

Results

Liquid–Liquid Phase Diagrams. The solubility measurements[4] on the system C_2H_6 + CF_4 are shown in Fig. 1. The critical solution temperature is 150.1°K. The phase diagram is symmetrical within experimental error, so the critical mole fraction may be taken as $(x_1)_c = (x_2)_c = 0.50$.

In addition, the unmixing temperatures of three other systems were determined near $x = 0.5$ and are shown in Table I.

Table I: Solubility Measurements Near $x = 0.5$

	System	Mole fraction x_2	$T_{unmixing}$, °K.
II	CH_2F_2 + $CClF_3$	0.493	178.0
III	CHF_3 + $CClF_3$	0.504	118.0
VII	CHF_3 + CF_4	0.592	131.4

These unmixing temperatures must be very nearly the same as the critical solution temperatures. The observed unmixing temperature for CHF_3 + CF_4 at $x_2 = 0.59$ is 0.6° higher than the unmixing temperature of 130.8°K. at $x = 0.60$ reported by Thorp and Scott[1]; we have not ascertained whether this small discrepancy is due to differences in purity of materials or to differences in temperature calibration.

Vapor Pressures and Excess Free Energies. Figures 2–8 show the measured total vapor pressures for the seven binary systems studied. The circles are the experimental points, while the full curves are those calculated in the data processing computer program.

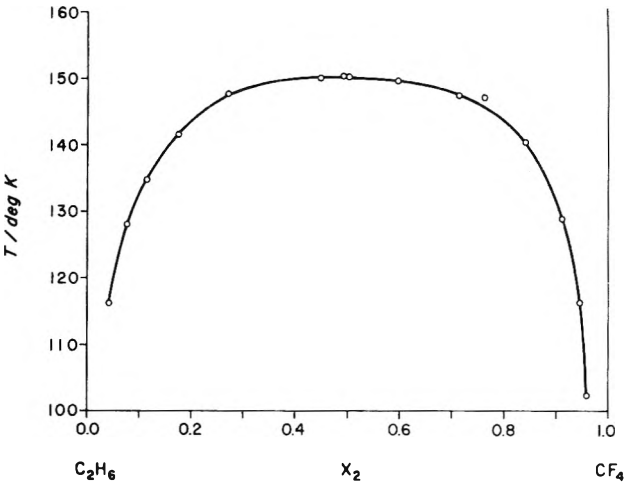

Figure 1. Liquid–liquid phase diagram for the system C_2H_6 + CF_4.

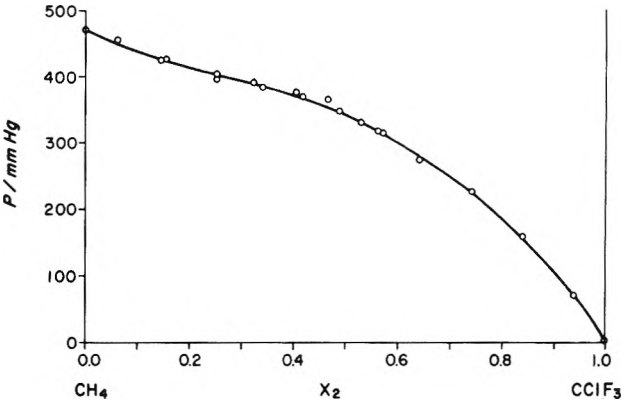

Figure 2. Total vapor pressure for the system CH_4 + $CClF_3$ at 105.1°K. The solid curve is calculated from eq. 1 using the parameters given in Table II.

The experimental data were processed by the computer program CH08B developed by Myers and Scott.[3] This program, a modification of the least-squares procedure proposed by Barker,[5] evaluates the set of coefficients α in an equation for the molar excess Gibbs free energy $\bar{G}^E$

$$\bar{G}^E/RT = x_1x_2[\alpha_0 + \alpha_1(x_1 - x_2) + \alpha_2(x_1 - x_2)^2 + \ldots] \quad (1)$$

(4) All the data shown in Fig. 1–8 (as well as the earlier data of ref. 1 and 2) will be found in numerical form in the Ph.D. dissertation of I. M. Croll, University of California, Los Angeles, Calif., 1958.

(5) J. A. Barker, *Australian J. Chem.*, 6, 207 (1953).

where x_1 and x_2 are the mole fractions of components 1 and 2.

Differentiation of eq. 1 yields the excess chemical potentials $\mu_1^E = RT \ln \gamma_1$ and $\mu_2^E = RT \ln \gamma_2$ (where the γ values are the activity coefficients). Of special interest are the limiting values $\ln \gamma_1^*$ and $\ln \gamma_2^*$ evaluated at infinite dilution

$$\ln \gamma_1^* = \lim_{x_1 \to 0} (\ln \gamma_1) = \alpha_1 - \alpha_2 + \alpha_3 - \ldots \quad (2a)$$

$$\ln \gamma_2^* = \lim_{x_2 \to 0} (\ln \gamma_2) = \alpha_1 + \alpha_2 + \alpha_3 + \ldots \quad (2b)$$

In practice the series in eq. 1 converges slowly, and an arbitrary decision about truncation must be made. In all but two systems studied, no significant improvement was obtained by including more than three coefficients, so the results in Table II are reported uniformly with the three coefficients α_0, α_1, and α_2. The results of recalculations of the previously reported measurements of Thorp and Scott are also included in Table II.

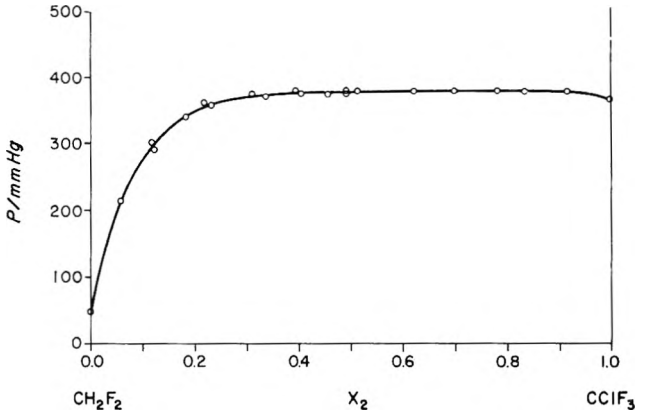

Figure 3. Total vapor pressure for the system CH_2F_2 + $CClF_3$ at 178.7°K. The solid curve is calculated from eq. 1 using the parameters given in Table II.

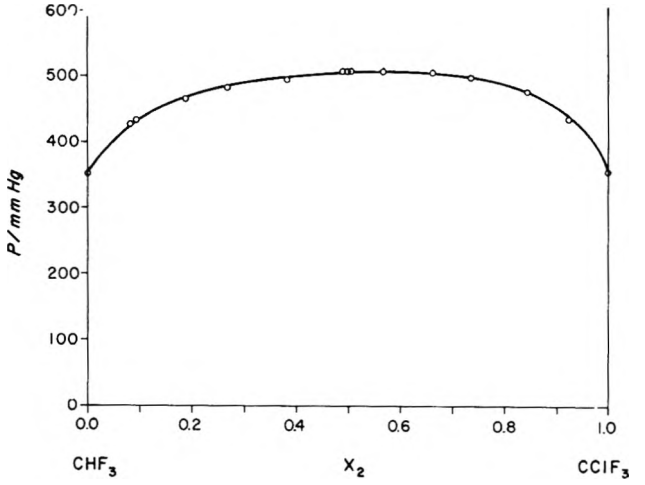

Figure 4. Total vapor pressure for the system CHF_3 + $CClF_3$ at 178.2°K. The solid curve is calculated from eq. 1 using the parameters given in Table II.

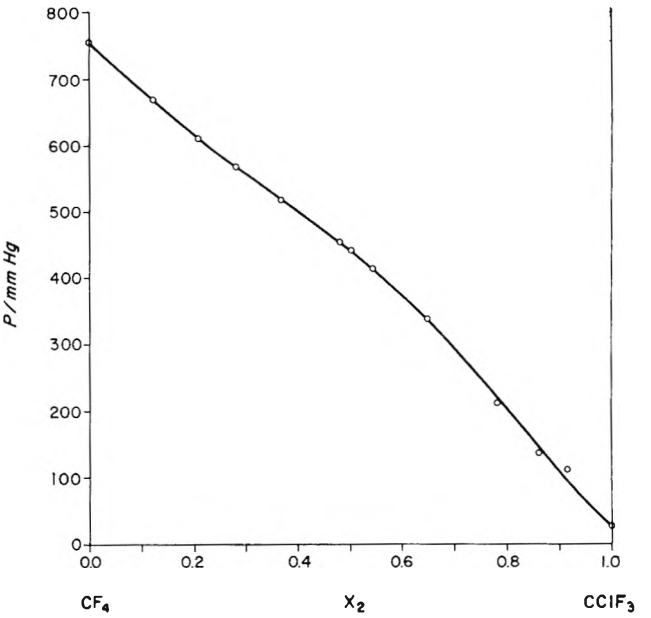

Figure 5. Total vapor pressure for the system CF_4 + $CClF_3$ at 145.2°K. The solid curve is calculated from eq. 1 using the parameters given in Table II.

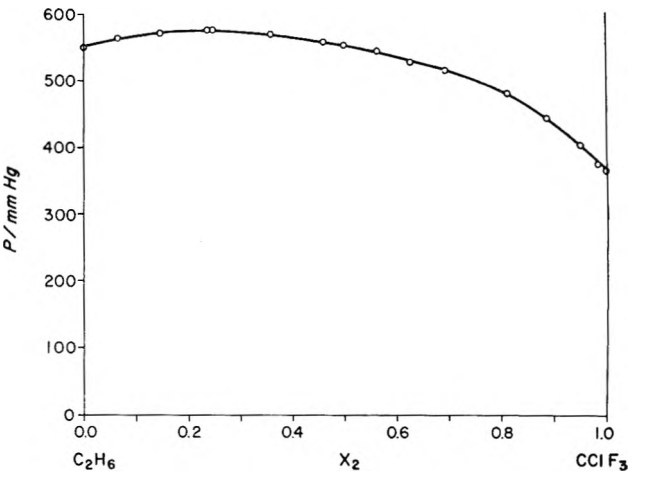

Figure 6. Total vapor pressure for the system C_2H_6 + $CClF_3$ at 178.7°K. The solid curve is calculated from eq. 1 using the parameters given in Table II.

Some comments on the computations may be helpful in interpreting the results shown in Table II.

(1) The Barker method and our program CH08B include corrections for gas imperfections and the effect of applied pressure upon vapor pressure. Table II lists the corrections used: $W_1 = (B_{11} - V_1)/RT$, $W_2 = (B_{22} - V_2)/RT$, and $\delta_{12} = (2B_{12} - B_{11} - B_{22})/RT$, where the B values are second virial coefficients (esti-

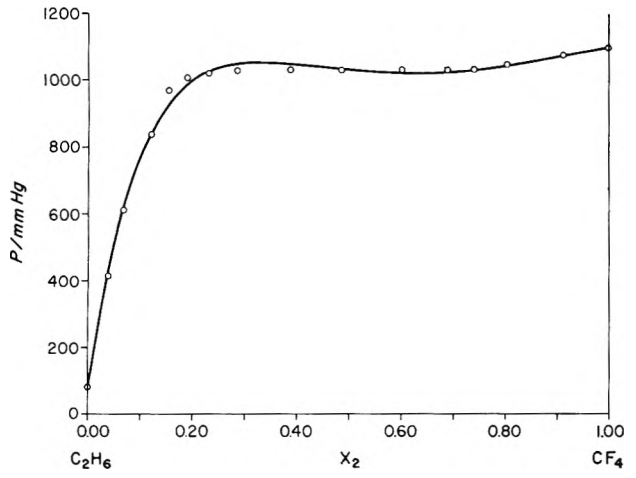

Figure 7. Total vapor pressure for the system C_2H_6 + CF_4 at 150.6°K. The solid curve is calculated from eq. 1 using the parameters given in Table II.

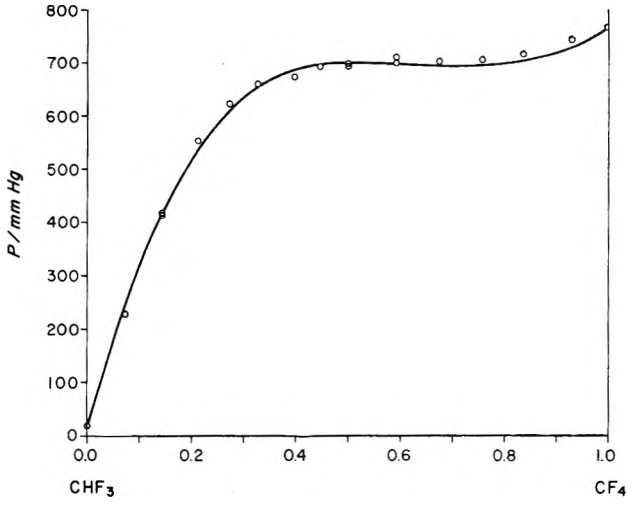

Figure 8. Total vapor pressure for the system CHF_3 + CF_4 at 145.2°K. The solid curve is calculated from eq. 1 using the parameters given in Table II.

mated using the Berthelot equation) and the V values are molar volumes of the liquids. However, the effect of these corrections, even at the highest pressures encountered, was extremely small, the largest being a change of 0.014 in α_1 for C_2H_6 + CF_4. Since the standard deviations of the coefficients are of this magnitude, the corrections might well have been neglected.

(2) The computer program yields the standard deviation σ_P for the set of observed pressures as well as standard deviations for the α values. These σ values range from 0.005 to 0.053 for α_0, from 0.009 to 0.10 for α_1, and from 0.015 to 0.13 for α_2; in every case the smallest deviations are for system VIIIB (CH_4 + CF_4 at 108.5°K.) and the largest for system

Table II: Excess Free Energy Coefficients from Vapor Pressures

	I	II	III	IV	V	VI	VII	VIII		IX	X	XI	XII	XIII
	CH_4 + $CClF_3$	CH_2F_2 + $CClF_3$	CHF_3 + $CClF_3$	CF_4 + $CClF_3$	C_2H_6 + $CClF_3$	C_2H_6 + CF_4	CHF_3 + CF_4	CH_4 + CF_4		CH_4 + Kr	CF_4 + Kr	CH_2F_2 + CHF_3	CHF_3 + C_2F_6	C_2H_6 + C_2F_6
T/°K.	105.1	178.7	178.2	145.2	178.7	150.6	145.2	105.5	108.5	115.5	117.1	175	175.4	176
$W_1 \times 10^5$	7.87	6.2	5.53	5.96	6.00	9.90	10.10	7.87	6.95	5.74	11.2	6.6	5.1	6.25
$W_2 \times 10^5$	34.50	7.20	7.26	13.00	7.20	5.34	5.96	15.20	13.90	7.54	7.26	5.1	8.6	8.45
$\delta_{12} \times 10^5$	10.50	0.0	0.00	0.99	0.00	0.73	0.56	1.15	0.99	0.14	0.65	0.0	0.1	0.00
α_0	1.19	2.295	1.394	0.37	0.750	2.25	1.95	1.80	1.62	0.22	1.25	−0.08	1.66	1.79
α_1	0.36	−0.15	−0.14	0.20	−0.03	0.02	−0.41	0.29	0.41	0.10	0.30	0.12	−0.04	−0.32
α_2	0.21	0.29	0.25	−0.14	0.08	0.08	0.02	−0.01	−0.10	0.06	0.23	−0.12	0.15	−0.00
ln γ_1	1.1	2.7	1.8	0.0	0.9	2.3	2.3	1.5	1.1	0.2	1.1	−0.3	1.8	1.5
ln γ_2	1.8	2.4	1.5	0.4	0.8	2.4	1.5	2.1	1.9	0.4	1.8	−0.1	1.8	2.1
σ_P/mm.	4.9	3.7	3.2	7.5	1.8	16.2	11.2	4.8	1.8	4.7	5.4	4.3	4.1	5.7
$100\sigma_P/P_{x=1/2}$	1.4	1.0	0.6	1.7	0.3	1.6	1.6	1.2	0.3	0.8	0.6	1.1	2.7	1.0

XI (CH_2F_2 + CHF_3). However the truncation of the series in eq. 1 to a trinomial (*i.e.*, the assumption that the truncated series is "correct" and that all the higher α values are exactly zero) makes these misleading as measures of reliability. The least-squares procedure leads further to standard deviations for the derived quantities ln γ_1^* and ln γ_2^* which are unrealistically small (less than 0.1). These limiting activity coefficients are meaningful thermodynamic properties of the mixtures and should not be artifacts of the assumed equation; yet they can fluctuate wildly as one computes them successively for the 1, 2, 3, 4, or 5-coefficient equations. (Scott and Dunlap[6] have discussed this problem of series truncation in relation to the evaluation of second virial coefficients.) To avoid this misleading impression of reliability we have suppressed the σ-values except for that of the vapor pressure itself. A measure of the relative precision is the ratio of this standard deviation to the vapor pressure of the equimolar solution $\sigma_P/P_{x=1/2}$.

(3) The inclusion of a coefficient α_3 for the system CHF_3 + CF_4 reduces the standard deviation σ_P of the observed vapor pressure from 11.2 to 4.9 mm. The system is not far above the critical solution temperature and four coefficients (1.920, −0.391, 0.015, −0.307) give a much better fit for the very flat vapor pressure curve.

Discussion

For many mixtures of nonelectrolytes, a reasonable zeroth approximation to the excess free energy per mole is the regular solution–solubility parameter equation[7,8]

$$\tilde{G}^E = \frac{x_1\tilde{V}_1 x_2\tilde{V}_2}{x_1\tilde{V}_1 + x_2\tilde{V}_2}(\delta_1 - \delta_2)^2 = (x_1\tilde{V}_1 + x_2\tilde{V}_2)(\delta_1 - \delta_2)^2\phi_1\phi_2 \quad (3)$$

where $\tilde{V}_1$ and $\tilde{V}_2$ are the molar volumes of the two pure liquids; x_1 and x_2, their mole fractions in solution; ϕ_1 and ϕ_2, their volume fractions; and δ_1 and δ_2, their "solubility parameters" (the square roots of the cohesive energy density or energy of vaporization per unit volume).

In 1958, Scott[9] reviewed the published data on fluorocarbon solutions and compared experimental values of the excess free energy with those predicted by eq. 3. For many such solutions, eq. 3 is reasonably adequate, but mixtures of fluorocarbons with aliphatic hydrocarbons are a striking exception, with excess free energies much larger than those corresponding to the factor $(\delta_1 - \delta_2)^2$. It will suffice here to make similar comparisons for the systems reported in this paper.

Table III summarizes the physical properties of the pure liquids: the normal boiling point T_b, the molar heat of vaporization $\Delta\tilde{H}_b^V$ at T_b, together with the molar volume $\tilde{V}$ and the solubility parameter δ at the relevant temperatures.

Table III: Physical Properties of the Pure Liquids

	T_b/ °K.	$\Delta\tilde{H}_{bV}$/ kcal.	T/ °K.	$\tilde{V}_T$/ cm.³	δ_T/ cal.$^{1/2}$ cm$^{-3/2}$
CH_4	111.7	1.96	105	37.0	6.8
CH_2F_2	221.6	5.1[a]	178	42	10.6
CHF_3	189.0	4.23	145	43.5	10.0
			178	46.7	9.3
CF_4	145.1	3.01	145	54.2	7.1
			150	54.9	7.0
$CClF_3$	191.8	3.85	105	57.4	8.9
			145	62.2	7.9
			178	66.5	7.3
C_2H_6	184.5	3.52	150	51.1	8.4
			178	54.3	7.6

[a] Estimated.

Table IV compares the observed free energies with those calculated from eq. 3.

If we use the rato $(\tilde{G}^E_{obsd} - \tilde{G}^E_{eq.\ 3})/RT$ as the measure of the failure of the simple theory, we see that it is the hydrocarbon + fluorocarbon system, C_2H_6 + CF_4, which is by far the most anomalous. In striking contrast to this system, the introduction of one chlorine atom into the otherwise completely fluorinated molecule produces the good agreement (no better can be expected) for mixtures of $CClF_3$ with both CH_4 and CF_4; this difference between CF_4 and $CClF_3$ is hard to explain.

The large excess free energy (169 cal. at 151°K. and $x = 0.5$) for the system C_2H_6 + CF_4 is confirmed by the high critical solution temperature of 150°K. This result is completely consistent with the similar ones for all other mixtures of aliphatic hydrocarbons and fluorocarbons (*e.g.*, CH_4 + CF_4, *n*-C_6H_{14} + *n*-C_6F_{14}), but, unlike the others, this system consists of two liquids of almost equal molar volumes, a feature which simplifies almost all theories of solutions. Prigogine[10]

(6) R. L. Scott and R. D. Dunlap, *J. Phys. Chem.*, **66**, 639 (1962).

(7) J. H. Hildebrand and R. L. Scott, "Solubility of Nonelectrolytes," 3d Ed., Reinhold Publishing Corp., New York, N. Y., 1950.

(8) J. H. Hildebrand and R. L. Scott, "Regular Solutions," Prentice-Hall, Inc., Englewood Cliffs, N. J., 1962.

(9) R. L. Scott, *J. Phys. Chem.*, **62**, 136 (1958).

(10) I. Prigogine, "The Molecular Theory of Solutions," North-Holland Publishing Co., Amsterdam, 1957, p. 420.

Table IV: Observed and Predicted Excess Free Energies

	System	T/°K.	$\tilde{G}^E$/cal. at $x = 1/2$ Observed	$\tilde{G}^E$/cal. at $x = 1/2$ Eq. 3	$\frac{\tilde{G}^E_{obsd} - \tilde{G}^E_{eq.3}}{RT}$	α_1/α_0	α_2/α_0	T_c/°K.
I	$CH_4 + CClF_3$	105.1	62	50	0.06	0.30	0.18	
II	$CH_2F_2 + CClF_3$	178.7	204	139	0.18	−0.07	0.13	*ca.* 178
III	$CHF_3 + CClF_3$	178.2	123	55	0.19	−0.10	0.18	*ca.* 118
IV	$CF_4 + CClF_3$	145.2	26	10	0.06	0.54	−0.39	
V	$C_2H_6 + CClF_3$	178.7	67	1	0.18	−0.04	0.11	
VI	$C_2H_6 + CF_4$	150.6	169	26	0.48	0.01	0.04	150.1
VII	$CHF_3 + CF_4$	145.2	140	101	0.13	−0.21	0.01	130.5

has attributed the large $\tilde{G}^E$ (86 cal. at 110°K. and $x = 0.5$) for the system $CH_4 + CF_4$ to the large difference in molar volumes and has obtained, from his corresponding-states-theory equations, a calculated $\tilde{G}^E = 55$ cal. and for the similar system $Kr + CF_4$, a calculated value even larger than that observed. However, this approach founders on this system $C_2H_6 + CF_4$. Scott[9] has shown that a corresponding-states calculation yields only about 9 cal. for $\tilde{G}^E$ at $x = 0.5$, less than 10% of the observed value. It is impossible to escape the conclusion that the difficulty in accounting for the free energies of these mixtures arises, not from anything in the model of the solution, but rather from the poor approximation that the magnitude of the fluorocarbon–hydrocarbon interaction energy is given by the geometric mean of the hydrocarbon–hydrocarbon and fluorocarbon–fluorocarbon energies.

Thorp and Scott[1] have cited the anomalously large excess free energies for mixtures of CHF_3 with CF_4 and C_2F_6 as evidence for hydrogen bonding in CHF_3. The systems $CH_2F_2 + CClF_3$ and $CHF_3 + CClF_3$ seem to fit in with this hypothesis.

The ratio α_1/α_0 is a measure of the skewness of the excess free energy function and, according to a volume fraction formulation such as eq. 3, should approximate $(\tilde{V}_2 - \tilde{V}_1)/(\tilde{V}_2 + \tilde{V}_1)$. Examination of the α_1 values (or the ratios) shows that the seven systems fall roughly into three groups: I and IV show positive α_1 values or a definite skewing of the excess free energy toward the region rich in the component of smaller molar volume, V and VI are nearly symmetrical ($\tilde{V}_2 \approx \tilde{V}_1$), and only II, III, and VII are skewed in a direction contrary to prediction. Since these three systems are the only ones which have CH_2F_2 or CHF_3 as a component their exceptional behavior may be related to hydrogen bonding.

The ratio α_2/α_0 is a measure of the flattening of the excess free energy curve. The large positive values of α_2/α_1 found[11] for the systems $C_5H_{12} + C_5H_{12}$ and $C_6H_{14} + C_6F_{14}$ near their critical solution temperatures have been attributed to clustering of the components. Our results here, however, cast doubt on this hypothesis since there is no consistency between the magnitude of α_2/α_0 and the nearness to the critical point.

Three of the systems (II, VI, and VII) have very flat regions in the vapor pressure curves, and one might suspect that we had measured the vapor pressure above a two-phase region. Indeed the computed vapor pressure curves (Fig. 3, 7, and 8) do show shallow maxima and minima. In actuality, however, the measurements were always made at temperatures above the critical solution temperatures.

Moreover, for the systems $CH_2F_2 + CClF_3$ (II) and $C_2H_6 + CF_4$ (VI), where the vapor pressure measurements were made very close to the critical temperature, the assumption that the liquid was a one-phase region was checked. For several mixtures in the middle of the composition range where dP/dx is nearly zero, the temperature was lowered after making the vapor pressure measurements, and the onset of phase separation was observed at temperatures about 0.5° below the operating temperatures.

One can attempt to calculate critical compositions and critical solution temperatures from the coefficients α. This requires two assumptions of questionable validity: (a) that the series of eq. 1 may be safely

Table V: Observed and Calculated Critical Values

	System	T_P/°K.	T_c/°K. Calcd.	T_c/°K. Obsd.	x_{1c} Calcd.	x_{1c} Obsd.
II	$CH_2F_2 + CClF_3$	178.7	187	178	0.65	...
III	$CHF_3 + CClF_3$	178.2	116	118	0.72	...
VI	$C_2H_6 + CF_4$	150.6	170	150	0.51	0.50
VII	$CHF_3 + CF_4$	145.2	154	131	0.61	0.57
			139[a]		0.54[a]	

[a] With four coefficients instead of three.

(11) R. D. Dunlap, R. G. Bedford, J. C. Woodbrey, and S. D. Furrow, *J. Am. Chem. Soc.*, **81**, 2927 (1959).

truncated with three coefficients and (b) that the excess free energy $\tilde{G}^E$ is temperature independent ($RT\alpha_n = g_n$ = constant). With these assumptions one obtains the numbers shown in Table V.

In general, the calculated critical solution temperature is higher than the actual. This is what one would expect from equations which cannot reproduce the very nearly flat coexistence curve (and free energy isotherms) in the region of the critical point. We see that the introduction of a fourth coefficient α_3 improves the agreement for $CHF_3 + CF_4$. Better agreement is hardly to be expected; indeed, the good agreement for $CHF_3 + CClF_3$ is almost certainly fortuitous in view of the great difference between the temperature T_P of the vapor pressure measurement and the critical solution temperature T_c. Similar conclusions have been reported by Williamson and Scott[12] for the systems perfluoroheptane + isooctane and perfluoro-*n*-hexane + *n*-hexane.

Acknowledgment. This research was supported by the Atomic Energy Commission.

(12) A. G. Williamson and R. L. Scott, *J. Phys. Chem.*, **65**, 275 (1961).

On the Theory of Imperfect Gases

by Bruce W. Davis[1]

Department of Chemistry, University of California, Riverside, California *(Received July 25, 1964)*

It is demonstrated that Mayer's theory of imperfect gases can be modified into a free volume theory by assuming a pair potential with a rigid sphere cutoff. Further simplifications and approximations yield a "van der Waals-like" equation of state. The resulting equation is

$$\frac{pv}{kT} = 1 + \frac{(b/v)}{[1 - {}^{7}/_{24}(b/v)]^{15/7}} - \frac{a_2}{vkT}$$

where $b = (2\pi/3)\sigma^3(T)$, $\sigma(T) = \sigma(2/(1 + \sqrt{1 + kT/\epsilon}))^{1/6}$, $a_2 = (16\pi/9)\sigma^3\epsilon C_1(T) \exp({}^{8}/_{35}\epsilon/kT)$, and $C_1(T) = [{}^{3}/_{2}(\sigma/\sigma(T))^3 - {}^{1}/_{2}(\sigma/\sigma(T))^9]$. Excellent numerical agreement is found between predicted and observed critical constants for argon. Although the liquid state is not formally included, the theory still gives a good estimate for the argon vapor pressure equation.

Introduction

Mayer's treatment of imperfect gases[2,3] has been well developed and gives, within the limitations of simplifying assumptions, a precise and useful expression for the canonical ensemble partition function. The evaluation of the partition function and related thermodynamic quantities is still relatively difficult so that a practical need for further simplification remains. By introducing a hard sphere cutoff in the pairwise interaction potential, it will be shown that the partition function may be put in the same form as that for a free volume model of liquids or gases. This modification makes no basic change in the problem of solving ir-

(1) Petroleum Research Fund Fellow, 1961–1964.

(2) J. E. Mayer and M. G. Mayer, "Statistical Mechanics," John Wiley and Sons, Inc., New York, N. Y., 1940, Chapter 13.

(3) T. L. Hill, "Statistical Mechanics," McGraw-Hill Book Co., Inc., New York, N. Y., 1956, Chapter 5.

reducible cluster integrals, but it does automatically separate out rigid sphere terms in the solution. In order to illustrate the approach, a comparison of a particularly simple version of the theory is then made with experimental results for argon.

Free Volume Partition Function

The canonical ensemble partition function[2] for a monatomic gas given in terms of irreducible cluster integrals, β_k, is

$$Q = \left[qev \exp\left(\sum_{k \geq 1} \frac{1}{k+1} \beta_k v^{-k} \right) \right]^N \qquad (1)$$

where

$$q = \left(\frac{2\pi mkT}{h^2} \right)^{3/2}$$

and v is the molecular volume ($v \equiv V/N$). Expressing eq. 1 in terms of virial coefficients, $B_n(T)$

$$Q = \left[qev \exp\left(- \sum_{n \geq 2} \frac{1}{n-1} B_n(T) v^{-n+1} \right) \right]^N \qquad (2)$$

Now suppose that there is hard sphere cutoff in the pairwise potential when molecules are separated by a distance $\sigma(v,T)$. This procedure permits the virial coefficients to be split into two parts, respectively, comprising "excluded volume" terms and "internal pressure" terms. In particular

$$\sum_{n \geq 2} \frac{1}{n-1} B_n(T) v^{-n+1} = \sum_{n \geq 2} \frac{\alpha_n}{n-1} \left(\frac{b}{v} \right)^{n-1} - \frac{1}{kT} \sum_{n \geq 2} \frac{1}{n-1} \left(\frac{a_n}{v} \right)^{n-1} \qquad (3)$$

where $b = (2\pi/3)\sigma^3(v,T)$, the α_n's are constants obtainable from calculations for rigid spheres, and the a_n's are in general functions of v and T determined by evaluation of cluster integrals over the region $\sigma(v,T)$ to $+\infty$ using an appropriate pairwise potential. Substituting eq. 3 into eq. 2

$$Q = \left[qev \exp\left(- \sum_{n \geq 2} \frac{\alpha_n}{n-1} \left(\frac{b}{v} \right)^{n-1} + \frac{1}{kT} \sum_{n \geq 2} \frac{1}{n-1} \left(\frac{a_n}{v} \right)^{n-1} \right) \right]^N \qquad (4)$$

If two definitions are made, *viz.*

$$v_f = v \exp\left(- \sum_{n \geq 2} \frac{\alpha_n}{n-1} \left(\frac{b}{v} \right)^{n-1} \right) \qquad (5)$$

and

$$\frac{\varphi}{2} = - \sum_{n \geq 2} \frac{1}{n-1} \left(\frac{a_n}{v} \right)^{n-1} \qquad (6)$$

then eq. 4 can be written

$$Q = \left[qev_f \exp\left(- \frac{\varphi}{2kT} \right) \right]^N \qquad (7)$$

Equation 7 is seen to be formally the same as a free volume partition function for gases or liquids.[4,5] Kirkwood[6] succeeded in casting a rigorous cell theory of liquids into the form of a free volume model. It is interesting that Mayer's theory of imperfect gases can also be made to conform to a free volume representation by such simple means.

Rigid Sphere Equation of State

The rigid sphere equation of state is contained in any complete equation of state derived according to the present model. For this reason the rigid sphere equation of state is discussed separately here.

It is found that

$$\frac{pv}{kT} = \left(\frac{\partial \ln v_f}{\partial \ln v} \right)_{T,N} = 1 + \sum_{n \geq 2} \alpha_n \left(\frac{b}{v} \right)^{n-1} \qquad (8)$$

(rigid spheres)

The α_n values for n up to six are known[7]: $\alpha_2 = 1$, $\alpha_3 = {}^5/_8$, $\alpha_4 = 0.28695$, $\alpha_5 = 0.1103 \pm 0.0003$, and $\alpha_6 = 0.0386 \pm 0.0004$. It has been shown that an excellent approximation to the complete summation, $\sum_{n \geq 2} \alpha_n (b/v)^{n-1}$, is the so-called Padé approximant.[7] It happens that this summation can also be adequately replaced by a binomial. Since no binomial can reproduce all of the known α_n values, a convenient compromise is chosen. The "ersatz" formula for eq. 8 is then

$$\frac{pv}{kT} \cong 1 + \frac{(b/v)}{[1 - {}^7/_{24}(b/v)]^{15/7}} \qquad (9)$$

The efficacy of eq. 9 is tested in Table I by comparing it with rigid sphere values of pv/kT obtained from the six-term virial series, the Padé approximant, and the molecular dynamics results. Equation 9 obviously gives close agreement with the molecular dynamics results although the Padé approximant does better.

Complete Equation of State

The complete equation of state is given by

$$\frac{pv}{kT} = \left(\frac{\partial \ln v_f}{\partial \ln v} \right)_{T,N} - \left(\frac{\partial(\varphi/2kT)}{\partial \ln v} \right)_{T,N} \cong 1 + \frac{(b/v)}{[1 - {}^7/_{24}(b/v)]^{16/7}} - \frac{1}{kT} \sum_{n \geq 2} \left(\frac{a_n}{v} \right)^n \qquad (10)$$

(4) J. O. Hirschfelder, D. Stevenson, and H. Eyring, *J. Chem. Phys.*, **5**, 902 (1937).

(5) T. L. Hill, *J. Phys. Colloid Chem.*, **51**, 1219 (1947).

(6) J. G. Kirkwood, *J. Chem. Phys.*, **18**, 380 (1950).

Table I: Values of pv/kT for a Fluid of Rigid Spheres Obtained from the Six-Term Virial Series, a Padé Approximant, Eq. 9, and Molecular Dynamics Results (MD)[a]

v/v_0	Six-term series	Padé	Eq. 9	MD
1.60	8.95	10.11	10.77	10.17
1.70	7.79	8.55	8.99	8.59
2.00	5.59	5.83	5.97	5.89
3.00	3.01	3.03	3.05	3.05
10.00	1.36	1.36	1.36	1.36

[a] Except for eq. 9, values were taken from ref. 7.

In order to evaluate the a_n's it is necessary to adopt some model for the pairwise potential. A fairly realistic representation can be achieved by using a 6:12 potential which has a suitable hard sphere cutoff. As a good approximation, let us assume that $\sigma(v,T)$ can be replaced by a characteristic distance, $\sigma(T)$, which is a function of temperature only. A good choice for $\sigma(T)$, at least for a dilute gas, is just the distance where the pairwise potential has a value of $+kT$.[8,9]

For this model the pair potential is then represented by

$$r < \sigma(T),\ u(r) = +\infty$$

$$r > \sigma(T),\ u(r) = 4\epsilon\left[-\left(\frac{\sigma}{r}\right)^6 + \left(\frac{\sigma}{r}\right)^{12}\right] \quad (11)$$

where $\sigma(T) = \sigma(2/(1 + \sqrt{1 + kT/\epsilon}))^{1/6}$. It is now fairly simple to find an expression for a_2 from eq. 11. Specifically

$$a_2 = kT2\pi \int_{\sigma(T)}^{\infty}\left[\exp\left(-\frac{u(r)}{kT}\right) - 1\right] r^2\, dr$$

$$= \frac{16\pi}{9}\sigma^3\epsilon c_1(T)\left[1 + {}^8/_{35}\frac{c_2(T)}{c_1(T)}\frac{\epsilon}{kT} + \ldots\right] \quad (12)$$

$$\cong \frac{16\pi}{9}\sigma^3\epsilon c_1(T)\exp\left({}^8/_{35}\frac{\epsilon}{kT}\right)$$

where

$$c_1(T) = \left[{}^3/_2\left(\frac{\sigma}{\sigma(T)}\right)^3 - {}^1/_2\left(\frac{\sigma}{\sigma(T)}\right)^9\right]$$

and

$$c_2(T) = \left[{}^{35}/_8\left(\frac{\sigma}{\sigma(T)}\right)^9 - {}^{42}/_8\left(\frac{\sigma}{\sigma(T)}\right)^{15} + {}^{15}/_8\left(\frac{\sigma}{\sigma(T)}\right)^{21}\right]$$

A "van der Waals-like" equation of state can now be written if a_3 and higher a_n's are ignored, *viz.*

$$\frac{pv}{kT} = 1 + \frac{(b/v)}{[1 - {}^7/_{24}(b/v)]^{{}^{15}/_7}} - \frac{a_2}{vkT} \quad (13)$$

Numerical Comparison of Theory with Experiment

Critical Constants. Argon is chosen as an example for comparison with eq. 13. The parameters for the 6:12 potential for argon are assumed to be those given by Michels, *et al.*,[10] *i.e.*

$$\epsilon/k = 119.8°\text{K.};\quad \sigma = 3.405\ \text{Å}. \quad (14)$$

The critical constants are then calculated using eq. 12, 13, and 14 and the conditions $(\partial p/\partial v)_c = 0$ and $(\partial^2 p/\partial v^2)_c = 0$. The results were obtained by iterative methods and are given in Table II.

Table II: Comparison of Experimental and Calculated Critical Constants

	kT_c/ϵ	$p_c v^*/\epsilon$	v_c/v^*	$p_c v_c/kT_c$
Eq. 13	1.23	0.122	3.62	0.360
Exptl.[a]	1.26	0.116	3.17	0.291

[a] See p. 245 of ref. 9.

Vapor Pressure Equation. Even though the present theoretical considerations do not properly include the liquid state, it is still interesting to ignore this limitation and proceed as if the properties of the liquid were correctly predicted. A particularly sensitive test is the vapor pressure equation which is obtained by equating the Gibbs free energies of the liquid and vapor phases at a particular temperature. It is convenient to carry out calculations for argon at its normal boiling point, assuming that the vapor is only slightly imperfect, *i.e.*, corrected up to the second virial coefficient. It follows that

$$\frac{pv^*}{\epsilon} = \left(1 - \frac{a_2}{v_g kT}\right)\frac{kTv^*}{\epsilon v_f^l} \times$$

$$\exp\left\{-\left[a_2\left(\frac{1}{v_l} - \frac{1}{v_g}\right) + p(v_g - v_l)\right]\Big/kT\right\} \quad (15)$$

where

$$v_g \cong kT/p\left[1 + \frac{bp}{kT} - \frac{a_2 p}{(kT)^2}\right] \quad (16)$$

(7) F. H. Ree and W. G. Hoover, *J. Chem. Phys.*, **40**, 939 (1964).

(8) J. Jeans, "The Dynamical Theory of Gases," Dover Publications, Inc., New York, N. Y., p. 281.

(9) J. O. Hirschfelder, C. F. Curtiss, and R. B. Bird, "Molecular Theory of Gases and Liquids," John Wiley and Sons, Inc., New York, N. Y., 1954, p. 157.

(10) A. Michels, H. Wijker, and H. Wijker, *Physica*, **15**, 627 (1949).

and

$$v_f^l \cong v_l \exp\left\{-\frac{(b/v)}{[1 - 0.2997(b/v)]^{1.043}}\right\} \quad (17)$$

(binomial approximation)

Combining eq. 15, 16, and 17 and evaluating the resulting equation numerically

$$\frac{pv^*}{\epsilon} = 2.80 - \frac{6.95\epsilon}{kT} \quad (18)$$

while the experimental result is[10,11]

$$\frac{pv^*}{\epsilon} = 2.98 - \frac{6.56\epsilon}{kT} \quad (19)$$

Discussion

In this study we have shown that a free volume partition function is obtained from Mayer's theory of imperfect gases when there is a hard sphere cutoff in the pairwise potential. The present approach gave a "van der Waals-like" equation of state similar to one developed by Hirschfelder, Stevenson, and Eyring.[4] It is hoped that eq. 13 will find some utility as an approximate equation of state because of its relative simplicity. Remarkably, this simple equation gives an excellent prediction of the observed critical constants for argon. The theory also yields a reasonable vapor pressure equation for argon even though the liquid state is not formally included.

Acknowledgments. The author gratefully acknowledges support by a predoctoral fellowship from a Petroleum Research Fund grant to Professor Conway Pierce. The author also wishes to thank Professor Hartland Schmidt for his helpful suggestions.

(11) E. A. Guggenheim, "Thermodynamics," North Holland Publishing Co., Amsterdam, 1957, p. 170.

Simple Hard-Disk Monolayer Isotherms with Phase Transitions[1]

by J. P. Stebbins and G. D. Halsey, Jr.

Department of Chemistry, University of Washington, Seattle 5, Washington *(Received July 27, 1964)*

Several monolayer isotherms appropriate for hard disks are considered. These include the Langmuir isotherm and several related to the Volmer isotherm. The approximations used in the derivation of the latter have been modified so as to lead to the correct limit at saturation and the correct second virial coefficient. These results are compared with the exact expansion as far as it is known. Monolayer transitions between the Volmer-type isotherm (at relatively low coverage) and the Langmuir isotherm (at higher coverage) are discussed for the case of adsorption on a structureless surface.

Introduction

The Langmuir[2] equation occupies a central position in the theoretical discussion of monolayer adsorption because of its simplicity of form and directness of derivation. The assumptions upon which it is based and its derivation from statistical mechanics are given by Fowler and Guggenheim.[2] Writing it in the form appropriate for consideration of molecular adsorption without dissociation, we have

$$k_L P = \theta/(1 - \theta) \quad (1)$$

(1) This research supported in part by the U. S. Air Force through the AFOSR.

(2) R. H. Fowler and E. A. Guggenheim, "Statistical Thermodynamics," Cambridge University Press, London, 1949, p. 426 ff.

where k_L is the Langmuir constant, made up of partition functions and other constants,[2] P is the gas pressure, and θ is the fractional coverage. The latter can be related to the surface concentration of molecules per unit area, Γ, by the relation

$$\vartheta = \Gamma/\Gamma_\infty \tag{2}$$

where Γ_∞ is the maximum concentration obtained as the pressure approaches infinity.

The Langmuir equation is suitable for the description of localized adsorption, where each adsorbed molecule is attached to a lattice site on the surface. Our purpose here is to compare it with similar equations appropriate to mobile monolayer adsorption, where the adsorbed molecule is free to translate in the plane of the surface and is constrained to interact solely with other adsorbed molecules.

We shall discuss only the simplest model, that of hard spheres or disks of diameter σ. For this comparison Γ_∞ will be identified with the maximum concentration of such disks when arranged in a close-packed triangular array. In this case

$$\Gamma_\infty = 2/\sqrt{3}\sigma^2 \tag{3}$$

Equation 2, in connection with any isotherm and the Gibbs adsorption equation, can be used to derive the related two-dimensional equation of state, which expresses the spreading pressure, ϕ, as a function of θ. For such an application the Gibbs adsorption equation takes the form

$$d\phi = NkT\Gamma \, d \ln P \tag{4}$$

This equation, when applied to the Langmuir isotherm, yields the equation of state[3]

$$\frac{\phi A}{NkT} = \frac{1}{\theta} \ln\left(\frac{1}{1-\theta}\right) \text{ (Langmuir)} \tag{5}$$

The Complete Volmer Equation. There is no simple isotherm corresponding to the Langmuir equation which is applicable to mobile monolayer adsorption over the entire range of θ (from 0 to 1). Fowler and Guggenheim[2] discuss only the region of low coverage, where Henry's law applies. In a recent discussion of the problem, Young and Crowell[4] present the well-known but seldom-used Volmer equation.[5] The original derivation includes a simplifying assumption that causes saturation to be reached at exactly one-half of the value predicted by eq. 2. The basis of the Volmer equation is the empirical equation of state

$$\phi(A - NA_0) = NkT \tag{6}$$

or, in terms of θ

$$\frac{\phi A}{NkT} = \frac{1}{1-\theta} \tag{6a}$$

where $A = 1/\Gamma$ and $A_0 = 1/\Gamma_\infty$, the "co-area" per molecule, analogous to the co-volume b, in van der Waals' equation. This yields, with the assumption that $A_0 << A$, the isotherm

$$k_V P = \theta/(1 - 2\theta) \text{ (Volmer)} \tag{7}$$

When eq. 7 is run through the reverse process we do not regain eq. 6a, but rather

$$\frac{\phi A}{NkT} = \frac{1}{2\theta} \ln\left(\frac{1}{1-2\theta}\right) \text{ (Volmer)} \tag{6b}$$

However, the equation of state, eq. 6, can be used together with the Gibbs equation, eq. 4, without any further approximation in the following way. Choosing $N = 1$ for simplicity and utilizing the relationship $\Gamma = 1/A$, eq. 4 may be rewritten

$$d\phi = \frac{kT}{A} d \ln P \tag{8a}$$

and eq. 6 becomes

$$\phi = \frac{kT}{A - A_0} \tag{8b}$$

then

$$d\phi = -\frac{kT}{(A - A_0)^2} dA = \frac{kT}{A} d \ln P \tag{8c}$$

or, rearranging

$$d \ln P = -\frac{A dA}{(A - A_0)^2} \tag{8d}$$

the right-hand side is a standard integral; thus we obtain

$$\ln P = \ln\left(\frac{1}{A - A_0}\right) + \frac{A_0}{A - A_0} + \text{constant} \tag{8e}$$

removing logarithms

$$P = \text{constant}\left(\frac{1}{A - A_0}\right) \exp\left(\frac{A_0}{A - A_0}\right) \tag{8f}$$

now, multiplying both sides by A_0 and introducing $\theta = A_0/A$, we obtain

(3) W. B. Innes and H. H. Rowley, *J. Phys. Chem.*, **45**, 158 (1941). The authors also demonstrate how the reverse process may be accomplished, *i.e.*, start with the two-dimensional equation of state and obtain the related isotherm.

(4) D. M. Young and A. D. Crowell, "Physical Adsorption of Gases," Butterworths Inc., Washington, D. C., 1962, p. 110.

(5) M. Volmer, *Z. physik. Chem.*, **115**, 253 (1925).

$$k_V P = \frac{\theta}{1-\theta} \exp\left(\frac{\theta}{1-\theta}\right)$$

("complete" Volmer) (9)

The result is a reasonably simple isotherm which we will designate as the "complete" Volmer equation. (A slightly different integration procedure yields the result

$$k_V P = \frac{\theta}{1-\theta} \exp\left(\frac{1}{1-\theta}\right) \qquad (9a)$$

Since the two equations differ only by a constant ratio, e, they are equivalent, but imply a different definition of k_V; we shall use the form of eq. 9.)

This isotherm can also be derived as a special case of the so-called van der Waals isotherm, developed by Cassel[6] and Hill.[7]

Comparison of Equations; Virial Expansions. The three isotherm equations, eq. 1, 7, and 9, each with the same initial slope, are plotted together in Fig. 1. Note that the "complete" Volmer equation is very slow to approach saturation, as compared to the Langmuir equation. The same phenomenon is reflected in the behavior of the equations of state, eq. 5, 6a, and 6b, which are shown in Fig. 2. The line $\phi A/NkT = 1$ has been included to indicate deviation from ideal gas behavior.

Now eq. 5, 6b, and 6a may all be expanded in powers of θ to yield, respectively

$$\frac{\phi A}{NkT} = 1 + \frac{\theta}{2} + \frac{\theta^2}{3} + \frac{\theta^3}{4} + \cdots \text{ (Langmuir)} \quad (10)$$

$$\frac{\phi A}{NkT} = 1 + \theta + \frac{4\theta^2}{3} + 2\theta^3 + \cdots \text{ (Volmer)} \quad (11)$$

$$\frac{\phi A}{NkT} = 1 + \theta + \theta^2 + \theta^3 + \cdots$$

("complete" Volmer) (12)

Equation 10 was originally given by Innes and Rowley,[3] while eq. 11 and 12 were first given by Volmer.[5] It is seen immediately that they are equations of state in the virial form.

Six virial coefficients of a hard-disk gas are available, the first three[8,9] being exact, while the last three[10] have been derived by utilizing Monte Carlo integrations. Now the virial equation of state for an imperfect two-dimensional gas may be written

$$\frac{\phi A}{NkT} = 1 + B_2\left(\frac{N}{A}\right) + B_3\left(\frac{N}{A}\right)^2 + B_4\left(\frac{N}{A}\right)^3 + \cdots \quad (13)$$

where the B's are the virial coefficients previously mentioned and are all functions of σ^2. In order to make a comparison with eq. 10, 11, and 12, eq. 13 must be rewritten in terms of θ. To maintain consistency, θ will

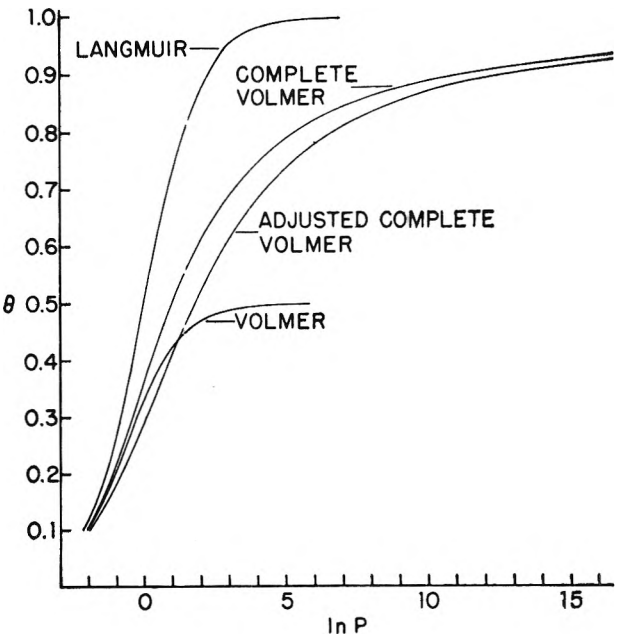

Figure 1. Monolayer adsorption isotherms for a hard-disk gas on a structureless surface.

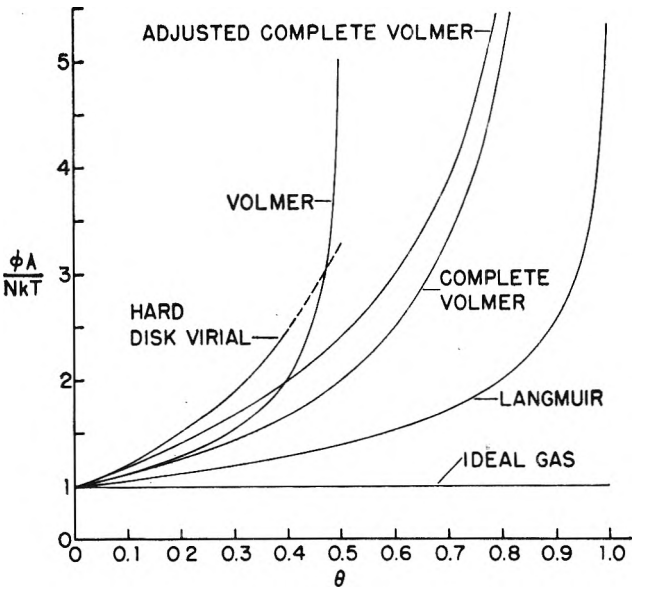

Figure 2. Two-dimensional equations of state for a hard-disk gas adsorbed on a structureless surface.

(6) H. M. Cassel, *J. Phys. Chem.*, **48**, 195 (1944).

(7) T. L. Hill, *J. Chem. Phys.*, **15**, 767 (1947).

(8) M. Metropolis, A. W. Rosenbluth, M. N. Rosenbluth, A. H. Teller, and E. Teller, *ibid.*, **21**, 1087 (1953).

(9) L. Tonks, *Phys. Rev.*, **50**, 955 (1936).

(10) F. H. Ree and W. G. Hoover, *J. Chem. Phys.*, **40**, 939 (1964).

be based on a close-packed triangular array. By simple geometry it may be shown[9] that the minimum area occupied by such an array is $(\sqrt{3}/2)N\sigma^2$, and thus θ is equivalent to $0.8660(N\sigma^2/A)$. Since each term of eq. 13 contains a factor $(N\sigma^2/A)^{n-1}$, where n is the term index, each coefficient of θ is obtained by multiplying the respective virial coefficient in eq. 13 by $(1.1547)^{n-1}$. The results of this calculation are given in Table I, where they are compared with the coefficients of the other three equations discussed. The hard disk virial equation of state has also been plotted in Fig. 2. By comparison of various equations of state in the closed and virial form we have found that truncating the series at six terms begins to add appreciable error beyond $\theta \approx 0.4$ and leads to completely erroneous results beyond $\theta \approx 0.5$. Thus the line has been plotted only to $\theta = 0.5$, with the region $\theta = 0.4$ to 0.5 given by a dashed line.

Table I: Comparison of Coefficients for the General Equation

$$\frac{\phi A}{Nkt} = 1 + C_1\theta + C_2\theta^2 + C_3\theta^3 + C_4\theta^4 + C_5\theta^5$$

Equation	C_1	C_2	C_3	C_4	C_5
Two-dimensional hard-disk gas	1.8138	2.5726	3.1787	3.6134	3.9109
"Complete" Volmer	1.0000	1.0000	1.0000	1.0000	1.0000
Volmer	1.0000	1.3333	2.0000	3.2000	5.3333
Langmuir	0.5000	0.3333	0.2500	0.2000	0.1667

The Adjusted Volmer Equation. As seen in Table I, none of the closed-form isotherms does a good job of reproducing the correct virial coefficients. It is possible to adjust the equation of state, eq. 6a, so that any number of early coefficients are exact. For example, if we wish the second virial coefficient to have the value C_1, we may use the equation of state

$$\frac{\phi A}{NkT} = \frac{1}{1-\theta} + (C_1 - 1)\theta \qquad (14)$$

The -1 in the parentheses cancels the second term of the expansion (eq. 12) and the value C_1 appears in its place. When put through the Gibbs adsorption formula, eq. 4, this yields what we will designate as the "adjusted complete" Volmer equation

$$k_V P = \frac{\theta}{1-\theta}\exp\left(\frac{\theta}{1-\theta} + 2(C_1 - 1)\theta\right)$$

("adjusted complete" Volmer) (15)

This result is little more complicated than the "complete" Volmer equation. It is plotted with the value $C_1 = 1.8138$ in Fig. 1. A plot of the equation of state, eq. 14, with the same value of C_1 is shown in Fig. 2.

Crossing of Isotherms. Thus far we have only compared isotherms with equal initial slopes, that is with $k_L = k_V$. The two constants are determined by different factors (*cf.* ref. 2) and there is no reason to suppose that they would be equal on a real surface. In fact, we might expect that the question of which model (localized or mobile) should be more applicable to a given surface–gas combination would depend, in a formal sense, on which constant was larger. It appears clear, however, that for a structureless surface, the mobile model would be appropriate in the region of small θ. In Fig. 3 a number of Langmuir isotherms with various k_L values are plotted, along with a single "complete" Volmer isotherm. Since the two types of isotherm equations are of different functional form and cover the same range of variables, it is possible for them to cross. The point of crossing (for a ln P *vs.* θ plot), obtained by equating the logarithmic forms of eq. 1 and 9, is

$$\theta_{cross} = -\frac{\ln K}{1 + \ln K} \qquad (16)$$

where

$$K = \frac{k_V}{k_L} \qquad (17)$$

This crossing occurs in a physically meaningful range of θ only when the ratio K is between 0 and 1. It is seen that, in general, the mobile isotherm has a lower relative pressure for the condition $\theta < \theta_{cross}$ while the Langmuir isotherms have a lower relative pressure beyond this point.

Although a structureless surface will favor mobile adsorption at coverages less than saturation, if the pressure (and thus the free energy) can be reduced by going to an ordered Langmuir structure at high coverage, this transition would be thermodynamically favored. We will now consider the effect of such a transition.

Application of the Rule of Equal Areas. Since the quantity adsorbed is plotted against ln P in Fig. 3, the area under each isotherm represents the free energy of formation of the adsorbed layer from $\theta = 0$ to the value of θ reached. This is so because the gas phase has been assumed ideal and at equilibrium the free energy of the two phases is equal; we have

$$\mu_{ads} = \mu_{gas} = \mu_{0\ gas} + kT \ln P_{gas} \qquad (18a)$$

$$\Delta F_{ads} = F_{ads} - F_{0\ gas} = \int_0^{\Gamma} (\mu_{ads} - \mu_{0\ gas})\, d\Gamma \qquad (18b)$$

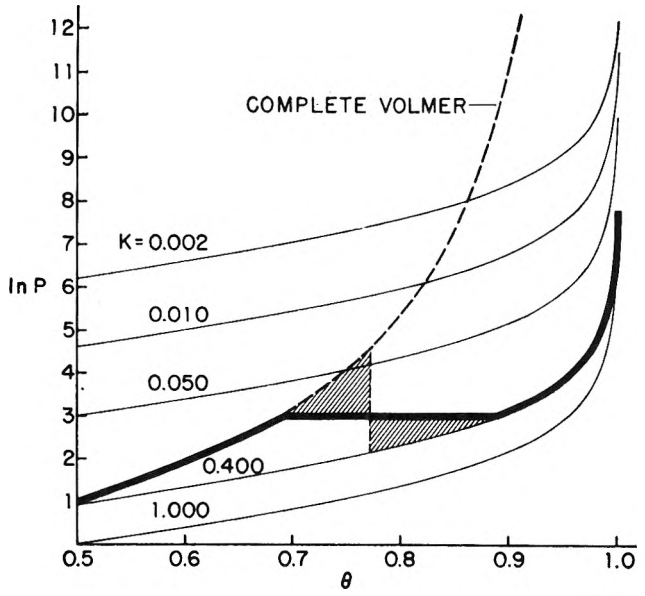

Figure 3. Construction of the composite isotherm with K = 0.4. The light continuous lines are Langmuir isotherms which are related to the "complete" Volmer isotherm by the attached K values. The vertical lightly dashed line indicates the coverage at which the free energies of the mobile ("complete" Volmer) and fixed (Langmuir) monolayers are equivalent. The heavy continuous line represents the composite isotherm, with the horizontal portion designating the mobile–immobile transition.

Now ln P as a function of θ may be derived and plotted from the isotherm equations, eq. 1 and 9. Since Γ, the surface concentration, is equivalent to $\Gamma_\infty\theta$, from eq. 2, $d\Gamma = \Gamma_\infty d\theta$. Thus we have

$$\Delta F_{ads}(\theta) = kT\Gamma_\infty \int_0^\theta \ln P \, d\theta \qquad (19)$$

It has been found that the value of θ where the two films become equal in free energy comes beyond θ_{cross}, at a point defined by ΔF (Langmuir) = ΔF ("complete" Volmer).

Performing the integration, as indicated by eq. 19, on both the Langmuir and the "complete" Volmer and equating the results as required, we obtain an expression which gives the θ for equal free energies

$$1 + \ln K = \frac{1}{\theta} \ln (1 - \theta) \qquad (20)$$

where K has been defined previously in eq. 17. A plot of the left-hand side of this equation as a function of θ will then permit a graphical determination of the equivalence point for any value of K.

For K = 0.4, the value of θ at which the two types of film have equal free energies of formation is indicated by the vertical dashed line in Fig. 3. Note that following this path implies a change in pressure at constant area, a situation somewhat analogous to the loop formed by the van der Waals equation when describing the P–V behavior of a substance below its critical temperature. In order to achieve a physically realizable condition, it is necessary to change concentration at constant pressure, meanwhile conserving the area (*i.e.*, the free energy) under the individual curves which describe the model up to and beyond the transition point. This equal area line[11] is shown in Fig. 3 as the horizontal portion in the isotherm and corresponds to the two-dimensional analog of a phase separation. The complete isotherm is shown as the heavy continuous line in the diagram.

Phase Diagram. We will show that it is difficult to make an accurate *a priori* estimate of K; we have, however, made equal area calculations for a number of values of K from 0 to 1 and determined for each the limits of θ at the beginning and end of the transition. These are shown as a function of K in Fig. 4. Now, since K is presumably some function of temperature, this figure may be regarded as a phase diagram displaying the solidus–liquidus behavior as some arbitrary function of temperature.

Estimation of the Ratio, K. Fowler and Guggenheim[12] develop thermodynamic relationships for both the mobile and fixed monolayers. In the former case, at high dilution where interactions between adsorbed molecules are negligible, they write for the free energy of the surface layer

$$F_{ads} = -NkT \ln a(T) + NkT \ln N - NkT \qquad (21)$$

where N is the number of atoms adsorbed in an area, A, and $a(T)$ is their partition function which includes the two-dimensional expression for translation, $2\pi mkTA/h^2$. The corresponding equation for μ, the chemical potential, is

$$\mu = \frac{\partial F_{ads}}{\partial N} = -kT \ln a(T) + kT \ln N \qquad (22)$$

In order to express this relationship in terms of θ, we substitute $N = \theta A/A_0$ to obtain

$$\mu_V = -kT \ln [(A_0/A)a(T)] + kT \ln \theta \qquad (23)$$

where the subscript V has been used to indicate that this equation, appropriate for the consideration of the mobile monolayer, corresponds to the low coverage re-

(11) Since one of the equations involved was a transcendental, and could not be solved explicitly, the equal areas were determined with the aid of a planimeter. The end-point values of θ have been checked and were found to correspond to equal spreading pressures.

(12) See ref. 2, p. 421 ff.

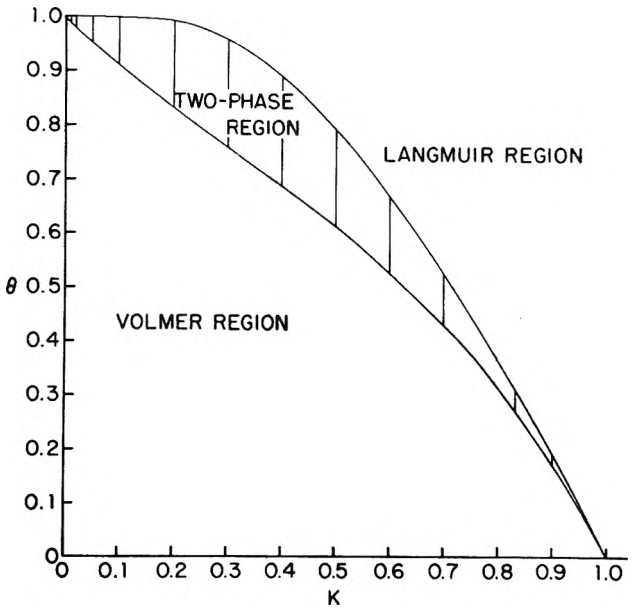

Figure 4. Phase diagram for a two-dimensional hard-disk gas adsorbed on a structureless surface. The Volmer region corresponds to a mobile monolayer and the Langmuir region to a fixed monolayer, while the two-phase region designates the transition between the two. The vertical lines appearing in the two-phase region correspond exactly to the horizontal portions of isotherms as constructed in Fig. 3.

gion, best described by the "complete" Volmer isotherm, eq. 9.

Relationships given in ref. 2 which are suitable for discussion of fixed monolayers may be modified for the condition of low coverage to yield

$$\mu_L = -kT \ln a_A(T) + kT \ln \theta \qquad (24)$$

where $a_A(T)$ is the partition function for atoms restricted to motions at fixed sites and the subscript L indicates that this equation corresponds to the high coverage region best described by the Langmuir isotherm, eq. 1.

Now eq. 18a gives the dependence of μ on ln P. In the present situation, combining eq. 18a and 23 we obtain

$$\mu_V = \mu_{gas} = \mu_{0\ gas} + kT \ln P_{gas} = -kT \ln [(A_0/A)a(T)] + kT \ln \theta \qquad (25)$$

while combining eq. 18a and 24 we obtain

$$\mu_L = \mu_{gas} = \mu_{0\ gas} + kT \ln P_{gas} = -kT \ln a_A(T) + kT \ln \theta \qquad (26)$$

The low pressure (dilute monolayer) limits of the logarithmic forms of eq. 1 and 9 may be written, respectively

$$\ln P_L = \ln k_L + \ln \theta \qquad (27)$$

$$\ln P_V = \ln k_V + \ln \theta \qquad (28)$$

Introducing eq. 27 and 28 into eq. 26 and 25, respectively, we have

$$\mu_{0\ gas} + kT \ln k_V = -kT \ln [(A_0/A)a(T)] \qquad (29)$$

$$\mu_{0\ gas} + kT \ln k_L = -kT \ln a_A(T) \qquad (30)$$

Finally, subtracting eq. 30 from eq. 29, cancelling common terms, and removing logarithms we obtain

$$\frac{k_V}{k_L} = K = \frac{a_A(T)}{(A_0/A)a(T)} \qquad (31)$$

If we factor out the translational portion of $a(T)$ and denote the remaining partition function for internal degrees of freedom as $j(T)$, we can write

$$K = \left[\frac{h^2}{2\pi mkTA_0}\right]\left[\frac{a_A(T)}{j(T)}\right] \qquad (32)$$

The factors in the right-hand bracket are vibrational partition functions. In the case where these factors are approximately equal, we can obtain an estimate of the magnitude of K by evaluating the left-hand bracket. As indicated by Fig. 4, the step height for a mobile–immobile transition becomes very small for K values very close to either 0 or 1, thus greatly reducing the probability of experimentally observing such a phenomenon. Calculations made for the noble gases at their boiling points in close-packed triangular array (where $A_0 = 0.866\sigma^2$), with atomic diameters taken from Hirschfelder, *et al.*,[13] indicate that only neon ($K \approx 0.1$) and argon ($K \approx 0.01$) fall within a range suitable for observation.

Discussion

It is apparent from Fig. 1 that the Langmuir isotherm is widely divergent in shape from those isotherms which are suitable for the description of mobile adsorption. If, for mathematical convenience, the former is utilized in a situation where one of the latter would give a more correct description, the result is, at best, a gross approximation. On the other hand, it is entirely possible for an adsorbate to establish itself in a regular array, with parameters characteristic of its own dimensions, on a structureless surface which would otherwise be expected to permit completely mobile adsorption. This behavior is analogous to the formation of a bulk crystal brought about solely by the influence of the intermolecular forces of its constituent particles. The only requisite for the formation of such a structure is that the transition results in a net lowering of the free energy of the system. It appears that, especially for an ordered

(13) J. O. Hirschfelder, C. F. Curtiss, and R. B. Bird, "Molecular Theory of Gases and Liquids," John Wiley and Sons, Inc., New York, N. Y., 1954, p. 1110.

structure with very few vacancies ($1 - \theta << 1$), the correct limiting form of the Langmuir equation is

$$1 - \theta = 1/k_L P \qquad (33)$$

Obviously then, at some intermediate value of θ, a transition to mobile adsorption must take place, since the latter is undoubtedly appropriate in the case of a structureless surface at low coverage.

We have proposed one possible way in which such a transition can be accomplished: by means of a discontinuous change in the surface density of the film. This corresponds, roughly, to a solid–liquid transition in the bulk phase. It is questionable whether any such transitions have been observed experimentally, since most of those reported to date have at least a probable explanation in the operation of attractive forces such as result in gas-to-liquid condensation in the bulk phase.

There is, however, at least one distinct difference between the two types of transition. The usual transition from a dilute to a condensed film that is caused by the operation of attractive forces results in a large step, of the order of magnitude of $\Delta\theta \approx$ unity,[14] whereas the steps we have calculated here have a maximum displacement of $\Delta\theta \approx 0.2$ and can be much smaller. A step which fits this latter description was encountered by Mastrangelo and Aston, in their study of the multilayer adsorption of helium.[15] It is realized, of course, that the simple classical theory reported here is inadequate to deal with the quantitative features of a multilayer helium isotherm, but the fact remains that the occurrence of this step has never been satisfactorily explained. It might be anticipated, on the basis of the rough estimations of K reported in the preceding section as well as the relatively small lateral interaction forces, that monolayer studies of neon adsorption in the vicinity of 20°K. would be the most favorable conditions under which to search for transitions of the type discussed here.

(14) G. Halsey, *J. Chem. Phys.*, 16, 931 (1948).

(15) S. V. R. Mastrangelo and J. G. Aston, *ibid.*, 19, 1370 (1951).

Kinetics of Periodate Hydration–Dehydration in Aqueous Solution

by K. Kustin and E. C. Lieberman

Department of Chemistry, Brandeis University, Waltham, Massachusetts 02154 *(Received August 22, 1964)*

The kinetics of the reaction $H_4IO_6^- \underset{k_H}{\overset{k_D}{\rightleftharpoons}} IO_4^- + 2H_2O$ (where k_D (sec.$^{-1}$) and k_H (sec.$^{-1}$) are the over-all first-order rate constants for dehydration and hydration) have been studied by the temperature-jump method. The rate constants at 20° and ionic strength 0.1 M are: $k_D = (5.6 \pm 0.6) \times 10^3$ sec.$^{-1}$ and $k_H = (1.9 \pm 0.2) \times 10^2$ sec.$^{-1}$. The reaction was studied in a pH range of 3.4 to 5.0. No catalytic effect of hydrogen ion was detected within experimental error. A two-step mechanism involving proton transfer *via* hydrogen bonding is postulated to explain the observed data.

Introduction

In a thermodynamic study of aqueous periodate solutions, Crouthamel, *et al.*,[1] showed that the species H_5IO_6, $H_4IO_6^-$, IO_4^-, and $H_3IO_6^{-2}$ and their equilibria were completely adequate to describe all observed behavior of acid solutions. Further evidence for the existence of these species has been the isolation of crystals such as H_5IO_6, $AgIO_4$, and KIO_4, and also

(1) C. Crouthamel, A. Hayes, and D. Martin, *J. Am. Chem. Soc.*, 73, 82 (1951) (*cf.* for references to earlier work).

$NaIO_4$, $(NH_4)_2H_3IO_6$, and $Ag_2H_3IO_6$, for which the crystal and molecular structures are known.[2]

The three equilibrium constants necessary for a complete description of the system are given in Table I, along with the equilibrium constants for the two indicators used in this study.

Table I: Stoichiometric Equilibrium Constants

$K_1 = \frac{[\overline{H^+}][\overline{H_4IO_6^-}]}{[\overline{H_5IO_6}]}$	$= 8.3 \times 10^{-4}$[a]
$K_2 = \frac{[\overline{H^+}][\overline{H_3IO_6^{-2}}]}{[\overline{H_4IO_6^-}]}$	$= 5.4 \times 10^{-7}$[a]
$K_D = \frac{[\overline{IO_4^-}]}{[\overline{H_4IO_6^-}]}$	$= 29$[a]
$K_{In_1} = \frac{[\overline{H^+}][\overline{In_1}]}{[\overline{HIn_1^+}]}$	$= 3.47 \times 10^{-4}$[b]
$K_{In_2} = \frac{[\overline{H^+}][\overline{In_2}]}{[\overline{HIn_2^+}]}$	$= 1.00 \times 10^{-5}$[b]

[a] See ref. 1, values corrected to 20°, ionic strength 0.1 *M*. [b] I. M. Kolthoff, *J. Phys. Chem.*, **34**, 1466 (1930). In_1, methyl orange; In_2, methyl red.

From these thermodynamic investigations it appeared that the equilibrium for the hydration–dehydration reaction was rapidly established. Therefore, we decided to undertake a temperature-jump study of this system at pH values around 4, where it is possible to observe the reaction of interest

$$H_4IO_6^- \underset{k_H}{\overset{k_D}{\rightleftharpoons}} IO_4^- + 2H_2O \qquad \text{(I)}$$

where k_D (sec.$^{-1}$) and k_H (sec.$^{-1}$) represent the first-order rate constants for the dehydration and hydration reactions, respectively. At the chosen pH of 4.2, for example, 99.8% of the periodate is present as some univalent species (either $H_4IO_6^-$ or IO_4^-); 0.2% is present as H_5IO_6; and essentially none is present as the divalent ion, $H_3IO_6^{-2}$.

Relaxation Spectra

In order to study the kinetics of reaction I by the temperature-jump technique, it was necessary to couple the system with an acid–base indicator to obtain an observable color change in the visible region of the spectrum. This coupling was accomplished *via* the following reactions

$$H_5IO_6 \rightleftharpoons H^+ + H_4IO_6^- \qquad \text{(II)}$$

$$HIn^+ \rightleftharpoons H^+ + In \qquad \text{(III)}$$

where Hin^+ and In represent the acidic and basic forms of methyl orange and methyl red, the two main indicators used in the study. Reactions II and III, which involve proton recombination, have relaxation times many orders of magnitude faster than the hydrolytic reaction I and, hence, are suitable as coupling reactions.

For the over-all reaction I the rate is

$$\frac{d[IO_4^-]}{dt} = k_D[H_4IO_6^-] - k_H[IO_4^-] \qquad (1)$$

In order to find the relaxation time for (I), the following relations

$$[x] = [\bar{x}] + \delta[x] \qquad (2a)$$

for all species, x, and

$$\delta[IO_4^-] + \delta[H_4IO_6^-] + \delta[H_5IO_6] = 0 \qquad (2b)$$

$$\delta[HIn^+] + \delta[In] = 0 \qquad (2c)$$

$$\delta[H^+] + \delta[H_5IO_6] + \delta[HIn^+] = 0 \qquad (2d)$$

$$k_D[\overline{H_4IO_6^-}] = k_H[\overline{IO_4^-}] \qquad (2e)$$

(where [x] is the instantaneous concentration of species x, $[\bar{x}]$ is the time-independent equilibrium concentration, $\delta[x]$ represents a small deviation from equilibrium and is time dependent, with $\delta[x] << [x], [\bar{x}]$) substituted into eq. 1 give

$$\frac{d(\delta[IO_4^-])}{dt} = \frac{-[IO_4^-]}{\tau} \qquad (3)$$

with

$$\frac{1}{\tau} = k_D(1 - \alpha) + k_H$$

where

$$\alpha = \left[\frac{[\overline{H^+}]}{[\overline{H^+}] + K_1 + [\overline{H_4IO_6^-}]\left(\frac{K_{In} + [\overline{H^+}]}{K_{In} + [\overline{H^+}] + [\overline{In}]}\right)}\right] \qquad (4)$$

Since the relaxation time, τ, is directly measurable by the temperature-jump method for a reaction with a finite heat of reaction,[3] k_D and k_H could be determined.

Experimental

The temperature-jump apparatus was the same one used in previous work in this laboratory by Hurwitz

(2) (a) E. A. Hazlewood, *Z. Krist.*, **98**, 439 (1938); (b) L. Helmholz, *J. Am. Chem. Soc.*, **59**, 2036 (1937); (c) L. Helmholz, *Struct. Rept.*, **9**, 215 (1942).

(3) M. Eigen and L. DeMaeyer in "Technique of Organic Chemistry," A. Weissberger, Ed., Vol. VIII, John Wiley and Sons, Inc., New York, N. Y., 1963, Part 2.

and Kustin[4] and is described in that paper as well as in others.[5] The final equilibrium temperature to which all rate constants are referred is 20 ± 1°. The relative error in the rate constants is ±10%. The reaction was followed by observing the change in optical density of the indicator at a single wave length (513 mμ for methyl orange, 525 mμ for methyl red); this change was oscilloscopically recorded and photographed.

Reagent grade sodium metaperiodate from the Fisher Scientific Co. was used without further purification, as was Fisher reagent grade sodium nitrate, used as an inert electrolyte to maintain a constant ionic strength of 0.1 *M*. The indicators, methyl orange and methyl red, from Eastman Organic Chemicals, were both recrystallized from water before using. Stock solutions of both indicators and $NaNO_3$ were used. Because of its low solubility, fresh samples of $NaIO_4$ were weighed out for each solution. Doubly distilled water was used in all preparations. The pH was adjusted on a Corning pH meter, Model 12, with dilute HNO_3 and NaOH. Measurements of pH after the solution was "T-jumped" showed no change in hydrogen ion concentration.

In the pH-dependence study, methyl orange was used as the indicator for pH 3.4–4.2, while methyl red was used for pH 4.6–5.0. It was observed that solutions of periodate and methyl orange or methyl red slowly faded upon standing. The rate was such that a period of about 24 hr. was required for most of the color to disappear. In control experiments on the Perkin-Elmer 202 UV-Vis spectrophotometer, it was found that at a constant concentration of indicator, the color fading was more rapid for larger periodate concentrations. From this fact it was assumed that some reaction (most likely oxidation) was occurring between periodate and both indicators. However, since the periodate and indicator were mixed just before the solution was used for a temperature-jump experiment, no more than 5–10 min. was permitted to elapse before the first oscillographs were taken.

Two other indicators were tried in the course of this work. With brom cresol green a small effect was observed, but it was not large enough to permit an accurate evaluation of the relaxation time. Brom phenol blue also showed a small effect when "T-jumped" once or twice. Further pulsing resulted in the apparent decomposition of this indicator so that no further investigation was possible. Nevertheless, the results of these experiments are in accord with those of the methyl orange–methyl red experiments. Thus, the effect observed with methyl orange and methyl red is not an artifact of these indicators.

Results

The results of the kinetic studies are shown in Tables II and III. Each relaxation time is an average of at least three photographic determinations. The rate constants were calculated from eq. 4.

Table II shows the results of the concentration dependence study at pH 4.2. As eq. 4 would indicate, there is no experimentally observable effect of periodate concentration on the relaxation time.

Table II: Concentration Dependence of τ[a]

$[IO_4^-]_0 \times 10^2$ *M*	τ, μsec.	k_D, sec.$^{-1}$	k_H, sec.$^{-1}$
1.00	180	6.0×10^3	2.1×10^2
2.00	190	5.6×10^3	1.9×10^2
4.00	200	5.2×10^3	1.8×10^2
6.00	190	5.4×10^3	1.9×10^2
8.00	180	5.7×10^3	2.0×10^2
	Av.	$(5.6 \pm 0.6) \times 10^3$	$(1.9 \pm 0.2) \times 10^2$

[a] pH 4.2; $[\text{methyl orange}]_0 = 2.0 \times 10^{-5}$ *M*; $\mu = 0.1$ *M*; temp. 20°.

Table III shows the results of the pH dependence study with $[IO_4^-]_0 = 0.02$ *M*. There is no significant dependence of rate on pH, and it thus appears that there is no hydrogen ion catalysis in the pH range studied.

Discussion

Comparison of these results with other reactions in the general class of hydration–hydrolysis shows that the periodate reaction is among the most rapid—a surprising result, in view of the large structural changes and complexity of the reaction. For example, the hydration rate constant for SO_2 is $k_H = 3.4 \times 10^6$ sec.$^{-1}$ [6]; halogen hydrolysis spans a broad range of relaxation times, but the largest k_H (for bromine) is 1.1×10^2 sec.$^{-1}$ [7]; the hydration rate constant for CO_2 is $k_H = 0.04$ sec.$^{-1}$.[8] Similar reactions involving the hydration–hydrolysis of various aldehydes and ketones are slower and usually show general acid–base catalysis.[9,10] In

(4) P. Hurwitz and K. Kustin, *Inorg. Chem.*, **3**, 823 (1964).

(5) G. Czerlinski and M. Eigen, *Z. Elektrochem.*, **63**, 652 (1959); G. G. Hammes and J. I. Steinfeld, *J. Am. Chem. Soc.*, **84**, 4639 (1962).

(6) M. Eigen, K. Kustin, and G. Maass, *Z. physik. Chem.* (Frankfurt), **30**, 130 (1961).

(7) M. Eigen and K. Kustin, *J. Am. Chem. Soc.*, **84**, 1355 (1962).

(8) B. H. Gibbons and J. T. Edsall, *J. Biol. Chem.*, **238**, 3502 (1963).

(9) R. P. Bell, "The Proton in Chemistry," Cornell University Press, Ithaca, N. Y., 1959, p. 151 ff.

(10) H. Strehlow, *Z. Elektrochem.*, **66**, 392 (1962).

Table III: pH Dependence of τ[a]

Indicator	pH	τ, μsec.	k_D, sec.$^{-1}$	k_H, sec.$^{-1}$
Methyl orange	3.4	200	6.7×10^3	2.3×10^2
Methyl orange	3.8	220	5.2×10^3	1.8×10^2
Methyl orange	4.2	190	5.6×10^3	1.9×10^2
Methyl red	4.6	190	5.4×10^3	1.9×10^2
Methyl red	5.0	190	5.3×10^3	1.8×10^2
		Av.	$(5.6 \pm 0.6) \times 10^3$	$(1.9 \pm 0.2) \times 10^2$

[a] $[IO_4^-]_0 = 2.00 \times 10^{-2}$ *M*; [methyl orange or methyl red]$_0 = 2.00 \times 10^{-5}$ *M*; $\mu = 0.1$ *M*; temp. 20°.

contrast, the hydration rate constant for periodate is $k_H = 1.9 \times 10^2$ sec.$^{-1}$ and is free from hydrogen ion catalysis in the pH range 3.4–5.0 as shown in Tables II and III.

Closer comparison between this and the previously mentioned reactions shows many differences. Let us first consider the faster hydration–hydrolysis reactions. The reactions of SO_2, the halogens, and CO_2 are those of pseudoacids. The SO_2 and CO_2 hydrolysis mechanisms most probably involve a single step. That is, the hydration is accomplished by the transfer of a hydroxyl ion from a water molecule to the substrate, during which process the freed hydrogen ion diffuses into the bulk of the medium. The change from metaperiodate to paraperiodate, on the other hand, involves (a) the "hydrolysis" of *two* water molecules with no increase in hydrogen ion concentration and (b) the change from tetrahedral to octahedral coordination, respectively. (This structural change is based upon the assumption that the known solid-state molecular structures are retained by the ions in solution.) These two facts necessitate a different explanation for the periodate reaction.

The results may be interpreted according to two schemes: a two-step mechanism with a pentacoordinated intermediate and a one-step mechanism with the "concerted" hydrolysis of two associated water molecules. The temperature-jump experiments do not distinguish between the two possibilities so long as the intermediate in the two-step mechanism is present in the steady state. As a consequence of this fact it is most correct to include both possibilities in the over-all mechanism, namely

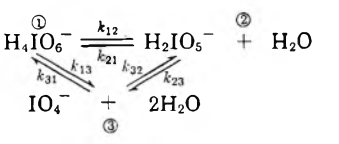

(IV)

Assuming that for the pentacoordinated intermediate, $H_2IO_5^-$, $(d/dt)(\delta[H_2IO_5^-]) = 0$, the rate constants k_D and k_H are then

$$k_D = \frac{k_{12}}{1 + k_{21}/k_{23}} + k_{31} \quad (5)$$

$$k_H = \frac{k_{32}}{1 + k_{23}/k_{21}} + k_{13} \quad (6)$$

On mechanistic grounds, pathway ① ⇌ ② ⇌ ③, the two-step mechanism, seems to have the greater likelihood. Unlike the SO_2 or CO_2 reactions, the number of ions does not increase upon hydrolysis, but a proton and hydroxyl ion have to be added to, and brought together from, separated sites on the periodate. Both periodate ions are relatively large, the distance between oxygen atoms along an edge in the octahedral $H_4IO_6^-$ being approximately 2.50 Å.[2a] This distance provides enough space for about two or three water molecules. Therefore, hydrogen bonding, which has also been shown to occur in the solid,[2a] could account for the rapid, reversible hydration–hydrolysis in a reaction such as that shown below for step ① ⇌ ②

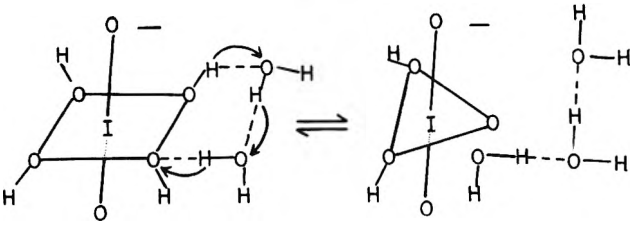

and similarly for the second step. In terms of this mechanism, we can see why the above-mentioned hydrolysis of aldehydes and ketones is slower. The relatively small length of the carbon–oxygen bond in the carbonyl group would not permit proton transfer through a network of hydrogen bonds.

It is also to be noted that there do not appear to be any *a priori* grounds for preferring a trigonal bipyramid to a square pyramid intermediate although the former is the more commonly encountered structure for a pentacoordinated compound and has consequently been employed in the illustration.[11] This type of reac-

tion, leading to the intermediate shown (or possibly one with a different pentacoordinated structure) provides an effective mechanism for accomplishing the structural changes, which would be consistent with the (relatively) short relaxation times. The rate constants for the two-step mechanism can be obtained from eq. 5 and 6 by dropping k_{31} and k_{13}, respectively. Without additional evidence, however, it is not possible to carry a kinetic analysis of this mechanism any further.

Some of the thermodynamic data give an indication that a one-step mechanism is not to be entirely discarded. The standard entropy change for reaction I is 44 e.u. Crouthamel, *et al.*, have estimated that the difference in the entropy of aquation between paraperiodate and metaperiodate (*viz.*, $\Delta S_{aq}(H_4IO_6^-) - \Delta S_{aq}(IO_4^-)$) is 23 e.u. The authors conclude that a considerable part of this large difference might be due to a difference in the solvent-orienting abilities of the two ions. Specifically, the greater charge localization at the two unprotonated oxygen atoms in paraperiodate ion produces more solvent structure organization at these two places than at the corresponding four sites on metaperiodate ion. Since significant solvent organization is thereby implicated in reaction I, the possibility of an orientation favorable enough to permit the simultaneous hydrolysis of two associated water molecules should not be omitted. In this case, the rate constants k_D and k_H would be given, simply, by k_{31} and k_{13}. However, this process seems to be less likely than the two-step mechanism on the grounds that such unique configurations would not occur as frequently as H-bond formation and subsequent proton transfer are known to occur.[12] Further work on acid–base catalysis in nonaqueous solvents will be undertaken in order to distinguish, experimentally, between the two mechanistic possibilities.

Acknowledgment. This investigation was supported by Public Health Service Research Grant GM-08893-03 from the National Institute of General Medical Science, Public Health Service.

(11) F. A. Cotton and G. Wilkinson, "Advanced Inorganic Chemistry," Interscience Publishers, Inc., New York, N. Y., 1962, p. 307.

(12) M. Eigen, *Angew. Chem.*, 75, 489 (1963).

NOTES

Competitive Scavenging of Methyl Radicals by Galvinoxyl and Iodine[1]

by Robert H. Schuler

Radiation Research Laboratories, Mellon Institute, Pittsburgh, Pennsylvania *(Received June 29, 1964)*

Bartlett and Funahashi[2] have recently studied the relative rates for reaction of galvinoxyl[3] and iodine with cyanoisopropyl radicals and found that the former rate is ten times greater. This result necessarily implies that, at least for the cyanoisopropyl radical, iodine is an inefficient scavenger and that the reaction is activation controlled. Work from these laboratories,[4] in which the absolute rate of scavenging of methyl radicals by iodine is determined by comparison with the rate of bimolecular combination of radicals, has indicated that the rate for reaction 1

$$CH_3\cdot + I_2 \longrightarrow CH_3I + I\cdot \qquad (1)$$

is in the range of 10^8–10^9 l. mole^{-1} sec.$^{-1}$ and is essentially diffusion controlled. In view of these facts a direct determination of the relative rates for the scavenging of methyl radicals by galvinoxyl and iodine seemed desirable. Since Bartlett and Funahashi have demonstrated the mutual compatability of these two scavengers such a direct determination is readily possible.

Experimental

Methyl radicals are generated by the radiolysis of 2,2,4-trimethylpentane for which $G(CH_3\cdot)$ had previ-

(1) Supported, in part, by the U. S. Atomic Energy Commission.

(2) P. D. Bartlett and T. Funahashi, *J. Am. Chem. Soc.*, 84, 2569 (1962).

(3) Formally known as 2,6-di-*t*-butyl-α-(3,5-di-*t*-butyl-4-oxo-2,5-cyclohexadiene-1-ylidene)-*p*-tolyloxy: G. M. Coppinger, *ibid.*, 79, 501 (1957).

(4) R. H. Schuler and R. R. Kuntz, *J. Phys. Chem.*, 67, 1004 (1963).

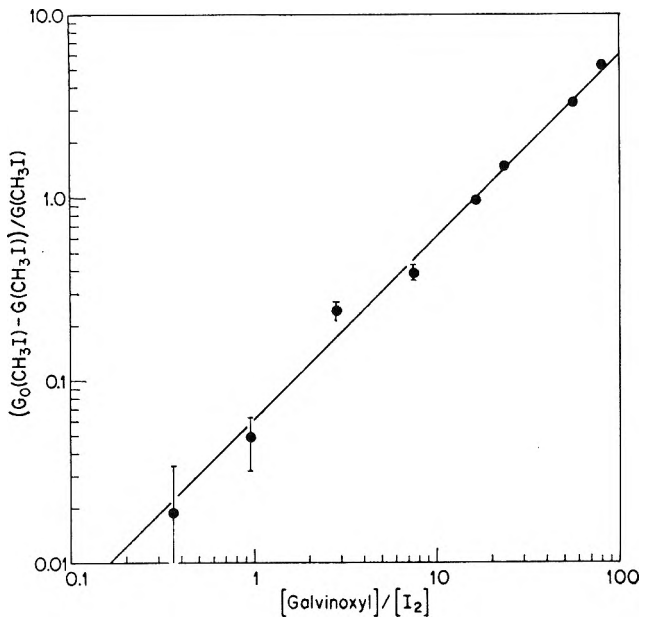

Figure 1. Ratio of scavenging of methyl radicals by galvinoxyl [$G_0(CH_3I) - G(CH_3I)$] and by iodine [$G(CH_3I)$]. Solid curve corresponds to simple competition (slope = 1), with the rates equal at [g]/[I_2] = 16. Error limits indicated are ±0.01 in ΔG.

ously been demonstrated to be 0.69. Reaction with iodine is measured directly from the formation of methyl iodide and with galvinoxyl (g) from the decrease in $G(CH_3I)$ at a particular ratio of (g)/(I_2). Since iodine concentrations were always in excess of 10^{-5} M complications due to abstraction of hydrogen from the solvent should be absent. Galvinoxyl concentrations were varied from 0.3 to 6 × 10^{-3} M and iodine concentrations from 0.01 to 3 × 10^{-3} M. The methyl iodide yields were determined by the radiochemical methods previously developed.[4]

Results and Discussion

The rate for reaction of methyl radicals with galvinoxyl

$$CH_3\cdot + g \longrightarrow \text{products} \qquad (2)$$

relative to (1) is given in Fig. 1. It is seen that a simple competition seems to exist with the rate for (2) only $^1/_{16}$ as large as that for (1). This somewhat decreased rate is not too surprising in view of the delocalization of the electron in the galvinoxyl radical and in view of possible steric complications in reaction with such a large scavenger molecule. Assuming that reaction 2 is at all rapid (*i.e.*, $k_2 > 10^7$ l./mole^{-1} sec.$^{-1}$) the present result confirms the previous conclusion that reaction 1 is essentially diffusion controlled. Apparently, the efficiency of iodine for reaction with cyanoisopropyl radicals is considerably less than for reaction with methyl radicals.

If the present result is combined with the previous estimate of 3 × 10^8 for k_1 then an absolute rate of 2 × 10^7 is obtained for k_2. Since, because of the high extinction coefficient for g ($E_{431} \sim 150{,}000$),[2] studies can be carried out at low concentrations, this low value for k_2 suggests that it should be possible to make a direct comparison of k_2 with the rate for bimolecular combination of radicals at moderate radiation intensities. Studies of this nature are in progress.

Acknowledgment. The author wishes to thank Mr. G. Buzzard for his assistance with the methyl iodide determinations reported here.

Diffusion Coefficients for One Composition of the System Water–Sucrose–Glycine at 25°[1]

by Peter J. Dunlop[2] and Louis J. Gosting

Chemistry Department and Institute for Enzyme Research, University of Wisconsin, Madison, Wisconsin 53706
(Received June 20, 1964)

Although a number of papers which present data for isothermal diffusion in ternary systems have appeared in the literature during the past decade, only a few[3-5] of these report data for two nonelectrolytes in water. As part of a program for studying diffusion in aqueous ternary systems by means of the Gouy diffusiometer it was decided to obtain some data for the system water–sucrose–glycine. This note reports values for the four diffusion coefficients for one composition of this system, together with auxiliary data for the partial specific volumes and the refractive index derivatives. Measurements were made at rather high solute concentrations in the hope that the cross-term diffusion coefficients would be large and capable of being determined quite accurately.

Experimental

We use the numbers 0, 1, and 2 to denote the components water, sucrose, and glycine, respectively.

(1) This investigation was supported in part by National Science Foundation Research Grant GP-179 and by National Institute of Arthritis and Metabolic Diseases (U.S.P.H.S.) Research Grant AM-05177 and Career Award K6-AM-16,715 (to L. J. G.).

(2) Department of Physical and Inorganic Chemistry, Adelaide University, South Australia.

(3) P. J. Dunlop, *J. Phys. Chem.*, **61**, 1619 (1957).

(4) F. E. Weir and M. Dole, *J. Am. Chem. Soc.*, **80**, 302 (1958).

(5) P. N. Henrion, *Trans. Faraday Soc.*, **60**, 75 (1964).

Table I: Data for the System Water–Sucrose–Glycine[a,b,c]

1	Expt. no.[d]	2	3	4	1
2	$(\rho_1)_A$	0.125006	0.124092	0.119962	0.118998
3	$(\rho_2)_A$	0.119970	0.120709	0.124238	0.125046
4	ρ_A	1.092673	1.092594	1.092405	1.092354
5	$(\rho_1)_B$	0.124970	0.125876	0.129998	0.130994
6	$(\rho_2)_B$	0.129972	0.129247	0.125734	0.124978
7	ρ_B	1.096471	1.096504	1.096696	1.096808
8	$\bar{\rho}_1$	0.124988	0.124984	0.124980	0.124996
9	$\bar{\rho}_2$	0.124971	0.124978	0.124986	0.125012
10	J_{exptl}	76.12	76.77	75.84	76.73
11	J_{calcd}	76.17	76.69	75.97	76.63
12	α_1	−0.0030	0.1496	0.8497	1.0069
13	$(\mathfrak{D}_A)_{exptl} \times 10^5$	0.71949	0.63789	0.40208	0.36910
14	$(\mathfrak{D}_A)_{calcd} \times 10^5$	0.71792	0.63907	0.40310	0.36827
15	$Q_{exptl} \times 10^4$	−58.6	−3.5	67.7	53.6
16	$Q_{calcd} \times 10^4$	−61.8	−0.5	69.7	51.6
17		$R_1 = 0.14007$		$R_2 = 0.16635$	
18		$\bar{v}_0 = 0.99954$	$\bar{v}_1 = 0.6273$	$\bar{v}_2 = 0.6192$	
19			$(D_{11})_V \times 10^5 = 0.3302 \mp 0.0023$		
20			$(D_{12})_V \times 10^5 = 0.0651 \mp 0.0032$		
21			$(D_{21})_V \times 10^5 = 0.0560 \pm 0.0033$		
22			$(D_{22})_V \times 10^5 = 0.6265 \pm 0.0044$		

[a] 0 = water, 1 = sucrose, 2 = glycine; $\bar{\rho}_1 = 0.125$, $\bar{\rho}_2 = 0.125$. [b] Units: concentrations ρ_i, g. cc.$^{-1}$; densities ρ, g. cc.$^{-1}$; reduced height–area ratios $\mathfrak{D}_A$, cm.^{2} sec.$^{-1}$; partial specific volumes $\bar{v}_i$, cc. g.$^{-1}$; refractive index derivatives R_i, cc. g.$^{-1}$, referred to the velocity of light in air at standard temperature and pressure and for wave length 5460.7×10^{-8} cm. in air; diffusion coefficients $(D_{ij})_V$, cm.^{2} sec.$^{-1}$, corresponding to volume-fixed flows, $(J_i)_V$, having units of g. cm.$^{-2}$ sec.$^{-1}$, and gradients of concentrations having units of g. cm.$^{-4}$. [c] Quantities which were calculated as intermediate data are $I_A = 373.66$, $S_A = 146.43$, $E_0 = -2.253$, $E_1 = 16.676$, and $E_2 = 11.691$. [d] Experiments are numbered chronologically.

Sucrose from the National Bureau of Standards (sample no. 17) was used without further purification. The glycine was part of a sample which had been once recrystallized for a previous study.[6] Procedures for preparing solutions and calculating their concentrations[7] have been described elsewhere,[8] except that here the concentration of each component, i, is denoted by ρ_i and expressed as g. cc.$^{-1}$. Doubly distilled water which had been saturated with air was used in all experiments. Each solution density, ρ, in g. cc.$^{-1}$ was obtained by averaging data from triplicate measurements in matched, single-neck, 30-ml. Pyrex pycnometers; the density of water at 25° was taken to be 0.997048 g. cc.$^{-1}$.

To obtain the desired diffusion data for the composition investigated, four diffusion experiments were performed with the Gouy diffusiometer used previously. The reader is referred to an earlier article[8] for information about the apparatus, for equations defining the various quantities, for description of the method of performing the experiments, and for calculation procedures for obtaining the final results. The same fused quartz diffusion cell was used for all experiments; its thickness, a, along the light path was 2.5074 cm., and the optical lever arm, b, was 307.06 cm. Each experiment was performed within ±0.006° of 25°, and the Stokes–Einstein relation was used to convert each reduced height–area ratio to $25.00_0°$.

Results

Table I summarizes all of the results from this study. Lines 2–9 give the solute concentrations, ρ_i, for the upper (A) and lower (B) solutions which were prepared for use in each diffusion experiment together with the corresponding measured densities and the mean solute concentrations, $\bar{\rho}_1 \simeq \bar{\rho}_2 \simeq 0.125$ g. cc.$^{-1}$. Measurements of the pH of the solutions for experiments 3 and 4 gave values between 6.0_8 and 6.1_0. The total number of fringes, J_{exptl}, obtained in each experiment is given in line 10. These values and the corresponding concentration differences, $\Delta\rho_i = (\rho_i)_B - (\rho_i)_A$, were used to compute[9] the values of the refractive index

(6) P. J. Dunlop, *J. Am. Chem. Soc.*, **77**, 2994 (1955).

(7) In calculating air buoyancy corrections the values 1.588 and 1.601 g. cc.$^{-1}$ were used for the densities of solid sucrose and glycine, respectively.

(8) L. A. Woolf, D. G. Miller, and L. J. Gosting, *J. Am. Chem. Soc.*, **84**, 317 (1962).

derivatives, R_1 and R_2, which are listed in line 17 of the table. Then from the R_i and the $\Delta\rho_i$ for each experiment, values of J_{calcd}, line 11, were calculated for comparison with J_{exptl} and, in addition, values were computed for α_1, the fraction of the total refractive increment between solutions B and A contributed by component 1, and are listed in line 12. The reduced height–area ratio, $(\mathfrak{D}_A)_{\text{exptl}}$, and the area, Q_{exptl}, of the fringe deviation graph for each experiment are listed in lines 13 and 15.

The desired volume-fixed diffusion coefficients, $(D_{ij})_V$, for this composition of the system, $\bar{\rho}_1 = \bar{\rho}_2 = 0.125$ g. cc.$^{-1}$, were computed[9] from the values of J_{exptl}, $\Delta\rho_i$, $(\mathfrak{D}_A)_{\text{exptl}}$, and Q_{exptl}, and are reported in lines 19–22. The estimates of accuracy shown were obtained by recalculating the $(D_{ii})_V$ after changing each Q_{exptl} by its estimated error; the upper sign corresponds to an increase of every Q by 0.0003 and the lower sign to a decrease of every Q by the same amount. It was found that an increase of each value of $(\mathfrak{D}_A)_{\text{exptl}}$ by 0.2% (without change in any Q) would increase each $(D_{ii})_V$ by less than 0.4% of its value. Values of I_A and S_A (eq. 42 of ref. 8) together with values of E_0, E_1, and E_2 (eq. 43 of ref. 8) which are intermediate quantities obtained in the calculation of the $(D_{ij})_V$ are reported in footnote *c* of Table I. The values of $(\mathfrak{D}_A)_{\text{calcd}}$ and Q_{calcd} in lines 14 and 16 were computed from the values of $\Delta\rho_i$, R_i, and the $(D_{ij})_V$ for comparison with the $(\mathfrak{D}_A)_{\text{exptl}}$ and the Q_{exptl}. These comparisons, and those of the J_{exptl} with the J_{calcd}, indicate somewhat greater deviations from the experimental data than have usually been obtained in this laboratory for other three-component systems. It is believed that all concentration differences, $\Delta\rho_i$, were sufficiently small so that the effects of concentration dependences of the $(D_{ij})_V$, of the R_i, and of the $\bar{v}_i$ do not affect the values reported in lines 17–22 by amounts significantly greater than the experimental errors of measurement. When the $\Delta\rho_i$ are sufficiently small, the volume-fixed frame of reference becomes identical with the cell-fixed frame of reference, and the $(D_{ij})_V$ may be identified with flows measured relative to the diffusion cell.[10] Application of criteria given elsewhere[11] indicates that in all four experiments reported in Table I the liquid columns in the diffusion cell were gravitationally stable.

To calculate the partial specific volumes, $\bar{v}_i$, of the components, the constants in the following equation were determined by the method of least squares to fit the density data in Table I.

$$\rho = 1.094573 + 0.3724(\rho_1 - 0.125) + 0.3805(\rho_2 - 0.125) \quad (1)$$

These constants, which express the density data with an average error of 0.0009%, were used to calculate the $\bar{v}_i$ in line 18 of Table I by using equations derived previously.[12]

(9) The procedure used for these calculations was the same as described in ref. 8, except they were performed on a Bendix G-15 computer using programs written in Intercom 1000 (double precision) format by R. P. Wendt, *J. Phys. Chem.*, **66**, 1279 (1962).

(10) J. G. Kirkwood, R. L. Baldwin, P. J. Dunlop, L. J. Gosting, and G. Kegeles, *J. Chem. Phys.*, **33**, 1505 (1960).

(11) See eq. 42 and 43 of G. Reinfelds and L. J. Gosting, *J. Phys. Chem.*, **68**, 2464 (1964), which are abbreviated forms of general gravitational stability criteria derived by R. P. Wendt, *ibid.*, **66**, 1740 (1962).

(12) P. J. Dunlop and L. J. Gosting, *ibid.*, **63**, 86 (1959).

Metathetical Reactions of Ion Pairs in Acetic Acid

by Elton Price and Ernest Grunwald

Bell Telephone Laboratories, Incorporated, Murray Hill, New Jersey 07971 *(Received July 3, 1964)*

Although the properties of ion pairs have been of theoretical interest for many years, thermodynamic data for metathetical reactions of ion pairs are relatively scarce. Such data can be obtained indirectly and with considerable labor from ion-pair dissociation constants.[1] As far as we know, the only previously reported direct methods of measurement are based on the analysis of the solubility of sparingly soluble salts in the presence of other salts,[1a,1c] or of the absorption spectra of the ion pairs when these depend on the nature of the counterions.[2]

We now wish to report a kinetic method that is based on nuclear magnetic resonance measurements of NH–COOH proton exchange in acetic acid.[3] The metathetical reactions for which the equilibrium constants can be measured by our method are represented by eq. 1, where BH^+ is any suitable alkylammonium ion and M^+ is any cation that does not have rapidly exchangeable protons.

$$BH^+Y^- + M^+OAc^- \overset{K_{eq}}{\rightleftharpoons} BH^+OAc^- + M^+Y^- \quad (1)$$

(1) (a) E. Griswold, M. M. Jones, and R. K. Birdwhistell, *J. Am. Chem. Soc.*, **75**, 5701 (1953); (b) M. M. Jones and E. Griswold, *ibid.*, **76**, 3247 (1954); (c) R. K. Birdwhistell and E. Griswold, *ibid.*, **77**, 873 (1955).

(2) M. M. Davis and H. B. Hetzer, *ibid.*, **76**, 4247, 6423 (1954).

(3) (a) E. Grunwald and E. Price, *ibid.*, **86**, 2965 (1964); (b) E. Grunwald and E. Price, *ibid.*, **86**, 2970 (1964).

In the present note, we let $BH^+ = (CH_3)_3NH^+$ and $M^+ = (CH_3)_4N^+$ or Na^+. The solvent is glacial acetic acid.

It has been shown[3] that in acetic acid, at electrolyte concentrations above 0.01 M, the rate of proton exchange of free BH^+ ions with the solvent is negligible compared to that of the acetate ion pairs, BH^+OAc^-. It has been shown, further, that the rate constant for proton exchange of BH^+Y^- is related to that for BH^+OAc^- approximately as the ratio of the basicity of Y^- relative to that of OAc^-.[4] It is therefore convenient, but not essential, that M^+Y^- be the salt of an acid that is at least two orders of magnitude stronger than acetic acid. In that case, the concentrations of the solute components can easily be adjusted so that proton exchange due to BH^+Y^- is negligible, and the observed rate of exchange, R, is directly proportional to the concentration of BH^+OAc^- in the equilibrium mixture. The relevant rate constant, $k = R/[BH^+OAc^-]$, is evaluated in a control experiment in which the only solute components are BH^+OAc^- and BH^+Y^-. The equilibrium constant can then be derived from rate measurements on systems in which the solute components are BH^+OAc^- and M^+Y^-.

The method is illustrated in Table I for some systems in which $Y^- = Cl^-$. The equilibrium constant, K_{eq}, is defined by

$$K_{eq} = \frac{[BH^+OAc^-][M^+Y^-]}{[BH^+Y^-][M^+OAc^-]} \qquad (2)$$

where the brackets denote molar concentrations. The precision of the K_{eq} values obtained by this method is about 10%.

It should be noted that the scope of this method is much wider than suggested by eq. 1. Given the values of K_{eq} for a series of salts M^+Y^-, further equilibrium constants for the ion-pair reactions among these salts can be derived by standard thermodynamic methods. Thus, the equilibrium constant for reaction 3, K_3, is

$$(CH_3)_4N^+Cl^- + Na^+OAc^- \rightleftharpoons (CH_3)_4N^+OAc^- + Na^+Cl^- \qquad (3)$$

equal to the ratio of K_{eq} for Na^+Cl^- to K_{eq} for $(CH_3)_4N^+Cl^-$. Using the data in Table I, the actual value obtained for K_3 is 0.170/0.510, or 0.33.

The present data, in agreement with earlier results,[1] indicate that equilibrium constants for metathetical reactions of ion pairs can differ appreciably from the purely statistical value of unity. The sensitivity of the present values of K_{eq} to ion-pair structure is also qualitatively consistent with existing data for ion-pair dissociation constants, K_d. The latter are related to K_{eq} according to eq. 4.

$$K_{eq} = \frac{K_d^{BH^+Y^-} K_d^{M^+OAc^-}}{K_d^{BH^+OAc^-} K_d^{M^+Y^-}} \qquad (4)$$

Bruckenstein and Kolthoff[5] find large differences among K_d values for acetate salts but very small differences among the corresponding chlorides. On that basis, the deviation from unity of the K_{eq} values in Table I may be ascribed largely to specific interactions in the acetate ion pairs rather than in the chloride ion pairs.

Table I: Equilibrium Constants for the Metathetical Reaction, $(CH_3)_3NH^+Cl^- + M^+OAc^- \rightleftharpoons (CH_3)_3NH^+OAc^- + M^+Cl^-$, in Acetic Acid at 25°

Solute components, M ($BH^+ = (CH_3)_3NH^+$)	$R^{a,b}$	K_{eq} or k
(a) Measurement of k (sec.$^{-1}$)[a]		
BH^+OAc^-, 0.0207; BH^+Cl^-, 0.0215	17.0	820
BH^+OAc^-, 0.0207; BH^+Cl^-, 0.0492	16.5	796
BH^+OAc^-, 0.0207; BH^+Cl^-, 0.0772	17.5	845
	Av.	820
(b) Measurement of K_{eq}		
BH^+OAc^-, 0.0200; $(CH_3)_4N^+Cl^-$, 0.0199	6.94	0.536
BH^+OAc^-, 0.0200; $(CH_3)_4N^+Cl^-$, 0.0516	3.15	0.520
BH^+OAc^-, 0.0200; $(CH_3)_4N^+Cl^-$, 0.0816	1.89	0.469
	Av.	0.510
Na^+OAc^-, 0.0180; BH^+Cl^-, 0.0993	8.69	0.170

[a] R = rate of NH–COOH proton exchange, in g.-atom/l. sec., $k = R/[BH^+OAc^-]$. [b] Calculated using eq. 2 and 3 of ref. 3b. The required n.m.r. parameters are δ (radians/sec.) = $846p_{Cl} + 690p_{OAc}$, J = 330 radians/sec., $1/T^1$ (sec.$^{-1}$) = $400p_{Cl} + 660p_{OAc}$, p_{Cl} = fraction of chloride salt in the salt mixture and p_{OAc} = fraction of acetate salt; $p_{Cl} = 1 - p_{OAc}$.

Experimental

Glacial acetic acid (Merck) was purified and dried as described previously.[3a]

Trimethylamine was obtained from Matheson and Co. in the form of a compressed gas. Trimethylammonium chloride (Eastman) was recrystallized twice from absolute ethanol. Tetramethylammonium chloride (Eastman) was recrystallized twice from absolute ethanol. Sodium acetate (Baker) was dried at 120° for 36 hr.

Rates of NH–COOH proton exchange were determined by nuclear magnetic resonance techniques

(4) Kinetic data for proton exchange of ammonium picrate, trichloroacetate, and acetate in acetic acid lead to a value of 0.9 for the slope of the Brønsted log k vs. log K_B plot: E. Grunwald and E. Price, *J. Am. Chem. Soc.*, 86, 4517 (1964).

(5) S. Bruckenstein and I. M. Kolthoff, *ibid.*, 78, 2974 (1956).

from the exchange broadening of the dominant n.m.r. line in the NH–COOH proton system. Experimental methods and rate calculations have been fully described elsewhere[3] and need not be repeated here. Values for relevant n.m.r. parameters were taken from the previous work[3b] and are listed in Table I, footnote *b*. Solute concentrations were in the range 0.01 to 0.2 *M*.

The following salts, when present as single solutes in acetic acid, were found to give negligible (<0.02 sec.$^{-1}$) exchange broadening of the COOH proton resonance at 25°: $(CH_3)_3NHCl$, NaCl, NaOAc, $(CH_3)_4NCl$, and $(CH_3)_4NOAc$. On the other hand, solutions of $(CH_3)_3NHOAc$, either as a single solute or in the presence of one of the previously mentioned salts, gave significant exchange broadening of the COOH proton resonance. The values of the exchange broadening permitted calculation of the exchange rate, R, which in turn permitted evaluation of $[(CH_3)_3NHOAc]$ as described in the text.

The Heat of Decomposition of Hydrogen Superoxide

by D. A. Csejka, F. Martinez, J. A. Wojtowicz, and J. A. Zaslowsky[1]

Olin Mathieson Chemical Corporation, Organics Division, New Haven, Connecticut *(Received June 26, 1964)*

The preparation of a thermally unstable hydrogen superoxide has been recently confirmed.[2,3] Although several values have been reported for its heat of decomposition,[4,5] the techniques employed have been relatively crude and the samples were not of known assay. A more precise determination on the basis of samples of known assay is presented.

Experimental

Apparatus. An ice calorimeter similar to that described by Giguère, Morissette, and Olmos[6] was employed. It was modified as follows. (a) A weighed glass vessel was placed in the central tube which holds the ice mantle. (b) The space between the central tube and vessel was filled with aqueous sulfuric acid (for rapid heat transfer). Samples were dropped into the vessel. The calorimeter was calibrated electrically; a value of 64.67 ± 0.09 (std. dev.) cal./g. of Hg was obtained (1 cal. = 4.1840 joules).

Materials. Hydrogen Superoxide. (1) Ozone was condensed on the walls of a U-trap cooled to −196° and exposed to hydrogen atoms as described.[3] The product was warmed to −135° under vacuum to remove unreacted ozone, recooled to −196°, and transferred to glass sample holders. Trace quantities of ozone remained.

(2) Water vapor was passed through a glow discharge tube, dissociated, and condensed at −196°. A neon sign transformer rated at 15 kv. and 30 ma. was used as the power source. Flow conditions were maintained using a Welch Duo-seal vacuum pump (1–2 mm. pressure).

Portions of each reaction product were decomposed by warming to −40°. The evolved oxygen was measured manometrically in a calibrated vacuum system. The residue was weighed and analyzed for hydrogen peroxide by permanganate titration.

Molar ratios of evolved oxygen to residual hydrogen peroxide were calculated. The amount of hydrogen superoxide in a calorimetric sample was determined from the molar ratio, the amount of residual hydrogen peroxide in the sample, and the equation

$$H_2O_4 \longrightarrow H_2O_2 + O_2$$

The molar ratio is the fraction of the residual hydrogen peroxide which was originally present as superoxide. In the case of the ozone–hydrogen atom product a ratio of 1.0 was used (1.0 ± 0.1 experimentally).

Amorphous ice–hydrogen peroxide samples of similar composition to the superoxide residue were prepared by condensing water–hydrogen peroxide vapor at −196°.

Procedure. Reaction product was transferred at −196° to thin-walled glass holders (5 × 0.5 cm.), warmed to −135° under vacuum for 30 min. to remove any liquid nitrogen or air, and recooled to −196° in a nitrogen atmosphere. The sample was transferred rapidly at −196° to the equilibrated calorimeter, and the heat evolved was determined by mercury weight. At the conclusion of the experiment the residue was weighed and analyzed for hydrogen peroxide; the amount of H_2O_4 was determined from the previous analyses.

(1) Address inquiries to D. A. Csejka. Work sponsored by Air Force Office of Scientific Research, Contract No. AF 49(638)-1137.

(2) N. I. Kobozev, I. I. Skorokhodov, L. I. Nekrasov, and E. I. Makarova, *Zh. Fiz. Khim.*, **31**, 1843 (1957).

(3) J. A. Wojtowicz, F. Martinez, and J. A. Zaslowsky, *J. Phys. Chem.*, **67**, 849 (1963).

(4) J. A. Ghormley, *J. Am. Chem. Soc.*, **79**, 1862 (1957).

(5) (a) L. A. Resnitskii, K. G. Khomyakov, L. I. Nekrasov, and I. I. Skorokhodov, *Zh. Fiz. Khim.*, **32**, 87 (1958); (b) I. I. Skorokhodov, L. I. Nekrasov, L. A. Reznitskii, K. G. Khomyakov, and N. I. Kobozev, *ibid.*, **33**, 2090 (1959).

(6) P. A. Giguère, B. G. Morissette, and A. W. Olmos, *Can. J. Chem.*, **33**, 657 (1955).

Table I: Heat of Decomposition at −196° of the Superoxide from Dissociated Water

Sample wt., (mg.)	$O_2(e)/H_2O_2$	Residue H_2O_2 wt., mg.	H_2O_4, mmole	Total heat, eq. I + II + III, cal.	Heat, eq. II, cal.	Heat, eq. III, cal.	Heat of decomposition, kcal./mole
191.5	0.160	30.5	0.144	21.70	23.92	0.43	−18.4
208.4	0.160	31.4	0.148	24.02	26.07	0.44	−16.8
231.2	0.177	50.7	0.264	24.47	28.52	0.79	−18.3
							Av. −17.8 ± 2.2 (95% certainty)

Table II: Heat of Decomposition at −196° of the O_3–H Atom Reaction Product

Sample wt., mg.	Residue H_2O_2 wt., mg.	H_2O_4, mmole	Total heat, eq. I + II + III,[a] cal.	Heat, eq. II, cal.	Heat, eq. III, cal.	Heat of decomposition, kcal./mole
20.6	3.6	0.105	−0.34	2.20	0.30	−27.1
23.3	4.4	0.129	−0.43	2.46	0.37	−25.3
49.3	6.6	0.193	+0.66	5.52	0.57	−28.1
						Av. −26.8 ± 2.6 (95% certainty)

[a] In eq. I and II, $x = 0$.

The transfers of aqueous hydrogen peroxide samples were conducted in a similar manner. All the samples were homogeneous since the peroxide assay was the same for samples from the same preparation.

To correct the observed heat for the heat capacity effect of the glass sample holders nine determinations using the holders were made. A value of 23.0 ± 1.1 (std. dev.) cal./g. for the heat absorbed from −196° to 0° was obtained.

Results

Thermal data of the following reactions were used to determine the heat of decomposition of the superoxide matrix at 196°

$$H_2O_4 \cdot xH_2O_2 \cdot yH_2O(s, -196°) \longrightarrow (x + 1)H_2O_2 \cdot yH_2O(s, -196°) + O_2(l, -196°) \quad (I)$$

$$(x + 1)H_2O_2 \cdot yH_2O(s, -196°) \longrightarrow (x + 1)H_2O_2 \cdot yH_2O(soln., 0°) \quad (II)$$

$$O_2(l, -196°) \longrightarrow O_2(g, 0°) \quad (III)$$

The heat absorbed from −196 to 0° of five amorphous ice–hydrogen peroxide samples having the same composition as the superoxide residue was determined. A value of 128.0 ± 1.2 (std. dev.) cal./g. for samples between 17.4 and 20.1 wt. % hydrogen peroxide was determined for eq. II. Thermodynamic data[7] were used to determine the heat absorbed in eq. III. The contribution to the heat of reaction of HO_2 radicals was neglected on the basis of their reported low concentration (about 0.3–0.4 wt. %) as determined by e.p.r. studies.[8] Furthermore, we have shown that at −135° the HO_2 radicals disappear rapidly. Samples were annealed at −135° for over 0.5 hr. prior to recooling to −196°.

Results for the decomposition of the hydrogen superoxide matrix are summarized in Tables I and II.

Uncertainty. The following significant uncertainties arose in these determinations. (1) Enthalpy change of ice–peroxide and superoxide from −196 to 0° including phase changes (1%); this contributes a 15% uncertainty in the heat of decomposition in the case of dissociated water and about 6% in the ozone reaction product; (2) molar ratio of oxygen evolved to hydrogen peroxide; in the dissociated water the error is about 5%. This contributes a 5% uncertainty to the heat of decomposition.

Discussion

The difference in the heats of decomposition of the two superoxide matrices, about 9 kcal./mole, is beyond

(7) (a) "Selected Values of Chemical Thermodynamic Properties," National Bureau of Standards Circular 500, U. S. Govt. Printing Office, Washington, D. C., 1952; (b) H. W. Woolley, *J. Res. Natl. Bur. Std.*, **40**, 163 (1948).

(8) R. L. Livingston, J. A. Ghormley, and H. Zeldes, *J. Chem. Phys.*, **24**, 483 (1956).

the experimental error and is attributed to either: (a) a difference in the matrix (one containing hydrogen peroxide, the other little or none), or (b) more probably to traces of ozone or nitrogen oxides in the ozone–hydrogen atom product. There were traces of ozone visible in the product. The ozone can react with hydrogen peroxide or decompose to liberate 57 kcal. or 34 kcal./mole of ozone, respectively.

The heat of decomposition of H_2O_4 at $-196°$ is -17.8 ± 2.2 kcal./mole. This differs considerably from the value of -44 kcal./mole reported by Ghormley[4] and -39 kcal./mole reported by Skorokhodov, *et al.*[5]

Ghormley assumed a superoxide assay without product analysis. Skorokhodov's calculation of the heat of decomposition is not clear.

The heat of formation of H_2O_4 at $-196°$ was estimated from data obtained in this research and those available in the literature.[9] The heat capacity of H_2O_2 from -196 to 25° was obtained from Giguère's data. The average C_p of H_2O_2 is 5.50 cal. mole^{-1} deg.$^{-1}$ from -196 to $-173°$, 6.85 cal. mole^{-1} deg.$^{-1}$ from -173 to $-143°$, 9.40 cal. mole^{-1} deg.$^{-1}$ from -143 to $-53°$, $2.31 + 0.03967T$ (°K.) cal./mole from -53 to $-2°$, 21.36 cal. mole^{-1} deg.$^{-1}$ from 0 to 25°. The heat of fusion of H_2O_2 at -0.43 is 2.9 kcal./mole. The average C_p of H_2 is 6.25 cal. mole^{-1} deg.$^{-1}$ from -196 to 25°. The average C_p of O_2 is 6.98 cal. mole^{-1} deg.$^{-1}$ from -183 to 25° and 13.0 cal. mole^{-1} deg.$^{-1}$ from -183 to $-196°$. The heat of vaporization of O_2 at $-183°$ is 1.6 kcal./mole.

It is assumed that there is no interaction of the matrix with H_2O_4 or H_2O_2 upon decomposition at $-196°$. The heat of formation of H_2O_2 at $-196°$ is -45.7 kcal./mole. Using the value of -17.8 kcal./mole for the reaction

$$H_2O_4 \cdot (xH_2O_2 \cdot yH_2O)(s) \longrightarrow H_2O_2 \cdot (xH_2O_2 \cdot yH_2O)(s) + O_2(l)$$

at $-196°$, the heat of formation of H_2O_4 is -27.9 kcal./mole.

The combination of HO_2 radicals is thought to lead to the formation of H_2O_4.[3] Using the data of Gray[10] for the heat of formation of gaseous HO_2 radicals (+5 kcal./mole) and assuming this radical has the same thermal properties as hydrogen peroxide, the heat of reaction at $-196°$ of

$$2HO_2(s) \longrightarrow H_2O_4(s)$$

is -4 kcal./mole H_2O_4.

(9) (a) P. A. Giguère, I. D. Liu, J. S. Dugdale, and J. A. Morrison, *Can. J. Chem.*, **32**, 117 (1954); (b) P. A. Giguère, B. G. Morissette, A. W. Olmos, and O. Knop, *ibid.*, **33**, 804 (1955); (c) "Selected Values of Chemical Thermodynamic Properties," National Bureau of Standards Circular 500, U. S. Govt. Printing Office, Washington, D. C., 1952; (d) H. W. Woolley, *J. Res. Natl. Bur. Std.*, **40**, 163 (1948); (e) H. W. Woolley, R. B. Scott, and F. G. Brickwedde, *ibid.*, **41**, 379 (1948).

(10) P. Gray, *Trans. Faraday Soc.*, **55**, 408 (1959).

Viscoelastic Properties of Plasticized Gelatin Films

by J. B. Yannas[1] and A. V. Tobolsky

Frick Chemical Laboratory, Princeton University, Princeton, New Jersey *(Received June 29, 1964)*

Features of the molecular structure of gelatin have been studied by a great variety of physicochemical approaches. In particular, the related problems of chain conformation, chain aggregation, and crystallinity of gelatin have received attention. Investigations of such as yet unresolved questions have been performed on gelatin samples which have covered the entire concentration range—from dilute solutions through gels to glassy films.[2]

Our own effort has centered on the measurement of viscoelastic properties of plasticized gelatin sheets and sheets of pure, unplasticized protein. So far, these measurements have given us useful insight into the characteristics of this interesting biopolymer.

Experimental

Limed ossein gelatin in powder form and sheets was obtained through the courtesy of Dr. D. Tourtellotte of Kind and Knox Gelatin Co., Camden, N. J. (Lot 4181-1). Gelatin prepared in identical fashion has been characterized by Scatchard, *et al.* (Knox Special Gelatin Type A).[3] It is a relatively monodisperse grade, the value of M_w/M_n being 1.61. Gelatin of this type has $M_n = 45{,}700$ and an isoionic point of 4.92. The moisture content is of the order of 10 wt. % and the ash content is of the order of 1 wt. %.

Dimethyl sulfoxide (J. T. Baker Chemical Co., purity 99.9%) was the main plasticizer used. Glycerol

(1) National Institutes of Health predoctoral fellow, Department of Chemistry, Princeton University, Princeton, N. J.

(2) J. D. Ferry, *Advan. Protein Chem.*, **4**, 21 (1948); A. G. Ward and P. R. Saunders, "Rheology," F. R. Eirich, Ed., Vol. 2, Academic Press, Inc., New York, N. Y., 1958; W. R. Harrington and P. H. von Hippel, *Advan. Protein Chem.*, **16**, 1 (1961).

(3) G. Scatchard, J. L. Oncley, J. W. Williams, and A. Brown, *J. Am. Chem. Soc.*, **66**, 1980 (1944).

(J. T. Baker Chemical Co., purity 96.0%) was also used as an alternate plasticizer in several instances.

Plasticized gelatin films were obtained by weighing amounts of gelatin powder, previously pulverized finely and dehydrated in a vacuum oven at 65° for several days, into aluminum dishes containing an excess of plasticizer. The initial protein concentration was of the order of 5 wt. %. The dishes were placed in a drying oven at 65 ± 1° and the plasticizer was allowed to evaporate slowly. Dishes were removed from the oven when the protein concentration in the films increased to the desired level (40–80 wt. %). Several films were also prepared using undried gelatin powder. In the undried form gelatin dissolved much more readily into the plasticizer giving films of superior clarity; these possessed identical viscoelastic properties with films that were prepared using dried gelatin powder. Immediately after removal from the oven, the films were cut up into rectangular strips; these were immersed in silicone oil (polydimethylsiloxane, Dow Corning Corp.) wherein they were tested. Strips of unplasticized protein were prepared by cutting up sheet gelatin after brief heating on a hot metal surface to impart flexibility; strips so obtained were dehydrated initially in a drying oven at 105° overnight and subsequently in a vacuum oven at 105° over a period of 4 days. Prolonged exposure of sheet gelatin to 105° (2 wk.) did not affect the magnitude of the properties measured.

The torsion modulus G of the strips measured after 10 sec. was obtained by a Clash–Berg torsional creep apparatus[4] in the region where the modulus exceeds 10^9 dynes/cm.^{2}. Below that level of the modulus, measurements were made in a modified Gehman apparatus.[5] Curves of log $3G$ *vs.* temperature were thus obtained for the various specimens within the experimentally accessible temperature range from −80 to 220°. The lower temperature limit was set by limitations of the apparatus used; the upper temperature range was imposed by the decomposition characteristics of the protein and by the volatility of the plasticizer.

The buoyant weight of specimens immersed in silicone oil was also measured over a considerable temperature range. A discontinuity in the slope of the buoyant weight *vs.* temperature curve indicated the presence of a glassy transition in the specimen. Such measurements of the glass transition temperature are entirely equivalent to those where a discontinuity in the slope of a specific volume *vs.* temperature curve is used as the criterion for the transition.

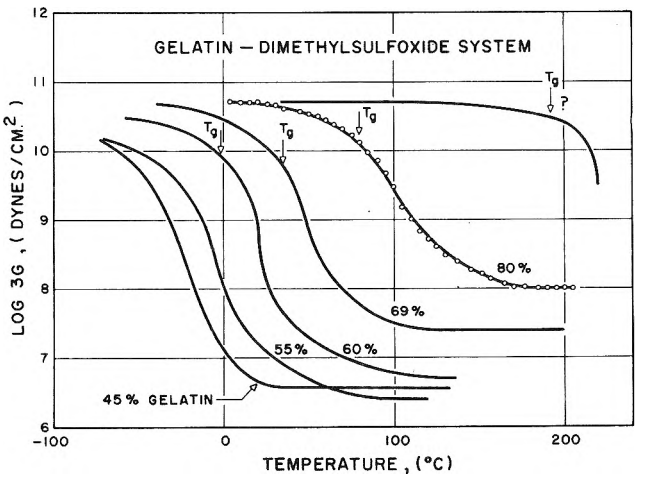

Figure 1. Ten-second modulus *vs.* temperature for gelatin–dimethyl sulfoxide sheets.

Results and Discussion

The log modulus *vs.* temperature curves for five specimens of gelatin plasticized with varying amounts of dimethyl sulfoxide (DMSO) are displayed in Fig. 1. The curve for the pure, unplasticized protein sheet is also shown; this curve is incomplete due to decomposition of the protein at *ca.* 220°. Arrows indicate the position of the glass transition temperature, T_g, as measured by the procedure illustrated in Fig. 2. The T_g of the pure protein is in the vicinity of 190°; its precise determination has eluded us so far owing to the experimental conditions which allow sufficient time for decomposition to occur and invalidate the data in that temperature region.

Values of T_g for the system gelatin–DMSO are listed in Table I. A tabulation of values of T_t (the

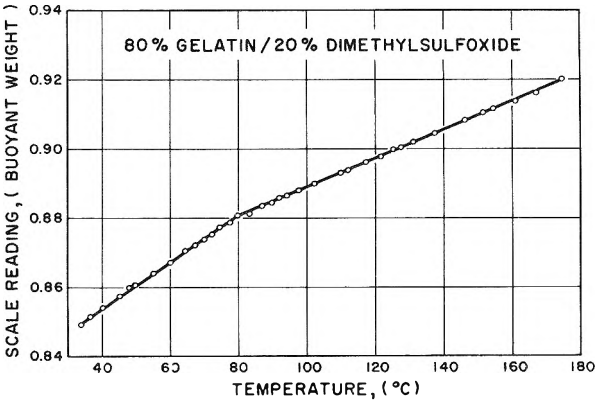

Figure 2. Buoyant weight *vs.* temperature for gelatin–dimethyl sulfoxide 80–20.

(4) R. F. Clash and R. M. Berg, *Ind. Eng. Chem.*, **34**, 1218 (1942).

(5) S. D. Gehman, D. E. Woodford, and C. S. Wilkinson, Jr., *ibid.*, **39**, 1108 (1947).

Table I: Viscoelastic Parameters of Gelatin Films

Gelatin concn., wt. %	Gelatin-DMSO T_g, °C.	Gelatin-DMSO T_i, °C.	Gelatin-glycerol T_i, °C.
40	...	−33	...
45	...	−31	...
50	...	−20	...
55	...	−13	−11
60	−3	17	30
65	23	...	...
69	35	50	53
75	60	...	...
80	80	112	110
100	(180–200)[a]	(220)[a]	(220)[a]

[a] Data uncertain owing to decomposition.

temperature at which $3G$ equals 10^9 dynes/cm.^{2}) for the systems gelatin–DMSO and gelatin–glycerol is also given there.

The results of Fig. 2 display a discontinuity in the slope of specific volume *vs.* temperature, rather than a discontinuity of the specific volume itself. This is an indication of a glass transition rather than a first-order transition (melting). The shape of the modulus–temperature curve in the neighborhood of the transition shows a change from glassy to leathery behavior, which is also indicative of a glass transition (see Fig. 1).

It is also observed (Fig. 1) that extended rubbery plateaus, where the modulus is relatively invariant with temperature, can be obtained even when the plasticizer concentration is as high as 55% wt. In no case was any melting or flow observed; instead, the specimens remained dimensionally stable and truly rubbery until loss of plasticizer started affecting the measurements.

The persistence of rubbery behavior in linear polymers over an extended temperature range is frequently evidence of the presence of a pseudo three-dimensional network structure. We believe that, in the case of plasticized gelatin, small protein crystallites are present even at very high plasticizer concentrations; these microcrystallites act as cross links which do not melt even at temperatures as high as 200° (Fig. 1). This interpretation is consistent with our belief that T_g for pure gelatin is in the vicinity of 190°.

In summary, we believe that gelatin plasticized with dimethyl sulfoxide and glycerol exhibits viscoelastic behavior typical of a plasticized microcrystalline polymer such as polyvinyl chloride.[6-8]

(6) A. V. Tobolsky, D. Carlson, and N. Indictor, *J. Appl. Polymer Sci.*, **7**, 393 (1963).

(7) A. V. Tobolsky and R. B. Taylor, *ibid.*, in press.

(8) M. Shen and A. V. Tobolsky, *Ind. Eng. Chem.*, in press.

Infrared Spectral Observation of Surface States

by George Blyholder and Edwin A. Richardson[1]

Department of Chemistry, University of Arkansas, Fayetteville, Arkansas *(Received July 15, 1964)*

In the course of studies[2] related to the surface interactions of α-Fe_2O_3 and polar adsorbates such as water and ammonia, a number of absorption bands in the infrared region (2 to 15 μ) were noted. These bands appear to be directly related to the solid adsorbent and only indirectly to the particular adsorbates employed. The purpose of this note is to describe the occurrence of these bands and their changes upon chemisorption and to propose several possible origins.

Experimental

A Perkin-Elmer Model 21 infrared recording spectrometer is employed. To expand the low transmission range of the instrument, the reference beam is partially blocked off with screen wires. The sample disk is mounted in a modified gas cell as described by Blyholder and Neff.[3] The effective range of the system is 2 to 13 μ. A conventional vacuum apparatus capable of maintaining 0.001 μ pressure is employed in degassing the disk.

Certified reagent grade iron(III) oxide obtained from Fisher Scientific Co. was employed without further treatment. Particle sizes are in the 5 μ range and the material has a surface area of about 15 m.^{2}/g. The far-infrared spectrum of this material indicates that it is essentially α-Fe_2O_3.[4]

About 0.3 g. of α-Fe_2O_3 is transferred to a 2.5-cm. diameter die and pressed at 8000 p.s.i. Before pressing, the die is heated in an oven at 140° to prevent sticking of the disk to the die face. By careful handling, the disk can be removed from the die without breaking and transferred to the cell described above.

The disks as prepared above contain considerable water and thus are not active in chemisorption. The activation process consists of degassing the disk at room temperature for several hours or until a pressure in the order of 0.05 μ can be maintained. The disk is then heated to 375° in an atmosphere of O_2 and maintained for several hours. This oxidizes any impurities which might cause subsequent reduction. The cell is then

(1) Abstracted in part from a thesis submitted in partial fulfillment of the Doctor of Philosophy degree, University of Arkansas.

(2) G. Blyholder and E. A. Richardson, *J. Phys. Chem.*, **66**, 2597 (1962).

(3) G. Blyholder and L. D. Neff, *ibid.*, **66**, 1464 (1962).

(4) Shell Oil Co., Houston, Texas, private communication.

evacuated and the temperature raised to 475° for the final activation step which is complete after about 16 hr. when the absorption spectrum of the disk no longer indicates the presence of hydroxyl groups.

The activated α-Fe_2O_3 disks readily chemisorbed water, ammonia, ethyl alcohol, and hydrogen sulfide. These gases all produced similar changes in the disk spectrum in the 7 to 10 μ range. The spectrum of the disk is obtained before and after addition of controlled amounts of adsorbate. Since water does not have any absorption bands in the 7 to 10 μ region, the data for water and ammonia are selected in this note to illustrate the phenomena.

Results

Figure 1 shows the transmission of α-Fe_2O_3 disks in the 2 to 13 μ region before and after activation.

Of special interest is the 6 to 9 μ region which is shown in detail in Fig. 2. The per cent transmission is given for a series of curves showing the changes in an activated disk of α-Fe_2O_3 which occur as increments of water are adsorbed on the surface. The range of water additions includes physical adsorption as well as chemisorption.

The spectrum of α-Fe_2O_3 in disk form shown in Fig. 1 is in approximate agreement with that obtained previously for α-Fe_2O_3 in powder form. The general increase in transmission in the 2 to 6 μ region is inversely proportional to the square of the wave length as is typical of scattering by particles[5] of the same order of magnitude in diameter as the wave length. In this region the adsorbed water exhibits two absorption bands, one at 3.0 and one at 6.2 μ as shown. The other bands appear to be properties of the α-Fe_2O_3.

The changes in infrared absorption which occur upon adsorption of H_2O are shown in Fig. 2. The temperature was maintained at 25° throughout and the spectrum obtained before and after increments of water were added to an activated disk. Similar data are obtained when ammonia, ethyl alcohol, or hydrogen sulfide are chemisorbed on the disk. Volumetric measurements indicated that additions of N_2, O_2, H_2, CO, SO_2, and Cl_2 were not adsorbed and these gases had no effect on the disk spectra. The first two curves for H_2O additions shown in Fig. 2 indicate the presence of only chemisorbed water. It is seen that the 6.6 and 7.88 μ bands remain unchanged. The strong 7.42 μ band and the weak 7.75 μ band are gradually diminished in intensity by the additions of water, bands at 7.62 and 8.2 μ appear and the 8.87 μ band increases in intensity. The addition of water also causes a slight general decrease in transmission in the 10 to 13 μ region.

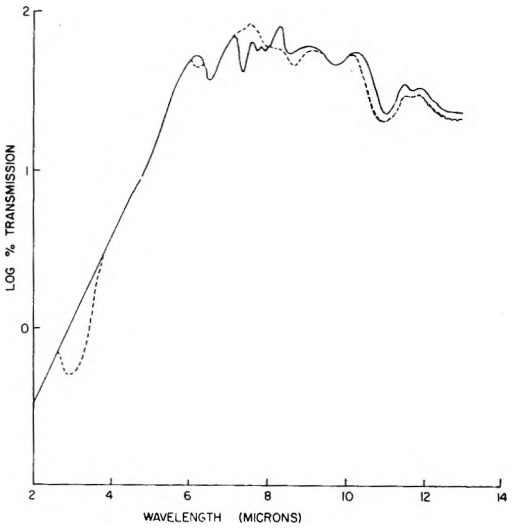

Figure 1. Transmission of 0.3-g. disk of α-Fe_2O_3: – – – –, raw disk; ———, activated disk.

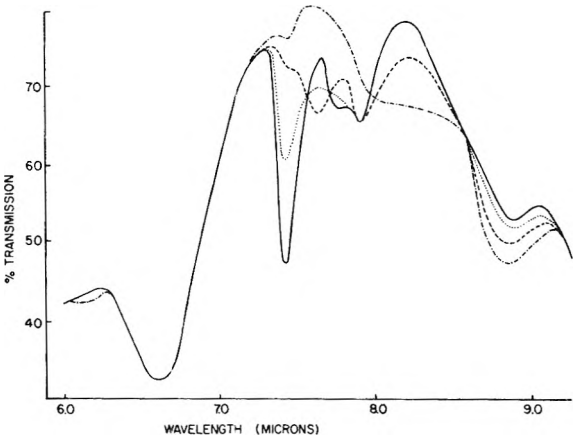

Figure 2. H_2O adsorbed on 0.3-g. activated disk of α-Fe_2O_3: ———, activated disk; . . . . . , 0.051 cc. (STP) of H_2O adsorbed; – – – –, 0.065 cc. (STP) of H_2O adsorbed; –·–·–·–, 0.181 cc. (STP) of H_2O adsorbed.

After the adsorption of 0.181 cc. (STP) of H_2O, the band at 6.2 μ in Fig. 2 indicates the presence of physically adsorbed water. With the appearance of physically adsorbed water, the band at 7.88 μ disappears and the same general trends established for the other bands continue for the physically adsorbed water as for the chemisorbed water. It is interesting to note that at about 7.54 and 7.7 μ, approximate isosbestic points appear. This indicates that the 7.42, 7.62, and 7.75 μ bands are related in some consistent manner to each other.

(5) D. H. Clewell, *J. Opt. Soc. Am.*, **31**, 521 (1941).

The spectral changes upon chemisorption of NH_3 on an activated disk are shown in Fig. 3. While the changes are similar to those produced by H_2O in that the 7.42 μ band disappears and new bands between 7.6 and 9.5 μ appear, there are some differences. One principal difference is that while H_2O produced very definite new bands, NH_3 smears out the new bands to create continuous absorption between 7.7 and 9.5 μ. The other principal difference is that whereas H_2O produced a new band at 7.62 μ, NH_3 increases the absorption between 7.8 and 8.0 μ where there already is an absorption band. Similarly to the behavior with H_2O, when enough NH_3 is present to produce an appreciable amount of physically adsorbed material the band at 7.9 μ diminishes.

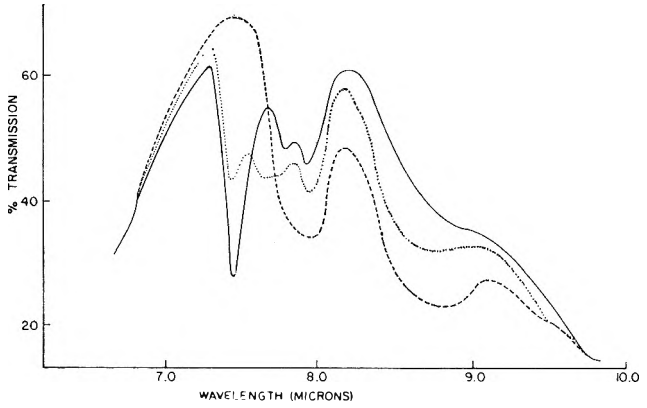

Figure 3. NH_3 adsorbed on 0.3-g. activated disk of α-Fe_2O_3: ———, activated disk; . . . . . , 0.051 cc. (STP) of NH_3 adsorbed; – – – –, 0.141 cc. (STP) of NH_3 adsorbed.

Measurements of the net change in area under the absorption bands relative to that obtained for the original activated disk in the 7 to 10 μ region are essentially zero for all adsorbates. If the oscillator strength is assumed to be constant, this indicates that a fixed number of oscillators are involved,[6] and thus the adsorbate does not create any new oscillators.

Discussion

Vibrational bands of the adsorbate are not expected to occur in the range 7 to 10 μ. The absence of an OH stretching band in the 2.7 to 3 μ region for the activated disk indicates that the original bands in the 7 to 9 μ region are not OH deformation bands. The absence of an OH stretching band after NH_3 chemisorption[2] indicates that the bands developed after gas adsorption are not OH deformation bands.

In this case chemisorption does not simply perturb surface levels in a continuous manner because as the surface coverage changes the energy levels do not change. Rather, the number of species giving rise to a particular transition changes. Since definite bands are observed, the species giving rise to them are presumed to have reasonably definite compositions and geometry. From the fact that different adsorbates give nearly the same bands, the surface states are presumed to arise from atoms already on the surface when it is "clean." The adsorbates used here all are similar in that they contain peripheral dipoles and hydrogen atoms capable of forming hydrogen bonds. When H_2O and NH_3 chemisorb on Fe_2O_3 it has been shown[2] that they probably occupy lattice positions on the surface and form hydrogen bonds. A lattice site has the definite composition and geometry necessary for the definite bands observed. When H_2O chemisorbs, it produces a OH^- ion and converts a surface O^{-2} ion to a OH^- ion. These OH^- ions would be expected to occupy lattice positions on the surface quite well and it is seen that definite bands are produced. NH_3 would not be expected to fit so perfectly in an oxide lattice as OH^- ions do and so the bands are less well defined. H_2S gives bands quite similar to those of H_2O. In physical adsorption, formation of hydrogen bonds on adsorption at definite sites could furnish the required definite interaction. Since the surface is heterogeneous, these bands would be expected to be rather broad as they are indeed observed to be in Fig. 2.

While the observed bands may be due to vibrations of the adsorbent, Fe_2O_3, the possibility of the bands in the 7 to 9 μ region being due to electronic transitions must be considered. The presence of surface electronic states is well known.[6,7]

One possible contributor to surface states is the Fe^{+2} ion. The presence of Fe^{+2} ions near the surface might be expected as a result of the prolonged evacuated heating process during activation. If the O_2 treatment at 375° is left out of the activation process, during the subsequent heating under vacuum at 475° the surface of the disk becomes covered with a layer of magnetite which renders the disk almost completely opaque. We suspect that some Fe^{+2} ions are produced in the activation process after the O_2 treatment.

Acknowledgment. This work was supported in part by a grant from the American Oil Company and in part by a grant from the Monsanto Chemical Company. Acknowledgment is made to the donors of the Petroleum Research Fund, administered by the American Chemical Society, for partial support of this research.

(6) F. Seitz, "Modern Theory of Solids," McGraw-Hill Book Co., New York, N. Y., 1940, pp. 320-326.

(7) J. Koutecky, *Phys. Rev.*, **108**, 13 (1957).

Direct Observation of Transient Intermediates in the Pulse Radiolysis of Isobutylene

by E. J. Burrell, Jr.[1]

Radiation Physics Laboratory, Engineering Department, E. I. du Pont de Nemours and Company, Wilmington, Delaware *(Received July 6, 1964)*

An ionic mechanism has been postulated for the radiation-induced polymerization of liquid isobutylene.[2-4] This note presents the results of the direct observation of the transient ionic species in this reaction and the determination of the absolute rate constant for termination.

Two principal methods of observation were employed: transient ultraviolet absorption spectroscopy and transient dielectric constant measurements. The radiation source was a Varian linear electron accelerator (Lineac) which introduces about 3 joules of energy/5-μsec. pulse of 6-Mev. electrons into the cold isobutylene sample.

A transient absorption at 2970 Å. in the isobutylene sample, which disappeared by a first-order process, was induced by the Lineac pulse. Trimethylcarbonium ions are thought to absorb in this region.[5] The lifetime and intensity of the absorption depend on temperature and various additives, such as O_2 and N_2O. These results are shown in Table I.

Table I: Radiation-Induced Transients at 2970 Å. in Liquid Isobutylene

Temp., °C.	Max. absorption, %	Additive	$t_{1/2}$, sec.	$k_{term.}$, sec.$^{-1}$
−60	10	None	0.1	...
−15	10	None	0.05	...
−59	5	O_2	0.1	...
−55	20	N_2O	0.10	7.0
−10	8	N_2O	0.040	17.0

The best data were obtained when N_2O was present at its saturation concentration. The N_2O molecule is known to attach electrons very efficiently at any low energy and apparently allows the ionic polymerization to proceed more efficiently. On the other hand, no signal as long as 1 msec. was observed for a saturated solution of N_2O in methylcyclohexane.

When oxygen-saturated isobutylene is irradiated, a rather weak signal with a first-order decay is observed at 2970 Å. This is in marked contrast to the very strong absorption with second-order decay observed in oxygen-saturated methylcyclohexane. The latter signal is due to the well-known termination of two peroxy radicals.[6]

Polymer was formed in the Lineac runs and typically had a molecular weight of 10,000 to 35,000 depending on temperature. These molecular weights were undoubtedly governed by chain transfer and are significant only in that polymer was formed.

The second method of observation consists in measuring the change in dielectric constant of liquid isobutylene induced by a Lineac pulse. A 12-leaf capacitor was constructed in a small Pyrex irradiation cell. The cell was filled with isobutylene at −78° and the cell capacitance balanced by means of a General Radio capacitance bridge, Type 716-CS1, energized by a 1.000-Mc. oscillator. The unbalance in the capacitance cell induced by the Lineac pulse was amplified by a factor of 10^6 and mixed with a 1.0-v. signal from a 1.001-Mc. oscillator, producing a 1-kc. beat. The resulting signal was fed through a tuned amplifier and presented on an oscilloscope whose sweep was triggered by the Lineac pulse.

The shape of such a signal implies that the formation of polymer (of different dielectric constant) is being observed rather than the direct observation of ion pairs. However, the signal is a measure of the same termination rate constant, being of the form $1 - e^{-kt}$. The first-order rate constant for termination measured in this way is 0.07 sec.$^{-1}$ at −78°. This is qualitatively consistent with optical runs at higher temperatures. This variation in termination rate constant with temperature is characteristic of ionic polymerizations, whereas the lifetimes of the transients observed are much too long for radiation-induced free radical reactions.

The dielectric constant cell could not be conveniently stabilized against temperature drift at any low temperature other than −78°. When optical runs were made at this temperature an insoluble polymer formed which scattered light. However, the transient signal

(1) Chemistry Department, Loyola University, Chicago, Ill.

(2) W. H. T. Davison, S. H. Pinner, and R. Worrall, *Chem. Ind.* (London), 1274 (1957).

(3) E. Collinson, F. S. Dainton, and H. A. Gillis, *J. Phys. Chem.*, **63**, 909 (1959).

(4) F. W. Lampe, *ibid.*, **63**, 1986 (1959).

(5) J. Rosenbaum and M. C. R. Symons, *Proc. Chem. Soc.*, 92 (1959); *Mol. Phys.*, **3**, 205 (1960); *cf.*, however, N. C. Deno, D. B. Boyd, J. D. Hodge, C. U. Pittman, Jr., and J. O. Turner, *J. Am. Chem. Soc.*, **86**, 1745 (1964).

(6) R. L. McCarthy and A. MacLachlan, *J. Chem. Phys.*, **35**, 1625 (1961).

observed in this case is still consistent if one assumes a transient form, $1 - e^{-kt^2}$, to take into account light scattering as a function of molecular weight of the growing polymer.

It was also noted that a Lineac pulse induced ion pairs in the liquid isobutylene as determined by collecting charge between the plates of a capacitor under an electric field of 4000 v./cm. An oscilloscope triggered by the Lineac beam monitored the charge collected. The current flowed only during the Lineac pulse and therefore consisted of electrons which were collected in times short compared to 5 μsec. and positive ions which did not move appreciably in this time. The charge collected from the sample was typically 6.5×10^{-6} coulomb as compared to the Lineac beam current which gave only 2.0×10^{-7} coulomb, thus establishing the presence of induced ion pairs as distinct from the Lineac beam current.

Acknowledgment. It is a pleasure to acknowledge P. C. Hoell and A. van Roggen for designing the apparatus for the transient dielectric constant measurements and V. F. Damme for constructing some of the equipment.

Conductance of the Alkali Halides. X. The Limiting Conductance of the Cesium Ion in Water at 25°

by Claude Treiner,[1] Jean-Claude Justice, and Raymond M. Fuoss[2]

Contribution No. 1764 from the Sterling Chemistry Laboratory of Yale University, New Haven, Connecticut *(Received July 14, 1964)*

Several recent determinations of the conductance of cesium salts in water lead to values for the cesium ion conductance which disagree by more than the estimated errors of measurement: 77.20 from cesium iodide[3] and 77.33, 76.46, and 76.92 from cesium chloride.[4-6] We present here data for cesium bromide, which give $\lambda_0(Cs^+) = 76.77$, which is in excellent agreement with the weighted average of the other determinations.

The cesium bromide was used as received from the Harshaw Chemical Co. ("random cuttings," from fused salt). It was stored over phosphorus pentoxide in an evacuated desiccator. Analysis by the flame photometer showed trace impurities as follows: 0.037% LiBr, 0.076% NaBr, 0.003% KBr, and 0.032% RbBr. These give a total correction[7] of -0.148 Λ-unit. All solutions were made up by weight. The water used had a conductance of 1.65×10^{-6}; the maximum solvent correction was 0.65%. The cell had a constant equal to 1.0115 ± 0.0001. Bridge, cell, and methods have been described previously.[8]

The conductance data (3 runs) are summarized in Table I. In order to obtain limiting conductances,

Table I: Conductance of Cesium Bromide in Water at 25°

10^4c	Λ	10^4c	Λ
82.824	146.85	24.447	150.46
65.955	147.64	13.136	151.66
41.442	149.12	99.290	146.19
24.924	150.41	71.182	147.42
14.540	151.50	48.769	148.65
78.639	147.06	27.465	150.21
56.192	148.21	15.101	151.41
40.152	149.20		

extrapolation was made on a Λ'–c plot by the method of least squares, using the equations[9]

$$\Lambda' = \Lambda \text{ (obsd.)} + Sc^{1/2} - Ec \log c \qquad (1)$$

$$\Lambda' = \Lambda_0 + Jc \qquad (2)$$

For the three runs, the values $\Lambda_0 = 155.157 \pm 0.013$, 155.135 ± 0.009, 155.143 ± 0.017 and $J = 180 \pm 2$, 186 ± 2, 186 ± 3 were found. These average to $\Lambda_0 = 155.15 \pm 0.02$ and $J = 184 \pm 2$. Correcting for the impurities, $\Lambda_0(CsBr) = 155.00 \pm 0.02$.

Using Longsworth's value[10] of 0.4906 for the transference number of potassium in potassium chloride, and Lind's value[8] of 149.89 for $\Lambda_0(KCl)$, we obtain $\lambda_0(K^+) = 73.54$. From Kay's extrapolations[11] of the data for potassium bromide,[12-14] we have $\Lambda_0(KBr) = 151.77$;

(1) DuPont Postdoctoral Research Fellow, 1963-1964; on leave of absence from the University of Paris.

(2) Grateful acknowledgment is made to the donors of the Petroleum Research Fund, administered by the American Chemical Society, for partial support of this work.

(3) J. E. Lind, Jr., and R. M. Fuoss, *J. Phys. Chem.*, **65**, 1414 (1961).

(4) W. E. Voisinet, Thesis, Yale University, 1951.

(5) J. C. Justice and R. M. Fuoss, *J. Phys. Chem.*, **67**, 1707 (1963).

(6) F. Accascina and M. Goffredi, University of Palermo, private communication.

(7) R. W. Kunze and R. M. Fuoss, *J. Phys. Chem.*, **67**, 914 (1963); see eq. 11.

(8) J. E. Lind, Jr., and R. M. Fuoss, *ibid.*, **65**, 999 (1961).

(9) R. M. Fuoss, *J. Am. Chem. Soc.*, **81**, 2659 (1959).

(10) L. G. Longsworth, *ibid.*, **54**, 2741 (1932).

(11) R. L. Kay, *ibid.*, **82**, 2099 (1960).

(12) B. B. Owen and H. Zeldes, *J. Chem. Phys.*, **18**, 1083 (1950).

subtracting the conductance of potassium gives $\lambda_0(Br^-) = 78.23$. Finally, from the corrected conductance of cesium bromide, we find $\lambda_0(Cs^+) = 76.77$.

A repeat run was also made on the cesium chloride used by Justice,[5] this time after fusing the salt in a platinum boat in a muffle furnace. The salt was kept molten for several minutes and then allowed to cool. Evidently the earlier samples still contained a little water after vacuum drying, because we now obtain $\Lambda_0 = 153.31$ by extrapolation of the data of Table II,

Table II: Conductance of Fused Cesium Chloride in Water at 25°

10^4c	Λ	$\delta\Lambda$
118.044	143.164	−0.017
87.936	144.496	0.028
67.898	145.480	−0.001
47.206	146.724	−0.006
23.859	148.587	−0.004

where the last column gives the difference between the observed conductances and those calculated by the equation

$$\Lambda = 153.310 - 95.65c^{1/2} + 26.25c \ln c + 138.8c \quad (3)$$

Applying the same correction (−0.258) as before for impurities gives $\Lambda_0(CsCl) = 153.05$; subtracting the chloride ion conductance[15] of 76.35 gives $\lambda_0(Cs^+) = 76.70$, in excellent agreement with the value from the bromide.

Averaging 77.20 from the iodide,[3] 76.92 from the chloride,[6] and our present values of 76.70 and 76.77 from the chloride and bromide, respectively, we obtain $\lambda_0(Cs^+) = 76.90 \pm 0.16$.

(13) G. C. Benson and A. R. Gordon, *J. Chem. Phys.*, **13**, 473 (1945).

(14) G. Jones and G. F. Bickford, *J. Am. Chem. Soc.*, **56**, 602 (1934).

(15) Correction to line 5 below Table II of ref. 5: replace 73.52 by 76.35 (or Cl by K^+).

The Use of Sodium Borohydride in Catalytic Deuterium Exchange Reactions[1]

by G. E. Calf and J. L. Garnett

School of Chemistry, The University of New South Wales, Kensington, N. S. W., Australia *(Received December 23, 1963)*

The problems associated with hydrogen reduction and activation of platinum oxide[2] and other transition metal oxides[3a,b] have already been discussed in the development of the associative and dissociative π-complex substitution mechanisms[4] for the metal catalyzed exchange of organic compounds with heavy water.[5,6] A different type of procedure for the reduction and activation of platinum oxide using organic compounds has also been reported.[7] This "self-activated" catalyst possesses certain advantages in isotopic hydrogen exchange experiments especially when combined with either ultraviolet or γ-radiation.[8]

It is the purpose of this present publication to report the use of a new method for the preparation of active transition metal catalysts for exchange reactions, namely, reduction in aqueous media with sodium borohydride. Brown and Brown[9,10] have already mentioned that the treatment of platinum metal salts with aqueous sodium borohydride yields finely divided black precipitates which are active catalysts for the hydrogenation of olefins. However, the exchange properties of these catalysts have not been investigated but should be important since the activity of the catalyst, particularly the site effect, depends markedly on the method of reduction and activation.[2]

Two types of metal catalyst systems have been studied, the water-soluble transition metal oxides and the soluble chloride salts. Benzene and ethylbenzene have been used as representative aromatic systems while hexane and cyclohexane were examined as examples of aliphatic reactivity.

Experimental

Apparatus, general procedures, and low voltage mass spectrometric analytical techniques have been outlined in an earlier publication.[2] For the hydrogen runs, reactions were performed with metallic oxide (100 mg.) prereduced with hydrogen or deuterium, benzene (4.0×10^{-2} mole), and heavy water (12.0×10^{-2} mole) at a temperature of 130° for 48 hr. as previously described.[2,5] In the hydride reductions, sodium borohydride (400 mg.) was added slowly to a suspension of the oxide (100

(1) Part XI of a series entitled "Catalytic Deuterium Exchange with Organics."

(2) J. L. Garnett and W. A. Sollich, *J. Catalysis*, **2**, 339 (1963).

(3) (a) J. L. Garnett and W. A. Sollich, *Nature*, **201**, 902 (1964); (b) J. L. Garnett and W. A. Sollich, to be published.

(4) J. L. Garnett and W. A. Sollich, *J. Catalysis*, **2**, 350 (1963).

(5) J. L. Garnett and W. A. Sollich, *Australian J. Chem.*, **14**, 441 (1961).

(6) J. L. Garnett and W. A. Sollich, *ibid.*, **15**, 56 (1962).

(7) J. L. Garnett and W. A. Sollich, *J. Phys. Chem.*, **68**, 436 (1964).

(8) W. G. Brown and J. L. Garnett, submitted for publication.

(9) H. C. Brown and C. A. Brown, *J. Am. Chem. Soc.*, **84**, 1493 (1962).

(10) H. C. Brown and C. A. Brown, *ibid.*, **84**, 1494 (1962).

mg.) in water (50 ml.), hydrolysis of the excess sodium borohydride was completed by warming the reaction to 70°, the prereduced catalysts were washed free from salts with water, the water was decanted, and the remaining reagents were added. Pumping off excess water prior to the last step resulted in appreciable loss in catalyst activity, presumably due to thermal sintering. For the soluble metal salts, the following modified hydride activation procedure was used. Sodium borohydride (400 mg.) was added slowly to a solution of the metallic chloride (containing the equivalent of 100 mg. of metal) in water (50 ml.). A finely divided black precipitate immediately formed with all salts except iridium, which necessitated warming to 70° for reaction completion. The precipitate was washed free from salts with water, the remaining reagents were added, and exchange was performed as previously, without shaking to accentuate differences in reactivity.[2]

Results and Discussion

The significant feature of the results (Tables I and II) is the general improvement in isotope incorporation of the aromatics from the hydride technique for almost all catalysts studied, the effect being particularly marked for ruthenium, rhodium, and iridium in Table I and for all metals in Table II. With the soluble metal chlorides, the only salts readily reduced by hydrogen were those of rhodium, palladium, and platinum, whereas all chlorides yielded active catalysts in borohydride reduction. For platinum oxide, accurate kinetic studies would be necessary before a decision as to whether sodium borohydride reduction was better than hydrogen could be substantiated since the benzene samples from hydrogen and hydride reduction procedures had both virtually reached equilibrium.

With nickel, rhodium, and palladium, reduction of the soluble salts yields a catalyst which is more active for deuterium exchange in both benzene and ethylbenzene than the corresponding oxide. The same result is obtained with ruthenium catalysts for the deuteration of benzene only. From Table I, sodium borohydride reduction of all catalysts is no better than hydrogen reduction for the exchange of aliphatic hydrocarbons as predicted by *π-complex chemisorption* theory.[5,11-13] A consistent predominance of ring deuteration in the ethylbenzenes is observed for all catalysts except nickel where the orientation effect favors the aliphatic side chain. Distribution studies with the labeled benzenes show that both stepwise and multiple exchange processes[2] occur with the two types of systems, *i.e.*, both hydrogen and borohydride activated catalysts.

As a synthetic tool for general deuterium and tritium labeling,[14] the sodium borohydride technique possesses several most important advantages. Reductions may now be performed very quickly and efficiently in minutes at 30° without the necessity for using vacuum line

Table I: Exchange Reactions with Metal Oxides Activated by Reduction with Hydrogen or Sodium Borohydride

Metal	Catalyst	Benzene,[a] atom % D	Benzene,[b] atom % D	Ethylbenzene,[b] atom % D	Hexane,[b] atom % D	Cyclohexane,[b] atom % D
Fe	Fe_2O_3	0.05	0.08	0.02	<0.01	0.02
Co	Co_2O_3	0.03	0.08	0.02	<0.01	0.04
Ni	NiO	0.04	0.05	0.01	<0.01	0.03
	Ni_2O_3	0.04	0.20	...	...	...
Ru	$RuO_2 \cdot H_2O$	0.13	8.1	1.10	<0.01	0.04
Rh	Rh_2O_3	2.13	8.4	9.6	<0.01	0.09
Pd	PdO	11.8	2.0	11.3	<0.01	0.04
Os	OsO_4	0.04	0.06	0.07	<0.01	0.04
Ir	$IrO_2 \cdot 2H_2O$	0.09	9.4	1.00	<0.01	0.90
	Ir_2O_5	0.01	0.1	...	...	...
Pt	$PtO_2 \cdot 2H_2O$	46.4	45.7	20.7	<0.05	0.20

[a] Method of catalyst preparation—hydrogen at 30°.[2] Equilibrium % D = D_∞ = 50.0%. [b] Method of catalyst preparation—sodium borohydride at 70°. D_∞ = 50.0% for benzene; 37.5% for ethylbenzene; 35.6% for hexane; 45.5% for cyclohexane.

Table II: Exchange Reactions with Metal Chlorides Activated by Reduction with Hydrogen or Sodium Borohydride

Metal	Catalyst	Benzene,[a] atom % D	Benzene,[b] atom % D	Benzene,[b] atom % D
Fe[c]	$FeCl_3$		0.04	0.01
Co[c]	$CoCl_2$		0.10	0.06
Ni[c]	$NiCl_2$		8.0	18.1
Ru[c]	$RuCl_3$		3.0	1.0
	K_2RuCl_5OH		12.9	
Rh	$RhCl_3$	4.5	38.0	25.0
Pd	K_2PdCl_4	0.7	38.4	25.1
Ir[c]	$(NH_4)_2IrCl_6$		6.1	...
Pt	H_2PtCl_6	13.9	46.1	25.9

[a] Method of catalyst preparation—hydrogen at 30°. D_∞ = 50.0%. [b] Catalyst preparation—$NaBH_4$. D_∞ = 50.0% for benzene, 37.5% for ethylbenzene. [c] Since little or no reduction of these aqueous chlorides was observed with hydrogen, there was correspondingly insignificant exchange in benzene.

(11) J. L. Garnett, *Proc. Roy. Australian Chem. Inst.*, **28**, No. 8, 328 (1961).

(12) E. Crawford and C. Kemball, *Trans. Faraday Soc.*, **58**, 2452 (1962).

(13) J. J. Rooney, *J. Catalysis*, **2**, 53 (1963).

(14) J. L. Garnett, *Nucleonics*, **20**, No. 12, 86 (1962).

techniques which hydrogen requires. Since relatively low temperatures are used in the hydride reduction process, the final catalyst suffers a minimum of deactivation from thermal sintering. This is an observation of value for the activation of catalysts such as nickel oxide which normally may only be prepared by hydrogen reduction at 300–400°. Since compounds exchanged in the presence of nickel exhibit a predominance of isotope incorporation in the aliphatic side chain, nickel is a valuable catalyst for *specific* labeling work and consequently rapid sodium borohydride reduction should be most useful.

Acknowledgment. The authors thank the Australian Institute of Nuclear Science and Engineering (Mr. E. A. Palmer) for assistance in the purchase of the heavy water, the N.S.W. State Cancer Council for the use of their facilities, Professor S. E. Livingstone for the gift of K_2RuCl_5OH, and Commander J. Mason for instrumentation advice.

Electron Spin Resonance Studies on the Photolysis of Azo Compounds at −196°

by P. B. Ayscough, B. R. Brooks, and H. E. Evans

Department of Physical Chemistry, The University, Leeds 2, England
(Received May 4, 1964)

The thermal and photochemical decomposition of azo compounds may, in general, be represented by the equation

$$R{-}N{=}N{-}R' \longrightarrow R + N_2 + R'$$

where R and R′ may be alkyl or aryl, substituted or unsubstituted. The reactions are kinetically first order with unusually high pre-exponential factors, and it has been suggested that the three fragments are produced simultaneously.[1] There is no evidence in the products[2,3] to suggest even the transient existence of radicals of structure R—N=N in the gaseous or liquid phase. However, in the solid, the chance of trapping such intermediates is greatly enhanced and e.s.r. methods provide a means of identification.

Six disubstituted azo compounds were examined during and after ultraviolet irradiation at −196°, namely, azomethane (I), azobenzene (II), phenylazoisobutyronitrile (III), azobisisobutyronitrile (IV), 2,6-dimethyl-4-cyano-4-phenylazoheptane (V), and dimethylazodiformate (VI). With the exception of azobenzene, all gave characteristic and readily identifiable spectra after 10–20 min. of irradiation in the e.s.r. cavity with light from a 250-w. medium-pressure mercury lamp (mainly 2537 Å.). I gave methyl radicals only, and VI gave methyl radicals, plus a narrow asymmetric singlet peak, probably due to $CH_3O\cdot$ or $CH_3OCO\cdot$ radicals. The spectrum observed during irradiation of III is shown in Fig. 1 while Fig. 2 shows the spectrum recorded during the photolysis of IV. V gave only the H atom doublet.

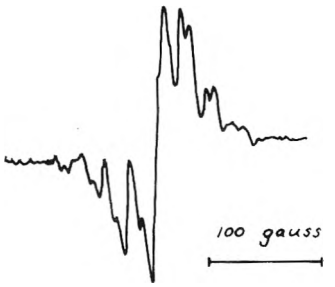

Figure 1.

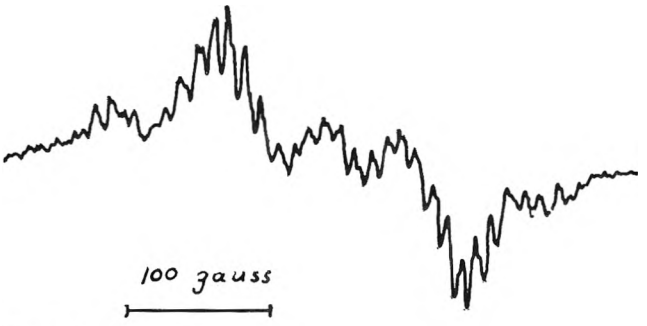

Figure 2.

The spectrum of ultraviolet-irradiated III has seven principal peaks, separated by 21 gauss, each with some subsidiary splitting; we suggest that it may be attributed to the radical $(CH_3)_2C{-}CN$. The methyl proton splittings are rather smaller than those observed in the isopropyl radical, while the minor splittings are in accord with the estimated values for nitrogen interaction in –CN (about 6 gauss, based on the observed values in aromatic nitriles).[4] The spectrum recorded during the photolysis of azobisisobutyronitrile (IV) is, however, quite different. Under low resolution, it consists of five broad peaks each separated by 65–70 gauss. The intensity ratios are approximately 1:2:2:

(1) B. G. Gowenlock, *Quart. Rev.* (London), **14**, 133 (1960).
(2) J. C. Bevington, *J. Chem. Soc.*, 3707 (1954).
(3) D. H. Grant and N. Grassie, *J. Polymer Sci.*, **42**, 588 (1960).
(4) P. H. Rieger and G. K. Fraenkel, *J. Chem. Phys.*, **37**, 2811 (1963).

2:1, suggesting interaction with two approximately equivalent nitrogen atoms. Under higher resolution, additional structure appears; the average peak separation is about 9 gauss (see Fig. 2). The magnitude of the major hyperfine interaction is compatible with a radical such as $N{=}N{-}C(CH_3)_2CN$ in which the unpaired electron has substantial 2s character. The subsidiary splitting would then be attributed to interaction with the methyl protons. Lack of resolution in the center of the spectrum is probably due to the presence of other radicals which become more significant on standing, so that after a few days at $-196°$ the spectrum resembles that shown in Fig. 1. The change is accelerated by further photolysis. We therefore conclude that the primary decomposition may be represented by the equation

$$NC{-}C(CH_3)_2N{=}NC(CH_3)_2{-}CN \xrightarrow{h\nu} NC{-}\dot{C}(CH_3)_2 + N{=}NC(CH_3)_2CN$$

but that the $\dot{N}{=}N{-}R$ radical decomposes readily even at $-196°$. It appears that $\dot{N}{=}N{-}CH_3$ and $\dot{N}{=}N{-}C_6H_5$ are even less stable, if formed at all.

These conclusions are in accord with the known exothermicity of the decomposition of alkylazo radicals.[5] Despite the difficulty of extracting reliable hyperfine splitting constants from spectra obtained from polycrystalline systems, the near-equivalence of the two nitrogen atoms supports the view of Gowenlock, *et al.*,[5] that the structure of the radical is not adequately represented as $\dot{N}{=}N{-}R$. Structures such as $N{\equiv}N{\cdot}R$ and $\dot{N}{\cdot\cdot}N{-}R$ with one- and three-electron bonds, respectively, must be important.

The behavior of V appears anomalous since only trapped hydrogen atoms were found, and these were not observed in the other systems. This difference is probably associated with the considerable strain in the bonds of the carbon atom adjacent to the azo nitrogens, which is apparent in molecular models. Not only is C–N fission facilitated (the rate of decomposition in solution is also greater than that of the other aromatic azonitriles examined)[6] but the possibility of the rupture of the radical $(CH_3)_2CHCH_2C(CN)CH_2{-}CH(CH_3)_2$ is enhanced. Breakdown to give hydrogen and isobutene or other unsaturated molecules is, thus, quite probable. The products of the pyrolysis of (V) also suggest that the reactions of the radicals are different from those of the other azonitriles[6] although the primary processes may well all be identical.

(5) B. G. Gowenlock, J. R. Majer, and D. R. Snelling, *Trans. Faraday Soc.*, 58, 670 (1962).

(6) B. R. Brooks and K. J. Ivin, unpublished results.

Acknowledgment. We are grateful to Dr. K. J. Ivin for helpful discussions during the course of this work and to the Department of Scientific Industrial Research for financial assistance.

A Method for the Determination of Rank in the Analysis of Absorption Spectra of Multicomponent Systems[1]

by R. M. Wallace and S. M. Katz

Savannah River Laboratory, E. I. du Pont de Nemours and Company, Aiken, South Carolina *(Received May 22, 1964)*

A method for the determination of the number of components in a series of solutions from their absorption spectra was developed by Wallace[2a]; a similar method was reported later by Ainsworth.[2b] The method is briefly the following. The absorption spectra of a series of solutions are measured in which exist a number of absorbing species whose relative concentrations change from one solution to the next. The absorbances A_{ij} measured at wave length i in the jth solution are arranged in a rectangular matrix and the number of components is determined from the rank of the matrix. The method for determining rank, which involved examining a number of submatrices for singularity based on a statistical criterion, proved to be quite cumbersome when large matrices were involved. We have developed an alternative method for determining rank that has proved easier to use and is ideally suited for machine computation.

The method consists of setting up, in addition to the absorbance matrix A, a companion matrix S, whose elements, S_{ij}, are the estimated errors of A_{ij}. A is then reduced by a series of elementary operations to an equivalent matrix, whose elements below the principal diagonal are all zero. S is also continually transformed during the reduction of A by computing new values of S_{ij} based on the propagation of errors in transforming A. The rank of A is then found from the number of nonzero rows in the reduced matrix.[3] The statistical criterion for a zero element

(1) The information contained in this article was developed during the course of work under Contract AT(07-2)-1 with the U. S. Atomic Energy Commission.

(2) (a) R. M. Wallace, *J. Phys. Chem.*, 64, 899 (1960); (b) S. Ainsworth, *ibid.*, 65, 1968 (1961).

(3) S. Perlis, "Theory of Matrices," Addison-Wesley Publishing Co., Reading, Mass., 1952, p. 45.

Table I

			Original A Matrix				
0.017	0.045	0.062	0.110	0.197	0.278	0.332	0.377
0.058	0.080	0.100	0.152	0.238	0.320	0.372	0.417
0.167	0.180	0.187	0.222	0.282	0.330	0.368	0.400
0.420	0.402	0.395	0.365	0.342	0.310	0.300	0.292
0.770	0.735	0.690	0.565	0.437	0.278	0.192	0.131
1.015	0.990	0.922	0.742	0.528	0.282	0.147	0.051
0.935	0.940	0.875	0.702	0.488	0.255	0.118	0.032
0.443	0.480	0.462	0.342	0.235	0.108	0.049	0.015
			Reduced A Matrix				
1.015	0.051	0.922	0.742	0.528	0.282	0.990	0.147
0	0.414	0.047	0.110	0.208	0.304	0.023	0.364
0	0	0.060	0.020	0.008	−0.010	0.048	0.009
0	0	0	−0.016	−0.007	−0.007	−0.005	−0.003
0	0	0	0	−0.006	−0.005	−0.006	0.001
0	0	0	0	0	0.005	0.003	−0.003
0	0	0	0	0	0	0.006	−0.004
0	0	0	0	0	0	0	0.004
			Reduced S Matrix				
0.003	0.003	0.003	0.003	0.003	0.003	0.003	0.003
0	0.003	0.004	0.004	0.003	0.003	0.004	0.003
0	0	0.004	0.004	0.004	0.004	0.005	0.004
0	0	0	0.005	0.005	0.005	0.007	0.005
0	0	0	0	0.006	0.006	0.008	0.006
0	0	0	0	0	0.010	0.013	0.008
0	0	0	0	0	0	0.017	0.012
0	0	0	0	0	0	0	0.021

in the reduced matrix on or above the principal diagonal is furnished by the transformed S matrix.

Details of the method follow. The A matrix is pivoted by an interchange of rows and columns to place the element whose absolute value is the largest in position 1,1; S is transformed by the same row–column interchanges used in A. The resulting A matrix is transformed to A' by the operation

$$A'_{ij} = A_{ij} - \frac{A_{i1}}{A_{11}} A_{1j} \qquad (1)$$

performed on all except the first row. This operation makes all elements in the first column identically zero except for the first one. S is transformed to S' by the equation for the propagation of errors in (1)[4]

$$S'_{ij} = \left[S_{ij}^2 + S_{1j}^2 \left(\frac{A_{i1}}{A_{11}}\right)^2 + S_{i1}^2 \left(\frac{A_{ij}}{A_{11}}\right)^2 + S_{11}^2 \left(\frac{A_{i1}A_{1j}}{A_{11}^2}\right)^2 \right]^{1/2} \qquad (2)$$

The submatrices formed by deleting the first row and column of A' and S' are then treated similarly to give A'' and S'' and so on until all the elements of the transformed A matrix below the principal diagonal are identically zero. It is then only necessary to compare elements on the principal diagonal of the transformed A and S matrices to determine how many rows are statistically nonzero, and therefore to find the experimental rank.

The main reason for pivoting the matrix to place the largest elements on the diagonal is to minimize the rate of propagation of errors. With this arrangement the coefficients of S_{1j}^2, S_{i1}^2, and S_{11}^2 on the right of eq. 2 can never exceed 1, and the value of an element in S' after an operation therefore cannot exceed twice the value of the largest of the elements in S that goes into its calculation. If the matrix A contains n rows and all the elements in the original S matrix are identical and equal to S_0, the largest possible value of S in the reduced matrix will be $2^{n-1}S_0$, but it will usually be much smaller.

We have written a "Fortran" program for the above procedure for the IBM 704 computer which will accept a 50 × 20 matrix. The only additional feature of this

(4) H. Margenau and G. M. Murphy, "The Mathematics of Physics and Chemistry," 2nd Ed., D. Van Nostrand Co., Princeton, N. J., 1956, p. 515.

program is that after each step in the reduction of A, each element is compared with the product of the corresponding element in S and some preselected criterion. If the absolute value of the element in A is less than or equal to that product, it is set identically equal to zero. If desired, the computer can be instructed to write only the rank of the matrix subject to the criterion.

The program has been tested successfully with several systems. The following example shows the application of the procedure to solutions containing methyl red at various values of pH. The original 8×8 A matrix and the reduced A and S matrices are shown in Table I. The original S matrix has been omitted because all its elements are identical and equal to 0.003, a reasonable estimate of the errors in absorbance measurements. Computations were carried out subject to a very small criterion so that elements were never arbitrarily set equal to zero.

The results show the definite existence of three colored components and perhaps a fourth, since the element 4,4 in the reduced matrix is three times its estimated error. This result agrees with that of Reilley and Smith,[5] who found three colored components in methyl red by another method. The failure to find more than two components previously by the matrix method[1] probably arose from the necessity to restrict the size of the matrix because of difficulties in computation introduced by the former method of determining rank.

(5) C. N. Reilley and E. M. Smith, *Anal. Chem.*, 32, 1233 (1960).

Studies on Solutions of High Dielectric Constant. V. Transport Number of Potassium Chloride in Formamide at Different Temperatures[1]

by Ram Gopal and OM Narain Bhatnagar[2]

Department of Chemistry, Lucknow University, Lucknow, India *(Received June 3, 1964)*

Studies on the transport numbers of ions in nonaqueous solutions are comparatively rare and are more so in solvents of high dielectric constant, other than water, such as formamide, N-methylformamide, N-methylacetamide, etc. This has blocked our understanding of the ionic conductance in nonaqueous solutions in which electrolytic conductance data are now available. Almost complete lack of experimental data on the effect of temperature on the transport numbers of ions, except in aqueous solutions, has restricted our knowledge of the ion–solvent interaction in nonaqueous solutions. An approximate cationic transport number of KCl in formamide at 25° has been reported by Dawson and Berger.[3] It is, therefore, considered desirable to determine the transport numbers of electrolytes in formamide more accurately and at different temperatures for a fuller understanding of the ion–solvent interaction. The present communication reports the cationic transport numbers of KCl in formamide at different temperatures and concentrations.

Experimental

A.R. grade potassium chloride, recrystallized and thoroughly dried, was used in making the solutions. Formamide (specific conductivity $\approx 10^{-4}$ mho) was dried over freshly ignited quicklime and distilled under reduced pressure until its conductivity fell to 10^{-5} mho or less and then was used immediately afterward. A Hittorf-number cell, similar to that used by MacInnes and Dole[4] with slight modifications to facilitate the taking out of the anode solution from the cell, was used in the experiments. The cathode of the cell was a silver chloride electrode and was prepared in the following manner. A silver wire was wound on a stout silver rod and the whole was made the anode and a platinum wire was the cathode of an electrolytic cell containing 1 N HCl as the electrolytic liquid. A current of 12–15 ma. was passed through the cell for 3 to 4 hr. The anode was taken out, washed carefully, dried, and used subsequently in the transport cell.

The anode of the transport cell was made from a silver wire, about 50 cm. long and 0.5 mm. in diameter. It was wound in the form of a spiral of about 6-mm. diameter. This size and shape of the anode was found to be appropriate to fit in the left arm of the cell and stout enough to stand mild jerks which are sometimes unavoidable in these experiments of long duration.

The solution of any desired concentration was prepared in a freshly distilled sample of formamide stored in a dry nitrogen box. The required amount of the electrolyte was taken in a 250-ml. graduated flask and its air was then replaced by dry nitrogen. Formamide was taken out of the dry nitrogen box and the solution was made as quickly as possible. The complete cell, filled with the solution and electrodes properly

(1) Work supported by the Council of Scientific and Industrial Research (CSIR), India.

(2) CSIR Junior Research Fellow.

(3) L. R. Dawson and C. Berger, *J. Am. Chem. Soc.*, 79, 4269 (1957).

(4) D. A. MacInnes and M. Dole, *ibid.*, 53, 1357 (1931).

fitted, was lowered in a thermostat running at the required temperature and was fixed on a stand. When the solution had attained the temperature of the bath, the electric current was switched on.[5] A current of 2–5 ma. was passed for 10–15 hr. from a battery of dry cells. After the experiment, the potassium content of the solution around the anode was estimated gravimetrically as dipotassium sodium cobaltinitrite. The potassium content of the original solution, as well as of the solution in the middle compartment of the cell, was checked gravimetrically. The transport number of the K^+ was calculated by the usual procedure. The experiment was repeated and the results were found to be reproducible within experimental error. The experiments were carried out at different temperatures and concentrations and the results obtained are summarized in Table I.

Table I: Transport Numbers of K^+ in Formamide at Different Temperatures and Concentrations

Concn. C, mole/l.	Transport number at t°C. (±0.05°)			
	25°	30°	40°	50°
0.1	0.4050	0.4150	0.4230	0.4312
0.2	0.3990	0.4070	0.4180	0.4259
0.25	0.3968	0.4040	0.4153	0.4228
0.3	0.3920	0.4015	0.4117	0.4214
0.4	0.3853	0.3959	0.4074	0.4174
0.5	0.3810	0.3901	0.4010	0.4120
0.00	0.4190	0.4265	0.4332	0.4400

In view of the very high resistance offered by the cell as well as the difficulties of accurate estimation of small quantities of potassium, investigations were confined to moderately higher concentrations. In order to evaluate the transport number of K^+ at infinite dilution, t_+^0, the procedure suggested by Longsworth[6] was followed. From the experimental values of transport numbers, t_+, at different concentrations at a fixed temperature, the Longsworth function $t_+^{0\prime}$ was calculated from the relation

$$t_+^{0\prime} = \frac{t_+\lambda' + {}^1/_2\beta\sqrt{c}}{\lambda' + \beta\sqrt{c}} = t_+^0 + BC \qquad (1)$$

The terms used have their usual significance. The values of λ^0, needed to obtain λ' at various temperatures, were obtained from the values of equivalent conductances at infinite dilution at 3, 20, 25, and 40°, given by Dawson and co-workers,[7] in the usual manner.[8] The values of $t_+^{0\prime}$ at various concentrations at a fixed temperature, calculated from eq. 1, were plotted against C. The curve was found to be approximately a straight line as can be seen from Fig. 1.

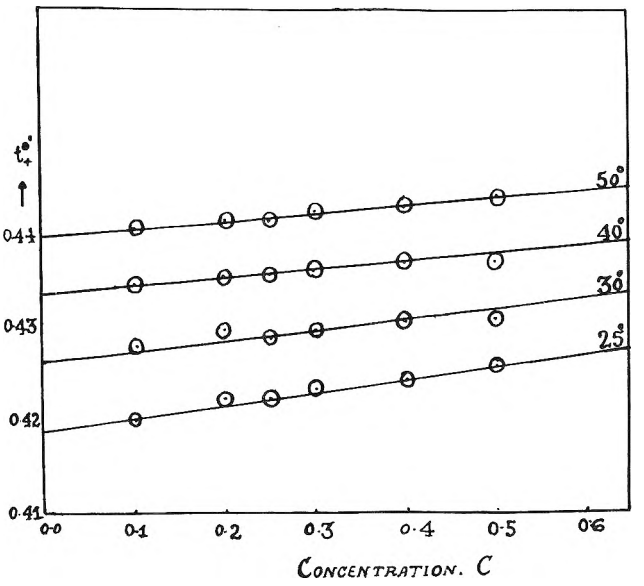

Figure 1. Plot of $t_-^{0\prime}$ *vs.* C at different temperatures.

The interpolation of the $t_+^{0\prime}$ *vs.* C curve to zero concentration gives t_+^0, the cationic transport number at infinite dilution, at the corresponding temperature. The values of t_+^0 thus obtained at different temperatures are also given in Table I.

Discussion

From the data given in Table I, it may be observed that the transport number at infinite dilution, t_+^0, of K^+ in formamide at 25° is slightly higher than that reported by Dawson and Berger.[3] The transport numbers at different concentrations differ from those in water in two respects. First, in formamide at any particular concentration, say 0.1 M, t_+ increases with rise in temperature, a behavior similar to that of Li^+ or Na^+ in water but opposite to that of K^+ in aqueous solutions.[8] Secondly, in formamide, at any temperature, the transport number decreases appreciably with increase in concentration whereas in water it remains almost a constant with only a very slight tendency to decrease. These marked differences in the behavior point to a difference in ion–solvent interaction in the two solvents. In water, as well as with

(5) Before switching on the current, a stream of dry nitrogen was bubbled through the solution in the two compartments of the cell. Then the nozzles of the nitrogen inlets were taken out of the solution and a slow current of dry nitrogen was allowed to sweep on the surface continuously during the experiments.

(6) L. G. Longsworth, *J. Am. Chem. Soc.*, 54, 2741 (1932).

(7) L. R. Dawson, T. M. Newell, and W. J. McCreary, *ibid.*, 76, 6024 (1954).

(8) H. S. Harned and B. B. Owen, "Physical Chemistry of Electrolytic Solutions," Reinhold Publishing Corp., New York, N. Y., 1958, p. 223.

rise in temperature, the open tetrahedral structure[9] in the presence of large inorganic ions like K^+, Rb^+, Cs^+, Cl^-, Br^-, I^-, etc., breaks down whereas this structure-breaking effect is of no importance for ions like Li^+ and Na^+ which have a much larger ion–dipole interaction resulting in appreciable solvation. In formamide, this structure is altogether missing and only some molecular association is present. Hence, all the ions in this solvent behave in the same manner irrespective of their sizes.

According to Kohlrausch,[10] the faster the ion, the smaller the temperature coefficient of its mobility and all the ions try to attain a transport number as close as possible to 0.5. This general rule is obeyed by KCl in formamide although, in aqueous solutions, it is an exception to the rule. It is obvious that the decrease in viscosity with rise in temperature cannot explain the general rule since both the ions will be affected in the same manner. According to Bredig,[11] due to the difference in the solvation of different ions, their effective volumes (in solution) are different and, generally, the smaller the ion (*i.e.*, the smaller the crystal radius), the larger its solvated ionic volume, the slower the movement, and the smaller the transport number. The effect of temperature on the transport numbers of cations and anions is, however, difficult to explain since both the increase[12-16] and decrease[17] in solvation with rise in temperature have been postulated. Further, relative changes in the sizes of cations and anions, with rise in temperature, are completely unknown. It is usually believed that in electrical conductance, it is only the "primary or chemical" solvation sphere, which is independent of temperature, that moves with the ion, leaving behind the "secondary or physical" solvation part, which is assumed to be temperature-dependent.[12,18] This concept fails to explain the temperature variation of the transport numbers because the moving ionic volume due to "primary" solvation remains unaltered with rise in temperature and hence the transport numbers of cations and anions should be independent of temperature, which is against the experimental facts. Assuming that the "primary" solvation is not affected at all by temperature changes, one is forced to conclude that the "secondary" solvation must be, partly at least, involved in the transport process, perhaps producing different amounts of drags on different ions when the temperature is raised. Beyond this it will be unsafe to speculate, since the variation of the total solvation (the primary plus secondary) with temperature is, more or less, an open question at present.

According to Eyring's theory of rate processes[19] as applied to the ionic transport,[20] the tangent to the log t_+^0/t_-^0 *vs.* $1/T$ curve gives the difference in the activation energies of K^+ and Cl^- ions according to the equation

$$\log \frac{t_+^0}{t_-^0} = \frac{\Delta E(Cl^- - K^+)}{2.303RT}$$

In formamide this plot is almost a straight line with a negative slope and the difference in the activation energies is about -450 cal., *i.e.*, the activation energy for the transport of K^+ is larger than for Cl^- by about 450 cal. This difference will, presumably, slowly level off at higher temperatures. In water it is positive and smaller.[21]

(9) J. D. Bernal and E. H. Fowler, *J. Chem. Phys.*, 1, 515 (1933).

(10) F. Kohlrausch and L. Holborn, "Das Leitvermögen der Elektrolyte," Teubner, Leipzig, 1916.

(11) G. Bredig, "Textbook of Physical Chemistry," S. Glasstone, Ed., Macmillan and Co., London, 1948, p. 920.

(12) F. S. Feates and D. J. G. Ives, *J. Chem. Soc.*, 2809 (1956).

(13) S. R. Gupta, G. J. Hills, and D. J. G. Ives, *Discussions Faraday Soc.*, 24, 150 (1957).

(14) M. Kaminsky, *ibid.*, 24, 177 (1957).

(15) E. R. Nightingale, *J. Phys. Chem.*, 63, 1384 (1959).

(16) L. R. Dawson, P. G. Sears, and R. H. Graves, *J. Am. Chem. Soc.*, 77, 1989 (1955).

(17) J. O'M. Bockris and B. E. Conway, "Modern Aspects of Electrochemistry," Butterworths Publications, London, 1954, p. 94.

(18) J. O'M. Bockris and B. E. Conway, *Quart. Rev.* (London), 3, 173 (1949).

(19) H. Eyring, *J. Chem. Phys.*, 4, 283 (1936).

(20) H. S. Slater, *ibid.*, 6, 331 (1938).

(21) R. W. Allgood, D. J. Le Roy, and R. Gordon, *ibid.*, 8, 418 (1940).

The Thermal Decomposition of Methylcyclobutane at Low Pressures[1,2]

by A. F. Pataracchia and W. D. Walters

Department of Chemistry, University of Rochester, Rochester, New York *(Received June 30, 1964)*

The thermal decomposition of cyclobutane near 450° has been found to be a unimolecular ring cleavage reaction which exhibits a falloff in the first-order rate constant in the pressure region below 20 mm.[3] Several comparisons of the low-pressure experimental results with unimolecular reaction rate theory have been made.[3b,c,d] The present study was undertaken to

(1) This work was supported by a grant from the National Science Foundation to the University of Rochester.

(2) Abstracted from the M.S. Thesis of A. F. Pataracchia, University of Rochester, 1961.

determine the influence of a change in structure from cyclobutane to methylcyclobutane upon the fall-off behavior. The effect of methyl substitution has already been studied for the case of the unimolecular isomerization of cyclopropane.[4] The homogeneous thermal isomerization of methylcyclopropane which yields four isomeric butenes was studied in the region 440–490° at pressures of 0.6 to 200 mm. A decrease in the over-all first-order rate constant was observed at about $^1/_{30}$ the pressure at which the same effect occurred in the isomerization of cyclopropane.[4] Thus an investigation of the effect of a methyl substituent upon the fall-off behavior of cyclobutane would be of interest also for comparison with the data for cyclopropane and methylcyclopropane. Earlier results on the pyrolysis of methylcyclobutane indicated that it should be suitable for such a study.[5]

Experimental

Materials and Apparatus. The methylcyclobutane used in this work was a sample which had been prepared in this laboratory by Das.[5] The methylcyclobutane had been obtained by the hydrogenation of methylenecyclobutane over Raney nickel at 50 p.s.i. with the temperature kept below 60°. Subsequent purification of the sample was carried out by gas chromatography with a 2-m. Perkin-Elmer column A (diisodecyl phthalate) at 33°. The purified sample after drying over Linde 4A Molecular Sieve had a minimum purity of 99.9%. The cyclobutane from a previous study[3a] which was used for some experiments was found to be 99.9% pure by a gas chromatographic analysis on a tetraisobutylene–firebrick column.

The reaction vessel and furnace were modifications of the apparatus used for several earlier experiments.[3a] The reactor was a 12-l. spherical Pyrex glass bulb with a thermocouple well extending into its center. For temperature uniformity the vessel was enclosed in a spherical aluminum shell 2.5 cm. thick (in the form of two separable hemispheres). The temperature of the reaction vessel was measured with five standardized platinum, platinum–13% rhodium thermocouples (one at the center of the vessel and four at various points on the surface of the glass vessel) which were connected to a Gray Model E3040 potentiometer. The average of the five values (with a mean deviation of about 0.25°) was taken as the reaction temperature.

The grease-free system for measurement, introduction, and removal of samples was connected to the reaction vessel through a 15-mm. mercury cutoff float valve, and the various parts were connected by 14-mm. tubing to permit rapid transfer of gases and efficient pumping. Before each experiment a pressure of less than 10^{-5} mm. was obtained. Prior to a series of experiments the surface of the reaction vessel was treated by decomposing the reactant in the vessel. For removal of the reaction mixture a trap adjacent to the first mercury float valve was fitted with a special dewar flask so that the coolant (liquid nitrogen) could be brought to a lower temperature by pumping with a mechanical-type oil pump. The pumping on the nitrogen coolant was begun at least 30 min. before the time of removal which usually corresponded to 25–37% decomposition. The pressure in the reaction vessel after product removal was less than 10^{-5} mm.

Analyses. The reaction mixtures were analyzed on a Perkin-Elmer Model 154D vapor fractometer equipped with a Model 194 printing integrator. The 2.7-m. chromatographic column (5-mm. i.d.) was packed with tetraisobutylene on 60–80 mesh Chromosorb. The column was operated at a temperature near 26° with a flow rate of 56 cc. of helium/min. To keep the vapor samples (which were expanded into the gas chromatograph) within definite limits attachments of different sizes were used with the gas sampling valve. Major peaks for ethylene, propylene, and methylcyclobutane were observed. From the size of the ethylene peak the proper attenuation could be selected to give the optimum size for the propylene peak for the comparison of its area with the area under the methylcyclobutane peak. A technique was developed in order to obtain for each reaction mixture a number of such area ratios which upon averaging would give a more reliable value than that from a single determination. The peaks for ethylene (1.5 min.) and propylene (3.7 min.) appeared during the first 4 min., but the peak for methylcyclobutane did not appear until about 40 min. later. With standard mixtures it was found that additional portions of the mixture could be expanded into the gas chromatograph after the ethylene and propylene had been detected and before the first methylcyclobutane peak was recorded. The successive expansions (2 to 7) gave a series of pairs of ethylene and propylene peaks followed by a series of methylcyclobutane peaks. The area under each propylene (or ethylene) peak was then compared with the area under the corresponding methyl-

(3) (a) C. T. Genaux, F. Kern, and W. D. Walters, *J. Am. Chem. Soc.*, **75**, 6196 (1953); F. Kern and W. D. Walters, *Proc. Natl. Acad. Sci. U. S.*, **38**, 937 (1952); (b) H. O. Pritchard, R. G. Sowden, and A. F. Trotman-Dickenson, *Proc. Roy. Soc.* (London), **A218**, 416 (1953); (c) J. N. Butler and R. B. Ogawa, *J. Am. Chem. Soc.*, **85**, 3346 (1963); (d) R. W. Vreeland and D. F. Swinehart, *ibid.*, **85**, 3349 (1963); R. W. Vreeland, Ph.D. Thesis, University of Oregon, 1961.

(4) J. P. Chesick, *J. Am. Chem. Soc.*, **82**, 3277 (1960).

(5) M. N. Das and W. D. Walters, *Z. physik. Chem.* (Frankfurt), **15**, 22 (1958).

cyclobutane peak. With proper attenuation there was no trend in the variation of the area ratio for the successively expanded portions. The average ratio for each reaction mixture was compared with a calibration curve prepared from samples of known compositions. When the peaks were not suitable for accurate measurement by the integrator, areas were determined in other ways and compared with standard samples measured in the same manner. Since $C_5H_{10} \rightarrow C_2H_4 + C_3H_6$, the gas chromatographic ratios could be used to obtain the percentages of decomposition.

On the assumption that two molecules of products are formed from one reactant molecule, the per cent decomposition was calculated also from a comparison of the total moles removed from the reaction vessel and the moles introduced. For 27 of the 30 experiments in which both PVT and g.c. results were available, the values from the PVT data (after 30% decomposition) averaged slightly higher than the g.c. values by an amount corresponding to +0.9% decomposition. The agreement seems satisfactory; it is to be noted that the per cent decomposition from PVT results will reflect the presence of all types of product molecules. The first-order rate constants were calculated from the propylene formed with the exception that the point at the lowest pressure in Fig. 2 was obtained from PVT results and the next point was based on the average for propylene and ethylene. In the calculations of the rate constants in this work the effect of a small dead space (0.3%) was taken into account and a small correction was applied for the time of removal of the reaction mixture.

In the present study prior to the work on methylcyclobutane, experiments were carried out with cyclobutane at initial pressures from 0.32 to 0.016 mm. near 449° in the same apparatus. A qualitative g.c. analysis of the products showed that ethylene was essentially the only product formed. Three preliminary experiments with $P_0 = 0.02$ mm. gave an average value of 2.05 for the (P_∞/P_0) ratio indicating the formation of two product molecules. The gas noncondensable in pumped liquid nitrogen was found to be only ~0.03% of the final products (after 24 hr.). Since the stoichiometry corresponded to that found at higher pressures ($C_4H_8 \rightarrow 2C_2H_4$), the per cent decomposition was determined from the ratio (moles removed from reaction bulb/moles introduced). The rate constants will be presented in the Results section, but after the report of the comprehensive low-pressure study of cyclobutane by Vreeland and Swinehart work with cyclobutane was discontinued.

Results

Experiments were performed to find out whether the decomposition at low pressures proceeds according to the equation

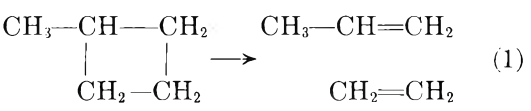

(1)

which represented 98–99% of the pyrolysis at 7–417 mm. and 410–450°.[5] The course of the reaction at pressures of 0.0026–0.45 mm. was indicated by the following results. With 0.3 mm. initial pressure at 450° the ratio of P_∞/P_0 was observed to be 2.02. In a test for side or subsequent reactions, the amount of gas noncondensable at ~−210° from an experiment with 0.28 mm. initial pressure carried to 23% reaction was found to be less than 2.5×10^{-6} mm. From the chromatographic analyses of the reaction mixtures it was possible to compare the amounts of ethylene and propylene in experiments at various pressures. The data summarized in Table I indicate that over the pressure range studied the ethylene and propylene are present in equivalent amounts. These findings provide evidence that under the conditions of this study the stoichiometry of the decomposition is in agreement with eq. 1.

Table I: Comparison of the Amounts of Ethylene and Propylene Formed in the Pyrolysis of Methylcyclobutane at Low Pressures[a]

Pressure range, mm.	Number of experiments	$P_{C_2H_4}/P_{C_3H_6}$
0.2–0.45	8	1.004 ± 0.006
0.05–0.20	8	1.016 ± 0.014
0.01–0.05	7	1.005 ± 0.023
0.0027–0.01	6	0.980 ± 0.020

[a] Temp., 400–440°; decomposition, 25–36%.

The chromatograms for experiments at the lowest pressures (~0.003 mm.) revealed three very small peaks at 2.2, 2.5 (between C_2H_4 and C_3H_6), and 4.8 min. (after C_3H_6). The substances were not identified, but the total of their areas amounted to only 0.03 ± 0.01 times the combined areas under the ethylene and propylene peaks. Of lesser importance was a small shoulder (sometimes a peak) near the beginning of the ethylene peak. In experiments at pressures of 0.3–0.4 mm. all of these minor features became less distinct (the curve between 2.2 and 2.5 min. being only slightly different from zero) and a maximum estimate

for them would be 0.001–0.008 times the combined areas of ethylene and propylene. Under the conditions used in this work, reactions other than (1) do not seem to occur to an extent that will significantly affect the rate constants calculated for (1). The absence of a peak near that of methylcyclobutane indicates that no appreciable isomerization takes place.

The decrease in the first-order rate constant as the initial pressure of methylcyclobutane is lowered to 0.0027 mm. at 420° is shown in Fig. 1, in which log k is plotted against log P_0. The data at 430° are shown in the form of a log (k/k_∞) *vs.* log P_0 plot. The values of k_∞ at 420 and 430° were taken to be 1.27×10^{-4} and 2.38×10^{-4} sec.$^{-1}$, respectively. In each case k_∞ was evaluated by the use of plots of k^{-1} *vs.* P_0^{-1} and k^{-1} *vs.* $P_0^{-0.5}$ for the present data plus some experiments from the earlier work.

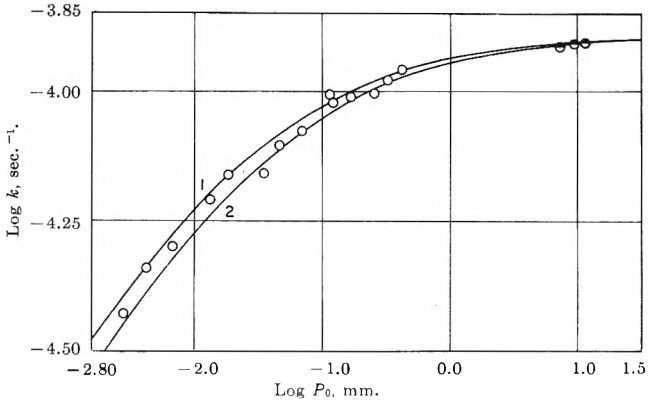

Figure 1. Change of first-order rate constant for methylcyclobutane with decreasing initial pressure at 420°: O, this study; ◓, data of Das.[5] Curves calculated from quantum form of Kassel theory: curve 1, $s = 28$; curve 2, $s = 27$; $\sigma = 5.9$ Å., $E = 62$ kcal./mole, $A = 4.46 \times 10^{15}$ sec.$^{-1}$, $\nu = 2.96 \times 10^{13}$ sec.$^{-1}$.

Although the effect of the initial pressure upon the activation energy was not studied in detail, some information was obtained from a few experiments at $P_0 = 0.4$ mm. and at $P_0 = 0.06$ mm. for the region 400–430° and from four experiments with P_0 near 0.0028 mm. at 410–440°. The activation energy at 0.4 mm. was 62 ± 1 kcal./mole. These preliminary results indicated that the activation energy probably decreases for pressures of 0.06 and 0.0028 mm. by about 3–4 and 5–6 kcal./mole, respectively.

Both the quantum and classical forms of the Kassel theory[6] were used for the calculation of fall-off curves. In Fig. 1 are shown the curves at 420° from the quantum form of the Kassel theory for the number of oscillators $s = 27$ and $s = 28$ (and with other parameters

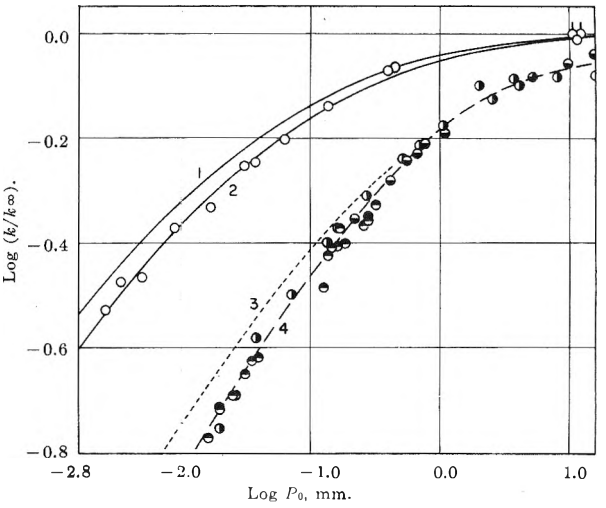

Figure 2. Comparison of the decrease in the first-order rate constant for methylcyclobutane at 430° with Kassel classical theory and with fall-off data for cyclobutane. Rate constant for methylcyclobutane at 430°: O, this work; Ō, data of Das.[5] Curve 1, $s = 24$. Curve 2, $s = 23$, $\sigma = 5.9$ Å., $b = 44.4$ ($b = E/RT$), $A = 4.4 \times 10^{15}$ sec.$^{-1}$. Curve 3, cyclobutane at 430° from ref. 3d. Curve 4, cyclobutane at 449°: ◑, Vreeland and Swinehart[3d] corrected to 449°; ◒, Kern, ref. 3a; ◓, this work.

as given below Fig. 1). These curves are in reasonable accord with the experimental results at 420° and a similar curve for $s = 28$ (not shown) agreed with the data at 430°. With the classical form of the Kassel theory the fall-off curves for $s = 24$ and $s = 23$ were obtained with the program of Schlag[7] for the Bendix G-15 computer (see curves 1 and 2, Fig. 2). The curve for $s = 24$ is slightly higher than the experimental data, but the curve for $s = 23$ fits the data well. The lower value of s for the classical form[8] compared to the quantum form would have been anticipated.

The effect that methyl substitution on cyclobutane produces upon the fall-off curve can be seen in Fig. 2. Curve 4 shows the decrease in the first-order rate constants obtained for cyclobutane at 449° from various studies. The results for cyclobutane in our apparatus at 449° seem to be in satisfactory agreement with the data of Vreeland and Swinehart at 449°.[3d] In the lower pressure region our methylcyclobutane fall-off curve at 430° is shifted toward lower pressures by 1.15–

(6) L. S. Kassel, "The Kinetics of Homogeneous Gas Reactions," Chemical Catalog Co., Reinhold Publishing Corp., New York, N. Y., 1932, pp. 100–103.

(7) E. W. Schlag, B. S. Rabinovitch, and F. W. Schneider, *J. Chem. Phys.*, **32**, 1599 (1960).

(8) The situation with respect to the classical form has been discussed by B. S. Rabinovitch and J. H. Current, *ibid.*, **35**, 2250 (1961); E. W. Schlag, *ibid.*, **35**, 2117 (1961); M. Vestal, A. L. Wahrhaftig, and W. H. Johnston, *ibid.*, **37**, 1276 (1962); G. M. Wieder and R. A. Marcus, *ibid.*, **37**, 1835 (1962).

1.2 log P_0 units compared to curve 3 for the cyclobutane fall-off at 430° observed by Vreeland and Swinehart.[3d] As would be expected, the difference (at the lower pressures) between the methylcyclobutane fall-off data at 430° and curve 4 for cyclobutane at the higher temperature (449°) is somewhat larger (1.25–1.4 log P_0 units). The value of $s = 23$ (Kassel classical) for methylcyclobutane may be compared with Vreeland and Swinehart's cyclobutane value of $s = 18$.[3d] In each case s is approximately 60% of the total number of vibrational degrees of freedom and on this basis the vibrational degrees of freedom of the added methyl group appear to participate almost as effectively in the activation process as the rest of the molecule. This finding would seem to be in accord with the concept of intramolecular energy transfer during the lifetime of the activated molecule. For methylcyclopropane[4] the value of $s = 19$ which gives a suitable Kassel classical fall-off curve represents an increase of 6 or 7 over the s appropriate for cyclopropane. Moreover, Flowers and Frey[9] found that the curve for $s = 23$ reproduces their fall-off data for 1,1-dimethylcyclopropane (which has the same number of vibrational degrees of freedom as methylcyclobutane). Also of interest is that the fall-off curve obtained by Chesick[10] for methylenecyclobutane lies between the curves for methylcyclobutane and cyclobutane.

In the low pressure work on cyclopropane[11] and cyclobutane,[3c,d] it has been observed that the curve for the decrease in rate constant tends to level off at pressures in the region 10^{-3} mm. and below. The data in Fig. 1 and 2 for methylcyclobutane do not extend to a pressure of 10^{-3} mm. and do not exhibit a noticeable leveling off.

Acknowledgment. The authors wish to thank Dr. E. W. Schlag for his computer program and Mr. Carl Whiteman for his assistance.

(9) M. C. Flowers and H. M. Frey, *J. Chem. Soc.*, 1157 (1962).

(10) J. P. Chesick, *J. Phys. Chem.*, **65**, 2170 (1961).

(11) A. D. Kennedy and H. O. Pritchard, *ibid.*, **67**, 161 (1963).

Solvent Dipole Competition for Interamide Hydrogen Bonds[1]

by James S. Franzen and Barbara C. Franzen

Department of Biochemistry and Nutrition, Graduate School of Public Health, University of Pittsburgh, Pittsburgh, Pennsylvania *(Received June 29, 1964)*

It has been demonstrated that the hydrogen-bonding interaction between amides is weakened by a dipolar solvent.[2] This earlier study has now been extended to another solvent system of varying dipolar character. By using either carbon tetrachloride, $\mu = 0.0$ D., or 1,1,1-trichloroethane, $\mu = 1.6$ D., or mixtures of the two, a range of solvent dielectric constants from 2.25 to 7.0 can be covered. This system is more appropriate than the *cis–trans*-dichloroethylene system used previously because no type of solvent–solute hydrogen bonding is possible. The extensive studies of Allerhand and Schleyer[3] have revealed no evidence for the participation of methyl groups in hydrogen bonding, and, therefore, any competitive effects by the solvent must be due to dipole–dipole interaction.

ε-Caprolactam was chosen as the hydrogen-bonding solute since it forms dimers only,[2,4] thus eliminating the need for making assumptions about relative magnitudes of equilibrium constants as is required for multiple equilibrium systems.[5] The extent of association was determined from the variation of the apparent extinction coefficient of the first overtone of the free N–H absorption according to the treatment of Lord and Porro.[4]

Experimental

The solvents employed were obtained from Fisher Scientific Co. Spectroanalyzed grade carbon tetrachloride was used without further treatment. The trichloroethane, however, exhibited a strong absorption band at about 275 mμ which was probably due to aromatic contamination. This solvent was, therefore, distilled through a 90-cm. electrically heated column packed with Berl saddles. Using a reflux ratio of 8:1, the fraction boiling at 72–73° and having no absorption band at 275 mμ was used for the hydrogen-bonding experiments. ε-Caprolactam from K and K Laboratories was dried overnight *in vacuo* at room temperature and used directly.

The spectral measurements of the unassociated N–H group in the near-infrared region were carried out as described in the earlier paper[2] except for a few minor changes. Since the Cary 14-R spectrophotometer was available, the reverse beam feature of this instrument was exploited. Thus instead of passing the entire wave length range of the source through the sample, only monochromatic radiation traversed the solutions. As a result, heating of the sample by the beam was reduced to

(1) This work was supported in part by a Public Health Service Research Grant (GM-10133-02) from the Division of General Medical Sciences.

(2) J. S. Franzen and R. E. Stephens, *Biochemistry*, **2**, 1321 (1963).

(3) A. Allerhand and P. von R. Schleyer, *J. Am. Chem. Soc.*, **85**, 1715 (1963).

(4) R. C. Lord and T. J. Porro, *Z. Elektrochem.*, **64**, 672 (1960).

(5) M. Davies and D. K. Thomas, *J. Phys. Chem.*, **60**, 763 (1956).

Table I: Values of Thermodynamic Functions for the Association of ϵ-Caprolactam

Solvent	T, °K.	D.	K, l. mole^{-1}	$\Delta G°$, kcal. mole^{-1}	$\Delta H°$, kcal. mole^{-1}	$\Delta S°$, cal. mole^{-1} deg.$^{-1}$
CCl_4	276	2.26	146 ± 6			
	298	2.22	74.2 ± 2.8	−2.53	−5.4	−9.8
	313	2.20	46.5 ± 1.9			
CCl_4–TCE (2:1)	276	3.54	58.0 ± 2.3			
	298	3.38	32.8 ± 1.3	−2.07		
CCl_4–TCE (1:1)	298	4.01	22.9 ± 0.9	−1.86		
TCE	276	7.67	23.8 ± 0.9			
	298	6.89	13.4 ± 0.5	−1.54	−4.9	−11.4
	313	6.38	8.7 ± 0.3			

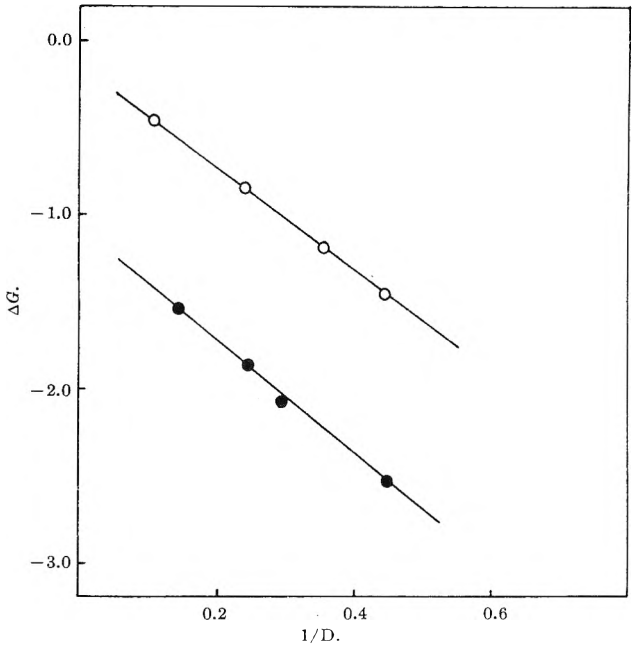

Figure 1. Dependence of the free energy of caprolactam association on the reciprocal of the solvent dielectric constant. The closed circles represent the data of this paper. The open circles represent data for the association of caprolactam in solvents composed of *cis*- and/or *trans*-dichloroethylene taken from the previous study.[2]

a negligible amount, and temperature control was certain to within ±0.5°. The temperature within the cell was monitored directly by the use of a thermocouple sealed in a glass capillary and press-fitted into the Teflon stopper supplied with the cell. An optical path of 10 cm. was used in all cases, since at the higher concentrations required for shorter cells the monomer–dimer equilibrium becomes complicated by the formation of larger aggregates.[4] The estimated maximum error in the reported equilibrium constants is 4%.

Dielectric constants of the solvents were determined by the resonance method with the apparatus described by Bender.[6]

Results and Discussion

As can be seen from Table I, the caprolactam dimer hydrogen bonds are quite sensitive to the composition of the solvent. This is also evident from Fig. 1, which shows that trichloroethane, μ = 1.6 D., is less effective in disrupting the dimer complex than *cis*-dichloroethylene, μ = 1.89 D. Such a relation is expected in view of the propensity of the π-electron cloud and of the C–H groups[3] of dichloroethylene for hydrogen-bonding to caprolactam monomers. The explanation of the linear relations in Fig. 1, however, is not fully established. Although the free energy of the association reaction varies directly with the reciprocal of the solvent dielectric constant, a theoretical description of the system in which the region between the hydrogen-bonded molecules is treated as a continuum[2] is not realistic. The observed linear relations may just be fortuitous since from a microscopic point of view there is no evident reason at present for expecting such behavior. It is more likely that the reduction in the extent of association with increasing dipolar nature of the solvent is due to solvent–solute dipole–dipole interactions.

In conclusion, it can be stated that there is a close relationship between hydrogen-bond strength and the molecular environment provided by the solvent. Accordingly, the recent studies of Ritchie and Pratt[7] emphasize the significance of solvation effects of this sort.

(6) P. Bender, *J. Chem. Educ.*, **23**, 179 (1946).

(7) C. D. Ritchie and A. L. Pratt, *J. Am. Chem. Soc.*, **86**, 1571 (1964).

Vapor ization Energy and Density Relations in Nonpolar Liquids

by A. A. Miller

General Electric Research Laboratory, Schenectady, New York *(Received July 3, 1964)*

The vaporization energy is important for the interpretation of liquid–vapor equilibrium. Also, the derived quantities, "cohesive energy density," ϵ/v, and "solubility parameter," $(\epsilon/v)^{1/2}$, have been suggested as empirical measures of intermolecular attraction in liquids.[1] This paper presents a simple relationship between vaporization energy and density which apparently has not yet been reported, and certainly not emphasized, in the literature.[2] The examples of nonpolar liquids which are considered are benzene, carbon tetrachloride, and six normal alkanes in the C_5 to C_{12} range.

Liquid densities were taken from A.P.I. Tables[3] and from Timmermans.[4] The latter was also the source of the orthobaric vapor densities. For benzene and *n*-heptane, the vaporization energies up to the boiling points, T_B, were computed from Haggenmacher's[5] values of the heat and external work of vaporization: $\epsilon = h - p\Delta v$. Between T_B and T_C, the Clapeyron equation was used

$$\epsilon = p(v_g - v_l)[(T/p)(dp/dT) - 1]$$

with the $dp/dT = \gamma_\sigma$ values reported by Rowlinson.[6] For carbon tetrachloride, the vaporization energies tabulated by Moelwyn-Hughes[7] between 0° and T_C were used directly.

Figure 1 shows that for each of these three liquids, the vaporization energy is a linear function of the liquid density over the entire liquid range. Extrapolation to $\epsilon = 0$, the critical point, gives the proper values of the critical densities, ρ_c.[8] Hence

$$\epsilon = k(\rho - \rho_c) \qquad (1)$$

where $k = d\epsilon/d\rho$. The values of k (cal. cc./g.^{2}) are 169, 43.5, and 185, for C_6H_6, CCl_4, and C_7H_{16}, respectively.

When extrapolated in the direction of higher densities, the lines in Fig. 1 should terminate at ϵ_0, ρ_0 for the hypothetical liquid at 0°K., where $\epsilon_0 = h_0$, the heat of vaporization. The latter can be derived from accurate vapor pressure equations, such as the Kirchoff–Rankine (K–R) equation, of the form: $\log p = A + B/T + C \log T$, where $h_0 = -2.3RB/M$ cal./g.[9]

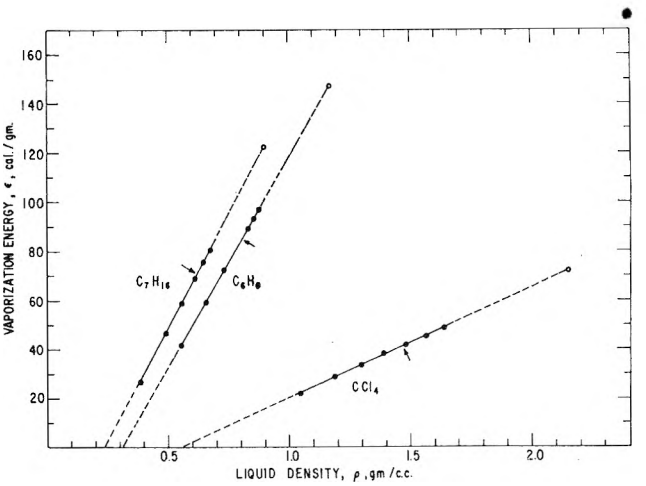

Figure 1. Vaporization energies *vs.* liquid densities for benzene, carbon tetrachloride, and *n*-heptane. Arrows indicate boiling points.

By an additional semiempirical term, Frost and Kalkwarf[10] extended the K–R equation to the critical point. The F–K constants have been reported by Thodos and co-workers for saturated aliphatic[11] and aromatic hydrocarbons,[12] and for CCl_4.[13] As should be expected, the F–K and the K–R[9] constants have similar values.

In the present context, the derivation of the K–R vapor pressure equation differs somewhat from the conventional method.[9] Starting with the exact Clapeyron equation, $dp/dT = h/T\Delta v$, with $h = \epsilon + p\Delta v$ and with the usual simplifications, applying up to approximately the boiling point ($\Delta v = v_g$ and $pv_g = RT$), we obtain $d \ln p/dT = \epsilon/RT^2 + 1/T$, but $d\epsilon/dT = (d\epsilon/d\rho)(d\rho/dT) = k(d\rho/dT)$ by eq. 1. Plots of ρ *vs.* T show that with nonpolar liquids for the small

(1) J. H. Hildebrand and R. L. Scott, "The Solubility of Nonelectrolytes," Reinhold Publishing Corp., New York, N. Y., 1950.

(2) J. R. Partington, "Advanced Treatise on Physical Chemistry," Vol. II, Longmans, Green and Co., London, 1951.

(3) F. D. Rossini, "Physical and Thermodynamic Properties of Hydrocarbons," A.P.I. 44, Carnegie Press, Pittsburgh, Pa., 1953.

(4) J. Timmermans, "Physico-Chemical Constants of Pure Organic Compounds," Elsevier Publishers, New York, N. Y., 1950.

(5) J. E. Haggenmacher, *Ind. Eng. Chem.*, **40**, 436 (1948).

(6) J. S. Rowlinson, "Liquids and Liquid Mixtures," Butterworths, London, 1959, Tables 2.3 and 2.4.

(7) E. A. Moelwyn-Hughes, "Physical Chemistry," Pergamon Press New York, N. Y., 1961, Table XVI-10.

(8) K. A. Kobe and R. E. Lynn, Jr., *Chem. Rev.*, **52**, 117 (1953).

(9) See E. A. Moelwyn-Hughes, ref. 7, p. 696 ff.

(10) A. A. Frost and D. R. Kalkwarf, *J. Chem. Phys.*, **21**, 264 (1953).

(11) N. E. Sondak and G. Thodos, *A.I.Ch.E. J.*, **2**, 347 (1956).

(12) D. L. Bond and G. Thodos, *J. Chem. Eng. Data*, **5**, 288 (1960).

(13) E. C. Reynes and G. Thodos, *Ind. Eng. Chem. (Fundamentals)*, **1**, 127 (1962).

expansions up to T_B, ρ is very nearly linear in T. Under these conditions,[14] $\epsilon = \epsilon_0 + aT$. Substitution in the Clapeyron equation and integration gives the Kirchoff–Rankine equation

$$\ln p = A - \epsilon_0/RT + [1 + a/R] \ln T \quad (2)$$

For C_6H_6, ϵ_0 (cal./g.) = 140, 153 (K–R),[9] 144 (F–K),[12] and 150, from latent heats determined in the 20–50° range[15] and extrapolated linearly to 0°K. A mean value, 147 (±6) cal./g., gives, by Fig. 1, ρ_0 = 1.17 (±0.04) g./cc. For CCl_4, ϵ_0 = 73 (K–R)[9] and 70.5 (F–K)[13] giving ρ_0 = 2.15 (±0.04) g./cc. These values are consistent with $\rho_0 \simeq 4\rho_c$ = 1.22 and 2.22 g./cc., respectively, which were found to apply in a free volume treatment of liquid viscosities for C_6H_6 and CCl_4.[16] For C_7H_{16}, ϵ_0 = 126 cal./g.,[11] and by Fig. 1, ρ_0 = 0.92 g./cc.

By eq. 1 and Fig. 1, we obtain the further relations

$$\epsilon_2 - \epsilon_1 = k(\rho_2 - \rho_1); \quad k = \epsilon_0/(\rho_0 - \rho_c);$$

$$\epsilon = \epsilon_0 + (d\epsilon/d\rho)(\rho - \rho_0) \quad (3)$$

The parameters for six normal alkanes are listed in Table I. The slopes, $d\epsilon/d\rho$, were derived from the linear ϵ *vs.* ρ plots based on the Haggenmacher values.[5] The B constant in the F–K equation[11] was used to obtain ϵ_0. As a convenient reference point, the ϵ, ρ data at 20° are listed.[17] With these data and eq. 3,

Table I: Vaporization Energy–Density Parameters for *n*-Alkanes, C_nH_{2n+2}

	$d\epsilon/d\rho$, cal. cc./g.^{2}	ϵ_0, cal./g.	20°: ϵ, cal./g.	20°: ρ, g./cc.	ρ_0, g./cc.	$\epsilon_0\rho_0$, cal./cc.
C_5	200	133	80.0	0.626	0.891	118
C_6	193	129	81.6	0.660	0.906	117
C_7	185	126	82.0	0.684	0.922	116
C_8	181	124	82.5	0.703	0.941	117
C_{10}	174	121	83.0	0.730	0.948	115
C_{12}	162	120	83.0	0.749	0.977	117

the values of ρ_0 were derived. For this series of *n*-alkanes, the "cohesive energy density" at 0°K., given by $(\epsilon/v)_0 = \epsilon_0\rho_0$, appears to be constant, 117 (±1) cal./cc. For the same series at 20°, the c.e.d. increases regularly from 50.2 to 62.1 cal./cc.[17]

The critical densities, ρ_c, calculated by eq. 1, are within 3% of the literature values,[8] and the ratio ρ_c/ρ_0 decreases slowly from 0.260 for C_5H_{12} to 0.243 for $C_{12}H_{26}$, paralleling the trend in the critical compressibility factor, $(PV/RT)_C$.[3,8] The ρ_0-values in Table I are within 1% of the zero-point densities for the crystalline *solids*.[18] However, they are consistently 2% higher than values given by the Doolittle relation,[19] $\rho_0 = e^{-10/M}$, which, in turn, are about 1% above values derived by Riedel.[20]

In an earlier paper,[16] the liquid viscosities of C_6H_6 and CCl_4 were related to the free volume fraction, defined as $f = (v - v_0)/v = (\rho_0 - \rho)/\rho_0$. From the present work, $f/f_c = (\epsilon_0 - \epsilon)/\epsilon_0$, where f_c refers to the critical point. For the nonpolar liquids considered here, $\rho_c/\rho_0 \simeq 0.25$ and $f_c \simeq 0.75$, with the values differing slightly for each liquid.

(14) Direct ϵ *vs.* T plots of the Haggenmacher values up to T_B show very little curvature. Since $h = \epsilon + RT$, for the conditions cited, h is also linear in T, which is the basis for usual derivation of the K–R equation.

(15) See J. R. Partington, ref. 2, p. 315.

(16) A. A. Miller, *J. Phys. Chem.*, 67, 2809 (1963).

(17) G. Allen, G. Gee, and G. J. Wilson, *Polymer*, 1, 458 (1960).

(18) See E. A. Moelwyn-Hughes, ref. 7, p. 320.

(19) A. K. Doolittle, *J. Appl. Phys.*, 22, 1471 (1951).

(20) L. Riedel, *Chem.-Ingr.-Tech.*, 26, 257 (1954).

The Conductance of Some Quaternary Ammonium Electrolytes in Hydrogen Cyanide

by R. H. Davies

Department of Chemistry, University College, Swansea, Wales

and E. G. Taylor

Thompson Chemical Laboratory, Williams College, Williamstown, Massachusetts (*Received July 13, 1964*)

The fact that earlier work in hydrogen cyanide[1] indicated unusual behavior of salts containing large ions has led us to reopen the investigation. Furthermore, the recent extension of the Onsager conductance equation, in addition to providing a reason for the anabatic behavior previously observed, may be applied to conductance data at higher concentrations than formerly used. We have also, therefore, taken the opportunity to show that the long-chain quaternary ammonium salts behave as normal electrolytes in hydrogen cyanide.

Experimental

Materials. Hydrogen cyanide as supplied (Imperial Chemical Industries, Ltd.) contained up to 1.8%

(1) J. E. Coates and E. G. Taylor, *J. Chem. Soc.*, 1245, 1495 (1936).

Table I: Preparation, Purification, and Melting Points of Salts

Starting materials	Product	Recrystallizing solvent	M.p., °C.
$(C_2H_5)_3N$, C_2H_5I	Et_4NI	Water–ethanol	300 dec.
	Et_4NPi	Water–ethanol	261
$(n\text{-}C_4H_9)_3N$, $n\text{-}C_4H_9I$	$n\text{-}Bu_4NI$	Water	144
	$n\text{-}Bu_4NNO_3$	Benzene	120
	$n\text{-}Bu_4NPi$	Ethanol	85
$(CH_3)_3N$, $n\text{-}C_{18}H_{37}I$	n-OctdMe$_3$NI (OTM)	95% ethanol	252
	n-OctdMe$_3$NCl	Methanol–acetone	225 dec.
	n-OctdMe$_3$NBr	Ethanol–acetone	248
$(C_2H_5)_3N$, $n\text{-}C_{18}H_{37}I$	n-OctdEt$_3$NI (OTE)	Ethanol–acetone	196
	n-OctdEt$_3$NCl	Acetone	153
	n-OctdEt$_3$NBr	Acetone	186
	n-OctdEt$_3$NNO$_3$	Acetone	160
	n-OctdEt$_3$NPi	Ethanol	58
$(n\text{-}C_{12}H_{25})(CH_3)_2N$, $n\text{-}C_{12}H_{25}I$	(Dod)$_2$(Me)$_2$NI (DDM)	Ligroin	138
	(Dod)$_2$(Me)$_2$NCl	Acetone	130
	(Dod)$_2$(Me)$_2$NPi	Ethanol	47
$(n\text{-}C_{12}H_{25})(CH_3)_2N$, $n\text{-}C_{18}H_{37}I$	(Octd)(Dod)(Me)$_2$NI	Acetone	146
	(Octd)(Dod)(Me)$_2$NPi	Ethanol	48

water together with 0.3% oxalic acid as a stabilizing agent. It was distilled to remove the oxalic acid and then shaken with P_2O_5 for several hours before being fractionated from fresh P_2O_5. A final distillation from magnesium perchlorate resulted in a product possessing a specific conductance of 3–5 $\times$ 10^{-7}, n.b.p. 25.7°. Later it was found that hydrogen cyanide recovered by distillation from the salt solutions was effectively purified by distilling from anhydrous sodium thiosulfate, the conductance falling to 5 $\times$ 10^{-8} and lower. All starting materials were carefully fractionated or recrystallized and the salts were subjected to multiple recrystallizations before use. The first step was the combination of the tertiary amine with the alkyl iodide to yield the quaternary ammonium iodide, which was converted into the other derivatives by metathesis with the appropriate silver compound. n-Dodecyldimethylamine (b.p. 118–119° at 5 mm.) was prepared by the methylation of n-dodecylamine[2]; n-octadecyl iodide (m.p. 35°) and n-dodecyl iodide (m.p. −2°) were obtained by iodination of the long-chain alcohols using phosphorus and iodine. Table I summarizes the procedures adopted. The salts were heated for several hours under vacuum at elevated temperature to constant weight.

Methods. Resistances were measured using a bridge similar to that described by Edelson and Fuoss.[3] The cells were of the flask type, fitted with small side chambers carrying the electrodes, which were lightly platinized. Cell constants were between 2 and 3 for the more concentrated solutions and about 0.5 for the dilute range. Runs were made using both the dilution and the concentration methods. Resistances were made with the cell immersed in an oil bath whose temperature was controlled to ±0.01°. Most measurements were made at 18° although 25° was used in several instances.

Solution densities were obtained using the dilatometric procedure described by Coates and Davies.[4] For concentrations up to 2% by weight at 18° the densities are given by the expression

$$\rho = 0.6900 + aw$$

where w is the salt concentration in grams per kilogram of solution. Values of a ($\times$ 10^4) are: Et_4NI, 4.35; Et_4NPi, 4.45; Bu_4NI, 3.35; Bu_4NNO_3, 2.75; Bu_4NPi, 3.60; OTMI, 2.95; OTMBr, 2.85; OTMCl, 2.40; OTMNO_3, 2.50; OTEI, 2.95; OTEBr, 2.75; OTECl, 2.30; OTENO_3, 2.60; OTEPi, 3.35; DDMI, 2.85; DDMCl, 2.25; DDMPi, 3.20; ODDPi, 3.00. At 25° it was found that the densities could be represented by the relation

$$\rho = 0.6797 + aw$$

The conductances of the salts in hydrogen cyanide are summarized in Tables II–V. At least two independent runs were made on each salt and the data given are for the more concentrated solutions. Where fewer than four points are given, these refer to individual

(2) R. A. Reck, H. J. Harwood, and A. W. Ralston, *J. Org. Chem.*, 12, 517 (1947).

(3) D. Edelson and R. M. Fuoss, *J. Chem. Educ.*, 27, 610 (1950).

(4) J. E. Coates and R. H. Davies, *J. Chem. Soc.*, 1194 (1950).

Table II: Conductance of Tetraethyl- and Tetra-*n*-butylammonium Salts in HCN at 18° (25° where Indicated)

10^4c	Λ	10^4c	Λ
Et_4NI		Et_4NPi	
112.00	333.3	87.43	260.8
71.19	337.6	52.90	265.3
40.49	342.4	27.12	270.1
22.15	346.5	18.20	272.1
Bu_4NI		Bu_4NNO_3	
110.1	281.1	124.7	272.4
66.22	286.9	90.07	275.6
37.07	292.0	59.20	279.7
23.10	295.0	30.92	284.2
Bu_4NPi		Et_4NPi (25°)	
90.03	209.2	86.14	277.9
56.78	213.6	52.14	282.5
34.60	217.2	26.73	287.3
20.28	220.5	17.93	289.5
Et_4NI (25°)		Bu_4NI (25°)	
21.83	367.6	36.53	310.3
2.480	376.8	23.07	313.2
Bu_4NNO_3 (25°)		Bu_4NPi (25°)	
30.46	301.7	55.95	228.0
27.04	302.9	19.89	235.2
19.12	305.1		

Table III: Conductance of *n*-Octadecyltrimethylammonium Salts in HCN at 18 and 25°

10^4c	Λ	10^4c	Λ
n-OctdMe$_3$NCl		*n*-OctdMe$_3$NCl (25°)	
80.30	270.0	79.12	287.0
53.86	273.8	53.08	290.8
35.45	276.3	34.93	293.5
18.14	280.1	17.87	297.4
n-OctdMe$_3$Br		*n*-OctdMe$_3$I	
76.79	270.3	136.4	265.3
44.87	275.0	89.35	270.2
21.56	279.7	49.61	275.6
10.54	283.0	27.58	279.8
n-OctdMe$_3$NI (25°)		*n*-OctdMe$_3$NBr (25°)	
134.5	281.5	21.25	296.7
48.89	292.4	5.627	302.9
27.17	296.8		
5.917	304.6		

Table IV: Conductance of *n*-Octadecyltriethylammonium Salts in HCN at 18 and 25°

10^4c	Λ	10^4c	Λ
n-OctdEt$_3$NCl		*n*-OctdEt$_3$NBr	
99.59	262.6	100.9	262.9
59.20	267.0	65.12	267.3
36.43	270.5	35.93	271.8
19.19	274.4	20.44	275.1
n-OctdEt$_3$NI		*n*-OctdEt$_3$NNO$_3$	
108.1	263.1	58.02	259.2
69.00	267.3	33.76	263.0
39.23	271.8	19.40	266.0
21.46	275.5	9.247	269.3
n-OctdEt$_3$NPi		*n*-OctdEt$_3$NCl (25°)	
71.97	191.2	98.13	279.1
39.42	196.0	25.53	289.3
19.47	200.1	18.91	291.2
9.679	202.9	10.80	294.0
n-OctdEt$_3$NI (25°)		*n*-OctdEt$_3$Br (25°)	
30.24	290.7	19.90	291.9
21.15	292.6	13.74	293.4
n-OctdEt$_3$NNO$_3$ (25°)			
19.12	282.8		
9.113	286.5		

Table V: The Conductance of Quaternary Ammonium Salts Containing Two Long Chains in HCN at 18 and 25°

10^4c	Λ	10^4c	Λ
Dod_2Me_2NCl		Dod_2Me_2NI	
59.67	263.1	73.4	261.6
30.08	267.9	45.17	266.1
14.29	271.5	23.86	270.5
7.112	274.4	11.43	274.1
Dod_2Me_2NPi		(Octd)(Dod)Me$_2$NPi	
58.88	188.1	93.7	173.8
33.89	192.4	59.50	178.4
17.07	196.5	30.21	183.4
7.425	200.2	19.15	186.1
(Octd)(Dod)Me$_2$NPi (25°)		Dod_2Me_2NCl (25°)	
92.33	185.4	14.08	288.4
58.63	190.3	3.254	293.6
29.76	195.7		
18.87	198.5	Dod_2Me_2NI (25°)	
		23.51	287.1
Dod_2Me_2NPi (25°)		4.698	294.9
16.82	209.9		
3.544	216.3		

cases in which certain of the solutions, after measurement at 18°, were placed in the 25° bath.

Despite the fact that the precision of the results is not better than 0.1%, the Onsager–Fuoss equation for unassociated electrolytes

$$\Lambda = \Lambda_0 - Sc^{1/2} + Ec \ln c + Jc$$

has been used to establish Δ_0 values by extrapolating plots of Λ' ($\Lambda + Sc^{1/2} - Ec \ln c$) *vs.* c to $c = 0$. The viscosity of hydrogen cyanide at 18° is 1.955×10^{-3} and at 25° it is 1.834×10^{-3}.[4] The dielectric constants at 18 and 25° were taken as 118.3 and 106.8, respectively.[5]

The slopes of the Λ'–c plots vary between 150 and 600 but because of the low precision and since both slight association and as yet uninvestigated viscosity corrections are undoubtedly included in the J value ($\Lambda' = \Lambda_0 + Jc$) it seemed pointless to calculate "a" values. It can however be stated that the slopes do correspond to center-to-center distances that are not totally unreasonable.

The values of Λ_0 are given in Table VI and are estimated to be good to within ±0.3. The values at 25° are given in parentheses and where only three figure numbers appear, these are to be regarded as good to about ±1.5 since they have been obtained by crude free-hand extrapolation from as few as two points on a Λ–$c^{1/2}$ plot.

Table VI: Limiting Equivalent Conductances of Salts in HCN at 18 and 25°

Salt	Λ_0	Salt	Λ_0
Et_4NI	358.8 (382)	Bu_4NI	307.5 (325)
Et_4NPi	282.9 (301.1)	Bu_4NPi	231.6 (246)
OTMCl	290.6 (309.4)	Bu_4NNO_3	297.9 (317)
OTMBr	291.4 (310)	OTECl	285.2 (302)
OTMI	293.0 (311.6)	OTEBr	286.5 (303)
DDMCl	281.0 (299)	OTEI	287.1 (303)
DDMI	283.0 (302)	$OTENO_3$	276.8 (295)
DDMPi	206.7 (222)	OTEPi	210.9
ODDPi	197.0 (210.5)		

Limiting equivalent ion conductances (Table VII) have been calculated based on the expression given for the tetra-*n*-butylammonium ion[6]

$$R^+D = 21.484 + 4.461D$$

and the Stokes relation $\lambda_0^+ = 0.82/R^+\eta$, giving for the Bu_4N^+ ion at 18 and 25° values of 90 and 96, respectively.

Table VII: Limiting Equivalent Ion Conductances in Hydrogen Cyanide at 18 and 25° (Values at 25° in Parentheses)

Ion	λ_0^+	Ion	λ_0^-
Et_4N^+	141 (151)	Cl^-	216 (229)
Bu_4N^+	90 (96)	Br^-	216 (229)
$OctdMe_3N^+$	75 (81)	I^-	218 (231)
$OctdEt_3N^+$	69 (73)	NO_3^-	208 (221)
$Dod_2Me_2N^+$	65 (72)	Pi^-	142 (150)
$(Octd)(Dod)Me_2N^+$	55 (61)		

(5) G. E. Coates and J. E. Coates, *J. Chem. Soc.*, 77 (1944).
(6) R. M. Fuoss, *Proc. Natl. Acad. Sci. U. S.*, **45**, 807 (1959).

Mutual Solubility of Perfluoroheptane with Carbon Tetrachloride and with Carbon Disulfide at 25°

by Kozo Shinoda and Joel H. Hildebrand

Department of Chemistry, University of California, Berkeley, California *(Received July 13, 1964)*

Fujishiro and Hildebrand,[1] in 1962, reported on the liquid–liquid solubility of cyclohexane and perfluorotributylamine at 25°. They pointed out the advantage of such measurements for systematic studies of solubility over the usual method of observing the temperature at which separation into two liquid phases occurs, saying: "This can be done accurately only in the region around the critical point, and most composition–temperature curves have not been carried very far down the descending branches. The reliable portions of available curves for different liquid pairs extend over different ranges of temperature, and it is difficult to make a systematic comparison of such systems at a common temperature. Parameters calculated from critical temperatures are unsatisfactory also because the structure of mixtures near the critical point is extremely complex, and not amenable to model treatments that are reasonably applicable outside this region. It is very desirable to have figures for liquid–liquid solubilities at a standard temperature, preferably at 25°, by determining the composition of both phases by analysis."

Such data offer the further advantages for systematic tests of theory that they are free, on the one hand, from the uncertainties of gas law deviations that are involved in studies by measurement of vapor pressures, and free, on the other hand, from the uncertainties involved in extrapolating liquid properties far below melting points when dealing with the solubility of solids.

(1) R. Fujishiro and J. H. Hildebrand, *J. Phys. Chem.*, **66**, 573 (1962).

Table I: Liquid–Liquid Solubilities, x, and Mole Fractions in Phases A and B at 25°

	A		B				
	x_A	φ_A	x_A	φ_A	$\delta_1 - \delta_2$	δ_1	δ_2
1. CCl_4	0.302[5,6]	0.157	0.970	0.933	3.08	8.6	5.5
2. C_7F_{16}	0.698	0.843	0.0299	0.067			
1. CS_2	0.140	0.042	~1.00	0.998	4.48	10.0	5.5
2. C_7F_{16}	0.860	0.958	5.4×10^{-4}	0.002			

Experimental

n-Perfluoroheptane was purified by the method described by Glew and Reeves.[2] Carbon tetrachloride and carbon disulfide were Spectro-quality reagents. They were distilled shortly before the experiments.

The solubility of C_7F_{16} in CS_2 and in CCl_4 is very small, so we applied the method devised by Reeves and Hildebrand[3] that measures the diminution in volume of the fluorocarbon after equilibrating with the other liquid, taking advantage of the fact that the latter wets glass preferentially.

Calibrated tubes were sealed to bulbs of about 130-cc. capacity. The volumes of these tubes, chosen after preliminary experiments, were 0.45 cc. for the CS_2 system and 2 cc. for the CCl_4 system. Measured volumes of the components were introduced into their respective vessels, which were then sealed and rocked in a thermostat. After saturation was reached, the remaining C_7F_{16} was collected in the calibrated side tube and its volume read. Corrections were made for the CCl_4 and CS_2 dissolved in the C_7F_{16}.

Concordant figures for the solubility of CCl_4 in C_7F_{16} were obtained by Hildebrand, Fisher, and Benesi[4] and by Kyle and Reed.[5]

Results and Discussion

Our results, together with those on CCl_4 in C_7F_{16} from ref. 5 and 6, are given in Table I, together with values of the difference between the solubility parameters that are calculated from the measurements by the equation used by Fujishiro and Hildebrand

$$\frac{RT}{2}\left(\frac{1}{v_1}\ln\frac{x_{1B}}{x_{1A}} + \frac{1}{v_2}\ln\frac{x_{2A}}{x_{2B}}\right) = (\varphi_{1B} - \varphi_{1A})(\delta_1 - \delta_2)^2 \quad (1)$$

The molal volumes of the components at 25° are: CCl_4, 97.1 cc.; CS_2, 60.7 cc.; C_7F_{16}, 225.6 cc. Equation 1 is obtained by combining the standard equation

$$RT \ln (a_2/x_2) = v_2\varphi_1^2(\delta_1 - \delta_2)^2 \quad (2)$$

with the corresponding equation for the other component.

The concordant values for $\delta_2 = 5.5$ for C_7F_{16} agree well within the usual limit of accuracy with the value 5.6 obtained for the system $Br_2 + C_7F_{16}$ by Reeves and Hildebrand,[3] calculated from the solubility of Br_2 in C_7F_{16}. These values of the solubility parameter of C_7F_{16} are distinctly less than the value, 5.85, derived from its energy of vaporization, a difference not unusual among systems departing appreciably from the simple model used in deriving eq. 2. However, the value here calculated agrees well with that found from the solubility of iodine, where $\delta_2 - \delta_1 = 8.6$, which with the standard value for I_2, 14.1, gives $\delta_1 = 5.5$. In this case, as in many others, a solubility parameter determined directly from solubility data is to be preferred, for practical purposes, over one based upon the heat of vaporization.[6]

Acknowledgment. This work has been supported by the Atomic Energy Commission.

(2) D. N. Glew and L. W. Reeves, *J. Phys. Chem.*, **60**, 615 (1956).

(3) L. W. Reeves and J. H. Hildebrand, *ibid.*, **60**, 949 (1956).

(4) J. H. Hildebrand, B. B. Fisher, and H. A. Benesi, *J. Am. Chem. Soc.*, **72**, 4348 (1950).

(5) B. B. Kyle and T. M. Reed, III, *ibid.*, **80**, 6170 (1958).

(6) For other examples, see R. L. Scott and J. H. Hildebrand, "Regular Solutions," Prentice-Hall, Englewood Cliffs, N. J., 1962, pp. 145–147.

The Production of Molecular Beams in the Mass Spectrometer[1]

by Benjamin P. Burtt and Jay M. Henis

Department of Chemistry, Syracuse University, Syracuse, New York 13210 *(Received July 17, 1964)*

In the course of studies of negative ion–molecule reactions in N_2O and CCl_3F at relatively high pressure in the mass spectrometer, evidence has been obtained to indicate that many of the accelerated negative ions lose their charge by collision in the analyzer tube.

The beam of particles impinging upon the collector plate contains more neutral atoms than negative ions.

The phenomenon of electron loss is not new, for Thomson[2] was one of the first to clarify some confusing observations made with early cathode ray tubes where the vacuum was poor. He showed that the charges on high-energy ions changed during their passage through the gas.

Physicists, using special equipment, have studied the charge-changing cross section using positive or negative ions of various types with energies of from 0.2 to 8000 kev. An excellent review is available by Allison and Garcia-Munoz.[3] However, the phenomenon should be called to the attention of those chemists who use mass spectrometers at relatively high pressure for the study of ion–molecule reactions (particularly where reactions of negative ions are concerned).

Since most modern spectrometers have differential pumping and the ions make no collisions in the analyzer tube, and since they usually are equipped with secondary electron repeller plates at the collector end of the tube, the phenomenon would not normally be observed.

At pressures of the order of 0.3 mm. in the ion source, the Cl^- peak in CCl_3F, for example, showed a valley on either side that dipped below zero current (*i.e.*, as if positive ions were being collected or as if the number of secondary electrons being ejected from the collector plate was greater than the number of Cl^- ions striking it). Curves of the form shown in Fig. 1 were obtained for O^- from N_2O as well as for F^- and Cl^- from CCl_3F.

As the pressure is raised, many Cl^- ions, after passing through the magnetic field, lose their charge on collision but are scattered only slightly from the original path (those that lose charge before reaching the magnetic field are not detected). These neutral particles with energies of 500 to 1000 v. eject secondary electrons from the grounded collector plate producing an apparent positive current. Application of a negative potential of 20 v. to the collector slit with respect to ground eliminates the effect and produces a normal peak with an intensity as much as 1000 times that obtained without the small electrostatic field.

That the secondary electrons are not all produced upon collision of Cl^- ions with the collector plate and that Cl atoms must be present are clear from the following experiment. At low pressure, when the Cl^- makes no collisions in the analyzer tube, the ion current increases by about 28% to a saturation value as the bias voltage on the collector slit is increased up to 20 v. In other words, 100 Cl^- ions striking the collector plate produce about 22 secondary electrons.

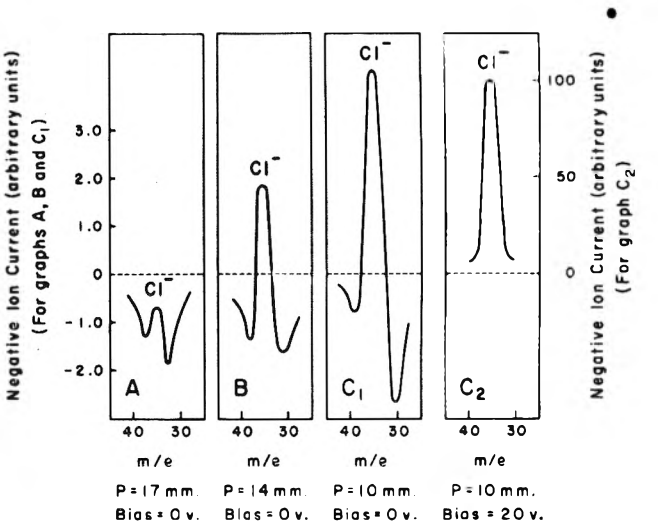

Figure 1. Ion current for the Cl^- peak in CCl_3F as a function of reservoir pressure. In graph C_2 the collector slit has a negative bias of 20 v. with respect to the collector plate. Note the change in scale in C_2.

Cl^+ ions are equally effective in producing secondary electrons (in that case the current decreases as the bias voltage is applied).

At a high pressure in the analyzer tube (0.010 mm.), there will be almost no observed Cl^- peak. However, when the collector slit is biased to 20 v., a large peak is obtained and the increase in ion current cannot be accounted for by secondaries from the Cl^- ions alone. However, the increase is explained if the bias voltage collects secondary electrons produced by Cl atom collision with the plate. Assuming that the Cl produces the same number of secondary electrons as the Cl^- and Cl^+ are observed to produce, it is possible to calculate the initial number of Cl^- ions that survive their passage through the magnetic field and the number of Cl atoms and Cl^- ions that eventually arrive at the plate. From these data, one can calculate the cross section σ in the usual manner

$$I = I_0 e^{-\sigma N p x}$$

where N is molecules/cc. at 1 mm., p is pressure in mm., x is the path length, and I and I_0 are, respectively, the ion current reaching the plate and the ion current entering the analyzer tube after passing through the magnetic field.

For example, in CCl_3F the electron detachment cross

(1) Supported in part by the U. S. Atomic Energy Commission.

(2) J. J. Thomson, "Rays of Positive Electricity," Longmans, Green and Co., London, 1921, pp. 134–142.

(3) S. K. Allison and M. Garcia-Munoz, "Atomic and Molecular Processes," D. R. Bates, Ed., Academic Press, New York, N. Y., 1962, pp. 722–782.

section at an ion energy of 1.0 ke.v. for F^- is 2.5×10^{-17} cm.^{2} while that for Cl^- is 5.5×10^{-17} cm.^{2}. These are rough values since the pressure of CCl_3F in the analyzer tube was known only approximately. The ratio of the two cross sections, 2.2, has greater validity and it can be compared to the ratio of 2.0 for Cl^- and F^- in krypton.[4]

The cross section for electron detachment for O^- in N_2O is found to be about 2.2×10^{-17} cm.^{2}. Of the three ions at 1.0 kev., O^- was most effective in producing secondary electrons, possibly because of its higher velocity. One O^- ion produced 0.55 electron, on the average; one F^- produced 0.46, and one Cl^- produced 0.22.

Kerwin and McGowan[5] have pointed out how a mass spectrometer can be used to study charge exchange of positive ions at high pressure, but they did not use the secondary electron emission as a tool. With equipment designed specifically for this purpose, it should be possible to use this method to obtain accurate values for cross sections for charge exchange.

Electron loss from negative ions produces a beam of neutral particles which might also be useful to studies of the chemistry of high energy molecular beams using the proper negative ion as a precursor. Equipment could be patterned after some of that used for the charge-changing cross section measurements described by Allison,[3] but ions could be fed into it from a mass spectrometer. In this way, the proper ion can be selected and a gas may be used that is easy to handle. For example, the CCl_3F is easier to use as a source of Cl^- or F^- than would be Cl_2 or F_2 or the corresponding hydrogen halides.

Negative ions would seem preferable to positive ions for the production of molecular beams for two reasons. First, the production of a neutral atom from a positive ion is a resonant process, and the electron must be captured into a particular state of the atom. The stripping of an electron from a negative ion should be more probable.

Secondly, many negative ions can be produced in large amounts by very low energy electrons. Only one or perhaps two types of ions will be produced, and these usually are in their ground state. To produce positive ions, greater ionizing energies are required, and a multitude of positive fragments is produced. The latter may have to be separated out, and the excited states of some ions may introduce complications.

In CCl_3F, for example, Cl^- and F^- are produced by a resonant process at 2.5 and 5.0 e.v., respectively.[6] O^- is produced efficiently from N_2O at 2.2 e.v.[7]

Acknowledgment. The writers are indebted to Professor Herbert Berry of the physics department of Syracuse University for his helpful comments and suggestions.

(4) J. B. Hasted, *Proc. Roy. Soc.* (London), **A212**, 235 (1952).

(5) L. Kerwin and W. McGowan, *Can. J. Phys.*, **41**, 316 (1963).

(6) Unpublished work from this laboratory; manuscript in preparation.

(7) R. K. Curran and R. E. Fox, *J. Chem. Phys.*, **34**, 1590 (1961).

Paramagnetic Resonance Study of Fermi Level Motion and Defect Formation in High-Resistivity Cadmium Sulfide Crystals

by G. A. Somorjai and R. S. Title

IBM Watson Research Center, Yorktown Heights, New York *(Received August 27, 1964)*

In this Note we wish to report how paramagnetic resonance measurements may be used to monitor Fermi level motion and the kinetics of defect formation in high-resistivity crystals and illustrate the technique with measurements on high-resistivity, sulfur-doped CdS crystals.

Electrical measurements in crystals with resistivities greater than about 10^8 ohm-cm. are difficult to make because of the low current levels involved. Changes in the resistivity, however, imply a change in the position of the Fermi level that can drastically affect other physical and chemical properties such as photoconductivity[1] or evaporation.[2]

A high resistivity implies that the Fermi level is close to the center of the band gap. A defect whose energy is near the center of the band gap will gain or lose electrons as the Fermi level passes through the level. If any of the charged states of the defect are paramagnetic, e.p.r. techniques can be used to monitor the motion of the Fermi level in the vicinity of the defect. We have found iron to be a suitable defect to monitor the motion of the Fermi level in sulfur-doped, high-resistivity CdS. Iron is present in the crystals (supplied by Eagle-Picher Co., Miami, Okla.) we studied in concentrations of $\simeq 5 \times 10^{16}$/cm.^{3}. In untreated crystals no paramagnetic resonance spectrum was observed at 77°K. In crystals fired in a sulfur

(1) R. H. Bube, "Photoconductivity of Solids," John Wiley and Sons, Inc., New York, N. Y., 1960.

(2) G. A. Somorjai, Proceedings of the International Conference on the Physics and Chemistry of Solid Surfaces, Providence, R. I., 1964.

atmosphere a resonance characteristic of Fe^{3+} was measured.[3] Samples fired in Cd vapor showed no Fe^{3+} spectrum. The heat treatment in sulfur vapor causes iron, which is present in CdS as Fe^{2+}, to convert to Fe^{3+}. The intensity of the Fe^{3+} paramagnetic resonance spectrum is found to be dependent on the sulfur pressure and on the temperature at which the sample is doped. The heat treatment in sulfur vapor results in a motion of the Fermi level through the Fe^{2+} level converting it to Fe^{3+}. The resonance detection of Fe^{3+} is therefore a convenient method of monitoring the Fermi level motion in high-resistivity, sulfur-doped CdS crystals. Besides the merit of being able to monitor Fermi level motion when other techniques are difficult to employ, this method is nondestructive and requires no electrodes on the sample. The technique, by careful choice of paramagnetic impurity, should be of general use in studying the kinetics of defect formation in high-resistivity solids.

Experimental

The ultra-high-purity grade crystals were cut (3 × 3 × 6 mm.) so that the *c*-face (0001) was perpendicular to the direction of the long axis. These samples were fired at 700–1100° in 5–30 atm. of sulfur for 48–72 hr.[4] to assure uniform dopant distribution throughout the crystal and were quenched to room temperature in order to freeze in the defect concentrations characteristic of the firing temperature. The doped crystals were orange in color[5] in contrast to the yellow color of the untreated specimens. The band gap at room temperature is 2.42 e.v. The resistivities of the treated samples were, as mentioned previously, high, ranging to beyond 10^{10} ohm-cm.

The paramagnetic resonance measurements were carried out at 77 and 300°K. The only spectrum observed in any of the crystals was due to Fe^{3+}, and this appeared only in crystals heat-treated in sulfur. The resonance spectrum of Fe^{3+} in CdS has been observed by Lambe, *et al.*[3] They found that the resonance was observable at 4.2°K. and only with light of wave length 550 mμ irradiating the crystal. They could observe no resonance at 77 or 300°K. We find similar results in untreated crystals. However, in crystals treated in a sulfur atmosphere the resonance due to Fe^{3+} is observable at 77 and 300°K. The resonance is not photosensitive at these temperatures. The parameters characterizing the resonance are as reported by Lambe, *et al.*[3] The intensity of the resonance absorption due to Fe^{3+} was found to depend on both the temperature and the pressure of the sulfur atmosphere in which the crystals were treated.

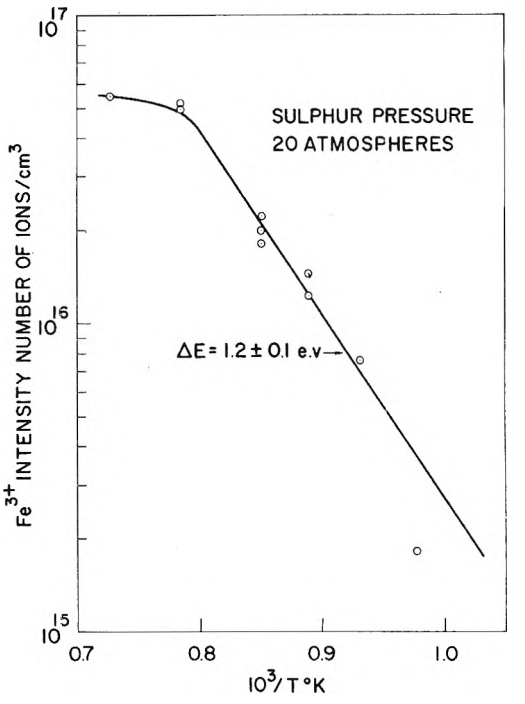

Figure 1. Fe^{3+} resonance intensity of sulfur-doped CdS single crystals as a function of the temperature of heat treatment at a constant sulfur pressure (20 atm.).

Results and Discussion

The dependence of the intensity of the Fe^{3+} resonance absorption on the temperature of the heat treatment for a constant sulfur pressure of 20 atm. is shown in Fig. 1. The intensity of the Fe^{3+} resonance signal is expressed in terms of the number of Fe^{3+} centers/cm.[3] that give rise to the signal. The logarithm of the intensity is plotted against the reciprocal of the temperature. At the highest temperatures there is an indication that the intensity of the Fe^{3+} absorption approaches a constant value. The other points fall more or less on a straight line. The slope of the straight-line portion may be used to determine an activation energy, $\Delta E = 1.2 \pm 0.1$ e.v. This activation energy is the net energy required for the over-all reaction that occurs during firing. It involves the sums of many energies such as the energy to remove an electron from Fe^{2+} in the CdS lattice, the energy involved in incorporating sulfur atoms into the lattice (energy gain), the energy required to create a Cd vacancy, as well as other energies. None of these

(3) J. Lambe, J. Baker, and C. Kikuchi, *Phys. Rev. Letters*, **3**, 270 (1959).

(4) G. A. Somorjai and D. W. Jepsen, *J. Chem. Phys.*, in press.

(5) F. A. Krëger, H. J. Vink, and J. vonden Boomgaard, *Z. physik. Chem.*, **203**, 1 (1954).

energies has been measured in CdS. Mandel[6] has estimated the energy required for vacancy formation in CdS to be 4.0 e.v. However, the accuracy is probably no better than ±0.5 e.v. Even if all the energies were known, a knowledge of the relative concentrations of the various defects involved would be required in order to separate the net activation energy into its various components. One can, however, state that, since the valence state of iron does change, the energy level of Fe^{2+} must be near the Fermi level which, in these high-resistivity samples, is close to the center of the band gap.

The intensity of the Fe^{3+} absorption at the highest temperatures, $\sim 5 \times 10^{16}$/cm.^{3}, corresponds to all iron in the lattice being present as Fe^{3+}. Spectroscopic analyses of the samples, both in our laboratory and by the Eagle–Picher Co., indicate an iron concentration of about 1 p.p.m. which corresponds to 5×10^{16}/cm.^{3}.

The dependence of the Fe^{3+} intensity on the sulfur pressure at a firing temperature of 900° is given in Fig. 2. The number of Fe^{3+} centers shows a maximum at 10 atm. and drops off to almost zero at 30 atm. The maximum value of 3×10^{16}/cm.^{3} is less than the total iron concentration in the lattice. This is known both from the results given in Fig. 1 and from the result given in Fig. 2 on a sample heat-treated in 10 atm. of sulfur, but at a higher temperature, 1100°. The maximum in the number of Fe^{3+} centers in the 900° curve of Fig. 2 cannot, therefore, be correlated with the exhaustion of the number of Fe^{2+} centers available for ionization. It is indicative of the formation of a new defect.

The qualitative model we use to understand the results of Fig. 1 and Fig. 2 is given in Fig. 3. In Fig. 3 the band gap of CdS is drawn, and the approximate positions of the various defects are indicated. In untreated crystals the concentration of sulfur vacancies V_S is assumed to be in excess of the concentration of cadmium vacancies V_{Cd}. In CdS a sulfur vacancy acts as a double donor and a cadmium vacancy as a double acceptor. At room temperature, the energy levels of V_S and V_{Cd} are such that almost all of these centers are ionized. The excess of V_S centers over V_{Cd} centers will therefore give rise to high conductivity n-type samples as observed.[5] The Fermi level in this material is near or in the conduction band. Heat treatment of the sample in cadmium vapor can only increase the ratio of V_S to V_{Cd} and make the material more n-type.[7] On the other hand, heat treatment of the samples in sulfur vapor will decrease the ratio of V_S to V_{Cd} and make the material less n-type, as is observed. In the high-resistivity samples, the Fermi

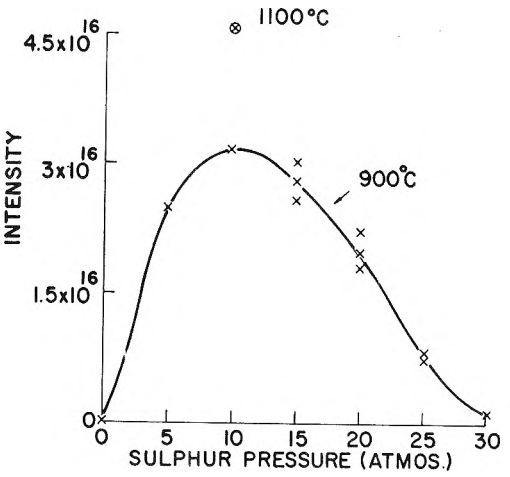

Figure 2. Fe^{3+} resonance intensity in sulfur-doped CdS single crystals as a function of sulfur pressure at a constant temperature (900°) of heat treatment.

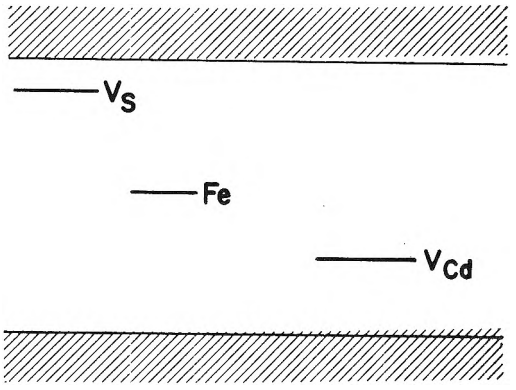

Figure 3. A model for the qualitative interpretation of the paramagnetic resonance experiments in sulfur-doped CdS single crystals.

level approaches the middle of the gap. Iron is assumed to be present as Fe^{2+} in the untreated crystals with an energy level close to the center of the band gap. As the Fermi level approaches the middle of the gap in the sulfur-doped samples, Fe^{2+} is converted to Fe^{3+} which accounts for our resonance observations.

The decrease in the intensity of the Fe^{3+} resonance absorption at sulfur pressures above 10 atm. (Fig. 2), even before all Fe^{2+} has been converted to Fe^{3+}, indicates that a new defect is formed. The decrease in the Fe^{3+} intensity in this case is not accompanied by a decrease in the resistivity, indicating that the defect is not electrically active. It is likely the product of a

(6) G. Mandel, *Phys. Rev.*, **134**, A1073 (1964).

(7) F. A. Kröger and H. J. Vink, "Solid State Physics," Vol. 3, F. Seitz and D. Turnbull, Ed., Academic Press, New York, N. Y., 1956, p. 310.

chemical reaction between Fe^{3+} and sulfur in the CdS crystal lattice at high sulfur pressures. Further work is required to clarify the detailed mechanism of this interaction.

The use of paramagnetic resonance of a deep-lying impurity to study Fermi level motion in high-resistivity materials should have general applicability and can take over when other electrooptical measurements of transport properties become difficult. It can be used to monitor the kinetics of defect formation in these materials in a nondestructive relatively simple manner.

Acknowledgments. We wish to gratefully acknowledge the help of J. A. Kucza for heat treatments of the crystals and E. E. Tynan for aid in taking the data.

ADDITIONS AND CORRECTIONS

1963, Volume 67

Bernard J. Wood, James S. Mills, and Henry Wise: Energy Accommodation in Exothermic Heterogeneous Catalytic Reactions.

Pages 1463–1465. Two errors, perpetrated in the derivations of the expressions relating the number densities of oxygen molecules and hydrogen atoms to their respective e.p.r. line intensities, affect the numerical values of the reaction energy accommodation coefficient, β. These errors were revealed to us by the analysis of Westenberg and de Haas in a recent paper [*J. Chem. Phys.*, **40**, 3087 (1964)]. We are grateful to these authors for their courtesy in providing us with a preprint of their contribution.

The term g_{eff} in the denominator of eq. 1 is incorrect as it stands and should be replaced by g^2/g_{eff} where g, the Lande factor, is 2.0023. Then, in eq. 3, g_{eff}/g becomes g/g_{eff}.

Because of an erroneous evaluation of the appropriate matrix element for atomic hydrogen, the right-hand side of eq. 2 is too large by a factor of 2. Hence, a 2 should appear in the denominator in eq. 3.

The value of $g_{eff} = (h/B)(d\nu/dH)$ is 1.40 for the particular O_2 transition observed in this study. In the paper, the quotient h/B was inadvertently omitted from the definition of g_{eff}, which led to the use of an incorrect value of 1.96 for g_{eff}.

Inserting the correct value for g_{eff} into the correct form of eq. 3 changes the values of the numerical coefficients in eq. 4 and 5 to 1.96×10^{-2} and 6.33×10^{14}, respectively. Since N_H appears in the denominator of eq. 13, the values of β reported in the paper should be increased by a factor of 2.68/1.96 = 1.37. The corrected values are tabulated below.

Table I: Corrected Values of Reaction Energy Accommodation Coefficient, β, for Hydrogen Atom Recombination on Metals

Catalytic surface	Temp., °K.	β (average)
Nickel	423	0.82 ± 0.15
Tungsten	443	1.08 ± 0.11
	480	1.11 ± 0.07
	773	1.17 ± 0.18
Platinum	376	0.67 ± 0.10
	378	0.78 ± 0.10
	588	0.34 ± 0.04
	813	0.26 ± 0.03

Page 1463. In footnote 8, the page number and year should be 1196 (1959) instead of 1788 (1961).

Page 1464. In eq. 9, the term D_{12} in the denominator should be deleted.—Bernard J. Wood.

Richard A. Holroyd and George W. Klein: Mercury-Photosensitized Decomposition of Aliphatic Hydrocarbons—Radical Detection with Ethyl-Carbon-14 Radicals.

Page 2274. The numbers on the ordinates of Fig. 1 and 2 are incorrect and should start from the origin 0, 1, 2, . . . instead of 1, 2, 3, ...

Page 2275. In footnote 8, the coefficients of (R_i) in the summation in the denominator are $a_i k_{mi}/k_{mE}$.—Richard A. Holroyd.

A. Chakravorty and F. A. Cotton: Stability Constants and Structures of Some Metal Complexes with Imidazole Derivatives.

Page 2879. Line 9 should read: Each solution was initially 0.001 M in metal ion, 0.002 M in ligand, 0.005 M in $HClO_4$, and 0.2 M in KNO_3. Lines 26–29 should read: Further, the present titrations were done in complete absence of chloride ions, so that any possible formation of chloro complexes was completely avoided.—A. Chakravorty.

1964, Volume 68

Peter J. Dunlop: Frictional Coefficients for Binary and Ternary Isothermal Diffusion.

Page 27. The second line above eq. 9 should read: . . . but that only q are independently since . . . . Equation 9 should read

$$[(v_i)_S - (v_k)_S] = [(v_i)_S - (v_j)_S] + [(v_j)_S - (v_k)_S]$$

Peter J. Dunlop

H. David Ellerton, Gundega Reinfelds, Dennis E. Mulcahy, and Peter J. Dunlop: Activity, Density, and Relative Viscosity Data for Several Amino Acids, Lactamide, and Raffinose in Aqueous Solution at 25°.

Page 400. In Table II, heading, . . . *vs.* molarity at 25° should read . . . *vs.* molality at 25°. Column 2, next to last line: combining eq. 1 and 2 . . . should read combining eq. 3 and 4 . . . .

Page 401. Column 1, eq. 5 should read

$$\Phi_1 = \Phi_1^\circ + \sum_{i=1}^{2} D_i C^i$$

Peter J. Dunlop

Thomas B. Hoover: Conductance of Potassium Chloride in Highly Purified N-Methylpropionamide from 20 to 40°.

Page 877. In the paragraph headed "Dielectric Constant," the phrase in parentheses should read (the conductance cell constant corresponds to 8.24 pf.).

Page 878. In Table II, columns headed Λ are actually Λ_η', as defined by eq. 6. A corrected table of molar conductances will be supplied by the author upon request.—Thomas B. Hoover.

Maurizio Cignitti and Thomas L. Allen: Nonbonded Interactions and the Internal Rotation Barrier.

Page 1292. K. S. Pitzer has pointed out to us that the conclusion of Blade and Kimball (mentioned in the Introduction) concerning the uncertainty about the shape of the ethane internal rotation barrier was erroneous, as explained by him in the following year [*Discussions Faraday Soc.*, **10**, 66 (1951)]. None of the

discussions or conclusions in the paper is affected by this addition.—THOMAS L. ALLEN.

J. P. Chan and W. F. Giauque: The Entropy of $NH_3 \cdot 2H_2O$. Heat Capacity from 15 to 300°K.

Page 3053. Lines 5 and 6 of the abstract have incorrect signs for ΔF and ΔH of the reaction $2H_2O(l) + NH_3(sat.\ l) = NH_3, 2H_2O(sat.\ l)$. They should be $\Delta F_{25°} = -2123$ cal./mole and $\Delta H_{25°} = -2842$ cal./mole. The values were given and used correctly in the text of the paper.—W. F. GIAUQUE

AUTHOR INDEX *to Volume 68, 1964*

SUBJECT INDEX *to Volume 68, 1964*